JOURNAL OF THE ELECTROCHEMICAL SOCIETY

ELECTROCHEMICAL SCIENCE AND TECHNOLOGY

SOLID-STATE SCIENCE AND TECHNOLOGY

REVIEWS AND NEWS
Call for Papers
Toronto, Ontario, Canada, Meeting



VOL. 131, NO. 11 NOVEMBER 1984

JESOAN 131 (11) 2467-2736, 463C-496C

FUTURE MEETINGS

TORONTO, ONTARIO, CANADA—MAY 12-17, 1985—HEADQUARTERS AT THE ROYAL YORK HOTEL

See the detailed Call for Papers published in the July-November 1984 issues of **This Journal.** Final program published in the March 1985 issue of **This Journal.**

LAS VEGAS, NEVADA—OCTOBER 13-18, 1985—HEADQUARTERS AT CAESAR'S PALACE

The detailed Call for Papers will be published in the December 1984-April 1985 issues of **This Journal.** Final program to be published in the August 1985 issue of **This Journal.**

Planned symposia for the Las Vegas Meeting include the following Divisions, Groups, Subcommittee, and subjects. **Battery**—Metal-Air Batteries; Battery Charging, Monitoring, and Control; Primary and Secondary Lithium Batteries; General Session: **Battery/Corrosion**—Corrosion in Battery and Fuel Cells: **Battery/Physical Electrochemistry**—Fundamentals of Porous Electrodes; Zinc Electrode Mechanisms and Kinetics: **Corrosion**—Acid Rain—Causes and Corrosion Effects; General Session: **Corrosion/Electronics**—Corrosion of Electronic Materials: **Dielectrics and Insulation/Electronics**—Dielectric Films on Compound Semiconductors; Adsorption Phenomena in Semiconductor Technology; Thin Film Interfaces and Interactions: **Electrodeposition**—Alloy Deposition; Use of Microcomputers and Automation in Electrochemical Investigations of Electroplating, Electroless Deposition, and Plant Operation and Control; Uses of Electrodeposition, Electroless Deposition, Electrophoretic Deposition, Anodization, Electromachining, and Polishing in Various Industries; General Session: **Electrodeposition/Industrial Electrolytic**—Effects of Additives and Impurities in Deposition Processes: **Electronics**—State-of-the-Art Program on Compound Semiconductors: **Electronics/Dielectrics and Insulation**—Reduced Temperature Processing for VLSI; Silicon-on-Insulator; Detection/Control of Effluents and Other Safety Considerations of VLSI Processing; Joint General Session; Joint Recent News Papers Session: **Electronics/Luminescence and Display Materials**—Fiber Optics Sensors: **Energy Technology**—Thermal Management of Electrochemical and Photovoltaic Devices; General Session: **Energy Technology/High Temperature Materials/Corrosion**—Heat Storage and Exchange Systems: **Energy Technology/Organic and Biological Electrochemistry**—Novel Approaches to Energy Conversion and Storage; Effects of Adsorbates on Photoelectrochemical Behavior: **High Temperature Materials**—High Temperature Materials Chemistry III; General Session: **High Temperature Materials/Dielectrics and Insulation**—Plasma Synthesis of High Temperature Materials: **High Temperature Materials/Physical Electrochemistry**—Electronic and Ionic Grain Boundary Transport: **Luminescence and Display Materials**—Organic Luminescence; General Session; Recent News Papers Session: **Luminescence and Display Materials/Electronics**—Materials for Optical Imaging; Active Matrix Addressing and Materials for Flat Panel Displays: **Physical Electrochemistry**—Fifth International Symposium on Molten Salts: **Physical Electrochemistry/Electrodeposition/Corrosion/Battery**—Electrosolidification and Crystallization: **Physical Electrochemistry/Electronics**—Electrochemistry in Semiconductor Technology: **Physical Electrochemistry/New Technology**—Application of Information Theory to Electrochemical Experimentation: **New Technology/Corrosion**—Mechanical and Corrosion Considerations of Single Crystals: **New Technology/Organic and Biological Electrochemistry**—Electrochemical Control of Biological Processes.

BOSTON, MASSACHUSETTS—MAY 4-9, 1986—HEADQUARTERS AT SHERATON BOSTON HOTEL

The detailed Call for Papers will be published in the July-November 1985 issues of **This Journal.** Final program to be published in the March 1986 issue of **This Journal.**

Planned symposia for the Boston Meeting include the following Divisions, Groups, Subcommittee, and subjects. **Battery/Physical Electrochemistry**—Electrochemical and Thermal Modeling of Batteries and Fuel Cells: **Corrosion**—General Session: **Dielectrics and Insulation/Electronics**—Patterning Science and Technology 1986; Electrolytic Capacitors and Anodic Oxidation; Medical Devices: **Dielectrics and Insulation/Electronics/High Temperature Materials**—Silicon Nitride: **Electronics**—Ion Implantation in Compound Semiconductors; State-of-the-Art Program in Compound Semiconductors: **Electronics/Dielectrics and Insulation**—Tutorial on Medical Electronics; Fifth International Symposium on Silicon Materials Science and Technology; Joint General Session; Joint Recent News Papers Session: **Electronics/Physical Electrochemistry/Energy Technology/New Technology**—Organic Semiconductors at the Molecular Level: **Energy Technology**—Strong Metal-Support Interactions in Catalysis; General Session: **Energy Technology/Dielectrics and Insulation/Electronics**—Materials and New Processing Techniques for Photovoltaics VI: **Energy Technology/Electrodeposition/Electronics**— Electrodeposition of Semiconductor Thin Films: **High Temperature Materials/Corrosion**—Surface Modification of High Temperature Materials; Fundamental Aspects of High Temperature Corrosion II: **High Temperature Materials/Corrosion/Dielectrics and Insulation**—Protective Coatings: **High Temperature Materials/Dielectrics and Insulation**—Preparation of Thin Films: **High Temperature Materials/Physical Electrochemistry/Industrial Electrolytic**—Ionic and Electronic Conductivity Mechanisms in Glasses; Diaphragms, Separators, and Fluorocarbon and Ion Exchange Membranes; Load Leveling and Energy Conservation in Industrial Electrolysis; Aqueous and Nonaqueous Industrial Electrolysis: **Physical Electrochemistry**—Ion Transfer at Liquid-Liquid Interfaces; Electrode Processes IV; General Session: **Physical Electrochemistry/High Temperature Materials/Energy Technology**—Electrochemical Sensors: **Physical Electrochemistry/New Technology**—Magnetic Effects in Electrochemistry: **New Technology/Corrosion**—Electrochemistry of Reactive Metals with Surface Oxide Films at Room Temperature.

THE ELECTROCHEMICAL SOCIETY BOOKS IN PRINT

Society Proceedings Series

The following softbound proceedings volumes are sponsored and published by The Electrochemical Society, Inc., 10 South Main Street, Pennington, NJ 08534-2896. Orders filled at the list price given, subject to availability. Enclose payment with order.

Electron and Ion Beam Science and Technology, Fifth International Conference. R. Bakish, Editor. A 1972 symposium. 420 pages, **$5.50.**

Electrochemical Bioscience and Bioengineering. H. T. Silverman, I. F. Miller, and A. J. Salkind, Editors. A 1973 symposium. 268 pages, **$8.00.**

Chlorine Bicentennial Symposium. T. C. Jeffery, P. A. Danna, and H. S. Holden, Editors. A 1974 symposium. 404 pages, **$11.00.**

Metal-Slag-Gas Reactions and Processes. Z. A. Foroulis and W. W. Smeltzer, Editors. A 1975 symposium. 1032 pages, **$20.00.**

Chemistry and Physics of Aqueous Gas Solutions. W. A. Adams, G. Greer, J. E. Desnoyers, G. Atkinson, G. S. Kell, K. B. Oldham, and J. Walkley, Editors. A 1975 symposium. 522 pages, **$11.00.**

Thermal and Photostimulated Currents in Insulators. D. M. Smyth, Editor. A 1975 symposium. 215 pages, **$7.00.**

International Symposium on Molten Salts. J. P. Pemsler, J. Braunstein, K. Nobe, D. R. Morris, and N. E. Richards, Editors. A 1976 symposium. 632 pages, **$16.00.**

Properties of High Temperature Alloys. Z. A. Foroulis and F. S. Pettit, Editors. A 1976 symposium. 851 pages, **$12.00.**

Semiconductor Silicon 1977. H. R. Huff and E. Sirtl, Editors. A 1977 symposium. 1100 pages, **$15.00.**

A History of The Electrochemical Society. The first 75 years. R. M. Burns with E. G. Enck, 160 pages. **$5.00.**

Semiconductor-Liquid Junction Solar Cells. A. Heller, Editor. A 1977 symposium. 340 pages, **$10.00.**

Load-Leveling. N. P. Yao and J. R. Selman, Editors. A 1977 symposium. 412 pages, **$13.00.**

High Temperature Metal Halide Chemistry. D. L. Hildenbrand and D. D. Cubicciotti, Editors. A 1977 symposium. 678 pages, **$17.00.**

Selected Topics in the History of Electrochemistry. George Dubpernell and J. H. Westbrook, Editors. A 1977 symposium. 523 pages, **$11.00.**

Laser and Electron Beam Processing of Electronic Materials. C. L. Anderson, G. K. Celler, and G. A. Rozgonyi, Editors. A 1979 symposium. 560 pages, **$13.00.**

Thin Film Interfaces and Interactions. J. E. E. Baglin and J. M. Poate, Editors. A 1979 symposium. 536 pages, **$16.00.**

Electrode Processes, S. Bruckenstein, J. D. E. McIntyre, B. Miller, and E. Yeager, Editors. A 1979 symposium. 500 pages, **$21.00.**

Power Sources for Biomedical Implantable Applications and Ambient Temperature Lithium Batteries. B. B. Owens and N. Margalit, Editors. A 1979 symposium. 652 pages, **$18.00.**

Electronic and Optical Properties of Polycrystalline or Impure Semiconductors and Novel Silicon Growth Methods. K. V. Ravi and B. O'Mara, Editors. A 1980 symposium. 280 pages, **$15.00.**

Electron and Ion Beam Science and Technology, Ninth International Conference, R. Bakish, Editor. A 1980 symposium. 672 pages, **$28.00.**

Lithium Nonaqueous Battery Electrochemistry. E. B. Yeager, B. Schumm, Jr., G. Blomgren, D. R. Blankenship, V. Leger, and J. Akridge, Editors. A 1980 workshop. 328 pages, **$18.00.**

Ion Exchange: Transport and Interfacial Properties. R. S. Yeo and R. P. Buck, Editors. A 1980 symposium. 396 pages, **$15.00.**

Materials and New Processing Technologies for Photovoltaics. J. A. Amick, E. Sirtl, P. Rai-Choudhury, and J. P. Dismukes, Editors. A 1980 symposium. 368 pages, **$14.00.**

Lithium Batteries, H. V. Venkatasetty, Editor. A 1980 symposium, 516 pages, **$26.00.**

Semiconductor Silicon 1981. H. R. Huff, R. J. Kriegler, and Y. Takeishi, Editors. A 1981 symposium. 1064 pages, **$25.00.**

Electrocrystallization. R. Weil and R. G. Barradas, Editors. A 1981 symposium. 352 pages, **$13.00.**

Chemical Vapor Deposition, Eighth International Conference. J. M. Blocher, Jr., G. E. Vuillard, and G. Wahl, Editors. A 1981 symposium. 836 pages, **$30.00.**

Corrosion and Corrosion Protection. R. P. Frankenthal and F. Mansfeld, Editors. A 1981 symposium. 304 pages, **$10.00.**

Third International Symposium on Molten Salts. G. Mamantov, M. Blander, and G. P. Smith, Editors. A 1981 symposium. 600 pages, **$23.00.**

Second International Symposium on Molten Salts. J. Braunstein and J. R. Selman, Editors. A 1978 symposium. 420 pages, **$16.00.**

High Temperature Materials Chemistry. D. D. Cubicciotti and D. I. Hildenbrand, Editors. A 1981 symposium. 498 pages, **$21.00.**

Electrocatalysis. W. E. O'Grady, P. N. Ross, Jr., and F. G. Will, Editors. A 1981 symposium. 428 pages, **$18.00.**

Photoelectrochemistry: Fundamental Processes and Measurement Techniques. W. L. Wallace, A. J. Nozik, S. K. Deb, and R. H. Wilson, Editors. A 1981 symposium. 736 pages, **$35.00.**

The Nickel Electrode. R. G. Gunther and S. Gross, Editors. A 1981 symposium. 324 pages, **$15.00.**

Semiconductor Technology. D. A. Doane, D. B. Fraser, and D. W. Hess, Editors. A 1982 symposium. 264 pages, **$18.00.**

Plasma Processing. J. Dieleman, R. G. Frieser, and G. S. Mathad, Editors. A 1981 symposium. 528 pages, **$25.00.**

VLSI Science and Technology. C. J. Dell'Oca and W. M. Bullis, Editors. A 1982 symposium. 392 pages, **$20.00.**

Materials and New Processing Technologies for Photovoltaics. J. P. Dismukes, E. Sirtl, P. Choudhury, and L. P. Hunt, Editors. A 1982 symposium. 544 pages, **$25.00.**

Inorganic Resist Systems. D. A. Doane and A. Heller, Editors. A 1982 symposium. 320 pages, **$15.00.**

Transport Processes in Electrochemical Systems. R. S. Yeo, T. Katan, and D-T. Chin, Editors. A 1982 symposium. 288 pages, **$18.00.**

Corrosion in Batteries and Fuel Cells and Corrosion in Solar Energy Systems. C. J. Johnson and S. L. Pohlman, Editors. A 1981 symposium. 554 pages, **$22.00.**

Electron and Ion Beam Science and Technology, Tenth International Conference, R. Bakish, Editor. A 1982 symposium. 474 pages, **$30.00.**

Membranes and Ionic and Electronic Conducting Polymers. E. B. Yeager, B. Schumm, Jr., K. Mauritz, K. Abbey, D. Blankenship, and J. Akridge, Editors. A 1982 symposium. 380 pages, **$22.00.**

Aggregation Phenomena of Point Defects in Silicon. E. Sirtl and J. Goorissen, Editors. A 1982 symposium. 216 pages, **$15.00.**

Corrosion in Fossil Fuel Systems. I. G. Wright, Editor. A 1982 symposium. 522 pages, **$20.00.**

Electrochemical Process and Plant Design. R. C. Alkire, T. R. Beck, and R. D. Varjian, Editors. A 1982 symposium. 288 pages, **$20.00.**

High Temperature Materials Chemistry II. Z. A. Munir and D. Cubicciotti, Editors. A 1983 symposium. 480 pages, **$30.00.**

Silicon Nitride Thin Insulating Films. V. J. Kapoor and H. J. Stein, Editors. A 1983 symposium. 522 pages, **$25.00.**

Defects in Silicon. W. M. Bullis and L. C. Kimerling, Editors. A 1983 symposium. 660 pages, **$30.00.**

Plasma Processing. G. S. Mathad, G. C. Schwartz, and G. Smolinsky, Editors. A 1983 symposium. 660 pages, **$35.00.**

Materials and New Processing Technologies for Photovoltaics. J. A. Amick, V. K. Kapur, and J. Dietl, Editors. A 1983 symposium. 512 pages, **$25.00.**

Electroplating Engineering and Waste Recycle—New Developments and Trends. D. D. Snyder, U. Landau, and R. Sard, Editors. A 1982 symposium. 428 pages, **$22.00.**

III-V Opto-Electronics Epitaxy and Device Related Processes. V. G. Keramidas and S. Mahajan, Editors. A 1983 symposium. 289 pages, **$25.00.**

Lithium Batteries. A. N. Dey, Editor. A 1983 symposium. 460 pages, **$35.00.**

Fourth International Symposium on Molten Salts. M. Blander, D. S. Newman, M-L. Saboungi, G. Mamantov, and K. Johnson, Editors. A 1983 symposium. 776 pages, **$35.00.**

Fundamental Aspects of Corrosion Protection by Surface Modification. E. McCafferty, C. R. Clayton, and J. Oudar, Editors. A 1983 symposium. 364 pages, **$25.00.**

Advances in Battery Materials and Processes. J. McBreen, R. S. Yeo, D-T. Chin, and A. C. C. Tseung, Editors. A 1983 symposium. 320 pages, **$26.00.**

The Electrochemistry of Carbon. S. Sarangapani, J. R. Akridge, and B. Schumm, Editors. A 1983 symposium. 648 pages, **$32.00.**

Ninth International Conference on Chemical Vapor Deposition. McD. Robinson, C. H. J. van den Brekel, C. W. Cullen, J. M. Blocher, Jr., and P. Rai-Choudhury, Editors. A 1984 symposium. 824 pages, **$36.00.**

VLSI Science and Technology/1984. K. E. Bean and G. A. Rozgonyi, Editors. A 1984 symposium. 520 pages, **$30.00.**

Porous Electrodes: Theory and Practice. H. C. Maru, T. Katan, and M. G. Klein, Editors. A 1982 symposium. 492 pages, **$18.00.**

Equilibrium Diagrams; Localized Corrosion. R. F. Frankenthal and J. Kruger, Editors. A 1984 symposium. 611 pages, **$36.00.**

Electrochemistry in Mineral and Metal Processing. P. E. Richardson, S. Srinivasan, and R. Woods, Editors. A 1984 Symposium. 677 pages, **$30.00.**

9/84

ห้องสมุดกรมวิทยาศาสตร์บริการ
28 มิ.ย. 2528

EDITOR
Norman Hackerman
Jackie Bourne, **Assistant to the Editor**

DIVISIONAL AND GROUP EDITORS

BATTERY
R. J. Brodd — G. F. Nordblom
Elton J. Cairns — Darrel Untereker
Eugene G. Gagnon

CORROSION
J. W. Faust, Jr. — Florian Mansfeld
R. P. Frankenthal — Ken Nobe
D. D. Macdonald — W. H. Smyrl
Barry R. MacDougall

DIELECTRICS AND INSULATION
Robert S. Alwitt — S. P. Murarka
Rudolf G. Frieser — George L. Schnable
Dennis Hess — Alan W. Swanson
Vikram J. Kapoor

ELECTRODEPOSITION
Ugo Bertocci — Y. Okinaka
Huk Y. Cheh — Mordechay Schlesinger

ELECTRONICS
Harry G. Brittain — David L. Nelson
D. M. Brown — Bertram Schwartz
Ted F. Ciszek — Thomas O. Sedgwick
George R. Cronin — Don W. Shaw
John A. DeLuca — Melvin Tecotzky
James S. Harris — C. C. Wang
Simon Larach — P. Wang
Subhash Mahajan — J. M. Woodall

ENERGY TECHNOLOGY GROUP
A. R. Landgrebe — M. Tomkiewicz
S. Srinivasan

HIGH TEMPERATURE MATERIALS
William A. Adams — Zuhair A. Munir
E. D. Cater — David A. Shores
Daniel Cubicciotti — Donald R. Vissers
Lee P. Hunt — Gene F. Wakefield
V. K. Kapur — Jack H. Westbrook
Peter J. Meschter

INDUSTRIAL ELECTROLYTIC
Richard C. Alkire — Scott Lynn
Ronald L. Dotson

ORGANIC AND BIOLOGICAL ELECTROCHEMISTRY
Martin Blank — John H. Wagenknecht
Glenn Dryhurst — Stanley Wawzonek
M. Dale Hawley

PHYSICAL ELECTROCHEMISTRY
Gregory C. Farrington — Barry Miller
David S. Ginley — William E. O'Grady
Adam Heller — Robert A. Osteryoung
Joseph T. Maloy — C. W. Tobias
Gleb Mamantov — F. G. Will
Richard L. McCreery — Ronald H. Wilson

News Editor—Jack H. Westbrook

JOURNAL OF THE
ELECTROCHEMICAL SOCIETY
(USPS 284-140)
ISSN 0013-4651

The JOURNAL OF THE ELECTROCHEMICAL SOCIETY (USPS 284-140) is published monthly by The Electrochemical Society, Inc. at 215 Canal St., Manchester, N.H. 03108. The address for the Executive Offices, Editorial and Advertising Office, and Circulation Department of The Electrochemical Society, Inc., is 10 South Main St., Pennington, N.J. 08534-2896. Subscription to members as part of membership service; subscription to nonmembers $135.00 plus $15.00 for postage outside U.S. and Canada. Single copies $7.00 to members, $12.00 to nonmembers.
© Copyright 1984 by The Electrochemical Society, Inc. Second Class Postage paid at Pennington, New Jersey and at additional mailing offices.
POSTMASTER: Send address changes to THE ELECTROCHEMICAL SOCIETY, INC., 10 South Main St., Pennington, N.J. 08534-2896.

November 1984

ELECTROCHEMICAL SCIENCE AND TECHNOLOGY

TECHNICAL PAPERS

The Mechanisms of Thionyl Chloride Reduction at Solid Electrodes
W. K. Isotone, R. J. Brodd 2467

Investigation of $SOCl_2$ Reduction by Cyclic Voltammetry and AC Impedance Measurements
M. J. Madou, S. Szpak 2471

Pore Development during Selective Leaching
A. D. Tomsett, D. J. Young, M. S. Wainwright 2476

Surface Dislocation Pinning by Adsorbed Ions and Water Molecules
C. J. van der Wekken 2481

AES/XPS Study of Transpassive Films on Iron in Nitrate Solution
M. Datta, H. J. Mathieu, D. Landolt 2484

Development of Silver-Palladium Alloy Plating for Electrical Contact Applications
U. Cohen, K. R. Walton, R. Sard 2489

A Quantitative Investigation of the Open-Circuit Photovoltage at the Semiconductor/Liquid Interface
N. S. Lewis 2496

Electrode Heat Balances of Electrochemical Cells
Y. Ito, H. Kaiya, S. Yoshizawa, S. K. Ratkja, T. Førland 2504

The Mechanism of Electrodeposition of Cadmium Sulfide on Inert Electrodes from Diethylene Glycol Solutions
A. S. Baranski, W. R. Fawcett 2509

Thin Film CdSe Electrodeposited from Selenosulphite Solution
M. Cocivera, A. Darkowski, B. Love 2514

Reduction of CO_2 on n-GaAs Electrodes and Selective Methanol Synthesis
K. W. Frese, Jr., D. Canfield 2518

Anode-Limited Cell Reversal in Lithium-Sulfur Oxyhalide Cells
A. I. Attia, C. Sarrazin, K. A. Gabriel, R. P. Burns 2523

Electrochemical Behavior of Water in Immobilized Salt Electrolytes. I. Electrical Conductivity and Thermal Measurements
R. Parash, F. Broitman, U. Mor, D. Ozer, A. Bettelheim 2531

Corrosion of the Wet-Seal Area in Molten Carbonate Fuel Cells. I. Analysis
R. A. Donado, L. G. Marianowski, H. C. Maru, J. R. Selman 2535

Corrosion of the Wet-Seal Area in Molten Carbonate Fuel Cells. II. Experimental Results
R. A. Donado, L. G. Marianowski, H. C. Maru, J. R. Selman 2541

Styrene Production from Ethylbenzene on Platinum in a Zirconia Electrochemical Reactor
J. N. Michaels, C. G. Vayenas 2544

A Theoretical Comparison of Flow-Through and Flow-By Porous Electrodes at the Limiting Current
T. Risch, J. Newman 2551

Electrochemical Studies of Antitumor Antibiotics. V. An Electrochemical Method of Measurement of the Binding of Doxorubicin and Daunorubicin
J. A. Plambeck, J. W. Lown 2556

Quantitative Comparison of Fermi Level Pinning at GaAs/Metal and GaAs/Liquid Junctions
G. Horowitz, P. Allongue, H. Cachet 2563

ELECTROCHEMICAL SOCIETY

Vol. 131 • No. 11

Mathematical Modeling of Liquid-Junction Photovoltaic Cells. I. Governing Equations
M. E. Orazem, J. Newman 2569

Mathematical Modeling of Liquid-Junction Photovoltaic Cells. II. Effect of System Parameters on Current-Potential Curves
M. E. Orazem, J. Newman 2574

Mathematical Modeling of Liquid-Junction Photovoltaic Cells. III. Optimization of Cell Configurations
M. E. Orazem, J. Newman 2582

Electrochemical Studies of Chromium in Molten LiF-NaF-KF (FLINAK)
T. Yoko, R. A. Bailey 2590

Cathodic Polarization of Aluminum in Alkylbenzene Electrolytes
G. A. Capuano, W. G. Davenport 2595

Electrochemical Properties of $WO_3 \cdot x(H_2O)$. III. Complex Plane Analysis of the Film on SnO_2.
N. Yoshiike, M. Ayusawa, S. Kondo 2600

TECHNICAL NOTES

The Decomposition of Propylene Carbonate in a Lithium/Metal Phthalocyanine Cell
M. Arakawa, J. Yamaki, T. Okada 2605

Electronic Conductivity Decrease in Porous NiO Cathodes during Operation in Molten Carbonate Fuel Cells
C. E. Baumgartner 2607

Improved H_3PO_4 Corrosion Resistance of Graphite/Phenolic Composites Suitable for 190°C Hydrogen/Air Fuel Cells
J. T. Hoggins, M. L. Deviney 2610

SOLID-STATE SCIENCE AND TECHNOLOGY

TECHNICAL PAPERS

Adsorption of Hydroxide and Sulfide Ions on Single-Crystal n-CdSe Electrodes
K. W. Frese, Jr., D. G. Canfield 2614

Effects of Additives on $ZnO-B_2O_3-SiO_2$ Passivation Glasses
Y. Misawa 2618

Electrical Characteristics of the RF Magnetron-Sputtered Tantalum Pentoxide-Silicon Interface
S. Seki, T. Unagami, B. Tsujiyama 2621

Wetting Angles and Surface Tension in the Crystallization of Thin Liquid Films
E. Yablonovitch, T. Gmitter 2625

Effect of Group V/III Flux Ration on Lightly Si-Doped Al_xGa_{1-x} As Grown by Molecular Beam Epitaxy
Y. Nomura, M. Mannoh, M. Mihara, S. Naritsuka, K. Yamanaka, T. Yuasa, M. Ishii 2630

Behavior of the Evaporated WO_3 Film in Li-Salt PC Electrolytes
N. Yoshiike, Y. Mizuno, S. Kondo 2634

The Etching of InP in HCl Solutions. A Chemical Mechanism
P. H. L. Notten 2641

Diffusion of Ion-Implanted Arsenic in Thermally Grown SiO_2 Films
R. Singh, M. Maier, H. Kräutle, D. R. Young, P. Balk 2645

Characteristics of Ion Implantation Damage and Annealing Phenomena in Semiconductors
J. Narayan, O. W. Holland 2651

TEM Cross Section Sample Preparation Technique for III-V Compound Semiconductor Device Materials by Chemical Thinning
S. N. G. Chu, T. T. Sheng 2663

DIVISION AND GROUP OFFICERS

Battery Division

Theodore Katan, Chairman
Sidney Gross, Vice-Chairman
Eugene Gagnon, Secretary-Treasurer
General Motors Corp.
Research Laboratories, Dept. 37
12 Mile and Mounds Rds.
Warren, MI 48090-9055

Corrosion Division

Florian Mansfeld, Chairman
Robert A. Rapp, Vice-Chairman
Edward McCafferty, Secretary-Treasurer
Naval Research Laboratory
Code 6314
Washington, DC 20375

Dielectrics and Insulation Division

Laura Rothman, Chairman
Robert B. Comizzoli, Vice-Chairman
D. L. Flowers, Treasurer
J. P. Dismukes, Secretary
Exxon Research & Engineering Company
Clinton Township
Route 22 East
Annandale, NJ 08801

Electrodeposition Division

Thomas C. Franklin, Chairman
Mordechay Schlesinger, Vice-Chairman
David S. Lashmore, Secretary-Treasurer
National Bureau of Standards
Dept. of Commerce
Washington, DC 20234

Electronics Division

Edward H. Nicollian, Chairman
Patricia L. Castro, Vice-Chairman (Semiconductors)
Prosenjit Rai-Choudhury, Vice-Chairman (New Electronic Technologies)
Mort Jones, Treasurer
W. Murray Bullis, Secretary
Fairchild Camera and Instrument Corporation
Research and Development Laboratory
Palo Alto, CA 94304

Energy Technology Group

A. J. Appleby, Chairman
V. K. Kapur, Vice-Chairman
D. S. Ginley, Treasurer
H. C. Maru, Secretary
Energy Research Corporation
3 Great Pasture Rd.
Danbury, CT 06810

High Temperature Materials Division

Lee P. Hunt, Chairman
Wayne Worrell, Senior Vice-Chairman
Frederick S. Pettit, Junior Vice-Chairman
Vishu D. Dosaj, Secretary-Treasurer
Dow Corning Corp.
Semiconductor Div.
Hemlock, MI 48626

Industrial Electrolytic Division

Robert S. Karpiuk, Chairman
W. Bruce Darlington, Vice-Chairman
Marino V. C. Woo, Secretary-Treasurer
930 Brown Road
Bridgewater, NJ 08807

Luminescence and Display Materials Group

C. W. Struck, Chairman
R. O. Petersen, Vice-Chairman
W. M. Yim, Secretary-Treasurer
RCA Laboratories
David Sarnoff Research Center
Princeton, NJ 08540

Organic and Biological Electrochemistry Division

Martin Blank, Chairman
Petr Zuman, Vice-Chairman
Dennis H. Evans, Secretary-Treasurer
Dept. of Chemistry
University of Wisconsin-Madison
1101 University Ave.
Madison, WI 53706

Physical Electrochemistry Division

Robert A. Osteryoung, Chairman
Larry R. Faulkner, Vice-Chairman
Jose Giner, Secretary-Treasurer
14 Spring Street
Waltham, MA 02154

SOCIETY OFFICERS AND STAFF

Paul C. Milner, President
AT&T Bell Laboratories
Room 1D-259
Murray Hill, NJ 07974

Richard C. Alkire, Vice-President
Dept. of Chemical Engineering
University of Illinois
Urbana, IL 61801

Ronald E. Enstrom, Vice-President
RCA Laboratories
Princeton, NJ 08540

Fritz G. Will, Vice-President
General Electric Company
Research and Development Center
Schenectady, NY 12301

James A. Amick, Secretary
Exxon Research & Engineering Company
Clinton Township
Route 22 East
Annandale, NJ 08801

Jerome Kruger, Treasurer
National Bureau of Standards
B254 Materials Building
Washington, DC 20234

V. H. Branneky, Executive Secretary
The Electrochemical Society, Inc.
10 South Main Street
Pennington, NJ 08534-2896

Roque J. Calvo, Assistant Executive Secretary
The Electrochemical Society, Inc.
10 South Main Street
Pennington, NJ 08534-2896

PUBLICATION STAFF

Sarah A. Kilfoyle, **Director of Publications**
Hugh P. Molloy
Dwayne L. Baron

PUBLICATION COMMITTEE

Robert P. Frankenthal, **Chairman**
James A. Amick
Norman Hackerman
Bertram Schwartz
Isaac Trachtenberg
Gary McGuire
Lee P. Hunt
Rolf H. Muller

Manuscripts submitted to the JOURNAL should be sent in triplicate to the Editorial Office at 10 South Main Street, Pennington, N.J. 08534-2896. They should conform to the revised "Instructions to Authors" available from Society Headquarters. Manuscripts so submitted, as well as papers presented before a Society technical meeting, become the property of the Society and may not be published elsewhere in whole or in part without written permission of the Society. Address such requests to the Editor.

The Electrochemical Society does not maintain a supply of reprints of papers appearing in its JOURNAL. A photoprint copy of any particular paper may be obtained from University Microfilms, Inc., 300 N. Zeeb St., Ann Arbor, Mich. 48106.

Inquiries regarding positive microfilm copies of issues should be addressed to University Microfilms, Inc., 300 N. Zeeb St., Ann Arbor, Mich. 48106.

Walter J. Johnson, Inc., 355 Chestnut St., Norwood, N.J. 07648, have reprint rights to out-of-print volumes of the JOURNAL, and also have available for sale back volumes and single issues with the exception of the last eight calendar years.

The JOURNAL OF THE ELECTROCHEMICAL SOCIETY combines the JOURNAL and TRANSACTIONS OF THE ELECTROCHEMICAL SOCIETY. Statements and opinions given in articles and papers in the JOURNAL OF THE ELECTROCHEMICAL SOCIETY are those of the contributors, and The Electrochemical Society, Inc. assumes no responsibility for them.

Claims for a missing issue should be reported within 60 days of normal delivery date to the Circulation Dept., The Electrochemical Society, Inc., 10 South Main Street, Pennington, N.J. 08534-2896.

Notice of a change in address should be sent to the Circulation Dept., The Electrochemical Society, Inc., 10 South Main Street, Pennington, N.J. 08534-2896. Include the mailing label or the number from the mailing label from your previous issue of the JOURNAL to ensure proper identification.

SOLID-STATE SCIENCE (Cont.)

Mass Spectrometric Transient Study of DC Plasma Etching of Si in NF_3 and NF_3/O_2 Mixtures
.....*T. Honda, W. W. Brandt* 2667

Photosensitivity and Contrast Determination of Photoresist by Laser Interferometry
.....*T. R. Pampalone, M. R. Hannifan, S. Jain, C. D. Krieger* 2670

Nonlinear Two-Step Diffusion in Semiconductors
.....*D. Anderson, K. O. Jeppson* 2675

Carrier Lifetime Reduction in Silicon by Proton Implantation Through MOS Structures
.....*A. Mogro-Campero, R. P. Love* 2679

The System AgI-AgBr: Energetic Consequences of Defect Equilibria in Single-Phase and Two-Phase Regions
.....*A. Khandkar, V. B. Tare, A. Navrotsky, J. B. Wagner, Jr.* 2683

Phase Relations and Thermochemistry of Iron-Aluminum-Sulfur System at 1173 K
.....*P. C. Patnaik, W. W. Smeltzer* 2688

Preparation and Properties of Amorphous Boron Films Deposited by Pyrolysis of Decaborane in the Molecular Flow Region
.....*K. Nakamura* 2691

Electrical Properties of Organometallic Chemical Vapor Deposited GaAs Epitaxial Layers
.....*D. H. Reep, S. K. Ghandi* 2697

Low Pressure Chemical Vapor Deposition of Tungsten on Polycrystalline and Single Crystal Silicon via the Silicon Reduction
.....*K. Y. Tsao, H. H. Busta* 2702

Charge Transfer via Interface States at Polycrystalline Cadmium Selenide Electrodes
.....*R. Haak, D. Tench, M. Russak* 2709

Activity Coefficients of Electrons and Holes in Semiconductors
.....*M. E. Orazem, J. Newman* 2715

TECHNICAL NOTES

Polarization Effects in Polyamides
.....*G. Samuelson, S. Lytle* 2717

Dependences of Magnetron-Sputtered SiO_2 Film Properties on Argon Pressure
.....*T. Yachi, T. Serikawa* 2720

The Growth of Epitaxial Layers of $Ga_{0.47}$ $In_{0.53}$ As by the Vapor-Phase Epitaxy-Hydride Method Using a Gallium-Indium Alloy Source
.....*T. E. Erstfeld, K. P. Quinlan* 2722

Hot Wall Si-CVD at Reduced Pressures
.....*C. Dominguez, G. Pastor, E. Lora-Tamayo, E. Dominguez* 2726

COMMENTS 2728

ACCELERATED BRIEF COMMUNICATIONS

Oxygen Reduction on Ruthenium Electrode Modified by Foreign Metal Adsorbates
.....*R. R. Adžić, N. A. Anastasijević, Z. M. Dimitrijević* 2730

A New Transition-Metal Penta-Chalcogenide Cathode for Secondary Lithium Cells
.....*S. Okada, H. Ohtsuka, T. Okada* 2732

Electrochemical Conversion of CrO_2
.....*D. Fousse, V. Jovancicevic, F. Tissier* 2734

REVIEWS AND NEWS

NEWS 467C

Call for Papers—Toronto, Ontario, Canada, Meeting 491C-496C

JOURNAL OF THE ELECTROCHEMICAL SOCIETY

ELECTROCHEMICAL SCIENCE AND TECHNOLOGY

NOVEMBER 1984

The Mechanisms of Thionyl Chloride Reduction at Solid Electrodes

W. K. Istone*,[1] and R. J. Brodd*,[2]

Ray O Vac Corporation, Madison, Wisconsin 53711

ABSTRACT

An experimental technique has been devised which allows *in situ* sampling of electrolyte from a functioning Li-$SOCl_2$ cell, followed by rapid FTIR analysis for soluble reaction products. Disulfur monoxide (S_2O) is observed as an intermediate discharge product. The half-life of S_2O is estimated to be about 20 min. The presence of S_2O is consistent with sulfur chemistry, as well as the accepted stoichiometry of the Li-$SOCl_2$ battery system. A possible safety hazard for low temperature discharges of Li-$SOCl_2$ cells is identified.

There has been great interest in the thionyl chloride-lithium battery system because of its high energy density and good high rate capability. There is general agreement that the overall discharge reaction for the system is

$$4Li + 2SOCl_2 = 4LiCl + S + SO_2$$

The details of the reaction are not yet known with certainty. Previous studies of the reaction mechanism have proposed various reaction pathways. Intermediates such as SO, S_2Cl_2, etc., have been postulated (1-4). It is important to know all aspects of the reaction characteristics in order to properly design the electrode structures (e.g., porosity) to accommodate reaction products, and to select materials of construction that are stable in SO, S_2Cl_2, $SOCl_2$, etc. It is also likely that the safety questions concerning thionyl chloride battery systems are related to the identity and stability of the reaction intermediates. Safety aspects include constructional features of the anode, the cathode, and the complete cell; they also prevent conditions such as internal shorts and the direct reaction of lithium and the sulfur reaction product.

In order to better understand the detailed steps and intermediates of the reaction mechanism, a technique described below has been devised to allow *in situ* sampling of electrolyte at the electrolyte surface. The materials present in the electrolyte are analyzed immediately utilizing Fourier transform infrared spectroscopy (FTIR). It is believed that the technique and relatively short analysis time (30s) have allowed us to confirm the existence of some reaction intermediates not previously observed.

Experimental

Thionyl chloride from Aldrich Chemical Company was redistilled in a glass and in Teflon still at ambient pressure under dry argon by the method of Wetter (5), with 160 ml additions of triphenyl phosphite to 1 liter of thionyl chloride. Care was taken to keep the pot below 82°C and column temperature below 78°C to prevent thermal decomposition of thionyl chloride. Fluka "puriss."-grade aluminum chloride was used as received. LiCl from Alpha Chemical Company was dried at 150°C *in vacuo* for 48h. The 1.6*M* $LiAlCl_4$ solutions were prepared in the argon dry box by slowly adding $AlCl_3$ to thionyl chloride to avoid heating and then slowly adding LiCl in slight excess. The resulting solutions were a very pale straw color. All pure chemicals and solutions were stored in glass inside an argon dry box.

Linear-sweep voltammetry experiments utilized a PAR Model 173 potentiostat and Model 175 waveform generator. Cell discharges were at constant current using a Keithley Model 227 constant current source.

The molar extinction coefficients are not known with certainty for the various reaction-product compounds in thionyl chloride. As a result, the absolute concentrations of the compounds cannot be determined. The amounts of materials were estimated on a relative basis. Since thionyl chloride is present in excess in all solutions, the peak for thionyl chloride at 2400 cm^{-1} was used as a reference. The height of the peak for a particular compound, relative to the height of the 2400 cm^{-1} peak, was used to follow changes in concentrations. This normalization procedure was used to eliminate errors due to changes in cell path length or instrumental conditions.

The experimental cell and sampling techniques were described previously (1). The FTIR cell was a Barnes micro flow-through cell having a path length of 0.1 mm. The cell material was KBr, with a total cell volume of 0.4 μl. The cell was connected by Teflon tubing to a syringe, which was used to draw samples of electrolyte into the FTIR cell. A valve prevented siphoning. A second piece of Teflon tubing connected the FTIR cell to the electrochemical cell, utilizing a stainless steel needle as a probe. The $SOCl_2$ slowly attacked the KBr cell, slightly changing its optical path. Therefore, the results reported here are semiquantitative in nature.

The electrochemical cell was contained in a glass vial containing 5 ml of 1.6*M* $LiAlCl_4$ in $SOCl_2$. A glass fiber mat separated the negative electrode (Foote Chemical Company pure lithium foil of 1 cm^2 area pressed into expanded stainless steel mesh) from the positive electrode (90% Shawinigan black, 10% PTFE, hot pressed at 275°C into expanded stainless steel grid to form a 1 cm^2 area electrode). The positive electrode made in this fashion had a porosity of about 60%. The stainless steel sampling probe was placed with its opening pressed against the face of the positive electrode. Experiments were also carried out with PTFE-bonded positive electrodes, using copper powder mixed with the Shawinigan black, as well as other solid planar materials, including glassy carbon, platinum, gold, nickel, and Type 316 stainless steel. The cell was assembled, filled, and sealed under argon atmosphere in a glove box, then transferred to the FTIR for discharge experiments.

The test cell was discharged at 5 mA/cm^2 constant current, with electrolyte samples of about 1 μl drawn for

* Electrochemical Society Active Member.
[1] Present address: St. Regis Technical Center, West Nyak, New York 10994.
[2] Present address: Standard Oil Company, Amoco Research Center, Naperville, Illinois 60566.

Table I. Infrared spectral assignments for thionyl chloride and related species (5-10)

Compound	Assignment (cm^{-1})
$SOCl_2$	1229*, 490, 443, 344, 284, 194
SO_2Cl_2	1414*, 1182, 560, 405, 388, 380, 362, 282, 218
SO_2	1332*, 1157
SO_3	1330, 1069*, 652, 532
SO	1124
S_2O	1165, 679*, 388
$(SO)_x$	1125
S_2Cl_2	538, 448, 438*, 242, 203
SCl_2	535*, 514, 208
$(AlCl_4)^-$	575*, 349, 180, 146
HCl	2886* (broad)
S	1290, 932, 841*, 686, 465

Underscoring denotes strong band.
* Denotes principal frequency for analytical purposes.

analysis before discharge began to establish base line and at 15 min intervals during discharge. The FTIR is a Nicolet MX-1. The 27 scans between 4400 and 225 cm^{-1}, taken to establish each spectrum, required 30s. Most experiments were carried out at a room temperature of 298 K (25°C). Some experiments were carried out at low temperatures of 273 K (0°C) and 260 K (−13°C) to establish the effect of temperature on the reaction rate and, if possible, to stabilize fast reacting species.

Results and Discussion

The infrared correlation chart (Table I) of species pertinent to sulfur oxyhalide chemistry was used to interpret the experimental results. The spectra obtained from the cell electrolyte were analyzed to determine which compounds are observed in analyzed electrolyte, whether these compounds are present as impurities or as the result of electrochemical discharge, and how the compounds' relative concentrations change as a function of experimental stand time and depth of discharge. The electrolytes are spiked with compounds of interest to confirm their presence, with the exception of SO_3 and S_2O.

Figure 1 shows a typical IR spectra taken during discharge of a Shawinigan-black, PTFE carbon cathode. The location of the significant peaks is noted during the experiments. An analysis of the spectra shows that small amounts of SO_2Cl_2, SO_2, S_2Cl_2, SCl_2, and HCl are present in the electrolyte as impurities at the beginning of the experiment. The HCl and SO_2 concentrations increase slightly with stand time, presumably as a result of moisture pickup from the cell walls. SO_3 is not observed initially and does not appear during stand time or during discharge. The SO and $(SO)_x$ species are difficult to detect because the proximity of the large $SOCl_2$ bands tend to mask them. The peak heights for S_2Cl_2 and SCl_2 remain constant throughout the experiments. Only the intensities of peaks assigned to SO_2 and S_2O are observed to change as a function of cell discharge. Matrix effects can result in wavelength shifts from the values reported for pure compounds, as opposed to the compound dissolved in 1.6*M* $LiAlCl_4$ in $SOCl_2$. For instance, the SO_2 peak reported at 1332 cm^{-1} appears at 1335 cm^{-1}, and the S_2O peak of 679 cm^{-1} appears at 689 cm^{-1} in $SOCl_2$ media. The other peaks for these compounds are also detected with similar matrix shifts, though the 1332 and 679 cm^{-1} are the easiest to monitor.

Figure 2 shows the change in relative concentration of SO_2 and S_2O as a function of cell discharge. It may be noted that the S_2O concentration increases to a maximum and then begins to decrease with time (mAh), whereas the SO_2 concentration increases and then appears to level off. We believe that the plateau in Fig. 2 is related to the steady-state concentration of SO_2 at the electrode surface under the experimental discharge conditions. Companion experiments run at a significantly higher discharge rate (50 mA/cm^2) show that the amount of SO_2 increases as a function of discharge time. Hence, the plateau of Fig. 2 may simply be related to the SO_2 diffusion away from the electrode surface in a steady-state situation. No new compounds were found at the higher current density. The results are similar to the results reported at lower current density, but with slightly higher concentrations of the S_2O intermediate. When an electrolyte sample from a discharged electrode is allowed to stand in the FTIR cell for a prolonged period (*e.g.*, 30 min), analyses show that the SO_2 concentration increases and the S_2O is deposited on the FTIR cell walls. Sulfur is a reaction product, and the S_8 species could be found as a reaction product. However, though S_8 has a weak absorption band at 686 cm^{-1}, it has a medium absorption band at 841 cm^{-1} which would not be interfered with in the observed spectra. Experimentally, no change around 841 cm^{-1} occurred, as would be expected. Also, on stand, no change should occur if S_8 is responsible for the 690 cm^{-1} band. This is consistent with the reported decomposition reaction for S_2O (7)

$$2S_2O = 3S + SO_2$$

Copper powder added to the positive electrode has been reported to improve the high rate capability of the Li-$SOCl_2$ cell (11). The copper reacts with $SOCl_2$ to produce insoluble CuCl. No new soluble materials were observed in thionyl chloride of cells containing copper. Only peaks for SO_2 and S_2O were observed. Figure 3 shows the change in relative concentrations of SO_2 and S_2O, using

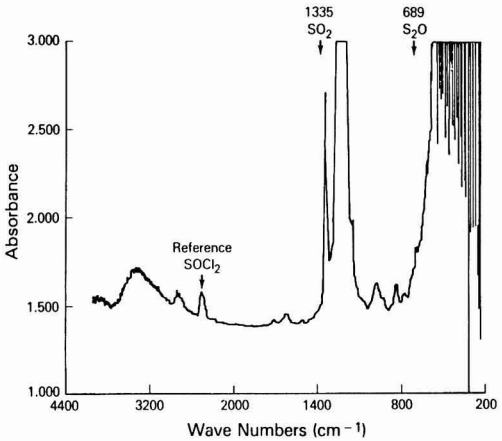


Fig. 1. Typical IR spectra showing S_2O, SO_2, and thionyl chloride reference peaks.

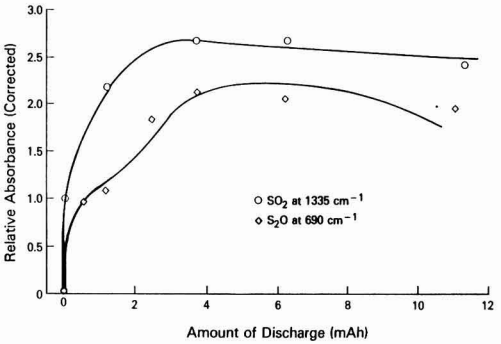


Fig. 2. Changes in the concentrations of SO_2 and S_2O as a function of thionyl chloride discharge (Shawinigan black cathode in 1.6*M* $LiAlCl_4$ ($SOCl_2$) at 25°C; discharge rate: 5 mA cm^{-2}).

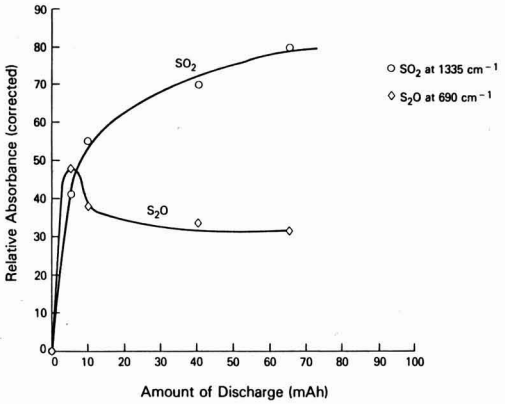


Fig. 3. Change in relative concentrations of SO_2 and S_2O using copper containing cathodes at 25°C (discharge rate: 5 mA cm^{-2}).

copper containing cathodes. The results are similar to those with only Shawinigan black.

Figures 4 and 5 show the effect of discharge at low temperature on the relative amounts of SO_2 and S_2O produced. The S_2O material is stabilized at the lower temperatures, and its concentration builds up to higher concentration levels at the lower temperature. It decomposes much more slowly at 273 and 260 K than at room temperature. From our results, we estimate that the half-life of S_2O at room temperature is of the order of 20 min.

Figure 6 shows a linear sweep for a glassy carbon cathode. The results are very similar to those reported for pyrolytic carbon (4). The main peak for $SOCl_2$ reduction is at 2.54V *vs.* Li, with some reaction at 1.1V *vs.* Li, presumably due to SO_2 reduction. On the second and third sweeps after the excursion into Cl_2 evolution, peaks at 3.61 and 3.32V were also observed. The peak at 3.61V is usually associated with Cl_2, but could be due in part to SO_3. The peak at 3.32V is thought to be due to SO_2Cl_2 formed during the excursion to higher voltages.

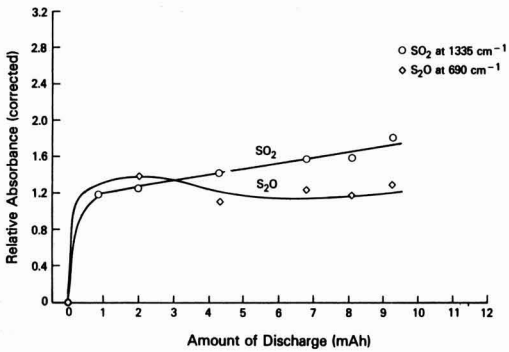


Fig. 4. Relative amounts of SO_2 and S_2O produced at 0°C (Shawinigan black cathode discharge rate: 5 mA cm^{-2}).

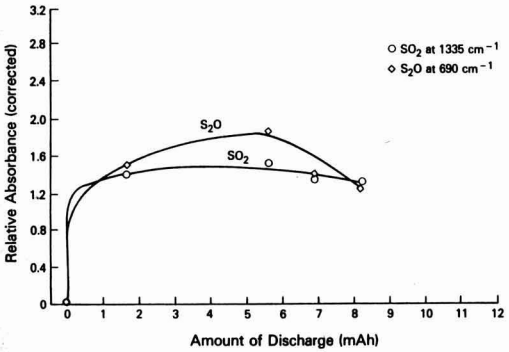


Fig. 5. Relative amounts of SO_2 and S_2O produced at −13°C (Shawinigan black cathode discharge rate: 5 mA cm^2).

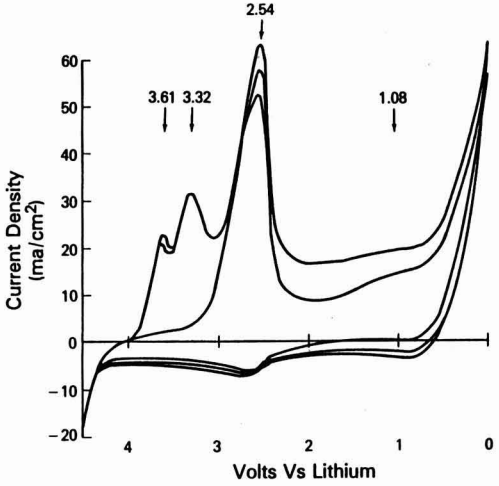


Fig. 6. Linear sweep voltammetry of a glassy carbon electrode in 1.6M $LiAlCl_4$ ($SOCl_2$).

The results reported here are not consistent with previous reports of reaction mechanism. Blomgren *et al.* (4) reported SCl and S_2Cl_2 as intermediates in $SOCl_2$ reduction. Both of these materials are active in the IR region under observation, but no changes in peak heights were observed in these compounds in the present study. None of the cells took on the blood red color usually associated with sulfur chlorides. Since their time frame for analysis was long, previous studies would not have observed the S_2O reported above. Blomgren *et al.* (4) proposed the following mechanism

$$SOCl_2 + e = SOCl^{\cdot} + Cl^-$$

$$2SOCl^{\cdot} = SO_2 + SCl_2$$

$$SCl_2 + e = SCl^{\cdot} + Cl^-$$

$$2SCl^{\cdot} = S_2Cl_2$$

$$S_2Cl_2 + 2e = 2S + 2Cl^-$$

The results here do not support the presence of sulfur chlorides as reaction intermediates. The reason for this difference is not obvious. Pure materials were used in both experiments. The only obvious difference is the different carbon electrode materials used in each study. Blomgren *et al.* did not use Shawinigan black, but a black produced by Union Carbide Corporation. They also used pressure-annealed pyrolytic graphite electrodes for linear sweep experiments. It is not clear why this difference should influence the reaction mechanism, if indeed it does.

Schlaikjer *et al.* (4) propose the following mechanism, which uses Teflon-bonded Shawinigan black electrode structures.

$$SOCl_2 + 2e = (SO) + 2Cl^-$$

$$(SO)_n = n/2S + n/2SO_2$$

They also report the possible formation of solid Li_2SO_3 in small amounts at low temperature discharge.

Dey *et al.* (3) proposed a mechanism somewhat similar to that of Blomgren *et al.*, involving the SO radical, but

ห้องสมุดกรมวิทยาศาสตร์บริการ

with formation of SOCl as the first step of the reduction. They did not report S_2Cl_2 and SCl_2 as intermediates

$$SOCl_2 + e = SOCl^{\cdot} + Cl^-$$

$$SOCl^{\cdot} + e = SO + Cl^-$$

$$nSO = (SO)_n$$

$$(SO)_n = n2S + n/2SO_2$$

The SO radical could follow the proposed reaction. However, according to Nickless, the usual path for SO reaction involves S_2O formation.

The identification of S_2O formation reported here would suggest the following mechanism

$$SOCl_2 + e = SOCl^{\cdot} + Cl^{\cdot}$$

$$SOCl^{\cdot} + e = SO + Cl^-$$

$$3SO = S_2O + SO_2$$

$$2S_2O = 3S + SO_2$$

The observation that S_2O is produced can be taken as proof that SO is formed in the thionyl reduction process. The formation of solid products such as Li_2SO_3 would not be expected unless there were excessive impurities in the $SOCl_2$ or there was a potential excursion of 4.0V *vs.* Li. If such an excursion occurred, SO_3 and SO_2Cl_2 could form, giving Li_2SO_3 and $Li_2S_2O_3$ on discharge. In the discharge of large cells, the IR spectra of discharged electrolyte indicates the presence of SO_3 when cells are held at 4.0V for a short period of time.

The formation of S_2O intermediate could explain some previous observations concerning the rate of SO_2 formation during discharge. It would be expected that smaller-than-stoichiometric quantites of SO_2 would be generated during the initial stages of cell discharge, owing to the stability of S_2O. Only toward the end of discharge, when S_2O production corresponds to the discharge rate, would the SO_2 production be directly proportional to discharge rate. As the stability of S_2O varies with temperature, low temperature discharges (especially at high rates) could lead to buildup of large S_2O concentrations. Warming these cells to room temperature could quickly lead to rapid decomposition of S_2O with rapid heat release and SO_2 pressure buildup.

Conclusions

1. It is possible to detect short-lived intermediates in thionyl chloride reduction using an *in situ* sampling technique, coupled with FTIR apparatus.
2. S_2O specie was identified and, therefore, by implication, the SO specie was identified as intermediates in electrochemical reduction of thionyl chloride.
3. The half-life of S_2O in thionyl chloride is about 20 min.
4. S_2O was identified as an intermediate with carbon, carbon-copper mixture, platinum, gold, nickel, and stainless steel electrodes.

Acknowledgments

This work was carried out at Inco Sterling Forest, with the financial support of Ray O Vac Corporation. The authors gratefully acknowledge the helpful discussions of N. Margalit. R. B. Roe, B. C. Bergum, and J. R. Thomas, as well as the assistance of D. Kerstanski and T. Gardinier in carrying out the experiments reported here. The authors also thank INCO, Limited and Ray O Vac Corporation for permission to publish this work.

Manuscript submitted Jan. 5, 1984; revised manuscript received June 26, 1984.

REFERENCES

1. J. C. Bailey and J. P. Kohut, "Power Sources 8," J. H. Thompson, Editor, p. 17, Academic Press, New York (1981).
2. C. R. Schlaikjer, T. Goebel, and N. Marimerc, *This Journal*, **126**, 513 (1979).
3. A. M. Dey and P. Bro, *ibid.* **125**, 1574 (1978).
4. G. E. Blomgren, V. Z. Leger, T. Kalnoki, M. L. Kronenberg, and R. J. Brodd, "*Power Sources 7*," J. H. Thompson, Editor, p. 583, Academic Press, New York (1979).
5. L. Friedman and W. P. Wetter, *J. Chem. Soc.*, 36 (1967).
6. K. Nakamoto, "Infrared Spectra of Inorganic and Coordination Compounds," John Wiley and Sons, New York (1963).
7. "Inorganic Sulfur Chemistry," G. Nickless, Editor, Elsevier, New York (1968).
8. D. L. Chua, S. L. Despande, and H. V. Venkatasetty, in "Battery Design and Optimization," S. Gross, Editor, p. 365, The Electrochemical Society Softbound Proceedings Series, Princeton, NJ (1979).
9. M. M. Yanak and W. K. Istone, Unpublished results.
10. H. G. Bernstein and J. Powling, *J. Chem. Phys.*, **18**, 1018 (1950).
11. L. R. Giattino, U.S. Pat. 4,262,065 (1981).

Investigation of $SOCl_2$ Reduction by Cyclic Voltammetry and AC Impedance Measurements

M. J. Madou*

SRI International, Menlo Park, California 94025

S. Szpak*

Naval Ocean Systems Center, San Diego, California 92152

ABSTRACT

Cyclic voltammetry and ac impedance measurements, covering the range 10^{-3}-10^4 Hz, were employed to investigate the reduction of thionyl chloride on glassy carbon surfaces and to determine the associated elementary processes. The quasi-exchange current density of the electroreduction of $SOCl_2$ is 6.4×10^{-7} A cm^{-2} and becomes larger in the presence of dissolved chlorine. Also, in the presence of Cl_2, the rest potential shifts to more positive values. At low overpotentials, the reduction of $SOCl_2$ is kinetically controlled. However, as the overpotentials are increased, a transition to mass-transport control occurs, even before the onset of passivation at +2.7V. The rate of mass transport is governed by the thickness and quality of the LiCl film.

The lithium thionyl chloride battery is one of the most energetic systems reduced to practice thus far and is well developed for lower power density requirements (1). However, to achieve high discharge rates, a new set of problems must be resolved, which requires a more detailed knowledge of the elementary processes that take place within the battery. In particular, reference is made to those processes that occur within the porous structure of the positive electrode.

The reduction of $SOCl_2$ was studied quite extensively (2-7). The reported results, however, are incomplete inasmuch as they do not provide useful data for electrode modeling which is essential for the rational design of high power output batteries (8, 9). In an attempt to provide this information, we will emphasize the description of the elementary processes rather than concentrate on the identification of reactive species (10, 11).

Experimental

Solutions.—Stock solutions having a composition of 1*M* $AlCl_3$, 1*M* $LiAlCl_4$, 1.6*M* $LiAlCl_4$, 2.2*M* $AlCl_3$, plus 1.9*M* $LiAlCl_4$ in $SOCl_2$ were used as supplied (source: Altus Corporation, San Jose, California 95112). Typical impurity levels, certified by the supplier, were Fe 1.8 ppm, SCl_2 0.1%, and OH 84 ppm in neutral solutions. The acidic solutions usually contained more OH (up to 251 ppm for the 1*M* $AlCl_3$ in $SOCl_2$).

Electrochemical cell and apparatus.—The electrochemical cell used in this investigation is shown in Fig. 1. A porous vitreous carbon and a flat glassy rod, press-fitted into a Teflon screw, were employed as the counter and working electrodes, respectively. Metallic Li and Mo were used interchangeably as reference electrodes. The cell volume was *ca.* 2 cm^3.

A Princeton Applied Research potentiostat/galvanostat, Model 173/176, and Universal Programmer, Model 175, were used to perform cyclic voltammetry. Measurements of the electrochemical transfer function were carried out using a Solartron Frequency Response Analyzer (FRA) Model 1172/1183/1185 in an experimental configuration described elsewhere (12).

Procedure.—All measurements were carried out in a dry box under a positive argon pressure. Before each measurement, the working electrode was polished with an Al_2O_3 aqueous slurry (particle size 1 μm) on a polishing cloth, followed by methanol wash, and then wiped dry with a lense paper. A fresh Li reference electrode was used for each set of impedance measurements and between sets of cyclic voltammograms. The porous vitreous carbon counterelectrode was replaced before each set of experiments.

Results and Discussion

The results and discussion section covers five topics: the choice of reference electrode, the concept of mixed potential and the quasi-exchange current density, the cyclic voltammetry data, the results of impedance measurements, and their relevance to battery modeling.

Choice of reference electrode.—Metallic Li is the reference electrode of choice in neutral solutions. It is not suitable in acidic electrolytes because of the dissolution of the protective LiCl film, which, for small cells, would substantially change the composition of the electrolyte phase. To avoid these difficulties, we have selected Mo as the reference electrode for most of the work in acidic solutions (13). These two reference systems were compared by measuring open-circuit potentials between a Mo electrode and a Li electrode in a U-type cell provided with a fritted glass disk between the cell compartments (*e.g.*, 1.6*M* $LiAlCl_4$ in $SOCl_2$), a V_{oc} of approximately 3.60V was measured. Upon the addition of an aliquot of 1*M* $AlCl_3$ solution in $SOCl_2$ to the Mo compartment, the V_{oc} increased to about 3.95V. Interestingly, these potentials are close to those reported for the carbon/lithium couple in neutral and acidic solutions (14). Such a relationship suggests that the Mo electrode acts as an electrode of the first kind and not as one of second kind, as concluded by Spandau and Brunneck (13), *i.e.*, it responds to the electron transfer associated with the fastest reaction, just as does the carbon electrode (15).

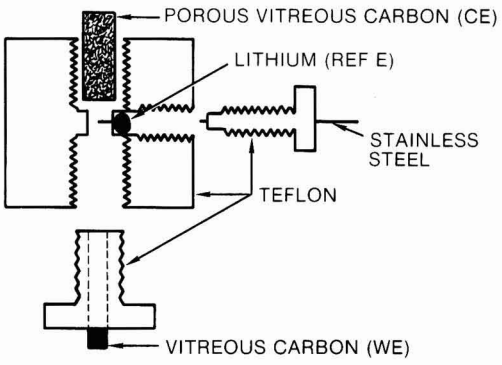


Fig. 1. Electrochemical cell, exploded view

* Electrochemical Society Active Member.

Table I. Summary of postulated overall cell reactions in neutral Li/$SOCl_2$ system (24)

Overall reaction	E_0, (V) (F/mol)	(calc.)
$4Li + 2SOCl_2 \rightarrow 4LiCl + S + SO_2$	2.00	3.72
$8Li + 3SOCl_2 \rightarrow 6LiCl + 2S + Li_2SO_3$	2.67	3.60
$8Li + 4SOCl_2 \rightarrow 6LiCl + S_2Cl_2 + Li_2S_2O_4$	2.00	3.50
$14Li + 6SOCl_2 \rightarrow 12LiCl + 4S + Li_2S_2O_6$	2.33	3.70
$10Li + 4SOCl_2 \rightarrow 8LiCl + 2S + Li_2S_2O_4$	2.50	3.57
$10Li + 4SOCl_2 \rightarrow 8LiCl + 3S + Li_2SO_4$	2.50	3.73
$8Li + 3SOCl_2 \rightarrow 6LiCl + S + Li_2S_2O_3$	2.67	3.56
$6Li + 4SOCl_2 \rightarrow 6LiCl + S_2Cl_2 + 2SO_2$	1.50	3.68
$10Li + 6SOCl_2 \rightarrow 8LiCl + 2S_2Cl_2 + Li_2S_2O_6$	1.67	3.64
$7Li + 4SOCl_2 \rightarrow 5LiCl + 3/2S_2Cl_2 + Li_2SO_4$	1.75	3.68
$6Li + 3SOCl_2 \rightarrow 4LiCl + S_2Cl_2 + Li_2SO_3$	2.00	3.52
$7Li + 3SOCl_2 \rightarrow 5LiCl + 1/2S_2 + Li_2S_2O_3$	2.33	3.52

Open-circuit potential and quasi-exchange current density.—The calculated values of open-circuit potential, listed in Table I, range from 3.52 to 3.73V for cells employing neutral electrolytes, with higher values in acidic electrolytes, *e.g.*, *ca.* 4.0V (14), *i.e.*, the same values that were recorded for the C/Li and Mo/Li couples. The gain in the open-circuit potential of *ca.* 0.4V in acidic electrolytes was attributed by Klinedinst and Domeniconi (14) to the difference in the Gibbs' free energy associated with the respective reactions. Using the available data for the equilibrium constant for the complexation reaction (*i.e.*, formation of $LiAlCl_4$), they estimated this gain to be between 0.53 and 0.63V. Experimentally, however, the gain is somewhat less, *viz.*, 0.35-0.4V.

A possible explanation for the discrepancy between the theoretical and experimental data is that, in adding the $AlCl_3$, not only the reaction product has changed (*i.e.*, $LiAlCl_4$ rather than LiCl) but also the reactant (*i.e.*, $AlCl_3 \cdot SOCl_2$ adduct rather than $SOCl_2$). There is, indeed, substantial evidence for the existence of the $AlCl_3 \cdot SOCl_2$ and $2AlCl_3 \cdot SOCl_2$ adducts by Raman spectroscopy (16), and for $AlCl_3 \cdot SOCl_2$ adduct by infrared spectroscopy (17). By taking the reaction of adduct formation, *i.e.*, starting with a more stable reactant, ΔG, and thus also ΔE, will be lowered, in contrast to the situation where no complexation has been taken into account.

In what follows, we will show that the experimentally determined cell potential is not the reversible potential, but is a mixed one, with a cathodic current involving the reduction of $SOCl_2$ or Cl_2 and the anodic current involving evolution of Cl_2 from either $SOCl_2$, $AlCl_4^-$, or LiCl.

An Evans-type representation of log *i vs. V* curves for the reduction and oxidation in neutral electrolyte is shown in Fig. 2. The cathodic and anodic branches were constructed with the aid of potential sweeps commencing at potentials slightly negative to the V_{oc} for the cathodic branch (curve a) and at 4.00V for the anodic branch (curve b). The development of a curvature and hysteresis indicates that the activation-controlled region is relatively narrow (between +3.55 and +3.00V), with a region for the reduction of both Cl_2 and $SOCl_2$ being between +3.55 and +3.25V only.

The anodic branch arises because of Cl_2 evolution generated by oxidation of $SOCl_2$, $AlCl_4^-$, or LiCl. The Cl_2 generated by the anodic excursion is subsequently reduced during the returned sweep with the amount of cathodic current depending on the anodic charge consumed.

Processes determining the V_{oc} and the quasi-exchange current density, i_o^q, are complex. Assuming that the amount of Cl_2 present (or generated) in the solution is small, it follows that the intersection of curves a and b determines both the V_{oc} and i_o^q. Extrapolation of data in Fig. 2 yields $V_{oc} = +3.55$V and $i_o^q = 6.4 \times 10^{-7}$ A cm^{-2}. Extrapolation of curves c and a yields higher values for the i_o^q and a more positive open-circuit potential. The sensitivity of both these quantities to the dissolved chlorine is an expected behavior, provided that the reduction of $SOCl_2$ is a rapid reaction.

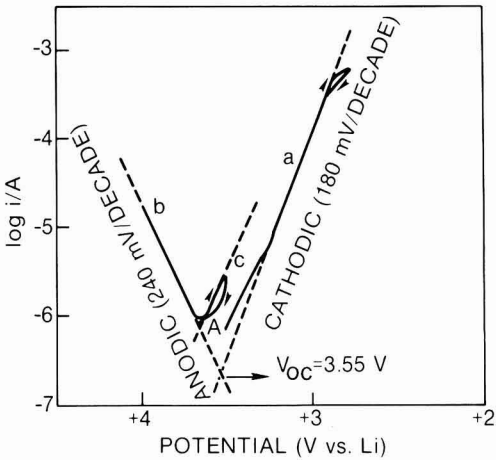


Fig. 2. Evans plot (log i vs. V). Electrolyte: 1.6M $LiAlCl_4$ in $SOCl_2$. Temperature: room. Electrode area: 0.314 cm^2. Reference Electrode: Li. Sweep rate: 10 mV s^{-1}.

Additional information concerning the magnitude of the electrode transfer resistance associated with the reduction of thionyl chloride can be extracted from data in Fig. 2. Using $i_o^q = 6.4 \times 10^{-7}$ A cm^{-2} and substituting into the Stern-Geary relationship, Eq. [1]

$$R_p = \vec{\beta} = \overleftarrow{\beta}/2.303 \times i_o^q \times A \times (\vec{\beta} - \overleftarrow{\beta}) \qquad [1]$$

a value of $R_p = 7 \times 10^4$ Ωcm is calculated. Here $\vec{\beta}$ and $\overleftarrow{\beta}$ are the anodic and cathodic Tafel coefficients, respectively, and A is the electrode area.

Cyclic voltammetry.—A typical voltammogram in a neutral electrolyte exhibits a large reduction peak (peak I), a rather broad peak located between +2.0 and +1.0V (peak II), followed by a rapid increase in current at *ca.* +1.0V (peak III). Upon reversal of the sweep, two anodic peaks appear at potentials of *ca.* +1.1 and +2.9V (peaks IV and V).

There is no disagreement in the identification of peak I and current onset III. However, the origin and structure of peaks II and V have not been resolved as yet. In fact, Behl (2) reported two barely perceptible peaks at +1.7 and +1.3V rather than one broad peak. The existence of these peaks has not been confirmed in this work or in work by others (4, 10, 19). The broad peak II is most likely due to the reduction of SO_2 (10, 19). However, even in SO_2-saturated neutral electrolytes, the peak height remains about the same because, to be reduced, SO_2 must diffuse through the passive film (2). As expected, the effect of SO_2 bubbling on the peak height is more evident in acid solutions since the excess of $AlCl_3$ partially dissolves the precipitated LiCl, thus making the surface accessible to the electroreduction of SO_2.

Commencing a cyclic voltammogram at a potential positive to the V_{oc} (*e.g.*, at +4.50V) and terminating the sweep at a potential positive to the appearance of peak II, two additional cathodic current peaks, peaks A and B, appear before the $SOCl_2$ reduction peak (Fig. 3, curve a). The first peak, peak A, at +3.60V, was attributed to the reduction of SCl_2 (8), and peak B, at +3.25V, to the reduction of Cl_2. To confirm this assignment, we have used a Cl_2-saturated electrolyte and commenced the sweep at potentials slightly cathodic to the V_{oc}. As illustrated in Fig. 3, curve b, peak B is substantially increased, *i.e.*, attributable to the reduction of Cl_2. Peak A, although present, was not affected by the presence of dissolved chlorine.

Figure 4 shows the dependence of reduction peak I on the scan rate. The substantial shift of the peak potential with the scan rate is indicative of the highly irreversible character of the $SOCl_2$ reduction. A plot of peak height i

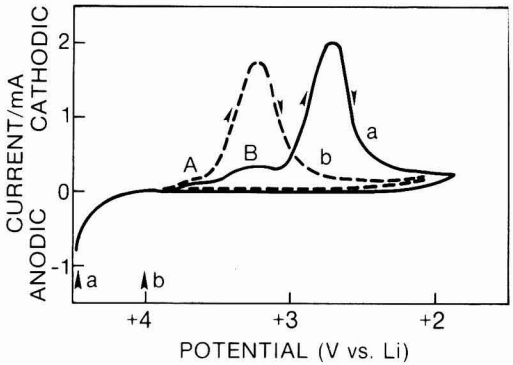


Fig. 3. Cyclic voltammograms on glassy carbon. Scan rate: 100 mV s^{-1}. Electrode area: 0.314 cm^2. Temperature: room. Reference electrode: Li. Electrolyte: 1M $LiAlCl_4$ in $SOCl_2$ (curve a) and 1M $LiAlCl_4$ + Cl_2 in $SOCl_2$ (curve b). Scan initiation: (curve a) +4.5V, (curve b) +4.0V.

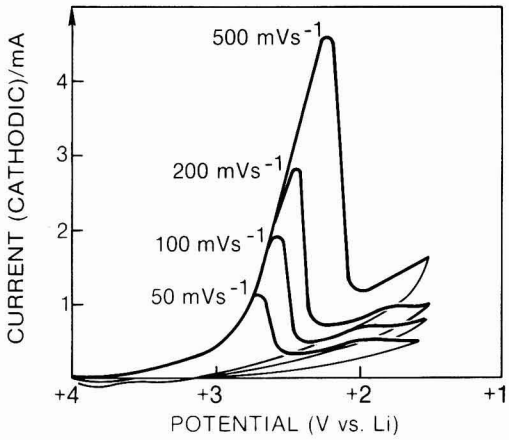


Fig. 4. Cyclic voltammograms as function of scan rate. Electrode: glassy carbon, area 0.314 cm^2. Electrolyte: 1M $LiAlCl_4$ in $SOCl_2$. Temperature: room. Scan rates indicated. Reference electrode: Li.

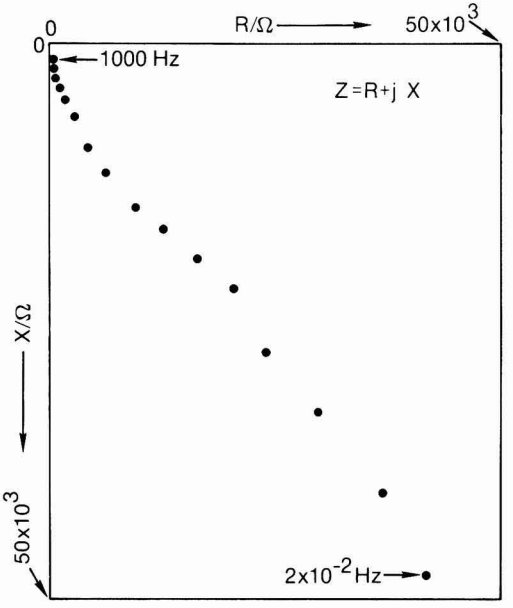
vs. $\sqrt{v}$ results in a straight line passing through the origin indicating a diffusion-controlled process, in agreement with results of Behl (20) and Doddapaneni (22). Since we did not find the usual effect of stirring of the electrolyte, the diffusion limitation suggested by the i *vs.* $\sqrt{v}$ plot cannot be due to the concentration polarization in the liquid phase. We conclude, therefore, that the diffusion limitation has its origin in the transport of species through the film produced on the electrode surface. The limiting diffusion current density in the electrolyte phase would have been much larger, on the order of Acm^{-2} (23).

Impedance measurements.—Impedance measurements were employed by Meitav and Peled (6) to study the behavior at the open circuit of stainless steel immersed in 1*M* $LiAlCl_4$ in $SOCl_2$ electrolyte. They concluded that the charge transfer reaction resistance is very high. Phillips *et al.* (7) found that also the reduction of $SOCl_2$ on vitreous carbon surfaces is slow. Qualitatively, these results are in agreement with the i_o^a and R_p values determined with the aid of the Evans plot (Fig. 2).

In an attempt to provide additional information, two sets of impedance measurements were made. In the first set, repetitive impedance data (with a 2 min delay time) were obtained at the V_{oc} and at very low cathodic overpotentials in neutral and acidic solutions. In the second set, impedance data were collected at higher cathodic overpotentials, also in neutral and acidic solutions.

A typical Nyquist plot (*i.e.*, a plot of the real *vs.* imaginary part of the electrode impedance) in acid solutions is shown in Fig. 5a, while the corresponding Bode plot (*i.e.*, a plot of the logarithm of the total electrode impedance *vs.* the ac frequency) is shown in Fig. 5b. A straightforward mathematical treatment shows that a semicircle intersecting the real axis at 90° in the Nyquist plot is indicative of a kinetically controlled reaction and can be represented by a simple RC parallel equivalent circuit. However, when a diffusional process is controlling the impedance factor, the Nyquist plot yields a straight line intersecting the real axis at 45°. The corresponding Bode plots are straight lines with slopes −1 and −1/2.

The separation and identification of contributing processes is clear in acid solutions (Fig. 5a and 5b). The Nyquist and Bode plots in neutral solutions are similar



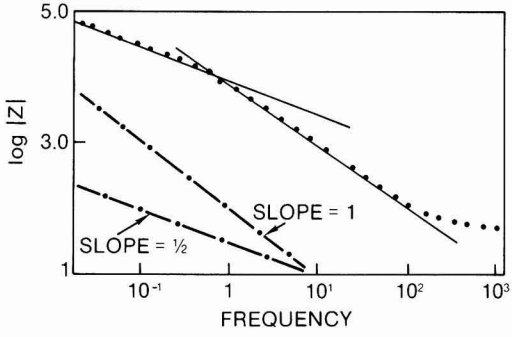


Fig. 5. Nyquist (a, left) and Bode (b, above) plots. Electrode: glassy carbon, area 0.314 cm^2. Electrolyte: 2.2M $LiAlCl_4$−1.9M $AlCl_3$ in $SOCl_2$. Temperature: room.

except that the kinetic and transport controlled processes are less clearly resolved. Here, the Nyquist plot in Fig. 6 is a large "depressed" semicircle, with its center below the real axis. The Bode plot (not shown) is a straight line with slopes approaching −1 and −1/2 at the highest and lowest frequencies, respectively. The diffusional process, we believe is associated with switch-on of Cl_2 in the solution.

Consecutive measurements at the V_{oc} or at low overpotentials were reproducible in the acidic electrolytes, while in neutral electrolytes, the impedance increased with each successive measurement. Such a behavior indicates that, in acid solutions, the electrode surface remains free from deposited LiCl, wheras in neutral solutions, the deposited LiCl changes the electrode impedance even at the open circuit. The presence of the deposited LiCl accounts for the difficulty in clearly separating and identifying participating processes.

Fitting the high frequency points in the Nyquist plot (Fig. 5a) to a semicircle yields a R_p of *ca.* $9.4 \times 10^3\ \Omega cm^{-2}$ and a value of C_p from the imaginary component of the impedance between 60 and 70 μFcm^{-2}, the latter being about twice that measured by Meitav and Peled on stainless steel (6).

Results of impedance measurements at different cathodic overpotentials are presented in Fig. 7, with the Nyquist plots on the left-hand side and the Bode plots on the right-hand side. These measurements were taken in steps at 200 mV starting at +3.3V (Fig. 7a) and terminating at +2.5V (Fig. 7e). In contrast to the electrode behavior of the open-circuit potential, no clear evidence for the dominance of transport properties can be presented at low cathodic overpotentials. This is an expected behavior because the diffusional process at low frequencies is associated with the reduction of Cl_2, which must disappear at potentials negative to the V_{oc}.

Results of the ac impedance measurements, summarized in Fig. 7a-7d, indicate that the electroreduction of $SOCl_2$ on glassy carbon is complex. The diameter of the single semicircle in Fig. 7a, *i.e.*, at 3.3V is almost the same as at the V_{oc}. If there were only one reduction process involved at V_{oc}, *e.g.*, the $SOCl_2$ reduction, we would expect the R_p to decrease exponentially with increasing overpotential. This clearly is not the case here and indicates that R_p at the V_{oc} is relatively small because of the contribution due to the reduction of Cl_2 at the V_{oc}. The diameter of the single semicircle in Fig. 7a and 7b decreases as the potential decreases from +3.3 to +3.1V. The approach to the real axis of the semicircles at high frequency is close to 90°, but the centers of the semicircles are found somewhat below the real axis. The Bode plots, Fig. 7a′ and 7b′, exhibit a slope approaching −1 over a wide frequency range. Taking the point at 0.1 Hz in these figures as representative for the R_p of a relatively LiCl-free surface, we can see that R_p has decreased over almost one order of magnitude with a change of 200 mV in electrode potential.

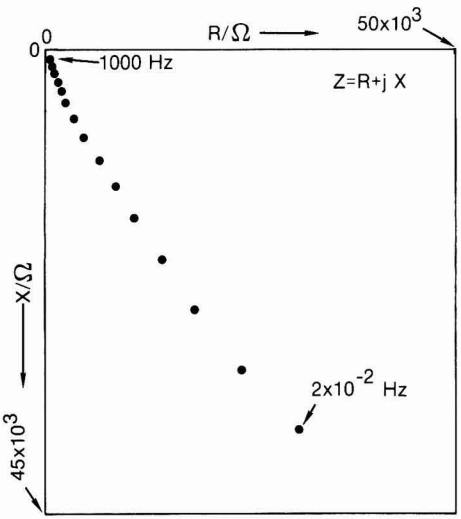


Fig. 6. Nyquist plot at rest potential. Electrode: glassy carbon, area 0.314 cm². Electrolyte: 1M $LiAlCl_4$ in $SOCl_2$. Temperature: room.

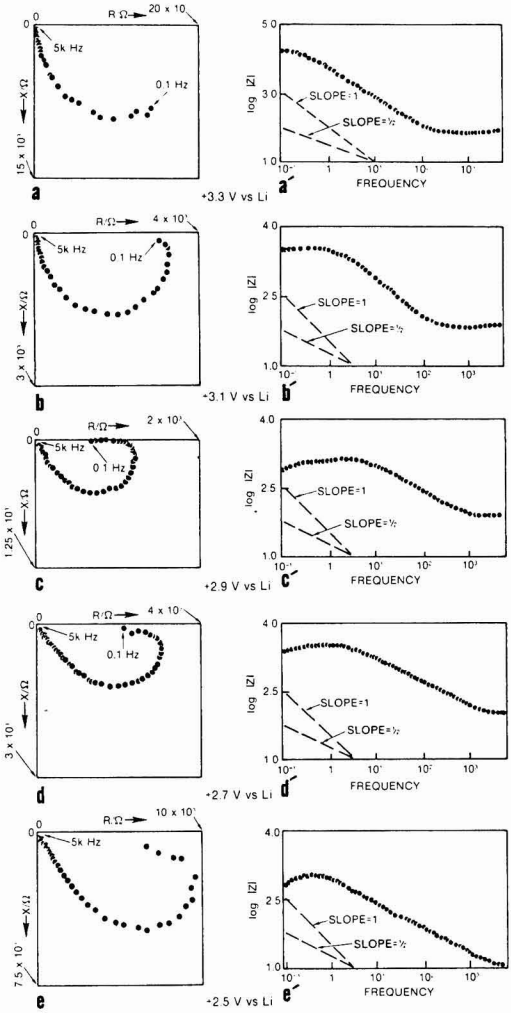


Fig. 7. Nyquist and Bode plots as function of overpotential. Electrode: glassy carbon, area 0.314 cm². Electrolyte: 1M $LiAlCl_4$ in $SOCl_2$. Temperature: room. Reference electrode: Li. Curve a: at +3.3V. Curve b: at +3.1V. Curve c: at 2.9V. Curve d: at +2.7V. Curve e: at +2.5V.

At electrode potentials close to the reduction peak of $SOCl_2$, the impedance spectra indicate diffusional behavior. The Nyquist plots, shown in Fig. 7c and 7d at +2.9 and +2.7V, respectively, exhibit an approach to the real axis at high frequencies of approximately 45°, and the corresponding Bode plots show lines with a slope approaching −1/2. The high frequency range, in which the diffusional character of the impedance becomes apparent, sets it apart from the diffusional process in solution, which has been discussed in connection with Fig. 5a and 5b. We note that within the low frequency range of the Nyquist plot in Fig. 7c, 7d, and 7e some points are lying along the real axis, indicating that R_p is increasing during the measurement. This change in R_p is due to the reduction of available area on the electrode surface because of deposition of LiCl.

Relevance to battery modeling.—In the "Cyclic voltammetry" section, we propose that a quasi-diffusional process arises during the $SOCl_2$ reduction, with its origin being the transport of species to or from the surface of the carbon electrode through voids in the LiCl film. The impedance spectra in Fig. 7a-7e support this picture. The approach of the intercept of the low frequency points toward the real axis in a Nyquist plot, for diffusion-controlled systems, is equal to the sum of series resistance R_s, here equal to the electrolyte resistance, R_p the electron transfer resistance, and R_d diffusion layer resistance. The magnitude of the diffusion layer resistance is proportional to the thickness of a layer through which diffusion takes place. Here, the thickness of the diffusion layer is that of a LiCl film deposited on a glassy carbon surface. Evidently, the cathodic polarization of carbon electrode reduces R_p but increases R_d owing to an increase in thickness of a LiCl film. The dominance of the R_d with the increase in cathodic polarization is clearly shown in Fig. 7d, where the diameter of the Nyquist plot begins to increase. As cathodic overpotentials are increased, to +2.5V (Fig. 7e), the electrode surface is completely covered, as evidenced by a sudden expansion of the Nyquist plot.

Upon starting the ac impedance measurements at +2.9V and stepping the dc bias towards more anodic potentials (again with 2 min delay) it was found that the quasi-diffusional behavior dominated the impedance even at +3.3V (*vs.* Li). Obviously, the thicker film formed at +2.9V was permanent and was not removed by reducing the cathodic polarization.

The quasi-diffusional behavior, *i.e.*, transport through solid LiCl film, similar to that in neutral solution, was never observed in acidic solutions, not even at potentials in the passive region. Despite this, the Nyquist plots showed points at low frequency lying along the real axis, indicating, again, the reduction in active area during the measurement. Evidently, in contrast to neutral solutions, in acidic electrolyte, the LiCl film remains sufficiently thin and does not result in quasi-diffusional behavior. The passivation of the electrode surface is likely to occur if the rate of LiCl complexation is slower than LiCl formation.

Conclusions

1. Metallic Li is a suitable reference electrode for measurements in neutral solutions, while Mo is preferable in acidic electrolytes.

2. The rest potential of a carbon electrode, immersed in $SOCl_2$, is a mixed potential, with the cathodic partial reaction being the reduction of $SOCl_2$ and the anodic branch arising from the oxidation of $SOCl_2$, $AlCl_4^-$, and Cl^-.

3. Reduction of $SOCl_2$ on a glassy electrode is a slow process with the quasi-exchange current density of 6.4×10^{-7} A cm^{-2}.

4. The reduction of $SOCl_2$ is kinetically controlled at low overpotentials. However, as these overpotentials are increased, a transition to diffusion control occurs, even before the onset of passivation at +2.7V.

5. All reactions, including SO_2 reduction, that take place at potentials more negative than +2.7V, are controlled by mass transport. The controlling factor is the thickness and porosity of the LiCl film rather than the conditions in the bulk electrolyte.

6. Once formed, the LiCl film cannot be removed by holding the electrode negative to the V_{oc}. Removal of this film requires potentials more positive than the V_{oc}.

7. In acidic solutions, the electrode surface remains free from deposited LiCl. Diffusional control through a LiCl film is possible only if the dissolution of the LiCl film is slower than its formation.

Acknowledgments

This work was funded by Naval Sea Systems Command (NAVSEA 63R-32) and constitutes a fraction of a program to establish a technology base for high discharge rate Li/SOCl batteries. We thank M. F. Romano (NAVSEA 63R-32) for his interest and support.

Manuscript submitted Aug. 4, 1983; revised manuscript received June 4, 1983.

The Naval Ocean Systems Center assisted in meeting the publication costs of this article.

REFERENCES

1. J. A. Christopulos and S. Gilman, *IEEC '75 Rec.*, 437 (1975).
2. W. K. Behl, *This Journal*, **101,** 367 (1979).
3. W. L. Bowden and A. N. Dey, *ibid.*, **127,** 1419 (1980).
4. D. L. Chua, S. L. Deshpande, and H. V. Venkatasetty, in "Battery Design and Optimization," S. Gross, Editor, p. 365, The Electrochemical Society Softbound Proceeding Series, Princeton, NJ (1979).
5. W. K. Behl, in "Proceedings of the 27th Power Sources Conference," Atlantic City, NJ, June 21-24, 1976, p. 30.
6. A. Meitav and E. Peled, *J. Electroanal. Chem.*, **134,** 49 (1982).
7. J. Phillips, J. C. Hall, and H. F. Gibbard, Abstract 65, p. 169, The Electrochemical Society Extended Abstracts, Vol. 80-2, Hollywood, FL, Oct. 5-10, 1980.
8. K.-C. Tsaur and R. Pollard, *This Journal*, **131,** 975 (1984).
9. K.-C. Tsaur and R. Pollard, *ibid.*, **131,** 984 (1984).
10. K. M. Abraham and R. M. Mank, *ibid.*, **127,** 1091 (1980).
11. S. Dullek, S. A. James, and W. P. Kilroy, *ibid.*, **128,** 508 (1981).
12. M. Madou and M. C. H. McKubre, *ibid.*, **130,** 1056 (1983).
13. H. Spandau and E. Brunneck, *Z. Anorg. Allg. Chem.*, **278,** 197 (1955).
14. K. A. Klinedinst and M. J. Domeniconi, *This Journal*, **127,** 530 (1980).
15. J. Devynck, A. Petit, M. C. Brage, and J. P. Descroix, Abstract 263, p. 423, The Electrochemical Society Extended Abstracts, Vol. 82-2, Detroit, MI, Oct. 17-21, 1982.
16. D. A. Long and R. T. Bailley, *Trans. Faraday Soc.*, **59,** 594 (1963).
17. J. P. Gabano and P. Lenfant, Abstract 37, p. 101, The Electrochemical Society Extended, Abstracts, Vol. 72-2, Los Angeles, Oct. 14-19, 1979.
18. M. Stern, and A. L. Geary, *This Journal*, **104,** 56 (1957).
19. G. E. Blomgren, T. Leger, M. L. Kronenberg, T. Kalnoki-Kio, and R. J. Brodd, in "11th International Power Sources Conferences," Brighton, England (1978).
20. W. K. Behl, *This Journal*, **127,** 1444 (1980).
21. J. R. Driscoll, G. L. Holleck, and D. E. Tolland, in "Proceedings of the 27th Power Sources Conference," Atlantic City, NJ, June 21-24, 1976, p. 28.
22. N. Doddapaneni, "Final Report for Period 10 April to 9 May 1982," ERADCOM, Fort Monmouth, NJ (1982).
23. G. L. Holleck and M. J. Turchan, in "Record of the Tenth Intersociety Energy Conversion Engineering Conference," Newark, Delaware, Aug. 18-22, 1975.
24. M. Domeniconi, K. Klinedinst, N. Marincic, C. Schlaikjer, R. Staniewicz, and L. Swette, Contract no. N-00014-76-C-0524, Oct. 1977.

Pore Development during Selective Leaching

A. D. Tomsett, D. J. Young,* and M. S. Wainwright

School of Chemical Engineering and Industrial Chemistry, University of New South Wales, Kensington, New South Wales 2033, Australia

ABSTRACT

The leaching kinetics of a Cu-50 weight percent Al alloy in aqueous NaOH have been studied. The product of the reaction, known as Raney copper, an important industrial catalyst, consists almost entirely of highly porous copper. In forming this material, the Al is selectively dissolved from the alloy, the rate of the leaching reaction being controlled by liquid-phase diffusion within the pores of the leach residue. At constant temperature, the spacing of these pores increases as the leaching rate decreases. As the temperature decreases, so does the pore spacing. The conversion of the original alloy phase, $CuAl_2$, to porous copper is considered as an example of a phase transformation, and the pore spacing is taken as a measure of the distance over which Cu-Al segregation must occur within the alloy. Models based on volume diffusion adjacent to the reaction front and on boundary diffusion at the front are used to describe the relationship between pore spacing and reaction rate. Application of these models to the experimental data, for a temperature of 20°C, yields estimates of $D = 6 \times 10^{-12}$ cm^2s^{-1} with an activation energy of 53 ± 2 kJ for volume diffusion and $D_B = 5 \times 10^{-10}$ cm^2s^{-1} with an activation energy of 62 ± 4 kJ for boundary diffusion. It is concluded that alloy segregation takes place at the leach reaction front by a mechanism of boundary diffusion.

The selective leaching in alkaline solution of aluminum from alloys to leave a porous, spongy residue is a well-known, but incompletely understood, phenomenon. Reactions of this type have been exploited since the days of Raney (1, 2) in the manufacture of high surface-area metal catalysts. The widespread use of Raney catalysts in a variety of chemical processes adds practical interest to fundamental questions about the nature of the leaching mechanism. Since the leach reaction determines the product morphology, it is possible that an understanding of the leaching mechanism will lead to the ability to control the morphology and, hence, the catalyst properties. The purpose of this study is to examine the relationships between leaching kinetics and product morphology.

A series of studies (3-6) has shown that caustic leaching of aluminum and zinc from alloys based on copper, nickel, and cobalt proceeds according to parabolic kinetics

$$X^2 = k_p t \qquad [1]$$

where X is the thickness of the reaction-product rim formed in time, t. The magnitude of k_p is found to be independent of the orientation of the parent alloy with respect to reaction direction. From these observations, it is concluded that the leach reaction rate is controlled by diffusion through the liquid occupying the pores of the reaction product. This conclusion is consistent with the magnitude of k_p and its activation energy.

During these reactions, the microstructure of the precursor alloy is reproduced in the reaction product. An example is shown in Fig. 1, where a Cu-Al alloy consisting of $CuAl_2$ grains separated by frozen Al-$CuAl_2$ eutectic is seen to produce grains of porous copper separated by void space. This observation, together with the fact that copper solubility in strong alkali is negligible, leads to the conclusion that the mechanism is one of selective dissolution and not dissolution reprecipitation. Similar findings apply to Ni-Al and Co-Al alloys.

In all cases, the product material is almost entirely composed of noble metal and is highly porous. The question therefore arises as to how rearrangement occurs within the solid to accommodate the loss of a large fraction of its constituent atoms in a reaction of the type

$$CuAl_2(s) + 2\,OH^- + 6H_2O = Cu(s) + 2Al(OH)_4^-(aq) + 3H_{2(g)} \qquad [2]$$

The reaction is presented schematically in Fig. 2. The highly ordered product morphology depicted is based on the observation (7) that pore sizes are very similar.

Theory

The transformation of a homogeneous parent phase into a highly ordered two-phase structure in which the reaction products appear in lamellar or rodlike form is a phenomenon familiar to metallurgists. Reaction morphologies of this sort are observed in eutectic and eutectoid transformations (8, 9)

$$\gamma \rightarrow \alpha + \beta \qquad [3]$$

and in discontinuous precipitation (10)

$$\alpha \rightarrow \alpha' + \beta \qquad [4]$$

where α, β, and γ denote different phases and α' denotes a distinctly different composition of a solid-solution phase α. In addition, reactions leading to the production of these cellular morphologies have been observed (11-13) in cases of reaction of the parent phase with an externally supplied gaseous reactant, R. Reactions of this type may be written

$$\gamma + R \rightarrow \alpha + \beta \qquad [5]$$

Although selective dissolution reactions have not hitherto been described in these terms, they appear to fall within this latter class. A brief review of the theory of cellular phase-transformation kinetics is therefore pertinent.

A simple description of transformation kinetics was first provided by Zener (14) on the supposition that segregation of the parent-phase constituent elements toward the tips of the advancing α and β lamellae occurs by diffusion within the parent phase itself. Assuming further that α-β-γ triple-phase junctions are at mechanical equilibrium, then the velocity, v, at which the reaction front advances into the parent phase, is given by

$$v = \frac{D}{S}\,\frac{A}{a}\left(1 - \frac{S_e}{S}\right) \qquad [6]$$

where D is the chemical diffusion coefficient in γ, S is

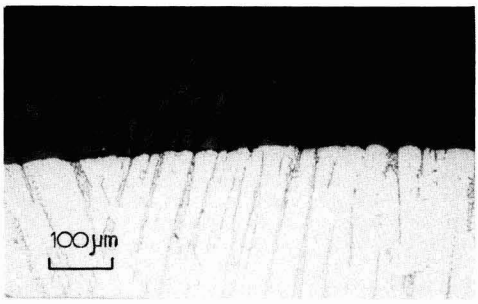


Fig. 1. Micrograph of section through partially leached Al-50Cu alloy

*Electrochemical Society Active Member.

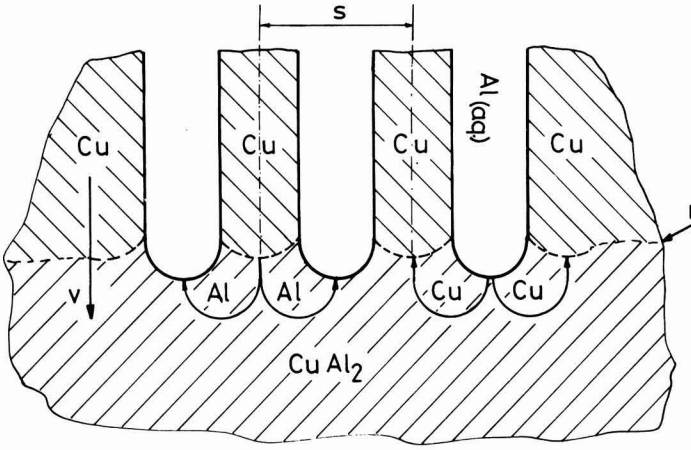


Fig. 2. Schematic representation of a $CuAl_2$-Cu grain and the alloy-reaction product interface.

the combined width of α and β lamellae, A is the relative supersaturation within the parent phase, and a is a geometric constant of order unity. The quantity S_c is a critical lamellar spacing at which the free energy per unit volume of two-phase product equals that of the parent phase and at which reaction ceases. This term arises through the surface free energy associated with the α-β interfaces which are created in the reaction. A complete local-equilibrium solution for eutectoids was provided by Hillert (15) by incorporating the Gibbs-Thompson effect for the pressure-composition variation in the parent phase along the curved interfaces, thereby evaluating the compositional differences driving the diffusion. Hillert in this way shows that

$$A = \frac{1}{f^{\alpha} f^{\beta}} \frac{C^{\gamma\alpha} - C^{\gamma\beta}}{C^{\beta} - C^{\alpha}} \qquad [7]$$

where $(C^{\gamma\alpha} - C^{\gamma\beta})/(C^{\beta} - C^{\alpha})$ is the ratio of the lateral concentration difference in front of limiting flat interfaces to that between the product phases. The constants f^{α} and f^{β} are, respectively, the ratios S^{α}/S and S^{β}/S; they are determined by the parent-phase composition.

Because the relationship between ν, S, and relative supersaturation permits an infinite number of solutions, a further condition must be imposed. Zener (14) and Hillert (15) suggest that the system stabilizes at a value of S for which ν is a maximum. If so, then

$$S = 2S_c = \frac{2\sigma^{\alpha\beta}}{RT(C^{\gamma\alpha} - C^{\gamma\beta})} \qquad [8]$$

where R is the gas constant and $\sigma^{\alpha\beta}$ is surface energy of the α-β phase boundary.

Alternatively, it has been proposed (16-18) that the rate of entropy production is a maximum, whence

$$S = 3S_c = 3\sigma^{\alpha\beta}/RT(C^{\gamma\alpha} - C^{\gamma\beta}) \qquad [9]$$

The consequences of the two optimizations are seen to be similar. Substitution from Eq. [7] and [9] to Eq. [6] leads to the result

$$\nu = \frac{2D}{af^{\alpha}f^{\beta}RT} \frac{\sigma^{\alpha\beta}}{C^{\alpha} - C^{\beta}} \frac{1}{S^2} \qquad [10]$$

A preferred mechanism of alloy segregation may be diffusion along the interface between the parent and product phases. In the present case, where $CuAl_2$ of tetragonal symmetry is converted to Cu of cubic symmetry, a discontinuous boundary between the two phases will certainly be formed. Boundary-diffusion theories were developed for discontinuous-precipitation reactions by Turnbull (10) and Cahn (16) and have been adapted to the eutectoid transformation by others (19-21). The resulting kinetic expression is

$$\nu = \frac{24D_B\delta K}{aRT} \frac{f^{\alpha}f^{\beta}\sigma^{\alpha\beta}}{C^{\alpha} - C^{\beta}} \frac{1}{S^3} \qquad [11]$$

where maximum entropy production has been adopted as the reaction constraint. In Eq. [11], D_B is the boundary diffusion coefficient, δ is the boundary width, and K is the coefficient representing partition of solute between bulk and boundary.

In the selective dissolution process represented by Eq. [2], the product phases are the liquid solution which fills the newly created pores and the copper which separates the pores. In terms of the foregoing theory, the spacing, S, which characterizes the product morphology, is given by the sum of the pore diameter and the width of the intervening copper region. Both size parameters are measurable, as is the reaction velocity, ν.

This paper reports measurements of pore spacings as a function of the selective-dissolution reaction rate. The relationship between pore spacing and reaction velocity is used to test the applicability of phase-transformation theory to the leaching process.

Experimental

An alloy of composition Cu-50.3 weight percent (w/o) Al was prepared by induction melting aluminum (99.9% pure) and copper (99.5% pure) using the method of Marsden *et al.* (22). For the leaching kinetic experiments, the homogeneous melt was cast onto a chilled copper mold to form a plate from which rectangular prisms were cut. The cast alloy consisted of $CuAl_2$, plus frozen Al-$CuAl_2$ eutectic. The prisms were reacted with thrice the amount of 20% w/w aqueous NaOH required to completely react with the aluminum in the alloy. This reaction was carried out isothermally at various temperatures. Partially extracted alloy pieces were removed after various reaction times of up to 24h and thoroughly washed with distilled water until the pH of the wash water was seven. The samples were then mounted in cold setting resin, cross sectioned at right angles to an original face of the specimen, and polished to a 1 μm finish. The depth of chemical attack was measured under an optical microscope using a graduated eyepiece.

Since the leaching reaction kinetics were parabolic, the average reaction rate over the complete course of leaching was lower for a large alloy particle than for a small one. It was therefore possible to investigate reaction morphology as a function of average leaching rate by using alloy samples having discrete particle size ranges. Samples consisting of a large number of particles were prepared by crushing and screening the alloy to yield approximately spherical particles in the size ranges

Table I. Surface and pore structure data for particles of alloy that are fully leached at 293 K

Particle size (μm)	Surface area (m^2g^{-1})	Pore diam (Å) $2r_p$	Pore diam (Å) $2r_a$	V_p (cm^3g^{-1})	Crystallite size (Å)	Interpore distance (Å)
105-180	31.44	236	268	0.214	88,85	129
353-420	25.28	316	316	0.203	84,79	177
710-850	23.48	342	330	0.197	87	194
1000-1180	23.96	338	328	0.197	89,81	192
1400-1676	23.89	342	324	0.197	85	194
2000-2360	21.35	382	366	0.195	79,85	218

specified in Table I. These samples were leached to completion at 20°C.

The extraction method used was similar to that reported by Friedrich *et al.* (4). A 40% w/w NaOH solution was added to the alloy pieces over a period of 0.75h so that the reaction temperature was kept to 20° ± 2.5°C. After extraction was complete, as determined by hydrogen evolution, the catalyst was thoroughly washed with distilled water until the pH of the wash water was seven.

The temperature dependence of the diffusion coefficient was also studied by leaching 1-1.18 mm particles at the temperatures given in Table II.

The composition of the alloy and leach residues was determined by atomic-absorption spectroscopy of acid-digested samples. The BET surface areas of the extracted materials were determined by a single-point chromatographic method (23).

Pore size distributions were calculated from nitrogen isotherms measured at −195°C, using a Micromeritics 2100E ORR surface area and pore-volume analyzer. Samples were transferred to the adsorption flask under water and evacuated at 130°C overnight. The degassed samples were weighed after completion of each experiment.

The crystallite size of the leach residues was estimated from x-ray line broadening of the Cu(200) diffraction line using the Scherrer equation, with corrections for instrumental broadening obtained from the silicon (220) diffraction line. The powdered catalysts were pyrophoric, and it was necessary to coat them with collodian prior to examination. CuK_α radiation was used, and the diffraction patterns were compared with those in the ASTM files to identify the compounds present.

Results

The interface between the unaffected alloy and the leach residue of the alloy (reacted at 50°C for 12h) is shown in Fig. 1. A clearly defined boundary which is parallel to the original alloy surface is discovered. As noted earlier, the $CuAl_2$ grains have leached to yield porous copper, and the eutectic material has been completely removed.

The thickness of the reaction-affected rim around the partially extracted alloy pieces, as a function of leaching time, is shown at various temperatures in Fig. 3. After an initial period of chemical-reaction control, the shapes of the curves indicate parabolic leaching kinetics. Therefore, the data have been replotted in Fig. 4, where the straight lines are the results of regression on Eq. [1]. An activation energy is determined from an Arrhenius plot for k_p and found to be 29 ± 2 $kJmol^{-1}$.

Table I gives the BET surface areas, pore radii, pore volumes, and crystallite sizes of the reaction product obtained from samples of various particle sizes. The pore volumes and mean pore radii are calculated from the nitrogen isotherm. The pore volume, V_p, is estimated from the amount of nitrogen adsorbed at a relative pressure of 0.99 and calculated as a normal liquid. The values of r_p correspond to the maxima in plots of $\Delta V_p/\Delta r_p$ *vs.* r_p. The pore size-distribution consists of a single, narrow peak. The average pore radius, r_a, is calculated by the equation for nonintersecting cylindrical pores, $r_a = 2V_p/S_{BET}$ (24).

The effect of extraction temperature on these properties is shown in Table II. Pore volumes are not measured in these experiments, and the average pore radius is calculated assuming V_p = 0.2 cm^3/g. The surface areas of

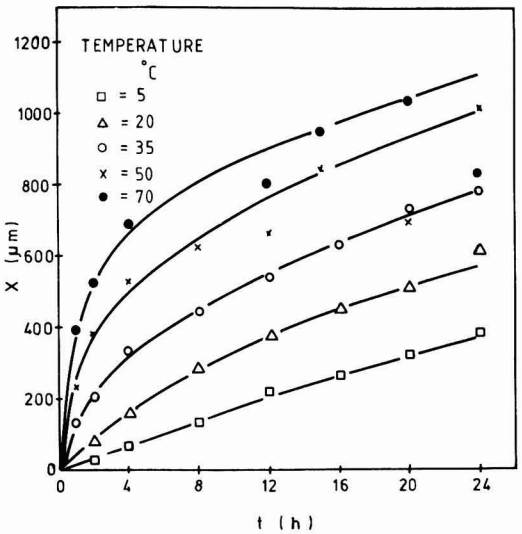


Fig. 3. Average thickness of reaction-affected rim as a function of leaching time.

Table II. The effect of the temperature of extraction on the surface area and pore structures of completely, leached 1.0-1.18 mm alloy particles[a]

Extraction temp (K)	Surface areas (m^2g^{-1}) S_{BET}[b]	Surface areas (m^2g^{-1}) S_{BET}	Pore diam (Å) $2r_p$	Crystallite size (Å)	Interpore distance (Å)
275	25.4	23.1	302	75	170
293	24.0	18.6	338	85	192
308	22.6	15.6	550	112	310
323	18.5	15.0	610	120	343
343	16.9	11.3	750	137	422
363	12.7	9.8	1076	146	606

[a] Data are for particles washed with 40% NaOH prior to washing with distilled water, unless otherwise stated.
[b] Particles washed with distilled water with no caustic wash.

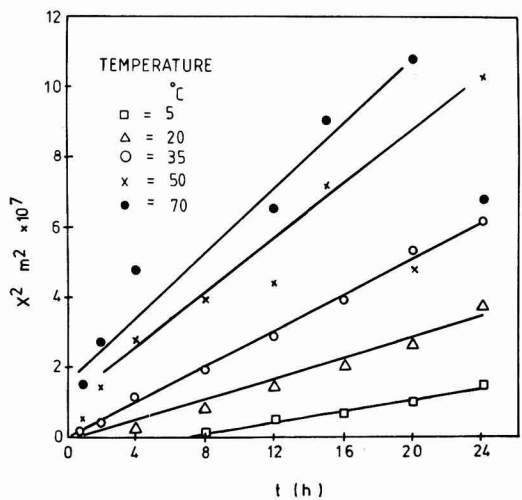


Fig. 4. Parabolic plots from Fig. 3

the copper are reported for samples with 40 w/o NaOH after washing with distilled water. The lower areas obtained after washing with NaOH are assumed to be due to removal of alumina produced in the reaction procedure. The atomic-absorption spectroscopy results show that in all leach residues, there is less than 3% aluminum, assumed to be present as alumina and evenly distributed over the reaction-product surface (15).

Discussion

The selective dissolution in alkali of aluminum from a Cu-50 w/o Al alloy proceeds according to parabolic kinetics, the reaction being controlled by liquid-phase diffusion within the reaction-product layer. Increasing the particle size of the alloy, which corresponds to decreasing the average reaction rate, results in a decrease in the surface area and an increase in the pore radius. However, the pore volume is approximately constant. Thus, the decrease in the average reaction rate results in an increase in the average diffusion distance, $\bar{S}$, at a fixed temperature. We now examine this correlation.

From Eq. [10] and [11], it is seen that the instantaneous reaction rate is related to $1/S^2$ for volume diffusion and $1/S^3$ for boundary diffusion. Because this rate varies with extent of reaction, the value of S also is predicted to vary. Because the measurements of pore size and copper crystallite size are obtained from the entire sample, they represent volume averages. It is therefore necessary to relate these averages to the instantaneous qualities. By definition

$$\overline{S^2} = \frac{\int S^2 dV}{\int dV}$$

where V represents volume. For spherical particles of radius B

$$\overline{S^2} = 3\int_0^B S^2 r^2 dr/B^3 \qquad [12]$$

where r is the radial coordinate within the sphere.

From Eq. [10], the diffusion distance is related to the diffusion coefficient and the velocity of the reaction front by

$$S^2 = \frac{\mathcal{K}D}{v} \qquad [13]$$

where

$$\mathcal{K} = 2\sigma^{CuP}/f^{Cu}f^{P}aRT(C^{Cu} - C^{P})$$

From Eq. [1] it follows that

$$v = \frac{dX}{dt} = \frac{k_p}{2X} \qquad [14]$$

Combining Eq. [13] and [14] yields

$$S^2 = \frac{2\mathcal{K}D}{k_p} X$$

which for a spherical particle becomes

$$S^2 = \frac{2\mathcal{K}D}{k_p}(B - r) \qquad [15]$$

Combination of Eq. [12] and [15], followed by integration, yields

$$\overline{S^2} = \frac{\mathcal{K}D}{2k_p} B \qquad [16]$$

The corresponding expression for boundary diffusion is found to be

$$\overline{S^3} = \frac{\mathcal{K}' D_B \delta K}{2k_p} B \qquad [17]$$

where

$$\mathcal{K}' = 24 f^{Cu}f^{P}\sigma^{CuP}/aRT(C^{Cu} - C^{P})$$

Equations [16] and [17] predict rather simple dependencies of $\bar{S}$ on B.

In order to calculate $\bar{S}$, both the pore diameter, $\bar{S}^P$, and the copper width, $\bar{S}^{Cu}$ are required. Knowing the pore volume and S^P, S^{Cu} is calculated on the presumption that the pores are uniform, cylindrical, and parallel. These presumptions are borne out by the shape of the N_2 desorption isotherms and by the agreement between r_p and r_a. Proceeding, then, on the basis that the pores' axes are arrayed on a square grid and that the intervening regions of solid are composed of pure, theoretically dense copper, the average interpore distances shown in Tables I and II are calculated. Similar values for $\bar{S}^{Cu}$ are calculated for hexagonally arrayed pores. Comparison of these numbers with the measured average crystallite sizes indicates poor agreement, although the trends with temperature are the same. Since average crystallite size is measured by x-ray line broadening, the average may be biased toward the smaller crystals in the total population. Because no analysis of the diffraction line shape has been performed, the values of $\bar{S}^{Cu}$ calculated from pore data are preferred.

Plots of $\overline{S^2}$ and $\overline{S^3}$ *vs.* B are shown in Fig. 5 and 6. In these plots, the first point, corresponding to a radius of 71 μm, is disregarded because the leaching kinetics (Fig. 4) show that the leaching reaction is under chemical-reaction control at this time. In both plots, the remaining data conform reasonably well with the predicted straight-line relationship. The good fit achieved by the two models does not differ at a statistically significant level. It is therefore concluded that pore spacing is indeed related to leaching rate through the alloy-segregation process. The two possible mechanisms of segregation, however, cannot be distinguished on this basis.

The volume diffusion coefficient is calculated from the slope of the $\overline{S^2}$ *vs.* B plot using Eq. [16] and the following values: $a = 1$; $f^{Cu} = 0.36$; $f^{P} = 0.64$; $\sigma^{CuP} = 300$ erg cm^{-2}; $C^{Cu} = 0.13$ mol cm^{-3}; $C^{P} = 0$; and $k_p = 3.97 \times 10^{-8}$ cm^{2}s^{-1}. The value obtained is $D = 6 \times 10^{-12}$ cm^{2}s^{-1}. Values for the diffusion coefficient in $CuAl_2$ are given by Smithells (26). Extrapolation of this high temperature data to 20°C yields a calculated value of 1×10^{-23} cm^{2}s^{-1}. In comparison, the value suggested by the application of the volume diffusion mechanism to the present results is seen to be rather high. A value of 1×10^{-12} cm^{2}s^{-1} has been deduced by Pickering and Wagner (27) for the diffusion of copper in a copper-gold alloy at 25°C and has been attributed to a divacancy mechanism. Such a mechanism might be oper-

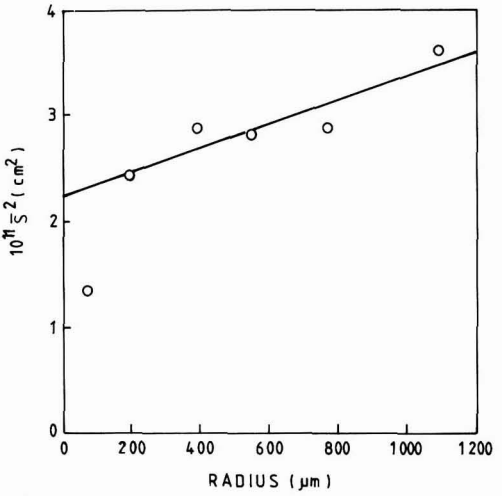


Fig. 5. Average diffusion distance squared as a function of particle radius.

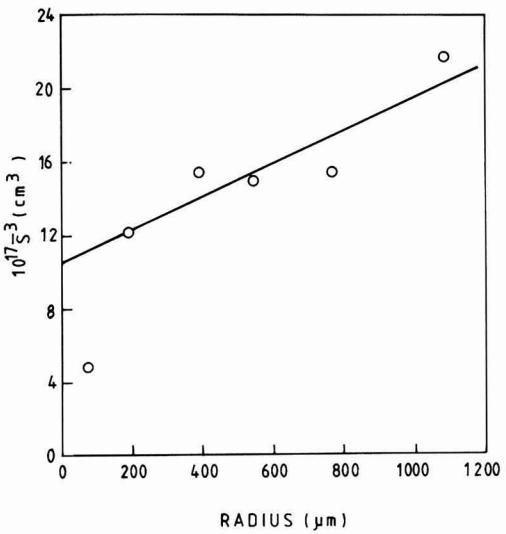


Fig. 6. Average diffusion distance cubed as a function of particle radius.

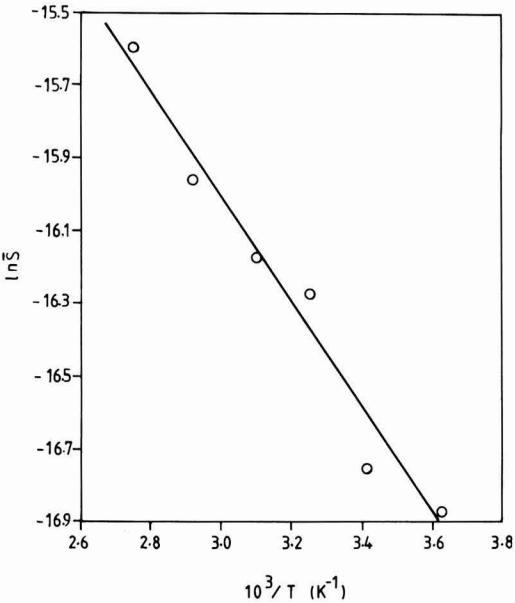


Fig. 7. Arrhenius plot according to Eq. [18] and [19]

ative in the present case, but no independent evidence for it exists.

If alloy segregation occurs via boundary diffusion, then Eq. [17] applies. In this case, the slope of the $\overline{S^3}$ *vs.* B plot leads to the estimate

$$D_B \delta K = 1 \times 10^{-16} \text{ cm}^3\text{s}^{-1}$$

Using the values $\delta = 10$Å and $K = 2$, it is found that $D_B = 5 \times 10^{-10}$ cm^{2}s^{-1}. Because of the absence of information on the $CuAl_2$/Cu boundary diffusion properties, it is difficult to comment on this value.

The temperature dependence of $\bar{S}$ can be deduced from Eq. [16] and [17] for the two modes of alloy segregation. Logarithmic differentiation for particles of fixed size leads to

$$\frac{\partial \ln \overline{S^2}}{\partial(1/T)} = -(Q_V - E_A)/R \qquad [18]$$

$$\frac{\partial \ln \overline{S^3}}{\partial(1/T)} = -(Q_B - E_A)/R \qquad [19]$$

where the linear term in T has been neglected. Here, Q_V is the activation energy for volume diffusion, Q_B the activation energy for boundary diffusion, and E_A the activation energy for the leaching reaction. The results in Table II for alloy particles of the same size, leached to completion at different temperatures, yield $\bar{S}$ as a function of T. These data are used to construct the Arrhenius plot shown in Fig. 7. From the slope of this plot and the measured value $E_A = 29$ kJ, it is calculated that if volume diffusion is operative, then $Q_V = 53 \pm 2$ kJ; whereas, if boundary diffusion is in effect, then $Q_B = 62 \pm 4$ kJ.

Activation energies for volume diffusion in $CuAl_2$ and Cu have been reported (26) as 127 and 211 kJ, respectively. The value estimated from the application of the volume diffusion model to the present results is seen to be quite inconsistent with these values. On the other hand, the value of Q_B estimated from the boundary diffusion model is about half the value expected for volume diffusion in $CuAl_2$ and is therefore quite reasonable.

The volume diffusion model has been found to lead to an inordinately low estimate of the activation energy. It also yields a remarkably high diffusion coefficient, for which no independent supporting evidence exists. For these reasons, the hypothesis that alloy segregation occurs via volume diffusion is rejected. Conversely, the boundary diffusion model has been found to yield an activation energy of the expected magnitude and a diffusion coefficient for which there is no reason to reject. In addition, the model correctly predicts the relationship between spacing and reaction rate. It is therefore concluded that alloy segregation at the leach reaction front occurs by a mechanism of boundary diffusion.

The qualitative consequences are clear. At a given temperature, the alloy diffusion coefficient is fixed, and the pore spacing is controlled by the leach reaction rate. An increase in reaction rate leads to a decrease in pore spacing. Because the pore volume is fixed by the leachable content of the alloy, a decrease in pore spacing leads to an increase in the number of pores and, hence, an increase in surface area. These effects have been demonstrated in the present work by varying the average leaching rate through particle size control. Other methods of controlling the reaction rate would presumably achieve the same purpose.

Changing the reaction temperature affects the leaching rate and the alloy diffusion coefficient. Because the activation energy for alloy diffusion is significantly greater than for leach reaction, the effect on solid diffusion outweighs the other. Thus, an increase in temperature increases the alloy segregation distance more than it does the leaching rate. Consequently, a decrease in pore spacing and an increase in surface area is achieved for alloy particles of fixed size by lowering the temperature. These effects have also been demonstrated in the present work.

Acknowledgments

The financial assistance of the Australian Research Grants Scheme is gratefully acknowledged. A. D. Tomsett acknowledges support from the Commonwealth Government Postgraduate Scheme.

Manuscript received Nov. 29, 1983.

The University of New South Wales assisted in meeting the publication costs of this article.

REFERENCES

1. M. Raney, U.S. Pat. 1,563,587 (1925).
2. M. Raney, *Ind. Eng. Chem.*, **32**, 1199 (1940).
3. D. J. Young, M. S. Wainwright, and R. B. Anderson, *J. Catal.*, **64**, 116 (1980).
4. J. B. Friedrich, D. J. Young, and M. S. Wainwright, *This*

Journal, **128**, 1840 (1981).
5. J. B. Friedrich, D.J. Young, and M. S. Wainwright, *ibid.* **128**, 1845 (1981).
6. J. P. Orchard, A. D. Tomsett, M. S. Wainwright, and D. J. Young, *J. Catal.*, **84**, 189 (1983).
7. J. B. Friedrich, M. S. Wainwright, and D. J. Young, *ibid.*, **80**, 1 (1983).
8. P. G. Shewman, "Transformations in Metals," p. 185, McGraw-Hill Book Company, New York (1969).
9. V. F. Zackay and H. I. Aaronson, Editors, "Decomposition of Austenite by Diffusional Processes," pp. 39, 131, Interscience Publishers (1962).
10. D. Turnbull, *Acta Metall.*, **3**, 55 (1955).
11. D. J. Young, W. W. Smeltzer, and J. S. Kirkaldy, *This Journal*, **123**, 1758 (1976).
12. J. Fridberg and M. Hillert, *Acta Metall.*, **25**, 19 (1977).
13. H. H. Hindam and W. W. Smeltzer, *This Journal*, **127**, 1419 (1980).
14. C. Zener, *Trans. AIME*, **167**, 550 (1946).
15. M. Hillert, *Jernkont. Ann.*, **141**, 757 (1957).
16. J. W. Cahn, *Acta Metall.*, **7**, 18 (1959).
17. M. P. Puls and J. S. Kirkaldy, *Metall. Trans.*, **3**, 2777 (1972).
18. J. S. Kirkaldy and R. C. Sharma, *Acta. Metall.*, **28**, 1009 (1980).
19. J. M. Shapiro and J. S. Kirkaldy, *ibid.*, **16**, 579 (1968).
20. M. Hillert, Monograph and Report Series No. 33, p. 231, Institute of Metals, London (1969).
21. B. Sundquist, *Acta Metall.*, **16**, 1413 (1968).
22. W. L. Marsden, M. S. Wainwright, and J. B. Friedrich, *Ind. Eng. Chem. Prod. Res. Dev.*, **19**, 551 (1980).
23. J. W. Evans, M. S. Wainwright, A. J. Bridgewater, and D. J. Young, *Appl. Catal.*, **7**, 75 (1983).
24. S. J. Gregg and K. S. W. Sing, "Adsorption, Surface Area and Porosity," p. 165, Academic Press, New York (1978).
25. S. D. Robertson and R. B. Anderson, *J. Catal.*, **23**, 286 (1971).
26. C. J. Smithells, "Metals Reference Book," Vol. 2, Butterworths, London (1955).
27. H. W. Pickering and C. Wagner, *This Journal*, **114**, 698 (1967).

Surface Dislocation Pinning by Adsorbed Ions and Water Molecules

C. J. van der Wekken

Laboratory of Metallurgy, Delft University of Technology, 2628 AL Delft, The Netherlands

ABSTRACT

Gold wire specimens were subjected to creep tests under constant load in various salt solutions. The effect of cathodic or anodic polarization on the creep behavior in deaerated acid solutions was found to depend on the nature of the ions present in the solution. Specific adsorption is a necessary but not sufficient condition for the pinning of surface dislocations by ions. A simple model for the observed rehbinder effects is proposed.

It has been shown previously (1, 2) that the effects of cathodic polarization on the creep rate of gold wire specimens cannot be explained in terms of changes in the surface stress. Instead, it was concluded from the experimental observations that in deaerated alkaline solutions specifically adsorbed hydroxyl ions have a strong pinning effect on surface dislocations in the metal. As the OH^- ions are desorbed during cathodic polarization near and beyond the point of zero charge (pzc), unpinning occurs which results in extra strain. Similar extra strain effects confirming the role of adsorbed OH^- ions were observed to occur when the pH was decreased by adding acid to the test solutions (2).

Measurements in acid $NaClO_4$ solutions (2) suggested that perchlorate ions are also able to pin dislocations. The effects were much smaller, however, than the effects caused by hydroxyl ions. In contrast Cl^- ions were concluded not to pin dislocations (1) since no extra strain was measured at potentials near the pzc in acid chloride solutions.

Extra strain effects ascribed to dislocation pinning by adsorbed water molecules (2) have been measured at potentials below −1000 mV *vs.* SCE. However, in the present study of effects due to adsorbed ions, the attention is focused on potentials above −1000 mV. The specimen is loaded at a potential E_{def} and subsequently polarized in the direction of the pzc. Dislocation pinning by anions is detected during cathodic pulsing after loading at $E_{def} >$ pzc. Pinning by cations may occur at $E_{def} <$ pzc and gives rise to extra strain during subsequent anodic pulsing. A variety of test solutions was employed in order to gain more insight into the nature of the dislocation pinning processes at the metal surface.

Experimental Procedure

The test apparatus has been described previously (1). The experimental procedure was essentially similar to that followed earlier (2). The annealed 99.999% pure gold wires of 0.15 μm diam and an average grain size of 15 μm were loaded in deaerated solutions to a stress of 85 MPa. The test solutions employed, prepared from reagent grade chemicals and high purity deionized (Milli-Q) water, are listed in Table I. The pH values of the solutions were measured at room temperature. The concentrations employed were 1*M* except for a 0.2*M* TlAc solution. The reasons for this lower concentration were the high cost of the chemical and its toxicity. Since earlier measurements (2) showed that larger effects could be expected at ~50°C than at room temperature, the present tests were performed at 50°C. After deaerating the test solutions and before applying the load, the specimen surface was prereduced for 1 min at −1300 mV, followed by a 1 min pulse at −800 mV *vs.* SCE.

Possible anion pinning was investigated by loading at either +400 or 0 mV and subsequently subjecting the specimen to a series of 1 min pulses of increasing magnitude in the cathodic direction, similar to the procedure employed earlier (1, 2).

In order to measure dislocation pinning by cations, the specimens were loaded at −800 mV *vs.* SCE and subjected to 1 min potential intervals following the sequence

Table I. Experimental test conditions and conclusions regarding dislocation pinning by various ions

Test solution	pH	E_{def} *vs.* SCE	Direction of potential pulses	Conclusion: extra strain due to dislocation pinning by
1*M* $NaClO_4$	0.6	0 mV	cathodic	ClO_4^-
1*M* Na_2SO_4	0.6	0 mV	cathodic	SO_4^{2-} (HSO_4^-)
1*M* $NaNO_3$	0.6	+400 mV	cathodic	NO_3^-
1*M* CsCl	0.6	+400 mV	cathodic	—
1*M* K I	0.6	0	cathodic	—
0.2*M* Tl Ac	4.2	+400 mV	cathodic	—
1*M* $NaClO_4$	0.6	−800 mV	anodic	—
1*M* CsCl	0.6	−800 mV	anodic	Cs^+
0.2*M* Tl Ac	4.2	−400 mV	anodic	—

−800, −600, −800, −400, −800, −200, −800, 0, −800, +200, −800, +400 mV. In the TlAc solution the specimen wire was loaded at E_{def} = −400 mV.

Results and Discussion

The extra strain effects resulting from the applied potential changes were measured in accordance with the definition given earlier (1) and plotted in extra strain-potential pulse (ES-PP) diagrams as shown in Fig. 1. A comparison between the extra strains measured previously in alkaline solutions (2) and the results presented in Fig. 1 shows that the effects measured in all the acid test solutions presently investigated are much smaller. If the present effects are also associated with surface dislocation pinning by adsorbed anions or cations, the pinning species can be identified. A list of pinning and non-pinning ions based on Fig. 1 can be derived. The result is shown in Table I. Considering the magnitude of the observed peaks in the ES-PP diagrams of Fig. 1 and taking into account the large effects caused by OH^- ions in previous studies, the dislocation pinning strength of adsorbed anions can be concluded to decrease as follows

$$OH^- >> ClO_4^- > SO_4^{2-} > NO_3^- > Cl^- = I^- = 0 \quad [1]$$

Literature data (3, 4) suggest that hydroxyl ions and Cl^- ions are adsorbed on gold with similar strength.

Taking the change in the pzc in 0.1*M* solutions (5) as a measure for the strength of specific adsorption on polycrystalline gold, then, yields the following sequence for the anions

$$I^- > OH^- \simeq Cl^- > NO_3^- > SO_4^{2-} > ClO_4^- \quad [2]$$

Comparing the pinning strength [1] and the strength of specific adsorption [2], it is observed that the sequences are reversed except for the position of OH^-. The observations for the CsCl solution constitute the first example of a rehbinder effect occurring during anodic polarization. Cs^+ cations, which are known to adsorb specifically on Hg, can be concluded from the present observations to adsorb specifically on gold as well. The large Tl^+ ions are probably adsorbed stronger than Cs^+. The fact that no extra strain effect was observed in the (less concentrated) Tl-Ac solution suggests that, probably, the sequences of pinning strength and specific adsorption strength for cations are also reversed. Earlier observations (1) indicated that not specifically adsorbed ions, *e.g.*, the cations in KCl and NaCl solutions, have some influence on the observed rehbinder effects. However, a necessary conditions for any extra strain effect in the potential region around the pzc is the occurrence of specific adsorption. If cathodic polarization is applied beyond −1000 mV SCE, a second peak is measured in the ES-PP diagram. This peak has been attributed to pinning by adsorbed water molecules (2).

It can be concluded from the available information that the observed rehbinder effects are primarily determined by contact adsorbed species in the first layer next to the metal surface.

A simple model for surface dislocation pinning in electrolyte solutions.—Figure 2 represents an example of a dislocation with Burgers vector b emerging at the metal surface. As the dislocation moves under the influence of a stress, a slip step is formed. Adsorbed ions I and water molecules W are present in the first adsorbed layer on the metal surface. As the area of the slip step is extended, the dislocation will disrupt the structure of the adsorbed layer. This implies that various interactions between metal atoms, ions, and water molecules will be broken (see Fig. 2). Previous explanations (6, 7) of rehbinder effects were based on the assumption that the energy necessary for the creation of a new surface area would determine the formation rate of new slip steps. The surface stress was considered to be a rate-determining parameter for the deformation process in the surface layer of the specimen. It is clear, however, that the surface stress is a macroscopic quantity which is related to some average value of the interactions mentioned above. It is to be expected that a surface dislocation moving under a certain stress will be stopped (pinned) by the strongest obstacles on its path. Let us consider a situation as represented in Fig. 2 and let the interactions I-Me and W-Me be strong. In that case, in addition to Me-Me bonds, I-W and W-W bonds across the slip plane must be broken if the dislocation is to move. The strongest of the latter two interactions will be likely to function as a barrier (pinning point) for further movement. Suppose that I-W bonds are pinning certain dislocations at a certain electrode potential. The pinning will be released as the ions I are desorbed by a change in electrode potential. The dislocation will then continue its movement in the slip plane and further on experience a weaker pinning by W-W interactions across

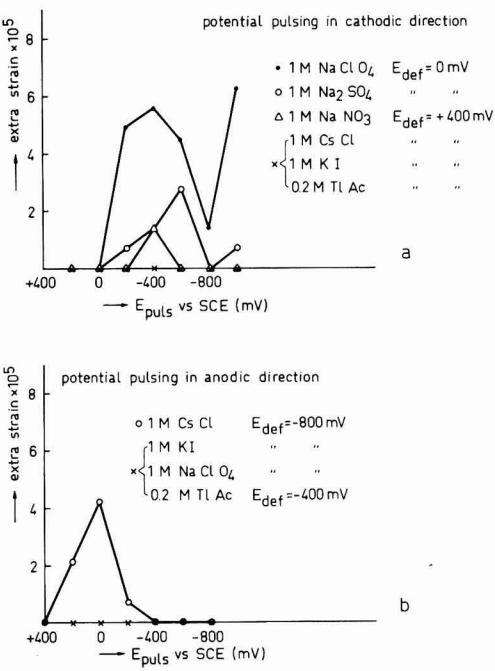


Fig. 1. Extra strain effects measured in deaerated acid salt solutions. a: Loading at a potential E_{def} above pzc and potential pulsing in cathodic direction. b: Loading at a potential E_{def} below pzc and potential pulsing in anodic direction.

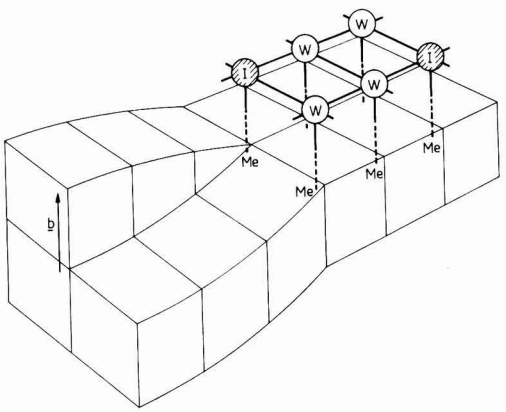


Fig. 2. Screw dislocation with Burgers vector *b* emerging at the surface of a metal electrode covered with contact adsorbed ions and water molecules.

its path. This type of pinning will be released as the adsorbed water is decomposed at potentials below −1000 mV. If the I-W interactions at the surface are weaker than the W-W bonds, pinning will only occur by the W-W interactions and no first peak will be measured in the ES-PP diagram. This is observed in the case of chloride solutions after loading at potentials anodic to the pzc and subsequent pulsing in the cathodic direction. Stronger I-W interactions can be expected for ions, which are known to be more strongly hydrated in the bulk of the solution. It is known that the strength of specific adsorption of ions and the strength of their interaction with hydration water molecules tends to be complementary (8). At the specimen surface, the I-W interaction may similarly increase as the strength of specific adsorption decreases. This could explain the reversed sequences [1] and [2] noted above. OH^- ions constitute an exception. These ions fit very well in the water structure. They are known as order producing ions (8, 9) in solutions, as is the case with F^-. However, the nature of their interactions with water molecules is different. Busing and Hornig (10) concluded that OH^- ions in aqueous solutions form a strong hydrogen bond with at least one water molecule. Not all surrounding water molecules are bonded with equal strength. Strong hydrogen bonds are expected to be retained in the case of specific adsorption. OH^- ions are thus strongly adsorbed, and simultaneously they have strong interactions with surrounding adsorbed water molecules. The strong I-W interactions in this case are probably the explanation for the large extra strain effects found in alkaline solutions.

Figure 2 represents only one possible example of the configuration of the lattice at the specimen surface around an emerging dislocation. Other situations are possible: for example, with the Burgers vector parallel to the specimen surface. What will happen in detail at the surface during slip depends on the relative strength of the various interactions between metal, adsorbed ions, and adsorbed water molecules, as well as on the local geometry of the slip process. It seems reasonable and in accordance with the experimental observations to conclude that the I-W and W-W interactions largely control the extra strain effects. The strength of the W-Me interactions is potential dependent. This has consequences for the magnitude of the second peak in the ES-PP diagram, as shown earlier (2). We may expect, for example, in the case of very weak Me-W interactions during loading—for gold at potentials near the pzc (2)—that during loading Me-W interactions will be broken before W-W interactions. Dislocation pinning will consequently be less, and a smaller second peak will be the result. This was indeed observed (2).

In the above discussion, the use of the term dislocation pinning is not necessarily meant to imply that dislocation movement is permanently blocked. It may well be that the stressed dislocations jump from one barrier to the next one of a similar type. Instead of "pinning," we could speak of "drag" in that case. From the present tests, it is not clear which term is more appropriate. Both more or less permanent pinning of dislocations as well as drag may play a role. While during loading the stress on the specimen is continually increased, the effective stress on dislocations during the primary creep stage after loading will decrease due to continuing work hardening of the specimen. The decreasing effective stress will lead to conditions where the dislocations become really pinned during longer periods at certain barriers. The removal of these barriers at the metal surface by means of variations in the potential is at the origin of the observed extra strain effects.

Conclusions

1. Specific adsorption is a necessary, but not a sufficient condition for dislocation pinning by ions.
2. The dislocation pinning strength of anions on gold has been observed to decrease according to the sequence

$$OH^- >> ClO_4^- > SO_4^{2-} > NO_3^- > Cl^- = I^- = 0$$

3. Cs^+ cations have been found to pin dislocations.
4. The pinning strength of adsorbed ions has been attributed to the strength of the interactions between the adsorbed ions and adsorbed water molecules. No extra strain effects due to the ions are observed when these interactions are weaker than the water-water interactions in the contact adsorbed layer.
5. The second peak in the ES-PP diagrams is due to interactions between adsorbed water molecules.
6. Dislocations are mechanical microprobes which can be used for the study of the structure of the compact double layer.

Manuscript submitted Oct. 11, 1983; revised manuscript received May 29, 1984.

Delft University of Technology assisted in meeting the publication costs of this article.

REFERENCES

1. C. J. van der Wekken, *This Journal*, **129**, 706 (1982).
2. C. J. van der Wekken, in "Extended Abstracts, 33rd ISE Meeting," M. Costa, Editor p. 28, ISE Lyon, (1982).
3. K.-F. Lin, *This Journal*, **125**, 1077 (1978).
4. D. D. Bodé, Jr., T. N. Anderson, and H. Eyring, *J. Phys. Chem.*, **71**, 792 (1967).
5. G. M. Schmid and M. E. Curley-Fiorino, in "Encyclopedia of Electrochemistry of the Elements," Vol. IV, A. J. Bard, Editor, p. 122, Dekker, New York (1975).
6. A. Pfützenreuter and G. Masing, *Z. Metallk.*, **42**, 361 (1951).
7. V. I. Likhtman, L. A. Kochanova, D. I. Leikis, and E. D. Shchukin, *Elektrokhimiya*, **5**, 729 (1969).
8. B. E. Conway, *Adv. Colloid Interf. Sci.*, **8**, 91 (1977).
9. G. R. Choppin and K. Buijs, *J. Chem. Phys.*, **39**, 2042 (1963).
10. W. R. Busing and D. F. Hornig, *J. Phys. Chem.*, **65**, 284 (1961).

AES/XPS Study of Transpassive Films on Iron in Nitrate Solution

M. Datta,* H. J. Mathieu, and D. Landolt*

Department of Materials, Swiss Federal Institute of Technology, CH-1007 Lausanne, Switzerland

ABSTRACT

Anodic films on iron formed in a forced convection system in the transpassive potential region in nitrate electrolytes at current densities up to 40 A/cm² have been studied by *in situ* coulometry and *ex situ* Auger electron spectroscopy (AES) and angle-resolved x-ray photoelectron spectroscopy (XPS). Qualitatively similar results on the variation of film thickness with applied current density are obtained by different methods. The transition from transpassive oxygen evolution to transpassive metal dissolution coincides with a marked decrease in film thickness and with the appearance of nitrogen in a reduced state at the metal-film interface.

Transpassive dissolution of iron and nickel in passivating electrolytes takes place at high current densities in the potential region beyond oxygen evolution and involves breakdown of passive films (1-3). Anodic films formed on iron and nickel in nitrate and chlorate electrolytes were investigated by Hoare and co-workers using potentiostatic polarization and coulometry in a stationary system (4-8). Their results showed that the film thickness increased in the passive potential region then decreased at the onset of the transpassive potential region. The behavior was attributed to an ion exchange mechanism (9), according to which electrolyte anions are incorporated into the film lattice by exchanging positions with oxygen ions leading to film dissolution. However, most of the data showing film thinning refer to a low current density region of exclusive oxygen evolution, and, therefore, their relation to transpassive dissolution, which occurs at much higher current densities, is not evident.

In a recent study, the present authors employed AES (Auger electron spectroscopy) and coulometry to investigate anodic films formed on nickel in the transpassive potential region in nitrate electrolytes under controlled hydrodynamic conditions in a flow channel cell (10). Results indicated that the passive film thickness reached its maximum as a function of current density in the oxygen evolution region. At higher current densities, nitrate ions were observed at the metal-oxide interface (10). In the present study, anodic films formed on iron in a concentrated nitrate electrolyte over a wide current density range in the transpassive potential region were investigated using XPS, AES, and coulometry. In particular, the study obtained information on the relationship among thickness, chemical nature of the films, and transpassive metal dissolution behavior. In addition to depth profiling, angle-resolved XPS was used for characterizing the films.

Experimental

Galvanostatic experiments were performed in a flow channel cell (11), through which the electrolyte was pumped at a constant linear velocity of 2.5 m/s. Cylindrical iron anodes (99.99%, single crystal,[1] [111] orientation), 8 mm diam were mechanically polished to 0.25 μm finish using diamond spray and ethanol as coolant. Only a part of the anode corresponding to the width of the channel (3 mm) was exposed to the electrolyte, while the remaining part was insulated by a Teflon spacer constituting the flow channel.

The applied anodic current density ranged from 1 mA/cm² to 40 A/cm². Anode potentials were recorded against a mercury sulfate electrode connected to the channel by a back-side capillary. The electrolyte solution (6*M* $NaNO_3$ + 0.1*M* NaOH) was prepared from analytical-grade chemicals and double-distilled water. An alkaline solution was employed to avoid self-activation of the anode after current interruption.

In coulometric studies, anodic oxide films formed at different current densities were reduced by a constant cathodic current (20 mA/cm²), and the quantity of charge for oxide reduction was evaluated from the measured potential-time traces. A switching system with mercury relays was employed for presetting anodic polarization time and for switching between anodic and cathodic currents. The anodic charge passed was kept small (0.5 C/cm²) to minimize possible changes in surface roughness due to dissolution. A digital oscilloscope (Explorer III, Nicolet Instruments) recorded anodic and cathodic potential transients.

For AES and XPS studies, anodically polarized electrodes were quickly removed from the cell, washed with distilled water, rinsed in ethanol, and dried in a cold air stream. They were kept in a desiccator until introduced into the UHV chamber of a combined XPS/AES system with double pass cylindrical mirror analyzer, differentially pumped raster ion gun, and x-ray source (Perkin-Elmer, Physical Electronics Division, Model 590/550 A). All samples were analyzed in the same position, corresponding to an angle of $\alpha = 42°$ between surface normal and CMA axis. In the XPS mode, the Mg x-ray source was operated at 10 keV and 40 mA with a pass energy of 50V. Binding energy calibration of the instrument was based on the measurement of the Au $4f_{7/2}$ peak at 83.8 eV. Depth profiling was performed by rastering a Kr^+ beam over an area of 1.5 × 1.5 mm or 6 × 7 mm in the AES or XPS mode, respectively. The ion gun, operated at 2 keV, was positioned at an angle of 39° with respect to the surface normal. For calibration purposes, a depth profile of a standard 10 nm Ta_2O_5 film was measured with each series of experiments (12).

Angle-dependent measurements with the CMA were performed using a drum with an angle resolving aperture of 12° (13). The take-off angle of electrons could be varied between 0° and 84° with respect to the surface normal without moving the sample. In these measurements, an Al x-ray source was employed.

Current efficiency for metal dissolution was determined from weight loss measurements using Armco iron (99.9%) anodes. The applied charge corresponded to a maximum dissolution depth of 20 μm.

Results

The galvanostatic anodic polarization curve for iron in 6*M* $NaNO_3$ + 0.1*M* NaOH at 2.5 m/s is shown in Fig. 1 as is the current efficiency calculated from weight loss measurements assuming divalent iron formation (14). At current densities below 8 A/cm², current efficiency is low because oxygen evolution is the main reaction. The current-potential curve exhibits Tafel behavior, with a slope of ~100 mV up to 0.2 A/cm², where the limiting current for OH^- discharge is reached (10). Measured potentials at higher current densities are strongly influenced by ohmic drops, which explains the shape of the current voltage curve above ~2 A/cm².

Figure 2 shows the charge necessary for reduction of films formed at different current densities. From the measured charge, the apparent film thickness was esti-

* Electrochemical Society Active Member.

[1] Supplier: Johnson Matthey Chemicals Limited, London, England.

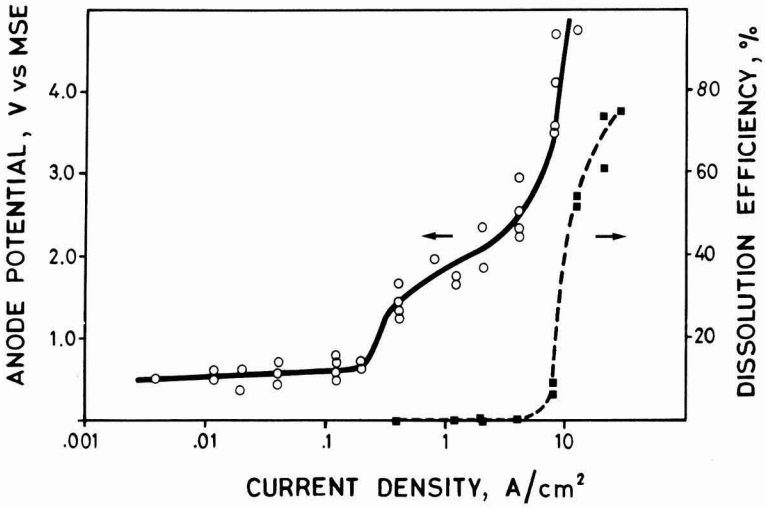


Fig. 1. Anodic potential (○) and current efficiency for iron dissolution (■) as a function of current density. Electrolyte: 6M $NaNO_3$ + 0.1M NaOH.

mated assuming that the film is Fe_2O_3 with a density of 5.24 g/cm³ (15) and that it is reduced at 100% current efficiency. The apparent film thickness as a function of current density exhibits two maxima: one at approximately 0.2 A/cm² corresponding to the limiting current density for the OH^- discharge, and the other at approximately 8 A/cm², beyond which the metal dissolution efficiency increases (Fig. 1).

Figure 3 shows Auger depth profiles of films formed at 0.042 A/cm² and 12.5 A/cm². The amplitude of the 703 eV iron, 503 eV oxygen, 272 eV carbon, and 379 eV nitrogen peaks were monitored as a function of time while sputtering the sample with Kr^+. The important difference between the two films is in their nitrogen profiles. For the films formed at 0.042 A/cm², the nitrogen peak amplitude decreases rapidly with sputtering, in a similar manner as for air-formed films (not shown). The observed surface nitrogen is due to adsorption from air. For the film formed at 12.5 A/cm², however, the nitrogen peak amplitude increases with time reaching a maximum at the oxide-metal interface.

The apparent film thickness was calculated from the sputter time corresponding to a decrease of the oxygen peak amplitude to 50% of its maximum value, assuming that the sputter rate of the film is the same as that of bulk Fe_2O_3. The relative sputter rate of Fe_2O_3 with respect to the Ta_2O_5 standard was determined from a single-crystal sample to be 0.92. The variation of the apparent film thickness as a function of applied current density (Fig. 4a) is qualitatively similar to that obtained by coulometry (Fig. 2), *i.e.*, two maxima are observed. Above 12 A/cm², the film thickness is independent of current density.

Using elemental sensitivity factors (16), the atomic concentration of nitrogen at the metal-oxide interface was estimated from AES depth profiles. The results (Fig. 4b) show that up to a current density of 1 A/cm² the nitrogen concentration is close to the AES detection limit, but beyond 1 A/cm², it increases with increasing current density to a value close to 5 atom percent (a/o) in the high rate metal dissolution region. A similar behavior was previously observed for nickel (10).

Films formed at different current densities were also analyzed by XPS without sputtering. The binding energies of different peaks were determined with respect to C 1s = 284.6 eV. The binding energy of the Fe $2p_{3/2}$ peak was 710.5 ± 0.2 eV, independent of applied current density, and the N 1s peak was at 398.1 ± 0.4 eV. Comparing the binding energies of the N 1s electrons for different com-

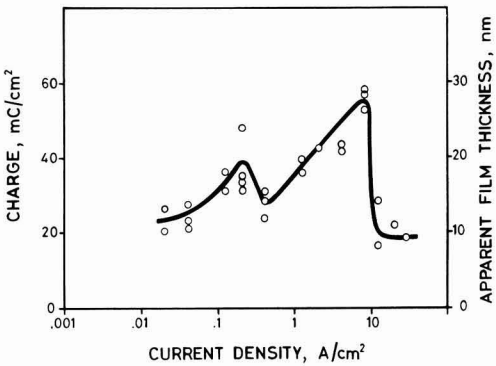


Fig. 2. Coulometrically measured charge for film reduction and estimated apparent film thickness as a function of current density.

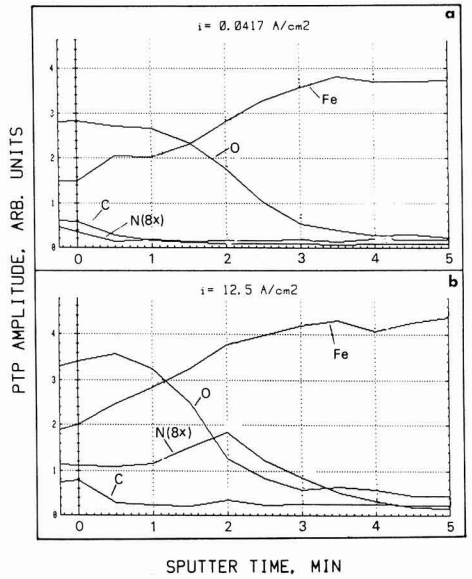


Fig. 3. AES depth profiles of films formed on iron at two different anodic current densities. Sputter rate of a standard Ta_2O_5 film is 1.86 nm/min under identical experimental conditions.

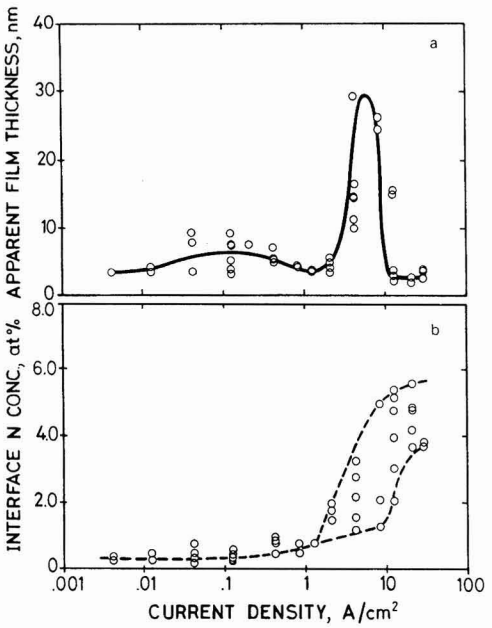


Fig. 4. Apparent film thickness (a) and nitrogen concentration at the metal-film interface (b) determined from AES depth profile data as a function of current density.

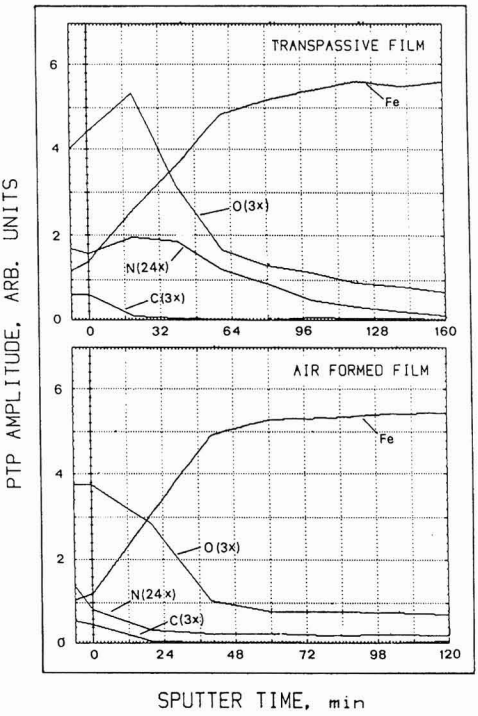


Fig. 5. XPS depth profiles of transpassive and air-formed films on iron. Sputter rate of a standard Ta_2O_5 film is 0.09 nm/min under identical experimental conditions.

pounds from the literature (17-20), it is concluded that the nitrogen in the transpassive film corresponds to the reduced form, N^{3-}.

Experiments described so far investigated the influence of applied current density on film properties. Further experiments were aimed at the more detailed characterization of transpassive films formed under high rate metal dissolution conditions. Samples polarized at 20 A/cm² were subjected to XPS sputter profiling and angle-resolved XPS measurements. The latter technique, in which the analysis information depth is varied by changing the take-off angle of emitted electrons, permits the characterization of very thin surface layers as a function of depth without the use of ion sputtering (21).

Figure 5 shows XPS sputter depth profiles of transpassive (a) and air-formed (b) films on iron. The data are qualitatively similar to those obtained by AES depth profiling of films formed under similar conditions. The nitrogen at the surface of the air-formed film is due to adsorption from air and disappears rapidly upon sputtering. Transpassive films exhibit nitrogen at the metal-oxide interface. From the XPS depth profiles, the thicknesses of the transpassive and air-formed films were estimated to be 3.7 and 2.4 nm, respectively, and compare well with the AES depth profile data (Table I).

The shapes of the Fe $2p_{3/2}$ spectra for transpassive and air-formed films depend on the take-off angle (Fig. 6). At $\phi = 0°$, a main peak at 710 eV and a shoulder at 707 eV are observed; these are attributed to oxidized iron and metallic iron, respectively (22-25). The intensity of the metallic iron peak decreases with increasing take-off angle and is almost completely absent at 57°, since at this angle most of the information is derived from the surface film.

The ratio of the signal intensity of oxidized and of metallic iron can be used to estimate the film thickness (12, 20). For a homogeneous oxide film (f) covering a flat substrate (m), the signal intensity ratio, $I_{Fe,f}/I_{Fe,m}$, is related to the film thickness, l, by (20)

$$l = -\lambda_{Fe,f} \cos\phi \ln\left[\frac{K}{K + \frac{I_{Fe,f}}{I_{Fe,m}}}\right] \quad [1]$$

with

$$K = \frac{\lambda_{Fe,f}\, n_{Fe,f}}{\lambda_{Fe,m}\, n_{Fe,m}} \quad [1a]$$

Here the iron ionization cross-sectional ratio between film and metal is taken as unity, $I_{Fe,f}$ and $I_{Fe,m}$ are the intensities of iron in the film and in the metal substrate, re-

Table I. Apparent film thickness on iron determined by different methods

Film	Estimated film thickness (nm) AES depth profiling*	XPS depth profiling*	Angle resolved XPS*	Coulometry**
Transpassive (at i = 20 A/cm²)	3.5 ± 0.3[a]	3.7 ± 0.2[b]	5.1 ± 0.5[c]	11.5 ± 0.5[a]
Exposed to electrolyte flow	2.8 ± 0.2[b]	—	—	10.1 ± 0.4[d]
Air-formed	2.1 ± 0.4[a]	2.4 ± 0.3[b]	4.5 ± 0.7[c]	—

* Referred to the sputter rate of Fe_2O_3 single crystal.
** Assuming the film to be Fe_2O_3.
Average of (a) 5, (b) 2, (c) 12, and (d) 8 measurements.

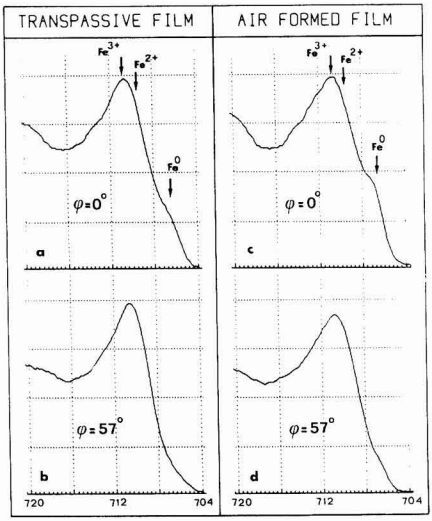


Fig. 6. Fe $2p_{3/2}$ spectra of transpassive (a, b) and air-formed (c, d) films on iron at different take-off angles. (a and c): $\phi = 0°$, (b and d): $\phi = 57°$.

spectively, $\lambda_{Fe,f}$ and $\lambda_{Fe,m}$ are mean free paths, $n_{Fe,f}$ and $n_{Fe,m}$ are atomic concentrations, and ϕ is the take-off angle of photoelectrons with respect to the surface normal. The values of constants used in Eq. [1] to evaluate film thickness are given in Table II.

To evaluate the signal intensity ratio, $I_{Fe,f}/I_{Fe,m}$, the Fe $2p_{3/2}$ spectra from 704 to 718 eV were resolved into four peaks (Fig. 7) at 706.6, 709.5, 710.6, and 714 eV that are attributed to Fe°, Fe^{2+}, Fe^{3+}, and a shake-up satellite signal of oxidized iron, respectively (23, 25, 27). The sum of the area intensities of Fe^{2+} and Fe^{3+} peaks was taken as a measure of the intensity of oxidized iron species. The contribution from the relatively small shake-up satellite signal was neglected. The transpassive and the air-formed film thicknesses thus determined from Eq. [1] are 5.1 ± 0.5 and 4.5 ± 0.7 nm, respectively (Table I).

The O 1s spectra of an air-formed and of a transpassive film were measured at different take-off angles. Three different peaks at 529.2, 530.9, and 532.2 eV were attributed to oxide (O^{2-}), hydroxide (OH^-), and water (H_2O), respectively (22-25, 28). Area intensities of these species were determined and are shown in Fig. 8 as a function of take-off angle. Little difference is observed between the two films. This behavior differs from that observed previously with nickel, where transpassive films contained significantly more O^{2-} than air-formed films (20). At the largest take-off angle, the ratio O^{2-}/OH^- decreases (Fig. 8), suggesting that the surface of the film contains more OH^- than the interior.

The energy of the N 1s peak measured at different take-off angles was the same and corresponded to that measured on an air-formed film. This indicates that the

Table II. Physical parameters used to calculate mean free path of Fe $2p_{3/2}$ photoelectrons in XPS

Material	Atomic density, n (mol/cm³)	Binding energy, E_b (eV)	Kinetic energy, E_K (eV)	λ* (nm)
Fe	0.141	706.6	775.4	1.24
Fe_2O_3	0.066	710.5	771.5	2.01

* Mean free path calculated using the empirical equations by Seah and Dench (26) for elements and inorganic compounds, respectively.

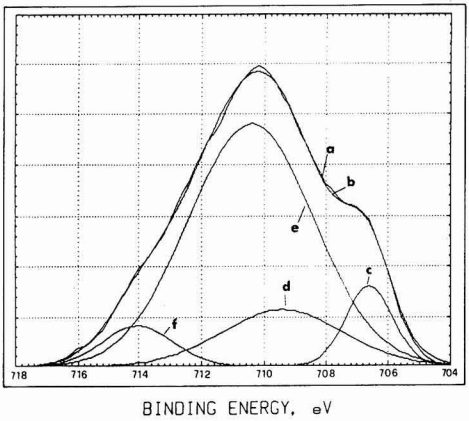


Fig. 7. Deconvoluted Fe $2p_{3/2}$ spectrum after background subtraction. a: Raw data. b: Fitted curve. c: Metallic iron. d: Fe^{2+}. e: Fe^{3+}. f: Satellite shake up signal of oxidized iron.

interface and the surface nitrogen are in the same chemically reduced state. The intensity of the N 1s signal on transpassive films showed no appreciable change with the variation of take-off angle, although one would have expected this based on the AES and XPS sputter profiles shown in Fig. 3 and 5. This is attributed to nitrogen adsorbed on the surface of the film; a high take-off angle the loss of intensity from the nitrogen at the film-metal interface is compensated by the increased intensity from adsorbed nitrogen.

Discussion

Characterization of anodic films by coulometry and by surface analytical techniques is subject to several limitations inherent in each method (10, 20). For example, coulometric data may include contributions from side reactions, and their interpretation requires a knowledge of film stoichiometry, density, and true surface area. AES/XPS analysis may be affected by sample transfer and contamination problems. In addition, the sputter rate is known approximately only, and the deconvolution procedures in XPS involve some degree of uncertainty. Therefore, data obtained for air-formed and transpassive

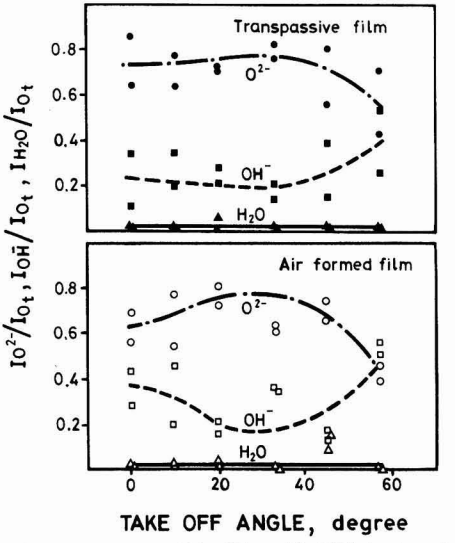


Fig. 8. Relative intensity of O^{2-}, OH^-, and H_2O XPS signals as a function of take-off angle for a transpassive and an air-formed film.

films at different current densities are of interest mostly on a comparative basis.

Film thickness as a function of current density shows two maxima (Fig. 2 and 4a). The first maximum lies close to the limiting current for OH^- discharge (Fig. 1), at which the local pH at the film-solution interface is diminished, favoring dissolution of surface hydroxyl species. This explains the decrease in film thickness in this region. Assuming film growth by high field conduction (29), the film thickness should increase with increasing potential resulting from higher applied current density. This leads to the observed increase in film thickness beyond the first maximum in Fig. 2 and 4a. At sufficiently high current density (anode potential), film breakdown occurs leading to high rate metal dissolution. This is evident in Fig. 9, which shows a scanning electron microphotograph of iron dissolved at 10 A/cm² for 0.7s. At a current efficiency of 20% (*cf.* Fig. 1), this corresponds to an average dissolution depth of 0.5 μm. The photograph confirms that the transpassive dissolution of iron takes place by local breakdown of the passive film at random sites, similar to observations for nickel in nitrate electrolytes (1). The apparent film thickness in the metal dissolution region is independent of applied current density.

Because of unavoidable transfer effects, the determination of transpassive film composition from XPS measurements is rather uncertain. However, AES and XPS depth profiles do exhibit a distinct nitrogen maximum at the metal-oxide interface at current densities corresponding to transpassive metal dissolution. This nitrogen originates from nitrate ions present in the electrolyte that might have penetrated through faults in the film (10).

The results of the present investigation provide new insight into the high rate transpassive dissolution behavior of iron in nitrate electrolytes. Under conditions of present experiments, transpassive dissolution in 6*M* $NaNO_3$ + 0.1*M* NaOH sets in at a current density of approximately 8 A/cm², and the metal dissolution efficiency is an increasing function of current density up to 30 A/cm². The apparent film thickness, however, remains constant beyond 12 A/cm² (Fig. 2 and 4a). The transpassive dissolution efficiency, therefore, is independent of film thickness, contrary to previous conclusions (4-8). The presence of nitrogen in the interior of the film suggests that passive films under these conditions are highly defective, so that electrolyte anions can penetrate locally up to the metal surface. It is probable that metal dissolution occurs at these sites, while oxygen evolution occurs on the rest of the surface. Micropits formed in this way, may grow until repassivation, *e.g.*, due to ohmic drop, occurs or until different micropits merge together. The current efficiency for transpassive dissolution, thus, would be governed by the kinetics of depassivation and repassivation phenomena, which determine the average surface fraction available for oxygen evolution and metal dissolution, respectively.

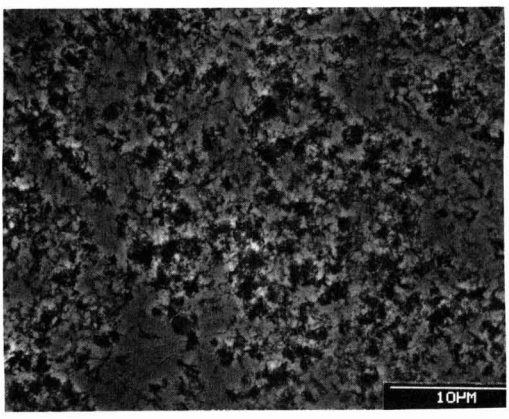


Fig. 9. SEM photograph of an iron sample after anodic dissolution in 6M $NaNO_3$ + 1M NaOH at 10 A/cm² for 0.7s.

Conclusions

1. For iron polarized in nitrate solution in the transpassive potential region, two states with respect to surface films have to be distinguished: oxygen evolution, where film thickness is a function of applied current density, and metal dissolution, where film thickness is independent of current density. This follows from both *in situ* coulometry and *ex situ* AES/XPS data.

2. In the metal dissolution region, current efficiency for metal dissolution is independent of apparent film thickness, and nitrogen in a reduced state is observed at the film-metal interface.

3. Obtained data suggest that the transition from transpassive oxygen evolution to high rate metal dissolution involves film breakdown initiated by penetration of anions through flaws.

Acknowledgments

The authors thank N. Xanthopoulos for experimental assistance. Thanks are also due to Dr. R. P. Frankenthal of AT&T Bell Laboratories for his valuable comments. This work was financially supported by the Fonds National Suisse de La Recherche Scientifique, Bern, Switzerland.

Manuscript submitted Oct. 17, 1983; revised manuscript received June 1, 1984.

The Swiss Federal Institute of Technology assisted in meeting the publication costs of this article.

REFERENCES

1. M. Datta and D. Landolt, *This Journal*, **124**, 483 (1977).
2. M. Datta and D. Landolt, *Electrochim. Acta*, **25**, 1263 (1980).
3. D. T. Chin and K. W. Mao, *J. Appl. Electrochem.*, **4**, 155 (1974).
4. J. P. Hoare, *This Journal*, **117**, 142 (1970).
5. K. W. Mao, M. A. LaBoda, and J. P. Hoare, *ibid.*, **119**, 419 (1972).
6. J. P. Hoare, *Nature (London) Phys. Sci.*, **241**, 44 (1973).
7. M. A. LaBoda, A. J. Chartrand, J. P. Hoare, C. R. Weise, and K. W. Mao, *This Journal*, **120**, 643 (1973).
8. J. P. Hoare, in "Passivity of Metals," R. P. Frankenthal and J. Kruger, Editors, p. 505, The Electrochemical Society Monograph Series, Princeton, NJ (1978).
9. T. P. Hoar, *Corros. Sci.*, **7**, 341 (1967).
10. M. Datta, H. J. Mathieu, and D. Landolt, *Electrochim. Acta*, **24**, 843 (1979).
11. M. Datta and D. Landolt, *ibid.*, **25**, 1255 (1980).
12. H. J. Mathieu and D. Landolt, *Surf. Interf. Anal.*, **6**, 82 (1984).
13. H. J. Mathieu and D. Landolt, *Appl. Surf. Sci.*, **10**, 455 (1982).
14. K. W. Mao, *This Journal*, **118**, 876 (1971).
15. "Handbook of Chemistry and Physics," 53rd Ed. p. B-99, CRC Press, Cleveland, OH (1972).
16. L. E. Davis, N. C. MacDonald, P. W. Palmberg, G. E. Riach, and R. E. Weber, "Handbook of Auger Electron Spectroscopy," 2nd Ed., p. 11, Physical Electronics Industries, Inc., Eden Prairie, MN (1976).
17. B. Folkesson, *Acta Chem. Scand.*, **27**, 287 (1973).
18. H. Schultheiss and E. Fluck, *J. Inorg. Nucl. Chem.*, **37**, 2109 (1975).
19. W. D. Wagner, W. M. Riggs, L. E. Davis, J. F. Moulder, and G. E. Muilenberg, "Handbook of X-ray Photoelectron Spectroscopy," Perkin Elmer Corp., Eden Prairie, MN (1979).
20. M. Datta, H. J. Mathieu, and D. Landolt, *Appl. Surf. Sci.*, **18**, 299 (1984).
21. C. S. Fadley, *Prog. Solid State Chem.*, **11**, 265 (1976).
22. K. Asami and K. Hashimoto, *Corros. Sci.*, **11**, 559 (1977).

23. N. S. McIntyre and D. G. Zetaruk, *Anal. Chem.*, **49**, 1521 (1977).
24. H. Konno and M. Nagayama, in "Passivity of Metals," R. P. Frankenthal and J. Kruger, Editors, p. 585, The Electrochemical Society Monograph Series, Princeton, NJ (1978).
25. C. R. Brundle, T. J. Chuang, and K. Wandelt, *Surf. Sci.*, **68**, 459 (1977).
26. M. P. Seah and A. W. Dench, *Surf. Interf. Anal.*, **1**, 2 (1979).
27. T. J. Chuang, C. R. Brundle, and K. Wandelt, *Thin Solid Films*, **53**, 19 (1980).
28. R. Kötz, H. Neff, and S. Stucki, *This Journal*, **131**, 72 (1984).
29. K. J. Vetter, "Electrochemical Kinetics," p. 759, Academic Press, New York (1977).

Development of Silver-Palladium Alloy Plating for Electrical Contact Applications

U. Cohen*,[1] K. R. Walton,[2] and R. Sard*,[3]

AT&T Bell Laboratories, Murray Hill, New Jersey 07974

ABSTRACT

Silver-palladium alloys were electroplated as high quality coatings from a concentrated chloride bath. Adherent, uniform, and coherent deposits were obtained with thicknesses of up to 20 μm. The alloys were found to be homogenous, single-phase solid solutions, with palladium content ranging from about 30% to 60%, depending on the operating variables. The microstructure of the plated Ag-Pd alloys consists of very fine grains (100-300Å). These alloys have a fcc crystal structure, and the lattice parameter varies continuously with composition. The useful plating rate with moderate agitation was found to be about 0.44 μm/min at 10 mA/cm², which is almost twice that of conventional cobalt-hardened gold, due to the current efficiency of nearly 100%. Alloys containing about 40% Pd were obtained with these conditions. High speed plating of the Ag-Pd alloy was achieved in a forced flow cell up to rates of about 9 μm/min. To achieve satisfactory deposits, it was generally necessary to use a thin (0.2-0.4 μm) soft gold underplating. Preliminary tests of electrical contact properties revealed that the Ag-Pd coatings possessed low contact resistance (about 1 mΩ at 100g load). Other relevant properties include intermediate Knoop microhardness (about 200 kg/mm² at 25g load) and an excellent resistance to formation of corrosion films in accelerated tests using flowers of sulfur. The present study indicates that the plated Ag-Pd coatings are superior in contact resistance stability to the bulk wrought alloy R156 (40%Ag-60%Pd). Finally, these coatings show satisfactory wear response in the selected tests provided a hydrocarbon lubricant is present.

The development of a suitable process for electroplating Ag-Pd would provide an attractive alternative to hard gold plating in a variety of electrical contact applications. The material cost per unit volume of a 40%Ag-60%Pd alloy is currently less than 20% that of pure gold.[4] The properties of metallurgically prepared Ag-Pd alloys are known to be suitable for contact materials (1, 2). In particular, savings in material costs and comparable corrosion behavior in tarnishing environments have led to the conversion of Bell System wire spring relays from pure Pd to this material (1).

The Ag-Pd alloy system consists of a homogenous solid solution phase over its entire composition range. The mechanical and electrical properties, therefore, should be easy to control and to reproduce. Problems associated with precipitation of a second phase in a mutiphase alloy, such as erratic, abrupt, or irreproducible changes in the properties, are thus eliminated. Small fluctuations in the alloy composition have only a minor effect on such properties because, in a homogeneous phase, properties vary gradually with the composition.

In his comprehensive treatise (3), Brenner reviewed the unsuccessful attempts up to that time to electroplate the Ag-Pd alloy from various baths. He commented, however, that the concentrated chloride bath, investigated by Graham *et al.* (4) for Ag-Pt alloy plating, should also be feasible for Ag-Pd alloy plating. Although the latter (4) mentioned briefly that they had obtained Ag-Pd alloy from a similar bath, they gave no details. Andreeva *et al.* (5) then reported Ag-Pd alloys using conditions similar to those specified by Graham *et al.* (4) for plating Ag-Pt alloys. Electrodeposition of the Ag-Pd alloy was also reported from a buffered ammoniacal electrolyte containing EDTA by Kudryavtsev *et al.* (6, 7). The ammoniacal plating system, however, appears to operate under conditions of silver diffusion-limited current, which adversely affects the deposition, composition, morphology, thickness, and rate of growth. We have chosen to work with the concentrated lithium chloride bath, which is simple and contains no additives or hazardous components. This electrolyte relies on the anomalous solubility of AgCl in the presence of chloride ion. At high concentrations of the latter, the solubility increases with the concentration of the chloride ion. The bath, however, is very aggressive towards base metals, causing vigorous displacement reactions with them. An intermediate layer of a more noble metal must thus be applied to protect the base metals against these reactions (8).

This paper describes our preliminary investigation related to: (*i*) the feasibility of electroplating high quality coatings of Ag-Pd alloy from the concentrated lithium chloride bath and (*ii*) initial characterization of the plated Ag-Pd coatings and their testings as contact materials. Desirable properties of an electrical contact include a low and stable contact resistance throughout service life and the ability to resist friction and wear. These requirements were discussed by Holm (9), and the contact resistance and wear resistance test methods were described by Antler (10). Comparative studies have been made here of the corrosion resistance, the electrical contact resistance, and the wear performance of the plated Ag-Pd alloys *vs.* the properties of a wrought Ag-Pd alloy (R156) and also *vs.* the properties of hard gold plating. This paper also briefly

* Electrochemical Society Active Member.

[1] Present address: Magnetic Peripherals, Incorporated, Santa Clara, California 95051.

[2] Present address: Exxon Research and Engineering Company, Linden, New Jersey 07036.

[3] Present address: Oxy Metal Industries, Warren, Michigan 48089.

[4] The product of a density factor (11.3/19.3 = 0.59) and a price factor $130/$390.

summarizes the results of a study of the morphology and microstructure of the plated Ag-Pd coatings (11). In another related study (12), the feasibility of a new method of plating cyclic multilayered alloys (CMA) was demonstrated by plating a wide variety of Ag-Pd structures.

Experimental

In the present work, the electrolyte for Ag-Pd alloy plating consisted of 500g of LiCl, 12g of AgCl, 3g of $PdCl_2$, 20 ml HCl, and 1000 ml of H_2O. After dissolving the salts, the bath was heated and brought to boiling (~130°C) to ensure complete dissolution of all salts, filtered (when hot), and cooled to the operating temperature (typically, 85°C). Moderate stirring was used during the plating, and the current density range studied initially was 0.5-20 mA/cm². Most samples, however, were plated at 5 ± 0.5 mA/cm².

Figure 1 illustrates the electroplating cell and associated electronics. The cell was a 500 ml reaction flask with an O-ring fitted cover that contained five standard tapered joints. Three electrodes, a thermometer, and a glass-stirrer were inserted through Teflon glands to the plating bath. The flask was immersed in a dark heating oil bath to provide uniform heating and to prevent photodissociation of wet solid AgCl. A stable plating bath temperature (within ± 0.5°C) was maintained with this arrangement.

Chemical analysis of the alloys was usually done with a nondispersive x-ray fluorescence (XRF) analyzer mounted on a scanning electron microscope (SEM). These analyses were corrected by comparison with several standard samples analyzed by wet chemical techniques and by electron microprobe. X-ray diffraction (XRD) was used for phase and texture analyses and for the determination of the lattice parameter. The coating morphology was studied by SEM and metallographic cross sections. Transmission electron microscopy (TEM) was used to study the grain size and microstructure (11). Knoop microhardness was tested at 25g force (with a Tukon instrument) on polished cross sections of coatings ≥ 10 μm thick.

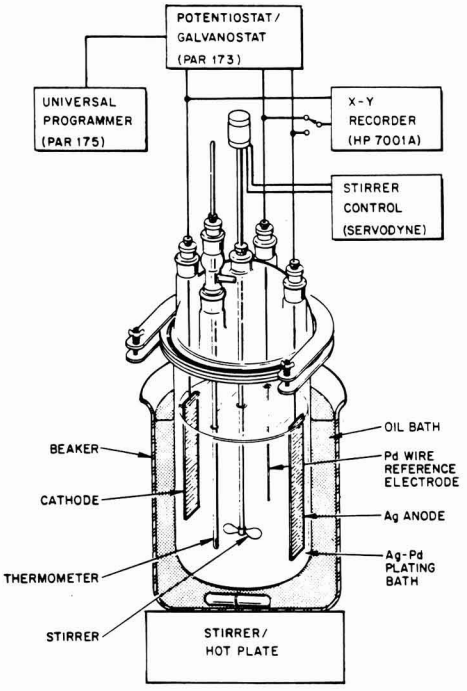


Fig. 1. Schematic of the experimental setup. The plating cell is immersed in a bath of oil. The oil bath is heated on a hot plate/stirrer equipped with a control thermistor sensor, which is immersed in the oil bath. A Pd wire immersed in the plating solution serves as an internal secondary reference electrode. A large plate (~ 25 cm²) of Ag metal serves as the anode. Electrical signals are provided to the cell from a potentiostat/galvanostat, PAR 173, combined with a signal programmer, PAR 175. The signals are recorded on an (HP-7004B) X-Y recorder.

Electrical contact resistance was measured using a four-wire technique. In the measuring system (13), a 0.05 cm diam gold wire bent around a 60° Teflon wedge is used as the contact member. With this system, contact closure takes place with virtually no contact wipe. Measurements were performed at 100g load both on samples and standards prior to and after exposure to aggressive environments.

Wear and friction behavior was studied using a rider/flat wear test fixture, which simulates the sliding of separable connectors. The wear behavior with actual connector hardware plated with an Ag-Pd finish was also evaluated. The rider/flat tester is shown schematically in Fig. 2. In this tester, a flat coupon slides back and forth (on the same track) under a 0.25 in. diam spherical rider. The latter is loaded with a known weight. The resulting frictional force is sensed by a transducer through a shaft coupled to the rider assembly and monitored on a chart recorder. The coefficient of friction, μ_f, for a given cycle in the rider/flat experiment, is obtained by dividing half the total swing in the frictional force during each cycle by the load on the rider. The implicit assumption here is that the sliding events in both directions are equivalent. For the accuracy of about 20% sought in this work, this assumption is believed valid. Rider/flat tests were conducted for 200 cycles at a rate of 27 cycles/min (about 1 cm/s). The load on the rider was either 70 or 255g. However, only the results at 255g load are reported here; the results at 70g load are similar and lead to the same interpretations and conclusions. The depth and width of the wear tracks on the flat coupon were determined quantitatively by a Dektak microprofiler equipped with a 5 μm diam diamond-tipped stylus. Qualitative examination of the degree of wear on the coupons was done using optical and scanning electron microscopy.

Results and Discussion

Substrate compatibility.—To determine the compatibility of base metal substrates to the concentrated chloride plating bath, Cu and Ni strips were immersed with no external current in a simulated plating bath (but milder and not including the $PdCl_2$, for simplicity). The bath contained 50g of LiCl, 0.4g of AgCl, 2 ml of HCl, and 100 ml of H_2O, and was held in the temperature range 70°-80°C. No stirring was used. A vigorous displacement reaction was observed when a Cu strip was immersed in the solution. The strip was soon covered with a very loose and spongy white silver deposit and, at the same time, the Cu strip partially dissolved. After a 60 min immersion, the strip was removed from the solution, the Ag deposit

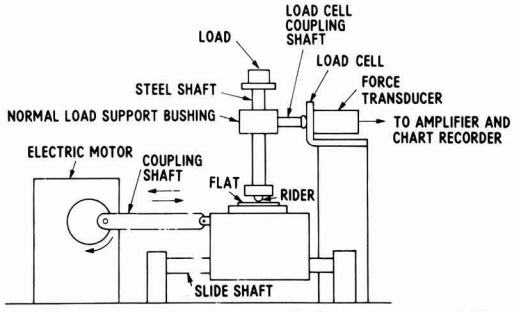


Fig. 2. Schematics of the wear tester. The load support is coupled by a shaft to a load cell (Statham UL4) and a force transducer (Statham UC3). Frictional forces experienced by the rider during sliding are transmitted to this unit. The transducer output is amplified and calibrated to read the frictional force in grams (accuracy to 0.1g) by a bridge amplifier (Statham SC1105).

scraped off, washed, and dried. The Ag deposit weight gain was 107.8 mg, and the Cu strip weight loss was 62.9 mg. These numbers may be compared with the respective atomic weights (107.87 for Ag, 63.54 for Cu), which indicate that the displacement reaction was

$$Cu + Ag(I) \rightarrow Cu(I) + Ag\downarrow$$

A more moderate displacement reaction was observed with a Ni strip. It was slowly covered with white Ag deposit of poor adherence. After an immersion of 17.5h, the strip was removed from the solution (which had become yellow-green in color). SEM examination of the deposit revealed individual Ag crystallites (10-20 μm) over most of the flat substrate surface and large Ag dendrites (400-600 μm on the strip edges). A total weight gain (strip plus deposit) of 110.1 mg was found. It may be noted that the Ag atom is almost twice the weight of the Ni atom, and that, for the displacement reaction

$$Ni + 2Ag(I) \rightarrow Ni(II) + 2Ag\downarrow$$

two Ag atoms are deposited for every dissolving Ni atom. Thus, a net weight gain is evidence of a displacement reaction.

Immersion of bare Cu and Ni substrates in the regular Ag-Pd alloy plating bath, under cathodic current, yielded loose powdery and spongy Ag-Pd deposits on Cu, and spontaneous peeling of the deposit from the Ni substrates. Current efficiencies, based on weight gain and Faraday's law, were much greater than 100%, indicating spontaneous displacement reactions had again occurred. These tests clearly demonstrate that the bare Cu and Ni substrates are imcompatible with the concentrated chloride bath, containing Ag (or Pd) ions.

Substrates of Cu and Ni, with protective Ag films 1 μm thick (especially if immersed under cathodic current), showed a significant improvement over the bare substrates. However, they still contained some unacceptable rough areas.

Bulk noble metal substrates, such as Pd, Au, and Ag, were generally found compatible and suitable for the plating of the Ag-Pd alloy. However, it was found that prolonged immersion of Ag metal in the plating bath with no external current could have deleterious effects, probably owing to the slow displacement reaction

$$2Ag + Pd(II) \rightarrow 2Ag(I) + Pd\downarrow$$

This reaction could result in poor adhesion and occasional cracking of the Ag-Pd coatings, probably owing to undercutting. The slow displacement reaction of Ag metal with the plating bath was also indicated by the observation that Ag strips, when immersed with no external current in the plating bath, exhibited immediate darkening of the Ag surface in contact with the bath. The metal surface when analyzed by XRF confirmed the presence of Pd metal. Further evidence was provided from SEM analysis of cross sections (12) and electrochemical potential measurements. The electrode potential gradually changed to less negative values *vs.* a Pd metal reference electrode. All these results indicate that Pd is more noble than Ag in this alloy plating system. By starting the plating of the alloy on Ag substrates immediately following immersion, or, preferably, by immersing under cathodic current; it was possible to eliminate the deleterious effects associated with these substrates.

It was found that the application of very thin (0.2-0.4 μm) protective undercoatings of soft gold could provide the most reliable protection to the base metal substrates against the displacement reactions. Soft gold plated from the citrate-buffered bath (14) provided better protection than hard-gold or gold-strike platings. This is believed to be due to the higher density (and lower porosity) of the soft gold. Without adequate substrate preparation, exposed pits or holes to the base metal will, of course, result in extensive displacement. Both unpolished and mechanically polished substrates of Cu, CDA725 alloy (89 w/o Cu-9 w/o Ni-2 w/o Sn), and Ni, when properly prepared and coated with 0.2-0.4 μm soft gold, proved to be excellent substrates for Ag-Pd alloy plating. The substrate preparation procedure outlined in Table I was developed to give reproducible results for the plating of the Ag-Pd coatings.

The plated Ag-Pd coatings, under favorable conditions, closely reproduced the substrate surface features. Figure 3a depicts the surface of a 2.5 μm thick Ag-Pd coating which was deposited at 5 mA/cm^2 on an unpolished CDA725 alloy substrate, with a nominal 0.3 μm soft gold undercoating. Another sample, prepared under identical conditions except that the alloy substrate was mechanically polished (0.3 μm alumina was the last abrasive) proved to be so smooth that it was featureless on the scale of 1 μm (*cf.* Fig. 3b). This type of surface finish is similar to that typically found with carefully prepared hard gold deposits.

Effects of current density and waveform.—DC plating.—The effects of current density were studied for the bath composition given above. Ag strips were used as substrates for these experiments. They were chemically etched in a mixture NH_4OH/H_2O_2 (1:1) for 5-10s, rinsed, and dried. They were then masked with adhesive plating tape to prevent nonuniformity stemming from edge effects, and to prevent plating of the strip back side. Coatings ~10 μm thick were deposited to facilitate characterization. Increasing the current density was found, in general, to produce Ag-Pd alloys with increased Ag content, as described more fully below. Table II summarizes the various effects of the current density; and the various surface morphologies are shown in the SEM photographs of Fig. 4. At the lowest current density, 0.5 mA/cm^2, the deposits were dark gray matte due to the three-dimensional growth features evident in Fig. 4a. At 2 mA/cm^2, the overall general appearance was similar. However, the microstructure was quite different, as shown in Fig. 4b. This structure gives rise to unfavorable properties, such as high contact resistance. At 5 mA/cm^2, the surface appeared much lighter, and the morphology was noticeably smoother (*cf.* Fig. 4c). At 10 mA/cm^2, similar deposits to those obtained with 5 mA/cm^2 were observed (*cf.* Fig. 4d). Plating with moderate stirring (about 10 cm/s flow rate) and with current density in the range of 5-10 mA/cm^2 was judged most favorable. A standard condition at 5 mA/cm^2 was thus adopted to prepare samples for additional measurements, as described below. At a current density of 20 mA/cm^2, deterioration of the coating was evident close to the edges, where the effective current density was highest. Spontaneous cracking was sometimes observed (*cf.* Fig. 4e and 4f). Thus, under the conditions used (*i.e.* moderate stirring), the useful plating current density is less than 20 mA/cm^2. It should be noted that, at 10 mA/cm^2, the plating rate of Ag-Pd was about 0.44 μm/min, which is almost twice that of hard gold plating.

Table I. Substrate preparation for plating

1. Degrease in acetone and trichloroethylene
2. Ultrasonic cleaning in Neutra-Clean 68 solution for about 1 min
3. Rinse in deionized (DI) water
4. Activate in dilute (1:1) HCl for about 30-60s
5. Rinse in DI water
6. Soft gold plate, 0.2-0.4 μm thick*
7. Rinse in DI water and dry**
8. Introduce to the Ag-Pd alloy plating bath under cathodic current†

* Procedure was to immerse (wet) substrates under cathodic current in a bath containing potassium gold cyanide (20 g/l), dibasic ammonium citrate (50 g/l), ammonium sulfate (50 g/l). Conditions were 65° ± 5°C, 8 ± 2 mA/cm^2, 30-45s, and moderate stirring.

** The substrates must not be introduced wet into the alloy plating bath since precipitation of AgCl due to local chloride dilution may occur on the surface, yielding coatings with poor adhesion (4). The preferred procedure is to dip the substrate, prior to plating, in a concentrated chloride solution.

† This is to insure that the thin gold layer is protective. Substrates with ≥0.4 μm soft gold undercoatings could be immersed in the plating bath with no external current for several minutes without deleterious effects.

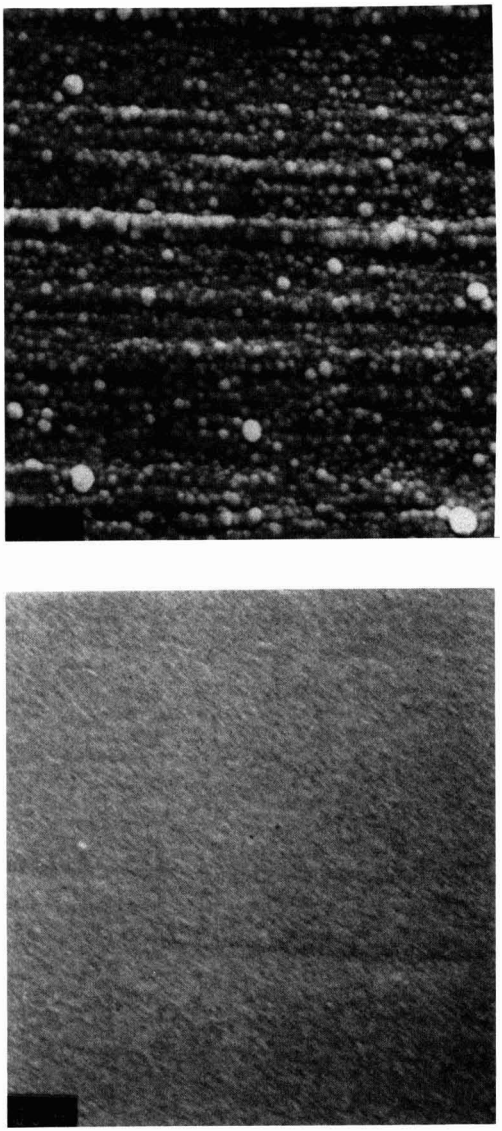


Fig. 3. SEM photographs of the surface of 2.5 μm thick Ag-Pd coatings plated at 5 mA/cm² using (a, top) unpolished CDA725 alloy substrate and (b, bottom) mechanically polished (with 0.3 μm alumina) CDA725 alloy substrate. Both substrates were plated with 0.3 μm soft gold prior to the Ag-Pd plating.

Much higher current densities were used in preliminary experiments with high speed plating of the Ag-Pd alloy in a forced flow cell (14). The solution velocity in the latter is estimated to be about an order of magnitude higher than in the stirred beaker. A precise value of the cathodic current density could not be determined because of some uncertainty regarding the plated area. Measurements of coating thickness on metallographic cross sections of a series of platings, obtained with a constant current and varying deposition time, revealed a linear thickness increase with plating duration. Assuming 100% current efficiency, an effective surface area of ~9.5 cm² was estimated. Smooth coatings could be obtained with total currents up to ~2000 mA. These conditions correspond to a current density of up to ~210 mA/cm² (or ~9 μm/min), which is roughly equivalent to rate attainable with high speed hard gold plating (14). Examination of the cross sections showed that even the very thin (~0.7 μm) coatings were continuous over the entire substrate surface. Some thick (> 7 μm) coatings showed initiation of nodular growth at locations of relatively higher current densities. The composition of a typical coating obtained at ~105 mA/cm² (or ~4.5 μm/min), was found by XRF analysis to be 62%Ag-38%Pd. The surface morphology of the coating, as revealed by SEM examination, was also very similar to the high quality coatings obtained with the much lower current density of 5 mA/cm² ~ 0.22 μm/min) under moderate stirring. Thus, the deleterious effects of high current densities on the morphology (*cf.* Fig. 4e and 4f) and excessive Ag content of the deposit, can be overcome by using a high speed flow cell.

Characterization of the plated Ag-Pd coatings.—Composition.—The composition of the coatings varied from about 70%Ag-30%Pd to about 42%Ag-58%Pd, depending on the current density and the rate of stirring. Generally, decreasing the current density or increasing the amount of stirring yielded alloy coatings with higher Pd content. This fact is further evidence that Pd is more noble than Ag in the alloy plating system. Data depicting the effect of dc current density on the alloy composition (for a constant stirring rate) are shown in Fig. 5.

Microstructure.—Transmission electron microscopy (TEM) examination revealed a microstructure of very fine grains (100-300Å). Voids of about 20-30Å in size were also noted at the grain boundaries. No second phase precipitates were observed. Electron and x-ray diffraction patterns indicated that the alloy coatings were homogeneous, single-phase solid solutions. These measurements also indicated that the fcc lattice parameter varies continuously with the composition in a similar manner to wrought Ag-Pd alloys (15). This dependency is shown in Fig. 6. The Ag-Pd coatings obtained with dc current had a strong fiber texture (preferred orientation) with the [100] direction perpendicular to the surface. As described elsewhere (11), plating of CMA coatings with cyclic current modulation tended to reduce degree of the preferred orientation. In particular, coatings with dense (or thin) multilayers exhibited more random orientation.

Microhardness.—Knoop microhardness was measured with a 25g load on polished cross sections of coatings with at least 10 μm thickness. A nominal value of about 200 kg/mm² was observed for optimal conditions. Some results are given in Table II.

Internal stress.—The internal macrostress of the Ag-Pd alloy coatings was continuously monitored using an electronic spiral contractometer (16, 17). The spirals were made of stainless steel 0.020 in. thick. They were plated with 2 μm Ni and with 2 μm soft gold. The gold, applied prior to the measurements, served to protect the spirals from the displacement reactions with the alloy plating bath.

Increasing the current density was found, in general, to decrease the tensile stress or to shift it to a compressive stress. The range of stress values observed for deposits 2.5 μm thick varied from slightly less than 1 kg/mm² tensile stress for coatings obtained at 2 mA/cm², to about the same magnitude of compressive stress for coatings obtained at 20 mA/cm². Temperature variations of ± 10°C (from the standard 85°C) had little effect on the macrostress. Thus, the magnitude of the internal macrostress found in the Ag-Pd coatings is rather small and is comparable to pure silver and other widely used electroplatings, such as acid-copper and sulfamate nickel. Moreover, these stress levels are substantially lower than the high values associated with such brittle platings as cobalt-hardened gold (16) and tin-nickel alloy.

Contact resistance.—Effects of tarnishing.—Contact resistance was measured with a four-point probe instrument with a 100g load. The contact resistance of the as-plated Ag-Pd coatings was typically about 1 mΩ. One

Table II. Results of dc experiments

Current density (mA/cm²)	Coating thickness (μm)	Composition XRF* (w/o)	KHN_{25}** (kg/mm²)	CR† (mΩ)	Remarks
0.5	~ 5.0	Ag 43.2 Pd 56.8	—	1.5	Dark gray matte deposits of uniform appearance and composition (see Fig. 4a).
2.0	~16.4	Ag 45.8 Pd 54.2	155-165	25	Uniform gray matte color. Unusual morphology responsible for high CR (see Fig. 4b).
5.0	~10.0	Ag 53.9 Pd 46.1	168-220 avg 200	1.3	Uniform light gray matte color (see Fig. 4c).
10.0	~10.0	Ag 54.6 Pd 45.4	192-212	3.0	Light gray matte color (see Fig. 4d).
20.0	~10.0	Ag 69.6 Pd 30.4	—	—	Very light gray color. Surface appears badly cracked and deteriorated with loose powdery spots (see Fig. 4e and 4f).

* Based on x-ray fluorescence intensity measurements relative to metallurgical alloy standard of 40%Ag-60%Pd. Also, checked with microprobe and wet chemical analysis.
** Knoop microhardness, 25g load.
† Four-wire contact resistance measurements at 100g force with soft gold probe (0.020 in. diam wrapped around 60° wedge).

week exposure at 50°C in an environment containing flowers of sulfur and 85% relative humidity (RH) had hardly any effect on this contact resistance with the plated Ag-Pd coatings. Wrought R156 alloy (40Ag-60Pd) exposed to the same environment exhibited a significant increase in its contact resistance. Whereas the mean change in contact resistance, ΔR, of the plated alloy was less than about 0.2-0.3 mΩ, the corresponding value of the R156 alloy was 4-6 mΩ. In these tests, 2.5 μm thick alloy deposits of about 40%Pd were plated on CDA725 substrates with a soft gold undercoat about 0.25 μm thick. Additional results are given in Ref. (12). Indeed, the corrosion resistance of the plated Ag-Pd coatings in this test was found quite similar to that of plated hard gold.

The superior corrosion resistance and contact resistance stability (CRS) of the plated alloys over the wrought alloy, R156, is quite surprising, since the latter contains more palladium. However, the plated alloys differ substantially from the wrought alloy in many respects. For example, the grain size of the wrought alloy is in the neighborhood of several micrometers (about two orders of magnitude larger than the grain size of plated alloys). Also, the plated alloys are more homogeneous in their composition than the wrought material. Wrought alloys may have a composition variation of several weight percent from grain to grain (18), owing to the influence of the anisotropic distribution coefficient during solidification. The finer grain size, as well as the homogeneity of

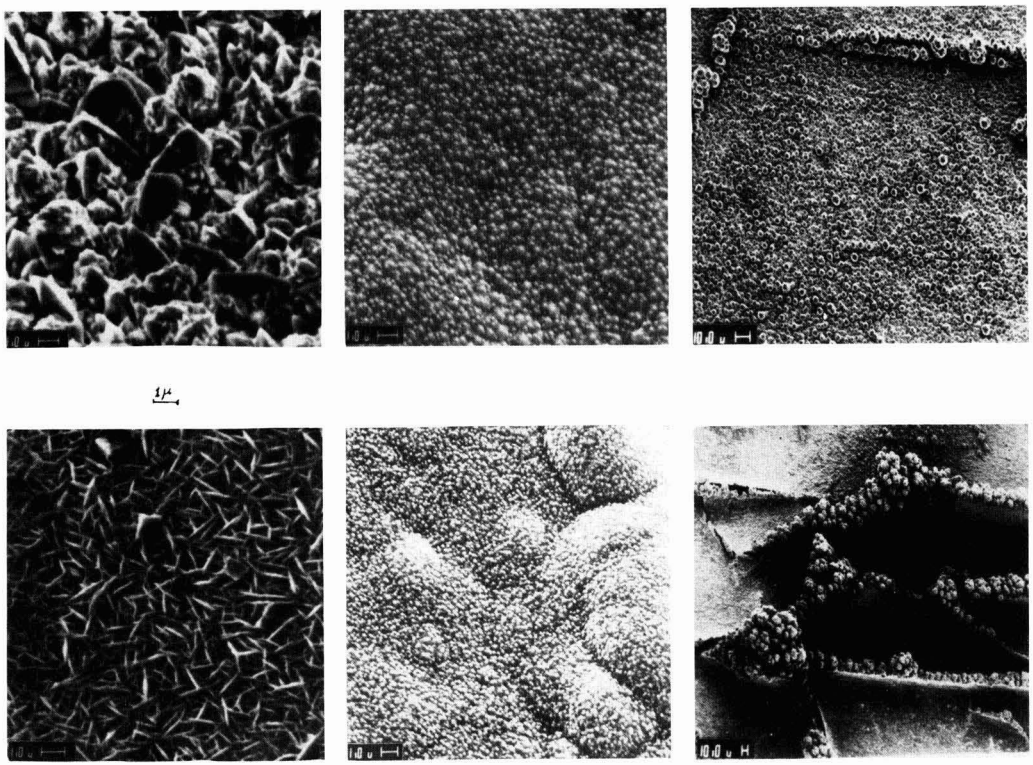


Fig. 4. SEM photographs of Ag-Pd alloy coatings obtained on Ag substrates with (a, top left) 0.5 mA/cm², (b, bottom left) 2 mA/cm², (c, top center) 5 mA/cm², (d, bottom center) 10 mA/cm², and (e, top right, and f, bottom right) 20 mA/cm². Figure 4e shows surface area in the center of the sample; 4f shows cracks closer to the sample edge, where there was higher current density. Note also the smaller magnifications of Fig. 4e and 4f.

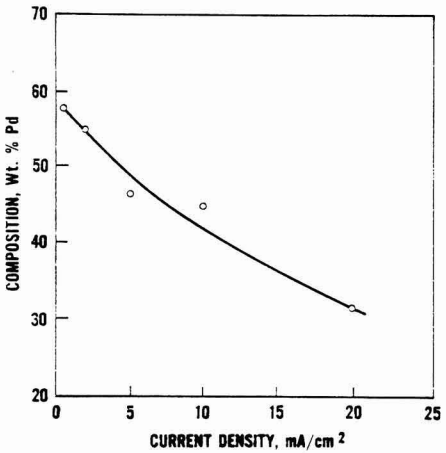


Fig. 5. Plated alloy composition vs. dc current density for low speed plating conditions.

the plated alloys, are likely to reduce the mobility of Ag atoms towards the surface, thereby reducing the formation of tarnish films in the sulfiding environment. It is also conceivable that certain impurities which are incorporated in the plated alloys help to reduce the mobility of Ag atoms towards the surface. The presence of incorporated Cl impurity in electroplated Ag-Pd CMA coatings was established by Auger electron spectroscopy (12). Incorporation of Cl in the plated Ag-Pd alloys could also contribute to their superior tarnish resistance over that of the wrought alloy.

Wear and friction.—Polished (rms surface roughness less than 0.5 μin.), and unpolished (rms less than 5 μin.) substrate coupons of CDA725 alloy were used as flats for the rider/flat wear tests. These were plated with either 2.5 μm of hard gold or with 2.5 μm of Ag-Pd alloy having a composition of 40 ± 2% Pd (preceded, as usual, by the 0.25 μm soft gold undercoating). The riders were hardened steel ball bearings (0.25 in. diam) plated first with 4 μm of nickel (Sel Rex 10-03S), then 0.25 μm of soft gold undercoating, and finally 5 μm of either the hard gold finish, or 5 μm of the Ag-Pd finish. Immediately prior to wear tests, both members of the test pair were carefully vapor degreased and then lubricated by dipping into a solution of Bareco wax (KS19416) in trichloroethane or a 2% synthetic hydrocarbon oil (Mobil RM109F).

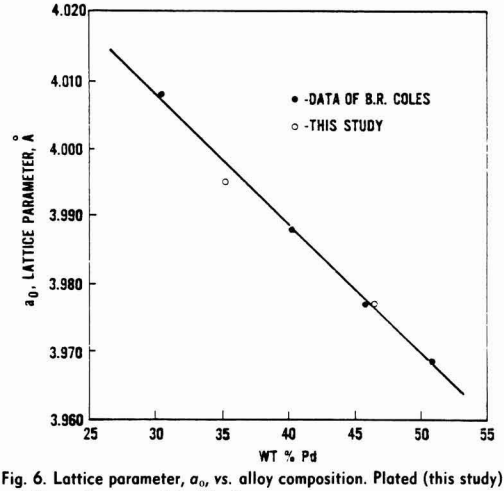


Fig. 6. Lattice parameter, a_o, vs. alloy composition. Plated (this study) and thermally prepared Ag-Pd alloys.

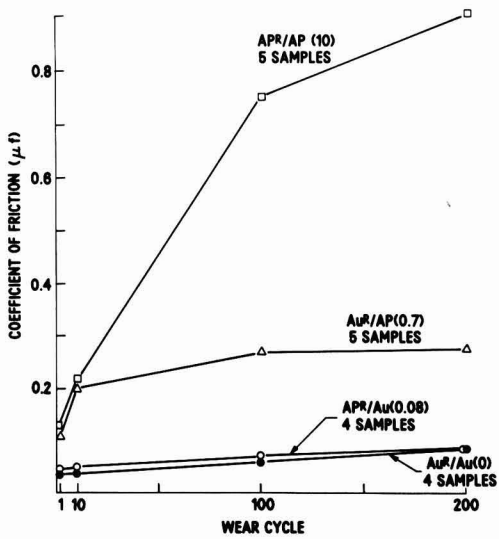


Fig. 7. The effect of contact finish variation on the wear and friction of rider/flat systems with microcrystalline wax lubrication, 225g load, 200 cycles, and polished CDA725 alloy substrates. Each data point represents the median value of 4 or 5 wear tests. AP^R/AP is alloy-plated rider/alloy-plated flat. Au^R/AP is gold-plated rider/alloy-plated flat. AP^R/Au is alloy-plated rider/gold-plated flat. Au^R/Au is gold-plated rider/gold-plated flat. The median wear depth in micrometers is indicated in parentheses.

The key results are summarized in Fig. 7 and 8 for the microcrystalline wax and hydrocarbon oil lubricants, respectively. It is clear from Fig. 7 that, with the solid lubricant (the microcrystalline wax), the hard gold-plated flats are superior to those with Ag-Pd-plated flats. In particular, the test pair with both rider and flat plated with Ag-Pd behaved very poorly. It is evident, however, that the pair with Ag-Pd-plated rider and hard gold-plated flat shows a wear response equivalent to the hard gold-plated pair. Figure 8 indicates that, with the liquid lubricant, all the test pair combinations are satisfactory and have essentially similar wear response (although there appears to be slightly better performance for the hard gold-plated

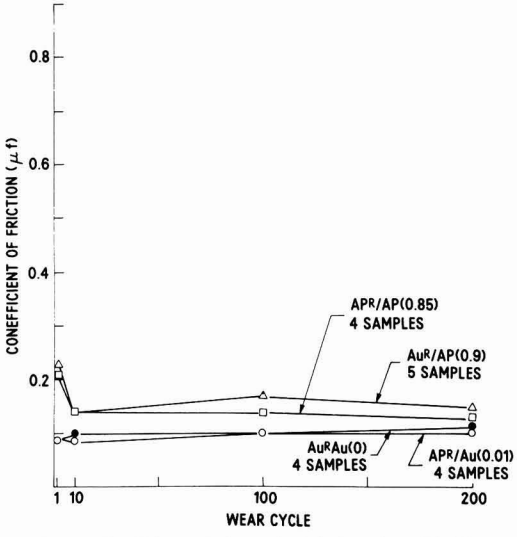


Fig. 8. As in Fig. 7, but with the synthetic hydrocarbon oil lubricant

flats). Surface roughness, in the range tested, appears to have little significance on the wear and friction performance. With both lubricants, the smoother substrates revealed a somewhat improved median wear response over the rougher substrates, but essentially identical friction coefficients. Coupons of bulk R156 alloy, when tested as flats with both lubricants under similar conditions, revealed significantly higher friction and wear than the plated Ag-Pd alloys. It should be noted that, without lubrication, both hard gold and the Ag-Pd alloys exhibited high coefficients of friction ($\mu_f \geq 0.6$) and disastrous wear (track depth up to 16 μm).

Some limited wear tests were also done with actual two-piece connector hardware of the type used in electronic switching systems. Standard 946/947 connectors with a mating load of 250g were the test vehicles. The male connector contact finish was 2.5 μm of hard gold plating. It was lubricated with the hydrocarbon oil prior to the testing. The female connectors were first plated with 2.5 μm of the Ag-Pd alloy finish and then tested by 200 mate/unmate cycles at a rate of 27 cycles/min, or about 1 cm/s as with the rider/flat tests. The median force of insertion was 1.8 kg for couples with Ag-Pd plated females (slightly higher than the 1.6 kg value for the reference pairs with soft gold inlay in place of the Ag-Pd alloy). Analysis by SEM and XRF mapping revealed some transfer of Ag-Pd to the male connector surface. However, there was no exposure of the base metal and no indication of unacceptable damage to any of the contacts after the 200 insertion cycles.

Summary

A simple, concentrated chloride electrolyte containing no additives or excessively hazardous components was used to demonstrate the potential benefits of Ag-Pd alloy plating. A very thin soft gold preplate (*i.e.*, 0.20-0.4 μm) was necessary to prevent displacement reactions with base metal substrates. Dense, uniform, single-phase alloys with Ag content of 40%-70% can be obtained at ~100% current efficiency. Decreasing the current density and increasing the amount of agitation increase the Pd content of the plated alloy. The lattice parameters, a_o, increases continuously with the Ag content of the alloy, in agreement with previous studies of Ag-Pd alloys (15).

Under optimal conditions, the following Ag-Pd alloy properties appear to be favorable for contact applications: (*i*) microhardness of ~200 (KHN_{25}), (*ii*) very low internal stresses (<1 kg/mm^2 compressive), (*iii*) with a hydrocarbon lubricant, wear and friction characteristics similar to hard gold plating, and (*iv*) the corrosion resistance in flowers of sulfur is better than R156 alloy and similar to hard gold plating.

The Ag-Pd alloy plating system appears to be an attractive potential substitute for hard gold in certain contact applications. However, more detailed study of the coating properties is required, as is continued development of a fully satisfactory plating process. The bath stability and aging due to photodissociation should be also studied in more detail.

Acknowledgments

The authors are indebted to F. B. Koch, R. A. Maher, S. Nakahara, G. J. Russ, and T. T. Sheng of Bell Laboratories for their help in various stages of this work.

Manuscript submitted June 11, 1982; revised manuscript received May 14, 1984. This was Paper 309 presented at the Denver, Colorado, Meeting of the Society, October 11-16, 1981.

AT&T Bell Laboratories assisted in meeting the publication costs of this article.

REFERENCES

1. T. R. Long and K. F. Bradford, in "Proceedings of the 8th International Conference on Electrical Contact Phenomena," Tokyo, Japan (1976).
2. W. A. Crossland and E. Knight, in "Proceedings of the Seminar on Electrical Contacts," p. 247, Chicago (1973).
3. A. Brenner, "Electrodeposition of Alloys: Principles and Practice," Academic Press, New York (1963).
4. A. K. Graham, S. Helman, and H. L. Pinkerton, *Plating*, **35**, 1217 (1948); *ibid.*, **36**, 47, 79 (1949).
5. G. P. Andreeva, N. P. Fedot'ev, and P. M. Vyacheslavov, in "Protective Metallic and Oxide Coatings, Metal Corrosion and Electrochemistry," N. P. Fedot'ev, Editor, Akademiya Nauk SSSR (1965); trans. published by Israel Program for Scientific Translations, Jerusalem, pp. 226-231 (1968).
6. N. T. Kudryavtsev, I. F. Kuschevich, and N. A. Zhandarova, *Z. Metallov.*, **7**, 206 (1971).
7. I. F. Kuschevich and T. Kudryavtsev, *ibid.*, **10**, 78 (1974).
8. U. Cohen and R. Sard, U.S. Pat. 4,269,671 (1981).
9. R. Holm, "Electric Contacts," New York (1967).
10. M. Antler, in "Properties of Electrodeposits—Their Measurement and Significance," R. Sard, H. Leidheiser, Jr., and F. Ogburn, Editors, p. 353, The Electrochemical Society Softbound Proceedings Series, Princeton, NJ (1975).
11. U. Cohen and S. Nakahara, "The Microstructure of Plated Ag-Pd Alloy Coatings," To be published.
12. U. Cohen, F. B. Koch, and R. Sard, *This Journal*, **130**, 1987 (1983).
13. G. J. Russ, *IEEE Trans. Compon. Hybrid. Manuf. Technol.*, **chmt-2**, 317 (1979).
14. D. E. Koontz and U. Landau, U.S. Pat. 4,001,093 (1977); D. Bacon, U. Landau, and R. L. Meek, *West. Elec. Eng.*, April 1978.
15. B. R. Coles, *J. Inst. Metals*, **84**, 364 (1956).
16. F. B. Koch, R. A. Maher, D. L. Simms, and R. Sard, *Plating*, **63**, 45 (1976).
17. R. A. Maher, Personal communication (1974).
18. J. E. Bennett and M. R. Pinnel, Personal communication (1973).

A Quantitative Investigation of the Open-Circuit Photovoltage at the Semiconductor/Liquid Interface

Nathan S. Lewis*

Department of Chemistry, Stanford University, Stanford, California 94305

ABSTRACT

A quantitative analysis of the theoretical value for the open-circuit photovoltage, V_{oc}, of a semiconductor/liquid junction reveals that control of bulk carrier transport properties is crucial to interpreting the observables at the semiconductor/liquid interface. Use of characterized semiconductor samples yields quantitative agreement between the maximum theoretical V_{oc} and experimentally observed values for both n-Si and p-Si surfaces in nonaqueous solvents. This accord between theory and experiment rules out deleterious effects of charged surface states on the V_{oc} of these interfaces. Lower than ideal V_{oc} values in other systems might reflect poor diffusion lengths in the semiconductor, classical tunneling over the barrier, or the effects of surface states. The observation of large photovoltages from n- and p-type-based semiconductor interfaces (n-Si, p-Si, n-GaAs, p-GaAs) in the same solvent is used to rule out a fixed density of charged surface states as the mechanism for obtaining constant photovoltages at these junctions. Direct support for this interpretation is obtained by techniques which verify the presence of mobile surface charge on p-type Si cathode surfaces in the inversion condition. Thus, control and investigation of bulk semiconductor properties that has been eminently significant to the understanding of p-n junction solar cells is also crucial to developing a rational understanding of the observables at the semiconductor/liquid interface.

The aim of this paper is to present a clarified treatment of the energetics at semiconductor/liquid interfaces. Recently, substantial effort has been directed into revision of the model which describes the relevant observables at a semiconductor/liquid junction. Rationales for junction properties include carrier inversion (1-3), pinning of the surface Fermi level by gap states (4-6), and hot carrier injection (7). Each of these models has been proposed to explain the behavior of a particular semiconductor/liquid combination. The specific conditions under which hot carrier injection may be observed have been discussed recently by Nozik (7), and this effect will not be the main focus of our discussion. Surface states have been frequently invoked to explain nonideal junction behavior at a variety of electrode surfaces (4-6). A key difference between carrier inversion and Fermi-level pinning by surface states is that the latter can (in principle) be manipulated by chemical treatment of gap states, while carrier inversion should not be sensitive to such effects.

We have previously demonstrated that modest interface parameters may not be intrinsic to the semiconductor/liquid junction, but can arise from nonideal bulk semiconductor properties (8) or from poor photoelectrochemical cell design (9). In the present work, the open-circuit photovoltage (V_{oc}), an especially important property of a semiconductor/liquid junction, is treated quantitatively. The ideal photovoltage for a semiconductor of bandgap E_g has been claimed to be the value of E_g itself (3, 4a, 10). Thus, constant photovoltages, less than $(1/q)E_g$ in value, have been stated to be diagnostic of surface states which pin the semiconductor Fermi level (3-6, 11). However, a quantitative analysis of the factors involved in the separation of photogenerated carriers indicates that at moderate light intensities (1 Sun), intrinsic bulk recombination kinetics of the semiconductor will prevent attainment of a photovoltage close to the value of $(1/q)E_g$. This maximum restriction on V_{oc} holds even in the absence of any other sources of recombination, and rigorously applies for all surface barrier devices (semiconductor/liquid junctions) and all p-n diodes (12, 13). In addition to presenting a theoretical framework within which to interpret experimental data for semiconductor/liquid interfaces, we describe experiments which rule out a fixed density of surface states as the dominant factor in determination of V_{oc} at p-type Si photocathodes, and present data which establish the presence of mobile surface charge (carrier inversion) at p-type Si surfaces in nonaqueous solvents.

Experimental

The mounting and characterization of semiconductor electrodes has been described previously (8, 9). Characterization of relevant samples is as follows: n-type Si, (100)-oriented, phosphorus-doped, 4-9 Ω-cm (Wacker Siltronic) ohmic contact with Ga-In eutectic or with phosphorus diffusion (950°C) followed by Al contact; p-type Si, (100)-oriented, boron-doped, 5-10 Ω-cm (Wacker Siltronic) ohmic contact by evaporation of Al and alloying at 650°C for 5 min; n-type GaAs, (100)-oriented, Si-doped, donor density = 8×10^{15} cm^{-3} ohmic contact by evaporation of In and annealing under N_2 at 450°C for 15 min; p-type GaAs, (100)-oriented, Zn-doped, acceptor density = 2×10^{16} cm^{-3} (Laser Diode Company) ohmic contact by evaporation of 98% Au/2% Ge alloy, followed by annealing under H_2 at 450°C for 5 min. Si surfaces were etched before use with 48% HF for 10s, followed by a rinse with H_2O, then by a rinse with solvent, and were air dried. GaAs surfaces were etched with 3:1:1 H_2SO_4:H_2O_2:H_2O, 1:1 H_2O_2:H_2SO_4, or 12*M* HCl, rinsed with H_2O, then rinsed with solvent, and air dried before use.

All open-circuit photovoltages were obtained by direct measurement of the voltage between the semiconductor electrode and a large area Pt counterelectrode. Measurements were conducted through a high input impedance voltmeter, and were recorded on a Houston Instruments Model 2000 X-Y chart recorder. The accuracy of these measurements was verified by recording current-voltage curves in a three-electrode configuration *vs.* a Pt wire reference electrode poised at the solution potential. Semiconductor surface conductivity measurements on Si cathodes were performed by monitoring the voltage drop across a calibrated 10 kΩ resistor placed in series with the conductivity cell. Voltage detection was performed with a Princeton Applied Research Model 124A Lock-In Amplifier. The lock-in amplifier supplied the applied voltage, which was a sine wave with a 10 mV amplitude and a frequency of 1 kHz. The output signal was recorded on a Linear Instruments Model 555 Strip Chart Recorder. Negligible changes in conductance were recorded when the semiconductor shunt was omitted from the apparatus.

The CH_3OH solvent was distilled in a nitrogen atmosphere from Mg, and was stored over activated 3Å molecular sieves until use. CH_3CN was distilled from P_2O_5 and stored over 3Å sieves until use. Cobaltocene was purchased from Strem Chemical, Incorporated, and was purified by sublimation. All manipulations with cobaltocene were performed in a Vacuum Atmospheres, Incorporated glove box because of the extreme air sensitivity of this compound. N,N′-dimethyl-4,4′-bipyridinium dichloride dihydrate was used as received from Aldrich Chemical Corporation. N,N′-dibenzyl-4,4′-bipyridinium dibromide was synthesized by addition of benzyl bromide to 4,4′-bipyridine in CH_3CN solvent, and was isolated by addition of diethyl ether. Decamethylferrocene was used as received from Strem Chemical Corporation. N,N,N′,N′-

*Electrochemical Society Active Member.

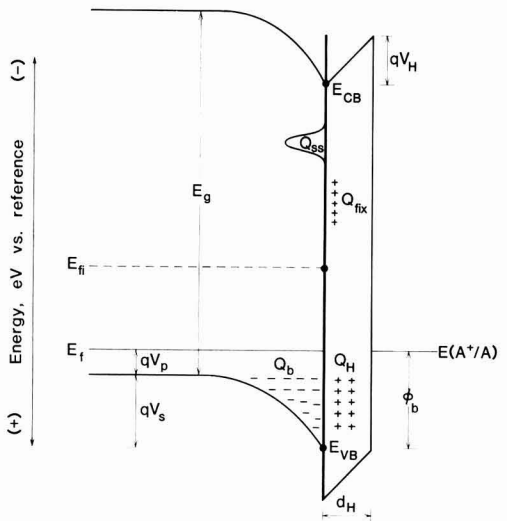
tetramethylphenylenediamine, 1,1′-dimethylferrocene, ferrocene, and acetylferrocene were purchased from Aldrich Chemical Corporation, and were recrystallized before use. Other oxidation states of all redox couples were obtained by constant potential electrolysis in a three-compartment electrochemical cell.

Expectations for the dependence of photovoltage upon solution redox potential.—A model of interface parameters at a p-type semiconductor/liquid junction is represented in Scheme I. Properties of interest include the energies of the semiconductor conduction and valence bandedges, E_{cb} and E_{vb}, the position of the Fermi level of the semiconductor, E_f, the position of the Fermi level of the intrinsic semiconductor when the band bending is zero, E_{fi}, the bandgap of the semiconductor, E_g, and the redox potential of the solution, $E(A^+/A)$. All potentials are defined in accord with the electrochemical scale where more negative potentials are closer to the vacuum level. The energy of the semiconductor Fermi level before equilibration with $E(A^+/A)$ is defined as the "flatband" condition, $E_{FB} \cong E_{vb} + kT \ln (N_A/N_v)$, where N_A is the bulk equilibrium hole concentration in the doped semiconductor and N_v is the effective density of states in the valence band. We assume that the back contact to the semiconductor is an ohmic or selective (for majority carriers) ohmic contact.

Equation [1] is appropriate to relate the band bending in the semiconductor, V_s, to $E(A^+/A)$, given values of fixed interfacial charge density, Q_{fix}, charge in surface states, Q_{ss}, and charge in the bulk semiconductor, Q_b

$$(qV_s = E_{vb} - q)E(A^+/A) - qV_p + q(d_H/\epsilon_H)(Q_b + Q_{fix} + Q_{ss}) \quad [1]$$

For values of V_s such that $E_f > E_{fi}$, Eq. [1] reduces to the conventional model of the semiconductor/liquid junction. For band bending such that E_f is negative of $2E_{fi} - E_{FB}$, a substantial contribution to the space charge in the semiconductor will come from accumulation of minority carriers. In this regime, the semiconductor is said to be in the strong inversion condition (1, 13), which can lead to V_{oc} values which are insensitive to the actual magnitude of $E_{vb} - qE(A^+/A)$. Under these conditions, the maximum band bending can reach $E_g - qV_p$ ($V_p \equiv (1/q)(E_{vb} - E_f)$ at zero band bending).



Scheme I. Representation of the energetic parameters of a semiconductor/liquid interface at charge transfer equilibrium. The energy scale is depicted using the electrochemical potential convention, where increasing negative potentials indicate energies closer to the vacuum level. The diagram is appropriate for a moderately doped, p-type semiconductor, and neglects image force effects or Schottky barrier lowering. The potential drop in the electrolyte is assumed to occur entirely across the Helmholtz layer, which is characterized by a thickness d_H with dielectric constant ϵ_H.

The maximum band bending under conditions where Q_{ss} dominates Q_b and Q_{fix} in Eq. [1] will be determined by the energetic distribution of the charged states relative to E_{vb} and E_{cb}. Thus, in the absence of surface chemistry with the electrolyte (a change in Q_{fix}), if the barrier height, ϕ_b, is limited by surface states, the maximum value of ϕ_b for a p-type semiconductor/liquid junction and the maximum value of ϕ_b for the corresponding n-type semiconductor/liquid junction will add up to no greater than $(1/q)E_g$ (3, 12, 13). In the absence of field shaping in an interfacial layer (15), V_{oc} at moderate light intensities will be substantially less than ϕ_b. Within this framework, if the maximum V_{oc} at a photocathode and at the corresponding photoanode should exceed (or even closely approach) $(1/q)E_g$, we can rule out Fermi-level pinning by a fixed surface-state density as the source of constant V_{oc} values with variation in $E(A^+/A)$. We discuss the experimental observation of such conditions below.

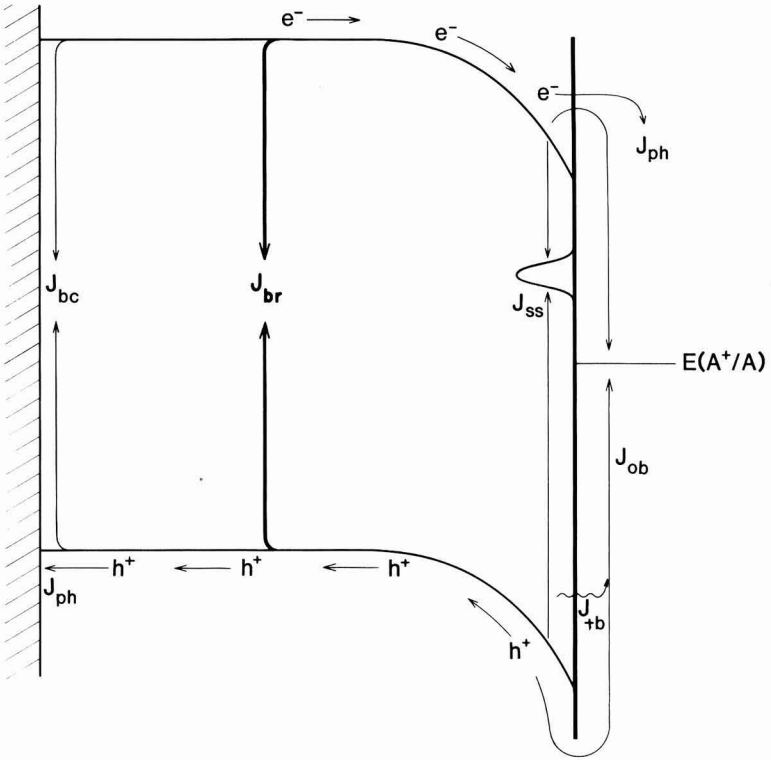
Maximum attainable photovoltages at a semiconductor/liquid interface.—V_{oc} values which are significantly less than $(1/q)E_g$ have been interpreted to indicate Fermi level pinning by interface states (3-6, 11, 16). Furthermore, the maximum V_{oc} value is commonly associated with the value of ϕ_b (±0.1V) (3, 4, 10c, 17), and nonidealities of V_{oc} are thus taken as indications of lower than theoretical ϕ_b values. In order to develop an explicit relationship between V_{oc} and ϕ_b at the semiconductor/liquid interface, we apply the procedures commonly used by physicists and physical electrochemists to relate E_g and V_{oc} in p-n junction cells and in electrolyte cells (12, 13).

The key notion is that V_{oc} is not an energetic parameter of the interface, but is determined by the generation, recombination, and transport of the minority and majority carriers throughout the semiconductor. Scheme II outlines most of the pertinent mechanisms for recombination of electron-hole pairs at a semiconductor/liquid interface. Depicted are mechanisms for loss of photogenerated carriers: direct and indirect bulk recombination, J_{br}; recombination at the back contact, J_{bc}; recombination via surface states, J_{ss}; thermionic emission of majority carriers over the barrier, J_{ob}; and tunneling or leakage (perhaps at chemical imperfections) through the barrier, J_{tb}. Most of these current densities are dependent upon the voltage developed in the cell. Additionally, the overall voltage profile of the recombination components yields the dark current-voltage curve for the interface. Also depicted is the current density for capture of photogenerated minority carriers by the electrolyte, J_{ph}, which will lead to useful energy extracted from the system.

The V_{oc} is defined as the potential at which the net collected current is zero; thus, recombination by any of the mechanisms indicated in Scheme II can lower V_{oc}. If no recombination occurred by any of the pathways indicated, then the maximum V_{oc} might approach $(1/q)E_g - V_p$. However, for real solids with finite mobilities of charge carriers and finite diffusion lengths, J_{br} will not approach zero. Collection of any photogenerated current by the electrolyte will necessarily lead to a change in the quasi-Fermi level for electrons from its value in the dark. This change in population will be "resisted" by the finite values of the minority carrier diffusion coefficient, D_n, (for a p-type semiconductor), and the minority carrier diffusion length, L_n. Thus, in the absence of surface recombination or leakage across the barrier, bulk recombination processes will define an upper limit on V_{oc} at a given photocurrent density.

The expression relating J_{br} to these bulk materials parameters is represented in Eq. [2] (12, 13)

$$J_{br}(V) = \frac{qD_n n_0}{L_n}\left(e^{\frac{qV}{kT}} - 1\right) = qN_C \frac{D_n}{L_n} e^{-(E_g - qV_p)/kT}\left(e^{\frac{qV}{kT}} - 1\right) \quad [2]$$



Scheme II. Representation of the kinetic parameters involved in separation of charge carriers at an illuminated semiconductor/liquid interface. Recombination by any of the mechanisms depicted can contribute to low open-circuit photovoltages in the system. If all other sources of recombination are suppressed, bulk recombination (by both direct and indirect mechanisms) will determine the upper limit on the attainable photovoltage at a given light intensity. Thus, the ultimate limit on the photovoltage represents a bulk property of the semiconductor itself, not a parameter of the semiconductor/liquid junction. Poor bulk properties can thus yield low photovoltages without implying the presence of surface states.

D_n is related to the mobility by $D_n = (kT/q)\mu$, and is thus a function of the semiconductor (the effective density of states in the conduction band), while L_n is a function of the particular crystal under study. N_C is the density of states in the conduction band, n_0 is the electron concentration in the bulk semiconductor before equilibration with the solution, and the other parameters have their usual meanings. Setting $J_{br} = J_{ph}$ will define the maximum possible V_{oc} at photocurrent density J_{ph} for a p-type semiconductor/liquid interface with fixed values of D_n, L_n, N_A, and E_g, and yields the approximate expression in Eq. [3] for V_{oc}. Similar treatments would apply to any semiconductor surface barrier device where photocurrent is to be collected

$$V_{oc} \cong \frac{kT}{q} \ln \frac{J_{ph}L_n}{qN_cD_n} + (1/q)E_g - V_p = \frac{kT}{q} \ln \frac{J_{ph}L_nN_A}{qD_nn_i^2} \quad [3]$$

At a semiconductor/liquid junction, under the usual conditions of low level injections, V_{oc} can never exceed the value determined from Eq. [3] (the "diffusion limit") without having an electrochemical corrosion reaction in series with stable photoelectrochemical power production. Table I indicates calculations of typical values of V_{oc} (max) for several common semiconductors under particular experimental conditions. Appropriate modifications can be made for the parameters in Eq. [2] or [3] to predict the theoretical V_{oc} at any photocurrent density given the appropriate materials parameters. It is emphasized that Eq. [2] and [3] refer specifically to p-type semiconductors, but analogous equations apply equally rigorously to n-type materials (replacing D_n with D_p, L_n with L_p, N_A with N_D, etc). The typical experimental variable which must be determined for a p-type crystal is L_n, with larger values of L_n indicating higher quality material. Notably, low L_n or N_A values can yield a low V_{oc} without surface states contributing to recombination. For accurate studies of the

Table I. Typical values of V_{oc} (max)

Semiconductor	Solvent	J_{ph} (mA/cm²)	N_{maj} (cm⁻³)	D_{min} (cm²/s)	n_i (cm⁻³)	L_{min} (μm)	V_{oc} (theory)[a] (V)	V_{oc} (obs.) (V)	Ref.
n-Si	CH_3OH	17.0	7.7×10^{15}	11.65	1.45×10^{10}	300	0.60	0.57-0.58	This work
n-Si	CH_3OH	17.0	9.3×10^{14}	11.65	1.45×10^{10}	700	0.56	0.51-0.52	(9)
p-Si	CH_3CN	21.0	2.1×10^{16}	34.97	1.45×10^{10}	400	0.55	0.48-0.50	(40)
n-GaAs	CH_3CN	22.0	8.0×10^{15}	10.9	1.8×10^{6}	2	0.94	0.72-0.75	(8a)
n-GaAs	H_2O	22	10^{16}	10.9	1.8×10^{6}	2	0.94	0.70-0.75	(41)
p-InP	H_2O	25	2.4×10^{17}	119	1.5×10^{7}	2	0.86	0.66-0.68	(24)
n-CdTe	CH_3CN	15	10^{16}	1.7	6.9×10^{5}	1	1.01	0.65-0.72	This work
n-$MoSe_2$[b]	CH_3CN	20	7×10^{16}	5	1.3×10^{10}	5	0.6	0.6	(1, 42)
n-$MoSe_2$[b]	H_2O	25	10^{17}	5	1.3×10^{10}	5	0.6	0.6	(42, 43)
n-WSe_2[b]	H_2O	15	10^{17}	5	1.9×10^{10}	5	0.6	0.7	(44)

[a] Calculated based on Eq. [3]. Relevant semiconductor parameters taken from Ref. (12, 13) and references therein. The theoretical value is calculated for an infinite crystal thickness, and thus ignores any further lowering of V_{oc} owing to the large surface recombination velocity of the back ohmic contact in typical experimental systems. The correction is on the order of 5%, and is not significant to the accuracy of the present values available for semiconductor/liquid junctions.

[b] The accuracy of these values are limited both by the dispersion in experimental V_{oc} values (1, 42, 43) and some uncertainty concerning the value of n_i for these crystals. We have used $E_g(MoSe_2) = 1.06$ eV, $E_g(WSe_2) = 1.16$ eV and approximate $N_c = N_v = 10^{19}$ for these materials (44).

semiconductor/liquid junction, it has been demonstrated that L_n (or L_p) must be sufficient to insure the collection of photogenerated carriers (8, 19). However, even values of L_n or L_p sufficient to produce unit quantum yields at short circuit with 632.8 nm irradiation might not suffice to obtain the V_{oc} values calculated for the highest quality material in Table I. Thus, although V_{oc} values have been interpreted to represent the chemical nature of the semiconductor/liquid interface (3-6, 10, 11, 17), it is seen that these V_{oc} values might in many cases primarily reflect the bulk properties of the semiconductor.

Although we have not considered any of the other recombination mechanisms depicted in Scheme II, we note that in most surface barrier devices the dominant recombination terms are leakage across the barrier and J_{ob}, the thermionic emission term (13, 20). For a finite barrier height, ϕ_b, classical emission over the barrier will ideally have a dependence on the cell potential as given in Eq. [4] and [5]

$$J_{ob} = J_o (e^{\frac{qV}{kT}} - 1) \quad [4]$$

$$J_o = A^*T^2e^{-(q\phi_b/kT)} \quad [5]$$

The effective Richardson's constant, A^*, is related to the free electron value by the ratio of effective electron (hole) mass in the semiconductor to the value in vacuum. If the dark current is dominated by J_{ob}, for a barrier height of $(1/q)E_g$ V_{oc} will be less than $(1/q)E_g$, and can be less than the V_{oc} value obtained from the diffusion limit of Eq. [3]. Use of the A^* appropriate for n-GaAs in Eq. [5] reveals that if V_{oc} for an n-GaAs anode is 0.90V at photocurrent densities of 20 mA/cm^2, this may be entirely consistent with a V_{oc} controlled by thermionic emission, and does not necessarily imply the presence of surface states. We note that use of expression [5] is predicated on the assumption of rapid carrier capture available in a metal, and liquids might require substantially different descriptions for the over-barrier component than given in Eq. [4] and [5]. The main point is that there are several mechanisms for obtaining low photovoltages at the semiconductor/liquid interface which do not require postulation of charge in surface states. Thus, in cases where V_{oc} is found to be substantially lower than the bulk diffusion limit, a detailed analysis of the junction properties is necessary in order to identify the dominant recombination term at the particular semiconductor/ liquid interface.

Results and Discussion

Comparison of theory and experiment: open-circuit photovoltage.—A comparison of the theoretical maximum V_{oc} values calculated from Eq. [3] with accurate experimental data indicates close agreement with ideal behavior in several systems. Listed in Table I are the calculated V_{oc}(max) from Eq. [3] and the experimental values of V_{oc} for semiconductor/liquid junctions where approximate estimates of the photocurrent density and the minority carrier diffusion length are possible. The quantitative comparison in Table I indicates that several of the common semiconductor/liquid junctions previously suggested to have severe limitations of V_{oc} due to Fermi-level pinning (3-5) actually display photovoltages which are close to the maximum possible values. As an example, p-type Si photocathodes have been stated to be Fermi-level pinned because V_{oc} is only 0.35-0.50V with laser excitation of up to 50 mW/cm^2 (11c, 21). At photocurrent densities of 25 mA/cm^2 on characterized silicon samples (Table I), we measure a V_{oc} of 0.48-0.52V for p-type Si in the cobaltocene $^{+/0}$/CH_3CN system. The theoretical value calculated from Eq. [3] (0.55V) is thus within 10% of the observed V_{oc}. Similar agreement between theory and experiment can be observed for n-Si/ferrocene junctions in CH_3OH solvent, where theory and data differ by less than 4% (9). We emphasize that the ideal values assume no losses from any of the other mechanisms depicted in Scheme II, and entirely neglect any contribution from the thermionic emission component or from recombination at the back contact. In view of the fact that we have not searched for conditions to optimize the performance of our liquid junctions, we are highly encouraged by the close accord between ideal expectations and actual experimental results.

It is interesting to compare the V_{oc} values obtained on these Si/liquid systems to the V_{oc} values obtained with Si p-n junctions. It has been suggested that when no surface states are present at a semiconductor/liquid interface, that the value of V_{oc} would approach that of a p-n junction. At 35 mA/cm^2 photocurrent density, typical p-n junctions (NASA Si secondary standard cells) exhibit a V_{oc} of 0.55-0.57V, and active area efficiencies of 12.5% (22). The n-Si/CH_3OH/ferrocene$^{+/0}$ photoelectrode system ($\rho \simeq 5$ Ω-cm) yields V_{oc} = 0.52-0.56 at 25 mA/cm^2, and total area efficiencies of 10.0% (without elimination of residual solution absorption or series resistance losses) (9). Thus, if similar substrates are employed, the photocurrent-voltage parameters attainable at the semiconductor/liquid interface compare favorably in V_{oc} to technologically advanced silicon solid-state systems.

A similar analysis can be applied to p-InP, where V_{oc} values of 0.80V have been obtained and assigned to surface states (3, 23). The bulk diffusion limit on V_{oc} for p-InP with an extremely long diffusion length ($L_n \cong 5$ μm) is approximately 0.9V. In the absence of leakage, and if the thermionic emission limit applies, a barrier height of $E_g - qV_p \cong 1.2$ eV might yield a V_{oc} (max) of only 0.8V. Although there is some discrepancy between the maximum bulk-diffusion-limited V_{oc} and the experimentally reported V_{oc} values, clearly indicating some other dominant recombination pathway at this junction, reference to Eq. [3] indicates that ideal junctions could not yield substantial (> 0.2V) improvements in V_{oc} over the reported data; thus, we conclude that surface-state pinning is not a severe limitation on the value of V_{oc} for p-InP cathodes in aqueous or nonaqueous solvents. This is consistent with the observation by Heller that the oxide on p-type InP will prevent surface states from significantly reducing the attainable V_{oc} value (24). Changes in stoichiometry at n-InP surfaces (owing to chemical reactions with the etchant, atmosphere, etc.) may prevent attainment of the maximum V_{oc} in photoanode-based systems, however, this does not necessarily mandate restrictions on V_{oc} for the p-InP system. The important concept is that Eq. [3] provides a quantitative framework to assess bulk *vs.* surface recombination effects at semiconductor/liquid interfaces.

For the systems listed in Table I (other than the Si-based junctions), it is clear that some improvement in experimental V_{oc} can be attained, and that bulk recombination does not limit the junction properties in all cases. Clearly, when surface etching is found to change junction properties, or when photocorrosion processes dominate the photovoltage, the surface will play an important role in determining the observed V_{oc}. In these cases, Fermi-level pinning may dominate the junction behavior, and this pinning can lead to lower than optimum V_{oc} values. However, Table I demonstrates that in some semiconductor/liquid systems, substantial improvements in V_{oc} could not be attained even if surface-state effects were minimized. We conclude that V_{oc} should be compared to the bulk-diffusion-limited value (and possibly to the ideal thermionic-emission-limited value) and not to the value of E_g, in order to ascertain a potential role for surface recombination at the semiconductor/liquid junction.

We also note that some reported values of V_{oc} significantly exceed the value calculated from the bulk diffusion limit (25, 26). We suggest that these particular interfaces must involve a parallel corrosion reaction which yields artificially high V_{oc} values. It is possible, of course, that the value of ϕ_b might actually exceed E_g if a fixed surface charge of the appropriate sign and density or an

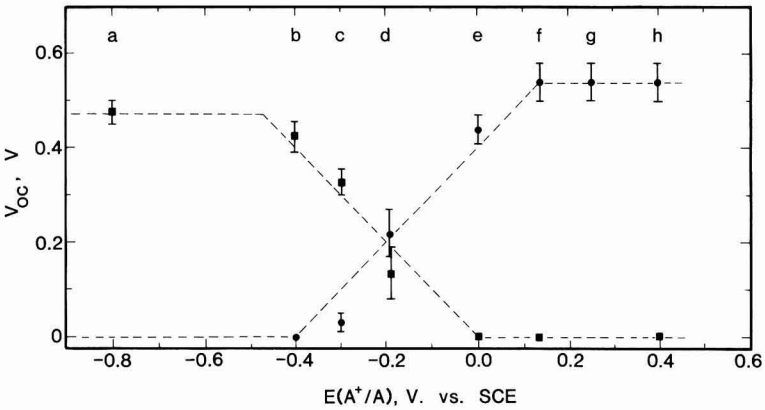


Fig. 1. Open-circuit photovoltage vs. solution redox potential for n-Si and p-Si photoelectrodes in 1.0M KCl/CH_3OH solution. The redox couples used were: (a) cobaltocene$^{+/0}$, (b) N,N′-dimethyl-4,4′-bipyridinium dichloride$^{2+/+}$, (c) N,N′-dibenzyl-4,4′-bipyridinium dibromide$^{2+/+}$, (d) decamethylferrocene$^{+/0}$, (e) N,N,N′,N′-tetramethylphenylenediamine$^{+/0}$, (f) dimethylferrocene$^{+/0}$, (g) ferrocene$^{+/0}$ and (h) acetylferrocene$^{+/0}$. A tungsten-halogen bulb was used to provide light intensities which yielded short-circuit photocurrent densities of 25-30 mA/cm^2.

oxide were present at the interface. This might produce suppression of the J_{ob} component, and other mechanisms might then dominate the dark current. Under no conditions, however, can the dark current be less than the bulk diffusion limit of Eq. [2]; therefore, higher V_{oc} values than those calculated from Eq. [3] must indicate chemical reactions with the electrolyte.

It can also be seen that V_{oc} measurements at any accessible light intensity generally will not provide an accurate estimate of ϕ_b. It has been stated that measurement of V_{oc} by cyclic voltammetry indicates ϕ_b to within 0.1V (3, 4, 21). Furthermore, it has been stated that V_{oc} measurements to determine ϕ_b are analogous to photoresponse measurements in the solid state (17). Photoresponse measurements on Schottky barriers are based upon internal photoemission from the metal into the semiconductor, and are a direct measure of ϕ_b, not V_{oc} (12, 27). We also emphasize the distinctions in Scheme I between ϕ_b, V_s, and V_{oc}.[1] Even in the absence of temperature effects and of recombination kinetics which are nonlinear with light intensity, plots (on linear axes) of the logarithmic dependence of the V_{oc} *vs.* incident light intensity can appear to exhibit a saturation value which does not reflect ϕ_b. Within the framework described above, V_{oc} should be correlated with V_s or ϕ_b only with a detailed understanding of the interfacial kinetics at the particular semiconductor/liquid junction system.

Comparison of maximum photovoltages for n-type and p-type semiconductors: distinguishing between Fermi-level pinning and carrier inversion.—Having established the theoretical upper limit on V_{oc}, it still remains of interest to determine the mechanism for constant photovoltages over a wide range of solution potentials, $E(A^+/A)$. In this work, two methods have been applied to differentiate between carrier inversion and Fermi-level pinning. One method, discussed below, is based on measurement of the near-surface conductivity of the semiconductor. Additionally, if the sum of the maximum barrier heights for an n-type semiconductor, ϕ_{bn}, and a p-type semiconductor, ϕ_{bp}, in the same solvent should substantially exceed E_g, then Fermi-level pinning by a fixed distribution of surface states inherent to the semiconductor/solvent interface can be ruled out. An even more severe restriction is that the sum of the maximum V_{oc} for the n- and p-type combination should not exceed $(1/q)E_g$. In principle, differential capacitance data can be used to extract the value of E_{FB}; however, frequency dependences of the measured capacitance generally complicate the analysis (29). The onset of photocurrent has also been used in some instances (5a, 30); however, it has not been unambiguously determined how to relate the kinetic parameters measured under these conditions (no well-defined solution redox potential, artificial suppression of dark current due to low concentrations of electroactive species) to the energetic parameter ϕ_b. We have thus carried out direct measurements of V_{oc} as a function of photocurrent density in various solutions (A^+/A) in both CH_3OH and CH_3CN solvent. The values of V_{oc} will determine lower limits of the sum of $\phi_{bn} + \phi_{bp}$ for the pairs of n- and p-type semiconductors.

For the redox couples (A^+/A), in order to insure rapid interfacial kinetics at the semiconductor/liquid interface, we choose outer sphere redox reagents which exhibit reversible electrochemistry at metal electrodes. Typical V_{oc} data for the n-type Si($N_D = 9 \times 10^{14}$ cm^{-3}), and p-type Si ($N_A = 2 \times 10^{15}$ cm^{-3}) electrode system are depicted in Fig. 1. The incident light intensity is sufficient to produce photocurrent densities of 25-30 mA/cm^2 in all cases, and the solutions contain high concentrations of both forms of the redox couple (where possible). We observe V_{oc} values of 0.54 ± 0.02V for n-Si in the ferrocene$^{+/0}$ system, and 0.45 ± 0.02V for p-Si in the cobaltocene$^{+/0}$ system. Further changes in redox potential do not yield higher value of V_{oc} at this photocurrent density in methanol solvent.

Similar photovoltage data, obtained by cyclic voltammetry for p-type Si in CH_3CN solvent (6a) and for n-type Si in C_2H_5OH (31) and CH_3CN solvent (6a), have been associated with ϕ_b, and have been used to propose Fermi-level pinning of the Si by surface states. In direct measurement of V_{oc} in a full cell configuration, at higher incident light intensities we observe $V_{oc} > 0.65$V for n-Si and $V_{oc} > 0.55$V for p-Si, for a sum of V_{oc} values of > 1.2V (E_g for Si at 300 K = 1.12 eV). The fact that the sum of the V_{oc} values exceeds $(1/q)E_g$ contradicts the notion that severe restrictions on V_{oc} are present due to a fixed set of charges in surface states.

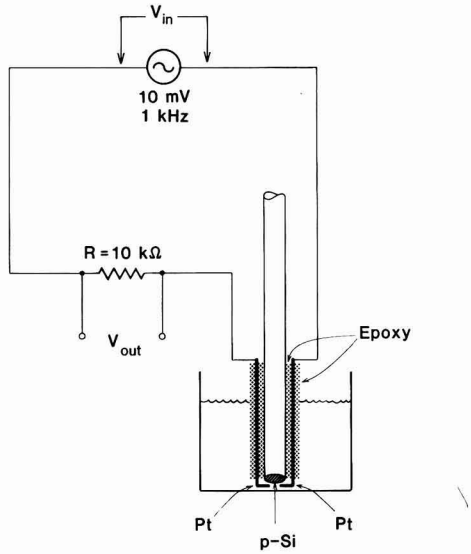
Data interpreted as evidence for surface states have been obtained previously for n- and p-type GaAs in CH_3CN solvent (5a). p-Type GaAs is reported to yield low V_{oc} values (0.2-0.3V) in both aqueous and nonaqueous solvents (32). In addition, constant (0.55-0.62V) photovoltages have been measured for n-type GaAs in CH_3CN solvent (33, 34). Therefore, it has been stated that n-GaAs and p-GaAs are Fermi-level pinned by surface states (4a, 5a). This is proposed to be consistent with the "1/3 rule" in semiconductor physics which empirically generalizes that surface states tend to reside at $E_{vb} - (1/3)\ E_g$ (12, 35). At light intensities ≅ 10 Suns, we observe V_{oc} values for n-type GaAs in ferrocene$^{+/0} > 0.85$V, and V_{oc} values for p-type GaAs in the cobaltocene$^{+/0}$ system of > 0.75V. We thus conservatively estimate $\phi_{bn} + \phi_{bp} > 1.6$ eV, which is in excess of E_g for GaAs (1.42 eV). Additionally, the barrier height for n-GaAs in CH_3CN (based on V_{oc} measurements) has been proposed to be in excess of 1.1 eV (34),

[1] For an ideal Si/Au Schottky diode (ideal diode quality factor, $n = 1.0$; dark current dominated by thermionic emission), V_{oc} at 30 mA/cm^2 photocurrent density will underestimate ϕ_b by 0.5V (28). Furthermore, light intensities of over 2000 W/cm^2 would be needed to obtain a 0.2V agreement between V_{oc} and ϕ_b. Lack of change in V_{oc} with increases in incident light intensity can reflect the onset of recombination processes in the bulk semiconductor or recombination at the interface, and need not imply that the flatband potential has been approached.

implying that surface states should be within 0.3 eV of the valence band, and should thus prevent substantial V_{oc} values at p-GaAs. The observation of $V_{oc} > 0.75$V in the p-GaAs/cobaltocene$^{+/0}$ system is inconsistent with these predictions. We thus conclude that Fermi level pinning by charge in a fixed density of interface states cannot account for the V_{oc} behavior of GaAs in CH_3CN solvent, and does not necessarily prevent design of efficient semiconductor/liquid junctions with these systems (8a).

We also note that the V_{oc} values for n-Si, p-Si, n-GaAs, and p-GaAs interfaces can substantially exceed those reported for direct Schottky contacts to noble metals such as Pt or Au (12). This cannot be simply due to Fermi-level pinning of ϕ_b, with more favorable interfacial kinetics resulting in higher V_{oc} values at liquid junctions. This possibility is excluded by the observation of V_{oc} values for liquid systems which exceed ϕ_b values for Au Schottky barriers. In contrast to the V_{oc} values of 0.54V for n-Si and 0.46V for p-Si CH_3OH junctions, surface-state pinning in Schottky barriers yields V_{oc} values of only 0.30V for n-Si/Pt interfaces, and yields low barrier height, "ohmic" contacts for p-Si/Pt and p-Si/Au junctions. In addition, we note that analogies (4a, 21) to the commonly quoted Schottky Fermi-level pinning behavior for covalent *vs.* ionic solids (36) clearly do not apply to the semiconductor/liquid interface, as evidenced by data showing extensive regions of ideal behavior for V_{oc} *vs.* $E(A^+/A)$ for liquid junctions with n-Si, p-Si (37), p-InP (24), n-CdTe (21a), a-Si:H (8b), and other small E_g semiconductors. Pinning of the Fermi level in solid-state systems can be associated with changes in surface stoichiometry upon formation of the Schottky barrier (38). The recombination induced by surface states which pin the Fermi level can only lower V_{oc} from the theoretical value defined by the diffusion limit of Eq. [3]. Different chemical interactions at liquid interfaces [including formation of surface oxides (9a)] may allow formation of more ideal junctions, and will preclude proposed generalizations of V_{oc} or ϕ_b values observed in Schottky systems to semiconductor/liquid junctions.

Surface conductivity measurements to verify carrier inversion.—An obvious difference between Q_b and Q_{ss} is that increases in Q_b should produce increases in mobile charge, while surface-state charge is essentially fixed. Thus, measurement of the near-surface conductivity should lead to a direct evaluation of the contribution of Q_b to the potential drop across the Helmholtz layer. Our measurement of the near-surface conductivity for p-Si photocathodes in CH_3CN solvent involves detection of the ac conductance between two Pt electrodes which are in close proximity to the semiconductor surface (Scheme III). If the semiconductor develops an inverted, conduct-



Scheme III. Diagram of cell arrangement for determination of near-surface conductivity of p-type silicon electrodes. The current response to an oscillating voltage signal applied between the two Pt wires is sensitive to the conductivity of the intermediate Si surface shunt. The method is only sensitive to mobile charge carriers. Thus, it will not detect charge in surface states, and will provide a method to distinguish between carrier inversion and Fermi-level pinning by surface states.

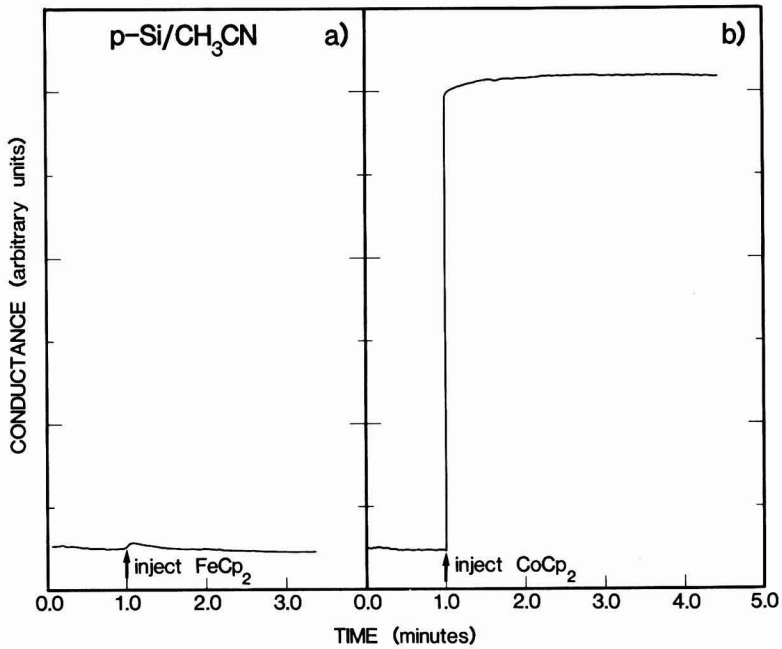


Fig. 2. Conductance between two Pt wires arranged as a Scheme III, under various experimental conditions. (a) Injection of 10 mM ferrocene into a 1.0 mM $LiClO_4$/CH_3CN solution yields no detectable change in measured conductance. (b) Injection of 1.0 mM cobaltocene yields a large, sustained change in measured conductance owing to the shunt formed by injection of mobile surface charge from the cobaltocene into the p-Si surface. Under our circuit conditions, the relationship between the measured change in conductance and the electron concentration in the semiconductor can be approximated by $N_e = (\Delta G_1)/(Ae\mu)$. Assumption of a 5×10^{-7} cm thick inversion layer in our 0.2×0.3 cm electrode yields $A = 1 \times 10^{-7}$ cm^2, $l = 0.3$ cm, and thus $N_e \cong 10^{17}$ cm^{-3} for a change in conductance of 5×10^{-6} Ω^{-1} cm^{-1}, as indicated.

ing surface layer, the conductance of the "cell" will change dramatically, and Q_b can thus be estimated directly. In our experiments, the reduced form of the redox couple A^+/A is injected into the solution, and the conductance between the Pt probe electrodes is monitored. This technique is similar to a method recently proposed by Gerischer (1c), which has roots in early field effect experiments on semiconductor surfaces. Because the semiconductor should be in depletion upon injection of the appropriate A, any increase in conductivity can be associated with the presence of mobile minority carriers near the surface, and would therefore imply the presence of carrier inversion.

Figure 2 displays the measured change in conductance between two Pt wires with a p-type Si surface ($N_A = 2 \times 10^{15}$ cm^{-3}) as the possible shunt. The experiments are performed in dry CH_3CN/1.0 m*M* $LiClO_4$. Injection of ferrocene yields little change in the conductance, but injection of cobaltocene produces a pronounced, stable increase in the signal. Because we have injected a neutral molecule into the solution, yet have produced an increase in the measured conductance, we associate this phenomenon with the formation of an inversion layer at the p-type Si cathode. Ferrocene is not a sufficiently strong reductant to effect carrier inversion in p-Si, and no increase in conductivity occurs.

Analysis of the geometry of our cell allows a rough estimate of the carrier concentration in the inversion layer. Assuming a 50Å inverted region, and a mobility of 480 cm^2/V-s, an electron concentration of 10^{17} carriers-cm^{-3} is calculated. This is consistent with the presence of strong inversion in the semiconductor, as might be expected for a redox couple with a formal potential as negative as cobaltocene $^{+/0}$.

Both carrier inversion ($Q_b > Q_{ss}$) and Fermi-level pinning ($Q_b < Q_{ss}$) have been proposed to explain the photoelectrochemistry of p-type Si in CH_3CN solvent (2, 39). The similarity of V_{oc} values for the cobaltocene$^{+/0}$ system in CH_3CN, and CH_3OH, the direct detection of mobile charge carriers at p-Si surfaces in CH_3CN, and the high efficiency of p-Si photocathodes in CH_3CN solvent (40) leads us to propose that carrier inversion is the dominant mechanism of developing charge across the Helmholtz layer for redox couples where $E(A^+/A) < -0.7$ V.vs. SCE (40).[2] Carrier inversion can provide a situation where design of efficient photoelectrodes is possible for both carrier types in the same solvent, and is consistent with accurate current-voltage data using high quality Si semiconductor samples.

Conclusions

The ultimate limit on the open-circuit photovoltage at a semiconductor/liquid interface can reflect the bulk recombination kinetics of the semiconductor itself. A quantitative treatment of these kinetics indicates that typical electrode samples may exhibit open-circuit photovoltages substantially below the value of the semiconductor bandgap, yet not possess any deleterious effects assignable to Fermi-level pinning. Lower than ideal open-circuit photovoltages may occur because of poor diffusion lengths in the bulk semiconductor, classical carrier emission over the surface barrier, or leakage across low barrier chemical imperfections at the semiconductor/liquid interface. Characterization and control of bulk semiconductor properties is thus crucial to obtaining meaningful data at the semiconductor/liquid interface. Saturation in open-circuit photovoltage with increases in incident light intensity can reflect recombination kinetics of the semiconductor, and may not yield the barrier height. Constant values of the open-circuit photovoltage with changes in solution redox potential can be consistent with carrier inversion at ideal semiconductor/liquid interfaces. The observation of large photovoltages for n- and p-type-based semiconductor interfaces in the same solvent can rule out pinning by a fixed density of charged surface states as the mechanism for obtaining constant photovoltages. Direct evidence for mobile minority charge carriers in the semiconductor can be obtained by ac conductivity techniques, and verifies the presence of an inversion layer for p-type Si cathodes in nonaqueous solvents. Application of the "1/3 bandgap" rule to p-type GaAs/liquid junctions is inappropriate, and in general, behavior of liquid contacts may not correlate with measured properties of Schottky barriers. Fermi-level pinning will prevent design of the most efficient semiconductor/liquid junctions, while carrier inversion may lead to interfaces which operate near the theoretical diffusion-limited photovoltage.

[2] Differential capacitance measurements have been suggested to rule out carrier inversion for p-Si in CH_3CN solvent (39) because the apparent E_{FB} position was found to change before a band bending of (1/2)E_g had been achieved. In this analysis, it is stated that qV_p of the p-Si ($N_A = 2 \times 10^{15}$ cm^{-3}) is 0.05 eV. However, for this doping level, we calculate $qV_p = 0.24$ eV (12, 13), and can thus use the original data to place E_{vb} at +0.4V *vs.* SCE. At this doping level, weak inversion could onset at −0.15V *vs.* SCE, strong inversion could then occur at −0.4V *vs.* SCE, and the data might be consistent with carrier inversion. Ideal behavior would predict that the reported analysis (39) of a straight line of slope ~ 0.5 for E_{FB} *vs.* $E(A^+/A)$ might actually be properly described as two distinct regions, each exhibiting a linear dependence of E_{FB} *vs.*E (A^+/A). Other workers have noted the anomalous behavior of differential capacitance data for p-Si in CH_3CN (6a), and additional data might be warranted to unambiguously describe the dependence of ϕ_b upon potential in this system. We also note that at the highest measured value of V_s, $q(\phi_b)$ is approximately 0.9 eV (if the proper E_{vb} is employed). Thus, if surface states do pin the Fermi level, they must be very close to E_{cb}, and should not appreciably limit V_{oc}. This notion is consistent with the excellent agreement between theory and experiment in Table I, and is strongly supported by other results in our laboratory, which describe the design of efficient p-Si-based photoelectrochemical cells in nonaqueous solvents (40).

Acknowlegment

We acknowledge helpful discussions with C. Gronet and R. Bube of Stanford University, as well as G. Cogan, J. Gibbons, and G. Moddel of SERA Solar Corporation, Santa Clara, California. This work was partially supported by the NSF through Stanford Center for Materials Research. N.S.L. also wishes to thank the IBM Corporation for generous support through receipt of a Young Faculty Development Award and support from NSF grant CHE-8312692.

Manuscript submitted Dec. 2, 1983; revised manuscript received Jan. 24, 1984.

REFERENCES

1. (a) J. Gobrecht and H. Gerischer, *Ber. Bunsenges, Phys. Chem.*, **82,** 1331 (1978); (b) W. Kautek and H. Gerischer, *ibid.*, **84,** 645 (1980); (c) C. D. Jaeger, H. Gerischer, and W. Kautek, *ibid.*, **86,** 20 (1982).
2. (a) J. A. Turner, J. Manassen, and A. J. Nozik, *Appl. Phys. Lett.*, **37,** 488 (1980); (b) ACS Symposium Series 146, "Photo effects at semiconductor—Electrolyte Interfaces," A. J. Nozik, Editor, p. 253, American Chemical Society, Washington, DC (1981).
3. J. A. Baglio, G. S. Calabrese, D. J. Harrison, E. Kamieniecki, A. J. Ricco, M. S. Wrighton, and G. D. Zoski, *J. Am. Chem. Soc.*, **105,** 2246 (1983).
4. (a) A. J. Bard, A. B. Bocarsly, F.-R. F. Fan, E. G. Walton, and M. S. Wrighton, *ibid.*, **102,** 3671 (1980); (b) L. F. Schneemeyer and M. S. Wrighton, *ibid.*, **101,** 6496 (1979).
5. (a) A. J. Bard, F.-R. F. Fan, A. S. Gioda, G. Nagasubramanian, and H. S. White, *Discuss. Faraday Soc.*, **70,** 19 (1980); (b) F.-R. F. Fan, H. S. White, B. L. Wheeler, and A. J. Bard, *J. Am. Chem. Soc.*, **102,** 5142 (1980); (c) R. E. Malpas, K. Itaya, and A. J. Bard, *ibid.*, **103,** 1622 (1981); A. J. Bard and S. N. Frank, *ibid.*, **97,** 7427 (1975); (e) P. A. Kohl and A. J. Bard, *ibid.*, **99,** 7531 (1977); (f) H. S. White, H. D. Abruna, and A. J. Bard, *This Journal*, **129,** 265 (1982); (g) D. Laser and A. J. Bard, *J. Am. Chem. Soc.*, **80,** 459 (1976).
6. H. J. Byker, V. E. Wood, and A. E. Austin, *This Journal*, **129,** 1983 (1982); (b) L. Nadjo, *J. Electroanal. Chem.*, **108,** 29 (1980); (c) J. L. Shulfort and A. M. Batiele, *Rev. Phys. Appl.*, **15,** 1209 (1980).
7. (a) A. J. Nozik, D. S. Boudreaux, R. R. Chance, and F. Williams, *Adv. Chem. Ser.*, **184,** 155 (1980); (b) D. S.

Boudreaux, F. Williams, and A. J. Nozik, *J. Appl. Phys.*, **51,** 2158 (1981).
8. (a) C. M. Gronet and N. S. Lewis, *Appl. Phys. Lett.*, **43,** 115 (1983); (b) C. M. Gronet, N. S. Lewis, G. W. Cogan, J. F. Gibbons, G. R. Moddel, and H. Weismann, *This Journal*, To be published.
9. (a) C. M. Gronet, N. S. Lewis, G. Cogan, and J. Gibbons, *Proc. Natl. Acad. Sci. USA*, **80,** 1152 (1983); (b) N. S. Lewis, R. Dominguez, C. M. Gronet, C. M. Lieber, M. D. Rosenblum, G. W. Cogan, J. F. Gibbons, and G. R. Moddel, in "Electrocatalysis," J. McIntyre, Editor, The Electrochemical Society Softbound Proceedings Series, Pennington, NJ, To be published.
10. (a) A. B. Ellis, S. W. Kaiser, J. M. Bolts, and M. S. Wrighton, *J. Am. Chem. Soc.*, **99,** 2893 (1977); (b) K. D. Legg, A. B. Ellis, J. M. Bolts, and M. S. Wrighton, *Proc. Natl. Acad. Sci. USA*, **74,** 4116 (1977); (c) M. S. Lin, N. Hung, and M. S. Wrighton, *J. Electroanal. Chem.*, **135,** 121 (1982).
11. (a) H. S. White, F.-R. F. Fan, and A. J. Bard, *This Journal*, **128,** 1045 (1981); (b) P. A. Kohl and A. J. Bard, *ibid.*, **126,** 59 (1979); (c) A. B. Boscarsly, D. C. Bookbinder, R. N. Dominey, N. S. Lewis, and M. S. Wrighton, *J. Am. Chem. Soc.*, **102,** 3683 (1980).
12. (a) S. M. Sze, "Physics of Semiconductor Devices," 2nd Ed., John Wiley and Sons, New York (1981); (b) A. L. Fahrenbruch and R. H. Bube, "Fundamentals of Solar Cells," Academic Press, New York (1983); (c) A. J. Hovel, "Solar Cells," Vol. 11 of Semiconductors and Semimetals, Academic Press, New York (1975); (d) S. J. Fonach, "Solar Cell Device Physics," Academic Press, New York (1981).
13. (a) V. A. Myamlin and Yu, V. Pleskov, "Electrochemistry of Semiconductors," Plenum Press, New York (1967); (b) W. Shockley, *Bell Syst. Tech. J.*, **28,** 435 (1949); (c) "Electrons and Holes in Semiconductors," Van Nostrand, Princeton, NJ (1950); (d) C. T. Sah, R. N. Noyce, and W. Shockley, *Proc. IRE*, **45,** 1128 (1957); (e) W. Shockley and H. J. Queisser, *J. Appl. Phys.*, **26,** 535 (1955); (f) M. Wolf, *IEEE Trans. Electron Devices*, **ed-27,** 751 (1980); (g) J. C. Fossum, *Solid State Electron.*, **19,** 269 (1976); (h) W. Van Roosbroeck, *J. Appl. Phys.*, **26,** 380 (1955).
14. H. Gerischer, *J. Electroanal. Chem.*, **58,** 263 (1975).
15. S. J. Fonash, *J. Appl. Phys.*, **47,** 3597 (1976).
16. (a) M. S. Wrighton, *Acc. Chem. Res.*, **12,** 303 (1979); (b) L. F. Schneemeyer and M. S. Wrighton, *J. Am. Chem. Soc.*, **102,** 6964 (1980).
17. (a) J. A. Baglio, G. S. Calabrese, E. Kamieniecki, R. Kershaw, C. P. Kubiak, A. J. Ricco, A. Wold, M. S. Wrighton, and G. C. Zoski, *This Journal*, **129,** 1961 (1982); (b) A. Aruchamy and M. S. Wrighton, *J. Phys. Chem.*, **84,** 2848 (1980); (c) S. Tanaka, J. A. Bruce, and M. S. Wrighton, *ibid.*, **85,** 3778 (1981).
18. W. R. Brandhorst, Jr., "Terrestrial-Photovoltaic Measurement Procedures," ERDA-NASA Technical Report 1022-77116, June 1977.
19. A. Heller, K. C. Chang, and B. Miller, *J. Am. Chem. Soc.*, **100,** 684 (1978).
20. W. A. Anderson, S. M. Vernon, A. E. Delahoy, J. K. Kim, and D. Mathe, *J. Vac. Sci. Technol.*, **13,** 1158 (1976).
21. (a) J. A. Bruce, T. Murahashi, and M. S. Wrighton, *J. Phys. Chem.*, **86,** 1152 (1982); (b) R. N. Dominey, N. S. Lewis, D. C. Bookbinder, J. A. Bruce, and M. S. Wrighton, *J. Am. Chem. Soc.*, **104,** 467 (1982); (c) D. C. Bookbinder, J. A. Bruce, N. S. Lewis, R. N. Dominey, and M. S. Wrighton, *Proc. Natl. Acad. Sci. USA*, **77,** 6280 (1980).
22. R. B. Godfrey and M. A. Green, *Appl. Phys. Lett.*, **34,** 790 (1979).
23. R. N. Dominey, N. S. Lewis, and M. S. Wrighton, *J. Am. Chem. Soc.*, **103,** 1261 (1981).
24. A. Heller, B. Miller, H. J. Lewerenz, and K. J. Bachmann, *ibid.*, **102,** 6555 (1980).
25. R. Noufi, D. Tench, and L. F. Warren, *This Journal*, **128,** 2596 (1981).
26. Y. Kamprakash, S. Basu, and D. N. Bose, *J. Indian Chem. Soc.*, **58,** 153 (1981).
27. D. L. Pulfrey and R. F. McQuat, *Appl. Phys. Lett.*, **24,** 167 (1974).
28. J. P. Ponpon and P. Siffert, *J. Appl. Phys.*, **47,** 3248 (1976).
29. (a) H. S. White, F.-R. F. Fan, and A. J. Bard, *This Journal*, **128,** 1045 (1981); (b) G. Nagasubramanian, B. L. Wheeler, G. A. Hope, and A. J. Bard, *ibid.*, **130,** 385 (1983); (c) E. C. Dutiot, R. L. Van Meirhaeghe, F. Cardon, and W. P. Gomes, *Ber. Bunsenges. Phys. Chem.*, **79,** 1206 (1975); (d) LaFlere, R. L. Van Meirhaeghe, F. Cardon, and W. P. Gomes, *Surf. Sci.*, **59,** 401 (1976); (e) J. N. Chazalviel, *This Journal*, **129,** 963 (1982).
30. F.-R. F. Fan, H. S. White, B. L. Wheeler, and A. J. Bard, *J. Am. Chem. Soc.*, **102,** 5142 (1980).
31. A. B. Boscarsly, E. G. Walton, M. G. Bradley, and M. S. Wrighton, *J. Electroanal. Chem.*, **100,** 283 (1979).
32. F.-R. F. Fan and A. J. Bard, *J. Am. Chem. Soc.*, **102,** 3677 (1980).
33. P. A. Kohl and A. J. Bard, *This Journal*, **129,** 603 (1979).
34. J. M. Bolts and M. S. Wrighton, *J. Am. Chem. Soc.*, **100,** 5257 (1978).
35. C. A. Mead and W. G. Spicer, *Phys. Rev. Lett.*, **10,** 471 (1963).
36. McGill, *J. Vac. Sci. Technol.*, **11,** 936 (1974).
37. A. Heller, H. J. Lewerenz, and B. Miller, *J. Am. Chem. Soc.*, **103,** 200 (1981).
38. R. J. Williams, *J. Vac. Sci. Technol.*, **8,** 929 (1981).
39. G. Nagasubramanian, B. L. Wheeler, F.-R. F. Fan, and A. J. Bard, *This Journal*, **129,** 1742 (1982).
40. C. M. Lieber, C. M. Gronet, and N. S. Lewis, *Nature (London)*, To be published.
41. B. A. Parkinson, A. Heller, and B. Miller, *This Journal*, **126,** 954 (1979).
42. J. Gobrecht, H. Tributsch, and H. Gerischer, *ibid.*, **125,** 2085 (1978).
43. G. Kline, K. Kam, D. Canfield, and B. A. Parkinson, *Solar Energy Mater.*, **4,** 301 (1981).
44. (a) J. A. Wilson and A. D. Yoffe, *Adv. Phys.*, **18,** 193 (1969); (b) W. Kautek, H. Gerischer, and H. Tributsch, *This Journal*, **127,** 2471 (1980); (c) F. Levy, Ph. Schmid, and H. Berger, *Philos. Mag.*, **34,** 1129 (1976).

Electrode Heat Balances of Electrochemical Cells

Application to Water Electrolysis

Y. Ito*

Department of Nuclear Engineering, Faculty of Engineering, Kyoto University, Sakyo-ku, Kyoto 606, Japan

H. Kaiya and S. Yoshizawa*

Department of Industrial Chemistry, Faculty of Engineering, Kyoto University, Sakyo-ku, Kyoto 606, Japan

S. K. Ratkje and T. Førland

Laboratory of Physical Chemistry, Norwegian Institute of Technology, University of Trondheim, Trondheim, Norway

ABSTRACT

Irreversible thermodynamics has been used to describe electrode heat balances of electrochemical cells. The specific example of electrolysis of water in molten sodium hydroxide is chosen for the purpose of illustration. Experimental data are presented for this system. The importance of a distinction between time and charge-dependent changes in entropy is pointed out. Only changes of the last type contribute to cell EMF's. The relation between EMF of thermocells, the temperature coefficient of an isothermal cell, and the electrode heat balances are discussed particularly. Results show a reasonably good agreement between theoretical predictions and experimental observations. With partial pressures of hydrogen and water vapor in the cathodic compartment of 0.8 and 0.2 atm, respectively, 63 kJ is evolved, and with partial pressures of oxygen and water vapor in the anodic compartment of 0.8 and 0.2 atm, respectively, 72 kJ is absorbed during the passage of 1F of current at 623 K.

When it is desired to improve the energy conversion efficiency or the temperature control of an electrochemical reactor, it is important to consider the overall energy flow through the reactor.

For example, if heat is not supplied to electrodes where an endothermic process takes place, a drop in temperature may result. This may lead to an increase in cell voltage, or, in molten salt electrochemical reactors, even freezing of the electrolyte. Conversely, if heat is not conducted from electrodes where exothermic processes take place, a rise in temperature may result. This may lead to a breakdown of the cell or electrolyte boiling. In order to maintain constant temperature at the electrodes, it is helpful to know the magnitude of the reversible heat changes during electrolysis. This includes the Peltier heat for each electrode (1).

It is the purpose of this article to show how reversible heat changes are related to electromotive forces of thermogalvanic cells, and how they can be estimated from EMF measurements. Experiments related to electrolysis of water in NaOH (1) are used to illustrate the theory, since this electrolytic process is promising for the future hydrogen energy system and the accumulation of thermodynamic and electrochemical data are desired for the further engineering development. The results are obtained using nonequilibrium thermodynamics (2). The approach by Førland and Ratkje (2) is chosen, since this describes electrochemical cells directly by local energy conversion processes. This is in contrast to conventional approaches which describe EMF by local electric potential differences due to charge separation (3, 4). The main features of the theory of Førland and Ratkje, in addition to the above, are (*i*) the use of single ion activities or electrochemical potentials is avoided. This is because energy changes are only defined and measurable with respect to electroneutral processes. (*ii*) The components of the system are components according to the phase rule. Components involved in electrode reactions are included. This ensures independent mass variables. (*iii*) The electric current is an independent flux of the system, since this can be controlled externally. (*iv*) The frame of reference is the wall of the cell container.

For isothermal systems, the superposition of time (diffusion) and charge-(migration) dependent processes has been pointed out (5, 6). In the nonisothermal case, we will show that a similar superposition is essential when characterizing entropy changes. This superposition separates irreversible (time dependent) and reversible heat changes. Furthermore, the nonisothermal transport processes will be described without using single ion entropies or electronic entropies.

*Electrochemical Society Active Member.

Entropy Production by Heat, Mass and Charge Transfer in a Continuous System

According to Førland and Ratkje (2) and Ratkje (7), the entropy production θ per unit volume and unit time at any point in the electrochemical system can be written

$$\theta = \nabla\left(\frac{1}{T}\right) J_{q'} - \frac{1}{T}\sum_{i=1}^{k} \nabla\mu_{iT} J_i - \frac{1}{T}\nabla\phi^{obs} I \qquad [1]$$

Current density is assumed to be constant through the system, so no local charge accumulation takes place. $J_{q'}$ is the measurable heat flux. $J_{q'}$ is equal to the heat flow which is required from two heat reservoirs on either side of a volume element to keep constant temperatures. J_i denotes the component fluxes of the k independent components, and I is the electric current density. The chemical potential gradient $\nabla\mu_{iT}$ contains only pressure and composition dependent terms. The symbol $\nabla\phi^{obs}$ denotes the differential EMF, measured with defined identical electrodes across the volume element. By integration across all volume elements the EMF of the system is obtained. This is illustrated in Fig. 1. T is the absolute temperature.

Fluxes of some components which form parts of the electrodes are completely coupled to the electric current

$$J_i = k_i \cdot I \qquad [2]$$

where k_i is an integer or ratio of integers. By inserting this condition into Eq. [1], we obtain

$$\theta = \nabla\left(\frac{1}{T}\right) J_{q'} - \frac{1}{T}\sum_{i=1}^{n} \nabla\mu_{iT} J_i - \frac{1}{T}\left(\nabla\phi^{obs} + \sum_{i=n+1}^{k} \nabla\mu_{iT} k_i\right) I \qquad [3]$$

This defines the electric force conjugate to the current as

$$\frac{1}{T}\nabla\phi = \frac{1}{T}\left(\nabla\phi^{obs} + \sum_{i=n+1}^{k} \nabla\mu_{iT} k_i\right) \qquad [4]$$

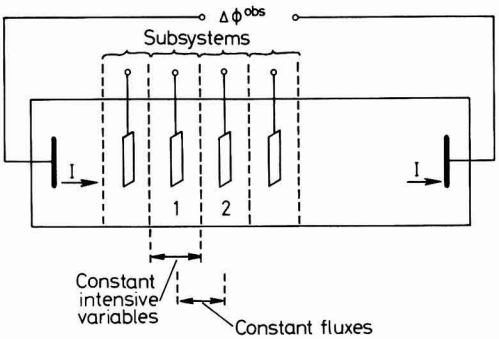


Fig. 1. Scheme of the electrochemical system

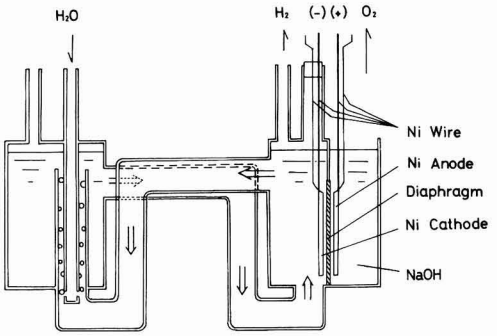


Fig. 2. Prototype cell for water vapor electrolysis

The quantity $\nabla\phi$ can be regarded as the effective electric potential gradient. The expression [3] for the entropy production can be used to define independent fluxes. This will be done below for our special systems, the water electrolysis system developed by Ito and co-workers (8, 9), and electrochemical systems related to this. The use of equations for specific systems is chosen on purpose to simplify reading. Generalizations to include more components are straightforward and will not give further physical insight.

The System

The electrolysis of water can be efficiently performed in the temperature range 330°-450°C by dissolving water vapor in molten sodium hydroxide (8, 9). The overall reaction is

$$H_2O \rightarrow H_2 + \frac{1}{2} O_2$$

This cell can be expressed as

$$Pt|H_2(g), H_2O(g)|NaOH(l)|O_2(g), H_2O(g)|Pt \qquad [5]$$

The cathodic and anodic reactions are written, respectively, as

$$2H_2O + 2e^- \rightarrow H_2 + 2\,OH^- \qquad [6]$$

and

$$2\,OH^- \rightarrow \frac{1}{2} O_2 + H_2O + 2e^- \qquad [7]$$

One possible cell construction is shown in Fig. 2. The cell is made entirely of nickel, and, in order to avoid bipolar effects, the inside of the anodic compartment is covered by an α-alumina wall. A porous α-alumina plate is used as a diaphragm. Water vapor is supplied to the left-hand side of the cell, and the electrolyte saturated with water circulates by a gas lift of both water vapor bubbles and evolved hydrogen gas in the direction given by the arrows in the figure.

During electrolysis heat will be evolved at the cathode and absorbed at the anode. In order to quantify this, the electrodes have been studied separately in the thermocell shown in Fig. 3. A gas mixture of either H_2O and H_2 or H_2O and O_2 was used for the right-hand side Pt-electrode of this figure. A sodium/β-alumina electrode at temperature T_1 was used as the constant reference electrode. The temperature T_2 of the gas electrode was varied. Porous α-alumina was used as a bridge between the two half cells. By subtracting the resulting EMF for two values of T_2, the EMF of the following thermocells are obtained

$$(T)\ Pt|H_2O(g), H_2(g)|NaOH(l)|H_2(g), H_2O(g)|Pt\ (T + \Delta T) \qquad [8]$$

$$(T)\ Pt|H_2O(g), O_2(g)|NaOH(l)|O_2(g), H_2O(g)|Pt\ (T + \Delta T) \qquad [9]$$

Fluxes and Forces of the Experimental System of Fig. 2 and 3

Apart from the gas components forming the electrodes ($H_2(g)$, $H_2O(g)$, $O_2(g)$), there is one component present in these systems, *i.e.*, NaOH. Using the general expression [3] for the entropy production, this gives for the fluxes and forces of the system

$$J_{q'} = L_{11}\nabla\left(\frac{1}{T}\right) - L_{12}\frac{1}{T}\nabla\mu_{1T} - \frac{1}{T}L_{13}\nabla\phi \qquad [10]$$

$$J_{NaOH} = L_{21}\nabla\left(\frac{1}{T}\right) - L_{22}\frac{1}{T}\nabla\mu_{1T} - \frac{1}{T}L_{23}\nabla\phi \qquad [11]$$

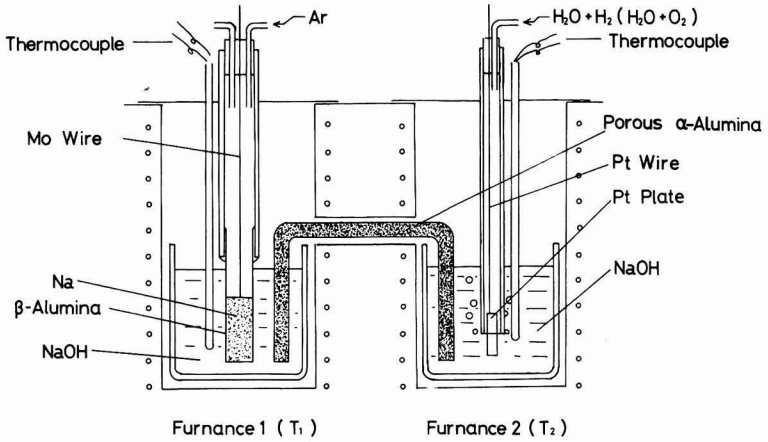


Fig. 3. Thermogalvanic cell arrangement.

$$I = L_{31}\nabla\left(\frac{1}{T}\right) - L_{32}\frac{1}{T}\nabla\mu_{1T} - \frac{1}{T}L_{33}\nabla\phi \qquad [12]$$

The problem is to find the meaning of the coefficients L_{ij} in each case. Furthermore, $\nabla\phi$ needs clarification when the electrodes are different, *e.g.*, during electrolysis.

One simplification may be introduced: we assume that the solubility of all gas components H_2O, H_2, and O_2 is so low (9) that the chemical potential, μ_{1T}, of NaOH is not significantly influenced by these components, so that $\nabla\mu_{1T} = 0$.

Superposition of Time and Charge Dependent Processes

For the interpretation of L_{ij}, it is important to acknowledge that the heat transferred consists of one time-dependent term $\Delta q'(t)$ and one charge-dependent term $\Delta q'(Q)$. This superposition can be seen as follows: by elimination of $\nabla\phi$ in Eq. [10] by Eq. [12], and setting $\nabla\mu_{1T} = 0$, we obtain

$$J_{q'} = \left(L_{11} - \frac{L_{13}L_{31}}{L_{33}}\right)\nabla\left(\frac{1}{T}\right) + \frac{L_{13}}{L_{33}}\cdot I \qquad [13]$$

The condition $\nabla\mu_{1T} = 0$ corresponds to the situation in which no concentration and/or pressure gradient exists in the system. The total heat transferred ($\Delta q'$) and the charge transferred (ΔQ) during a short time interval, Δt, are $J_{q'}\cdot\Delta t$ and $I\cdot\Delta t$ respectively. Thus

$$\Delta q' = \left(L_{11} - \frac{L_{13}L_{31}}{L_{33}}\right)\nabla\left(\frac{1}{T}\right)\cdot\Delta t + \frac{L_{13}}{L_{33}}\cdot\Delta Q \qquad [14]$$

This equation shows that the transferred heat consists of one time-dependent term, which is the first term on the right-hand side, and one charge-dependent term. The latter is time independent, its sign reversed by reversing the sign of ΔQ. This part of the heat transfer is reversible. The heat balance is

$$\Delta q' = \Delta q'(t) + \Delta q'(Q) \qquad [15]$$

The presence of gradients in chemical potentials will not change the general form (15), but will merely give an additional contribution to both the time-dependent and charge-dependent parts of $\Delta q'$.

The entropy change per Faraday corresponding to $\Delta q'(Q)$ is

$$S'(Q) = \frac{q'(Q)}{T\cdot\Delta Q} \qquad [16]$$

The heat $\Delta q'(Q)$ will contain the heat associated with the electrode reactions, but $\Delta q'(Q)$ will also contain contributions from the reversible transport process through the electrolyte and metal leads. This means that the coefficient ratio L_{13}/L_{33} is also determined by the mechanism of transport

$$L_{13}/L_{33} = TS'(Q) \qquad [17]$$

Furthermore, by expressing $\nabla\phi$ by Eq. [12], we obtain

$$(\nabla\phi)_{I=0,\ \nabla\mu_{1T}=0} = -\frac{L_{31}}{L_{33}}\frac{\nabla T}{T} \qquad [18]$$

By application of Onsager relations, we see that the coefficient ratio (17) determines the electric work that can be obtained from the system

$$(\Delta\phi)_{I=0,\ \nabla\mu_{1T}=0} = -\Delta T\,S'(Q) \qquad [19]$$

For a temperature difference ΔT, it is thus only the heat $\Delta T\,S'(Q)$ which can be reversibly converted to electric work or vice versa. Equation [19] will next be used to find contributions to EMF or electric work done in the outer circuit.

Reversible Entropy Changes during Electrolysis or EMF Measurements

Consider first the thermocell given by Eq. [8], and a small volume element, as given by Fig. 1. When electrons pass from left to right in the outer circuit, the following reaction takes place at the left-hand side electrode

$$\frac{1}{2}H_2(g) + NaOH(l) = H_2O(g) + Na^+ + e^- \qquad [20]$$

The entropy change due to formation of $H_2O(g)$ and removal of $H_2(g)$ and NaOH(l) is equal to

$$\Delta S_1 = S_{H_2O(g)} - \frac{1}{2}S_{H_2(g)} - t_{NaOH}S^\circ_{NaOH} \qquad [21]$$

where $t_{NaOH} = t_{Na^+}$ (transport number of Na^+) is the number of moles of NaOH transferred from left to right per Faraday. All entropies on the right-hand side of Eq. [21] are state functions. By inserting the experimental values of $P_{H_2O} = 0.2$ atm and $P_{H_2} = 0.8$ atm and using literature data (10), we obtain the entropy change of the left-hand region of the cell per Faraday transferred

$$\Delta S_1 = 150.0\ JK^{-1}F^{-1} - t_{NaOH}S^\circ_{NaOH(l)} \qquad [22]$$

This is the entropy change of the left-hand part of the system due to composition changes caused by charge transfer. Since this is a reversible entropy change, it is equal to the entropy transferred from a heat reservoir at the left-hand side, $S'_{(Q)1}$, minus the transported entropy $\bar{\bar{S}}_{(Q)}$ due to the charge transport process in the electrolyte. The term corresponding to $\bar{\bar{S}}_{(Q)}$ due to transport of charge in metallic leads will be neglected here (Peltier heat for metals is small). The terminology is according to Agar (4). The entropy balance is shown in Fig. 4. We have

$$\Delta S_1 = S'_{(Q)1} - \bar{\bar{S}}_{(Q)} \qquad [23]$$

or

$$S'_{(Q)1} = \Delta S_1 + \bar{\bar{S}}_{(Q)} \qquad [24]$$

For the present system, measurements show that $S'_{(Q)1}$ is positive, which means that a negative Peltier heat $TS'_{(Q)}$ is transferred reversibly over a temperature interval of dT. For dT positive, electric work must be supplied, *i.e.*, the EMF is negative. Combining Eq. [18], [24], and [22], one obtains in the one dimensional case

$$\frac{d\phi_1}{dT} = -(\Delta S_1 + \bar{\bar{S}}_{(Q)}) \qquad [25]$$

$$\frac{d\phi_1}{dT} = -150.0\ JK^{-1}F^{-1} + t_{NaOH(l)}S^\circ_{NaOH(l)} - \bar{\bar{S}}_{(Q)} \qquad [26]$$

The second type of cell investigated, given by Eq. [9],

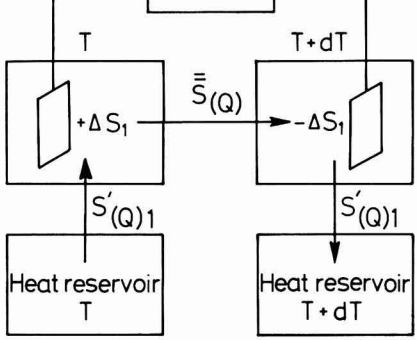


Fig. 4. Entropy balance for a thermogalvanic cell. ΔS_1 is entropy change due to change in composition. ΔS_1 is obtained from changes in state functions. $\bar{\bar{S}}_{(Q)}$ is transported entropy caused only by the transport of electric charge in the electrolyte. $\bar{\bar{S}}_{(Q)}$ depends on mechanism of charge transport. $S'_{(Q)1}$ is entropy supplied to or from heat reservoirs in equilibrium with sections of the cell. $S'_{(Q)1}\cdot T$ is the Peltier heat.

can be treated in a similar way. The reaction at the left-hand side electrode is now

$$\mathrm{NaOH(l)} = \frac{1}{4}\,SO_{2(g)} + \frac{1}{2}\,\mathrm{H_2O(g)} + \mathrm{Na^+} + e^- \qquad [27]$$

The entropy change at the left-hand side of the cell is

$$\Delta S_2 = \frac{1}{4}\,S_{O_{2(g)}} + \frac{1}{2}\,S_{H_2O(g)} - t_{NaOH}\,S^\circ_{NaOH} \qquad [28]$$

where the last term is the same as the last term in Eq. [22]. With $P_{O_2} = 0.8$ atm and $P_{H_2O} = 0.2$ atm, we have

$$\Delta S_2 = 170.2\ JK^{-1}\,F^{-1} - t_{NaOH}\,S^\circ_{NaOH} \qquad [29]$$

An entropy balance gives (compare Eq. [23])

$$S'_{(Q)2} = \Delta S_2 + \bar{\bar{S}}_{(Q)} \qquad [30]$$

where $\bar{\bar{S}}_{(Q)}$ has the same value as in Eq. [24]. Thus, the thermoelectric EMF $d\phi_2/dT$ is given by

$$\frac{d\phi_2}{dT} = -\,(\Delta S_2 + \bar{\bar{S}}_{(Q)})$$

$$= -170.2\ JK^{-1}\,F^{-1} + t_{NaOH}\,S^\circ_{NaOH} - \bar{\bar{S}}_{(Q)} \qquad [31]$$

This completes the analysis of the heat change at the separate electrodes and how this change can be obtained experimentally by EMF measurements. When we need to know the details of the thermoelectric power, additional experiments must be performed to obtain t_{NaOH} and $\bar{\bar{S}}_{(Q)}$, but, at present, the analysis given above is sufficient for our purpose.

It remains to be shown how the thermoelectric powers of the thermocells [8] and [9] are related to the EMF of the formation cell [5].

Thermogalvanic Electric Power and Isothermal Temperature Coefficient

It will be shown below that the EMF of the two thermocells [8] and [9] are related to the temperature coefficient $d\phi_2/dT$ of the isothermal cell [5]. Consider for this purpose the simple combination of cells given by Fig. 5. In this case, all electrodes contain the same metal, Pt. If, further, the junctions between Pt and other leads (*e.g.*, Cu) are all at the same temperature, one can see that the reversible heats absorbed both at T_1 and T_2 cancel. It is shown in Fig. 5 how the transfer of charge results totally in zero transfer of heat. This heats Δq_{iTj} in Fig. 5, corresponding to the last term $\Delta q'(Q)$ in Eq. [15]. This gives for the complete circuit

$$\Delta\phi_1 + \Delta\phi_3 + \Delta\phi_2 + \Delta\phi_4 = 0 \qquad [32]$$

under the condition for the junctions given above. Further

$$\Delta\phi_1 = \frac{d\phi_1}{dT}\,\Delta T;\quad \Delta\phi_2 = -\,\frac{d\phi_2}{dT}\,\Delta T \qquad [33]$$

and

$$-\Delta\phi_3 = \Delta\phi_4 + \frac{\partial\phi_3}{\partial T}\,\Delta T \qquad [34]$$

Thus

$$\frac{d\phi_1}{dT} - \frac{d\phi_2}{dT} = \frac{d\phi_3}{dT} \qquad [35]$$

This relation makes possible a consistency check on separate measurements, since all terms in Eq. [35] can be measured independently of each other.

Interpretation of Flux Equations for the Formation Cell

The results obtained from the analysis of the thermogalvanic cells [8] and [9] can be related to electrolysis—conditions in the isothermal cell given by Eq. [5]. Since the electrolyte is almost pure NaOH(l), $\nabla\mu_{1T} = 0$. The electric force of Eq. [10]-[12] is now related to the observed EMF by Eq. [4]

$$\nabla\phi = \nabla\phi^{obs} - \left(-\nabla\mu_{H_2O} + \frac{1}{2}\,\nabla\mu_{H_2}\right) \qquad [36]$$

with traces of H_2 and O_2 present anywhere along with local test electrodes, we can assume local equilibrium and

$$\frac{1}{2}\,\mu_{H_2} = \frac{1}{2}\,\mu_{H_2O} - \frac{1}{4}\,\mu_{O_2} \qquad [37]$$

We are then obliged to reduce the number of components by one, and have chosen to exclude O_2. Formation of 1/4 O_2 is then described as formation of 1/2 H_2O and removal of 1/2 H_2. This means that we may regard the total electrode reaction as a transfer of H_2O and H_2. The limits for the chemical potential of H_2 are the value at the cathode and given from Eq. [37] at the anode. This means by inserting into Eq. [36] and integrating for isothermal conditions that

$$\Delta\phi = \Delta\phi^{obs} - \Big[-\Delta\mu_{H_2O} + \frac{1}{2}\left(\mu_{H_2(2)} - \mu_{H_2O(1)} + \frac{1}{2}\,\mu_{O_2(1)}\right)\Big]$$

or

$$\Delta\phi = \Delta\phi^{obs} - \Delta G \qquad [38]$$

where ΔG is the Gibbs free energy change of the formation cell, and $\Delta\mu_{H_2O} = 0$. By inserting Eq. [38] into Eq. [12], we can find an expression for $\Delta\phi^{obs}$. An equation like [34] cannot be written for the entropy, and it is thus not possible to eliminate O_2 as a component when reversible entropy changes are considered. The reversible transfer of entropy is as before the sum of the entropy changes at the electrodes and the entropy of transport in the electrolyte and metallic leads.

With a temperature gradient across the cell [5], the processes taking place will in total be identical to the processes taking place in a cell [8] with the temperature gradient in series with an isothermal cell [5]. The processes in both these cells can then be described by Eq. [10]-[12]. Alternatively, the entropy balance may be analyzed in a way similar to that shown in Fig. 4. It should be noticed, however, that, since the transport mechanism in the electrolyte is different in cell [5] from that in cells [8] and [9],

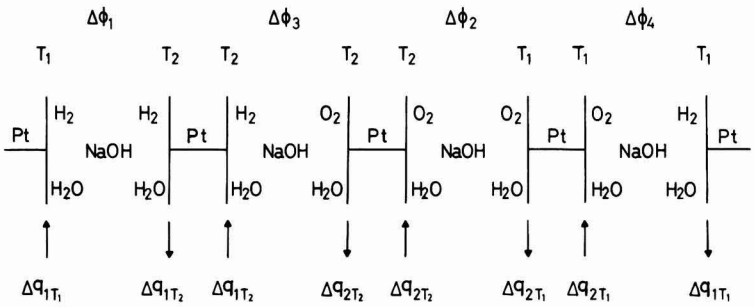


Fig. 5. A combination of thermocells and formation cells which together give zero EMF, T_1 and T_2 are temperatures while q_1 and q_1 are absorbed heats.

t_{NaOH}, ΔS_1, ΔS_2, and $\bar{\bar{S}}_{(Q)}$ will have different values and thus the reversible entropy $S_{(Q)1}$ absorbed from the heat reservoirs will be different. For this type of thermogalvanic cell with different electrodes, the entropy absorbed from the left-hand side heat reservoir is different from the entropy donated to the right-hand side heat reservoir.

In this section, we have focused attention on the effect of heat transport, and how this can be described when no concentration gradients are present. The presence of concentration gradients will give irreversible heat changes. Soret equilibrium is defined when migration balances diffusion ($J_i = 0$). This condition can easily be introduced in the flux Eq. [10]-[12], and can be used to quantify diffusional heat effects. This is outside the practical scope of this case.

Experimental

The thermogalvanic cell was constructed as shown in Fig. 3. Molten sodium hydroxide was contained in two separate high purity α-alumina beakers (SSA-S, 99.5%), and their electrolytic contact was achieved by a porous α-alumina bridge, which was completely wetted by molten sodium hydroxide.

A gas mixture of either H_2O and H_2 or H_2O and O_2 was supplied through a high purity α-alumina pipe to make a three-phase zone on the platinum working electrode submerged in the molten sodium hydroxide in the right-hand-side beaker. A gas mixture was prepared by passing H_2 or O_2 gas through a water pool maintained at a fixed temperature. The composition was determined by the flow rate measurement of H_2 or O_2 before passing through the water pool, together with the weight gain of a $CaCl_2$ column due to the absorption of the water in the gas mixture coming out from the cell. The composition determined in these ways coincided well with the value estimated from the vapor pressure data of the water. A sodium/β-alumina reference electrode was prepared by making a liquid sodium pool at the bottom of the β-alumina tube. This tube was connected to a high purity β-alumina pipe by using alumina cement. Argon gas was supplied into the tube as a cover gas to prevent the oxidation of the liquid sodium. To obtain reversibility of the reference electrode, cathodic and anodic currents were applied alternatively through the reference electrode before thermoelectric power measurements. By this pretreatment, wetting of the inner and outer surface of the β-alumina tube by liquid sodium and molten sodium hydroxide, respectively, was achieved to ensure good electrolytic contact.

The temperature of furnace 1 was set at a constant temperature T_1 and the temperature T_2 of furnace 2 was raised, and the electromotive force between the platinum working electrode and the sodium/β-alumina reference electrode was measured at various T_2 values.

Results and Calculations

The results are presented in Fig. 6 and 7. From these figures, we obtain

$$\frac{d\phi_1}{dT} = -1.05 \pm 0.02 \text{ mV K}^{-1} = -101 \pm 2 \, JK^{-1} \text{ F}^{-1} \qquad (T_1 = 340.5°\text{C}) \qquad [39]$$

and

$$\frac{d\phi_2}{dT} = -1.19 \pm 0.04 \text{ mV K}^{-1} = -115 \pm 4 \, JK^{-1} \text{ F}^{-1} \qquad (T_1 = 336°\text{C}) \qquad [40]$$

These results can be checked for internal consistency by application of Eq. [35]. The isothermal temperature coefficient is

$$\frac{d\phi_3}{dT} = \frac{1}{4} S_{O_2} + \frac{1}{2} S_{H_2} - \frac{1}{2} S_{H_2O} = \Delta S \qquad [41]$$

where ΔS refers to 1F. For the present conditions (P_{O_2} = 0.8 atm, P_{H_2} = 0.8 atm, P_{H_2O} = 0.2 atm)

$$\Delta S = \frac{1}{2}\left(150.7 + R \ln \frac{1}{0.8}\right) + \frac{1}{4}\left(226.3 + R \ln \frac{1}{0.8}\right) - \frac{1}{2}\left(212.9 + R \ln \frac{1}{0.2}\right) = \underline{20.2 \, JK^{-1} \text{ F}^{-1}}$$

This result may be compared to the difference between the experimental results 115 − 101 = $\underline{14 \, JK^{-1} \text{ F}^{-1}}$ (see Eq. [35]).

A more complete analysis of the thermogalvanic cells would include independent measurements of t_{NaOH} and the entropy of transport $\bar{\bar{S}}_{(Q)}$. The most important thing is, however, to estimate the single electrode heat changes at each electrode and not their difference. When the entropy of transport is to be included in the calculation of electrode compartment heat changes, they are found from Eq. [31] and [26]. Partial pressures of hydrogen and water vapor in the cathodic compartment of 0.8 atm and 0.2 atm, respectively, give 63 kJ F^{-1} evolved at the cathode. Partial pressures of oxygen and water vapor in the anodic compartment of 0.8 and 0.2 atm, respectively, give 72 kJ F^{-1} absorbed at the anode. In both cases the charge transferral is 1F at 623 K.

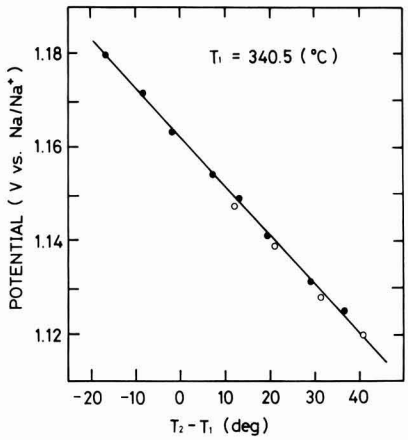


Fig. 6. Electromotive force of thermogalvanic cell consisting of two hydrogen electrodes (cell 8). ○: Measured when ($T_2 - T_1$) was increased. ●: Measured when ($T_2 - T_1$) was decreased.

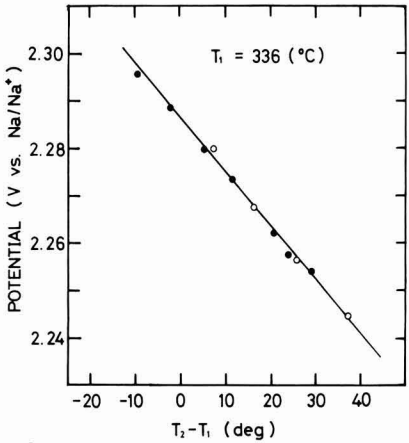


Fig. 7. Electromotive force of thermogalvanic cell consisting of two oxygen electrodes (cell 9). ○: Measured when ($T_2 - T_1$) was increased. ●: Measured when ($T_2 - T_1$) was decreased.

Conclusion

A theoretical procedure has been developed for the purpose of calculating the heat evolution at each electrode in electrochemical reactors. The heat change at the electrode includes the Peltier heat and heat reversibly transferred by the electrolyte. Thermoelectric power measurements can be interpreted by the sum of these heat changes and the heat change due to the entropy of transport.

The procedure has been illustrated by using the results obtained for water electrolysis in molten sodium hydroxide. For the conditions given, the total heat changes in the electrode compartments are 63 kJ F^{-1} at the cathode and -72 kJ F^{-1} at the anode.

Acknowledgment

This work was carried out under support from Grant no. 320 from the Japanese Ministry of Education, Science and Culture.

Manuscript submitted Nov. 4, 1983; revised manuscript received June 15, 1984.

Kyoto University assisted in meeting the publication costs of this article.

LIST OF SYMBOLS

I	current density ($F \cdot s^{-1} \cdot m^{-2}$)
J_i	mass flux of component i ($mol \cdot s^{-1} \cdot m^{-2}$)
$J_{q'}$	thermal flux ($J \cdot s^{-1} \cdot m^{-2}$)
k_i	complete coupling coefficient between mass flux of component i ($i = n + 1 \sim k$) and current density ($mol \cdot F^{-1}$)
L_{11}	Onsager coefficient ($J \cdot m^{-1} \cdot s^{-1} \cdot K$)
L_{12}	Onsager coefficient ($mol \cdot m^{-1} \cdot s^{-1} \cdot K$)
L_{13}	Onsager coefficient ($F \cdot s^{-1} \cdot m^{-1} \cdot K$)
L_{21}	Onsager coefficient ($mol \cdot m^{-1} \cdot s^{-1} \cdot K$)
L_{22}	Onsager coefficient ($J^{-1} \cdot mol^2 \cdot m^{-1} \cdot s^{-1} \cdot K$)
L_{23}	Onsager coefficient ($mol \cdot m^{-1} \cdot s^{-1} \cdot V^{-1} \cdot K$)
L_{31}	Onsager coefficient ($F \cdot m^{-1} \cdot s^{-1} \cdot K$)
L_{32}	Onsager coefficient ($J^{-1} \cdot F \cdot mol \cdot m^{-1} \cdot s^{-1} \cdot K$)
L_{33}	Onsager coefficient ($F \cdot m^{-1} \cdot s^{-1} \cdot V^{-1} \cdot K$)
Q	charge ($F = 96487$ $Cmol^{-1}$)
q'	heat transferred through unit area ($J \cdot m^{-2}$)
$S'(Q)$	Peltier entropy ($J \cdot F^{-1} \cdot K^{-1}$)
S	transported entropy ($J \cdot F^{-1} \cdot K^{-1}$)
S_i	partial molar entropy of component i ($J \cdot mol^{-1} \cdot K^{-1}$)
S°_i	standard partial molar entropy of component i ($J \cdot mol^{-1} \cdot K^{-1}$)
T	temperature (K)
t	time (s)
t_i	transference number of component i ($mol \cdot F^{-1}$)

Greek letters

ϕ	"effective" potential ($J \cdot F^{-1}$)
ϕ^{obs}	observed potential ($J \cdot F^{-1}$)
μ_i	chemical potential of component i ($J \cdot mol^{-1}$)
θ	entropy production per unit volume per unit time, ($JK^{-1} \cdot s^{-1} \cdot m^{-3}$)
∇	grad operator (m^{-1})

Subscripts

i, j, l	mass component i, j, l
Q	charge
q'	heat

REFERENCES

1. Y. Ito, F. R. Foulkes, and S. Yoshizawa, *This Journal*, **129**, 1936 (1982).
2. T. Førland and S. K. Ratkje, *Electrochim. Acta*, **25**, 157 (1980).
3. T. Jacobsen and G. H. J. Broers, *This Journal*, **124**, 207 (1977).
4. J. N. Agar, "Advances in Electrochemistry and Electrochemical Engineering," Vol. 3, P. Delahay, Editor, p. 31, Interscience, New York, (1963).
5. T. Førland, L. Thulin, and T. Østvold, *J. Chem. Ed.*, **48**, 741 (1971).
6. A., Ekman, S. Liukkonen, and K. Kontturi, *Electrochim. Acta*, **23**, 243 (1978).
7. S. K. Ratkje, *K. Norske Vidensk. Selsk. Skr.*, **6** (1982).
8. Y. Ito, H. Kaiya, and S. Yoshizawa, in "Proceedings of the 3rd World Hydrogen Energy Conference," 221 (1980).
9. Y. Ito, H. Kaiya, and S. Yoshizawa, *Energy Dev. Jpn.*, **3**, 153, (1981).
10. I. Barin and O. Knacke, Editors, "Thermochemical Properties of Inorganic Substances," Springer Verlag, Berlin (1973).

The Mechanism of Electrodeposition of Cadmium Sulfide on Inert Electrodes from Diethylene Glycol Solutions

A. S. Baranski* and W. R. Fawcett*,[1]

Guelph-Waterloo Centre for Graduate Work in Chemistry, University of Guelph, Guelph, Ontario, Canada N1G 2W1

ABSTRACT

The mechanism of electrodeposition of CdS from diethylene glycol solutions containing a cadmium salt and elemental sulfur was investigated. At fresh gold and platinum electrodes, the potential at which CdS is formed is strongly dependent on Cd^{++} concentration and independent of sulfur concentration; the opposite is true at an electrode covered with a coherent layer of CdS. The properties of the electrodeposited films are strongly dependent on the nature of the anion in the electrolyte. In the presence of Cl^- and Br^- anions, mixed Cd-CdS films are formed under specified conditions. A detailed analysis of the effect of Cl^- anion showed that the results obtained were due to a change in the nature of the predominant form of Cd(II) in solution from Cd^{++} to $CdCl_4^=$.

Recently, a simple electrochemical method for depositing thin polycrystalline films of metal sulfides and selenides on conducting substrates was developed in this laboratory (1-4). In this technique, metal chalcogenides are electrodeposited at the cathode in a cell containing a solution of the metal salt and elemental chalcogen at an elevated temperature. There is a limited choice of solvents from which deposition is possible. Moreover, as one would expect, the structural and electrical properties of the deposit are strongly dependent on the nature of the electrolyte and solvent, and composition of the solution. In a previous paper (2), it was shown that CdS grown from dimethylsulfoxide (DMSO) solutions exhibits high specific resistivity and has a tendency to crack. Similar problems exist if DMSO is replaced by other highly basic solvents such as N,N-dimethylformamide, pyridine, hexamethylphosphoramide or 1-methyl-2-pyrrolidone. However, deposition from solvents of low basicity, such as propylene carbonate, acetonitrile, or ethanol, results in the formation of a Cd-CdS mixed film. It was subsequently discovered that CdS could be grown from ethyl-

* Electrochemical Society Active Member.
[1] Present address: Department of Chemistry, University of California, Davis, California 95616.

ene glycol (EG) or diethylene glycol (DEG) solutions with much better physical properties suitable for use in photovoltaic devices. DEG is more convenient in this regard because of the higher solubility of sulfur.[2] The physical properties of CdS film grown from DEG solutions containing 10% water by volume and saturated with sulfur have been characterized (5). In the present paper, we report the results of a study of the mechanism of CdS deposition from DEG solutions.

Experimental

The electrochemical measurements were carried out with a PAR Model 173 potentiostat. In most cases, the working electrode was a Pt wire, 0.25 mm diam and 1.5 cm long. In some experiments, a gold electrode with an area of 0.12 cm^2 or a glassy carbon electrode with an area of 0.3 cm^2 was employed. The counterelectrode was a Pt cylinder with an area of 3 cm^2. The reference electrode was constructed from a Cd rod immersed in a 0.05*M* $Cd(ClO_4)_2$ solution in DEG. The reference electrode system was kept at the same temperature as the main cell and was connected to it through a sintered glass disk. The temperature was maintained constant to within ±0.1°C by circulating paraffin oil from a constant temperature bath through a jacket surrounding the cell and reference electrode.

The solvent, diethylene glycol, was dried for 24h over 4Å molecular sieves and then distilled under argon at reduced pressure from a Vigreaux column 1m high. The purified salts, $Cd(ClO_4)_2$, $CdCl_2$, $LiClO_4$, and NaI were dried for 24h at 120°C under vacuum. NH_4Cl, NH_4Br, and NH_4ClO_4 were dried for 24h at 60°C under vacuum. Sublimated sulfur was recrystallized from benzene and dried at 60°C.

Results and Discussion

The electrochemical studies of the mechanism of CdS deposition were carried out by cyclic voltammetry in DEG solutions containing $LiClO_4$ as supporting electrolyte in the temperature range 70°-130°C. In this medium, sulfur is reduced quasi-reversibly at gold and glassy carbon electrodes and irreversibly at platinum. The current-voltage curves were similar to those observed in other nonaqueous media for the reduction of S_8 (6): accordingly, it is assumed that the first step in the reduction process is the formation of the $S_8^=$ anion. The standard potential for the reaction $S_8 + 2e \rightarrow S_8^=$ in DEG at 100°C was 0.055V against the Cd/Cd^{++} reference electrode. Noting that the potential for the reaction $Cd^{++} + 2e \rightarrow Cd$ is 0 V against the same reference electrode when the concentration of Cd^{++} is 0.05*M*, and that the free energy of formation of CdS from metallic Cd and sulfur in a saturated DEG solution at 100°C is −139.6 kJ mol^{-1}, the reversible potential for the reaction

$$8Cd^{++} + S_8\,(\text{sat'd}) + 16e \rightarrow 8CdS \qquad [1]$$

is 0.72V at 100°C. The potential for this process and the reduction of sulfur both depend very little on temperature.

Typical current-voltage curves observed in a DEG solution containing 0.05*M* $Cd(ClO_4)_2$ and 0.2*M* $LiClO_4$, and saturated with S_8 at various electrodes at 120°C are shown in Fig. 1. At a fresh Au electrode, a distinct prepeak is observed at 0.56V. At Pt, the peak occurs at a less positive potential and is not as sharp. In addition, the potential of the prepeak depends strongly on Cd^{++} concentration, the potential shift being 80 mV for a tenfold increase in Cd^{++} concentration at Pt. However, the peak potential is virtually independent of sulfur concentration (Fig. 2). If the metallic electrode is already covered with a coherent layer of CdS, the prepeak does not appear. Similar observations were made earlier for deposition from DMSO solutions (7). On the basis of the present results and those obtained earlier (7), it is concluded that the prepeak is due to the reduction of Cd^{++} at a pre-existing layer of metal sulfide formed by reaction of the metal electrode with

[2] The solubility of sulfur at 120°C is 0.62 and 0.14g per 100 ml of DEG and EG, respectively.

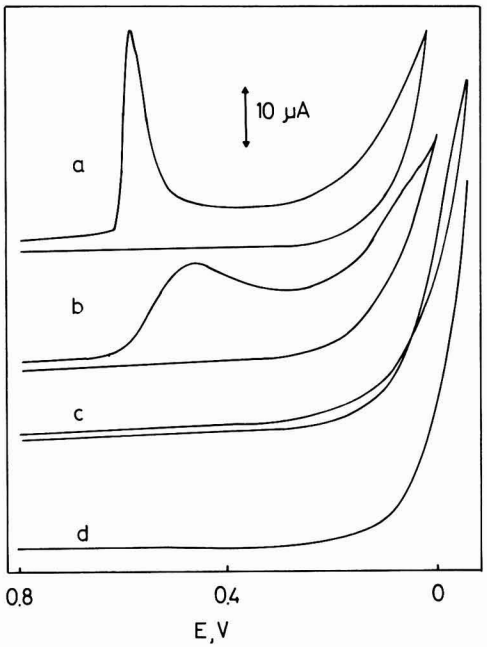


Fig. 1. Cyclic voltammetric curves for the electrodeposition of CdS at (a) gold, (b) platinum, (c) glassy carbon, and (d) CdS (thickness ~1 μm) on Pt. The electrolyte solution contained 0.05M $Cd(ClO_4)_2$, 0.2M $LiClO_4$ and saturated sulfur in diethylene glycol; the sweep rate was 50 mV s^{-1}, and temperature 120°C. The electrode areas were 0.12 cm^2 for Pt, Au, and CdS, and 0.3 cm^2 for glassy carbon.

sulfur in solution; the electrode reaction results in the metal sulfide being converted to CdS. Representing the metal composing the electrode (Au or Pt) as M, the reaction scheme may be written

$$8M + S_8 \rightarrow 8MS_{ads} \qquad [2]$$

$$MS_{ads} + Cd^{++} + 2e \rightarrow CdS_{ads} + M \qquad [3]$$

Strong chemisorption of sulfur on Au and Pt from DEG solutions was demonstrated experimentally in the same way as described previously for DMSO solutions (7). However, this process does not occur at glassy carbon, no prepeak being observed at this electrode.

The present investigation was chiefly directed to determination of the mechanism of CdS deposition on an electrode already covered with a coherent film of CdS. In this case, the nature of the substrate electrode has no influence on the electrode process. The study was carried out by analyzing Tafel plots (ln *i* against electrode potential) obtained for different solution compositions and at various temperatures. The electrode was prepared by covering a Pt wire (surface area ~0.12 cm^2) with a layer of CdS ~1 μm thick;[3] the CdS layer was deposited from the system under investigation at a constant current density of 0.25 mA cm^{-2}. Then, the electrode was polarized with a linearly changing potential, typically at a rate of 20 mV s^{-1}, and the current-potential curve recorded. During the experiment, the solution resistance was carefully compensated, and concentration polarization avoided by stirring the solution using a magnetic stirrer. Furthermore, only currents less than one-tenth of the limiting current were considered in the analysis. Under these conditions, the current-voltage curves were independent of the thickness of the CdS layer, the potential sweep rate, and the rate of solution stirring.

[3] The thickness of the deposit was estimated assuming that the electrodeposition process consumed 100% of the charge passed, and that the density of the CdS film is the same as bulk CdS (4.82 g cm^{-3}).

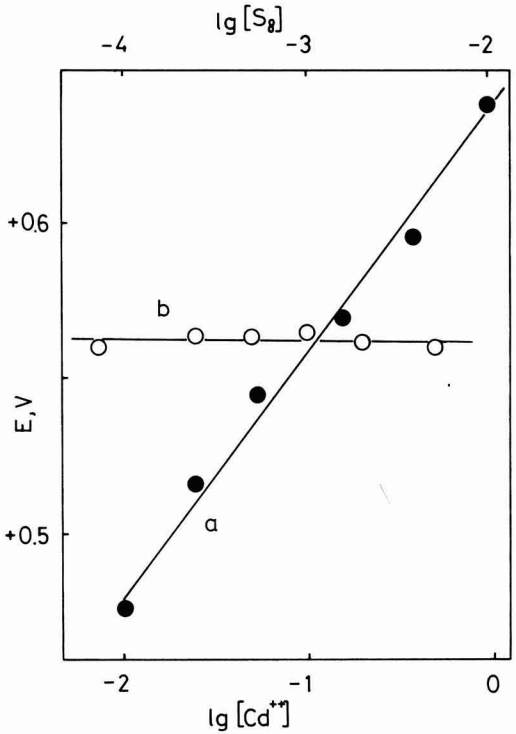


Fig. 2. The dependence of the half-peak potential on (a) Cd^{++} concentration and (b) sulfur concentration for the prepeak corresponding to CdS deposition on Pt at 120°C in a DEG solution containing (a) 0.2M $LiClO_4$, saturated with sulfur and varying concentrations of Cd as indicated or (b) 0.1M $Cd(ClO_4)_2$, 0.2M $LiClO_4$, and varying concentrations of S_8 as indicated.

In all cases, it was found that the electrode process was controlled by irreversible electron transfer. The experimental transfer coefficient calculated from the slope of the Tafel plots was 0.57 ± 0.05. Tafel plots obtained for different sulfur concentrations in DEG solutions containing 0.02*M* $Cd(ClO_4)_2$ and 0.24*M* $LiClO_4$ are shown in Fig. 3. As the sulfur concentration increases, the plots are shifted in the direction of positive potentials. The change in the logarithm of the current density was linear with that of the sulfur concentration at constant potential; the order of the electrode process with respect to sulfur, determined from the slope of this plot, is 1.05 ± 0.1.

In another experiment, the concentration of sulfur was kept constant and that of $Cd(ClO_4)_2$ varied from 0 to 0.1*M*, the ionic strength of the solution being maintained constant by addition of the appropriate concentration of $LiClO_4$. The resulting Tafel plots showed no effect of Cd^{++} concentration on the electrode process (Fig. 4). However, when the solution contained no Cd^{++} ions, a decrease in the Tafel slope was observed at high currents. The latter result is probably due to strong adsorption of the $S_8^=$ anion on the CdS electrode. This adsorption may have an auto-inhibiting effect on further sulfur reduction. The Tafel plot for the reduction of sulfur on Pt from a DEG solution containing 0.3*M* $LiClO_4$ is also shown in Fig. 4. It is interesting to note that the reduction of sulfur is much more irreversible on CdS than on Pt.

On the basis of the data presented in Fig. 3 and 4, the following mechanism for CdS deposition on CdS is proposed

$$S_8 + 2e \rightarrow (S_8^=)_{ads} \quad \text{slow} \qquad [4]$$

$$(S_8^=)_{ads} + Cd^{++} \rightarrow CdS + S_7 \quad \text{fast} \qquad [5]$$

S_7 and other sulfur species containing less than eight sulfur atoms are expected to be more reactive than S_8 (8), and may undergo subsequent electron transfer processes

$$S_{n\leq 7} + 2e \rightarrow (S^=_{n\leq 7})_{ads} \quad \text{fast} \qquad [6]$$

$$(S^=_{n\leq 7})_{ads} + Cd^{++} \rightarrow CdS + S_{n-1} \quad \text{fast} \qquad [7]$$

The deposition of CdS from DEG solutions was very strongly temperature dependent. Tafel plots obtained for deposition of CdS from DEG solutions containing 0.1*M* $(Cd(ClO_4)_2$, 0.1*M* $LiClO_4$, and saturated with sulfur are shown at various temperatures in Fig. 5. On the basis of these data, the enthalpy of activation of the electrodeposition process was found to be 95 ± 20 kJ mol^{-1}.

It is interesting to note that, except at the highest temperatures, the deposition of CdS occurs at potentials more negative than the reversible potential for the

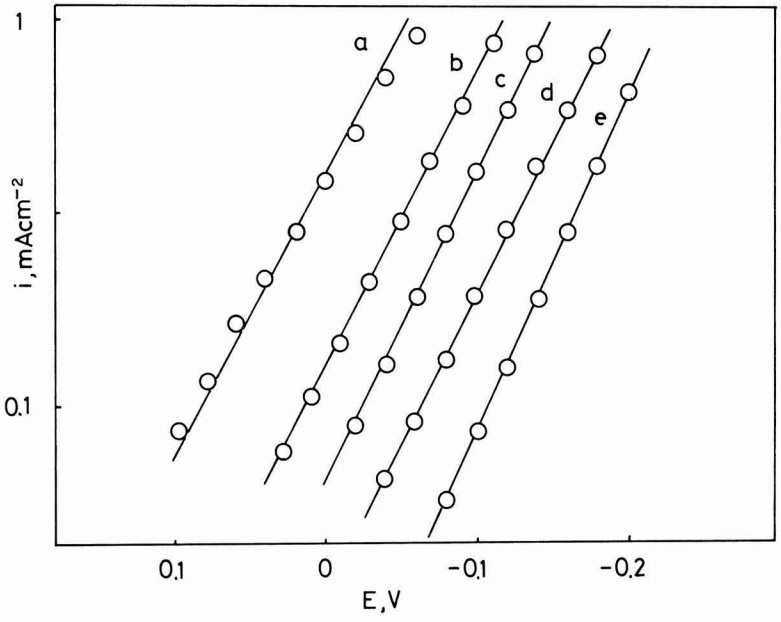


Fig. 3. Tafel plots for the deposition of CdS on a Pt electrode covered with a coherent film of CdS at 130°C from a DEG solution containing 0.02M $Cd(ClO_4)_2$, 0.24M $LiClO_4$, and various concentrations of S_8: (a) 0.007M; (b) 0.003M; (c) 0.0016M; (d) 0.0008M; and (e) 0.0004M. The ordinate scale is logarithmic.

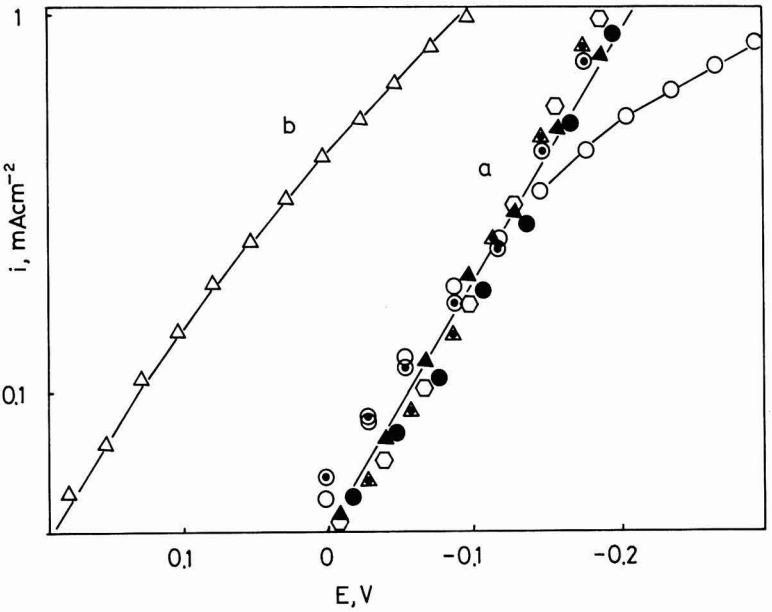


Fig. 4. Tafel plots for the deposition of CdS on (a) a Pt electrode covered with a coherent film of CdS at 130°C from a DEG solution containing 0.001M S_8 and various concentrations of $Cd(ClO_4)_2$: (○) 0; (▲) 0.005M; (⊙) 0.01M; (●) 0.02M; (○) 0.005M; and (△) 0.1M. The ionic strength was maintained constant at 0.3M by adding $LiClO_4$. Curve b is the Tafel plot for the reduction of sulfur at a fresh Pt electrode at 130°C in a DEG solution containing 0.001M S_8 and 0.3M $LiClO_4$. The ordinate scale is logarithmic.

Cd/Cd^{++} system. It was found that the deposition of Cd on CdS in the absence of sulfur is a fast diffusion-controlled process in this potential region. However, x-ray analysis of deposits obtained from DEG solutions at 90°C containing 0.002M S_8, 0.1M $LiClO_4$, and varying concentrations of $Cd(ClO_4)_2$ in the range from 0.005-0.1M showed no excess of Cd in the CdS deposit. Apparently, when sulfur is present in solution, the reduction of Cd^{++} is strongly inhibited by the adsorption of molecular sulfur on the surface of the CdS electrode.

In previous work (5), it was found that addition of small amounts of water to the electroplating solution significantly improved the adhesion of the electrodeposited CdS film to the substrate. In the present study, it was shown that addition of water in quantities up to a mole fraction of 0.57 (~20% H_2O by volume) had a surprisingly small effect on the deposition process (Fig. 6). The observed change in the slope of the Tafel plots is probably caused by a change in double layer structure at the semiconductor/solution interface.

The role of the supporting electrolyte in the electrode process was also studied. It was shown that the cation does not play any significant role, the same Tafel plots being obtained when Li^+ was replaced by Na^+, K^+, or NH_4^+. However, the role of the anion is very important. Replacement of ClO_4^- by BF_4^-, $CH_3SO_3^-$, Cl^-, or Br^- usually resulted in the formation of a dark dendritic deposit composed of a mixture of Cd and CdS. The effect of halide ions was particularly interesting and was studied in more detail. In this regard, the percentage of metallic Cd in a mixed Cd-CdS deposit was determined by chronopotentiometry. When a mixed film is deposited at

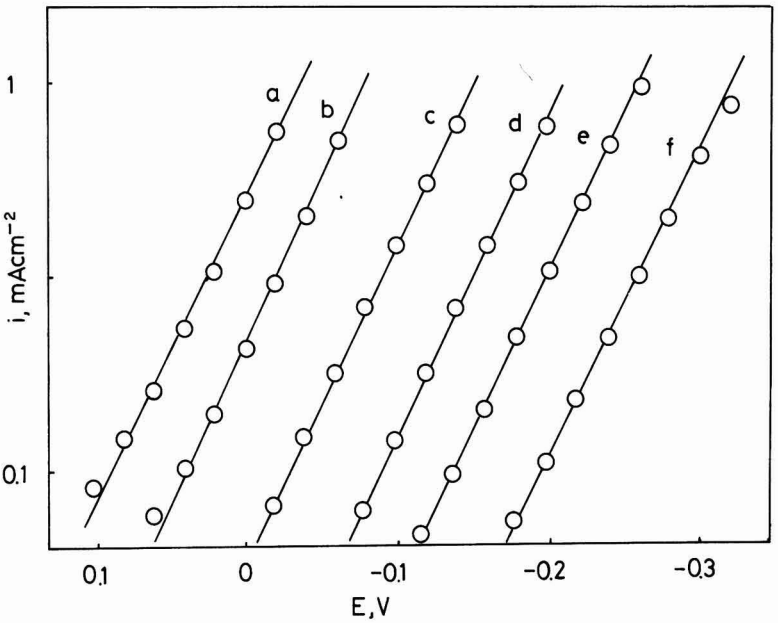


Fig. 5. Tafel plots for the deposition of CdS on a Pt electrode covered with a coherent film of CdS from a DEG solution saturated with sulfur and containing 0.1M $Cd(ClO_4)_2$ and 0.1M $LiClO_4$ at various temperatures: (a) 130°C; (b) 123°C; (c) 108°C; (d) 95°C; (e) 82°C; and (f) 70°C. The ordinate scale is logarithmic.

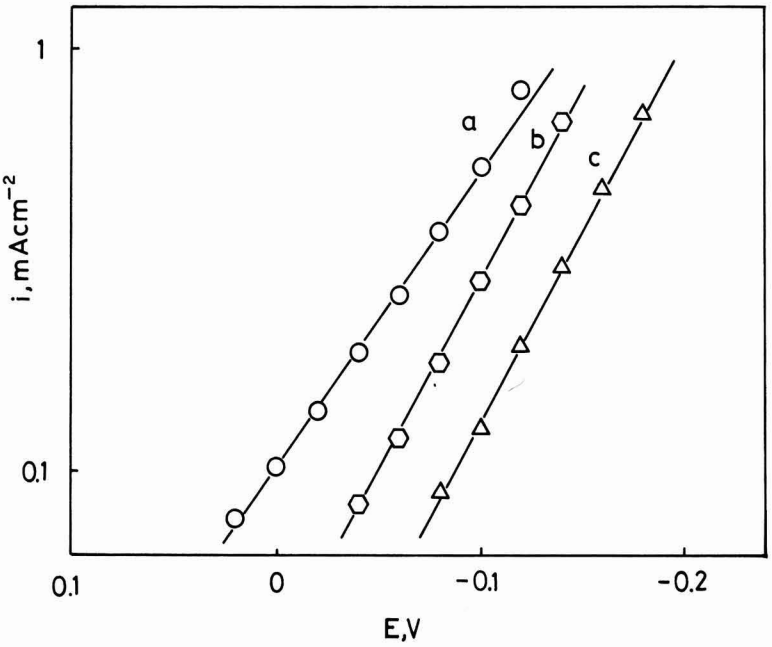


Fig. 6. Tafel plots for the deposition of CdS on a Pt electrode covered with a coherent film of CdS at 110°C from a DEG solution saturated with sulfur and containing 0.1M $Cd(ClO_4)_2$, 0.1M $LiClO_4$, and different amounts of water: (a) 0; (b) 5%; and (c) 20% by volume. The ordinate scale is logarithmic.

constant current by reduction, only the metallic Cd is oxidized when the current is reversed. Thus, the ratio of the transition time in the oxidation process to the reduction time is equal to the mole fraction of Cd in the deposit. This experiment was carried out under conditions for which the mixed deposit is not too thick, thereby ensuring that all available Cd was oxidized on current reversal. Chronopotentiometric experiments were run with varying concentrations of NH_4Cl, NH_4Br, NaI, and water at different temperatures. Some of the results are presented in Fig. 7. The addition of iodide anion had no effect on the ratio of Cd to CdS in the deposit, pure CdS being formed over the entire concentration range studied. However, in the cases of Cl^- and Br^- anions, pure CdS can be electrodeposited only when the concentration of these ions is very low or very high. Lowering the temperature, or adding water to the deposition bath results in a slight decrease in range of concentrations over which pure CdS can be deposited, but the general characteristics of the dependence remain the same.

In order to investigate the role of halide ions further, the stability constant for formation of the $CdX_4^{=}$ ion was determined on the basis of EMF measurements using the following cell

$$Cd/0.05M\ Cd(ClO_4)_2,$$

$$1M\ NH_4ClO_4 \text{ in aqueous DEG}//0.05M\ Cd(ClO_4)_2,$$

$$xM\ NH_4X, (1-x)M\ NH_4ClO_4 \text{ in aqueous DEG/Cd} \quad [8]$$

where X represents Cl^-, Br^-, or I^-, and the solvent contained 10% H_2O by volume. In the presence of the large excess of halide ions the tetrahalocadmium(II) ion ($CdX_4^{=}$) was formed with the logarithm of the stability constant ($\log \beta_4$) equal to 8.4, 9.0, and 9.9 for Cl^-, Br^-, and I^-, respectively, at 110°C. In Fig. 8, the equilibrium potentials for the $Cd/CdCl_x^{2-x}$ system (curve a) and the potentials for deposition of CdS at a current density of 0.5 mA cm^{-2} (curve b) are shown as a function of the Cl^- ion concentration in the DEG solution. It is noteworthy that for Cl^- concentrations less than 0.002M, the deposition of pure CdS occurs at a potential about 100 mV more negative than the equilibrium potential for the Cd/CdX_x^{2-x} system. This was attributed to strong inhibition of Cd^{++} reduction by adsorbed molecular sulfur on the CdS surface. However, as the Cl^- ion concentration increases, the inhibition by sulfur becomes less effective, probably because Cl^- ions are coadsorbed on the CdS surface and provide bridging sites for the adsorption of Cd^{++} (9). As a result, a mixture of Cd and CdS is formed in the electrode process, and the overpotential decreases. For higher Cl^- ion concentrations, a substantial shift in the $Cd/CdCl_x^{2-x}$ equilibrium potential in the negative direction is observed due to formation of the complex ions $CdCl^+$, $CdCl_2$, $CdCl_3^-$, and $CdCl_4^-$. Finally, when the $Cd/CdCl_x^{2-x}$ potential becomes more negative than the potential for CdS formation, pure CdS is deposited in the electrode process. The higher overpotential for CdS formation in the presence of high Cl^- ion concentrations is attributed to the inhibiting effect of adsorbed Cl^- ions on the reduction of sulfur.

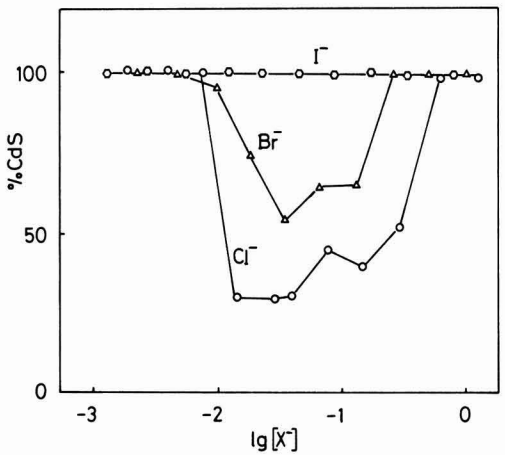


Fig. 7. The percentage of CdS in mixed Cd-CdS deposits obtained from solutions containing halide ions against the logarithm of the halide ion concentration. The electrolyte solution in DEG was saturated with sulfur and contained 0.05M Cd(II) and 10% H_2O by volume. The deposition current was 0.5 mA cm^{-2}, and the temperature 110°C.

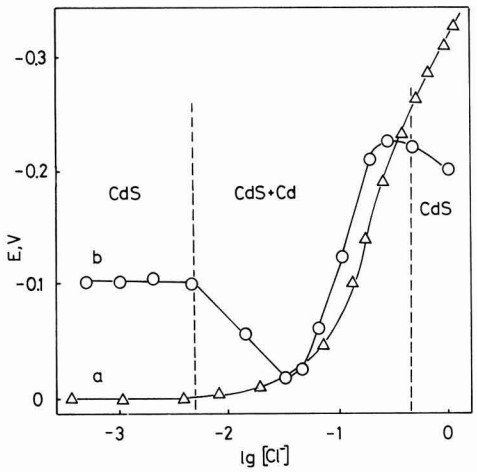


Fig. 8. A plot of (a) the equilibrium potential for the $Cd/CdCl_x^{2-x}$ couple and (b) the deposition potential for mixed Cd-CdS films against the logarithm of chloride ion concentration in the electroplating bath. The electrolyte solution in DEG was saturated with sulfur and contained 0.05M Cd(II) and 10% H_2O by volume. The deposition current was 0.5 mA cm^{-2}, and the temperature 110°C.

The addition of Cl^- ions to the electroplating bath causes marked changes in the orientation of the electrodeposited CdS crystallites (5). For Cl^- ion concentrations less than 0.005*M*, the crystallites are randomly oriented, but for Cl^- ion concentrations greater than 0.5*M*, they are strongly oriented with the c-axis perpendicular to the substrate. It is reasonable to assume that the extent of Cl^- ion adsorption varies with the crystallographic orientation of the exposed CdS face. This will result in differences in the rate of growth of different faces of the crystallites, and consequently, the promotion of one orientation in thicker deposits.

Conclusions

The growth of CdS during electrodeposition from DEG solution at a CdS surface is controlled by the reduction of sulfur. The anion formed in the electrode process, presumably $S_8^=$, subsequently reacts with Cd^{++}, causing the deposition of CdS. The process is strongly affected by the nature of the anions in the electrolyte. In the case of ClO_4^- anion, which is probably not strongly adsorbed on the electrode, the deposition of CdS occurs at potentials more negative than the standard potential of the Cd/Cd^{++} system. However, the reduction of Cd^{++} and subsequent formation of a Cd-CdS mixture is inhibited, most likely, by the adsorption of molecular sulfur on the CdS surface. This inhibition is not as effective in the presence of Cl^- or Br^- anions. In this case, the deposition of pure CdS is only possible if the equilibrium potential of the Cd/Cd(II) system is shifted by complex ion formation to a potential more negative than the reduction potential of S_8 at CdS.

The formation of the first monolayer of CdS on metallic electrodes occurs by a different mechanism. In this case, the rate of reaction is independent of sulfur concentration but depends strongly on Cd^{++} concentration. These observations are attributed to the initial formation of a monolayer of metallic sulfide on the metal electrode which is reduced to CdS at the appropriate potential in the presence of Cd^{++} ions. The initial stages of the formation of CdS in DMSO were also studied at gold electrodes by Roe *et al.* (10), who concluded that the first monolayer was formed by reaction of sulfur with cadmium already on the electrode as a result of underpotential deposition. No evidence in support of their proposal was obtained in our earlier work (7) or in that reported here.

Acknowledgments

The financial support of the Natural Sciences and Engineering Research Council, Canada (NSERC) and of the Technology Development Corporation, Canada through operating grants is gratefully acknowledged.

Manuscript submitted March 5, 1984; revised manuscript received June 13, 1984.

The Natural Sciences and Engineering Research Council, Canada, assisted in meeting the publication costs of this article.

REFERENCES

1. A. S. Baranski and W. R. Fawcett, *This Journal*, **127**, 766 (1980).
2. A. S. Baranski, W. R. Fawcett, A. C. McDonald, R. M. de Nobriga, and J. R. MacDonald, *ibid.*, **128**, 963 (1981).
3. A. S. Baranski, W. R. Fawcett, K. Gatner, A. C. McDonald, J. R. MacDonald, and M. Selen, *ibid.*, **130**, 579 (1983).
4. A. S. Baranski, W. R. Fawcett, and C. Gilbert, *ibid.*, **130**, 2423 (1983).
5. A. S. Baranski, M. S. Bennett, and W. R. Fawcett, *J. Appl. Phys.*, **54**, 6390 (1983).
6. J. Badoz-Lambling, R. Bonnaterre, G. Cauquis, M. Delamer, and G. Demange, *Electrochim. Acta*, **21**, 119 (1976).
7. A. S. Baranski, W. R. Fawcett, and A. C. McDonald, *J. Electroanal. Chem.*, **160**, 271 (1984).
8. F. N. Tebbe, E. Wasserman, W. G. Peet, A. Vatvars, and A. C. Hayman, *J. Am. Chem. Soc.*, **104**, 4971 (1982).
9. F. C. Anson, *Acc. Chem. Res.*, **8**, 400 (1975).
10. D. K. Roe, Li Wenzhao, and H. Gerischer, *J. Electroanal. Chem.*, **136**, 323 (1982).

Thin Film CdSe Electrodeposited from Selenosulfite Solution

Michael Cocivera,* Andrzej Darkowski, and Bruce Love

Guelph Waterloo Center for Graduate Work in Chemistry, University of Guelph, Guelph, Ontario, Canada N1G 2W1

ABSTRACT

Thin film CdSe on titanium is electrodeposited by reduction of an aqueous solution containing the selenosulfite anion and a nitrilotriacetate complex of cadmium ion. Films having thickness between 1.3 and 2.6 μm and surface areas of 1 cm^2 give photoconversion efficiencies between 5.5% and 5.9% when used in a photoelectrochemical cell and illuminated with an ELH lamp.

A number of workers (1-4) have reported the preparation of thin film CdSe for solar cells by means of electrodeposition from an aqueous solution containing Cd^{2+} and H_2SeO_3. A substantial excess of selenium is detected in films prepared in this manner (1, 3). To remove a major portion of this excess, the films must be annealed at temperatures as high as 750°C (3).

It has been suggested that selenium incorporation occurs according to the reaction

*Electrochemical Society Active Member.

$$2CdSe + H_2SeO_3 + 4H^+ \rightarrow 2Cd^{2+} + 3Se + 3H_2O$$

Consequently, use of a selenium precursor that is formally in a lower valence state might avoid undesirable side reactions of this type. For this purpose, we have developed (5) an electrodeposition process that involves the reduction of selenium, which is in the form of the selenosulfite anion $SeSO_3^{2-}$. This species is prepared *in situ* by dissolving elemental selenium in an aqueous sodium sulfite solution. The selenosulfite anion has also been employed to form CdSe films by a chemical process rather than an electrochemical process (6). In addition, thin film CdSe has been electrodeposited from cyanide solution in which elemental selenium has been dissolved; however, the reported efficiencies are low (7).

We find that electrodeposition of CdSe from aqueous selenosulfite solutions results in films having a Cd/Se ratio close to 1. The process consistently provides 1 cm^2 films having efficiencies between 5.5% and 5.9%.for conversion of light power into electrical power using unfiltered light from an ELH lamp. Furthermore, the solution seems fairly stable since a 24h old solution provides films that also have efficiencies around 5.5%. Selenosulfite electrodeposited films appear to adhere quite well to titanium, whereas flaking has been reported for films electrodeposited from H_2SeO_3 solutions (4). A similar problem has been found for films grown by the chemical bath process using selenosulfite solution unless the film is grown in stages (6). In addition, the chemical bath solutions apparently cannot be used for periods longer than about 1h (6). Selenosulfite has been used previously under conditions that are different from those presented below to electrodeposit CdSe films, which were reported to be of inconsistent quality and had a maximum of only 1% light conversion efficiency (8).

Experimental

Electrodeposition of CdSe.—Thin film CdSe is deposited at a titanium cathode at room temperature using a two-electrode cell in which the anode is cadmium metal. A constant potential of 0.30V between these electrodes was maintained using a Bioanalytical Systems (BAS) CVIB. Under these conditions, there is an initial transient reduction current that decays to near zero in about 10s. The current density then gradually increases to 0.34 mA/cm^2 over a period of *ca.* 100s and continues to increase gradually to 0.47 mA over a period of 15 min. By including a saturated calomel electrode (SCE) in the cell, we find that the titanium electrode potential is −1.07V *vs.* SCE.

The electrodeposition solution is prepared by mixing 30 ml of aqueous selenosulfite solution with 10 ml of aqueous cadmium nitrilotriacetate solution. The selenosulfite solution is prepared by dissolving 0.120g of elemental selenium powder (0.050 molar) in an aqueous solution containing 3.0g of sodium sulfite (0.75 molar) at *p*H 9. The cadimum solution was prepared by dissolving 0.20g of $CdCl_2 \cdot 2.5H_2O$ (0.088 molar) into an aqueous solution containing 0.103*M* sodium nitrilotriacetate (NTA) at *p*H 8. After mixing, the combined solution remains clear and colorless over a period of about 8h. Over a period of 24h, a very thin redish brown film of either CdSe or Se forms on the walls of the flask; however, the solution remains clear and colorless. The electrodeposition is performed at *p*H 9 and room temperature using an air-saturated solution. The anode is not isolated from the cathode. Magnetic stirring is maintained during deposition.

Preparation of the titanium electrode prior to film deposition involved abrading the rectangular titanium plates using no. 400 emery paper. The plate was then soaked in chromic acid at 90°C for 3 min, rinsed in distilled water, and soaked in *ca.* 1*M* sodium hydroxide at 80°C for 5 min. It was then rinsed in distilled water and dried.

Electrolysis for 1h provides a film thickness of 1.3-1.6 μm. This thickness is determined in two ways. First, the weight of the film scraped from molybdenum foil was compared with the tabulated density of CdSe (9). Second, a Sloan Dektak stylus-type device was used at two positions on a CdSe film deposited on indium tin oxide-coated glass. Based on the weight of the film and the number of coulombs passed, the electrodeposition appears to be 88% efficient. The weight of the film was determined after the film has been annealed at 500°C. At this temperature, vaporization of the film does not appear to be extensive.

Cyclic voltammetry.—Cyclic voltammetry (CV) at the titanium electrode was performed with the BAS CVIB in a three-electrode cell containing the SCE as the reference electrode and cadmium metal as the auxiliary electrode. In addition to the electrodeposition solution, measurements were made at room temperature on a solution containing only the selenosulfite, on a solution containing only the cadmium complex, and on a solution of cadmium ion in the absence of NTA.

Composition of CdSe film.—Two methods were used to determine the composition of the film: polarography and Rutherford backscattering spectroscopy (RBS). For the polarographic determination, the analytical solution was prepared by treating the film on titanium with nitric acid at 50°C to dissolve cadmium as Cd^{2+} and selenium as H_2SeO_3. The $E_{1/2}$ for the reduction waves for Cd^{2+} and H_2SeO_3 occur at −0.745 and −1.500 (SCE). The polarographic analysis gives a Cd/Se ratio of 1.2. Preliminary RBS analysis of the surface composition of the CdSe film indicates a similar ratio (1.1 ± 0.1). More extensive studies of surface and depth profiles will be reported later. For this analysis, a 3 MV Van de Graaff accelerator provided 1.6 MeV helium nuclei.

Surface morphology.—An Etec Autoscan scanning electron microscope that employs the backscattered electron technique was used to observe the surface structure of the film before and after various annealing treatments. Photographs of the micrographs were taken on Kodak FXP/20 film using a Graphex lens and apperture.

Performance.—The photoresponse of the CdSe film was determined in a photoelectrochemical cell (PEC) using an aqueous solution containing 1/1/1*M* Na_2S/S/NaOH. The two-electrode cell contained the CdSe photoanode connected by a variable resistor (EICO resistance decade box) to a cathode that consisted of brass wire mesh coated with Cu_2S (10). No external bias was applied. The voltage across the load was measured with a digital voltmeter. Unfiltered light from a 300W CGE Quartzline ELH lamp was used. Power output from the lamp was determined with an Eppley thermopile. Prior to power measurements, the films were etched in 9*N* HCl, soaked in 1*N* NaCN, and treated with 1*M* $ZnCl_2$ (11).

Results and Discussion

The selenosulfite anion and the cadmium complex are made *in situ* in separate solutions, which are then mixed. The selenosulfite anion is prepared by dissolving elemental selenium in 0.6*M* sodium sulfite. The cadmium complex is prepared by dissolving cadmium chloride in 0.028*M* sodium nitrilotriacetate. The cadmium complex [stability constant $10^{9.8}$ (12)] is used to reduce the concentration of free cadmium ion. Otherwise, the chemical reaction (6, 13)

$$Cd^{2+} + 2\ OH^- + SeSO_3^{2-} \rightarrow CdSe + SO_4^{2-} + H_2O$$

occurs to an appreciable extent during the time of the electrolysis. By means of this complex, the solution remains stable for at least 24h. Furthermore, control experiments indicate that this chemical reaction provides no detectable CdSe film on the titanium during the period used for the electrolysis.

The CdSe film is electrodeposited at a titanium cathode from an air-saturated aqueous solution containing 0.02*M* selenosulfite anion and 0.02*M* cadmium cation complexed to nitrilotriacetate anion. This deposition is performed at room temperature and *p*H 9 using a two-electrode cell in which cadmium metal is employed as the anode. A constant potential of 0.30V is maintained be-

tween the electrodes, giving a current density that gradually rises from 0.34 to 0.47 mA/cm² during the deposition period. A time period of 1h provides a film thickness between 1.3 and 1.6 μm. So far, these conditions provide the CdSe film with the best light power to electrical power conversion efficiency (5.5-5.9%) for this system. Furthermore, these conditions provide consistent quality films from one solution to the next. Five solutions gave films having efficiencies beween 5.5% and 5.9%. An added advantage is that the solutions are sufficiently stable so that electrolyses can be repeated several times. In addition, solutions left overnight without any special protection provide films with photoconversion efficiencies as good as those obtained from fresh solutions.

The film on titanium appears dark gray with a slight sheen. It adheres well to titanium. Adhesion to other substrates, such as molybdenum, platinum, and indium tin oxide-coated glass, is not as good. Polarographic analysis indicates that the ratio Cd/Se is 1.2 in the film, and Rutherford backscattering spectroscopy indicates a ratio of 1.1 ± 0.1 using the surface energy approximation (14). Based on this composition, comparison of the weight of the films with the number of coulombs passed indicates that the efficiency of the electrodeposition process is 88%. For this determination, the film was annealed at 500°C for 30 min.

Prior to photoconversion efficiency measurements, the CdSe film was annealed in air to 550°C for 30 min to activate it. We found that this temperature provided suitable activation without causing substantial loss of material due to vaporization. A similar observation has been reported earlier (6). Careful temperature control seems to be important since films annealed at 500° and 550°C give photoconversion efficiencies of 4.5% and 5.8%, respectively, at 70 mW insolation. Above 550°C, vaporization appears to become significant. After annealing, the surface of the film was prepared by etching with 9*N* HCl, soaking in 1*N* NaCN, and treatment with 1*M* $ZnCl_2$ (10).

The efficiency for the conversion of light power into electrical power was determined using a photoelectrochemical cell (PEC) that contained an aqueous solution of $Na_2S/S/NaOH$ in the molar ratio 1/1/1. In this cell, the CdSe photoanode was connected by a variable resistor to the counterelectrode, which consisted of brass mesh coated with Cu_2S (11). No external biasing was applied. The photovoltage across the resistor was measured using a digital voltmeter. Unfiltered light from a Quartzline ELH lamp was used for excitation. The photovoltage measured in this manner for the film were quite stable with no appreciable variation during irradiation for periods up to 15 min. Dark voltages were negligible at all loads below 1 kΩ. Above 1 kΩ, the dark voltage increased with resistance to a maximum value around 50 mV at open circuit.

Figure 1 illustrates the photocurrent/photovoltage characteristics for two CdSe films having thicknesses of *ca.* 1.3 and 2.6 μm. There appears to be little difference between the results at the two thicknesses. For three 1 cm² CdSe films (*ca.* 1.3 μm thick) deposited from three separate fresh solutions, the average efficiency for the conversion of light power to electrical power is 5.74 ± 0.09% for 70 mW insolation. For these samples and those discussed below, the dark voltages were usually negligible, *i.e.*, no more than one or two millivolts except at open circuit, for which the dark voltage could be as large as 50 mV. Open-circuit photovoltages at 70 mW insolation are typically between 600 and 700 mV. Variation between 40 and 100 mW insolation gave open-circuit photovoltages in this range also. The photoresponse of each film was quick; response time appeared to be limited by the response of the voltmeter. At all loads, the photovoltage/photocurrent was stable during the illumination period, typically about 15 min. Short-circuit current density at 70 mW insolation was in the range 12.4-14.4 mA/cm² and fill factors were in the range 0.40-0.47. Figure 2 illustrates the photoresponse as a function of light power. The conversion efficiency decreases somewhat as the light intensity increases. Thus at 40, 70, 80, and 100 mW insolation, the conversion efficiency is 5.9%, 5.9%, 5.1%, and 4.7%, respectively, for a film having a surface area of 1 cm². When the surface area was increased to 3.2 cm², the efficiency decreased to 4.0% at 70 mW. Aging the electrolysis solution does not appear to adversely affect the quality of the film. Thus a conversion efficiency of 5.4% is obtained for a film grown from a solution that has been exposed to air for 24h at room temperature.

The effect of other conditions on the properties of the CdSe film are currently under study. Preliminary results indicate that current densities higher than 0.500 mA/cm² give films having efficiencies somewhat lower (*ca.* 5.0%). Larger selenosulfite anion concentrations have a similar effect.

Scanning electron microscopy reveals the effect of temperature on the surface morphology of the CdSe film. Figure 3A illustrates the surface morphology of the CdSe film on titanium after deposition for 1h and prior to any temperature treatment. At the present time, it is not clear if the cracks occur during electrodeposition or if they result when the film is dried at room temperature. The characteristic cauliflower appearance (3) found for H_2SeO_3-grown CdSe is not evident with our film. Annealing at 500°C in air for 30 min followed by 9*N* HCl etch gives the surface illustrated in Fig. 3B. The consequences of the annealing on the surface are not clear at this time.

A cyclic voltammogram (CV) of the deposition solution at room temperature is illustrated in Fig. 4. Second and subsequent scans exhibit currents higher than the first one given in Fig. 4, and the first peak shifts 70 mV in the positive direction. The CV's were obtained under condi-

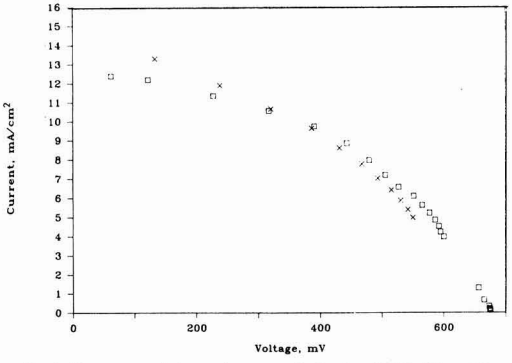


Fig. 1. Photocurrent/photovoltage results for 1 cm² CdSe films at two thicknesses: (□) 1.3 and (X) 2.6 μm. Conditions: PEC containing aqueous polysulfide; 70 mW unfiltered light from an ELH lamp; no externally applied bias.

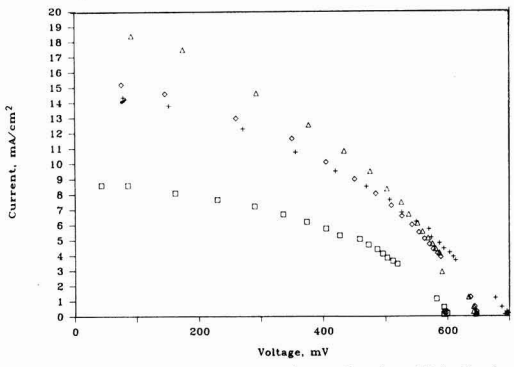


Fig. 2. Photocurrent/photovoltage results as a function of light flux for 1 cm² CdSe film 1.3 μm thick in PEC containing aqueous polysulfide. □: 40 mW + 70 mW. ◇: 80 mW. △: 100 mW.

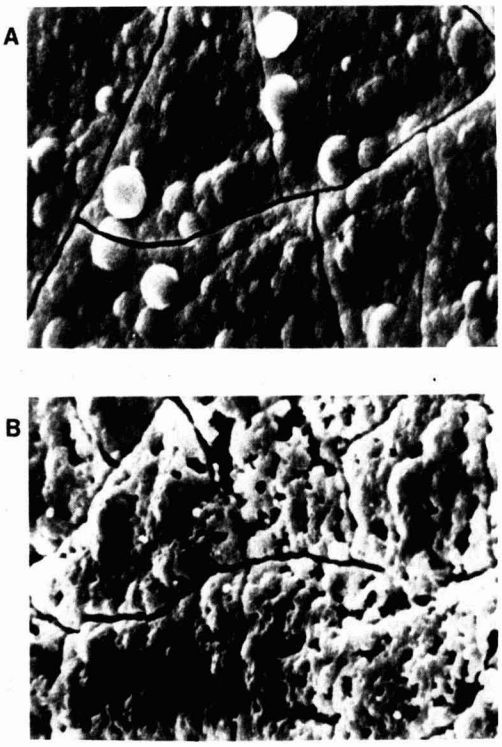


Fig. 3. Scanning electron micrographs of electrochemically deposited CdSe films on titanium. Magnification, 3250X; angle, 45°. A: As deposited. B: Annealed at 500°C for 30 min in air.

tions very close to those employed for film preparation, *i.e.*, same concentrations and electrode except the surface area of the titanium was reduced to 0.08 cm^2.

For several reasons, the details of the electrodeposition process are not clear at this time. First, CV of Cd^{2+} + NTA exhibits a peak at potential close to that in Fig. 4. Second, CV of $SeSO_3^{2-}$ exhibits peak 200 mV more negative than first peak in Fig. 4. Third, in both these cases, the current is not enhanced on the second and subsequent scans. Fourth, polarographic studies of the reduction of the various species alone and when mixed indicates that the mixture exhibits an additional wave that may result from an interaction between $SeSO_3^{2-}$ and either free or complexed cadmium ion. Consequently, the results thus far indicate several possibilities that are currently under study.

Acknowledgments

We thank Professor W. R. Fawcett for sharing the polarographic analyzer and the Sloan Dektak with us, and Professor J. R. MacDonald for allowing the use of the Van de Graaff accelerator. We are pleased to acknowledge helpful discussions with Dr. A. S. Baranski. This work was supported in part by the Natural Sciences and Engineering Research Council of Canada.

Manuscript submitted April 9, 1984; revised manuscript received June 20, 1984.

The University of Guelph assisted in meeting the publication costs of this article.

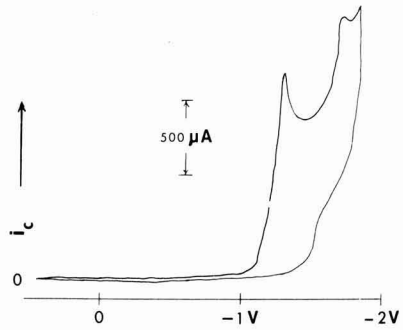


Fig. 4. Cyclic voltammogram at room temperature and 100 mV/s for an aqueous solution containing 0.6M sulfite, 0.02M selenosulfite, 0.022M cadmium chloride, and 0.28M sodium nitrilotriacetate at pH 9. Titanium electrode area is 0.08 cm^2. Reference is SCE.

REFERENCES

1. M. Skyllas-Kayacos and B. Miller, *This Journal*, **127,** 869 (1980).
2. G. Hodes, J. Manassen, and D. Cahen, *Nature (London)*, **261,** 403 (1976); *Bull. Isr. Phys. Soc.*, **22,** 100 (1976).
3. M. Tomkiewicz, I. Long, and W. S. Parsons, *This Journal*, **129,** 2016 (1982).
4. R. A. Boudreau and R. D. Rauh, *Solar Energy Mater.*, **7,** 385 (1982).
5. Preliminary report: M. Cocivera, *Chem. Commun.*, 938 (1984).
6. R. A. Boudreau and R. D. Rauh, *This Journal*, **130,** 513 (1983).
7. M. Skyllas-Kazacos, *J. Electroanal. Chem.*, **148,** 233 (1983).
8. M. Skyllas Kazacos and B. Miller, *This Journal*, **127,** 2378 (1980).
9. "CRC Handbook of Chemistry and Physics," 46th Ed., R. C. Weast, Editor, p. B161, Chemical Rubber Co., Cleveland, OH (1965).
10. G. Hodes, D. Cahen, J. Manassen, and M. David, *This Journal*, **127,** 2252 (1980).
11. G. Hodes, J. Manassen, and D. Cahen, *ibid.*, **127,** 544 (1980).
12. T. S. West, "Complexometry with EDTA and Related Reagents," 3rd Ed., p. 221, BDH Chemicals Ltd., Poole (1969).
13. G. S. Klevonov and N. A. Ostrapkevich, *Zh. Prikl. Khim.*, **35,** 1199 (1962).
14. W. K. Chu, J. W. Mayer, and M. A. Nicolet, "Backscattering Spectrometry," Chap. 2, Academic Press, New York (1978).

Reduction of CO_2 on n-GaAs Electrodes and Selective Methanol Synthesis

K. W. Frese, Jr.* and D. Canfield

SRI International, Materials Research Laboratory, Menlo Park, California 94025

ABSTRACT

Faradaic efficiencies and current voltage characteristics for the reduction of CO_2 to CH_3OH on n-GaAs (111 As) single-crystal electrodes have been determined. The yield of CH_3OH is ~ 100% for current densities of ~ 140 $\mu A/cm^2$ at −1.2 to −1.4V *vs.* SCE. The excess current due to CO_2 was found to have a threshold at pH ~ 3.6 and a maximum at pH ~ 4.3. The current also exhibited a rotation-independent j/v characteristic that is interpreted as a rate-determining surface chemical combination step involving adsorbed H atoms and a carbon containing intermediate. The pH dependence of the saturation current is modeled with a kinetic scheme involving the parallel reduction of H^+ and CO_2.

Over the past 40 years, there have been a number of studies dealing with CO_2 reduction at metal electrodes (1, 2). Recently, we have been investigating the reduction of CO_2 at semiconductor electrodes. One goal of the semiconductor approach is to utilize the electrochemical properties of p-type photocathodes to convert sunlight and CO_2 into useful fuels. It is known that CO_2 can be reduced to methanol and small amounts of methane on certain semiconductor electrodes in aqueous solutions (3-6). Our results (7) on electrolysis of CO_2 solutions using n- or p-GaAs and p-InP electrodes show that methanol is the major product (pH 4-6). These studies involving semiconductor electrodes, however, have mainly concerned product identification and yield.

Our purpose is to investigate aspects of the kinetics of CO_2 reduction on semiconductor electrodes. In this paper, we report measurements of the current voltage characteristics of a rotating disk n-GaAs electrode as a function of pH and rotation rate in the presence of N_2 and CO_2.

The faradaic efficiency for CH_3OH as a function of current density has also been determined. The results, especially the saturation current for CO_2 reduction, are modeled by kinetic analysis of a set of tentative elementary steps.

Experimental

Single-crystal disks, 5 mm diam, were mounted in a Pine Rotating-ring disk arrangement. Rotation speed was controlled by means of a Pine analytical rotator.

The crystal face was n-GaAs (111 As). The electrodes were first etched with 1% Br_2/CH_3OH and rinsed for 10s with 1*M* HCl. The GaAs electrodes were further etched in 1% sodium hypochlorite/0.1*M* Na_2 EDTA at pH 10. All etching was done with a wet cotton tip applicator. Finally, all electrodes were rinsed with distilled water.

All solutions were prepared with distilled, deionized water and reagent-grade chemicals, unless otherwise noted. High purity N_2 was passed through the electrolyte to remove dissolved oxygen. The electrode potential was swept at 1 V/min by means of a Pine RDE-3 potentiostat. The initial voltage for all sweeps was −0.5V SCE. All experiments were performed at room temperature, 22°C.

Electrolyte pH was controlled by addition of H_2SO_4 or NaOH solutions. When pH was varied, it was checked before and after each scan to make sure it had not changed.

Experimental Results

Current-voltage curve.—Current-voltage curves for n-GaAs (111)As in N_2-saturated and CO_2-saturated Na_2SO_4 electrolyte (pH = 4.0) are shown in Fig. 1. Before these curves were obtained, the rotating disk electrode was held at −1.2V *vs.* SCE in the same N_2-saturated electrolyte but with pH = 3.4 and 1600 rpm rotation speed. It was observed that the current increased with time until a steady current of 2.5 mA/cm^2 was reached after a period of about 10 min. A typical current-time curve is shown in the inset in Fig. 1. This pretreatment was chosen because we wanted to make measurements with the surface conditions close to those obtained in our extended electrolysis experiments (7) that are performed at −1.2 to −1.4V *vs.* SCE in a similar electrolyte (pH = 4-5). In those experiments, we always observed changes in the initial current voltage characteristics for about 30-60 min, then steady conditions are found for at least 70h. The probable cause for the longer current transient is that the pH is higher than in the present case.

Returning to Fig. 1, the onset for excess current due to CO_2 is −0.95V. Both curves with N_2 or CO_2 showed saturation behavior starting to −1.1 to −1.2V. This portion of the curve corresponds to diffusion-limited H^+ reduction, and in the case of CO_2 solution to the simultaneous reduction of H^+ and CO_2. Beyond −1.4V, a steep rise in current was observed with either gas present. This current is apportioned between H_2O and CO_2 reduction. It should be noted that the pH of the electrolyte was constant before and after each measurement. The saturation currents (N_2 present) depended on rotation speed, but the magnitude of the excess current due to CO_2 was almost constant up to −1.4V at pH 4.

Effect of rotation speed.—Figure 2 illustrates the dependence of the excess current in the presence of CO_2 as a function of rotation rate and electrode potential. These curves were constructed by direct subtraction of points on the N_2 and CO_2 curves at each voltage. The rotation rate was varied from 100 to 2500 rpm. This electrode was also pretreated as in Fig. 1. It can be seen that at pH 4.2, the excess CO_2 current was independent of rotation speed and showed saturation behavior over a voltage range between −1.15 and −1.40V. The saturated current density was ~ 1.4×10^{-4} A/cm^2. At potentials negative of −1.4V,

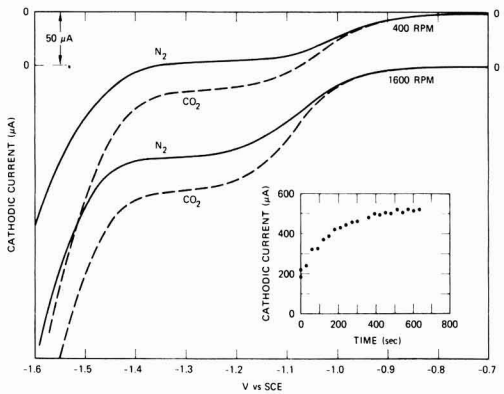


Fig. 1 Current-voltage curves in N_2 and CO_2 saturated 0.2M Na_2SO_4 solution, pH = 4.0, for n-GaAs (111) As face disk at two rotation speeds. Inset shows pretreatment current as function of time at −1.2 vs. SCE, pH = 3.4 same electrolyte (N_2). Area 0.2 cm^2.

*Electrochemical Society Active Member.

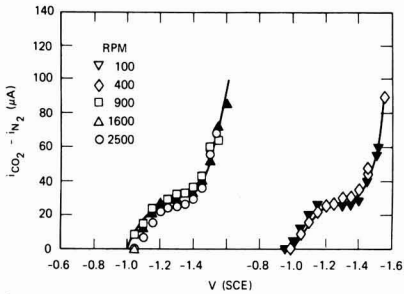


Fig. 2. Excess cathodic current due to CO_2 vs. electrode potential and rotation speed. n-GaAs, (111) As, in CO_2-saturated 0.1M Na_2SO_4. pH = 4.2. Area, 0.2 cm^2. Pretreatment as in Fig. 1.

an increase in excess current was observed. This characteristic also appeared to be independent of rotation rate.

A more detailed study of the rotation dependence of the cathodic current in the presence of N_2 or CO_2 was made. The results are shown in Fig. 3. With only N_2 present at pH = 4.2, a diffusion-limited H^+ reduction wave was obtained as shown by the linear plot of i vs. $(rpm)^{1/2}$. A diffusion coefficient of 7.0×10^{-5} cm^2/s was calculated from the slope assuming a proton activity coefficient (8) of 0.76. This diffusion coefficient was obtained at 22°C; correction to 25°C using 3.1 kcal/mol (9) activation energy yields 7.4×10^{-5} cm^2/s, in good agreement with data obtained in KCl electrolyte (9). When the electrolyte was saturated with CO_2, plots of i vs. $(rpm)^{1/2}$ were again linear with nearly the same slope as in the N_2-saturated case. Importantly, the intercepts of these plots were nonzero and depended on the electrode potential. A plot of the intercept vs. potential is shown in the inset to Fig. 3. Note the similarity of this i-V curve obtained in CO_2-saturated solution and those shown in Fig. 2 that were calculated by difference from data pairs in CO_2 and N_2 saturated electrolytes at constant rotation speed.

Effect of pH.—Cathodic current vs. pH and electrode potential was measured in both N_2- and CO_2-saturated electrolytes. The results for a rotation speed of 400 rpm are shown in Fig. 4. The lower curves in each panel correspond to the N_2 case, and the upper curves to the CO_2 case. In order to obtain reproducible results over the whole pH range that we investigated, we had to etch the

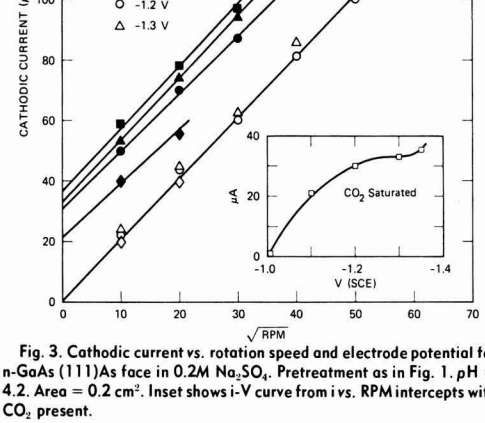


Fig. 3. Cathodic current vs. rotation speed and electrode potential for n-GaAs (111)As face in 0.2M Na_2SO_4. Pretreatment as in Fig. 1. pH = 4.2. Area = 0.2 cm^2. Inset shows i-V curve from i vs. RPM intercepts with CO_2 present.

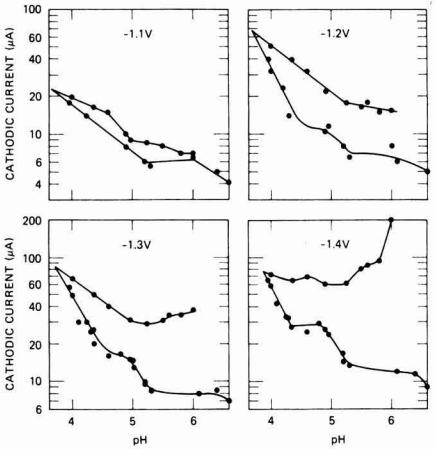


Fig. 4. Current vs. pH at various electrode potentials for n-GaAs (111)As in N_2- (lower curve) and CO_2- (upper curve) saturated electrolytes. 0.2M Na_2SO_4. Etch pretreatment only. Rotation speed, 400 RPM. Electrode area, 0.2 cm^2.

crystal before each i-V scan at a given pH. Therefore, the electrode was given the same etch pretreatment before each data point in Fig. 4. This treatment consisted of a 2s rinse in 1M HCl, 10s distilled H_2O rinse, followed by a 20s etch with 1% v/v sodium hypochlorite in pH 9 aqueous solution, and final H_2O rinse. In all cases, the etched electrodes shed rinse water immediately on contact. Generally, these surfaces are considered to be much closer to stoichiometric than the cathodically pretreated ones (Fig. 1-3). In the pretreated case, some surface roughening and cathodic corrosion giving at least a Ga monolayer is expected.

Inspection of the curves in Fig. 4 reveals that excess CO_2 current was first detected at pH values of 3.6, 3.7, 3.7, and 3.9 for −1.1, −1.2, −1.3, and −1.4V, respectively. The reaction orders for H^+ reduction with N_2, d log i/dpH were 0.37, 0.95, 0.91, and 0.97 for the same electrode potentials. The numbers were calculated from the straight lines in the most acid region of the plot. These unit reaction orders are consistent with diffusion-controlled reduction of hydrogen ions. Another approximate calculation of D_{H^+} was performed by extrapolation of the current at −1.3V (N_2 present) to pH = 0. A diffusion coefficient of 7.0×10^{-5} cm^2/s was found, in good agreement with our earlier determination. Under less acidic conditions, the reaction order approached zero and then came close to unity again. The deviation in reaction order with respect to the hydrogen ion may be caused by reduction of a thin (perhaps mono) layer of adsorbed species which are more stable at certain pH values. We assume this effect is constant for both N_2- and CO_2-saturated electrolytes. The electrolyte was saturated with CO_2, and the i-V curves at each pH were determined, again, after a standard etch for each pH value. The general pattern was that the apparent reaction order with respect to hydrogen ion decreased when CO_2 was present.

Then, plots of $i_{CO_2} - i_{N_2}$ vs. pH at a fixed potential were constructed; the results are shown in Fig. 5. The excess current began at a pH of 3.5-3.9 and increased to a maximum at pH 4.3 and then, depending on voltage, increased sharply again.

Finally, the $i_{CO_2} - i_{N_2}$ data were plotted vs. electrode potential with pH as a variable, as shown in Fig. 6. Strikingly different i-V curves at each pH were observed. The onset potential was similar to that already observed in Fig. 1 and 2, namely, ~ −1.0V. At pH 4.0, a saturation current was also found between −1.2 and −1.4V. As the pH increased, the saturation portion narrowed and a sharp increase became very noticeable. At pH 6, the saturation characteristics completely disappeared. Tafel plots of the

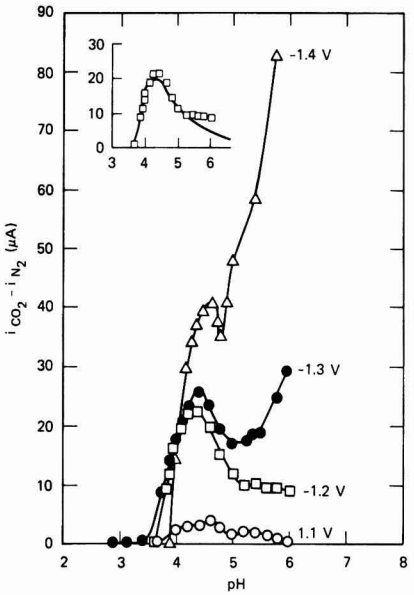


Fig. 5. Excess current due to CO_2 vs. pH, electrode potential. n-GaAs (111) As. Rotation speed, 400 rpm. Area, 0.2 cm². 0.2M Na_2SO_4. Inset shows kinetic model fit for pH variation of saturation current, $i_{Co_2} - i_{N_2}$. Solid line calculated, data squares from −1.2V curve below.

i-V curves for pH 5.8-6.0 and the more cathodic portion of the pH 5.5 curve are shown in the inset. The Tafel slopes were 220-230 mV.

Electrolysis and chemical analysis.—We performed long-term (17-20h) electrolysis experiments using two different Na_2SO_4 electrolytes that were saturated with CO_2, initial pH 4.2. The details of these experiments, analytical procedures, and more complete results have been tabulated (7). The objective was to determine the reduction products and obtain faradaic efficiencies.

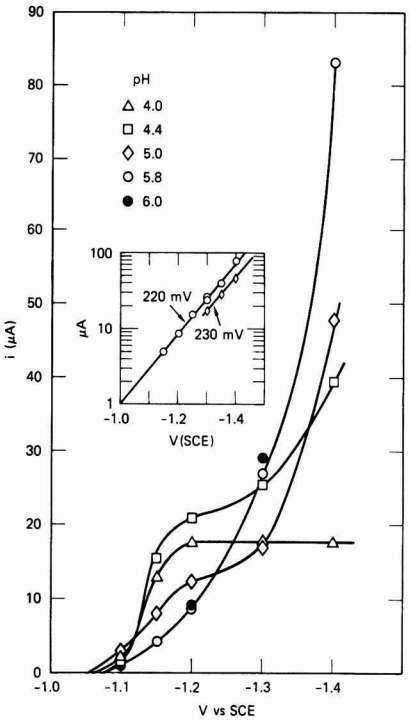


Fig. 6. Current-voltage curves for CO_2 reduction at various pH values using n-GaAs (111)As in 0.2M Na_2SO_4. Inset shows Tafel plots for most alkaline pH values. Area, 0.2 cm².

Analysis for methane, methanol, formaldehyde, and CO was performed. The electrolysis was conducted at various current densities (based on geometrical area) using n-GaAs (111)As crystals similar to those that were used in the i-V measurements reported above.

Occasionally, only traces of CH_4 were observed. Faradaic efficiencies for formaldehyde were always very low, < 1%. Also, efficiencies for CO were usually ~ 1%. However, the efficiencies for methanol were high and depended on current density, as shown in Fig. 7. Note that in an electrolyte made from 99.999% Na_2SO_4 and high purity water, no methanol was formed. This effect will be discussed more fully in later reports. The results with the Ga (111) face were similar except that methanol was produced in either reagent-grade or high purity electrolyte.

At a current density of ~ 1.4×10^{-4} A/cm², the efficiency for methanol was 100%. At 5×10^{-4} A/cm², the methanol efficiency dropped to low values with either face.

Electrolysis of similar electrolytes at pH 5.8-6, gave some formate ion product, as shown by qualitative analysis using the mercuric chloride test (10). Formate has been shown to be the major product on Hg electrodes (11) in this same pH range. Methanol has also been found at pH up to 6.7 with current efficiencies > 10%.

Discussion

In this section, we will discuss our results in light of a plausible reaction mechanism for CO_2 reduction. A number of key experimental observations can be summarized as follows. The excess current due to CO_2 saturates at ~ 140 μA/cm² (cathodically pretreated surface, Fig. 2 and 3) and at ~ 90 μA/cm² on an as-etched surface (Fig. 6). This saturation current is independent of rotation speed from 100 to 2500 rpm. This behavior suggests that the current is controlled by a chemical surface reaction with nearly saturation coverage with adsorbed intermediates. The faradaic efficiency for CH_3OH reaches 100% at a current density of ~ 140 μA/cm². This value is remarkably close to the saturation current for a similarly activated electrode. Also, the pH has a pronounced influence on the excess current, $i_{CO_2} - i_{N_2}$. Two critical pH values were found (Fig. 5); a low value when the excess current is immeasurably small, and a higher value where a maximum occurs. Finally, the reduction of H^+ is diffusion controlled in the presence of CO_2 (Fig. 3). According to the analysis of Pleskov (12), plots of current density *vs.* $(rpm)^{1/2}$ like those in Fig. 3 (CO_2 present) indicate that rapid diffusion-controlled H^+ reduction occurs in parallel with a slower

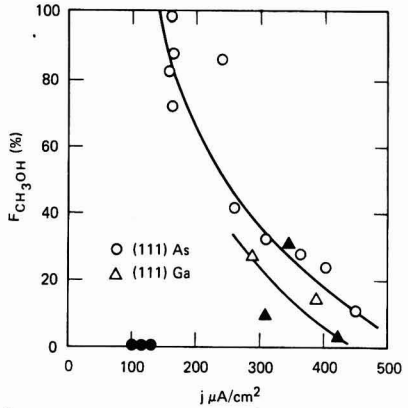


Fig. 7. Faradaic efficiency for CH_3OH on n-GaAs in CO_2-saturated 0.2M Na_2SO_4. Open symbols = reagent grade salt/distilled water. Solid symbols = 99.999% salt/1.7 × 10^7 Ω · cm water. 10^{17} donors/cm³.

activation-controlled process. This factor is used in formulating the parallel reaction mechanism below. An increase in current at more cathodic voltages (Fig. 2 and 6) indicates a change in mechanism. At pH values 5-6, Tafel slopes of 220-230 mV/decade were observed. We will first focus on the saturation current and the effect of pH.

The data presented here do not, of course, allow for identification of the chemical species involved in all the mechanistic steps. However, the data do provide important clues concerning the overall reaction sequence and the rate-determining step in CO_2 reduction to methanol.

In the following discussion, we will assume that under reaction conditions, the GaAs rotating disk electrode surface contains adsorbed hydrogen atoms. It is further assumed that the steady-state coverage with hydrogen, θ, is mainly controlled by the convective diffusion of H_3O^+ ions. The value of θ will depend on the rate of removal of H atoms and the diffusion properties. In the following, the subscript "a" indicates adsorbed on the surface. When the combination reaction is rate determining in the hydrogen evolution reaction, HER, we have

$$2H_a \xrightarrow{k_c} H_2 \qquad [1]$$

By equating the current for Eq. [1] with the Levich equation (12), we obtain

$$\theta = \left(\frac{A}{k_c}\right)^{1/2} (\text{rpm})^{1/4} (H^+)^{1/2} \qquad [2]$$

where $A = 0.017 (D_{H^+})^{2/3}$; D and H^+ are expressed in units of 10^{-5} cm/s and mol/liter, respectively. Similarly, when the electrochemical desorption is rate determining

$$H^+ + e^- + H_a \xrightarrow{k_e} H_2 \qquad [3]$$

and

$$\theta = \frac{A(\text{rpm})^{1/2}}{k_e} \qquad [4]$$

According to Eq. [2], the hydrogen coverage depends on the square root of the proton concentration and depends slowly on rotation rate. For the second case of electrochemical desorption, θ is independent of H^+ and varies more strongly with stirring.

Now, consider the following elementary scheme of steps to account for the saturation of j_{CO_2}-j_{N_2} and its pH dependence.

$$n H^+ + n e^- \underset{k-1}{\overset{k_1}{\rightleftarrows}} n\, H_a \qquad [I]$$

$$2H_a \xrightarrow[\text{rds}]{k_c} H_2 \qquad [II]$$

$$CO_2 + e^- + H^+ \underset{k-3}{\overset{k_3}{\rightleftarrows}} \cdot COOH_a \qquad [III]$$

$$H_a + \cdot COOH_a \xrightarrow[\text{rds}]{k_4} I \qquad [IV]$$

followed by four additional hydrogenation steps to give methanol via additional intermediates, I. We have no specific evidence for the identity of these intermediates, I. For example, I in step [IV] could be CO_{ad}. For H_2 and CH_3OH reduction products, n would equal seven. Adsorbed formate radicals are believed to be the precursor to CO_2 in the oxidation of formic acid (13) and to be the product of the one electron reduction of CO_2 on Hg electrodes (11, 14).

The key to explaining the saturation current and its pH dependence is the assumption that the rate of CO_2 reduction (methanol formation) is limited by a surface chemical reaction involving H_a. For simplicity let us say that step [IV] is rate limiting. The total current in the presence of CO_2 is then given by

$$j_{CO_2} = 2k_c\theta^2 + 6k_4\theta\gamma \qquad [5]$$

where γ is the surface coverage with formate radicals. An expression for γ can be obtained by the usual steady-state method. Under saturation conditions, we simply write $\theta + \gamma = 1$. Other analogous rate-determining steps involving H_a and species I would lead to a relation similar to Eq. [5] (consecutive step reaction). Using our expression for θ (combination reaction) Eq. [2], and conservation of sites, we obtain the following expression for the experimentally determined j_{CO_2}-j_{N_2}

$$j_{CO_2}\text{-}j_{N_2} = 6k_3B(H^+)^{1/2}\,[1 - B(H^+)^{1/2}] \qquad [6]$$

where

$$B = [A/k_c]^{1/2}\,(\text{rpm})^{1/4}$$

According to Eq. [6], the excess current should go to zero when $(H^+)_o = k_c/A(\text{rpm})^{1/2}$; and it should be maximum at $(H^+)_{max} = k_c/4A(\text{rpm})^{1/2}$. In addition, the model predicts $pH_{i=max} - pH_{i=o} = \log 4$. From Fig. 5, we see that for -1.2V, the excess current is maximum at pH = 4.3 and goes to zero at pH = 3.6. Therefore ΔpH = 0.7 agrees with the predicted value log 4 = 0.6.

We can calculate a value for k_c in current density units by applying the equation for $(H^+)_{max}$ just mentioned above. Using the appropriate constants for A, and an activity coefficient of 0.76, we obtain $k_c = 3.2 \times 10^{-4}$ A/cm^2. Using this value of k_c, we can calculate $B = 62.4M^{-1}$. Returning to Eq. [6] and noting the saturation current at pH = 4.2 of 90 μA/cm^2 (Fig. 6), we can calculate that $k_4 = 6.1 \times 10^{-5}$ A/cm^2.

It is of interest to compare the surface combination rate constants determined here with those deduced (15) from limiting current behavior for Cl_2 evolution. Here, the reaction rate is limited by combination of Cl atoms on the surface. On oxide-free Pt electrodes in anhydrous trifluoroacetic acid, k_c ranges from 300 to 1500 μA/cm^2, depending on coverage of Cl atoms. Our values, particularly for the H atom combination are in the same range. A more realistic comparison would involve rate calculations based on details of the energy surfaces for the adsorbed H_a and $COOH_a$ on the GaAs electrode. Unfortunately, these are not available.

At this stage, we can calculate the complete pH dependence of the saturation current using Eq. [6] and our rate constants. The inset to Fig. 5 shows the model prediction (solid line) and the data points for -1.2V. The fit is seen to be good. If θ were determined by the electrochemical desorption in the HER Eq. [4], no maximum is predicted in the saturation current *vs.* pH. At pH > 5, the observed current is slightly above the calculated curve; this is probably due to a faster process taking over. This also explains why the -1.4V peak (Fig. 5) appears larger than the -1.2 and -1.3V peaks.

We now consider some other features of the j_{CO_2}-j_{N_2} curve. As we have seen, at more cathodic potentials (Fig. 2, 5, and 6), different i-V characteristics were observed. At pH 4.2, a rotation-independent increase in excess current was found, beginning at -1.4V (Fig. 2). The Tafel shapes for these two plots are 152 and 134 mV/decade. It is not clear if these slopes depend on rotation rate or if the data is imprecise. At pH 5-6, the i-V curves are dominated by characteristics with Tafel slopes of 220-230 mV decade (400 rpm) and no saturation effect is observed.

From the earlier discussion concerning the saturation current, it is clear that under our reaction conditions the surface is nearly saturated with adsorbed intermediates. Therefore, Temkin-type analysis with the possibility of activated adsorption must be applied (16).

We have not done a complete analysis of these effects, and, therefore, a detailed interpretation of the Tafel slopes must be postponed. However, we note that Tafel slopes of 224 mV/decade were already observed (14) for CO_2 reduction on Hg electrodes in $NaHCO_3$ solution. In that case (11, 14), the rate-determining step ($j > 10^{-5}$ A/cm^2) was concluded to be

$$CO_2 + e^- + H_2O \rightarrow COOH_{ad} + OH^-$$

The reaction product was stated to be formate (98% current efficiency). At pH > 5, it is reasonable to expect that the coverage on GaAs with H_{ad} is also low and hydrogen has to be obtained from H_2O.

Now consider the effect of current density on the faradaic efficiency, F_{CH_3OH}, for methanol. These measurements were made at −1.3 to −1.4V (SCE) in CO_2-saturated solutions with an initial pH of 4.1-4.2. There is a close correspondence between this current density of F_{CH_3OH} = 100% and the saturation current in Fig. 2 for a cathodically pretreated electrode. Both these values are ~ 140 $\mu A/cm^2$. If the total current is increased beyond this value, the yield of methanol should drop if the limiting rate of methanol formation corresponds to the saturation current. This appears to be the case as shown in Fig. 7. Apparently, another CO_2 reduction product is formed at high current densities as demonstrated by the drop in methanol yield and the simultaneous rise in excess current, as shown in Fig. 2. This current may correspond to the reduction of the adsorbed formate radicals that were postulated to be reactants in the surface chemical rate-limiting step of methanol synthesis.

According to our model, the yield of CH_3OH will depend on the coverage of H atoms. Recall that we assume only H_a and I, which may be · COOH, are the only important intermediates in the mechanism. Using Eq. [5] and the observed rate constants, k_c and k_i, we can write

$$F_{CH_3OH} = \frac{6k_i\theta\gamma}{j_{CO_2}} = \frac{1}{1 + 1.75\left(\frac{\theta}{1-\theta}\right)} \qquad [7]$$

It may be seen that methanol yield increases as θ decreases. For θ = 0.5 and 0.1, F_{CH_3OH} is 0.36 and 0.84, respectively. Even though $k_i < k_c$, the yield of methanol can reach high values as found experimentally. In the limit of θ = 0, Eq. [7] is undefined.

The question of the acidity of the postulated adsorbed formate radicals is not completely answerable at this time. It has been suggested that adsorbed CO_2^- is the dominant first electron product based on the reported pK_a of 1.4 (18) for free aqueous formate radicals. However, the value of 3.9 has also been reported (19) for the same radical. We reason that is more appropriate to estimate the acidity of adsorbed formate radicals by analogy to organic acids. There appears to be little quantitative data on the pK_a's of metallocarboxylic acids (20, 21); however, many organic acids with different hydrocarbon substituents have been studied. In many cases (22), the pK_a's are in the range of 4.7 to 5.0. In addition, substituent effects can change the K_a's by an order of magnitude. If bonding of radicals occurs to the more electropositive Ga atoms on the surface, then the pK_a of the adsorbed radical might exceed 5.0. The negative charge at the cathodic surface may also act to further increase the pK_a. For example (22), introduction of the $—CO_2^-$ group for a methyl hydrogen in acetic acid raises pK_a from 4.76 to 5.69. Finally, adsorbed CO_2^- would be less favorable, owing to lateral repulsions on the surfaces. In summary, because of the above chemical and physical effects, protonated CO_2^- radicals are a distinct possibility as suggested in our mechanism, step [III], for pH ≤ 5.

Summary

Carbon dioxide can be reduced to methanol on n-GaAs (111 As) electrodes with high faradaic efficiencies for current densities of ~150 $\mu A/cm^2$. Methanol synthesis appears to be limited by a surface chemical step involving adsorbed hydrogen and an unidentified surface intermediate. Possible intermediates are CO_{ad}; formyl, —COH; hydroxycarbene, —CH—OH; hydroxymethyl, CH_2—OH; or methoxy, —O—CH_3.

Analysis of the pH dependence of the saturation current led to information on the HER. We used the assumption that hydrogen is formed by the combination reaction. This step was already proposed as part of the HER on GaAs electrodes (17). A chemical rate constant of 3.2 × 10^{-4} A/cm^2 for the H_a combination was obtained. The pH dependence of the saturation current in the presence of CO_2 could be fit with parameters derived from the data. The analysis gave a chemical rate constant of 6.1 × 10^{-5} A/cm^2 for the rate-determining step.

The results given here show that very complex catalytic reactions can be performed on semiconductor surfaces in electrochemical cells. A start has been made towards understanding such mechanisms as CH_3OH synthesis. There appears to be pH and voltage range for certain mechanisms or products.

The onset potentials for CH_3OH synthesis are quite cathodic, which means, the energy efficiency, for the process is low. The use of p-type cathodes and/or n-type photoanodes in electrolysis cells could significantly alter this situation.

Manuscript submitted July 11, 1983; revised manuscript received June 8, 1984. This was Paper 517 presented at the San Francisco, California, Meeting of the Society, May 8-13, 1983. This work was supported by the Gas Research Institute.

SRI International assisted in meeting the publication costs of this article.

REFERENCES

1. P. G. Russel, N. Kovac, S. Srinivasan, and M. Steinberg, *This Journal*, **124,** 1329 (1977) and references therein.
2. S. Kapusta and N. Hackerman, *ibid.*, **130,** 607 (1983).
3. M. Halmann, *Nature*, **275,** 115 (1978).
4. T. Inoue, A. Fujishima, S. Konishi, and K. Honda, *ibid*, **277,** 637, (1979).
5. B. Aurian-Blajeni, M. Halmann, and J. Manassen, *Solar Energy*, **25,** 165 (1980).
6. K. W. Frese, Jr. and D. G. Canfield, SRI Quarterly Report no. 1 July (1982) and SRI Quarterly Report no. 2 October (1982), "Reduction of CO_2 to Methanol and Methane by Photo and Dark Reactions on Semiconductor Electrodes," Sponsored by Gas Research Institute, 1982.
7. D. Canfield and K. W. Frese, Jr., *This Journal*, To be published.
8. R. A. Robinson and R. H. Stokes, *Trans. Faraday Soc.*, 612 (1949).
9. Von B. Gostisa-Mihelcic, W. Veilstick, and A. Heindrichs, *Ber. Bunseges. Phys. Chem.*, **76,** 21 (1972).
10. F. Feigl, V. Amger, and R. Oesper, "Spot Tests in Organic Analysis" p. 453 Elsivier Publishing, Amsterdam (1966).
11. W. Paik, T. N. Andersen, and H. Eyring, *Electrochim. Acta*, **14,** 1217 (1969).
12. F. Opekar and P. Beran, *J. Electronal. Chem.*, **69,** 1 (1976).
13. J. Horiuti, in "Physical Chemistry, An Advanced Treatise", Vol. IXB, H. Eyring, Editor, p. 1, Academic Press, New York (1970).
14. J. Ryu, T. N. Andersen, and H. Eyring, *J. Phys. Chem.*, **76,** 3278 (1972).
15. B. E. Conway and D. M. Novak, *J. Electroanal. Chem.*, **99,** 133 (1979).
16. B. E. Conway, "Principles of Electrode Kinetics," Ronald Press (1965).
17. K. D. N. Brummer, *This Journal*, **114,** 74 (1967).
18. G. V. Buxton and R. M. Sellers, *J. Chem. Soc. Faraday Trans.*, **69,** 555 (1973).
19. A. Fojtik, G. Czapski, and A. Henglein, *J. Phys. Chem.*, **74,** 3204 (1970).
20. R. Laine and R. B. Wilson, in "Aspects of Homogeneous Catalysis," Vol. 5, R. Ugo, Editor, D. Reidel Publishing Co. (1984).
21. N. Grice, S. C. Kao, and R. Pettit, *J. Am. Chem. Soc.*, **101,** 1627 (1979).
22. H. C. Brown, D. H. McDaniel, and O. Haflinger, in "Determination of Organic Structure by Physical Methods," E. A. Braude and F. C. Nachod, Editors, Academic Press, New York (1955).

Anode-Limited Cell Reversal in Lithium-Sulfur Oxyhalide Cells

Alan I. Attia*,[1] and Christian Sarrazin

Gould Research Center, Rolling Meadows, Illinois 60008

Kenneth A. Gabriel and Richard P. Burns

Department of Chemistry, University of Illinois at Chicago, Chicago, Illinois 60680

ABSTRACT

In situ infrared spectroscopy and mass spectrometry were used to investigate the gas and liquid phases in lithium-sulfur oxyhalide cells driven into anode-limited reversal at 1-5 mA/cm². In the lithium-thionyl chloride system the species HCl, CS_2, SO_2, S_2O, SCl_2, and SO_2Cl_2 were identified in the gas phase and HCl, $AlCl_3OH^-$, SO_2, SO_2Cl_2, and $SOCl^+$ $AlCl_4^-$ in the liquid phase. A species giving rise to three absorption bands at 1337, 1070, and 665 cm^{-1} was observed in the liquid phase of that system during anode-limited reversal only, and in the lithium sulfuryl chloride system during normal discharge and during reversal; this compound was tentatively identified as $Li(SO_2, SO_2Cl_2)^+$ $AlCl_4^-$ and is analogous to the well-known complexes involving $LiAlCl_4$, SO_2, and $SOCl_2$. The lithium-sulfuryl chloride cell behaved similarly to the thionyl chloride cell, specifically with respect to formation of SO_2- and $SOCl^+$-like species—the latter tentatively identified as SO_2Cl^+. Indirect evidence suggests that chlorine may accumulate in both systems at −20°C, but at 25°C its accumulation in the cells is prevented by its reaction with SO_2 to form SO_2Cl_2.

In the ten years since the feasibility of lithium-sulfur oxyhalide cells was first recognized (1), remarkable progress has been made in hardware development; however, their widespread use has been impeded, owing to the safety hazards associated with their relatively high energy density. Conflicting reports exist as to the cause of several explosions involving the lithium-thionyl chloride system. Explosions have been observed in anode-limited cells driven into reversal (2); a hazard also exists in cathode-limited cells since they contain both lithium and sulfur at the end of discharge, and the highly exothermic formation of Li_2S may be possible at elevated temperatures (3, 4). In addition, poor mechanical design is suspected in some cases.

The lithium-sulfuryl chloride cell which does not form any sulfur during discharge is potentially safer than $Li/SOCl_2$ (5). However, the relatively high corrosion rate of lithium in that system limits its use to special high rate reserve applications.

Resolution of the unpredictable safety hazards associated with these systems may only be possible by analytical determination of their causes, and several investigations have been conducted along these lines. Istone and Brodd (6) have performed an *in situ* infrared study of the electrolyte of $Li/SOCl_2$ cells and observed that only two absorption bands change in intensity during normal discharge, one at 1335 cm^{-1} due to SO_2 formation, the other at 689 cm^{-1} which they assigned to S_2O. Elemental sulfur was also seen to deposit on the spectroscopic cell walls. These authors proposed a mechanism involving formation of SO_2 and S_2O with subsequent decomposition of the S_2O to sulfur and SO_2. This mechanism had been previously rejected on the basis of stoichiometry by Schlaikjer *et al.* (7), who postulated instead the formation of a sulfur monoxide polymer according to the reaction

$$2n\text{Li} + n\text{SOCl}_2 = 2n\text{LiCl} + (\text{SO})n \quad [1]$$

followed by decomposition of the polymer to produce elemental sulfur and SO_2.

Spectroelectrochemical studies first carried out by Abraham and Mank (8) then by Salmon *et al.* (9) have provided evidence that the principal reaction at the anode current collector on reversal is

$$2\text{SOCl}_2 = 2\text{SOCl}^+ + \text{Cl}_2 + 2e^- \quad [2]$$

Salmon *et al.* further speculated that several electrochemical reactions involving SO_2 were also occurring

$$\text{SO}_2 = \text{SO}^{++} + \text{O} + 2e^- \quad [3]$$

$$\text{SO}_2 + \text{Cl}_2 = \text{SO}^{++} + 2\text{Cl}^- + \text{O} \quad [4]$$

$$\text{Cl}_2 + \text{O} = \text{Cl}_2\text{O} \quad [5]$$

IR absorption bands at 1070 and 690 cm^{-1} were assigned by these authors to SO^{++} and Cl_2O, respectively. Abraham and Mank had observed the 1070 cm^{-1} band in their investigation but assigned it to an S-O stretching vibration of a sulfur-oxy compound. Under the same conditions, they also observed a band at 1415 cm^{-1}, which they assigned to SO_2Cl_2.

Evidence for a significant involvement of aluminum chloride species in the IR absorption spectrum was obtained by Bailey and Blomgren (10), who identified several aluminates in Li_2CO_3-$AlCl_3/SOCl_2$ electrolyte giving rise to absorptions at 3200-3400 ($AlCl_3OH^-$), 800, and 695 cm^{-1}. The last two bands were assigned to the oxychloro-aluminate species with the suggested structure $Li_2(AlCl_3)_2O$. They corroborated their results using ^{27}Al NMR spectroscopy.

More recently, McDonald (11) was able to show by mass spectroscopy the generation of substantial amounts of hydrogen and nitrogen in $Li/SOCl_2$ batteries.

In order to clarify these issues, we have re-examined the IR absorption spectrum of the electrolytes of lithium thionyl chloride and lithium-sulfuryl chloride cells during normal discharge and anode-limited reversal, at current densities between 1 and 5 mA/cm², and temperatures between −20° and 25°C. Furthermore, we have carried out a mass spectrometric analysis of the gases evolved from a $Li/SOCl_2$ cell during discharge and anode-limited reversal at 25°C.

Experimental

The cell.—The electrochemical cell used for all our experiments is shown in Fig. 1. It consists of two concentric electrodes supported within a nickel cylinder. The cathode is a thin (20 cm² × 20 mil) carbon-Teflon porous electrode pressed on a nickel grid spot welded to the wall of the cylinder. The lithium anode (8 cm² × 5 mil) is pressed on a nickel foil substrate spot welded around a stainless steel central post. The electrodes are about 0.5 cm apart and separated by a double layer of 0.005 in. glass mat. The cell can be coupled directly to a mass spectrometer via a valve system, as shown in Fig. 2, or to an IR spectroscopic cell via a pump to circulate the electrolyte between the electrochemical cell and the spectroscopic cell. The volume of solution in the cell is 14 ml. An additional volume of 2 ml is circulating through the pump and spectroscopic cell. The head space volume is 1 ml.

Mass spectra.—A Perkin-Elmer (PE270) mass spectrometer with a home-built all-glass gas inlet system was used

*Electrochemical Society Active Member.

[1]Present address: Gould, Incorporated, Micro Power Products Division, Eagan, Minnesota 55121.

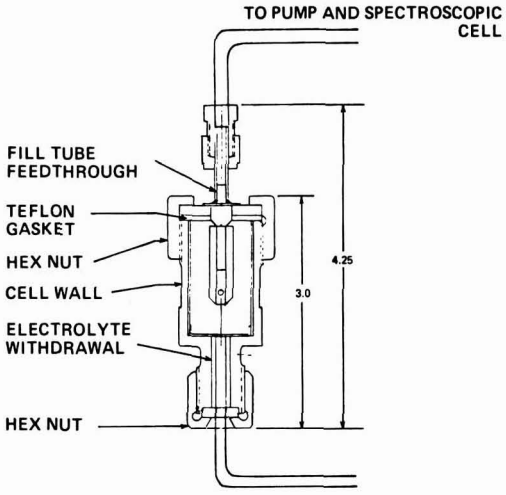


Fig. 1. Electrochemical cell for flowing electrolyte system

for *in situ* gas-phase analysis (Fig. 2). This sampling system consists of two (V_1 and V_2) stainless steel shut-off nonrotating stem valves from Circle Seal. The sampling volume contained between V_1 and V_2 is approximately 0.5 cm^3. The glass inlet system includes four Teflon stopcocks (V_3-V_6), with V_4 providing access to a roughing pump and V_6 leading to the mass spectrometer ion source. V_5 gives access to a perfluorokerosene (PFK) reservoir, which is used in the calibration of the mass scale. Exact mass experiments were performed on an AEI MS-30 double focusing mass spectrometer equipped with an Anatron peak matching unit. These measurements were carried out with known perfluorokerosene fragments as the mass reference (12). Intensity *vs.* time data were obtained with 80 eV electron energy on the PE270 mass spectrometer and with 70 eV electron energy on the MS-30 mass spectrometer.

Infrared spectra.—The IR absorption spectra were obtained with a Nicolet 5MX/1200S FTIR spectrometer. Silver chloride windows were used for the spectroscopic cell with a 0.1 mm optical path length. All spectral frequencies are accurate to within ± 4 cm^{-1}; for the purpose of quantitative analysis, peak heights above the base line were measured. For badly overlapping bands, we used the tangent line technique to obtain reproducible results, or spectral subtractions.

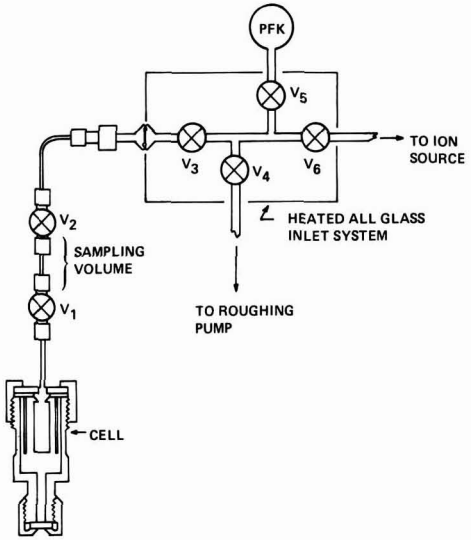


Fig. 2. Mass spectrometric sampling system

Chemicals.—$SOCl_2$ and SO_2Cl_2 were double-distilled before use. $LiAlCl_4$ was used as received from Anderson Physics.[2] The electrolyte solutions, 1.4*M* $LiAlCl_4$ in $SOCl_2$ and 1.5*M* $LiAlCl_4$ in SO_2Cl_2 were prepared in a dry room shortly before filling the electrochemical cell.

Spiking and calibration experiments.—Mixtures of known composition were used for calibration and identification of possible products of discharge. These mixtures were prepared in a dry room or glove box and transferred to the spectroscopic cells in a dry environment. The calibration for $SOCl^+$ was obtained by dissolving known amounts of $AlCl_3$ in pure thionyl chloride, assuming 100% conversion of the $AlCl_3$ to $SOCl^+AlCl_4^-$.

S_2O synthesis.—We attempted to synthesize S_2O in a vacuum line using the reaction between $SOCl_2$ and Ag_2S at 160°C, as described by Nickless (13).

Results and Discussion

Qualitative IR studies.—Typical spectra of electrolyte from Li/$SOCl_2$ and Li/SO_2Cl_2 cells driven into anode-limited reversal are shown in Fig. 3(a) and 3(b). The most prominent absorption bands are tabulated in Table I together with their most likely assignment based on previously published results (6-10, 14) or the present work. The spectra for these electrolytes during normal discharge show only the formation of SO_2 at these relatively low current densities of 1-5 mA/cm^2.

To identify the various absorption bands, we spiked several solutions of $SOCl_2$ or SO_2Cl_2 with known compounds and compared the resulting IR spectra with the electrolyte spectra during normal discharge and reversal. The results of these tests are shown in Table II.

Water has a substantial effect on the absorption spectrum of $SOCl_2$. Addition of water to pure $SOCl_2$ results in the formation of HCl (2790 cm^{-1}) and SO_2 (1335 and 1144 cm^{-1}). However, the same addition to 1.4*M* $LiAlCl_4/SOCl_2$

[2]Anderson Physics Laboratory, Urbana, Illinois 61801.

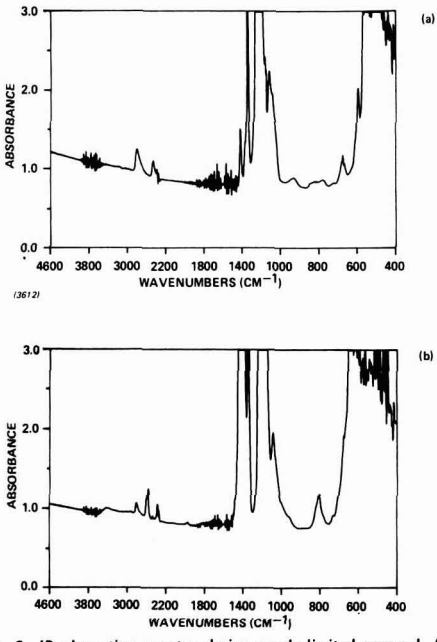


Fig. 3. IR absorption spectra during anode-limited reversal. (a): Li/$SOCl_2$ system. (b): Li/SO_2Cl_2 system.

Table I. Observed frequencies and assignments for $Li/SOCl_2$ and Li/SO_2Cl_2 systems in reversal

Frequency (cm^{-1})	Assignment	Ref.
	$Li/SOCl_2$ – 1.4*M* $LiAlCl_4$	
3400	$AlCl_3OH^-$	(10)
2790	HCl	
2450, 1225, 775, 927	$SOCl_2$	(14)
1408, 1160, 570	SO_2Cl_2	(14)
1335, 1144	SO_2	(13)
1115	$SOCl^+AlCl_4^-$	(8)
1337, 1070, 665	$Li(SO_2, SO_2Cl_2)^+AlCl_4^-$	This work
822	Oxychloroaluminate	(10)
694	Oxychloroaluminate	(10)
	Li/SO_2Cl_2 – 1.5*M* $LiAlCl_4$	
3444	$AlCl_3OH^-$	(10)
2811, 2569, 2360, 1413, 1180, 1000, 796, 575	SO_2Cl_2	(14)
1335	SO_2	(13)
1337, 1068, 668	$Li(SO_2, SO_2Cl_2)^+AlCl_4^-$	This work
692	Oxychloroaluminate	(10)
1084, 1059	$SO_2Cl^+AlCl_4^-$	This work

Table II. Spiking experiment

	Observed frequencies (cm^{-1})
$SOCl_2$ neat	2450, 1225, 927, 776, 722, 636, 616, 590, 569, 549
Water added to $SOCl_2$	2790, 1335, 1144[a]
$SOCl_2$/1.4*M* $LiAlCl_4$	2445, 1225, 924, 777, 722, 638, 617, 591, 577
Water added to $SOCl_2$/1.4*M* $LiAlCl_4$	3400, 2790, 1333, 1144, 694[b]
SO_2Cl_2 added to $SOCl_2$	1412, 1169, 800, 570[a]
HCl to $SOCl_2$	2790[a]
SO_2 to $SOCl_2$	1144, 1335[a]
$AlCl_3$ to $SOCl_2$	1117, 557[a]
SO_2 and SO_2Cl_2 $SOCl_2$/1.4*M* $LiAlCl_4$	1070, 668, 1337, 1408, 594[b]
SCl_2 or S_2Cl_2 to $SOCl_2$/1.4*M* $LiAlCl_4$	1070, 668, 1337, 1408, 594[b]
Water to $SOCl_2/AlCl_3$	1335, 1144, 1115, 822[a]
SO_2Cl_2 neat	2814, 2586, 2368, 1415, 1180, 996, 793, 775, 723, 570
$SO_2Cl_2/LiAlCl_4$	2811, 2569, 2360, 1413, 1180, 1000, 796, 775, 723, 575
$AlCl_3$ to SO_2Cl_2	1090, 1053[c]
$SO_2 + SO_2Cl_2/LiAlCl_4$	1335, 1068, 668[d]

[a] Frequencies observed in addition to those in $SOCl_2$.
[b] Frequencies observed in addition to those in $SOCl_2$/1.4*M* $LiAlCl_4$.
[c] Frequencies observed in addition to those in SO_2Cl_2.
[d] Frequencies observed in addition to those in $SO_2Cl_2/LiAlCl_4$.

electrolyte gives rise to two more absorption bands at 694 and 3400 cm^{-1} ($AlCl_3OH^-$). The addition of $AlCl_3$ and water to $SOCl_2$ results in the formation of $AlCl_3OH^-$ (3400 cm^{-1}), but the absorption band at 694 cm^{-1} does not appear, while two other poorly resolved bands at 803 and 822 cm^{-1} appear instead.

Absorption bands at 3400, 800-820, and occasionally 694 cm^{-1} are evident in both the $LiAlCl_4/SOCl_2$ and $LiAlCl_4/SO_2Cl_2$ electrolyte spectra, indicating water contamination (HCl is not formed in the Li/SO_2Cl_2 system) (13). The same absorptions have been observed by Bailey and Blomgren in the Li_2CO_3-$AlCl_3/SOCl_2$ system and were assigned to $AlCl_3OH^-$ (3400 cm^{-1}) or oxychloroaluminate species (800, 695 cm^{-1}). With great precaution, we were able to reduce considerably the absorption at 694 cm^{-1} during normal discharge, but it was nearly impossible to eliminate water contamination completely, and its effects were more noticeable towards the end of the relatively long period of reversal.

The addition of $AlCl_3$ to $SOCl_2$ gives rise to strong absorption bands at 1115 and 557 cm^{-1} owing to the complex $SOCl^+AlCl_4^-$ (2). On reversal, the $Li/SOCl_2$ cell shows the same absorption bands, indicating formation of $SOCl^+AlCl_4^-$. An analogous $SO_2Cl^+AlCl_4^-$ (15) compound is formed in the Li/SO_2Cl_2 system upon addition of $AlCl_3$ or during anode-limited reversal, with characteristic absorption bands at 1090 and 1053 cm^{-1} reflecting the two S-O stretching frequencies expected from SO_2Cl^+. Any absorption band at the lower frequency range would be hidden under the strong SO_2Cl_2 absorption band at 570 cm^{-1}.

Addition of SCl_2 or S_2Cl_2 to $LiAlCl_4/SOCl_2$ in the presence of SO_2 results in a slow increase in the IR absorptions at 1070, 665, and 1337 cm^{-1}, together with the formation of SO_2Cl_2, as evidenced by the characteristic absorption bands at 1408 and 570 cm^{-1}. [The IR absorptions due to the sulfur chlorides (13) occur below 550 cm^{-1} and cannot be detected by our instrument.] The same effect is observed with addition of SO_2Cl_2 and SO_2 to $LiAlCl_4/SOCl_2$. This characteristic triplet (1070, 665, 1337 cm^{-1}) appears only during anode-limited reversal in the $Li/SOCl_2$ system, while it is observed during normal discharge in the Li/SO_2Cl_2 system.

A compound with this characteristic IR spectrum was isolated from SO_2Cl_2 or $SOCl_2$ electrolytes following evaporation of the solvent. This compound decomposes abruptly at 40°C, releasing SO_2. It appears that its formation requires the presence of SO_2Cl_2, SO_2, and either $LiAlCl_4$ or $AlCl_3$. A reasonable assignment for the bands might be the S-O stretching vibrations and Al-Cl stretching modes of a complex similar to those observed by Barbier (16) between SO_2, $SOCl_2$, and $LiAlCl_4$. Subsequently, we refer to this complex as $Li(SO_2, SO_2Cl_2)^+AlCl_4^-$.

In our attempt to synthesize S_2O, we were only able to observe one (1168 cm^{-1}) of the three absorption bands characteristic of this compound (13). Attempts to condense S_2O in $SOCl_2$ at 77 K resulted only in the formation of a red polysulfur oxide which decomposed to S and SO_2 upon heating to room temperature. We concluded that the absorption which Istone and Brodd (6) observed at 688 cm^{-1} and assigned to S_2O, in effect, must have been due to the interaction of water with neutral electrolyte. Salmon's assignment of a 690 cm^{-1} absorption to Cl_2O (9) also overlooks the strong interaction of water with the electrolyte, which may, if excessive, mask the absorption band at 665 cm^{-1} formed only during anode-limited reversal in the $Li/SOCl_2$ system. Actually, mass spectrometry shows the presence of small amounts of S_2O in the gas phase but no trace of Cl_2O (see below).

In situ mass spectrometry.—The $Li/SOCl_2$ systems was studied mass spectrometrically using the apparatus shown in Fig. 2. The *in situ* experiment, which lasted 69.25h, involved the discharge of a single cell at 8 mA (1 mA/cm^2 based on the anode) for a period of about 20h, followed by a period of reversal at 50 mA which lasted approximately 50h (Fig. 4).

The quantity of gas used in sampling was significant with respect to the head space, and the effect is shown in Fig. 4 as the short-term "sampling spikes." There was no

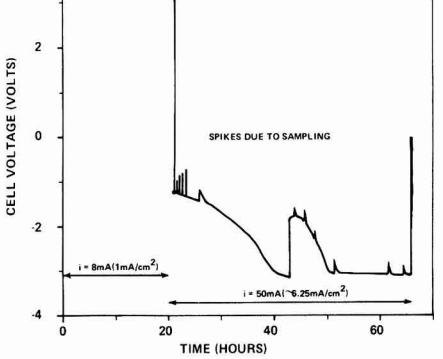


Fig. 4. Discharge curve of $Li/SOCl_2$ cell used for mass spectrometric analysis.

pause between end of discharge and the onset of cell reversal. The rate of discharge was increased sixfold during reversal in order to accelerate reaction progress. Infrared analysis had already shown that this change in current density did not affect the reaction mechanism, but rather simply accelerated the reaction progress.

Fifteen sets of mass spectra were recorded from time zero at the beginning of the discharge through time 69.25h at the end of the experiment. No spectra were recorded on the complete cells stored without discharge. Reversal occurred at time $t = 21$h, and the reversal process was continued through $t = 66$h. The last set of spectra was recorded at time $t = 69.25$h. Tabulated intensities for nominal masses appearing between masses 35 and 138 are given in Table III.

Masses below mass 35 were not included because these masses primarily arise from residual gases in the mass spectrometer and inlet system. The cell used in this study contained $SOCl_2$ in excess, and the vapor pressure remained essentially constant during the experiment reported here. Therefore, the partial pressures of the various species can be estimated using the known vapor pressure of $SOCl_2$, the ion intensities reported in Table III, and estimates of the relative ionization cross sections. All intensity data are relative to the intensity of mass 83 ($SOCl^{35+}$) which is set arbitrarily at 100. The uncertainty in the intensity data is estimated to be ±20%.

Pure samples of SCl_2, $SOCl_2$, and SO_2Cl_2 were introduced into the mass spectrometer, their spectra recorded and the peak intensities were entered in Table IV. The inlet system used in these experiments contributed to the peak at mass 36. This peak arises from the reaction between the chlorine containing sample and adsorbed water and/or hydrocarbons in the inlet system. Under the carefully controlled inlet conditions used with these samples, the intensity of mass 36 remained constant to within 20%. Thus, in subsequent experiments, it will be assumed that the inlet reactions are constant to within 20% and that large changes in the intensity of mass 36 are due to factors other than the inlet system. All of these spectra were recorded with an electron energy of 80 eV.

Three exact mass experiments at nominal masses 50, 76 and 80 yielded the following exact mass values: 49.99597 (±30 ppm), 75.94528 (±20 ppm), and 79.94057 (±20 ppm), respectively.

The results clearly show the presence of molecular HCl, SO_2, CS_2, S_2O, SCl_2, $SOCl_2$, and mass 134 species (mainly SO_2Cl_2, with, probably, some S_2Cl_2). The data also reveal the presence of high levels of chlorine fragments as well as low concentrations of CF_2^+ fragments. Species with nominal mass exceeding 140 were also observed toward the later stages of reversal.

The plots of intensity *vs.* time of HCl and Cl^+ (Fig. 5 and 6) indicate that their concentrations remain constant in the gas phase during normal discharge but increase during anode-limited reversal after an induction period of 5h. We have investigated the contribution to mass 36 and have found that the intensity of the mass 36 (HCl) signal can be reduced by improving the inlet system to the mass spectrometer. However, not all of the mass 36 can be removed by the improved inlet; thus, part of mass 36 may arise from cell components containing chlorine and hydrogen. Water contamination may, in part, be introduced from the cathodes which are formed by an aqueous process.

The plots of CS_2 and S_2O (Fig. 7 and 8) show little variation in the concentration of these species with time during both discharge and reversal, while the plots for SCl_2 (Fig. 9) and SO_2Cl_2 (Fig. 10) indicate that these compounds are only formed during reversal, also following a 5h induction period.

The increase in the concentration of HCl following reversal indicates a source of hydrogen which may be the residual water in the electrolyte or, more likely, the adsorbed water on the carbon cathode.

The mass spectrometric analysis of SO_2 confirms our infrared results: SO_2 appears to be the major product of discharge. If the data for SO^+ and SO_2^+ intensities are plotted (Fig. 11), interesting results are obtained. This figure clearly shows that the SO_2^+ rate of increase is larger than that for SO^+ fragments. Furthermore, it is seen that the difference in concentration between SO_2^+ and SO^+ increases rapidly after the onset of reversal and then reaches a steady value. It is worth noting that the ratio of SO^+ to SO_2^+ intensities is approximately 0.5 for pure SO_2 (18). Thus, it is clear that the SO^+ intensity in the discharge mode is higher than that accounted for by SO_2 fragmentation alone. Upon reversal, the SO^+/SO_2^+ ratio decreases and approaches its limiting value predicted by SO_2 fragmentation only.

Table III. Mass intensity *vs.* time data for the *in situ* experiment

Mass \ Time (h)	0	0.1	1.25	2.33	18.5	20.33	21.00[a]	24.00	26.00	42.33	45.00	48.75	50.25	66.00[b]	69.25
35	18.2	—	25.0	13.2	23.8	16.3	12.2	12.1	20.7	51.3	93	55.9	57.6	52.9	47.4
36	34.7	27.3	37.6	43.3	165	50.5	54.3	40.3	85.5	212	224	385	395	376	357
37	6.5	5.1	8.9	4.8	10.2	5.9	4.1	4.9	6.0	16.7	29.5	17.8	19.2	18.7	17.1
38	27.7	19.1	23.1	14.5	52.5	18.0	18.2	15.6	31.5	69.1	72.1	129	135	120	108
48	92.8	—	68.8	48.1	87.8	—	115	163	170	171	238	256	302	146	128
50	6.9	5.9	8.3	2.4	5.0	11.6	6.5	8.6	12.0	10.5	27.5	12.6	6.1	10.2	9.7
64	93.4	—	62.4	65.2	111	—	145	279	292	307	444	565	648	340	320
67	8.5	9.7	11.6	5.9	5.1	6.6	5.1	7.2	8.5	6.8	28.4	12.5	19.2	11.4	13.2
69	0	4.4	4.9	2.5	3.3	2.8	2.7	2.1	3.7	5.0	12.1	4.8	7.0	9.1	9.1
76	9.7	11.9	27.0	9.6	14.3	25.0	16.3	17.3	14.9	13.7	14.7	15.0	7.9	8.6	8.4
78	0.8	1.1	2.4	0.7	1.2	2.6	1.4	1.5	1.1	1.5	1.0	1.1	0.5	0.6	0.7
80	23.8	27.2	23.7	20.6	16.0	19.9	15.9	19.1	22.2	19.8	28.4	31.9	22.0	19.3	20.0
82	2.0	2.5	2.6	2.0	1.3	1.8	2.0	1.6	1.7	1.7	2.5	2.8	1.8	1.5	1.7
83	100	100	100	100	100	100	100	100	100	100	100	100	100	100	100[c]
85	35.6	37.5	37.5	39.0	35.3	38.9	39.1	39.4	44.4	37.6	42.4	39.5	40.0	42.3	38.9
99	0	0	0	0	0	0	0	0	0	2.11	1.39	1.34	1.10	0.77	0.87
101	0	0	0	0	0	0	0	0	0	1.05	0.70	0.58	0.56	0.32	0.40
102	0	0	0	0	0	0	0	0	0	1.95	9.12	7.21	7.21	6.39	4.15
104	0	0	0	0	0	0	0	0	0	1.26	6.60	5.33	5.00	5.05	2.99
106	0	0	0	0	0	0	0	0	0	0.49	1.12	0.94	0.98	1.24	0.71
118	20.0	18.7	19.1	14.6	14.3	15.9	14.2	14.6	15.0	15.3	16.9	14.8	14.6	12.2	14.7
120	13.8	13.1	14.2	11.6	11.0	12.4	10.6	10.6	9.6	11.4	11.4	11.3	11.0	8.9	10.9
122	2.0	2.1	2.1	2.4	2.2	2.0	2.0	2.0	2.1	2.1	2.7	2.0	2.1	2.0	2.0
134	0	0	0	0	0	0	0	0	0	1.43	1.14	1.17	0.67	0.52	0.64
136	0	0	0	0	0	0	0	0	0	0.78	0.80	0.80	0.37	0.34	0.38
138	0	0	0	0	0	0	0	0	0	0.25	0.22	0.21	0.14	0.07	0.07

[a] Time at onset of reversal.
[b] Last data set obtained before conclusion of reversal.
[c] All intensities are relative to the intensity of mass 83, which is set arbitrarily to 100.

Table IV. Mass spectral intensities for pure SCl_2, $SOCl_2$, and SO_2Cl_2

Mass	SCl_2	$SOCl_2$	SO_2Cl_2	Mass	SCl_2	$SOCl_2$	SO_2Cl_2
30	0	0	0	86	0	0	0
31	0	0	0	87	0	0.62	0
32	64.4	100*	36.5	88	0	0	0
33	0	0	0	89	0	0	0
34	1.34	1.13	0.93	90	0	0	0
35	12.1	17.7	6.67	91	0.96	0	0
36	75.3	91.4	18.7	92	0	0	0
37	4.10	6.55	2.76	93	1.09	0	0
38	26.2	27.7	9.41	94	0	0	0
39	1.92	0	1.46	95	4.76	0	0
40	4.45	7.25	3.58	96	1.11	0	0
41	4.5	0	0.93	97	3.70	0	0
42	1.86	0	1.46	98	0	0	0
43	1.95	2.23	2.50	99	0	0	35.3
44	1.73	2.80	3.63	100	0	0	1.17
45	0	0	0	101	0	0	12.9
46	0	0	0	102	67.8	0	0
47	0	0	0	103	0.83	0	1.17
48	1.74	49.8	53.5	104	43.7	0	0
49	0	0.92	0.93	105	0.96	0	0
50	0	2.81	4.09	106	8.60	0	0
51	2.85	0	0.93	107	0.91	0	0
52	2.21	0	0	108	0	0	0
53	0	0	0	109	0	0	0
54	0	0	0	110	0	0	0
55	6.69	0	0.90	111	0	0	0
56	2.15	0	0	112	0	0	0
57	5.24	0	0.98	113	0	0	0
58	0	0.75	0.91	114	0	0	0
59	0	0	0	115	0	0	0
60	0	0.63	0.78	116	0	0	0
61	0	0	0	117	0	0	0
62	0	0	0	118	0	3.6	0
63	0	0	0	119	0	0	0
64	4.00	31.1	100*	120	0	2.5	0
65	0	0	2.28	121	0	0	0
66	0	2.06	7.54	122	0	0.58	0
67	100*	3.44	0.92	123	0	0	0
68	0.95	0	0	124	0	0	0
69	36.4	1.32	6.27	125	0	0	0
70	9.72	0	1.27	126	0	0	0
71	2.71	0	0	127	0	0	0
72	5.56	0	1.17	128	0	0	0
73	0	0	0	129	0	0	0
74	1.03	0	0	130	0	0	0
75	0	0	0	131	0	0	0
76	2.54	2.56	2.16	132	0	0	0
77	0	0	0	133	0	0	0
78	0	0	0	134	0	0	6.84
79	1.05	0	0	135	0	0	0
80	0	3.00	0	136	0	0	5.08
81	3.63	0.23	0	137	0	0	0
82	1.30	0	0	138	0	0	1.17
83	3.5	41.5	0	139	0	0	0
84	0	0	0	140	0	0	0
85	1.79	14.5	0				

*Most intense peak.

Thus, the foregoing analysis indicates that during discharge SO^+ intensity results from at least two major contributions. The first is from SO_2 fragments, and the second arises from $SOCl_2$ fragmentation. However, as the cell is brought into reversal, the SO_2 becomes the major source of SO^+ production.

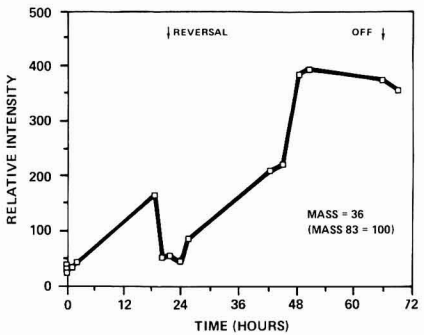


Fig. 5. Mass 36 (HCl^{35}) vs. time (h)

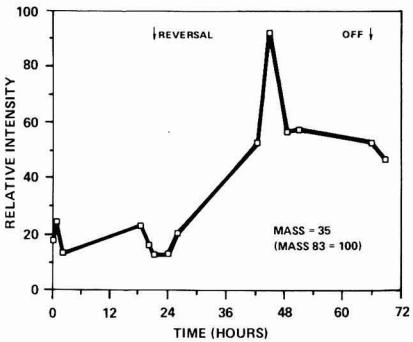


Fig. 6. Mass 35 (Cl^{35}) vs. time (h)

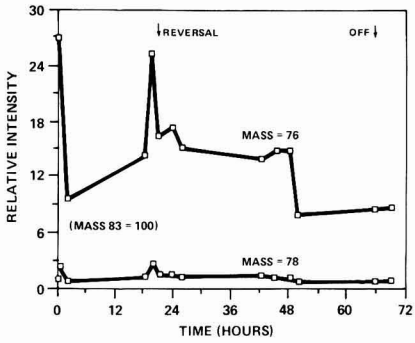


Fig. 7. Mass 76 and 78 (CS_2) vs. time (h)

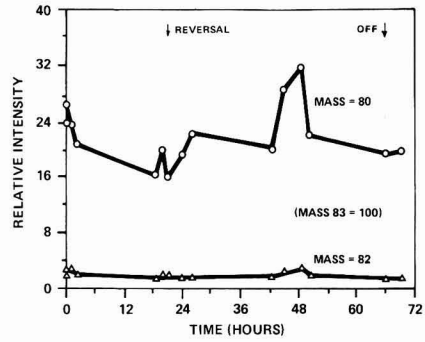


Fig. 8. Mass 80 and 82 (S_2O) vs. time (h)

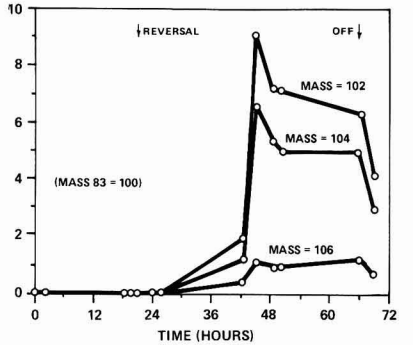


Fig. 9. Mass 102, 104, and 106 (SCl_2) vs. time (h)

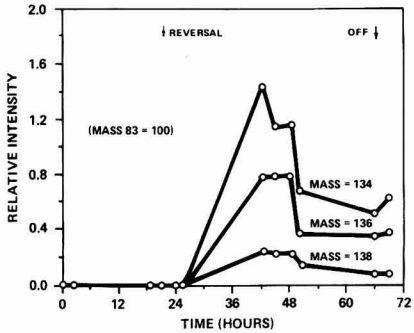


Fig. 10. Mass 134, 136, and 138 vs. time (h)

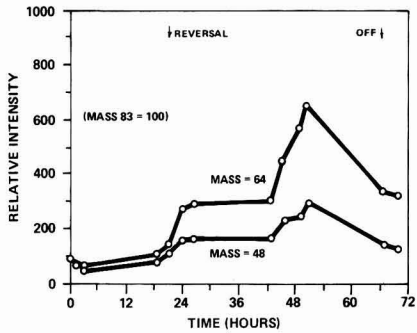


Fig. 11. Mass 48 and 64 (SO^+ and SO_2^+) vs. time (h)

Mass 80 was identified as S_2O by exact mass measurements. This is not surprising, as Meshi and Myer (17) had previously identified both S_2O and CS_2 as products in a discharge-tube reaction between elemental sulfur and SO_2. Furthermore, thermal decomposition of $SOCl_2$ has been shown to yield S_2O as a product (17). It is worth noting, however, that the amount of S_2O in the gas phase remains fairly constant throughout the experiment and appears independent of any electrochemical process.

The mass triplet 102, 104, and 106, characteristic of SCl_2, appears only in reversal after an induction period of 5h. The species giving rise to masses 67 and 69 (Table III) can arise from fragmentation of SCl_2. However, since no SCl_2 parent is detected at and prior to $t = 26$h, the intensities measured for this doublet at and prior to $t = 26$ do not arise from SCl_2. This result also implies that species other than SCl_2 give rise to masses 67 and 69 in the cell. It is important to note that chlorine dioxide (ClO_2, mass 67, 69) can give rise to these masses. However theoretical isotopic abundance considerations neither confirm nor rule out ClO_2 as species giving rise to masses 67 and 69. It is also noteworthy that the absence of both parent (masses 86, 88, and 90) peaks and fragments (masses 51, 53) in the mass spectrum strongly suggests that Cl_2O is not present in measurable concentration in this system.

The mass triplet 134, 136, 138 also detected during reversal after a 5h induction period could arise from either S_2Cl_2 or SO_2Cl_2. S_2Cl_2 has been suggested as a possible reaction product by Schlaikjer *et al.* (7) as follows

$$3S + 2SOCl_2 = SO_2 + 2S_2Cl_2 \qquad [6]$$

Thus S_2Cl_2 may be present in this system, but our infrared results suggest that SO_2Cl_2 is the major component. Mass 50 (Fig. 12) was positively identified as CF_2^+ by exact mass analysis. Its presence throughout the periods of discharge and reversal implies a chemical or electrochemical attack on the Teflon binder at the cathode during both discharge and reversal.

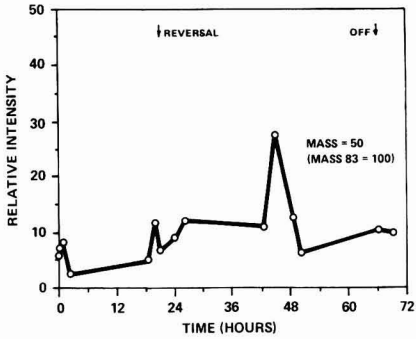


Fig. 12. Mass 50 (CF_2^+) vs. time (h)

Quantitative FTIR studies.—Li/SOCl₂, normal discharge.—A total of eight cells were discharged and driven into reversal under various conditions ranging from −20° to +25°C and 1-5 mA/cm².

During normal discharge, the only noticeable change is the increase in SO_2 concentration. At 25°C, SO_2 appears to increase linearly until the cell is fully discharged then levels off. At −20°C, a slight curvature is noticeable at the beginning of the discharge. This also holds true for the Li/SO_2Cl_2 system. Typical results are shown in Fig. 13. Average results for four of the cells are tabulated in Table V. In every case, the amount of SO_2 produced during normal discharge was always found to be only a fraction of that predicted by the usually accepted equation for the discharge of this cell

$$4Li + 2SOCl_2 = S + SO_2 + 4LiCl \qquad [7]$$

Li/SOCl₂, anode-limited reversal.—On reversal, the most noticeable changes in the IR spectrum are due to formation of SO_2Cl_2 (1408 and 580 cm^{-1}), $SOCl^+$ (1115 and 557 cm^{-1}), and what we tentatively identified as the weakly bound complex Li (SO_2, SO_2Cl_2)$^+AlCl_4^-$ absorbing at 1070, 665, and 1337 cm^{-1} (this last band appears as a shoulder on the very large SO_2 peak). Typical results are plotted in Fig. 14 and 15 for ambient temperature operation, and in Fig. 16 and 17 for operation at −20°C.

A small amount of water contamination is always present and is the cause for the three broad bands at 3400 cm^{-1} ($AlCl_3OH^-$), 2900 cm^{-1} (HCl), and 800-820 cm^{-1} (oxychloroaluminate).

At room temperature, SO_2Cl_2 increases steadily after a short induction period then appears to level off. $SOCl^+$ starts increasing immediately, levels off to a steady-state value, and disappears fairly rapidly after the current is turned off. The peaks at 1070 and 665 cm^{-1} also show an initial increase, then an apparent leveling off.

At low temperature (−20°C), one should note the immediate and sharp increase in the $SOCl^+$ species (0.65 mol/Faraday) (see Fig. 17). Obviously, at room temperature regenerative processes are fast and prevent accumulation of large amounts of $SOCl^+$. The SO_2Cl_2 concentration (see

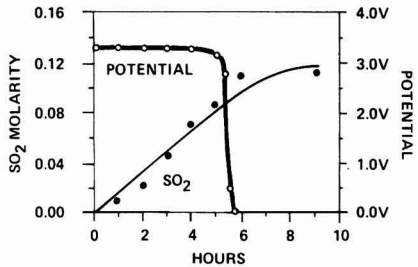


Fig. 13. SO_2 formation during discharge of anode-limited $Li/SOCl_2$ cells: i = 40 mA (5 mA/cm²).

Table V. SO_2 production during normal discharge

Cell	Discharge conditions	SO_2
SC-69	(5 mA/cm², 25°C)	0.14 mol/Faraday
SC-71	(5 mA/cm², 25°C)	0.17 mol/Faraday
SC-77	(1 mA/cm², 25°C)	0.17 mol/Faraday
SC-81	(1 mA/cm², −20°C)	0.13 mol/Faraday

Fig. 17) levels off at a fairly low value. However, upon heating to room temperature, a dramatic jump in SO_2Cl_2 concentration occurs, pointing to the accumulation of unstable species (most likely Cl_2) during the reversal period at low temperature. Water contamination and the large $SOCl^+$ concentration precluded our plotting the increases in absorption of 665 and 1070 cm^{-1} for the low temperature run.

Li/SO_2Cl_2.—As with the Li/$SOCl_2$ system, the major reaction product during normal discharge is SO_2. Its concentration appears to increase linearly at room temperature, but somewhat nonlinearly at −20°C. The SO_2 concentration levels off after reversal (see Fig. 18).

Qualitatively, the results are identical at room temperature and at −20°C, but at −20°C an analysis of the potential evolution, especially during reversal, shows a small plateau at −2.8V and a larger one not very flat at −5.5/−6V followed by a sharp decrease after about 15h to −12V at which point the current is cut off (see Fig. 19). When the cell is allowed to recover, the voltage stabilizes at −0.8/−0.6V, then goes to 0V upon warming up to room temperature. This small polarization left on recovery at low temperature could be attributed to the formation of a species stable at −20°C.

Absorption bands at 1070, 1337, and 665 cm^{-1} appear during normal discharge and continue increasing slowly in intensity during reversal (see Fig. 20). The three peaks appearing during the normal discharge as they do in a mixture of SO_2, $LiAlCl_4$, and SO_2Cl_2 without the passage of current suggest a chemical reaction. The appearance of the same peaks in the Li/$SOCl_2$ cells on reversal is probably due to the formation of SO_2Cl_2 during the overdischarge and its subsequent reaction with $LiAlCl_4$ and SO_2. The product of this reaction has been tentatively identified as $Li(SO_2, SO_2Cl_2)^+AlCl_4^-$.

Additional peaks appear on reversal at 1090 and 1059 cm^{-1}, which quickly disappear on recovery. Those facts

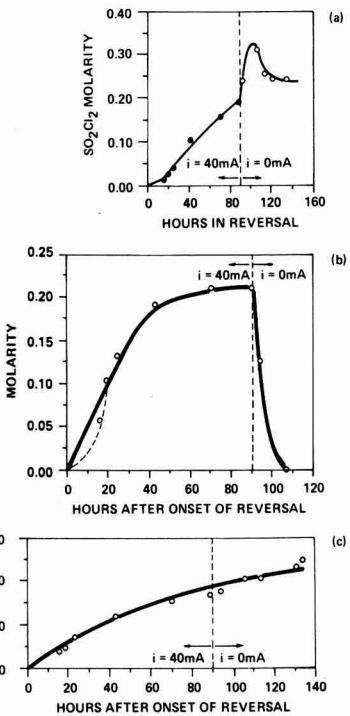


Fig. 14. Formation of (a) SO_2Cl_2, (b) $SOCl^+$, and (c) $Li(SO_2, SO_2Cl_2)^+AlCl_4^-$ during reversal of anode-limited Li/$SOCl_2$ cell. i = 40 mA (5 mA/cm²). T = 25°C.

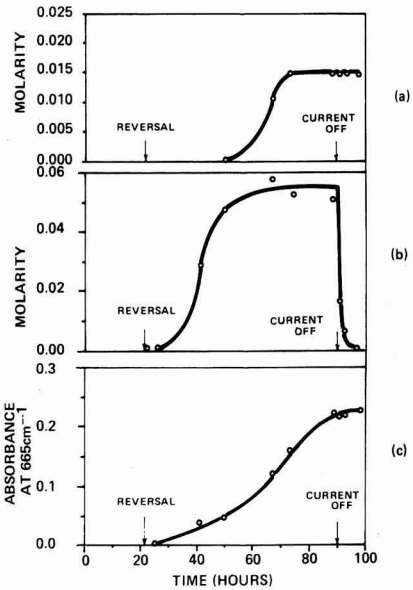


Fig. 15. Formation of (a) SO_2Cl_2, (b) $SOCl^+$, and (c) $Li(SO_2, SO_2Cl_2)^+AlCl_4^-$ during reversal of anode-limited Li/$SOCl_2$ cell. i = 7.4 mA (1 mA/cm²). T = 25°C.

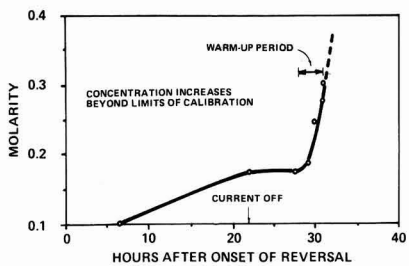


Fig. 16. Formation of SO_2Cl_2 during reversal of anode-limited Li/$SOCl_2$ cell at −20°C and warm-up to 25°C. i = 40.5 mA/(5 mA/cm²).

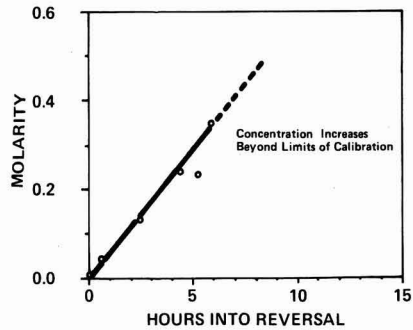


Fig. 17. Formation of $SOCl^+$ during reversal of anode-limited Li/$SOCl_2$ cell at −20°C. i = 40.5 mA (5 mA/cm²).

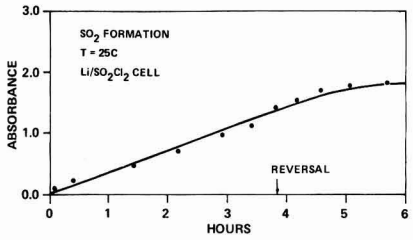


Fig. 18. Formation of SO_2 during discharge and reversal of anode-limited Li/SO_2Cl_2 cell at 25°C. i = 40 mA (5 mA/cm²).

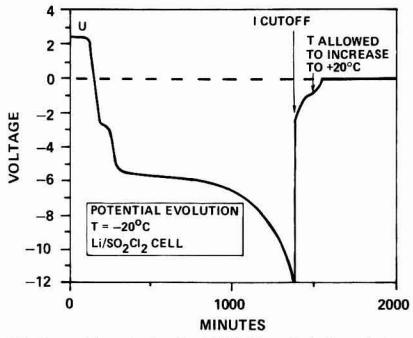


Fig. 19. Potential evolution for Li/SO_2Cl_2 cell during discharge and anode-limited reversal at −20°C. i = 40 mA (5 mA/cm²).

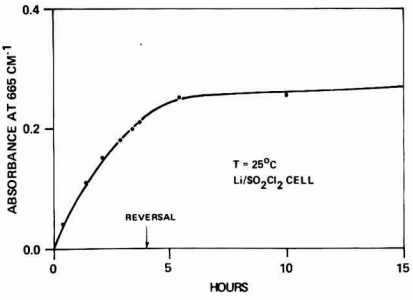


Fig. 20. Formation of $Li(SO_2, SO_2Cl_2)^+AlCl_4^-$ during discharge and reversal of Li/SO_2Cl_2 cell at 25°C and i = 40 mA (5 mA/cm²).

suggest the formation of a complex analogous to $SOCl^+AlCl_4^-$ in the Li/$SOCl_2$ system. This complex is proposed to be $SO_2Cl^+AlCl_4^-$ (15) and may be formed as follows

$$2SO_2Cl_2 = 2SO_2Cl^+ + Cl_2 + 2e^- \quad [8]$$

$$Cl_2 + SO_2 = SO_2Cl_2 \quad [9]$$

$$SO_2Cl^+ + AlCl_4^- = SO_2Cl^+AlCl_4^- \quad [10]$$

Conclusions and Summary

Mass spectrometry and infrared spectroscopy have been used to investigate both the gas and liquid phases in lithium-sulfur oxyhalide cells during normal discharge and anode-limited reversal.

By measuring the spectra *in situ*, we were able to minimize the interaction of moisture with the electrolyte. Quantitative and reproducible results have been obtained and definite trends have been demonstrated. With the two techniques, we were able to corroborate our results.

In the lithium-thionyl chloride system, the species HCl, CS_2, SO_2, S_2O, SCl_2, and SO_2Cl_2 were identified in the gas phase, and HCl, $AlCl_3OH^-$, SO_2, SO_2Cl_2, $SOCl^+AlCl_4^-$ in the liquid phase. A species giving rise to absorptions at 1337, 1070, and 665 cm^{-1} was observed in the liquid phase during anode-limited reversal; this last compound is tentatively identified as $Li(SO_2, SO_2Cl_2)^+AlCl_4^-$ and is analogous to the complexes characterized by Barbier (16) involving $LiAlCl_4$, SO_2, and $SOCl_2$ instead of SO_2Cl_2.

The gas phase concentrations of CS_2 and S_2O were essentially constant throughout the experiment. These species may not necessarily arise from electrochemical processes but are probably minor products of chemical reactions either in the cell or the inlet system. Fragments identified as CF_2^+ were observed in measurable amounts. The origin of these fragments is most likely the Teflon binder used in the construction of the porous carbon electrode.

The sulfuryl chloride cell behaved similarly to the thionyl chloride cell, specifically with respect to formation of SO_2 and the formation of $SOCl^+$-like species tentatively identified as SO_2Cl^+. Moreover, this system exhibited the same sensitivity to water and the same behavior at −20°C as the thionyl chloride system. During normal discharge a compound absorbing at 665, 1070, and 1337 cm^{-1} was formed immediately upon generation of SO_2. This compound was isolated from SO_2Cl_2 solutions containing $LiAlCl_4$ and SO_2, it decomposes at approximately 40°C with evolution of SO_2, and is the same as the $Li(SO_2, SO_2Cl_2)^+AlCl_4^-$ complex observed in the thionyl chloride system.

The formation of chlorine in both systems is quite likely but its accumulation in the cells at room temperature is prevented by reaction with SO_2 to form SO_2Cl_2. At low temperatures, chlorine does accumulate but reacts quite rapidly on warming up to form SO_2Cl_2.

Finally the effect of water contamination was characterized. Water tends to form strongly IR absorbing species with $AlCl_3$ or $AlCl_4^-$. This fact should be taken into account in interpreting the results of previous investigations.

Acknowledgments

This work was supported in part by the Naval Surface Weapons Center under Contract no. N60921-81-C-0363. Portions of the material contained in this article were prepared in collaboration with Mr. Christian Sarrazin, a French scientist working at Gould, Incorporated, Gould Research Center under a cooperative agreement of the governments of the United States of America and France through the Foreign Science/Engineer Exchange Program, administered by the Department of Defense. Mr. Sarrazin is a staff member of Direction des Recherches Etudes et Techniques/G7-1, 75015 Paris, France.

Manuscript submitted Nov. 18, 1983; revised manuscript received July 9, 1984.

Gould, Incorporated assisted in meeting the publication costs of this article.

REFERENCES

1. J. Auborn, K. W. French, S. I. Lieberman, U. K. Shan, and A. Heller, *This Journal*, **120**, 1613 (1973).
2. K. M. Abraham, P. G. Gudrais, G. L. Holleck, and S. B. Brummer in "Proceedings of the 28th Power Sources Symposium," Atlantic City, NJ, June 12-15, 1978, The Electrochemical Society, Inc. p. 255 (1979).
3. A. N. Dey, in "Proceedings of the 28th Power Sources Symposium," Atlantic City, NJ, June 12-15, 1978, The Electrochemical Society, Inc., p. 251 (1979).
4. S. Dallek, S. D. James, and W. P. Kilroy, *This Journal*, **128**, 508 (1981).
5. W. K. Behl, *ibid.*, **127**, 1444 (1980).
6. W. K. Istone and R. J. Brodd, *ibid.*, **129**, 1853 (1982).
7. C. R. Schlaikjer, F. Goebel, and N. Marincic, *ibid.*, **126**, 513 (1979).
8. K. M. Abraham and R. M. Mank, *ibid.*, **127**, 2091 (1980).
9. D. J. Salmon, M. E. Peterson, L. L. Henricks, L. L. Abels, and J. C. Hall, *ibid.*, **129**, 2496 (1982).
10. J. C. Bailey and G. E. Blomgren, in "Electrocatalysis," W. E. O'Grady, P. N. Ross, Jr., and F. G. Will, Editors, p. 485, The Electrochemical Society Softbound Proceedings Series, Pennington, NJ (1982).
11. R. C. McDonald, *This Journal*, **129**, 2453 (1982).

12. "Perfluorokerosene Mass Spectral Table," PCR Research Chemical, Inc., Gainesville, FL.
13. G. Nickless, "Inorganic Sulfur Chemistry," p. 409 Elsevier, Amsterdam (1978).
14. R. J. Gillespie and E. A. Robinson, *Can. J. Chem.*, **39**, 2171 (1961).
15. J. C. Bailar, Jr., H. J. Emeleus, Sir R. Nyholm, A. F. Trotman-Dickenson, Editors, "Comprehensive Inorganic Chemistry," Vol. 2, p. 858, Pergamon Press, New York (1973)
16. Y. Bedfer, J. Corset, M. C. Dhumelincourt, F. Wallart, and P. Barbier, *J. Power Sources*, **9**, 267 (1983).
17. D. J. Meshi and R. J. Myers, *J. Am. Chem. Soc.*, **78**, 6220 (1956).
18. "EPA/NIH Mass Spectral Data Base," Vol. 1, p. 11, Dec. 1978.

Electrochemical Behavior of Water in Immobilized Salt Electrolytes

I. Electrical Conductivity and Thermal Measurements

Rachel Parash, Frederico Broitman, Uri Mor, Dan Ozer, and Armand Bettelheim

Nuclear Research Center-Negev, Beer-Sheva, Israel

ABSTRACT

The meaning of moisture content of a pelletized LiCl-KCl-MgO mixture is discussed in terms of different states of interaction in which water may exist in the specimen. According to electrical conductivity measurements, differential thermal analysis, and thermogravimetric experiments in the ambient to ≈400°C range, water comes off the pellet by an endothermic process that involves the migration of water to the surface of the pellet where it vaporizes (T = 25°-130°C). Exothermic reactions involving oxide ions and traces of water and hydrogen chloride are suggested to exist in the 130°-250°C range. This is followed (T > 250°C) by a hydrolytic and endothermic reaction, which converts chloride ions to hydroxide ions and hydrogen chloride.

The investigation of water in pelletized LiCl-KCl-MgO mixtures is of interest for the development of primary as well as secondary batteries for load leveling and electric vehicle applications. The presence of water as well as contaminants formed near the electrodes during exposure to humid air could affect cell performance and accelerate self-discharge (1).

To prevent direct reaction between the anolyte and catholyte, a separator must be employed to physically separate the anode from the cathode, which in most cases consists of a lithium alloy and FeSx (x = 1 or 2), respectively (2). An effective separator must be ionically conducting and chemically inert to all the cell components. Two concepts were considered for the separators (2, 3): (*i*) a refractory powder compact composed of the electrolyte (usually a LiCl-KCl eutectic mixture) and binder (such as SiO_2 or MgO) and (*ii*) separator pads fabricated from boron nitride or yttria fiber pads impregnated with electrolyte. The choice of the binder is based upon its ability to gel or immobilize the electrolyte, which would otherwise flow when subjected to the battery operation temperature, some 150°C above the electrolyte melting point. In the present study, the separator is a pelletized mixture of electrolyte composed of LiCl + KCl (64-36 mole percent [m/o]) in the presence of MgO (50 weight percent [w/o]) as binder.

The most troublesome aspect of preparing a pure electrolyte fusion arises from the highly deliquescent property of the lithium chloride. Unless special precautions are taken, hydrolytic decomposition occurs as the temperature is raised

$$H_2O + Cl^- \rightleftarrows OH^- + HCl \qquad [1]$$

Consequently, the melt becomes contaminated with alkaline products (4-7). Various methods have been proposed and used to prevent hydrolytic decomposition during the preparation of anhydrous and fused alkali metal chlorides. The difficulty of removing the last traces of residual moisture from the salts has often necessitated rather arduous drying procedures (8, 9). A high degree of purity of the LiCl-KCl melts has been achieved by treating the fused salt with hydrogen chloride gas (10) or chlorine (11).

The extreme sensitivity of electrical methods of analysis to chemical and structural transformations has been highlighted in several publications (12-14). From an application viewpoint, the practical potential of electrochemical methods such as electrical conductivity measurements has been demonstrated in a wide variety of geological problems related to underground resources (15). It is the purpose of this paper to seek a correlation between the trends observed in the electrical and thermal behavior of pelletized LiCl-KCl-MgO mixtures containing various amounts of water. A wide variety of techniques, ac electrical conductivity (EC), thermogravimetric analysis (TGA), and differential thermal analysis (DTA), was employed for the detection and characterization of the different states of water in the specimen.

Experimental

AR-grade LiCl, KCl, and MgO (Merck) were used.

The water content of the LiCl-KCl-MgO mixtures after weighing, blending, and mixing was determined by Karl Fisher titrations (16). Pellets of variable water concentrations were obtained by heating the pellet at ≈150°C for several hours in a dry glove box (RH ≤ 0.5%). Water concentration after pelletizing was calculated by weight-loss measurements.

A schematic diagram of the electrical conductivity (EC) apparatus and furnace arrangement are illustrated in Fig. 1. The apparatus described here can be used for EC measurements on pressed disks up to a maximum temperature of about 500°C. The furnace is a ceramic block, and temperature is detected by two Chromel-Alumel thermocouples. One of them controls the rate of temperature rise via a proportional band temperature programmer; the other measures the temperature of the pellet and its EMF output is recorded on the X-axis of a Type 3078 Yokogawa X-Y recorder.

The samples were pressed in the form of disks using a stainless steel piston and die and a Beckman 30 ton hydraulic press. The disks, 28.6 mm diam and 4.5 mm thick, were held by a spring between two stainless steel electrodes.

AC electrical conductivity (EC) measurements were carried out using a Wayne Kerr B642 or B605 bridge. No control of the sample chamber atmosphere was necessary because of its geometry, the atmosphere surrounding the sample was essentially a "self-generated" one containing water vapor (17).

Differential thermal analysis (DTA) and thermogravimetric analysis (TGA) were performed on a Netzch differential thermo-analyzer 404 and a Setaram thermo-

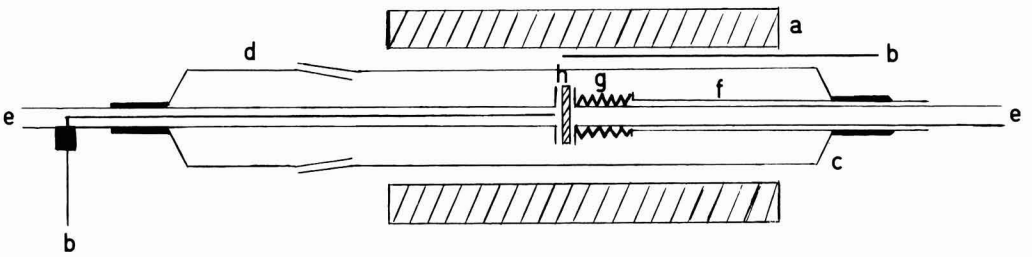


Fig. 1. Cell for EC measurements. a: Furnace. b: Thermocouples. c: Glass cell. d: Glass joint. e: Stainless steel electrodes. f: Stainless steel electrodes guide. g: Stainless steel spring. h: Pellet.

balance, respectively. Dehydration conditions in the sample chamber of the DTA and TGA were similar to those used in the EC measurements, *i.e.*, a self-generated atmosphere of water vapor. Alumina crucibles containing small portions (< 20 mg) of the pelletized salts were used for the thermal methods.

A Shaw hygrometer (Model Sha-3) with a medium (yellow spot) sensor range was used to detect water vapor evolved from a pellet subjected to heat-treatment in the apparatus shown in Fig. 1.

Results and Discussion

Room temperature measurements made at 1.5 kHz between two metallic collectors positioned at opposite sides of a pellet (Fig. 1) showed an increase in the ac conductance when the pellet was exposed to ambient atmosphere (RH = 50%). Passing a dry gas (air or argon, RH < 0.5%) through the porous structure of the pellet at ambient temperature caused a decrease in conductance, as shown in Fig. 2. Moreover, this procedure caused a gradual decrease in weight, probably due to loss of surface adsorbed water. A total weight loss of about 0.3 w/o was detected for a pellet initially containing 2 w/o water.

Figure 3 shows the electrical conductance of a LiCl-KCl-MgO pellet as function of temperature, measured at three different frequencies. The increase in electrical conductivity with temperature can be related to ohmic conduction which follows the well-known relationship (18)

$$\sigma_{ohmic} = \sigma_0 \exp(-E_a/RT) \quad [2]$$

where E_a is the activation energy for the mobility of the current carriers, and σ_0, the pre-exponential factor, is related to the lattice vibration frequency. Conductivity in alternating current fields, however, is the sum of ohmic and polarization components expressed as

$$\sigma_{total} = \sigma_{ohmic}(T) + \sigma_{pol}(\nu, T) = \sigma_0 \exp(-E_a/RT) + 2\pi\nu\epsilon'' \quad [3]$$

where σ_{pol} represents the contribution of polarization current to the total conductivity σ_{total}, ν is the operating frequency, and ϵ'' is the loss factor. As can be seen from Fig. 3, the conductivity in the temperature range 25°-250°C increases by a factor of about two when the frequency is increased by two orders of magnitude. This indicates that the ohmic conductivity is the dominant factor in the total conductivity of the pellet. Polarization effects superimposed on the ohmic contribution to the conductivity are found only at temperatures below 70°C, as indicated by the small peaks in the conductivity curves at low frequencies (19).

As with other dynamic thermoanalytical techniques, the EC curve of a sample was influenced by the heating rate. At higher heating rates, the peaks were much smaller and broader. Low heating rates allow more time for the dissociation of hydrates and for bulk water vapor to diffuse to the vicinity of the electrodes.

Peaks I and II (appearing at 60°-65° and 80°-110°C, respectively) are correlated with the loss of absorbed water (peak I) and vaporization of liquid water which is in equilibrium with hydrates (peak II). Similar EC results were reported for the $CuSO_4 \cdot 5H_2O$ salt (17). For lithium chloride, the dehydration process could be described by the following scheme

$$LiCl \cdot nH_2O \rightarrow LiCl + nH_2O_{(l)}$$
$$H_2O_{(l)} \rightarrow H_2O_{(g)} \quad [4]$$

According to Duval (20), a water molecule is associated with two lithium chloride molecules, *i.e.*, $n = \frac{1}{2}$. The presence of liquid water, as given in reaction [4], forms a saturated solution, which permits an increase in current flowing through the sample. As this water vaporizes, the current decreases to the level of the original substance (17).

The process taking place at region III in the EC curve (Fig. 3) will be described in the context of the DTA and TGA results. The conductance rises at $T > 250$°C (not shown in the figure) until a steady value is obtained at the melting point of the electrolyte (about 370°C for the present composition of LiCl-KCl). At 450°C, the conductivity of the LiCl-KCl-MgO mixture is about one order of magnitude lower than the reported value in the absence of binder (21): 0.13 and 1.5 mho · cm^{-1}, respectively. It should be noted that part of the samples showed a tendency to exhibit conductivity that "smeared" over a broad temperature region extending from 200° to 400°C. The loss of resolution in region III is presumably due to overlapping of the temperature regimes of the processes contributing to the electrical conductivity in the intermediate region 200°-250°C (processes II, III, and high ionic mobility above 250°C).

The EC curves in the 25°-125°C range for pellets containing various initial water concentrations are shown in Fig. 4. Conductivity in this temperature range increases when the water content in the pellet is increased and decreases in subsequent heating cycles. The disappearance of peaks I and II in the absence of water seems to be related to the lack of mobility of the current carriers ($\sigma_{ohmic} \rightarrow 0$ in Eq. [2]). As it can be seen from Fig. 4, the relative heights of peaks I and II vary independently on the total

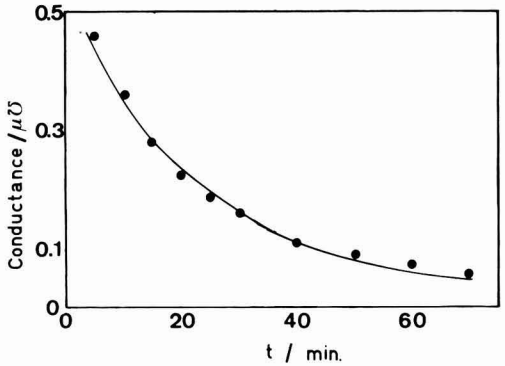


Fig. 2. The decrease of conductance at 1.5 kHz as function of time for a pellet (50 w/o electrolyte + 50 w/o MgO) at room temperature when a dry (RH = 0.5%) gas (air or Ar) is allowed to flow (rate = 1 liter/min^{-1}) through the sample (initial water concentration ≃ 2 w/o).

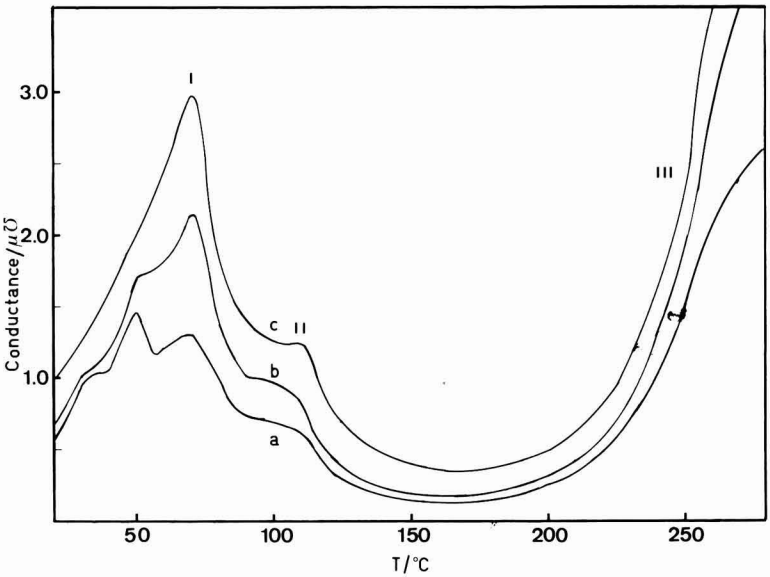


Fig. 3. Conductance vs. temperature at different frequencies, (a) 0.1, (b) 1, (c), 10 kHz, for a pellet (50 w/o electrolyte + 50 w/o MgO) containing an initial water concentration of 3 w/o.

water content in the various pellets. This is probably due to the variation of the time required to prepare the different samples, and hence to the different amounts of adsorbed water in the specimen.

For comparison of the trends observed in the electrical behavior, DTA experiments were carried out on pellets of the same composition (50 w/o electrolyte and 50 w/o magnesia). The first heating cycle yielded (Fig. 5) endothermic effects at 80°, 120°, 320°, and 382°C (peaks I, II, IV, and V, respectively). The last endothermic peak (peak V), appearing at 382°C in the first heating cycle and 370°C in the second cycle, and the reverse (exothermic) process at 320°C (peak V') are attributed to the solid-liquid and liquid-solid transitions, respectively. The shift of the electrolyte melting point to a higher temperature in the heating part of the first cycle could arise from changes of thermal conductivity or strain effects in nucleation. The first heating-cooling treatment probably eliminates effects arising from sample compaction due to sintering (12). The hysteresis in the transformation temperature in

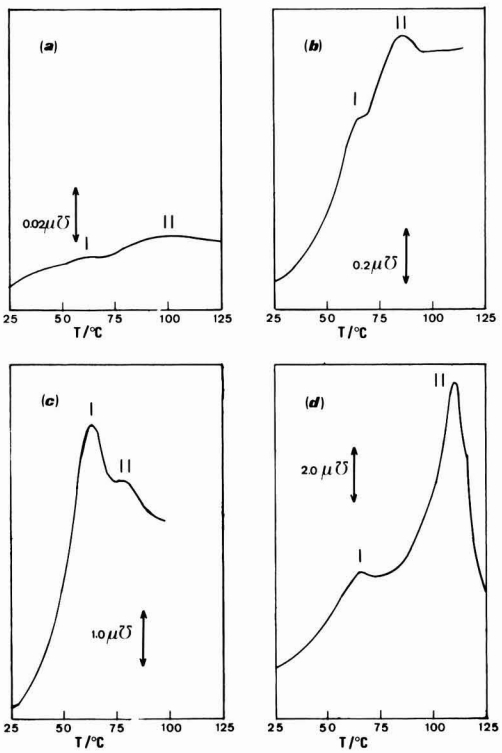


Fig. 4. Conductance vs. temperature at 1.5 kHz for pellets initially containing (a) 0.5, (b) 1.3, (c) 1.8, and (d) 2.6 w/o water.

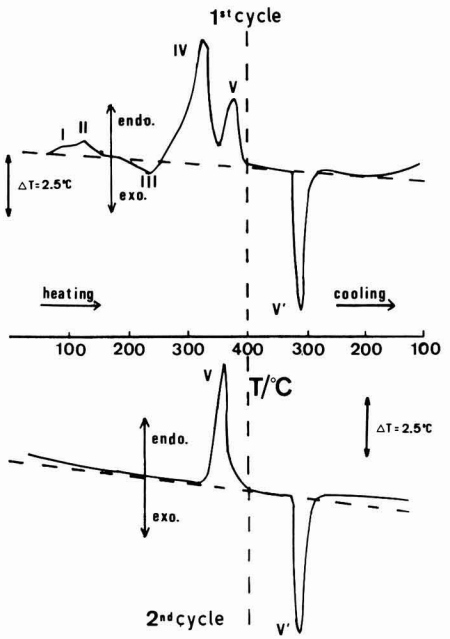


Fig. 5. DTA curves (first and second heating-cooling cycles) for a 50 w/o electrolyte + 50 w/o MgO mixture (heating-cooling rate = 5°C · min^{-1}).

the two directions could be reduced by reducing the heating-cooling rate.

Since the endothermic peaks at 80° and 120°C (peaks I and II) appeared only in the first heating cycle, they seem to be due to processes involving water being expelled during the first heating cycle. The origin of the first two effects is the same as described for the EC behavior in regions I and II (Fig. 3 and 4). The exothermic broad effect at 200°-250°C (region III in Fig. 5) seems also to be related to an increase in electrical conductance (region III in Fig. 3). The following exothermic reactions are consistent with the EC and DTA results and are known to occur in similar electrolytes (10, 11)

$$O^{2-} + H_2O \rightleftarrows 2\,OH^- \quad [5]$$

$$OH^- + HCl \rightleftarrows Cl^- + H_2O \quad [6]$$

Moreover, for LiCl-KCl mixtures in the absence of MgO, only endothermic peaks corresponding to the loss of adsorbed water (peak I), vaporization of liquid water (peak II), and to the electrolyte solid-liquid transition (peak V) were observed. This is in accordance with the suggestion that the exothermic effect (peak III) is related to reactions involving oxide and hydroxide ions (such as reactions [5] and [6]). The endothermic process IV taking place between regions III and V is suggested to be the result of the hydrolytic decomposition, in which the electrolyte becomes contaminated with alkaline products and HCl is lost from the system, *i.e.*, reaction [6] from right to left. Such reaction occurring at temperatures near fusion has been reported in several publications (10, 11).

The weight loss temperature dependence of the alkali chlorides has been investigated by Duval (20) using a thermogravimetric balance. An almost horizontal stretch between 80° and 96°C in the TGA curve of lithium chloride was interpretated to correspond to the composition $LiCl \cdot \frac{1}{2}H_2O$ (20). A typical TGA curve for the LiCl-KCl-MgO mixture is shown in Fig. 6. The lost weight processes found at 50°-70°C and 70°-130°C correspond to the loss of surface adsorbed water and the evolution of water vapor after hydrate dissociation. Moreover, the overall weight loss in the ambient-130°C range is quite identical to the initial water content of the sample, determined by a Karl Fisher titration to be 2.5 w/o. The surprisingly large weight loss (≃ 6 w/o) found in the 130°-170°C region seems to correspond to the conductance increase in region III (Fig. 3) and to the exothermic activity (peak III in Fig. 5) observed after dehydration. Since this TGA effect in region III was neither reported for LiCl (20) nor detected in the present study for LiCl-KCl in the absence of MgO, it seems to be related to a reaction consuming oxide ions and converting to a volatible product, *i.e.*, water. This suggestion is also consistent with the EC results, since electrical conductivity is sensitive to water evolution.

To detect water vapor in the gas evolved from pellets subjected to heat-treatment, a hygrometer was connected to the apparatus shown in Fig. 1 and relative humidity

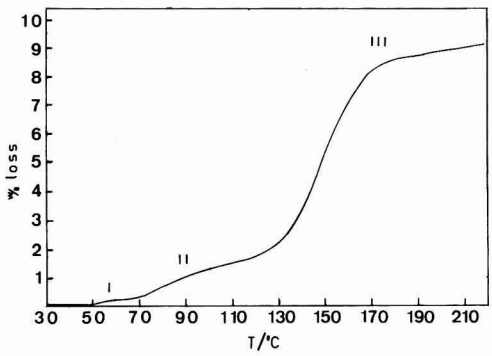


Fig. 6. TGA curve for a sample (50 w/o electrolyte + 50 w/o MgO) initially containing ≃ 2.5 w/o water.

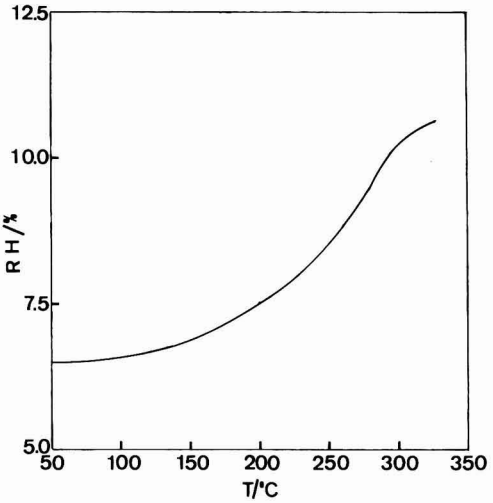


Fig. 7. Relative humidity *vs.* temperature of the gas evolved from a pellet (50 w/o electrolyte + 50 w/o MgO) which has been preheated and cooled (150°-25° C) several times. The system was continuously flushed with dry argon (RH < 0.5%, flow rate = 2 $cm^3 \cdot min^{-1}$).

was recorded as function of temperature. Contrary to the EC, DTA, and TGA experiments, a small and constant flow of dry argon (RH < 0.5%) was allowed to flush the system (the electrodes also serving as gas inlets). To eliminate the contribution of water evolved in the 25°-150°C region to the relative humidity, several heating-cooling cycles were applied until a constant value of RH was obtained in this temperature range. The RH *vs.* temperature curve obtained (Fig. 7) showed an increase in relative humidity at $T > 150$°C, confirming water vapor evolution in this temperature range.

Conclusions

Electrical conductance as function of temperature of several eutectic mixtures has been reported in the literature. However, all reported data concern temperatures above melting point of the electrolyte (21). In the present study, ac conductivity measurements were particularly conducted below the melting temperature of the pelletized LiCl-KCl (64-36 m/o) mixture in the presence of MgO. The electrochemical data were compared to those obtained using differential thermal and thermogravimetric analysis and were related to the various states of water present in the pelletized mixture. There are distinct changes taking place at temperatures right from the ambient value, and at least three main different processes seem to be related to the presence of water in the pellet; the processes are listed below.

1. Initially, the pellet dries by a process that involves the migration of water to the surface of the pellet, where it vaporizes (T = 25°-130°C).

2. In the temperature region 30°-250°C, exothermic reactions give rise to an increase in electrical conductivity and to a large weight loss effect. Hygrometric measurements indicate the evolution of water in this temperature range. This is suggested to be the product of the thermochemically favorable reaction between oxide or hydroxide ions and hydrogen chloride (reaction [6] from left to right). However, the intensity of the EC, DTA, and TGA effects in region III is much larger than expected to arise from the small amounts of HCl present in the electrolyte (5). Further studies are needed to investigate the exact nature of the processes involved in these temperatures.

3. Further heating ($T > 250$°C) causes hydrolytic decomposition of the electrolyte, *i.e.*, equilibrium [6] is shifted from right to left, yielding hydrogen chloride and hydroxide ions. The voltammetric detection of water as well as

hydrolytic products in fused pelletized electrolytes ($T >$ 370°C) will be described in a future publication (22).

REFERENCES

1. W. Borger, D. Kunze, and H. S. Panesar, *Prog. Batt. Solar Cells*, **3**, 251 (1980).
2. D. R. Vissers, *NATO Conf. Ser., Ser. 6*, **2**, 47 (1980).
3. J. P. Mathers, T. M. Olszanski, and J. E. Battles, *This Journal*, **124**, 1149 (1977).
4. K. W. Fung and G. Mamantor, *Adv. Molten Salt Chem.*, **2**, 199 (1973).
5. S. H. White, in "Ionic Liquids," D. Inman and D. G. Lovering, Editors, Chap. 12 Plenum Press, New York (1981).
6. R. Combes, in "Ionic Liquids," D. Inman and D. G. Lovering, Editors, Chap. 15, Plenum Press, New York (1981).
7. A. A. El Hosary, D. H. Kerridge, and A. M. Shams El Din, in "Ionic Liquids," D. Inman and D. G. Lovering, Editors, Chap. 16, Plenum Press, New York (1981).
8. S. Senderoff and A. Brenner, *This Journal*, **101**, 16 (1954).
9. H. J. Gardner, C. T. Brown, and G. J. Janz, *J. Phys. Chem.*, **60**, 1458 (1946).
10. H. A. Laitinen, W. S. Ferguson, and R. A. Osteryoung, *This Journal*, **104**, 516 (1957).
11. D. L. Maricle and D. N. Hume, *ibid.*, **107**, 354 (1960).
12. R. Nottenburg, K. Rajeshwar, M. Freeman, and J. Du Bow. *Anal. Chem.*, **51**, 1149 (1979).
13. K. Rajeshwar, R. Nottenburg, M. Freeman, and J. Du Bow, *Thermochim. Acta*, **33**, 157 (1979).
14. K. Lonvik, K. Rajeshwar, and J. B. Du Bow, *ibid.*, **42**, 11, (1980).
15. G. V. Keller and F. C. Frischknecht, "Electrical Methods in Geophysical Prospecting," Pergamon Press, New York (1966).
16. A. I. Vogel, "A Textbook of Quantitative Inorganic Analysis Including Elementary Instrumental Analysis," 3rd Ed., p. 944, Longmans, London (1961).
17. W. W. Wendlandt, *Thermochim. Acta*, **1**, 11 (1970).
18. A. B. Lidiard, in "Encyclopedia of Physics, Vol. 20, Electrical Conductivity II," S. Flugge, Editor, p. 246 Springer-Verlag, Berlin, (1957).
19. K. Rajeshwar, R. Nottenburg, J. Du Bow, and R. Rosenvold, *Thermochim. Acta*, **27**, 357 (1978).
20. C. Duval, "Inorganic Thermogravimetric Analysis," p. 165, Elsevier, Houston, (1953).
21. E. R. Van Artsdalen and I. S. Yaffe, *J. Phys. Chem.*, **59**, 118 (1955).
22. F. Broitman, R. Parash, U. Mor, D. Ozer, and A. Bettelheim, In preparation.

Corrosion of the Wet-Seal Area in Molten Carbonate Fuel Cells

I. Analysis

R. A. Donado, L. G. Marianowski, and H. C. Maru[1]

Institute of Gas Technology, Chicago, Illinois 60616

J. R. Selman*

Department of Chemical Engineering, Illinois Institute of Technology, Chicago, Illinois 60616

ABSTRACT

Severe corrosion can occur in the seal area between the cell housing and the electrolyte tile of a molten carbonate fuel cell even if an optimal selection of the active cell materials has been made. Thermodynamic calculations and an approximate mixed-potential analysis indicate that several minor corrosion cells are active at open circuit, and a major corrosion cell is established when the cell is under load. Extensive corrosion can be expected on the anode side of the wet seal, although effects at the cathode side are minor.

The available literature related to gas-seal techniques and methods of minimizing corrosion, particularly in the seal area of a molten carbonate fuel cell, is very limited. In early work on cell development, several types of assemblies comprising all-ceramic components were used, *e.g.*, by Broers *et al.* (1), Salvadori (2), and Kronenberg (3), but such assemblies are bulky and have low resistance to thermal shock. More recently, investigators have used cells and cell stacks formed by pressing together a series of flat-plate cell components (filter-press arrangement) and utilizing a wet seal (4, 5).

In the wet-seal technique, metal flanges are pressed against the flat surface of an electrolyte "tile," *i.e.*, a porous, inert matrix filled with electrolyte. At the cell operating temperature, sufficient free liquid is present to wet the metal surfaces and form a gas seal, as schematically represented in Fig. 1. The concept was first applied by Davtyan (6) when working with "solid electrolyte" fuel cells in 1946. Later investigations by Broers (6) revealed that the electrolyte was not really a solid but contained molten salts such as phosphates and tungstates. Chambers and Tantram (7), using a eutectic mixture of lithium and sodium carbonates held in a porous, sintered magnesia disk, formed a cell or battery by sandwiching the disk, with its attached electrodes, to metal flanges. Similar sandwich-type cells were investigated by Peattie and Trachtenberg (8). The wet-seal approach was also used in a previous project carried out at IGT (9). Critical improvements in seals and seal design for single, flanged cells are described in patent citations (10, 11). A review of more recent developments is given by Pigeaud *et al.* (5).

Because the wet-seal technique involves metal-electrolyte contact in a gas-deficient region of the cell, one may expect one or more corrosion cells to form. Experience with single, flanged cells has shown that corrosion of the seal-area metal can be severe and may lead to a poor seal and rapid deterioration of cell performance as a result of gas leakage. Severe corrosion in the wet-seal area also aggravates carbonate loss from the tile and may cause catastrophic failure (4). In fuel-cell stacks the cells are separated by a bipolar plate, which forms a wet seal with the electrolyte tile in each cell of the stack. The bipo-

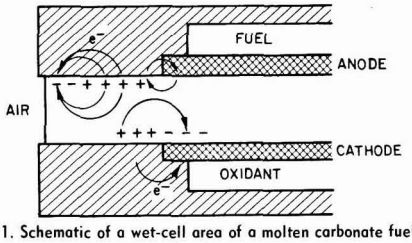


Fig. 1. Schematic of a wet-cell area of a molten carbonate fuel cell

*Electrochemical Society Active Member.

[1]Present address: Energy Research Corporation, Danbury, Connecticut 06810.

lar plate, for which stainless steel is a candidate material, experiences similar corrosion problems as the anode and cathode flanges in a single cell.

Although wet-seal corrosion and its prevention have received some attention in the electrochemical literature (12), no systematic study has been made of the corrosion mechanism and of the corrosion rates at various points in the wet-seal area. In this paper, we compare thermodynamically the corrosion cells operating in the wet-seal area and report corrosion rates under conditions simulating those in a fuel cell. A further objective is to clarify how corrosion can be prevented and to determine the level to which corrosion rates can be reduced. In this paper, the possible mechanisms of corrosion are presented and analyzed. This analysis cannot predict the actual corrosion rates, for which experiments are necessary. The experimental results are presented in the following paper (13).

Conversion and Corrosion Reactions

The main electrode reactions occurring in a molten carbonate fuel cell are at the fuel (negative) electrode or anode

$$H_2 + CO_3^{2-} \rightarrow H_2O + CO_2 + 2e^- \quad [1]$$

and at the oxygen (positive) electrode or cathode

$$1/2\ O_2 + CO_2 + 2e^- \rightarrow CO_3^{2-} \quad [2]$$

The overall cell reaction is

$$H_2 + 1/2\ O_2 \rightarrow H_2O \quad [3]$$

Although the cell also converts CO, the direct electrochemical oxidation of CO, analogous to Eq. [1], appears to be very slow. It is generally assumed that CO oxidation takes place via the water-gas shift equilibrium

$$CO + H_2O \rightarrow CO_2 + H_2 \quad [4]$$

The fuel electrode and the negative flange of the cell housing (Fig. 1) are continuously in contact with fuel gas containing H_2, CO, H_2O, and CO_2, with N_2 constituting the balance. The oxygen electrode and the positive flange are continuously in contact with oxidant gas containing O_2, CO_2, and a small amount of H_2O, with N_2 constituting the balance. The gas compositions used here to illustrate corrosion processes are shown in Table Ia; they correspond to reformed naphtha as fuel and standard oxidant (70% air, 30% CO_2) as oxidant gas.

A large cell operating under an electrical load has an appreciable degree of conversion, typically 75% for the fuel gas and 50% for the oxidant. The resulting outlet compositions of fuel and oxidant are also shown in Table Ia.

The local driving force for conversion, Eq. [3], is determined by the equilibrium potentials of electrode reactions [1] and [2], which depend on the local gas compositions. This is illustrated in Table Ib, based on standard thermodynamic data (14, 15). The reference potential is that of oxygen reduction, Eq. [2], the reference oxidant consisting of 33% oxygen and 67% CO_2. Because the equilibrium potentials of Eq. [1] and [2] vary from point to point along the electrodes, the driving force for conversion, Eq. [3], varies correspondingly. Consequently, the distribution of the current in a cell with appreciable conversion is nonuniform. Analyses of current distribution in scaled-up cells have been presented by Sampath *et al.* (16) and Wilemski *et al.* (17).

Variations in local gas composition also cause variations in the local driving force for corrosion. The negative half (flange) of the cell housing is in contact, over its entire interior surface, with fuel gas of varying composition. Likewise, the inside of the positive half contacts oxidant of varying composition. In addition, both halves are in contact with ambient air, at and around the open end of the wet seal, where some electrolyte creepage usually occurs. The equilibrium potential of oxygen reduction from air is included in Table Ib.

Table Ia. Compositions of gases used in this work (m/o)

	H_2	CO_2	H_2O	CO	N_2	O_2
Fuel inlet	60.9	8.4	21.6	9.1	—	—
Fuel outlet	10.3	39.6	45.4	4.6	—	—
Air	—	0.03	2.5	—	Bal	20.5
Oxidant inlet	—	29.2	2.8	—	53.7	14.3
Oxidant outlet	—	18.7	3.6	—	68.8	9.0
Reference gas	—	66.7	—	—	—	33.3

Table Ib. Equilibrium potentials of reactions [1] and [2] with respect to standard oxygen electrode (33.3% oxygen, 66.7% CO_2)

	Reaction	Potential at 923 K
Fuel inlet	1	−1121
Fuel outlet	1	−960
Air	2	−310
Oxidant inlet	2	−50
Oxidant outlet	2	−76

Corrosion cells are formed by local oxidation (dissolution) and reduction reactions occurring in adjacent areas of the same, electronically conducting surface. In the present case, these adjacent areas are located on the inside surface of the anodic or cathodic flange and on the porous electrode enclosed by the flange. The oxidation (dissolution or corrosion) reactions can be represented in a general way by the following equations written for a two-valent metal

$$M \leftrightarrows M^{2+} + 2e^- \quad [5]$$

$$M + O^{2-} \leftrightarrows MO + 2e^- \quad [6]$$

$$M + 2\ OH^- \leftrightarrows MO + H_2O + 2e^- \quad [7]$$

$$M + CO_3^{2-} \leftrightarrows MO + CO_2 + 2e^- \quad [8]$$

Similar reactions may be written for a trivalent metal. The reduction reactions contributing to corrosion cells are gas-electrode reactions, principally oxygen reduction, Eq. [2], and possibly reduction of H_2O by the reverse reaction of Eq. [1].

In the treatment of corrosion presented here, the possibility of carbide formation (carburization) is not considered, although carbides can form in the metal phase beneath the oxide scale, if the oxygen activity is very low. Rapp *et al.* (21) have analyzed the conditions for carbide formation in detail and confirmed their predictions experimentally. Shores and Singh (22) have demonstrated the presence of carburization in laboratory cell current collectors. However, it is unlikely that the oxygen activity in the wet seal area will be low enough to cause carburization, except possibly very close to the inner edge of the anode-side flange, at open-circuit conditions or at very small conversions. The experimental results to be presented in Part II (13) show that this assumption is correct.

The electrode reactions, Eq. [5]-[8], are not independent. They involve dissolved gases and ionic species which locally participate in dissociation and hydrolysis equilibria

$$CO_3^{2-} \rightleftarrows CO_2 + O^{2-} \quad [9]$$

$$CO_3^{2-} + H_2O \rightleftarrows CO_2 + 2\ OH^- \quad [10]$$

The water-gas shift equilibrium, Eq. [4], is also applicable. All of these reactions are rapid, at least compared with the rate of corrosion reactions [5]-[8], so that local equilibrium may be assumed. Thus, at any point of the flange surfaces, the equilibrium potentials of electrode reactions [5]-[8] are identical, and we may evaluate the potential by the Nernst equation applied to one of them; for example, Eq. [8]

$$E = E^0\,(MO, CO_2/M, CO_3^{2-}) + RT/2F \ln \frac{(MO)\,(CO_2)}{(M)\,(CO_3^{2-})} \quad [11]$$

The oxide MO is assumed to be insoluble, or sparingly soluble, so its activity is equal to, or close to, unity. In fact, stainless steel passivates; that is, it forms a coherent, conducting oxide layer that reduces the corrosion rate appreciably (18). This oxide layer may consist in part of mixed oxides such as $LiFeO_2$ and $LiCrO_2$, which are also insoluble or sparingly soluble and do not significantly affect the electrode potential. In the transpassive region, these surface layers disintegrate under formation of loosely adherent metal oxides; in a strongly oxidizing, basic (*i.e.*, alkali oxide-rich) environment, such as exists at the cathode under load, chromium may be oxidized further to the very soluble chromate ion

$$Cr + 4CO_3^{2-} \rightarrow CrO_4^{2-} + 4CO_2 + 6e^- \quad [12]$$

$$E = E^0(CrO_4^{2-}, CO_2/Cr, CO_3^{2-}) + RT/6F \frac{(CrO_4^{2-})(CO_2)^4}{(Cr)(CO_3^{2-})^4} \quad [13]$$

In Table II, the equilibrium potentials of various metals according to Eq. [11], based on standard thermodynamic data (14, 20), are collected; the gas compositions are those of Table Ia. Iron, chromium, and nickel are of interest not only as constituents of Type 300 stainless steels, but also as electrode materials. In the latter category, copper and cobalt are of interest. The table also includes structural materials such as tantalum, vanadium, and other refractory metals. Among the light metals included are aluminum and titanium, which form insulating oxides.

From Tables Ib and II, one can immediately ascertain which corrosion cells are thermodynamically possible. For example, all three components of stainless steel will have a tendency to corrode at those points of the flange where contact with air and electrolyte occurs. The driving force for these corrosion cells is, from Tables Ib and II

Chromium	−310 −(−1834)	= 1524 mV
Iron	−310 −(−1346)	= 1036 mV
Nickel	−310 −(−1087)	= 777 mV

However, whether corrosion really takes place and, if so, at what rate, depends on the actual electrode potential at the point in question. Corrosion takes place only if the actual electrode potential is more positive than the equilibrium potential of the anodic (dissolution, corrosion) reaction. The rate of corrosion depends on the available driving force (actual potential minus equilibrium potential of the anodic reaction). Therefore, one may expect important differences in the corrosion picture when the cell is under load, as compared to that at open circuit. Thus, it is well known that at high current densities the porous anode material, mainly consisting of nickel, may become oxidized. Table II indicates that this is only possible if the actual electrode potential of the anode, with respect to a 33% oxygen, 67% CO_2 reference electrode, is more positive than, for example, −862 mV if the CO_2 partial pressure is 0.084 atm, as for reformed naphtha at inlet conditions. Such an electrode potential, though unacceptably high (positive) for state-of-the-art fuel cell anodes under standard operating conditions (4), may occasionally be reached at very high current densities. However, from Table Ib it can be seen that in a cell at open circuit, oxidation of nickel by the reverse reaction of Eq. [1] is thermodynamically impossible unless the H_2O and CO_2 partial pressures in the fuel gas are increased far in excess of those in reformed naphtha at 75% conversion.

In a cell at open circuit, the negative and positive flanges are not electronically connected. Each flange then assumes a mixed potential corresponding to zero net current of the various electrochemical reactions that exchange electrons via the flange. The mixed potential is the result of a complex interaction between the electrochemical reactions (corrosion and reduction) and the supply, by diffusion, of dissolved gases to various points of the wet-seal area. In the carbonate fuel cell at open circuit, a small fraction of the feed gas on both sides is continually being consumed by chemical reaction; that is, there is a small but stationary flux of dissolved gas into the tile toward the opposing electrode or toward the air interface of the wet seal. Hydrogen diffusing from the fuel electrode toward the oxygen electrode and the air/tile interface reacts with oxygen and is consumed (chemical discharge). Furthermore, a small fraction of the feed gases on either side may be involved in corrosion cells (circuits); on the cathode side, some oxygen is reduced, and on the anode side, some H_2O may be reduced. These corrosion cells are parasitic or cooperative, depending on whether or not they consume part of the feed gases. At open circuit, the changes in gas composition are usually of no practical significance. Corrosion cells involving oxygen from air are indifferent with respect to conversion.

In all of the above cases, only those corrosion reactions (dissolution or oxidation) can take place whose equilibrium potential is more negative than the mixed potential assumed by the flange.

The same applies to a fuel cell under load, that is, producing a current. However, the analysis is easier because the electrode potential is controlled externally through the load rather than through the spontaneous interaction of diffusion and reactions in the wet-seal area. The corrosion cells (circuits) are now superimposed on the main cell current, due to fuel conversion, as schematically shown in Fig. 2. One may still distinguish cooperative, parasitic, and indifferent corrosion cells. Thus, a corrosion cell restricted to the anode flange, in which some H_2O is reduced to hydrogen, decreases fuel conversion for a given cell current; it is, therefore, cooperative. Corrosion cells that involve both flanges may also be established, as shown in Fig. 2; such cells parallel the main cell reaction and increase the external current, while also increasing oxidant conversion for a given main cell current due to fuel conversion.

In reality, of course, the various corrosion cells (circuits) do not exist as separate entities in the overall current distribution between the flanges. The resulting current distribution at the flanges can be interpreted in terms of corrosion cells. This is convenient in cases like the present one, where the exact, quantitative analysis of the potential distribution would require much mathematical effort.

Table II. Equilibrium potentials at 925 K *vs.* standard oxygen reference electrode (33.3% oxygen, 66.7% CO_2)

Material	Reaction	Potential (mV) Air 0.03% CO_2	Fuel inlet 8.4% CO_2	Fuel outlet 39.6% CO_2	Oxidant inlet 29.2% CO_2	Oxidant outlet 18.7% CO_2
Cu	$Cu(c) + 1/2\ O_2(g) = CuO(c)$	−674	−449	−388		
Ni	$Ni(c) + 1/2\ O_2(g) = NiO(c)$	−1087	−862	−801	−813	−830
Co	$Co(c) + 1/2\ O_2(g) = CoO(c)$	−1156	−931	−872	−882	−899
Fe	$0.947Fe(c) + 1/2\ O_2(g) = Fe_{0.947}O(c)$	−1346	−1121	−1060	−1072	−1090
Cr	$2Cr(c) + 3/2\ O_2(g) = Cr_2O_3(c)$	−1834	−1609	−1548	−1560	−1578
Nb	$2Nb(c) + 5/2\ O_2(g) = Nb_2O_5(c)$	−1836	−1611	−1550		
Ta	$2Ta(c) + 5/2\ O_2(g) = Ta_2O_5(c)$	−1980	−1755	−1694		
V	$2V(c) + 3/2\ O_2(g) = V_2O_3(c)$	−2014	−1789	−1728		
Ti	$Ti(\alpha) + O_2(g) = TiO_2(c)$	−2296	−2071	−2010		
Zr	$Zr(\alpha) + O_2(g) = ZrO_2(\alpha)$	−2665	−2440	−2379		
Al	$2Al(c) + 3/2\ O_2(g) = Al_2O_3$ (Cor)	−2675	−2450	−2389		

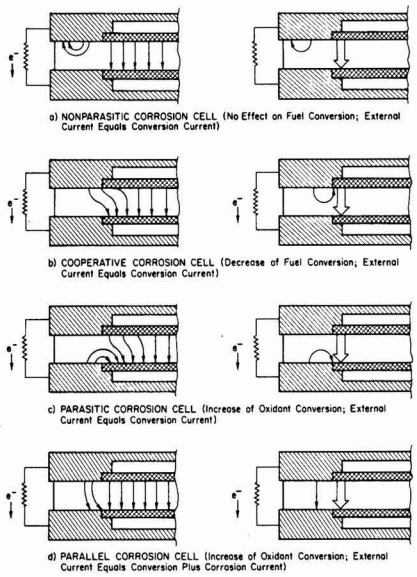


Fig. 2. Types of corrosion cells existing in the wet-cell area. Left: current distribution in the electrolyte. Right: schematic in terms of corrosion cells. The bold arrow represents the main cell current due to fuel conversion in the absence of corrosion.

Corrosion Regions and Solute Fluxes

To distinguish the various corrosion cells in the wet-seal area, we identify first the approximate gas compositions adjacent to various regions of the cell housing. These are schematically indicated in Fig. 3.

Surrounding the anode is region A, which has a high concentration of H_2 and CO, and which also contains a considerable amount of H_2O (see Table Ia). From this region, H_2 and CO diffuse toward the edge of the flange. From the edge of the flange (regions C and F), O_2 (as air) diffuses toward region A. H_2 and O_2 react in a zone (indicated by a dotted line) at region B where, consequently, the H_2O concentration is high. Because the solubility and diffusivity of H_2 are appreciably larger than those of O_2 in molten carbonate (17), the location of region B is closer to the outer edge of the seal area than to the inner edge.

The reaction zone between H_2 (or CO) and O_2 within the tile is schematically indicated by the dotted line in Fig. 3. From region B, this line curves toward that part of the tile that lies between the electrodes. The reaction zone is region G, which is closer to the cathode than to the anode.

Region D, near the edge of the cathode, contains a relatively high concentration of O_2 and CO_2, while region F, near the outer edge, contains a high concentration of O_2 but is low in CO_2. The concentration of H_2O goes from relatively low in region D to very low in region F. This is schematically indicated in Table III. Region E, unlike the opposite region at the anode side (region B), is characterized by conditions that are not very different from adjacent regions.

To analyze the corrosion effects, it is desirable next to assess the relative importance of the various fluxes of

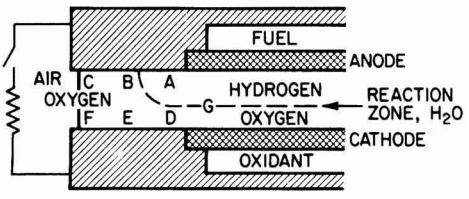


Fig. 3. Regions in the wet seal according to major dissolved-gas species

Table III. Dissolved gas concentrations in various regions of the wet seal (schematically) in percent of total gas pressure

Region	H_2 + CO	CO_2	O_2	H_2O
A	70	8	0	22
B	0	(8)*	0	(92)
C	0	0.1	19	0.1
D	0	29	14	3
E	0	(10)	(17)	(1)
F	0	0.1	19	0.1

* The concentrations in regions B and E are determined by the reaction of converging fluxes, and could be estimated by a rather involved mathematical analysis. The values in parentheses are rough estimates only for purpose of illustration.

dissolved gas in the wet-seal area. These fluxes may reinforce or may counteract the corrosion cells that arise spontaneously. The concentration differences (Table III) and the distances between various regions lead us to conclude that certain fluxes are very important and others secondary, as indicated by solid and dashed arrows in Fig. 4. It should be noted that the tile thickness is only about one-fifth of the length dimension of the flange, so fluxes across the tile are relatively more important than those along the flanges. Also, H_2O fluxes are in first approximation equivalent to CO_2 fluxes because of the hydrolysis equilibrium (Eq. [10]).

Analysis: Corrosion at Open Circuit

The corrosion picture at open circuit is simplified by the observation that in cells of reasonably large size, the open-circuit potentials of the fuel electrode and the oxidant electrode are practically equal to the equilibrium potentials of the respective conversion reactions, that is, H_2 oxidation (reaction [1]) and O_2 reduction (reaction [2]). Therefore, we can make use of Table IV, in which are collected the equilibrium potentials of the primary corrosion and reduction reactions in the various regions.

At the anode side, little iron dissolution should be expected in regions A and B. Only if the fuel gas is richer in H_2O and CO_2 than assumed in Table Ia will it be likely that there is a strong corrosion cell between regions A and B. However, between regions B and C, the conditions are fulfilled for dissolution of iron under simultaneous reduction of O_2. The driving force for this cell, indicated by i_1 in Fig. 5, is considerably larger than that for corrosion between regions A and B (i_3).

Chromium dissolution can occur over the entire anode wet seal, compensated for by reduction of O_2 from air in region C. Corrosion of chromium, like that of iron, will be most intense just outside region B.

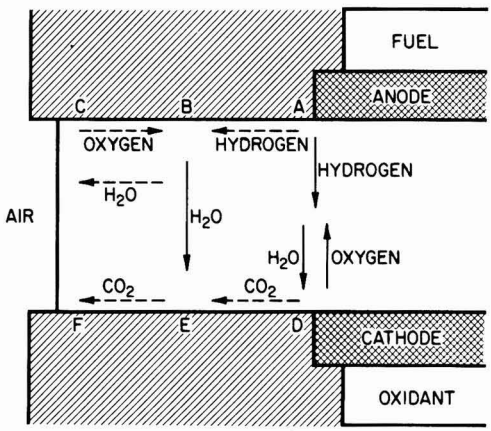


Fig. 4. Primary fluxes (solid arrows) and secondary fluxes (dashed arrows) of dissolved gas at open circuit.

Table IV. Equilibrium potentials of electrode reactions in various regions of the wet seal (in mV at 925 K vs. the 33% oxygen, 66.7% CO_2 reference electrode

Region	H_2O/H_2	$O_2, CO_2/CO_3^{2-}$	FeO/Fe	Cr_2O_3/Cr	NiO/Ni
A	−1120		−1120	−1610	−860
B			−1050	−1611	−864
C		−310	−1350	−1830	−1090
D		−50	−1070	−1560	−810
E		−50	−1110	−1603	−856
F		−310	−1350	−1830	−1090

Figure 5 indicates schematically how the positive and negative areas on the anode side of the wet seal are distributed, correponding to the prevailing fluxes (H_2O from B to C and E; CO_2 from B to C; O_2 from C to B; and H_2 from A to B).

At the cathode side, where the open-circuit potential is very close to −50 mV, metal dissolution compensated by oxidant reduction is possible everywhere. It is most likely to be intense in region D, where the distance to the cathode itself is shortest. The distribution of positive and negative sites indicated in Fig. 5 is in agreement with a CO_2 flux from region D to E. In region D, one would expect corrosion to be serious, since the driving force for metal oxidation is very large (Table IV). However, the compensating oxygen reduction apparently proceeds at a very small rate: the cathode open-circuit potential is close to equilibrium for this reaction. This suggests that the corrosion rate may, after all, be quite small compared to that at the anode because the kinetics of O_2 reduction in molten carbonate are known to be very much slower than those of H_2 oxidation (15).

Analysis: Corrosion under Load

In a cell under load, some changes may be expected in the picture of Fig. 3. Region B, where H_2 from (A) combines with O_2 from (C), will be located closer to (A) because the concentration of H_2 at (A) is now lower, except at the fuel inlet. At the cathode, the flux of CO_2 from region D, via (E) to (F), will be smaller than at open circuit for similar reasons. The flux of H_2O across the tile, although still very prominent, will be smaller than at open circuit and shifted toward the inner edge of the wet seal.

Again considering the equilibrium potentials shown in Table IV, we note that these are valid only at the feed gas inlet points. The potentials at outlet may be found from Tables I and II; they are graphically illustrated in Fig. 6.

The most important differences, however, have to do with the actual electrode potentials of anode and cathode. These are considerably different from the open-circuit

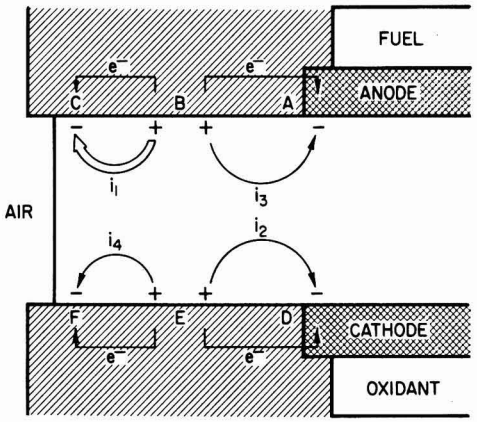


Fig. 5. Corrosion cells in the wet-seal area as open circuit

values (Fig. 6). Also, anode and cathode are connected electronically through the load, thereby opening the possibility of cross-tile corrosion cells. The consequences of the new situation are shown schematically in Fig. 7.

At the anode side, where the operating potential is −950 mV, corrosion cell i_1, in region C, is likely to extend further toward the inner edge of the wet seal. Also, under fuel outlet conditions the H_2O concentration at (A) may be high enough to make the anodic leg of corrosion cell i_3, at and near (B), extend further toward the inner edge of the seal. This is equivalent to an increase of corrosion current i_3 and a decrease of fuel conversion (cooperative corrosion). Nevertheless, i_3 remains quite small because the driving force is small.

The salient feature of Fig. 7, however, is the corrosion cell across the tile, between regions B and E. This is a major corrosion cell because the driving force is large and the distance over which it operates is small. Cell i_5 is made possible by the electronic connection between the flanges. The current is in first approximation inversely dependent on the load, as is the main conversion current of the fuel cell. We note also that the corrosion current i_5 is reinforced by the flux of H_2O, and equivalently of CO_2 by equilibrium (10), across the tile from region B to E.

At the cathode side, the corrosion cell i_2 is weakened or suppressed, as is cell i_4, by the negative shift of the electrode potential under load (cathodic protection).

To quantify the various corrosion tendencies in first approximation, we observe that the driving force for cor-

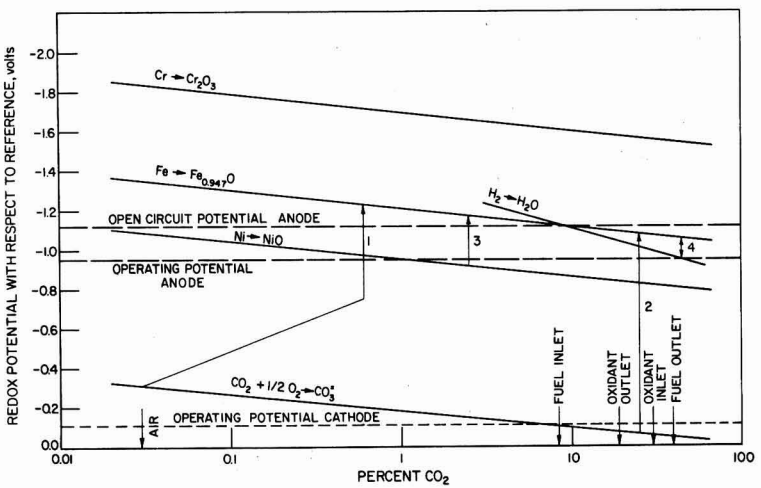


Fig. 6. Equilibrium potentials of electrode reactions vs. the 33.3% oxygen and 66.7% CO_2 reference electrode as a function of CO_2 partial pressure. Operating potentials of anode and cathode, as well as anode open-circuit potential, are indicated.

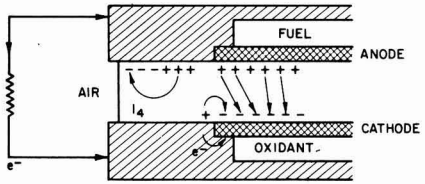


Fig. 7. Corrosion cells in the wet-seal area under load

rosion cell i_2 of Fig. 7 is, for iron corrosion, approximately $-50 - (-1110) = +1060$ mV at open circuit, but decreases to $-100 - (-1110) = 1010$ mV under load, similarly for cell i_4. The principal corrosion cell on the anode side is at open-circuit cell i_1, which has a driving force of $-310 - (-1050) = +740$ mV; however, under load the principal corrosion cell is i_5, with driving force $-100 - (-950) = +850$ mV over a much smaller distance.

Thus, corrosion at the cathode side of the wet seal should be decreased and the anode side should experience more intense corrosion. Correspondingly, the corroded area of the anode side may be expected to increase under load, although the cathode side should be largely immune.

Corrosion of Various Metals in an Operating Cell

At the anode operating potential of −950 mV, chromium and iron will be oxidized (Fig. 6), but nickel, cobalt, and copper will not (Table II). The thermodynamic data also indicate that somewhat less corrosion of iron should be observed at the fuel outlet side of the cell because the equilibrium potentials for metal oxidation become more positive with increasing partial pressure of CO_2 (Fig. 6). In terms of the corrosion cells of Fig. 7, this means a strong cathodic component of i_3 (H_2O being reduced in region A) and possibly a shift of the anodic leg of i_3, as well as i_5, toward the outer edge of the wet seal. However, this does not necessarily imply that the total rate of corrosion in the wet-seal area is less.

For the corrosion of chromium, fuel inlet or outlet conditions make little difference because the driving force for corrosion is large. If, as has been suggested (19), corrosion of stainless steel takes place by intergranular attack of chromium, there would not be any significant effect of fuel gas composition. However, the picture is complicated by the formation of mixed oxides, such as $LiCrO_2$ and $LiFeO_2$, whose solubility and conductivity are influenced by the basicity of the melt and by the relative concentrations of the alkali ions. For lack of adequate information about these fundamental chemical aspects of corrosion in molten carbonates, the present approximate analysis must suffice.

The analysis in this paper is based primarily on tendencies indicated by thermodynamic equilibria combined with a semi-quantitative assessment of the actual corrosion cells in the wet-seal area. A more exact prediction of the intensity of corrosion and its distribution would follow from a complete mathematical model of the potential, current, and species concentration distributions in the wet-seal area and adjoining regions. Solving such a model would require not only extensive computational effort, but also reliable kinetic information, for example, on the dissolution and passivation of stainless steel and the reduction of oxygen at steel or various metal oxides.

Under these conditions, it is easier to simulate wet-seal conditions experimentally in a model cell. The results of model experiments are reported in the second part of this paper (13).

Summary

A semi-quantitative analysis of the mixed-potential conditions in the wet-seal area of a molten carbonate fuel cell leads to the following conclusions.

1. At open circuit, the anode side will corrode mostly near the center of the wet seal compensated by reduction of atmospheric O_2 near the outer edge. Corrosion close to the inner edge of the seal is only expected if the fuel is very rich in H_2O and CO_2. The cathode side will corrode near the inner edge of the seal, compensated by reduction of oxidant in the porous cathode.

2. Under load, anode wet-seal corrosion will take place much more intensively than at open circuit and over a greater area. The compensating reaction is reduction of oxidant gas, or atmospheric oxygen, at the cathode flange. Corrosion of the cathode side is less intensive than at open circuit owing to cathodic protection under load.

3. Owing to higher H_2O and CO_2 partial pressures at fuel outlet conditions, somewhat more corrosion should be observed at the inner edge of the anodic wet seal near the fuel outlet than at fuel inlet. This effect should be very clear if the corrosion process involves iron oxidation directly, if it takes place via chromium oxidation, the differences should be minor.

Acknowledgments

The work reported here was sponsored by the U. S. Department of Energy through Argonne National Laboratory. Guidance and suggestions by the program manager, Dr. John P. Ackerman, are very much appreciated. One of the authors (J. R. Selman) also acknowledges support by the Office of Basic Energy Sciences, U. S. Department of Energy.

Manuscript submitted June 14, 1984; revised manuscript received Feb. 27, 1984.

The Institute of Gas Technology assisted in meeting the publication costs of this article.

REFERENCES

1. G. H. J. Broers, M. Schenke, and G. G. Piepers, *Adv. Energy Convers.*, **4**, 127 (1964).
2. A. Salvadori, P. Lovy, and M. Beigelman, U.S. Pat. 3,359,134 (1967).
3. M. L. Kronenberg, U.S. Pat. 3,216,911 (1965).
4. J. R. Selman and L. G. Marianowski, in "Molten Salt Technology," D. H. Lovering, Editor pp. 323-393, Plenum Press, New York, (1982).
5. A. Pigeaud, A. J. Skok, P. S. Patel, and H. C. Maru, *Thin Solid Films*, **83**, 449 (1981).
6. G. H. J. Broers, Thesis, University of Amsterdam, Amsterdam (1958).
7. H. H. Chambers and A. D. S. Tantram, in "Fuel Cells," Vol. 1, G. Y. Young, Editor, pp. 94-108, Reinhold, New York (1960).
8. C. J. Peattie, I. Trachtenberg, and J. K. Truitt, in "Proceedings of the First Australian Conference Electrochemistry," J. A. Friend and F. Gutmann, Editors, pp. 683-688, Pergamon Press, Oxford, England (1963).
9. Institute of Gas Technology, "Development of Molten Carbonate Fuel Cells," A. G. A. Project DC-4-1 Final Report, Chicago, March 1967.
10. C. R. Schroll, U. S. Pat. 3,855,002 (1974).
11. A. Z. Borucka, U. S. Pat. 3,723,186 (1973).
12. R. B. Swaroop, J. W. Sim, and K. Kinoshita, *This Journal*, **125**, 1799-1800 (1978).
13. R. A. Donado, L. G. Marianowski, H. C. Maru, and J. R. Selman, *ibid.*, **131**, 2541 (1984).
14. D. R. Stull and H. Prophet, "JANAF Thermochemical Tables," 2nd Ed., p. 37, NSRDS-NBS, Washington, DC (1971).
15. J. R. Selman and H. C. Maru, in "Advances Molten Salt Chemistry 4" G. Mamantov and J. Braunstein, Editors, pp. 157-389 (1981).
16. V. Sampath, A. F. Sammells, and J. R. Selman, *This Journal*, **127**, 79 (1980).
17. T. L. Wolf and G. Wilemski, *ibid.*, **130**, 48 (1983).
18. G. J. Janz and A. Conte, *Electrochim Acta*, **9**, 1277 (1964).
19. B. K. Anderson, Thesis, Technical University of Denmark, Lyngby, Denmark (1975).
20. I. Barin, O. Knacke, and O. Kubaschewski, "Thermochemical Properties of Inorganic Substances" (1973) and Supplement (1977), Springer Verlag, Dusseldorf.
21. R. A. Rapp, in "Proceedings of the DOE/EPRI Workshop on Molten Carbonate Fuel Cells," EPRI-WS-78-135, Nov. 1979, p. 230 (1979).
22. D. A. Shores and P. Singh, Papers 254 and 387 presented at the Electrochemical Society Meeting, Montreal, Quebec, Canada, May 9-14, 1982.

Corrosion of the Wet-Seal Area in Molten Carbonate Fuel Cells

II. Experimental Results

R. A. Donado, L. G. Marianowski, and H. C. Maru[1]

Institute of Gas Technology, Chicago, Illinois 60616

J. R. Selman*

Department of Chemical Engineering, Illinois Institute of Technology, Chicago, Illinois 60616

ABSTRACT

Experimental results for anode wet-seal corrosion in molten carbonate fuel cells generally agree with postulated mechanisms that involve corrosion couples acting along or across the seal area. The corrosion rate of Type 316 stainless steel in the anode wet-seal area under all test conditions is unacceptably high. Substitution of an aluminum containing alloy, such as Kanthal A-1, reduces the anode wet-seal corrosion by at least two orders of magnitude. The corrosion rate of Type 316 stainless steel in the cathode wet seal is about two orders of magnitude lower than in the anode wet seal.

In Part I (1), we presented an approximate thermodynamic analysis of the mechanisms that cause corrosion of the molten carbonate fuel cell hardware. Two corrosion cells of relatively minor intensity should be active at open circuit: flange metal/air at the anode side and flange metal/oxidant gas at the cathode side. A major corrosion cell, anode-side flange metal/cathode-side oxidant, should be established under load. The analysis predicted a greater corrosion rate of the anode wet seal than of the cathode wet seal.

In this part, we present the results of corrosion experiments carried out to test the thermodynamic predictions, and we identify practical solutions to the wet-seal corrosion problem. The experiments were carried out at varying electrode potential (cell at open circuit or under load), fuel utilization (inlet or outlet), and material (316 stainless steel or Kanthal A-1).

Apparatus and Experimental Conditions

As discussed in Part I, several corrosion cells may be expected to operate in the wet-seal area of molten carbonate fuel cells (1). Because of the design limitations of scaled-up cells, such as the difficulty of access for reference electrodes, the corrosion mechanism cannot be studied quantitatively in actual operating cells. Therefore, out-of-cell testing is required. However, great care must be taken to assure that the characteristic design parameters controlling corrosion rates, for example, tile thickness, diffusion path lengths, and local gas compositions, are comparable to those in actual cells. Several test configurations were evaluated and tested before the design shown in Fig. 1 was adopted. In the test-stand design of Fig. 1, the test-specimen (J) for the anode wet seal, 3.8 cm diam, was welded to a ring (L) previously welded to a Type 316 stainless-steel tube. An electrolyte tile (I) was placed on the specimen. The test specimen was 0.64 cm larger in diameter than the electrolyte and was welded around the edge of the ring to minimize any changes in the grain structure that could occur during the welding operation. The specimen was then machined to accommodate a ring-shaped anode. Perforations in the specimen provided fuel access to the electrode. The cathode compartment was similar to that of the anode, except that a hole in the center of the cathode and a cathode current collector was provided for the reference electrode. The electrolyte and the wet-seal area, 0.64 cm wide, had the same thickness and width, respectively, as in a working cell. The active cell area was 2.5 cm^2; the electrodes were 1.91 cm diam with a 0.66 cm diam center hole.

The corrosion tests were operated at 923 K (650°C) for 1000h using electrolyte tiles 0.178 cm thick. The carbonate content of the electrolyte tiles was approximately 60 weight percent (w/o). A Li_2CO_3/K_2CO_3 eutectic carbonate mixture (62 mole percent [m/o] Li_2CO_3/38 m/o K_2CO_3) was used. The compositions of the test gases are presented in Table I. In the tests operated under load, the anode potential was potentiostatically kept constant at −1000 mV with respect to the 67% CO_2/33% O_2-gold reference electrode described by Borucka (2) and Argano *et al.* (3).

Table I. Gas compositions (m/o)

	H_2	CO_2	H_2O	CO	O_2	N_2
Fuel inlet*	60.9	8.4	21.6	9.1	—	—
Fuel outlet**	31.5	21.9	37.0	9.6	—	—
Oxidant'	—	29.2	2.8	—	14.3	53.7
Reference electrode	—	66.7	—	—	33.3	—

* Reformed naphtha fuel.
** Reformed naphtha fuel (37% H_2 utilization).
' Standard oxidant.

Results

Corrosion at open circuit.—Tests at open circuit were carried out to observe the corrosion caused at the anode side by the metal/air and the metal/fuel corrosion cells (i_1 and i_3 in Fig. 5 of Part I). Both cells cause corrosion in the wet-seal area of the test cell, but the metal/fuel cell would cause more corrosion near the inner edge of the wet-seal area.

Typical corrosion results at open circuit are shown in Fig. 2. The sampling locations are indicated in Fig. 3. Figure 2 demonstrates that the most severe corrosion occurs at sites 3 and 4, which are at the edge of the tile and

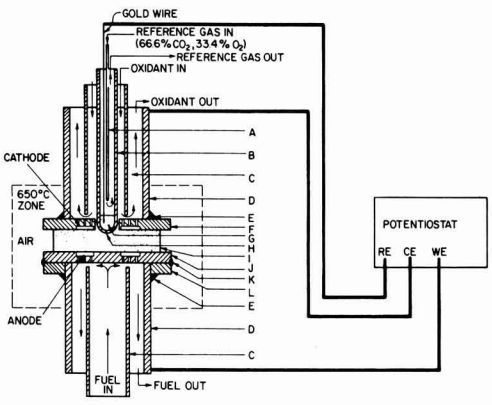


Fig. 1. Corrosion test cell. F: Cathode specimen. I: Tile. J: Anode test specimen. L: Support ring.

*Electrochemical Society Active Member.
[1]Present address: Energy Research Corporation, Danbury, Connecticut 06810.

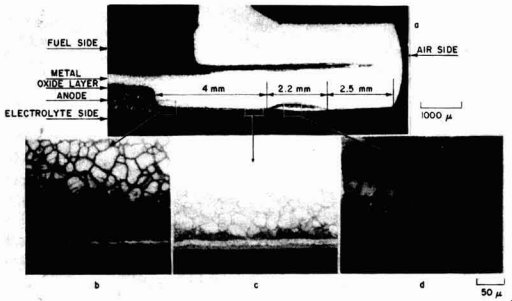


Fig. 2. Test results for Type 316 SS at open circuit. a: Cross section of entire anodic wet-seal flange and support ring. b, c, and d: Photomicrographs of coupons at indicated locations.

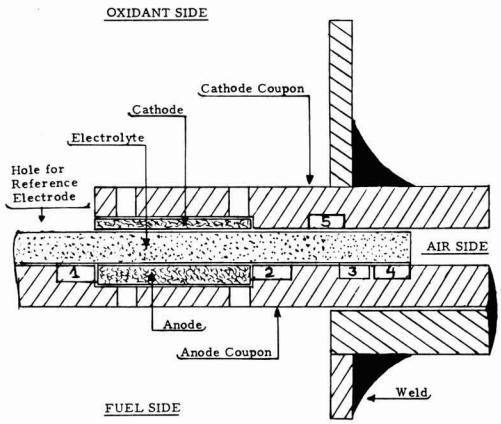


Fig. 3. Sampling sites (1-5)

nearest to the ambient air environment. This agrees with the analysis (1), which predicted that the affected area would be beyond the center of the wet seal: the metal/air corrosion cell, i_1, is stronger than the metal/H_2O cell, i_3. The corrosion in areas 3 and 4 is very similar to that caused by excess OH^- and O^{2-} ions, as described by Andersen (4), who worked with basic alkali carbonates and alkali oxides. Corrosion at the center (site 1) and the inside (site 2) of the wet seal is much less severe.

Corrosion under load.—Corrosion testing under load conditions was carried out at fuel inlet and fuel outlet conditions. Photomicrographs from test cells are shown in Fig. 4 and 5. In both types of tests, very severe corrosion is observed. A much greater rate of corrosion is observed at the inside of the anode wet seal (site 2) and its central portions (site 1) than at the outer edge; repeat tests showed similar results. Corrosion rates at these same sites (1 and 2) were much smaller in our experiments at open circuit, where the metal/air cell (i_1) had a limited operating range. Clearly, there is a shift in potential distribution in

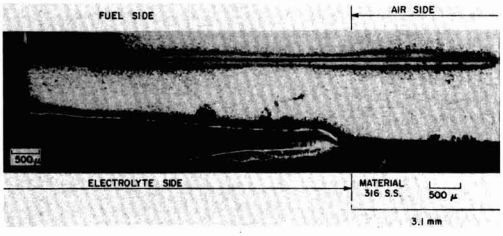


Fig. 4. Test results for Type 316 SS under load at fuel inlet conditions

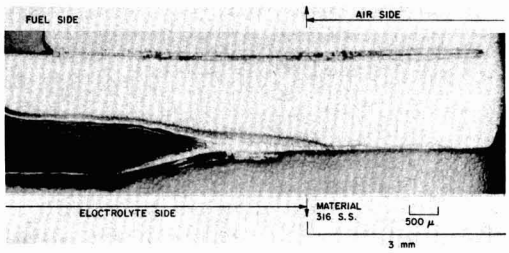


Fig. 5. Test results for Type 316 SS under load at fuel outlet conditions

the wet-seal area upon electrically loading the cell; this is caused by a new, across-tile metal/oxidant corrosion cell (i_5). The latter is the principal corrosion-causing cell when an external current is drawn.

The test cells also show somewhat greater corrosion rates at fuel outlet conditions than at fuel inlet. As our analysis predicted (1), at fuel inlet conditions corrosion cell i_3 (metal/H_2O) is relatively ineffective because of the high H_2 activity in the gas phase. This protection decreases with the conversion of the fuel, and at the fuel-outlet conditions iron will tend to corrode over a much wider area adjacent to the porous anode. Therefore, it is likely that the somewhat greater corrosion observed at fuel-outlet conditions in our experiments is indeed the result of the much lower H_2/H_2O ratio than at fuel inlet (0.85, compared to 2.82 at inlet).

Careful visual examination of the cathode coupon was carried out after termination of each test. In all the tests, a brownish, rust-like, apparently thin, oxide layer covered the surface of the coupon; the oxide layer was very uniform, with almost no sign of corrosion. To verify this, we sectioned the cathode wet-seal coupon from one test operated at open circuit. Corrosion (caused by the metal/oxidant cell, i_2) is expected to be at a maximum under these conditions. The corrosion observed at the cathode wet seal (Fig. 6) is not severe and is uniform across the sample. The corrosion morphology of the specimen nearest the porous cathode did not differ significantly from that closer to the tile-air interface.

Rates of Corrosion

Experiments under load at −1000 mV *vs.* the 67% CO_2/33% O_2 reference electrode show that the most severe corrosion of the Type 316 stainless-steel wet seal occurs at the anode side and at the inner portion of the seal. The rate of corrosion caused by the metal/oxidant cell, i_5, across the tile, was an order of magnitude greater than

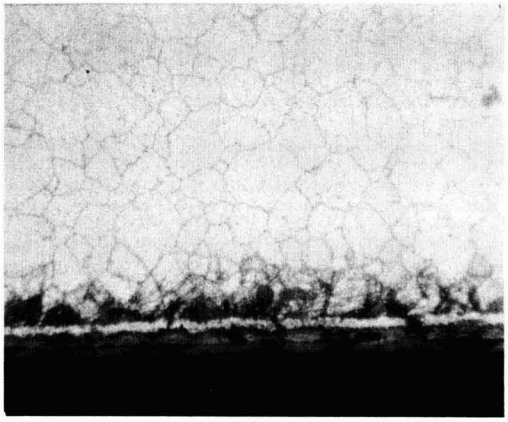


Fig. 6. Typical corrosion of the cathode wet-seal area

Table II. Corrosion of Type 316 stainless steel as a wet-seal material

	Site[a]	Open circuit	Load
		(mm/1000h)	
	1	0.035-0.041	0.43-0.60[c]
	1		0.970[d]
Anode	2	0.035-0.041	0.470-0.62[c]
	2		0.45[d]
	3	0.015[b]	
	4	0.079-0.109	
Cathode	5	0.008-0.010	0.008-0.010

[a] See Fig. 3 for location.
[b] Minimum corrosion.
[c] Maximum for fuel inlet gas conditions.
[d] Maximum for fuel outlet gas conditions.

that caused by the metal/air cell, i_1, and the metal/H_2O cell, i_3, at open circuit. The corrosion rate under load at the anode side was two orders of magnitude greater than that by the metal/oxidant cell, i_2, at the cathode wet seal under open-circuit conditions.

Corrosion rates measured in 1000h of testing under the same gas environment are collected in Table II. The metal/oxidant cell across the tile, i_5, combined with the metal/H_2O cell, i_3, under load causes 0.43-0.62 mm of corrosion. This is to be compared with the metal/H_2O cell, i_3, alone at open circuit, which is responsible for 0.036-0.040 mm, and the metal/air cell, i_1, alone at open circuit, which causes 0.08-0.11 mm of corrosion in 1000h. A somewhat greater rate of corrosion of Type 316 stainless steel is observed under fuel outlet conditions (0.45 to 0.97 mm) than under inlet conditions (0.43 to 0.62 mm). On the cathode side, at open circuit, the metal/oxidant cell, i_2, does not cause more than 0.01 mm. The latter, very low corrosion rate indicates that most of the driving force of this cell (1022 mV at open circuit) is spent in overcoming a high ohmic resistance caused by the oxide layer.

Corrosion Protection by Alumina

The corrosion rates reported above for the anode side of the wet seal are prohibitive, both at open circuit and under load. Since the largest amount of corrosion is clearly associated with the metal/oxidant cell, i_5, across the tile, corrosion protection by means of an insulating gasket covering the wet-seal faces would be an obvious solution. Such a gasket would function as a barrier to the ions and dissolved gas molecules diffusing or migrating across the tile in the wet-seal area. However, a gasket would not offer long-term protection unless it was intimately bonded to the base metal of the wet-seal flanges. Various possibilities were explored, of which alumina or compounds derived from alumina appeared most promising.

In long-term laboratory cell testing, dense alumina has been shown to be stable for over 40,000h (5). However, its direct use in the wet-seal area would be impractical from the viewpoint of thermal expansion matching in scaled-up cells, and it would also be expensive. Therefore, indirect means of forming a protective oxide layer based on Al_2O_3 were explored. Alloys known to form protective layers of aluminum oxide and aluminized metals were tested. At 923 K, the redox potential of aluminum in an air atmosphere (0.03% CO_2) is −2675 mV with respect to the (67% CO_2, 33% O_2) reference electrode. In a fuel inlet or outlet atmosphere (Table I), its potential is −2450 or −2389 mV, respectively. These potentials indicate that in an operating cell (anode potential −950 mV or more positive), aluminum will readily be oxidized, possibly at a faster rate than chromium, because the latter has a more positive redox potential. To investigate this possibility, we operated test cells with a Kanthal A-1 (Fe-Cr-Al alloy containing 5% aluminum) anode wet seal.

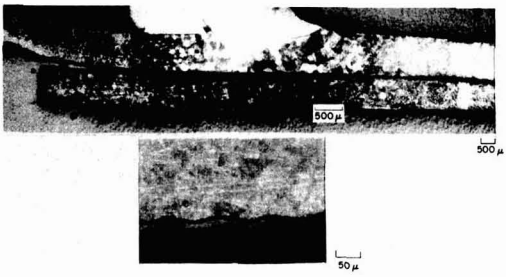


Fig. 7. Test results for Kanthal A-1 (anode wet seal) at fuel inlet conditions. The oxide coating is clearly visible in the photomicrograph at high magnification.

Visual examination of the Kanthal wet seal revealed no points of high, localized corrosion; this was confirmed by photomicrographs (Fig. 7). An almost-uniform corrosion from the fuel side to the air side of the wet seal is observed; the intensity of the corrosion is small, even though the cell was accidentally operated at 1098-1123 K for 8-15h, during which time corrosion might be expected to be accelerated by the higher temperature.

Thus, Fe-Cr-Al alloys are definitely more suitable than austenitic stainless steels as anode wet-seal material. A further possibility would be that corrosion protection could be achieved by a metallic diffusion coating of aluminum on stainless steel. This was investigated next in assemblies in which the flange surfaces had been treated by aluminum diffusion (5). Aluminized wet seals, which form an insulating layer of Al_2O_3 and or $LiAlO_2$ *in situ* during the thermal start-up of the cell, have shown negligibly small corrosion rates (less than 0.025 mm in 5000h of testing) (6). This indicates that the cell endurance desired for economic viability (40,000h) can be achieved inasmuch as wet-seal corrosion is concerned.

Summary

The experimental results presented in this paper confirm the validity of the thermodynamic and mixed-potential analysis presented earlier (1). Much greater corrosion of the anode wet seal than of the cathode wet seal is observed; for Type 316 stainless steel, the corrosion rates in a cell under load are greater by two orders of magnitude than open-circuit values. Typically, anode wet-seal corrosion of 316 stainless steel proceeds at a rate of 0.5-1 mm/1000h.

Kanthal A-1 steel (Fe-Cr-Al alloy containing 5% aluminum) was tested to assess the effectiveness of an alumina or aluminate barrier interrupting the principal, cross-tile, metal/oxidant corrosion cell. The rate of corrosion of Kanthal A-1 was small and almost uniformly distributed (0.02 mm/1000h). The results indicate that aluminum diffusion coatings are effective corrosion barriers. In long-term tests of aluminized wet seals, negligible corrosion (less than 0.025 mm in 5000h) was observed (6). This satisfies economic viability requirements.

The low rate of corrosion at the cathode side of the wet seal indicates that Type 316 stainless steel satisfies endurance requirements for molten carbonate fuel cell stacks without further modifications.

Acknowledgments

The work reported here was sponsored by the U. S. Department of Energy through Argonne National Laboratory. Guidance and suggestions by the program manager, Dr. John P. Ackerman, are very much appreciated. One of the authors (J. R. Selman) also acknowledges support by the Office of Basic Energy Sciences, U. S. Department of Energy.

Manuscript submitted June 14, 1982; revised manuscript received Feb. 27, 1984.

The Institute of Gas Technology assisted in meeting the publication costs of this article.

REFERENCES

1. R. A. Donado, L. G. Marianowski, H. C. Maru, and J. R. Selman, *This Journal*, **131**, 2535 (1984).
2. A. Borucka, "Fuel Cells," Paper presented at the 154th

National Marketing Division, Fuel Chemistry, American Chemical Society, Chicago, Sept. 10-15, 1967.
3. E. S. Argano and J. Levitan, *This Journal*, **116**, 153 (1969).
4. B. K. Anderson, Ph.D. Thesis, Technical University of Denmark, Lyngby, Denmark (1975).
5. J. R. Selman and L. G. Marianowski, in "Molten Salt Technology," D. H. Lovering, Editor, pp. 323-393, Plenum Press, New York (1982).
6. E. H. Camara, L. G. Marianowski, and R. A. Donado, U. S. Pat. 4,160,067 (1979).

Styrene Production from Ethylbenzene on Platinum in a Zirconia Electrochemical Reactor

J. N. Michaels*,[1] and C. G. Vayenas[2]

Department of Chemical Engineering, Massachusetts Institute of Technology, Cambridge, Massachusetts 02139

ABSTRACT

The vapor-phase electrochemical oxidative dehydrogenation of ethylbenzene on platinum-paste electrodes was studied at 575°-600°C in a stabilized-zirconia electrochemical reactor. Styrene and carbon dioxide were the major products. The dehydrogenation rate increased markedly with anodic current, reaching an ethylbenzene-concentration-dependent asymptote at large current densities. The rate of deep oxidation of ethylbenzene to CO and CO_2 was linear in current density. Both rates were strongly inhibited by gas-phase hydrogen. These results can be rationalized by an electrode mechanism in which the dominant charge-transfer reaction is exchange between chemisorbed oxygen on the electrode and oxygen ions in the electrolyte lattice. Styrene and CO_2 were formed primarily by catalytic reactions of ethylbenzene and neutral dissociatively adsorbed oxygen, although at least one other parallel charge-transfer reaction was evident. The current dependence of the dehydrogenation rate results from an oxidative dehydrogenation reaction on the surface whose rate is sensitive to the amount of oxygen on the electrode surface. A simple kinetic model is presented which quantitatively describes these experimental observations.

Styrene is presently produced commercially by the vapor-phase dehydrogenation of ethylbenzene over promoted iron oxide, molybdenum oxide, or mixed iron-oxide/molybdenum-oxide catalysts (1, 2). The reaction is endothermic and equilibrium-limited; under operating conditions of 580°C and atmospheric pressure, the equilibrium constant is 0.19 (3). Ethylbenzene is, therefore, diluted 1:15 in steam to increase the equilibrium conversion to styrene and to maintain the reaction temperature. Under these conditions, conversion is 55%-60% per pass (2).

A significant fraction of the cost of styrene manufacture lies in the separation of styrene from unreacted ethylbenzene. For this reason, alternative processes have been sought which increase the per-pass yield of styrene. The most widely studied among these is oxidative dehydrogenation with a suitable oxidant, such as oxygen or sulfur dioxide (4-10). A second alternative is coproduction of styrene and propylene oxide via the Oxirane process (11).

This work is part of an investigation of a third alternative, electrochemical oxidative dehydrogenation of ethylbenzene. In this process, ethylbenzene is fed to a solid-oxide electrolytic cell, reacting with electrochemically supplied oxygen to form styrene and water. This process offers three potential advantages over the conventional dehydrogenation process. First, because the overall reaction in this cell is the oxidative dehydrogenation of ethylbenzene by oxygen, the equilibrium limitation is eliminated. Second, electricity can be directly cogenerated with styrene production at an efficiency which is not Carnot-limited. Third, because of the absence of equilibrium or flammability limits, dilution of ethylbenzene is unnecessary, permitting construction of smaller reactors.

It should be noted that the economic desirability of cogenerating electricity is not obvious. Recent work by Spillman *et al.* (28) suggests that net expenditure of electrical energy to boost styrene production might be preferable to power cogeneration. Our work does not aim to evaluate the economics of electro-oxidative dehydrogenation. Rather, it attempts to illustrate the physical feasibility of the process and to understand the electrochemical kinetics of partial and complete oxidation of ethylbenzene. For this reason, no effort has been made to optimize the electrochemical reactor, nor to characterize the sources of electrical inefficiency.

The electro-oxidative dehydrogenation process is shown schematically in Fig. 1. The electrochemical reactor consists of two porous electrodes flanking a section of an oxygen-ion conducting solid electrolyte, such as yttria-stabilized zirconia. At the cathode, molecular oxygen is reduced to oxygen ions. These ions pass through the electrolyte to the anode, where they subsequently react with ethylbenzene to form styrene, water, and other by-products.

This work is an investigation of the anodic kinetics and reaction mechanism of electro-oxidative dehydrogenation of ethylbenzene. Such a study is useful in guiding the choice of suitably active and selective electrocatalysts for this process. We believe that the anodic electrode mechanism in such a system is likely to be a complex combination of electrochemical and purely catalytic steps. The simplest type of mechanism is one in which the sole charge-transfer reaction is exchange between chemisorbed oxygen on the electrode and oxygen ions in the electrolyte. In Kroger-Vink notation, this electrochemical step is

$$O_O^x = O(a) + V_O^{\cdot\cdot} + 2e'$$

where O_O^x is a lattice oxygen, $V_O^{\cdot\cdot}$ is an oxygen ion vacancy in the electrolyte, O(a) is a chemisorbed oxygen atom on the electrode surface, and e' is an electron. In this mechanism, the oxidation of ethylbenzene and other reactive species occurs by reactions with neutral chemisorbed oxygen. On the other hand, multiple charge-transfer reactions of other chemisorbed, oxidizable species with oxygen ions may occur simultaneously. For example, chemisorbed carbon monoxide or hydrogen may participate in the following reactions

$$CO(a) + O_O^x = CO_2(g) + V_O^{\cdot\cdot} + 2e'$$

$$2H(a) + O_O^x = H_2O(g) + V_O^{\cdot\cdot} + 2e'$$

Such charge-transfer reactions have been observed in similar electrochemical systems (19, 24).

*Electrochemical Society Active Member.
[1]Present address: Department of Chemical Engineering, University of California, Berkeley, California 94720.
[2]Present address: Department of Chemical Engineering, University of Patras, Patras, Greece.

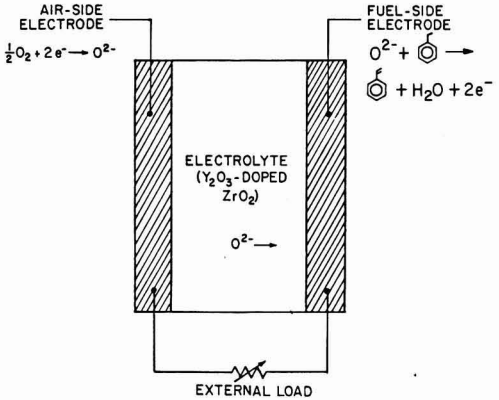


Fig. 1. Schematic of electro-oxidative dehydrogenation

This paper discusses the anode kinetics of the electrochemical cell

$$Pt/C_8H_{10}, C_8H_8, H_2O/ZrO_2(Y_2O_3)/air/Pt$$

Platinum has been chosen as the electrocatalyst in this investigation because of its activity for ethylbenzene dehydrogenation (12) and the simplicity of depositing porous, conductive films onto zirconia (13). The kinetics of styrene formation and carbon dioxide formation are discussed, and a simple electrode mechanism is proposed which quantitatively models these results. Particular attention is paid to determining the major steps in the electrode mechanism and whether multiple charge-transfer reactions occur on platinum.

Experimental

Two electrochemical reactors were constructed from 8 weight percent (w/o) yttria-stabilized zirconia tubes (Zircoa Products) having dimensions 46 cm long, 1.9 cm od, and 1.6 cm id. One of these reactors, shown schematically in Fig. 2, was designed to minimize the occurrence of homogeneous reactions of ethylbenzene; it was used in all experiments at 600°C. The active volume of this reactor was reduced from 19.5 to 2.13 cm^3 by insertion of a 44 cm long, 1.5 cm diam fused-quartz rod; the rod was centered in the zirconia tube with gold shims. Platinum-paste working electrodes were deposited on the center 10 cm of the inside and outside tube surfaces. Each working electrode was flanked by two 1 cm^2 platinum-paste reference electrodes. Platinum-paste leads were deposited from each electrode to the appropriate ends of the zirconia tube. The second reactor, used in all experiments below 600°C, had neither reference electrodes, nor a quartz rod. The active volume of this reactor was 19.5 cm^3. Each reactor was heated by a Lindberg Sola Basic tubular furnace controlled by a Love Controls Corporation Model 49 proportioning temperature controller.

Platinum-paste electrodes were deposited by painting the cleaned, masked-zirconia surfaces with one to three coats of Engelhard A-3788 fluxed platinum ink. Each coat was air dried at 60°-70°C, then calcined in air at 850°C for 30 min. The temperature was raised from room temperature to 850°C at approximately 200°C/h. Freshly deposited electrodes were dull gray in color and adhered well to the electrolyte surface. Their specific surface area was approximately 300 $cm^2/(cm^2$ superficial area) (13). The end-to-end resistance of the working electrodes at 25°C ranged between 1 and 2.5Ω. External connections to these electrodes are discussed in detail elsewhere (14).

Each reactor was shielded from extraneous electrical noise by insertion into a grounded 30 cm long, 3.8 cm od stainless steel tube. Air flowed through the annular space between the shield and reactor at a nominal flow rate of 100 cm^3 (STP)/min. At this flow rate, both the pressure drop and external mass transfer resistance were negligible, and the oxygen partial pressure at the cathode surface remained constant at 0.21 atm.

The reactors were controlled galvanostatically by an AMEL Model 549 potentiostat/galvanostat. The current and voltages between any pair of electrodes were measured with Fluke Model 8600A digital multimeters (voltmeter input impedance $10^7\Omega$). The cell working voltage and the anodic overpotential were monitored continuously with a two-pen chart recorder (input impedance $10^6\Omega$). The anodic overpotential was measured using the adjacent downstream reference electrode. Because these electrodes were made of the same material and, therefore, catalyzed the same electrode reactions, the measured overpotential was insensitive to the overall conversion of ethylbenzene.

In a typical experiment, feed conditions and the cell current density were set, and the system was allowed to reach steady-state conditions. The approach to steady state was followed by monitoring the cell working voltage and, when possible, the anodic overpotential. When the voltages stabilized, the feed and product-stream compositions were analyzed by on-line gas chromatography, and the cell current, the feed and product volumetric flow rates, and all relevant voltages were measured. All results discussed below are steady-state results.

The reactors were differential with respect to ethylbenzene conversion; total conversion was limited to 15% or less in all experiments. Reaction rates, therefore, were calculated directly from product flow rates. Reaction rates, rate constants, and cell current are normalized by the area of active electrolyte.

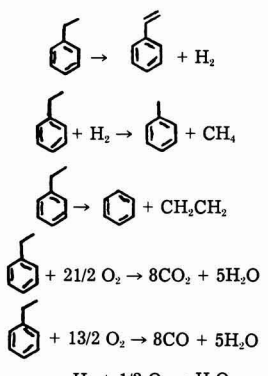
The experimental flow system and gas-chromatographic analytical system are discussed in detail elsewhere (14, 15).

Results

Three experiments are discussed below. In the first, ethylbenzene diluted with helium was fed to the reactor, and the rates of product formation were measured as a function of current density. In the second, hydrogen was added to the ethylbenzene/helium feed stream, and the same measurements repeated. In the third, oxygen was added to the ethylbenzene/helium feed stream, and the rates of product formation were measured at open circuit.

In all experiments, detectable products included H_2, CO, CO_2, water, methane, ethylene, benzene, toluene, and styrene. Neither working electrode lost electrochemical activity during the duration of the experiments. The carbon atom balance closed to within ±2%, suggesting that coke formation on the anodic surface is insignificant.

The overall reactions which occur in the electrolytic cell may be summarized as follows



This list is not exhaustive; rather, it represents the predominant reactions responsible for the final product distribution. Because this reaction system is so complex, it is convenient to lump the production of CO and CO_2 and that of benzene and toluene in the analysis of the rate data. The rate of formation of CO and CO_2 is termed the

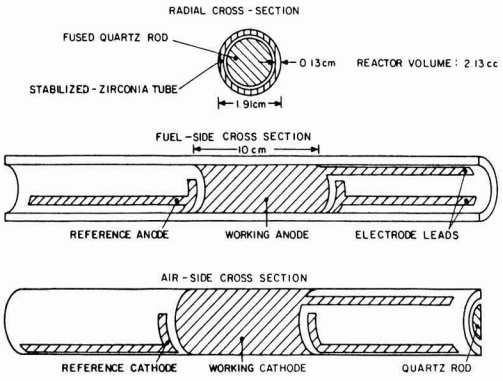


Fig. 2. Stabilized-zirconia electrochemical reactor: annular geometry

"deep oxidation" rate and is designated by r_{DO}; the rate of benzene and toluene formation is called the "dealkylation" rate and is designated by r_{DA}. The rate of styrene production is synonymous with the "dehydrogenation" rate and is designated by r_{DH}.

Due to the diversity of the experimental measurements, the discussion of results is divided into two subsections. The division is based on the primary goals of this work: elucidation of the prominent steps in the electrode mechanism; and detection of the predominant charge-transfer reactions. The behavior of the dehydrogenation, deep oxidation, and dealkylation rates are discussed in the first subsection. These measurements are summarized in Fig. 3-6. The current-voltage characteristics of the anode and the effect of gas-phase oxygen on the reaction rates, summarized in Fig. 7 and 8, are discussed in the second subsection.

Electrode mechanism.—Dehydrogenation.—When no hydrogen or oxygen is present within the feed, the dehydrogenation rate is strongly current dependent, as shown in Fig. 3a. At low ethylbenzene concentrations and moderate current densities, the rate of styrene production is as much as six times larger than that at open circuit; the enhancement of the dehydrogenation rate saturates at large current densities. This behavior suggests that dehydrogenation of ethylbenzene occurs by two pathways on the platinum electrode. The first pathway is a nonoxidative reaction which produces styrene and hydrogen. The second pathway is an oxidative pathway which ultimately produces styrene and water, whose rate is dependent on the supply of oxygen to the electrode surface.

Further evidence of this dual-pathway dehydrogenation mechanism is furnished by the experiments with hydrogen/ethylbenzene mixtures. As shown in Fig. 4a, the dehydrogenation rate at a given current density decreases as the hydrogen concentration in the feed increases. This indicates that dehydrogenation of ethylbenzene is inhibited by hydrogen. This inhibition is evident only at nonzero current densities; the open-circuit dehydrogenation rate is independent of the hydrogen concentration. These results suggest that styrene is formed in two parallel, independent surface reactions: a nonoxidative pathway which is insensitive to current density and hydrogen concentration; and an oxidative pathway which is current dependent and strongly inhibited by gas-phase hydrogen.

Deep oxidation.—The deep oxidation rate in the absence of gas-phase hydrogen is linear in current density and zero order in ethylbenzene, as shown in Fig. 3b. Oxygen atom balances indicate that all of the electrochemically supplied oxygen is accounted for by the formation of CO, CO_2, and water; no oxygen is detected in the gas phase. The linearity of the rate, therefore, is simply a consequence of Faraday's law. The rate of production of all oxygenated species must be proportional to the current density and independent of gas-phase composition. Although

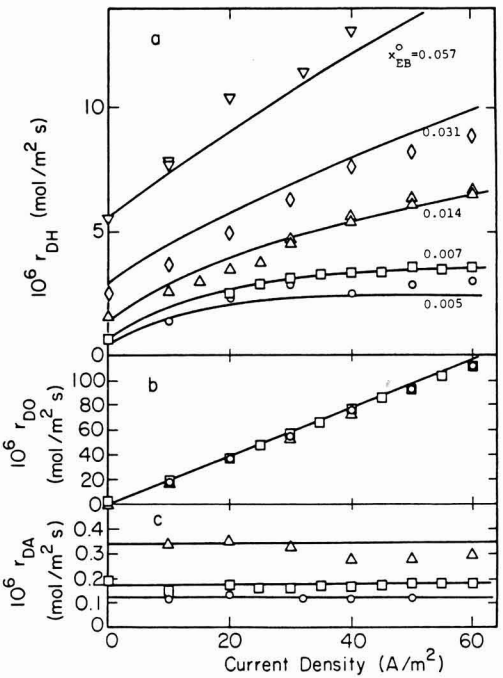


Fig. 3. Reaction rates at 575°C. Feed ethylbenzene mole fraction: ○ 0.48%; □ 0.70%; △ 1.44%; ◇ 3.12%; ▽ 5.72%. (a, Top) dehydrogenation rate; (b, middle) deep oxidation rate; (c, bottom) dealkylation rate: — Calculated rate.

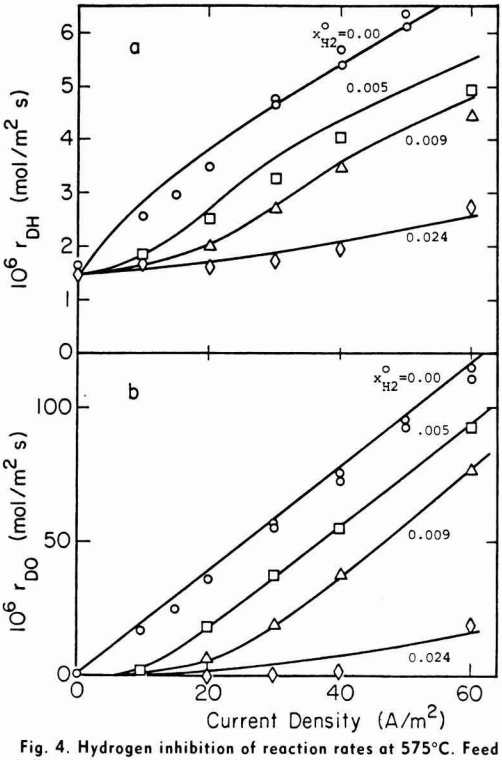


Fig. 4. Hydrogen inhibition of reaction rates at 575°C. Feed ethylbenzene mole fraction: 1.48%. Feed hydrogen mole fraction: ○ 0.00%; □ 0.51%; △ 0.94%; ◇ 2.36%. (a Top) dehydrogenation rate; (b bottom) deep oxidation rate. — Calculated rate.

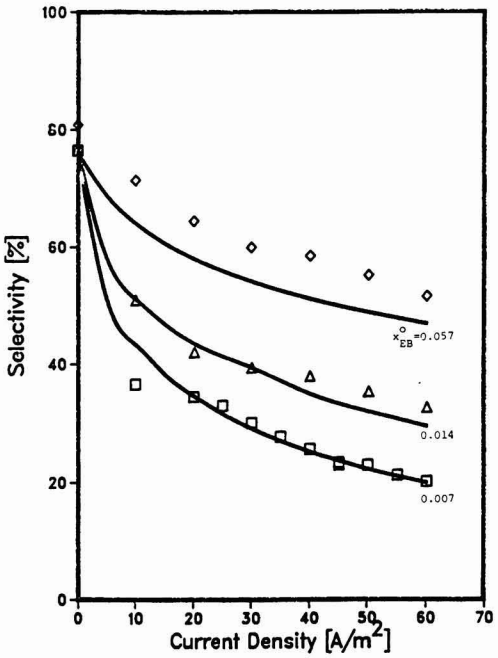


Fig. 5. Selectivity to styrene at 575°C. Feed ethylbenzene mole-fraction: □ 0.70%; △ 1.44%; ▽ 5.72%. — Calculated selectivity.

small amounts of water are produced by oxidative dehydrogenation of ethylbenzene, all of the oxides of carbon and most of the water are produced by deep oxidation. Therefore, the deep oxidation rate should be nearly linear in current and independent of ethylbenzene concentration, as observed. It is interesting to note that the absence

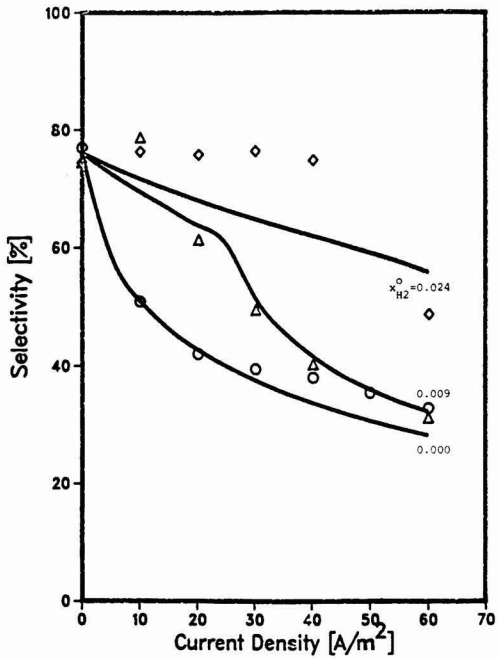


Fig. 6. Hydrogen enhancement of selectivity to styrene at 575°C. Feed ethylbenzene mole fraction: 1.48%. Feed hydrogen mole fraction: ○ 0.00%; △ 0.94%; ◇ 2.36%. — Calculated selectivity.

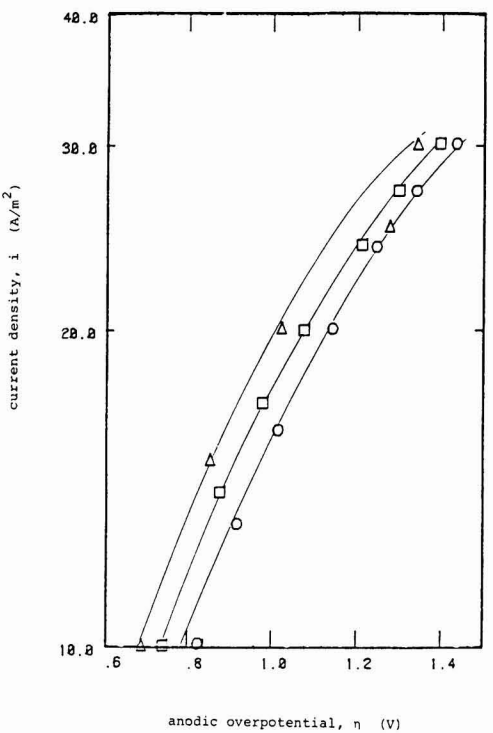


Fig. 7. Anodic overpotential at 600°C. Feed ethylbenzene mole fraction: ○ 0.47%; □ 0.86%; △ 1.94%. — Calculated overpotential.

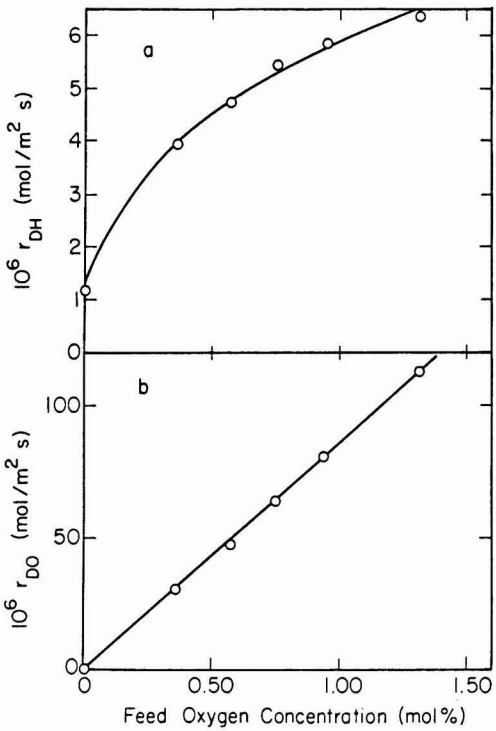


Fig. 8. Effect of gas-phase oxygen on open-circuit reaction rates at 575°C. Feed ethylbenzene mole fraction: 1.42%. (a Top) dehydrogenation rate; (b bottom) deep oxidation rate.

of oxygen evolution at the anode implies that the deep oxidation of ethylbenzene is oxygen limited.

As shown in Fig. 4b, the deep oxidation rate is strongly inhibited by addition of hydrogen to the gas phase. In contrast to the dehydrogenation rate, the deep oxidation rate is reduced to zero by large hydrogen concentrations. This behavior is suggestive of simple competition between hydrogen and ethylbenzene for available oxygen on the electrode surface in parallel surface reactions. The large inhibition of r_{D0} implies that oxidation of hydrogen on the surface is significantly faster than that of ethylbenzene.

Dealkylation.—In contrast to the dehydrogenation and deep oxidation rates, the dealkylation rate is independent of current density. This is shown in Fig. 3c. This behavior suggests that dealkylation is a nonelectrochemical, catalytic reaction which occurs in parallel with dehydrogenation and deep oxidation of ethylbenzene.

Selectivity to styrene.—The experimental results shown in Fig. 3 and 4 may be simply summarized by plotting the selectivity to styrene as a function of current density. This has been done in Fig. 5 and 6, respectively, where some of the data shown in Fig. 3 and 4 have been removed for clarity. The selectivity to styrene in these figures is defined as the ratio of the dehydrogenation rate to the total rate of consumption of ethylbenzene.

In the absence of gas-phase hydrogen, the selectivity decreases markedly with current density, as shown in Fig. 5. This current dependence is the result of deep oxidation of ethylbenzene. The selectivity decreases with decreasing ethylbenzene concentration at nonzero current densities because the deep oxidation rate is zero order in ethylbenzene, while the dehydrogenation rate is positive order. At open circuit, no CO_2 is formed, and the selectivity is 78% and is concentration independent; this value is determined by the relative rates of dehydrogenation and dealkylation, which are each first order in ethylbenzene.

The selectivity in the presence of significant amounts of gas-phase hydrogen is shown in Fig. 6. The selectivity increases and becomes less sensitive to changes in current density as the hydrogen concentration increases. Both of these effects are due primarily to the inhibition of the deep oxidation rate by hydrogen.

Charge-transfer reactions.—The results discussed above present an overview of the important steps in the anode reaction mechanism. It is clear that some steps in this mechanism are nonoxidative and, therefore, purely catalytic. However, among the oxidative reactions, it is not possible to distinguish between catalytic reactions with neutral chemisorbed oxygen and charge-transfer reactions with oxygen ions. This question is addressed most directly by measurement of the anodic overpotential. Tafel plots of the anodic overpotential measured at 600°C are shown in Fig. 7. These measurements are not compensated for the ohmic drop between the reference and working electrodes; this is the source of the curvature of the plots. Unfortunately, the ohmic resistance was not determined by current interruption; therefore the data were fit by the high-field limit of the Butler-Volmer equation, modified to account for the significant ohmic contribution to the overpotential.

$$\eta_m = \frac{RT}{\alpha \mathbf{F}} \ln (i/i_o) + IR_E$$

where η_m is the measured overpotential, η is the activation overpotential, α is the transfer coefficient, i_o is the exchange-current density, $\mathbf{F}$ is the Faraday constant, R is the gas constant, T is the absolute temperature, I is the total cell current, and R_E is the uncompensated resistance. The solid lines in Fig. 7 are calculated with $\alpha = 1.0$, $R_E = 5.5\Omega$, and exchange-current densities of 0.015, 0.028, and 0.060 A/m^2 at feed ethylbenzene mole fractions of 0.0047, 0.0086, and 0.0194, respectively. As discussed in detail in the following section, a transfer coefficient of unity is consistent with oxygen oxidation/reduction's being the major anodic charge-transfer reaction. On the other hand, the ethylbenzene-concentration dependence of i_o suggests that an additional exchange reaction also occurs in the electrode mechanism.

The variation of the open-circuit dehydrogenation and deep oxidation rates with oxygen partial pressure also suggests that oxygen exchange is the dominant anodic charge-transfer reaction. As shown in Fig. 8, the dehydrogenation rate increases rapidly to a constant value as the oxygen pressure increases, and the deep oxidation rate is first order in oxygen. Furthermore, oxygen is fully consumed in the production of CO, CO_2, and water. These results are qualitatively similar to the electrochemical results shown in Fig. 3. This similarity suggests that the reactions of oxygen and ethylbenzene are insensitive to the source of oxygen. This is consistent with an electrode mechanism in which ethylbenzene reacts with neutral chemisorbed oxygen in nonelectrochemical steps.

Discussion

These results strongly suggest that electro-oxidation of ethylbenzene on platinum occurs mainly by chemical, rather than electrochemical, steps. Oxygen ions are rapidly oxidized to neutral adatoms, and these subsequently react with ethylbenzene and hydrogen to form styrene, CO_2, and water. Dehydrogenation of ethylbenzene occurs by two parallel surface reactions, one nonoxidative, the other oxidative. Deep oxidation of ethylbenzene and hydrogen are rate limited by oxygen supply to the electrode surface. Small amounts of toluene and benzene are formed in parallel, purely catalytic reactions.

These ideas are incorporated into the following kinetic model, which quantitatively describes the observed electrode kinetics. This model does not attempt to describe all of the reaction steps and intermediates involved in ethylbenzene dehydrogenation and deep oxidation. That would be a formidable task and is not justified by the extent of the data. Rather, emphasis is placed on developing the simplest model which captures the important aspects of the qualitative mechanism described above and adequately describes the experimental observations. Additional details of this model are presented in Ref. (15). For simplicity, the dealkylation reactions are ignored due to their small contribution to the overall conversion of ethylbenzene. Deep oxidation of styrene and production of carbon monoxide are also neglected.

This model contains three major assumptions. First, oxygen exchange is the sole charge-transfer reaction. Second, two forms of uncharged oxygen coexist on the platinum surface. The first form is mobile, chemisorbed oxygen, which reacts with adsorbed hydrocarbons and hydrogen to form CO_2 and water. The second form is a surface "oxide" which oxidatively dehydrogenates adsorbed ethylbenzene to styrene and water. This assumption is supported by studies of cyclohexane dehydrogenation on platinum single crystals; these studies show the dehydrogenation rate to be enhanced by preoxidation of the crystal surface (15, 27). The third assumption is that interchange between the two forms of oxygen is rapid and can be modeled as an equilibrium. Thus, an increase in the coverage of chemisorbed oxygen increases the coverage of the oxide and concommitantly increases the oxidative-dehydrogenation rate.

The catalytic surface is therefore modeled to have two types of sites, S1 and S2. All gas-phase species absorb and react on S1 sites. Nothing in the gas-phase adsorbs on S2 sites. Rather, S2 sites are "oxidized" by available chemisorbed oxygen and subsequently react with adjacent adsorbed ethylbenzene molecules to form styrene and water. Ethylbenzene and styrene are assumed to be in adsorption equilibrium on S1 sites at suitably low coverages such that their isotherms are linear. This assumption appears to be justified by the low desorption temperature of benzene on clean and carbon-covered platinum surfaces (18). Hydrogen and oxygen adsorb dissociatively on the S1 sites; hydrogen is assumed to be in adsorption equilibrium and at low coverage (25, 26).

Because the deep oxidation reactions are oxygen limited, oxygen is not in adsorption equilibrium.

In the absence of gas-phase oxygen, the sole source of oxygen atoms to S1 sites on the anode is the oxygen-exchange reaction

$$O_O^x \rightarrow O(a) + V_O^{\cdot\cdot} + 2e' \quad [1]$$

Since this is the only charge-transfer step in the mechanism, Faraday's law requires that the rate of oxygen adsorption on S1 sites equals the oxygen ion flux to the anode, $j_O = i/2\mathbf{F}$. Once adsorbed on the anode, the oxygen atoms can react with adsorbed ethylbenzene and hydrogen to produce CO_2 and water. It is assumed that the rate-determining step in each reaction is first order in the adsorbed reactants with the rate constants shown in Eq. [2] and [3]

$$C_8H_{10}(a) + O(a) \xrightarrow{k_{DO}} 8CO_2(g) + 5H_2O(g) \quad [2]$$

$$H(a) + O(a) \xrightarrow{k_{HO}} H_2O(g) \quad [3]$$

These reactions are written nonstoichiometrically to emphasize the molecularity of their rate-determining steps. Furthermore, chemisorbed oxygen can oxidize S2 sites. It is assumed that surface oxidation is rapid and that equilibrium between adsorbed oxygen and the oxidized surface is achieved at steady state. If the oxide has stoichiometry S20, this equilibrium is written

$$O(a) + S2 \overset{K_*}{=} S1 + S20 \quad [4]$$

where K_* is the oxidation equilibrium constant.

Finally, ethylbenzene dehydrogenation is assumed to occur by two parallel reactions. The first is a nonoxidative surface reaction whose rate-determining step is first order in adsorbed ethylbenzene

$$C_8H_{10}(a) \xrightarrow{k_{DH}} C_8H_8(a) + 2H(a) \quad [5]$$

The second is an oxidative reaction which is first order in ethylbenzene and oxidized sites

$$C_8H_{10}(a) + S20 \xrightarrow{k_*} C_8H_8(a) + H_2O(g) \quad [6]$$

k_{DH} and k_* are the rate constants of the nonoxidative and oxidative dehydrogenation rate-determining steps, respectively.

Reaction rates and selectivities calculated with this model are shown by the solid lines in Fig. 3-6. Because hydrogen conversion in most measurements is large, calculation of the rates required integration of the appropriate rate expressions over the hydrogen profiles in the reactor. Details of these calculations are presented elsewhere (14, 15). The model correctly predicts the "Langmuir-type" behavior of the dehydrogenation rate and the ethylbenzene-concentration independence of the deep oxidation rate at low hydrogen concentrations. The inhibitory effect of hydrogen is also correctly described. The "break" in the selectivity at the intermediate hydrogen concentration shown in Fig. 6 is a real effect. This occurs at the current density at which the hydrogen conversion first reaches 100%. At larger current densities, the hydrogen concentration is zero in an increasing fraction of the reactor, and the deep oxidation rate is uninhibited in the same region. Because the uninhibited rate is so much greater than the rate in the presence of hydrogen, quantitative conversion of hydrogen in the latter stages of the reactor results in a dramatic loss of selectivity to styrene. The large discrepancy between the measured selectivity and calculated selectivity at the highest hydrogen concentration is caused by inaccurate measurement of very small carbon dioxide concentrations.

This model oversimplifies the electrochemistry at the platinum anode by assuming a single charge-transfer reaction. If the only exchange reaction at the electrode-electrolyte interface were oxygen exchange (Eq. [1]), the anodic overpotential would be well described by the Butler-Volmer equation with transfer coefficients of unity (19-23)

$$i = i_o [\exp(\eta\mathbf{F}/RT) - \exp(-\eta\mathbf{F}/RT)] \quad [7]$$

This agrees well with the measured overpotential. However, the exchange current density should vary with the surface coverage of chemisorbed oxygen, according to (20)

$$i_o = 2eK_r[\theta_0(1 - \theta_0)]^{1/2} \quad [8]$$

where e is the electronic charge, K_r is the geometric average of the forward and reverse rate constants of reaction [1], and θ_0 is the oxygen surface coverage at open circuit. At the temperatures of interest, the coverage of chemisorbed oxygen should be small (18), and the exchange current should decrease monotonically with decreasing oxygen coverage. Since deep oxidation of ethylbenzene is oxygen limited, increasing the ethylbenzene concentration should decrease the steady-state oxygen coverage by increasing the surface reaction rate. Thus, i_o should decrease with increasing ethylbenzene concentration. The measured exchange current density displays the opposite behavior. Therefore, it appears that a second exchange reaction occurs in parallel with reaction [7]. Because of the extent of deep oxidation and dehydrogenation of ethylbenzene, it is likely that there is a significant amount of hydrogen on the electrode surface. Thus, a possible charge-transfer reaction is direct oxidation of adsorbed hydrogen atoms

$$2H(a) + O_O^x = H_2O + V_O^{\cdot\cdot} + 2e' \quad [9]$$

This exchange reaction has been observed previously on nickel electrodes (24). When the surface coverage of hydrogen is small, the exchange current of this reaction should increase with increasing hydrogen coverage. Thermal programmed desorption results suggest that hydrogen is in dissociative-adsorption equilibrium and is at low coverages under conditions of interest (25, 26); therefore, hydrogen coverage increases with increasing hydrogen partial pressure. Because the dehydrogenation rate is positive order in ethylbenzene, the average hydrogen concentration in the reactor increases and increasing ethylbenzene concentration. For this reason, the exchange current of reaction [1] also should increase with increasing ethylbenzene mole fraction.

Conclusion

The dehydrogenation rate of ethylbenzene is significantly enhanced by electrochemical supply of oxygen to a platinum-paste anode. In the absence of significant amounts of gas-phase hydrogen, the major by-product is CO_2. Addition of hydrogen to the reactor feed inhibits dehydrogenation and deep oxidation; in the limit of large hydrogen partial pressures, the dehydrogenation rate approaches its value at open circuit, and the deep oxidation rate approaches zero.

The anodic electrode kinetics are well described by a model which assumes that the sole electrochemical reaction is exchange of dissociatively adsorbed oxygen and oxygen ions in the electrolyte lattice. Electrochemically supplied oxygen adatoms subsequently react with adsorbed ethylbenzene and hydrogen to form carbon dioxide and water, or with the platinum surface to form a surface oxide. Adsorbed ethylbenzene reacts with this oxide in an oxidative-dehydrogenation reaction to form styrene and water. This surface reaction is responsible for the electrochemical enhancement of the dehydrogenation rate.

This kinetic model oversimplifies the anodic electrode mechanism by assuming oxygen exchange is the sole charge-transfer reaction. The current-voltage characteristics of the anode suggest that oxygen exchange is indeed an important step in the mechanism. However, at least one other parallel charge-transfer reaction is apparent.

From a practical standpoint, the performance of these reactors is hampered by platinum's activity as a nonspecific oxidation catalyst. A better choice for the anodic material might be an active and selective oxidative-dehydrogenation catalyst with suitably large electrical conductivity. Another possible improvement is suggested by the inhibitory effect of hydrogen. If a hydrogen-rich mixture of styrene and ethylbenzene were produced in the vicinity of a platinum anode, hydrogen could be selectively oxidized from the mixture electrochemically, shifting the equilibrium toward styrene and potentially generating electricity. This could be accomplished by packing a platinum-anode solid-oxide fuel cell with a commercial dehydrogenation catalyst. Preliminary work with both of these approaches is reported elsewhere (14).

Acknowledgments

The authors thank Professor James Wei at MIT and Ms. Karrie Hanson at University of California, Berkeley for their contributions to this work. The project was supported by the Department of Energy, Grant no. DE-AC02-80ER10694.

Manuscript submitted Feb. 27, 1984; revised manuscript received June 8, 1984.

LIST OF SYMBOLS

(a) chemisorbed species
(g) gas-phase species
e electronic charge
$\mathbf{F}$ Faraday's constant
I total current
i current density
i_o exchange-current density
j_0 oxygen ion flux to anode
K_f geometric-average rate constant for oxygen exchange
K_* surface oxidation equilibrium constant
k_i rate constant of ith reaction
k_* surface oxidation-dehydrogenation rate constant
R gas constant
R_E uncompensated electrode resistance
r_i rate of ith reaction
T absolute temperature

Greek Symbols

α transfer coefficient
η activation overpotential
η_m measured overpotential
θ_0 surface coverage of chemisorbed oxygen

Subscripts

DA dealkylation
DH dehydrogenation
DO deep oxidation
HO hydrogen oxidation

REFERENCES

1. W. W. Kaeding, *Catal. Rev.*, **8(2),** 307 (1973).
2. C. L. Thomas, "Catalytic Processes and Proven Catalysts," pp. 47-48 Academic Press, New York (1970).
3. L. Gutman, E. F. Westrum, and K. S. Pitzer, *J. Am. Chem. Soc.*, **95,** 1246 (1943).
4. T. G. Alkhazov, A. E. Lisovskii, M. G. Safarov, and A. M. Dadsheva, *Kinet. Katal.* **13,** 509 (1972).
5. A. Cortes and J. L. Seoane, *J. Catal.*, **34,** 7 (1974).
6. Z. Dziewieke and A. Makawski, *React. Kinet. Catal. Lett.*, **13,** 51 (1980).
7. K. Fujimoto and T. Kunugi, *Ind. Eng. Chem., Proc. Des. Dev.*, **20,** 319 (1981).
8. C. R. Adams and T. L. Jennings, *J. Catal.*, **17,** 152 (1970).
9. N. J. Gaspar, A. D. Cohen, M. Vadekar, and I. S. Pasternak, *Can. J. Chem. Eng.* **53,** 79 (1975).
10. M. Vadekar, I. S. Pasternak, and N. J. Gaspar, *ibid.*, **52,** 788 (1974).
11. "SRI International Chemical Economics Handbook," Stanford Research Institute, Menlo Park, CA, (1982).
12. F. E. Shepard and J. J. Rooney *J. Catal.*, **3,** 129 (1964).
13. R. D. Farr, MS. Thesis, MIT, Cambridge, MA (1979).
14. J. N. Michaels, Sc.D. Thesis, MIT, Cambridge, MA (1983)
15. C. G. Vayenas and J. N. Michaels, *J. Catal.*, **85,** 477 (1984).
16. R. C. Reid, J. M. Prausnitz, and T. K. Sherwood, "The Properties of Liquids and Gases", pp. 629-65 McGraw Hill, New York (1977).
17. C. G. Vayenas, B. Lee, and J. N. Michaels, *J. Catal.*, **66,** 36 (1980).
18. J. L. Gland, *Surf. Sci.*, **93,** 487 (1980).
19. T. H. Etsell and S. N. Flengas, *Chem. Rev.*, **70,** 339 (1970).
20. D. Y. Wang and A. S. Nowick, *This Journal*, **126,** 1159 (1979).
21. T. H. Etsell and S. N. Flengas, *ibid.*, **118,** 1890 (1971).
22. D. Braunstein, D. S. Tannhauser, and I. Riess, *ibid.*, **128,** 82 (1981).
23. D. Y. Wang and A. S. Nowick, *ibid.*, **126,** 1166 (1979).
24. E. J. L. Schouler, M. Kleitz, E. Forest, E. Fernandez, and P. Fabry, *Solid State Ionics*, **5,** 559 (1981).
25. R. W. Mcabe and L. D. Schmidt, *Surf. Sci.*, **60,** 85 (1976).
26. S. M. Davis and G. A. Somorjai, *ibid.*, **91,** 73 (1980).
27. C. E. Smith, J. P. Biberian, and G. A. Somorjai, *J. Catal.*, **57,** 426 (1979).
28. R. W. Spillman, R. M. Spotnitz, and J. T. Lundquist Jr., *Chemtech*, **14,** 176 (1984).

A Theoretical Comparison of Flow-Through and Flow-By Porous Electrodes at the Limiting Current

Tim Risch*,[1]

Acurex Corporation, Aerotherm Division, Mountain View, California 94039

John Newman**

Materials and Molecular Research Division of Lawrence Berkeley Laboratory, and Department of Chemical Engineering, University of California, Berkeley, California 94720

ABSTRACT

A limiting current model for the potential and concentration distribution for a flow-by porous electrode of infinite length to width ratio is developed and compared to previous models of Alkire and Ng and Fedkiw. For flow-by electrodes of practical interest, the maximum solution phase potential drop is shown to be dependent upon one relevant parameter: the product of the electrode width and the reciprocal of the penetration depth, ad. Criteria delineating the optimal electrode configuration are given using this potential difference as a basis for comparison. Results of the comparison show that the criteria are dependent upon reactant conversion but independent of any specific mass-transfer correlation.

Packed-bed porous electrodes have become increasingly attractive in the past several years for use in a number of industrially important processes. These electrodes have been suggested for such diverse applications as removal of dilute metal ions from waste streams (1), electroorganic synthesis (2), and off-peak energy storage (3).

Two principal configurations for packed-bed electrodes have been developed: the flow-through configuration, where fluid flow and current are parallel; and the flow-by configuration, where the fluid flows perpendicularly to the current. Both configurations are illustrated in Fig. 1, where the porous electrodes are represented by rectangles and the separators by dashed lines. For simplicity, we choose to represent the counterelectrodes as planar electrodes; however, in general, the counterelectrodes can also be porous electrodes.

Figure 1a illustrates a flow-through electrode with an upstream counterelectrode. An upstream counterelectrode is favored over a downstream counterelectrode in the flow-through configuration, because it gives a lower ohmic potential drop, particularly at high conversions (4). The Y direction denotes the direction of fluid flow in the figure. For the flow-through configuration, the flow is divided as it enters and flows in different directions through the working electrode and counterelectrode. Current generated within the porous electrode flows in the same spatial direction as the fluid flow.

Figure 1b illustrates a flow-by configuration. For the flow-by configuration, the fluid flow is again divided, but here the flow to the working electrode and counterelectrode remains in the same direction. In this configuration, current generated within the porous electrode travels generally in the X direction, which is perpendicular to the direction of the fluid flow.

Bennion and Newman (1) developed a one-dimensional model for the flow-through electrode assuming its performance to be limited only by the transport of reactants from the bulk stream to the surface of the electrode. More realistic one-dimensional models for the flow-through electrode not restricted to this "limiting current" assumption have subsequently been developed (5). These models incorporate equilibrium constraints, finite rate kinetics, and parasitic side reactions in addition to the transport of reactants.

Because the fluid and current travel in the same direction in the flow-through configuration, the analysis remains one-dimensional even in the general case. In the flow-by configuration, however, the general analysis is necessarily two-dimensional. The absence of a common space variable for the fluid and current flow requires that the analysis be formulated in terms of partial differential equations, unless simplifications are made.

Alkire and Ng (6, 7) simplified the analysis of the flow-by electrode by assuming current flow to travel directly perpendicular to the fluid flow. This assumption reduces the equation for the potential distribution from a partial differential equation to an ordinary differential equation. Recently, Fedkiw (8) analyzed the special case of a flow-by electrode at the limiting current by including the two-dimensional nature of the current distribution and the effects of the finite electrode length. However, he included in his analysis a single specific dependence of the mass-transfer coefficient on velocity. Stork *et al.* (8, 9), in two recent papers, give theoretical and experimental results for the potential distribution in a flow-by electrode. The theoretical model they present is essentially the same limiting current analysis given by Fedkiw. Some experimental measurements of the potential distribution inside a flow-by electrode are also given which compare well with results of their calculations.

Alkire and Ng (6, 7), Trainham and Newman (2), and Fedkiw (8) have all considered the selection of the optimum electrode configuration for a given application. Trainham and Newman developed a method, applicable below the limiting current, to select the optimum con-

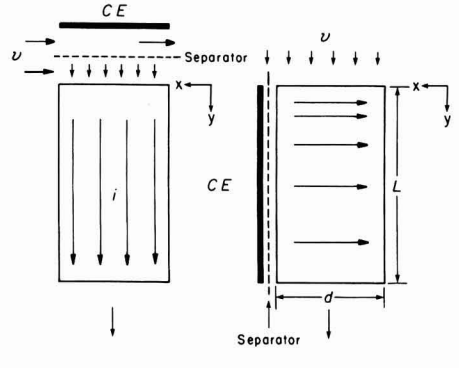


Fig. 1. Porous electrode configurations (a): flow-through electrode, upstream counterelectrode. (b): Flow-by electrode.

*Electrochemical Society Student Member.
**Electrochemical Society Active Member.
[1]Present address: Acurex Corporation, Aerotherm Division, Mountain View, California 94039.

figuration. Alkire and Ng, followed by Fedkiw, considered the choice of the optimum configuration at the limiting current. Alkire and Ng maximized the volumetric current density to compare the two configurations. Fedkiw compared the maximum solution-phase potential drop for the flow-through configuration to the maximum solution phase potential for the flow-by electrode. Equal electrode volumes and identical flow velocities were chosen as fixed quantities for these two comparisons. At the limiting current, the maximization of the volumetric current density or the minimization of the maximum ohmic potential drop lead to the same result.

The results of Alkire and Ng and Fedkiw can be reconciled by an order-of-magnitude analysis. This can be useful in determining the approximate conditions under which the flow-by configuration is superior to the flow-through configuration at the limiting current. Consider a flow-through and a flow-by electrode of equal dimensions and feed flow rates and with identical packings and feed compositions. Each reactor has a length L, width d, and height W. At the limiting current, the reactant flows through the electrode and reacts at a rate determined solely by the type of packing and the magnitude of the fluid flow. The distribution of the reaction and the total current will therefore be identical in the two reactors. For high conversions of reactant to product, most of the reactant will be depleted in a region very near the front of the electrode. The characteristic length of this region is the penetration depth, denoted by $1/\alpha$. Most of the current in the flow-through electrode with an upstream counter-electrode, must travel an approximate distance $1/\alpha$, through an area of Wd. The majority of the current in the flow-by electrode, however, need only travel a distance comparable to the width of the electrode d, through an area of W/α. The superior electrode configuration is the configuration that yields a lower ohmic potential drop. The ohmic potential drop is the product of the total current times the length of travel divided by the cross sectional area to current flow. A comparison of the ohmic drop shows that the flow-by electrode configuration is preferred for high conversions if the approximate condition

$$\alpha d < 1 \qquad [1]$$

is satisfied. This result is identical to the result obtained by Alkire and Ng when they maximized the volumetric current density to compare configurations.

At low conversions, however, the penetration length eventually becomes comparable to the electrode length. In this limit, the current in the flow-through electrode now flows a distance L, rather than $1/\alpha$. Likewise, in the flow-by electrode, the current flows through an area of WL. Equating the ohmic potential drop in the low-conversion limit results in the criterion that the flow-by configuration is favored for

$$\frac{L}{d} > 1 \qquad [2]$$

Equation [1] shows that, at high conversions, the parameter αd is of primary importance in distinguishing the optimum electrode configuration and in determining the maximum potential drop in the flow-by configuration. At low conversions, Eq. [2] shows L/d can be expected to be the parameter of primary importance in determining the optimum configuration.

In this paper, we propose a limiting form solution to the two-dimensional potential distribution for large αd. This solution shows that the maximum solution-phase potential drop for the flow-by electrode is primarily dependent upon the parameter αd, with only a secondary dependence upon L/d. We then reexamine potential distribution derived by Fedkiw to determine the conditions under which the two-dimensional nature of the current distribution and the effects of the finite electrode should be included. This new solution, along with the expressions derived by Fedkiw and Alkire and Ng, is presented in a form that is not restricted to the single mass-transfer correlation presented by Fedkiw.

Finally, the flow-by and flow-through configurations are compared using the maximum solution phase potential drop as a basis for comparison. Criteria are given delineating the optimum electrode configuration which depend upon reactant conversion. Results of this comparison show that the two configurations can be compared independent of any specific mass-transfer relationship.

Potential Distribution

The starting point for the analysis will be the theoretical framework for porous electrodes developed by Bennion and Newman (1) and extended by Newman and Tiedemann (11). The porous electrode is treated as a superposition of two continua, representing the fluid phase and the solid phase. A single reaction of the form

$$\sum_i s_i M_i^{z_i} \rightarrow ne^- \qquad [3]$$

will be assumed to occur within the electrode. Under these assumptions, the electrode reaction appears as a homogeneous source or sink term within the conservation of species equation. A solution with excess supporting electrolyte and a uniform solution conductivity will be assumed as well as a dilute solution of reacting species. Diffusion and dispersion will be neglected. Also, the velocity within the electrode is assumed to be plug-flow, one-dimensional in the Y direction only. Under these conditions, at steady state, conservation of the reactant species for both the flow-through and flow-by electrode can be expressed as

$$v\frac{dc}{dy} = -ak_m c \qquad [4]$$

with the boundary condition

$$\text{at } y = 0,\ c = c_F \qquad [5]$$

Solution of Eq. [4] subject the boundary condition of Eq. [5] yields

$$c = c_F e^{-\alpha y} \qquad [6]$$

where

$$\alpha = \frac{ak_m}{v} \qquad [7]$$

The reciprocal of the parameter α can be thought of as a penetration length. The penetration length defines the distance where the reactant is depleted to $1/e$ of its inlet composition, or, as an order of magnitude, the length of the region where most of the reaction occurs within the electrode.

At the end of the bed ($y = L$), the concentration of the flowing stream will have reacted to the largest extent. Here, the concentration of the reactant will be denoted as c_L. Equation [6] then gives at the end of the bed

$$c_L = c_F e^{-\alpha L} \qquad [8]$$

This may be rearranged for αL in terms of the inlet and outlet concentrations as

$$\alpha L = \ln \frac{c_F}{c_L} \qquad [9]$$

Equation [9] shows that the parameter αL effectively specifies the conversion of reactant within the electrode.

Now that the concentration distribution has been established, the solution to the potential distribution may proceed. For a uniform conductivity and negligible diffusion potential, Ohm's law governs the potential distribution within the fluid phase

$$i_2 = -\kappa\nabla\Phi_2 \qquad [10]$$

Faraday's law relates the transfer current to the local rate of mass transfer within the electrode

$$j = \frac{n\mathbf{F}ak_m c}{s_R} \quad [11]$$

One must also employ the relationship

$$\nabla \cdot i_2 = j \quad [12]$$

which defines the transfer current as the divergence of the total current. Substituting the concentration distribution obtained in Eq. [6] into Eq. [11] and using Eq. [10] and [12], we obtain

$$\nabla^2\Phi_2 = -\frac{n\mathbf{F}ak_m c_F}{s_R\kappa} e^{-\alpha y} \quad [13]$$

In contrast to the solution for the concentration distribution, the solution to the potential distribution depends upon the electrode configuration.

Bennion and Newman (1) solved Eq. [13] for a one-dimensional flow-through electrode. Alkire and Ng (6) solved Eq. [13] for the flow-by electrode assuming potential variation only in the direction perpendicular to fluid flow. This assumption reduces Eq. [13] from a partial differential equation to an ordinary differential equation. Fedkiw (8) solved Eq. [13] for two-dimensional current flow in a flow-by electrode of finite length.

Here, we propose to examine the limiting case of a flow-by electrode with an infinite aspect ratio. Thus, our case will reflect the condition

$$R = \frac{L}{d} \to \infty \quad [14]$$

The potential distribution is obtained by solving Eq. [13] subject to the boundary conditions

$$\text{at } y = 0, \frac{\partial\Phi_2}{\partial y} = 0 \quad [15]$$

$$\text{as } y \to \infty, \frac{\partial\Phi_2}{\partial y} \to 0 \quad [16]$$

$$\text{at } x = 0, \frac{\partial\Phi_2}{\partial x} = 0 \quad [17]$$

and

$$\text{at } x = d, \Phi_2 = V \quad [18]$$

Solution to Eq. [13] by separation of variables subject to the boundary conditions in Eq. [15] through [18] yields

$$\frac{\Phi_2 - V}{\frac{n\mathbf{F}c_F V^2}{s_R\kappa ak_m}} = \left(\frac{\cos \alpha x}{\cos \alpha d} - 1\right) e^{-\alpha y} + 2\alpha d \sum_{n=0}^{\infty} (-1)^n \left(\frac{1}{\lambda_n^2} - \frac{1}{\lambda_n^2 - (\alpha d)^2}\right) \cdot e^{-\lambda_n y/d} \cos \lambda_n x/d \quad [19]$$

where

$$\lambda_n = \frac{(2n+1)\pi}{2} \quad [20]$$

To the designer, the maximum variation in solution phase potential may be a quantity of greater interest rather than the potential distribution within the electrode. To relate the relevant design variables to the maximum variation in solution potential, the results of the potential distribution will be used. For the flow-by electrode configuration, the semi-infinite potential distribution indicates that the maximum solution phase potential drop occurs at the front of the electrode, $y = 0$, between the two electrode boundaries, $x = 0$ and $x = d$. This is the position where the greatest current is flowing. The maximum solution phase potential difference in dimensionless form is given as

$$\frac{\Phi_2(x=0, y=0) - V}{\frac{n\mathbf{F}c_F V^2}{s_R\kappa ak_m}} = \frac{\Delta\Phi_2}{\frac{n\mathbf{F}c_F V^2}{s_R\kappa ak_m}} = \frac{\Delta\Phi_2}{\frac{\epsilon n\mathbf{F}c_F D_0}{s_R\kappa}} \frac{\text{Sh}}{\text{Pe}^2}$$

$$= \frac{1}{\cos \alpha d} - 1 + 2\alpha d \sum_{n=0}^{\infty} (-1)^n \left(\frac{1}{\lambda_n^2} - \frac{1}{\lambda_n^2 - (\alpha d)^2}\right) \quad [21]$$

This result can be compared to the results obtained by other investigators. The Alkire-Ng approximation gives for the maximum solution phase potential difference

$$\frac{\Phi_2(x=0, y=0) - V}{\frac{n\mathbf{F}c_F V^2}{s_R\kappa ak_m}} = \frac{\Delta\Phi_2}{\frac{\epsilon n\mathbf{F}c_F D_0}{s_R\kappa}} \frac{\text{Sh}}{\text{Pe}^2} = \frac{1}{2}(\alpha d)^2 \quad [22]$$

The solution obtained by Fedkiw, which includes the effects of the finite electrode length, can be represented as

$$\frac{\Phi_2(x=0, y=0) - V}{\frac{n\mathbf{F}c_F V^2}{s_R\kappa ak_m}} = \frac{\Delta\Phi_2}{\frac{\epsilon n\mathbf{F}c_F D_0}{s_R\kappa}} \frac{\text{Sh}}{\text{Pe}^2} = f(\alpha d, \alpha L) \quad [23]$$

where $f(\alpha d, \alpha L)$ represents a complicated function of the variables αd and αL previously derived by Fedkiw (8).

For the flow-through electrode, the maximum solution-phase potential drop occurs between the front and the rear of the electrode, $y = 0$ and $y = L$. From Bennion and Newman (1), this is

$$\frac{\Phi_2(y=0) - \Phi_2(y=L)}{\frac{n\mathbf{F}c_F V^2}{s_R\kappa ak_m}} = \frac{\Delta\Phi_2}{\frac{\epsilon n\mathbf{F}c_F D_0}{s_R\kappa}} \frac{\text{Sh}}{\text{Pe}^2}$$

$$= 1 - e^{-\alpha L}(1 + \alpha L) \quad [24]$$

In Fig. 2, we have plotted the dimensionless maximum potential drop times the ratio of the Sherwood number to the square of the Péclet number for a flow-by electrode. The variable αd has been chosen as the independent variable. We have included curves for a semi-infinite electrode and curves for electrodes of finite aspect ratio. Curves for the finite aspect ratio electrodes were obtained from the work of Fedkiw. In addition, the solution given by Alkire and Ng is shown. These curves are independent of any specific mass-transfer relationship.

The dotted lines plotted on Fig. 2 represent the limiting behavior of the flow-by electrode potential distribution for large values of αd. We have determined these by solving the following problem which is suggested by the limiting physical behavior of the electrode. For a fixed bed aspect ratio R, a large value of αd implies a large value of αL, and consequently a high conversion. Reactants are therefore consumed in a region very near the front of the electrode. For a reactor of very large αL, the volume of the reactor where a significant portion of

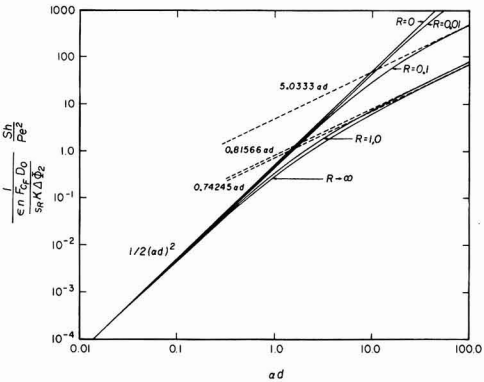


Fig. 2. Dimensionless maximum potential drop times the ratio of the Sherwood number to the square of the Péclet number for the flow-by electrode of various aspect ratios as a function of αd.

the reaction occurs approaches zero. The current generated within the bed can then be approximated as a uniform line source of current along the front of the reactor, and Laplace's equation can be used to solve for the potential distribution within the bed. Details of the problem formulation and the calculations are given in the Appendix.

Figure 2 clearly demonstrates five points.

1. The dimensionless maximum potential drop times the ratio of the Sherwood number to the square of the Péclet number calculated by the finite-electrode solution, the semi-infinite-electrode solution, and the Alkire and Ng solution all approach the same limit as αd becomes small.

2. The maximum dimensionless potential drop times the ratio of the Sherwood number to the square of the Péclet number approaches a limit for R becoming large. At large values of αd and large aspect ratios this relationship becomes proportional to αd. In the limit of small αd, this relationship approaches a value given by $1/2(\alpha d)^2$.

3. The maximum dimensionless solution phase potential drop times the ratio of the Sherwood number to the square of the Péclet number for finite R asymptotically becomes proportional to αd at large values of αd. The value of this proportionality constant is determined by the magnitude of R.

4. The effect of the finite electrode length is important only for values of R approximately less than one and then only at large values of αd.

5. The Alkire and Ng one-dimensional solution is seen to reflect the limit as the aspect ratio of the flow-by electrode tends toward zero for all values of αd. This contrasts with earlier work, which has suggested the Alkire and Ng solution results only as the aspect ratio R goes to infinity (8).

If the maximum dimensionless solution phase potential drop times the ratio of the Sherwood number to the square of the Péclet number for the flow-through electrode were plotted on this graph, the resulting curves would be horizontal straight lines. Equation [24] shows that for the flow-through electrode this quantity is not dependent upon the parameter αd.

Comparison of Configurations

As a first approximation, the optimum electrode configuration for a specified conversion might be found by assuming that the dimensionless potential drops times the ratio of the Sherwood number to the square of the Péclet number are equal. We satisfy this requirement by fixing equal potential drops for each configuration and by assuming that each electrode is constructed from the same materials and processes solutions with identical properties. Additionally, we restrict the comparison to equal ratios of the Sherwood number to the square of the Péclet number. This last constraint requires both the flow-through and flow-by electrodes to have identical volumes, flow rates, and consequently, equal pressure drops. In Fig. 3, we have plotted the values of αd and R (as functions of αL) which give equal dimensionless maximum potential drops times the ratio of the Sherwood number to the square of the Péclet number for the flow-through electrode and for the flow-by electrode. We have also designated the regions where each type of configuration is preferred. Again, the variable αL can be used to represent the reactor conversion. The maximum dimensionless potential drop times the ratio of the Sherwood number to the square of the Péclet number for the flow-through electrode has been calculated using Eq. [24]. We have included the three possibilities for evaluating this quantity for the flow-by electrode. First, the flow-by electrode is assumed to be infinitely long, and Eq. [21] is used. We can also assume the one-dimensional potential variation of Alkire and Ng might be appropriate and use Eq. [22]. Finally, the effects of the finite electrode length also can be included. The relationship given by Fedkiw could also be used. For this finite electrode case, an additional constraint must be imposed since this function explicitly depends on the aspect ratio. The value of R is computed from

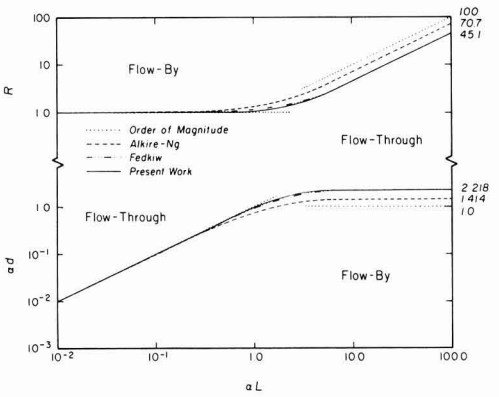


Fig. 3. Values of αd and R for equal dimensionless potential drops times the ratio of Sherwood number to the square of the Péclet number for the flow-through electrode and the flow-by electrode using: order-of-magnitude expressions, Alkire and Ng expression, semi-infinite electrode, and Fedkiw expression. These two representations are equivalent since $R = \alpha L/\alpha d$.

$$R = \frac{L}{d} = \frac{\alpha L}{\alpha d} \qquad [25]$$

Thus, the value of αd and the value of R are found for each value of αL such that the maximum dimensionless potential drops times the ratio of the Sherwood number to the square of the Péclet number are equal. For comparison, we have also included the results of the order of magnitude analysis which were derived in the introduction.

We emphasize here that this comparison of the two electrode configurations does not require that we specify a mass-transfer coefficient relationship. This comparison does not depend upon the Sherwood-Péclet number relationship. Fedkiw compared the two configurations in a similar way, except that he introduced a specific Sherwood-Péclet number relationship in his comparison. The comparison presented here is considered to be preferable because it is not restricted to a single correlation.

Figure 3 establishes several important points. At low values of αL and, consequently, low conversion, the aspect ratio and the value of αd for equal potential drops are independent of the flow-by potential drop relationship. The Alkire and Ng one-dimensional approximation, the semi-infinite electrode approximation, and the finite electrode relationship all predict the same geometry. In this low conversion range, $\alpha L < 1$, the aspect ratio for equal potential drops is seen to approach one. The value of αd, given equal electrode cost, is seen to approach a limiting relationship of

$$\alpha d = \alpha L \qquad [26]$$

The conclusion to be made here is that a flow-by electrode is favored at low conversions if it can be constructed with an aspect ratio greater than one. Otherwise, a flow-through electrode would be a better choice. Equation [26] is identical to Eq. [2], obtained by the order-of-magnitude analysis in the introductory section.

At higher conversions, values of αL greater than about 2, the criterion that specifies the optimum configuration changes. In this region, the value of R delineating the optimum electrode configuration no longer is constant. Also, the one-dimensional Alkire and Ng approximation deviates from the two-dimensional solutions. Since the one-dimensional approximation overpredicts the potential drop, it results in a criterion giving a lower flow-by aspect ratio. The two-dimensional potential distributions

are thus seen to affect the choice of electrode configurations only at high conversions. From Fig. 3, we can see that at high conversion one would choose a flow-by electrode only if the resulting aspect ratio is greater than 0.45 times αL. According to Fedkiw (8), the flow-by configuration was preferred over the flow-through configuration for

$$R \geq 5 \quad [27]$$

One can see, however, that this relationship holds only for values of αL near 10. In terms of αd, the flow-by electrode is superior at high conversions only if

$$\alpha d < 2.218 \quad [28]$$

Except for the factor of 2.218, Eq. [28] is consistent with Eq. [1], obtained by an order-of-magnitude estimate in the introductory section. This factor accounts for the variation of current across the flow-by electrode and the two-dimensional current flow, which was not included in the earlier analysis.

Figure 3 also demonstrates another significant point. The curves for the optimum electrode configuration given by the finite length electrode or the semi-infinite electrode are very nearly the same. At high and low conversions, the criterion becomes independent of whether one considers the finite electrode length. Only for a region of αL near one, does the effect of the finite electrode length on the criterion become noticeable. From Fig. 2, one can see that only when the aspect ratio approaches one at high conversions does the effect of the finite electrode length on the potential drop become noticeable. But at large conversions, or large αL, it is impractical to construct a flow-by electrode with an aspect ratio near one. Consequently, considering the potential distribution in a flow-by electrode of finite length is not really important for practical flow-by designs when the maximum potential drop is used as a basis for comparison. The potential distribution for an electrode with an infinite aspect ratio gives results which are practically identical, but in a less complicated expression.

Conclusions

The two-dimensional potential distribution for a flow-by porous electrode of infinite length to width ratio operating at the limiting has been derived. It is shown that the maximum solution-phase potential drop depends primarily on the ratio of the electrode width and the penetration depth αd. The potential drop for practical flow-by designs depends only weakly upon the length-to-width ratio. This result has been compared to the potential drop for a finite length electrode given by Fedkiw and the one-dimensional potential drop of Alkire and Ng.

The flow-through and flow-by electrode configurations have been compared at the limiting current using the maximum solution-phase potential difference as a basis for comparison. This comparison is independent of any specific mass-transfer coefficient correlation. Criteria delineating the optimal electrode configuration have been given which depend upon the reactant conversion. At low conversion, a flow-by electrode is favorable, providing that it can be constructed with a length-to-width ratio greater than one. At high conversions, however, a flow-by electrode is favorable if the ratio of the electrode width and penetration depth is less than 2.218.

Acknowledgment

This work was supported by the Assistant Secretary of Conservation and Renewable Energy, Office of Energy Systems Research, Energy Storage Division of the U. S. Department of Energy under Contract DE-AC03-76SF00098.

Manuscript submitted Feb. 13, 1984; revised manuscript received June 14, 1984.

The University of California assisted in meeting the publication costs of this article.

APPENDIX

Asymptotic Solutions for Large Values of αd

Consider a flow-by reactor with a given aspect ratio R. For large enough values of αd and large αL, most of the reactant will be consumed in a region very close to the electrode entrance. Consequently, the current will appear to be generated from a uniform line source near the front of the electrode. The applicable differential equation is thus Laplace's equation

$$\nabla^2\Phi_2 = 0 \quad [A\text{-}1]$$

subject to the boundary conditions

$$\text{at } y = 0, \frac{\partial\Phi_2}{\partial y} = -\frac{i_2}{\kappa} \quad [A\text{-}2]$$

$$\text{at } y = L, \frac{\partial\Phi_2}{\partial y} = 0 \quad [A\text{-}3]$$

$$\text{at } x = 0, \frac{\partial\Phi_2}{\partial x} = 0 \quad [A\text{-}4]$$

and

$$\text{at } x = d, \Phi_2 = V \quad [A\text{-}5]$$

The solution to the above problem is

$$\frac{\Phi_2(x = 0, y = 0) - V}{\frac{n\mathbf{F}c_F v^2}{s_R \kappa a k_m}} = \frac{\Delta\Phi_2}{\frac{\epsilon n \mathbf{F} c_F D_0}{s_R \kappa}} \frac{\text{Sh}}{\text{Pe}^2} = \alpha d \sum_{n=0}^{\infty} \frac{2(-1)^n}{\lambda_n^2 \tanh \lambda_n R} \quad [A\text{-}6]$$

where

$$\lambda_n = \frac{(2n + 1)\pi}{2} \quad [A\text{-}7]$$

The above equation thus shows that at fixed R, the dimensionless potential drop times the ratio of the Sherwood number to the square of the Péclet number becomes proportional to αd at large αd. The constant of proportionality is determined the value of R. These are the dotted lines plotted in Fig. 2.

LIST OF SYMBOLS

a	specific interfacial surface area (cm^2/cm^3)
c	pore averaged concentration (mol/cm^3)
d	flow-by electrode bed width perpendicular to fluid-flow direction (cm)
D_0	free stream diffusion coefficient of reacting species (cm^2/s)
$\mathbf{F}$	Faraday constant (96,485 C/eq)
i_2	total current density within electrolyte phase (A/cm^2)
j	transfer current density (A/cm^3)
k_m	mass transfer coefficient (cm/s)
L	bed depth in direction of fluid flow (cm)
M	arbitrary species
n	number of electrons transferred in reaction
Pe	Péclet number (V/aD_0)
R	bed aspect ratio (L/d)
Sh	Sherwood number ($\epsilon k_m/aD_0$)
s_R	stoichiometric coefficient of reactant
v	superficial fluid velocity (cm/s)
V	reference potential of flow-by electrode at $y = d$ (V)
z	charge number (eq/mol)

Greek characters

α	reciprocal of penetration length ak_m/v (cm^{-1})
$\Delta\Phi_2$	maximum allowable solution potential drop (V)
ϵ	bed porosity or void fraction
κ	conductivity of fluid phase in bed ((Ω cm)$^{-1}$)
λ	dimensionless eigenvalue
Φ_2	solution potential, V

Subscripts

i	species number
n	eigenvalue number
F	feed condition
L	exit condition

REFERENCES
1. D. Bennion and J. Newman, *J. Appl. Electrochem.*, **2**, 113 (1972).
2. J. L. Fitzjohn, *Chem. Eng. Prog.*, **71**, 85 (1975).
3. J. A. Trainham and J. Newman, *Electrochim. Acta*, **26**, 455 (1981).
4. J. A. Trainham and J. Newman, *This Journal*, **125**, 58 (1978).
5. J. A. Trainham and J. Newman, *ibid.*, **124**, 1528 (1977).
6. R. Alkire and P. Ng, *ibid.* **121**, 95 (1974).
7. R. Alkire and P. Ng, *ibid.*, **124**, 1220 (1977).
8. P. Fedkiw, *ibid.*, **128**, 831 (1981).
9. A. Stork *et al.*, *Electrochim. Acta.*, **27**, 293 (1982).
10. A. Stork *et al.*, *ibid.*, **27**, 301 (1982).
11. J. Newman and W. Tiedemann, in "Advances in Electrochemistry and Electrochemical Engineering", Vol. 11, Heinz Gerischer and Charles Tobias, Editors, Wiley Interscience, New York (1978).

Electrochemical Studies of Antitumor Antibiotics

V. An Electrochemical Method of Measurement of the Binding of Doxorubicin and Daunorubicin Derivatives to DNA

James A. Plambeck* and J. William Lown

Department of Chemistry, University of Alberta, Edmonton, Alberta, Canada T6G 2G2

ABSTRACT

A procedure has been developed for the measurement in aqueous solution of the association constant with native DNA of an agent which is electrochemically reducible. A fresh mercury drop is extruded into a solution containing both the agent and DNA, surface adsorption is reproducibly conditioned ($-0.4V \leq E \leq -1.0V$, 90s, followed by $-0.4V$, 90s), and the peak current is measured during a rapid voltage scan. A suitable plot of current as a function of DNA concentration yields the desired constant. Data are given for a significant series of substituted daunorubicin and doxorubicin compounds and for control compounds.

Since the concept of intercalation into DNA was first formulated by Lerman (1) in 1961, it has become widely recognized that many compounds of pharmacological interest, including anticancer drugs and antibiotics as well as certain carcinogens, function by binding to duplex nucleic acids (2). The anthracyclines (*e.g.*, adriamycin, daunorubicin, aclacinomycin) constitute one of the most widely studied types of such drugs owing to their established clinical efficacy against a wide range of malignancies; they are regarded as amongst the most promising of anticancer drugs (3, 4). The molecular mechanism of action of the anthracyclines is complex and appears to involve free radical generation (5, 6), lipid peroxidation (7), DNA damage (8, 9), and possible covalent attachment (10), as well as intercalative binding (2-4, 11). Nevertheless, the ability of anthracyclines to undergo intercalative binding to DNA has shown a consistent correlation with antitumor properties (3, 4, 11).

One of the parameters which characterizes this phenomenon is the binding constant K_b (12), also known as the apparent association constant K_{app}. Other parameters include sequence preference or specificity and spatial and functional group parameters determining molecular recognition (2, 3, 11, 12). Consequently, there is an urgent need for a direct, sensitive, and accurate method to quantify the binding to DNA of the growing number of new anthracyclines which are being prepared in order to improve their therapeutic index or especially to combat their main clinical limitation, severe cardiotoxicity (13, 14).

The methods which have been developed to measure binding constants of anthracyclines and other drugs fall into two categories (*i*) those that follow changes in properties of the drug, and (*ii*) those that monitor changes in the polynucleotide (12). Methods of the first type include measurement of (*i*) changes in the UV and visible absorption characteristics of the anthracycline chromophore (2, 15-17), (*ii*) changes in the fluorescence of the chromophore (15, 18-20), and (*iii*) circular dichroism characteristics (21-23). In addition, those methods for determining K_b values which depend on properties of the DNA include (*i*) viscosity changes (15, 16, 24), (*ii*) buoyant density and sedimentation coefficient differences (15, 16, 24), (*iii*) melting temperature changes (11, 24, 25), (*iv*) equilibrium dialysis (16, 22, 26), and (*v*) removal of the supercoiling in native covalently closed circular DNA (2, 27).

Many of these methods are tedious experimentally or require either rather large amounts of the anthracyclines or expensive circular DNA's. Moreover, the reported association constants for daunorubicin (12) cover the range 1.3 to 9.3×10^6 liter/mol, indicating a lack of agreement using the different methods. In this paper, we describe a new method based on the electrochemical characteristics of both free and intercalatively bound drugs. The method is experimentally convenient and sensitive so that it requires only small amounts of materials. In principle, it can be applied to a wide range of intercalating drugs, provided they bear an electrochemically active moiety. We report also further studies upon DNA and the drugs required to establish this technique.

Early applications of electroanalytical techniques to solutions of nucleic acids have been reviewed (28, 29). Of the four bases present in deoxyribonucleic acid (DNA), adenine and cytosine are reducible at mercury electrodes whether free or bound to the nucleotide chain. Native DNA is not reducible at the dropping mercury electrode because the stability of the intact double helix makes the reducible bases inaccessible to the electrode. When the integrity of the double helix is altered, as by heating above the melting point or by induced breaks in the helix, reduction of bases can be observed.

AC methods have been employed by Barker (30) and Malfoy and Reynaud (31-33). Valenta and Nürnberg (34-44) have employed dc voltammetric methods in the fast sweep mode at a stationary mercury electrode and reviewed the results (45-47). Of significance to this work is their finding that native DNA can be reduced at mercury electrodes after adsorption and unwinding of the double helix (39, 47). Less extensive studies have also been carried out by Berg and co-workers (48, 49).

Theory

The constant to be measured is the equilibrium constant for the formation of the anthracycline-DNA complex (ADNA) from unbound anthracycline (A) and uncomplexed DNA (DNA), which in terms of concentrations may be written as

$$K = c(\text{ADNA})/c(\text{A})\ c(\text{DNA})$$

*Electrochemical Society Active Member.

None of these species is easily measured directly, but the total concentration of anthracycline, $cT(A)$, and the total concentration of DNA, $cT(DNA)$, are established as conditions of the experiment and by definition

$$cT(A) = c(A) + c(ADNA)$$

$$cT(DNA) = c(DNA) + c(ADNA)$$

To express units consistently, if $cT(A)$ is in units of mol/dm^3, and each molecule of anthracycline is understood to occupy one binding site, then $cT(DNA)$ must be expressed in units of binding sites/dm^3 rather than mol/dm^3. The number of binding sites/dm^3 will depend upon the molecular weight of the DNA and its concentration, which are expressible as mol bases/dm^3, and the number of bases required to form a binding site. Since the molecules are intercalated in the helix, a minimum of four bases (two pairs) is required to form a binding site. However, it is improbable that the intrinsic binding to all types of four-base sites with different base pair compositions is identical, and the effect of bases other than nearest neighbors upon the binding may be significant (2). At the very low levels of saturation used in this study, only the most favorable sites should be occupied, and as a consequence the constants measured here should refer to an average of only the most favorable sites. Thus, the interaction constants measured by this method should be smaller than those measured by methods involving saturation of the DNA and should be more comparable to clinically realizable conditions.

When the concentration of DNA is expressed in this way and only a small proportion of the possible binding sites are occupied, then $c(ADNA)$ is much less than $cT(DNA)$ so that $c(DNA)$ is approximately equal to $cT(DNA)$. Thus measurement of the $c(ADNA)/c(A)$ ratio establishes the value of the binding constant K

$$K\,cT(DNA) = c(ADNA)/c(A)$$

Experimentally, we find that for at least all of the antibiotics reported here, and for others of different structure but containing at least one group reducible at a potential not more negative than −1.25V against SCE, application of the method described in this paper yields a curve of current against sweep potential having one (occasionally more) peaks at approximately the polarographic or cyclic voltammetric reduction potential of the anthracycline. The current I at this peak is directly proportional to $cT(A)$ in the absence of DNA, and thus to $c(A)$. In no case is an additional peak observed in the presence of DNA save for the reduction of DNA itself and consequent hydrogen evolution, but these are too negative to interfere with measurement of I; addition of DNA reduces the value of I, but the potential of the peak remains unaffected.

Since the current I arises from reduction of A whether bound or unbound

$$I = k'c(A) + k''c(ADNA)$$

In the presence of A and absence of DNA, there can be no contribution from the bound anthracycline and such a value $I(0)$ equals $k'cT(A)$ which is also $k'cT(A)$. At the other extreme of an infinite excess of DNA, the concentration of unbound anthracycline must go to zero and thus such a value $I(\text{inf.})$ equals $k''c(ADNA)$. Then

$$I(0) - I = k'cT(A) - (k'c(A) + k''c(ADNA))$$

$$I(0) - I = (k' - k'')\,c(ADNA)$$

$$I - I(\text{inf.}) = k'c(A) + k''c(ADNA) - k''c(ADNA) = k'c(A)$$

$$[I(0) - I]/[I - I(\text{inf.})] = c(ADNA)/c(A) = K\,cT(DNA)$$

Experimental

The experiments were carried out using a Princeton Applied Research (PAR) Polarographic Analyzer Model 174A, PAR Controller Model 315, and Static Mercury Drop Electrode Model 303, a Biomation Model 805 Waveform Recorder, and a Houston Instrument Type 2000 X-Y recorder. Both McIlvane and acetate buffers were used; *0.1M McIlvane buffers of pH 5.6 and 6.0* were prepared using reagent-grade dibasic sodium phosphate and citric acid. The ionic strength of the McIlvane buffers was adjusted to 1.0*M* using reagent-grade potassium chloride (29). The 0.1*M* acetate buffers of *p*H 5.6 and 6.0 were prepared using sodium acetate, acetic acid, and $10^{-4}M$ disodium EDTA dihydrate in 0.1*M* KCl. All buffers were prepared from triply distilled water. The acetate buffer of *p*H 5.6 so prepared was used in all experiments unless otherwise specified.

Calf thymus DNA was obtained from Sigma Chemical Company, *E. coli* DNA from Aldrich Chemical Company, and *B. subtilis* DNA (Grade A) from Calbiochem. The antibiotic daunorubicin **1b** was obtained from Sigma Chemical Company; its anhydrous molecular weight was 564.0. Compound AD32, **1o**, was kindly provided by Dr. M. Israel of the Sidney Farber Cancer Institute. Other anthracyclines were obtained from Dr. E. M. Acton of SRI International. Their structures are given in Fig. 1.

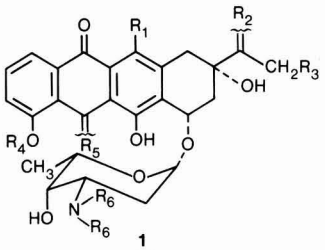
The procedure used was similar to those established by Nürnberg *et al.* (50). The "conditioning" potential E_c, the "deposition" potential E_s, and the final potential E_f were set on the potentiometers of the Model 315. The "deposition" potential and time are so noted on the Model 315, which was designed for use in anodic stripping voltammetry, but here represent only a second stage of conditioning. Both the "conditioning" time t_c and "deposition" time t_s were 90s. The internal switch in the PAR Model 174A was set to the position for 10 times higher sweep rates, which permits sweep rates of up to 5 V/s.

The Model 303 was set to HMDE mode with large drop size, each drop having a surface area of 2.83×10^{-2} cm^2. A fresh drop was used for each measurement. The reference electrode was AgCl/Ag-saturated KCl in a glass frit; all potentials were measured and are given with respect to this reference. A platinum wire served as an auxiliary electrode. All measurements were made at room temperature under an atmosphere of purified nitrogen after deaeration with nitrogen.

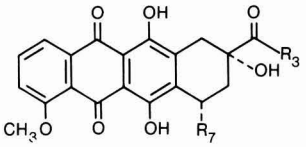
For 90s, the mercury drop was subjected to a constant applied "conditioning" potential whose values could be varied between −0.40 and −1.60V. After 90s, the potential was stepped to a constant "deposition" potential of −0.40V and was held there for a further 90s. Finally, the potential was driven by a rapid cathodic sweep with a rate of 1 or 5 V/s to the negative limit of potential at about −1.8V. The current values were stored in the Biomation Model 803 which was set for pretriggered recording with 1800 delay interval and single triggering mode. The stored voltammogram was plotted, using the Houston recorder in x-t mode, as provided by the Biomation Model 803; typical curves are shown in Fig. 2. The Biomation unit was triggered from the pen-drop switch closure of the Model 315 using an external battery. Similar results, though with less precise output, were obtained using an R564B storage oscilloscope (Tektronix).

For all of the solutions studied, the experimental curves were superimposable for successive fresh drops of the same size (as provided by the mechanical operation of the Model 303) in the same solution. Drops of nonreproducible size, or use of the same drop twice, gave totally nonreproducible results. Replicate runs on new solutions and using fresh drops were within ±4%-5% on the basis of peak height.

The functions of peak current derived in the theory section of this paper were calculated and plotted against the concentration of DNA either manually or by computer (Amdahl 470/V7, Calcomp plotter, *IG package at University of Alberta Computing Services). Typical plots are given in Fig. 5 and 6. The association constant is obtainable from the linear portion of the slope of Fig. 5. In terms of originally measured quantities, this slope has the units of μg anthracycline complexed per cm^3 of DNA stock solution added, but use of the original anthracycline concentration (nominally 5.0×10^{-6} mol/dm^3), the concentration of the DNA stock solution (nominally 1.050 mg/cm^3



1



2

1a R_1=OH, R_2=O, R_3=OH, R_4=CH_3, R_5=O, R_6=H
1b R_1=OH, R_2=O, R_3=H, R_4=CH_3, R_5=O, R_6=H
1c R_1=H, R_2=O, R_3=OH, R_4=CH_3, R_5=O, R_6=H
1d R_1=H, R_2=O, R_3=H, R_4=CH_3, R_5=O, R_6=H
1e R_1=H, R_2=O, R_3=OH, R_4=H, R_5=O, R_6=H
1f R_1=H, R_2=O, R_3=H, R_4=H, R_5=O, R_6=H
1g R_1=OH, R_2=(H,OH) R_3=OH, R_4=CH_3, R_5=O, R_6=CH_2Ph
1h R_1=OH, R_2=(H,OH) R_3=H, R_4=CH_3, R_5=NH, R_6=H
1i R_1=OH, R_2=(H,OH) R_3=H, R_4=CH_3, R_5=O, R_6=$-(CH_2)_2CHOCH_3(CH_2)_2-$
1j R_1=OH, R_2=O, R_3=H, R_4=CH_3, R_5=O, R_6=$(CH_2)_2O(CH_2)_2-$
1k R_1=OH, R_2=O, R_3=H, R_4=CH_3, R_5=O, R_6=$-(CH_2)_5-$
1l R_1=OH, R_2=O, R_3=H, R_4=CH_3, R_5=O, R_6=(2′-tetrahydropyranyl)
1m R_1=OH, R_2=O, R_3=H, R_4=CH_3, R_5=O, R_6=$-(CH_2)_2CHOCH_3(CH_2)_2-$
1n R_1=OH, R_2=O, R_3=H, R_4=CH_3, R_5=O, R_6=$-(CH_2)_2S(CH_2)_2-$
1o R_1=OH, R_2=O, R_3=$OCO(CH_2)_4CH_3$, R_4=CH_3, R_5=O, R_6=(H,$COCF_3$)
1p R_1=OH, R_2=(H,OH) R_3=H, R_4=CH_3, R_5=O, R_6=H

2a R_3=OH, R_7=OH
2b R_3=H, R_7=OH
2c R_3=OH, R_7=H
2d R_3=H, R_7=H

Fig. 1. Structures of anthracyclines (1) and aglycones (2).

calf thymus DNA of od 21 measured at 260 nm), and the relationship that one od unit is equivalent to 50 $\mu g/cm^3$ or 1.49×10^{-4} mol phosphate/dm^3 or mol bases/dm^3 permits calculation of the association constant in molar quantities, liter/mol phosphate or liter/mol bases.

Coulometric measurements were made upon the recorder output curves using a planimeter and converted to the original input time base. The method of obtaining the base line for the peaks near −1.5V was that of Valenta and Grahmann (37). In the peaks at −0.65V, the base line of the output curves with base electrolyte alone and the base lines of the curves with DNA and/or daunorubicin **1b** were the same. Planimeter measurements were also made upon molecular models of **1b** to establish the area they would occupy. A single molecule of **1b** can occupy a surface area of *ca.* 1.50 nm^2 (flat) and *ca.* 0.64 nm^2 (on edge).

Results

Preliminary tests were made using 1.0×10^{-4} mol/dm^3 Cd(II) in pH 5.6 McIlvane buffer. At a conditioning potential of, or positive of, −1.0V, a single sharp asymmetric peak (sharp rise, exponential fall) was observed at a peak

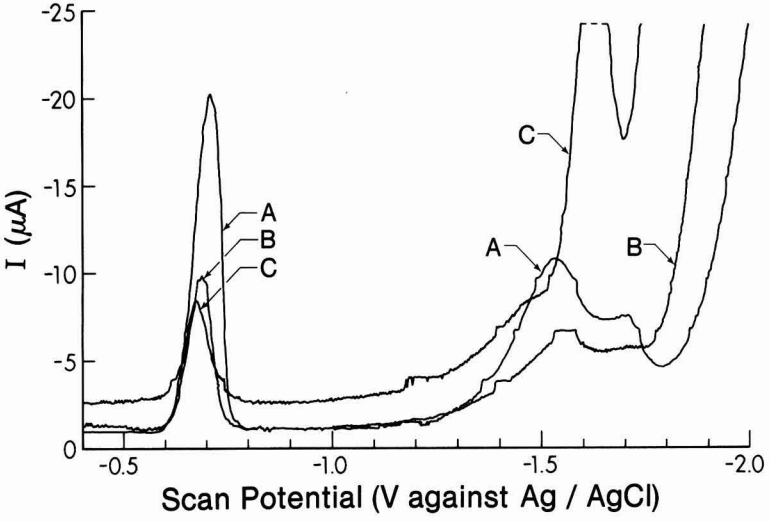


Fig. 2. Typical biomation output plots. Data for 5×10^{-6} mol/dm^3 doxorubicin (**1a**) in acetate buffer, conditioning potential −0.4V. Curve A: no added DNA. B: calf thymus DNA concentration 10.4 $\mu g/cm^3$. C: calf thymus DNA concentration 59.4 $\mu g/cm^3$. Vertical scale of C, only, exaggerated by a factor of 2.5.

potential (E_p) of −0.63 ± 0.01V. At "conditioning" potentials more negative than −1.0V, the current no longer fell exponentially. This is expected because the conditioning potential is now sufficiently negative to deposit more cadmium onto (or into) the HMDE than is removed during the "deposition" time at −0.4V. Addition of sufficient EDTA to give a 0.02 mol/dm³ solution shifted the cadmium reduction peak negative to −1.70V; its fall then merged with the solvent discharge current. In the EDTA solution, the peak shape and height were not affected by the "conditioning" potential. This behavior is expected for aqueous Cd(II) and its EDTA complex, which are reversibly reduced on mercury.

DNA.—Calf thymus DNA was used both in McIlvane and acetate buffer. The addition of DNA to buffer caused the appearance of a single sharp asymmetric peak at about −1.5V and a positive shift of the onset of hydrogen evolution from *ca.* −1.83V (*p*H 6.0, 0.1*M* acetate buffer + 0.1*M* KCl) to *ca.* −1.6V (same system + DNA). The bacterial DNA gave sharper peaks, as expected, owing to its lower molecular weight. All three forms of DNA gave only a single peak at about −1.5V at all values of the conditioning potential less than −1.5V. Its height increased with scan rate, and varied with the type and concentration of DNA used (Table I). This peak is attributed to the reduction of the adenine and cytosine bases of the adsorbed DNA (34-47); for DNA alone, our results are comparable to those of Nürnberg *et al.*

Anthracyclines.—Solutions of **1b** in the absence of DNA gave a single, sharp, well-defined, approximately symmetric peak at −0.625 ± 0.005V (full width at half-maximum 0.08 ± 0.02V, except for extremely low concentrations). The peak potential did not change with **1b** concentration or with scan rate. The peak current was directly proportional to the concentration of **1b** up to about 2 mol/dm³, at which point the current increase became less than proportional (Fig. 3). Direct proportionality is found from 10 nmol/dm³ to over 500 nmol/dm³ (Fig. 4); the lower limit is due to inability to easily distinguish the peak from base-line noise. Solutions of **1b** which contained no DNA also gave a peak or shoulder at the approximate potential of reduction of the bases of DNA, −1.535V. This is due to the additional reduction of **1b** at these more negative potentials (53, 54). The behavior of the other anthracyclines studied paralleled that of daunorubicin. In all cases, the easiest reduction of the anthracyclines is sufficiently positive of either their own second reduction or the reduction of DNA that the current returns to the base line before these processes begin.

Table I. Effect of conditioning potential upon reduction of DNA

Calf thymus DNA; 84 μg/cm³ McIlvane buffer, *p*H 6.0; scan from "deposition" potential of −0.4V.

E_c (V)	E_p (V) (5 V/s)	Q (μC/cm²) (5 V/s)	E_p (V) (1 V/s)	Q (μC/cm²) (1 V/s)
−0.4	−1.605	9.6	−1.525	17.6
−0.6	−1.605	12.3	−1.525	15.8
−0.8	−1.610	14.2	−1.525	12.9
−1.0	−1.655	12.1	−1.525	18.8
−1.2	−1.625	18.0	−1.535	24.9
−1.3	−1.620	18.1	−1.540	27.4
−1.35	−1.605	10.4	−1.530	25.6
−1.4	−1.595	5.5	−1.6?	4.0

Calf thymus DNA; 84 μg/cm³ acetate buffer, *p*H 6.0, scan rate 1 V/s from −0.4V "deposition" potential, EDTA when present 1×10^{-4} mol/dm³.

E_c (V)	E_p (V) (w/o EDTA)	Q (μC/cm²) (w/o EDTA)	E_p (V) (w/EDTA)	Q (μC/cm²) (w/EDTA)
−0.4	−1.535	5.08	−1.535	4.51
−0.6	−1.535	5.64	−1.540	5.16
−0.8	−1.535	5.57	—	—
−1.0	−1.540	6.77	—	—
−1.2	−1.530	10.64	−1.550	8.95
−1.3	—	—	—	—
−1.35	−1.540	9.35	−1.560	8.79
−1.4	−1.545	3.14	—	—

Bacterial DNA; *E. coli* DNA 40 μg/cm³, *B. subtilis* DNA 66.7 μg/cm³; scan rate 1 V/s from "deposition" potential of −0.4V; acetate buffer *p*H 5.6.

E_c (V)	*E. coli* DNA E_p (V)	*E. coli* DNA Q (μC/cm²)	*B. subtilis* DNA E_p (V)	*B. subtilis* DNA Q (μC/cm²)
−0.4	−1.515	2.66	−1.530	8.87
−0.6	−1.520	2.82	−1.530	8.38
−0.8	−1.525	3.07	−1.510	8.46
−1.0	−1.525	2.90	−1.520	9.11
−1.2	−1.525	3.30	−1.525	9.59
−1.3	−1.525	4.67	−1.525	11.20
−1.35	−1.525	4.28	—	—
−1.4	−1.530	2.58	−1.525	6.21

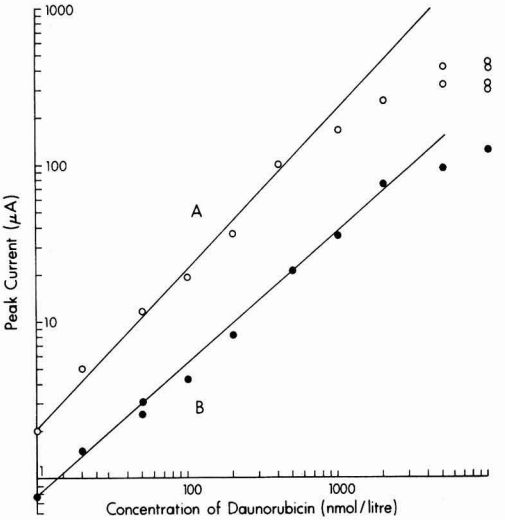


Fig. 3. Effect of concentration upon daunorubicin (1b) reduction. Aqueous buffer. Open circles (A) obtained at 5 V/s. Closed circles (B) obtained at 1 V/s. Log-log plot. Peak potential: −0.65V.

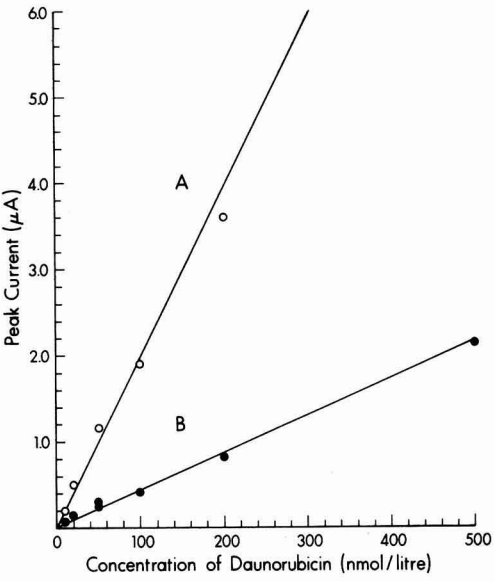


Fig. 4. Effect of low concentrations of daunorubicin (1b) upon peak current. Aqueous buffer. Open circles (A) obtained at 5 V/s. Closed circles (B) obtained at 1 V/s. Peak potential: −0.65V. Point on A at 500 nmol/liter is at 10.0 μA, offscale.

DNA-anthracycline complexes.—The electrochemical behavior of solutions containing both DNA and the individual anthracycline is similar to the sum of the behavior of separate solutions of the two components. The first reduction of **1b** at −0.625V shifts negative in the presence of DNA by not more than 50 mV; the peak is broadened and slightly reduced in height as compared to **1b** alone. The second reduction of **1b** is indistinguishable from the reduction of the adsorbed adenine and cytosine bases of DNA near −1.55V. As a consequence, we are unable to measure the effect of the anthracycline upon the DNA present, although at relatively low levels of anthracycline that effect is, within experimental error, absent. The sharp drop-offs in peak current and charge as the "conditioning" potential becomes more negative than −1.3V are due to partial reduction of the adsorbed material while the "conditioning" potential is still held, well before the onset of the recorded voltammetric sweep. These observations apply to all of the other anthracyclines studied as well.

The association constants of the anthracyclines with DNA were calculated according to the procedure described from the values of the peak current as a function of DNA concentration. These are given in Tables II-V. The values reported in Tables II-IV are arbitrarily given to three places following the decimal point to ensure that any real differences in potential dependence are not lost. The reproducibility of completely separate experiments on different solutions is of the order of 5%, and the smaller number of figures given in the summary of Table V reflect this.

This procedure has been optimized for daunorubicin by adjusting the DNA increments and values to give a slope of about 50° in the plots of the type given in Fig. 5. For association weaker or stronger than that of daunorubicin by a factor greater than ten, the line approaches horizontal or vertical. Classes of compounds with much stronger association than daunorubicin, which may be those of greatest anticancer interest, are better studied with smaller or more dilute DNA additions.

The number of moles of bases of DNA per mole of anthracycline can be calculated from the total stoichiometric ratio in the solution. A plot of this ratio against the signal due to unbound anthracycline, which can be taken as proportional to the ratio of the peak current, less the peak current at an infinite excess of DNA, to the peak current measured in the absence of DNA, can give an indication of the number of base pairs of the DNA involved in direct interaction with the antibiotic (Fig. 6). This is essentially a titration of the anthracycline with DNA; the estimation of the number of bases/binding site uses only the initial rapid decrease.

In all cases, the number of bases per anthracycline calculated from the intercept of diagrams such as Fig. 6 was between 5 and 8.

Table II. Association constants in aqueous solution

Compound	K (l/mol phosphate × 10^5)					$I(\infty)$[1]
	−0.4V	−0.6V	−0.8V	−1.0V	Mean	[% $I(0)$]
1a	0.688	0.755	0.889	0.856	0.797	4
1b	0.638	0.477	0.433	0.513	0.515	8
1c	0.765	0.738	0.792	0.738	0.758	3
1d	0.463	0.463	0.470	0.490	0.472	14
1e	0.366	0.460	0.436	0.315	0.394	2
1f	0.299	0.144	0.174	0.179	0.199	2
1h	0.342	0.329	0.409	0.403	0.371	4
1i	2.070	1.805	1.362	1.342	1.645	0
1j	1.644	1.752	1.299	1.393	1.522	0
1k	1.611	2.460	1.342	1.483	1.474	0
1l	0.359	0.352	0.466	0.366	0.378	7
1m	3.215	2.685	2.725	2.547	2.793	0
1n	1.812	1.342	1.544	1.409	1.527	0
1o	NS	NS	NS	NS	NS	—
1p	0.268	0.208	0.235	0.188	0.225	6

[1] Percent response in effectively "infinite" DNA excess as compared to total absence of DNA.
NS = not soluble.

Table III. Association constants in 3% CH_3CN

Compound	K (l/mol phosphate × 10^5)					$I(\infty)$[1]
	−0.4V	−0.6V	−0.8V	−1.0V	Mean	[% $I(0)$]
1a	0.839	0.805	0.966	1.037	0.912	5
1b	0.698	0.839	0.923	0.883	0.836	6
1c	0.503	0.738	0.718	0.691	0.663	3
1d	0.389	0.470	0.383	0.463	0.426	9
1e	0.322	0.228	0.352	0.362	0.316	3
1f	0.262	0.322	0.329	0.430	0.336	8
1g[2]	0.072	0.109	0.050	0.071	0.076	15
1h	0.356	0.383	0.456	0.443	0.411	5
1i	1.628	2.070	1.970	1.718	1.847	0
1j	1.883	1.570	1.386	1.319	1.540	0
1k	1.779	1.594	1.678	1.594	1.661	0
1l	0.416	0.440	0.473	0.466	0.449	7
1m	1.342	1.812	1.846	1.826	1.706	0
1n	1.544	1.805	1.715	2.577	1.910	0
1o	0.060	0.128	0.077	0.091	0.089	47
1p	0.208	0.201	0.268	0.221	0.225	8
2a[2]	0.215	0.174	0.141	0.142	0.168	36

[1] Percent response in effectively "infinite" DNA excess as compared to total absence of DNA.
[2] 5% CH_3CN.

Table IV. Association constants in 30% CH_3CN

Compound	K (l/mol phosphate × 10^5)					$I(\infty)$[1]
	−0.4V	−0.6V	−0.8V	−1.0V	Mean	[% $I(0)$]
1a	0.446	0.436	0.544	1.517	0.486	9
1b	0.503	0.560	0.537	0.356	0.489	10
1c	0.336	0.329	0.201	0.282	0.287	10
1d	0.218	0.255	0.228	0.181	0.221	18
1e	0.074	0.114	0.107	0.181	0.119	2
1f	0.228	0.255	0.228	0.299	0.253	8
1h	0.044	0.034	0.040	0.067	0.046	29
1i	0.356	0.336	0.302	0.292	0.322	0
1j	0.923	1.047	0.859	0.953	0.946	0
1k	0.560	0.604	0.423	0.128	0.429	0
1l	0.453	0.299	0.208	0.201	0.290	7
1m	1.117	1.235	1.510	0.775	1.159	0
1n	0.537	0.537	0.205	0.369	0.412	0
1o	0.054	0.060	0.027	0.037	0.044	12
1p	0.141	0.154	0.154	0.134	0.146	29
2b	0.255	0.201	0.195	0.148	0.200	40
2d	0.050	0.034	0.040	0.054	0.045	20

[1] Percent response in effectively "infinite" DNA excess as compared to total absence of DNA.

Table V. Summary of mean association constants

Compound	Mean K[1] (l/mol phosphate × 10^5)		
	Aqueous	3% CH_3CN	30% CH_3CN
1a	0.80	0.91	0.49
1b	0.52	0.84	0.49
1c	0.76	0.66	0.29
1d	0.47	0.43	0.22
1e	0.39	0.32	0.12
1f	0.20	0.34	0.25
1g	NS	0.08[2]	—
1h	0.38	0.41	0.05
1i	1.65	1.85	0.32
1j	1.52	1.54	0.95
1k	1.47	1.66	0.43
1l	0.38	0.45	0.29
1m	2.79	1.71	1.16
1n	1.53	1.91	0.41
1o	NS	0.09	0.04
1p	0.23	0.23	0.15
2a	—	0.17[2]	—
2b	NS	NS	0.20[4]
2d	NS	NS	0.04

NS = not soluble.
[1] Value in table should be multiplied by 10^5 to give K in l/mol phosphate.
[2] 5% CH_3CN.
[3] No detectable complexation; value << 0.05.
[4] Scattered data plots.

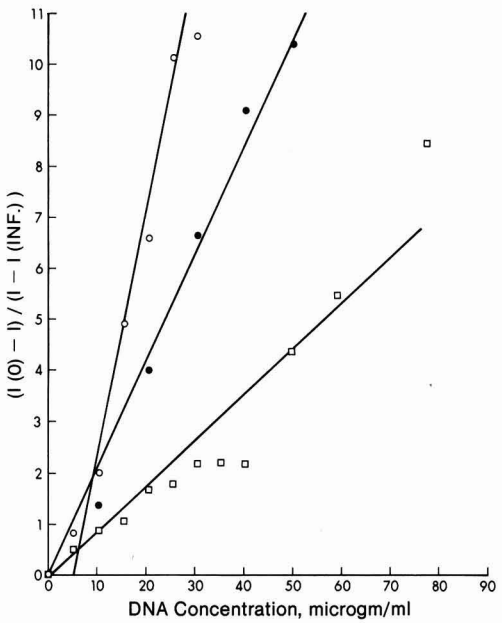


Fig. 5. Typical plots used to obtain association constants. Strong association, open circles (1j); moderate association, closed circles (1a); weaker association, open squares (1f). All in aqueous solution, conditioning potential −0.4V, scan rate 5 V/s.

Additional electrochemical studies of these compounds are given elsewhere (59).

Discussion

The interfacial mercury/aqueous electrolyte region has been used as a model for electrically charged biological membranes, the interactions of DNA with the electrode being then taken as relevant to the interactions of cellular DNA with cell membranes. While doubly helical native DNA is not reducible from solution, it can undergo the sequence adsorption, dehydration, strand separation, and base reorientation which renders the reducible adenine and cytosine bases accessible to electron transfer (43). Their irreversible reduction to strongly adsorbed products blocks the surface of the electrode to further adsorption of DNA. These products, in common with other nitrogen heterocyclic compounds, are catalysts for hydrogen evolution on mercury. The parameters known to affect the adsorption, and hence observable reduction, of DNA on fresh mercury electrodes include ionic strength, *p*H, percentage of A-T content in the DNA, and molecular weight, in addition to the experimentally adjustable parameters of adsorption time, potential of the electrode during adsorption, and rate of the voltammetric scan (43). Denatured DNA, in which the bases are already accessible, and mononucleotides are reducible through the latter part of the same mechanism. The data of this study for solutions of DNA alone are consistent with previous studies (43) and the above mechanism.

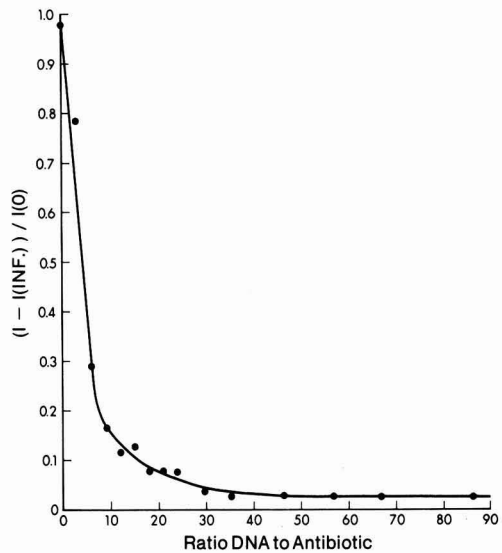


Fig. 6. Typical plot of moles of DNA base/mol agent. Data for 1a, aqueous solution, conditioning potential −0.4V, scan rate 5 V/s.

Anthracyclines.—Generation of fresh drops in the solution containing both the DNA and the anthracyclines known (51-54 and references therein) to interact with it, followed by the double potential step-sweep method under the conditions already established (50) as appropriate for study of DNA itself should demonstrate any effect of interaction with DNA upon the reduction of DNA. At the lowest anthracycline concentrations used, no such effect is observed.

If the behavior of the anthracyclines alone under the same conditions is established, any effect of interaction with DNA upon the redox properties of the anthracyclines should also be noticeable. This second factor is relevant to the possible reductive activation of an anthracycline once bound to DNA (51-54). We find no evidence of any such effect. The results obtained show that for anthracyclines alone the initial reduction studied by this method occurs at the same potential as is observed in the more conventional techniques of polarography and cyclic voltammetry. For daunorubicin either alone or in the presence of DNA, the peak current gives a linear response to concentration down to about 10 nmol/dm^3, suggesting further development of this technique as a clinical analytical method.

DNA-anthracycline complexes.—The data presented by Berg and co-workers on the association constant of actinomycin with DNA obtained by pulse polarography (49) and of other anthraquinones with DNA obtained by classical polarography (55) employed experiments in which the decrease of polarographic response to a fixed total concentration of the antibiotic upon successive additions of calf thymus DNA was interpreted as being due to the complexation of the antibiotic with DNA. The complex was taken as having no polarographic response (55) or (49) as having a response at the same potential as the uncomplexed antibiotic with, however, a much slower rate of diffusion due to the attachment of DNA. This interpretation seems unlikely; it is more probable that the effects observed are due to time-dependent (and possibly also potential-dependent) competitive adsorption of the antibiotic and DNA, which would also account for the observed diminution of antibiotic response with increasing DNA concentration. Such effects, while necessarily present in dc polarographic techniques, are not a complication in the present procedure only because the equilibration time at constant potential is long enough to achieve equilibrium (or at least a highly reproducible steady state), while the scan rate is fast enough to prevent significant change from equilibrium before the measurement is complete. We have found 90s a practical minimum equilibration time and 1 V/s the minimum useful scan rate to obtain reproducible results with calf thymus DNA.

Molinier-Jumel *et al.* (58) gave a value of 0.78×10^5 liter/mol phosphate for **1b** with sonicated calf thymus DNA using ac polarography in aqueous solution. The compound was added in increments to a solution with a fixed DNA concentration. Our comparable value using

the reverse procedure described here is 0.52×10^5, in reasonable agreement.

Electrode coverage by mononucleotides is undoubtedly greater than for DNA, if only because the guanine and thymine bases in DNA are not reducible though they are presumably also adsorbed. In acid (pH 3.0 ± 0.5) aqueous solution, the protonated mononucleotide adenosine gives a reduction charge of 40 $\mu C/cm^2$ for the adsorbed material between −0.2 and −0.4V (36); values higher than this are obtained for the compact stage of adsorption. Protonated cytidine has about half the occupied area of adenosine (56, 57). Our values are at or below these limits (Table I).

The charge expected for a two-electron reduction of a complete or maximum daunorubicin monolayer with molecules oriented parallel to the electrode surface is 21.4 $\mu C/cm^2$, while 50 $\mu C/cm^2$ could be expected for the less likely perpendicular orientation. This is quite consistent with the values of 13-17 $\mu C/cm^2$ actually obtained for daunorubicin in the absence of DNA.

Conclusion

The method described herein seems well suited to studies of the influence of structural variations in both anthracycline and sugar to the binding of the anthracyclines to DNA. The association constants do not vary significantly with potential when the conditioning potential ranges from −0.4 to −1.0V against SCE, nor does the addition of 3% acetonitrile alter their values (although 30% decreases them significantly). The configuration of DNA on the electrode surface is therefore reproducibly established by the experimental conditions used and it is to that configuration that the binding occurs.

The association constant reported herein for doxorubicin (**1b**) is significantly higher than that for daunorubicin (**1a**). The same difference is found for the corresponding pairs **1d, 1c** and **1f, 1e,** leading to the conclusion that replacement of the hydroxyl group at R3 with hydrogen reduces binding to DNA. This is in accord with the greater ΔT_m value observed for doxorubicin than for daunorubicin, but not in accord with all of the values reported by other methods (12), which generally give values for doxorubicin of 20% lower than for daunorubicin. Values obtained with solution rather than electrode methods also tend to be consistently higher and may refer to DNA of a considerably more accessible (to anthracyclines) configuration than that on electrode surfaces.

Binding of the aglycones **2a-2d** is much less than for the anthracyclines with attached sugars. The ratio of $I(\text{inf.})/I(0)$ is greater than 30%, indicating that much of the aglycone remains unbound even at mole ratios greater than 300:1 bases:aglycone. It is clear that the sugar materially assists in the binding of the anthracyclines to DNA.

Acknowledgments

The authors are grateful to Z. Kherani for experimental measurements. This work was supported by grants from the Natural Science and Engineering Research Council of Canada (to J.A.P. and to J.W.L.), and by a grant from the National Cancer Institute of Canada and a contract with the National Foundation for Cancer Research (to J.W.L.).

Manuscript submitted Nov. 28, 1983; revised manuscript received July 2, 1984.

The University of Alberta assisted in meeting the publication costs of this article.

REFERENCES

1. L. S. Lerman, *J. Mol. Biol.*, **3,** 18 (1961).
2. M. J. Waring, in "The Molecular Basis of Antibiotic Action," E. F. Gale, E. Cundliffe, P. E. Reynolds, M. R. Richmond and M. J. Waring, Editors, p. 173, John Wiley and Sons, New York (1972).
3. F. Arcamone, in "Topics in Antibiotic Chemistry," Vol. 2, P. Sammes, Editor, p. 102, John Wiley and Sons, New York (1978).
4. A. Di Marco, F. Arcamone, and F. Zunino, in "Antibiotics III—Mechanism and Action of Antimicrobial and Antitumor Agents," J. W. Corcoran and F. E. Hahn Editors, pp. 101-128, Springer, New York (1975).
5. N. R. Bachur, S. L. Gordon, and M. V. Gee, *Molec. Pharmacol.*, **13,** 901 (1977).
6. J. W. Lown, H. H. Chen, J. A. Plambeck, and E. M. Acton, *Biochem. Pharmacol.*, **28,** 2563 (1979).
7. T. Goodman and P. Hochstein, *Biochem. Biophys. Res. Commun.*, **77,** 797 (1977).
8. V. Berlin and W. A. Haseltine, *J. Biol. Chem.*, **256,** 4747 (1981).
9. J. W. Lown, S. K. Sim, K. C. Majumdar, and R.-Y. Chang, *Biochem. Biophys. Res. Commun.*, **76,** 705 (1977).
10. B. K. Sinha and C. F. Chignell, *Chem. Biol. Interact.*, **28,** 301 (1979).
11. D. W. Henry, in "Cancer Chemotherapy," A. C. Sartorelli, Editor, ACS Symposium Series 30, American Chemical Society (1976).
12. S. Neidle, in "Topics in Antibiotic Chemistry," Vol. 2, P. Sammes, Editor, p. 230, John Wiley and Sons, New York (1978).
13. G. Bonadonna and S. Monfardini, *Lancet*, **1,** 837 (1969).
14. B. Smith, *Br. Heart J.*, **31,** 607 (1969).
15. E. Calendi, A. Di Marco, M. Reggiani, B. Scarpinato, and L. Valentini, *Biochim. Biophys. Acta*, **103,** 25 (1965).
16. F. Zunino, R. Gambetta, A. Di Marco, and A. Zaccona, *ibid.*, **277,** 489 (1972).
17. A. Di Marco, F. Zunino, R. Silverstrini, C. Gambarracci, and R. A. Gambetta, *Biochem. Pharmacol.*, **20,** 1323 (1971).
18. A. Di Marco, A. M. Casazza, R. Gambetta, R. Supino, and F. Zunino, *Cancer Res.*, **36,** 1962 (1976).
19. F. Zunino, R. Gambetta, A. Di Marco, G. Luoni, and A. Zaccara, *Biochem. Biophys. Res. Commun.*, **69,** 744 (1976).
20. K. C. Tsou and K. F. Yip, *Cancer Res.*, **36,** 3367 (1976).
21. D. G. Dagleish, G. Fey, and W. Kersten, *Biopolymers*, **13,** 1752 (1974).
22. G. J. Baggay, D. Grier, R. E. Fingeole, R. Reimer, S. Levy, S. W. Pearce, and W. D. Wilson, *Biochem.*, **15,** 2062 (1976).
23. T. R. Kough and M. A. Young, *Nature*, **269,** 627 (1977).
24. W. Kersten, H. Kersten, and W. Szybalski, *Biochem.*, **5,** 236 (1966).
25. A. Di Marco and F. Arcamone, *Arnzeim. Forsch.*, **25,** 368 (1975).
26. Y. M. Huang and D. R. Phillips, *Biophys. Chem.*, **6,** 363 (1977).
27. M. J. Waring, *J. Mol. Biol.*, **54,** 247 (1976).
28. B. Janik and P. J. Elving, *Chem. Rev.*, **68,** 295 (1968).
29. E. Palecek, in "Progress in Nucleic Acid Research and Molecular Biology," Vol. 9, J. N. Davis and W. E. Cohn, Editors, p. 31, Academic Press, New York (1969).
30. G. C. Barker and D. McKeown, *Bioelectrochem. Bioenerg.*, **3,** 373 (1976).
31. B. Malfoy, J. A. Reynaud, and P. J. Sicard, *ibid.*, **1,** 126 (1974).
32. B. Malfoy and J. A. Reynaud, *J. Electroanal. Chem.*, **67,** 359 (1976).
33. B. Malfoy, J. A. Reynaud, and P. J. Sicard, *Bioelectrochem. Bioenerg.*, **1,** 126 (1974).
34. D. Krznaric, P. Valenta, and H. W. Nürnberg, *J. Electroanal. Chem.*, **65,** 863 (1975).
35. P. Valenta, H. W. Nürnberg, and D. Krznaric, *Bioelectrochem. Bioenerg.*, **3,** 418 (1976).
36. D. Krznaric, P. Valenta, H. W. Nürnberg, and M. Branica, *J. Electroanal. Chem.*, **93,** 411 (1978).
37. P. Valenta and P. Grahmann, *ibid.*, **49,** 41 (1974).
38. P. Valenta and H. W. Nürnberg, *ibid.*, **49,** 55 (1974).
39. P. Valenta, H. W. Nürnberg, and P. Klahre, *Bioelectrochem. Bioenerg.*, **1,** 487 (1974).
40. P. Valenta, H. W. Nürnberg, and P. Klahre, *ibid.*, **2,** 204 (1975).
41. B. Malfoy, J. M. Sequaris, P. Valenta, and H. W. Nürnberg, *ibid.*, **3,** 440 (1976).
42. J. M. Sequaris, B. Malfoy, P. Valenta, and H. W. Nürnberg, *ibid.*, **3,** 461 (1976).
43. H. W. Nürnberg and P. Valenta, *Croat. Chem. Acta*, **48,** 623 (1976).
44. H. W. Nürnberg and P. Valenta, in "Proceedings of the Colston Conference No. 29 (Bristol 1978)," pp. 201-229, Scientechnica, Bristol (1979).
45. J. M. Sequaris, P. Valenta, H. W. Nürnberg, and B. Malfoy, *Bioelectrochem. Bioenerg.*, **5,** 483 (1978).
46. J. M. Sequaris, P. Valenta, H. W. Nürnberg, and B. Malfoy, in "Proceeding of the Colston Conference No. 29 (Bristol 1978)," pp. 230-234, Scientechnica, Bristol (1979).
47. P. Valenta and H. W. Nürnberg, *Biophys. Struct. Mech.*, **1,** 17 (1974).
48. J. Flemming and J. Berg, *Bioelectrochem. Bioenerg.*, **1,** 459 (1974).

49. H. Berg and H. Schütz, in "Proceedings of the Second Conference on Applied Physical Chemistry," Vol. 1, Ilova Buzas, Editor, pp. 497-489, Akad. Kiado, Budapest (1971).
50. B. Malfoy, J. M. Sequaris, P. Valenta, and H. W. Nürnberg, *J. Electroanal. Chem.*, **75,** 455 (1977).
51. G. M. Rao, J. W. Lown, and J. A. Plambeck, *This Journal*, **124,** 195 (1977).
52. G. M. Rao, A. Begleiter, J. W. Lown, and J. A. Plambeck, *ibid.*, **124,** 199 (1977).
53. G. M. Rao, J. W. Lown, and J. A. Plambeck, *ibid.*, **125,** 534 (1978).
54. G. M. Rao, J. W. Lown, and J. A. Plambeck, *This Journal*, **125,** 540 (1978).
55. H. Berg and K. Eckhardt, *Z. Naturforsch.*, **25B,** 362 (1969).
56. Y. M. Temerk, P. Valenta, and H. W. Nürnberg, *J. Electroanal. Chem.*, **100,** 77 (1979).
57. Y. M. Temerk and P. Valenta, *ibid.* **93,** 57 (1978).
58. C. M. Molinier-Jumel, B. Malfoy, M. A. Reynaud, and G. Aubel-Sadrom, *Biochem. Biophys. Res. Commun.*, **84,** 441 (1978).
59. J. A. Plambeck, J. W. Lown, S. F. Yen, E. M. Acton, and J. H. Peters, Submitted to *Biochem. Pharmacol.*

Quantitative Comparison of Fermi Level Pinning at GaAs/Metal and GaAs/Liquid Junctions

G. Horowitz

CNRS, Laboratoire de Photochimie Solaire, 94320 Thiais, France

P. Allongue and H. Cachet

G.R.4 du CNRS, "Physique des Liquides et Electrochimie," associé à l'Université Pierre et Marie Curie, 75230 Paris Cedex 05, France

ABSTRACT

Flatband potential (V_{FB}) of (100)-oriented n-GaAs electrodes in various aqueous solutions have been determined by ac impedance measurements. The Nernstian variation of V_{FB} with pH (−60 mV/pH) was verified in both indifferent electrolytes and redox-couple solutions. Taking into account this pH dependence, the barrier height ϕ_B of the n-GaAs/liquid junction with various redox couples could be calculated. ϕ_B was determined at the point of zero zeta potential (PZZP), where the voltage drop due to specific adsorption of OH groups vanishes. A pH (PZZP) of 2.8 was estimated from published data for the electron affinity of GaAs. The variation of ϕ_B as a function of redox potential at the GaAs/liquid junction could then be quantified through the slope S of the ϕ_B (V_{redox}) straight line. A value of $S \simeq 0.8$ was found, showing that Fermi level pinning is much weaker than at the GaAs/metal junction, at which one has $S \simeq 0.05$. The behavior is confirmed by published data on p-GaAs and polymer-coated n-GaAs. We discuss these results within the framework of recent works on the semiconductor/metal Schottky barrier.

Considerable attention has been brought recently to the problem of Fermi level pinning at semiconductor/liquid junctions. A recent report of the Institute for Science Information on the 1980 Chemistry papers most cited in 1980-1982 (1) showed that an article by Bard *et al.* (2) devoted to this problem has been cited 60 times during that period. In this article, was presented a model to account for the fact that the photovoltage measured on semiconductor electrodes (n-GaAs, p-GaAs, and p-Si) in acetonitrile solutions of various redox couples did not follow a linear variation as a function of the redox potential as would be expected according to the classical (Schottky) model for semiconductor/liquid junction, in which the band-edge positions at the semiconductor surface are fixed with respect to the solution levels (3). The modified model advanced by Bard *et al.* referred to the concept of Fermi level pinning due to surface states, which had been first proposed by Bardeen (4) to explain the observation that for most covalent semiconductors (Si, Ge, GaAs, InP, . . .) the semiconductor/metal barrier height is independent of the metal.

More recently, measurements have been reported on n-GaAs photoanodes protected against photocorrosion with various polymer films: polypyrrole (PPy) (5), polystyrene pendant $Ru(bpy)_3^{2+}$ (PSt-bpy-Ru) (6), and poly-3-methylthiophene (PMeT) (7). Open-circuit voltages V_{oc} greater than 1V have been reached with such electrodes. Furthermore, a quasi-linear variation of V_{oc} with redox potential is observed, suggesting that Fermi level pinning does not occur. The question then arises whether this behavior is characteristic of the n-GaAs/liquid junction or comes from modifications in the surface states when a conducting polymer is put between the semiconductor and the solution.

However, recent investigations on the semiconductor/metal interface led to the conclusion that the phenomenon responsible for the narrow range of barrier heights observed on GaAs/metal junctions is not the presence of intrinsic surface states (the so-called Tamm and Shockley surface states) at the semiconductor surface. Brillson (8) attributes this narrow range to a microscopic charge redistribution at the semiconductor/metal interface that depends on the chemical reactivity of the metal coverage. More recently, measurements on (110)-cleaved GaAs in ultrahigh vacuum (UHV) led Spicer *et al.* (9) to think that the pinning is due to extrinsic surface states due to defects produced at the semiconductor surface by the presence of the metal adatoms. Bolmont *et al.* (10) think that these surface states are rather due to a reconstruction of the GaAs surface by chemical bondings of the metal atoms with the semiconductor atoms. It thus seems established that the presence of the metal is necessary to induce the surface-state distribution leading to Fermi level pinning. Since the chemical reactivity of a liquid electrolyte is different from that one of a metal, one can expect a different behavior between the two kinds of junctions as far as the barrier formation is concerned. In this paper, we report flatband potential and open-circuit potential measurements performed on PMeT-coated and bare n-GaAs in contact with aqueous solutions of various redox couples. The results suggest that Fermi level pinning is much less important at the n-GaAs/liquid junction than at the n-GaAs/metal junction. This result is compared to recently published data on p-GaAs/liquid junctions and discussed within the framework of recent theories on the semiconductor/metal junction.

Experimental

Nonintentionally doped n-type (100)-oriented GaAs single-crystal slices were purchased from RTC (Caen, France). Ohmic contacts were made by vacuum evaporating Ge (12 weight percent [w/o]) Au alloy and annealing at

400°C under N_2. The electrodes were then mounted on glass tubes with Torr Seal (Varian) resin and the active surface polished with 1 μm diamond paste. Before each measurement, the electrode surface was chemically etched in either H_2SO_4:H_2O_2:H_2O (1:1:1 volume ratio) mixture or in Br_2-MeOH solution. Both of these etching procedures led to similar experimental results.

Electrodeposition of polymer films was performed under illumination in 0.1*M* supporting salt, 1*M* distilled 3-methylthiophene, acetonitrile solutions, as described in a previous paper (7). The thickness of the film was monitored by measuring the charge with a digital coulometer. Typical thickness was about 0.1 μm.

Electrolytic solutions were prepared with reagent-grade chemicals and doubly distilled water. The various redox couples employed are listed in Table IV. For $[Fe(CN)_6]^{4-/3-}$ and $Fe^{2+/3+}$ couples, the concentrations were 0.1*M*. I^-/I_3^- and Br^-/Br_2 couples were obtained by adding 0.01*M* I_2 and 0.1*M* KI, and 0.01*M* Br_2 and 0.1*M* KBr, respectively, to 0.1*M* H_2SO_4 solutions. $Fe^{II/III}$ citrate was prepared by adding 0.1*M* $Fe(ClO_4)_2$ to a solution containing 1*M* NaH_2 citrate and 1*M* $NaClO_4$. The solution was then buffered to *p*H 9.4 by adding ammonia. S^{2-}/S_n^{2-} solutions were obtained by equimolar dissolution of Na_2S and S in KOH or NaOH solutions. The preparation of Se^{2-}/Se_2^{2-} solutions has been described elsewhere (11).

Impedance measurements were made in a classical three-electrode cell with a saturated calomel (SCE) reference and a Pt counterelectrode. Impedance was determined over a wide frequency range by using a 1174 Solartron frequency response analyzer equipped with a data management system.

Results

The correlation between the open-circuit voltage (taken as the difference between the photocurrent onset potential V_{on} and the redox potential V_{redox}) and V_{redox} for polymer-coated n-GaAs-based PEC cells is shown in Fig. 1. The data were taken from Ref. (6) for PSt-bpy-Ru- and Ref. (7) for PMeT-protected electrodes. The slope of the least squares fit straight line is 0.81, a value close to unity. This suggests that very weak Fermi level pinning occurs at polymer-coated n-GaAs/liquid junction. A similar behavior has been reported for n-GaAs/PPy electrodes (5), although no data were given for this system.

In order to determine whether this behavior is brought by the polymer film or is characteristic of the n-GaAs/liquid junction, measurements of the flatband potential V_{FB} were carried out on PMeT-coated and bare electrodes in various redox couples. V_{FB} was obtained by ac impedance measurements over a wide frequency range (25 Hz-250 kHz). Impedance data were analyzed by means of a nonlinear least squares fit method, according to the equivalent circuits given in Fig. 2. In the complete circuit (Fig. 2a) the Helmholtz layer capacitance C_H is generally omitted since it is at least two orders of magnitude greater than the space charge layer capacitance C_{sc}. Analyses according to this complete circuit led to low values for the dispersion capacitance C_{ss} ($C_{ss}/C_{sc} < 0.1$), suggesting a low density of surface states. Consequently, most of the impedance data could be analyzed according to the simplified circuit given in Fig. 2b. Typical values for the series and parallel resistances R_s and R_p are 10 $\Omega \cdot cm^2$ and 10,000 $\Omega \cdot cm^2$, respectively. Good linear Mott-Schottky (M-S) plots for C_{sc} were obtained in all cases, for both polymer-coated and bare electrodes. The average of the slopes gave a donor concentration of 2.8 ($\pm$0.2) $\times 10^{16}$ cm^{-3}. The value given by the manufacturer is 1.9 $\times 10^{16}$ cm^{-3}. This slight increase corresponds to a roughness factor of 1.2.

Table I gives the values for V_{FB} obtained on bare and PMeT-coated n-GaAs in I^-/I_3^-, $Fe^{2+/3+}$, and Br^-/Br_2 solutions. If we discard the measurement on coated electrode in $Fe^{2+/3+}$ solution, a mean value of -0.88 ± 0.04 V/SCE is obtained. The mean deviation is inside the range of experimental error (a mean deviation of $\pm$0.5V is generally taken for impedance determinations of V_{FB}) and two main results can then be deduced from the data given in Table I: (*i*) V_{FB} is equivalent at bare and PMeT-covered electrodes. Again, a similar invariance has been observed on PPy- (5) and PSt-bpy-Ru-coated n-GaAs (6). (*ii*) V_{FB} does not depend upon the redox potentials, at least over the potential range covered by the three redox couples used.

It was, of course, necessary to extend the potential range of our V_{FB} determinations towards more negative values of V_{redox}, but some preliminary measurements had to be done in order to check the dependence of the flatband potential upon two other parameters of the solution: *p*H and redox-ion concentration.

The variation of V_{FB} with pH in indifferent electrolyte solutions is shown in Fig. 3. Data were obtained on (100)-oriented GaAs. Other data on the same orientation reported by Janietz *et al.* (12) and Haroutiounian *et al.* (13) are also drawn in Fig. 3, together with data reported by Laflere *et al.* (14) on $(\bar{1}\bar{1}\bar{1})$-oriented GaAs surface. The slope of the least squares fit straight line is -60 mV/pH with a correlation factor of 0.997. The well-known Nernstian behavior (3) is then observed on both surface orien-

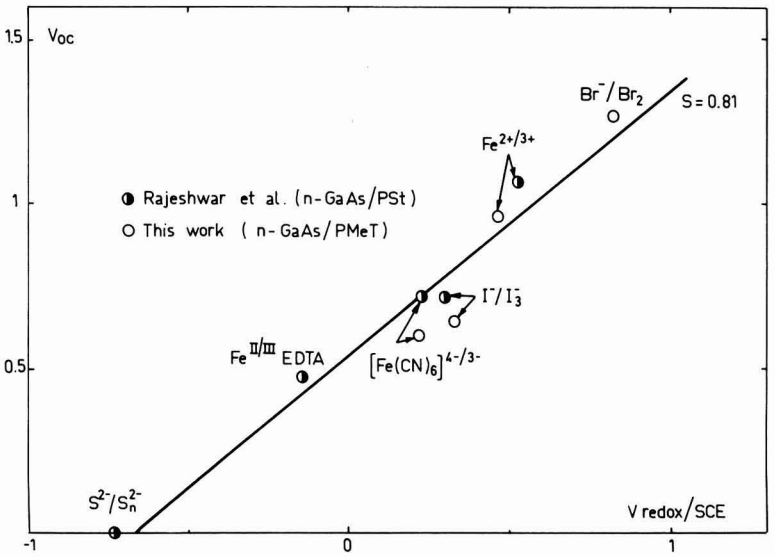


Fig. 1. Variation of the open-circuit potential V_{oc} (taken as the difference between the onset potential and redox potential) at PMeT- and PSt-bpy-Ru-coated n-GaAs in aqueous solutions of various redox couples. Data for GaAs/PSt taken from Rajeshwar *et al.* (6).

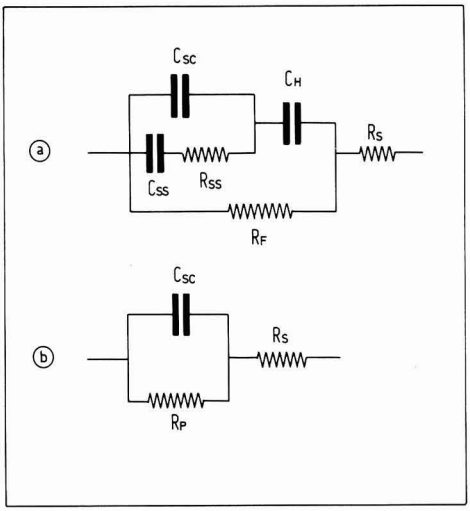


Fig. 2. (a): Equivalent circuit of a semiconductor/liquid junction. C_{sc} : space charge layer capacitance; C_H : Helmholtz layer capacitance; C_{ss} and R_{ss} : surface-state capacitance and resistance; R_F : Faradaic resistance; R_s : series resistance. (b): Simplified equivalent circuit used for analyzing impedance data.

tations. This result disagrees with that one reported by Rajeshwar and Mraz (15), who found a slope of −15 mV/pH on (100)-oriented n-GaAs.

The pH variation of V_{FB} was also measured with a redox couple added to the solution. The ideal redox couple for such a measurement is $[Fe(CN)_6]^{4-/3-}$, which is soluble at all pH. Furthermore, its redox potential remains constant at +0.22 V/SCE, except at pH < 2, where it shifts towards positive potentials. Figure 3 shows that V_{FB} is shifted to positive potentials in the presence of $[Fe(CN)_6]^{4-/3-}$ couple. Importantly, V_{FB} still follows a Nernstian behavior:

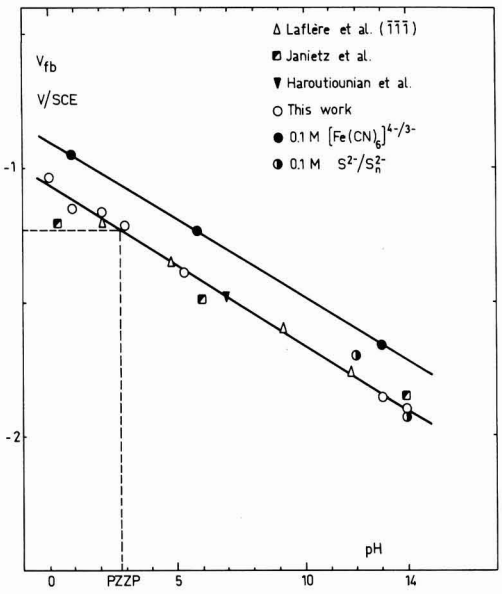


Fig. 3. Variation of the flatband potential V_{FB} as a function of the pH of the solution, for redox-free, and $[Fe(Cn)_6]^{4-/3-}$ and S^{2-}/S_n^{2-} containing, solutions. Dotted line shows the determination of the PZZP (see text). Data were taken from Ref. (12-14). All data on (100) GaAs unless otherwise stated.

Table I. Redox and flatband potentials of bare and PMeT-covered n-GaAs in three different redox couples. All solutions have a pH of 0.9 (0.1M H_2SO_4)

Redox couple	V_{redox}/SCE	V_{FB}/SCE Bare	V_{FB}/SCE PMeT-coated
I^-/I_3^-	0.33	−0.81	−0.87
$Fe^{2+/3+}$ (H_2SO_4 0.1M)	0.42	−0.89	−0.71
Br^-/Br_2	0.83	−0.91	−0.92

the slope of the least squares fit straight line is −59 mV/pH, which is the exact theoretical value. The variation of V_{redox} at low pH does not induce any deviation of V_{FB}. This confirms the independence of V_{FB} with V_{redox}.

Similar experiments were made with S^{2-}/S_n^{2-} couple at pH 12 and 14. No significant shift of V_{FB} is observed when this redox couple is added to the solution, and a similar pH dependence is obtained. We shall then assume in the following that the flatband potential always follows a Nernstian variation with pH for all redox couples added to the solution.

The last preliminary verification was to check the variation of V_{FB} with redox-ion concentration. Experiments were made with various concentrations of $[Fe(CN)_6]^{4-/3-}$ at pH 13 (0.1M KOH) and S^{2-}/S_n^{2-} at pH 14 (1M KOH). Results are given in Table II and III. A mean value of −1.90 ± 0.04 V/SCE is obtained with S^{2-}/S_n^{2-} couple: this variation is within the experimental error. As far as $[Fe(CN)_6]^{4-/3-}$ couple is concerned, the variation occurring between 10^{-3} and $10^{-4}M$ corresponds to the shift observed in Fig. 3: the flatband potential behaves as if the effect of the redox-couple disappears when its concentration is lower than $10^{-3}M$. Anyhow, we are still far from the −59 mV/decade variation reported by Ginley and Butler (16) for the CdS/Na_2S junction, which was attributed to an adsorption of HS^- ions at the CdS surface. We can then assume that V_{FB} is insensitive to the redox ion concentration.

The flatband potential was determined for two more redox couples: Se^{2-}/Se_2^{2-} (pH 14) and $Fe^{III/II}$ citrate (pH 9.4). All our results are gathered in Table IV. The value corresponding to H_2/H^+ couple was taken from Fig. 3. In order to compare the results obtained for all redox couples, V_{FB} data were recalculated at pH = 2.8 by assuming a variation of −59 mV/pH. The reasons for this choice will be explicited in the discussion section. All data obtained on bare electrodes are plotted in Fig. 4, together with the values measured on PMeT- and PSt- [from Ref. (6)] coated n-GaAs. The redox-potential range is now almost 2V, and a slight variation of V_{FB} can be noted, with a slope of *ca.* 0.2.

Discussion

The classical model of the semiconductor/metal barrier was first developed by Schottky (17). This model pre-

Table II. Flatband potential of n-GaAs in 0.1M KOH (pH 13) with various concentrations of $[Fe(CN)_6]^{4-/3-}$ ions

$[Fe(CN)_6]^{4-/3-}$	V_{FB}/SCE
$10^{-1}M$	−1.66
$10^{-3}M$	−1.63
$10^{-4}M$	−1.83
$10^{-5}M$	−1.89

Table III. Flatband potential of GaAs in 1M KOH (pH 14) with various concentrations of $[S^{2-}/S_n^{2-}]$ ions

$[S^{2-}/S_n^{2-}]$	V_{FB}/SCE
1M	−1.85
$10^{-1}M$	−1.92
$10^{-3}M$	−1.93
$10^{-4}M$	−1.88

Table IV. Redox potentials, flatband potentials, and barrier heights of bare n-GaAs in various redox couple aqueous solutions. Data for H_2/H^+ couple taken from Fig. 3. Barrier height ϕ_B calculated from Eq. [3] with $\Delta V_{fc} = 0.07V$ (see text)

Redox couple	V_{redox}/SCE	ϕ_{redox} (eV) ($E_o = 4.9$ eV)	V_{FB}/SCE	pH	V_{FB}/SCE (pH 2.8)	ϕ_B (eV)
Se^{2-}/Se_2^{2-}	−0.95	3.95	−2.05	14	−1.39	0.51
S^{2-}/S_n^{2-}	−0.73	4.17	−1.90	14	−1.24	0.58
$Fe^{II/III}$ citrate	−0.43	4.47	−1.70	9.4	−1.31	0.95
$[Fe(CN)_6]^{4-/3-}$ (0.1M KOH)	+0.22	5.12	−1.66	13	−1.06	1.35
$[Fe(CN)_6]^{4-/3-}$ (0.1M H_2SO_4)	+0.30	5.20	−0.95	0.9	−1.06	1.41
I^-/I_3^-	+0.33	5.23	−0.81	0.9	−0.92	1.32
$Fe^{2+/3+}$ (0.1M H_2SO_4)	+0.42	5.32	−0.89	0.9	−1.00	1.49
Br^-/Br_2	+0.83	5.73	−0.91	0.9	−1.02	1.92
H_2/H^+ (pH 2.8)	−0.41	4.49	−1.23	2.8	−1.23	0.86

dicts that the barrier height ϕ_B should be given (for an n-type semiconductor) by the difference between the metal work function ϕ_m and the semiconductor electron affinity χ_s. The concept of Fermi level pinning was first introduced by Bardeen (4) to explain the observed independence of the barrier height upon the metal work function for some semiconductors. This phenomenon was believed to result from a significant density of intrinsic (Tamm and Shockley) surface states at the semiconductor surface. Later, Cowley and Sze (18) showed that the Schottky and Bardeen models are the limiting cases of a more general expression for the barrier height that can be reduced to Eq. [1]

$$\phi_B = S\phi_m + \text{const.} \quad [1]$$

where S is dimensionless parameter depending on the semiconductor. From the study of the value of S for a large number of semiconductors, Kurtin *et al.* (19) showed that S can be quantitatively related to the ionicity of the semiconductor, which they measured as the difference ΔX in the electronegativities of the two constituents

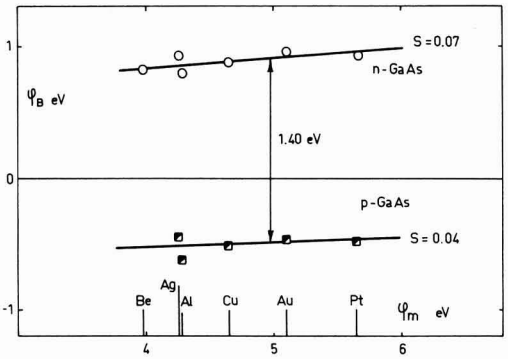


Fig. 5. Variation of the Schottky barrier height ϕ_B of a GaAs/metal junction as a function of the metal work function ϕ_m. Data for ϕ_B taken from Ref. (20), and for ϕ_m from Ref. (21).

of the semiconductor compounds (ΔX is taken as 0 in the case of an element semiconductor): S remains small for $\Delta X < 0.7$ and then changes rapidly to a value equal to unity when $\Delta X > 0.7$. A fundamental difference was then shown between ionic (*e.g.*, oxide) and covalent (*e.g.*, III-V compound) semiconductors. A similar result was obtained by Brillson (8) by taking the heat of compound formation as the measure of the ionicity.

The variation of ϕ_B with ϕ_m for GaAs is shown in Fig. 5. Data for ϕ_B were taken from Ref. (20). They were obtained by capacitance measurements on vacuum-cleaved surfaces. Recent determinations of metal work functions were taken from Ref. (21). A value of S of 0.07 is obtained for n-type and 0.04 for p-type GaAs. A quantitative comparison of Fermi level pinning at GaAs/metal and GaAs/liquid junctions can be made by calculating the value of S at the GaAs/liquid junctions. Figure 6 shows how ϕ_B can be determined from the value of V_{FB}. The dependence of the flatband potential as a function of the

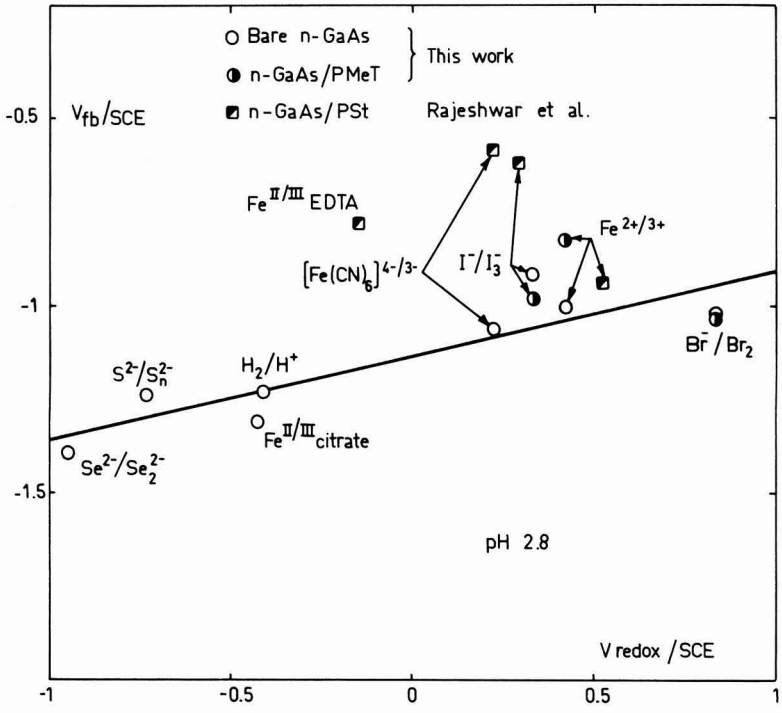


Fig. 4. Variation of the flatband potential with the redox potential at bare and polymer-coated GaAs. Values of V_{FB} recalculated for a pH of 2.8 by assuming a variation −59 mV/pH. Data for PSt-coated GaAs taken from Ref. (6).

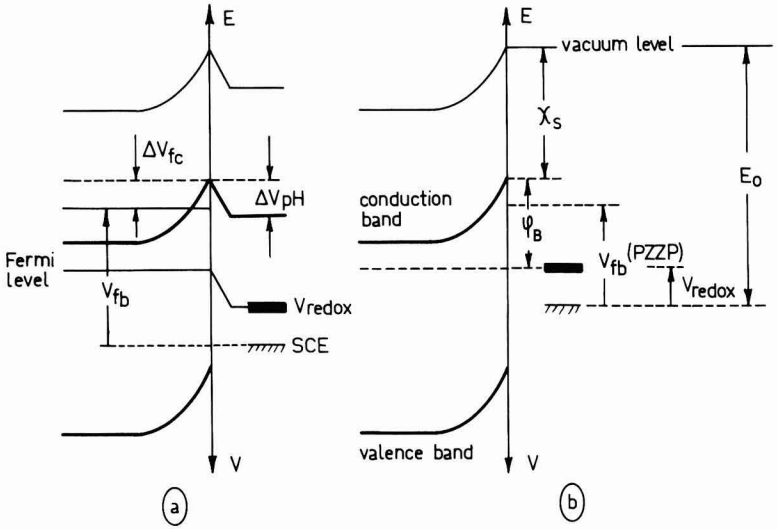


Fig. 6. Energetic diagram of a n-type semiconductor/liquid junction at equilibrium (a) general case and (b) at the point of zero zeta potential. Flatband (V_{FB}) and redox (V_{redox}) potentials are referred to SCE level; semiconductor electron affinity χ_s is defined with respect to the vacuum level. Energy and potential scales may be related through the equation: $E = E_o + qV$, where q is the absolute electron charge. The meaning of other symbols is given in text. The variations of the vacuum level represent the existence of local electric fields.

pH is taken into account through a potential drop ΔV_{pH} due to specific OH groups adsorption (Fig. 6a). As pointed out by Butler and Ginley (22), there exists a value of the pH where $\Delta V_{pH} = 0$, called the point of zero zeta potential (PZZP) (Fig. 6b). This point can be determined from the value of the electronic affinity of the semiconductor χ_s through Eq. [2]

$$\chi_s = E_o + q[V_{FB}(\text{PZZP}) - \Delta V_{fc}] \quad [2]$$

where E_o is a constant relating the reference electrode to the vacuum level and $\Delta V_{fc} = (kT/q) \ln (N_c/N_d)$ the difference between the Fermi and the bottom of the conduction band (N_c is the density of states at the bottom of the conduction band, and N_d the donnor impurity concentration). For n-GaAs and $N_d = 10^{16}$ cm^{-3}, one has $\Delta V_{fc} = 0.07$V. ϕ_B can then be calculated by using Eq. [3]

$$\phi_B = q[V_{redox} - V_{FB}(\text{PZZP}) + \Delta V_{fc}] \quad [3]$$

For the SCE a value of 4.75 eV is often taken for E_o (23). More recent determinations gave $E_o = 4.97$ eV (24). We shall take a value of 4.9 eV for E_o. The electron affinity of GaAs has been reported from photoelectric measurements to be 4.07 eV for the (110) face (25) and 3.63 eV for the (111) face (26).

A discussion on Schottky-barrier height measurements by Geppert *et al.* led to a value of 3.57 eV (27). However, a theoretical value for χ_s can be calculated according to Mulliken (28) and Nethercot (29) by using the following relations

$$\chi_s = E_F^i - 1/2\, E_\kappa \quad [4]$$

$$E_F^i = (M_A M_B)^{1/2} \quad [5]$$

$$M_A = 1/2\, (I_1 + A_f) \quad [6]$$

where E_F^i is the intrinsic Fermi level, E_κ the bandgap, M_A the Mulliken potential of element A, I_1 the first ionization potential, and A_f the atomic electron affinity. Values for I_1 and A_f can be found in Ref. (21) and (30). We calculated an electron affinity of 3.40 eV for GaAs. From these four different determinations, a reasonable value of 3.60 eV can be assumed for χ_s. It can now be seen that at the PZZP we have $V_{FB} = (\chi_s - E_o)/q + \Delta_{fc} = 3.60 - 4.9 + 0.07 = -1.23$ V/SCE. By carrying this value in Fig. 3, the point of zero potential is found to occur at pH = 2.8.

Values for ϕ_B calculated from Eq. [3] are given in Table IV, along with the redox "work function" ϕ_{redox}, which we define as

$$\phi_{redox} = E_o + qV_{redox}$$

A plot of these data is given in Fig. 7. A value of $S = 0.78$ is obtained. This value is very close to that one deduced from V_{oc} measurements (Fig. 1) and again suggests a very slight Fermi level pinning at the n-GaAs/aqueous solution interface.

Also shown in Fig. 7 are values of the barrier height at a p-GaAs/acetonitrile-solution junction, calculated from flatband potential measurements recently reported by Nagasubramanian *et al.* (31). Equation [3] was used for this calculation, with $\Delta V_{fc} = 0.12$V. Data were not corrected for a ΔV_{pH} because this kind of correction is not likely to occur in acetonitrile solutions. A value of $S = 0.69$ is obtained. The mean difference between the two straight lines for n- and p-type GaAs is 1.40 eV, a value very close to the bandgap (1.43 eV). However, this result may be fortuitous because of the uncertainty on the values for χ_s and E_o. Moreover, the SCE scale may be shifted from water to acetonitrile solutions.

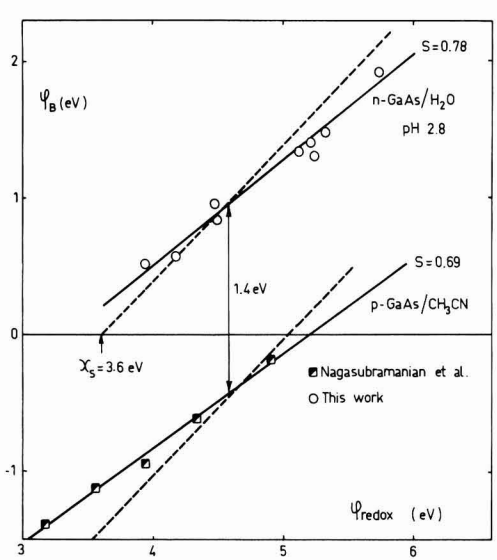


Fig. 7. Same as Fig. 5 for a GaAs/liquid junction. ϕ_B taken from Table IV for n-GaAs and calculated from data in Ref. (31) by using Eq. [2] for p-GaAs. Dotted line gives the values of ϕ_B that would be expected in the absence of Fermi level pinning.

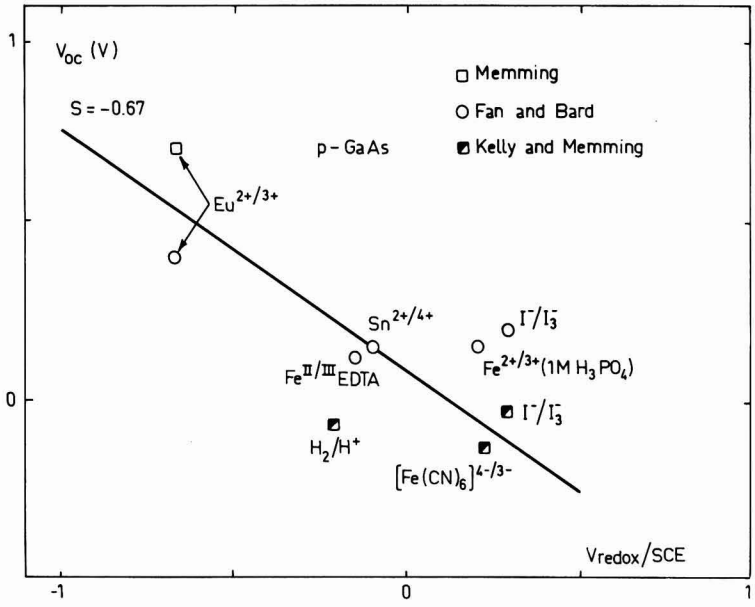


Fig. 8. Same as Fig. 1 for a bare p-GaAs electrode. Data taken from Ref. (32-34).

Finally, Fig. 8 shows the variation of the open-circuit potential for a p-GaAs/aqueous solution junction. Data were taken from Ref. (32-34). As previously, V_{oc} was taken as $V_{on} - V_{redox}$. Negative values of V_{oc} correspond to systems unable to work as energy converters. The slope of the straight line is −0.67 (this slope is negative because we are now dealing with a p-type semiconductor), in excellent agreement with the value deduced from flatband potential measurements.

The dispersion of the data in Fig. 8 can be explained by the fact that the onset potential of a semiconductor/liquid junction is not uniquely determined by the position of the bandedges at the semiconductor surface but also by the kinetics of electron transfers at the interface. A similar dispersion may be observed in Fig. 1.

A quantitative comparison of Fermi level pinning between GaAs/metal and GaAs/liquid junctions can now be made with the help of the parameter S. Figures 5 and 7 unambiguously show that Fermi level pinning at GaAs/liquid junction is considerably less pronounced than at GaAs/metal junction. This is the main result of this paper and it will now be discussed. From the classical Bardeen theory of Fermi level pinning by intrinsic surface states, one should expect from Fig. 5 a distribution of surface states centered at about 0.5 eV above the top of the valence band. From results of several experimental groups, it now appears firmly established that there is no intrinsic surface states in the bandgap of GaAs [see, e.g., Ref. (9) and references therein]. This is explained by a lattice rearrangement (or relaxation) of the surface, which moves the surface states out of the bandgap. The Fermi level pinning is then attributed to extrinsic surface states brought by the metal deposition, either through defects produced at the semiconductor surface (9) or by a restoration of the initial (nonrelaxed) surface (10). However, Brillson (8) suggests that the concept of Fermi level pinning should be replaced by that of microscopic charge redistribution at the semiconductor/metal junction, controlled by the degree of chemical reactivity between the semiconductor and metal atoms. The common characteristic of these models is that the "Fermi level pinning" at the semiconductor/metal junction is mainly induced by chemical reactions between the semiconductor and the metal overlayer. From our results and the preceding models, it can be concluded that the chemical reactivity of an aqueous electrolyte with GaAs surfaces is not able to induce a surface-state distribution sufficiently high to promote full Fermi level pinning.

However, a slight degree of Fermi level pinning is observed at GaAs/liquid junctions. Some ideas can be put forward to give the beginning of an explanation for this phenomenon: (*i*) Recent investigations on the kinetics of charge transfer at both n-type (35) and p-type (34) GaAs/liquid junctions under illumination suggest that (extrinsic or intrinsic) surface states do exist at the GaAs surface, but that the occupation rate of these states depends on kinetic factors. This is proved particularly by the shift of V_{FB} under illumination, and the fact that no surface states can be detected in the dark. (*ii*) A GaAs surface in contact with an aqueous or acetonitrile solution is far more "dirty" than a UHV-cleaved face. The formation of oxides has been shown to occur by simply dipping GaAs in water (36). The presence of extrinsic surface states is then likely, since it has been shown that the chemisorption of a submonolayer of oxygen suffices to induce such states (9).

As a final remark, the weak Fermi level pinning at the GaAs/liquid junction should permit high open-circuit voltages. Such high values have been already observed at polymer-protected n-GaAs electrodes with oxidizing redox couples such as $Fe^{2+/3+}$, I^-/I_3^-, or Br^-/Br_2. Similar results can be expected with p-GaAs and reducing redox systems. This idea is supported by a value of 0.7V measured by Memming (32) on a p-GaAs/$Eu^{2+/3+}$ cell. This result is noteworthy since the barrier height at p-GaAs/metal junction is always lower than 0.5V.

Acknowledgments

The authors are very grateful to Dr. C. A. Sebenne (Laboratoire de Physique des Solides, Université Pierre et Marie Curie, Paris, France) and Dr. F. Garnier (Laboratoire de Photochimie Solaire, CNRS, Thiers, France) for valuable discussions. This work was supported by the GRECO 130061 of the CNRS.

Manuscript submitted March 15, 1984; revised manuscript received June 4, 1984.

REFERENCES

1. E. Garfield, *Current Contents*, **35**, 5 (1983).
2. A. J. Bard, A. B. Bocarsly, F.-R. F. Fan, E. G. Walton, and M. S. Wrighton, *J. Am. Chem. Soc.*, **102**, 3671, (1980).
3. H. Gerischer, in "Physical Chemistry: An Advanced

Treatise," Vol. IXA, H. Eyring, D. Henderson, and W. Sost, Editors, p. 467, Academic Press, New York (1970).
4. J. Bardeen, *Phys. Rev.*, **71**, 717 (1947).
5. R. Noufi, D. Tench, and L. F. Warren, *This Journal*, **127**, 2310 (1980).
6. K. Rajeshwar, M. Kaneko, and A. Yamada, *ibid.*, **130**, 38 (1983).
7. G. Horowitz, G. Tourillon, and F. Garnier, *ibid.*, **131**, 151 (1984).
8. L. J. Brillson, *Phys, Rev. Lett.*, **40**, 260 (1978); *J. Vac. Sci. Technol.*, **16**, 1137 (1979).
9. W. E. Spicer, P. W. Chye, P. R. Skeath, C. Y. Su, and I. Lindau, *ibid.*, **16**, 1422 (1979).
10. D. Bolmont, P. Chen, V. Mercier, and C. A. Sebenne, in "Proceedings of the 16th International Conference on Physics of Semiconductors," Montpellier, France, Sept. 6-10, 1982; *Physica B&C*, **117, 118**, 816 (1983).
11. A. Bourrasse, H. Cachet, G. Horowitz, and S. Le Crom, *Rev. Phys. Appl.*, **17**, 801 (1982).
12. P. Janietz, R. Weiche, J. Westfahl, R. Landsberg, and R. Dehmlow, *J. Electroanal. Chem.*, **106**, 23 (1980).
13. E. Haroutiounian, J.-P. Sandinu, P. Clechet, P. Lamouche, and J.-R. Martin, *This Journal*, **131**, 27 (1984).
14. W. H. Laflere, F. Cardon, and W. P. Gomes, *Surf. Sci.*, **59**, 401 (1976).
15. K. Rajeshwar and T. Mraz, *J. Phys. Chem.*, **87**, 742 (1983).
16. D. S. Ginley and M. A. Butler, *This Journal*, **125**, 1968 (1978).
17. W. Schottky, *Naturwiss.*, **26**, 843 (1938).
18. A. M. Cowley and S. M. Sze, *J. Appl. Phys.*, **36**, 3212 (1965).
19. S. Kurtin, T. C. McGill, and C. A. Mead, *Phys. Rev. Lett.*, **22**, 1433 (1969); T. C. McGill, *J. Vac. Sci. Technol.*, **11**, 935 (1974).
20. C. A. Mead and W. G. Spitzer, *Phys. Rev.*, **134**, A713 (1964).
21. "CRC Handbook of Chemistry and Physics," 61st ed., R. C. Weast, Editor, pp. E83-84, CRC Press, Cleveland, OH (1981).
22. M. A. Butler and D. S. Ginley, *This Journal*, **125**, 228 (1978).
23. F. Lohmann, *Z. Naturforsch., Teil A*, **22**, 813 (1967).
24. R. Gomer and G. Tryson, *J. Chem. Phys.*, **66**, 4413 (1977).
25. G. W. Gobeli and F. G. Allen, *Phys. Rev. A*, **137**, 245 (1965).
26. J. Wojas, *Acta Phys. Polonica*, **35**, 1025 (1969).
27. D. V. Geppert, A. M. Cowley, and B. V. Dore, *J. Appl. Phys.*, **37**, 2458 (1966).
28. R. S. Mulliken, *J. Chem. Phys.*, **2**, 782 (1934); *ibid.*, **3**, 573 (1935).
29. A. H. Nethercot, Jr., *Phys. Rev. Lett.*, **33**, 1088 (1974).
30. H. Hotop and W. C. Lineberger, *J. Phys. Chem. Ref. Data*, **4**, 539 (1975).
31. G. Nagasubramanian, B. L. Wheeler, and A. J. Bard, *This Journal*, **130**, 1680 (1983).
32. R. Memming, *ibid.*, **125**, 117 (1978).
33. F.-R. F. Fan and A. J. Bard, *J. Am. Chem. Soc.*, **102**, 3677 (1980).
34. J. J. Kelly and R. Memming, *This Journal*, **129**, 730 (1982).
35. P. Allongue, H. Cachet, and G. Horowitz, *ibid.*, **130**, 2352 (1983).
36. H. Cachet, R. Calsou, M. Froment, and H. Mathlouthi, *J. Microsc. Spectrosc. Electron.*, **7**, 9 (1982).

Mathematical Modeling of Liquid-Junction Photovoltaic Cells

I. Governing Equations

Mark E. Orazem[1] and John Newman*

Materials and Molecular Research Division of Lawrence Berkeley Laboratory and Department of Chemical Engineering, University of California, Berkeley, California 94720

ABSTRACT

The equations which govern the liquid-junction photovoltaic cell are presented in the context of a one-dimensional mathematical model. This model treats explicitly the semiconductor, the electrolyte, and the semiconductor-electrolyte interface in terms of potentials and concentrations of charged species. The model incorporates macroscopic transport equations in the bulk of the semiconductor and electrolyte, coupled with a microscopic model of the semiconductor-electrolyte interface. Homogeneous and heterogeneous recombination of electron-hole pairs is included within the model. Recombination takes place at the semiconductor-electrolyte interface through interfacial sites, which can enhance the recombination rate. The coupled nonlinear ordinary differential equations of the model were posed in finite-difference form and solved numerically. The results are presented in succeeding papers.

The liquid-junction photovoltaic cell is an electrochemical system with one or two semiconducting electrodes. This system has undergone intense study since the early 1970's as a means of converting solar energy to chemical or electrical energy (1-8). A number of articles review the physics of the liquid-junction cell, the role of the semiconducting electrode, and the literature [see *e.g.*, Ref. (9-19)].

A mathematical model is presented here which treats explicitly all components of the liquid-junction photovoltaic cell. The results of the model, obtained through numerical computation, are used to gain insight into the cell behavior and into the factors influencing cell design.

Development of a mathematical model constitutes an important step toward understanding the behavior and predicting the performance of the liquid-junction photovoltaic cell. Coupled phenomena govern the system, and the equations describing their interaction cannot, in general, be solved analytically. Two approaches have been taken in developing a mathematical model of the liquid-junction photovoltaic cell: approximate analytic solution of the governing equations and numerical solution. These are reviewed elsewhere (20).

The use of a digital computer in the numerical solution of the equations governing the liquid-junction cell eliminates the need for restrictive assumptions. The numerical approach was taken in this work (20) and has been used in the modeling of solid-state devices (21-26). Laser and Bard (27-30) developed a computer program which was used to calculate open-circuit photopotentials, the transient behavior of the system following charge injection, and the time dependence of photocurrents in liquid-junction cells. Time-dependent material balances of holes and electrons and Poisson's equation described the semiconductor. The interface was included in terms of charge and flux boundary conditions. The model was limited by lack of convergence for electrode thicknesses greater than that of the space-charge region and did not treat explicitly the electrolyte and counterelectrode.

A number of computer programs related to the liquid-junction photovoltaic cell have been developed. Leary *et al.* (31), for example, calculated carrier concentrations in

* Electrochemical Society Active Member.
[1] Present address: Department of Chemical Engineering, University of Virginia, Charlottesville, Virginia 22901.

polycrystalline films using a numerical solution of Poisson's equation coupled with overall charge neutrality within spherical grains. Their model was used for analysis of semiconductor gas sensors. A computer program has been presented by Davis and colleagues (32-34) which uses simultaneous calculation of surface and solution equilibrium states to obtain the equilibrium condition of electrical double layers.

Physical Model

A one-dimensional representation of the liquid-junction photovoltaic cell is presented in Fig. 1. This model includes macroscopic representations of the counterelectrode, the electrolytic solution, and the semiconductor coupled with a microscopic representation of the interface between the semiconductor and the solution. The semiconductor-electrolyte interface couples the macroscopic equations which govern the adjacent bulk phases.

The interface is represented by four planes, inner and outer Helmholtz planes on the electrolyte side of the interface and inner and outer surface states on the semiconductor side. The outer Helmholtz plane (OHP) is the plane of closest approach for (hydrated) ions associated with the bulk solution. The inner Helmholtz plane (IHP) passes through the center of ions specifically adsorbed on the semiconductor surface. The outer surface state (OSS) represents the plane of closest approach for electrons (and holes) associated with the bulk of the semiconductor. The inner surface state (ISS) is a plane of surface sites for adsorbed electrons.

This model of the semiconductor-electrolyte interface is an extension of the classical diffuse-double-layer theory (35-37). Charge adsorbed onto the IHP and the ISS planes is balanced by charge in the diffuse region of the electrolyte and the space-charge region of the semiconductor. The net charge of the interface, including surface planes and diffuse and space-charge regions, is equal to zero.

Within the model, single-step reactions relate concentrations and potentials at interfacial planes. A continuous spectrum of energy levels at the ISS is represented by three discrete energy levels (designated v, t, and c). Conduction electrons are adsorbed via reaction [1] (see the interface in Fig. 1) from the OSS to high-energy sites at the ISS, via reaction [10] to intermediate energy sites at the ISS, and via reaction [11] to low energy sites at the ISS. Via reaction [2], low-energy electrons at the ISS can occupy vacancies in the valence band, or holes, at the OSS. Intermediate energy electrons can transfer from the ISS to the OSS through reaction [12], and high energy electrons can transfer through reaction [13]. Reactions [3] and [4] allow the shifting of electrons from one energy level to another.

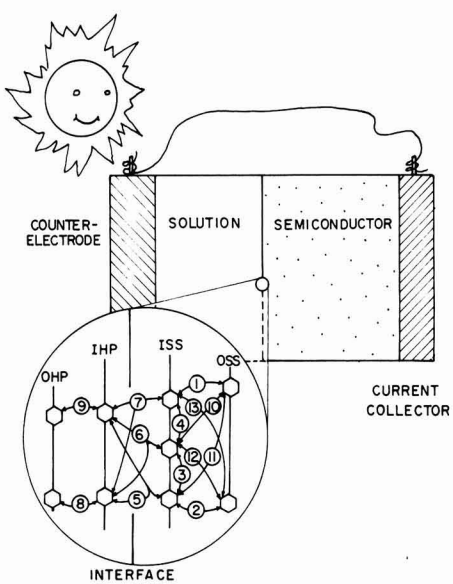


Fig. 1. Mathematical model of the liquid-junction photovoltaic cell

Ionic species from the solution are adsorbed into the IHP by reactions [8] and [9]. Two adsorbed species are considered here. It is assumed that other ionic species in the solution do not adsorb and do not participate in the electrochemical reactions. Relaxation of this assumption involves the inclusion of additional ion-adsorption and charge-transfer reactions. Reactions [5], [6], and [7] are the charge-transfer reactions that take place among adsorbed ions at the IHP and adsorbed high, intermediate, or low energy electrons at the ISS. Charge-transfer reactions allow passage of electrical current from the semiconductor to the solution.

Theoretical Development

The equations governing the liquid-junction photovoltaic cell in the dark or under steady-state illumination are developed here in terms of the model presented above. The governing relationships can be developed separately for the semiconductor and the electrolyte. The microscopic model of the semiconductor-electrolyte interface couples the equations governing the macroscopic systems.

Semiconductor.—The electrochemical potential of a given species can arbitrarily be separated into terms representing a reference state, a chemical contribution, and an electrical contribution

$$\mu_i = \mu_i^\theta + RT \ln (c_i f_i) + z_i \mathbf{F} \Phi \qquad [2]$$

where Φ is a potential which characterizes the electrical state of the phase and can be arbitrarily defined. The potential used here is the electrostatic potential which is obtained through integration of Poisson's equation (38). Equation [2] can be viewed as the defining equation for the activity coefficient, f_i.

The flux of an individual species within the semiconductor is driven by a gradient of electrochemical potential, which corresponds to gradients of potential and concentration [see *e.g.*, Chap. 11 in Ref. (39) and Gerischer (40)]. Under the assumption that the individual ionic activity coefficients are constant with a value of one,[2] the flux of holes is given by

$$N_{h^+} = - u_{h^+} \mathbf{F} p \frac{d\Phi}{dy} - D_{h^+} \frac{dp}{dy} \qquad [3]$$

and the flux of electrons by

$$N_{e^-} = u_{e^-} \mathbf{F} n \frac{d\Phi}{dy} - D_{e^-} \frac{dn}{dy} \qquad [4]$$

The concentrations of electrons and holes are represented by n and p, respectively, and the mobilities u_i are related to the diffusivities D_i by the Nernst-Einstein equation

$$D_i = RT u_i \qquad [5]$$

Homogeneous reaction takes place in the semiconductor; thus a material balance for a given species, say holes,[3] yields

[2] The assumption of constant activity coefficients, valid for dilute solutions, is appropriate for most semiconductors. The carrier concentrations in semiconductors is usually less than 0.0001M, which is low as compared to dilute aqueous solutions. The assumption of constant activity coefficients is in harmony with a Boltzmann distribution of electrons and holes. Use of Fermi-Dirac distributions for these charged species results in activity coefficients that are functions of concentration [see Ref. (46)].

[3] The development presented here, while applicable to p-type semiconductors, is oriented toward analysis of an n-type semiconductor in which holes are the minority carrier. Material balances of holes and electrons are not independent, and conservation of the minority carrier was chosen to improve the numerical computational accuracy.

$$\frac{dN_{h^+}}{dy} = R_{h^+} \quad [6]$$

where R_{h^+} is the net rate of production of holes under steady-state conditions.

The rate of production of holes is, by stoichiometry, equal to the rate of production of electrons and is governed by three concurrent processes: generation by absorption of light, generation by absorption of heat, and recombination of electrons and holes (*i.e.*, transfer of an electron from the conduction band to the valence band)

$$R_{h^+} = G_L + G_{th} - R_{rec} \quad [7]$$

Mathematical models of the homogeneous recombination process have been developed which incorporate single-step electron transfer from one energy level to another. They differ in the assumption of the presence or absence of impurities within the semiconductor which allow electrons to have energies between the conduction and valence-band energies (41, 42).

Most semiconducting materials contain impurities or imperfections within their lattice structure which may be described as fixed sites with valence-band electron energies within the semiconductor bandgap. The trap-kinetics model allows recombination to occur through these sites (see Fig. 2). Absorbed radiation drives an electron from the valence band to the conduction band, and all recombination and thermal generation reactions are assumed to occur through trap sites. This model results in

$$R_{h^+} = \eta m q_0 e^{-my} - \frac{N_t k_2 (np - n_i^2)}{\dfrac{k_1(N_v - p) + k_3(N_c - n)}{k_4} + \dfrac{k_2}{k_4} p + n} \quad [8]$$

where k_1, k_2, k_3, and k_4 are the rate constants for the corresponding reactions shown in Fig. 2. The intrinsic concentration is given by

$$n_i = \left[\frac{k_1 k_3 (N_c - n)(N_v - p)}{k_2 k_4}\right]^{1/2} \quad [9]$$

The electron and hole concentrations are generally small as compared to the respective conduction and valence-band site concentrations. The intrinsic concentration is therefore constant, and the reaction rate can be characterized with three lumped rate constants [$N_t k_2$, ($k_1 N_v$ + $k_3 N_c$)/k_4, and k_2/k_4]. Homogeneous electron-hole recombination was assumed in the mathematical model to occur through trap sites (Eq. [8] and [9]).

The expression for the intrinsic concentration (Eq. [9]) is consistent with the expression derived through statistical-mechanical models (see Eq. [32] of Chap. 6, Ref. (20)). The intrinsic concentration can be considered to be a constant for a given semiconductor only if the ratios n/N_c and p/N_v are negligibly small as compared to unity. This condition is consistent with the assumption of unity activity coefficients for electrons and holes. The value of the intrinsic concentration derived from statistical-mechanical arguments serves as a relationship among the kinetic parameters in Eq. [9].

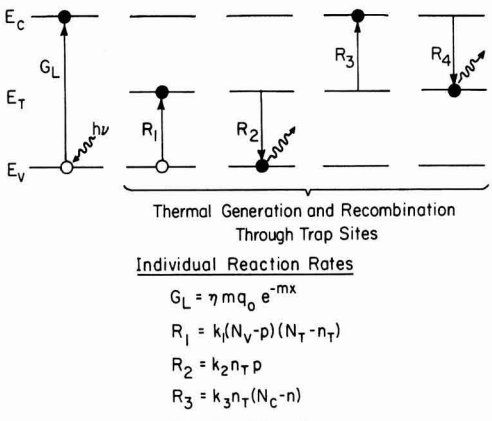


Fig. 2. Schematic representation of single-trap recombination kinetics in the semiconductor.

The divergence of the current is zero at steady state; therefore the fluxes of holes and electrons are related by

$$\frac{dN_{e^-}}{dy} - \frac{dN_{h^+}}{dy} = 0 \quad [10]$$

A material balance on electrons, analogous to Eq. [5], could be used to replace Eq. [10].

Poisson's equation

$$\frac{d^2\Phi}{dy^2} = -\frac{\mathbf{F}}{\epsilon_{sc}}[p - n + (N_d - N_a)] \quad [11]$$

relates the potential to the charge distribution. The concentrations of ionized electron donors and acceptors are represented by N_d and N_a, respectively. The Debye length

$$\lambda_{sc} = [\epsilon_{sc} RT/\mathbf{F}^2(N_d - N_a)]^{1/2}$$

characterizes the distance over which the potential varies in the semiconductor. It typically has a value of 1×10^{-6} to 2×10^{-5} cm.

The degree of ionization of donors or acceptors is dependent upon the concentrations of charged species within the semiconductor and upon the temperature. Complete ionization has been assumed in this work. This assumption is reasonable at room temperatures and is consistent with the assumption of unity activity coefficients.

Electrolyte.—For a one-dimensional case, neglecting convective effects, the flux of an ionic species is governed by potential and concentration gradients

$$N_i = -z_i u_i c_i \mathbf{F} \frac{d\Phi}{dy} - D_i \frac{dc_i}{dy} \quad [12]$$

Under the assumption that homogeneous reactions do not take place, conservation of mass yields a uniform flux at steady state, *i.e.*

$$\frac{dN_i}{dy} = 0 \quad [13]$$

The potential and concentrations of charged species are related by Poisson's equation

$$\frac{d^2\Phi}{dy^2} = -\frac{\mathbf{F}}{\epsilon_{sol}} \sum_i z_i c_i \quad [14]$$

Electroneutrality of the electrolyte is not assumed here because the diffuse region near the interface plays an important role in the microscopic model of the interface. The Debye length in the solution is given by

$$\lambda_{sol} = [\epsilon_{sol} RT/\mathbf{F}^2 \sum_i z_i^2 c_{i,\infty}]^{1/2}$$

and typically has a value of 1×10^{-8} to 1×10^{-7} cm.

The relationships presented above are sufficient to describe the electrolytic solution. An additional relationship yields the current density as a function of the ionic fluxes

$$i = \mathbf{F} \sum_i z_i N_i \quad [15]$$

Within the semiconductor, this can be regarded as an integrated form of Eq. [10].

Semiconductor-electrolyte interface.—A general interfacial reaction can be expressed as

$$\sum_i s_i M_i^{z_i} \rightarrow ne^- \quad [16]$$

where s_i is the stoichiometric coefficient of species i, M_i is a symbol for the chemical formula of species i, and n is the number of electrons transferred. [See Chap. 8 in Ref. (39).] For single-step reactions, n is equal to one.

The rate of a single-step reaction 1 at the interface is given by

$$r_l = k_{f,l} \exp\left[\frac{(1-\beta_l)\mathbf{F}\Delta\Phi_l}{RT}\right]\prod_i c_i^{p_{i,l}} - k_{b,l}\exp\left[\frac{-\beta_l\mathbf{F}\Delta\Phi_l}{RT}\right]\prod_i c_i^{q_{i,l}} \quad [17]$$

where β_l is a symmetry factor (usually assumed to be equal to 1/2), $k_{f,l}$ and $k_{b,l}$ are forward and backward reaction rate constants, respectively, and $\Delta\Phi_l$ is the potential driving force for the given reaction, l. The potential driving force enters into reactions involving charge transfer from locations of one potential to locations of another.

The reaction orders for a given species i in the forward and reverse directions are $p_{i,l}$ and $q_{i,l}$, respectively. They are determined from the stoichiometric coefficients, $s_{i,l}$

$$\text{If } s_{i,l} = 0;\ p_{i,l} = 0, \text{ and } q_{i,l} = 0$$

$$\text{If } s_{i,l} > 0;\ p_{i,l} = s_{i,l}, \text{ and } q_{i,l} = 0$$

$$\text{If } s_{i,l} < 0;\ p_{i,l} = 0, \text{ and } q_{i,l} = -s_{i,l}$$

The reaction rates are written in terms of the equilibrium constants as

$$r_e = k_{b,l}\left\{K_l \exp\left[\frac{(1-\beta_l)\mathbf{F}\Delta\Phi_l}{RT}\right]\prod_i c_i^{p_{i,l}} - \exp\left[\frac{-\beta_l\mathbf{F}\Delta\Phi_l}{RT}\right]\prod_i c_i^{q_{i,l}}\right\} \quad [18]$$

The equilibrium constant used here is the ratio of the forward and backward rate constants

$$K_l = \frac{k_{f,l}}{k_{b,l}} \quad [19]$$

Six of the 13 equilibrium constants are independent and can be calculated as functions of equilibrium interfacial concentrations and potentials

$$K_l = \exp\left[-\frac{\mathbf{F}}{RT}\Delta\Phi_l\right]\prod_i c_i^{-s_{i,l}} \quad [20]$$

A discussion of the calculation of equilibrium concentrations and potentials and the subsequent calculation of equilibrium constants is presented elsewhere [see Chap. 6, Ref. (20)]. The remaining constants can be calculated from Eq. [20] or from the following identities

$$K_4 = \frac{K_3(N_d - N_a)^2}{K_1K_2n_i^2} \quad [21a]$$

$$K_6 = K_5/K_3 \quad [21b]$$

$$K_7 = K_6/K_4 \quad [21c]$$

$$K_{10} = K_1K_4 \quad [21d]$$

$$K_{11} = K_{10}/K_3 \quad [21e]$$

$$K_{12} = K_2/K_3 \quad [21f]$$

and

$$K_{13} = K_{12}K_4 \quad [21g]$$

Within the parametric studies which follow (44), one independent rate constant is assumed to be characteristic of each of four groups of interfacial reactions. The four groups, shown in Fig. 1, are reactions [1], [2], [10]-[13] (OSS-ISS), reactions [3] and [4] (ISS), reactions [5]-[7] (ISS-IHP), and reactions [8] and [9] (IHP-OHP). The individual rate constants for each reaction l are related to the characteristic rate constant by

$$k_{b,l} = k_l^0 K_l^{-1/2} \quad [22]$$

and

$$k_{f,l} = k_{b,l}K_l = k_l^0 K_l^{1/2} \quad [23]$$

where k_l^0 is the pre-exponential part of the rate constant, with a characteristic value for a given reaction type, and β was given a value of one-half. These equations are consistent with Eq. [18] and [19].

Material balances govern the interface under steady-state conditions. These are expressed by continuity of flux at the OSS and the OHP

$$N_{e^-}|_{oss} = \sum_l -s_{e^-,l}r_{l,iss} \quad [24]$$

$$N_{h^+}|_{oss} = \sum_l -s_{h^+,l}r_{l,iss} \quad [25]$$

and

$$N_i|_{ohp} = \sum_l -s_{i,l}r_l \quad [26]$$

and material balances for each adsorbed species i at the ISS and the IHP

$$\sum_l s_{i,l}r_{l,iss} = 0 \quad [27]$$

and

$$\sum_l s_{i,l}r_{l,ihp} = 0 \quad [28]$$

Gauss's law can be applied to the region between the OSS and ISS

$$(\Phi_{oss} - \Phi_{iss}) = \frac{\delta_1}{\epsilon_{sc}}\left[\frac{\epsilon_2}{\delta_2}(\Phi_{iss} - \Phi_{ihp}) + \mathbf{F}\left(\sum_{iss}\gamma_i - g^+_{iss}\right)\right] \quad [29]$$

and between the ISS and the IHP

$$(\Phi_{iss} - \Phi_{ihp}) = \frac{\delta_2}{\epsilon_2}\left[\frac{\epsilon_{sol}}{\delta_3}(\Phi_{ihp} - \Phi_{ohp}) - \mathbf{F}\left(\sum_{ihp} z_i\gamma_i\right)\right] \quad [30]$$

The evaluation of Gauss's law in the region between the OSS and the ISS includes a term for a fixed positive charge at the ISS, q^+_{iss}, which was set equal to zero in this study.

Boundary conditions.—The semiconducting electrode is bounded at one end by the electrolyte and at the other end by a metallic current collector. The boundary conditions at the semiconductor-electrolyte interface are incorporated into the model of the interface. The boundary conditions at the semiconductor-current collector interface are that the potential is zero, the potential derivative is equal to a constant, determined by the charge assumed to be located at the semiconductor-current collector interface (this constant was set equal to zero in this study), and all the current is carried by electrons (the flux of holes is zero). The boundary conditions in the electrolytic solution are set a fixed distance (10 Debye lengths) from the interface. This distance may be considered to be a diffusion layer. The boundary conditions are that the potential gradient is continuous and that all concentrations have their bulk value.

Counterelectrode.—In the region sufficiently far from the interface that electroneutrality holds, the potential distribution is linear and is a function of current density. The potential drop in the region between the counterelectrode and the outer limit of the diffusion layer is given by

$$V_{IR} = \frac{Li}{\kappa} \quad [31]$$

where κ is the solution conductivity and L is the distance between the counterelectrode and the outer edge of the diffusion layer. The conductivity of dilute solutions is related to ionic mobilities and concentrations by

$$\kappa = \mathbf{F}^2 \sum_i z_i^2 u_i c_i \quad [32]$$

The potential drop across the counterelectrode-electrolyte interface is given by

$$V_{CE} = V^o_{CE} + \eta_{CE} \quad [33]$$

where V^o_{CE} is the equilibrium potential drop across the interface and η_{CE} is the total counterelectrode reaction overpotential. The total overpotential is related to the current density through the Butler-Volmer reaction model (39, 43)

$$i = i_o \left\{ \left[1 - \frac{i}{i_{4,lim}} \right] \exp \left[\frac{(1-\beta)n\mathbf{F}}{RT} \eta_{CE} \right] - \left[1 + \frac{i}{i_{3,lim}} \right] \exp \left[-\frac{\beta n \mathbf{F}}{RT} \eta_{CE} \right] \right\} \quad [34]$$

where i_o is the exchange current density associated with the bulk concentrations of reactants, $i_{k,lim}$ is the diffusion-limited current density associated with species k, and n is the number of electrons transferred in the counterelectrode reaction.

Conclusion

The equations which govern the liquid-junction photovoltaic cell are presented in the context of a one-dimensional mathematical model. This model treats explicitly the semiconductor, the electrolyte, and the semiconductor-electrolyte interface in terms of potentials and concentrations of charged species. The model incorporates macroscopic transport equations in the bulk of the semiconductor and electrolyte, coupled with a microscopic model of the semiconductor-electrolyte interface. Homogeneous and heterogeneous recombination of electron-hole pairs is included within the model. Recombination takes place at the semiconductor-electrolyte interface through interfacial sites, which can enhance the recombination rate. The coupled nonlinear ordinary differential equations of the model were posed in finite-difference form and solved numerically (44). Such numerical solution of the governing equations reduces the number of restrictive assumptions needed to solve the problem. The model can be used to gain insight into the effect of cell parameters on cell performance (44) and can be coupled with primary resistance calculations to optimize cell configurations (45).

Acknowledgment

This work was supported by the United States Department of Energy under Contract no. DE-AC03-76SF00098 through the Director, Office of Energy Research, Office of Basic Energy Sciences, Chemical Sciences Division, and through the Assistant Secretary of Conservation and Renewable Energy, Office of Advanced Conservation Technology, Electrochemical Systems Research Division.

Manuscript submitted June 24, 1983; revised manuscript received May 11, 1984. This was Paper 471 presented at the Minneapolis, Minnesota, Meeting of the Society, May 10-15, 1981.

The University of California assisted in meeting the publication costs of this article.

LIST OF SYMBOLS

c_i molar concentration of species i (mol/cm³)
D_i diffusivity of species i (cm²/s)
E_i energy of species or site i (eV)
ΔE_i ionic adsorption energy (J/mol)
f_i molar activity coefficient of species i
$\mathbf{F}$ Faraday's constant, 96,487 C/eq
G_{th} rate of thermal electron-hole pair generation (mol/s-cm³)
G_L rate of photo electron-hole pair generation (mol/s-cm³)
i current density (mA/cm²)
i_o exchange current density (mA/cm²)
$k_{f,l}$ forward reaction rate constant for reaction l
$k_{b,l}$ backward reaction rate constant for reaction l
k_k rate constants for homogeneous reaction k
K_l equilibrium constant for reaction l
m solar absorption coefficient (1/cm)
M_i symbol for chemical formula of species i
n number of electrons involved in electrode reaction
n electron concentration (mol/cm³)
n_i intrinsic electron concentration (mol/cm³)
N total site concentration (mol/cm³)
N_a total bulk electron-acceptor concentration (mol/cm³)
N_d total bulk electron-donor concentration (mol/cm³)
N_i flux of species i, (mol/cm²s)
p hole concentration (mol/cm³)
$p_{i,l}$ heterogeneous reaction order
$q_{i,l}$ heterogeneous reaction order
q_o incident solar flux (mol/s-cm²)
r_i heterogeneous reaction rate (mol/s-cm²)
R universal gas constant, 8.3143 J/mol-K
R_i net rate of production of species i (mol/s-cm³)
R_{rec} net rate of electron-hole recombination (mol/s-cm³)
$s_{i,l}$ stoichiometric coefficient of species i in an electrode reaction
T absolute temperature (K)
u_i mobility of species i (cm²-mol/J-s)
V potential drop across depletion layer (V)
W depletion layer thickness (cm)
y distance variable (cm)
z_i charge number of species i

Greek characters

β symmetry factor
γ_k surface concentration of energy or species k (mol/cm²)
Γ_k total surface-site concentration of energy or species k (mol/cm²)
δ_k distance between interfacial planes (gap denoted by k) (cm)
ϵ permittivity (C/V-cm)
η photon efficiency
η_k total overpotential at interface k (V)
Θ fractional occupation of surface sites
κ conductivity (mho/cm)
λ Debye length (cm)
μ_i electrochemical potential of species i (J/mol)
Φ electrical potential (V)

Superscripts

o equilibrium
θ secondary reference state at infinite dilution
* secondary reference state in semiconductor

Subscripts

bulk associated with the bulk
c associated with conduction band in semiconductor
CE associated with the counterelectrode
cell associated with the cell
e^- relating to electrons
h^+ relating to holes
ihp associated with inner Helmholtz plane
iss associated with inner surface states
k dummy subscript
l associated with reaction l
o equilibrium value or initial value
ohp associated with outer Helmholtz plane
oss associated with outer surface states
sc associated with semiconductor
sol associated with solution
t associated with trap band in semiconductor
v associated with valence band in semiconductor
1 associated with the region between the OSS and the ISS
2 associated with the region between the ISS and the IHP
3 associated with the region between the IHP and the OHP

REFERENCES
1. A. Fujishima and K. Honda, *Nature*, **238**, 37 (1972).
2. J. Manassen, D. Cahen, and G. Hodes, *ibid.*, **263**, 97 (1976).
3. A. J. Bard, *J. Photochem.*, **10**, 59 (1979).
4. H. Ehrenreich and J. H. Martin, *Phys. Today*, **32**, 25 (1979).
5. M. S. Wrighton, *Acc. Chem. Res.*, **12**, 303 (1979).
6. H. Gerischer, *Pure Appl. Chem.*, **52**, 2649 (1980).
7. A. J. Bard, *Science*, **207**, 139 (1980).
8. A. Heller, *Acc. Chem. Res.*, **14**, 154 (1981).
9. M. Green, in "Modern Aspects of Electrochemistry," Vol. 2, J. O'M. Bockris, Editor, Chap. 5, Academic Press, New York (1959).
10. H. Gerischer, in "Advances in Electrochemistry and Electrochemical Engineering," Vol 1, P. Delahay, Editor, Chap. 4, Interscience, New York (1961).
11. M. D. Archer, *J. Appl. Electrochem.*, **5**, 17 (1975).
12. K. Rajeshwar, P. Singh, and J. Dubow, *Electrochim. Acta*, **23**, 1117 (1975).
13. L. A. Harris and R. H. Wilson, *Ann. Rev. Mater. Sci.*, **8**, 99 (1978).
14. A. J. Nozik, *Ann. Rev. Phys. Chem.*, **29**, 189 (1978).
15. M. Tomkiewicz and H. Fay, *Appl. Phys.*, **18**, 1 (1979).
16. R. H. Wilson, in "CRC Critical Reviews in Solid State and Materials Science," p. 1, CRC Press, Cleveland, OH (1980).
17. R. Memmings, *Electrochim. Acta*, **25**, 77 (1980).
18. S. R. Morrison, "Electrochemistry at Semiconductor and Oxidized Metal Electrodes," Plenum Press, New York (1980).
19. S. U. M. Kahn and J. O'M. Bockris, in "Modern Aspects of Electrochemistry," Vol. 14, J. O'M. Bockris, B. E. Conway, and R. E. White, Editors, Chap. 3, Plenum Press, New York (1982).
20. M. E. Orazem, Ph.D. Thesis, University of California, Berkeley, CA (1983).
21. J. R. Macdonald, *Solid State Electron.*, **5**, 11 (1962).
22. A. De Mari, *ibid.*, **11**, 33 (1968).
23. A. De Mari, *ibid.*, **11**, 1021 (1968).
24. S. C. Choo, *IEEE Trans. Electron Devices*, **ed-18**, 574 (1971).
25. S. C. Choo, *ibid.*, **ed-19**, 954 (1972).
26. J. E. Sutherland and J. R. Hauser, *ibid.*, **ed-24**, 363 (1977).
27. D. Laser and A. J. Bard, *This Journal*, **123**, 1828 (1976).
28. D. Laser and A. J. Bard, *ibid.*, **123**, 1833 (1976).
29. D. Laser and A. J. Bard, *ibid.*, **123**, 1837 (1976).
30. D. Laser, *ibid.*, **126**, 1011 (1979).
31. D. Leary, J. O. Barnes, and A. G. Jordan, *ibid.*, **129**, 1382 (1982).
32. J. A. Davis, R. O. James, and J. O. Leckie, *J. Colloid Interface. Sci.*, **63**, 480 (1978).
33. J. A. Davis and J. O. Leckie, *ibid.*, **67**, 91 (1978).
34. J. A. Davis and J. O. Leckie, *ibid.*, **74**, 32 (1980).
35. D. C. Grahame, *Chem. Rev.*, **41**, 441 (1947).
36. J. F. Dewald, in "Semiconductors," N. B. Hannay, Editor, Chap. 17, Reinhold, New York (1959).
37. M. J. Sparnaay, "The Electrode Double Layer," Pergamon Press, New York (1972).
38. R. Parsons, in "Modern Aspects of Electrochemistry," Vol. 1, J. O'M. Bockris, Editor, pp. 103-179, Academic Press, New York (1954).
39. J. Newman, "Electrochemical Systems," Prentice-Hall, Englewood Cliffs, NJ (1973).
40. H. Gerischer, in "Physical Chemistry: An Advanced Treatise," Vol. IX, H. Eyring, Editor, Chap. 5, Academic Press, New York (1970).
41. J. L. Moll, "Physics of Semiconductors," McGraw-Hill, New York (1964).
42. R. A. Smith, "Semiconductors," Cambridge University Press, London (1959).
43. P. Delahay, "Double Layer and Electrode Kinetics," Interscience, New York (1965).
44. M. E. Orazem and J. Newman, *This Journal*, **131**, 2574 (1984).
45. M. E. Orazem and J. Newman, *ibid.*, **131**, 2582 (1984).
46. M. E. Orazem and J. Newman, *ibid.*, **131**, 2715 (1984).

Mathematical Modeling of Liquid-Junction Photovoltaic Cells

II. Effect of System Parameters on Current-Potential Curves

Mark E. Orazem[1] and John Newman*

Materials and Molecular Research Division of Lawrence Berkeley Laboratory, and Department of Chemical Engineering, University of California, Berkeley, California 94720

ABSTRACT

The one-dimensional mathematical model presented in a previous paper was used to calculate the effect of system variables on the performance of an n-type GaAs semiconducting anode in contact with an 0.8*M* K_2Se, 0.1*M* K_2Se_2, 1.0*M* KOH electrolytic solution. The performance of the semiconductor electrode is influenced by kinetic limitations to interfacial reactions, dopant concentration, semiconductor thickness, the direction of illumination, and the amount of light absorbed in the semiconductor. An optimal dopant concentration and semiconductor thickness can be calculated for a given system.

The liquid-junction photovoltaic cell is an electrochemical system with one or two semiconducting electrodes. This system has undergone intense study since the early 1970's as a means of converting solar energy to chemical or electrical energy (1-8). A number of articles review the physics of the liquid-junction cell, the role of the semiconducting electrode, and the literature. See *e.g.*, Ref. (9-19).

A mathematical model of the liquid-junction photovoltaic cell was presented in a previous paper (20). The results of the model, obtained through numerical computation, are used here to gain insight into the cell behavior and into the factors influencing cell design. This model can also be coupled with primary resistance calculations to optimize the design of cell configurations (21).

A one-dimensional mathematical model of the liquid-junction photovoltaic cell has been developed (20) which treats explicitly the semiconductor, the electrolyte, and the semiconductor-electrolyte interface in terms of potentials and concentrations of charged species. A one-dimensional representation of the model is presented in Fig. 1 of the first paper in this series (*This Journal*, p. 2569). This model includes macroscopic representations of the counterelectrode, the electrolytic solution, and the semiconductor coupled with a microscopic representation of the interface between the semiconductor and the solution. The semiconductor-electrolyte interface couples the macroscopic equations which govern the adjacent bulk phases.

Semiconductor-electrolyte interface.—A description of the semiconductor-electrolyte interface appears on page 2571 of *This Journal*.

Numerical method.—The coupled nonlinear ordinary differential equations of the model were posed in finite-

*Electrochemical Society Active Member.
[1]Present address: Department of Chemical Engineering, University of Virginia, Charlottesville, Virginia 22901.

Table I. Input parameters for the semiconductor

Semiconductor: n-GaAs		
Valence band site concentration	N_v	1.16×10^{-5} mol/cm^3 (7×10^{18} cm^{-3})
Conduction band site concentration	N_c	7.80×10^{-7} mol/cm^3 (4.7×10^{17} cm^{-3})
Bandgap	E_g	1.4 eV
Dopant concentration	$N_d - N_a$	9.96×10^{-8} eq/cm^3 (6×10^{16} cm^{-3})
Electron diffusivity	D_{e^-}	222.0 cm^2/s
Hole diffusivity	D_{h^+}	6.46 cm^2/s
Permittivity	ϵ_{sc}	1.06×10^{-12} C/V-s
Solar absorption coefficient	m	4.40×10^5 cm^{-1}
Solar spectrum efficiency	η	0.3735
Total incident radiation (AM-2)	q_o	7.139×10^{-7} mol/cm^2-s 882 W/m^2
Homogeneous recombination rate constants	$N_i k_2$	1.89×10^9 s^{-1}
	$(k_1 N_v + k_3 N_c)/k_4$	100
	k_2/k_4	2.56×10^{-3} cm^3/mol

difference form and solved numerically for the cell under equilibrium and steady-state conditions (25). The equations were properly linearized, posed in finite-difference form, and solved using Newman's BAND method (28), coupled with Newton-Raphson iteration. Calculation of a current-potential curve involved iterative solution of the system of coupled equations for input values of solar illumination and current density. Numerical accuracy was enhanced by definition of concentration variables that are uniform under equilibrium conditions. The concentration and potential variables in the semiconductor were[2]

$$AN = \frac{n}{N_d - N_a} e^{-\phi}$$

and

$$P = \frac{p}{N_d - N_a} e^{\phi}$$

where

$$\phi = \frac{\mathbf{F}\Phi}{RT}$$

Under equilibrium conditions, the dimensionless potential varied in the semiconductor from zero to around 40.

Numerical accuracy was further improved by partial decoupling of the three equations governing the semiconductor. The large number of equations associated with the semiconductor-electrolyte interface involve variables that appear only at that location. These equations were transformed into a smaller number of equations involving only bulk phase variables in a local inversion routine. A general method for local inversion is presented by White (48).

Results

Computed results for the mathematical model of the liquid-junction photovoltaic cell are presented in the following section. The parameter values chosen for the model are consistent with an n-type GaAs anode in contact with a 0.8*M* K_2Se, 0.1*M* K_2Se_2, 1.0*M* KOH solution. The redox couple was assumed to be Se_2^{2-}/Se^{2-}, and the semiconductor was illuminated at the semiconductor-electrolyte interface. Input parameter values are as presented in Tables I-III unless stated otherwise. Dependent parameters calculated from the input data are presented in Table IV.

The n-type GaAs system was chosen for analysis to allow comparison to the experimental work of Heller and Miller (8, 27, 28). Their cell achieved a 12% power efficiency based upon incident radiation, an open-circuit potential of 0.7V, and a closed circuit current of 24 mA/cm^2. A description of their experimental electrodes, cell, and measuring techniques is presented in Ref. (29). Their cell efficiency includes the effects of reflection losses and electrolyte resistance. The influence of kinetic and mass-transfer limitations to current flow at the counterelectrode were reduced by using a counterelectrode to semiconductor area ratio of 50. The Se_2^{2-}/Se^{2-} redox couple was chosen to limit the corrosion of GaAs under 1000 W/m^2 illumination to a few micrometers per year (approximately 0.04 mA/cm^2) (30-32).

The discussion of the effect of kinetic, bulk semiconductor, and interfacial parameters does not include the effect of IR drop in the electrolyte or kinetic and mass-transfer limitations at the counterelectrode (see the "Counterelectrodes" section of the previous paper). The

[2]A list of symbols appears on page 2573 of *This Journal*.

Table II. Input parameters for the semiconductor-electrolyte interface

ISS site	k	v	t	c	
ISS site energy	E_k	1.3	1.4	1.5	eV
ISS site density	γ_k	0.3334	0.3333	0.3333	
Total ISS site concentration	Γ_{iss}			4.019×10^{-12} mol/cm^2 (2.42×10^{12} cm^{-2})	
Total IHP site concentration	Γ_{ihp}			1.200×10^{-13} mol/cm^2 (7.23×10^{10} cm^{-2})	
IHP adsorption energy	ΔE_3			0.0 J/mol	
	ΔE_4			0.0 J/mol	
Equilibrium OSS potential	Φ_{oss}			5.93 mV	
Equilibrium charge on interface				-0.1298 μC/cm^2	
Distance between OSS and ISS	δ_1			1.0×10^{-8} cm	
Distance between ISS and IHP	δ_2			2.0×10^{-8} cm	
Distance between IHP and OHP	δ_3			2.0×10^{-8} cm	
Permittivity between ISS and IHP	ϵ_2			6.93×10^{12} C/V-cm	
Rate constants					
(OSS-ISS)	k_{etr}			1.0×10^{25} cm^3/mol-s	
(ISS)	k_{sft}			1.0×10^{29} cm^2/mol-s	
(ISS-IHP)	k_{cht}			1.0×10^{29} cm^2/mol-s	
(IHP-OHP)	k_{ads}			1.0×10^{23} s^{-1}	

Table III. Input parameters for the electrolyte

Electrolyte: 0.8*M* K_2Se, 0.1*M* K_2Se_2, 1.0*M* KOH					
Species index	k	1	2	3	4
Species		K^+	OH^-	Se_2^{2-}	Se^{2-}
Charge number	z_k	+1	−1	−2	−2
Bulk concentration	$c_{k,\infty}$	0.0028	0.0010	0.0001	0.0008 mol/cm^3
Diffusivity ($\times 10^5$)	D_k	1.957	5.260	1.000	1.000 cm^2/s
Permittivity	ϵ_{sol}			6.930×10^{-12} C/V-cm	
Conductivity	κ			0.3 $(\Omega$-cm$)^{-1}$	
Temperature	T			300 K	

Table IV. Values calculated from input parameters

Semiconductor		
Fermi level	E_f	1.347 eV
Intrinsic concentration	n_i	5.228×10^{-18} mol/cm^3 (3.15×10^6 cm^{-3})
Minority carrier diffusion length	L_p	5.846×10^{-4} cm
Debye length	λ_{sc}	1.689×10^{-6} cm
Electrolyte		
Debye length	λ_{sol}	1.967×10^{-8} cm

contribution of these phenomena is discussed in the "Cell Design" section (see also the next paper).

Interfacial kinetic limitations.—The values of the interfacial rate constants can affect the open-circuit cell potential, the value of the limiting current, and the shape of the current-potential curve. Most (> 99%) of the recombination under open-circuit illumination occurs at the interface. Homogeneous recombination is included in the model, but does not play a major role for the range of parameters studied.

Ion-adsorption reactions.—Current-potential curves are presented in Fig. 1 with the interfacial rate constant for adsorption and desorption of ions onto the inner Helmholtz plane as a parameter (reactions [8] and [9] in Fig. 1 of the first paper). In each case, the cell potential is a maximum at open circuit (700.5 mV) and decreases as the anodic current increases. A limiting current is observed due to limitations of mass transfer and generation of holes in the semiconductor.

The ion-adsorption rate constant influences the limiting current and the shape of the current-potential curve. A dramatic decrease in the maximum power obtained from this system is observed for the cases with small ion-adsorption rate constants. Kinetic limitations to ion adsorption are seen to have a major effect on cell performance.

Concentration distributions of holes and electrons in the semiconductor are presented in Fig. 2 and 3 for a system with no interfacial kinetic limitations and for a system with kinetic limitations to ion adsorption, respectively. The equilibrium and illuminated open-circuit concentration distributions for the two cases are identical. Under equilibrium conditions, the concentration of holes (curve a) is essentially zero in the bulk of the semiconductor and increases near the negatively charged interface. Conduction electrons are depleted near the interface and reach a value of 0.328 dimensionless units at the current collector, where the concentrations are scaled by the dopant concentration ($N_d - N_a$). The electron concentration in a neutral region of the semiconductor would have a value essentially equal to 1.0. The equilibrated semiconductor of Fig. 2 can therefore be described as having an inversion region extending from the semiconductor-electrolyte interface to 0.5 Debye lengths from the interface and a depletion region extending to the current collector.

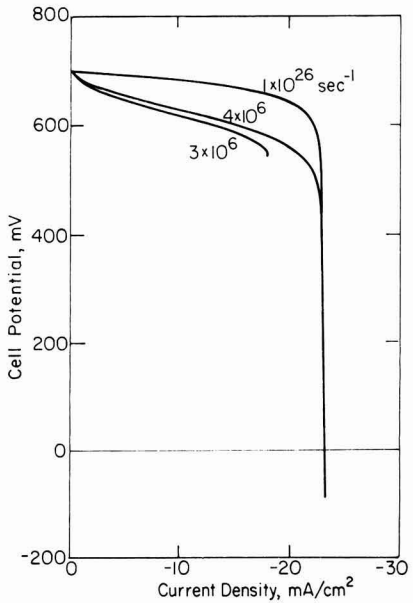


Fig. 1. Computed current-potential curves for an n-type GaAs anode with ion-absorption rate constant as a parameter.

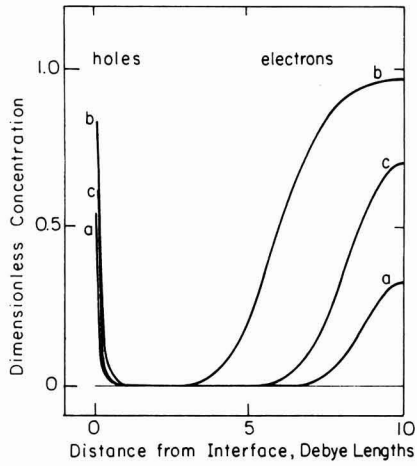


Fig. 2. Concentration distribution for the liquid-junction cell with no kinetic limitations ($k_{ads} = 1.0 \times 10^{26}$ s^{-1}). Curve a, open circuit in the dark; curve b, open circuit under illumination; and curve c, near short circuit ($i = -23.1$ mA/cm^2) under illumination.

The positive background charge density has a value of 1.0; the semiconductor has a net positive charge which is balanced by charge associated with the diffuse region of the electrolyte and the interface. System electroneutrality is maintained. The potential gradient, the driving force for migration of charged species, is balanced by the concentration gradient, which drives diffusion. The net flux of each species in the semiconductor is equal to zero at equilibrium.

Illumination under open-circuit conditions produces electron-hole pairs, which are separated by the potential

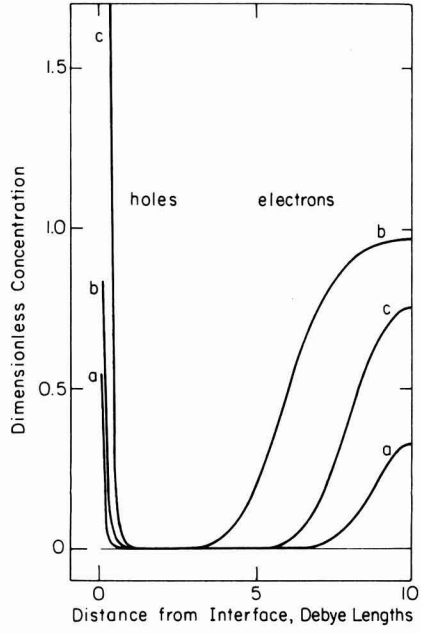


Fig. 3. Concentration distribution for the liquid-junction cell with kinetic limitations to ion adsorption ($k_{ads} = 4.0 \times 10^6$ s^{-1}). Curve a, open circuit in the dark; curve b, open circuit under illumination; and curve c, near short circuit ($i = -23.1$ mA/cm^2) under illumination.

gradient. The concentration of holes increases near the interface, and the concentration of electrons increases near the current collector (curve b). As the system without kinetic limitations approaches short circuit (curve c in Fig. 2), the concentrations of holes and electrons approach the equilibrium distributions. The system under kinetic limitations to ion adsorption, in contrast, experiences an increase in hole concentration at large current densities (curve c in Fig. 4).

The model also allows calculation of the potential distribution in the semiconductor and throughout the cell. Kinetic limitations at the interface are compensated by increased changes of potential across the reaction planes. A small ion-adsorption rate constant is therefore compensated by increased potential and concentration driving forces at the interface. In this way, kinetic limitations influence the cell performance.

Charge-transfer reactions.—Current-potential curves are presented in Fig. 4 with the rate constant for charge transfer from the inner surface states of the semiconductor to the inner Helmholtz plane as a parameter (reactions [5], [6], and [7] in Fig. 1 of the previous paper). The cell potential has a maximum value under open-circuit illumination and decreases as the anodic current increases. Kinetic limitations to charge transfer adversely influence the power performance of the cell. A small charge-transfer rate constant is compensated by increased potential and concentration driving forces.

Electron-adsorption reactions.—The influence of electron-adsorption rate constants (reactions [1], [2], [10], [11], [12], and [13] in Fig. 1 of the previous paper) upon the current-potential curve is presented in Fig. 5. A small electron-adsorption rate constant reduces the net rate of recombination of holes and electrons at the surface and thus increases both the cell potential and the value of the limiting current.

Surface-shift reactions.—The rate constants for reactions which allow electrons to move from one energy level at the interface to another (reactions [3] and [4] in Fig. 1 of the previous paper) do not have any independent effect upon the cell potential or the value of the limiting current. These rate constants affect only the path by which recombination may take place.

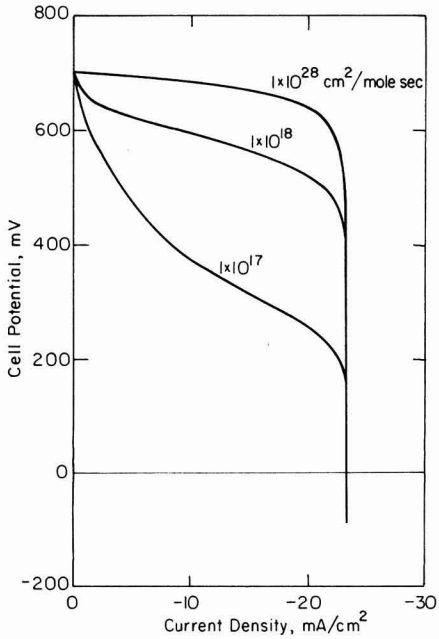


Fig. 4. Computed current-potential curves for an n-type GaAs anode with charge-transfer rate constant as a parameter.

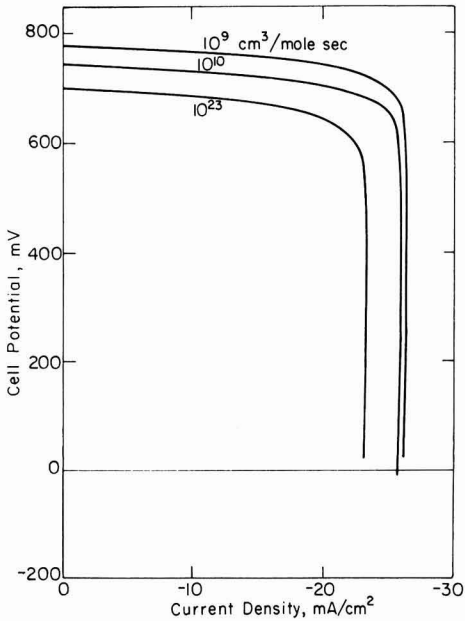


Fig. 5. Computed current-potential curves for an n-type GaAs anode with electron-adsorption rate constant as a parameter.

Bulk semiconductor properties.—Bulk semiconductor properties can greatly influence the performance of the liquid-junction photovoltaic cell. Some properties which can be controlled in semiconductor manufacture and cell design are the dopant concentration, the thickness of the semiconductor, and the amount of light absorbed in the semiconductor. The influence of the solar absorption coefficient is also presented. This parameter is generally fixed for a given semiconductor.

Dopant concentration.—Current-potential curves are presented in Fig. 6 for concentrations of positive background charge ranging from 0.0396×10^{-7} to 2.500×10^{-7} eq/cm^3 (2.4×10^{15} to 1.5×10^{17} cm^{-3}) and for a semiconductor thickness of 10 Debye lengths. For low to moderate levels of doping, the open-circuit cell potential is independent of dopant concentration. The open-circuit cell potential decreases with very large doping levels due to a decrease in the equilibrium flatband potential. For low to moderately large levels of doping, the charged portion of the equilibrated semiconductor adjacent to the interface consists of an inversion region and a depletion region. Electroneutrality of the interfacial region can be satisfied in the very highly doped semiconductor by a region of low electron concentration. No inversion layer is observed, and the potential variation in the semiconductor (*i.e.*, the flatband potential) is reduced.

The short-circuit current is independent of dopant concentration for the highly doped semiconductor and is reduced at very low dopant levels because of enhanced homogeneous recombination of electron-hole pairs. This effect is dependent upon the rate constants for homogeneous recombination.

The semiconductor Debye length is inversely proportional to the square root of the dopant concentration. If the semiconductor thickness were held constant at a value of 1.69×10^{-5} cm, as opposed to 10 Debye lengths, similar results would be observed for high dopant concentrations. At low dopant concentrations, the semiconductor thickness would be smaller than the space-charge region thickness, and the cell potential would be reduced

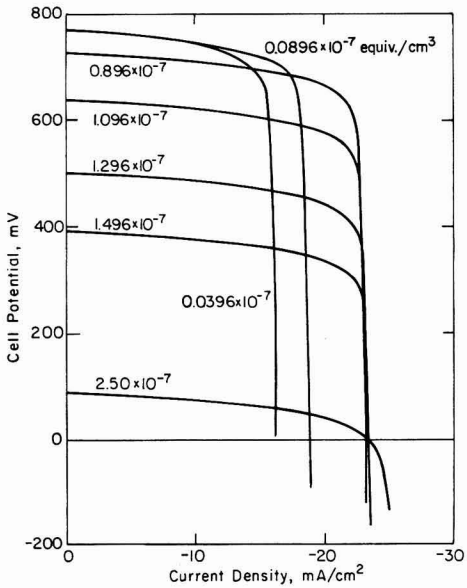


Fig. 6. Computed current-potential curves for an n-type GaAs anode with dopant concentration as a parameter.

(see next section). A change in the Debye length influences the utilization of the incident radiation (see the "Solar absorption coefficient" section below), but the change in cell performance due to this effect is small.

Maximization of power density yields an optimal dopant concentration for the n-GaAs system of about 9.0×10^{-8} eq/cm³. The donor concentration in the work presented by Heller and Miller (27, 28) was 6×10^{16} carriers/cm³ (or 9.96×10^{-8} eq/cm³).

Semiconductor thickness. The effect of semiconductor thickness on the cell performance is presented in Fig. 7 for a characteristic depth of light adsorption of 228.2A (corresponding to 1.35 Debye lengths). The cell potential increases as the thickness increases from 5 to 13 Debye lengths. The current-potential curve is essentially unchanged for an increase in thickness from 13 to 30 Debye lengths. A very thick semiconductor is expected to decrease the system performance because of resistive losses in the semiconductor. For the system described here, however, the resistance losses should be insignificant, even for 1 mm thick crystals. A semiconductor thickness less than the normal space-charge region is associated with saturation of charge in the semiconductor. All mobile electrons are driven from the semiconductor in response to the negatively charged interface, and a large potential gradient across the semiconductor cannot be sustained. This may be regarded to be a limitation to the flatband potential and, therefore, a limitation to the cell potential.

Solar absorption coefficient.—The characteristic length for absorption of light can be compared to the Debye length by the dimensionless absorption coefficient $m\lambda_{sc}$. The open-circuit cell potential is presented in Fig. 8 as a function of the dimensionless absorption coefficient. A maximum in cell potential is observed in the region where the characteristic length for absorption of light is of the same order as the Debye length. The cell potential is relatively insensitive to the dimensionless absorption coefficient within the range of 0.2 to 3.0. Variation of dimensionless absorption coefficient from 0.04 to 10 (two-and-one-half orders of magnitude) results in a deviation from an average open-circuit cell potential of only 14 mV. The optimal value for the dimensionless absorption coefficient was around 0.425, where the characteristic length for light absorption is 2.4 Debye lengths. The absorption coefficient for single-crystal GaAs, averaged over photons with energy greater than the bandgap energy, is 4.4×10^5 cm^{-1}. This value corresponds to a dimensionless absorption coefficient of 0.743 and to a characteristic absorption depth of 1.35 Debye lengths.

Solar flux.—The amount of light absorbed within the semiconductor has a strong effect on cell performance. As seen in Fig. 9, light scattering or reflective losses can reduce the limiting current from −23.2 mA/cm² under full AM-2 irradiation (modeled here with a single mean absorption coefficient) to −14.0 mA/cm² under 60% AM-2 irradiation. The 40% decrease in limiting current is accom-

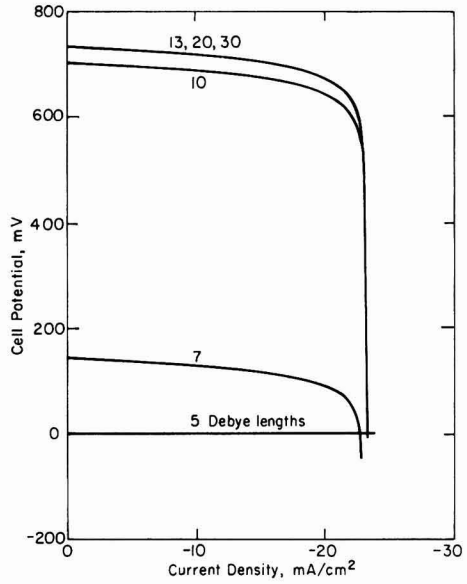


Fig. 7. Computed current-potential curves for an n-type GaAs anode with semiconductor thickness as a parameter.

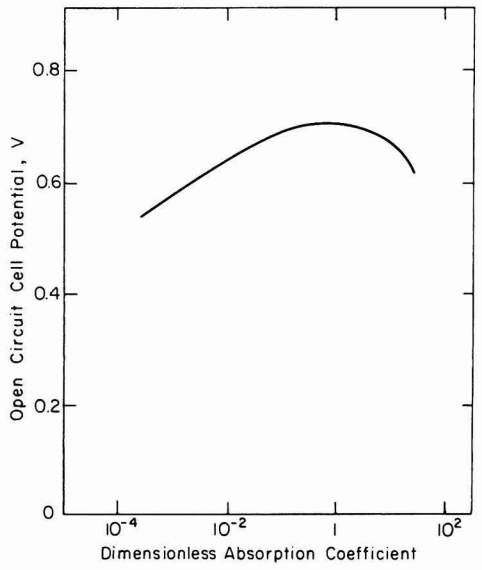


Fig. 8. Open-circuit cell potential as a function of dimensionless solar absorption coefficient.

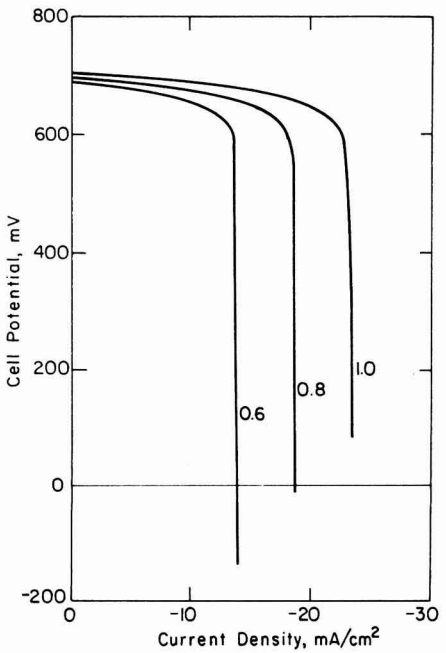


Fig. 9. Computed current-potential curves for an n-type GaAs anode with fractional absorption of incident AM-2 radiation as a parameter.

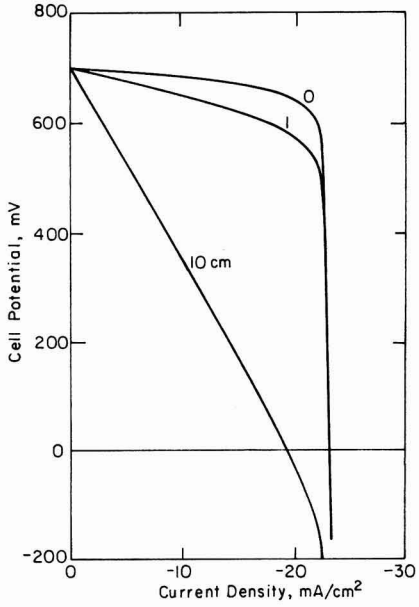


Fig. 10. Computed current-potential curves for an n-type GaAs anode with the separation between the counterelectrode and the semiconductor as a parameter. Solution resistance has been included.

panied by a 1% decrease in open-circuit cell potential. The amount of light absorbed within the semiconductor is directly related to the generation of the limiting species, holes, and therefore primarily affects the limiting current.

Cell design.—Under electrolyte-side illumination and without interfacial kinetic limitations, electrolyte resistance, and counterelectrode effects, the maximum power efficiency of the cell was calculated to be 15.0%. This is the value that one might observe if the power density is calculated using a potential drop measured between the semiconductor electrode and a reference electrode reversible to the redox reaction and located just outside the diffusion region. The resistance of the electrolyte, mass-transfer and kinetic limitations at the counterelectrode, and the choice of front- or back-illumination will affect this value.

Electrolyte and counterelectrode.—Resistance in the electrolyte and kinetic and mass-transfer effects at the counterelectrode decrease the maximum power-density of the liquid-junction photovoltaic cell. The current-potential curve for a system with no interfacial kinetic limitations (see Fig. 2) is presented in Fig. 10 with electrolyte resistance included. The conductivity of the electrolyte was assumed to be 0.3 Ω^{-1} cm^{-1}. The cell potential at a given current is reduced by an amount which is proportional to the current density and to the distance L between the counterelectrode and the semiconductor. A 10 cm separation between the counterelectrode and the semiconductor reduces the maximum power efficiency of the cell to 4.0%.

The same base current-potential curve is presented in Fig. 11 and 12 with the effect of kinetic and mass-transfer limitations at the counterelectrode included. The reaction

$$2Se^{2-} \rightarrow Se_2^{2-} + 2e^- \qquad [2]$$

was assumed to follow the sequence

$$Se^{2-} \rightarrow Se^-_{ads} + e^- \qquad [3a]$$

$$2Se^-_{ads} \rightarrow Se_2^{2-} \qquad [3b]$$

Under the assumption that the second step is equilibrated, the current density at the counterelectrode can be expressed by

$$i = i_o \left\{ \left[1 - \frac{i}{i_{4,\text{lim}}} \right] \exp\left[\frac{(1-\beta)\mathbf{F}}{RT} \eta_{CE} \right] - \left[1 + \frac{i}{i_{3,\text{lim}}} \right]^{1/2} \exp\left[-\frac{\beta \mathbf{F}}{RT} \eta_{CE} \right] \right\} \qquad [4]$$

where i_o is the exchange current density associated with the bulk concentrations of reactants

$$i_o = \mathbf{F} k^{\beta}_{a,f} c^{\beta}_{4,\infty} \left[\frac{k_{a,b} k_{b,b}^{1/2}}{k_{b,f}^{1/2}} c_{3,\infty}^{1/2} \right]^{(1-\beta)}$$

$i_{3,\text{lim}}$ is the diffusion-limited current density associated with species Se_2^{2-}, $i_{4,\text{lim}}$ is the diffusion-limited current density associated with species Se^{2-}, and n is equal to one.

The effect of diffusion limitation to currents at the counterelectrode is presented in Fig. 11 with diffusion-limited current density at the counterelectrode as a parameter. Diffusion-limited current densities of 20 mA/cm² for Se_2^{2-} and 80 mA/cm² for Se^{2-} correspond to a Nernst stagnant diffusion layer thickness of about 0.010 cm. An exchange-current density of 100 mA/cm² was assumed. The influence of the exchange current density on the current-potential curve is presented in Fig. 12. Diffusion-limited currents of 20 and 80 mA/cm² were assumed for the Se_2^{2-} and the Se^{2-} species, respectively. Kinetic limitations, either at the counterelectrode or the semiconductor, cause an inflection point in the current-potential curve.

The calculated maximum power efficiency is 11.8% for a cell with a 1.0 cm gap between the semiconductor and the counterelectrode, an exchange current density of 100 mA/cm², and diffusion-limited currents of 20 and 80 mA/cm² at the counterelectrode for the Se_2^{2-} and the Se^{2-} species, respectively. Reduction of illumination due to absorption in the electrolyte and reflection were not included.

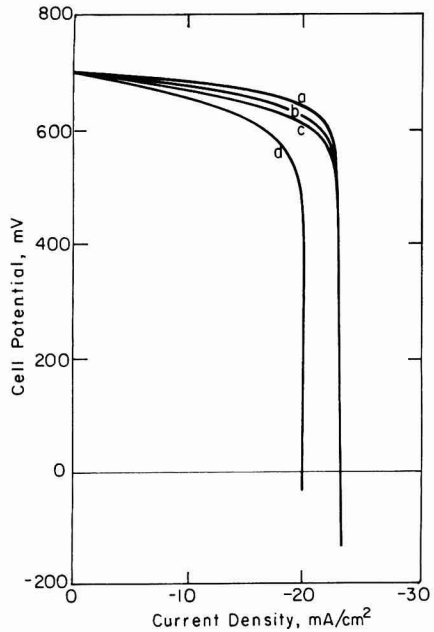


Fig. 11. Computed current-potential curves for an n-type GaAs anode with diffusion-limited current density at the counterelectrode as a parameter. Curve a, counterelectrode effects not included; curve b, $i_{lim,3}$ = 20 mA/cm² and $i_{lim,4}$ = 20 mA/cm²; curve c, $i_{lim,3}$ = 10 mA/cm² and $i_{lim,4}$ = 40 mA/cm²; curve d, $i_{lim,3}$ = 5 mA/cm² and $i_{lim,4}$ = 20 mA/cm².

Front- and back-illumination.—The semiconductor can be illuminated at the semiconductor-electrolyte interface (front illumination) or at the semiconductor-current collector interface (back illumination). The influence of the direction of illumination is strongly dependent upon the relative rates of recombination in the bulk and at the interfaces involved.

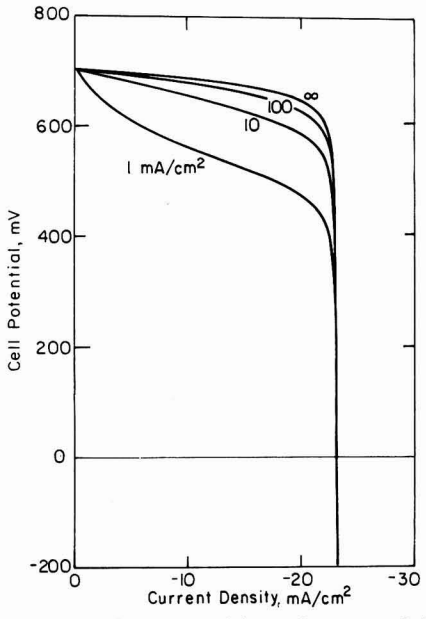


Fig. 12. Computed current-potential curves for an n-type GaAs anode with counterelectrode exchange-current density as a parameter. Kinetic and mass-transfer effects at the counterelectode have been included.

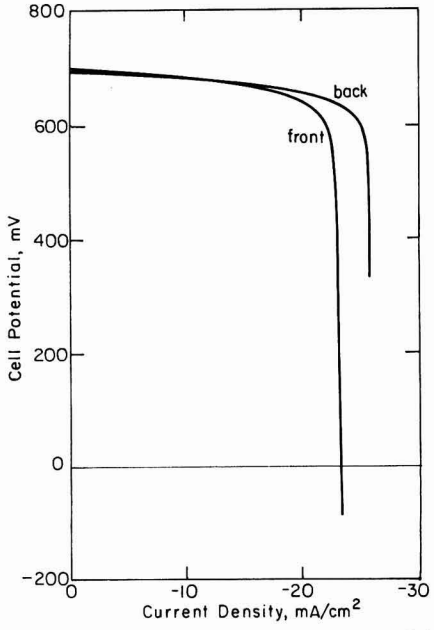


Fig. 13. Computed current-potential curves for an n-type GaAs anode with the direction of illumination (front or back illumination) as a parameter.

Under the conditions of a negligible surface recombination at the semiconductor-current collector interface and of a small rate of homogeneous recombination as compared to the rate of recombination at the semiconductor-electrolyte interface, back-illumination increases the power output. This effect is illustrated in Fig. 13, where current-potential curves for the case with no interfacial kinetic limitations are presented for the semiconductor under front and back-illumination. The limiting current under back-illumination is −25.6 mA/cm², and the maximum power efficiency is 17.0%. The limiting current under front-illumination is −23.2 mA/cm², and the maximum power efficiency is 15.0%. Generation of electron-hole pairs in regions where recombination is facilitated reduces the power output.

Discussion

Experimental results reported in the literature show the general shape of the current-potential curves presented in this paper. Small scale systems are generally designed with large counterelectrode areas (to minimize any limitation to current flow at the counterelectrode) and a small depth of electrolyte over the semiconductor surface (to minimize losses of illumination by absorption in the electrolyte). Current-potential curves thereby obtained include effects of electrolyte resistance and illumination losses.

Inflection points are observed for many experimental systems, *e.g.*, TiO_2 in 1.0*M* NaOH (33), TiO_2 in 0.1*M* Na_2SO_4 at *p*H less than 10 (adjusted with NaOH and H_2SO_4) (34), $PbFe_{12}O_{19}$, $Hg_2Ta_2O_7$, $CdFe_2O_4$, and $Pb_2Ti_{1.5}W_{0.5}O_{6.5}$ in 0.2*M* NaOH (35), n- and p-type GaP in liquid ammonia (36), p-GaP in 0.5*M* H_2SO_4 (37), WO_3 in 1*M* sodium acetate (38), $KTaO_3$ in 8.6*M* NaOH (39), CdS in 0.1*M* NaOH (40), CdS in 1.0*M* NaI, 1.0*M* $Na_2S_2O_3$, and 0.1*M* I_2 (41), and untreated polycrystalline GaAs with a selenium redox couple (8). These inflection points are indicative of kinetic limitations to charge-transfer or to ion-adsorption reactions at the semiconductor-electrolyte interface (as shown by the

parameter variation in Fig. 1 and 2 in the "Interfacial kinetic limitations" section). Other systems, *e.g.*, ruthenium-treated polycrystalline GaAs (8, 42) and single-crystal GaAs (43) in contact with a selenium redox couple, CdS and Bi_2S_3 in contact with a sulfide-polysulfide redox couple (44), CdS in 1*M* KCl, 0.8*M* CH_3COOH, and 0.2*M* CH_3COOH (45), and p-InP in contact with a vanadium redox couple (8), do not exhibit inflection points. The interfacial reactions are equilibrated for these systems.

The results of the mathematical model presented in this paper are compared to experimental results in Fig. 14. The solid line represents the experimental current-potential curve for a ruthenium-treated n-GaAs photoanode in contact with a selenium redox couple (27, 28). The dashed lines are calculated results in which interfacial reactions were assumed to be equilibrated. Both calculated curves include a 7% loss of illumination; the lower curve includes an electrolyte resistance of 3 Ω-cm^2. The model parameters are presented in Tables I, II, and III. Bulk transport properties were obtained from the literature; values were assumed for properties characteristic of the semiconductor-electrolyte interface. The model agrees with the experimental results near open circuit, but exhibits a sharper limiting current plateau than the experimental results indicate. This discrepancy may be due to convective overpotential losses due to the textured surface of the semiconductor electrode. An increase in the homogeneous recombination rate constants decreases the sharpness of the potential drop near limiting current but also decreases the cell potential.

Some of the model parameters are associated with characteristics of the current-potential curve. In the absence of counterelectrode effects, the magnitude of the limiting current is determined by the intensity of illumination, and the shape of the curve is determined by kinetic parameters. Kinetic limitations to charge-transfer and to ion-adsorption reactions result in an inflection point. Kinetic limitations at the counterelectrode can also cause an inflection point. The magnitude of the open-circuit potential is a function of the equilibrium potential difference between the semiconductor and the solution. Within the model, this parameter is represented by the equilibrium OSS potential. The surface site energy distribution also influences the open-circuit cell potential. These parameters could be varied by selection of different semiconductor-electrolyte combinations. The open-circuit cell potential is also affected by semiconductor properties, such as bandgap energy and absorption coefficient.

Analytic models of the liquid-junction cell are described in Ref. (46). These models can match experimental current-potential curves but show maxima in electron and hole concentrations near the boundary between space-charge and neutral regions. These maxima were not seen in the results of the mathematical model and are probably due to imposition of boundary or matching conditions between those regions.

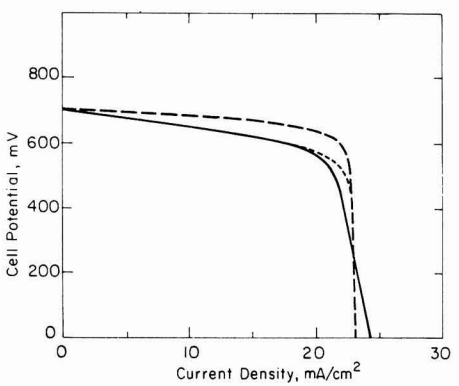


Fig. 14. Comparison of computed current-potential curves (dashed lines) to experimental results (solid line) for an n-type GaAs anode in contact with a selenium redox couple.

Conclusions

Kinetic limitations to interfacial charge-transfer and ion-adsorption reactions drastically reduce the power output of the liquid-junction cell. A small interfacial rate constant is compensated by increased potential and concentration driving forces, thus influencing the cell performance.

The cell performance is strongly influenced by bulk-semiconductor and cell-design properties such as the dopant concentration, the semiconductor thickness, and the amount of light adsorbed in the semiconductor. An optimal dopant concentration and semiconductor thickness can be calculated for a given semiconductor system. The resistance of the electrolyte and kinetic and mass-transfer limitations at the counterelectrode influence cell performance and may play an important role in the optimal design of a liquid-junction photovoltaic cell.

Acknowledgment

This work was supported by the United States Department of Energy under Contract no. DE-AC03-76SF00098 through the Director, Office of Energy Research, Office of Basic Energy Sciences, Chemical Sciences Division, and through the Assistant Secretary of Conservation and Renewable Energy, Office of Advanced Conservation Technology, Electrochemical Systems Research Division.

Manuscript submitted June 24, 1983; revised manuscript received May 11, 1984. This was Paper 471 presented at the Minneapolis, Minnesota, Meeting of the Society, May 10-15, 1981.

The University of California assisted in meeting the publication costs of this article.

REFERENCES

1. A. Fujishima and K. Honda, *Nature*, **238,** 37 (1972).
2. J. Manassen, D. Cahen, and G. Hodes, *ibid.*, **263,** 97 (1976).
3. A. J. Bard, *J. Photochem.*, **10,** 59 (1979).
4. H. Ehrenreich and J. H. Martin, *Phys. Today*, **32,** 25 (1979).
5. M. S. Wrighton, *Acc. Chem. Res.*, **12,** 303 (1979).
6. H. Gerischer, *Pure Appl. Chem.*, **52,** 2649 (1980).
7. A. J. Bard, *Science*, **207,** 139 (1980).
8. A. Heller, *Acc. Chem. Res.*, **14,** 154 (1981).
9. M. Green, in "Modern Aspects of Electrochemistry," Vol. 2, J. O'M. Bockris, Editor, Chap. 5, Academic Press, New York (1959).
10. H. Gerischer, in "Advances in Electrochemistry and Electrochemical Engineering," Vol 1, P. Delahay, Editor, Chap. 4, Interscience, New York (1961).
11. M. D. Archer, *J. Appl. Electrochem.*, **5,** 71 (1975).
12. K. Rajeshwar, P. Singh, and J. DuBow, *Electrochim. Acta*, **23,** 1117 (1975).
13. L. A. Harris and R. H. Wilson, *Ann. Rev. Mater. Sci.*, **8,** 99 (1978).
14. A. J. Nozik, *Ann. Rev. Phys. Chem.*, **29,** 189 (1978).
15. M. Tomkiewicz and H. Fay, *Appl. Phys.*, **18,** 1 (1979).
16. R. H. Wilson, in "CRC Critical Reviews in Solid State and Materials Science," p. 1, CRC Press, Cleveland, OH (1980).
17. R. Memming, *Electrochim. Acta*, **25,** 77 (1980).
18. S. R. Morrison, "Electrochemistry at Semiconductor and Oxidized Metal Electrodes," p. 10, Plenum Press, New York (1980).
19. S. U. M. Kahn and J. O'M. Bockris, in "Modern Aspects of Electrochemistry," Vol. 14, J. O'M. Bockris, B. E. Conway, and R. E. White, Editors, Chap. 3, Plenum Press, New York (1982).
20. M. E. Orazem and J. Newman, *This Journal*, **131,** 2569 (1984).
21. M. E. Orazem and J. Newman, *ibid.*, **131,** 2582 (1984).
22. D. C. Grahame, *Chem. Rev.*, **41,** 441 (1947).
23. J. F. Dewald, in "Semiconductors," N. B. Hannay, Editor, Chap. 17, Reinhold, New York (1959).
24. M. J. Spernaay, "The Electrode Double Layer," Pergamon Press, New York (1972).
25. M. E. Orazem and J. Newman, Paper 471 presented at

the Minneapolis, MN, Meeting of the Society, May 10-15, 1981.
26. J. Newman, *Ind. Eng. Chem. Fundam.*, **7**, 514 (1968).
27. A. Heller and B. Miller, in "Interfacial Photoprocesses: Energy Conversion and Synthesis," M. S. Wrighton, Editor, Chap. 12, Advances in Chemistry Series 184, The American Chemical Society, Washington, DC (1980).
28. B. A. Parkinson, A. Heller, and B. Miller, *Appl. Phys. Lett.*, **33**, 521 (1978).
29. A. Heller, K. C. Chang, and B. Miller, *This Journal*, **124**, 697 (1977).
30. K. C. Chang, A. Heller, B. Schwartz, S. Menezes, and B. Miller, *Science*, **196**, 1097 (1977).
31. A. B. Ellis, J. M. Bolts S. W. Kaiser, and M. S. Wrighton, *J. Am. Chem. Soc.*, **99**, 2848 (1977).
32. M. S. Wrighton, J. M. Bolts, A. B. Bocarsly, M. C. Palazzotto, and E. G. Walton, *J. Vac. Sci. Technol.*, **15**, 1429 (1978).
33. Y. Nakato, N. Takamori, and H. Tsubomura, *Nature*, **295**, 312 (1982).
34. W. Gissler, P. L. Lensi, and S. Pizzini, *J. Appl. Electrochem.*, **6**, 9 (1976).
35. H. H. Kung, H. S. Jarrett, A. W. Sleight, and A. Ferretti, *J. Appl. Phys.*, **48**, 2463 (1977).
36. J. Belloni, G. Van Amerongen, M. Herlem, J.-L. Sculfort, and R. Heindl, *J. Phys. Chem.*, **84**, 1269 (1980).
37. M. P. Dare-Edwards, A. Hamnett, and J. B. Goodenough, *J. Electroanal. Chem.*, **119**, 109 (1981).
38. M. A. Butler, R. D. Nasby, and R. K. Quinn, *Solid-State Commun.*, **19**, 1011 (1976).
39. A. B. Ellis, S. W. Kaiser, and M. S. Wrighton, *J. Phys. Chem.*, **80**, 732 (1977).
40. R. Memming, *Ber. Bunsenges. Phys. Chem.*, **81**, 732 (1977).
41. H. Gerischer and J. Gobrecht, *ibid.*, **80**, 327 (1976).
42. W. D. Johnston, Jr., H. J. Leamy, B. A. Parkinson, A. Heller, and B. Miller, *This Journal*, **127**, 90 (1980).
43. H. Gerischer, *J. Electroanal. Chem.*, **82**, 133 (1977).
44. B. Miller and A. Heller, *Nature*, **262**, 680 (1976).
45. R. A. L. Vanden Berghe, W. P. Gomes, and F. Cardon, *Ber. Bunsenges. Phys. Chem.*, **77**, 289 (1973).
46. M. E. Orazem, Ph.D. Thesis, University of California, Berkeley, CA (1983).

Mathematical Modeling of Liquid-Junction Photovoltaic Cells

III. Optimization of Cell Configurations

Mark E. Orazem[1] and John Newman*

Materials Molecular Research Division of Lawrence Berkeley Laboratory, and Department of Chemical Engineering, University of California, Berkeley, California 94720

ABSTRACT

A one-dimensional mathematical model of the liquid-junction photovoltaic cell was coupled with primary resistance calculations to predict the optimal performance of three cell configurations. Two cells are considered in which the semiconductor is illuminated from the electrolyte side and one in which the semiconductor is illuminated from the current-collector side. An economic analysis is presented based upon these results. The performance of the liquid-junction photovoltaic cell is dependent upon the design, surface area, and placement of the counterelectrode and current collectors.

Most studies of the liquid-junction photovoltaic cell have been oriented toward developing an understanding of the semiconducting electrode which characterizes the cell [see, *e.g.*, Ref. (1-19)]. This work describes the design and optimization of liquid-junction photovoltaic devices. The advantages and problems inherent in the liquid-junction cell are reviewed, and a mathematical model of the liquid-junction cell (20, 21) is used to predict the optimal performance of various cell configurations. An economic analysis is presented based upon these results.

The liquid-junction photovoltaic cell has appeal because, in contrast to solid-state junctions, the junction between electrolyte and semiconductor is formed easily and allows use of polycrystalline semiconductors. The electrochemical nature of the cell allows both production of electricity and generation of chemical products which can be separated, stored, and recombined to recover the stored energy. These features could make the liquid-junction cell an economical alternative to solid-state photovoltaic devices for solar energy conversion.

Liquid-junction cells also have the advantages that are attributed to other photovoltaic devices. Photovoltaic power plants can provide local generation of power on a small scale. The efficiency and cost of solar cells is independent of scale, and overall efficiency is improved by locating the power plant next to the load. Nuclear and fossil-fuel burning plants, in contrast, are economical only if built on a large scale (on the order of 1000 MW) (22).

The design of a liquid-junction photovoltaic cell requires selection of an appropriate semiconductor-electrolyte combination and design of an efficient cell configuration. The selection of a semiconductor is based upon the bandgap, which provides an upper limit to the conversion efficiency of the device, and the choice of electrolyte is governed by the need to limit corrosion. The optimal design of the liquid-junction photovoltaic cell is aided by use of mathematical models.

Bandgap.—Photovoltaic cells rely on the unique properties of semiconductors to convert incident radiation to electrical current. The semiconductor property of interest is the moderate gap between the valence and the conduction-band energy levels. Incident photons of light with energy greater than or equal to the bandgap energy transfer their energy to valence-band electrons, producing conduction-band electrons and vacancies in the valence band.

An upper limit to the efficiency of photovoltaic devices can be established, based upon the bandgap and the solar spectrum, without consideration of cell configuration. This "ultimate efficiency" is given by (11)

$$\eta_{ult} = \frac{E_g \int_{E_g}^{\infty} N(E)\, dE}{\int_0^{\infty} E\, N(E)\, dE} \qquad [1]$$

where E_g is the semiconductor bandgap energy, E is the photon energy, and $N(E)$ is the number density of incident photons with energy E. The fraction of the power in the solar spectrum that can be converted to electrical power is a function of the bandgap of the semiconductor. Photons with energy less than the bandgap cannot produce electron-hole pairs. Photons with energy greater than the bandgap yield the bandgap energy (23-25).

* Electrochemical Society Active Member.
[1]Present address: Department of Chemical Engineering, University of Virginia, Charlottesville, Virginia 22901.

The "ultimate efficiency" of Eq. [1] represents an upper limit to conversion of solar energy (11, 26, 27); factors such as reflection and absorption losses of sunlight, kinetic and mass-transfer limitations, and recombination will reduce the efficiency. These effects are included in the "cell configuration" section. A bandgap between 1.0 and 1.5 eV is generally considered to be appropriate for efficient conversion of solar energy.

Corrosion.—The application of liquid-junction technology to photovoltaic power conversion is limited by problems associated with the semiconductor-electrolyte interface. Primary among these problems is corrosion. Efficient conversion of solar energy requires a bandgap between 1.0 and 1.5 eV and most semiconductors near this bandgap corrode readily under illumination. Semiconductors with large bandgaps (4-5 eV) tend to be more stable, but cannot convert most of the solar spectrum.

Among the approaches taken to solve this problem, the most successful concern the matching of an electrolyte to the semiconductor. The rate of corrosion is reduced if the semiconductor is in equilibrium with the corrosion products. The rate of corrosion can also be reduced by using a redox couple which oxidizes easily. The oxidation of the redox couple Se_{x+1}^{2-}/Se_x^{2-}, for example, has been shown to compete successfully with photocorrosion reactions for holes in n-type GaAs electrodes (8, 28).

p-Type semiconductors used as cathodes are more stable than the more common and generally more efficient n-type semiconducting anodes. The inefficiency of p-type photocathodes has been attributed to the presence of surface states near the valence band energy. A stable p-type photocathode has been developed, however, with a solar conversion efficiency of 11.5% (29). Protective films have been proposed to be a solution to electrode corrosion. The electrode, in this case, would be a small bandgap semiconductor covered by a film composed of either a more stable large bandgap semiconductor, a conductive polymer, or a metal. A large Schottky barrier is frequently present at such semiconductor-metal and semiconductor-semiconductor interfaces which blocks the flux of holes from the semiconductor to the electrolyte. In cases where the photocurrent is not blocked, corrosion can take place between the semiconductor and the protective film (17, 30). Menezes *et al.* (31) discuss the difficulties in avoiding absorptive losses in the metal film while maintaining sufficient integrity to serve the semiconductor corrosion protection function. Frese *et al.* (32) have, however, reported a measurable improvement in the stability of GaAs with less than a monolayer gold metal coverage. Thin conductive polypyrrole films appear to be successful in inhibiting corrosion in some electrolytes (33-38). In addition, insulating polymer films deposited on grain boundaries can improve the performance of polycrystalline semiconductors by reducing surface recombination rates (39).

Mathematical model.—Development of a mathematical model constitutes an important step toward design and optimization of the liquid-junction photovoltaic cell. A one-dimensional mathematical model has been developed (20, 21) which treats explicity the semiconductor, the electrolyte, and the semiconductor-electrolyte interface in terms of potentials and concentrations of charged species. The model incorporates macroscopic transport equations in the bulk of the semiconductor and electrolyte. Homogeneous and heterogeneous recombination of electron-hole pairs is included within the model. Recombination takes place at the semiconductor-electrolyte interface through interfacial sites, which can enhance the recombination rate. Surface sites at the semiconductor-metal interface were not included within the model.

The coupled nonlinear ordinary differential equations of the model were posed in finite-difference form and solved numerically. The mathematical model can be used to gain insight into the operation of cells with semiconducting electrodes, and to optimize their design. The model was used here to calculate the effect of cell design on the performance of an n-type GaAs semiconducting anode in contact with an 0.8*M* K_2Se, 0.1*M* K_2Se_2, 1.0*M* KOH electrolytic solution. The choice of this semiconducting electrode system was based upon the work of Heller and associates (8, 40-42). Cell design parameters are presented in Table I, and the parameters used in modeling the liquid-junction cell are presented elsewhere (20, 43).

Table I. Counterelectrode parameters

Diffusion-limited current density	$i_{3,\mathrm{lim}}$	20.0 mA/cm²
	$i_{4,\mathrm{lim}}$	80.0 mA/cm²
Exchange current density	i_o	100.0 mA/cm²

Cell Configuration

The optimal design of liquid-junction photovoltaic cells shares constraints with solid-state photovoltaic cells (44, 45). Current collectors cast shadows and can reduce the amount of sunlight absorbed in the semiconductor. A constraint unique to the liquid-junction cell is the placement of the counterelectrode relative to the semiconductor-electrolyte interface. Mass-transfer and kinetic limitations at the counterelectrode and resistance of the electrolyte can play important roles in the optimal design of the liquid-junction photovoltaic cell. These considerations are treated qualitatively by Parkinson (46).

Under electrolyte-side illumination and without illumination losses, interfacial kinetic limitations, electrolyte resistance, and counterelectrode limitations, the maximum power efficiency of the cell was calculated (43) to be 15.3%. The corresponding value under back (or current-collector) side illumination was calculated (43) to be 17.2%. These are the values that one might calculate using a potential drop measured between the semiconductor electrode and a reference electrode reversible to the redox reaction and located just outside the diffusion region. The resistance of the electrolyte, illumination losses, and mass-transfer and kinetic limitations at the counterelectrode affect these values and are influenced by cell design. The difference between front and back illumination is due to the assumption that facilitated recombination does not take place at the semiconductor-current collector interface.

The performance of three cell configurations was calculated for operation under AM-2 solar illumination (882 W/m²). The semiconductor was assumed to be in the form of a thin film [see Mitchell for a review of thin-film photovoltaic technologies (47)]. Interfacial kinetic limitations were not included (20, 43). The one-dimensional model of the liquid-junction cell was coupled with the resistance to current flow associated with the two-dimensional systems. Some methods for calculation of this resistance were reviewed by Fleck *et al.* (48).

System 1: wire counterelectrode.—The liquid-junction photovoltaic cell with a wire-grid counterelectrode is presented in Fig. 1a. The cell consists of a semiconductive film supported on a metallic current collector, a wire-grid counterelectrode, and a transparent glass cover plate. The space between the cover plate and the semiconductor is filled with the electrolyte. The glass plate is an essential part of the cell because it keeps the system clean and allows optimal orientation of the cell for collection of sunlight. This cell is designed for conversion of solar energy into electrical energy; no provision is made for separation of chemical products. A two-dimensional representation of the cell is presented in Fig. 1b.

Sunlight absorbed in the semiconductor must pass through the cover plate, past the counterelectrode, and through the electrolyte. Reflection at each of the interfaces (air-glass, glass-electrolyte, and electrolyte-semiconductor), absorption in the glass and electrolyte, and screening by the counterelectrode decrease the amount of light which can be used for generation of electron-hole pairs. Absorption losses in the electrolyte can be limited by maintaining a small gap between the counterelectrode and the semiconductor. A wide spacing

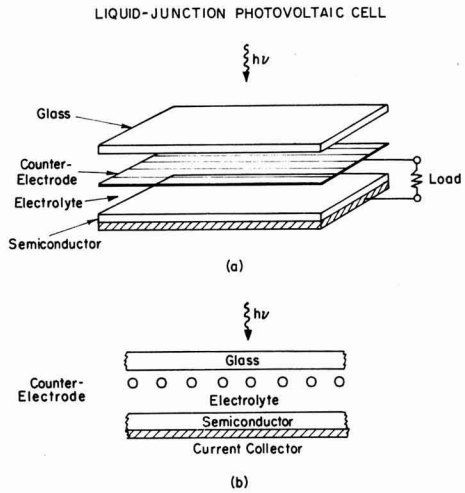


Fig. 1. Design of the liquid-junction photovoltaic cell. System 1: wire counterelectrode.

of counterelectrode elements reduces the screening of the semiconductor but also increases the influence of kinetic and mass-transfer effects at the counterelectrode as well as ohmic drop.

The one-dimensional model of the liquid-junction photovoltaic cell was used with averaged uniform current density and solar flux. The shadow of the counterelectrode was implicitly assumed to be diffuse. Resistive losses in the electrolyte were calculated from a two-dimensional solution of Laplace's equation (49-53). The potential drop in the electrolyte was given by Eq. [14] in Ref. (53). The current density at the counterelectrode was assumed to be uniform and was related to the semiconductor current density by

$$i_{ce} = i_{sc}\left(\frac{L}{\pi D}\right) \qquad [2]$$

and the counterelectrode shadow was assumed to reduce the magnitude of incident light by a factor of $(1 - D/L)$. The effective solar flux was therefore given by

$$q_{sc} = q_o\left(1 - \frac{D}{L}\right)(1 - \rho_{air\text{-}glass})e^{-(mx)_{glass}} (1 - \rho_{glass\text{-}soln})e^{-(mx)_{soln}}(1 - \rho_{soln\text{-}sc}) \qquad [3]$$

where ρ_{j-k} is the reflectance associated with the interface j - k and m is the extinction coefficient for a given phase of depth x.

The design parameter for this cell design is the ratio of the counterelectrode element spacing to the counterelectrode element diameter, L/D. When L/D has a value of one, the semiconductor is completely shaded from illumination; when L/D is very large, counterelectrode limitations dominate.

The power density of the cell with a counterelectrode radius of 0.05 cm is presented in Fig. 2 as a function of current density with L/D as a parameter. The maximum power density is presented in Fig. 3 as a function of L/D. The separation between the cover plate and the counterelectrode was 0.5 cm, and the separation between the semiconductor and the counterelectrode was 0.5 cm. The electrolyte depth was therefore 1.1 cm. The optimal value of L/D is 14, and the maximum power density obtained is 63.5 W/m^2. The current density under the optimal condition is 11.8 mA/cm^2 delivered at a cell potential of 538.7 mV. The maximum power efficiency of the wire-counterelectrode cell was 7.2%.

Kinetic limitations at the counterelectrode further reduce this efficiency. An exchange current density of

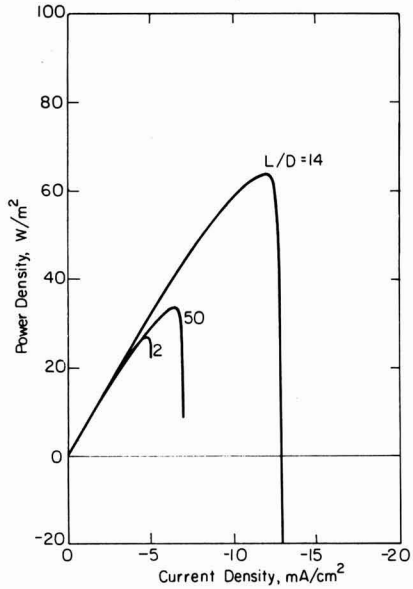


Fig. 2. Power density as a function of current density for system 1 with a counterelectrode element diameter of 0.10 cm.

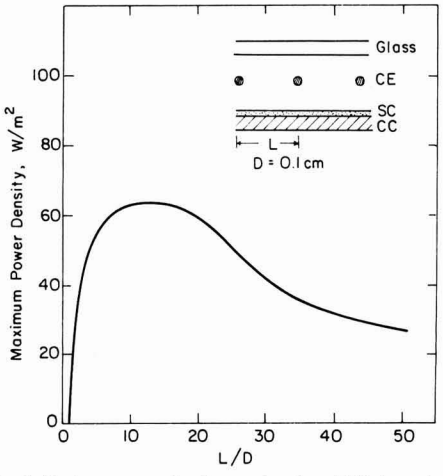


Fig. 3. Maximum power density as a function of L/D for system 1 with a counterelectrode element diameter of 0.10 cm.

1 mA/cm^2 leads to a 5.5% power efficiency at an optimal L/D of 10.

System 2: slotted semiconductor.—The liquid-junction cell configuration with a slotted-semiconductor electrode is presented in Fig. 4. A glass cover plate protects the cell. Sunlight passes through the cover plate and the electrolyte to illuminate the semiconductor surface. Electrical current passes between the semiconductor and the counterelectrode through slots cut in the semiconductor. This configuration has the advantage that no shadows are cast upon the semiconductor; furthermore, reaction products can be separated if a membrane is placed between the semiconductor and the counterelectrode.

The primary current distribution and the resistance of a cell containing a slotted electrode were calculated using numerical methods coupled with the Schwarz-Christoffel transformation (20, 54). The cell resistance is a function of three geometric ratios, chosen to be t/G, h/G, and L/h

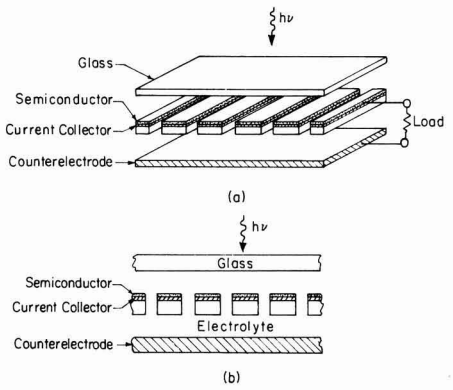


Fig. 4. Design of the liquid-junction photovoltaic cell. System 2: slotted semiconductor.

where L is the half-length of the protruding electrode assembly, t is the thickness of the protruding electrode assembly, G is the half-gap between the electrode assemblies, and h is the separation between the electrode and the upper insulating wall. h is also the separation between the counterelectrode and the lower edge of the semiconductor-electrode assembly.

The performance of this cell is a function of four geometric parameters. The distance betwen the counterelectrode and the semiconductor assembly was chosen to be 0.5 cm, and the semiconductor assembly thickness was assumed to be 0.1 cm. The primary resistance for this system is presented in Fig. 5 as a function of L/D with h/G as a parameter. The maximum power density is presented in Fig. 6 as a function of L/h and h/G as a parameter. L/h was varied by varying the half-length; h/G by varying the half-gap. The maximum power density for this system is obtained with a small gap. For $h/G = 0.5$ ($G = 1$ cm), the maximum power density was 47.8 W/m², and the maximum power efficiency was 5.4%. The current density under maximum power conditions was 15 mA/cm² delivered at 477.6 mV. For $h/G = 10$ ($G = 0.05$ cm), the maximum power density was 67.7 W/m², and the maximum power efficiency was 7.7%. At maximum power, the current density 15.2 mA/cm² delivered at 534.6 mV.

System 3: back-illuminated semiconductor.—A cell design is presented in Fig. 7, in which the semiconductor is illuminated from the current-collector side. The semiconducting film is deposited on a pane of transparent conducting glass. A current collecting grid is used to offset the low conductivity of the glass. The semiconductor is separated from the counterelectrode by a gap

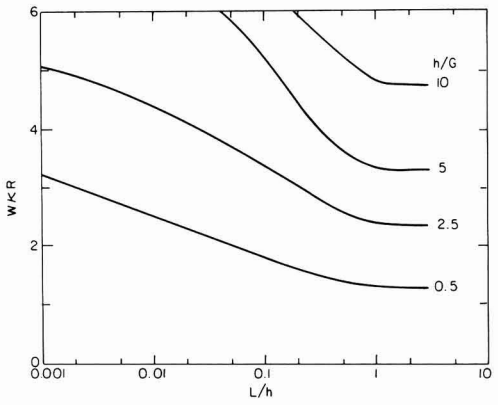


Fig. 5. Primary cell resistance as a function of L/h for system 2 with h/G as a parameter.

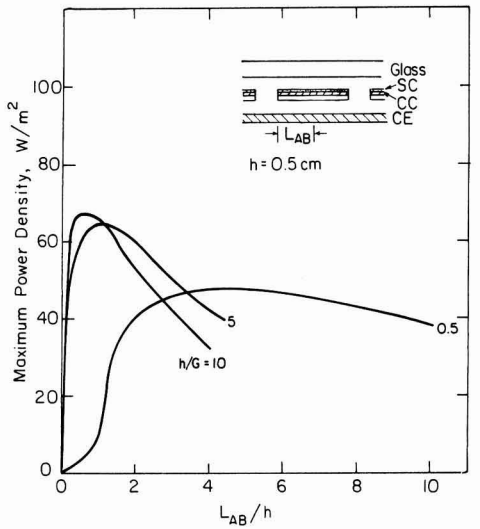


Fig. 6. Maximum power density as a function of L/h for system 2 with h/G as a parameter.

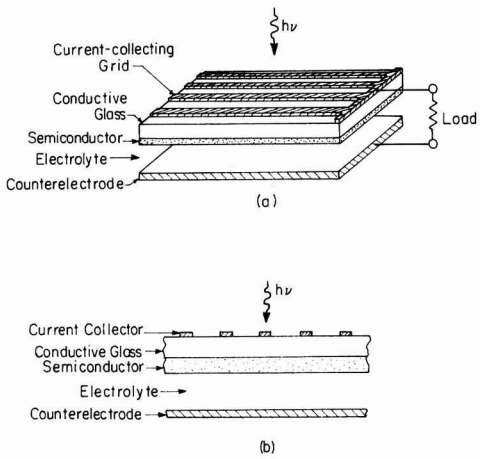


Fig. 7. Design of the liquid-junction photovoltaic cell. System 3: back-illuminated semiconductor.

filled with electrolyte. This design could be used with a membrane within the gap, which would allow separation of reaction products at each of the electrodes.

The potential drop between the semiconductor and the current collecting grid can be obtained through application of the general solution to the resistance of a rectangular conductor with arbitrarily placed electrodes presented by Moulton (55, 56).

The transparent conducting support for the semiconducting film was assumed to be SnO_2, which is commonly used as a transparent electrode. SnO_2 is a large bandgap semiconductor and is essentially transparent to light with energy below 3.7 eV. The properties of SnO_2 have been reviewed by Jarzebski and Marton (57-59). The conductivity of the transparent material was assumed to be 50 mho/cm, and the total absorption and reflection losses at the air-SnO_2 interface for a 1/8 in. thick plate were assumed to be 8%. The reflectance at the SnO_2-GaAs interface was assumed to be 5%. The separation between the counterelectrode and the semiconductor was 0.5 cm.

The maximum power density is presented in Fig. 8 as a function of the ratio of the current-collector-element

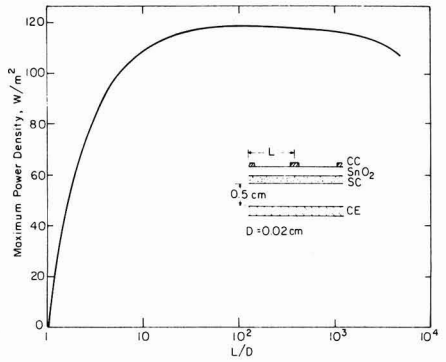


Fig. 8. Maximum power density as a function of L/D for system 3 with a current-collector element thickness of 0.01 cm.

spacing to the element width L/D. When L/D is equal to one, the semiconductor is completely blocked, and the power density is zero. When L/D is large, the resistance of the SnO_2 becomes important. The optimal value of L/D is around 100; the maximum power density is 118.5 W/m², and the power efficiency is 13.4%. The current density under optimal operating conditions is 21.0 mA/cm² delivered at a cell potential of 564.3 mV.

The excellent performance of this cell design as compared to systems 1 and 2 can be misleading. Facilitated recombination at the semiconductor-metal interface was not included in the model. The back-illuminated system does have inherent advantages over front-illuminated cells. Optical losses, for example, can be smaller, and separation of electrochemical products is feasible. The relative rates of electron-hole recombination at the semiconductor-metal and the electrolyte-semiconductor interfaces, however, will influence the relative merit of front and back illumination.

Intensity of Illumination

The intensity of solar illumination varies with location, cloud cover, day of year, and time of day. In addition, mirrors and lenses can be used to concentrate the sunlight and reduce the amount of semiconducting material incorporated into the cell. The prediction of the performance of a given design of the liquid-junction photovoltaic cell must therefore consider the effect of the intensity of illumination.

The maximum power efficiency is presented as a function of illumination intensity in Fig. 9, 10, and 11 for systems 1, 2, and 3, respectively. The cells were designed with the design parameters calculated to be optimal under AM-2 illumination. The power efficiency decreases with increasing illumination due to the influence of electrolyte resistance and kinetic and mass-transfer limitations at the counterelectrode. These phenomena become increasingly important as current densities increase, and mass-transfer limitations at the counterelectrode result in an upper limit for cell currents.

The maximum power efficiency for systems 2 and 3 without counterelectrode limitations is also presented in Fig. 10 and 11. These results are appropriate for cells with porous counterelectrodes. A porous counterelectrode may not be feasible for system 1 because of the need in this system to pass sunlight through the counterelectrode. The efficiency still decreases with illumination intensity due to electrolyte resistance.

The maximum cell current obtained under large magnitudes of illumination depends upon the ratio of the counterelectrode area to the semiconductor area. This ratio must be large for liquid-junction photovoltaic cells designed for large intensities of illumination. Replacement of the flat-plate counterelectrode with a porous electrode (60) can increase the counterelectrode area of systems 2 and 3. Inclusion of a cooling system in the cell design becomes important under these conditions. The electrolyte itself can serve as a heat-exchange medium in photoelectrochemical systems.

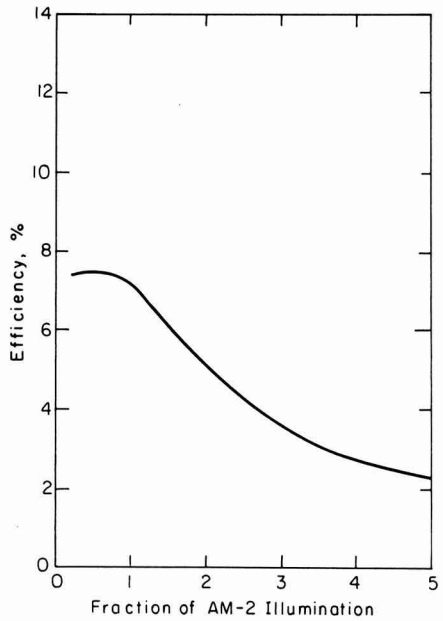


Fig. 9. Maximum power efficiency as a function of the fraction of AM-2 illumination (882 W/m²) for system 1 with L/D = 14.

Discussion and Economic Analysis

The cells discussed in the previous sections can be divided into two groups, front and back illuminated, within which they can be compared fairly. The comparison of front- and back-illuminated cells depends upon the relative rates of recombination at the semiconductor-metal

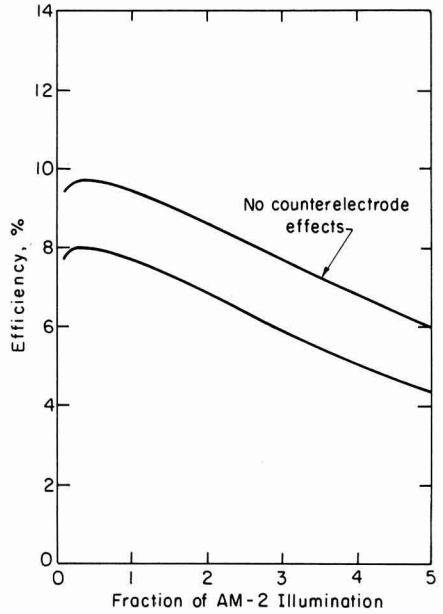


Fig. 10. Maximum power efficiency as a function of the fraction of AM-2 illumination (882 W/m²) for system 2 with h/G = 10 and L/h = 0.5.

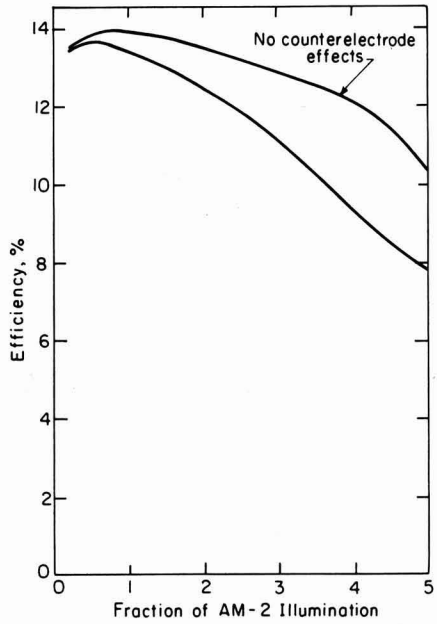


Fig. 11. Maximum power efficiency as a function of the fraction of AM-2 illumination (882 W/m²) for system 3 with a current-collector half-width of 0.01 cm and with $L/D = 100$.

and electrolyte-semiconductor interfaces, and these rates will differ from one system to another.

The calculated power efficiencies are presented in Table II for the front-illuminated systems. Semiconductor effects, such as recombination, reduce the power efficiency from a value of 37%, based solely upon bandgap, to 15.3%. Reflection losses, with an arbitrarily chosen 8% efficiency of illumination, reduce this value to 12.2%. This value can be compared to the 12% efficiency obtained in the experimental work of Heller and Miller (8, 40, 41). The effect of cell design and illumination losses is to reduce the performance to 7.2% for system 1 and 7.7% for system 2.

The calculated power efficiencies are presented in Table III for the back-illuminated system. Semiconductor effects reduce the power efficiency from a value of 37%, based solely upon bandgap, to 17.2%. Enhanced recombination at the semiconductor-current collector interface was not included in these calculations. The effect of cell design and illumination losses is to reduce the power efficiency to 13.4%.

The calculated performance could be improved by making distances between semiconductor and counter-

Table II. Power efficiency under front illumination

	No illumination losses	Illumination losses*	Experimental results
Optimal bandgap	45	36 (80%)	
GaAs bandgap	37	30 (80%)	
Semiconductor-electrolyte junction	15.3	12.2 (80%)	12.0
Cell design (1)	10.1	7.2 (55.4%)	
Cell design (2)	9.8	7.7 (71.6%)	

* In some cases, the number in parenthesis represents the fraction of AM-2 illumination (above the bandgap) which actually enters the semiconductor, after accounting for reflection, shadowing, and absorption in the intervening phases. In other cases, where detailed calculations were not made, it represents the ratio to column 1 because the nonlinear effect of illumination could not be assessed.

Table III. Power efficiency under back illumination

	No illumination losses	Illumination losses*
Optimal bandgap	45	36 (80%)
GaAs bandgap	37	30 (80%)
Current collector and semiconductor-electrolyte junction	17.2	13.8 (80%)
Cell design (3)	15.4	13.4 (86.5%)

* In some cases, the number in parenthesis represents the fraction of AM-2 illumination (above the bandgap) which actually enters the semiconductor, after accounting for reflection, shadowing, and absorption in the intervening phases. In other cases, where detailed calculations were not made, it represents the ratio to column 1 because the nonlinear effect of illumination could not be assessed.

electrode smaller, reducing the effect of electrolyte resistance. The values chosen for this analysis were based primarily on mechanical considerations. A spacing of 0.5 cm was used between all cell elements. A smaller spacing could result in shorting of the counterelectrode and the semiconductor and/or trapping of gas bubbles. The influence of the counterelectrode could be reduced by increasing the flow rate or degree of mixing near the counterelectrode, thereby increasing the limiting current. Kinetic limitations at the semiconductor-electrolyte interface were not considered here and may greatly reduce the performance of some semiconductor systems.

Current-potential curves are presented in Fig. 12 for the front-illuminated cells. The optimally designed cells of systems 1 and 2 are compared to the cell without interfacial kinetic limitations, counterelectrode limitations, and electrolytic resistance. The cell with a slotted semiconductor has a larger power efficiency than the wire-grid counterelectrode cell and can be designed for separation of chemical products. The analysis of the system designed for separation of chemical products would include the electrical resistance of the membrane.

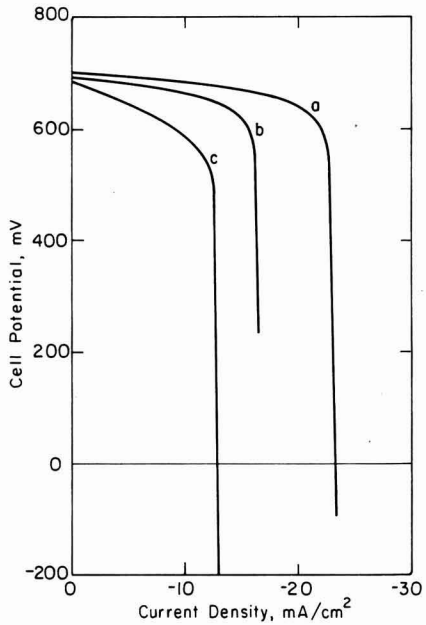


Fig. 12. Cell potential as a function of current density for (a) a front-illuminated semiconductor without kinetic, electrolyte-resistance, and counterelectrode limitations; (b) system 1 with a counterelectrode element diameter of 0.10 cm and with $L/D = 14$; and (c) system 2 with $h/G = 10$ and $L/h = 0.5$.

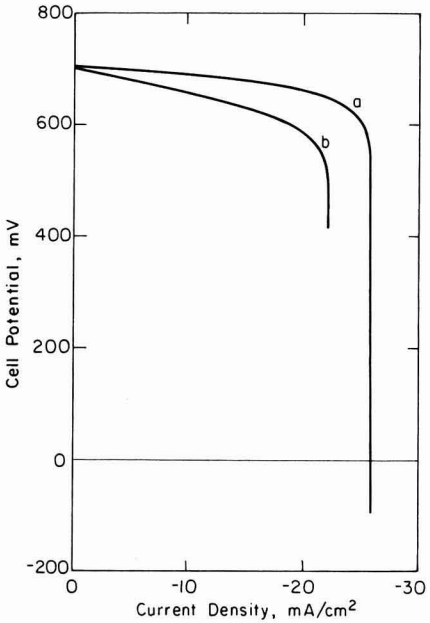


Fig. 13. Cell potential as a function of current density for (a) a back-illuminated semiconductor without kinetic, electrolyte-resistance, and counterelectrode limitations; and (b) system 3 with a current-collector element half-thickness of 0.01 cm and with L/D = 100.

Current-potential curves are presented in Fig. 13 for the back-illuminated cell. The optimally designed cell of systems 3 is compared to the cell without interfacial kinetic limitations, counterelectrode limitations, and electrolytic resistance. The back-illuminated design is appealing because chemical products can be separated and because of reduced losses of illumination.

The following discussion of cell economics is appropriate for all photovoltaic devices. The allowable capital investment for the cell is given by

$$I = 8.76\, P_{in}\, \eta \Delta c y_e \qquad [15]$$

where P_{in} is the annual incident illumination intensity average over 24h in watts per square meter, η is the cell efficiency, Δc is the difference in selling price and operating cost in dollars per kilowatt-hour, and y_e is the break-even point in years. This equation is presented as a nomogram in Fig. 14. The power output of the liquid-junction cell is presented in Fig. 14a as a function of the incident solar illumination with the average efficiency of the device as a parameter. The incident solar illumination is averaged over a 24h period. On this basis, the average insolation of the continental United States is 200-250 W/m² (11). Lenses or mirrors could be used to increase the amount of sunlight striking the semiconductor surface. The annual return on investment is presented in Fig. 14b as a function of the power output with power cost as a parameter. The total initial investment is presented in Fig. 14c as a function of the averaged annual investment with cell break-even period as a parameter.

Based upon a 7.7% power efficiency (averaged over 24h), 250 W/m² incident illumination (averaged over 24h), 0.05 dollars/kWh profit, and a break-even period of 5 yr, an investment of 42 dollars/m² is justified for the complete cell. Based upon a 13.4% power efficiency (averaged over 24h) an investment of 73 dollars/m² is justified for the complete cell.

An increase of solar illumination by a factor of five while reducing the efficiency to 6% (system 2 with a porous counterelectrode) yields an acceptable initial investment of 164 dollars/m². An efficiency of 10.4% (system 3 with a porous counterelectrode) yields an acceptable initial investment of 285 dollars/m². If the mirrors and lenses needed to concentrate sunlight are cheaper than the semiconducting film, the cell may be most economical under high illumination. Maintenance of a high efficiency under high illumination is possible only with the back-illuminated cell of Fig. 7 and the front-illuminated cell of Fig. 4, both coupled with porous counterelectrodes.

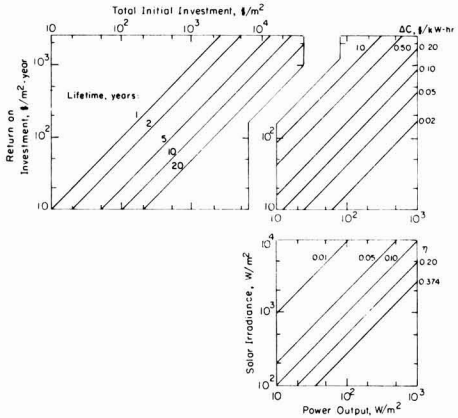


Fig. 14. Economic analysis of the liquid-junction photovoltaic cell. a (bottom): Power output as a function of the incident solar illumination with power efficiency as a parameter. b (top right): Averaged annual return on investment as a function of the power output with power cost as a parameter. c (top left): Total initial investment as a function of averaged annual return on investment with cell lifetime as a parameter.

The values presented here can be compared to the estimate presented by Weaver *et al.* (61) of 0.34 dollars/peak W. This estimate is based on materials cost and assumes a cell efficiency of 13%. Under AM-2 illumination, this value corresponds to 39 dollars/m².

Conclusions

The optimization of the liquid-junction photovolatic cell depends upon the choice of semiconductor, electrolyte, and cell design. The system studied in this work, n-GaAs with a Se_2^{-2}/Se^{-2} redox couple, is close to optimal with respect to utilization of solar irradiation and therefore provides a best-case estimate of liquid-junction cell efficiency. This system, however, exhibits a small rate of corrosion under illumination (a few micrometers per year) (62).

The performance of the liquid-junction photovoltaic cell is strongly dependent upon the design, surface area, and placement of the counterelectrode and current collectors. This system may be economical under concentrated illumination or where the power produced has high value.

Acknowledgment

This work was supported by the United States Department of Energy under Contract no. DE-AC03-76SF00098 through the Director, Office of Energy Research, Office of Basic Energy Sciences, Chemical Sciences Division, and through the Assistant Secretary of Conservation and Renewable Energy, Office of Advanced Conservation Technology, Electrochemical Systems Research Division.

Manuscript submitted June 24, 1983; revised manuscript received May 11, 1984.

The University of California assisted in meeting the publication costs of this article.

REFERENCES

1. A. Fujishima and K. Honda, *Nature*, **238**, 37 (1972).
2. J. Manassen, D. Cahen, and G. Hodes, *ibid.*, **263**, 97 (1976).

3. A. J. Bard, *J. Photochem.*, **10,** 59 (1979).
4. H. Ehrenreich and J. H. Martin, *Phys. Today,* **9,** 25 (1979).
5. M. S. Wrighton, *Acc. Chem. Res.*, **12,** 303 (1979).
6. H. Gerischer, *Pure Appl. Chem.*, **52,** 2649 (1980).
7. A. J. Bard, *Science,* **207,** 139 (1980).
8. A. Heller, *Acc. Chem. Res.*, **14,** 154 (1981).
9. M. Green, in "Modern Aspects of Electrochemistry," Vol. 2, J. O'M. Bockris, Editor, Chap. 5, Academic Press, New York (1959).
10. H. Gerischer, in "Electrochemistry and Electrochemical Engineering," Vol 1, P. Delahay, Editor, Chap. 4, Interscience, New York (1961).
11. M. D. Archer, *J. Appl. Electrochem.*, **5,** 71 (1975).
12. K. Rajeshwar, P. Singh, and J. Dubow, *Electrochim. Acta,* **23,** 1117 (1975).
13. L. A. Harris and R. H. Wilson, *Ann. Rev. Mater. Sci.*, **8,** 99 (1978).
14. A. J. Nozik, *Ann. Rev. Phys. Chem.*, **29,** 189 (1978).
15. M. Tomkiewicz and H. Fay, *Appl. Phys.*, **18,** 1 (1979).
16. R. H. Wilson, in "CRC Critical Reviews in Solid State and Materials Science," pp. 1-41, CRC Press, Cleveland, OH (1980).
17. R. Memming, *Electrochim. Acta,* **25,** 77 (1980).
18. S. R. Morrison, "Electrochemistry at Semiconductor and Oxidized Metal Electrodes," p. 10, Plenum Press, New York (1980).
19. S. U. M. Khan and J. O'M. Bockris, in "Modern Aspects of Electrochemistry," Vol. 14, J. O'M. Bockris, B. E. Conway, and R. E. White, Editors, Chap. 3, Plenum Press, New York (1982).
20. M. E. Orazem, Ph.D. Thesis, University of California, Berkeley, CA (1983).
21. M. E. Orazem and J. Newman, *This Journal,* **131,** 2569 (1984).
22. H. Oman and J. W. Gelzer, in "Energy Technology Handbook," D. M. Considine, Editor, pp. 6.56-6.80, McGraw-Hill, New York (1977).
23. J. J. Loferski, *J. Appl. Phys.*, **27,** 777 (1956).
24. J. J. Loferski, *Proc. IEEE,* **51,** 667 (1963).
25. J. J. Wysocki, *Solar Energy,* **6,** 104 (1962).
26. M. Wolf, *Proc. IRE,* **48,** 1246 (1960).
27. W. Shockley and H. J. Queisser, *J. Appl. Phys.*, **32,** 510 (1961).
28. K. C. Chang, A. Heller, B. Schwartz, S. Menezes, and B. Miller, *Science,* **196,** 1097 (1977).
29. A. Heller, B. Miller, and F. A. Thiel, *Appl. Phys. Lett.*, **38,** 282 (1981).
30. H. Gerischer, in "Proceedings of the 2nd International Photovoltaic Solar Energy Conference," R. van Overstraeten and W. Palz, Editors, pp. 408-431, D. Reidel, Boston (1979).
31. S. Menezes, A. Heller, and B. Miller, *This Journal,* **127,** 1268 (1980).
32. K. W. Frese, Jr., M. J. Madou, and S. R. Morrison, *ibid.*, **128,** 1939 (1981).
33. R. Noufi, D. Tench, and L. F. Warren, *ibid.*, **127,** 2310 (1980).
34. R. Noufi, D. Tench, and L. F. Warren, *ibid.*, **128,** 2596 (1981).
35. T. Skotheim, I. Lundstrom, and J. Prejza, *ibid.*, **128,** 1625 (1981).
36. F.-R. F. Fan, B. L. Wheeler, A. J. Bard, and R. N. Noufi, *ibid.*, **128,** 2042 (1981).
37. R. A. Bull, F.-R. F. Fan, and A. J. Bard, *ibid.*, **129,** 1009 (1982).
38. T. Skotheim, L.-G. Petersson, O. Inganas, and I. Lundstron, *ibid.*, **129,** 1737 (1982).
39. H. S. White, H. D. Abruna, and A. J. Bard, *ibid.*, **129,** 265 (1979).
40. A. Heller and B. Miller, in "Interfacial Photoprocesses: Energy Conversion and Synthesis," M. S. Wrighton, Editor, Chap. 12, Advances in Chemistry Series 184, The American Chemical Society, Washington, DC (1980).
41. B. A. Parkinson, A. Heller, and B. Miller, *Appl. Phys. Lett.*, **33,** 521 (1978).
42. K. C. Chang, A. Heller, B. Schwartz, S. Menezes, and B. Miller, *Science,* **196,** 1097 (1977).
43. M. E. Orazem and J. Newman, *This Journal,* **131,** (1984).
44. H. J. Hovel, "Solar Cells," Vol. 11 of Semiconductors and Semimetals, R. K. Willardson and A. Beers, Series Editors, Academic Press, New York (1975).
45. P. A. Iles, Paper 1 presented at the 9th IEEE Photovoltaic Specialists Conference, Silver Springs, MD, 1972.
46. B. Parkinson, *Solar Cells,* **6,** 177 (1982).
47. K. W. Mitchell, *Ann. Rev. Mater. Sci.*, **12,** 401 (1982).
48. R. N. Fleck, D. N. Hanson, and C. W. Tobias, "Numerical Evaluation of Current Distribution in Electrochemical Systems," Lawrence Berkeley Laboratory Report UCRL-11612 (1964).
49. C. Kasper, *Trans. Electrochem. Soc.*, **77,** 353 (1940).
50. C. Kasper, *ibid.*, **77,** 365 (1940).
51. C. Kasper, *ibid.*, **78,** 131 (1940).
52. C. Kasper, *ibid.*, **78,** 147 (1940).
53. C. Kasper, *ibid.*, **82,** 153 (1942).
54. M. E. Orazem and J. Newman, *This Journal,* To be published.
55. H. F. Moulton, *Proc. London Math. Soc. Ser. 2,* **3,** 104 (1905).
56. F. Bowman, "Introduction to Elliptic Functions with Applications," John Wiley and Sons, New York (1953).
57. Z. M. Jarzebski and J. P. Marton, *This Journal,* **123,** 199C (1976).
58. Z. M. Jarzebski and J. P. Marton, *ibid.*, **123,** 299C (1976).
59. Z. M. Jarzebski and J. P. Marton, *ibid.*, **123,** 333C (1976).
60. D. Canfield and S. R. Morrison, "Electrochemical Storage Cell Based on Polycrystalline Silicon," Lawrence Berkeley Laboratory Report LBL-14639 (1982).
61. N. L. Weaver, R. Singh, K. Rajeschwar, P. Singh, and J. DuBow, *Solar Cells,* **3,** 221 (1981).
62. M. S. Wrighton, J. M. Bolts, A. B. Bocarsly, M. C. Palazzotto, and E. G. Walton, *J. Vac. Sci. Technol.*, **15,** 1429 (1978).

Electrochemical Studies of Chromium in Molten LiF-NaF-KF (FLINAK)

Toshinobu Yoko[1] and Ronald A. Bailey

Department of Chemistry, Rensselaer Polytechnic Institute, Troy, New York 12181

ABSTRACT

The mechanism of the reduction of Cr(III) in molten FLINAK was studied using cyclic voltammetry and chronopotentiometry over a temperature range of 612°-983°C and a Cr(III) concentration of 0.07 to 0.13 mol/l. Two reduction and two oxidation steps were observed, but extensive differences in the electrochemistry were seen over the measured temperature range. Cr(III) is reduced to Cr(II) followed by a two-electron reduction of Cr(II) to Cr metal and both reduction processes are quasi-reversible. The product of the first reduction process is soluble at 983°C, but is insoluble at lower temperatures.

Electroplating of refractory metals (IV, V, and VI transition groups) from molten salts has been explored for several years, most notably in the work of Senderoff and Mellors in the 1960's (1-8). More recently, there has been renewed interest in this technique (9, 10). In spite of the earlier work (2, 3, 4, 8), however, it is hard to say that the mechanisms of the electroplating of these refractory metals from molten salts are completely understood, especially for chromium (8, 11-14). The primary objective of this research is to elucidate the mechanisms of the electrode reduction of Cr(III) in molten LiF-NaF-KF eutectic (46.5 mole percent [m/o] LiF, 11.5 m/o NaF, 42.0 m/o KF, [FLINAK]) based on the results of cyclic voltammetry and chronopotentiometry.

Experimental

Each fluoride salt used was reagent grade. After being well mixed and dried in a vacuum oven at 160°C for over a week, the powdered mixture was melted, then filtered in an argon atmosphere to remove black material using a nickel crucible which had many layers of platinum screen welded over a hole in its bottom. The filtered salt was pre-electrolyzed at about 1.5V using a vitreous carbon anode and a stainless steel cathode until the current density of the cathode dropped to around 0.3 mA/cm^2; this eliminated metal ion impurities. After pre-electrolysis, the background voltammograms for pure melts were flat between +1.0 and −1.0V. That is, there were no reduction or oxidation waves detectable at the highest sensitivity used over the voltage range scanned in the experiments.

Cr(III) was added either as CrF_3 (Cerac, 99.5%), or as K_3CrF_6, which was prepared by the method of Christensen (15). The K_3CrF_6 was examined using x-ray diffraction analysis, and no other lines were detected. Analysis of one preparation gave 18.5% Cr (18.4% calculated). Both materials gave identical electrochemical behavior.

Figure 1 shows a schematic diagram of the cell assembly used. To minimize the effect of cell resistance between the electrodes, a three-electrode system was employed. For both measurements, a vitreous carbon (Atomergic Chemicals Corporation) auxiliary electrode (1/4 in. diam) and a small Pt plate (1 × 1 cm, area 2 cm^{-2}) quasi-reference electrode were used. A very fine Pt microelectrode (0.12 mm diam, 5 mm long) and a Pt cylindrical working electrode (2.3 mm diam, 11.3 mm long) were used as the working electrodes for cyclic voltammetry and chronopotentiometry, respectively.

Although attempts were made to use a boron nitride insulator for the working electrode to obtain a precise area, this failed because of the conductivity of the BN above 600°C, probably as a result of porosity due to leaching of the binder.

The controlled potential cyclic voltammeter used was designed and built in this laboratory. With this instrument, scan rates from 0.01 to 80 V/s are available, and cell currents up to 500 mA can be measured. A constant current power supply (HP Model 6212A) was used for chronopotentiometry. Waves were recorded by means of either a Tektronix Type 564 storage oscilloscope or an Omnigraphic Series 2000 X-Y recorder. Data were measured either from the large X-Y recorder chart or from enlarged photographs; transition times were evaluated according to Kuwana's method (16), and those reported for the second wave are measured from the end of the first wave.

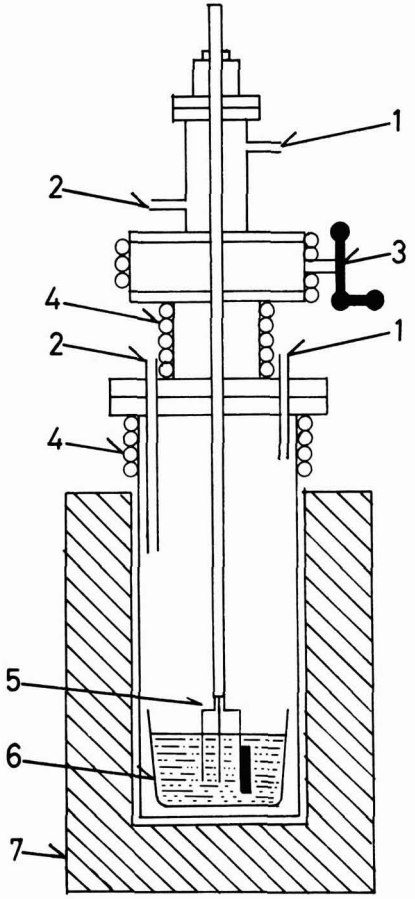


Fig. 1. Schematic diagram of the electrochemical cell. 1: Gas outlet. 2: Gas inlet. 3: Gate valve. 4: Water cooling coil. 5: Electrodes. 6: Ni crucible and molten salt. 7: Furnace.

[1]Present address: Department of Industrial Chemistry, Faculty of Engineering, Mie University, Tsu, Mie-Ken, 514, Japan.

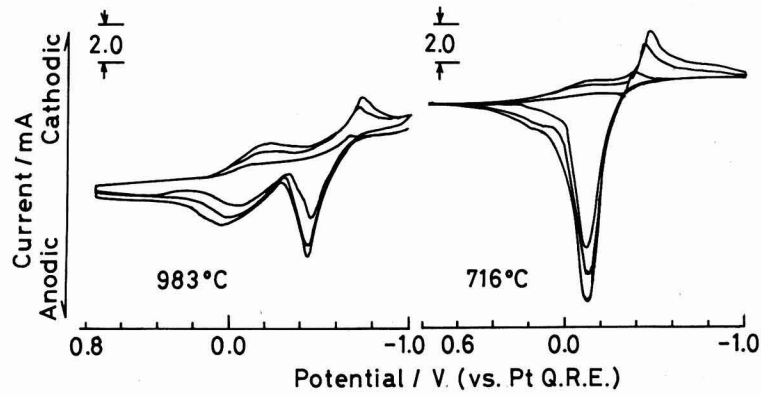
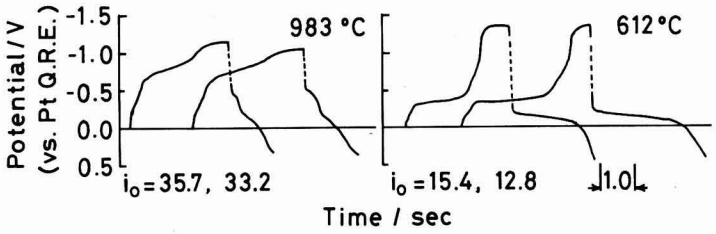


Fig. 2. Top: cyclic voltammograms for the reduction of Cr(III) in molten FLINAK. Scan rate: 8.0, 5.0, and 1.0 V s^{-1}. Concentration of Cr(III): 0.10 mol l^{-1}. Bottom: chronopotentiograms for the reduction of Cr(III) in molten FLINAK. Concentration of Cr(III): 0.10 mol l^{-1}. i_0: current density/10^{-2} mA m^{-2}.



All measurements were done in an argon atmosphere.

Results and Discussion

Both cyclic voltammetry and chronopotentiometry were performed over a temperature range of about 600° to 1000°C and a Cr(III) concentration of 0.07-0.13 mol/l. Figure 2 shows typical results taken at a Cr(III) concentration of 0.1 mol/l at temperatures of 983°, 716°, and 612°C. As shown in all of these figures, two reduction and two oxidation steps are evident. The first reduction step and the second oxidation step became indistinct at lower temperatures and lower scan rates, eventually almost merging with the others. This is mainly due to the tendency of the second reduction and first oxidation peaks to shift anodic with decreasing scan rate, decreasing temperature, and increasing concentration of Cr(III).

The shape of the first reduction wave in cyclic voltammetry is not in the form of a peak, but is a simple plateau at lower scan rates and lower temperatures. However, at higher scan rates, and especially at higher temperatures, it develops into a peak. The nature of the first reduction wave will be discussed later in more detail.

In Fig. 3, relationships between $i_0\tau^{1/2}$ and current density i_0 obtained from chronopotentiometry are shown for both reduction steps at different temperatures; $i_0\tau^{1/2}$ varies with current density at higher temperature and lower current density values, especially for the second reduction step, but becomes constant at higher current density. In Fig. 4, transition time constants, $i_0\tau^{1/2}/C$, where C is the concentration of Cr(III), at different temperatures are shown plotted against concentration of Cr(III) for both reduction steps. It is seen from Fig. 4 that the transition time constant of the first reduction step is substantially invariant at each temperature, in spite of some scatter of the data. The data for the second step show more deviation. In view of the high temperatures involved and the consequent possibility of convection, we do not consider that these deviations from constant values are unreasonable or represent real trends. That is, these results do not provide any indication that the electrode reaction of either reduction step has complications related to adsorption or coupled homogeneous chemical reactions (17, 18), although a reversible charge transfer followed by a reversible chemical reaction (ErCr) would also give a constant value. The deviation of $i_0\tau^{1/2}$ from the constancy observed at lower current density in Fig. 3 probably also is due to the convection of the bath melt. This is supported by the results from cyclic voltammetry.

In Fig. 5, relationships between peak current, i_p, of the cyclic voltammograms and the square root of the scan rate, $V^{1/2}$, are shown for both reduction steps at different temperatures. The value of i_p for the second wave was ob-

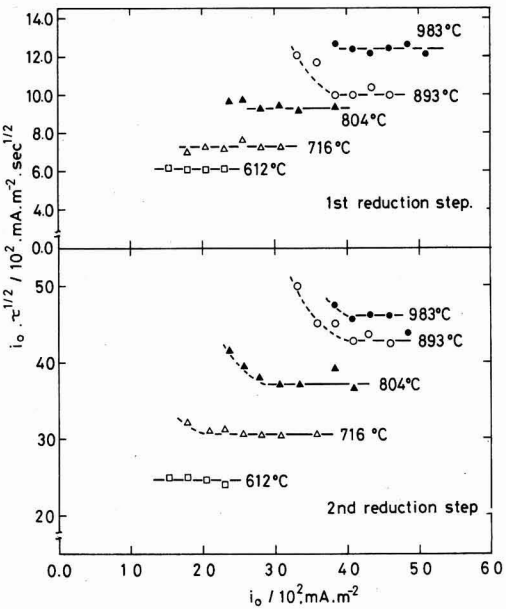


Fig. 3. Plots of $i_0\tau^{1/2}$ vs. i for the first and second reduction steps of Cr(III) in molten FLINAK. Concentration of Cr(III): 0.11 mol l^{-1}. Pt working electrode area: 0.98 × 10^{-4} m^2.

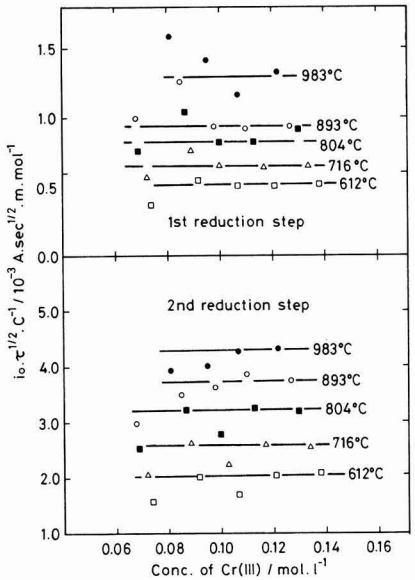


Fig. 4. Plots of $i_0\tau^{1/2}/C$ vs. C [concentration of Cr(III)] for the first and second reduction steps.

tained by extrapolating the first wave to provide a new base line; this was relatively straightforward at low scan rates, but involved more uncertainty at high scan rates and high temperatures, where a peak appeared on the first wave. A good linear relationship between i_p and $V^{1/2}$ is observed for the first reduction step, except at higher temperatures and lower scan rates. However, for the second reduction, the deviation from this relationship becomes significant at both lower and higher scan rates. The deviation of i_p at lower scan rates seems to be due to

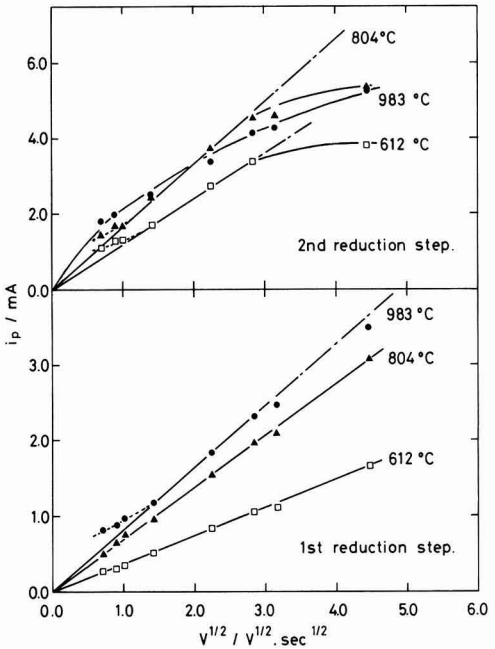


Fig. 5. Plots of i_p vs. $V^{1/2}$ for the first and second reduction steps of Cr(III) in molten FLINAK. Concentration of Cr(III): 0.11 mol l^{-1}. Pt microelectrode area: 2.02 × 10^{-6} m^2.

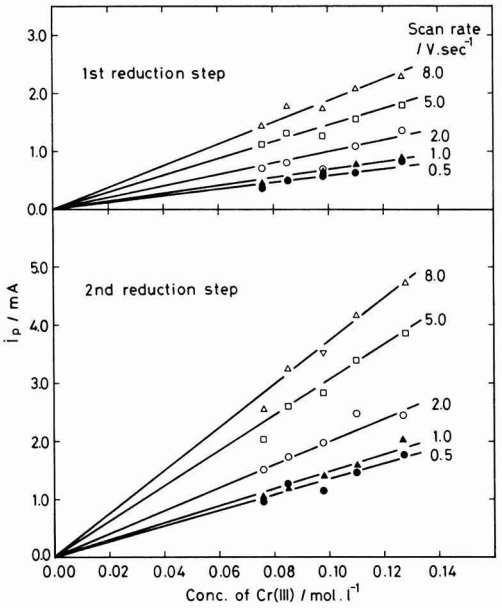


Fig. 6. Plots of peak current i_p vs. concentration of Cr(III) for the first and second reduction steps at 893°C.

the same cause as that of $i_0\tau^{1/2}$ at lower current density. The deviation of i_p at higher scan rates might suggest a slower reaction in the second reduction step, but may also reflect more uncertainty in the extrapolated base line for the second wave. The dependence of i_p on the concentration of Cr(III) for both reduction steps is shown in Fig. 6; i_p at each scan rate satisfies a linear function of Cr(III) concentration which goes through the origin over a wide range of concentrations of Cr(III). These observations mean that both reduction processes are diffusion or kinetically controlled, but are not adsorption or catalytic ones as just mentioned above (19). At the same time, this fact shows that there is no significant effect of uncompensated resistance between the electrodes (19).

In Tables I and II, scan rate and concentration dependence of the peak potentials (E_p) and current density and

Table I. Concentration dependence of peak potentials and quarter-wave potentials. Scan rate (voltammetry): 2.0 V s^{-1}. Current density (chronopotentiometry): 45.9 × 10^2 mA m^{-2}. Temperature: 983°C

Concentration of Cr(III) (mol l^{-1})	E_p/V First wave	E_p/V Second wave	$E_{\tau/4}$/V First wave	$E_{\tau/4}$/V Second wave
0.07	−0.186	−0.774	—	—
0.08	−0.164	−0.762	−0.32	−0.782
0.10	−0.156	−0.746	−0.259	−0.792
0.11	−0.192	−0.734	−0.202	−0.764
0.12	—	—	−0.206	−0.752

Table II. Scan rate dependence of peak potentials (voltammetry) and current density dependence of quarter-wave potential (chronopotentiometry). Concentration of Cr(III): 0.11 mol l^{-1}, 983°C

Scan rate (V s^{-1})	E_p (V) First wave	E_p (V) Second wave	Current density (mA m^{-2})	$E_{\tau/4}$ (V) First wave	$E_{\tau/4}$ (V) Second wave
1.0	−0.126	−0.738	33.2	−0.135	−0.610
2.0	−0.152	−0.749	35.8	−0.145	−0.616
5.0	−0.162	−0.786	38.4	−0.156	−0.628
8.0	−0.173	−0.796	40.9	−0.178	−0.637
10.0	−0.186	−0.815	43.5	−0.194	−0.646
20.0	−0.234	−0.857	46.0	−0.244	−0.656

concentration dependencies of the quarter-wave potential ($E_{\tau/4}$) are shown for both reduction steps. As seen from these tables, for both reduction steps, E_p and $E_{\tau/4}$ shift cathodic with increasing scan rate and current density and anodic with increasing concentration of Cr(III). None of logarithmic plots of cyclic voltammograms and chronopotentiograms such as log $(i_p/i - 1)$, log $(i - i_p)$, log $(\tau^{1/2}/t^{1/2} - 1)$, and log $(\tau^{1/2} - t^{1/2})$ are linear with potential, and it is clear that neither reduction step can be reversible.

As we cannot estimate from the slopes of such plots how many electrons are involved in each reduction step, we have to resort to another means to determine this. Berzins and Delahay (20) derived the equation which predicts the number of electrons involved in the stepwise diffusion-controlled electrode process

$$\frac{\tau_2}{\tau_1} = 2\frac{n_2}{n_1} + \left(\frac{n_2}{n_1}\right)^2 \quad [1]$$

where τ_i and n_i are the transition time and number of electrons in each step, respectively. As $n_1 + n_2$ equals 3 in our case, the two different values of n_1 and n_2 are considered as follows

Case I: if $n_1 = 1$ and $n_2 = 2$ then $\frac{\tau_2}{\tau_1} = 8$

Case II: if $n_1 = 2$ and $n_2 = 1$ then $\frac{\tau_2}{\tau_1} = 1.25$

The average values measured at different temperatures are listed in Table III. The values at higher temperatures are nearly 8 and correspond to case I. Indeed, this is the expected mode of behavior of Cr(III), and has been observed earlier in this melt (8). However, while the behavior at 983°C is as expected, at lower temperature reduction must occur in a more complicated manner as considered later. Equation [1] applies strictly only to diffusion-controlled electrode processes.

In order to clarify the nature of the first reduction step further, reversal techniques were employed for both chronopotentiometry and cyclic voltammetry. Ratios of the forward to the reverse transition time, τ_f/τ_r, for the first wave measured at various temperatures are listed in Table IV. This value is a very powerful tool for determining whether the product of the electrode reaction is soluble or insoluble (18). At 983°C, the ratio τ_f/τ_r is nearly 3, which means that the reduced product is soluble. However, this value becomes nearly unity below 893°C, so the product of the first reduction step is considered to be insoluble. This result agrees with the result previously mentioned: that is, at lower temperatures the ratio τ_{2r}/τ_{1r} shown in Table III gets larger than 8 with decreasing temperature, owing to the formation of the insoluble product of the first reduction step. There is less diffusion of the product of step 1 from the electrode surface, therefore leading to a larger amount of material available for the second reduction step. Smith (21) has obtained similar chronopotentiometric behavior in this system.

Cyclic voltammograms of only the first wave were taken at 893° and 983°C. Following Nicholson's semiempirical method (22), ratios of the anodic to the cathodic peak current, i_{ap}/i_{cp}, were obtained and given in Table V with the peak separation potentials. As seen from this table, peak separation gets larger with increasing scan rate, although at lower scan rates it approaches the value which is predicted for the reversible system. The ratio of i_{ap}/i_{cp} increases to more than unity with increasing scan rate, and shows the value of about 1 at lower scan rates. Both quantities show smaller values than expected for reversible behavior at the lowest scan rates examined, especially at 983°C. Peak current ratios of less than 1 can be rationalized on the basis of nonreversible behavior, while the cause of small peak separations may arise from uncertainties in determining peak position as the wave becomes flatter and less well defined at low scan rates.

When the results obtained for the first reduction wave are compared with the diagnostic criteria for typical electrode processes (Table VI), it is seen that the closest agreement is with either a quasi-reversible case, or with an ErCr process (for example, a reaction of Cr(II), perhaps with F^-, to form a metal cluster compound). Behavior of the i_{ap}/i_{cp} and τ_f/τ_r ratios is not consistent with the latter mechanism, however, so that a quasi-reversible process is considered most probable on the basis of the discrepancy of these ratios.

We cannot overlook the possibility that the Cr(II) might disproportionate by the following reaction

$$3Cr(II) \rightarrow 2Cr(III) + Cr(metal)$$

as pointed out by Mellors and Senderoff (8), and Redman (23). We also found that 8 weight percent of CrF_2 added into molten FLINAK for electrolysis did disproportionate and small amounts of Cr metal deposited on the surface of the Ni container after a week's experiment. The electrochemical results for a solution made from CrF_2 were qualitatively the same as when Cr(III) was used. However, it is believed that this disproportionation reaction is slow and is not detected within the range of the scan rates used in our experiments. Since our experiments have been carried out at a relatively high temperature (600°-1000°C) and the effect of convection in the melt becomes significant, reproducible measurements cannot be obtained at lower scan rates (≤ 1.0 V/s) and lower current density where the detection of a catalytic reaction might be feasible.

Table III. Temperature dependence of the ratio of the transition time of the second to the first reduction step, τ_{2r}/τ_{1r}. Concentration of Cr(III): 0.09 mol l^{-1}

Temp. (°C)	983	893	804	716	612
τ_{2r}/τ_{1r}	8.0	8.6	9.3	11.3	13.4

Table IV. Ratio of the forward to the reverse transition time for the first wave at different temperatures. Concentration of Cr(III): 0.13 mol l^{-1}

Temp. (°C)	Current density (10^2 mA m^{-2})	Transition time Forward τ_f (s)	Reverse τ_r (s)	τ_f/τ_r τ_f/τ_r
983	51.0	0.102	0.039	2.6
	40.8	0.156	0.047	3.3
893	46.0	0.067	0.071	0.93
	35.8	0.110	0.098	1.1
804	30.7	0.157	0.126	1.2
	25.6	0.201	0.193	1.0
716	25.6	0.114	0.112	1.0
	20.5	0.186	0.169	1.1
612	20.6	0.119	0.123	0.97
	18.0	0.158	0.150	1.1

Table V. Ratios of the anodic to the cathodic peak current i_{ap}/i_{cp}, peak potentials and their peak separation at different scan rates. Concentration of Cr(III) = 0.11 mol l^{-1}

Temp. (°C)	Scan rate (V s^{-1})	i_{ap}/i_{cp}	E_{cp} (V)	E_{ap} (V)	$E_{cp} - E_{ap}$ (V)
983	20	1.27	−0.286	−0.091	−0.377
	10	1.18	−0.236	−0.085	−0.321
	8	1.12	−0.226	−0.075	−0.301
	5	1.02	−0.213	−0.070	−0.283
	2	0.95	−0.186	−0.051	−0.237
	1	0.92	−0.157	−0.049	−0.201
					−0.253*
893	50	1.34	−0.339	−0.206	−0.545
	20	1.22	−0.226	−0.135	−0.351
	10	1.17	−0.199	−0.109	−0.308
	5	1.22	−0.173	−0.091	−0.264
	1	1.02	−0.152	−0.073	−0.225
					−0.234*

* Theoretical values calculated based on the reversible process (as $n = 1$).

E_{ap}, E_{cp}: Anodic and cathodic peak potential, respectively.

Table VI. Comparison of the results obtained for the first reduction step with the diagnostic criteria for typical electrode processes

Electrode process	$i_p/V^{1/2}$ vs. V	$i\,\tau^{1/2}$ vs. i	i_{ap}/i_{cp} vs. V	E_p vs. V	$E_{\tau/4}$ vs. i	$E_{\tau/4}$ vs. C	τ_f/τ_r vs. i
Observed	const.	const.	increasing	cathodic	cathodic	anodic	1[a] 3[b]
Reversible	const.	const.	1[c]	const.	const.	anodic[c] const.[d]	1[c] 3[d]
Quasi-rev.	const.	const.	> 1[d]	cathodic	cathodic	anodic	1[c] 3[d]
Irrev.	const.	const.	0	cathodic	cathodic	anodic	0 or 1[c] 0 or 3[d]
Cr.Er.	decreasing	decreasing	increasing from 1 at low V	anodic	—	—	3
Er.Cr.	const.	const.	decreasing from 1 at low V	cathodic	cathodic	anodic	increasing
Catalytic	*	increasing from 1	*	anodic or const.	anodic	—	—

Cr.Er.: Reversible chemical reaction preceding a reversible charge transfer.
Er.Cr.: Reversible charge transfer followed by a reversible chemical reaction.
* Decreasing at low V and constant at high V.
[a] Below 893°C.
[b] At 983°C.
[c] Insoluble product.
[d] Soluble product.

Table VII. Temperature dependence of the ratio of the transition time of the second reduction to the first oxidation step τ_{2f}/τ_{1r}. Concentration of Cr(III): 0.09 mol l^{-1}

Temp. (°C)	983	893	804	716	612
τ_{2f}/τ_{1r}	0.58	0.66	0.86	0.98	1.1

The ratios of the transition times of the second reduction to the first oxidation step, τ_{2f}/τ_{1r}, obtained at different temperatures are listed in Table VII. At lower temperatures, this ratio is very close to unity, but decreases with increasing temperature. Since the second reduction step has been found to be a quasi-reversible reduction of Cr(II) to Cr metal, this value should be unity. Possibly, alloy formation of deposited Cr metal with the Pt electrode might be responsible for the reduction of the ratio at higher temperatures.

Manning and Dale (11) have carried out voltammetric measurements on Cr(II) (as CrF_2) in $LiF\text{-}BeF_2\text{-}ZrF_4$ at 500°C and found that the reduction of Cr(II) to Cr metal in this melt is a quasi-reversible process. Their result reasonably agrees with ours.

The diffusion coefficient, D, of the electroactive species can be estimated from the Sand equation (24)

$$i_0\tau^{1/2} = \frac{nFC(\pi D)^{1/2}}{2} \qquad [2]$$

where i_0 is the current density, τ the transition time, C the concentration of electroactive species, and the remaining terms have their usual significance. The result is shown plotted as the logarithm against the reciprocal of absolute temperature in Fig. 7; the result is a straight line. The diffusion coefficients of Cr(III) obtained in molten FLINAK seem to be low (983°C: 1.84×10^{-6}, 893°C: 1.19×10^{-6}, 804°C: 0.95×10^{-6}, 716°C: 0.59×10^{-6}, 612°C: 0.36×10^{-6} cm²/s), even allowing for some uncertainty (± ~20%), mainly in the surface area of the working electrode and the concentration of Cr(III). The activation energy for the diffusion of Cr(III) calculated from the slope in Fig. 7 is 9.5 kcal/mol. Although small diffusion coefficients and large activation energies have been found for some other transition metals in molten FLINAK, the diffusion coefficients are still a factor of 5 or more greater than those obtained here (25, 26). This may suggest the existence of a large and stable complex anion like CrF_6^{3-} in the melt; Cr(III) does exhibit a maximum in ligand field stabilization energy and consequently in complex stability and inertness to ligand exchange.

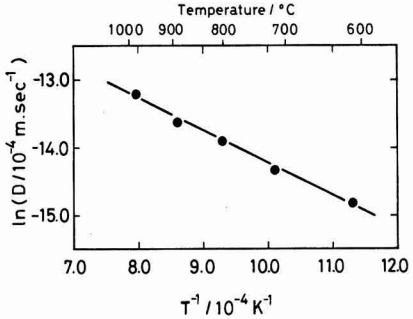


Fig. 7. Plots of ln D vs. $1/T$ for Cr(III) in molten FLINAK

In summary, Cr(III) in molten FLINAK is reduced in two steps over the temperature range 600°-983°C. The first step is the relatively slow reduction of Cr(III), to give a product which is soluble at 983°C and insoluble, but still electroactive, below 893°C. This step is most probably quasi-reversible, although the behavior of some parameters is not totally straightforward and some complications from chemical reactions are possible. The second step is the reduction of Cr(II) to Cr(O). This is also quasi-reversible, with indications from voltammetric peak currents that it is slow especially at higher temperatures.

In electroplating of Cr from molten FLINAK, there is a correlation between the physical nature of the electrodeposited metal and the changing nature of the electrochemistry with temperature. At low temperatures, the deposit consists of extensive dendrites imbedded in the salts. At high temperatures, dendrite formation is reduced and smoother plates are obtained. The results of the Cr electroplating will be reported separately.

Acknowledgments

The authors wish to thank Dr. George J. Janz (R.P.I.) for his helpful discussions and other assistance through the course of this study. Financial support was provided by the Army Research Office under Contract no. DAAG29-79-C-0035.

Manuscript submitted Oct. 10, 1982; revised manuscript received June 29, 1984. This was Paper 490 presented at the Minneapolis, Minnesota, Meeting of the Society, May 10-15, 1981.

REFERENCES

1. G. W. Mellors and S. Senderoff, *Plating*, **51**, 972 (1964).
2. G. W. Mellors and S. Senderoff, *This Journal*, **112**, 266 (1965).
3. S. Senderoff, G. W. Mellors, and W. J. Reinhard, *ibid.*, **112**, 840 (1965).
4. G. W. Mellors and S. Senderoff, *ibid.*, **113**, 60 (1966).
5. S. Senderoff and G. W. Mellors, *ibid.*, **113**, 66 (1966).
6. S. Senderoff and G. W. Mellors, *ibid.*, **114**, 556 (1967).
7. S. Senderoff and G. W. Mellors, *ibid.*, **114**, 586 (1967).
8. G. W. Mellors and S. Senderoff, in "Applications of Fundamental Thermodynamics to Metallurgical Processes," G. R. Fitterer, Editor, p. 81, Gordon and Breach Science Publishers, New York (1967).
9. I. Ahmad, W. A. Spiak, and G. J. Janz, *J. Appl. Electrochem.*, **11**, 291 (1981).
10. D. Inman and S. H. White, *ibid.*, **8**, 375 (1978).
11. D. L. Manning and J. M. Dale, in "Molten Salts," G. Mamantov, Editor, p. 563, Marcel Dekker, New York (1969).
12. I. I. Naryshkin, V. P. Yurkinskii, and P. T. Stangrit, *Electrokhimiya*, **5**, 1043 (1969).
13. K. Cho and T. Kuroda, *Denki Kagaku*, **39**, 206 (1971).
14. D. Inman, J. C. L. Legey, and R. Spencer, *J. Electroanal. Chem.*, **61**, 289 (1975).
15. O. T. Christensen, *J. Pract. Chem.*, **35**, 161 (1887).
16. R. N. Adams, "Electrochemistry at Solid Electrodes," p. 183, Marcel Dekker, Inc., New York (1969).
17. I. J. Bard and L. R. Faulkner, "Electrochemical Methods—Fundamentals and Applications," Chap. 7, 11, John Wiley and Sons, New York (1980).
18. D. D. Macdonald, "Transient Techniques in Electrochemistry," Chap. 5, Plenum Press, New York (1977).
19. A. M. Bond, "Modern Polarographic Methods in Analytical Chemistry," Chap. 3, 5, Marcel Dekker, New York (1980).
20. T. Berzins and P. Delahay, *J. Am. Chem. Soc.*, **75**, 4205 (1953).
21. J. F. Smith, Materials Research Corp., Orangeburg, NY, Private communication.
22. R. S. Nicholson, *Anal. Chem.*, **37**, 1406 (1965).
23. J. D. Redman, O.R.N.L. 2626 M.S.R.P., Q.P.R. 94 (1958).
24. P. Delahay, "New Instrumental Methods in Electrochemistry," pp. 117, 180, Interscience Publishers, Inc., New York (1954).
25. D. L. Manning, *J. Electroanal. Chem.*, **6**, 227 (1963); *ibid.*, **7**, 302 (1964).
26. F. R. Clayton, G. Mamantov, and D. L. Manning, *This Journal*, **120**, 1193 (1973); *ibid.*, **121**, 86 (1974).

Cathodic Polarization of Aluminum in Alkylbenzene Electrolytes

G. A. Capuano*

Department of Chemistry, University of Quebec in Montreal, Montreal, Quebec, Canada H3C 3P8

W. G. Davenport

Department of Metallurgical Engineering, University of Arizona, Tucson, Arizona, 85721

ABSTRACT

Cathode overpotentials for the plating of aluminum from ethylbenzene toluene 1:1, 50 weight percent $AlBr_3$ electrolytes have been measured as a function of current density, temperature, and specific conductances. The exchange current density (i_o) and the heat of activation ($\Delta H)_\eta$ were determined to be 10^{-3} A/cm^2 and 2.6 to 4.5 kcal/mol, respectively. Stoichiometries of plating are proposed, and the observed transfer coefficient of 1.3 is shown to be consistent with monomeric aluminum complexes as the active plating species. Solutions prepared from anhydrous alkyl benzene and $AlBr_3$ are shown to be insufficiently conductive for aluminum plating. HBr increases the conductivities for optimal plating conditions.

The use of alkylbenzene electrolytes for the electrodeposition of aluminum and aluminum-copper alloys has been extensively studied in our laboratories during the past few years (1-10).

The plating solution consists of a 1:1 mixture (by volume) of ethylbenzene and toluene, containing 50 weight percent (w/o) $AlBr_3$. Some gaseous HBr is added to insure a specific conductance of 2-4 $\times 10^{-3}\ \Omega^{-1}\ cm^{-1}$ and to provide bromide ions to complex the excess of aluminum ions obtained whenever cathode efficiencies are lower than 100%.

From the faradaic cathodic efficiencies obtained in our electroplating work (3, 8), the range of conductivities mentioned above is considered optimal for plating. All our kinetic data were determined, therefore, over this conductivity range.

The object of this paper is to describe and interpret cathode polarization experiments on the above-described system. The basic measurements were cathode overpotential as a function of current density, temperature, and specific conductance. The results are interpreted in terms of the exchange current density (i_o), the heat of activation (ΔH), and the transfer coefficient α. Plating stoichiometries are proposed.

Some aromatic complexes of aluminum.—When aluminum halides are dissolved in aromatic hydrocarbons, different types of complexes are formed, depending on the number and type of constituents used for their formation.

Binary mixture.—Brown and Wallace (11) and Brown and Brady (12) suggested that π complexes form when aluminum bromide is dissolved in an aromatic solvent such as benzene or toluene, *i.e.*

$$Al_2X_6 + ArH \rightleftarrows \underset{(\pi\ \text{complex})}{(Al_2X_5 \cdot ArH)^+} + X^- \qquad [1]$$

where ArH is an aromatic hydrocarbon and X a halide.

These complexes have a very low degree of dissociation because their saturated solutions have specific conductances of the order of $10^{-9}\ \Omega^{-1}\ cm^{-1}$ when prepared from rigorously dried $AlBr_3$ and aromatic solvents (13). Lebedev and Korshak (14-16) suggested that the formula for the complex compound of aluminum halides with an organic solvent is

$$Al_2X_6 + n_{slv} \rightleftarrows (AlX_2 \cdot n_{slv})^+ + (AlX_4)^- \qquad [2]$$

where slv denotes solvent.

Kessler and co-workers (17) considered this scheme to be the most probable and adopted the value of 2 for n.

Ternary mixtures.—Brown and Wallace (18) reported on the basis of vapor pressure compositions-phase studies the formation of σ complexes or salts of carbonium ions $(ArH_2)^+$ and $Al_2X_7^-$ or AlX_4^- when hydrogen bromide and

*Electrochemical Society Active Member.

aluminum bromide react with the aromatic hydrocarbons, *i.e.*

$$ArH + HX + Al_2X_6 \rightleftharpoons ArH_2^+ + Al_2X_7^- \quad [3]$$

or

$$ArH + HX + \tfrac{1}{2}Al_2X_6 \rightleftharpoons ArH_2^+ + AlX_4^- \quad [4]$$

However, benzene and toluene could only produce dimeric complexes at room temperature as in Eq. [3], whereas solvent molecules having more or larger lateral chains such as m-xylene, and mesitylene, produced more readily the monomeric form of the aluminum complex as in Eq. [4].

The formation of these ions can explain the good conductivity of the solution when the hydrogen halide is added to an electrolyte containing aluminum bromide dissolved in an aromatic solvent.

Electrodeposition of aluminum from aromatic hydrocarbons.—Levinskieve and Simanavicius (19) suggested the following scheme for the electrodeposition of aluminum from a xylene-$AlBr_3$-HBr system

$$[AlBr_2 \cdot n(C_6H_4)(CH_3)_2]^+ + 3e \rightarrow Al + n(C_6H_4)(CH_3)_2 + 2Br^- \quad [5]$$

This is in agreement with the Lebedev and Korshak suggestion (Eq. [2]) and the Brown and Wallace findings (Eq. [4]).

This paper is essentially an investigation into cathode overpotentials at different current densities, temperatures, and specific conductances, with the aim of understanding to a greater extent the aluminum electroplating process.

Experimental

The experimental cell and auxiliary equipment used in the experiments have been described in a previous paper (5). The cell consists essentially of a cylindrical glass body with (*i*) working electrodes occupying the cross section of the cell at each end and (*ii*) a reference electrode behind the cathode, penetrating to the front through a 0.8 mm glass-lined hole. The thickness of the glass lining has been measured to be 0.001 cm, and it represents the distance between the capillary tip and the cathode surface. The amount of IR voltage drop for electrolytes having conductivities of 2 and $4 \times 10^{-3}\ \Omega^{-1}\ cm^{-1}$ at current densities of 10 mA cm^{-2} are 5 and 2.5 mV, respectively, from the equation

$$E_{IR} = \frac{i_c \delta}{K} \quad [6]$$

where i_c is the cathodic current density, δ the glass wall thickness, and K is the specific conductance of the electrolyte (20). However, no corrections were made since the actual values of the E_{IR} are likely to be considerably lower due to edge effects which tend to increase the potential around the cathode hole due to field distortion (21, 22) and also because the capillary tip is displaced horizontally from rather than in front of the cathode.

Materials.—Aluminum bromide was prepared from super-pure aluminum (99.99%) and Fisher reagent-grade bromine. Ethylbenzene and toluene were both Fisher reagent-grade products. Preparation of the electrolyte has been described elsewhere (1-4). The conductivity of the plating solution was adjusted by bubbling gaseous HBr through the solution.

Procedure.—One liter of freshly prepared electrolyte, conditioned by 5-8h of aluminum plating at 10 mA/cm^2 in order to remove traces of more noble metals (impurities), was used in all the experiments. The cathode area was 30 cm^2. Four anodes of the same surface area were placed around the cathode (3).

The cell was protected from moisture in a closed system. After filling the cell, the first experimental step was to plate aluminum onto the platinum cathode and reference electrode for 30-60 min. Once this was done, the electrodes were connected in their working and measuring circuits and plating was begun under controlled current density conditions. The electrolyte near the cathode was stirred by means of a micromagnetic Teflon-covered bar. The overpotentials were measured by a galvanostatic (point by point) procedure. Plating was carried out for 1 min before the cathode overpotential was measured.

Following each measurement, the current density was increased and the procedure was repeated at the new current density. After each set of experiments at one temperature, the cell was emptied, cleaned, filled with fresh electrolyte (from the 1 liter batch), and the experiments were repeated at a higher temperature. All the overpotentials reported were measured against a reference (reversible) aluminum electrode (RAl) located behind the cathode, containing the same solution under study and at the same temperature (5).

Results and Discussion

The polarization studies showed (Fig. 1) that the cathode overpotential (η) as a function of current density is significantly lowered with increasing specific conductance. However, at specific conductance greater than $8 \times 10^{-3}\ \Omega^{-1}\ cm^{-1}$, under galvanostatic conditions, the aluminum coating on the platinum cathode redissolved. At specific conductances of $1 \times 10^{-3}\ \Omega^{-1}\ cm^{-1}$, however, there was such an ohmic drop across the cell that it was impossible to reach the 15 mA/cm^2 current density with the potentiostat maximum output of 20V. Furthermore, when the aluminum bromide and the alkylbenzene were rigorously dried by redistillation under nitrogen in a dry box, current densities were not higher than 1 mA/cm^2 even for potentials up to 20V applied between the anode and the cathode. The specific conductance was of the order of $10^{-9}\ \Omega^{-1}\ cm^{-1}$.

Thus, the polarization study complements that on the beneficial effect of HBr on the faradaic cathode efficiency in the region of conductances from 2 to $4 \times 10^{-3}\ \Omega^{-1}\ cm^{-1}$, as reported in previous papers (3, 8).

The effect of specific conductance on overpotentials.—The observed decrease in cathode overpotential

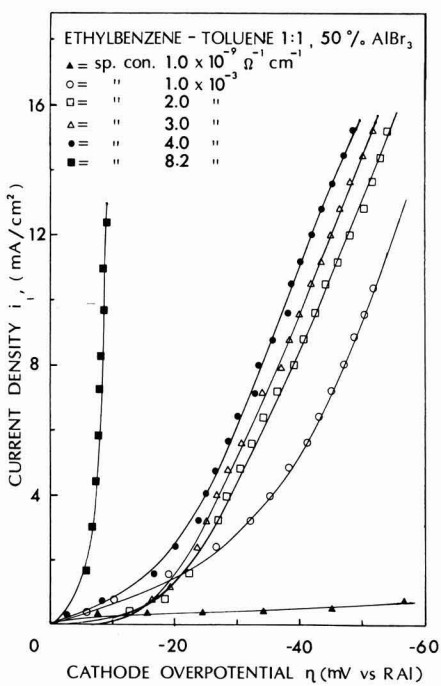


Fig. 1. Cathode overpotentials vs. current density for ethylbenzene-toluene 1:1 vol:50 w/o $AlBr_3$-HBr at the specific conductances shown.

with increasing specific conductance (Fig. 1 to 4) can be explained in terms of an increase in the concentration of the active aluminum bearing ions, *i.e.*, π complexes (Eq. [7]). These complexes are formed by the addition of HBr on the alkylbenzene and $AlBr_3$ electrolyte, as shown in Eq. [7], which is a combination of Eq. [2] and [4]

$$2Al_2Br_6 + 2HBr + (2 + n)ArH \rightarrow \underset{\sigma \text{ complex}}{2ArH_2^+} + \underset{}{3AlBr_4^-} + \underset{\pi \text{ complex}}{(AlBr_2 nArH)^+} \quad [7]$$

The Butler-Volmer equation gives

$$i = i_o(e^{\overleftarrow{\alpha}F\eta/RT} - e^{\overrightarrow{\alpha}F\eta/RT}) \quad [8]$$

where

$$i_o = FKc\ CA^{n+}e^{-\overrightarrow{\alpha}F\eta/RT} = FKcCD\ e^{\overleftarrow{\alpha}F\eta/RT})$$

and i is the net current density, i_o the exchange current density, Kc the rate constant, CA^{n+} the positive electroactive ion concentration, CD the reduced ions concentration, $\overrightarrow{\alpha}$ the cathodic transfer coefficient, $\overleftarrow{\alpha}$ the anodic transfer coefficient, η the $\Delta\phi - \Delta\phi_e$ overpotential, $\Delta\phi_e$ the equilibrium potential, $\Delta\phi$ the applied potential, and **F**, R, and T have their usual significance.

Equation [8] predicts that an increase in the concentration species "CA^{n+}," *i.e.*, the π complex in Eq. [7], causes an increase in current density at any applied cathodic potential, $\Delta\phi$. Similarly, an increase in CA^{n+} means that a lower potential $\Delta\phi$ is required to achieve any desired current density. Since $\eta = \Delta\phi - \Delta\phi_e$, where $\Delta\phi_e$ is the equilibrium rest potential across the electrode interface, the lower required applied potential $\Delta\phi$ (for any current density) is equivalent to the presence of a lower overpotential η at the cathode.

Tafel plots.—Figures 2, 3, and 4 present the (point by point) galvanostatic current overpotential relationship, for the cathodic reduction of aluminum at four different temperatures in alkylbenzene-$AlBr_3$-HBr electrolytes,

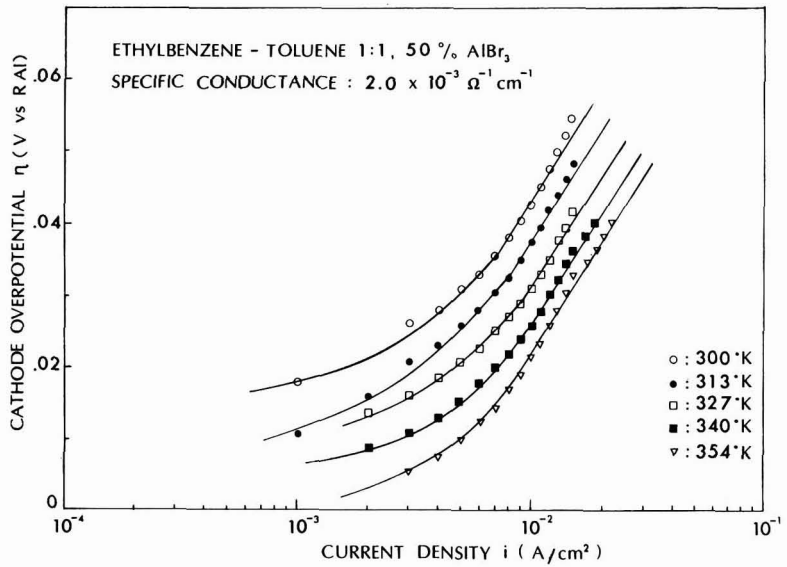


Fig. 2. Tafel plot at the temperatures shown, for ethylbenzene-toluene 1:1 vol:50 w/o $AlBr_3$-HBr at a specific conductance of $2.0 \times 10^{-3}\ \Omega^{-1}\ cm^{-1}$.

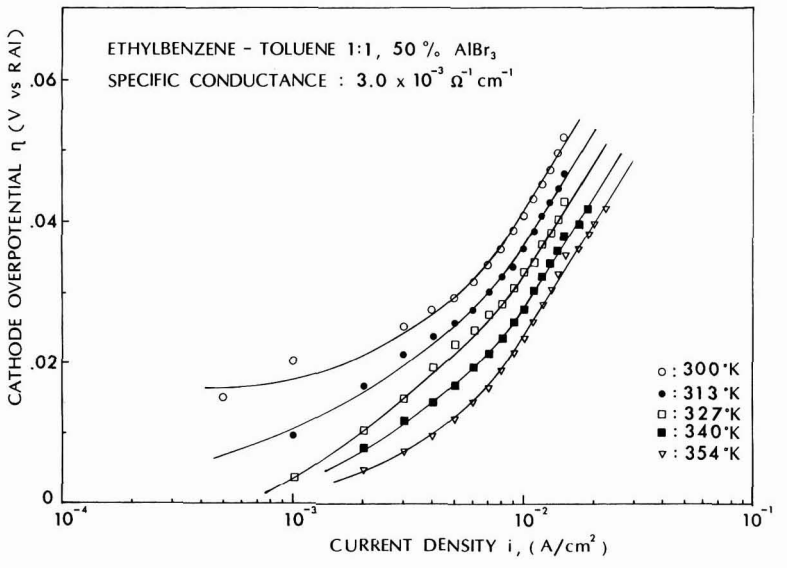


Fig. 3. Tafel plot at the temperatures shown, for ethylbenzene-toluene 1:1 vol:50 w/o $AlBr_3$-HBr at a specific conductance of $3.0 \times 10^{-3}\ \Omega^{-1}\ cm^{-1}$.

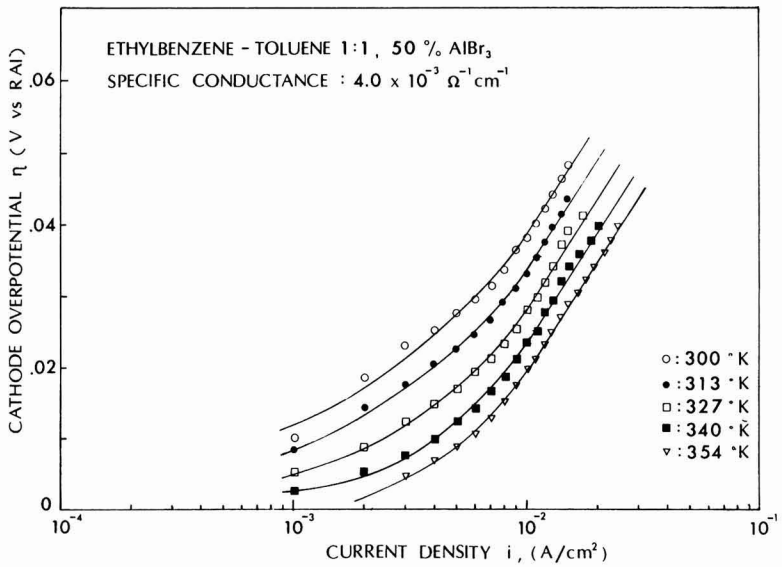


Fig. 4. Tafel plot at the temperatures shown, for ethylbenzene-toluene 1:1 vol:50 w/o $AlBr_3$-HBr at a specific conductance of $4.0 \times 10^{-3}\ \Omega^{-1}\ cm^{-1}$.

having HBr added to yield specific conductances of 2, 3, and $4 \times 10^{-3}\ \Omega^{-1}\ cm^{-1}$, respectively.

These plots display a linear relationship between the cathode overpotentials and the log of the current density, above overpotential values of 30 mV. This is to be expected if the Tafel equation

$$\eta = \frac{2.30RT}{\overrightarrow{\alpha}\mathbf{F}} \log i_o - \frac{2.30RT}{\overrightarrow{\alpha}\mathbf{F}} \log i_c \qquad [9]$$

is obeyed and there is a controlling charge-transfer step.

Exchange current density.—The values of the exchange current density (i_o) were calculated by extrapolating the Tafel line to $\eta = 0$. For the three experimental electrolytes studied (specific conductance 2.0, 3.0, and $4.0 \times 10^{-3}\ \Omega^{-1}\ cm^{-1}$) and the data at 40°C (Fig. 2, 3, and 4), the i_o values were found to be approximately 2×10^{-3} A/cm² (Table I).

Mechanism of aluminum deposition.—It is difficult to isolate the precise mechanism of aluminum deposition as there are numerous views on the types of complexes which can form between aluminum halides and aromatic hydrocarbons. However, the basic differences between the structures suggested are that, in one case, aluminum bromide exists in a monomeric form exemplified by the complex $(AlBr_2 \cdot n\text{ArH})^+$ (Eq. [2]) and, in the other, aluminum bromide would combine into a dimeric form, *e.g.*, $(Al_2Br_5 \cdot n\text{ArH})^+$ (Eq. [1]).

Brown and Wallace (18) and Choi and Brown (23) found that unbranched or lower branched aromatic solvent molecules such as benzene and toluene produced mostly dimeric complexes (Eq. [3]). Solvent molecules with more or larger lateral chains, such as xylene and mesitylene, or alkyl benzenes having a higher basicity than toluene, generate mainly monomeric complexes, as shown in Eq. [4].

Table I. Calculated kinetic parameters from Tafel lines (40°C)

Specific conductance ($\Omega^{-1}\ cm^{-1}$)	i_o (mA cm^{-2})	Tafel slope (V decade)	Cathodic transfer coefficient* (α)
4.0×10^{-3}	2.2	0.046	1.35
3.0×10^{-3}	2.0	0.048	1.3
2.0×10^{-3}	1.9	0.050	1.25

* Transfer coefficient: $\alpha = 2.3\ RT/b\mathbf{F}$, where b is Tafel slope.

Ethylbenzene provides highly basic alkylbenzenes such as diethylbenzene, ethylmethylbenzene, etc., through disproportionation reactions (10).

Capuano and Davenport, in an early publication (1), presented photographs showing the effects of several aromatic solvents on the quality of aluminum coatings. In fact, one can notice in Fig. 2 in Ref. (1) that no acceptable aluminum coatings are obtained from unbranched or lower branched solvents such as benzene or toluene. The quality of the aluminum coating improved, however, with xylene, and became excellent with ethylbenzene. This is consistent with the formation of monomeric aluminum complexes in solvent molecules having more or larger lateral chains than benzene and toluene. This supports the hypothesis that the presence of an aluminum complex in its monomeric form is prerequisite for aluminum electrodeposition in alkylbenzene-$AlBr_3$-HBr electrolytes.

The slope of the experimental Tafel lines yields an average cathodic transfer coefficient $\overrightarrow{\alpha}$ of 1.3, close to 1.5. Similar values for the anodic transfer coefficient $\overleftarrow{\alpha}$, are then predicted for Eq. [10]

$$\overrightarrow{\alpha} + \overleftarrow{\alpha} = \frac{n}{\nu} \qquad [10]$$

These results indicate that if n (the total number of electrons transferred in the overall reaction) is equal to 3, *i.e.*, if aluminum is present in a monomeric form, ν (the number of times the rate-determining step takes place for the overall reactions to occur once) equals 1.

Assuming then from the foregoing discussion that an ethylbenzene-toluene-$AlBr_3$-HBr electrolyte produces monomeric aluminum complexes, the following plating reaction is proposed

$$(AlBr_2\ nC_6H_5C_2H_5)^+ + 3e^- \rightarrow Al + nC_6H_5C_2H_5 + 2Br^- \qquad [11]$$

Considering the fact that the Br^- is not likely to be in a free state, Eq. [11] can be written as

$$2(AlBr_2\ nC_6H_5C_2H_5)^+ + 3e^- \rightarrow Al + AlBr_4^- + 2nC_6H_5C_2H_5 \qquad [12]$$

This is in agreement with Brown and Wallace (18) (Eq. [4]), Lebedev and Korshak (14-16) (Eq. [2]), and Levinskieve and Simanavicius (19) (Eq. [5]).

Heat of activation.—An electrochemical Arrhenius plot at some typical electrode overpotentials as derived from

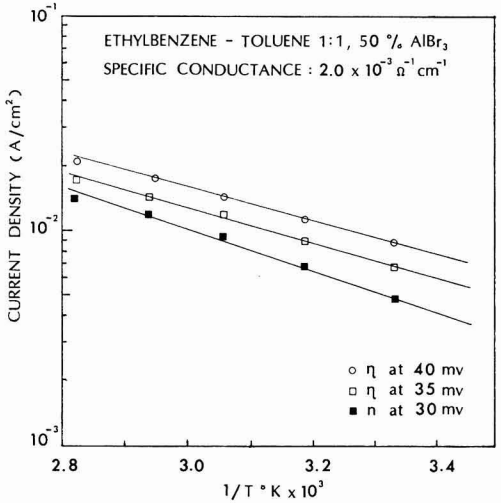


Fig. 5. Current density vs. $1/T$ (where T is the absolute temperature) plot adopted from Fig. 2, in order to determine the heat of activation $(\Delta H)_\eta$ at the overpotentials shown.

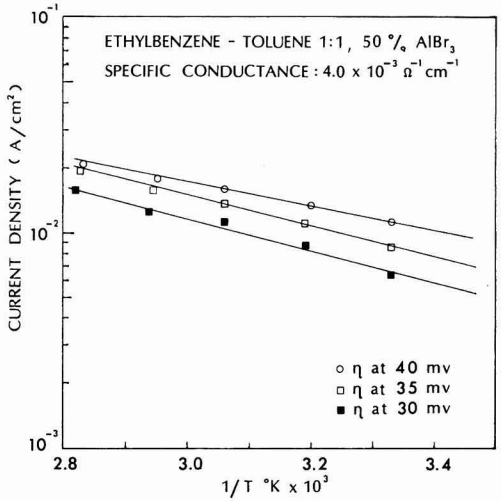


Fig. 6. Current density vs. $1/T$ (where T is the absolute temperature) plot adopted from Fig. 4, in order to determine the heat of activation $(\Delta H)_\eta$ at the overpotentials shown.

Fig. 2 and Fig. 4 is presented in Fig. 5 and Fig. 6. The heat of activation as given by the differential $(\partial \log i/\partial 1/T)_{\eta_0}$ lies between 2.6 and 4.5 kcal, depending on the electrode potential and the specific conductance. The complete results are given in Table II. These results compare well with the values obtained (4 kcal/mol) by Simanavicius *et al.* (24) for the Hurley and Wier (25) electrolyte (aluminum bromide and an ethyl-pyridinium bromide in toluene). It has been generally agreed (26) that the heat of activation in the electrodeposition of metals from aqueous solution is of the order of 10-30 kcal/mol. The values from the present work and values obtained by Simanavicius *et al.* (24) indicate, however, that the activation energies for plating metals from organic electrolytes are almost an order of magnitude less than the heats of activation for plating from aqueous electrolytes.

This result suggests that the bond energy of aluminum bromide in the alkylbenzene complexes is considerably lower than the hydration energy of metal ions in aqueous solutions.

Conclusions

1. A study of cathodic overpotentials of ethylbenzene-toluene $AlBr_3$-HBr electrolyte showed that charge-transfer overpotentials were of the order of 40 mV at current density of 10 mA/cm². The overpotentials decrease with increasing specific conductances and temperature of the electrolyte.

2. Exchange current density (i_o) at specific conductances of 2-4 $\times 10^{-3}$ Ω^{-1} cm^{-1} and a temperature of 40°C are approximately 2×10^{-3} A/cm², and the heat of activation $(\Delta H)_\eta$ varies from 2.6 to 4.5 kcal/mol. The relatively high values of exchange current density and the relatively low value of heat of activation indicate that aluminum is released rather easily from its organic complexes to plate on an aluminum cathode.

3. A cathodic transfer coefficient α of 1.3 is consistent with monomeric aluminum complexes being the active species during plating.

4. Solutions prepared from anhydrous alkylbenzene and aluminum bromide are not conductive enough for electroplating aluminum.

HBr is a suitable reagent for adjusting the conductivity of the solution to its optimum operating condition.

Table II. Calculated heat of activation for some typical electrode overpotentials at different specific conductances for the temperature range of 300-354 K

Specific conductance (Ω^{-1} cm^{-1})	Cathode overpotentials (mV)	Heat of activation (kcal/mol)
2×10^{-3}	30	4.5
	35	4.2
	40	3.5
4×10^{-3}	30	3.5
	35	3.1
	40	2.6

Acknowledgment

The authors wish to thank the Natural Sciences and Engineering Research Council of Canada and the Quebec Ministry of Education for financial support of this work.

Manuscript submitted July 11, 1983; revised manuscript received May 7, 1984.

The University of Quebec assisted in meeting the publication costs of this article.

REFERENCES

1. G. A. Capuano and W. G. Davenport, *This Journal*, **118,** 1688 (1971).
2. G. A. Capuano and W. G. Davenport, *Plating*, **60,** 251 (1973).
3. G. A. Capuano, R. Lafortune, and C. Gobeil, *Plating Surf. Finish.*, **64,** 59 (1977).
4. G. A. Capuano, J. Caza, and N. Homsy, in "1st International Symposium on Electrodeposition of Aluminum," Proceedings Session G-3, pp. 1-7 (1981).
5. G. A. Capuano and W. G. Davenport, *This Journal*, **122,** 453 (1975).
6. G. A. Capuano and W. G. Davenport, Canadian Pat. 945,935 (1974); U.S. Pat. 3,775,260 (1973).
7. R. Lafortune, J. T. Bourret, and G. A. Capuano, *Can. J. Chem.*, **56,** 2375 (1978).
8. G. A. Capuano, R. Ducasse, and W. G. Davenport, *J. Appl. Electrochem.*, **9,** 7 (1979).
9. R. Ducasse and G. A. Capuano, *Plating Surf. Finish.*, **68,** 78 (1981).
10. H. Antoun, A. Hade, and G. A. Capuano, *This Journal*, **129,** 40 (1982).
11. H. C. Brown and W. J. Wallace, *J. Am. Chem. Soc.*, **75,** 6265 (1953).
12. H. C. Brown and J. D. Brady, *ibid.*, **74,** 3570 (1952).
13. D. D. Eley and P. J. King, *J. Chem. Soc.*, 2517 (1952).
14. N. N. Lebedev, *JOCH*, **22,** 1505 (1948).
15. V. V. Korshak and N. N. Lebedev, *ibid.*, **18,** 1766 (1948).

16. N. N. Lebedev, *ibid.*, **21,** 1780 (1951).
17. O. M. Kessler, N. M. Alpatov, and O. R. Orpow, *Adv. Chem.*, **33,** 261 (1964).
18. H. C. Brown and W. J. Wallace, *J. Am. Chem. Soc.*, **75,** 6268 (1953).
19. L. Simanavicius and A. Levinskieve, *Liet: TSR Mokslu Akad. Darb. Ser. B*, **4,** 39 (1966).
20. S. Barnartt, *This Journal*, **108,** 102 (1961).
21. S. Barnartt, *ibid.*, **99,** 549 (1952).
22. R. Piontelli, *Gazz. Chim. Ital.*, **83,** 357, 370 (1953).
23. S. V. Choi and H. C. Brown, *J. Am. Chem. Soc.*, **88,** 903 (1966).
24. L. Simanavicius and P. Dobrovolskis, *Issled. Obl. Ogazhdeniya Metal, Water. Respubl. Kouf. Ele. Ktrochium. Litkov. S.S.R.*, **11,** 192 (1971).
25. F. H. Hurley and T. P. Wier, *This Journal*, **98,** 207 (1951).
26. J. O'M. Bockris, in "Modern Aspects of Electrochemistry," Vol. 2, J. O'M. Bockris, Editor, Butterworth Scientific Publication, London (1954).

Electrochemical Properties of $WO_3 \cdot x(H_2O)$

III. Complex Plane Analysis of the Film on SnO_2

Nobuyuki Yoskiike, Masatake Ayusawa, and Sigeo Kondo

Matsushita Electric Industrial Company, Limited, Central Research Laboratory, Moriguchi, Osaka 570, Japan

ABSTRACT

Complex plane analysis of evaporated WO_3 films on SnO_2 coated glass substrate has been performed in propylene carbonate electrolytes as a function of frequency from 100 kHz to 100 mHz at various applied voltages. It has been confirmed that the electron injection process at the SnO_2 electrode/WO_3 film interface, the electrochemical charge-transfer process in the WO_3 film and a diffusion-controlled process in the bulk are important processes at high ($f > 1$ kHz), medium (1 kHz $> f >$ 3 Hz), and low frequencies ($f <$ 3 Hz), respectively. The change of electrochromic activity of various $WO_3 \cdot x(H_2O)$ films depends mainly on the charge-transfer process in the film; the charge-transfer impedance increases with hydroxylation of WO_3 layer and, furthermore, increases drastically with hydrated crystallization.

WO_3 is one of the most useful materials for electrochromic displays (ECD) (1-6). A model for coloration by Faughnan *et al.* (3) explained reasonably well that double injection of electrons and protons into the film accompanies the formation of tungsten bronze. (The bronze has a stable memory effect and can be switched back into the original colorless state by reversing the current.) Recent studies (7-13) have confirmed that water in the film plays an important role for the coloration and bleaching mechanism.

The states of water in the WO_3 film may be classified into three groups: physisorbed water, chemisorbed water as hydroxylation, and hydrated water having a crystal structure. We (14, 15) have recently confirmed the influence of these three states on the electrochemical properties of evaporated WO_3 films. In particular, we have reported that water adsorbed on the film from ambient air after the ventilation of the vacuum evaporation chamber not only provides a fast electrochromic reaction at first, but also reacts gradually with WO_3 by hydroxylation and/or hydrolysis to shift the potential of the cathodic reaction to negative potentials. Then the hydroxylated film loses the electrochromic coloration density at the same applied voltage as before (14). We have also reported that the formation of tungstate crystals ($WO_3 \cdot H_2O$ and/or $H_2WO_4 \cdot H_2O$) by storing in high humidity air causes remarkable deterioration of the electrochromic activity of the film (15). The relationship between the electrochromic activity and the state of the water in $WO_3 \cdot x(H_2O)$ has been clarified, but it is still not clear what kind of processes in the electrochromic reaction are being affected.

The mechanism and the coloration dynamics of the WO_3 film have been roughly clarified by many authors. Faughnan *et al.* (3, 16) measured a $t^{-1/2}$ dependence of current flow during the coloration reaction of the WO_3 film in H_2SO_4 aqueous solutions under low applied voltage and suggested a barrier-limited current of proton transport across the WO_3/electrolyte interface as controlling. They (17) found $t^{-3/4}$ and $V^{1/2}$ dependence of current flow during the bleaching process under other constant applied voltages and suggested a field-driven space-charge-limited current of proton in those cases.

Mohapatra (18) also reported similar dynamics in the Li_xWO_3/Li system. Green *et al.* (19-20) studied the thermodynamics of the diffusion process with WO_3/solid electrolyte and WO_3/liquid electrolyte junctions using the galvanostatic method. However, although complex plane analysis is a most useful method, there are few studies of WO_3 film using this method. Ho *et al.* (21) have reported kinetic data such as chemical diffusion coefficient, partial ion conductivity, and thermodynamic enhancement factor, with $Li_xWO_3/LiAsF_6$ in propylene carbonate/Li system using this method. They suggested that the interfacial charge-transfer reaction at the WO_3/electrolyte interface is important at short time ($t <$ 0.5s), but at longer times the rate of Li injection is determined by the diffusion kinetics.

This paper describes studies on $WO_3 \cdot x(H_2O)$ using complex plane techniques. The relationships between reaction processes and various states of water in $WO_3 \cdot x(H_2O)$ are discussed for the actual operating conditions of display devices.

Experimental

Preparation of WO_3 films.—WO_3 films were deposited on SnO_2-coated glasses (100 Ω/cm^2) by an electron beam evaporation method. WO_3 targets (99.99%) were supplied by Furuuchi Kagaku Company, Limited. The deposition rate was 4 to 5 Å/s, the deposition angle was varied within 40° with a planetary rotation, and the substrate temperature was usually maintained at 80°C after being kept at 110°C for 5 min. The total gas pressure in the chamber during the evaporation process was controlled by a gas-introduction method at 4-5 $\times$ 10^{-5} torr. Deposited WO_3 films were analyzed by electron diffraction and found to be amorphous. Packing density of the film calculated from film thickness and weight was 5.3-5.7 g/cm^3. The refractive index deduced from the interference patterns of visible absorption and film thickness was 1.85.

For the purpose of investigating the influence of humidity on the evaporated films, the films were stored in humidity- and temperature-controlled air at different conditions (Nagano Kagakukikai, Model NEW LH-20).

Electrochemical measurements.—Complex plane analyses were made using a pseudo-three-electrode configuration. The working electrode was the WO_3/SnO_2 electrode, in which the WO_3 film thickness and area were 3000Å and 0.3 cm^2, respectively. In order to avoid interference arising from the SnO_2/electrolyte interface, the SnO_2 elec-

trode surface was coated by a thin glass-plate insulator exposing only a part of the WO_3 film (0.3 cm^2). The counterelectrode was a carbon electrode plate having a large surface area (the specific surface area of the carbon was 220 m^2/g). The potential drift of the electrode during the measurements was negligibly small ($\Delta V < 1$ mV), so that the counter and reference electrode leads were combined (hence, pseudo-three electrode). The potential of the counterelectrode was monitored by a saturated calomel electrode (SCE).

The electrolytes were propylene carbonate (PC) solutions containing 0.3*M* $LiClO_4$ and 0.03*M* $LiBF_4$. PC (Wako Junyaku) was freshly distilled under vacuum. $LiClO_4$ (purity 99%, Mitsuwa Kagaku) and $LiBF_4$ (purity > 98%, Morita Kagaku) were used. Ar gas was bubbled before measurements.

Frequency response analysis was performed with the working electrode held at constant voltage by an electrochemical interface (Solartron Model 1186, England). A small alternating signal from a frequency response analyzer (Solartron Model 1170) was then superimposed on the constant voltage.

The amplitude of the signal which was applied to the sample was always 5 mV, and the frequency range covered extended from 100 kHz down to 100 mHz. Output data were the average values of ten sampling times and were plotted through a plotter interface (Solartron Model 1180).

Cyclic voltammetry measurements were performed with a potentiostat (Hokuto Denko, Model HA-301), which was supplied with voltage from a function generator (same company, Model HB-104). The counterelectrode was a Pt plate and the reference a SCE. The electrolyte was the same as the electrolyte used for complex plane measurements.

H_2O content of the electrolytes was checked in each case by an aquacounter (Hiranuma Seisakusho, Model AQ-3B). The concentrations were typically 0.03-0.05*M*.

Results and Discussions

Complex impedances of the WO_3 (3000Å thick) film on SnO_2 stored in air at 25°C for 1h after the evaporation were measured under various applied voltages, as shown in Fig. 1 and 2.

Figure 1 shows the complex impedance data under conditions of working electrode potentials from +500 to +300 mV *vs.* SCE, and counterelectrode potential constant at +370 mV *vs.* SCE. Figure 2 shows the complex impedance data for more negative working electrode potentials between +250 and −200 mV *vs.* SCE. In Fig. 1 and Fig. 2, the first semicircle was observed from 100 down to 1 kHz. It became small at more negative potentials of the working electrode and too small to be recognized at potentials more negative than +100 mV *vs.* SCE. The second semicircle was observed clearly from 1 kHz down to 3 Hz at potentials more negative than +400 mV and corresponds to a charge-transfer-controlled process. The second one also became small with more negative potential conditions.

The impedance plots for frequencies lower than 3 Hz approached a line parallel to the imaginary axis and were therefore assigned to finite diffusion control rather than a semi-infinite diffusion-controlled process.

These impedance results can be represented, as a rule, by the circuit of Fig. 3 (21-25). In Fig. 3, R_1 is the uncompensated ohmic resistance of the electrolyte and electrode. C_1 and θ_1 are the capacitance and the resistance associated with the first semicircle, respectively. C_2 and θ_2 are the capacitance and the charge-transfer resistance, respectively, associated with the second semicircle, and Zw is a complex impedance arising from the diffusion of the electroactive species, associated with the straight line for lower frequencies.

Furthermore, θ_1 can be obtained from the following equation

$$\left(R - R_1 - \frac{\theta_1}{2}\right)^2 + X^2 = \left(\frac{\theta_1}{2}\right)^2 \qquad [1]$$

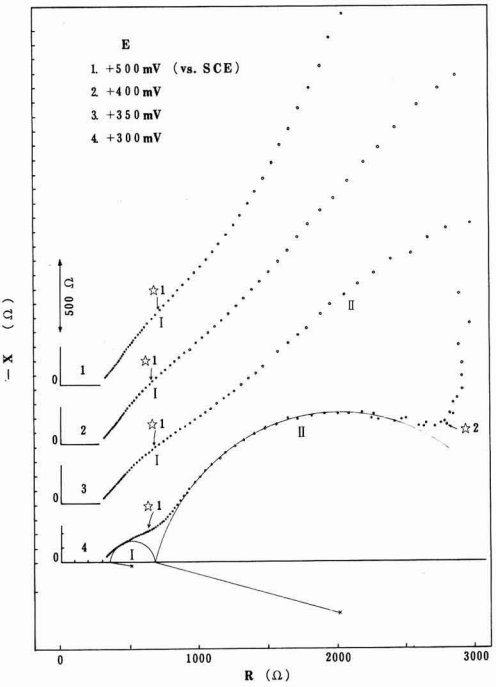


Fig. 1. Complex impedance data of the WO_3 film (3000Å thick, 0.3 cm^2) stored in air at 25°C for 1h. I is the first semicircle, and II is the second semicircle. *1 and *2 are 1.1 kHz and 3.5 Hz, respectively.

where R and X are the real and imaginary parts of the complex impedance, respectively.

C_1 can be obtained from the following equation

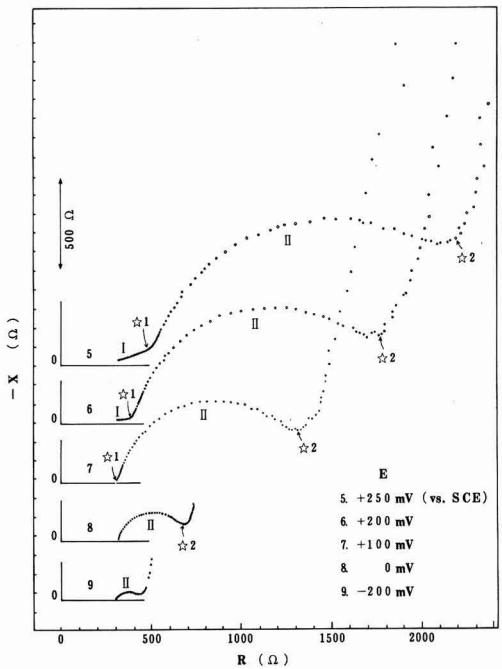


Fig. 2. Complex impedance data of the same sample as shown in Fig. 1.

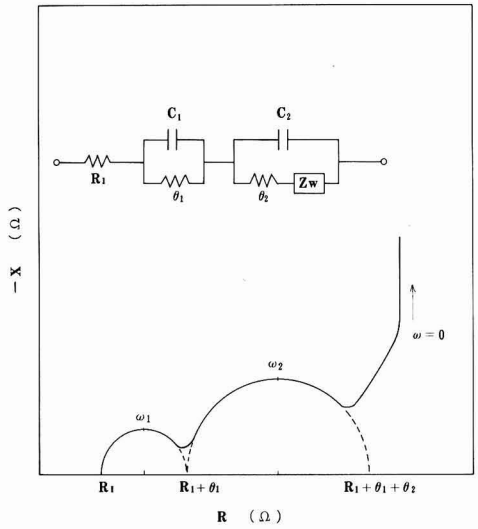


Fig. 3. Admittance plots for the circuit containing two R-C circuits and a finite diffusion-controlled process.

$$C_1 = \frac{1}{\theta_1 \omega_1} \quad [2]$$

where ω_1 is the radial frequency corresponding to the top of the first semicircle.

θ_2 can be obtained from

$$\left(R - R'_1 - \frac{\theta_2}{2}\right)^2 + X^2 = \left(\frac{\theta_2}{2}\right)^2 \quad [3]$$

where $R'_1 = R_1 + \theta_1$.

C_2 can be obtained from

$$C_2 = \frac{1}{\theta_2 \omega_2} \quad [4]$$

where ω_2 is the radial frequency corresponding to the top of the second semicircle.

The equivalent circuit shown in Fig. 3 is independent of the counterelectrode, because the counterelectrode was a large surface carbon electrode having a large double layer capacity (more than 1 mF). Thus, the complex impedance is determined by the reaction processes on the WO_3 electrode only. R_1 was about 290Ω, and was independent of the electrode potential.

In order to clarify the properties of the two semicircles, complex impedances of various WO_3 films having different thickness (500-5000Å) were measured. R_1 and θ values for each semicircle were calculated using a computer method in which three ideal plots for the semicircle were chosen and Eq. [1] and/or [3] were used. R_1 was 270 ± 30Ω and was independent of the thickness of the WO_3 films. The θ values for films of various thickness are shown in Fig. 4 and 5 as a function of the WO_3 electrode potential. In Fig. 4, the θ_1 values, corresponding to the first semicircle observed from 100 kHz down to 1 kHz, increase with the potential of the WO_3 electrode. The θ_1 value of 5000Å thickness WO_3 film was not obtained because of unstable plots.

The θ_1 values were independent of the WO_3 film thickness between 500 and 3000Å, so that θ_1 can be assigned to the charge-transfer impedance at the SnO_2 electrode/WO_3 interface or the WO_3/electrolyte interface, but not to a bulk property.

We consider the following four points: (*i*) the coloration of WO_3 is caused by the double injection of electrons from the electrode and cations from the electrolyte (3), and not caused by an electrochemical reaction such as a reaction W = 0 to W-O-H at the WO_3/electrolyte interface; (*ii*) the first semicircle is found at high frequency (1 kHz to 100 kHz); (*iii*) the interface of the WO_3/electrolyte is not a flat plane, but a porous xerogel structure (12), so that the interface taking part in the cation injection process will increase with the WO_3 film thickness; and (*iv*) the small capacitance can exist at the electrode/WO_3 interface in which WO_3 was evaporated as grains on the electrode surface (25) because of the following two reasons: the energy level of the conduction band of n-SnO_2 does not overlap the level of n-WO_3, and, strictly speaking, the contact of n-SnO_2/n-WO_3 may not be an ohmic contact; electron transfer from the SnO_2 electrode to the WO_3 layer may be slightly blocked at grain boundaries of WO_3 (25). There-

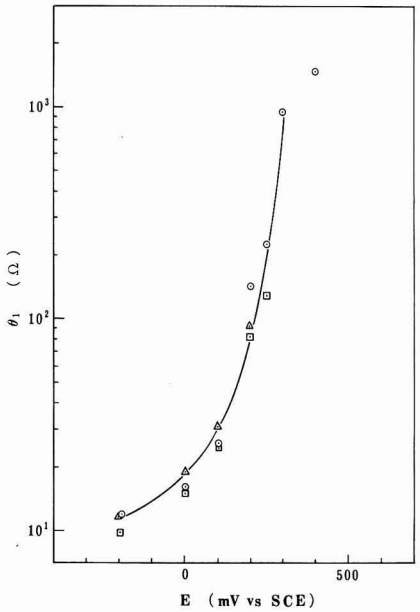


Fig. 4. Potential dependence of the resistance (θ_1) corresponding to the first semicircle (I). The thickness of the WO_3 films (0.3 cm²) are 500 (△), 1000 (□), and 3000Å (○).

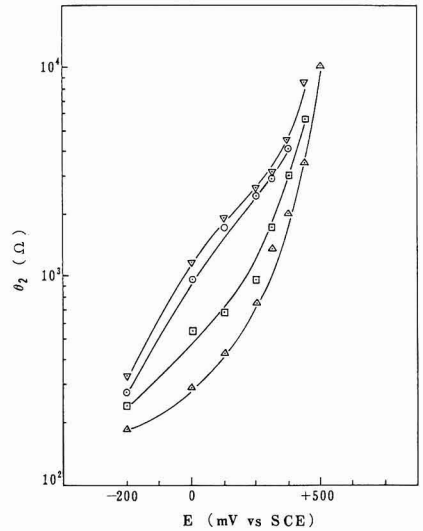


Fig. 5. Potential dependence of the resistance (θ_2) corresponding to the second semicircle (II). The thickness of the WO_3 films (0.3 cm²) are 500 (△), 1000 (□), 3000 (○), and 5000Å (▽).

fore, it may be reasonable to say that the first semicircle results from a circuit involving the capacitance (C_1) and the resistance (θ_1) corresponding to the electron injection process at the electrode/WO_3 interface.

In Fig. 5, the θ_2, corresponding to the second semicircle observed from 1 kHz down to 3 Hz, increases with the potential of the WO_3 electrode and increases with film thickness. However, the injection of cations into the WO_3 film would not only occur at the WO_3 surface interface, but also occur at voids in the porous WO_3 film (12). Then the semicircle corresponding to the cation injection process would be dependent on the WO_3 film thickness.

Therefore, θ_2 would be the charge-transfer impedance corresponding to an electrochemical reaction process such as the cation injection.

Various $WO_3 \cdot x(H_2O)$.—We prepared the following four kinds of $WO_3 \cdot x(H_2O)$ films after evaporation on SnO_2 electrodes: (*i*) as-deposited WO_3 film containing small amount of H_2O; (*ii*) $WO_3 \cdot x(H_2O)$ film containing much physisorbed water by storing in air at 25°C 50% (relative humidity) for 16h (14); (*iii*) hydroxylated $WO_3 \cdot x(H_2O)$ film having many OH groups by storing in air at 25°C 50% (RH) for 168h (14); and (*iv*) hydrated $WO_3 \cdot x(H_2O)$ film having $WO_3 \cdot H_2O$ and/or $H_2WO_4 \cdot H_2O$ crystal structures by storing in air at 40°C 95% (RH) for 24h (15).

Cyclic voltammograms of these $WO_3 \cdot x(H_2O)$ films were measured in PC electrolyte and are shown in Fig. 6. The cathodic current is associated with coloration of the film and the anodic current is associated with bleaching. $WO_3 \cdot x(H_2O)$ films containing much physisorbed water have a fast electrochromism (EC) and both hydroxylated $WO_3 \cdot x(H_2O)$ films and hydrated $WO_3 \cdot x(H_2O)$ films having crystal structures lose EC activity. We earlier discussed these properties in more detail (14, 15).

Complex impedances of these films were measured at various working electrode potentials. Both C_1 and C_2 values were calculated by Eq. [2] or [4] and are shown in Fig. 7. The capacitance of the WO_3 thin film bulk layer (C_2) was several μF, which was about 30 times the magnitude of the capacitance (C_1) of the electrode/WO_3 interface. The θ values of each process were calculated and are shown in Fig. 8 and 9.

Compositions (x) of M_xWO_3 bronze ($M:H^+$ or Li^+) under the various working electrode potentials were calculated from the injected charge and are shown in Fig. 10 as a function of the electrode potential. Both θ_1 and θ_2 are represented as a function of composition (x) in Fig. 11.

From these results, we conclude first concerning the fast electron injection process at the electrode/WO_3 interfaces that (*i*) the interface of an as-deposited film may be in a nonequilibrium state, thus giving rise to unstable complex impedances; (*ii*) the impedance decreases to one-half with an increase of physisorbed water in the WO_3 film and doubles with hydroxylation of the film and is relatively insensitive to hydrated crystallization; (*iii*) there is a linear relationship between the impedance and the composition, x, of M_xWO_3 bronze; and (*iv*) the capacitance is about 10^{-7} F and not strongly dependent on the condition of water in the $WO_3 \cdot x(H_2O)$.

Second, concerning the charge-transfer process such as the cation injection process in the WO_3 film: (*i*) the as-deposited film is unstable; (*ii*) the electrochemical charge

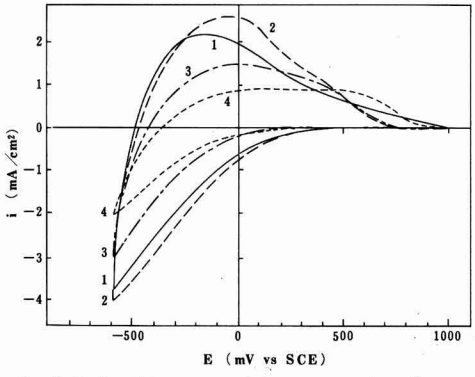


Fig. 6. Cyclic voltammograms of the WO_3 films (3000Å thick, 0.3 cm²). Scan rate: 200 mV/s. 1: As-deposited film. 2: WO_3 containing physisorbed water. 3: Hydoxylated film. 4: Hydrated film.

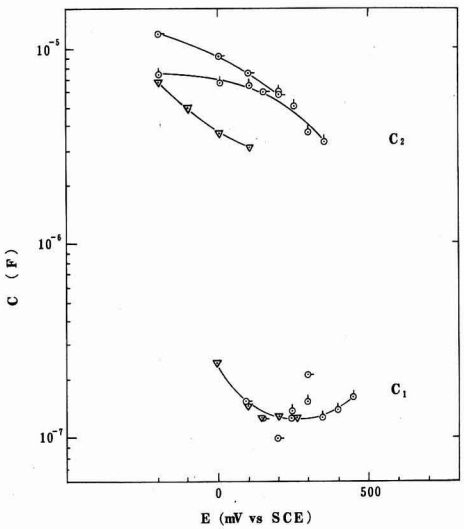


Fig. 7. Potential dependences of the equivalent circuit capacitances. WO_3 films (3000Å, 0.3 cm²) are the film containing physisorbed water (Ⓘ), the hydroxylated film (⊖), and the hydrated film (▽).

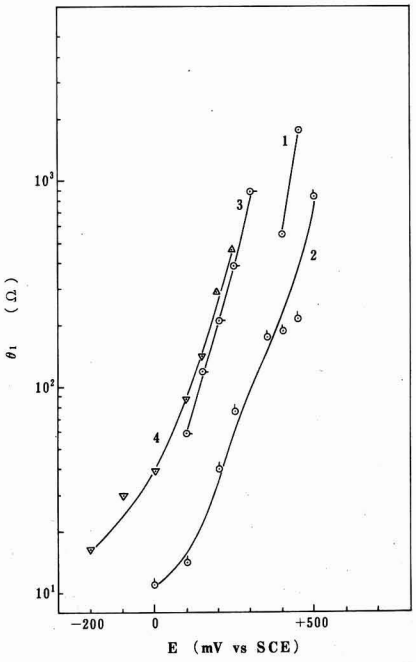


Fig. 8. Potential dependences of θ_1. 1: As-deposited WO_3 film (○). 2: WO_3 film (3000Å, 0.3 cm²) containing physisorbed water (Ⓘ). 3: Hydroxylated film (⊖). 4: Hydrated film (▽).

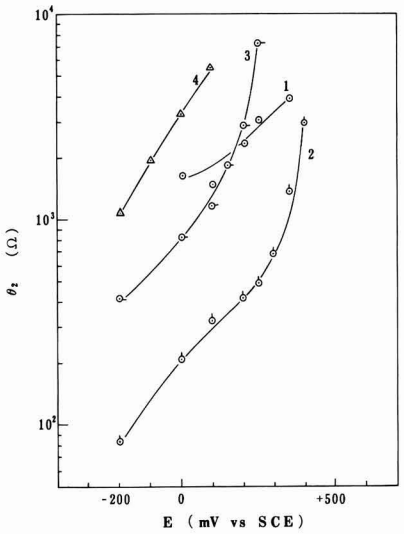


Fig. 9. Potential dependences of θ_2. Sample numbers represent the same samples shown in Fig. 8.

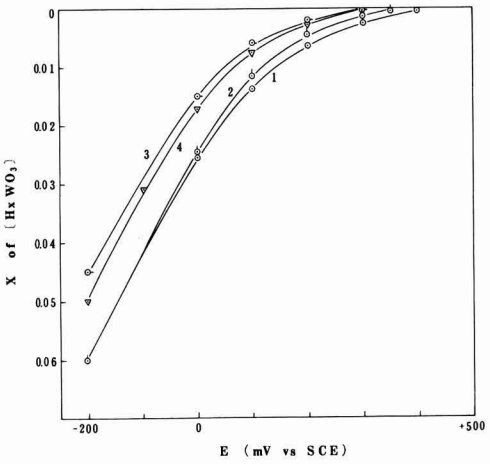


Fig. 10. Coulometric titration curve for M_xWO_3. Sample numbers represent the same samples shown in Fig. 8.

transfer impedance in the film is about one order of magnitude larger than the electron injection impedance; and (*iii*) it decreases to about one-sixth to one-seventh with an increase of physisorbed water and increases about three times with hydroxylation of the film and about ten times with hydration. θ_2 values for four kinds of $WO_3 \cdot x(H_2O)$ films, in case of a composition $x = 0.01$ of M_xWO_3 bronze, are tabulated in Table I.

Conclusion

The coloration reaction process was separated into three processes using complex plane analysis; the electron injection process at the electrode/WO_3 interface having the double layer capacitance (10^{-7}F) (100 kHz > f > 1 kHz), the electrochemical charge transfer through the cation-injection process in the WO_3 film having an impedance one order of magnitude larger than the electron injection impedance (1 kHz > f > 3 Hz), and a slow diffusion-controlled process in the bulk (f < 3 Hz).

Remarkably, the fast electron injection process at the interface is not influenced by the condition of the water incorporation in the WO_3 films, but the electrochemical charge-transfer process in the WO_3 film clearly is. The electrochemical charge-transfer process in the WO_3 is the most important process in determining EC reaction speed for display devices.

Table I. θ_2 values in case of a composition $x = 0.01$ of M_xWO_3 bronze

	$WO_3 \cdot x(H_2O)$	θ_2 (Ω)
1	As-deposited film	1.6×10^3
2	Containing physisorbed water	4×10^2
3	Hydroxylated film	9×10^2
4	Hydrated film	4.5×10^3

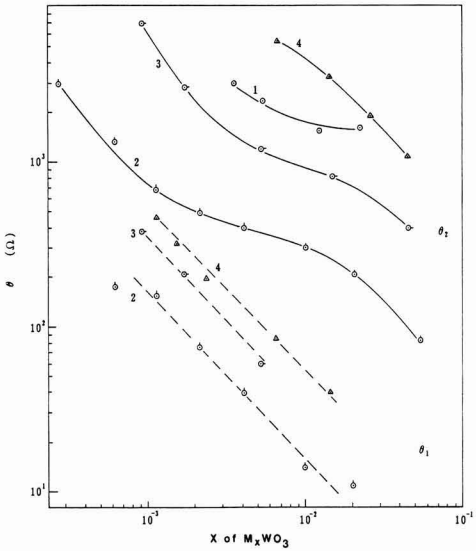


Fig. 11. Composition dependences of θ_1 and θ_2. Sample numbers represent the same samples shown in Fig. 8.

Acknowledgments

The authors thank Dr. E. Hirota, the assistant director of Central Research Laboratory, for support in this work and Dr. S. Sekido for helpful discussions.

Manuscript submitted Dec. 21, 1983; revised manuscript received June 25, 1984.

Matsushita Electrical Industrial Company, Limited assisted in meeting the publication costs of this article.

REFERENCES

1. S. K. Deb, *Appl. Opt. Suppl.*, **3,** 192 (1969).
2. C. J. Schoot, J. J. Ponjee, H. T. Van dam, R. A. Van doorn, and P. T. Bolwijn, *Appl. Phys. Lett.*, **23,** 64 (1973).
3. B. W. Faughnan, R. S. Crandall, and P. M. Heyman, *RCA Rev.*, **36,** 177 (1975).
4. J. D. E. McIntyre, G. Beni, and J. L. Shay, Abstract of the 20th EMC, Santa Barbara, 1978.
5. M. M. Nicholson and R. V. Galiardi, SID 1978 Digest, p. 24.
6. N. Yoshiike, S. Kondo, and M. Fukai, *This Journal*, **127,** 1496 (1980).
7. R. Hurditch, *Electron. Lett.*, **11,** 142 (1975).
8. H. R. Zeller and H. V. Beyeller, *Appl. Phys.*, **13,** 231 (1977).
9. B. Reichman and A. J. Bard, *This Journal*, **126,** 583 (1979).
10. A. Deneuville, P. Gerard, and P. Billat, *Thin Solid Films*, **70,** 203 (1980).
11. Y. Hajimoto, M. Matsushita, and S. Ogura, *J. Electron. Mater.*, **8,** 301 (1979).
12. L. Pickelman and P. Schlotter, Eurodisplay '81, München, FRG, Sept. 16-18, 1981.

13. T. C. Arnoldussen, *This Journal*, **128**, 117 (1981).
14. N. Yoshiike and S. Kondo, *ibid.*, **130**, 2283 (1983).
15. N. Yoshiike and S. Kondo, *ibid.*, **131**, 809 (1984).
16. R. S. Crandall and B. W. Faughnan, *Appl. Phys. Lett.*, **28**, 95 (1976).
17. B. W. Faughnan, R. S. Crandall, and M. A. Lampert, *ibid.*, **27**, 275 (1975).
18. S. K. Mohapatra, *This Journal*, **125**, 284 (1978).
19. M. Green, *Thin Solid Films*, **50**, 145 (1978).
20. M. Green, W. C. Smith, and J. A. Weiner, *ibid.*, **38**, 89 (1976).
21. C. Ho, I. D. Raistrick, and R. A. Huggins, *This Journal*, **127**, 343 (1980).
22. J. E. B. Randles, *Discuss. Faraday Soc.*, **1**, 11 (1947).
23. J. E. Bauerle, *J. Phys. Chem. Solids*, **30**, 2657 (1969).
24. S. Haruyama, *Denki Kagaku*, **39**, 536 (1971); *ibid.*, **39**, 658 (1971).
25. T. Takahashi, H. Iwahara, and Y. Suzuki, *ibid.*, **39**, 665 (1971).

Technical Notes

The Decomposition of Propylene Carbonate in a Lithium/Metal Phthalocyanine Cell

M. Arakawa, J. Yamaki,* and T. Okada

Nippon Telegraph and Telephone Public Corporation, Ibaraki Electrical Communication Laboratory, Tokai, Ibaraki-ken, 319-11, Japan

Recently, considerable attention has been focused on batteries composed of lithium anodes, cathodes, and organic electrolytes. This has been particularly true of lithium secondary batteries employing topochemical reactions (1-3).

We have reported on metal phthalocyanine (MPc) as a cathode active material, and its charge and discharge characteristics (4). Gas evolution, however, was observed in lithium batteries using MPc as the cathode active material. Gas evolution from the graphite electrode in lithium batteries was first reported by Dey *et al.* (5). However, the electrochemical characteristics and the gas evolution reaction mechanism were not clarified sufficiently.

Studies of the effect of MPc on electrocatalysis have been widely carried out for O_2 reduction reactions in aqueous electrolytes (6, 7). The decrease of electrocatalytic activity was reported in the order: Fe > Co > Ni > Cu > H_2 (8). This indicates a significant dependence of the central metal on electrocatalytic activity, though its role is not yet sufficiently understood.

In this paper, we report the catalytic effect of MPc on the gas evolution reaction.

Experimental

The experimental setup is schematically shown in Fig. 1. Test cell was set in the vacuum line and evacuated. A constant current discharge and stepwise potentiostatic discharge were then carried out, using a constant current and a constant voltage source (Hokuto Denko Company). The volume of gas evolved during the discharge test was measured using the oil manometer of the vacuum line, and its components were identified with a mass spectrometer.

The test cell was composed of a lithium anode, a cathode, and a reference electrode as shown in Fig. 2. The cathode was made up of MPc (M = H_2, Li_2, Na_2, CrF, Mn, Fe, Co, Cu, GaCl, Ag, Cd) (Eastman Kodak Company), carbon powder (Akzo Corporation, Ketjenblack EC), and polytetrafluoroethylene (PTFE, Daikin Kogyo Company Limited, F103). The mixing ratio of MPc, carbon powder, and PTFE was 49, 48, and 3 weight percent (w/o), respectively. The mixture (0.05g) was pressed at 30 kg/cm^2 to form a 13 mm diam disk. The lithium electrode was 13 mm diam and 0.24 mm thick disk. Lithium metal was also used for the reference electrode. Propylene carbonate (PC) containing 1*M* $LiClO_4$ (Tomiyama Pure Chemical Industries Limited) was used as the organic electrolyte. Water content was less than 20 ppm. All test cells were constructed in a dry box filled with dry argon gas.

Results and Discussion

Discharge tests were carried out galvanostatically at 3 mA for cathodes containing several kinds of MPc. Gas evolution volume during discharge down to 0.5V is summarized in Table I. A typical gas evolution curve is shown in

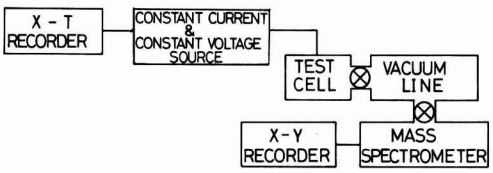


Fig. 1. Block diagram of gas evolution measurement system

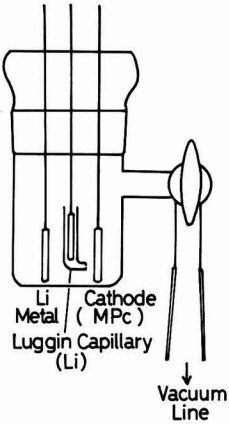


Fig. 2. Cell for gas evolution measurement.

* Electrochemical Society Active Member.

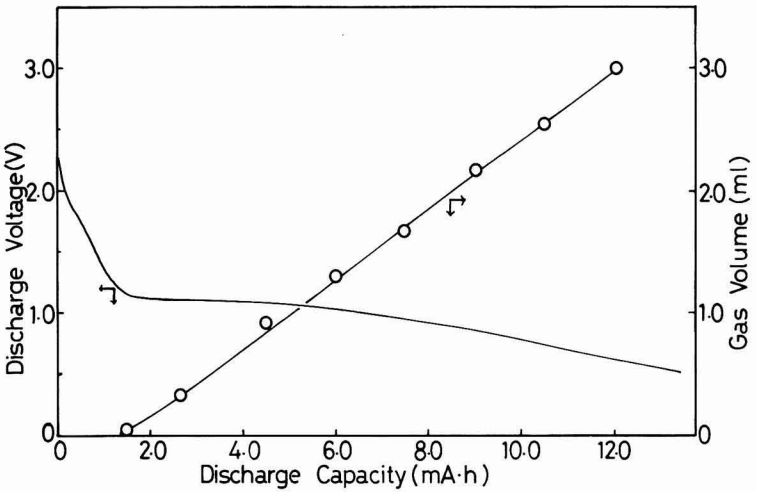


Fig. 3. A typical gas evolution characteristic in Li/MPc cell. M = Fe, 3 mA constant current discharge.

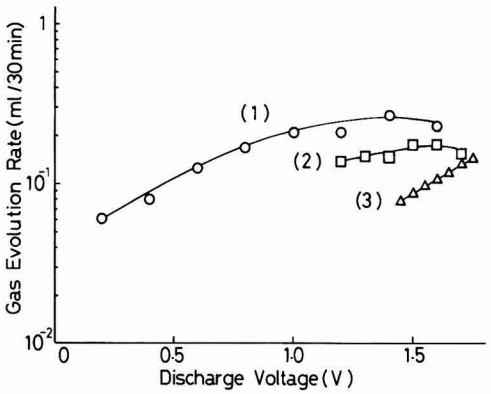


Fig. 4. Dependence of gas evolution rate on discharge voltage in Li/FePc cell with 1M $LiClO_4$/PC. (1): 0.2V stepwise discharge. (2): 0.1V stepwise discharge. (3): 0.05V stepwise discharge.

Fig. 3. The principal component of the evolved gas was identified as propylene from mass peaks (m/e = 39, 41, and 42). In the cells containing FePc, CoPc, or MnPc, the evolved gas volume was very large. The effect of carbon on gas evolution cannot be neglected in the low voltage region. However, under the conditions reported here, the contribution from the carbon is estimated from the blank test to be less than 0.30 ml. A detailed study of the effect of carbon is now being carried out.

Table I. Gas evolution characteristics of various MPc's

MPc	Gas volume (V_g)* (ml)	Ratio (R)** (%)	Discharge capacity (Q_d) (mA · h)	Net capacity (mA · h)
H_2Pc	0.19	5.05	9.0	8.55
Na_2Pc	0.08	4.25	4.5	4.31
Li_2Pc	0.02	0.90	5.3	5.25
CrFPc	0.58	15.88	8.7	7.31
MnPc	1.27	24.70	11.1	8.36
FePc	3.15	55.42	13.6	6.06
CoPc	1.75	46.50	9.0	4.82
NiPc	0.85	20.41	10.0	7.96
CuPc	0.12	4.42	6.5	6.21
GaClPc	0.03	0.89	3.5	3.47
AgPc	0.64	11.89	12.8	11.28
CdPc	0.04	0.89	5.3	5.25

* V_g is converted into the volume at 0°C, 1 atm.
** R is derived from Eq. [3].

A lithium cell containing FePc (Li/FePc) was employed to investigate the gas evolution reaction more closely. Stepwise potentiostatic discharge (0.05, 0.1, and 0.2V, respectively) was carried out at intervals of 30 min. The results are shown in Fig. 4. A simple relation was not observed between the gas evolution rate and discharge voltage. The rate varied according to the changes in the constant voltage step width. Namely, the gas evolution rate depends on not only the cathode voltage, but also the discharge condition. This indicates the electrochemical charge transfer process is not the rate-determining step for the gas evolution reaction.

This view is supported by the results of discharge tests performed galvanostatically at 1, 3, and 6 mA for Li/FePc cells. The evolved gas volume was plotted against discharge capacity (Fig. 5). The gas volume was proportional to the discharge capacity and independent of discharge current. This indicates that the rate-determining step of the gas evolution reaction is a reaction product formation process. The electrochemical reaction product ($FePcLi_r$) from FePc and Li^+ may react chemically with PC and produce gas (Eq. [1] and [2])

$$MPcLi_r + 2Li^+ + 2e^- \rightarrow MPcLi_{r+2} \quad [1]$$

$$MPcLi_{r+2} + C_3H_6CO_3 \rightarrow MPcLi_r + C_3H_6 + 2Li^+ + CO_3^{2-} \quad [2]$$

This was confirmed by adding PC to the $FePcLi_r$, which was formed by the reaction of FePc with n-butyl lithium.

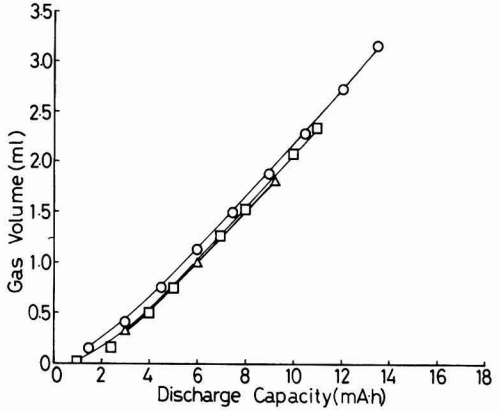


Fig. 5. Dependence of evolved gas volume on discharge capacity. □: 1 mA constant current discharge (CCD). ○: 3 mA CCD. △: 6 mA CCD.

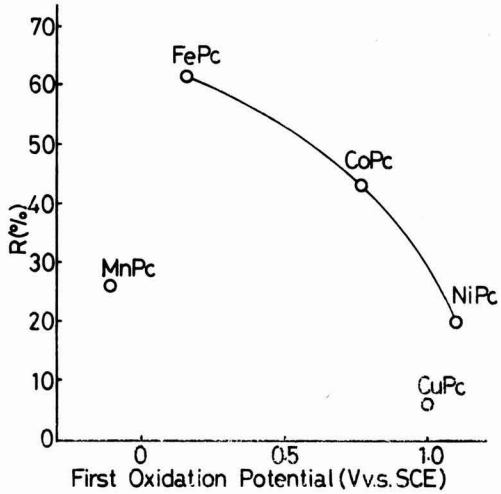


Fig. 6. Gas evolution ratio (R) derived from Eq. [3] plotted against the first oxidation potential of MPc taken from Ref. (9).

PC was added, and it immediately reacted to generate propylene gas.

Based on these results, the activity of $MPcLi_x$ was estimated using the ratio (R) given by Eq. [3]. R means the ratio of the quantity of electricity for gas evolution to discharge capacity

$$R = \frac{2 \times 26.8\ V_g/22.4}{Q_d} \qquad [3]$$

where V_g and Q_d represent gas volume and discharge capacity, respectively. The ratios for several MPc are shown in Table I. Remarkable activity is observed for FePc and CoPc.

Gas evolution ratios (R) were plotted against the first oxidation potentials of MPc (Fig. 6). The data reported by Manassen and Bar-Ilan were used for first oxidation potential values of the various MPc's (9). The relation shows that group VIII central metal MPc's have higher gas evolution activity than the other group. However, the reason for this activity difference has not been investigated in this work. Within the same group, the gas evolution activity increased with a decrease of oxidation potential. This may indicate that the order of the first oxidation potential of $MPcLi_x$ is similar to that of MPc, and that the reactivity of reaction represented by Eq. [2] depends on the first oxidation potential of $MPcLi_x$; that is, the reaction (Eq. [2]) proceeds more easily when the charge transfer from $MPcLi_x$ to PC occurs more easily.

Conclusion

Gas evolution from the phthalocyanine electrode in lithium batteries was observed. During the discharge tests, the evolved gas volume was proportional to the discharge capacity. The principle component of the gas was identified as propylene. The activity of MPc was estimated based on discharge capacity. The activity decreased in the order of FePc > CoPc > MnPc > NiPc > CrFPc > AgPc. H_2Pc, Li_2Pc, Na_2Pc, GaClPc, and CdPc did not have much activity. Propylene gas is probably generated by the chemical reaction between PC and the discharge product of phthalocyanine.

Manuscript submitted April 30, 1984; revised manuscript received *ca.* June 13, 1984.

Nippon Telegraph and Telephone Public Corporation assisted in meeting the publication costs of this article.

REFERENCES

1. B. Scrosati, *Electrochim. Acta*, **26**, 1559 (1981).
2. K. M. Abraham, *J. Power Sources*, **7**, 1 (1981).
3. K. M. Abraham, P. B. Harris, and D. L. Natwig, *This Journal*, **130**, 2309 (1983).
4. J. Yamaki and A. Yamaji, *ibid.*, **129**, 5 (1982).
5. A. N. Dey and B. P. Sullivan, *ibid.*, **117**, 222 (1970).
6. M. Savy, P. Andro, C. Bernard, and G. Magner, *Electrochim. Acta*, **18**, 191 (1973).
7. J. Zagal, P. Bindra, and E. Yeager, *This Journal*, **127**, 1506 (1980).
8. J. P. Randin, *Electrochim. Acta*, **19**, 83 (1973).
9. J. Manassen and A. Bar-Ilan, *J. Catal.*, **17**, 86 (1970).

Electronic Conductivity Decrease in Porous NiO Cathodes during Operation in Molten Carbonate Fuel Cells

Charles E. Baumgartner*

General Electric Company, Corporate Research and Development, Schenectady, New York 12301

The electronic conductivity of nascent and doped NiO has been extensively examined over the past several decades (1-16). Stoichiometric NiO is an insulator at room temperature with a specific resistivity of $\sim 10^{13}$ Ω cm (1, 5). The introduction of monovalent ions, such as lithium, into the NiO lattice on Ni lattice sites can decrease the room temperature resistivity by as much as 13 orders of magnitude. This pronounced effect was first explained by Verwey *et al.* (1-3), who postulated that coincident with the incorporation of each Li^+ ion was the formation of a trivalent nickel ion (Ni^{+3}) located on a Ni^{+2} lattice site, thereby reserving the overall crystal charge neutrality. The observed conductivity enhancement results from the mixed valency of nickel atoms located on equivalent, adjacent lattice sites. Following this mechanism, it was postulated, and later proven by Verwey (3), that doping NiO with equimolar concentrations of both a monovalent and a foreign trivalent species would yield an electronic conductivity resembling undoped NiO. This result has been subsequently demonstrated by other authors (6, 15) and is, in part, responsible for the differences in absolute Li-doped NiO conductivity values found in the literature. A recent review by Jarzebski (17) historically details the published NiO electronic conductivity data.

A state-of-the-art molten carbonate fuel cell (MCFC) utilizes a porous Li-doped NiO cathode. The structure is typically prepared by the oxidation of a porous nickel plaque *in situ* to the fuel cell cathode compartment, the lithium dopant originating from the Li_2CO_3:K_2CO_3 electrolyte. The resulting porous structure, containing an equilibrium Li concentration of approximately 0.02 cation fraction, possesses a 923 K (MCFC operating temperature) specific conductivity of $\sim 2\ (\Omega\ cm)^{-1}$. In most present fuel cell designs, the cathode is in intimate contact with a ribbed stainless steel current collector which, during cell operation, oxidizes to form a scale containing predominantly Fe_2O_3, $LiFeO_2$, Li_2CrO_4, and K_2CrO_4. The chromates

* Electrochemical Society Active Member.

are highly soluble in the molten alkali carbonate electrolyte and therefore dissolve from the cathode/current collector interface to leave behind a predominately iron oxide scale. The incorporation of either Fe^{+3} or Cr^{+3} into the NiO structure, from either the current collector or its dissolved corrosion products, would be expected to significantly decrease the cathode's electronic conductivity and thereby increase, with time, the voltage drop associated with cell operation.

This communication quantifies the specific conductivity penalty associated with Fe^{+3} addition to 0.02 cation fraction Li-doped NiO samples (*i.e.*, $Li_{0.02}Fe_xNi_{0.98-x}O$) and estimates this mechanism's impact on MCFC performance from Fe and Cr analysis of post-cell-tested NiO cathodes.

Experimental

Fe_2O_3-doped $Li_{0.02}Ni_{0.98}O$ powders were prepared by the thermal decomposition (823 K) of reagent-grade $FeOH(C_2H_3O_2)_2$, $Li(C_2H_3O_2) \cdot H_2O$, and $NiCO_3$ powders which were previously well mixed in an acetone/acetic acid vehicle. Following decomposition, samples were air fired for 10h at 1023 K and washed in dilute acetic acid to remove nonincorporated Li salts. Elemental analysis was performed by atomic absorption spectroscopy, and the Ni^{+3} content obtained independently using the method described by Goodenough *et al.* (18).

Electronic conductivity measurements were made using a standard four-probe, ac impedance technique on pressed, sintered pellets using the apparatus diagrammed in Fig. 1. The pellets, 1.25 cm diam × ~0.6 cm thick, were prepared by pressing the powders at ~120 MPa and sintering under a blanket of powder of the same composition in air at 1325 K for 1h. Chemical analysis showed the pellets' composition to be unchanged by sintering. Following sintering, the faces of the pellets were polished smooth, sputtered with ~1 μm gold, and two gold wires were attached to each face using silver paint (du Pont conductor composition 4922). The samples, supported using alumina holders (not shown in Fig. 1) and contained within an alumina tube furnace under a 30% CO_2/air atmosphere, were heated to 823 K overnight to cure the silver paint. Sample conductivities were obtained as a function of signal frequency (50-20,000 Hz) during both heating (823-1123 K) and cooling (1123 K to ambient) cycles using a PAR 5204 Lock-In Analyzer coupled to a PAR 371 Signal Source (Princeton Applied Research, Princeton, New Jersey).

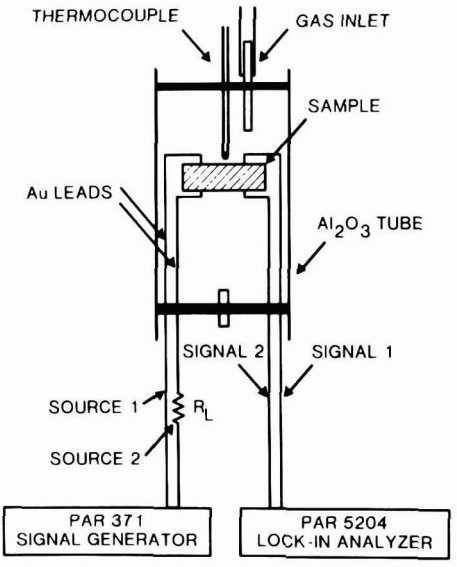


Fig. 1. Four-probe ac impedance measurement apparatus

Post-cell-tested NiO cathodes were obtained from MCFC's operated at 923 K for times between 50-10,080 h.[1] All cells were assembled using a Ni (10 weight percent [w/o] Cr) anode, a hot-pressed $LiAlO_2/Li_2CO_3/K_2CO_3$ electrolyte structure, and a porous nickel cathode. The cathode oxidized during heat-up to the 923 K cell operating temperature to form a porous NiO structure; lithium incorporated into the NiO lattice from the Li_2CO_3 containing electrolyte gave a final cathode composition of 0.02 ± 0.002 cation fraction Li (*i.e.*, $Li_{0.02}Ni_{0.98}O$). Cathode current collectors were fabricated using 316 stainless steel in all cases.

Cathodes, obtained following cell testing, were thoroughly freed of Li_2CO_3 + K_2CO_3 electrolyte by washing with 50% aqueous acetic acid under a vacuum of ~10^{-2} torr. The cathodes were then sectioned according to their structural location within the cell and analyzed for Fe and Cr by Auger electron spectroscopy (Physical Electronics Industries Model 548 ESCA/Auger spectrometer).

Results and Discussion

The composition of prepared Fe^{+3}-doped $Li_{0.02}Ni_{0.98}O$ samples (*i.e.*, $Li_{0.02}Fe_xNi_{0.98-x}O$) are given in Table I. Total Fe, Ni, and Li concentrations were obtained by atomic absorption spectroscopy, and the Ni^{+3} content obtained titrimetrically using the method of Goodenough *et al.* (18). Lithium concentrations were maintained at 0.02 cation fraction while iron was varied between 0.00 and 0.02 cation fraction. Samples prepared with Fe concentrations exceeding ~0.015 cation fraction possessed a Ni^{+3} concentration below the quantitative detection limit; however, it is apparent from the results presented in the table that Fe enters the NiO lattice as Fe^{+3}, thereby quantitatively reducing the Ni^{+3} concentration. This is in agreement with Verwey and others (1, 3, 12, 15).

The specific conductivity measured at 1 kHz as a function of temperature for the various samples is shown in Fig. 2. Frequencies between 50 and 20,000 Hz were scanned at each temperature with less than 2% frequency dependence observed, confirming that the measured values were indeed the samples' bulk conductivity. The measured 923 K specific conductivity at 1 kHz decreased from 33.0 to 3.5 × 10^{-2} $(\Omega\ cm)^{-1}$ as the Fe^{+3} concentration increased from 0.00 to 0.02 cation fraction. In addition to a decrease in the magnitude of the conductivity, Fe^{+3} addition also resulted in changes to both the nature and the slope of the conductivity/temperature relationship. Prior to Fe^{+3} addition, two activation energies are apparent, with the transition from one to the other occurring at ~625 K. Activation energies of 0.68 and 3.9 kcal/mol obtained at temperatures above and below the transition temperature, respectively, are in reasonable agreement with Nowotny and Wagner's results (15) of 1.56 and 5.4 kcal/mol obtained for a 0.008 cation fraction Li-doped NiO sample.

It is evident from the data presented above that the incorporation of current collector corrosion products (*e.g.*, Fe^{+3}, Cr^{+3}) into the lattice of a Li-doped NiO cathode would impact significantly on fuel cell performance. The measured porous cathode specific conductivity of 2$(\Omega\ cm)^{-1}$ presently leads to a one-dimensional IR loss at a

[1]The 10,080h sample was supplied by the Institute of Gas Technology, Chicago, Illinois.

Table I. Compositional analysis of $Li_{0.02}Fe_xNi_{0.98-x}O$ powders, in cation fraction

[Li]	$[Fe]_{total}$	$[Ni^{+3}]_{theoretical}$	$[Ni^{+3}]_{experimental}$
0.020	0.000	0.020	0.021
0.021	0.006	0.015	0.015
0.020	0.010	0.010	0.010
0.019	0.013	0.006	0.006
0.020	0.014	0.006	0.005
0.020	0.017	0.003	—
0.020	0.019	0.001	—
0.020	0.020	0.000	—

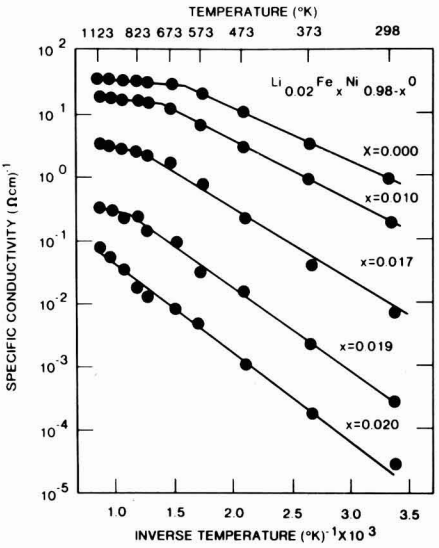


Fig. 2. Temperature dependence of specific conductivity for various compositions of Fe^{+3}, doped $Li_{0.02}Ni_{0.98}O$.

current density of 160 mA/cm² of about 3 mV for the 0.038 cm thick cathode. Conductivity decreases, as determined above for samples doped with 0.02 cation fraction Fe^{+3}, would increase this resistive drop by almost three orders of magnitude if the dopant were uniformly distributed throughout the structure. Both the iron and chromium content of porous NiO cathodes obtained from MCFC's were analyzed via Auger electron spectroscopy (AES) following alkali carbonate removal from the cathode structure by acetic acid washings. Chromates, present in the electrolyte by dissolution of Li_2CrO_4 and K_2CrO_4 corrosion products, are also entirely removed from the porous structure during this washing. Following washing, the cathodes were sectioned into four distinct areas according to their location within the cell. These areas were: region 1, in direct contact with the stainless steel current collector; region 2, adjacent to region 1, in contact with the open gas passage; region 3, located within the body of the cathode; and region 4, in contact with the electrolyte structure.

Nine cathodes were analyzed, encompassing cells operated between 50 and 10,080h. All samples showed similar results in that all regions in direct contact with the current collector (region 1) contained iron within the NiO lattice. No iron was found in regions 2, 3, or 4, and no chromium was observed in any specimen. Chromates were, however, present in the electrolyte of several samples, as noted by the yellow color of the acetic acid wash solutions. Figure 3 displays a typical AES result, Fig. 3A showing the spectrum obtained on region 1 of a cathode on test for 2485h, and Fig. 3B showing the spectrum obtained from region 2 of the same sample. The two spectra are virtually identical with the exception of the iron peak in area 3A. From this spectrum, an iron concentration of between 0.03 and 0.04 cation fraction was estimated; such a concentration is more than sufficient to neutralize the conductivity gain associated with the 0.02 cation fraction Li incorporation. No correlation was found between the observed iron level and the length of cell test.

The cathode AES results, coupled with the previous conductivity determinations, would lead to the prediction that a fairly resistive interface could exist between the cathode and current collector in operating MCFC's. The thickness of this resistive layer was determined for several cathodes from cells operated for various lengths of time by repetitive Auger analysis following argon ion etching. The results obtained on cathodes from cells

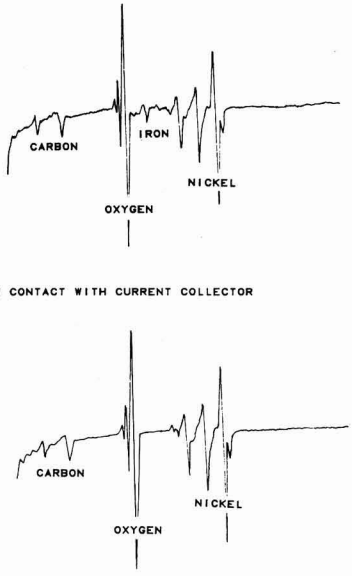


Fig. 3. Auger electron spectra of Li-doped NiO cathode from MCFC operated 2485h. Region 1 was in contact with stainless steel current collector: region 2 was the adjacent location in contact with open gas channel.

tested for 515, 2485, and 10,080h are shown in Fig. 4. All samples possessed initial Fe levels similar to that shown in Fig. 3, and the depth profiles are therefore plotted on a relative ordinate. Whereas the absolute Fe level found at the NiO surface could not be correlated with the duration of cell test, longer cell tests did show a greater Fe penetration depth. However, even after 10,080h on test, iron has penetrated only superficially into the NiO grains, diffusing to a depth of ~10 nm. Therefore, even though Fe^{+3} or Cr^{+3} incorporation into a $Li_{0.02}Ni_{0.98}O$ MCFC cathode

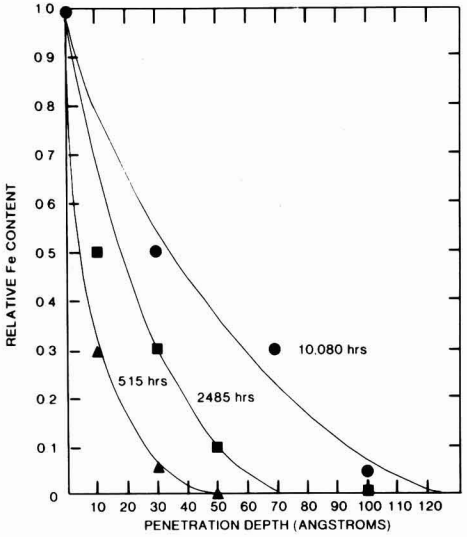


Fig. 4. Fe penetration profiles into the NiO lattice obtained by AES with Ar^+ milling. All samples were cathode regions in direct contact with the stainless steel current collectors.

could dramatically reduce fuel cell performance by decreasing cathode conductivity, such a mechanism apparently plays an insignificant role as neither impurity readily enters the Li-doped NiO cathode structure under experimental fuel cell operating conditions.

Conclusions

The 923 K specific electronic conductivity of 0.02 cation fraction Li-doped NiO ($Li_{0.02}Ni_{0.98}O$) was shown to decrease from 33.0 to 3.5×10^{-2} $(\Omega\ cm)^{-1}$ upon the addition of an equivalent doping level of Fe^{+3}. However, the impact of this conductivity degradation mechanism on the performance of MCFC's containing $Li_{0.02}Ni_{0.98}O$ cathodes was shown to be insignificant from iron and chromium analyses of post-tested cathodes. Although appreciable iron impurity levels were found within the NiO lattice in regions where the cathode contacted the stainless steel current collector, iron penetration into the grains was restricted to a distance of only 10 nm in 10,080h. The results indicate that impurity diffusion into the cathode should have little or no impact on fuel cell performance.

Acknowledgments

The author wishes to acknowledge the assistance of Mr. K. P. Zarnoch for the conductivity measurements. The Department of Energy is acknowledged for its support of this work under contract no. DE-ACO2-80ET17019.

Manuscript submitted May 19, 1983; revised manuscript received May 28, 1984. This was Paper 371 presented at the Montreal, Quebec, Canada, Meeting of the Society, May 9-14, 1982.

General Electric Company assisted in meeting the publication costs of this article.

REFERENCES

1. E. J. W. Verwey, *Chem. Weekblad*, **44**, 705 (1948).
2. E. J. W. Verwey, P. W. Haaijman, F. C. Romeijn, and G. W. van Oosterhout, *Philips Res. Rep.*, **5**, 173 (1950).
3. E. J. W. Verwey, "Semiconducting Materials," pp. 151-161, Butterworths, London (1951).
4. F. J. Morin, *Phys. Rev.*, **83**, 1005 (1951).
5. F. J. Morin, *ibid.*, **93**, 1195, 1199 (1954).
6. W. D. Johnson, *J. Chem. Ed.*, **36**, 605 (1959).
7. S. van Houten, *J. Chem. Phys. Solids*, **17**, 7 (1960).
8. S. Fujime, M. Murakami, and E. Hirahara, *J. Phys. Soc. Jpn.*, **16**, 183 (1961).
9. S. P. Mitoff, *J. Chem. Phys.*, **35**, 882 (1961).
10. A. J. Bosman, H. J. Van Daal, and G. F. Knuvers, *Phys. Lett.*, **19**, 372 (1965).
11. S. Koide, *J. Phys. Soc. Jpn.*, **20**, 123 (1965).
12. A. J. Bosman and C. Crevecoeur, *Phys. Rev.*, **144**, 763 (1966).
13. Ya. M. Ksendzov, B. K. Avdeenko, and V. V. Makarov, *Sov. Phys. Solid State*, **9**, 828 (1967).
14. I. G. Austin, A. J. Springthorpe, B. A. Smith, and C. E. Turner, *Proc. Phys. Soc.*, **90**, 157 (1967).
15. J. Nowotny and J. B. Wagner, Jr., *Bull. Acad. Pol. Sci.*, **21**, 931 (1973).
16. N. G. Eror and J. B. Wagner, Jr., *Phys. Status Solidi*, **35**, 641 (1969).
17. Z. M. Jarzebski, "Oxide Semiconductors," Engl. transl., B. R. Pamplin, Editor, International Series, Monographs in Science and Solid State, Vol. 4, pp. 150-189, Pergamon Press, 1973.
18. J. B. Goodenough, D. G. Wickham, and W. J. Craft, *J. Appl. Phys.*, **23**, 382 (1958).

Improved H_3PO_4 Corrosion Resistance of Graphite/Phenolic Composites Suitable for 190°C Hydrogen/Air Fuel Cells

J. T. Hoggins and M. L. Deviney

Ashland Chemical Company, Ventures Research Division, Dublin, Ohio 43017

Electrocatalyst life, bipolar plate chemical resistance to hot H_3PO_4, and bipolar plate mechanical strength and dimensional stability have been indentified as the major obstacles to the long-term service life of the hydrogen-air fuel cell (1-3). Composite bipolar plates prepared by molding graphite powder with phenol-formaldehyde resin binder have been studied by the Army and its contractors (4-6).

In an earlier Ashland investigation (7) concerned with fabrication of improved bipolar plates, two phenolic resins, Arofene® 877LF (Ashland Chemical Company) and A-33 (an experimental styrenated resin), were shown to exhibit good corrosion resistance to hot H_3PO_4. A near optimum graphite powder loading for the composite was established along with a high density blend composition. In addition, an improved two-step molding technique was developed. The purpose of the present study was to further investigate the fabrication processes for the resin/graphite composite bipolar plates. As part of this investigation, we examined methods of treating bipolar plates so that essentially all etchable substances and possible poisons could be removed prior to fuel cell operation.

It was suspected that corrosion products from the phenolic resin could leach from the acid reservoir in the bipolar plate and be deposited on the catalyst. These could block the active sites, thus poisoning the catalyst.

Experimental

The initial experimental program consisted of monitoring the corrosion of test composite coupons fabricated from C^{14} labeled resins and the graphite powder mixture. This was done by liquid scintillation counting of solution extracts from composite plates immersed in hot H_3PO_4. The radiochemical procedure for monitoring corrosion offered two advantages. First, different positions of the resin molecular structure could be labeled; thus, the point of attack could be determined. Second, by monitoring the concentration of resin products in acid, problems in measuring accurate weight losses in these graphite composites were avoided.

Later in the program, an alternative method to monitor corrosion was developed to eliminate the costly and time consuming step of radio-labeled resin synthesis. It was observed that the color of the acid samples corresponded well with the concentration of resin in the acid. Therefore, optical (visible) spectrometry was studied as a potential method for measuring the concentration of resin in the acid. The optical spectrometry method was calibrated using the samples from the test with radio-labeled coupons. There was a linear correspondence between optical spectrometric absorption and radiochemically determined concentration. This good agreement allowed the use of commercially available resins in corrosion studies. Another advantage of visible spectrometry over the radiotracer method is that visible spectrometry takes advantage of the color quenching which must be corrected for in the radiochemical method.

Synthesis of C^{14} labeled Arofene 877LF and A-33 resins.—The methylene "bridging" position was chosen as the C^{14} labeling position because the "bridge" was con-

sidered a likely point of attack (probably leading to polymer chain scission) by hot H_3PO_4.

The laboratory synthesis procedures used were scaled-down versions of commercial Ashland procedures. About 700g of resin was synthesized in each batch. The only significant synthesis modification was the addition of the C^{14} labeled formaldehyde earlier, and at a lower temperature, than the main formaldehyde charge. The purpose of this modification was to minimize volatility losses and to insure complete utilization of the C^{14} labeled formaldehyde. Radiochemical yields were about 90%. The physical property data on the Arofene 877LF and A-33 resins related to the present study are presented in Table I. The test methods used were all ASTM procedures.

Molding coupons and bipolar plates.—The conditions for fabrication of the coupons were as described in Ref. (7). A vacuum ($\sim 10^{-1}$ torr) postcuring was applied on some coupons.

Corrosion tests.—These coupons (25 × 75 × 3 mm) were suspended by Teflon (trademark of E. I. du Pont de Nemours and Company) strings into a Teflon cup containing 93.5 ml of (85.6%) H_3PO_4 (Baker Chemical Company). The assembly was placed in an oven at 190°C for extended periods of time (up to 2000h). At various intervals, 0.3 ml of acid was removed for measurement of the concentration of resin dissolved in the acid and was replenished by 0.3 ml of fresh preheated acid.

Counting procedures for corrosion tests.—The 0.3 ml acid sample was diluted 9 to 1 with H_2O. Then 1 ml of diluted etching product was placed in 10 ml dioxane scintillation cocktail (for more concentrated samples, less of the diluted acid was used to reduce color quenching). The dioxane solutions were counted in a Beckman LS-100 liquid scintillation counter. A spiking procedure was used to determine the counting efficiency. This procedure required 50 μl of C^{14} radiochemical standard (New England Nuclear lot no. 697-242, containing 4.5×10^5 dpm/ml activity) in each sample cocktail solution. Counting efficiency was calculated by comparison of the spiked solution counts with raw counts from the sample.

Table I. Physical properties of resin

Resin	Melt point (°C)	150°C Melt time (s)	125°C Flow* (mm)	150°C Cure time* (s)
C^{14} labeled 877LF	92	165	44	73
Arofene 877LF lot 7198F	78	140	52	72
C^{14} labeled A-33 batch 1	74	142	152	222
C^{14} labeled A-33 batch 2	76	256	25	154
A-33 pilot plant lot 7214	77	264	60	114

* Determined with 10% hexamethylenetetramine added to the resin.

Visible optical spectrometry.—The 0.3 ml samples from the corrosion test were diluted with 9.7 ml of fresh H_3PO_4. A portion of the diluted sample was put in a cuvette and then placed in a Bausch and Lomb Spectrometer Model 100 tuned to 590 nm. This wavelength was determined to be the optimum wavelength by a broad scan of the sample. Fresh acid was used as a reference. The absorbance of the sample was then measured. For calibration, the absorbances were measured on samples of known concentrations. These concentrations were determined from C^{14} radiochemical measurements of corrosion extracts.

Results and Discussion

The results for several coupons from the initial tests are shown in Table II. First, it was apparent that some coupons exhibited very good corrosion resistance (less than 0.2% weight loss of the resin), while others, supposedly molded under identical conditions, showed poor corrosion resistance (more than 5% weight loss). Physical examination of the coupons after corrosion tests showed that the more corroded coupons had swelled considerably (up to about 17% increase in thickness). The scatter in

Table II. Results of etching

Coupon	Binder	w/o Furfural	Postcure	Final % etched	Total time (h)	Remarks
T-16	C^{14} 877LF	0	Regular	0.13	271	
T-22	C^{14} 877LF	0	Regular	5.50	281	9% HMTA
T-59	C^{14} A-33 (B2)	0	Regular	0.75	2011	
T-60	C^{14} A-33 (B1)	0	Regular	0.30	2011	
L-1	C^{14} A-33 (B2)	0	Regular	2.86	750	
L-2	C^{14} A-33 (B2)	0	Vacuum	0.10	750	
L-3	C^{14} A-33 (B2)	0	Regular	3.30	750	9% HMTA
L-4	C^{14} 877LF	0	Regular	5.37	750	
L-5	C^{14} 877LF	0	Regular	9.10	750	9% HMTA
L-6	C^{14} A-33 (B1)	0	Vacuum	0.40	750	
L-7	C^{14} A-33 (B1)	0	Regular	4.80	750	Prolonged molding
L-8	C^{14} A-33 (B1)	0	Regular	4.25	750	Prolonged molding, 9% HMTA
L-9	C^{14} A-33 (B2)	0	Regular	3.08	456	
L-10	C^{14} A-33 (B2)	0	Regular	3.42	456	
M-1	Arofene 877LF	0	Regular	12.71	456	Molding: Held at 220°C (20 min) → outgas
M-2	Arofene 877LF	0	Vacuum	2.65	456	Molding: Outgas → Held at 220°C (20 min)
M-3	Arofene 877LF	1	Regular	3.45	456	
M-4	Arofene 877LF	1	Regular	1.22	456	
M-5	Arofene 877LF	0	Vacuum	3.35	456	
M-8	Arofene 877LF	0	Regular	4.95	456	
M-9	Arofene 877LF	0	Regular	3.10	456	Molding: Outgas held at 220°C (20 min)
M-10	Arofene 877LF	0	Regular	12.30	456	
M-11	A-33 pilot plant	1.5	Regular	6.00	538	11.5% HMTA
M-12	A-33 pilot plant	1.5	Vacuum	0.21	538	
M-13	A-33 pilot plant	1.5	Vacuum	1.45	538	
M-14	Arofene 877LF	1.5	Vacuum	0.28	538	
M-15	Arofene 877LF	1.5	Vacuum	0.33	538	
M-16	C^{14} A-33 (B2)	1.5	Vacuum	0.31	538	
M-17	C^{14} A-33 (B2)	1.5	Vacuum	0.40	538	
M-18	Arofene 555	0	Vacuum	0.43	528	Purified by steam
M-19	Arofene 877LF	0	Regular	4.20	528	
M-20	Arofene 877LF	0	Vacuum	7.10	528	
M-21	Arofene 877LF	1.5	Vacuum	1.75	528	
M-22	Arofene 877LF	1.5	Vacuum	0.38	528	
M-30	Arofene 877LF	0	Vacuum	>10.0	96	Extracted with acetone before acid etch

these early results prompted a more thorough investigation into optimizing the curing conditions for the composites and more careful control over the molding and curing processes.

A second observation was that the corrosion process is complete in about 300h, regardless of the amount of total etching. A possible mechanism for this passivation is that H_3PO_4 attacks both low molecular weight resin and resin with a low cross-link density. Apparently, the etching ceases when low molecular weight resin materials are depleted, and only fully cross-linked material remains in the coupon. The total amount leached may be a function of both the total amount of low cross-link density resin and the total surface area in contact with the phosphoric acid. To minimize the exposed surface area, it is necessary for the resin to wet the graphite particles as well as possible. Two methods to achieve better wetting were investigated. The first was through enhanced flow characteristics of the resin, and second involved the use of a wetting agent. Molding techniques were varied to increase the flow during curing, but to no avail (see Table II).

Other possible sources of corrosion products are unreacted phenol and formaldehyde, and impurities such as low molecular weight phenol-formaldehyde reaction species. To minimize these, post curing was done in a vacuum furnace. This vacuum curing treatment resulted in some improvement in corrosion resistance. However, the corrosion of some coupons was unacceptably high: > 2.5% in two cases.

It was apparent from the data that an improvement in resin flow properties during molding (in the early stages of cure where the cross linking degree is low) was very desirable. Resin flow is usually enhanced when the free phenol content of the resin is low. The phenol was removed from the resin by steam stripping as a last step during synthesis. The coupon, M-18, prepared from low phenol resin (Arofene 555) showed good corrosion resistance.

The use of a chemical additive, furfural, to improve particle wetting resin flow during molding was another approach investigated. Initial results indicated much lower corrosion of test coupons in 190°C H_3PO_4. To check reproducibility, several additional coupons containing this flow enhancing additive were tested, and results were very favorable. Fairly consistent, low (< 0.3% weight loss) results were obtained in most cases. The earlier problems of higher corrosion rates and inconsistent results thus appeared to have been due to insufficient resin flow in the mold before cross linking becomes the dominant factor. Use of the resin formulations with slower cure rate properties and an additive for improved particle wetting and resin flow appear to be the keys to enhanced corrosion resistance for bipolar plates.

The mechanism for passivation is unknown, but, as noted before, essentially all corrosion takes place in the first 300h as shown in Fig. 1. This was also observed in a test where the acid was changed for each sampling (coupon T-22). Therefore, pre-etching the bipolar plate acid reservoir with H_3PO_4 could be beneficial. However, pre-etching with an organic solvent, acetone (note coupon M-30, Table II), was extremely deleterious. The coupon severely cracked and corrosion was very pronounced.

Conclusions

Arofene A-33 and 877LF, when molded and cured using the improved techniques developed in this study, are promising candidates for use in preparing composite (graphite powder/phenolic resin) bipolar plates, which are highly resistant to corrosion by 190°C H_3PO_4. These results suggest that a hot H_3PO_4 pretreatment of the bipolar plate reservoir area could result in little or no etching by H_3PO_4 in subsequent fuel cell operations. The main features of the modified curing/molding procedure developed (but not fully optimized) here for bipolar plate fabrication are the use of a chemical additive, furfural, molding techniques to improve particle wetting and resin flow properties during cure, and the employment of an extended (20h) vacuum oven postcure of the plates. Improved particle wetting and resin flow during molding can lead to a stronger, less permeable composite. Therefore, it may be possible to lower the bipolar plate resin content below 25% (the amount used in this study). This could result in greater electrical conductivity for the bipolar plate, without introducing increased plate porosity (which would lead to increased H_2 permeability and greater susceptibility to H_3PO_4 attack). This would require verification.

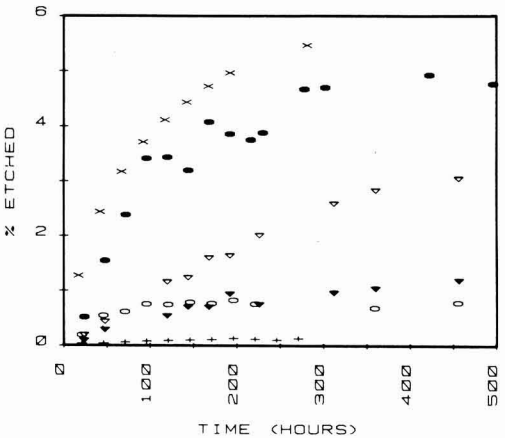


Fig. 1. w/o Resin leach from typical test coupons vs. time in H_3PO_4 at 190°C. +: Coupon T-16 (see Table II), coupon L-7. ∇: Coupon L-9. ∇: Coupon M-4. o: Coupon T-59. x: Coupon T-22.

Steam stripping of the phenolic resin to remove excess phenol and reaction by-products may be a useful technique for improving test coupon resistance to hot H_3PO_4. This approach is suggested by the limited results obtained here, but considerably more work is needed for verification.

Acknowledgments

The authors wish to express their gratitude to several persons whose assistance contributed greatly to the success of this project: Corbett L. Taylor, for performing the majority of the experimental work, particularly in the radiochemical analysis and resin curing areas; G. Fred Watts, for his expert counseling services in phenolic resins chemistry area; Alan H. Boyer, who carried out most of the synthesis of radio-labeled resins; and John E. Martin, who provided important counsel concerning experimental techniques developed during their previous related fuel cell contract.

Manuscript submitted Dec. 9, 1982; revised manuscript received March 28, 1984.

Ashland Chemical Company assisted in meeting the publication costs of this article.

REFERENCES

1. S. G. Abens, B. S. Baker, and I. Michalko, "Fuel Cell Stacks," Final Technical Report, Contract no. DAAK02-74-C-0367, June, 1977, Sponsored by U.S. Army Mobility Equipment R&D Command, Ft. Belvoir, VA.
2. A. Kaufman, "Phosphoric Acid Fuel Cell Stack and System Development," Technical Progress Report for Quarter Ending Sept. 30, 1979, Contract no. DE-AC-03-78-ET 15366, Sponsored by U.S. Dept. of Energy, Administered by NASA Lewis Research Center, Cleveland, OH.
3. G. A. Gruver, R. F. Pascoe, and H. R. Kunz, *This Journal*, **127**, 1219 (1980).
4. P. Stonehart, J. MacDonald, V. Jalan, and J. Baris, pp. 102-105, Extended Abstracts of the National Fuel Cell Seminar, Bethesda, MD, June 26-28, 1979.
5. L. G. Christner, "Technology Development for Phos-

phoric Acid Fuel Cell Powerplant (Phase II)," 3rd Quarterly Report for Contract no. DEN 3-67, June, 1979, Sponsored by U.S. Dept. of Energy, Administered by NASA Lewis Research Center, Cleveland, OH (DOE/NASA/0067-79-2), NASA Report no. CR-159705.

6. H. C. Maru, L. G. Christner, S. G. Abens, and B. S. Baker pp. 86-90, Extended Abstracts of the National Fuel Cell Seminar, Bethesda, MD, June 26-28, 1979.
7. P. M. Colling, J. E. Martin, and R. V. Norton, "Selection and Evaluation of Carbon-Resin Composites for Bipolar Plates for Hydrogen Fuel Cells," Final Technical Report, Contract no. DAAK70-77-C-0151, Completed Sept. 1978, Sponsored by U.S. Army Mobility Equipment R&D Command, Ft. Belvoir, VA.

JOURNAL OF THE ELECTROCHEMICAL SOCIETY

SOLID-STATE SCIENCE AND TECHNOLOGY

NOVEMBER 1984

Adsorption of Hydroxide and Sulfide Ions on Single-Crystal n-CdSe Electrodes

K. W. Frese, Jr.* and D. G. Canfield

SRI International, Menlo Park, California 94025

ABSTRACT

Flatband potentials were determined for n-CdSe ($11\bar{2}0$) electrodes as a function of OH^- and SH^- concentrations. Surface coverage was calculated from the observed flatband potential shift. The Frumkin isotherm was applied to the data, and thermodynamic parameters were determined. The standard free energies of adsorption for OH^- and $S^=$ were found to be −2.3 and −6.9 kcal/mol, respectively. At high SH^- concentrations, there was evidence for a decrease in the repulsive interactions of the $S^=$ and OH^- ions.

The n-CdSe/sulfide electrolyte redox system has been studied extensively in relation to solar-to-electrical energy conversion devices. Although it is known that this system possesses a high degree of stability with respect to photoanodic corrosion, the details of the corrosion-redox competition processes are not completely understood.

An important detail of the electron-transfer process in this system is surface adsorption and dissolution of sulfide and sulfur species, respectively. We have begun a study of the adsorption properties of the CdSe/sulfide electrolyte system. Because the alkaline polysulfide electrolyte can be complicated by different polysulfide species with perhaps different adsorption characteristics, we thought it useful to first study the adsorption process under simpler conditions. These conditions obtain in $NaOH/Na_2SO_4$ electrolytes and in $NaOH/Na_2S$ electrolytes without dissolved sulfur. In this report, we focus on measurements of flatband potentials at room temperature in the dark. A distinction has to be made between measurements in the dark and under illumination. In the former case, the corrosion of the electrode and thus changes in the surface caused by the measurements are minimized, whereas in the latter case, corrosion products and the effect of illumination could significantly complicate the characteristics of the system.

Experimental

All measurements were made on single-crystal n-CdSe ($11\bar{2}0$) electrodes (Cleveland Crystals). The donor densities were 1×10^{17} cm^{-3}. The electrode surface was chemomechanically polished with 1% (V/V) Br_2/CH_3OH. After mounting in epoxy (Epoxy Patch) and in between capacitance/voltage measurements, the crystals were rinsed with 1*M* HCl to remove sulfide layers, and then cleaned with a cotton-tip applicator soaked in 1% Br_2/CH_3OH mixed with 50% by volume 1*M* HCl. This cleaning was followed by rinsing with distilled deionized water. All chemicals were reagent grade.

Capacitance/voltage sweep measurements were made at 50 kHz using a lock-in amplifier. A constant ac current was passed through the cell, and the 90° out-of-phase component of the voltage across the CdSe-Pt foil electrode was measured. AC voltages were typically 1-10 mV. Previous capacitance measurements (1) on these same crystals showed that the space-charge capacitance was independent of frequency (10^3-10^5 Hz). High purity N_2 was passed through the electrolyte before and during the measurements. All capacitance measurements were made within 15 min of the time of introduction of the electrode into the electrolyte.

*Electrochemical Society Active Member.

Theory

Flatband potential and surface coverage.—The flatband potential, V_{FB}, is a property of a semiconductor-electrolyte system that is essentially a measure of the energy of the conduction band of the material. In general, the measured flatband potential can be related to its value when no excess charge exists on the surface, V_{FB}^o, and the voltage drop across the Helmholtz double layer when net charge resides on the electrode surface. We can express this relationship as

$$V_{FB} = V_{FB}^o \pm \frac{Q_{ad}}{C_H} \quad [1]$$

where C_H is the integral capacitance of the Helmholtz double layer. The chemical and physical structure of this interfacial region at the semiconductor-liquid junction is not fully known. It is expected that the concepts of inner and outer Helmholtz planes (2) that were developed for metal/electrolyte interfaces apply in the semiconductor electrode case. The shift in V_{FB} relative to the neutral condition is positive or negative, depending on the sign of the net surface charge. The quantity Q_{ad} (C/cm²) is assumed to be given by

$$Q_{ad} = q_o (\Sigma z_i n_i^+ - \Sigma z_j n_j^-) \quad [2]$$

where n is the number of adsorbed species per square centimeters and q_o is the elementary charge. z is the integral charge on the ion. If there are N total sites for adsorption, the surface coverage, θ, for the ith species is given by $\theta_i = n_i/N$. When $n_i = N$, θ is θ_{sat}, the saturation coverage.

Now consider the simplification that only one negatively charged species adsorbs on the electrode surface, *e.g.*, OH^-, with surface coverage, θ.

Then

$$V_{FB} = V_{FB}^o - \frac{q\theta N}{C_H} \quad [3]$$

and the flatband potential saturates at

$$V_{FB}^{sat} = V_{FB}^o - \frac{qN}{C_H} \quad [4]$$

By solving Eq. [3] for θ, and eliminating qN/C_H by means of Eq. [4], we find

$$\theta = \frac{V_{FB} - V_{FB}^{0}}{V_{FB}^{sat} - V_{FB}^{0}} \quad [5]$$

This simple result states that the fractional occupancy of surface sites is given by the ratio of the shift in flatband potential relative to the neutral condition to the total shift from neutral to saturation condition. Application of Eq. [5] assumes that V_{FB}^{sat} can be observed experimentally. Calculation of V_{FB}^{sat} appears to be unreliable at present. However, V_{FB}^{0} values can be predicted with reasonable accuracy (3).

Isotherms.—The thermodynamic equilibrium constant for the adsorption process

$$X^- + M \overset{K_0}{\rightleftarrows} MX_{ad}^- \quad [6]$$

is

$$K_0 = \frac{a_s}{a_v a_{el}} \quad [7]$$

where a_s and a_{el} are the activities of the adsorbing species on the surface and in the electrolyte, respectively, and a_v is the activity of vacant sites. According to the general isotherm of Frumkin (4), $a_s = \theta\, e^{f\theta}$, $a_v = (1 - \theta)$, and $a_{el} = a_{x^-}$. For simple adsorption such as reaction [6], the Frumkin isotherm is

$$\ln\left(\frac{\theta}{1-\theta}\right) + f\theta = \ln K_0 + \ln a_{x^-} \quad [8]$$

The parameter f, in units of kT, represents the interaction energy between adsorbed particles. This energy may be repulsive ($f > 1$) or attractive ($f < 1$).

The parameter, f, generally depends on coverage and the density of electrons or holes on the electrode surface. In the case of semiconductors in the dark, the electrode charge is normally quite small (low density of ionized electronic surface states). At the flatband condition, the space charge is zero by definition. To a first approximation, neglect of electronic (as opposed to adsorbed) charge is permissible. If so, then f may be related to various models of the interface. For example, according to the induced dipolar heterogeneity model of Boudart (5)

$$f = \frac{2\Pi\, q_0 N\, M_0}{kT\left(1 + \frac{9\alpha}{a^3}\theta\right)} \quad [9]$$

where N is the density of available sites, M_0 is a dipole moment normal to the surface, α is the polarizability of the adsorbing particles, and a is the distance between dipoles. For 10^{14} particle/cm^2, $M_0 = 1.0$ Debye, and $\alpha = 0$, $f = 7.3$, a very reasonable value (6, 7). Mutual polarization effects will lower f depending on α, a, and the coverage.

The Bockris-Devanathan-Müller isotherm (2, 8), that describes ion-ion interactions, can also provide an estimate of f. When the electrode charge is negligible

$$f = \frac{M' q_0^2\, r_{ion}^2\, (z\,N)^{3/2}}{\epsilon\, kT}\, \theta^{1/2} \quad [10]$$

where M' is a geometrical factor, r is the radius of the adsorbing ion, and the dielectric constant, $\epsilon \approx 6$. Using $M = 15.3$ (8), $N = 10^{14}$ cm^{-2}, $z = 1$, and $r_i = 2.5 \times 10^{-8}$ cm, we find $f = 8.9$ for $\theta = 1$. Both models predict reasonable values of f and are useful for rationalizing and predicting changes in adsorption characteristics as system properties vary.

Surface substitution reaction.—Now consider a situation where the electrode is saturated with an adsorbed charged species and another more strongly adsorbing species is introduced into the electrolyte. Specifically, consider the equilibrium

$$M\,OH^-_{ad} + SH^-\,(aq) \overset{K_s}{\rightleftarrows} M\,S^-_{ad} + H_2O\,(l) \quad [11]$$

where M stands for an adsorption site.

The equilibrium constant for this substitution reaction may be written

$$K_s = \frac{\theta_2 e^{f_2\theta_2}\, a_{H_2O}}{\theta_1 e^{f_1\theta_1}\, a_{SH^-}} \quad [12]$$

where the subscript 2 refers to adsorbed $S^=$ ion and 1 refers to adsorbed OH^- ion. According to our data (see Fig. 2 and the results below), the CdSe surface is saturated with OH^- at the time SH^- ions were introduced into the 1M NaOH electrolyte. Therefore we describe the system by reaction [11]. Accordingly, it is assumed that $\theta_1 + \theta_2 = 1$. When the surface contains two interacting species, such as $S^=$ and OH^-, the f's have a more complicated meaning than that implied in Eq. [9] or [10]. A theory that counts the interaction between different kinds of particles is needed to describe the system.

For the present, we have to assume that like and unlike ion interactions are included in the f's in Eq. [12]. Assuming a_{H_2O} is unity and $\theta_1 + \theta_2 = 1$, Eq. [12] may be written using $\theta_{S^=}$ for θ_2

$$\theta_{S^=} + \frac{1}{f_1 + f_2}\ln\left(\frac{\theta_{S^=}}{1-\theta_{S^=}}\right) = \frac{1}{f_1 + f_2}\ln a_{SH^-} + \frac{f_1}{f_1 + f_2} + \ln K_s \quad [13]$$

This equation will be applied below.

Results

Adsorption of OH^-.—Typical Mott-Schottky plots for CdSe ($11\bar{2}0$) in 0.1M Na_2SO_4 are shown in Fig. 1. The concentration of OH^- was varied by the addition of NaOH. The plots were linear over a wide voltage range. The measured capacitance followed the $1/C^2$ relation for surface barriers as small as 0.2V. This behavior suggests that the density of active electronic surface states in the upper part of the bandgap is quite low. Our previous measurements (1) with the same crystals in neutral Na_2SO_4 solution indicated interface state densities of 10^{12}-10^{13} cm^{-2} at 0.1-0.5 eV below the conduction bandedge. The interface is assumed to be formed by the CdSe and a thin (perhaps permeable and chemically active) layer of elemental Se. The Se results from the oxidative etch with Br_2. Apparently, the more-alkaline conditions, as in Fig. 1, play a role in reducing the interface state density. A possible explanation is that OH^- ions bond to sites with Cd^{2+} character and thus remove the postulated acceptor-state levels.

The flatband potentials determined from Fig. 1 were plotted against OH^- concentration, and the results are shown in Fig. 2. The inset to Fig. 2 shows how V_{FB} varies with log [OH^-]. Interpolated values of V_{FB} are listed at various OH^- concentrations in Table I. The flatband po-

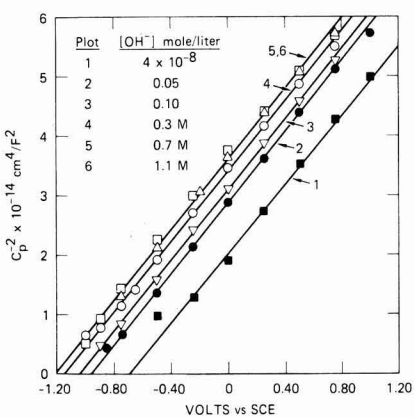


Fig. 1. Mott-Schottky plots for n-CdSe ($11\bar{2}0$) in 0.1M Na_2SO_4 at 50 kHz. NaOH added. $N_0 = 7.6 \times 10^{16}$ cm^{-3}.

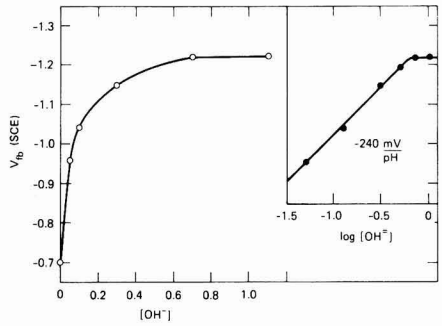


Fig. 2. Flatband potential vs. [OH⁻] for n-CdSe (11$\bar{2}$0) in 0.1M Na_2SO_4. Data from Mott-Schottky plots at 50 kHz.

tential was strongly dependent on [OH⁻], and at sufficiently large concentrations, a saturation V_{FB} of −1.22V *vs.* SCE was observed. The results suggest a strong adsorption of OH⁻ ions on the CdSe surface.

The behavior of V_{FB} in the pH range 4-11 is unusual. We (1) and others (9) have reported that V_{FB} is −0.7V *vs.* SCE and is independent of [OH⁻] in this intermediate pH range. Therefore, in the discussion to follow we will assume that OH⁻ or H⁺ are not strongly adsorbing for [OH⁻] < $10^{-3}M$. And accordingly, we will assume that V_{FB} = −0.7V corresponds to the neutral surface charge (adsorbed) condition, *i.e.*, V_{FB}° = −0.7V (see below).

Adsorption of $S^{=}$.—The adsorption of sulfide ions was studied by measuring the flatband potential shift as a function of Na_2S in 1*M* NaOH. Mott-Schottky plots are shown in Fig. 3. These parallel plots of $1/C^2$ *vs.* *V* indicate that the addition of Na_2S leads to a further negative shift in V_{FB}. We assume that $S^{=}$ replaces OH⁻ on the surface until saturation is reached.

The results of V_{FB} determinations are plotted in Fig. 4 as a function of Na_2S concentration. Interpolated values are given in Table II.

Discussion

OH⁻ adsorption.—The surface coverage with OH⁻ was calculated using Eq. [5] and V_{FB}° = −0.70 and V_{FB}^{sat} = −1.22V. The results are plotted in Fig. 5 according to the logarithmic form of the Frumkin isotherm, Eq. [8]; the interaction parameter was calculated from the slope, $d\theta/d \ln c$ and found to be 1.7. This value indicates a weak interaction between the adsorbed OH⁻ ions. A value of the equilibrium constant for adsorption can be made by direct calculation by means of Eq. [8], for θ = 0.5. Using an

Table I. Flatband potentials and derived values of surface coverage of OH⁻ on n-CdSe (11$\bar{2}$0)

[OH⁻] (*M*)	V_{FB} (SCE)	θ
0.00	−0.700	0.0
0.01	−0.765	0.13
0.02	−0.840	0.23
0.03	−0.865	0.32
0.04	−0.915	0.41
0.05	−0.955	0.49
0.06	−0.980	0.54
0.07	−1.005	0.59
0.08	−1.020	0.62
0.09	−1.030	0.63
0.10	−1.040	0.65
0.15	−1.080	0.73
0.20	−1.110	0.81
0.30	−1.150	0.86
0.40	−1.176	0.92
0.50	−1.195	0.95
0.60	−1.210	0.98
0.70	−1.220	1.00

Electrolyte: 0.1*M* Na_2SO_4 with NaOH added.
Calculations based on Eq. [5] with V_{FB}° = −0.70V (SCE).

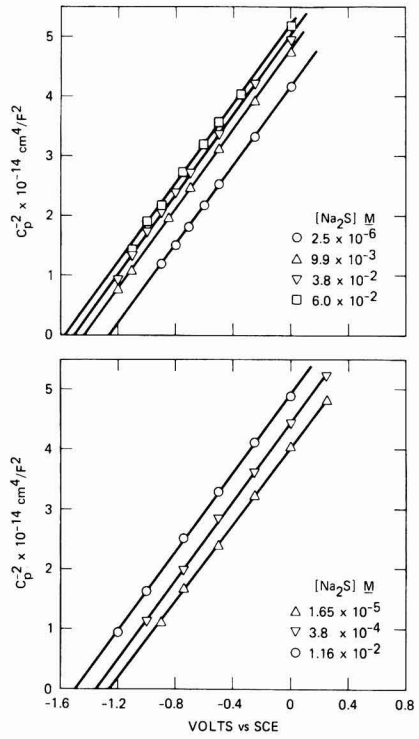


Fig. 3. Typical Mott-Schottky plots for n-CdSe (11$\bar{2}$0) in 1M NaOH with added Na_2S. 50 kHz.

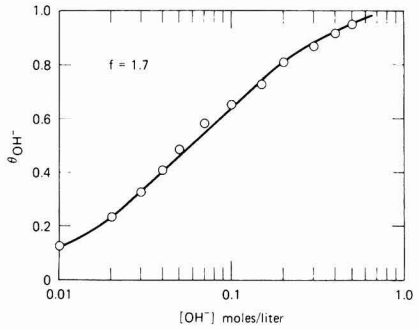


Fig. 4. Logarithm plot of θ_{OH^-} vs. concentration of OH⁻ for n-CdSe (11$\bar{2}$0) in 0.1M Na_2SO_4.

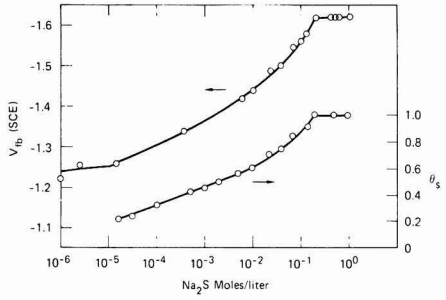


Fig. 5. Logarithm plot of flatband potential and surface coverage with sulfide for n-CdSe (1120) vs. concentration of Na_2S.

Table II. Flatband potentials and derived values of surface coverage of $S^=$ on n-CdSe ($11\bar{2}0$)

$[Na_2S]$ (mol/liter)	V_{FB} (SCE)	θ*
0.00	−1.220	0
1.5×10^{-5}	−1.260	0.22
3.0×10^{-5}	−1.280	0.24
1.0×10^{-4}	−1.310	0.33
5.0×10^{-4}	−1.356	0.43
1.0×10^{-3}	−1.370	0.46
2.0×10^{-3}	−1.390	0.50
5.0×10^{-3}	−1.420	0.57
1.0×10^{-2}	−1.440	0.61
2.2×10^{-2}	−1.490	0.72
4.0×10^{-2}	−1.505	0.75
7.0×10^{-2}	−1.550	0.85
1.0×10^{-1}	−1.561	0.87
1.5×10^{-1}	−1.580	0.91
2.0×10^{-1}	−1.620	1.0
5.0×10^{-1}	−1.620	1.0
1.0×10^{-1}	−1.620	1.0

Electrolyte: 1*M* NaOH with Na_2S added.
* Calculated using $qN/C_H = 0.46$V.

activity coefficient of 0.8 for 0.058*M* OH^- (Fig. 5), K_0 is found to be 50.4. The standard free energy change was calculated to be −2.3 kcal/mol. This value can be compared with $\Delta G^0 = -3.7$, −3.4, and +2.6 calculated (10) for adsorption of OH^- on Au, Ag, and Hg electrodes, respectively.

Aqueous sulfide chemistry.—Before detailed interpretation of the flatband potential data, the chemistry of Na_2S solutions has to be briefly considered. The addition of Na_2S to an aqueous solution results in nearly complete hydrolysis leading to an essentially equimolar solution of SH^- and OH^-. The equilibrium constant for the hydrolysis (11)

$$S^=(aq) + H_2O \rightleftarrows SH^-(aq) + OH^-(aq) \qquad [14]$$

is $\sim 1.1 \times 10^3$. In 1*M* OH^-, ~ 0.1% of sulfide is present as $S^=$. This means that $SH^-_{(aq)}$, is the dominant precursor to adsorbed $S^=$.

Another important aspect is the very probable large increase in acidity of SH^- when adsorbed on the surface. The chemical evidence for this expectation is the following. First, the pK_a for SH^- is 17.1 at room temperature (11). The pK_a of AgSH is 5.3 (12). Thus, the K_a increases by ~12 orders of magnitude by interaction of SH^- with a metal that is adjacent to Cd in the periodic table. Next, consider the enhancement in acidity of SH^- when it complexes with sulfur atoms to form polysulfide species. The pK_a's for HS_2^-, HS_3^-, HS_4^-, and HS_5^- were calculated to be 9.5, 7.4, 6.2, and 5.6, respectively (13). Clearly, complexation of SH^- with metals or nonmetals greatly increases its acidity. The above discussion allows us to conclude that any adsorbed SH^- will be nearly quantitatively converted to $S^=_{ad}$ in 1*M* NaOH.

The coverage with sulfide was calculated on the assumption that $\theta_{OH^-} + \theta_{S^=} = 1$, and the results are shown in Table II. Equation [3] was used with $qN/C_H = 0.46$V and θ was replaced by $(1 + \theta_{S^=})$. The value 0.46 is one-half the shift in V_{FB} from −0.70 to −1.62V, the saturation value for $S^=$. Saturation with $S^=$ with a double-negative charge should cause a shift twice that for saturation with OH^-, a single-negative species, if the number of sites is constant. Comparison of ΔV_{FB} of 0.52 (OH^-) with 0.92 ($S^=$) shows that this expectation is found experimentally. The coverage values, $\theta_{S^=}$, were plotted *vs.* log $[SH^-]$, as shown in Fig. 4. The slope of the linear portion gives a first approximation to $(f_1 + f_2)^{-1}$. Various values of $f_1 + f_2$ were chosen until Eq. [13] was satisfied. The best fit was obtained for $f_1 + f_2 = 12.4$. For $\theta_{S^=} > 0.6$, the data did not fit Eq. [13], as discussed below. This large $f_1 + f_2$ value compared to $f_{OH^-} \approx 2$ is not too surprising. The large negative charge and size of $S^=$ causes $f_{S^=}$ to be larger (Eq. [10]). In addition, f_{OH^-} is increased because OH^- ions interact with some $S^=$ on the surface. However, $S^=$ ions interact with OH^-, and thus $f_{S^=}$ is probably decreased. In order to calculate the equilibrium constant for the surface substitution reaction [11], an estimate of f_{OH^-} in the presence of $S^=_{ad}$ is needed. We reasoned that this number should be greater than 2 but less than $1/2\ (f_1 + f_2) = 12.4$. A midrange value of 5 was assumed to be a reasonable compromise. Now K_s can be calculated using Eq. [13], $\theta = 0.5$, $C_{SH} = 2.0 \times 10^{-3}$, and an activity coefficient of 0.75 for SH^- ion in 1*M* NaOH solution. The calculation gives $K_s = 1.9$ and $\Delta G_s^0 = -0.37$ kcal/mol.

A calculation of the free energy change for adsorption of $S^=$ can also be made using the thermodynamic data derived here. Consider the following series of reactions and corresponding standard free energy changes.

ΔG^0(kcal/mol)	
$M - OH^-_{ad} + SH^- \rightleftarrows MS^=_{ad} + H_2O$	−0.37
$M + OH^- \rightleftarrows MOH^-_{ad}$	−2.3
$S^= + H^+ \rightleftarrows SH^-$	−23.3
$H_2O \rightleftarrows H^+ + OH^-$	+19.1
$M + S^= \rightarrow MS^=_{ad}$	− 6.9

The value of ΔG^0 for adsorption of $S^=$ is found to be −6.9 kpm.

There is one other aspect of the sulfide coverage data that is of interest that is not predicted by Eq. [13]. The increase in slope of the θ *vs.* log *C* plot for $\theta \geq 0.6$ is unusual. Normally, the Frumkin isotherm with repulsive interaction shows a decrease in slope, leading to saturation for $\theta \geq 0.8$. Evidently, the nature of the interaction between the adsorbed ions changes in the direction of less repulsion as θ increases before saturation of the surface. A possible explanation is that a new phase forms on the surface, such as CdS or a sulfur layer. The former may require removal of Se, while the later may require at least partial oxidation of the adsorbed sulfide ions. Both of these processes, sulfur-selenuim exchange and sulfur layer formation, are thought to occur on CdSe surfaces in contact with sulfide electrolytes in photoelectrochemical solar cells.

Summary

The adsorption of OH^- and $S^=$ ions on n-CdSe single-crystal electrodes was studied. Both ions reach saturation coverage for concentrations of 0.1-0.7*M*. Standard free energies of adsorption were −2.3 and −6.9 kcal/mol for OH^- and $S^=$, respectively. The corresponding quantity for the substitution reaction involving OH^-_{ad} and $S^=_{ad}$ was −0.37 kcal/mol. The repulsive interaction of $S^=$ (and possibly OH^-) appears to weaken at high Na_2S electrolyte concentrations. The formation of a new phase in the near surface region may be implicated.

Acknowledgment

This research was supported by the Solar Energy Research Institute under Contract XE-2-0273-1.

Manuscript submitted Feb. 16, 1983; revised manuscript received July 9, 1984.

SRI International assisted in meeting the publication costs of this article.

REFERENCES

1. K. W. Frese, Jr., *J. Appl. Phys.*, **53,** 1571 (1982).
2. J. O'M. Bockris, M. A. V. Devanathan, and K. Müller, *Proc. R. Soc. A*, **274,** 55 (1963).
3. K. W. Frese, Jr., *J. Vac. Sci. Technol.*, **16,** 1042 (1979).
4. "Electrosorption," E. Gileadi, Editor, Plenum Press, New York (1967).
5. M. Boudart, *J. Am. Chem. Soc.*, **74,** 3556 (1952).
6. B. E. Conway and E. Gileadi, *Trans. Faraday. Soc.*, **58,** 2493 (1962).
7. B. E. Conway, "Theory and Principles of Electrode Processes," Ronald Press, New York (1965).
8. H. Wroblowa and K. Müller, *J. Phys. Chem.*, **73,** 3528 (1969).
9. A. B. Ellis, S. W. Kaiser, J. M. Bolts, and M. S. Wrighton, *J. Am. Chem. Soc.*, **99,** 2839 (1977).
10. D. D. Bode, Jr., *J. Phys. Chem.*, **76,** 2915 (1972).

11. W. Giggenbach, *Inorg. Chem.*, **10**, 1333 (1971).
12. W. L. Freyberger and P. L. DeBruyn, *J. Phys. Chem.*, **61**, 586 (1957).
13. M. C. M. McKubre and D. D. Macdonald, "Electrochemical Removal of Dissolved Sulfide from Geothermal Brines," Final Report from SRI International to the Environmental Protection Agency, EPA Contract no. 63-07-2778 (1981).

Effects of Additives on ZnO-B_2O_3-SiO_2 Passivation Glasses

Yutaka Misawa

Hitachi Limited, Hitachi Research Laboratory, Hitachi, Ibaraki, Japan

ABSTRACT

The addition of BaO, Sb_2O_3, or Bi_2O_3 to glass A with composition (weight percent [w/o]) 65.4 ZnO-24.5 B_2O_3-10.1 SiO_2 resulted in more negative surface charge density and increase in the thermal expansion coefficient (α). The glass B, 63 ZnO-29 B_2O_3-8 SiO_2 (w/o) showed finer crystals by the addition of ZnO (1 w/o) or glass A without affecting the surface charge density or α. The effects of additives on the DTA characteristic temperatures of the two glasses are also presented.

ZnO-B_2O_3-SiO_2 glasses are suitable passivants for high voltage silicon power devices such as thyristors, transistors, and diodes. One advantage of using this glass is that surface charge density of the glass/Si system can be controlled by changing the glass composition (1), *i.e.*, the surface electric fields of the devices can be modified on demand. However, a new problem occurred when the ratios of B_2O_3 to SiO_2 were increased to shift the surface charge density in the negative direction (2). The problem consisted of an increase in crystal size.

Thus, to produce the passivation glass with a large negative surface charge density and fine crystals for high power devices, two approaches have been considered.

In method 1, a shift to more negative surface charge density of the glass with a small negative surface charge density and fine crystals is achieved by addition of another material. In method 2, forming finer crystals of the glass with a large negative surface charge density and large crystals is also achieved by addition of another material. For ZnO-B_2O_3-SiO_2 glass, Moriguchi *et al.* (3) reported that Sb_2O_3, CeO_2, and PbO were additives which lower the flowing point and crystallization point for the DTA curve and make the thermal expansion coefficient larger. However, Ta_2O_5 was an additive which did not change the flowing point, crystallization point, or thermal expansion coefficient, but did shift the surface charge density slightly in the positive direction.

In this report, method 1 was examined adding various metal oxides to glass A (ZnO:65.4, B_2O_3:24.5, SiO_2:10.1 w/o). Method 2 was investigated adding glass A or ZnO to glass B(ZnO:63, B_2O_3:29, SiO_2:8 w/o).

Experimental

Glass preparation.—In method 1, metal oxide components of glass A and 5 w/o of BaO, Al_2O_3, Ga_2O_5, SnO, PbO, ZrO_2, Sb_2O_3, Bi_2O_3, TiO_2, V_2O_5, Nb_2O_5, or Ta_2O_5 additive were mixed in a revolving mixer and used as glass materials. V_2O_5, Sb_2O_3, and PbO, which are low melting point materials, were heated at 500°C, while other materials were heated at 850°C to remove water and organic contaminations before weighing. Subsequent preparation procedures were the same as reported before (1, 2).

In method 2, glass A, with crystallized glass A or ZnO as additive, was mixed with glass B in a revolving mixer. Crystallized glass A was prepared as follows. Glass A powder was fired at 740°C for 40 min in air and then ground to give the same mean particle size distribution as glass A. ZnO was used like the glass materials.

Measurements.—Physical properties of glasses were measured by differential thermal analysis (DTA), thermal expansion coefficient measurements, and scanning electron microscope (SEM) observations.

Surface charge densities of the glass/silicon system were measured with metal-glass-silicon (MGS) capacitors. Sample preparation and measurement methods have been reported previously (1, 2).

Results and Discussion

The effects of additives for glass A with a small negative surface charge density and fine crystals are shown in Fig. 1. as DTA curves of glass A and glass A with added Sb_2O_3. For the latter, a second crystallization point (T_{c2}) was not distinctly observed. Table I shows characteristic points for DTA curves of glass A with various metal oxides added. Characteristic points such as softening point (T_s), crystallization starting point (T_{cs}), and first crystallization point (T_{c1}) shift to lower temperatures on addition of any of the metal oxides. The oxides seemed to act as nucleating agents. Furthermore, the second crystallization points were not distinctly observed for all additives except TiO_2. Glass A with added TiO_2 showed distinct DTA characteristics. The boundary between T_s and T_{cs}

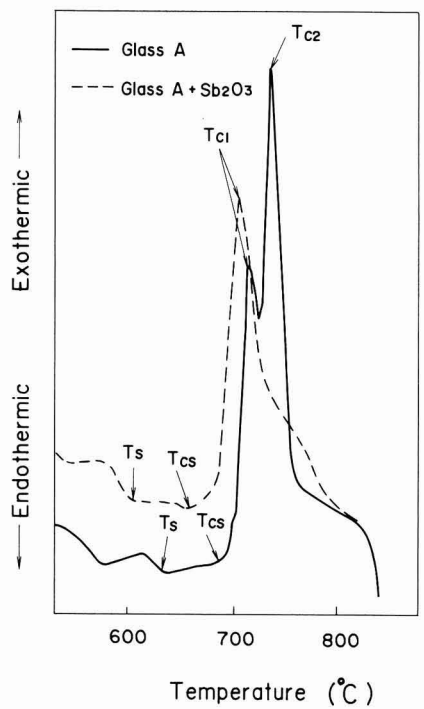


Fig. 1. DTA curves of glass A with and without added Sb_2O_3

Table I. Characteristic points for DTA curves of glass A with various metal oxides added

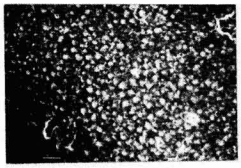
Additive	T_s (°C)	T_{cs} (°C)	T_{c1}* (°C)	T_{c2}* (°C)
BaO	603	657	693 (133)	
Al_2O_3	620	673	710 (150)	
Ga_2O_3	590	645	690 (138)	
SnO	618	665	715 (125)	
PbO	600	654	690 (165)	
TiO_2	595	595	635 (2)	700 (48)
ZrO_2	600	650	703 (130)	
Sb_2O_3	610	665	714 (75)	
Bi_2O_3	600	656	700 (110)	
V_2O_5	600	650	710 (60)	
Nb_2O_5	595	653	700 (95)	
Ta_2O_5	604	667	703 (100)	
None	636	690	724 (93)	755 (163)

* Numbers in parentheses are peak height in arbitrary units.

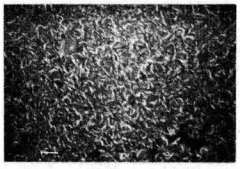
was unclear, and T_{c1} was very low in comparison with those of other glasses. Figure 2 shows typical photomicrographs for glasses fired on silicon at 700°C. Crystals in these glasses were different; they were larger than those in glass A and finer than those in glass B. Table II shows thermal expansion coefficients of glasses fired at 680° or 700°C. The thermal expansion coefficients for glass A with added metal oxide were all larger than that of glass A alone, except for ZrO_2 and Ga_2O_5 additives. It was expected that the thermal expansion coefficients of glass A with added metal oxide would be lower than that of glass A alone, because the crystallization points of these modified glasses were all lower than that of glass A alone. However, the results contradicted the expectations. The effects of metal oxides on the thermal expansion coefficients were larger than that of the degree of crystallization.

Table III shows the surface charge densities of glasses fired on n-type silicon at 680° or 700°C. The additives which shifted the surface charge density in the positive direction and accumulated the surface of n-type silicon are Al_2O_3, Ga_2O_5, SnO, PbO, TiO_2, ZrO_2, Nb_2O_5 and Ta_2O_5. These additive metals are from groups IIIB, IV, and VA of the periodic table. The additives which shifted the surface charge density in the negative direction and inverted the surface of n-type silicon are BaO, Sb_2O_3, and Bi_2O_3. These are from groups IIA and VB of the periodic table.

The effects of additives on the properties of glass B with large negative surface charge density and large crystals are shown in Fig. 3 as determined from DTA curves.



(a) Glass A



(b) Glass A with 5 wt% Bi_2O_3

Fig. 2. Typical micrographs for glasses fired on silicon at 700°C for 40 min.

Table II. Thermal expansion coefficients of glass A with various metal oxides added

Additive \ Glass firing temperature	Thermal expansion coefficient (10^{-7}/°C) 680°C	700°C
BaO	39.5	38.9
Al_2O_3	42.6	
Ga_2O_5	38.9	
SnO	42.4	
PbO	42.8	
TiO_2	44.5	
ZrO_2	34.8	
Sb_2O_3	43.0	39.6
Bi_2O_3	40.0	39.4
V_2O_5	45.8	39.8
Nb_2O_5	42.9	
Ta_2O_5	42.4	
None	39.0	34.0

Table III. Surface charge densities of glass A with various metal oxides added

Additive \ Glass firing temperature	Surface charge density (10^{-11} cm^{-2}) 680°C	700°C
BaO	−1.0 to −1.2	−3.4 to −3.7
Al_2O_3	+1.6 to +2.4	
Ga_2O_5	+2.2 to +3.9	
SnO	+1.6 to −3.6	
PbO	+2.2 to +3.9	
TiO_2	+4.1 to +5.7	
ZrO_2	+3.0 to +3.8	
Sb_2O_3	−1.7 to −3.4	−7.4 to −8.6
Bi_2O_3	−2.0 to −2.8	−6.4 to −8.9
V_2O_5	−0.4 to +0.3	−1.4 to −2.1
Nb_2O_5	+2.0 to +2.4	
Ta_2O_5	+2.3 to +2.5	
None	0 to −1.0	−1.0 to −3.0

Softening points of all the glasses changed hardly at all with additions. Crystallization starting point, first, and second crystallization point first decreased sharply and then by a slow increase by the addition of the additives. This tendency is independent of additives. Thus the additives were functioning as nucleating agents as stated before. However, T_{c2} did not disappear. And in particular,

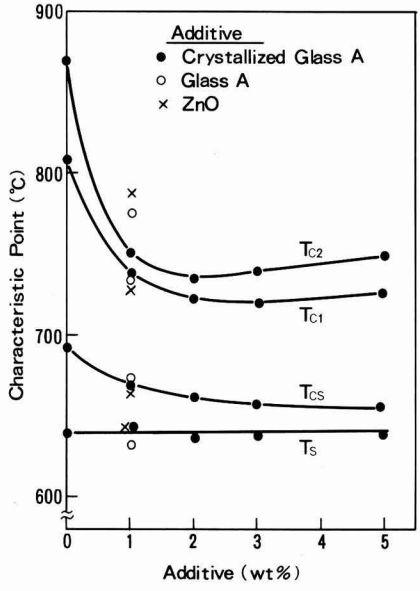


Fig. 3. Effects of additives on characteristic points of glass B as determined from DTA curves.

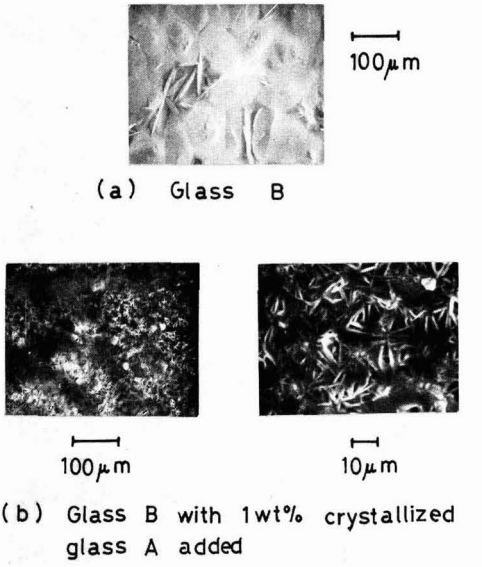


Fig. 4. Typical micrographs for glasses fired on silicon at 680°C or 700°C for 40 min.

variations of T_{c1} and T_{c2} were large with addition of only a small amount of additive. For 1 w/o additive, T_{cs} and T_{c1} did not differ for different additives. However, the variation of T_{c2} for glass B with crystallized glass A added was the largest. That is, crystallized glass A was most effective as a nucleating agent.

Phases of crystallization were observed by SEM. Figure 4 shows several photomicrographs for the glasses fired on silicon at 680° or 700°C. Large needlelike crystals were observed in glass B, as reported before (2). However, in glass B with additives, fine crystals were observed, as in glass A alone. Fine crystals formed because crystallization proceeded easily.

Figure 5 shows the relationship between the ratio of additives and thermal expansion coefficient of glass B fired at 680° or 700°C. Thermal expansion coefficients of glass B with added ZnO or crystallized glass A decreased with the ratio of additive. The thermal expansion coefficient of glass B with crystallized glass A was smaller than that with ZnO. This could be attributed to the difference in T_{c2}. The effect of the additive on the thermal expansion coefficient of glass B was opposite of

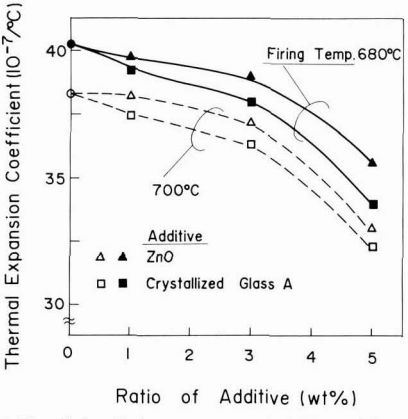


Fig. 5. The relationship between amount of additive and thermal expansion coefficient of glasses fired at 680° or 700°C.

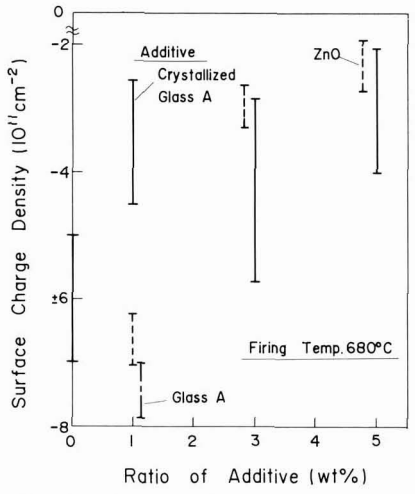


Fig. 6. The effect of amount of additive and surface charge density of glasses fired at 680°C.

that for glass A. This could be assumed to originate from the difference in the addition methods.

Figures 6 and 7 show the relationships between ratio of additive and surface charge density of the glass fired on silicon at 680° or 700°C. Surface charge density shifted in the positive direction with increasing ratio of additive. The shift was smallest for the glass B with added glass A.

Figure 8 shows the relationship between surface charge density and glass firing temperature. Surface charge density shifted to a more negative charge with higher firing temperature. This tendency was the same as that of glasses with no additive (1).

Conclusions

The effects of additives on DTA characteristics, crystal morphology, thermal expansion coefficient, and surface charge density of ZnO-B_2O_3-SiO_2 glasses were investigated.

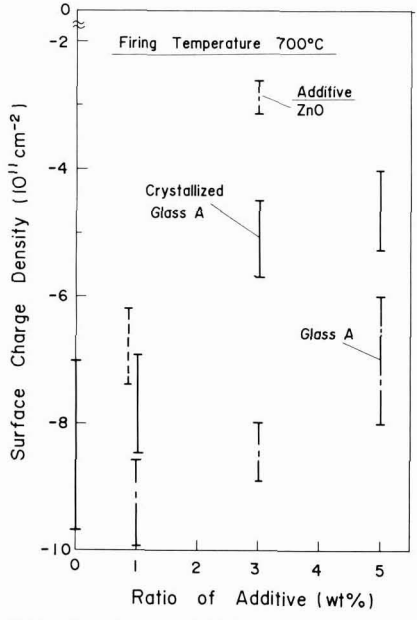


Fig. 7. The effect of amount of additive and surface charge density of glasses fired at 700°C.

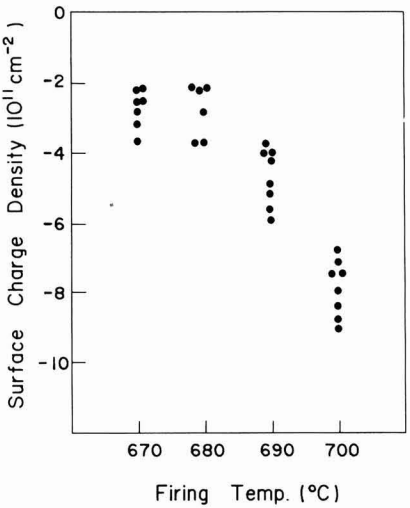


Fig. 8. The effect of firing temperature on surface charge density of glass B with 1 w/o crystallized glass A added.

The addition of metal oxides influenced the properties of glass A, which had a small negative surface charge density and fine crystals, as follows. Characteristic points such as T_s, T_{cs}, and T_{c1} of glass A decreased, and T_{c2} was not distinctly observed on addition of metal oxide. The thermal expansion coefficients of glass A increased. The surface charge density of the glass/silicon system shifted negatively with the addition of metal oxides, if the metal belonged to groups IIA or VB (*e.g.*, BaO, Sb_2O_3, or Bi_2O_3). It shifted to positive with the addition of metal oxides, if the metal belonged to groups IIIB, IV, or VA (*e.g.*, Al_2O_3, Ga_2O_5, SnO, PbO, TiO_2, ZrO_2, V_2O_5, Nb_2O_5, or Ta_2O_5).

The addition of glass A or ZnO influenced the properties of glass B, which had a large negative surface charge density and large crystals, as follows. T_{cs}, T_c, and T_{c2} of glass B decreased, and the crystals in the glass were finer. The thermal expansion coefficient of glass B decreased with increasing ratio of additive. The surface charge density shifted positively with increasing ratio of additive. However the shift was negligible in the case of the glass with 1 w/o additive. Hence, glass B with 1 w/o additive meets the objectives of this work, which was the development of a glass with large negative surface charge and fine crystals.

Acknowledgments

The author wishes to thank Mr. Y. Ikeda and Drs. M. Okamura, H. Hackino, and M. Monma for their helpful suggestions and encouragement during this study and Mr. M. Takahashi for technical assistance.

Manuscript submitted April 16, 1984; revised manuscript received July 9, 1984.

Hitachi Limited assisted in meeting the publication costs of this article.

REFERENCES

1. Y. Misawa, H. Hackino, S. Hara, and M. Hanazono, *This Journal*, **131,** 359 (1984).
2. Y. Misawa, *ibid.*, To be published.
3. Y. Moriguchi, K. Miwa, M. Kanno, H. Kawamura, and T. Shibuya, in "Proceedings of First Symposium on Semiconductors and Integrated Circuits Technology, Tokyo," p. 10 (1971).

Electrical Characteristics of the RF Magnetron-Sputtered Tantalum Pentoxide-Silicon Interface

Shunji Seki, Takashi Unagami, and Bunjiro Tsujiyama

Nippon Telegraph and Telephone Public Corporation, Ibaraki Electrical Communication Laboratory, Tokai, Ibaraki 319-11, Japan

ABSTRACT

Tantalum pentoxide (Ta_2O_5) films were deposited onto single-crystalline silicon as gate insulators by RF magnetron sputtering. Capacitance-voltage characteristics were measured to determine the interface properties between Ta_2O_5 and Si. After annealing at 450°C in H_2 ambient, a negative interface charge that is fully localized in the low dielectric constant transition layer at the interface was observed. It has also been clarified that the rest of the film is homogeneous, whose dielectric constant is almost close to that of the bulk of Ta_2O_5. It has been shown that Ta_2O_5 gate insulator with relatively good interface properties can be fabricated at low temperatures using RF magnetron sputtering.

In recent years, tantalum pentoxide (Ta_2O_5) film is of interest for use as a gate insulator in MOS devices. The higher dielectric constant of Ta_2O_5, compared with that of SiO_2, makes it attractive for the fabrication of high quality MOS devices with high transconductance and low threshold voltage. Furthermore, since high quality Ta_2O_5 films can be fabricated at low temperatures using RF magnetron sputtering (1), it also offers the opportunity for removing some of the problems encountered with conventional MOS devices with thermally grown SiO_2 as a gate insulator.

The characteristics of MOS devices will be strongly dependent on the interface properties between the gate insulator and the silicon layer, in addition to the quality of the gate insulator itself. Because of its excellent properties, thermally grown SiO_2 has been used for years as gate insulators in MOS devices. However, since the thermal oxidation is performed at 900°C or higher, the oxidation process prohibits the use of the thermal oxide on devices fabricated on a low melting point substrate. Furthermore, the high temperature oxidation generates stacking faults and dislocations in the silicon substrate, and it also changes the impurity distribution previously formed in the substrate. These structural defects and the variation of the impurity profiles induce the degradation in the performance of MOS devices. In order to remove these problems, gate insulator fabrication processing at low temperatures becomes necessary.

Several attempts have been made to employ Ta_2O_5 films as gate insulators in MOS devices, using chemical vapor deposition (2) and thermal oxidation of a deposited Ta film (3, 4). However, the interface properties between Ta_2O_5 and Si fabricated by these processes were inferior to those between SiO_2 and Si. More than -5 to -10×10^{11}

cm^{-2} interface charge density remained at flatband condition, which was much higher than that between SiO_2 and Si. In order to obtain high quality MOS devices, it is necessary to reduce the interface charge density between Ta_2O_5 and Si.

The authors have investigated the interface properties between the silicon layer and the Ta_2O_5 gate insulator formed by RF magnetron sputtering. This paper reports the results of these experiments, and also shows the ability to produce a relatively good quality Ta_2O_5 gate insulator at low temperatures using RF magnetron sputtering.

Experimental

Al/Ta_2O_5/Si structure devices were used to investigate the interface behavior. All of the MOS capacitors were fabricated on p-type, <100>-oriented, 1.2-1.8 Ω-cm silicon wafers. Si wafers were chemically cleaned using mixtures of H_2O_2 and H_2SO_4 (volume ratio of H_2O_2/H_2SO_4 = 1/4). Then, they were rinsed in deionized water. Immediately before being installed into the sputtering chamber, the wafer was dipped into dilute HF to remove the oxide formed during previous processing steps. Sputtering was performed using an ULVAC SBH-2204 RS RF magnetron sputtering system. Instead of a conventional oil diffusion pump, a 3000 liter/s cryogenic pump was used to eliminate contamination. The Ta_2O_5 target was 10 cm diam and 5 mm thick. The target to substrate distance was kept at 5 cm. The sputtering gas consisted of mixtures of argon and oxygen (partial pressure ratio of Ar/O_2 = 8/2). The sputtering chamber was evacuated to less than 1×10^{-7} torr prior to sputtering, and then backfilled with the sputtering gas. The sputtering pressure was varied from 4×10^{-3} to 2×10^{-2} torr. The Ta_2O_5 target was presputtered for at least 1h. Typical deposition rate ranged from 2 to 6 nm/min. Aluminum dot electrodes of 300 μm diam were electron-beam deposited onto the sputtered Ta_2O_5 surface. To minimize the radiation damage produced during the MOS capacitor fabrication steps, the wafers were annealed in the hydrogen ambient. After a final H_2 anneal, the high frequency capacitance-voltage characteristics were measured with automatic capacitance meters (HP 4275A and HP 4274A). These measurements were performed for more than 20 MOS capacitors fabricated on the same silicon substrate.

In-depth composition profiles of the deposited Ta_2O_5 were measured by Auger electron spectroscopy (AES) with simultaneous Ar sputtering. For the AES measurements, samples were taken from the sputtering chamber and were then mounted in an ultrahigh vacuum chamber of the AES measurement equipment (Φ 590). Measurements were performed under conditions of a 5 kV excitation voltage and a 0.5 μA beam current. Typical sputtering rate of Ta_2O_5 films was 3 nm/min for a 3 kV sputtering voltage and a 5 mA emission current.

Experimental Results

H_2 annealing effect.–To find H_2 annealing effect on the interface charge density, capacitance-voltage characteristics of MOS capacitors, which had been annealed in the hydrogen ambient at different temperatures, were measured at frequencies ranging from 1 kHz to 1 MHz. In these cases, annealing was performed after the aluminum electrode deposition, which is hereafter referred to as the postmetallization annealing. Annealing temperatures were varied from 350° to 450°C, and the annealing time was retained for 30 min. Figure 1 shows capacitance-voltage characteristics for MOS capacitors which were not annealed. A strong frequency dispersion was observed in their C-V curves. This is due to the existence of the high density of interface states with various response time constants. Two parameters were used to indicate the H_2 annealing effect: the interface charge density calculated from the flatband voltage measured at 1 MHz, and the flatband voltage difference between the low frequency C-V curve taken at 1 kHz and the high frequency C-V curve taken at 1 MHz.

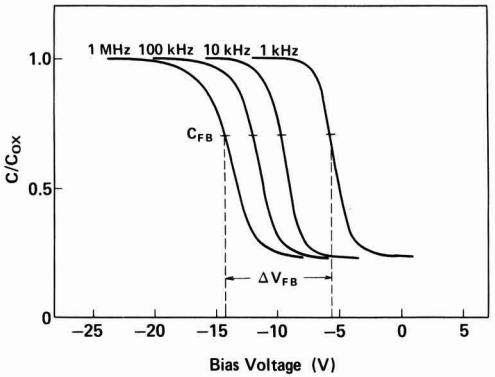


Fig. 1. Frequency dispersion in capacitance-voltage characteristics for MOS capacitors without the postmetallization annealing. The Ta_2O_5 thickness is 110 nm. The interface charge density, calculated from the V_{FB} measured at 1 MHz and the ΔV_{FB} inserted in the figure, were used to indicate the annealing effect.

Figure 2 shows variations in the interface charge density and the flatband voltage difference with annealing temperatures. The interface charge density decreases monotonically as the annealing temperature goes up from 350° to 450°C. After annealing at 450°C, the interface charge polarity changed to negative, and the value of -3.1×10^{11} cm^{-2} was obtained. Flatband voltage difference also decreases uniformly with increasing annealing temperature. After annealing at 450°C, the flatband voltage difference in between low and high frequency C-V curves was reduced to less than 0.04V. It has been clarified that H_2 annealing has a great effect on the reduction in the interface charge density in Al/Ta_2O_5/Si structures.

In order to make the interface charge density much lower, the annealing process was newly introduced after the Ta_2O_5 deposition process. The purpose of this annealing process, hereafter referred to as the postsputtering annealing, is to reduce the radiation damage produced during the sputtering process. In these cases, wafers were annealed at 450°C in the hydrogen ambient for 30 min before the aluminum metallization, and the postmetallization annealing temperature was varied.

Figure 3 shows the variations in the interface charge density and the flatband voltage difference with postmetallization annealing temperatures. The interface

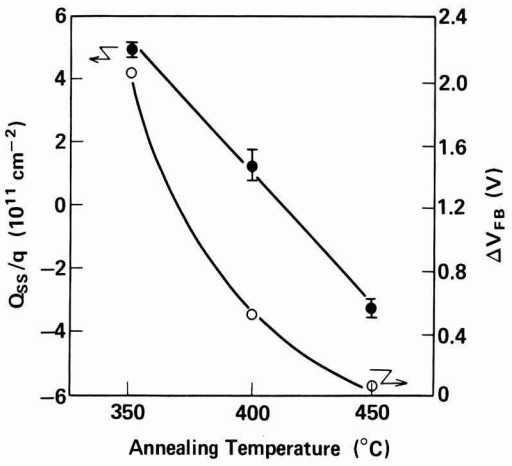


Fig. 2. Variations in interface charge density Q_{SS}/q and flatband voltage difference ΔV_{FB} with changes in postmetallization annealing temperature. The Ta_2O_5 thickness is 80 nm.

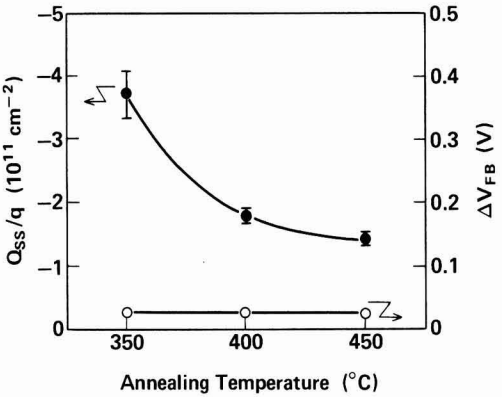


Fig. 3. Variations in Q_{SS}/q and ΔV_{FB} with changes in postmetallization annealing temperature. Samples had been annealed at 450°C in the hydrogen ambient before metallization. The Ta_2O_5 thickness is 80 nm.

charge density and the flatband voltage difference on the case involving postsputtering annealing without postmetallization annealing were 4.2×10^{11} cm^{-2} and 0.19V, respectively. Differing from the results shown in Fig. 2, the interface charge polarity changed to negative, even though the postmetallization annealing temperature was 350°C. The value of interface charge density decreases as the postmetallization annealing temperature rises from 350° through 450°C. After annealing at 450°C, the interface charge density was reduced to as low as $\div 1.4 \times 10^{11}$ cm^{-2}. Flatband voltage difference was made as low as 0.03V almost invariable in the postmetallization annealing temperature over 350°C. And the reproducibility of these results was good. It has become clear that the interface charge density can be reduced to as low as -1.4×10^{11} cm^{-2} by the optimum combination of postmetallization annealing with postsputtering annealing. These are the lowest values which have been reported so far. These results imply that postsputtering annealing has an effect on the reduction of the radiation damages induced during the sputtering process.

The surface-state density was calculated from the high frequency (1 MHz) capacitance-voltage characteristics using the Terman method (5). The surface-state density distributions, before and after annealing in the hydrogen ambient, are compared in Fig. 4. The surface-state density for as-deposited samples was on the order of 10^{12} states cm^{-2} eV^{-1} in the middle of the energy gap and increased rapidly toward the bandedges. After the samples had been annealed at 450°C in the hydrogen ambient, the surface-state density was reduced to as low as 1.5×10^{11} states cm^{-2} eV^{-1} near the midgap, which is one order of magnitude lower than that reported previously (3).

Interface charge density dependence on gate insulator thickness.—It has become clear from the results mentioned in the previous section that the interface charge after annealing at 450°C in the hydrogen ambient is characterized by a negative charge and behaves like fixed charges in the Al/Ta_2O_5/Si structures. To clarify the charge distribution in the gate insulator, variations in the interface charge density with changes in the gate insulator thickness were investigated. Results are shown in Fig. 5. The interface charge density is within the range from -3.0×10^{11} to -3.8×10^{11} cm^{-2} as varying the gate insulator thickness from 17 to 110 nm. The interface charge density is independent of the gate insulator thickness in the thickness range studied. If the charge distribution were uniform in the gate insulator, the interface charge density would increase monotonically with increasing gate insulator thickness. Hence, these results indicate that the charge distribution is not uniform in the gate insulator.

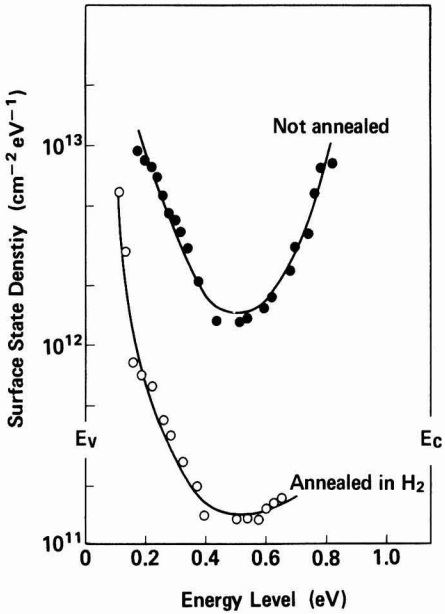


Fig. 4. Surface-state density distribution for Al/Ta_2O_5/Si MOS capacitors. Combination of postsputtering annealing with postmetallization annealing reduced the surface-state density to as low as 10^{11} cm^{-2} eV^{-1}. The Ta_2O_5 thickness is 110 nm.

Dielectric constant dependence on gate insulator thickness.—In order to clarify dielectric properties of Ta_2O_5 sputtered on single-crystalline Si, the relationship between the dielectric constant of the gate insulator and the gate insulator thickness was studied. The dielectric constant of the gate insulator was calculated from the capacitance of MOS capacitors in the accumulated region measured at 1 MHz. Figure 6 shows the variations in gate insulator dielectric constant with changes in thickness. The dielectric constant increases monotonically with increasing gate insulator thickness. For the sample 17 nm thick, the dielectric constant is 3.9, which is much lower than that of Ta_2O_5 itself and is close to that of SiO_2. As the thickness increases, the dielectric constant becomes higher and reaches 12.5 for the 110 nm thick sample. These results imply that the dielectric constant is not uniform throughout the whole thickness of deposited Ta_2O_5.

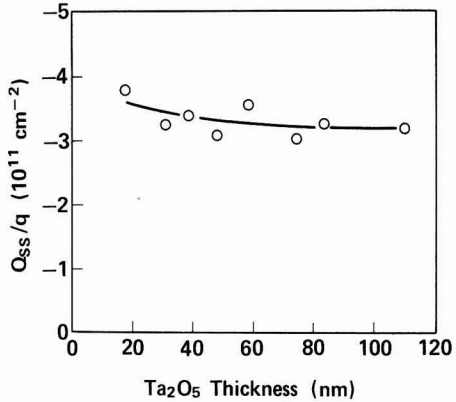


Fig. 5. Variation in interface charge density with changes in Ta_2O_5 gate insulator thickness. The interface charge density was calculated from the flatband voltage measured at 1 MHz.

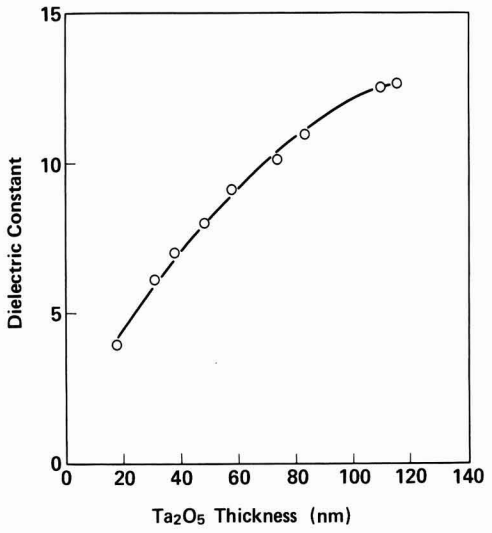


Fig. 6. Variation in Ta_2O_5 gate insulator dielectric constant with changes in the gate insulator thickness. Dielectric constant was calculated from the capacitance in the accumulated region at 1 MHz.

To clarify the reason for the variation in the dielectric constant, the dielectric constant profile within the deposited film was calculated from the results shown in Fig. 6. Figure 7 shows the dielectric constant profile, which was obtained by approximating the film with a series of discrete homogeneous layers. The bars shown in Fig. 7 represent the average value of the dielectric constant for each layer. The lowest average value was taken as the dielectric constant for the sample with the Ta_2O_5 thickness of 17 nm. The dielectric constant for the second layer was then obtained by reevaluating the dielectric data, using a multilayer model consisting of the first layer and the second layer. This calculation was repeated for each successive layer. The results indicate the existence of low dielectric constant layer near the Ta_2O_5/Si interface. It has also been shown that the dielectric constant is almost uniform throuhgout the rest of the film and is almost close to that of the bulk of Ta_2O_5.

To confirm the correctness of the model, etch-back experiments were performed. The sample with the oxide thickness of 110 nm was etched back to 50 nm. Following the etch-back step, aluminum electrodes were deposited on it to fabricate the MOS capacitor. From the measurement of the capacitance, the dielectric constant of the oxide was calculated to be 8.5. This value fits well with the results shown in Fig. 6. It is, therefore, concluded that the outer part of the film is homogeneous, and that the thickness of the transition layer is independent of the total thickness of gate insulator.

Composition profiles.–AES measurements of in-depth composition profiles are shown in Fig. 8. The vertical axis is proportional to the relative concentration, and the sputtering time indicated by the horizontal axis is related to the depth counted from the outer surface.

A remarkable feature is that the relative composition ratio of Ta/O is fairly constant through the whole thickness of the film, except for near the silicon interface, where the relative composition ratio becomes larger. This is not unique to the case of this film, but has been observed for other films with different thicknesses as well. The variation of the relative composition ratio of Ta/O near the interface is assumed to be related to the formation mechanism of tantalum oxide on silicon.

Discussion

The results shown in Fig. 7 can be explained by a model with a relatively narrow transition layer at the interface, where the rest of the film is homogeneous. This transition layer is considered to be attributed to the imperfect tantalum compound formed in the early stage of Ta_2O_5 formation on silicon. It is assumed that the dielectric constant becomes lower in this transition layer, owing to its structure imperfection. Following the transition layer formation, nearly perfect tantalum oxide will form on it. Hence, the outer part of the film becomes homogeneous, and the value of the dielectric constant in this region is close to that of the bulk of Ta_2O_5.

This model is confirmed by in-depth composition profiles obtained from the AES measurements. As shown in Fig. 8, the composition profile of the film is divided into two regions based on the relative composition ratio of Ta/O: (*i*) the outer part of the film, where the relative composition ratio of Ta/O is constant, and (*ii*) the region near the silicon interface, where the relative composition ratio becomes larger. Results shown in Fig. 8 indicate that the deposited film is homogeneous except for transition region near the interface. From the composition profiles, the thickness of this transition region is estimated to be in the range from 10 to 15 nm. Based on the assumption that the composition of the outer part of the film is Ta_2O_5, the larger relative composition ratio implies the existence of the imperfect tantalum compound or lower tantalum oxide in the transition region.

It has already been reported by Revez *et al.* (2) and Smith *et al.* (3), that the interface charge is also negative

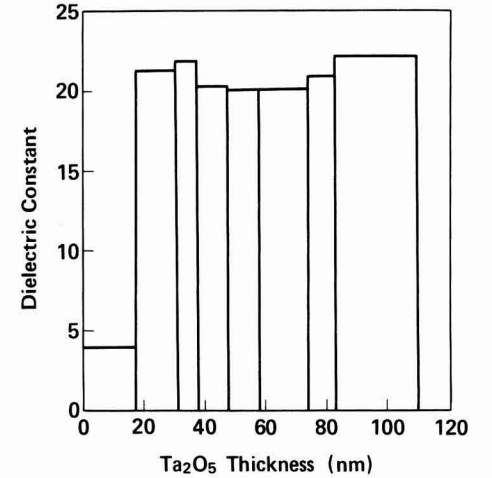


Fig. 7. Variation in dielectric constant with changes in distance from gate insulator/silicon interface. Data were obtained by approximating the Ta_2O_5 film with a series of discrete homogeneous layers.

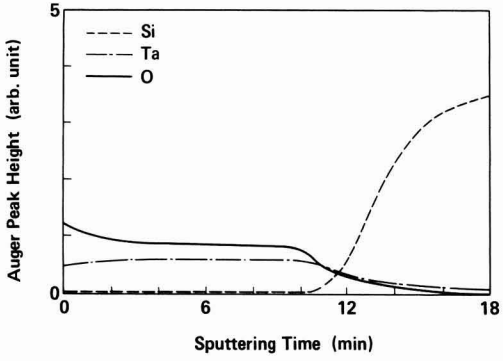


Fig. 8. In-depth composition profiles of Ta_2O_5 deposited on silicon. The sample was annealed at 450°C in the hydrogen atmosphere. Sputtering rate for Ta_2O_5 was 3 nm/min.

in the Ta_2O_5/Si system, when Ta_2O_5 gate insulator is fabricated with thermal oxidation of deposited Ta on Si. They investigated variations in refractive index of the film with changes in the film thickness in detail. However, the spatial distribution of these negative charges and the origin of these negative charges have not been clarified. The results shown in Fig. 5 indicate the fully localized distribution of the negative charge near the interface. As the interface charge density for the sample with 17 nm gate insulator thickness is almost the same as that for the sample with thicker gate insulator, the negative charge distribution will be localized within a thin layer at the Ta_2O_5/Si interface, which is less than 17 nm thick.

Taking the aforementioned results into consideration, it has become clear that the negative charges are fully localized in the low dielectric constant, narrow transition layer formed at the silicon interface. Even though the Si wafer is etched with dilute HF just before sputtering, oxide will reform quickly. The transition layer will be formed as the result of the interaction of this initial Si oxide film and/or Si surface with sputtered particles. If the transition layer consists of imperfect tantalum compound and/or lower tantalum oxide, it is suspected that the negative charge is due to the structure imperfections, such as the nonbridging oxygens, which are known to act as electron traps (6).

Conclusion

In the present study, Ta_2O_5 films have been deposited onto single-crystalline Si wafers using RF magnetron sputtering, and capacitance-voltage characteristics have been measured to determine the interface properties between Ta_2O_5 and Si. After annealing at 450°C in the hydrogen ambient, the interface charge in Al/Ta_2O_5/Si structures is characterized by a negative charge and is found to behave like a fixed charge. To obtain good quality interface, the postsputtering annealing has been newly introduced in addition to the conventional postmetallization annealing. At the optimized annealing conditions, the interface charge density was reduced to as low as -1.4×10^{11} cm^{-2} at flatband, and the surface-state density of 1.5×10^{11} cm^{-2} eV^{-1} was obtained near the midgap. These are the lowest values in the Ta_2O_5/Si system which have been reported so far.

It has been clarified that the deposited oxide consists of two regions: a low dielectric constant, narrow transition layer at the silicon interface, and the higher dielectric constant, homogeneous layer. The thickness of this transition layer is in the range 10-15 nm, which is independent of the total thickness of Ta_2O_5 film. Moreover, it has been shown that the negative charges are fully localized in this transition layer. From the results of the present work, it has been pointed out that the negative charge in the Ta_2O_5/Si system results from imperfect tantalum compound formed in the early stage of Ta_2O_5 formation on single-crystalline silicon.

In the present Ta_2O_5 gate insulator fabrication processes, the highest temperature was restrained to under 450°C in the postannealing process. The present work demonstrates that a relatively good quality Ta_2O_5 gate insulator can be fabricated at low temperatures using RF magnetron sputtering.

Acknowledgments

The authors would like to thank Mr. K. Murase for his encouragement during the course of this work. The authors are also grateful to Dr. M. Ojima for the AES measurements.

Manuscript submitted Aug. 1, 1983; revised manuscript received June 22, 1984.

Nippon Telegraph and Telephone Public Corporation assisted in meeting the publication costs of this article.

REFERENCES

1. S. Seki, T. Unagami, and B. Tsujiyama, *J. Vac. Sci. Technol. A*, **1**, 1825 (1983).
2. E. Kaplan, M. Balog, and D. Frohman-Bentchkowsky, *This Journal*, **123**, 1570 (1976).
3. A. G. Revesz and J. F. Allison, *IEEE Trans. Electron Devices*, **ed-23**, 527 (1976).
4. D. J. Smith and L. Young, *ibid.*, **ed-28**, 22 (1981).
5. L. M. Terman, *Solid State Electron.*, **5**, 285 (1962).
6. A. Szekeres, S. Alexandrova, and K. Kirov, *Phys. Status Solidi A*, **62**, 727 (1980).

Wetting Angles and Surface Tension in the Crystallization of Thin Liquid Films

Eli Yablonovitch and Tom Gmitter

Exxon Research and Engineering Company, Annandale, New Jersey 08801

ABSTRACT

The behavior of thin liquid films is known to be dominated by surface tension forces. We show that the crystallization of thin liquid films requires that two wetting angle conditions be simultaneously satisfied: (*i*) relating to the liquid-vapor interface, and (*ii*) relating to the crystal-liquid interface. The balance between capillary pressure and thermal gradient forces shows that the equilibrium freezing point of thin films is actually depressed below the bulk freezing point. The magnitude of the effect is 1 K in an 800Å thick film. These observations suggest that small-scale thickness fluctuations may be responsible for the initiation of subgrain boundaries in the growth of crystalline silicon films.

The crystallization of thin liquid silicon films is a promising method (1) for producing single-crystal films of good electronic quality. These films will have important device applications in radiation hardening, dielectric isolation, high voltage integrated circuits, etc.

It is well known (2) that capillary forces, surface tension, and wetting play a vital role in the behavior of thin liquid films. In this article, we will derive the wetting angle requirements which permit the crystallization of thin liquid films to proceed. We will see that the success with liquid silicon films encapsulated in silicon dioxide is the result of a particularly fortuitous combination of wetting angles for those two materials.

Wetting Angle Requirements

In general, there is no assurance that a thin liquid film will be stable. There is the well-known tendency for the liquid film to "ball up" and form droplets on the surface of the substrate. The condition for spreading of the liquid film on a substrate is that its wetting angle should be identically zero. Since this is very rare, a different approach is used. We will show that a solid capping layer on the liquid film greatly relaxes this severe wetting angle constraint, and permits wetting under more easily satisfied conditions.

For practical stability, the liquid film should spread to fill any possible voids in the film, as shown in Fig. 1. Let

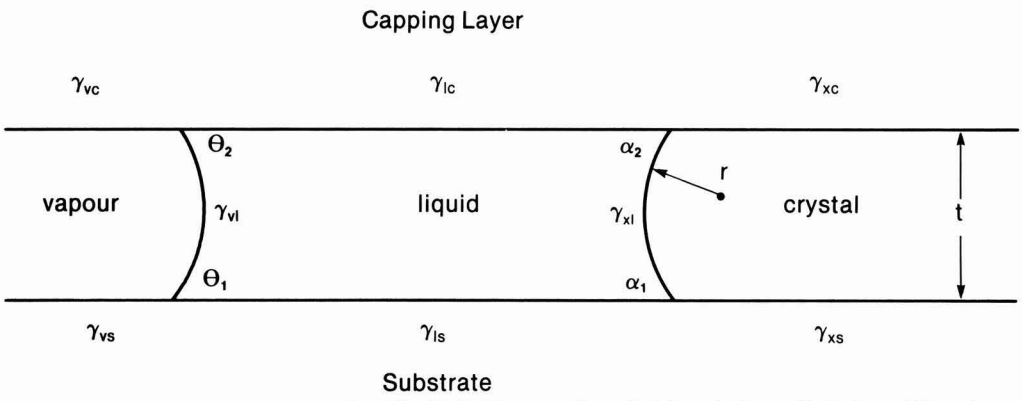


Fig. 1. A vertical cross-section through the thin liquid film. The liquid-vapor wetting angle, θ, is required to provide absolute stability against any voids which might be present in the film. The crystal-liquid angle α is required for high quality crystal growth and to prevent heterogeneous nucleation on the substrate. Note the radius of curvature r.

γ_{ls} and γ_{lc} be the surface energy (or tension) of the liquid with respect to the substrate and capping layer. Let γ_{vs} and γ_{vc} be the surface energy of the bare substrate and capping layer, respectively. The spreading of the liquid film should result in a net reduction of surface energy. Therefore

$$\gamma_{ls} + \gamma_{lc} - (\gamma_{vs} + \gamma_{vc}) < 0 \qquad [1]$$

The Young-Dupre equation (2) for wetting angles, $\gamma_{vs} - \gamma_{ls} = \gamma_{vl} \cos \theta$, may be used to simplify inequality [1]

$$\cos \theta_1 + \cos \theta_2 > 0 \qquad [2]$$

Inequality [2] states the wetting condition; the sum of the cosines of the wetting angles with respect to the substrate and the capping layer must be greater than zero. If the substrate and capping layer are made of the same material, then inequality [2] simply says that the wetting angle θ must be less than 90°. The wetting angle of liquid silicon on silica at the melting point has been independently measured (3) to be 87°, *i.e.*, barely within the regime of stability! This must be regarded as extremely fortuitous. Of course, without a capping layer we go back to the condition $\theta_1 = 0$, *i.e.*, wetting would be almost hopeless.

Since the surface tension γ_{vs} of the silica surface is thought to drop with increasing temperature, the angle θ_1 is thought (4) to become > 90° at temperatures 50-100 K above the silicon melting point. This probably explains the very narrow temperature window of stability in the crystallization of liquid silicon films on pure fused silica substrates. As a practical matter, it was found that the addition of a small amount of nitrogen (1) to the SiO_2 permitted the wetting conditions to be satisfied much more readily. The wetting angle of liquid silicon on Si_3N_4 is much less than 90°, having been measured (5) to be around 25°. It is understandable then that the addition of a small amount of Si_3N_4 to the SiO_2 might lower the wetting angle away from the condition of borderline stability, therefore broadening the temperature window of stability.

Thus far, we have considered wetting angles at the liquid-vapor interface, which controls the stability of the liquid film. Now we want to consider the crystal-liquid wetting angles, which will control the quality of crystal growth. It is a maxim (6) among crystal growers that the growth front should be convex away from the crystal. This permits any spurious crystal orientations to grow out to the edge and terminate there. A convex shape is guaranteed by wetting angles α_1 and α_2 both less than 90°. When α is greater than 90°, the Young-Dupre equation implies that γ_{xs}, the crystal-substrate interfacial energy, would be small, permitting easy heterogeneous nucleation of spurious grains at the surface of the substrate. In addition, the leading edge of the crystal growth would be a cusp at one or both interfaces. Good crystalline quality is inherently unstable at such a cusp.

Therefore, the wetting angle requirement for good crystalline quality is that the angle α_1 enclosed by the liquid at the interface between the crystal and the substrate should be less than 90°. Likewise, the angle α_2 with respect to the capping layer should be less than 90°.

Recently, Celler (8) observed the angle formed by liquid silicon between crystalline silicon and silica. The angle he observed is $60° < \alpha < 90°$, again fortuitously in the favorable range for good crystal growth. The two wetting angle conditions may now be summarized as (*i*) $\cos \theta_1 + \cos \theta_2 > 0$, and (*ii*) $\alpha_1 < 90°$ and $\alpha_2 < 90°$.

Capillary and Thermal Gradient Forces

The convex interface in Fig. 1 between the crystal and the liquid experiences a pressure due to its curvature. This is a type of capillary pressure which can be computed from the equation of Young and Laplace (2)

$$P = \gamma_{xl}\left[\frac{1}{r} + \frac{1}{R}\right] \qquad [3]$$

where γ_{xl} is the interfacial tension between crystalline and liquid silicon, r is the radius of curvature in the plane of Fig. 1, and R is the radius of curvature in the orthogonal plane coming out of the page. The smaller radius, r, may also be written as $r = t/2 \cos \alpha$, where t is the thickness of the film.

If the growth front is straight (looking down at the film from above) then $R = \infty$. A top view of the growing crystal-liquid interface in Fig. 2(a) shows not that the growth front is straight, but, rather that it is scalloped. The growing front is made up of a series of curved sections joined at cusps. The grain boundaries between adjacent crystal domains meet the growth interface at the tip of the cusps, as indicated schematically in Fig. 2(b). Because of this scalloped structure, the convex radius of curvature R of each scallop is finite.

The structure we observe differs from the faceted structure seen in the beautiful photographs by Geis *et al.* (1). We have found that the structure of the crystallization front depends on the speed of growth. At low speeds, $\approx 10^{-3}$ cm/s, the growth front is scalloped, as shown in Fig. 2(a). At higher speeds, some fraction of the cusps become deep, V-shaped facets. As the growth speed increases, more of the cusps become faceted. At a speed of 3×10^{-2} cm/s, the entire growth front is faceted, similar to Fig. 6 of Ref. (1). The facets are <111> crystal faces which form because of the kinetic barrier against crystal growth on that face. When the sample scanning direction is reversed, the facets disappear, but the scalloped structure remains. The reversibility of the scalloped structure indicates that it is

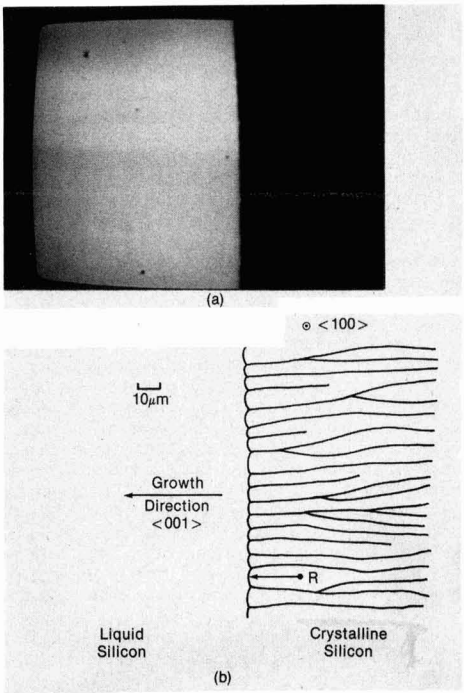


Fig. 2. (a) A video photograph of the crystal-liquid interface as seen in top view of the film. The crystal is the dark region on the right. Notice the presence of "scallops" on the growth front. The scallops join together at small pointed cusps, which are also seen on the growth front. (b) A schematic illustration of the grain boundary structure which might be visualized behind the growth front of Fig. 2(a). This grain boundary structure is typical of thin film crystal growth and has been observed in our experiments as well as others. It is implicit that the grain boundaries meet the growth front at the cusps. Note that *R* is the radius of curvature of a "scallop." A key question is: what is responsible for the nucleation of fresh grain boundaries in single-crystal material?

a minimum free energy configuration. In this article, we will explore mostly the regime of slow crystal growth. Nevertheless, we expect that many of the conclusions will apply equally well to more rapid crystal growth, where kinetic growth limitations begin to play a role.

In addition to the interfacial pressure due to the two radii of curvature r and R, Eq. [3], there is also a pressure term associated with the thermal gradient. Let z be the direction of crystal growth. The free energy associated with supercooling a layer of material of thickness dz is

$$\Delta G = \Delta S\,(T - T_m)\,dz\,dA \qquad [4]$$

where ΔS is the entropy of melting per unit volume, T_m is the melting temperature, and dA is the area of the growth front. Assuming a linear temperature gradient, $(T - T_m) = (z - z_m)dT/dz$, Eq. [4] may be rewritten as an equation for interfacial pressure

$$P = \Delta S \frac{dT}{dz}(z - z_m) \qquad [5]$$

where z_m defines the melting temperature isotherm. The pressure in Eq. [5] tends to push the crystal-liquid interface toward the position of the macroscopic melting point. That force is counteracted by the curvature pressure of the Young-Laplace Eq. [3], which pulls in the direction of supercooling. The actual amount of supercooling to be expected can be obtained by combining Eq. [3] and [5]

$$\Delta S \frac{dT}{dz}(z - z_m) = \gamma_{xl}\left[\frac{1}{r} + \frac{1}{R}\right] \qquad [6]$$

Equation [6] gives the balance between capillary pressure and thermal gradient forces. Of the two terms on the right-hand side, the most important is $1/r$, since it is largest. If the other term is temporarily neglected, and $r = t/2 \cos \alpha$, then Eq. [6] simplified to

$$\Delta S \frac{dT}{dz}(z - z_m) = \gamma_{xl}\frac{2 \cos \alpha}{t} \qquad [7]$$

Equation [7] shows that the equilibrium freezing point is depressed by surface tension forces in thin films. This may be seen even more clearly by substituting for the right-hand side of Eq. [7] using the Young-Dupre equation

$$\Delta S \frac{dT}{dz}(z - z_m)\,t = 2(\gamma_{xs} - \gamma_{ls}) \qquad [8]$$

Equation [8] shows that the difference in surface free energy on the substrate between crystal and liquid is balanced by the volume free energy of supercooling. The equilibrium freezing point of thin films is therefore depressed by surface energy contributions. In the next section, we describe an experimental determination of the magnitude of this effect.

Freezing Point Depression

Equation [8] shows that fluctuations in thickness t can lead to variations in the positioning of the crystal growth front. Because of the importance of this phenomenon, we have made direct experimental confirmation of the effect and its magnitude.

In our experiment, thin films of silicon are deposited on top of fused quartz substrates and capped with SiO_2. As shown in Fig. 3, the substrates are heated from below by CO_2 laser radiation, and the melt front is observed from above by a high power optical microscope. Since SiO_2 is opaque to CO_2 laser radiation, the silicon films are heated only indirectly by conduction. A knowledge of the thermal conductivity of quartz and the gaussian mode parameters of the laser beam permits a calculation of the radial temperature distribution on top of the substrate. We observe the effect of thickness variations on the microscopic position of the melting front and the freezing front of the thin film. In order to make a more precise measurement, we found it advantageous for both a thick film and a thin film to be present simultaneously. The thick film was 7000Å of polycrystalline Si deposited by chemical vapor deposition (CVD). This was capped by 2000Å of CVD SiO_2. A second thin silicon layer only 800Å thick was then deposited and patterned by photolithography into stripes 35 μm wide. The whole structure was then capped again by 2000Å of CVD SiO_2. A cross section of the final structure is shown in Fig. 4(b). By making the upper layer

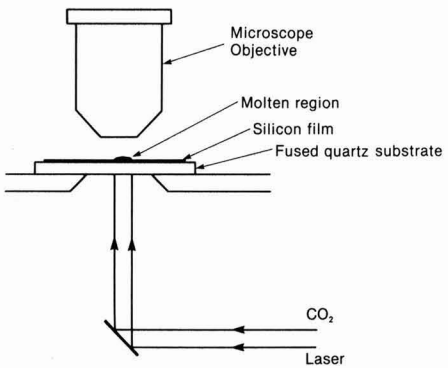


Fig. 3. The experimental arrangement used to produce the photographs in Fig. 2(a) and 4(a) was very simple. The CO_2 laser was fully absorbed in the fused quartz substrate, and the heating was by conduction.

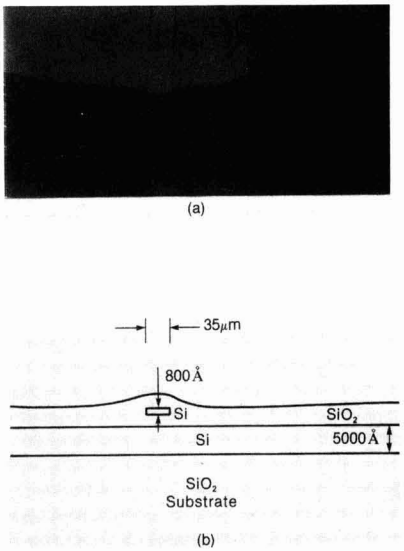


Fig. 4. (a) This photograph shows the depression of the freezing point in a thin film stripe in comparison to the thick film on which it rests. The dark region is crystalline silicon, and its crystallization front lags behind by approximately 1 K in the thin region relative to the thick region. The overall curvature is due to the round laser spot. (b) The cross section of the double layer structure of the film in Fig. 4(a). The Si, SiO_2, and Si layers were deposited in sequence. Then the thin silicon layer was patterned, and a final SiO_2 layer was applied.

in the form of narrow thin stripes, the position of the melt front in both the thin film and the thicker film can be observed simultaneously. Since the SiO_2 interlayer is only 2000Å thick, the temperature difference between the two films due to thermal radiation from the top surface is only 0.02 K, which is much smaller than the temperature shift we are seeking.

A micrograph of the position of the two crystallization fronts is shown in Fig. 4(a). The overall curvature of the growth front is indicative of the round melted spot produced by the laser beam. Away from the center of the melted region the temperature drops. From Fig. 4(a) the freezing point temperature is clearly lower in the thin stripe than in the thicker material beneath it.

The shift in the freezing point of the thin stripe relative to the thick film was a strong function of the thickness of the stripe. There was no shift if the stripe had the same thickness as the underlying thick film. As the stripe thickness was reduced, the temperature shift rose roughly as the reciprocal of thickness t, in good agreement with Eq. [7].

Owing to the opacity of the substrate to the CO_2 laser, strong thermal gradients are produced, and thermal conductivity rather than radiation is the dominant thermal transport mechanism. We present a calculation of the radial thermal conductivity of a disk heated by a gaussian laser beam in the Appendix to this article. The result of that calculation is that the radial temperature gradient is given by

$$\frac{dT}{dr} = \frac{2r}{\omega^2} \frac{K_{av}}{RK(T)} \Delta T \qquad [9]$$

where r is the radial distance from the center of the heated spot, ω is the gaussian radius of the laser beam, $K(T)/K_{av} = 1.17$ is the ratio of the thermal conductivity (9) of fused quartz at the melting point to the average thermal conductivity up to the melting point, $R = 2.02$ is the numerical value of an exponential integral, and ΔT is the overall temperature difference between the center of the heated spot and the edge of the fused quartz disk. The temperature gradient in Fig. 4(a) is approximately 0.15 K/μm.

As the molten zone in Fig. 4(a) was moved back and forth, for example by moving the sample relative to the laser beam, a hysteretic effect was observed, *i.e.*, the thickness-induced shift in freezing point was different from the corresponding shift in melting point. Upon freezing of a stripe about 800Å thick, the freezing point was depressed by 1 K relative to the thicker film beneath it. Upon remelting that same stripe, the melting point was virtually unchanged relative to the thicker film beneath it. Such hysteresis is common (2) in wetting angle measurements. An important distinction is therefore made between advancing wetting angles and receding wetting angles.

Such hysteresis is thought to be due to a change in surface energy of an interface due to its previous history. A freshly made crystal-SiO_2 interface has fairly high energy. After a period of time, there is probably significant reconstruction which lowers the surface energy. This may play the following role in our experiment. When the crystal advances into the liquid, it is forced to make a fairly energetic interface with the SiO_2, lowering the freezing point. When the liquid silicon advances into the crystal, it eliminates a low energy reconstructed crystal-SiO_2 interface. In that case, there is little or no melting point depression. Since we are interested in the crystallization of thin films, we will deduce the surface energies from freezing measurements rather than melting measurements.

Substituting the observed freezing point shift of thin stripes into Eq. [8] and using $\Delta S = 2.5$ J/K cm^3 for the entropy of melting, we obtain for $(\gamma_{xs} - \gamma_{ls})$ the value of 80-100 erg/cm^2. As far as we know, there are no previous measurements that this numerical value might be checked against.

There are two precautions that should be mentioned in making this measurement. At the melting temperature of silicon, amorphous SiO_2 is a glass with a finite viscosity and is not absolutely rigid. We found that it was necessary to complete the measurements fairly quickly (< 10s at the melt) in order to avoid severe thickness distortions of the thin stripe. The thickness was double-checked after freezing by profilometry and interferometry. The second precaution has to do with the initial melting of the polycrystalline film. As we have mentioned, there is little or no melting point depression of the crystallized film. Nevertheless, there is a large melting point depression of the as-deposited polycrystalline silicon. This is probably due to the excess free energy associated with the large grain boundary density in the as-deposited film. These observations, which monitor the initial polycrystalline film rather than the crystallized film, are not incorporated with the data in this paper. Only the results on the crystallized film are summarized in Table I.

Instability of the Crystallization Front

We have learned from the previous section that the freezing point is a function of film thickness. Equation [8] connects the film thickness with the position z of the crystal growth front. A local fluctuation in film thickness can cause the crystal growth front to move forward or backward locally relative to the rest of the front. The key question in thin film crystal growth is how to produce the largest possible single-crystal domains. In this

Table I. The hysteresis between freezing and melting is thought to be due to reconstruction of the crystalline silicon-SiO_2 interface, lowering its surface energy

	Temperature depression in an 800Å thick film relative to bulk ΔT	Surface energy difference with respect to SiO_2 substrate $(\gamma_{xs} - \gamma_{ls})$
Freezing	1 K	80-100 erg/cm^2
Melting	≈ 0 K	≈ 0 erg/cm^2

section, we suggest that locally concave regions of the growth front caused by local thickness fluctuations may be the birthplace of fresh subgrain boundaries. This would tend to limit the maximum possible crystal-domain size.

As indicated schematically in Fig. 2(b), and has been observed in virtually all thin film crystallization experiments, grain boundaries run together and recombine during crystal growth. Simultaneously, fresh grain boundaries initiate in previously single-crystal material. Both processes are shown schematically in Fig. 2(b), which is representative of typical (1, 10) photographs of grain boundary structure. It is the second of these two processes, the birth of fresh grain boundaries, which we must confront.

In the second section of this article, we mentioned the crystal grower's maxim (6) that the growth front should always be convex away from the crystal. It is very difficult to visualize how a fresh subgrain boundary may nucleate from single-crystal material. What we propose here is that concave regions of the growth front are the birthplace of fresh subgrain boundaries. In these regions, dislocations would tend to become locked into place and lead eventually to small-angle grain boundaries.

Although the growth front might be concave in top view, nevertheless, a cross-section view as shown in Fig. 1 would still remain convex, as demanded by the second wetting angle condition. Therefore, the actual three-dimensional geometry of that region is a saddle point. We are actually proposing that crystal growth at saddle points permits the initiation of small-angle grain boundaries.

As discussed in the third section and shown in Fig. 2(a), the growth front itself is scalloped, meeting the pre-existing subgrain boundaries at cusps. Each scallop represents a single crystal domain and has a finite radius of curvature R. This convex curvature tends to stabilize the domain structure and inhibit the birth of fresh subgrain boundaries. A local thickness fluctuation will have no effect unless it is deep enough to retard the growth front sufficiently to change it from convex curvature to locally concave. If the scallop radius of curvature R is very small, it would take an extremely deep and spatially localized thickness fluctuation to change it from convex to concave. Conversely, if the scallop is wide, representing a large crystal grain, the scallop radius of curvature R is large indicating a relatively straight growth front. In that case, even a small thickness fluctuation can change R from convex to concave. Thus, large grains are relatively unstable to grain boundary nucleation and they tend to split in two. Meanwhile, small grains tend to be stable and to avoid further subdivision. Therefore, the grain boundary structure represented in Fig. 2(b) tends to be stabilized around a certain crystal-domain width.

In conclusion, we have shown that thickness fluctuations could be responsible for the initiation of subgrain boundaries by producing locally concave regions of the growth front. A scalloped growth front, consisting of a series of domains of convex curvature, tends to be stable against growth front fluctuations. The balance between these two tendencies produces the actual grain structure that is observed.

Conclusions

The crystallization of thin liquid films demands that two wetting angle conditions be simultaneously satisfied: (*i*) regarding the liquid-vapor interface on the substrate, and (*ii*) regarding the crystal-liquid interface on the substrate.

The position of the crystal growth interface is determined by the balance between capillary forces, which tend to push the growth front to temperatures below the bulk freezing point, and thermal gradient forces which tend to pull the growth front toward the freezing point. The balance between these forces results in an equilibrium depression of the freezing point of thin films of about 1 K for an 800Å thick film. This implies a surface tension difference ($\gamma_{xs} - \gamma_{ls}$) of approximately 80-100 erg/cm^2.

The coupling between thickness and growth front position provides a mechanism for a crystal-growth instability. Thickness fluctuations can produce locally concave regions of the growth front, where subgrain boundaries could initiate. The convex curvature of the scalloped growth front counteracts this effect and tends to stabilize the crystal domain structure.

Acknowledgments

We gratefully acknowledge the assistance of Mike Schneider, Bob Weinberger, Harry Deckman, and John Dunsmuir. We also thank Professor Hank Smith for his comments on the manuscript.

Manuscript received April 23, 1984.

Exxon Research and Engineering Company assisted in meeting the publication costs of this article.

APPENDIX

In this Appendix, we derive the thermal gradient produced in a thermally conducting disk by a gaussian laser beam. The CO_2 laser is absorbed within 10 μm of the surface of fused quartz. In principle, both conduction and radiation could play a role in transporting this heat. For the t = 0.75 mm thickness fused quartz plates used in these experiments, radial thermal conduction plays the major role, owing to the strong thermal gradient induced by the laser beam with radiative heat loss being only a small correction.

The power per unit area absorbed from a gaussian laser beam is

$$P(r) = \frac{2P_o}{\pi\omega^2} \exp\left\{-\frac{2r^2}{\omega^2}\right\}$$

where ω is the gaussian radius of the laser beam, about 2.8 mm in our case. P is its total power, about 30W and r is the distance from the central axis of the beam. The total power inside a spot of radius r is

$$H(r) = P_o\left(1 - \exp\left\{-\frac{2r^2}{\omega^2}\right\}\right)$$

The thermal conduction equation in the radial direction is

$$H(r) = \frac{K(T)\, 2\pi r t\, dT}{dr} \qquad \text{[A-1]}$$

where $K(T)$ is the temperature dependent thermal conductivity of fused quartz. Integrating Eq. [A-1] yields

$$\frac{P_o}{2\pi t}\int_o^r \left(1 - \exp\left\{-\frac{2r^2}{\omega^2}\right\}\right)\frac{dr}{r} = \int_{T_{max}}^{T_{min}} K(T)\, dT \qquad \text{[A-2]}$$

The integral in Eq. [A-2] is an "Exponential Integral," which is (11) approximately $R = [\ln (2r^2/\omega^2) + 0.577]/2 = 2.02$ in our geometry. Let us write the difference between the temperature T_{max} at the center of the laser spot and T_{min} the temperature at the edge of the fused quartz disk as $\Delta T = T_{max} - T_{min}$. Then the integrated heat flow equation can be written

$$\frac{P_o}{2\pi t} = \frac{K_{av}\, \Delta T}{2.02} \qquad \text{[A-3]}$$

Simplifying [A-1] by taking $r < \omega$ we obtain

$$\frac{dT}{dr} = \frac{P_o}{2\pi t}\frac{2r}{K(T)\,\omega^2} \qquad \text{[A-4]}$$

Substituting [A-4] in [A-3]

$$\frac{dT}{dr} = \frac{2r}{\omega^2}\frac{K_{av}}{RK(T)}\Delta T$$

which is the same as Eq. [9] in the text.

REFERENCES

1. M. W. Geis, H. I. Smith, D. J. Silversmith, R. W. Mountain, and C. V. Thompson, *This Journal*, **130,** 1178 (1983).
2. A. W. Adamson, "Physical Chemistry of Surfaces," Third ed., John Wiley and Sons, New York (1976).

3. K. M. Kim, S. Berkman, H. E. Temple, and G. W. Cullen, *J. Cryst. Growth*, **50**, 212 (1980).
4. S. Berkman, Private communication.
5. T. J. Whalen and A. T. Anderson, *J. Am. Ceram. Soc.*, **58**, 396 (1975); E. Kuroda, M. Matsuda, and M. Maki, *Phys. Status Solidi A*, **48**, 105 (1978).
6. J. C. Brice, "The Growth of Crystals from Liquids," see especially p. 209, North-Holland, Amsterdam (1973).
7. D. P. Woodruff, "The Solid-Liquid Interface," see especially p. 31, Cambridge University Press, London (1973).
8. G. K. Celler, Private communication.
9. "Handbook of Thermophysical Properties of Solid Materials," Vol. III, "Ceramics," A. Goldsmith, T. E. Waterman, and H. J. Hirschhorn, Editors, see especially p. 893, Pergamon Press, New York (1961).
10. M. W. Geis, H. I. Smith, B. Y. Tsaur, J. C. C. Fan, D. J. Silversmith, and R. W. Mountain, *This Journal*, **129**, 2812 (1982).
11. M. Abramowitz and I. A. Stegun, "Handbook of Mathematical Functions," see especially p. 228, Dover, New York (1965).

Effect of Group V/III Flux Ratio on Lightly Si-Doped $Al_xGa_{1-x}As$ Grown by Molecular Beam Epitaxy

Y. Nomura, M. Mannoh, M. Mihara, S. Naritsuka, K. Yamanaka, T. Yuasa, and M. Ishii

Optoelectronics Joint Research Laboratory, Nakahara, Kawasaki, 211 Japan

ABSTRACT

Optical and electrical properties of lightly Si-doped $Al_xGa_{1-x}As$ ($x \approx 0.2$) layers grown by molecular beam epitaxy under various V/III flux ratios (1 to 4) and at various substrate temperatures (720°-780°C) have been studied by low temperature (≈4 K) photoluminescence and Hall measurements. Bound exciton (BE) peak intensity and Hall mobility increase with decreasing flux ratio and increasing substrate temperature. An excess reduction in the flux ratio causes the condensation of group III metals on epilayers. An optimum flux ratio was found to be 2.3 for the highest substrate temperature investigated here, 780°C. The peak intensity of the defect complex has been shown to be correlated with the growth conditions. It is suggested that the defect complex includes defects dominant under excess arsenic population. Reflection electron diffraction patterns from the growing $Al_{0.2}Ga_{0.8}As$ layers have been related to the growth conditions and the qualities of the epitaxial layers. A sample with the highest BE peak intensity and smooth surface has been grown with a metal-rich structure (3 × 1) present on the surface. A structure (1 × 1) has reproducibly been observed at intermediate amounts of group V/III composition on the surface between those for the (3 × 1) and the arsenic-stabilized (2 × 4) structures. Growth conditions which result in surfaces with a (1 × 1) structure are found to cause surface roughening on the epilayers.

Novel devices with $Al_xGa_{1-x}As$/GaAs heterostructures, such as the high electron mobility transistor and lasers with extremely low threshold current density, have been fabricated by virtue of excellent controllability of film thickness and doping profile of molecular beam epitaxy (MBE) (1, 2).

The quality of $Al_xGa_{1-x}As$ is important for high performance devices (3). The substrate temperature during growth affects optical properties of $Al_xGa_{1-x}As$ layers grown by MBE (4, 5). The group V/III flux ratio is also an important growth parameter because it influences formation of nonstoichiometric defects that act as nonradiative centers (6). From a view of device applications of MBE-grown $Al_xGa_{1-x}As$, in-depth understanding of the effect of the growth conditions on optical and electrical properties and surface morphologies is necessary, but little information has been available, particularly about the relation between the V/III flux ratio and the properties of $Al_xGa_{1-x}As$.

Reflection electron diffraction (RED) patterns have often been used as indicators of growth conditions for GaAs growths on (001)-plane GaAs substrates by MBE. By real-time observation of RED patterns, empirical relationships have been established between the relative and absolute incident fluxes of Ga atoms and arsenic molecules and the surface reconstruction as a function of the substrate temperature (7, 8). This has enabled conditions to be defined for growth of stoichiometric epitaxial GaAs. In contrast, the relation between RED patterns and the growth conditions for $Al_xGa_{1-x}As$ has not been reported.

In this paper, we report the effect of the V/III flux ratio and the substrate temperature on the optical and electrical properties of lightly Si-doped $Al_xGa_{1-x}As$ layers grown by MBE. The layers were characterized by low temperature (≈4 K) photoluminescence (PL) and Hall measurements. The results show that both the optical and electrical qualities improve with decreasing flux ratio and increasing substrate temperature. We have also investigated RED patterns from growing $Al_{0.2}Ga_{0.8}As$ layers and have related these patterns to the growth conditions and the qualities of the epitaxial layers. We have found that high quality $Al_xGa_{1-x}As$ layers with smooth surfaces are grown with the appearance of a (3 × 1) reconstruction pattern on the surface.

Experimental

The $Al_xGa_{1-x}As$ layers were grown on semi-insulating (001)-plane GaAs substrates in a Varian MBE/GEN II system. The structure of samples consisted of a 2 μm, undoped GaAs buffer; a 1 μm, Si-doped $Al_xGa_{1-x}As$ layer ($n \lesssim 1 \times 10^{16}$ cm^{-3}); and a 250Å, undoped GaAs cap layer. Elemental Al, Ga, As, and Si were used as source materials. All the $Al_xGa_{1-x}As$ layers were grown under group V/III flux ratios, $\gamma = As_4/(Al + Ga)$, from 1 to 4 by changing the arsenic pressure and at substrate temperatures from 720° to 780°C. The molecular beam fluxes were estimated from pressure readings of an ion gauge that could be placed at the growth position of the substrate (9). The Al and Ga pressures were determined before elevating the cell temperature of the arsenic source. The growth rate of $Al_xGa_{1-x}As$ layers was approximately 1 μm/h. The Al mole fraction, x, in the $Al_xGa_{1-x}As$ layers was determined from the energy of the BE emission and was found to be 0.19-0.25. The substrate temperature was measured by a spring-loaded thermocouple (W-Re) pressed to the rear of a Mo heating block, on which the substrate was mounted. The substrate temperature was also checked by a pyrometer with emissivity setting at 0.6. To assure the accuracy of the temperature, we observed the removal temperature of the native oxides from GaAs substrates and determined it to be about 590°C, which is close to previously reported datum, 580°C (10). Peak heights of the dominant residual gasses of $^{18}H_2O^+$ and $^{28}CO^+$ in the growth chamber, determined by a quadrupole mass analyzer, were always kept low during growth.

Table I. The electron concentrations and Hall mobilities of lightly Si-doped $Al_xGa_{1-x}As$ layers grown under various growth conditions

Sample	x	Substrate temp (°C)	Flux ratio	n (10^{15} cm^{-3})	μ (cm^2 V^{-1} s^{-1})
(a)	0.22	750	1.1	1.4	3870
(b)	0.21	750	1.4	1.4	1820
(c)	0.19	750	1.9	Highly resistive	
(d)	0.22	780	2.3	8.8	3520
(e)	0.23	780	2.8	9.4	3030
(f)	0.21	780	3.8	10	3010

PL measurements were made at liquid helium temperature (≈4 K). The 6471Å line of a Kr ion laser was used as the excitation source. The incident excitation intensity was approximately 1 W/cm^2. Luminescence was analyzed by a 1-m monochromator and detected with a cooled photomultiplier with an S-1 response. The slit width was adjusted to 100 μm or less, resulting in a resolution of less than 1Å.

Hall measurements (van der Pauw technique) were made on cloverleaf-shaped samples at room temperature.

Surface structures were examined *in situ* by glancing incidence reflection electron diffraction at an accelerating voltage of 8 keV.

Results and Discussion

Table I summarizes measured free electron concentrations and mobilities of the samples grown under various V/III flux ratios and at substrate temperatures, 750° and 780°C. Si atoms are dominantly incorporated as donors in MBE-grown $Al_xGa_{1-x}As$ layers. Although the Si cell temperature of 1050°C was maintained over the growths, the electron concentrations for the samples (d), (e), and (f) grown at 780°C were higher than those for the samples (a), (b), and (c) grown at 750°C, indicating a decrease of compensation of the donors by acceptors. The dependence of electron concentration on the flux ratio is small at 780°C. On the contrary, the samples grown at 750°C and under high flux ratios ($\gamma > 1.9$) were highly resistive, and Hall measurements were not possible. This is probably caused by a full depletion of the $Al_xGa_{1-x}As$ layer owing to low carrier concentrations (11).

The principal result shown in Table I is that lower flux ratios yield higher electron mobilities. The dependence of mobility on the flux ratio is small at 780°C, whereas the mobility for samples grown at 750°C decrease rapidly with the flux ratio. We attribute the reduction in the mobility of the relatively compensated sample (b) to the scattering of free electrons by increased space-charge regions at the heterostructure interface and the surface, as suggested by Stringfellow (12).

PL spectra in Fig. 1(a)-1(f) are from the samples (a) to (f) in Table I. The PL spectra show peaks due to the BE transition, the Si donor to carbon acceptor (DA) pair recombination, and the defect complex in order of increasing wavelength. These assignments have been made according to our previous work (13).

The half-widths of the BE peaks, 4 meV in Fig. 1(a) and 1(d), are comparable to the half-widths observed in high quality GaAs with a similar carrier concentration, indicating the high quality of the $Al_xGa_{1-x}As$ layers. The BE peak intensities are dominated by excitons bound to silicon donors. We assume that high BE peak intensities reflect high qualities of $Al_xGa_{1-x}As$ layers. It is known that the intensity of the BE peak relative to intensity of the other recombination peaks depends on doping concentration and the laser excitation (14). Since the doping and laser excitation were not changed in this work, only residual impurities and defects that act as nonradiative recombination centers and deep level emission centers will reduce the peak intensity.

We studied the BE intensity as a function of the flux ratio and the substrate temperature to determine the optimum growth condition. The results are shown in Fig. 2, including additional data with x ranging from 0.19 to 0.25. Figure 2 shows that the BE peak intensity increases with decreasing flux ratio and increasing substrate temperature. We note that the curve for T_s = 780°C exhibits a maximum at the flux ratio of 2.3. The degradation at the lower flux ratio, 1.2, is caused by condensation of group III metal on the surface due to extremely high evapora-

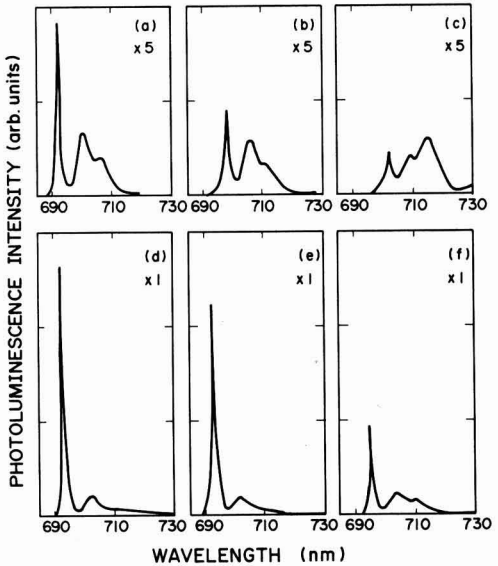


Fig. 1. PL spectra from the samples (a) to (f) from Table I

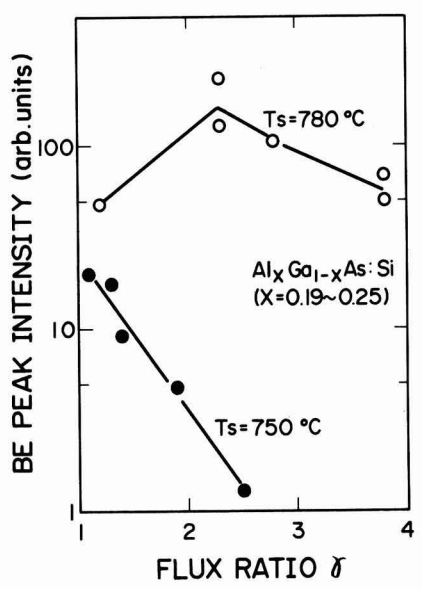


Fig. 2. BE peak intensity as a function of the flux ratio for substrate temperatures of 750° and 780°C.

tion of arsenic molecules. Thus, in order to obtain high quality $Al_xGa_{1-x}As$, the flux ratio should be adjusted to near 2.3. The results are consistent with the results of the Hall measurements; sample (d) among the samples grown at 780°C has the highest electron mobility. Samples grown at a substrate temperature, 720°C, and under flux ratios ranging from 1 to 2.5, had lower PL intensities than those in Fig. 1.

The carbon acceptor-related emission intensity increases monotonically with decreasing flux ratio and increasing substrate temperature, as shown in Fig. 1. This is mainly due to reduction of nonradiative centers, as indicated by BE intensity changes in Fig. 2. This reveals that the carbon incorporation rate is relatively insensitive to the growth conditions but gradually increases with decreasing flux ratio and increasing substrate temperature. The flux ratio dependence of the carbon incorporation rate agrees with the case of GaAs (15).

The defect complex luminescence in GaAs has been suggested to be associated with carbon impurities (16). However, the detailed nature of the defect complex has not been determined even in the case of GaAs (16). Figure 1 shows that the defect complex peak intensity closely correlates with the growth conditions; the intensity decreases with decreasing flux ratio and is not observed at high substrate temperatures and low flux ratios. A slight shift of the complex peak toward a higher energy with an increased excitation intensity is observed, indicating that the peak is due to DA pair recombination (17). It is natural to attribute the donor to Si. The acceptor could be attributed to defects dominant under excess arsenic conditions.

Figure 3 shows RED patterns in [$\bar{1}\bar{1}0$] azimuth from $Al_{0.2}Ga_{0.8}As$ surfaces which were grown at T_s equal to (a) 700°, (b) 750°, and (c) 780°C and under a constant flux ratio of 1.7. To determine the structures, RED patterns in [$1\bar{1}0$] azimuth were also observed. It was revealed that the RED patterns in Fig. 3 corresponded to (a) (2 × 4), (b) (1 × 1), and (c) (3 × 1) structures. However, it was difficult to distinguish diffraction features associated with centered structures in common with other RED work (8). Thus, we will refer only to primitive two-dimensional lattice structures. This does not mean that centered structures were not present, only that RED did not distinguish, for instance, c (2 × 8) and (2 × 4) (8).

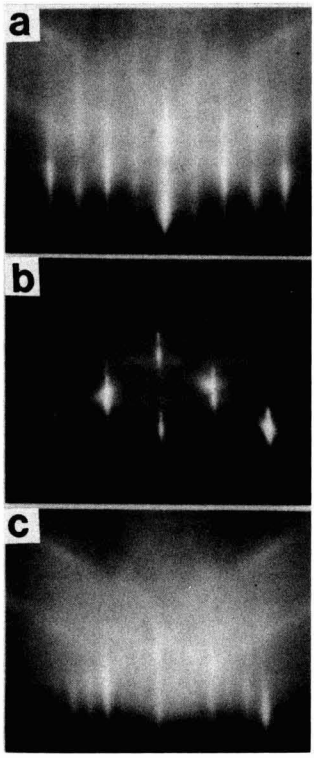


Fig. 3. RED patterns in [$\bar{1}\bar{1}0$] azimuth, for $Al_{0.2}Ga_{0.8}As$ surfaces growing at a rate of 1 μm/h and under a flux ratio of 1.7. The substrate temperatures are (a) 700°, (b) 750°, and (c) 780°C.

The structures shown in Fig. 3 could be reversibly changed from one to another by changing the substrate temperature only. These structures could be reproducibly observed from wafer to wafer. The metal-rich reconstruction (4 × 2) commonly observed for (001)-plane GaAs surfaces was not observed for $Al_xGa_{1-x}As$ surfaces in the temperature range studied here. It could, however, be observed by depositing Al and Ga without the arsenic flux on the (3 × 1) surface but immediately changed to a (1 × 1) structure due to the lack of surface mobility of metal atoms (18).

The structures shown in Fig. 3 also depend on the flux ratio. Figure 4 shows the map where the flux ratios that provide the structures are plotted as a function of the substrate temperature. In Fig. 4, points A and D correspond to the growth conditions of samples (a) and (d) in Table I that have the highest mobilities and BE peak intensities for substrate temperatures of 750° and 780°C, respectively. The surface of sample (d) is smooth, as is shown in Fig. 5a. The samples grown at the point marked by an asterisk, only 15% below the flux ratio at point D, exhibit matt surfaces due to condensation of group III metals. Therefore, we believe that excess arsenic evaporates during growth under the conditions corresponding to the (3 × 1) structure.

The (1 × 1) structure shown in Fig. 3(b) has not been observed for GaAs, but is common with surfaces including Al (18). The (1 × 1) structure suggests roughness of the surface. Figure 5 shows surface morphologies of $Al_xGa_{1-x}As$ layers ($x \approx 0.2$) grown under conditions of (T_s, γ) equal to 780°C, 2.3 (a), 750°C, 2.3 (b), and 720°C, 3.0 (c). These growth conditions are found, in Fig. 4, to be associated with (a) (3 × 1), (b) (1 × 1), and (c) (2 × 4) structures.

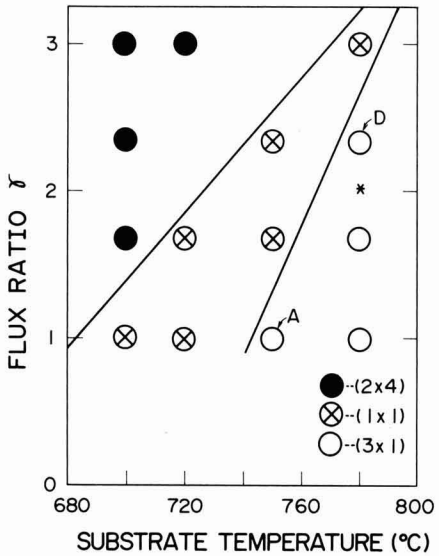


Fig. 4. Relationship between surface structures of growing $Al_{0.2}Ga_{0.8}As$ and growth conditions. The structures are ● = (2 × 4), ⊗ = (1 × 1), and ○ = (3 × 1), as indicated. Characters A and D indicate the growth conditions for samples (a) and (d) in Table I and Fig. 1. Samples grown under the condition marked by the asterisk exhibit matt surfaces.

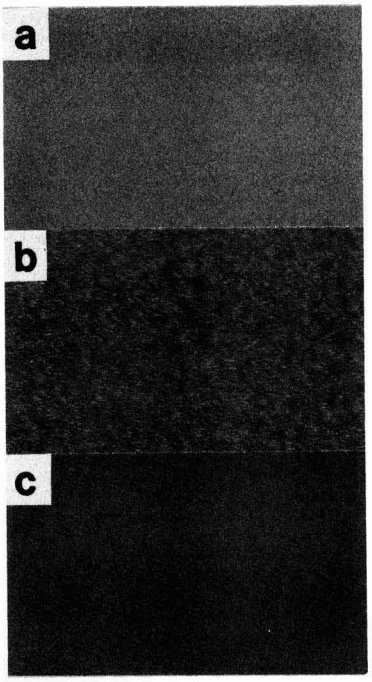


Fig. 5. Phase contrast photomicrographs of 1 μm $Al_xGa_{1-x}As$ ($x \approx 0.2$) layers grown under the conditions of (Ts, γ) equal to (a) (780°C, 2.3), (b) (750°C, 2.3), and (c) (720°C, 3.0).

The (2 × 4) and (3 × 1) structures correspond to the smooth surfaces, but surface roughening is observed for the (1 × 1) structure, as shown in Fig. 5. Morkoc *et al.* have demonstrated that the surface morphology first degrades and later improves with increasing substrate temperature from 620° to 700°C for $x > 0.4$ and a constant V/III flux ratio of 4 (19). Our results show that such degradation occurs also for $x \approx 0.2$ under flux ratios lower than 3. These results now manifest that the growth condition for high quality $Al_xGa_{1-x}As$ layers with smooth surfaces is rather critical and is restricted to the vicinity of point D in Fig. 4.

Conclusions

The effect of the growth conditions, V/III flux ratio, and substrate temperature on low temperature PL spectra and Hall mobilities of lightly Si-doped $Al_xGa_{1-x}As$ layers ($x \approx 0.2$) grown by MBE has been investigated. The Hall mobilitzy and PL intensity increase with decreasing flux ratio increasing substrate temperature. The optimum flux ratio, 2.3, was obtained at a substrate temperature of 780°C. The peak intensity of the defect complex has been shown to be correlated with the growth conditions. It is suggested that the defect complex includes defects dominant under excess arsenic population.

The RED patterns from the growing $Al_{0.2}Ga_{0.8}As$ layers have been investigated and related to the growth conditions and the qualities of the epitaxial layers. The results show that the sample with the highest BE peak intensity and smooth surface has been grown with the (3 × 1) structure present on the surface.

Acknowledgment

This work was supported by the Agency of Industrial Science and Technology, MITI, of Japan in the frame of the National Research and Development Project "Optical Measurement of Control Systems."

Manuscript submitted Jan. 9, 1984; revised manuscript received June 22, 1984. This was Paper 335 presented at the San Francisco, California, Meeting of the Society, May 8-13, 1983.

Optoelectronics Joint Research Laboratory assisted in meeting the publication costs of this article.

REFERENCES

1. T. Mimura, S. Hiyamizu, T. Fujii, and K. Nanbu, *Jpn. J. Appl. Phys.*, **19**, L225 (1980).
2. W. T. Tsang, *Appl. Phys. Lett.*, **40**, 217 (1982).
3. W. T. Tsang, *ibid.*, **33**, 245 (1978).
4. G. Wicks, W. I. Wang, C. E. C. Wood, L. F. Eastman, and L. Rathbun, *J. Appl. Phys.*, **52**, 5792 (1981).
5. V. Swaminathan and W. T. Tsang, *App. Phys. Lett.*, **38**, 347 (1981).
6. W. T. Tsang and V. Swaminathan, *ibid.*, **39**, 486 (1981).
7. A. Y. Cho, *J. Appl. Phys.*, **42**, 2074 (1971).
8. J. H. Neave and B. A. Joyce, *J. Cryst. Growth*, **44**, 387 (1978).
9. C. E. C. Wood, D. Desimone, K. Singer, and G. W. Wicks, *J. Appl. Phys.*, **53**, 4230 (1982).
10. A. Y. Cho, *Thin Solid Films*, **100**, 291 (1983).
11. A. Chandra, C. E. C. Wood, D. W. Woodard, and L. F. Eastman, *Solid State Electron*, **22**, 645 (1979).
12. G. B. Stringfellow, *J. Appl. Phys.*, **50**, 4178 (1979).
13. M. Mihara, Y. Nomura, M. Mannoh, K. Yamanaka, S. Naritsuka, K. Shinozaki, T. Yuasa, and M. Ishii, Paper presented at the 1983 Electronic Materials Conference, University of Vermont, Burlington, VT.
14. E. Hanamura, *J. Phys. Soc. Jpn.*, **28**, 120 (1970).
15. O. Tejayadi, Y. L. Sun, J. Klem, R. Fischer, M. V. Kleivn, and H. Morkoc, *Solid-State Commun.*, **46**, 251 (1983).
16. F. Briones and D. M. Collins, *J. Electron. Mater.*, **11**, 847 (1982).
17. R. Dingle, *Phys. Rev.*, **184**, 788 (1969).
18. W. I. Wang, *J. Vac. Sci. Technol. B*, **1**, 574 (1983).
19. H. Morkoc, T. J. Drummond, W. Kopp, and R. Fisher, *This Journal*, **129**, 824 (1982).

Behavior of the Evaporated WO_3 Film in Li-Salt PC Electrolytes

Nobuyuki Yoshiike, Yasuo Mizuno, and Shigeo Kondo

Matsushita Electric Industrial Company, Limited, Central Research Laboratory, Moriguchi, Osaka 570, Japan

ABSTRACT

Electrochemical properties of evaporated amorphous WO_3 films on conductive glass substrates have been studied in propylene carbonate electrolytes, and the degradation of the electrochromic activity of the WO_3 film on storage in the electrolyte and the prevention of the degradation of the film have been investigated by cyclic voltammetry. The WO_3 films have also been analyzed by XPS, SIMS, and FT-IR spectra. We have confirmed that the thermodynamic degradation is accelerated by H_2O and $LiClO_4$ in the electrolyte. It is proposed that: first, H_2O contributes to the change of WO_3 into $W(OH)_x$; second, Li^+ exchanges with the H^+ of $W(OH)_x$; and then these reactions result in the formation of Li_2WO_4; and, consequently, in the negative shift of the cathodic reaction potential of the film. We have also confirmed that the degradation is prevented by addition of an acid, such as H_3PO_4 or acrylic acid, to the $LiClO_4$ PC electrolyte and by using $LiBF_4$ as a supporting electrolyte in place of $LiClO_4$.

Since the important paper of Deb (1), there have been numerous studies (2-8) of the electrochromic (EC) properties of WO_3 films. Electrochromic displays (ECD) using WO_3 thin films will be classified into three groups: WO_3/liquid electrolyte, WO_3/solid electrolyte, and WO_3/dielectric layer systems. The WO_3/liquid electrolyte systems have been studied frequently, and EC properties of this system, such as response and memory, are superior to other systems. Faughnan (5) reported a WO_3/glycerol-H_2SO_4 liquid electrolyte system which had a fast response, but it had problems of the dissolution of the WO_3 film on the shelf and the corrosion of transparent electrode during color/bleach cycling (9). In order to overcome these problems, nonaqueous organic solvents have been investigated as the electrolyte solvent. Randin (9) reported that evaporated WO_3 film dissolved about 10% under storage for 90 days at 50°C in acetonitrile and dimethylformamide, etc., but the film dissolution was negligibly small in γ-butyrolactone and propylene carbonate (PC) under the same conditions. Furthermore, Li salts have been used in the supporting electrolytes as a cation source in place of protons because the mobility of Li is the next highest. Problems of the dissolution and the corrosion have been solved by using $LiClO_4$ PC electrolyte.

However, even in the WO_3/$LiClO_4$ PC system, the problem of degradation of electrochromic activity on storage for long time and/or cyclic drive still remained.

Schlotter *et al.* (10) reported that the degradation with cycling was caused by ion exchange between Li and protons of $W(OH)_x$. Morita *et al.* (11) also reported that the origin of the mechanism dominating the degradation was essentially the accumulation of Li in the film with SIMS data and Auger analysis.

In this paper, the mechanism of degradation of the WO_3 film on storage in Li salts-PC electrolytes and preventive methods for the degradation will be described.

Experimental

Preparation of WO_3 films.—WO_3 films were deposited by an electron beam evaporation method. WO_3 targets (99.99%) were supplied by Furuuchi Kagaku Company, Limited. The deposition rate was 4-5 Å/s the deposition angle was varied within 40° with a planetary rotation, and the substrate temperature was usually maintained at 80°C after keeping at 110°C for 5 min. The total gas pressure in the chamber during the evaporation process was controlled by N_2 gas-introduction method to be 5-6.5 × 10^{-2} Pa. Deposited WO_3 films were analyzed by electron diffraction and found to be amorphous. The packing density of the film calculated from film thickness and weight was 5.38 g/cm³, and the refractive index evacuated from the interference patterns of visible absorption and film thickness was 1.85.

The substrates were In_2O_3-coated glass (20 Ω/cm²) used for electrochemical measurements, XPS, and SIMS analyses, and Si wafers for IR spectra.

Electrochemical measurements.—Cyclic voltammetry measurements were performed with a potentiostat (Hokuto Denko, Model HA-301), which was supplied with voltage from a function generator (same company, Model HB-104). Coulometric measurements were performed with a coulomb meter (same company, HF-201). The WO_3 film thickness and area were 3000Å and 0.3 cm², respectively. The counterelectrode was a Pt plate, and the reference electrode was a saturated calomel electrode (SCE). The electrolytes were propylene carbonate (PC) solutions containing 0.3*M* $LiClO_4$. PC (the first grade, Wako Junyaku) was freshly distilled under vacuum, $LiClO_4$ (purity 99%, Mitsuwa Kagaku) was used. Ar gas was bubbled before measurements.

H_2O content in the electrolytes was checked in each case by the Karl-Fisher method with an Aquacounter (Hiranuma Seisakusho, Model AQ-3B), and these concentrations were typically 0.01-0.03*M*.

Analyses of WO_3 films.—IR spectra were taken with a FT-IR spectrometer (Nihon Denshi, Model JIR-40D). For these measurements, the film thickness of WO_3 on a Si wafer was 3000Å. Resolution was 8 cm^{-1}, and the number of sampling for one measurement was 400 cycles.

X-ray photoelectron spectroscopy (XPS) measurements were performed using a VG ESCALAB-5 electron spectrometer with Al Kα x-ray sources (10 kV, 20 mA). The energy resolution for the Ag $3d_{5/2}$ photopeak was 1.1 eV at 20 eV pass energy. The normal pressure in the analyzer chamber was below 6 × 10^{-8} Pa.

Three kinds of powder, WO_3 (99.9%, Mitsuwa Kagaku) H_2WO_4, and Li_2WO_4 (Superfine grade, Kanto Kagaku), were used for IR and XPS analyses as reference samples.

Secondary ion mass spectrometry (SIMS) measurements were performed using a CAMECA IMS-3F, the primary ion was O_2^+, and its ion beam current and energy were 500 nA and 8 keV, respectively.

Preparation of ECD cells.—ECD cells used for life test were constituted as follows: In_2O_3 (20 Ω/cm²)/WO_3 (3000Å, 1.9 cm²)/Li salt-PC electrolyte (2 ml)/carbon counterelectrode.

Results and Discussions

Degradation of WO_3 film in $LiClO_4$ PC electrolytes.—The electrochemical properties of the WO_3 films which were stored in 0.3*M* $LiClO_4$ PC electrolytes containing H_2O less than 0.01*M* were investigated. The storage experimental conditions were as follows: WO_3 films (3000Å thick, 0.3 cm²) evaporated on In_2O_3-coated glass were dipped completely in 1 ml of PC elctrolytes in glass tubes (8 mm diam), air in the tubes was replaced by Ar gas, the glass tubes were sealed by melting and stored at 70°C for various storage times. After storage, the WO_3 films were taken out from the tube and rinsed quickly with acetone, then dried with a N_2 gas blower. Cyclic voltammograms of the WO_3 films were measured in

freshly prepared 0.3*M* $LiClO_4$ PC electrolyte, and shown in Fig. 1.

In Fig. 1, the cathodic current is associated with the coloring process of the film and the anodic current following scan reversal with the bleaching process. The starting potential (E_c) where the cathodic current of the WO_3 film begins to flow, was about +360 mV *vs.* SCE for the as-deposited WO_3 film, whereas that of the WO_3 film stored in the $LiClO_4$ PC electrolyte for 20h at 70°C was +50 mV *vs.* SCE: that is, the starting potential (E_c) was drastically shifted to the negative side by storage in the $LiClO_4$ PC electrolyte at high temperature for relatively short time. The shift continued gradually with storage time after the initial drastic shift. These cathodic shifts result in the decrease of the injection charge in the coloration reaction, which contributes to the degradation of electrochromic activity of the WO_3 film. With respect to the anodic oxidation of the colored WO_3 film, the anodic reaction become fast with the storage.

The thickness of the WO_3 film stored in the electrolyte at 70°C for 500h (Fig. 1, curve 5) was confirmed to be unchanged, so that the dissolution of the WO_3 film was negligibly small. In spite of various kinds of WO_3 films having various E_c corresponding to the states of water in WO_3 (12 ~ 13), the potential shifts of these WO_3 films had the same tendency.

The relationship between the cathodic reaction potential shift and the quantity of $LiClO_4$ PC electrolyte in glass tubes was investigated and shown in Fig. 2. It is shown that the potential shift is increased with increase of amount of $LiClO_4$ PC electrolyte used for storage. Therefore, the degradation of electrochromic activity the WO_3 film is accelerated with the quantity of the electrolyte.

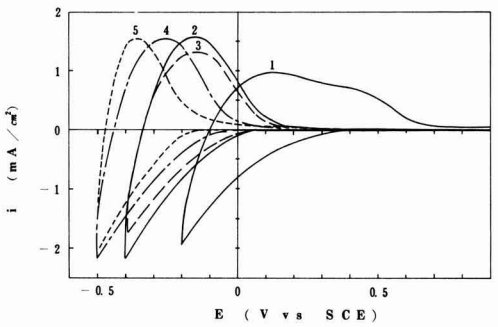


Fig. 1. Cyclic voltammograms for WO_3 films (3000Å, 0.3 cm^2) in the freshly prepared 0.3M $LiClO_4$ PC electrolyte at 0.2 V/s scan rate. 1: As-deposited. 2: Stored in 3 ml 0.3M $LiClO_4$ PC electrolyte at 70°C for 20h. 3: Stored for 43h. 4: Stored for 113h. 5: Stored for 500h.

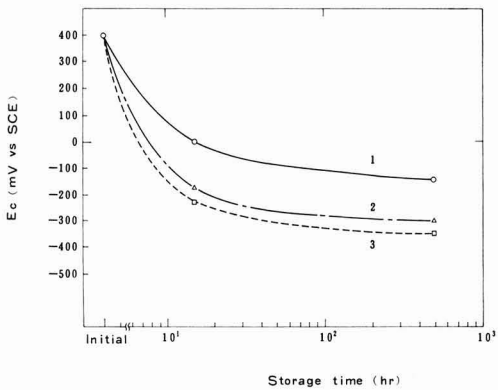


Fig. 2. Plots of starting potentials of cathodic reactions for WO_3 films at 0.2 V/s scan rate as a function of storage time at 70°C in 0.3M $LiClO_4$ PC electrolyte. The quantity of the electrolyte for the storage was (1) 0.3, (2) 3, and (3) 15 ml.

The decrease of the injected charge on storage in PC electrolyte also depends on the concentration of the supporting electrolyte ($LiClO_4$), as shown in Fig. 3. In Fig. 3, Q_w is the cathodic injected charge of the WO_3 film stored in PC electrolytes for 15h at 70°C under the condition of the cyclic voltammetry from +1.0V to −600 mV *vs.* SCE with 200 mV/s scan rate, and Q_{wo} is the initial value.

In actual electrochromic display (ECD) cells, the degradation of electrochromic activity on storage at high temperature was observed and is shown in Fig. 4. In Fig. 4, Q_w is the cathodic injected charge, which is proportional to coloration optical density under the condition of applied pulse voltage between the WO_3 working electrode and the counterelectrode for 1s and Q_{wo} is the initial value, after the aging of cells at 70°C for 15h.

We confirmed that the potential shift of the counterelectrodes of the cells after the aging was negligibly small, so that the degradation of the electrochromic activity of ECD cells on storage at high temperature corresponds to the cathodic potential shift of the WO_3 film. Therefore, the degradation is accelerated with H_2O in PC electrolyte, as shown in Fig. 4.

The temperature dependence of the degradation of ECD cells is shown in Fig. 5. In Fig. 5, there is a linear relationship between log (t) and $1/T$, where t is storage time and T is storage temperature (K).

However, the Arrhenius equation for the rate constant k is

$$k = Ae^{-E_a/RT} \quad [1]$$

where A is a constant, R is the gas constant, and E_a is the activation energy of the reaction.

If we postulate that the degradation function $f(x)$ is represented as follows

$$f(x) = kt \quad [2]$$

we obtain

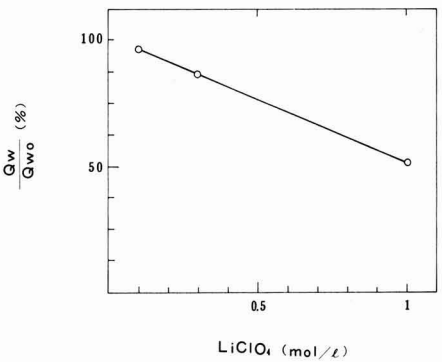


Fig. 3. Plots of Q_w/Q_{wo} as a function of $LiClO_4$ concentration in the electrolyte used for the storage.

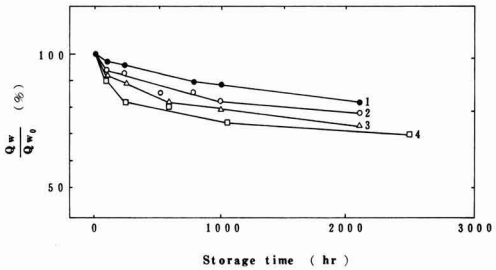


Fig. 4. Plots of Q_w/Q_{wo} of various ECD cells as a function of storage time at 60°C. H_2O concentration in the 0.3M LiClO, PC electrolyte was (1) 0.014, (2) 0.017, (3) 0.035, and (4) 0.072M.

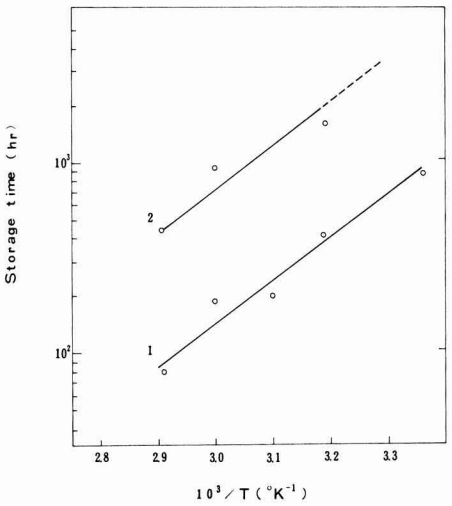


Fig. 5. $1/T$ dependence of lifetime of ECD cells until (1) the degradation Q_w/Q_{wo} = 0.9 and (2) Q_w/Q_{wo} = 0.8. Storage in 0.3M $LiClO_4$ + 0.036M H_2O PC electrolyte at 70°C.

$$t = \frac{1}{A} f(x)\, e^{E_a/RT} = ce^{E_a/RT} \qquad [3]$$

where $c = 1/A\, f(x)$, and $f(x)$ is equal to Q_w/Q_{wo}, so that we can obtain the quantity of E_a using Eq. [3]. From the slope in Fig. 5, E_a was estimated to be 4.5 kcal/mol.

Consequently, from the results mentioned above, the degradation of the electrochromic activity on storage corresponds to the cathodic potential shift, which is caused by some thermodynamic reactions of the WO_3 layer with Li content and H_2O content.

Mechanism of degradation.—SIMS of the WO_3 films stored in PC electrolyte were measured, and their depth profiles are shown in Fig. 6. In Fig. 6, sample 1 was only washed with PC solvent and acetone successively, and it was dried by a N_2 gas blower. Sample 2 was dipped in 0.3M $LiClO_4$ PC electrolyte containing 0.01M H_2O for 10s and then treated the same as sample 1. Sample 3 was stored in 0.3M $LiClO_4$ PC electrolyte containing 0.01M H_2O in a sealed glass tube for 120h at 70°C, and then treated the same as sample 1.

A molecular ion of OLi^+ (mass = 22) was used for the evaluation of Li content in WO_3 film, because of two facts that secondary ion intensities of Li^+ (mass = 7) and Li^+ isotope (mass = 6) were too strong to get a good linearity between Li content and the signal intensity, and that OLi^+ (mass = 23) overlaps Na (mass = 23).

Each signal intensity of OLi^+ was normalized using a signal intensity of a main component, W^+ isotope (mass = 184). It can be said that Li^+ permeates smoothly into the WO_3 layer by quick dipping in the electrolyte for relatively short time (10s) and accumulates homogeneously in the film, and that the permeation of Li into the layer is accelerated by storing at high temperature.

It was difficult to wash away Li in the layer, even in the case of sample 2.

In spite of smooth permeation of Li, ClO_4^- did not permeate into the WO_3 layer (see the Cl depth profiles in Fig. 6). From these results, the degradation of the WO_3 film would correspond to an accumulation of Li in the film, but the degradation will not directly depend on Li concentration in the film. This is because if the degradation which associates with the negative potential shift of the cathodic reaction potential were only caused by accumulation of Li in the film, the negative potential shift of the WO_3 film by quick dipping in $LiClO_4$ PC electrolyte would be observed, compared with the potential of the WO_3 film in non-Li electrolyte (*e.g.*, H_2SO_4 solution); but,

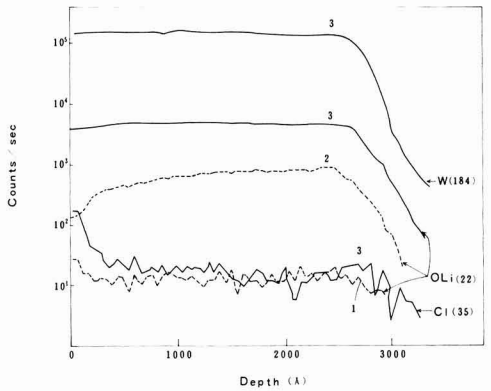


Fig. 6. SIMS depth profiles of WO_3 films. 1: No treatment. 2: Dipped in the $LiClO_4$ PC electrolyte for 10s. 3: Stored in the electrolyte for 120h at 70°C.

in fact, the cathodic reaction potential of as-deposited WO_3 film in $LiClO_4$ PC electrolyte is located at the more positive side about 250 mV more than that of same film in H_2SO_4 electrolyte (12). Therefore, it is better for the degradation process to be discussed on the basis of Li which can be separated from free Li^+, remains in the void of the film, and/or is injected in Xerogel structure (10) and has a interaction with W-O such as W-O-Li.

FT-IR spectra of the WO_3 film stored in 0.3M $LiClO_4$ PC electrolyte at 70°C for 500h in a sealed glass tube are shown in Fig. 7.

The O-H stretching broad peak at 3400 cm^{-1} was decreased, and the W-O stretching broad peak (~650 cm^{-1}) changed to a broad peak having several shoulders on storage.

IR spectra of WO_3, H_2WO_4, and Li_2WO_4 powders are shown in Fig. 8 for comparison.

From these results, IR spectrum of the degradated WO_3 film may be similar to a mixed spectrum of H_2WO_4 and a small amount of Li_2WO_4, so that it seems that the internal surface of $W(OH)_x$ would change to Li_2WO_4 on storage in $LiClO_4$ PC electrolyte.

The $W_{4f7/2}$ electrons binding energy and O_{1s} electrons binding energy of WO_3 film and powders of WO_3 derivatives were measured using XPS analysis and are shown in Fig. 9-10 with reference data of WO_3, H_2WO_4, and Li_2WO_4 (14-21).

The uncertainty of measured binding energy was estimated to be ±0.3 eV, and the electron escape depth of $W_{4f7/2}$ electrons was estimated approximately to be 20Å by Penn's equations (22).

The $W_{4f7/2}$ and O_{1s} electrons binding energies of the WO_3 film which was stored in air for 144h after the evaporation will be in agreement with those of WOOH (14) within the experimental error. The surface of the WO_3 film before dipped in PC electrolyte will be a $W(OH)_x$ structure as shown in Fig. 9, 10 and Ref. (10, 12).

The $W_{4f7/2}$ electrons binding energy of the WO_3 film stored in 0.3M $LiClO_4$ PC electrolyte for 144h at 70°C is essentially identical with that of WO_3 and Li_2WO_4 powder measured in our laboratory. It can be said that the surface of the degradated WO_3 film is constructed with WO_3 or Li_2WO_4: however, if we consider the SIMS and IR experimental results, the surface of the degradated WO_3 film will be constructed with Li_2WO_4.

Consequently, it seems reasonable to assume that the surface state of the WO_3 film is changed by the H-Li ion exchange in $LiClO_4$ PC electrolyte such as in the following thermodynamic reaction

$$\text{W-OH} + \text{Li}^+ \rightarrow \text{W-O Li} + \text{H}^+ \qquad [5]$$

and this exchange reaction will result in the formation of Li_2WO_4.

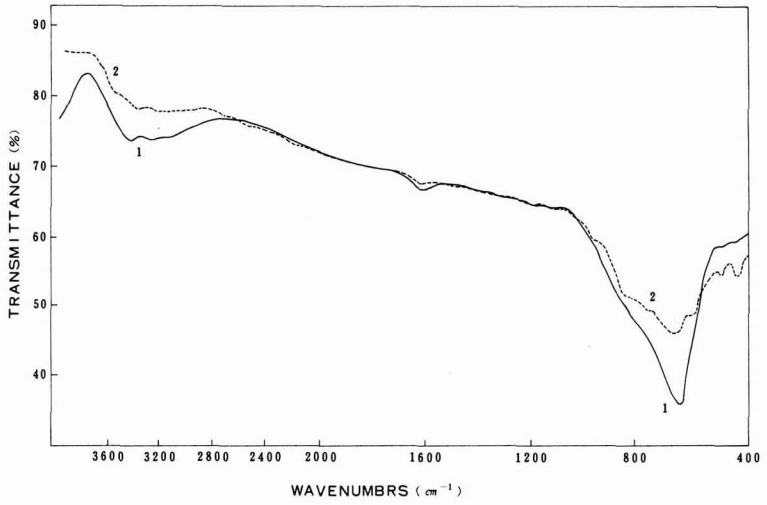


Fig. 7. FT-IR spectra of WO_3 films (1) as-deposited and (2) stored in 0.3M $LiClO_4$ PC electrolyte at 70°C for 500h.

Prevention of degradation.—Cyclic voltammograms of WO_3 films which were stored in various kinds of electrolytes in sealed glass tubes were measured and are shown in Fig. 11-12. The storage experimental conditions were as follows: WO_3 films (3000Å thick, 0.3 cm^2) on In_2O_3-coated glass were dipped completely in PC electrolytes in glass tubes (8 mm diam), air in the tubes was replaced by Ar gas, the glass tubes were sealed by melting, and then stored at 70°C for various storage times. After storage, the WO_3 films which were taken out from the electrolyte were rinsed quickly with acetone and dried with a N_2 gas blower.

In Fig. 11, the starting potential (E_c) of the cathodic reduction of the WO_3 film was shifted to negative side about 300 mV on storage in 0.3*M* $LiClO_4$ PC electrolyte at 70°C for 1000h, but that of the WO_3 film stored in 0.3*M* $LiClO_4$ PC electrolyte containing 0.01 volume percent (v/o) H_3PO_4 under the same condition was scarcely shifted and the degradation of electrochromic activity was not observed.

In Fig. 12, the starting potential (E_c) of the cathodic reduction of the WO_3 film stored in 0.3*M* $LiClO_4$ PC electrolyte containing 5 v/o acrylic acid was also scarcely shifted to negative side.

From these results, the degradation of the WO_3 film in Li salt PC electrolyte, corresponding to the ion exchange between Li and H of $W(OH)_r$, will be prevented by the addition of an acid to the electrolyte. However, propylene carbonate is easy to decompose under coexistence of acids; therefore, it is undesirable to add a strong acid to the electrolyte.

Furthermore, we have found that the degradation of the WO_3 film is also prevented by using $LiBF_4$ as a supporting electrolyte.

Cyclic voltammograms of the WO_3 films stored in 0.3*M* $LiBF_4$ PC electrolyte containing 0.01*M* H_2O in sealed glass tubes at 70°C were measured and are shown in Fig. 13. The storage experimental conditions were as same as mentioned above.

In Fig. 13, compared to the case of $LiClO_4$ supporting electrolyte, as shown in Fig. 11, curve 2, the starting potential (E_c) of the cathodic reduction of the WO_3 film was rarely shifted to negative side by the storage at 70°C for 1000h. Moreover, there was no observation of gas evolution by decomposition of PC solvent.

The preventive effect on the degradation of the WO_3 film in $LiBF_4$ PC electrolyte can be attributed to the facts that $LiBF_4$ is especially effective in this regard, as can be

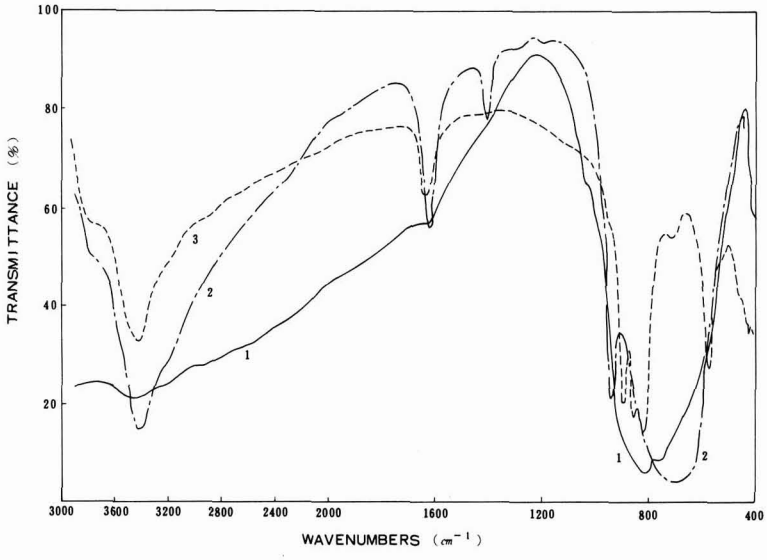


Fig. 8. FT-IR spectra of (1) WO_3 powder, (2) H_2WO_4 powder, and (3) Li_2WO_4 powder.

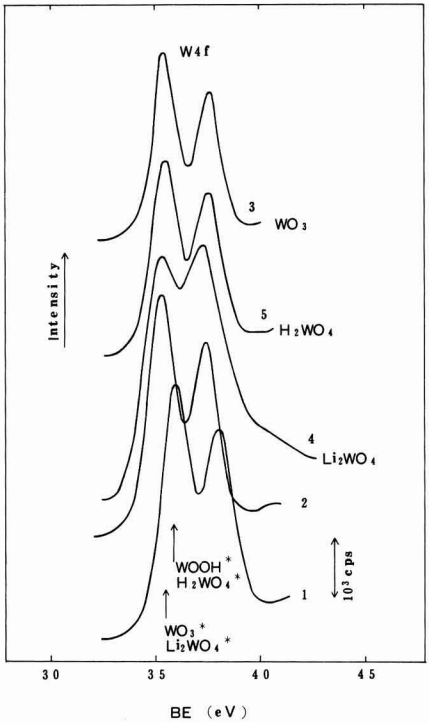


Fig. 9. XPS spectra of $W_{4f7/2}$. 1: As-deposited WO_3 films. 2: Stored in 0.3M $LiClO_4$ PC electrolyte at 70°C for 144h. 3: WO_3 powder. 4: Li_2WO_4 powder. 5: H_2WO_4 powder. Reference data (14-21).

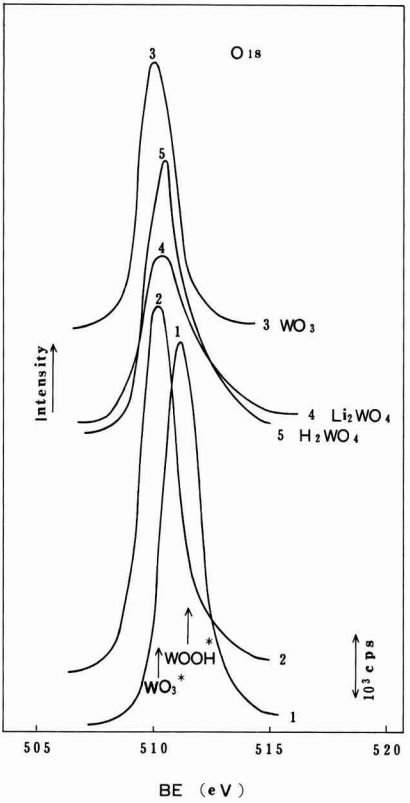


Fig. 10. XPS spectra of O_{1s} of the same samples as shown in Fig. 9. Reference data (14-21).

seen from aqueous PH determination (generally acidic, if hydrolyzed) (23), and that $LiBF_4$ is able to dissociate H^+ from H_2O containing in the electrolyte.

An FT-IR spectrum of the WO_3 film on a Si wafer stored in 0.3*M* $LiBF_4$ PC electrolyte in a sealed glass tube at 70°C for 500h is shown in Fig. 14 with reference IR data.

In Fig. 14, showing long-time storage in $LiBF_4$ PC electrolyte, the shoulder of O-H stretching broad peak at 3400 cm^{-1} was decreased as same as in $LiClO_4$ PC electrolyte, while the W-O stretching broad peak at 650 cm^{-1} was rarely changed. WO_3 film in $LiBF_4$ PC electrolyte was more stable than in $LiClO_4$ PC electrolyte.

A SIMS depth profile of the WO_3 films stored in 0.3*M* $LiBF_4$ PC electrolyte is shown in Fig. 15.

Sample 1 was merely dipped in 0.3*M* $LiClO_4$ PC electrolyte for 10s; sample 2 was stored in 0.3*M* $LiBF_4$ PC electrolyte for 120h at 70°C; and sample 3 was stored in 0.3*M* $LiClO_4$ PC electrolyte for 120h at 70°C.

Molecular ion of OLi^+ (mass = 22) was used for the evaluation of Li content in WO_3 films, and each signal inten-

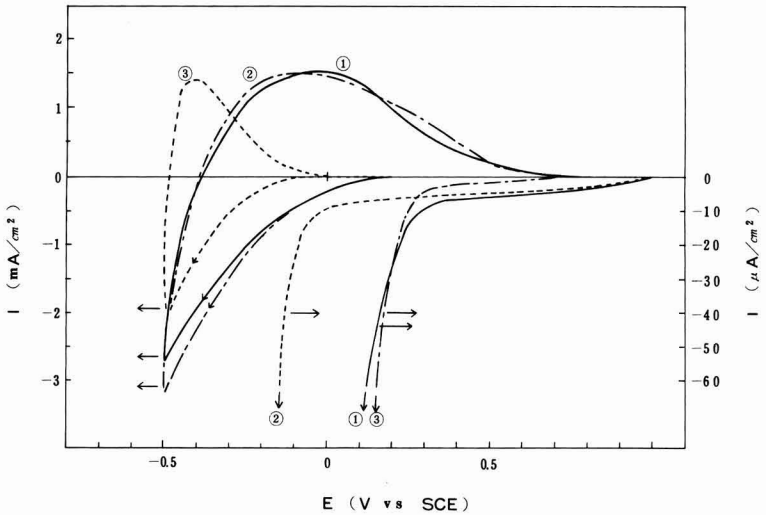


Fig. 11. Cyclic voltammograms for WO_3 films (3000Å, 0.3 cm^2) in freshly prepared 0.3M $LiClO_4$ PC electrolyte at 0.2 V/s scan rate. 1: As-deposited. 2: Stored in 1 ml 0.3M $LiClO_4$ + 0.3M H_2O PC electrolyte at 70°C for 1000h. 3: Stored in 1 ml 0.3M $LiClO_4$ + 0.01 v/o H_3PO_4 PC electrolyte at 70°C for 1000h.

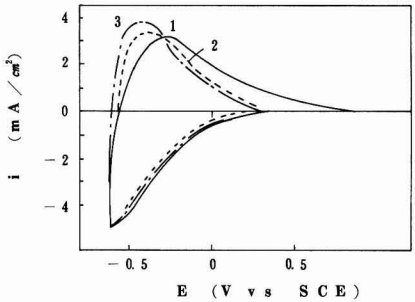


Fig. 12. Cyclic voltammograms for WO_3 films (3000Å, 0.3 cm²) in freshly prepared 0.3M $LiClO_4$ PC electrolyte at 0.2 V/s scan rate. 1: As-deposited. 2: Stored in 0.3 ml 0.3M $LiClO_4$ + 5 v/o acrylic acid PC electrolyte at 70°C for 500h 3: Stored for 1000h.

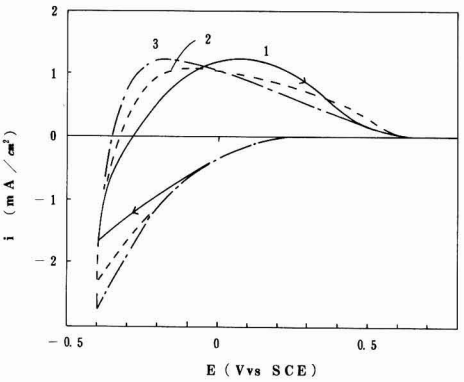


Fig. 13. Cyclic voltammograms of WO_3 films (3000Å, 0.3 cm²) in freshly prepared 0.3M $LiClO_4$ PC electrolyte at 0.2 V/s scan rate. 1: As-deposited. 2: Stored in 0.3M $LiBF_4$ + 0.01M H_2O PC electrolyte at 70°C for 500h. 3: Stored for 1000h.

sity of OLi was normalized using a signal intensity of a main component W^+ (mass = 184).

Li content of the WO_3 film stored in $LiBF_4$ PC electrolyte was about one-half smaller than that of the case of $LiClO_4$ (Fig. 15). Considering the free Li^+ remaining in the void of the WO_3 film by merely dipping in $LiClO_4$ PC electrolyte (Fig. 15, curve 2), it can be assumed that the ion exchange between Li^+ and H^+ of $W(OH)_r$ is depressed in $LiBF_4$ PC electrolyte.

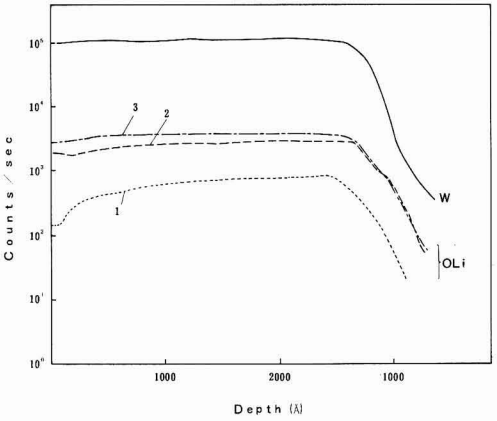


Fig. 15. SIMS depth profiles of WO_3 films. 1: Dipped in 0.3M $LiClO_4$ PC electrolyte for 10s. 2: Stored in 0.3M $LiBF_4$ PC electrolyte for 120h at 70°C. 3: Stored in 0.3M $LiClO_4$ PC electroloyte for 120h at 70°C.

In actual ECD cells, the degradation of electrochromic activity on storage at 70°C was investigated and is shown in Fig. 16.

The electrolytes of samples 1 and 2 were 0.3*M* $LiBF_4$ and 0.3*M* $LiClO_4$ PC solutions, respectively. The quantities of cathodic injected charge into the WO_3 films were measured under the condition of applied pulse voltages between the WO_3 electrode and the counterelectrode for 1s. Q_{wo} is the initial value of the quantity of cathodic injected charge into the WO_3 film after aging for 15h at 70°C, and Q_w is that of stored for various storage times after aging, in which Q_w is approximately proportional to coloration optical density. The potential drift of counterelectrode of the cells on storage at 70°C for 1000h after the aging was negligibly small. In Fig. 16, it is confirmed that the degradation of the electrochromic activity of ECD cells using $LiBF_4$ as the supporting electrolyte was remarkably small, compared with that of using $LiClO_4$.

The temperature dependence of the degradation of the ECD cells is shown in Fig. 17. There are linear relationships between log t and $1/T$, where t is storage time until $Q_w/Q_{wo} = 0.9$, and T is storage temperature (K). From the slopes of straight lines in Fig. 17, the activation energies of the degradation reaction of ECD cell using $LiBF_4$ PC electrolyte and $LiClO_4$ PC electrolyte were estimated 7.0 and 4.5 kcal/mol, respectively. Therefore, $LiBF_4$ PC sys-

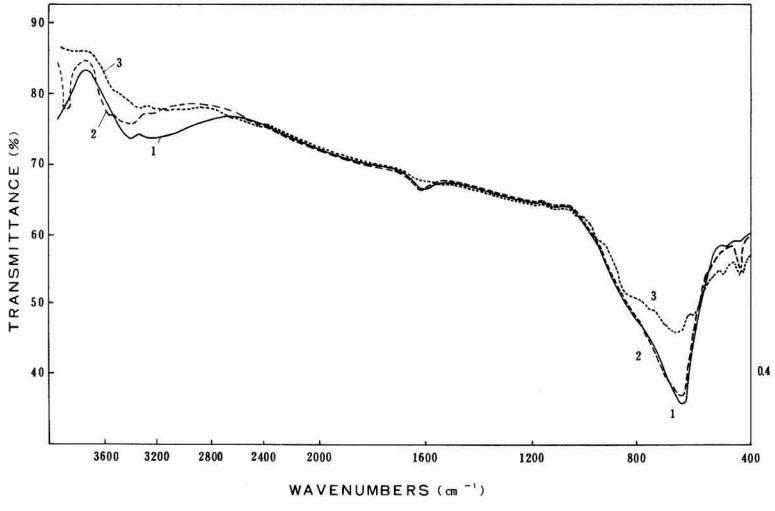


Fig. 14. FT-IR spectra of WO_3 films on Si wafers. 1: As-deposited. 2: Stored in 0.3M $LiBF_4$ PC electrolyte at 70°C for 500h. 3: Stored in 0.3M $LiClO_4$ PC electrolyte at 70°C for 500h.

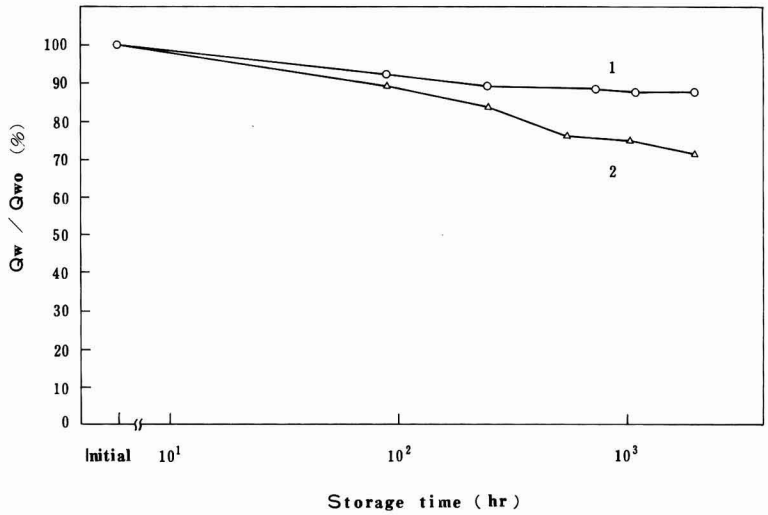


Fig. 16. Plots of Q_w/Q_{wo} of ECD cells as a function of storage time at 70°C in the electrolyte. 1: 0.3M $LiBF_4$ + 0.2M H_2O. 2: 0.3M $LiClO_4$ + 0.3M H_2O.

tem has a larger amount of the activation energy for the degradation reaction corresponding to the ion exchange between Li^+ and H^+ of $W(OH)_r$ than that of $LiClO_4$ PC system. It is, therefore, preferable to use $LiBF_4$ as the supporting electrolyte for ECD cells using WO_3 film.

Conclusion

The cathodic reduction potential of the evaporated WO_3 film is shifted to negative side on storage in $LiClO_4$ PC electrolyte, and this causes the degradation of the electrochromic activity of the film.

The degradation depends not only on the H_2O concentration, but also on the $LiClO_4$ supporting electrolyte concentration.

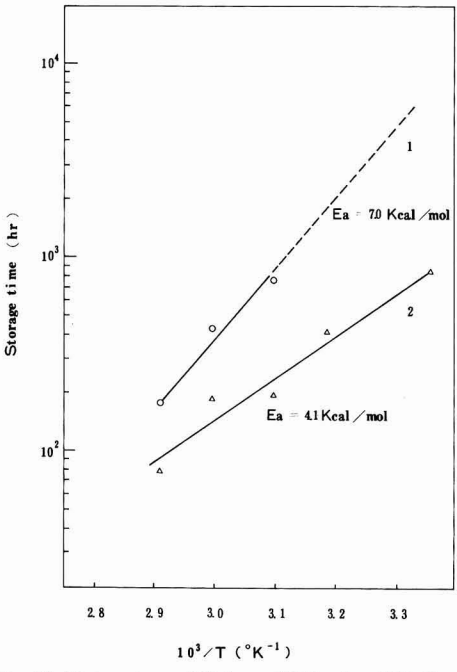


Fig. 17. 1/T dependence of lifetimes of ECD cells until Q_w/Q_{wo} = 0.9. Electrolyte, (1) 0.3M $LiBF_4$ + 0.02M H_2O and (2) 0.3M $LiClO_4$ + 0.3M H_2O.

It seems reasonable, for the degradation, to assume that H_2O in the electrolyte contributes at first to the change of WO_3 into $W(OH)_r$ and then Li^+ exchanges with the H^+ of $W(OH)_r$ and that the exchange results in the formation of Li_2WO_4.

The degradation of the WO_3 film in Li salt PC electrolyte caused by the ion exchange between Li^+ and H^+ of $W(OH)_r$ can be prevented by the addition of acids and/or acidity compounds (*e.g.*, $LiBF_4$) to PC electrolyte; however, an acid is undesirable for an additional agent because it causes decomposition of PC, then $LiBF_4$ is a preferable supporting electrolyte to prevent not only the ion exchange, but also the decomposition of PC.

Acknowledgments

We are grateful to Dr. E. Hirota, the Assistant-Director of Central Research Laboratory for permission to publish the paper and for encouragement. We thank S. Kohiki, K. Tsukamoto, and M. Kamikawaji, members of TechnoResearch Department, for performing the XPS, SIMS, and FT-IR observations and for helpful discussions.

Manuscript submitted Jan. 9, 1984; revised manuscript received June 1, 1984.

Matsushita Electrical Industrial Company, Limited assisted in meeting the publication costs of this article.

REFERENCES

1. S. K. Deb., *Philos. Mag.*, **27,** 801 (1973).
2. R. Hurditch, *Electron Lett.*, **11,** 142 (1975).
3. R. S. Crandall and B. W. Faughnan, *Appl. Phys. Lett.*, **26,** 120 (1975).
4. I. F. Chang, B. L. Gilbert, and T. I. Tan, *This Journal*, **122,** 955 (1975).
5. B. W. Faughnan, R. S. Crandall, and P. M. Heyman, *RCA Rev.*, **36,** 177 (1975).
6. B. W. Faughnan, R. S. Crandall, and A. M. Lampert, *Appl. Phys. Lett.*, **27,** 275 (1975).
7. R. S. Crandall and B. W. Faughnan, *ibid.*, **28,** 95 (1976).
8. N. H. Hersh, W. E. Kramer, and J. H. McGee, *ibid.*, **27,** 646 (1975).
9. J. P. Randin, *J. Electro. Mater.*, **7,** 47 (1978).
10. P.Schlotter and L. Pickelmann, *ibid.*, **11,** 207 (1982).
11. H. Morita and H. Washida, *Oyo Butsuri*, **51,** 488 (1982).
12. N. Yoshiike and S. Kondo, *This Journal*, **130,** 2283 (1983).
13. N. Yoshiike and S. Kondo, *ibid.*, **131,** 809 (1984).
14. T. L. Barr, *J. Phys. Chem.*, **82,** 1801 (1978).
15. P. Biloen and G. T. Pott, *J. Catal.*, **30,** 169 (1973).
16. C. D. Wagner, D. A. Zatko, and R. H. Raymond, *Anal. Chem.*, **52,** 1445 (1980).
17. T. L. Barr, *J. Phys. Chem.*, **82,** 1801 (1978).
18. G. E. Mcguire, G. K. Schweitzer, and T. A. Carlson, *Inorg. Chem.*, **12,** 2450 (1973).
19. C. D. Wagner, *J. Vac. Sci. Technol.*, **15,** 518 (1978).

20. R. J. Cotton and J. W. Rabalais, *Inorg. Chem.*, **15,** 236 (1976).
21. K. T. Ng and D. M. Hercules, *J. Phys. Chem.*, **80,** 2094 (1976).
22. D. R. Renn, *J. Electron. Spectro. Relat. Phenom.*, **9,** 26 (1976).
23. J-P. Gabano, "Lithium Balleries," p. 27, Academic Press, New York (1983).

The Etching of InP in HCl Solutions: A Chemical Mechanism

P. H. L. Notten

Philips Research Laboratories, 5600 JA Eindhoven, The Netherlands

ABSTRACT

The etch rate of InP in solutions of high HCl concentration was shown to be independent of the applied potential in a wide potential range negative with respect to the flatband value. Dissolution of the solid led to the formation of PH_3. The etch rate, which was not mass-transport controlled, was first order in molecular HCl concentration. The results lead us to conclude that, in HCl etchants, InP is dissolved by a purely chemical mechanism. The influence of chemical etching on the anodic behavior of InP in these electrolytes is described.

Aqueous etching of III-V materials is often an important step in device technology (1, 2). While anodic etching is sometimes used (3), the necessity of making electrical contact to slices of small dimensions is invariably a disadvantage. Methods not involving an external current or voltage source are therefore favored (1, 2). Such methods can be divided into two classes: "electroless" and "chemical" dissolution. Electroless dissolution involves two separate potential-dependent electrochemical reactions: the oxidation of the solid and the reduction of an oxidizing agent. The principle is illustrated in Fig. 1 for the etching of a p-type III-V semiconductor (4). For these materials, holes in the valence band are required at the surface for bond breaking. As a result, the anodic dissolution current increases at potentials close to the flatband value (V_{FB}) as shown in curve (a). For electroless dissolution, holes must be supplied by an oxidizing agent in solution. If the distribution function of the oxidizing agent overlaps with the valence band of the semiconductor, then reduction via hole injection into the valence band is expected [curve (b)]. Here, we have assumed that the reduction reaction is diffusion controlled, *i.e.*, the cathodic partial current is independent of potential. Curve (c) represents the total measured current-potential curve in the electrolyte containing the oxidizing agent. At the rest potential, the anodic and cathodic partial currents are equal. If the potential is changed from this value using an external source, then the etch rate of the semiconductor will, of course, also change.

Gerischer and co-workers (5, 6) have shown that semiconductors can be dissolved by a purely chemical mechanism, which is characterized by the absence of any influence of the surface carrier concentration on the etch rate. Such behavior is observed with bifunctional agents, such as halogen or H_2O_2 molecules, which are capable of forming two new bonds with the semiconductor surface more or less simultaneously. For GaAs dissolution in bromine solution, for example, they suggest a coordinated reaction sequence involving the breaking of Ga-As and Br-Br bonds and the simultaneous formation of Ga-Br and As-Br bonds.

Etchants based on HCl are widely used for InP semiconductor devices (7, 8). The presence of other acids in the HCl solution has a significant influence on the etch rate. However, InP does not dissolve in conventional etchants involving simple oxidizing agents. In order to resolve the question of the dissolution mechanism, we studied both the etching and electrochemistry of p-InP in various HCl solutions.

Experimental

The p-type InP slices used in this work were made from liquid-encapsulated Czochralski material with a carrier density in the range 1-2 × 10^{18} cm^{-3}. The (100) face was exposed to the solution. The diameter of the electrodes was 3 mm, with the exception of the InP rotating disk, which had a diameter of 4 mm.

The current-potential measurements were carried out under potentiostatic control in a conventional cell using a Pt counterelectrode and a saturated calomel electrode (SCE) as reference. All potentials are given with respect to this SCE. A Solartron 1172 Frequency Response Analyser was employed for determining the flatband potentials. All impedance measurements were carried out at a frequency of 10 kHz.

The total dissolution rate of InP at various potentials was determined analytically by measuring the indium concentration in the etching solution by induced-coupled-plasma (ICP) emission spectrometry. The etchant was passed over the InP electrode, which was mounted in a glass microelectrochemical flow cell as described by Haroutiounian *et al.* (9). Indium concentrations as low as 0.5 ppm could be determined with a relative accuracy of about 5%. An LKB Varioperpex peristaltic pump was used to pump the solution through the flow cell. The flow rate of the solution, mainly deter-

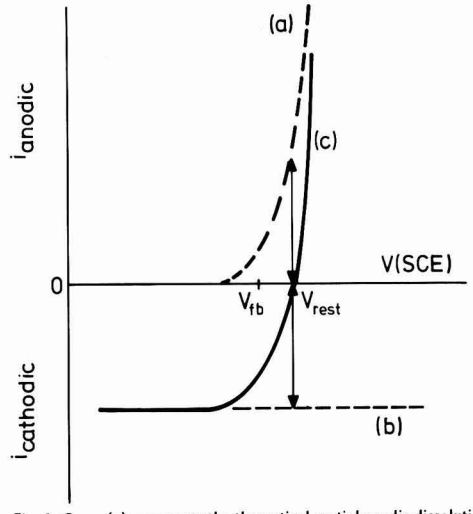


Fig. 1. Curve (a) represents the theoretical partial anodic dissolution current of a p-InP electrode in the dark, and curve (b) the diffusion-limited reduction current of an oxidizing agent as a function of the potential. Curve (c) gives the total current-potential curve.

mined by the lower limit of the indium detection, was in the range from 0.2 to 1.0 ml/min.

The gas was analyzed qualitatively using the color-detector tube method ("Dräger" tube), which in our case gave a color reaction specific for phosphine. A gas burette was used for the quantitative gas analysis.

Results

Flow-cell experiments.—In Fig. 2, results are given for the potentiostatic etching of p-InP in the dark in HCl solutions. Figure 2a shows the current-potential curves of this electrode in 3*M* and 6*M* HCl. At negative potentials the current is very low in both cases. In the vicinity of the flatband potential (V_{FB} = 0.73V *vs.* SCE) the anodic current increases, as expected. It should be noted that the anodic curve for the 6*M* HCl solution is shifted slightly in the cathodic direction with respect to that for the 3*M* solution.

The total dissolution rate, according to the ICP analysis, is shown in Fig. 2b as a function of the potential. For the 3*M* HCl solution, the dissolution rate follows the current closely. At negative potentials the etch rate (r_t) is very low and increases considerably near the flatband potential. If we assume that in this case etching is due solely to anodic dissolution, then it can be easily shown that six holes are required to dissolve one InP entity. The total etch rate potential curve for the 6*M* HCl case differs markedly from that of the corresponding current-potential curve. This difference is most obvious at negative potentials, at which the InP dissolves at a rate essentially independent of applied potential. Since no cathodic reaction occurs in this range, we must conclude that InP is chemically dissolved by HCl. If we assume that anodic dissolution in 6*M* HCl here also requires six holes per InP, then the chemical etch rate can be calculated from the total etch rate and the measured anodic current. Figure 2c shows that the chemical etch rate (r_{chem}) remains constant, even at potentials at which the electrode dissolves anodically.

A further example is shown in Fig. 3 for 1.5*M* HCl in concentrated acetic acid solution. Etchants based on HCl and acetic acid are often used in InP technology (7). Figure 3a shows the current-potential curve, and Fig. 3b the calculated chemical etch rate as a function of the electrode potential. The results in the cathodic region are similar to those found with 6*M* HCl solution; the current is low and a high chemical etch rate is found. The slow increase of the chemical etch rate with potential is probably due to a roughening of the electrode surface during the experiment. The increase in the anodic current at potentials near V_{FB} is considerably lower than that found in a HCl solution of the same concentration but without acetic acid. A dramatic decrease of the chemical dissolution rate is observed when the anodic dissolution starts. In this potential range, we observed the formation of an orange-colored film at the electrode surface. Phosphorus was found in this film by EDAX analysis. Obviously, a passivating film is formed during anodic dissolution. This film inhibits both the anodic and the chemical dissolution reactions.

It should be noted that the chemical dissolution rate depends markedly on the surface condition of the InP electrode. Since induction effects are observed, care must be taken to ensure a constant dissolution rate before measurements are made. This can be done by pre-etching the electrode in the same etching solution.

The results shown so far suggest that the chemical etch rate of InP is strongly dependent on HCl concentration. This dependence was studied by varying the HCl concentration over a wide range for two different systems. An InP crystal was chemically etched in these solutions in the flow cell (the measured current was zero), and the chemical dissolution rate was again analytically determined by ICP emission spectrometry. The results are shown in Fig. 4. For curve (a), the concentration was varied by diluting concentrated HCl with water. At 9*M* HCl, the chemical dissolution rate is high and decreases rapidly as the HCl concentration is lowered. For a 5*M* HCl

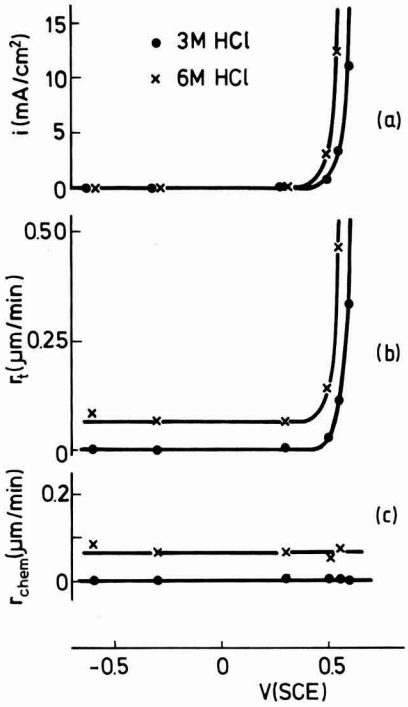


Fig. 2. Potentiostatically measured current-potential curves (a), total etch rate as a function of the electrode potential (b), and chemical etch rate as a function of the electrode potential (c) for a p-InP electrode in the dark in a 3M HCl (●) and 6M HCl (x) solution in water.

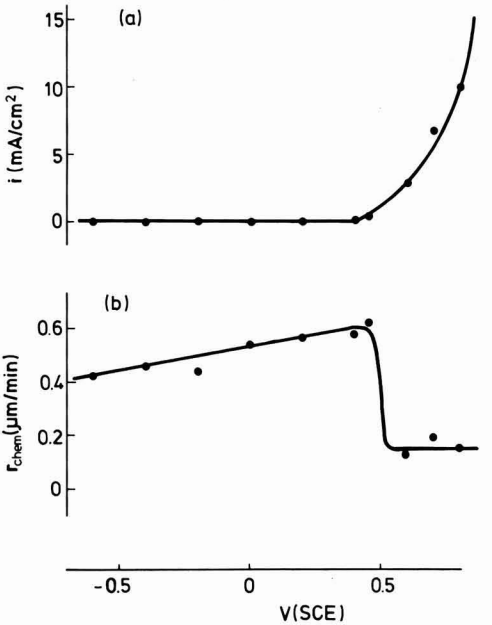


Fig. 3. Potentiostatically measured current-potential curve (a) and chemical etch rate as a function of the electrode potential (b) in the dark for a p-InP electrode in a solution of 1.5M HCl in concentrated acetic acid.

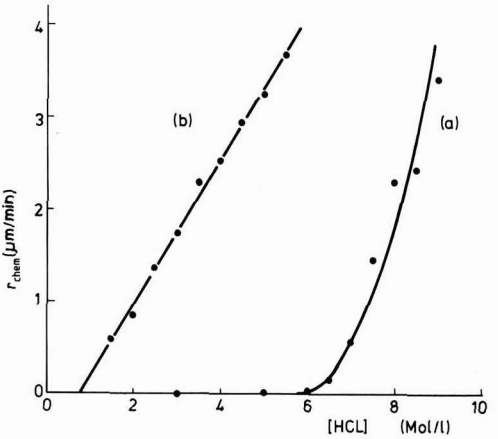


Fig. 4. Chemical etch rate as a function of the HCl concentration for a p-InP crystal in the dark. The HCl concentration was varied by diluting with water [curve (a)] and concentrated acetic acid [curve (b)].

concentration, the etch rate is less than 40 Å/min and even lower for more dilute solutions. For curve (b), concentrated HCl was diluted with concentrated acetic acid. It is striking that here a linear relationship between etch rate and HCl concentration is observed and that the etch rate is significantly higher than in the corresponding HCl-H_2O solutions.

To decide whether the dissolution is a diffusion or a kinetically controlled process, the etch rate was measured as a function of the rotation rate using a p-InP rotating disk electrode at open circuit. Figure 5 shows that the chemical etch rate measured in a 3*M* HCl in concentrated acetic acid solution is essentially independent of the rotation rate (*N*). This means that the rate of the dissolution reaction is kinetically controlled.

Gas analysis.—When an InP crystal was dissolved at the rest potential in a concentrated HCl solution, gas evolution was observed at the solid surface. Using the color-detector method, we showed that this gas was phosphine. A clear color change was indeed observed even with the most insensitive tubes. We determined the gas quantitatively with a gas burette and showed that the phosphorus is converted for 100% (± 1%) as PH_3.

Electrochemical measurements.—The current-potential curves of p-InP in 1*N* H_2SO_4 and in different HCl solutions in the dark are shown in Fig. 6. In all cases, the blocking current in the cathodic region was very low (< 0.02 mA/cm²). The onset of the anodic current in the case of 1*N* H_2SO_4 [curve (a)] occurs near the flatband potential (V_{FB} = 0.73V), as expected. The anodic current for 1*M* HCl [curve (b)] is shifted some 150 mV in the negative potential direction with respect to the H_2SO_4 case. With an increase in the HCl concentration, this effect becomes more pronounced. For the 9*M* HCl solution, the shift amounts to about 350 mV. When the curve was measured again in 1*N* H_2SO_4 after the HCl experiments, exactly the same result was obtained as in the first measurement [curve (a)].

We also measured the Mott-Schottky plots for each of the solutions used in Fig. 6. The flatband potential did not depend on the HCl concentration: V_{FB} = 0.725 ± 0.050V in all cases. The slope of the Mott-Schottky plots decreased somewhat as the HCl concentration was increased. This is probably due to an increase in the surface area of the electrode due to roughening as a result of etching. A similar effect can also be seen in Fig. 3b.

Discussion

From Fig. 2 and 4, it is obvious that chemical dissolution occurs in aqueous solution when the HCl concentration exceeds a certain critical value. The rate is strongly dependent on the HCl concentration and becomes very low at values lower than 5*M* [see Fig. 4, curve (a)]. This suggests that the etch rate depends on the degree of dissociation of HCl molecules. Although it is clear that at low concentrations the dissolution of HCl is complete, there is a considerable discrepancy in the literature with respect to higher concentrations (10). Calculations based on vapor pressure measurements and on Hammett functions show that the concentration of undissociated HCl begins to increase significantly above 5 mol/l (11, 12). In order to avoid the uncertainty involved when HCl is diluted with water, we studied the dissolution rate in HCl-acetic acid solutions. The disssociation constant of HCl in acetic acid ($K_a = 10^{-8.55}$) is much lower than in water ($K_a = 10^{+3}$) (13). Consequently, the degree of dissociation of HCl in acetic acid is negligible, even at low HCl concentrations. The chemical etch rate could therefore be studied as a function of the molecular HCl concentration. The linear dependence of the chemical dissolution rate on the HCl concentration in concentrated acetic acid [Fig. 4, curve (b)] indeed confirms that chemical dissolution is determined by the molecular HCl concentration. The

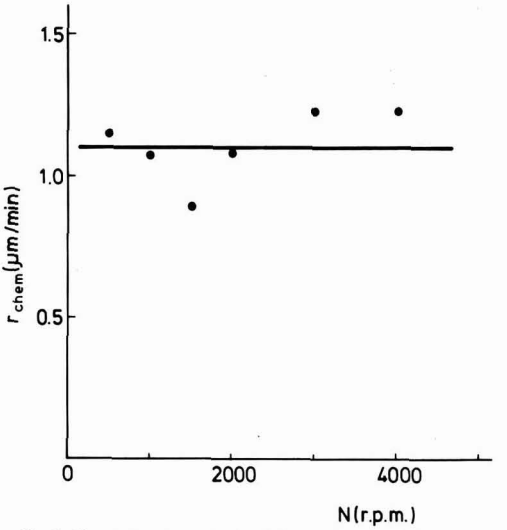


Fig. 5. Chemical etch rate in the dark as a function of the rotation speed of a p-InP electrode in a solution of 3M HCl in concentrated acetic acid.

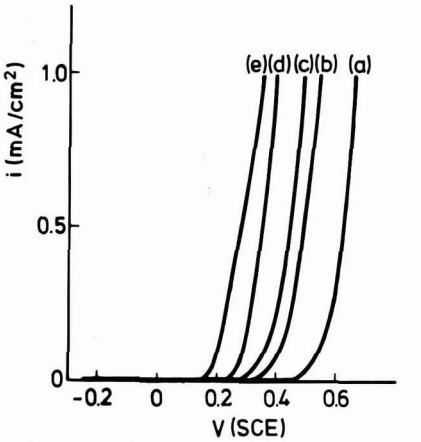
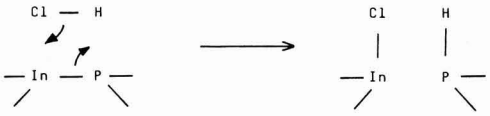


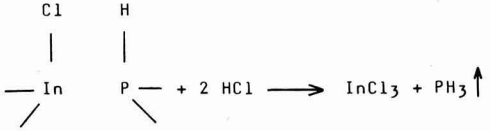
Fig. 6. Current-potential curves for a p-InP electrode in the dark in 1N H_2SO_4 (a), 1M HCl (b), 5M HCl (c), 7M HCl (d), and 9M HCl (e) in water. Scan rate: 10 mV/s.

high etch rate of HCl solutions diluted with concentrated acetic acid compared to that for aqueous solutions, also found by Adachi (7), can be understood in this way. Figure 5 shows that the etch rate is independent of the rotation rate of an InP electrode meaning that the chemical etch rate is kinetically determined by these HCl molecules.

The mechanism presented by Gerischer and Wallem-Mattes for the chemical dissolution of semiconductors involves symmetrical bifunctional etching agents such as H_2O_2 and halogen molecules (5, 6). Although we are, in the present work, dealing with an asymmetrical HCl molecule, we propose a reaction scheme similar to that for symmetrical agents. The first step involves a synchronous exchange of bonds: In-Cl and P-H bonds replace the original H-Cl and In-P bonds. This is very likely the rate-determining step



Since the indium and phosphorus atoms at the surface are triply bonded to neighboring atoms, two further bonds must be broken in an analogous manner to remove each atom from the lattice



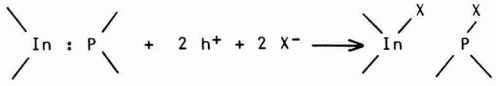
Indium is therefore dissolved as hydrolyzed $InCl_3$ and PH_3 is evolved as a gas. Such a mechanism can account for the etching results observed.

The chemical etch rate of InP in HCl solution is independent of potential. At potentials near the flatband value (Fig. 2 and 3) the p-InP electrode dissolves anodically. The rate of the anodic etching increases as the surface hole concentration is increased, *i.e.*, as the potential is made more positive. In aqueous HCl solutions, we have shown that six holes are required to dissolve one In-P entity. This means that both In and P are oxidized to the trivalent state, as is common for III-V materials (3-6). With a considerable concentration of acetic acid in the HCl solution, however, a film is formed on the electrode which inhibits both the chemical and anodic dissolution (Fig. 3). EDAX measurements have shown that this layer contains phosphorus but no indium or chlorine. We suspect that, in this case, phosphorus is not oxidized directly during anodic dissolution

$$InP + 3h^+ \rightarrow In^{III} + P$$

A similar three-hole mechanism has been shown for GaP (14).

It is obvious from Fig. 6 that the chemical dissolution rate strongly influences the electrochemical behavior of InP. Anodic dissolution starts at a more negative potential as the HCl concentration is increased, although the flatband potential does not change. This must mean that the activation energy for electrochemical dissolution is lowered by chemical etching. A similar effect has been demonstrated by Gerischer and Wallem-Mattes (6) for the dissolution of GaAs in bromine solution. As in the GaAs case, this result can be explained if we assume that rupture of the first In-P surface bond is rate determining for anodic dissolution



If this bond is broken during a chemical attack by HCl, then the remaining bonds are more easily attacked anodically and the onset potential for anodic dissolution is consequently lowered, indicating that it is, indeed, likely that the first step is the rate-determining dissolution step.

Conclusions

The dissolution of InP in concentrated HCl solutions follows a chemical mechanism in which undissociated HCl molecules play a decisive role. It seems likely that other etchants for InP, such as HBr and Br_2 (7, 8), are based on a similar mechanism. The reason why InP does not undergo electroless dissolution in conventional etchants containing oxidizing agents is probably related to the presence of a thin, highly resistant oxide layer on the semiconductor (15). Such a layer, which can inhibit either the dissolution of the solid or hole injection from the oxidizing agent, is unlikely to be present at the high HC concentrations used here.

Acknowledgment

The author wishes to thank Dr. J. J. Kelly, Mr. J. E. A. M. van den Meerakker, and Dr. R. Memming (Philips Forschungslabor, Hamburg, Germany) for helpful discussions, and the Analytical Department of Ir. P. J. Rommers for the indium analyses.

Manuscript submitted March 19, 1984; revised manuscript received June 11, 1984.

Philips Research Laboratories assisted in meeting the publication costs of this article.

REFERENCES

1. W. Kern, *RCA Rev.*, **39**, 278 (1978).
2. R. P. Tijburg and T. van Dongen, *This Journal*, **123**, 687 (1976).
3. M. M. Faktor, T. Ambridge, C. R. Elliott, and J. C. Regnault, Curr. Top. *Mater. Sci.*, **6**, 1 (1980).
4. H. Gerischer and I. Mattes, *Z. Phys. Chem. N. F.*, **49**, 112 (1966).
5. H. Gerischer and W. Mindt, *Electrochim. Acta*, **13**, 1329 (1968).
6. H. Gerischer and I. Wallem-Mattes, *Z. Phys. Chem. N.F.*, **64**, 187 (1969).
7. S. Adachi and H. Kawaguchi, *This Journal*, **128**, 1342 (1981).
8. S. Adachi, Y. Noguchi, and H. Kawaguchi, *ibid.*, **129**, 1053 (1982).
9. E. Haroutiounian, J. Sandino, P. Clechet, D. Lamouche, and J. Martin, *ibid.*, 131, 27 (1984).
10. "Gmelins Handbuch der Anorganischen Chemie," Chlor (6), Ergänzungsband, Teil B - Lieferung 1, p. 223, Verlag Chemie, GmbH, Weinheim, Germany (1968).
11. A. Eucken, *Z. Elektrochem.*, **52**, 255 (1948).
12. W. Kangro, *Z. Phys. Chem.*, **32**, 273 (1962).
13. W. Huber, "Titrations in Nonaqueous Solvents," pp. 215, 226, Academic Press, New York (1967).
14. R. Memming and G. Schwandt, *Electrochim. Acta*, **13**, 1299 (1968).
15. A. Heller, R. Vadimsky, W. Johnston, Jr., K. Strege, H. Leamy, and B. Miller, in "Proceedings of the 15th IEEE Photovoltaics Specialists Conference, Kissimmee, Florida, May 1980," p. 1422, IEEE, New York (1981).

Diffusion of Ion-Implanted Arsenic in Thermally Grown SiO_2 Films

R. Singh,[1] M. Maier, H. Kräutle, D. R. Young,[2] and P. Balk*

Institute of Semiconductor Electronics, Technical University Aachen, D-5100 Aachen, Germany

ABSTRACT

The diffusion of As implanted in thermally grown SiO_2 was studied at temperatures in the range 1000°-1200°C using N_2 and O_2 as ambients. Concentrations were between 3×10^{15} and 3.5×10^{16} As^+ ions cm^{-2}. Energies of 60 and 340 keV were used. Because of As loss due to evaporation, significant quantitative data could only be obtained for deep implants. N_2-annealed samples exhibit low diffusion rates at high concentrations (above the middle of the 10^{19} cm^{-3} range). Larger diffusion rates are observed at lower concentrations. In the samples treated in O_2, the opposite concentration dependence of the diffusivity is observed. The shape of the profiles suggests that in both cases a high and a low concentration phase exists. A model is presented assuming that in O_2 a fully oxidized structure and in N_2 an oxygen deficient network is obtained as a first step in the annealing process. There are indications that the ambient also affects the diffusion rate during further high temperature treatment of these structures, probably through the concentration of oxygen vacancies.

Dopants introduced into gate oxide films during implantation of the channel in MOSFET devices or by outdiffusion from a polysilicon gate may act as trapping centers for charge carriers (1). For this reason, it is of interest to know the diffusion behavior and understand the trapping properties of such elements in thermally grown SiO_2.

In a recent study in this laboratory (2) on electron trapping in As-implanted SiO_2, different trapping states were found after annealing depending on the nature of the coimplant (O^+ or Si^+) or on the annealing ambient (O_2 or N_2). This was interpreted to mean that the conditions under which the implantation damage is being annealed determine the "microscopic location" of the As in the oxide structure. It may be expected that the diffusion mechanism of As will also depend on its mode of incorporation into the SiO_2 network.

Indeed, it had been reported by Wada and Antoniadis (3) that the diffusion rate of As implanted in SiO_2 is concentration and ambient dependent. Specifically, an enhancement of the As diffusion (compared to that in a N_2 ambient) was reported for the case that the process was carried out in O_2 and the silicon substrate was being oxidized simultaneously. The enhancement was attributed to the flow of oxygen through the oxide or, as a more likely cause, to the generation of some point defect at the Si-SiO_2 interface during oxidation. However, it was concluded that the mere presence of excess oxygen in the oxide does not suffice to create the faster rate of diffusion.

In the present study, we have attempted to shed some further light on the question of the diffusion mechanism of As in SiO_2. With some exceptions, we have confirmed the observations of Wada and Antoniadis. However, to arrive at a correct interpretation of the data, it is necessary to recognize that diffusion of implanted As is a two-step process: incorporation of As into the SiO_2 network and diffusion of the incorporated As. Both steps may, in principle, be affected by the experimental conditions, specifically by the annealing ambient. It will be shown in this paper that, even though a number of questions remain open, a consistent picture of the overall process is obtained by taking these aspects into account.

Experimental

To study the diffusion of implanted As in SiO_2, concentration profiles were determined for four groups of diffusion experiments. In the first two, some of the experiments of Wada and Antoniadis were repeated to clarify the role of the rate of oxidation in O_2 on the diffusion process. In the third experiment, the effects of implanted dose, annealing temperature, and ambient, and in the fourth that of "mixed" annealing treatments, using O_2 and N_2 consecutively, were studied. Annealing temperatures were 1000°, 1100°, and 1200°C.

All substrates were (100)-oriented 22-32 Ωcm p-type silicon wafers. For the first experiment, to determine the effect of an ongoing oxidation process, these substrates were first oxidized in dry O_2 at 1000°C to approximately 100 nm. Subsequently, some of these samples were implanted with a dose of 10^{16} As^+ ions (60 keV) cm^{-2}. Half of the latter group was additionally implanted with 5×10^{15} N_2^+ ions (80 keV) cm^{-2}, giving a nitrogen profile with centroid at the Si-SiO_2 interface to block further oxidation. The inhibition or retardation of oxidation by this method, caused by the formation of a nitride layer near the interface and first demonstrated by Josquin and Tamminga (4), was confirmed by us. For example (Fig. 1), starting with an initial oxide of 102 nm, after 8h of further oxidation at 1000°C the N_2^+-implanted oxide had become thicker by only 15 nm, and that of the sample implanted with As^+ but not with N_2^+ had increased by an amount more than ten times larger, *i.e.*, 177 nm. Since for oxidation times > 10h the oxide thickness started to increase significantly, we limited the diffusion experiment at 1000°C to 8h only. All values of SiO_2 film thickness quoted were determined by ellipsometry with an accuracy of ± 1%.

For the second experiment, to explore the interaction between the oxidation and diffusion processes, samples with different oxide thicknesses (177 and 1040 nm) and

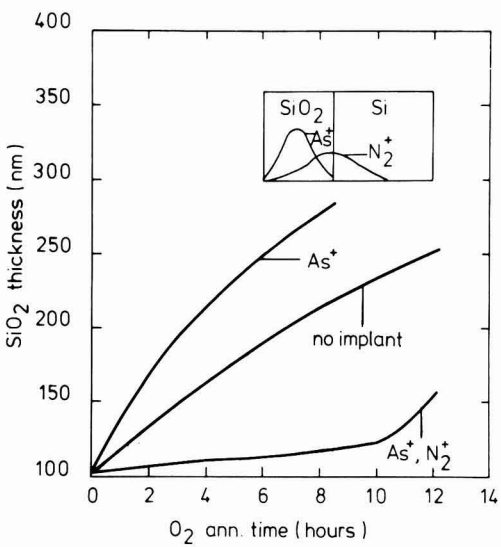


Fig. 1. Inhibition of oxidation by N_2^+ implantation (5×10^{15} cm^{-3} at 80 keV) for samples with and without As^+ implant (10^{16} cm^{-2} at 60 keV). Insert: as-implanted profiles.

*Electrochemical Society Active Member.

[1]Present address: Solid State Physics Laboratory, Delhi, India.

[2]Present address: IBM Research Center, Yorktown Heights, New York 10598.

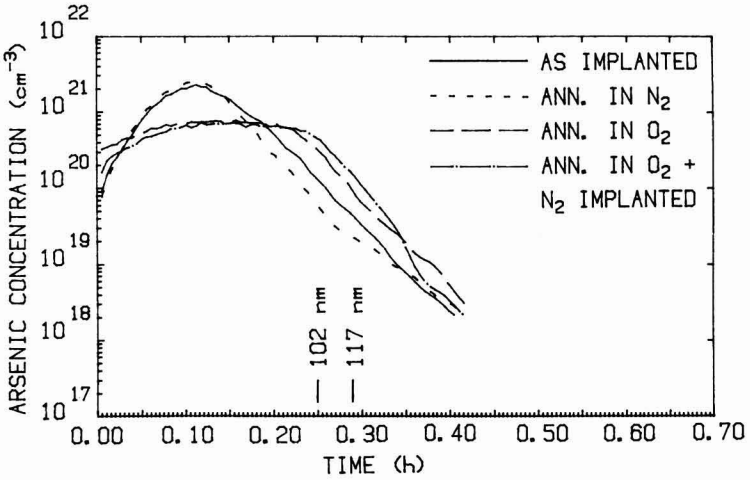


Fig. 2. As concentration vs. sputtering time for as-implanted (10^{16} cm^{-2} at 60 keV) sample and upon annealing in N_2 or O_2 at 1000°C (8h); the fourth sample had additionally been implanted with N_2^+ (5×10^{15} cm^{-2} at 80 keV) to inhibit oxidation. Position of SiO_2/Si interface is indicated (as-implanted and annealed in N_2: 102 nm, N_2 implanted and annealed in O_2: 117 nm).

thus different rates of oxidation during O_2 annealing were prepared. The oxidation was carried out in wet O_2 at 1000°C and was followed by 30 min of N_2 annealing at the same temperature. The As^+ implant was again of the same dose (10^{16} cm^{-2}) and at the same energy (60 keV) as in the first case.

The samples used for the third and fourth experiments had a 934 nm thick oxide, grown at 1000°C in wet O_2; they were again given a preimplantation N_2 anneal at 1000°C. As implants As^+ doses of 3.5×10^{16} and 3×10^{15} cm^{-2} at 340 keV were selected.

Concentration-depth profiles were determined from SIMS measurements using an Atomika instrument. A 10 keV O_2^+ primary ion beam, incident at an angle of 10° with respect to the surface normal, was employed for sputter erosion of the samples. The quadrupole mass spectrometer of the SIMS instrument was tuned to $^{75}As^+$ secondary ions and to $^{28}Si_2^+$ secondary ions of the matrix for reference purposes. The interference of $^{29}Si^{30}Si^{16}O^+$ molecular ions (mass 75) with the $^{75}As^+$ ions was suppressed by appropriate energy filtering. To minimize the charge up of the SiO_2 surface, the oxide was simultaneously bombarded with 2 keV electrons incident at 60° with respect to the surface normal. The change of intensity of the Si_2^+ ion signal at the SiO_2-Si interface was used to calibrate the sputter-time scale in terms of a depth scale. The error in the depth scale is about ±5%. A calibration of the $^{75}As^+$ signal intensity normalized to the $^{28}Si_2^+$ signal was obtained by equating the integrals of the background-subtracted depth profiles to the implanted dose of the unannealed samples, which is known with an accuracy of ±5%. The integrals of the depth profiles of unannealed samples were reproducible within ±15%. The resulting error in the As concentration scale is ±20%. As a check, some RBS measurements were also carried out. Even though the RBS analysis yields a somewhat poorer depth resolution than SIMS, all qualitative features of the profiles were confirmed. However, for determination of the total amount of As present in the samples, the RBS method offers greater accuracy. The RBS data led to the conclusion that the loss of As due to outdiffusion was underestimated in some cases (by as much as 10% of the total amount present) in the SIMS study.

Results and Discussion

Effect of ongoing oxidation process.—Results from the first group of experiments, where we studied the effect of retarded oxidation by a nitride layer prepared by N_2^+ ion implantation near the Si-SiO_2 interface, are presented in Fig. 2. The energy of the implanted As^+ ions had been chosen to place the maximum of the distribution in the middle of the oxide film at a projected range of 46 nm. This value is close to the values of 47 nm from photo I-V measurements and 46 nm from a SIMS analysis for samples with the same implant as reported by earlier workers (1). The profile obtained after an 8h N_2 anneal at 1000°C shows some narrowing at higher concentrations compared to the As-implanted distribution and exhibits a pronounced tail in the lower concentration range. It should be noticed that the tail lies mainly in the Si substrate. This tailing, but also the narrowing at higher concentrations, could possibly be explained from the relatively high value of the diffusion coefficient of As in the Si substrate [4×10^{-15} cm^2s^{-1} at 1000°C (5), compared to 3×10^{-17} cm^2s^{-1} for As in SiO_2 (3)], which acts as a sink for the dopant.

The profile for the samples annealed for the same length of time at the same temperature in O_2 exhibit a strikingly different appearance. They are broad and flat at the top and do not show a corresponding smear-out at low concentrations. The profile for the sample without N_2^+ implant is somewhat narrower at high concentrations, which cannot be explained from out-diffusion into the substrate, since the interface has moved outside the range of the figure (from 102 to 279 nm) as a consequence of the oxidation process taking place during the O_2 anneal. Comparing the profiles for samples with and without N_2^+ implantation, which exhibit oxidation rates differing by more than an order of magnitude during the diffusion process in O_2, it must be concluded that, even though we do observe the speed up compared to a N_2 anneal, as reported by Wada and Antoniadis, there is no evidence in our data that the rate of the oxidation process affects the diffusion.

To exclude the possibility that the presence of nitrogen or the damage caused by implantation of this element in the SiO_2 would enhance the diffusion rate, thereby "compensating" for a very slow rate of diffusion in pure and defect-free SiO_2, the diffusion of implanted As in a thin (177 nm) and thick (1040 nm) sample were compared (Fig. 3). In this case, the average oxidation rates of the samples during O_2 annealing differed by a factor of nearly three, and in the early stages of the process by even more. However, again any indication of a correlation between oxidation rate and diffusion rate fails. Also, during the N_2 anneal (in this experiment annealing times of 30h at 1000°C were used, instead of 8h, as in the first experiment), there is a distinct change of profile, but certainly not so pronounced as upon O_2 annealing.

It is difficult to derive quantitative information from the data in Fig. 2 and 3 since our measurements indicate that during some of the diffusion experiments considerable amounts of As are lost, most likely because of evapo-

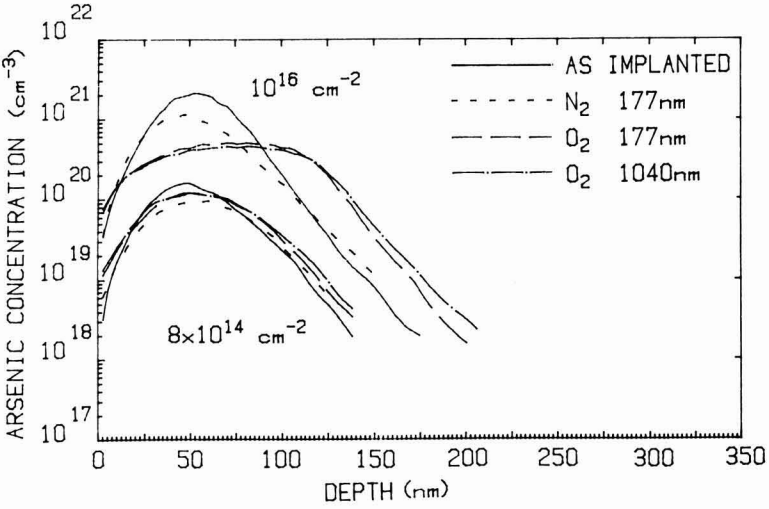


Fig. 3. Diffusion of As (10^{16} cm^{-2} and 8×10^{14} cm^{-2} at 60 keV) in thin (177 nm) and thick (1040 nm) oxides in O_2 at 1000°C (30h). For comparison, diffusion in N_2 at same conditions is also shown.

ration, as also mentioned by Wada and Antoniadis (3). This loss is particularly pronounced for the shallow implants used in experiments 1 and 2. It amounts to 50% (0%) for the O_2-annealed samples and 30% (25%) for the N_2-annealed sample with high (low) As dose of Fig. 3, to 35%-40% for the samples annealed in O_2 in Fig. 2, whereas upon the N_2 treatment, no loss could be detected. For this reason, we used in the experiments described below considerably deeper As^+ implants (340 keV) and consequently thicker oxide films (934 nm).

Ambient dependence.—Having established that the diffusion rate of As in SiO_2 does not depend on the rate of an oxidation process of the silicon taking place simultaneously, we will deal with the difference in diffusion rate for N_2 and O_2 ambients. Figures 4-7 show profiles observed for different annealing temperatures (1000°, 1100°, and 1200°C) and for two (3.5×10^{16} and 3×10^{15} As ions cm^{-2}) deep (340 keV) implants.

The profiles obtained upon N_2 anneal at 1000°C (30h), 1100°C (17h), and 1200°C (5h) (Fig. 4 and 5) clearly show two regions: one at higher concentrations (for example, $> 3 \times 10^{19}$ cm^{-3} at 1200°C), where the profile narrows down, and a second region at concentrations below these limits, where relatively rapid diffusion occurs. The concentration around the maximum does not change at all, or, for the lower concentration implant, only in a modest fashion. This behavior suggests the presence of a stable high concentration phase, as also proposed by Wada and Antoniadis (3), which acts as a source for the diffusion into the low concentration range. The diffusion coefficients in the low concentration range amount to 6.2×10^{-17} cm^2s^{-1} at 1000°C, to 1.0×10^{-15} cm^2s^{-1} at 1100°C, and to 1.1×10^{-14} cm^2s^{-1} at 1200°C. Contrary to the samples of Fig. 4, where there was no measurable loss of As due to evaporation (RBS yielded 6% outdiffusion), in Fig. 5 the loss amounted to 6% at 1000°, 15% at 1100°, and 30% at 1200°C. This ties in with the change of profile near the surface in the latter case.

The corresponding data for O_2 annealing are shown in Fig. 6 and 7. Particularly striking is the flat appearance of the distribution obtained for the high concentration implant; at 1000°C, only diffusion near the top of the distribution is visible. Apparently, at all temperatures the rate decreases towards lower concentrations. The measured loss of As is quite in line with these observations: for the 3.5×10^{16} cm^{-2} implant, it increases from 7% to 1000°C to 24% at 1100°C and 35% at 1200°C. For the 3×10^{15} cm^{-2} implant (Fig. 7), it ranged from 0% at 1000°C and 1100°C to 14% at 1200°C. The diffusion coefficients at lower concentrations are 4.0×10^{-16} cm^2s^{-1} at 1100°C and 2.7×10^{-15} cm^2s^{-1} at 1200°C.

It thus appears that the concentration dependences of the diffusion rates in O_2 and N_2 show opposite trends.

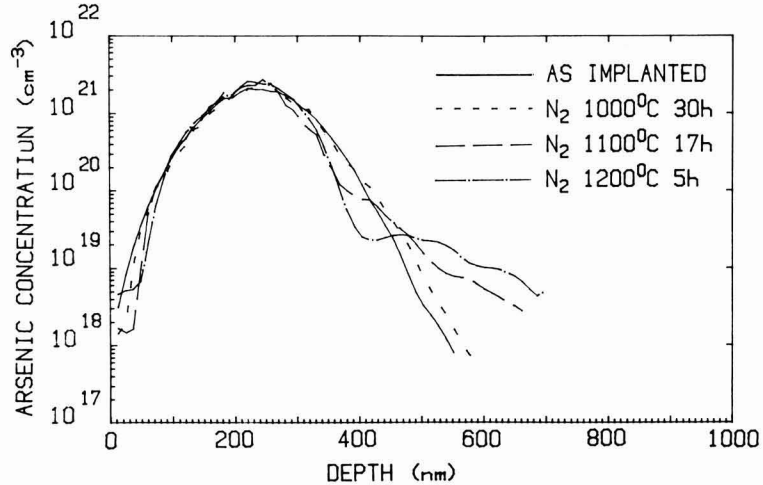


Fig. 4. As diffusion in 934 nm oxide in N_2 at 1000° (30h), 1100° (17h), and 1200°C (5h). Implant: 3.5×10^{16} cm^{-2} at 340 keV.

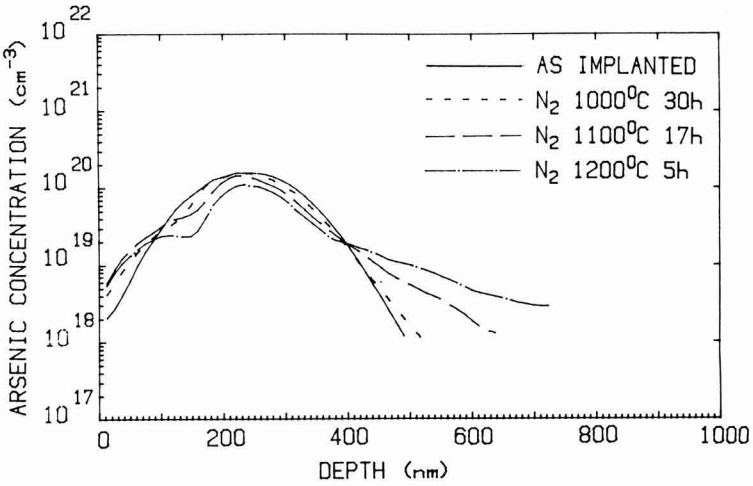


Fig. 5. As diffusion in 934 nm oxide in N_2 at 1000° (30h), 1100° (17h), and 1200°C (5h). Implant: 3×10^{15} cm^{-2} at 340 keV.

This complex behavior was further investigated in the fourth group of experiments.

The diffusion mechanism of implanted As.—In order to obtain a better understanding of the diffusion mechanism of As implanted in SiO_2 it is important to consider the following: upon implantation of As in SiO_2, the solid has become disordered. The oxygen available in the material does not suffice to reach the fully oxidized stage for both Si and As. This can only be achieved by introducing additional oxygen into the structure, for example, by annealing in O_2, which would lead to the formation of an arsenic silicate ($(As_2O_3)_x$-$(SiO_2)_{1-x}$) ($x \approx 0.04$, 1200°C) glass. In contrast, when annealing in N_2, Si and As will compete for oxygen. It is not clear whether here an arsenic silicate glass plus interstitial Si and As will form or if an incompletely oxidized network containing configuration like $O_3 \equiv$ As-Si $\equiv O_3$[3] with direct bonding between As and Si are obtained. However, it appears likely that the rate of diffusion should depend on the manner in which the As has been built into the network. Once a thermodynamically stable atomic configuration has been attained, there could, in principle, be a second effect of the ambient, namely, on the diffusion of the As built into the network, via the stoichiometry (vacancy content) of the oxide structure.

To explore this question, a fourth set of experiments was carried out. Again, implants of 3×10^{15} and 3.5×10^{16} As^+ ions cm^{-2} in thick oxide films (934 nm) were used, and annealing for 5h at 1200°C was studied. It may be seen that for the 3.5×10^{16} cm^2 implant (Fig. 8), a 5 min O_2 anneal followed by a 5h N_2 treatment has nearly the same effect as a treatment for 5h in O_2 only. Apparently, a very brief O_2 anneal is sufficient to reach a fully oxidized state of the oxide system. In fact, such a transition requires only the presence of a slight amount of O_2 in the neutral ambient: it was observed that starting the annealing step in a neutral ambient without previously thoroughly flushing the furnace tube after introducing the sample led to oxygen-saturated behavior. The subsequent diffusion step appears to be nearly independent of the ambient. Even though a 5 min N_2 anneal may be able to restore the network in a manner typical for the N_2 ambient, the following 5h O_2 anneal appears to first turn the system into the more stable fully oxidized state. Consequently, again the profile characteristic for the network structure obtained for an O_2 treatment is observed.

The loss by evaporation was 35% for 5h O_2 anneal only, 47% for 5 min O_2 + 5h N_2, and 43% for 5 min N_2 + 5h O_2; these values are relatively large but hardly distinguisha-

[3]Here and in the following, the symbol $O_3 \equiv$ As-Si $\equiv O_3$ is used to indicate an oxygen-deficient silicon oxide configuration $O_3 \equiv$ Si-Si $\equiv O_3$ (fully oxidized oxide: $O_3 \equiv$ Si-O-Si $\equiv O_3$), where one Si atom has been replaced by an As atom. The question of the different valency of As (3 to 5) compared to that of Si (4) is not being discussed; only the presence of direct As-Si and Si-Si bonds (or possibly also of As-As bonds) is being alluded to.

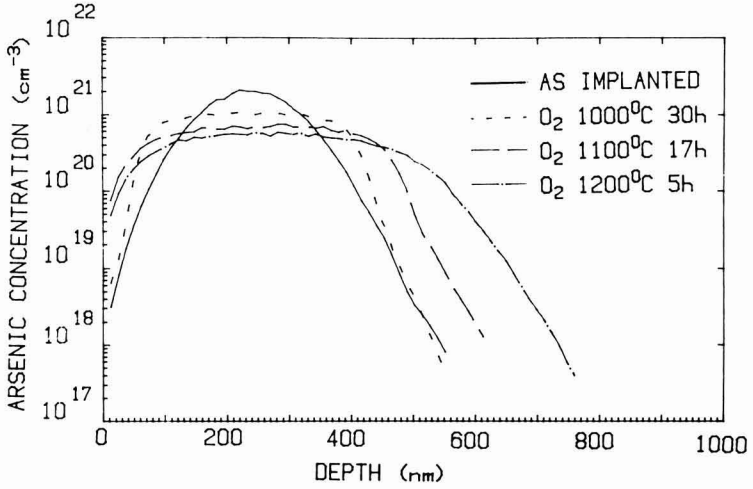


Fig. 6. As diffusion in 934 nm oxide in O_2 at 1000° (30h), 1100° (17h), and 1200°C (5h). Implant: 3.5×10^{16} cm^{-2} at 340 keV.

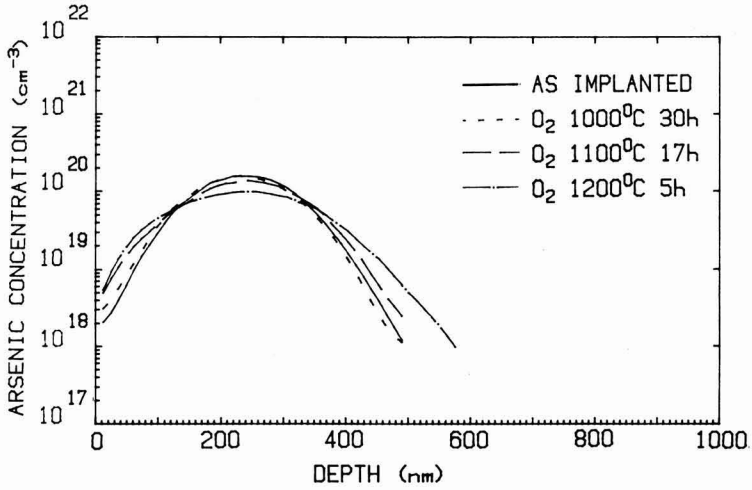


Fig. 7. As diffusion in 934 nm oxide in O_2 at 1000° (30h), 1100° (17h), and 1200°C (5h). Implant: 3×10^{15} cm^{-2} at 340 keV.

ble. For the case of 5h annealing in N_2 only, in the sample of Fig. 4 could no loss be detected. During 5 min treatment in O_2 or N_2, no measureable diffusion could be observed; the profiles were identical to the as-implanted distribution.

In the samples with lower concentration implants (Fig. 9), slight differences between the "mixed annealing" and O_2 annealing steps become visible. The samples which had been exposed to N_2 in a "mixed anneal" exhibit a somewhat wider profile (*i.e.*, faster diffusion at lower concentrations) than those which had been treated with O_2 only. Thus, the slope of these profiles is less steep and becomes closer to that of the samples annealed in N_2 only. Accordingly, the diffusion coefficient of the "mixed annealed" samples lies between O_2 and N_2 (3.7×10^{-15} cm^{2}s^{-1}). The samples which had been exposed to O_2 experienced a smaller loss of As (22% for 5 min O_2 + 5h N_2, 19% for 5 min N_2 + 5h O_2, 12% for the sample treated in O_2 only) compared to 30% for treatment in N_2 only.

The diffusion constants derived from our data in the lower concentration range have been plotted in Fig. 10. They show the lower values for the O_2 than for the N_2 ambient (by roughly a factor of three). An intermediate value is found for mixed ambients. It may be seen that this behavior is opposite to that reported in Ref. (3). The reason for this discrepancy is not clear to us.

Summing up, the findings of this section support the concept that upon annealing in N_2 or O_2 implanted As$^+$ ions are incorporated into the oxide system in a different fashion. In fact, it appears that N_2 anneal gives rise to two types of structures. One of these is observed only if As concentrations in the 10^{20} cm^{-3} range or higher are introduced. In this structure, the dopant is effectively immobilized. Parallel to the dopant incorporated in the first type of structure, As is also taken up in a second "site," where it diffuses at relatively high speeds. In the case of O_2 anneal, the situation is reversed: here there is a strong broadening of the profile at high concentrations, but slower diffusion at low concentrations. The behavior during N_2 anneal is suggestive of the presence of two phases; this could also be the case in the O_2-treated samples.

It is worth noting that the diffusion behavior of As using a N_2 ambient is not specifically related to this ambient; annealing in Ar for 5h at 1200°C led to a profile indistinguishable from that obtained in N_2. Moreover, N incorporation into the bulk of the oxide film was not found within the detection limit (10^{18} cm^{-3}) for this element in SiO_2 using SIMS.

Incorporation of As on different sites upon O_2 or N_2 anneal was also suggested in Ref. (2): for an O_2 anneal, formation of an "As-O complex" was proposed, whereas the two centers found upon N_2 anneal were tentatively equated with As incorporated on Si sites, since their concentrations were reduced when Si was implanted simultaneously with As. It was assumed that the remaining As would occupy interstitial sites in the latter case. In

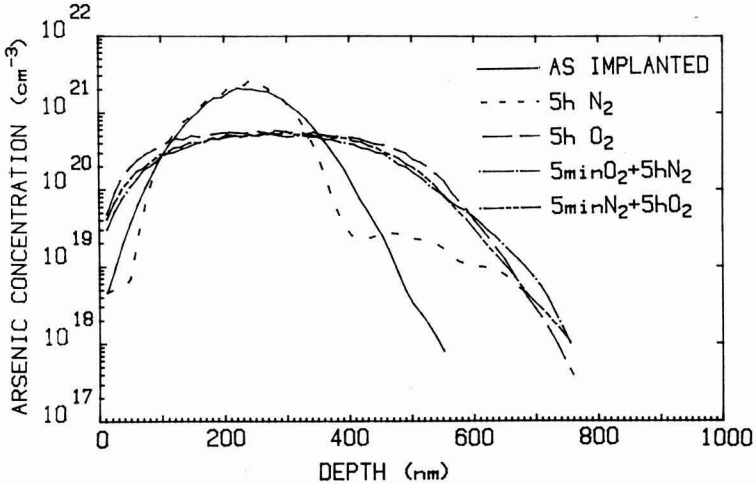


Fig. 8. As diffusion in 934 nm oxide at 1200°C in N_2 (5h), O_2 (5h), O_2 (5 min) plus N_2 (5h) or N_2 (5 min) plus O_2 (5h). Implant: 3.5×10^{16} cm^{-2} at 340 keV.

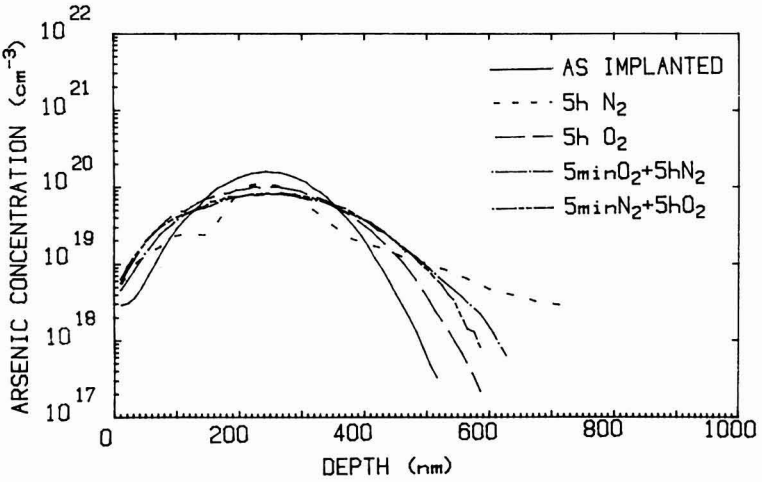


Fig. 9. As diffusion in 934 nm oxide at 1200°C in N_2 (5h), O_2 (5h), O_2 (5 min) plus N_2 (5h) or N_2 (5 min) plus O_2 (5h). Implant: 3×10^{15} cm^{-3} at 340 keV.

comparing these data with ours, it should be remembered that the implantations in Ref. (2) were done at a dose of only 8×10^{12} cm^{-2} at 80 keV, leading to maximum concentrations at least two orders of magnitude smaller than the lowest in our experiments. Thus, the conclusions in Ref. (2) are only relevant for the low concentration range in our data.

From a study of As_2O_3-SiO_2 glasses, used as diffusion sources, it is known that phase separation occurs when the As_2O_3 concentration in the arsenic silicate layer reaches a few mole percent (6). This suggests that, like observed for the phosphosilicate (7, 8) and borosilicate glasses (9), the high concentration phase is probably a liquid at the annealing temperature. It should be noted that one is dealing here with fully oxidized systems, like in our case of O_2 annealing.

Finally, it has been reported (10) from an XPS study of P-implanted SiO_2 that N_2 and O_2 annealing lead to different spectra. In both cases, P appears to be incorporated in the lattice in PO_4 configurations; upon N_2 annealing an additional peak, indicative of P-Si bonds, appears. In Ref. (10), this peak is attributed to interstitial phosphorus, but in our opinion these data do not exclude the possibility of the occurrence of $O_3 \equiv Si\text{-}P \equiv O_3$ configurations.

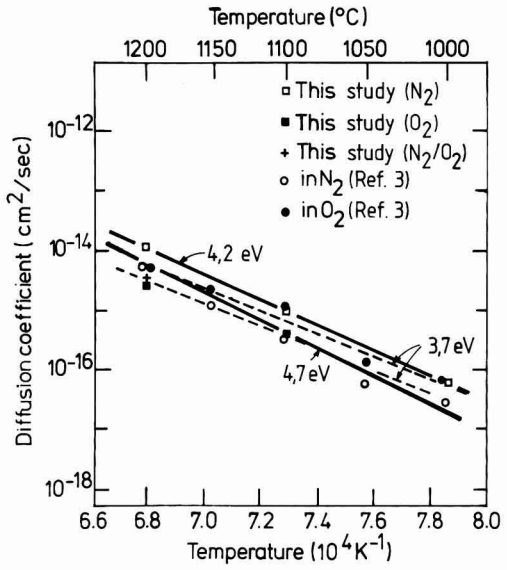


Fig. 10. Arrhenius plot of diffusion constants for As diffusion in SiO_2 in different ambients. For comparison, data from Ref. (3) are also shown. Full lines connect open symbols (N_2 ambient), dashed lines closed symbols (O_2 ambient). Dashed line through O_2 squares from this study was drawn parallel to the corresponding line from Ref. (3).

The above considerations lead to the following tentative interpretation of our experimental data: upon O_2 annealing of As-implanted SiO_2, the system becomes fully oxidized and an arsenic silicate glass forms. Since there is no direct evidence that As exists in the form of As_2O_5 in this glass, its composition will be designated by $(As_2O_3)_x$-$(SiO_2)_y$. In analogy to the phosphosilicate glass system, we will assume that As replaces Si in the oxide network. This would also explain its low diffusivity. At higher concentrations, a second phase will form, which presumably is liquid at the temperature of annealing. During annealing, this phase will dissolve SiO_2 from both sides until it reaches the composition of the liquidus resulting in the flat and broad profile observed in our data.

We propose that the N_2-annealed samples most likely contain direct Si-As bonds in the form of $O_3 \equiv Si\text{-}As \equiv O_3$ configurations. Such bonds are probably relatively weak, so that $O_3 \equiv Si^{\cdot}$ and $O_3 \equiv As^{\cdot}$ dangling bond configurations are obtained. As atoms should be able to move through the network by reaction of $O_3 \equiv As$ with $O_3 \equiv Si\text{-}Si \equiv O_3$ configurations to form $O_3 \equiv Si\text{-}As \equiv O_3$ and $O_3 \equiv Si^{\cdot}$. This is responsible for the relatively rapid diffusion at lower As concentrations. Even though diffusion via interstitial As atoms cannot be excluded, the rather similar values obtained for the activation energies for diffusion in N_2 and O_2 appear to support the above mechanism. The immobile phase observed at high concentrations should also be oxygen deficient. Because of the very low diffusivity of As in this phase, it should be a solid, with As incorporated in the network. However, at the present time, we have no clear ideas about the structure of this phase.

It appears feasible that the ambient will additionally affect the rate of diffusion once the O-deficient or fully oxidized systems have formed. Most likely, a N_2 anneal creates a small concentration of oxygen vacancies (2) of the form $O_3 \equiv Si^{\cdot}\ ^{\cdot}Si \equiv O_3$. Such "stretched Si-Si-bonds" (11) are of the same nature as the $O_3 \equiv Si\text{-}As \equiv O_3$ configuration and should enhance the rate of As diffusion in the system. This should become particularly apparent in the fully oxidized system where the initial concentration of vacancies is low. Indeed, the data of the region of low As concentration for the samples submitted to a "mixed" 5 min O_2 plus 5h N_2 anneal suggest that this enhancement does indeed occur. However, further experiments would be necessary to substantiate this point.

Conclusions

Our study shows that the diffusion of As in thermally grown SiO_2 is a complex phenomenon. In agreement with expectations from a simple model, one has to consider two consecutive process steps: restoration of the network structure damaged by implantation, and diffusion of As in the restored network. Both steps are likely to be ambient dependent.

The data presented in this paper suggest that two different oxide structures are obtained: an oxygen deficient one in N_2 (or Ar), and a fully oxidized structure in O_2. In both cases, As is incorporated into the network of the glassy oxide, and for N_2-annealed samples possibly additionally on interstitial sites.

The observation of a relatively high diffusion rate at high As concentrations and a very low one at lower concentrations in O_2-annealed samples leads to the conclusion that a separate high concentration liquid phase is formed in fully oxidized samples. The opposite behavior is exhibited by the N_2 heated samples. Again, a two-phase model is proposed, in this case with an immobile high concentration solid phase.

A report in the literature, claiming that a considerably enhanced rate of diffusion in O_2 is observed when simultaneously oxidation of the substrate takes place, could not be confirmed. However, we did find indications that the ambient affects the diffusion rate via the oxygen vacancy concentration in the system.

Acknowledgments

The authors like to thank Dr. O. Meyer, Kernforschungszentrum, Karlsruhe, Germany, for performing a number of RBS measurements. Mrs. D. Laschet has given valuable support in preparing the samples.

Manuscript submitted Dec. 29, 1983; revised manuscript received June 14, 1984.

Technical University Aachen assisted in meeting the publication costs of this article.

REFERENCES

1. R. F. Dekeersmaeker and D. J. DiMaria, *J. Appl. Phys.*, **51,** 1085 (1980).
2. S. Alexandrova and D. R. Young, *ibid.*, **54,** 174 (1983).
3. Y. Wada and D. A. Antoniadis, *This Journal*, **128,** 1317 (1981).
4. W. J. M. J. Josquin and Y. Tamminga, *This Journal*, **129,** 1803 (1982).
5. D. A. Antoniadis, A. M. Lin, and R. W. Dutton, *Appl. Phys. Lett.*, **33,** 1030 (1978).
6. M. Ghezzo and D. M. Brown, *This Journal*, **120,** 110 (1973).
7. T. Y. Tien and F. A. Hummel, *J. Am. Ceram. Soc.*, **45,** 422 (1962).
8. J. M. Eldridge and P. Balk, *Trans. Metall. Soc. AIME*, **242,** 539 (1968).
9. T. J. Rocket and W. R. Forster, *J. Am. Ceram. Soc.*, **48,** 75 (1965).
10. K. Hoh, M. Saitoh, and Y. Miura, *This Journal*, **128,** 1613 (1981).
11. K. L. Ngai and C. T. White, *J. Appl. Phys.*, **52,** 320 (1981).

Characteristics of Ion-Implantation Damage and Annealing Phenomena in Semiconductors

J. Narayan* and O. W. Holland

Solid State Division,[1] Oak Ridge National Laboratory, Oak Ridge, Tennessee 37831

ABSTRACT

The nature of ion-implantation damage in silicon and gallium arsenide as a function of implantation and substrate variables has been investigated using electron microscopy and Rutherford backscattering techniques. With no annealing effects, the crystalline-to-amorphous transition occurs at a critical energy of 12 eV/atom for silicon. By increasing the dose rate or the substrate temperature, "defect-free" regions with no dopant redistribution are obtained. There is a dose rate or substrate temperature window in which voids are formed, producing undesirable effects. The annealing effects at high dose rates are interchangeable with substrate temperature. A high fraction of dopants in both Si and GaAs is found to be in electrically active substitutional sites after high dose rate or high temperature implants. The origin and thermal annealing of underlying dislocation bands have been examined in detail. Subsequent annealing behavior of underlying dislocation bands is critically determined by the nature of the as-implanted states.

Ion implantation is now a well-established technique for a controlled introduction of dopants in semiconductors. Ion-implantation-induced damage must be removed in order to achieve a "complete" electrical activation of dopants and to recover carrier mobility (1). The conventional method of removing ion-implantation damage involves isothermal annealing treatments in a furnace in the temperature range of 900°-1000°C for about 30 min. Recently, more advanced methods based on rapid heating or annealing have been developed for removing ion-implantation damage. The annealing methods based on solid-phase and liquid-phase crystallization (2-6) have been successfully utilized to remove the damage. In both conventional and advanced annealing methods, the nature of ion-implantation damage before annealing is thought to determine the amount of residual damage and concomitant electrical activation and mobility achieved after annealing.

The purpose of this paper is twofold. The first purpose is to show that the nature of residual damage after ion implantation is a strong function of ion implantation and substrate variables. The ion-implantation variables of particular interest are the total dose, dose rate, and mass and energy of the incident ions. The substrate variables include the temperature and the mass. The second purpose of this paper is to show that different ion-implantation states exhibit different annealing behavior and electrical recovery of dopants. The mechanisms of dynamic *in situ* annealing during ion implantation and of subsequent annealing behavior are discussed for Si and GaAs. The correlations between residual ion-implantation damage and concentration of substitutional (electrically active) dopants in Si and GaAs specimens are presented. The paper is divided into the following sections: ion-implantation fundamentals; dose rate and substrate temperature effects in silicon; dose rate effects in different orientations; dose rate and substrate temperature effects in GaAs; thermal annealing of different ion-implantation states; and annealing effects in underlying dislocation bands and gettering.

*Electrochemical Society Active Member.

[1]Operated by Martin Marietta Energy Systems, Incorporated, under Contract no. DE-ACO5-840R21400 for the U.S. Department of Energy, Oak Ridge, Tennessee 37831.

Experimental

Single crystals of silicon having <100> and <111> orientations (500 μm thick, 2-6 Ω-cm, Czochralski grown) were implanted with $^{28}Si^+$, $^{30}Si^+$, $^{75}As^+$, and $^{209}Bi^+$ ions. Implantation current varied from 1-500 $\mu A\ cm^{-2}$, ion energy from 100-250 keV, total dose from $1.0 \times 10^{14}\ cm^{-3}$ to $5.0 \times 10^{16}\ cm^{-2}$, and substrate temperature from liquid helium (He) to room temperature. No effort was made to heat-sink the samples during implantation. The <100> GaAs specimens were implanted with $^{28}Si^+$ ions using a similar range of implant and substrate variables. For some Si and GaAs specimens, *in situ* heating was applied while ion implantation was carried out at low dose rates. The ion-implanted silicon and gallium arsenide samples were analyzed by cross-sectional electron microscopy and Rutherford backscattering/channeling techniques at room temperature for a detailed determination of residual damage and lattice location of dopants. Lattice location of dopants is directly related to their electronic properties. The Si^+-implanted GaAs samples were analyzed by MeV proton-induced x-ray excitation (PIXE) to determine the lattice location of silicon (7). For other studies, an analysis of the energy spectra of light ions backscattered from the sample under channeling and nonchanneling conditions is used for lattice-site determination. However, backscattering techniques are sensitive only to heavy impurities in light substrates and, therefore, are not suitable for GaAs work. The distinct separation of the Si characteristic x-rays from those of the host lattice makes lattice location studies possible in this material through the analysis of x-ray spectra (otherwise impossible using other ion scattering techniques). High resolution electron microscopy studies were conducted using a JEOL 200CX electron microscope operated at 200 kV with a spherical aberration coefficient (C_s) of 1.2 mm. The images were taken under axial illumination with optimum defocus, which is about 1.2 times the Scherzer defocus limit of -65 nm.

Results and Discussion

Ion-implantation fundamentals.—During ion implantation, when an energetic ion penetrates a solid, it collides with the electrons and nuclei of the solid. The energy lost in electronic excitations ultimately appears as heat. The initial energy of the primary ion can be partitioned into the amount lost in electronic excitations, and the remaining energy (E_D) goes into production of displacements. This displacement or ion-implantation damage is created as Frenkel (vacancy and interstitial) pairs, whose number is given by the modified Kinchin and Pease (8) expression $\kappa E_D/2E_d$, where κ (~ 0.8) is the displacement efficiency and E_d is the displacement threshold energy (~ 15 eV for silicon) (9). The vacancies and interstitials accumulate as a function of implanted dose, and at a critical value of 12 eV/atom for E_D, there is a first-order phase transition from crystalline to amorphous phase. This value of 12 eV/atom, or $6.0 \times 10^{23}\ eV/cm^3$ in silicon, is determined near 4 K, where annealing effects are negligible (10, 11). At higher temperatures, mobility of vacancies and interstitials becomes high enough that they annihilate each other or cluster to form dislocation loops. During ion implantation, if the regions of crystals exceed the critical energy for amorphization, they undergo a first-order phase transformation. It has been shown that for self-ions in silicon, overlap of damage produced by several ions is required because individual ions can deposit only about 3 eV/atom (11, 12). The ions, having mass equal to higher than that of antimony, can deposit 12 eV/atom or higher and, therefore, produce amorphous regions directly (11).

Figure 1A is a high resolution micrograph showing an amorphous region in a silicon specimen implanted with 100 keV, $1.0 \times 10^{14}\ cm^2$, $^{30}Si^+$ ions at liquid He temperature. The specimens that were implanted with $5.0 \times 10^{13}\ cm^{-2}$ Si^+ (100 keV), at liquid He temperature or at room temperature, showed the presence of dislocation loops and not of amorphous regions. As the implanted dose was increased to $2.0 \times 10^{14}\ cm^{-2}$, the small amorphous regions overlapped and created a large band of amorphous region. However, in this amorphous phase, the presence of microcrystallites is clearly delineated, as indicated by the arrow in Fig. 1B. Figure 1C shows a micrograph just below the critical dose of amorphization. There are many amorphous regions present at this dose, including a twinning partial dislocation, the core region of which is encircled in the micrograph. The line in the micrograph shows the trace of a twinning plane. Figure 1D shows a cross-section micrograph from a specimen implanted with a dose of $4.0 \times 10^{14}\ cm^{-2}$, where the interface between crystalline and amorphous phase appears to be atomically sharp, confirming the first-order phase transition. Some microcrystallites (as shown by the arrow) are also present in this specimen. It is interesting to note that the amorphous-crystalline interface is fairly undulated, presumably because of ion-range straggling.

The displacements below the amorphous-crystalline interface are created because of ion-range straggling. The interstitials in this region can cluster at higher temperatures to form visible dislocation loops. The average size of the vacancy loops has been shown to be much smaller ($\sim$ 5-10Å) than that of interstitial loops (13), normally below the resolution limit of the strain-contrast imaging mode of the microscope.

The sequence of ion implantation as a function of increasing dose, discounting the annealing effects, can be described as follows. First, the region corresponding to the Gaussian damage peak turns amorphous after attaining 12 eV/atom of damage energy. This band then expands toward both the surface and deeper regions of the crystal with increasing implanted dose as these regions accumulate the critical energy for amorphization. Figure 2A shows a buried amorphous layer after a dose of $2.0 \times 10^{14}\ cm^{-2}$ (100 keV, $^{30}Si^+$ ions). A high resolution micrograph from the near-surface region is shown in Fig. 2B, where the crystalline and amorphous boundary is clearly delineated. Although the amorphous-crystalline boundary is jagged, it is atomically sharp. The microcrystallites are present in the amorphous region. As the implanted dose is further increased, the amorphous-crystalline boundaries at both ends expand, ultimately creating amorphous layers followed by a band of dislocation loops. Figure 3 shows such layers for two different doses, 5.0×10^{14} and $5.0 \times 10^{15}\ cm^{-2}$ (100 keV, $^{30}Si^+$). The thickness of the amorphous layer was found to increase from 2200-2660Å as the dose increased from 5.0×10^{14} (Fig. 3A) to $5.0 \times 10^{15}\ cm^{-2}$ (Fig. 3B). Figure 3C is a microdiffraction pattern from $5.0 \times 10^{14}\ cm^{-2}$ specimens, showing two clear rings, which correspond to the first and second neighbor distances, and a faint third ring. For a dose of $1.0 \times 10^{16}\ cm^{-2}$, the thickness of the amorphous layer was found to be 2830Å. With further increase in dose, however, the increase in thickness was small because of saturation and the importance of sputtering effects.

Dose rate/substrate temperature effects in Si $^{28}Si^+$ implantation.—It has been shown that by increasing the ion-implantation current, the substrate temperature can be raised. Therefore, the annealing effects achieved by high dose rate implants (without additional sample heating) can be simulated by *in situ* heating of the substrate while implanting at low dose rates. By increasing the dose rate (ion-implantation current), it is possible to create "defect-free" regions near the surface, followed by a broad band of dislocation loops and tangles. An example is shown in Fig. 4A for a 200 keV Si^+ implant at 200 $\mu A\ cm^{-2}$ to a dose of $1.0 \times 10^{16}\ cm^{-2}$. In this case, no additional heating was applied during implantation. The cross-sectional TEM micrograph shows a top 2100Å wide "defect-free" region, followed by a 3000Å wide region containing dislocation loops and tangles. The annealed layer has the same orientation as the underlying substrate. Figure 4B shows a random and <110>-aligned spectrum from these specimens. The aligned yield in the top 2100Å region is close to that of virgin crystals, which is in good agreement with TEM observations. The aligned yield increases below 2100Å, because of the presence of disloca-

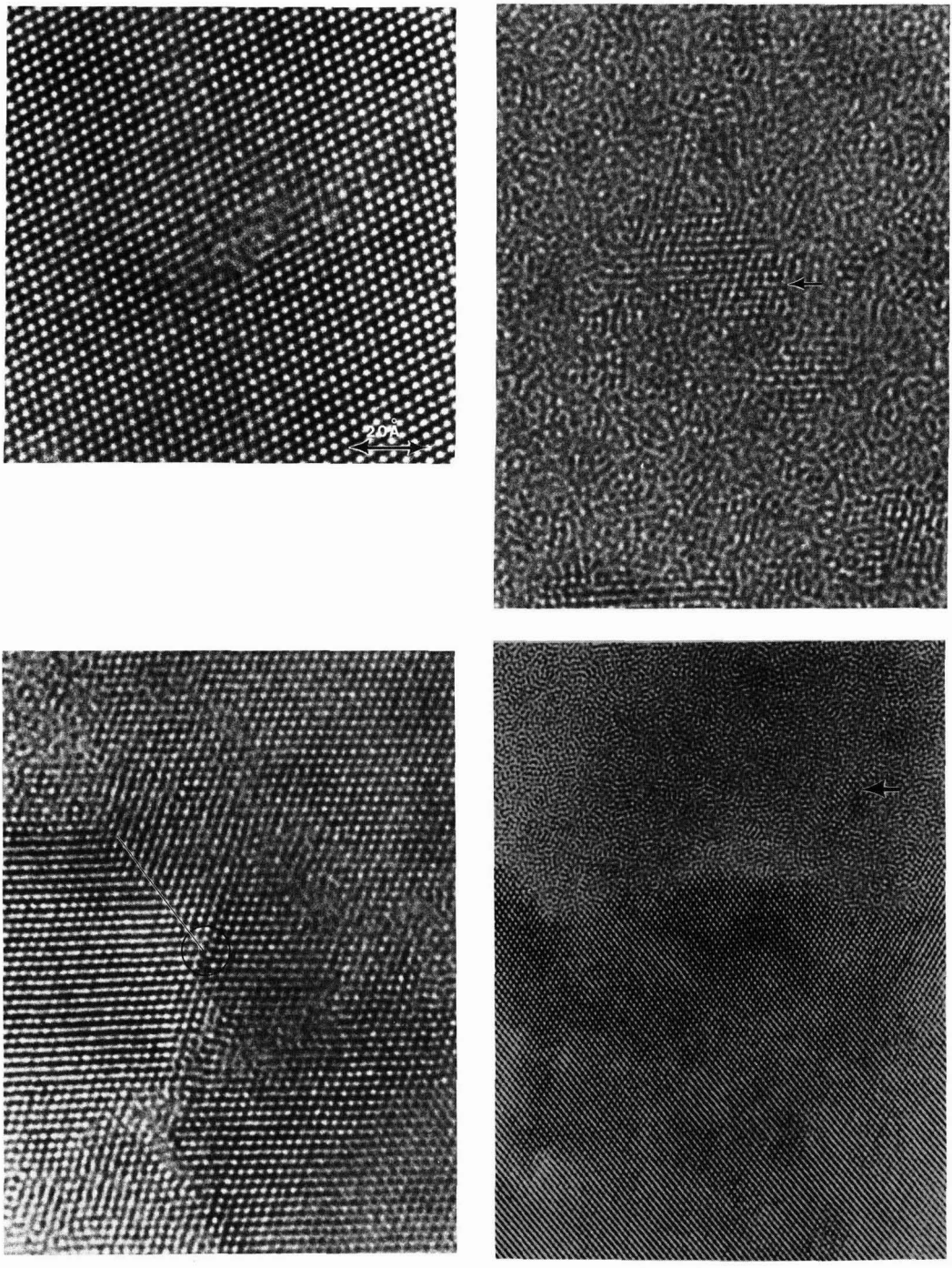
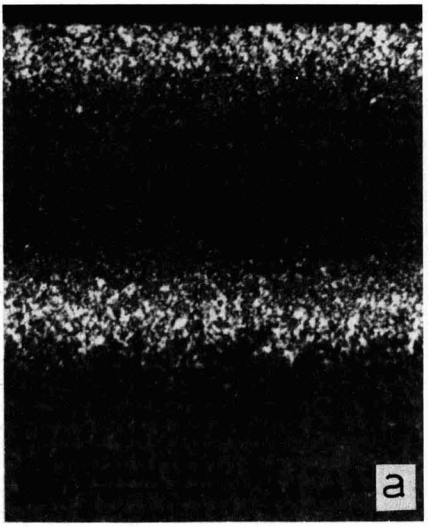


Fig. 1. A (top left): High resolution electron micrograph showing an amorphous cascade region in a specimen implanted with 100 keV $^{30}Si^{+}$ ions to a dose of 1.0×10^{14} cm^{-2}. B (top right): High resolution micrograph of amorphous silicon implanted with 100 keV $^{30}Si^{+}$ ions to a dose of 2.0×10^{14} cm^{-2}. C (bottom left): High resolution micrograph showing amorphous regions and a twinning partial dislocation (encircled) below the critical dose of amorphization. D (bottom right): High resolution electron micrograph (cross-sectional) showing the interface between the amorphous and crystalline silicon. Notice the presence of a microcrystallite in the amorphous region (indicated by arrow).

tions, but it does not reach the random or amorphous value. These results should be contrasted with low dose-rate Si^{+} implants (see Fig. 19), where an amorphous layer followed by a band of dislocation loops is observed.

Figure 5 shows results from 80 keV $^{28}Si^{+}$ implants in silicon. After implantation to a dose of 1.0×10^{16} cm^{-2} at an implantation current of 120 μA cm^{-2}, we found a buried amorphous layer, as shown in Fig. 5A. The cross-sectional



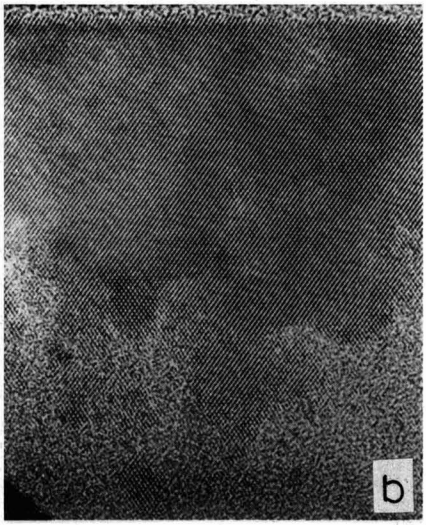
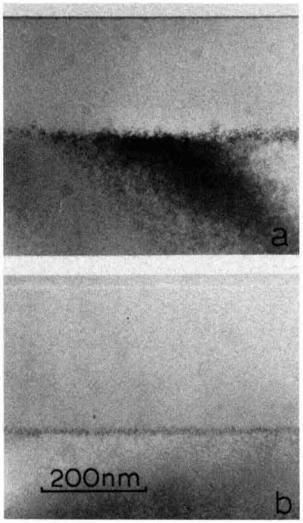


Fig. 2. Cross-sectional electron micrographs showing buried amorphous layers in specimens implanted with 100 keV $^{30}Si^{+}$ (dose 2.0×10^{14} cm^{-2}). A: Dark-field. B: High resolution micrograph.



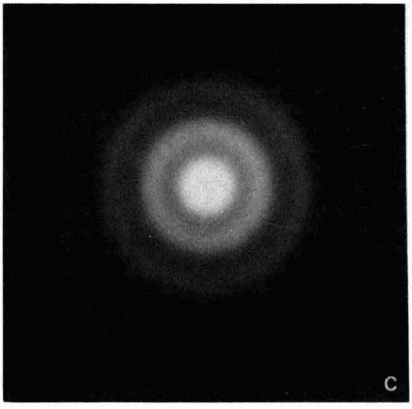
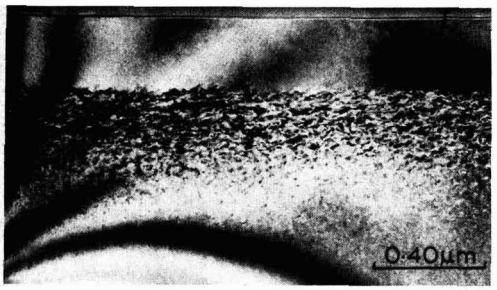


Fig. 3. Cross-sectional electron micrographs showing an increase in amorphous layer thickness with dose. A: 100 keV $^{30}Si^{+}$, dose = 5.0×10^{14} cm^{-2}. B: Dose = 5.0×10^{15} cm^{-2}. C: Microdiffraction pattern corresponding to A.

micrograph shows about a 350Å wide "defect-free" region, followed by a 700Å wide amorphous region. Below the amorphous layer, a 200Å wide defect-free layer is formed, which is followed by a 600Å wide region of dislocation loops and tangles. The RBS results from these specimens are shown in Fig. 5B. From the comparison of <110>-aligned spectra and random spectra, we find that the reduced yield in the top layer in as-implanted specimens is consistent with TEM observations. Below this region, the aligned yield approaches the random yield, corresponding to the presence of a 700Å wide amorphous layer. The aligned yield drops again, corresponding to the defect-free region below the amorphous layer. The yield increases again, owing to the presence of dislocations; however, the yield does not drop to a virgin value in the substrate, owing to previous dechanneling events. The as-implanted specimens containing buried amorphous layers were annealed at 550°C, and it was found that two amorphous-crystalline interfaces moved toward each other and ultimately produced a band of dislocation loops near the center. This is consistent with a small peak in the aligned spectrum at a 700Å depth after annealing the as-implanted specimens for 50 min at 550°C. This peak was reduced or almost annealed out by further annealing at 850°C for 10 min, but the large dislocation loops in this layer, particularly in the underlying layer, remain. This is consistent with increased dechanneling in the aligned spectrum below 1200Å.

$^{75}As^{+}$ implantation.—Figures 6-9 show results from high dose-rate, 100 keV As^{+} implants in <100> silicon. Figure 6A is a TEM cross-sectional micrograph at 200 μA cm^{-2} to a dose of 1.0×10^{16} cm^{-2}; it shows a defect-free region (~ 500Å wide), followed by a band of dislocation loops and tangles (~ 1000Å wide). A microdiffraction pattern from the implanted layers of these specimens is shown in Fig. 6B, in which diffraction spots are sharp and regular, corresponding to a <110> orientation. At 40 μA cm^{-2}, there is a 1100Å wide amorphous layer followed by a 150Å wide defect-free region and a 300Å wide dislocation band, as shown in Fig. 6C. A microdiffraction pattern from the amorphous band is shown in Fig. 6D, which contains the characteristic rings of amorphous phase. The defect-free region is formed by a solid-phase epitaxial growth process at this dose rate because of beam heating. It is apparent that by increasing the dose rate, the SPE



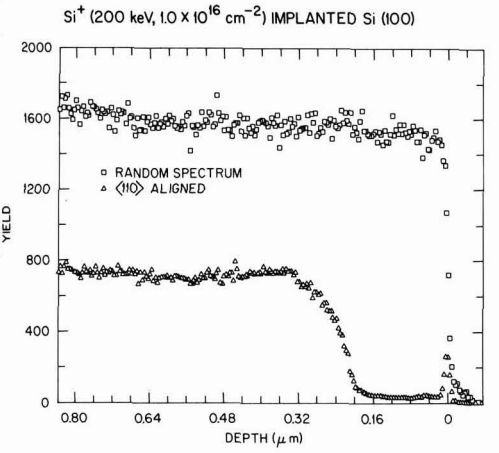


Fig. 4. A(top): Cross-sectional electron micrograph showing the formation of defect-free region in silicon-implanted (100) silicon (200 keV $^{30}Si^+$, 1.0×10^{16} cm^{-2}, 200 μA cm^{-2}). B(bottom): 2.0 MeV He^+ RBS spectra (random and <110>-aligned) from the specimen shown in A.

growth rate can be enhanced and annealing in the top region achieved. The dislocation loops and tangles are formed by clustering of point defects with number densities below that required for amorphous phase transformation. Figure 7 shows 2.0 MeV $^4He^+$ random and <110>-aligned spectra from high (Fig. 6a) and low (Fig. 6c) dose-rate implants and virgin crystals. The low dose-rate implants show ~1500Å thick defective layers. It should be noted that the 150Å wide defect-free band below the amorphous layer is not resolved in the aligned silicon spectrum for low dose-rate implants, presumably because of limited system resolution. The aligned silicon spectrum from high dose-rate implants shows reduced

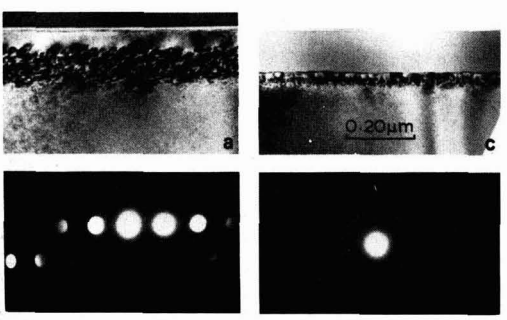
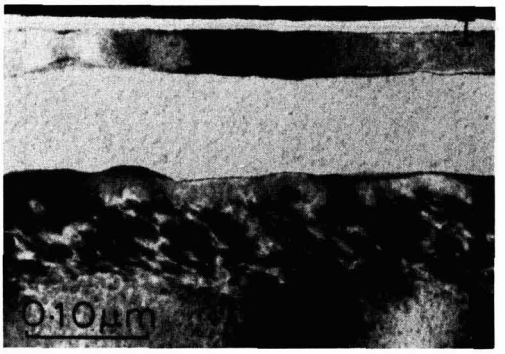


Fig. 6. Dose-rate effects in arsenic-implanted (100) silicon. A: 1.0×10^{16} cm^{-2} at 200 μA cm^{-2}. B: Microdiffraction pattern corresponding to A. C: 1.0×10^{16} cm^{-2} at 40 μA cm^{-2}. D: Microdiffraction pattern from C.



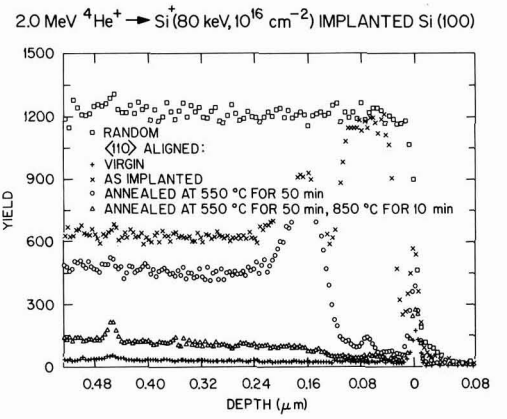


Fig. 5. A(top): Cross-sectional electron micrograph showing a buried amorphous layer in silicon-implanted (100) silicon (80 keV $^{30}Si^+$, 1.0×10^{16} cm^{-2} with a dose rate of 120 μA cm^{-2}). B(bottom): 2.0 MeV He^+ RBS spectra (random and <110>-aligned) after annealing at 550° and 850°C (from specimen shown in 1A).

yield in the top 500Å wide region corresponding to the defect-free region in the cross-sectional TEM micrograph. From the aligned and <110> random spectra of arsenic, it was found that up to 90% of the arsenic in substitutional sites were in certain regions. It is most interesting to note that the arsenic depth distribution remains Gaussian and largely unchanged during high dose-rate implants. Hall measurements showed a high electrical activation of arsenic of up to 70%.

When the dose rate was increased to 400-500 μA cm^{-2}, we observed the formation of voids in the top 500Å wide region with a 50Å average diameter. The voids in Fig. 8a exhibit a characteristic light contrast for overfocus conditions and a characteristic dark contrast for underfocus

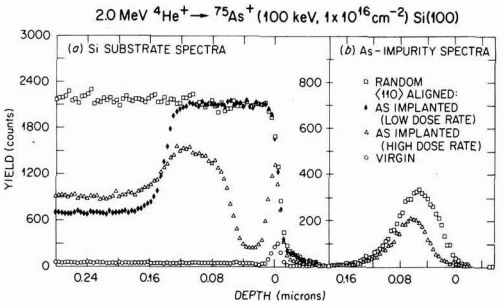


Fig. 7. 2.0 MeV He^+ RBS spectra (random and <110>-aligned) from the high and low dose-rate specimens shown in Fig. 6.

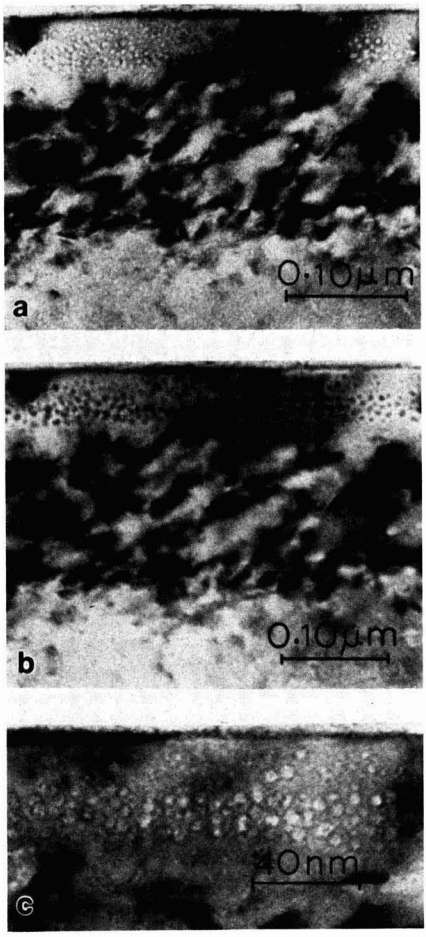


Fig. 8. Formation of voids in high dose-rate implanted (100) silicon specimen (100 keV As^+, 1.0×10^{16}, ~400 $\mu A\ cm^{-2}$) under different focusing conditions. A: Cross-sectional electron micrograph showing voids in overfocus (light contrast) conditions. B: Underfocus (dark contrast) conditions. C: Voids with light contrast in overfocus conditions at a higher magnification.

conditions (15) [Fig. 8b]. A small area at a higher magnification is shown in Fig. 8c, where voids are shown under a light contrast. Figure 9 is a plan-view micrograph showing voids in light contrast (overfocus conditions) in the top region. The formation of voids occurs because the interstitials have faster mobility and are lost to the surface or other sinks. The vacancies, which in comparison with interstitials represent the slower moving species, cluster to form voids (16).

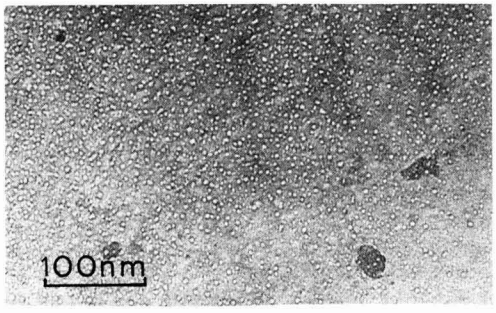


Fig. 9. Plan-view electron micrograph showing voids in light contrast (overfocus) conditions.

From these observations and a previous work (14), we have derived the following mechanism of annealing at high dose rates. During the initial phase of the ion implantation, buried amorphous layers or near-surface amorphous layers are formed, depending upon energy and mass of the incident ions and upon mass of the substrate. These variables determine the profile of the deposited damage energy. Lower energy of the incident ions and higher mass of the incident ions and substrate create amorphous layers near the surface. Buried amorphous layers are formed by higher energy of the incident ions and lower mass of the incident ions and substrate. For example, 100 keV $^{28}Si^+$ tend to form buried amorphous layers, whereas $^{75}As^+$ ions form near-surface amorphous layers. The amorphous layers anneal by solid-phase epitaxial growth as the implantation is continued. The heat generated by the ion beam raises the substrate temperature. A typical substrate temperature of 750°C was measured during a 200 $\mu A\ cm^{-2}$ (120 keV) Si^+ implant. Thus, SPE growth at high temperatures provides a primary mechanism of annealing at high dose rates. The kinetics of SPE growth have been extensively studied by RBS, TEM, and time-resolved reflectivity techniques (17). The interface velocity follows an Arrhenius relation $V = V_0 \exp(E_1/kT)$, where $V_0\langle 100\rangle = 3.07\ 10^8$ cm s^{-1}, and $E_a = -2.68$ eV. The pre-exponential factor V_0 is orientation dependent, given by $(V_0\langle 111\rangle = 24\ V_0\langle 100\rangle = 4\ V_0\ \langle 110\rangle$ (3). If the amorphous layers are not formed because the regions could not attain the critical energy of 12 eV/atom for amorphization, the recombination of interstitials and vacancies is a dominant mechanism of annealing. The cascades representing vacancy-rich regions may provide nuclei for void formation. It is noted that dopant depth profiles remain unchanged during high dose-rate implants. This is consistent because the average dopant diffusion distance ($\sqrt{2D\tau}$) during ion implantation (using the typical values of diffusion coefficients of arsenic in silicon at elevated temperatures, and using diffusion time, τ, the time of the ion implantation as the upper limit) is estimated to be less than 10Å.

Dose-rate effects in different orientations.—Since *in situ* solid-phase epitaxial (SPE) growth is a primary mechanism of annealing at high dose rates for high dose implants, it is interesting to study dose-rate effects in different orientations. The <111> Si specimens implanted with $^{75}As^+$ ions at a dose rate of 200 $\mu A\ cm^{-2}$ contain an amorphous layer followed by a small defect-free region, similar to the microstructure obtained at 40 $\mu A\ cm^{-2}$ in <100> specimens (shown in Fig. 6c). These results reflect a much smaller growth rate in <111> orientations than that in <100> orientations. The experimental results and theoretical models predict SPE growth rates to be slower by a factor of 24 in <111> orientations and a factor of 6 in <110> orientations, as compared with <100> orientations. Figure 10 shows a comparison between <100> and <111> orientations. These samples were implanted with 40 keV, $^{30}Si^+$ to 1.5×10^{16} cm^{-2} dose at liquid-nitrogen temperature at ~5 $\mu A\ cm^{-2}$ and then implanted with 120 keV $^{28}Si^+$ to 1.0×10^{16} cm^{-2} dose at ~200 $\mu A\ cm^{-2}$. In <100> orientations, we found a 1700Å wide region to be fairly "defect free," except for a few polycrystalline regions near the surface. This region was followed by a 2000Å wide band of dislocation loops and tangles (Fig. 10a). A microdiffraction pattern from the recrystallized region is shown in Fig. 10c, where regularity and sharpness of diffraction spots are indicative of the perfection of the lattice.

The <100> Si results are in contrast to those of the <111> orientations, where we found 1700Å wide polycrystalline followed by a 2000Å wide band of dislocation loops and tangles (Fig. 10b). In the second region, a high number density of microtwins were also present.

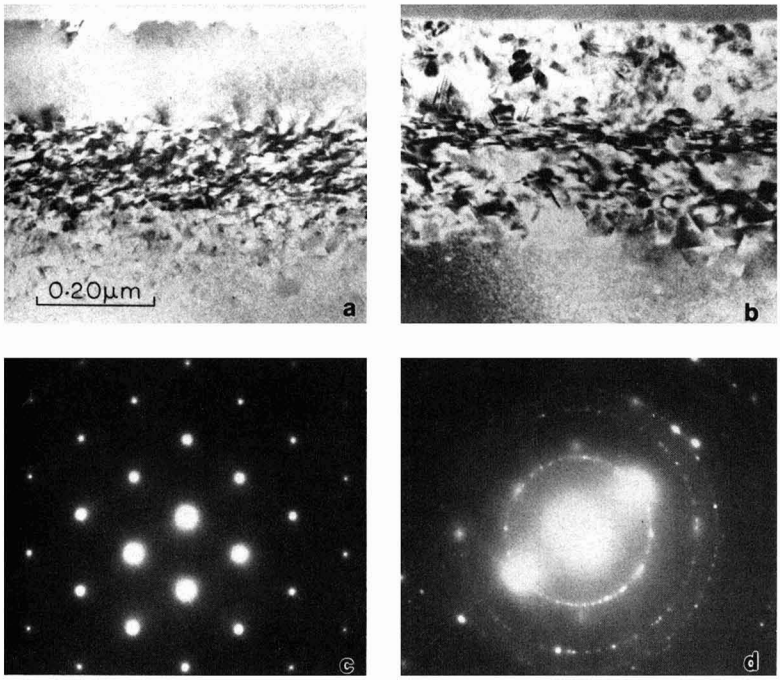


Fig. 10. Comparison of high dose-rate effects in <100>- and <111>-oriented silicon specimens implanted with 40 keV $^{30}Si^+$ to 1.5×10^{16} cm^{-2} dose at LN_2 (~ 5 μA cm^{-2}) and then implanted wih 120 keV $^{28}Si^+$ to 1.0×10^{16} cm^{-2} dose. A: Cross-sectional electron micrograph, (100) Si specimens. B: (111) specimens. C: Microdiffraction pattern from A. D: Microdiffraction pattern from B.

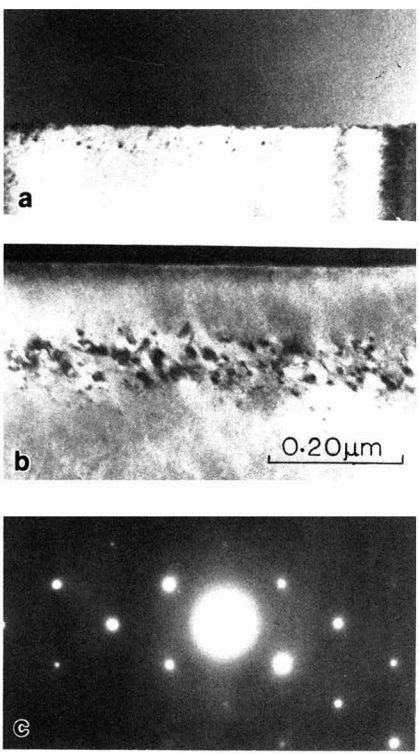


Fig. 11. Substrate temperature effects in (100) GaAs after ion implantation with 120 keV $^{28}Si^+$ to a dose of 5.0×10^{15} cm^{-2}. A: (110) cross-sectional electron micrograph with a dose rate ~ 5 μA cm^{-2} while substrate is at room temperature. B: ~ 5 μA cm^{-2} while substrate is at 200°C. C: (110) microdiffraction pattern from the specimen shown in B.

Figure 10d shows a microdiffraction pattern from the top layer, where diffraction rings are consistent with the polycrystalline structure of Fig. 10b. It is envisaged that SPE growth in <100> orientations is rapid enough to be completed before the nucleation of polycrystalline regions ahead of the crystallizing interface can occur (17). However, in <111> orientations, since the SPE growth rate is 24 times slower than that in <100> orientations, the crystallites can nucleate ahead of the crystallizing interface (3). Once these crystallites nucleate, interface-controlled growth cannot occur, and the whole layer turns polycrystalline.

Dose rate and substrate temperature effects in GaAs.—We have studied dose rate effects in <100> GaAs and compared the results with those obtained by heating the substrate during ion implantation. The ion implantation at low dose rates of $\sim$ 5-10 μA cm^{-2} typically results in the formation of amorphous layers followed by bands of dislocation loops. A typical example is shown in Fig. 11a, after 120 keV $^{28}Si^+$ implantation to a dose of 5.0×10^{15} cm^{-2}. The number density of dislocation loops in the underlying dislocation band is found to be lower in this case than that found in silicon for the same implant condi-

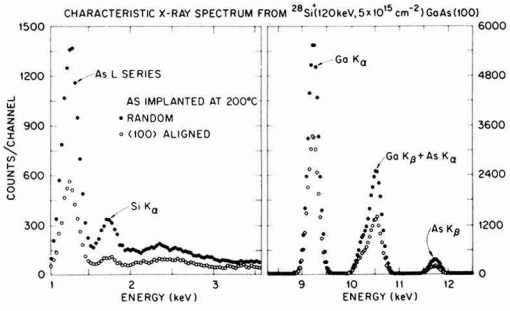


Fig. 12. Characteristic x-ray spectrum from specimens shown in Fig. 11b, showing random and <100>-aligned x-ray yields.

tions. By heating the substrate to 200°C during implantation, we found a 1100Å wide, defect-free region followed by a 900Å wide band of dislocation loops, as shown in Fig. 11b. Figure 11c is a microdiffraction pattern from the annealed region; it shows sharp and regular diffraction, as corresponded with a <110> orientation.

Figure 12 shows a characteristic x-ray spectrum taken in random and <100>-aligned directions. The differences in aligned and random spectra of Ga and As confirm good annealing of the lattice. The SiKα yield in random and <100>-aligned directions shows that more than 90% of Si is in substitutional sites. Thus, these results indicate that high electrical activation of dopants can be achieved by implantation at high temperatures. The silicon profiles were found to be Gaussian from SIMS-measurements, similar to the as-implanted profile, which indicates that annealing does not involve long-range migration of defects. This is consistent with SPE growth and close-pair recombination of vacancies and interstitials.

The annealing results similar to those obtained by heating the substrate can also be obtained by increasing the dose rate. Figure 13 shows a TEM cross-sectional micrograph from specimens implanted at 160 μA cm^{-2} to a dose of 5.0 × 10^{15} cm^{-2} (100 keV ^{28}Si$^+$ ions). The micrograph shows a ~ 1100Å wide, defect-free region followed by a 1000Å wide band of dislocation loops. As is shown in Fig. 11, heating the sample to 200°C produces qualitatively similar results. Figure 14 shows RBS results from specimens implanted at high currents ranging from 120 to 160 μA cm^{-2}. The dechanneling as a function of depth decreases with increasing dose rate, and the yields are close to virgin crystals for specimens implanted with 160 μA cm^{-2}.

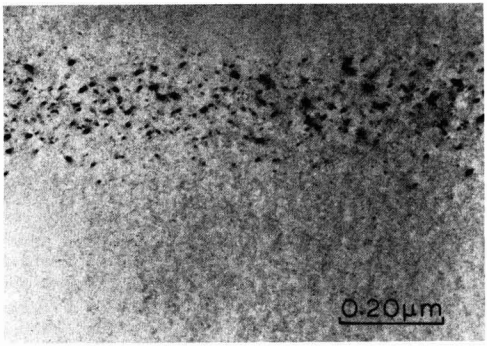


Fig. 13. Cross-sectional electron micrograph from (100) GaAs specimens implanted with 100 keV ^{28}Si$^+$ ions to a dose of 5.0 × 10^{15} cm^{-2} (dose rate = 160 μA cm^{-2}).

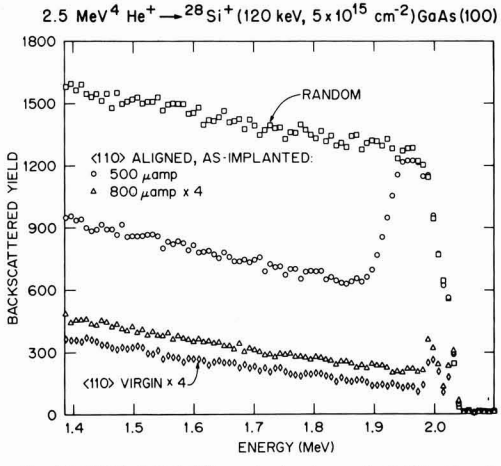


Fig. 14. 2.0 MeV He$^+$ RBS spectra (random and <110>-aligned) from ^{28}Si$^+$ (120 keV, 5.0 × 10^{15} cm^{-2}) implanted specimens at 120 and 160 μA cm^{-2} specimens.

Thermal annealing of different ion implantation states.—We now present a detailed characterization of some ion implantation states and their subsequent annealing behavior. At low dose rates, we produce buried amorphous layers, which expand toward the surface and into the deeper regions of the crystal as the implanted dose is increased. At a certain dose, which is critically determined by the ion implantation and substrate variables, we obtain a continuous amorphous layer, which extends from the surface to a certain depth and is followed by a band of dislocation loops. In this section, we divide the discussion into two parts: (*i*) annealing of amorphous layers; and (*ii*) annealing of dislocation loops in the underlying dislocation band.

The annealing of amorphous layers occurs by an interface-controlled crystallization process commonly referred to as solid-phase epitaxial (SPE) growth. An example is shown in Fig. 15, where by annealing at 550°C for 25 min, the interface moved toward the surface by a distance of 1050Å. The specimens after ion implantation (100 keV ^{30}Si$^+$ to 5.0 × 10^{15} cm^2 dose) contained a 2830Å amorphous layer followed by a band of dislocation loops. This band of dislocation loops is left behind during SPE growth.

Figure 16 shows an implantation state (100 keV ^{30}Si$^+$ to 5.0 × 10^{14} cm^{-2} dose at liquid nitrogen temperature) where the amorphous layer does not extend to the surface entirely. Figure 16a shows a bright-field, cross-sectional TEM micrograph in which dark regions near the surface represent crystalline islands. The sample contains a 2150Å wide amorphous layer followed by a band of dislocation loops. Figure 16b shows a high resolution micrograph of the near-surface region. The crystalline islands contain two sets of fringes corresponding to (111) and ($\bar{1}$11) planes in <01$\bar{1}$> orientation. The size of crystalline islands varies from 6 to 30Å. It is interesting to note the presence of a 15Å thick oxide layer above the crystalline islands. The structure of the oxide is noncrystalline. If such samples are annealed, the SPE growth occurs both from the front and back sides of the specimens, as shown in Fig. 16c. The thickness of the SPE-grown back and front layers is 750Å and 450Å, respectively. The front amorphous-crystalline interface is considerably more undulated than the back interface. However, both the front and back SPE-grown layers have exactly the same orientation as the substrate, as shown by the microdiffraction patterns in Fig. 17. Figures 17a and 17b are microdiffraction patterns of front and back SPE-grown layers, respectively, both of which have identical <110> diffraction patterns. A microdiffraction pattern from the amorphous layer is shown in Fig. 17c, which contains characteristic amor-

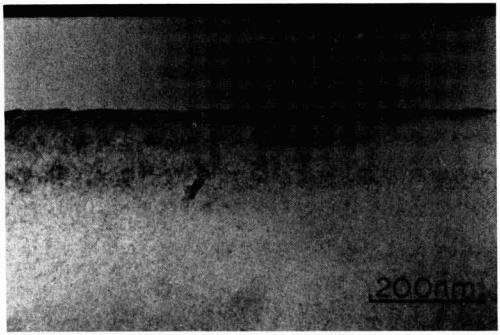


Fig. 15. Cross-sectional electron micrograph from ^{30}Si$^+$-implanted (100) Si specimen after annealing at 550°C for 20 min. The substrate was kept close to liquid He temperature and implanted with 100 keV ^{30}Si$^+$ to a dose of 5.0 × 10^{15} cm^{-2}.

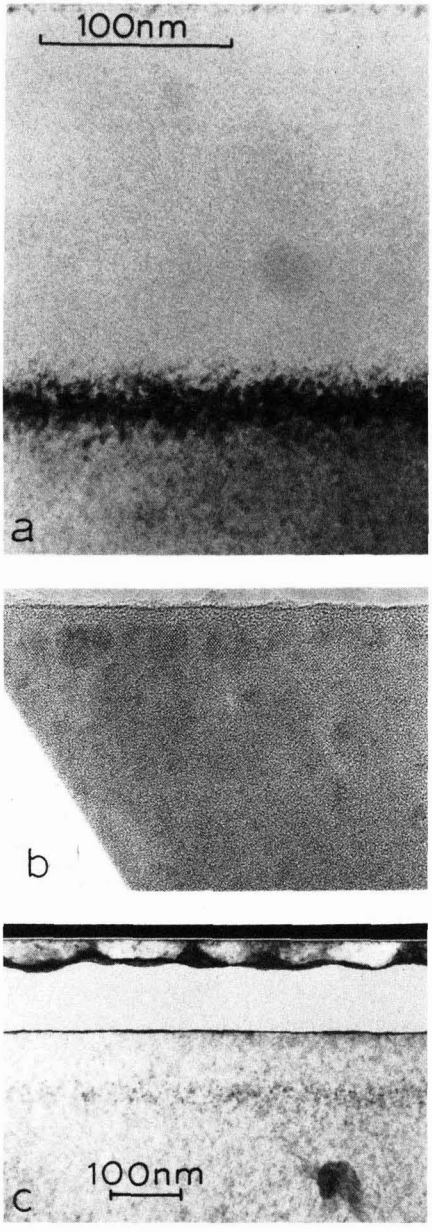


Fig. 16. A: Cross-sectional electron micrograph of as-implanted (100) Si specimens (100 keV $^{30}Si^{+}$, 5.0×10^{14} cm^{-2}) containing crystalline islands near the surface. B. High resolution micrograph of A showing crystalline islands and the native oxide ~15Å thick. C: After isothermal annealing at 550°C for 10 min.

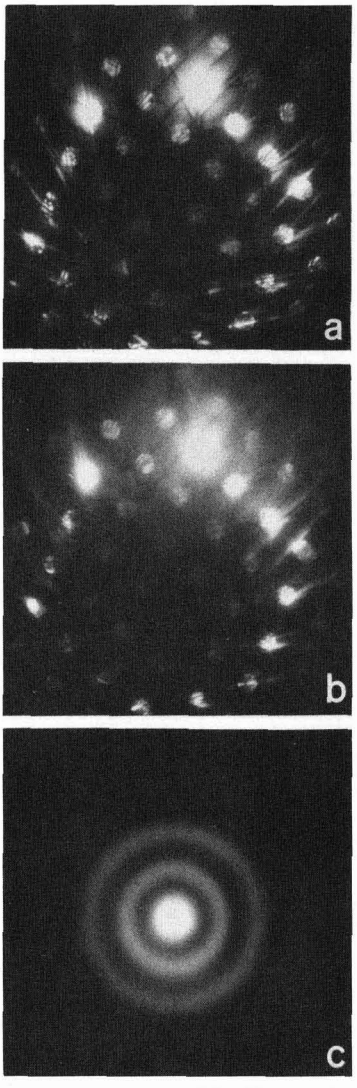


Fig. 17. Microdiffraction patterns of the different regions of specimens shown in Fig. 16C. A: Front layer. B: Back layer. C: Middle amorphous layer.

phous rings. As the time of isothermal annealing was increased to 40 min at 550°C, the front and back crystallizing interfaces were found to meet at a depth of about 880Å. The dark line in Fig. 18a shows that defects associated with the interface at 880Å are limited to within a 10Å wide region. The nature of these defects was analyzed by plan-view electron microscopy, and the results are shown in Fig. 18b. The defects in this band consist of defect clusters and dislocation loops of interstitial nature. An approximate determination of concentration of point defects showed that the number of interstitials is equal to the number of implanted Si^{+} ions. Recent RBS experiments (14) on high dose-rate annealing have shown that if buried amorphous layers are formed during early states of ion implantation, the annealing occurs by SPE growth from both front and back sides.

Annealing effects in underlying dislocation bands and gettering.—We now discuss the nature and annealing of dislocation bands below the amorphous layers. The dislocation loops in the region are formed as a result of clustering of point defects that escape amorphous regions. Due to ion-range straggling, the number density of displacements in this region does not reach the critical value needed for amorphization. The number density of dislocation loops in this region is critically determined by ion implantation and substrate variables. The specific damage-energy density (the number of displacements per unit volume) and ion range straggling are primarily determined by the atomic mass of the projectile and substrate and the energy of the projectile. This, in turn, determines the number of point defects that can escape the amor-

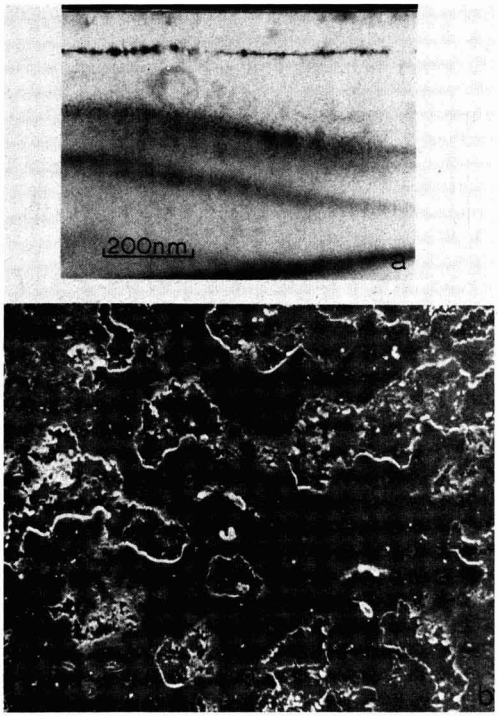


Fig. 18. Defect microstructures of specimens shown in Fig. 16C after thermal annealing at 550°C for 40 min. A: Cross-sectional micrograph. B: Plan-view micrograph of dislocation loops and tangles.

phous regions. The mobility of defects and subsequent clustering into dislocation loops are determined by the substrate temperature. The dislocation loops are observed (by conventional TEM imaging techniques) to be of an interstitial nature. The size of vacancy loops is usually much smaller (5-10Å) than that of interstitial loops. The number density of dislocation loops decreases with decreasing substrate temperature. Figures 19a and 19b show a comparison between room temperature and liquid nitrogen temperature implants (200 keV $^{28}Si^+$ to 1.5×10^{16} cm^{-2} dose). These specimens were annealed at 550°C/5 min so that underlying dislocation bands could be delineated. The nature of the dislocation band also affects the defect density in the SPE-grown layers. In room temperature implants, the amorphous-crystalline interface intersects dislocation loops whose average size is much larger than that in the liquid nitrogen temperature implants. As a result, during SPE growth, these dislocations continue to grow with the interface and create a network of high number density of hairpin dislocations. The number density of loops in the underlying dislocation band also decreases with increasing mass of the projectile or the substrate. An example is shown in Fig. 19c for a bismuth implant (200 keV, 1.0×10^{16} cm^{-2} dose) in silicon. With increasing mass of the projectile, specific deposited damage energy increases, resulting directly in amorphous cascades and allowing the escape of a smaller number of defects to form loops.

The dislocation loops should be minimized or, preferably, removed because they are detrimental to electrical characteristics of p-n junctions. The dislocations with energy levels close to the middle of the bandgap provide efficient recombination centers. The dislocations are also known to provide trap centers via electronic and elastic interactions. The dislocations in these bands are particularly undesirable, owing to their close proximity to the metallurgical junction. The annealing characteristics of dislocation loops during heat-treatment are determined

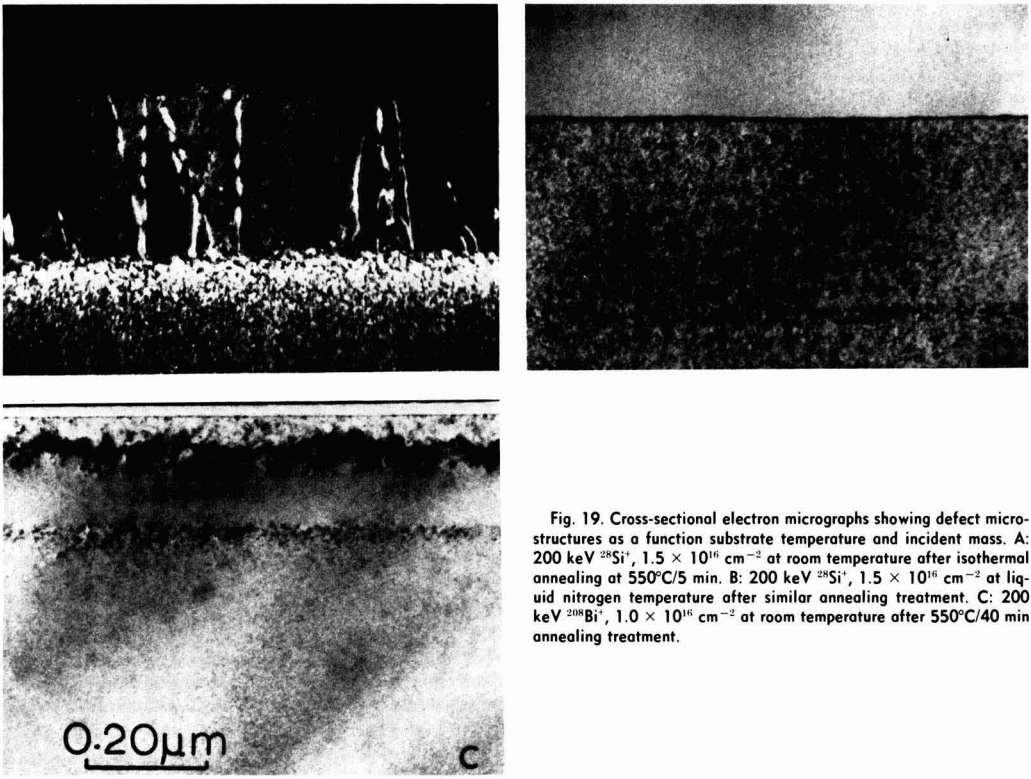


Fig. 19. Cross-sectional electron micrographs showing defect microstructures as a function substrate temperature and incident mass. A: 200 keV $^{28}Si^+$, 1.5×10^{16} cm^{-2} at room temperature after isothermal annealing at 550°C/5 min. B: 200 keV $^{28}Si^+$, 1.5×10^{16} cm^{-2} at liquid nitrogen temperature after similar annealing treatment. C: 200 keV $^{209}Bi^+$, 1.0×10^{16} cm^{-2} at room temperature after 550°C/40 min annealing treatment.

by the average size and number density of loops. If the distance between two loops is less than twice the diameter of the larger loops, these two loops may coalesce by glide and climb processes and form larger loops (18). If the loops are farther apart, they shrink by a normal bulk diffusion process (19). Figure 20 illustrates the subsequent annealing behavior of two different ion implantation (100 keV As^+, 1.0×10^{16} cm^{-2} dose) states shown in Fig. 6a (high dose rate) and Fig. 6c (low dose rate). The dislocation tangles in the high dose-rate samples evolve into a complicated network of dislocations upon subsequent thermal annealing (at 850°C/30 min). It was found that the carrier concentration and mobility are degraded after the above annealing treatment, presumably because of segregation and trapping of dopants at the dislocations. In the case of low dose-rate samples, the amorphous layers grow by a solid-phase epitaxial growth process, and the loops coarsen by loop coalescence. Sometimes a network is generated by a well-known dislocation reaction: $a/2\langle 101\rangle + a/2\langle 01\bar{1}\rangle \rightarrow a/2\langle 110\rangle$, as shown by the 1 in Fig. 20b. The electrical properties (carrier concentration and mobility) of these specimens were found to improve continuously with subsequent annealing treatment after SPE growth.

The dislocations in the underlying dislocation bands provide effective impurity/dopant traps via elastic and electronic interactions. The dislocations can also be used to tie up or remove unwanted impurities by trapping them at the dislocations. We illustrate antimony trapping or segregation at the dislocations in Fig. 21. The (100) Si specimens were implanted with 200 keV, 4.4×10^{15} Sb^+ cm^{-2} dose; they were annealed at 550°C/20 min for SPE growth of the amorphous layers and subsequently heat-treated at 900°C for 30 min. After the latter heat-treatment, large precipitates were formed at the dislocations, making

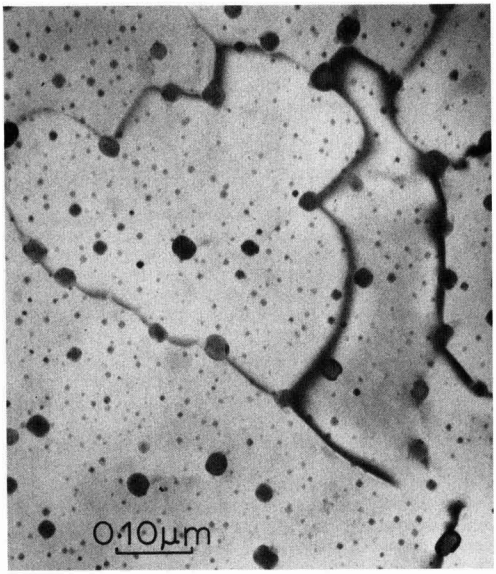


Fig. 21. Plan-view electron micrograph showing gettering of antimony by dislocations after heat-treatment of Sb^+-implanted (200 keV, 4.4×10^{15} cm^{-2}) specimens, 550°C/20 min and 900°C/30 min.

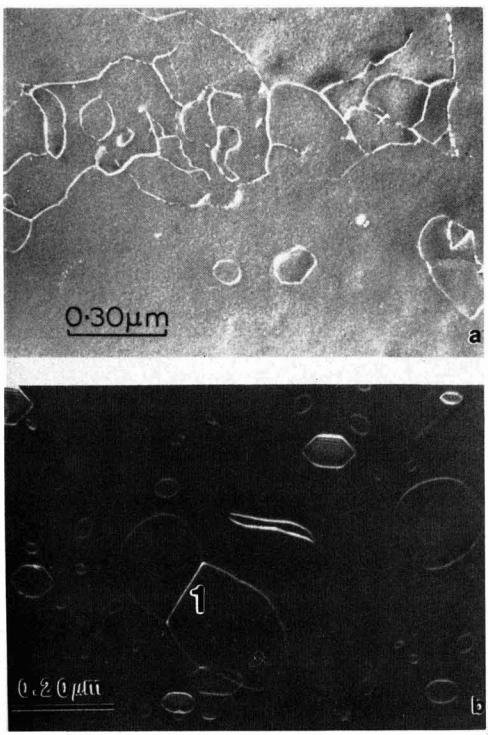


Fig. 20. Comparison of subsequent annealing behavior of high and low dose-rate As^+-implanted specimens. A: High dose-rate specimens of Fig. 6A after isothermal annealing at 850°C/30 min. B: Low dose-rate specimens of Fig. 6B after the same heat-treatment.

them efficient traps for dopants. Figure 22 illustrates gettering of fluorine by dislocations in a BF_2^+-implanted (100) Si, which was annealed at 1100°C for 5s in a rapid thermal annealing apparatus. The as-implanted specimens (50 keV BF_2^+, 1.0×10^{15} cm^{-2} dose) contained a 500Å wide amorphous layer followed by a band of dislocation loops. After the rapid thermal annealing treatment, the loops coarsened and gettered the fluorine, as indicated by the formation of fluorine bubbles near the dislocations (see bubbles as white spots in the micrograph). The secondary ion-mass spectrometry results on fluorine

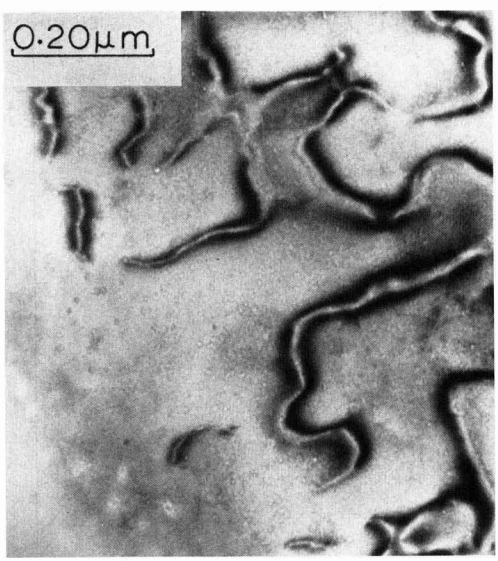


Fig. 22. Plan-view electron micrograph showing gettering of fluorine by dislocations after rapid thermal annealing (1100°C for 5s) of BF_2^+-implanted specimens (50 keV BF_2^+, 1.0×10^{15} cm^{-2}).

profiles show a peak corresponding to the dislocation band. It is interesting to note that loops are confined in a rather narrow band because the segregation of fluorine inhibits the glide of dislocations. It was found that, by further annealing, the dislocations and fluorine are removed simultaneously.

Conclusion

We have shown that the nature of ion implantation damage is a strong function of implantation and substrate variables. In silicon, crystalline to amorphous phase transformation occurs above a critical damage energy of 12 eV/atom if there are negligible annealing effects. This value is very close to the displacement threshold. For other materials, the critical specific damage energy is expected to scale according to the displacement threshold energy. By increasing the dose rate, the substrate temperature is increased, which enhances the SPE growth rate of amorphous layers and/or the recombination of close pairs of vacancies and interstitials. The as-implanted profiles in high dose-rate implants were found to be unchanged because of negligible diffusion distances of dopants, as estimated from time and temperature of implants. The specimens implanted at high dose rates contain defect-free, self-annealed layers followed by a wide band of dislocation loops. In the defect-free, self-annealed layers, up to 90% of the arsenic was found to be in substitutional (electrically active) sites. During high dose-rate implants, buried or near-surface amorphous layers are formed, the annealing of which involves SPE growth from both the front and back sides (buried layers) or growth from the back side (near-surface layers). At still larger dose rates, there is a region in the implantation current where we obtain undesirable void structure. A comparison of microstructures obtained at high dose rates and high substrate temperatures shows that these two parameters are interchangeable. The number density of dislocation loops in the underlying dislocation band can be manipulated by ion implantation and substrate variables. The average size and number density of loops play a critical role in the development of network of dislocations during subsequent annealing. These dislocations provide strong recombination and trap centers for impurities and dopants. By moving their locations away from the junctions, these dislocations can be used to getter unwanted impurities that adversely affect the p-n junction characteristics.

Acknowledgments

We are grateful to D. Fathy, S. J. Pennycook, and O. S. Oen for useful discussions.

Manuscript submitted April 4, 1984; revised manuscript received July 10, 1984.

Oak Ridge National Laboratory assisted in meeting the publication costs of this article.

REFERENCES

1. K. A. Pickar, *Appl. Solid State Sci.*, **5,** 152 (1975).
2. J. Narayan and O. W. Holland, *Appl. Phys. Lett.*, **41,** 239 (1982).
3. J. Narayan, O. W. Holland, and B. R. Appleton, *J. Vac. Sci. Technol. B*, **1,** 871 (1983).
4. T. O. Segwick, *This Journal*, **130,** 484 (1982).
5. C. W. White, J. Narayan, and R. T. Young, *Science*, **204,** 461 (1981).
6. J. Narayan, J. Fletcher, C. W. White, and W. H. Christie, *J. Appl. Phys.*, **52,** 7128 (1981).
7. P. P. Pronko, A. K. Rai, O. W. Holland, B. R. Appleton, and J. Narayan, *ibid.*, **53,** 5621 (1982).
8. G. H. Kinchin and R. S. Pease, *Rep. Prog. Phys.*, **18,** 1 (1955); M. J. Norgett, M. T. Robinson, and I. M. Torrens, *Nucl. Eng. Des.*, **33,** 50 (1975).
9. J. W. Corbett and J. C. Bourgoin, in "Point Defects in Solids," J. H. Crawford and L. M. Slifkin, Editors, p. 1, Plenum Press, New York (1975).
10. J. R. Dennis and E. B. Hale, *J. Appl. Phys.*, **49,** 1119 (1978).
11. K. B. Winterbon, P. Sigmund, and J. B. Sanders, *Mat. Fys. Medd. Dan. Vid. Selsk.*, **37** (1970).
12. P. Sigmund, *Appl. Phys. Lett.*, **25,** 169 (1974).
13. B. C. Larson, R. T. Young, and J. Narayan, in "Neutron Transmutation Doping in Semiconductors," J. M. Meese, Editor, p. 281, Plenum Press (1979).
14. O. W. Holland and J. Narayan, *Appl. Phys. Lett.*, **44,** 748 (1984).
15. M. R. Rulhe, in "Radiation-Induced Voids in Metals," J. W. Corbett and L. C. Ianniello, Editors, p. 255, National Technical Information Service (CONF-710601), Washington, DC (1972).
16. R. Bullough and R. C. Perrin, in "Radiation-Induced Voids in Metals," J. W. Corbett and L. C. Ianniello, Editors, p. 769, National Technical Information Service (CONF-710601), Washington, DC (1972).
17. S. A. Kokorowski, G. L. Olson, and L. D. Hess, *J. Appl. Phys.*, **53,** 921 (1982).
18. J. Narayan and J. Washburn, *ibid.*, **43,** 4862 (1972); *Philos. Mag.*, **26,** 1179 (1972).
19. I. R. Sanders and P. S. Dobson, *J. Mater. Sci.*, **9,** 1987 (1974).

TEM Cross Section Sample Preparation Technique for III-V Compound Semiconductor Device Materials by Chemical Thinning

S. N. G. Chu* and T. T. Sheng

AT&T Bell Laboratories, Murray Hill, New Jersey 07974

ABSTRACT

A cross section sample preparation technique is described for the TEM studies of III-V compound semiconductor device materials. In this technique, a grid-masking method is introduced for selective-area perforation using chemical etching. By epoxy bonding a TEM specimen grid onto the surface of a face-to-face or face-to-back epoxy-bonded thin cross section sample stack, perforations by chemical etching are confined to the regions inside the meshes. Selective-area perforation can easily be achieved by accurately positioning the masking grid and monitoring the perforation under a microscope. Since many perforations can be made in the selected area, the chance of obtaining a cross section sample containing the device structure is greatly increased. Furthermore, the masking grid mechanically reinforces the perforated sample and hence eliminates problems associated with sample handling. Examples of the use of this technique for InP/InP(substrate) single-layer and p⁺-InGaAsP/p-InP/InGaAsP/n-InP/InP(substrate), multilayer laser device structures, grown by vapor-phase epitaxy, are demonstrated. The technique is also applicable to GaAlAs/GaAs multilayer structures, and, in addition, greatly facilitates the selective-area perforation of plan-view TEM samples.

Cross-sectional transmission electron microscopy (XTEM) has proven itself to be a powerful technique for the study of the generation and evolution of defect structures during heteroepitaxy of III-V compound semiconductor device materials (1, 2). In silicon integrated-circuit processing, XTEM is now routinely used for the characterization of process-related problems (3). The essential part of the XTEM technique, however, is the preparation of cross section samples containing the desired device structure.

Because most semiconductor devices consist of layers with thicknesses ranging from a few hundred angstroms to several microns near the surface of the wafer, reproducible XTEM samples are generally difficult to prepare. For example, sample preparation requires that the perforation, by ion milling or chemical etching, occur not only near the edge of the cross section, but right at where the desired device structure is located as well. Edge erosion of the sample is another problem. Unless the edge is well protected, the device structure is usually eroded before a perforation occurs.

These difficulties in the preparation of XTEM sample of silicon integrated circuits were overcome by Sheng *et al.* (3) using an epoxy embedding technique combined with large area ion milling. Direct application of this technique to InGaAsP/InP heterostructure-device materials, however, was found to be difficult simply because of the extreme fragility of the III-V materials compared with silicon. In this work, we report a new chemical thinning technique for the preparation of XTEM samples for III-V compound semiconductor device structures. We also introduce a grid masking method that allows us to control precisely the selected-area perforation. Finally, the XTEM for InP/InP single-layer and InGaAsP/InP multilayer structure materials are demonstrated.

Sample Preparation Technique

Thin cross section samples were cleaved from device wafers along a (011) plane. The cleaving process was facilitated by thinning the device wafer, from the back side, to less than 0.3 mm, using chemical-mechanical polishing in 2% Br_2-methanol solution. The cross section samples were epoxy bonded to form a stack with the device structures either face to face or face to back, as shown in Fig. 1, using extra-fast setting epoxy by Hardman, Incorporated (Belleville, New Jersey 07109). Excess epoxy was squeezed out between the samples. For best results in the subsequent thinning process, the thickness of the epoxy film was kept to a minimum. The cross section sample stack was then thinned by polishing it from both sides to a final thickness of about 20 μm.

*Electrochemical Society Active Member.

The details of the polish thinning process are as follows. The cross section stack was first bonded to a slide cover-glass, which in turn was bonded to a titanium disk (part of the sample polishing holder). A transparent crystal bond or soft wax can be used as a bonding material. The sample stack was surrounded with InP substrate wafers, as shown in Fig. 2, to prevent the edges of the stack from being rounded off during the polishing process. The stack was polished on one side to smooth the cross section surface and then turned over and polished to a final thickness of around 20 μm. Figure 3 shows Nomarski interference micrograph of a polished cross section sample stack.

Perforation by chemical etching immediately adjacent to the epoxy joint in the device region was accomplished by using a grid masking technique. A 100-mesh molybdenum grid was epoxy bonded onto the cross section stack, as shown in Fig. 4, using the same epoxy described before. Such grid masking requires careful alignment of the openings in the epoxy-coated grid to expose the device region, and can be done by using the grid-mounting jig shown in Fig. 5. With the cross section stack still on the titanium disk (Fig. 5), the disk is attached to the alignment block using double-sided adhesive tape. The sample

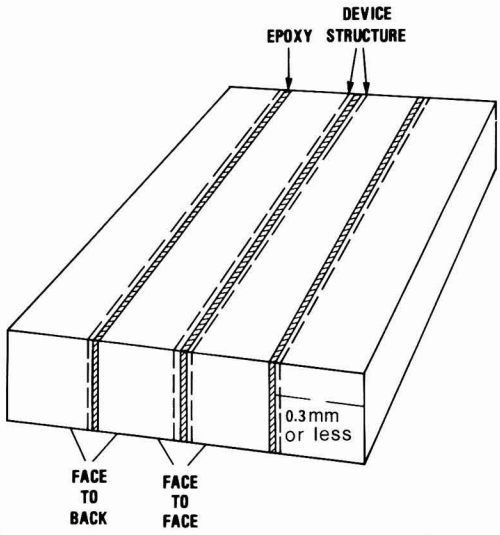


Fig. 1. Schematic diagram of face-to-face and face-to-back cross section sample stack bonded by epoxy.

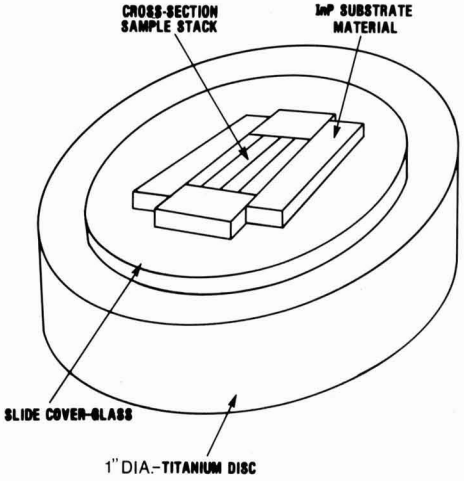


Fig. 2. Schematic diagram of a cross section sample stack surrounded by InP substrate wafer, ready for initial polish thinning.

stack is centered by adjusting the four alignment screws on the grid mounting device. It is then visually aligned by moving one of the epoxy-bonded interfaces to the center of the device using the transparent alignment cover. An epoxy-coated 3 mm diam molybdenum grid is placed over a 2 mm diam hole inside the grid mounting cover, and is lightly held in place by the epoxy on the grid to the edge of the hole. The grid mounting cover is then turned over and slid onto the grid mounting device until it contacts the stop ring which prevents the grid from contacting the sample surface.

Precise alignment of the grid to expose the desired area is then accomplished under a stereo microscope by adjusting the position of the sample with respect to the grid. The stop ring is released and the grid mounting cover lowered until the grid rests on the surface of the sample. Gentle pressure on the grid mounting cover transfers the grid onto the surface of the cross section stack.

Two important points should be noted: (i) only a thin layer of epoxy should be applied to the grid. Excess epoxy tends to smear out and cover the openings of the

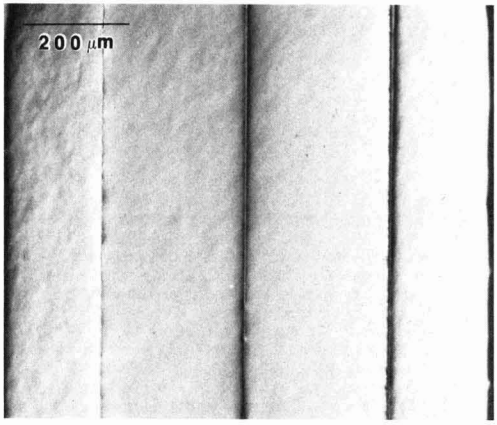


Fig. 3. Optical micrograph of the surface of a polished cross section couple. The dark strip is the epoxy.

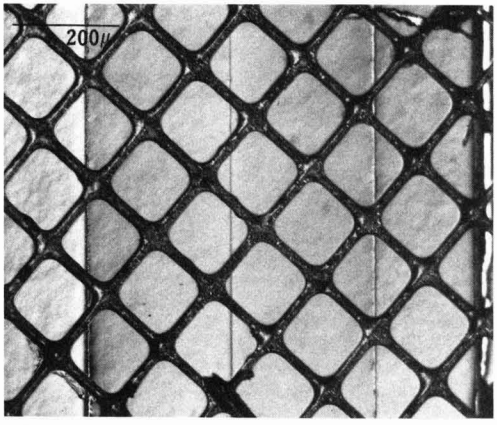


Fig. 4. Optical micrograph of a masking grid epoxy bonded to the surface of a thin cross section sample stack.

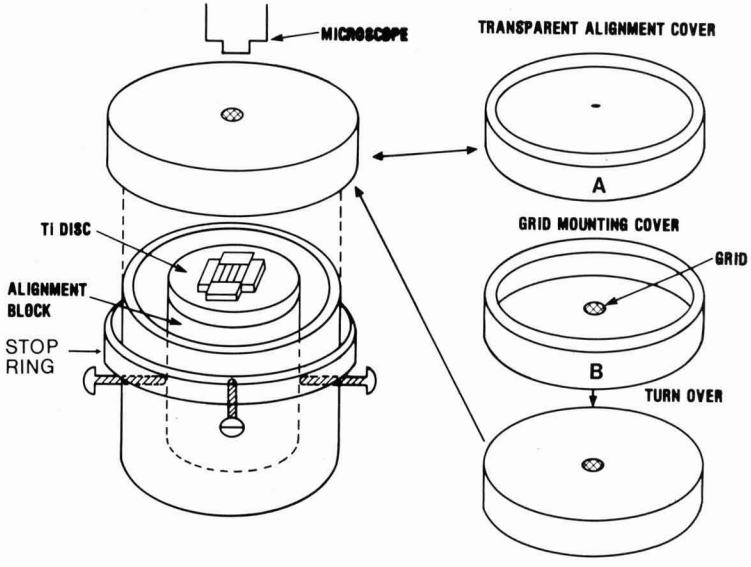


Fig. 5. Schematic diagram of the grid mounting device. Cover A is for initial alignment of the sample. Cover B is for mounting the grid.

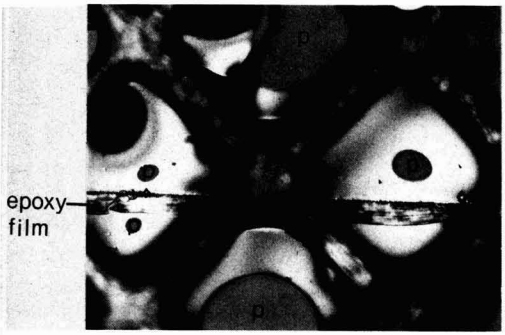


Fig. 6. Optical micrograph showing typical perforations occurring inside the mesh near the device structure. The dark ribbon is the epoxy film; perforations are labeled P.

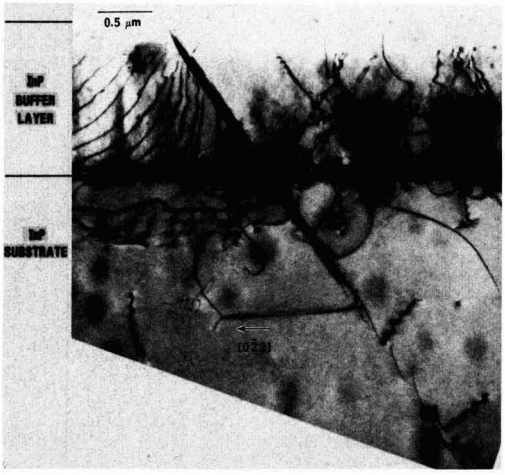


Fig. 7. XTEM of 1.3 μm InP buffer grown by VPE on InP substrate

grid. (*ii*) Any movement of the grid parallel to the surface must be prevented after the grid is transferred to the cross section stack. To avoid having the grid accidentally cover the entire device region, the edge of the cross section is aligned along the diagonal of the square mesh as shown in Fig. 4. The sample is then transferred with the cover glass onto a quartz disk.

The final perforation is done inside a crystalline dish by dripping 0.5% Br_2-methanol solution onto the masked-sample surface. A stereo microscope equipped with both reflection and transmission illumination is used to monitor the perforation. Because perforations are made only inside the meshes, each mesh becomes an individual sample. Grid masking, therefore, greatly increases the success of obtaining a good XTEM sample. The etching process is stopped by applying a jet of methanol to the sample using a squeeze bottle. Small variations in thickness always exist across the polished cross section sample stack. As a result, perforations inside the mesh normally occurred progressively from mesh to mesh, starting from the thinnest area. It is important to stop the etching at the right moment, since the thin area around the perforation tends to be etched away very rapidly. The

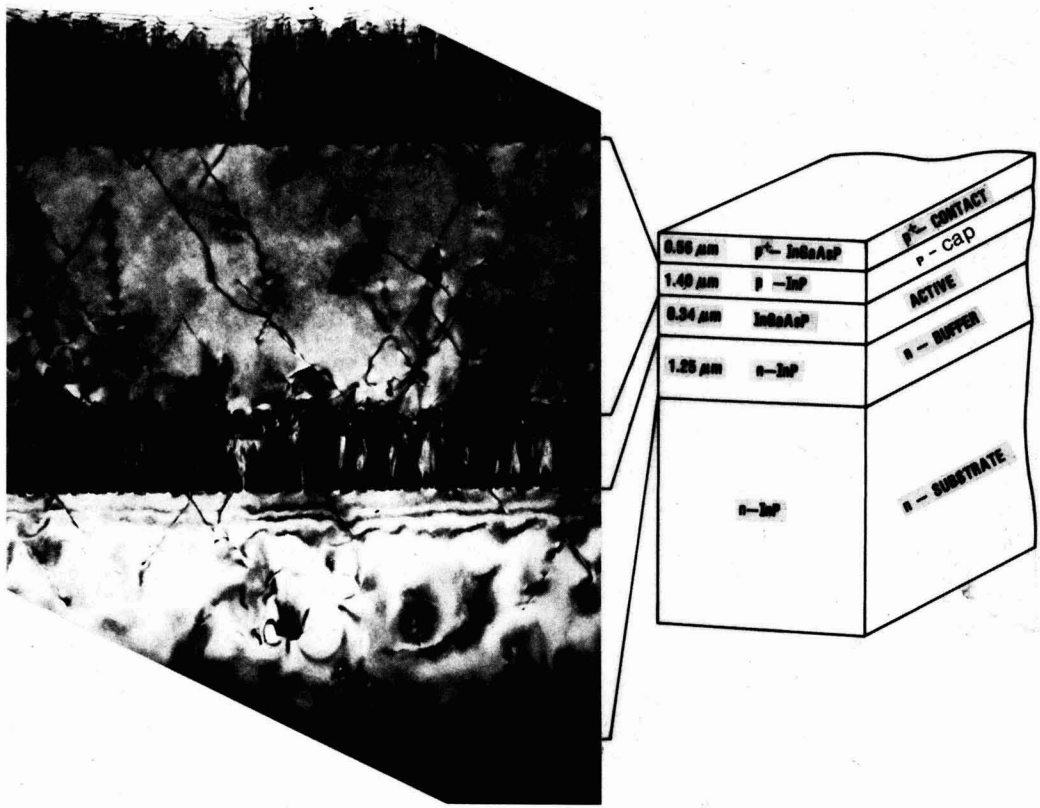




Fig. 9. A tilted cross section view of the p-InP/InGaAsP (active) n-InP regions, showing the interfaces.

proper thickness at which to stop etching was judged by the transparency of the film as observed under the microscope using transmission illumination. When the proper transparency was achieved, the sample bonded to the grid was removed from the cover glass by soaking in acetone or trichlorethylene. Finally, the cross section sample is examined in the transmission electron microscope. Micrographs reported in this paper were taken using a JEOL 200-A instrument.

Results and Discussion

Figure 6 is an optical micrograph showing perforations that occur successively inside two meshes near the device structures. The semitransparent regions surrounding some of the perforations extend all the way to the device regions — a condition that is ideal for TEM studies. Since epoxy does not react with Br_2-methanol, the epoxy film between the cross section remained as the semiconductors on both sides were etched away. The dark ribbon in Fig. 6 is the epoxy film that fell and covered one of the face-to-face epoxy-joined device structures.

A TEM cross section view of a 1.3 μm InP buffer layer grown by vapor-phase epitaxy on a (100) InP substrate is shown in Fig. 7. The InP epitaxial layer was contaminated by gallium during growth. It is therefore lattice mismatched to the InP substrate. This is shown by the presence of the straight interfacial-misfit dislocations oriented along the $[0\bar{1}1]$ direction. The dislocation networks on both sides of the interface were generated at the interface and propagated along the {111} planes. Furthermore, the dark band oriented along the $[\bar{1}\bar{1}2]$ direction was verified to be a stacking fault. The detailed study of the gallium contamination of InP grown by vapor-phase epitaxy will be discussed in another paper (4).

The TEM cross section view of an InGaAsP/InP laser structure grown by vapor-phase epitaxy on a (100) InP substrate is shown in Fig. 8. The multilayer structure consists of 1.25 μm thick n-type InP buffer layer, a 0.34 μm thick undoped InGaAsP active layer, a 1.4 μm thick p-type InP cap layer, and a 0.56 μm thick p^+-InGaAsP contacting layer. High density threading dislocations generated at the binary/quaternary interface, and threading through the quaternary layers can be seen in both active and p-contacting layers. These dislocations lie either in the {111} planes or along a direction close to [100]. Furthermore, areas of diffuse dark contrast close to the [100] orientation are also present, similar to those observed by Al-Jassim *et al.* (1) in InGaAs/InP VPE structures. An examination of the threading dislocation density between the active layer and p-InP shows that the majority of the dislocations are either bent into the interface or recombined at the interface.

This bending and recombining is also seen in the tilted cross section view shown in Fig. 9. The threading dislocations recombine and form large dislocation tangles, only a few of which are propagated into the p-InP region. The lower interface shows a network of strain fields where the threading dislocations originate. The detailed characterization of the defect structure and the interfaces will be discussed in another paper. Similar quality of cross-sectional TEM samples have been achieved using the same technique on GaAlAs/GaAs and InAlAs/InGaAs/InP multilayer structures.

Conclusion

We have described a technique for preparing cross section samples for TEM studies of III-V compound semiconductor device materials using a chemical thinning technique. An essential aspect of the technique is the use of a grid masking method that makes it possible to exercise precise control over the selected-area perforation in the device regions. Since the perforation is confined to the area inside the mesh, each mesh becomes an individual sample, greatly increasing the probability of obtaining a good XTEM sample. The masking grid also mechanically reinforces the thin cross section of the sample, thereby alleviating sample handling problems. We have used the technique to prepare XTEM samples for InP/InP single-layer and InGaAsP/InP multilayer laser structures. The technique can also be applied to GaAlAs/GaAs and InAlAs/InGaAs/InP device structures, and, in addition, greatly facilitates the preparation of plan-view TEM samples.

Acknowledgments

The authors are grateful for the support and encouragement of W. D. Johnston, Jr., R. B. Marcus, and J. V. DiLorenzo. Appreciation is also due to S. Mahajan for the technical instruction of TEM, K. E. Strege for providing us with the VPE sample, and C. M. Jodlauk for technical assistance. The valuable discussion with T. Boone on the polishing technique is acknowledged.

Manuscript submitted April 2, 1984; revised manuscript received May 18, 1984.

AT&T Bell Laboratories assisted in meeting the publication costs of this article.

REFERENCES

1. M. M. Al-Jassim, M. Hockly, and G. R. Booker, in "Defects in Semiconductors," J. Narayan and T. Y.

Tan, Editors, p. 521, North-Holland, Amsterdam (1981).
2. G. H. Olsen, and M. Ettenberg, in "Crystal Growth," Vol. 2, C. H. L. Goodman, Editor, p. 1, Plenum Press, New York (1974).
3. T. T. Sheng and R. B. Marcus, *This Journal*, **127**, 738 (1980).
4. S. N. G. Chu, F. A. Stevie, A. T. Macrander, R. F. Karlicek, C. C. Chang, C. M. Jodlauk, K. E. Strege, D. L. Mitcham, and W. D. Johnston, Jr., Submitted to *This Journal*.

Mass Spectrometric Transient Study of DC Plasma Etching of Si in NF_3 and NF_3/O_2 Mixtures

T. Honda[1] and W. W. Brandt

Department of Chemistry and Laboratory for Surface Studies, University of Wisconsin-Milwaukee, Milwaukee, Wisconsin 53201

ABSTRACT

DC plasma etching experiments were performed on thin wafers of polycrystalline Si, using a pulse injection technique developed earlier, with NF_3 or NF_3/O_2 mixtures as etchants. The addition of O_2 was found to have no measurable effect on the etching rate, and steady-state concentrations of various radicals present in the plasma shifted relatively little. A fairly simple reaction scheme is presented which is consistent with these results. The NF_3 etching rates measured after oxidizing or nitriding the Si surface by plasma methods were explored to some extent as well.

It is very clear from the literature that plasma etching rates and related data obtained in different laboratories can normally not be compared in a quantitative fashion, since the experimental procedures, and, in fact, the quantities measured in each case, may differ. To arrive at reliable comparisons, the procedures must be standardized. At present, because of the large parameter space involved (1), this uniformity is an immediate and realistic objective only if the results which are to be compared are obtained in a single laboratory, using identical procedures, in short succession.

The present study represents such an attempt; the experimental procedures, including the sample preparation, were exactly the same as those used in several preceding studies (2, 3); only the etchant was changed, using NF_3 and NF_3/O_2 mixtures. The fragmentation of NF_3 in the plasma is likely to yield very few fragments, in contrast to SF_6 or SF_6/O_2 mixtures used earlier, judging from the published mass spectra of this gas (4-6). The tedious mass spectrometric fragmentation corrections needed to determine the concentrations of various excess species in the plasma are thus expected to be much simpler than those encountered in the earlier studies (2, 3, 7).

A second important reason for this study lies in that actinometric methods, based on optical emission measurements, are sometimes of no help in establishing the reaction mechanism of a system. For example, the plasma-etch rate of Si in NF_3/He mixtures fails to correlate with the concentration of electronically excited fluorine present in the plasma. Presumably the excitation transfer from He* (2^1S) to NF_3, with the simultaneous formation of excited F

$$He^*(2^1S) + NF_3 \rightarrow NF_2 + F^* + He \qquad [1]$$

becomes relatively important in certain mixtures, compared to direct electron impact excitation. There seem to be no actinometric results available on NF_3/O_2 mixtures thus far, but, eventually, such data, together with the results from this study, could help in determining the scope and reliability of actinometry in plasma etching studies (9, 10).

As an important by-product of this study, further information has been gathered concerning the detailed mass spectrometric procedures used in this and in previous studies (2, 3, 7), notably with respect to the unavoidable random errors, and minor systematic errors which have been identified earlier.

[1]Present address: Department of Chemical Engineering, Tokyo Institute of Technology, O-Okayama, Meguro-Ku, Tokyo, Japan.

Experimental

Most of the procedures used in this work are exactly the same as those used in the earlier studies (2, 3). Only the exposure of the polycrystalline Si sample to active O_2 and N_2 plasmas constitutes new types of experiments. The conditions are as shown in Table I.

Results and Discussion

Early during this study, it was recognized that the m/e = 71 and 52 signals, which are the major peaks in the NF_3 mass spectrum, and represent NF_3^+ and NF_2^+, respectively, were always proportional to each other, and that their ratio was within the range of literature values (4-6). If plasma-generated NF_2 radicals were present, henceforth termed "excess NF_2," the NF_2^+ peak should be larger than that found in the standard NF_3 mass spectra. There was no such excess NF_2 outside the experimental errors, and, as a consequence, only the 52 peak was measured in the bulk of this study and taken to be a convenient measure of unfragmented or produced NF_3 present in the plasma.

The peak at m/e = 85, representing SiF_3^+, served as a simple measure of the etch rate, as in earlier studies (2, 3). As illustrated in Fig. 1, this peak was found to be proportional (*i*) to the NF_2^+ signal, representing the unfragmented NF_3 in the plasma cell, and (*ii*) to the difference in the NF_2^+ peak before and after igniting the plasma, and thus to the amount of NF_3 fragmented in the plasma.

The signals at m/e = 33 and 14, representing NF^+ and N^+, respectively, were corrected for the contributions from the NF_3 mass spectrum, and are also plotted in Fig. 1. The signals thus represent "excess NF^+" and "excess N^+," respectively, which arise from NF and N radicals or ions formed in the plasma. The excess N^+ is seen to be proportional to the NF_2^+ and SiF_3^+ signals, and therefore to the etch rate, while the excess of NF^+ varies with the square of the NF_2^+ peak height (see Fig. 2).

Table I. Experimental conditions for O_2- and N_2-plasma treatment. Discharge voltage: 900V

Plasma gas	Pressure (torr)	Time (min)	Current (mA)
O_2	0.7	120	6.7
N_2	2.4	60	7.0

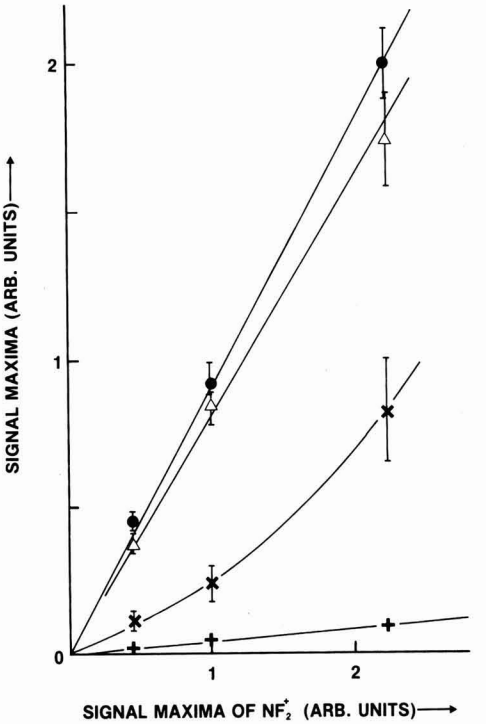


Fig. 1. Mass spectrometric signal maxima as a function of the amount of NF_3 injected with each pulse, as measured by the maximum of the NF_2^+ signal. ●: SiF_3^+. ×: NF^+. +: N^+. △: (NF_2^+ signal maximum from the inactive cell) - (same quantity where plasma is ignited). The NF^+ and N^+ signals are corrected for the contributions arising from the mass spectrometric fragmentation of NF_3.

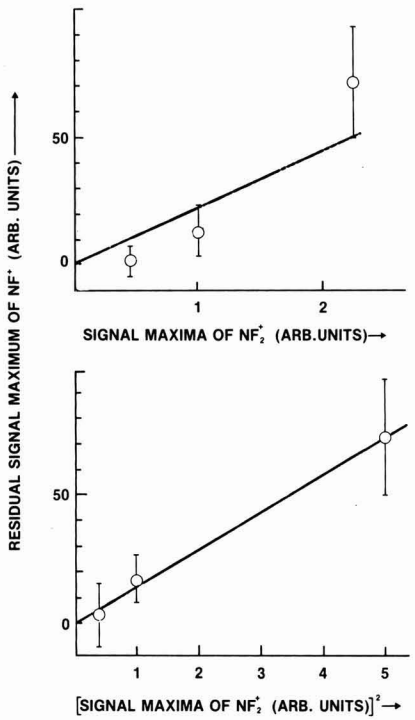


Fig. 2. Residual signal maximum of NF^+, after subtracting the estimated SiF_2^{++} contribution to the m/e = 33 signal from the measured signal height (see test), against the signal maxima of NF_2^+ (top), and against the same quantities squared (bottom).

Except for the last finding, one can summarize this as follows: there is essentially no measurable excess NF_2^+, little excess NF^+, and a somewhat larger excess N^+—in short, the F-depleted fragments tend to accumulate in the plasma, as one would expect.

The results presented here are consistent with a relatively simple reaction scheme

$$NF_3 \rightleftarrows NF_2 + F \quad [2]$$

$$NF_2 \rightleftarrows NF + F \quad [3]$$

$$NF \rightleftarrows N + F \quad [4]$$

$$Si + 2F \rightleftarrows SiF_2 \quad [5]$$

$$Si + NF_2 \rightleftarrows SiF_2 + N \quad [6]$$

$$SiF_2 + 2F \rightarrow SiF_4 \quad [7]$$

$$SiF_2 + NF_2 \rightarrow SiF_4 + N \quad [8]$$

Reactions [5] and [7] may well involve two separate steps which need not be discussed at length; the SiF_2 intermediate in the etching process has been documented by several spectroscopic studies (11, 12).

Reactions [6] and [8] are consistent with the fact that there is no measurable excess of NF_2 radicals in the plasma.

From the results analyzed in Fig. 2, one may postulate that in addition to the above reactions the disproportionation of NF_2

$$2NF_2 \rightarrow NF + NF_3 \quad [9]$$

plays an important role. There are possible variations of this scheme which cannot be eliminated from the present data alone, such as a modified reaction [8]

$$Si + 2NF_2 \rightarrow SiF_2 + 2NF \quad [8a]$$

Next, measured SiF_3^+ signal heights, which are considered a simple measure of the etch rate, are independent of the amount of oxygen added to the plasma, within experimental errors, as shown in Fig. 3. There is a slight decrease of the m/e = 52 signal, *i.e.*, of the amount of unfragmented NF_3 present. A corresponding slight increase of the SiF_3^+ signals is to be expected, but this effect is smaller than the experimental uncertainties.

Related to this, the changes in mass signals 33, 14, and 19, representing NF^+, N^+, and F^+, respectively, must be considered. Unfortunately, the F concentrations are too low to be measurable, but the trends in the 33 and 14, as shown in Fig. 3, lead to some insight.

The 33 peak has contributions from NF (radicals or ions) and SiF_2^{++}. NF probably reacts with plasma-generated O when O_2 is present, according to

$$NF + O \rightarrow NO + F \quad [10]$$

The NF contribution to the m/e = 33 signal initially present in O_2-free plasmas is thus expected to vanish as O_2 is added while the m/e = 30 peak, representing NO, increases at the same rate, as seen in Fig. 3. The m/e = 33 signal, which remains at high O_2 concentrations, presumably arises from the SiF_2^{++} peak in the SiF_4 mass spectrum; this is consistent with the measured SiF_3^+ signals and the literature spectra (4-6). The m/e = 30 signal continues to increase with increasing O_2 concentration in the plasma, balancing the previously mentioned increase in NF_3 fragmentation (decrease of NF_2^+ signal). In view of reaction [10], and within the experimental uncertainties, NF and F seem to be equally effective in the etching process.

The m/e = 14 signal as plotted in Fig. 3 is practically constant throughout this series; either reactions [6] and [8] are not shifted by the addition of oxygen, or the contri-

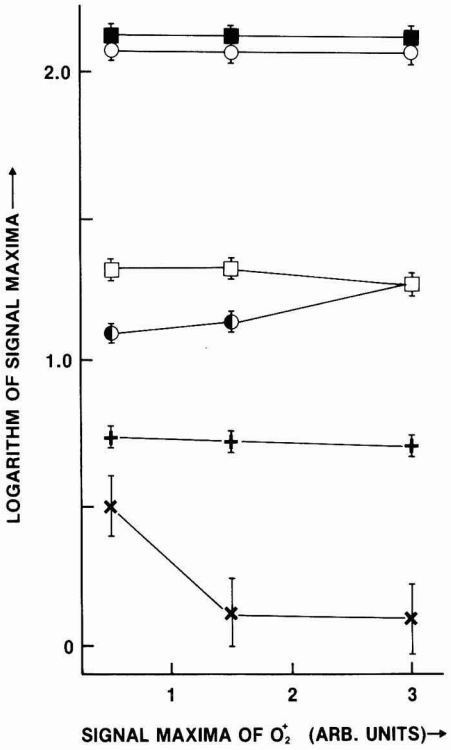


Fig. 3. Logarithm of signal maxima of various species against the signal maxima of O_2^+, as a measure of the strength of the O_2 pulses injected. ○: SiF_3^+. ■, □: NF_2^+ from the nonenergized plasma cell and in the presence of the plasma, respectively. ×, +, and ◐: signals at m/e = 33, 14, and 30, respectively.

butions to the signal height from NO and NF are about equal, per unit concentration. In this context, one must recall that the contribution to the mass 14 signal arising from unfragmented NF_3 was subtracted earlier, and that NF_2 radicals are not present to a measurable extent.

Small m/e = 44 and 82 peaks were found in this study, both decreasing with increasing O_2 pressure. One can expect a small amount of $SiOF_2$ to form in this system, giving rise to SiO^+ and $SiOF_2^+$ signals, at 44 and 82, respectively, but the concentrations of $SiOF_2$ should increase with O_2 concentration. Other unidentified traces may be involved here.

The sample surface and plasma cell walls remain very clean during the NF_3 and NF_3/O_2 etching experiments, so only volatile products are formed, except perhaps for small amounts of SiF_2 and $SiOF_2$.

Further support for the above interpretation is found in the kinetic results as presented in Fig. 4. As discussed in the earlier study (3). the apparent first-order constants determined from the slopes of the descending branches of the signal transients (2, 3) reflect the rate of the effusion process whenever one is dealing with chemically inert species. The NF_2^+ signals, representing unfragmented NF_3 present in the plasma cell, decay quickly, even somewhat faster than other inert species measured earlier regardless of whether the plasma indicated is ignited or not (see range b in Fig. 4). The SiF_3^+ apparent rate constants, by contrast, seem to be somewhat lower than the new NF_2^+ reference values, indicating some delay in the release of SiF_4 from the sample surface. This effect was just barely noticeable in the SF_6/Si system (2) and in the SF_6/O_2-Si system studied earlier (3).

NF^+ and N^+ signals also decay slowly, on this basis, and conceivably a portion of these species are formed, while the etching activities are dying down, after each injection

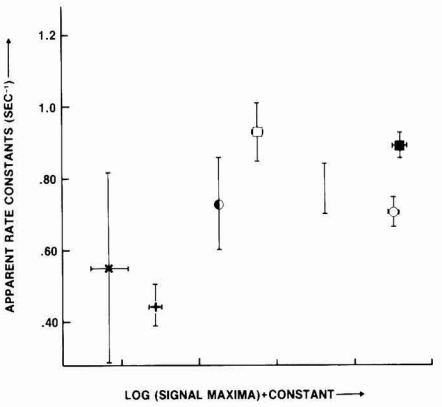


Fig. 4. Apparent rate constants, obtained from descending branches of transient signals, against natural logarithm of maximum signal. Data for low oxygen concentrations, corresponding to data near ordinate of Fig. 2. ■, □: NF^+ before and after ignition of the plasma, respectively. ×, +, ◐:signals at m/e = 33, 14, and 30, respectively. ○: SiF^+. B designates the range of other apparent rate constants in the absence of a plasma is shown, w.o. data point symbol. All data are corrected, according to Graham's law, to account for the different effusion rates. For this purpose, NF_2^+ is assumed to arise from NF_3, NO^+ from NO, SiF_3^+ from SiF_4, NF^+ from NF, and N^+ from N [see text, and Ref. (3)]. All corrections are relative to SiF_4, as in Ref. (3).

of etchant gas. Possibly, NF_2 radicals, while present in the gas phase only in negligibly small amounts, are adsorbed at the surface undergoing etching, and cause reactions such as [6], [8], and/or [8a] to continue in the forward direction, even after the plasma activity ceased. Correspondingly, a small component of the SiF_3^+ signals, measured to evaluate the descending branches of the transient curves and to calculate the apparent rate constants, arises from that SiF_4 which is formed at the end of etching pulses. The fraction concerned is small: from Fig. 4, one obtains about 5%.

On the basis of these considerations, the overall reaction can be summarized approximately as

$$2Si + 3NF_3 \rightarrow 2SiF_4 + NF + 2N \qquad [11]$$

where NO appears in place of NF, whenever a sufficient amount of O_2 is present.

Finally, to gain some insight concerning the Si surface events, some plasma experiments were carried out to modify this surface. From Fig. 5, it appears that an oxide layer was created by exposure of the Si sample to an O_2 plasma, as described above. The layer is slowly removed by subsequent NF_3 etching, while Ar sputtering, under the conditions used, is quite ineffective for this purpose.

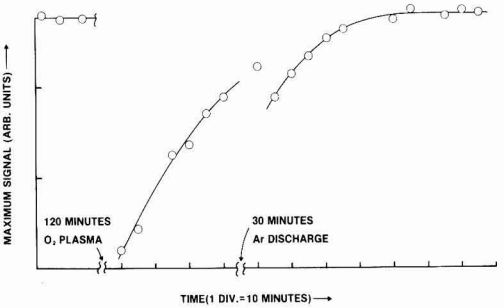


Fig. 5. Logarithms of maximum signals of SiF_3^+, representing the etch rate, as a function of time. After the initial etching an O_2 plasma was produced for 120 min, at a pressure of 0.7 torr (see Table 1). Later on, a continuous Ar discharge was applied, modified by pulses of NF_3, which resulted in the measured points. One ordinate division corresponds to a signal increase by a factor of 1.65.

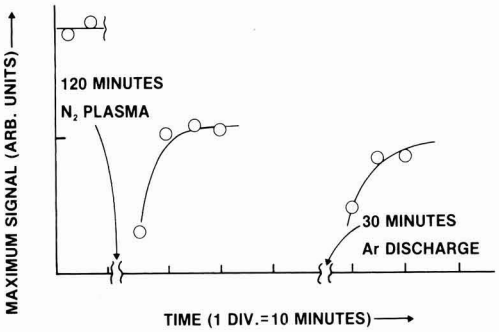


Fig. 6. Same as Fig. 5, for N_2 plasma exposure, for 60 min at 2.4 torr (see Table I). Ordinate scale factor: 1.29.

The exposure to a N_2 plasma leads to the formation of a nitride layer which appears to be even more tenacious under NF_3 etching, except initially, where there is a rapid increase in etching rate after N_2-plasma exposure (see Fig. 6). Intermittent Ar sputtering appears to render this layer even more resistant to etching.

The exploratory experiments described here essentially show the versatility and scope of the pulse etching procedure.

Conclusions

The pulse injection procedure developed earlier was used to gain some detailed insight into the chemistry of the plasma etching of polycrystalline Si under NF_3 or NF_3/O_2 mixtures.

As shown in reaction [11], aside from the principal product SiF_4, small amounts of NF and N were formed during that process, and in addition NO, whenever O_2 was present in the mixture. NF_2 radicals were not present in the gas phase in measurable amounts, but from a consideration of probable reaction steps, reactions [2]-[10], and the apparent first-order rate constants for the disappearance of various species after each pulse, it was concluded that NF_2 is probably adsorbed at the surface, during etching. Oxygen additions have no measurable effect on the etching rates, and little effect on the concentrations of most species measured, with the important exceptions of NF which decreases, and of NO which increases, with oxygen concentrations.

Acknowledgments

The authors are indebted to the National Science Foundation for support of these studies, and to Professor d'Agostino for valuable comments concerning the reaction mechanism.

Manuscript submitted Feb. 28, 1984; revised manuscript received July 16, 1984.

REFERENCES

1. J. W. Coburn, *Plasma Chem. Plasma Proc.*, **2**, 1 (1982).
2. W. W. Brandt and T. Honda, in "Proceedings of the Sixth International Symposium on Plasma Chemistry," M. I. Boulos and R. J. Munz, Editors, p. 604, IUPAC, McGill University, Montreal, Que., Canada (1983).
3. W. W. Brandt and T. Honda, Submitted to *Plasma Chem. Plasma Proc.*
4. W. H. Beattie, *Appl. Spectrosc.* **29**, 334 (1975).
5. A. Cornu and R. Massot, "Compilation of Mass Spectral Data," Vol. 1, Heyden & Son, London (1975); E. Stenhagen, S. Abrahamsson, and F. W. McLafferty, Editors "Atlas of Mass Spectral Data," Wiley-Interscience, New York (1969).
6. W. H. Dibeler and F. L. Mohler, *J. Res. Natl. Bur. Stds.*, **40**, 25 (1948).
7. J. J. Wagner and W. W. Brandt, *Plasma Chem. Plasma Proc.*, **1**, 201 (1981).
8. N. J. Ianno, K. E. Greenberg, and J. T. Verdeyen, *This Journal*, **128**, 2174 (1981).
9. R. d'Agostino, V. Colaprico, and F. Cramacrossa, *Plasma Chem. Plasma Proc.*, **1**, 365 (1981); references therein.
10. R. d'Agostino, Personal communication.
11. T. J. Chuang, *J. Appl. Phys.*, **51**, 2614 (1980).
12. C. I. M. Beenakker, J. H. J. van Dommelen, and J. Dieleman, in "Plasma Processing," R. G. Frieser and C. J. Mogab, Editors, p. 302, The Electrochemical Society Softbound Proceedings Series, Pennington, NJ (1981).

Photosensitivity and Contrast Determination of Photoresist by Laser Interferometry

T. R. Pampalone,[1,*] M. R. Hannifan, S. Jain, and C. D. Krieger

American Hoechst Corporation, AZ Photoresist Products, Somerville, New Jersey 08876

ABSTRACT

A laser interferometry technique was used to determine the photosensitivity and contrast values of positive photoresist. The precision of the technique was determined to be 2.7% (1σ) for photosensitivity and 2.1% (1 σ) for contrast. The linear correlation of photosensitivity with film thickness was used to normalize the data. The utility of the technique as a quality control tool was demonstrated by analysis of 52 serially produced lots of 1350J photoresist.

Linewidth control during microlithographic fabrication of devices is critically dependent on the inherent photosensitivity of the resist. Some lot-to-lot variability in resist photosensitivity is expected by the device fabricator, and adjustments in exposure dose are routinely made on the line to compensate for this variability, most often using the critical dimensions of the device as the basis for the adjustment (1). Resist manufacturers do their best to minimize this lot-to-lot variability in photosensitivity by blending of raw materials or finished product to average out individual differences. However, one of the difficulties in achieving uniformity of photosensitivity is the variability of the test itself.

Several attempts to quantify the photosensitivity of a positive resist have been reported. One method measures the rate of photobleaching of the resist sensitizer, using monochromatic UV light as the irradiating source (2). The method assumes that the rate of photochemical conversion of sensitizer is a predictor of resist photosolubility, independent of processing conditions. This assumption is valid if the composition of the nonphotochemical components of the resist remain absolutely consistent so as not to change the physiochemical characteristics of the system. In practice, the latter situation seldom occurs. In or-

* Electrochemical Society Active Member.
[1] Present address: RCA Corporation, Solid State Division, Somerville, New Jersey 08876.

der to maintain consistent functional performance of the resist, resist manufacturers purposefully choose resins of varying molecular weight and developer solubility in the formulation to compensate for a particularly fast or slow sensitizer.

A functional measure of the photosensitivity of a resist is the "depth-of-penetration test" (3), which measures the thickness of resist film removed for a given amount of exposure energy under specific and controlled processing conditions. Recommended development time is 5 min. The thickness removed can be measured by a stylus measuring device if a ruled grating is used as the optical mask, and a plot of depth of penetration *vs.* exposure energy is constructed. From the plot, the minimum exposure energy to achieve complete dissolution of the film can be extrapolated. The precision associated with the test is ±5% (3), although for development times in the more-realistic 1-2 min range, the precision of the method is considerably less. A slight modification of the depth-of-penetration technique flood-exposes the sample and measures the thickness of film with an optical film thickness analyzer before and after development (4).

Rather than measure the thickness of film removed for a given exposure, one can measure the rate of film dissolution as a function of sensitizer photobleaching (5). Since for every resist there are inherent solubility rates for the dissolution of nonexposed and fully exposed resist, under fixed processing conditions, these solubility rates can be expressed as parameters to characterize the resist photosensitivity. A parameter related to contrast can then be calculated from the solubilty parameters.

Although the approach has a good theoretical basis and generates functional data, it does not appear to be easily applicable to rapid resist characterization or have the rigor necessary for quality control.

In order to be useful to device fabricators, techniques to characterize the photosensitivity and contrast of photoresist must meet these criteria: (*i*) the results must be functional, derived under processing conditions the device actually undergoes; (*ii*) the results must be directly applicable to some device fabrication need, such as closely predicting the linewidth and edge acuity; (*iii*) the results must have good precision under production support conditions, which often differ considerably from the laboratory; and (*iv*) the technique must be responsive to small photoresist variations.

The laser interferometry technique described within has been under evaluation for over a year and meets these criteria. It functionally measures the dissolution properties of the total resist film, rather than the photochemical change of one component. In contrast, the Dill (7) procedure measures parameters (called "ABC") associated only with the photobleachability of the sensitizer (called photoactive compound, PAC) and neglects the contribution of the other components to dissolution rate. The Neureuther (5) technique uses laser interferometry to monitor development rate of the resist and generates data which can provide theoretical comparisons of resist lots. However, the data provided are not easily translated into the process-control parameters of interest to device makers. By comparison, the most useful application of the laser interferometry technique presented here appears to be quality control of photoresist on device fabrication lines. Contrast values indicate the attainable image resolution of the resist lot. Photosensitivity values provide a measure of lot-to-lot photosensitivity uniformity and can be used as a straightforward basis for making on-line exposure adjustments, if necessary. For instance, a ±10% variation in photosensitivity values determined by this technique results in linewidth variation of approximately ±0.1 μm for a pattern generated with a Perkin-Elmer 220 Projection Aligner and consisting of 2 μm equal lines and spaces (6). The IC manufacturer, knowing that the photosensitivity value of a particular lot of photoresist is 10% higher than average, can increase exposure dose by 10% to maintain the same critical dimensions of the device.

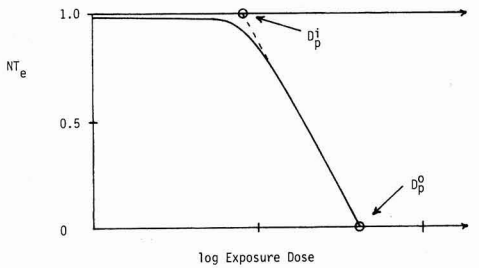


Fig. 1. Exposure curve for determining photosensitivity and contrast values. D_p^o = Exposure dose where NT_e = 0 (mJ/cm²). D_p^i = Exposure dose where NT_e = 1.0 (mJ/cm²). NT_e = Normalized film thickness. Contrast = $|[\log D_p^o/D_p^i]^{-1}|$ = |slope|. Photosensitivity = D_p^o (mJ/cm²).

The purpose of this paper is to review the laser interferometry procedure for determining photosensitivity and contrast of photoresist and show application of the technique for quality control. The laser inter-

Table I. Photosensitivity and contrast values for 1350J

Lot no. 1350J	T_o (μm)	Contrast	D_p^o (mJ/cm²)	D_{pc}^o (mJ/cm²)
1	1.701	1.447	100	107
2	1.732	1.540	98	101
3	1.816	1.558	105	99
4	1.707	1.547	99	105
5	1.806	1.554	106	101
6	1.766	1.471	98	97
7	1.680	1.598	102	111
8	1.837	1.467	106	97
9	1.814	1.506	104	98
10	1.790	1.534	106	103
11	1.799	1.507	105	101
12	1.785	1.467	106	103
13	1.806	1.583	105	100
14	1.805	1.647	100	95
15	1.792	1.587	101	97
16	1.764	1.513	108	108
17	1.741	1.405	97	99
18	1.797	1.435	95	91
19	1.761	1.487	93	93
20	1.783	1.350	104	101
21	1.807	1.589	102	97
22	1.808	1.549	102	97
23	1.756	1.462	87	88
24	1.798	1.442	101	97
25	1.770	1.473	91	90
26	1.765	1.633	108	107
27	1.765	1.570	103	102
28	1.785	1.513	111	108
29	1.771	1.521	108	107
30	1.786	1.570	106	103
31	1.773	1.428	112	110
32	1.779	1.517	108	106
33	1.716	1.598	98	103
34	1.765	1.559	101	100
35	1.779	1.561	99	97
36	1.762	1.563	100	100
37	1.733	1.677	93	96
38	1.733	1.678	94	97
39	1.746	1.616	93	95
40	1.743	1.590	95	97
41	1.739	1.526	96	98
42	1.770	1.416	109	108
43	1.747	1.563	101	103
44	1.714	1.613	101	106
45	1.748	1.510	105	106
46	1.735	1.620	98	101
47	1.719	1.574	89	94
48	1.757	1.663	100	100
49	1.723	1.781	86	90
50	1.761	1.518	108	108
51	1.746	1.494	110	112
52	1.747	1.645	94	95
n	52	52	52	52
$\bar{x}$	1.764	1.543	100.9	100.4
σ	0.033	0.080	6.2	5.7
% RSD = $100\sigma/\bar{x}$	1.89	5.2	6.1	5.7

ferometry technique has been used widely by other workers (7) to characterize photoresist, and has been drafted into an ASTM test method (8).

Experimental

Determination of photosensitivity and contrast values.—The laser interferometry procedure is described fully in the ASTM method (8). Twelve 2 in. polished silicon wafers were spin coated at 4000 rpm with the 1350J photoresist and soft-baked 30 min at 90°C in an air circulating oven. The thickness variability for 12 wafers prepared in this manner was typically 0.008 μm (1σ). Each of the 12 wafers was exposed with a UV dose in the range 25-100 mJ/cm², using an Oriel Corporation broadband 200W UV illuminator. The thickness of coated resist was measured in the center of each wafer using a Rudolf FTM (film thickness monitor). The wafers were each developed in 1:1 AZ Developer at 24°C, without agitation, and the loss of film was monitored by laser interferometry. From the resultant exposure curve of normalized film thickness remaining after 1 min development and the log exposure dose (Fig. 1), the photosensitivity and contrast values were determined for each of the 52 lots analyzed (Table I). The photosensitivity value (D_p^o) is the minimum UV dose required for complete film dissolution in the specified development time. In practice, the photosensitivity value is the exposure value when the linear portion of the exposure curve is extrapolated to zero normalized thickness. Contrast is the slope of the linear portion of the exposure curve (Fig. 1). Points within the linear limits of the exposure curve typically have a correlation coefficient of 0.98 or better. A reference 1350J resist was analyzed periodically to verify the reproducibility of the exposure and processing conditions.

Correlation of photosensitivity values with film thickness.—The photosensitivity values of 1350J (lot A), spin-coated at varying thicknesses, were determined and correlated with film thickness. Thicknesses from 3.3 to 1.6 μm were attainable by adjusting spin speed. After dilution to 26.5% solids, with AZ Thinner, coating thicknesses of 1.7-0.9 μm were attainable, and after dilution to 16.5% solids, coating thicknesses of 0.9-0.4 μm were attainable. The photosensitivity values obtained were recorded as a function of film thickness (Table II and Fig. 2). The correlation of photosensitivity value with film thickness was repeated for nine additional, randomly chosen lots of 1350J. For these additional runs, only six thicknesses were used, spanning the range of from 2.06 to 1.57 μm. The slope (mJ/cm² μm) of the least squares fit for each correlation, as well as the corresponding correlation coefficient, were calculated and statistically analyzed (Table III).

The contribution of substrate reflectivity to photosensitivity values.—The development rates of exposed resist were monitored by laser interferometry to determine the contribution of the silicon substrate reflectivity to the photosensitivity values. The 1350J resist (lot A) was coated to thicknesses of 2.20, 1.45, and 0.49 μm on silicon wafers, with and without a proprietary antireflective coating. The antireflective coating was 1.88 μm thick and absorbed all of the normal incident light in the actinic range as determined by percent transmission measurements. After UV exposure with 25 mJ/cm², the development rate of each wafer was monitored by laser interferometry, and the result plotted as film thickness removed *vs.* time (Fig. 3 and 4).

Table II. Photosensitivity values (D_p^o) as a function of film thickness (T_o)

1350J (30.5% solids)		(26.5% solids)		(16.5% solids)	
T_o (μm)	D_p^o (mJ/cm²)	T_o (μm)	D_p^o (mJ/cm²)	T_o (μm)	D_p^o (mJ/cm²)
3.270	330	1.697	114	0.883	52
3.080	268	1.562	96	0.569	40
2.543	208	1.466	82	0.469	36
2.500	197	1.366	81	0.415	34
2.056	145	1.176	69	0.408	33
1.915	131	1.051	65		
1.906	126	0.959	56		
1.823	121	0.893	51		
1.814	116				
1.751	114				
1.745	107				
1.661	94				
1.576	90				
1.421	74				
1.382	73				
1.345	70				
1.305	68				
1.202	59				

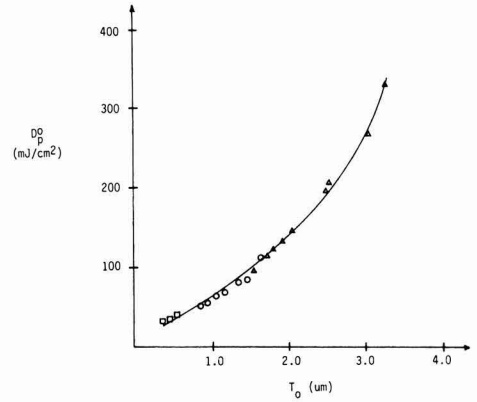


Fig. 2. Photosensitivity values (D_p^o) *vs.* film thickness (T_o). △: 30.5% solids. ○: 26.5% solids. □: 16.5% solids.

Results and Discussion

Photosensitivity values corrected for film thickness.—In Table III are listed the photosensitivity values obtained as a function of film thickness for 1350J (lot A) at 30.5% solids and after dilution to 26.5% and 16.5% solids. T_o is the mean thickness of resist coated on the 12 wafers used for each photosensitivity determination. These results are plotted in Fig. 2. The slope of the least squares fit for a thickness range of 2.06-1.57 μm is statistically consistent for randomly chosen lots of 1350J, as shown in Table III. This consistency is not unexpected since the sensitizer and resin components are individually characterized and selected in formulating each resist lot. From the average

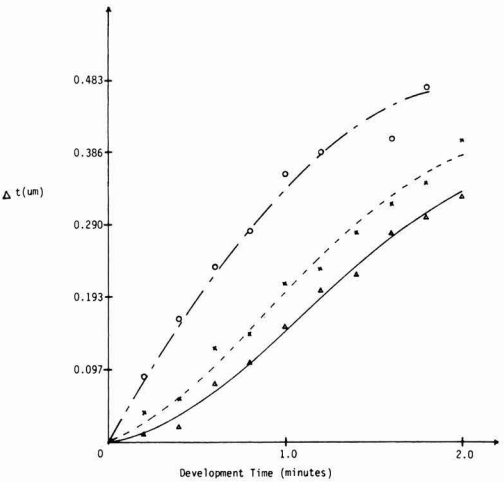


Fig. 3. Film thickness removed (μm) *vs.* development time (min). Polished silicon substrate, 25 mJ/cm² exposure. — — —: 0.49 μm film. - - - - - - - - -: 1.45 μm film. ————: 2.20 μm film.

Table III. Linear slope of photosensitivity values (D_p^o) vs. film thickness (T_o) for random lots of 1350J

Lot no. of 1350J	Slope* (mJ/cm²)(μm)	Correlation coefficient
A	115.2	0.992
B	118.2	0.999
C	111.9	0.999
D	115.9	0.989
E	112.2	0.999
F	108.6	0.980
G	113.0	0.980
H	114.3	0.983
I	111.2	0.986
J	118.2	0.995
$\bar{x}$	113.8	0.990
σ	3.3	
% RSD = $100\sigma/\bar{x}$	2.9	

* 2.06-1.57 μm thickness range.

slope value of 113.8 mJ/cm² μm for 1350J are calculated the photosensitivity values corrected for film thickness (D_{pc}^o). For AZ 1350J spun at 4000 rpm, the average dry coating thickness is formulated to 1.760 μm. Therefore, the corrected photosensitivity value (D_{pc}^o) for 1350J is derived from the relationship

$$D_{pc}^o = D_p^o + (1.760\ \mu m - T_o)\ (113.8\ mJ/cm^2\ \mu m)$$

where D_p^o is the uncorrected photosensitivity value and T_o is the mean film thickness for the 12 wafers used in the determination. The correction is best suited to small film thickness variations. The inherent 3% error in the correction factor (Table III) corresponds to an error in correction of less than 1 mJ/cm² for the thickness range under consideration. The thickness range for the 52 lots reported in this study (Table I) is 1.85-1.65 μm.

Photosensitivity and contrast values for 1350J.— Presented in Table I are the photosensitivity and contrast values for 52 serially produced lots of 1350J resist. Each lot of resist was spun on 12 silicon wafers at 4000 rpm and the resultant mean thickness (T_o) was recorded. The photosensitivity values (D_p^o) of all the lots were corrected (D_{pc}^o) to a 1.760 μm film thickness using the correction formula given above. From Table I, the mean corrected photosensitivity value (D_{pc}^o) for the 52 lots is 100.4 mJ/cm² with a 5.7% (% RSD) lot-to-lot variability.

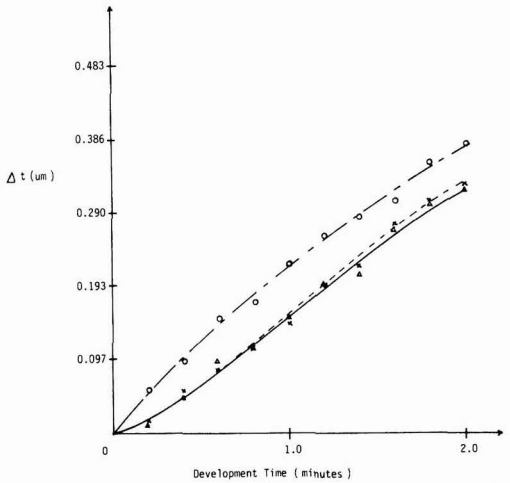


Fig. 4. Film thickness removed (μm) vs. development time (min). Antireflective substrate. 25 mJ/cm² exposure. — — —: 0.49 μm film. - - - - - - - - -: 1.45 μm film. ————: 2.20 μm film.

Precision of laser interferometry technique.—The repeatability precision of the laser interferometry technique was determined for 1350J (lot A) by the same operator using the same equipment. The statistical data and results are given in Table IV. The technique is shown to have a 1σ precision of 2.7% (% RSD) for photosensitivity and 2.1% for contrast values.

Substrate reflectivity contribution to photosensitivity values.—As pointed out by Willson (9), the choice of method of defining resist sensitivity requires careful interpretation. His major concern is the contribution of substrate reflectivity, necessary to monitor film thickness loss, to the photosensitivity value. It is interesting to know how much, if any, of the reflected, actinic light affects the photosensitivity measurement. A direct observation of the reflectivity contribution was observed by analyzing the laser interferograms of 0.49, 1.45, and 2.20 μm resist films after 25 mJ/cm² exposure. The plot of film thickness removed *vs.* development time (Fig. 3) illustrates the differential dissolution rates for the three films. (Deviation of the points from the curves is due mainly to standing wave effects.) The development rates for the 2.20 and 1.45 μm films are similar; however, the 0.49 μm film dissolves considerably faster. When the experiment is repeated, using an antireflective coating (Fig. 4), the dissolution rates of the 2.20 and 1.45 μm film are unchanged; the 1.45 μm film is now dissolving at the same rate as is the 2.20 μm film, and the 0.49 μm film is dissolving slower than before. Internal reflections and partial reflection at the photoresist-antireflective coating interface may still affect the dissolution rates despite the elimination of the reflection of normal incident light. The effect is more pronounced with thinner films owing to the higher relative intensity of incident light throughout the film and the interface. Residual solvent content of resist films after soft-bake is well known to affect dissolution rates (10). However, analysis of residual solvent in the 0.49 and 1.45 μm resist films by quantitative infrared analysis (using transparent double-polished silicon wafers and scanning the 1720 cm^{-1} carbonyl frequency) (11) showed that both films after soft-bake contained no detectable differences in percent ethoxyethyl acetate.

The data in Table II (photosensitivity value *vs.* film thickness) can be plotted as film thickness *vs.* log photosensitivity value. Each point on this curve represents a measured photosensitivity value for the respective film thickness on a substrate. In contrast, an exposure curve plot represents the film thickness removed after development for the respective log exposure dose. The plot of film thickness *vs.* log photosensitivity value (from Table II) superimposed upon an exposure curve of film loss *vs.* log exposure dose for a thick (3.2 μm) film illustrates the contribution of substrate reflectivity to photosensitivity (Fig. 5).

In Fig. 5, the film thickness *vs.* log photosensitivity value plot (line no. 1) is superimposed upon the mean exposure curve for triplicate analyses of a 3.20 μm film (line

Table IV. Precision of the laser interferometry technique

Trial no.	T_o μm	D_p^o mJ/cm²	D_{pc}^o mJ/cm²	Contrast
1	1.751	99	100	1.61
2	1.732	96	99	1.65
3	1.708	98	104	1.66
4	1.723	98	102	1.63
5	1.741	95	97	1.67
6	1.760	99	99	1.62
7	1.713	95	100	1.68
8	1.757	100	100	1.66
9	1.737	104	107	1.58
10	1.727	95	99	1.68
11	1.732	96	99	1.69
$\bar{x}$	1.735	98	101	1.65
σ	0.017	2.8	2.7	0.03
% RSD = $100\sigma/\bar{x}$	0.98	2.8	2.7	2.1

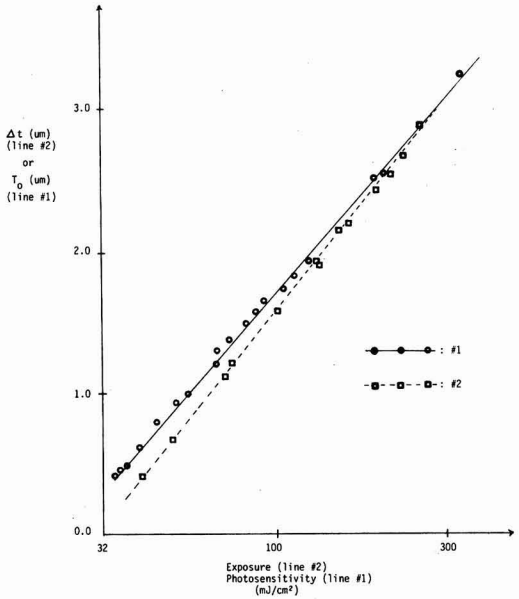


Fig. 5. No. 1: Initial film thickness (T_0) vs. exposure required for complete dissolution in 1.0 min development. No. 2: Film loss (Δt) in 1.0 min development vs. exposure given a "thick" film.

no. 2). The divergence of the two lines reflects the magnitude of the contribution of substrate reflectivity to photosensitivity. Reflectivity contribution to resist photosensitivity has been well documented, especially for thin films on highly reflective substrates (12). Quantifying reflectivity effects is possible in this case because the light source is broadband and standing wave effects are minor. This would not be so for narrow bandwidth light sources such as projection aligners or steppers.

Determination of lot-to-lot photosensitivity uniformity.—From Table I, the standard deviation of corrected photosensitivity values (D_{pc}^{o}) is 5.7 mJ/cm², and from Table IV, the standard deviation of the laser interferometry technique is 2.7 mJ/cm². Using analysis of variance (13), which assumes the total variance is the sum of separate variances

$$\sigma^2_{\text{Total}} = \sigma_1^2 + \sigma_2^2$$

the variance for resist photosensitivity (σ_R^2) can be approximated

$$(5.7)^2 = \sigma_R^2 + (2.7)^2$$

$$\sigma_R^2 = 25.2$$

The standard deviation for resist photosensitivity is

$$\sigma_R = 5.0 \text{ mJ/cm}^2$$

Therefore, the lot-to-lot photosensitivity uniformity for 1350J resist at the 1σ level is approximately ±5 mJ/cm², or ±5% (σ), since x = 100.4 mJ/cm². By the same analysis of variance procedure, the lot-to-lot contrast uniformity for 1350J at the 1σ level is ±0.074, or +4.8%, since x = 1.543.

Conclusions

The laser interferometry technique can be successfully used to characterized the photosensitivity and contrast of positive resist. The 1σ precision for the technique was found to be 2.7% for photosensitivity and 2.1% for contrast values. A correction for film thickness can be applied in the normal working range of 1350J to improve the measurement. The technique is particularly well suited for lot-to-lot quality control (QC) testing of photoresist. QC analysis of 52 lots of 1350J photoresist showed the percent relative standard deviation (% RSD) for photosensitivity and contrast to be 5.7% and 5.2%, respectively. The % RSD for photosensitivity and contrast corrected by analysis of variance was 5.0% and 4.8%, respectively.

Research work is now underway to improve the precision of the laser interferometry technique and correlate photosensitivity and contrast values with critical dimensions, wall angles, and other lithographic outcomes. The techniques described here are being used to monitor and qualify raw materials and manufactured lots of photoresist.

Manuscript submitted Dec. 9, 1983; revised manuscript received May 20, 1984.

American Hoechst Corporation assisted in meeting the publication costs of this article.

REFERENCES

1. J. N. Helbert, C. C. Walker, P. A. Seese, and A. J. Gonzales, *SPIE Semicond. Microlithogr.*, **275**, 182 (1981); K. Kadota, Y. Taki, and S. Shimizu, *ibid.*, **275**, 173 (1981).
2. D. F. Ilten and R. J. Sutton, *This Journal*, **119**, 539 (1972); F. J. Loprest and E. A. Fitzgerald, *Photogr. Sci. Eng.*, **15**, 260 (1971).
3. D. J. Elliot, in "Integrated Circuit Fabrication Technology," Chap. 13, p. 325, McGraw-Hill Book Company, New York (1982).
4. M. J. Bowden, *This Journal*, **128**, 195C (1981).
5. D. J. Kim, W. G. Oldham, and A. R. Neureuther, in "Kodak Microelectronics Seminar, Proceedings of Interface '82," p. 100 (1982).
6. T. R. Pampalone, M. R. Hannifan, S. Jain, and C. D. Krieger, In preparation.
7. F. H. Dill, W. P. Hornberger, P. S. Hauge, and J. M. Shaw, *IEEE Trans. Electron Devices*, **ed.-22**, 445 (1975); F. H. Dill, A. R. Neureuther, J. A. Tuttle, and E. J. Walker, *ibid.*, **ed.-22**, 456 (1975); K. L. Konnerth and F. H. Dill, *Solid State Electron.*, **15**, 371 (1972); M. Exterkamp, W. Wong, H. Damar, A. R. Neureuther, C. H. Ting, and W. G. Oldham, *SPIE*, **334**, 182 (1982).
8. T. R. Pampalone and R. F. Doll, "Recommended Practice for Determining Contrast and Photosensitivity of a Photoresist," ASTM Document no. 8A60, Subcommittee F1.08, American Society for Testing and Materials, Philadelphia.
9. G. C. Willson, in "Introduction to Microlithography," Chap. 3, p. 105, American Chemical Society, Washington, DC (1983).
10. J. M. Shaw, M. A. Frisch, and F. H. Dill, *IBM J. Res. Dev.*, **21**, 219 (1977).
11. T. R. Pampalone, M. R. Hannifan, S. Jain, and C. D. Krieger, In preparation.
12. F. Jones, M. Hatzakis, and H. Rothmann, in "Kodak Microelectronics Seminar, Proceedings of Interface '79." p. 113 (1979).
13. ICI Staff, in "Statistical Methods in Research and Production," O. L. Davis and P. L. Goldsmith, Editors, Chap. 8, Longman Group Limited, London (1972).

Nonlinear Two-Step Diffusion in Semiconductors

D. Anderson

Institute for Electromagnetic Field Theory, Chalmers University of Technology, S-412 96 Göteborg, Sweden

K. O. Jeppson

Research Laboratory of Electronics, Chalmers University of Technology, S-412 96 Göteborg, Sweden

ABSTRACT

At high concentrations, impurity diffusion in semiconductors tends to be governed by nonlinear diffusion processes. Using similarity analysis, analytical solutions are here found for the impurity profile resulting from a two-step diffusion process where the drive-in step involves a nonlinear diffusion process. Comparison with previously published experimental results shows very good agreement.

In the fabrication of many semiconductor devices, solid-state diffusion is a common method for the introduction of impurities into the semiconductor material. The desired impurity profile is often established by means of a two-step process. In the first predeposition step, a certain total number of impurities is deposited in a shallow region close to the surface of the material, either by ion implantation or by an initial diffusion process. The second drive-in step involves a diffusive redistribution of the impurities, usually resulting in much deeper penetration into the material (1).

For low impurity concentration, the diffusion processes are governed by linear diffusion equations and exact solutions in terms of Gaussian or erfc functions are available. Although there has recently been some discussion about the most convenient approximation for the final impurity profile resulting from two-step diffusion processes (2, 3), the analytical understanding of the evolution of the impurity profiles is generally very good, owing to the extensive knowledge existing for the linear diffusion equations, *cf.* Ref. (4).

However, many modern semiconductor applications involve high impurity levels, in which case the corresponding diffusion processes may become strongly nonlinear, and the simple linear diffusion equation is well known to give results which are not in agreement with experimental results (5).

The physical mechanism causing nonlinear diffusion of impurities in, *e.g.*, silicon has recently been summarized by Fair (6, 7). According to the vacancy model, the diffusion of substitutional impurities is a result of the interaction with vacant states in the silicon. These vacancies may be neutral or charged. The concentration of neutral states at any temperature is independent of the impurity concentration, C, while the number of charged vacancies depend on the impurity concentration. The intrinsic diffusion coefficient D_i, at low doping levels ($C < n_i$) may be written as

$$D_i = D^o + D^+ + D^- + D^= \qquad [1]$$

where D^o, D^+, D^-, and $D^=$ represent the effective diffusivities under intrinsic conditions for the neutral, positive, singly, and doubly negative charged states, respectively. For extrinsic conditions, the diffusion coefficient may be written as

$$D = h[D^o + D^+(n_i/n) + D^-(n/n_i) + D^=(n/n_i)^2] \qquad [2]$$

where n is the electron concentration

$$n = \frac{C}{2}\left\{1 + \left[1 + \left(\frac{2n_i}{C}\right)^2\right]^{1/2}\right\} \qquad [3]$$

and h is the self electric-field enhancement factor

$$h = 1 + \frac{C}{2n_i}\left[\left(\frac{C}{2n_i}\right)^2 + 1\right]^{-1/2} \qquad [4]$$

Usually, at high doping levels, one of the charged-state diffusivities becomes dominant, so the effective diffusion coefficient may be written

$$D = 2D_i(C/n_i)^\gamma \qquad [5]$$

where $\gamma = 1$ for boron and arsenic, and $\gamma = 2$ for phosphorous. However, the diffusion of phosphorous in silicon is complicated by the dissociation of the doubly negative charged vacancies at doping levels of about 10^{20} cm^{-3}. At lower levels, this dissociation results in an enhanced tail diffusion.

As compared to the linear case, the analytical understanding of nonlinear diffusion processes is strikingly poor, and resort is mostly taken to numerical computations (6). As far as we know, within the context of semiconductor applications, the only attempt towards an analytical investigation of nonlinear diffusion processes has been made by Nakajima *et al.* (9), Fair (10, 11), and Fair and Tsai (12, 13) for arsenic and boron diffusion. This approach relies on the approximation of the impurity profile by Chebyshev polynomials in the variable $x/t^{1/2}$ suggested by Nakajima *et al.* where x and t denote space and time coordinates, respectively (see Appendix A). This is a good approach for diffusion involving a constant surface concentration, but is not appropriate in the case of a two-step diffusion, where the diffusive redistribution occurs under the condition of a constant total number of impurities. The proper variable in this case turns out to be $x/t^{1/(\gamma+2)}$, *i.e.*, $x/t^{1/3}$ and $x/t^{1/4}$ for $\gamma = 1$ and $\gamma = 2$, respectively.

The purpose of the present work is to demonstrate that similarity methods (14) provide a powerful and flexible tool for a systematic study of the nonlinear diffusion equations which occur in solid-state high concentration impurity diffusion. Furthermore, the analytic solutions which are obtained are exact, attractively simple, and yield very good agreement with experimental results.

Analysis

We restrict the present analysis to the case of a two-step process where the first step establishes a very shallow impurity profile containing a given total dose, Q_o. For high impurity concentration, the second drive-in step is assumed to be governed by a diffusion equation of the form

$$\frac{\partial C}{\partial t} = \frac{\partial}{\partial x}\left(D\frac{\partial C}{\partial x}\right) \qquad [6]$$

where the diffusion coefficient, D, depends nonlinearly on the impurity concentration, C, as given by Eq. [5], *i.e.*, $D_o = 2D_i$

$$D = D_o\left(\frac{C}{n_i}\right)^\gamma \qquad [7]$$

A systematic and very powerful tool for analyzing diffusion equations is similarity methods (14), which have the

attractive advantage of being equally applicable to linear and nonlinear equations. Following the similarity approach, we look for solutions of Eq. [6] and [7] in the form

$$C(x, t) \sim t^{\alpha}\phi(\xi) \quad [8]$$

where the similarity variable, ξ, is given by

$$\xi = \frac{x}{t^{\beta}} \quad [9]$$

The unknown function, $\phi(\xi)$, as well as the parameters α and β, are determined by inserting the expression into the diffusion equation and using the appropriate boundary or initial conditions. If the initial shallow impurity profile can be approximated as a delta function and the total number of diffusing impurities is assumed constant, the exact solution of Eq. [6] and [7] can be written in the suggestive form (see Appendix B)

$$C(x, t) = C_S(t)\left(1 - \frac{x^2}{x_F^2(t)}\right)^{1/\gamma} \quad [10]$$

where the surface concentration, $C_S(t)$, and the penetration depth, $x_F(t)$, are given by

$$C_S(t) = \left(\frac{\gamma}{2(\gamma+2)I_\gamma^2} \cdot \frac{Q_o^2 n_i^\gamma}{D_o t}\right)^{1/(\gamma+2)}$$

$$x_F(t) = \left(\frac{2(\gamma+2)}{\gamma I_\gamma^\gamma} \cdot \frac{Q_o^\gamma D_o t}{n_i^\gamma}\right)^{1/(\gamma+2)} \quad [11]$$

In Eq. [10] and [11], I_γ is a numerical factor given by $I_1 = 2/3$ and $I_2 = \pi/4$.

In particular, we find from Eq. [10] and [11] for $\gamma = 1$ and $\gamma = 2$, respectively

(i) $\gamma = 1$

$$C(x, t) = C_S\left(1 - \frac{x^2}{x_F^2}\right) \quad [12]$$

where

$$C_S = \frac{3^{1/3}}{2}\left(\frac{Q_o^2 n_i}{D_o t}\right)^{1/3} \cong 0.57\left(\frac{Q_o^2 n_i}{D_i t}\right)^{1/3}$$

$$x_F = 9^{1/3}\left(\frac{Q_o D_o t}{n_i}\right)^{1/3} \cong 2.62\left(\frac{Q_o D_i t}{n_i}\right)^{1/3} \quad [13]$$

(ii) $\gamma = 2$

$$C(x, t) = C_S\left(1 - \frac{x^2}{x_F^2}\right)^{1/2} \quad [14]$$

where

$$C_S = \left(\frac{2}{\pi}\right)^{1/2}\left(\frac{Q_o^2 n_i^2}{D_o t}\right)^{1/4} \cong 0.67\left(\frac{Q_o^2 n_i^2}{D_i t}\right)^{1/4}$$

$$x_F = \left(\frac{8}{\pi}\right)^{1/2}\left(\frac{Q_o^2 D_o t}{n_i^2}\right)^{1/4} \cong 1.90\left(\frac{Q_o^2 D_i t}{n_i^2}\right)^{1/4} \quad [15]$$

We emphasize the characteristic time dependence of C_S and x_F involving $t^{1/3}$ and $t^{1/4}$ for $\gamma = 1$ and $\gamma = 2$, respectively, as opposed to the ordinary $t^{1/2}$ dependence of the conventional Boltzmann transformation. This feature has caused some confusion in previous investigations of nonlinear diffusion in semiconductors, *cf.* Ref. (11-13, 15).

The delta function approximation for the initial impurity distribution is a good approximation when the final width of the profile, as resulting from the drive-in step, is much larger than the width of the initial profile. Actually, the drive-in profile asymptotically approaches the similarity profile as t increases, irrespective of the form of the first impurity deposition. In situations where the width of the initial profile does play a non-negligible role, it can easily be incorporated into the analysis (see Appendix B). In particular, Eq. [10]-[15] are still valid, provided we redefine the surface concentration and the penetration depth according to (*cf.* eq. [13] and [15])

(i) $\gamma = 1$

$$C_S = \frac{3^{1/3}}{2}\left(\frac{Q_o^2 n_i}{D_o t}\right)^{1/3}\left(1 + \frac{x_o^3}{9Q_o D_o t/n_i}\right)^{-1/3}$$

$$x_F = 9^{1/3}\left(\frac{Q_o D_o t}{n_i}\right)^{1/3}\left(1 + \frac{x_o^3}{9Q_o D_o t/n_i}\right)^{1/3} \quad [16]$$

(ii) $\gamma = 2$

$$C_S = \left(\frac{2}{\pi}\right)^{1/2}\left(\frac{Q_o^2 n_i^2}{D_o t}\right)^{1/4}\left(1 + \frac{\pi^2}{64}\frac{x_o^4}{Q_o^2 D_o t/n_i^2}\right)^{-1/4}$$

$$x_F = \left(\frac{8}{\pi}\right)^{1/2}\left(\frac{Q_o^2 D_o t}{n_i^2}\right)^{1/4}\left(1 + \frac{\pi^2}{64}\cdot\frac{x_o^4}{Q_o^2 D_o t/n_i^2}\right)^{1/4} \quad [17]$$

and x_o is the width of the initial profile.

Discussion

The general shape of the doping profile given by Eq. [10] is shown in Fig. 1 for $\gamma = 1$ and $\gamma = 2$, together with the Gaussian profile and the Chebyshev polynomial approximation (9-13). In this plot, the impurity concentration is normalized to the surface concentration and plotted against normalized junction depth. (For the Gaussian and Cheyshev profiles, the junction depth was chosen as the depth at which the concentration falls to 1% of the surface concentration.) As expected analytically, and also observed experimentally (8-13), the solutions to the nonlinear diffusion equations are much steeper, giving more abrupt junctions than the linear Gaussian profile.

For arsenic, only the neutral and singly negative charged vacancies are responsible for the impurity diffusion. The diffusivity of arsenic may then be written

$$D = D^o + D^- \frac{n}{n_i} \quad [18]$$

but since $\beta = D^-/D^o \cong 1$, the diffusion process is strongly nonlinear for $C >> n_i$, and the resulting profile may be described by Eq. [10] and [11] where $\gamma = 1$. In Fig. 2, the

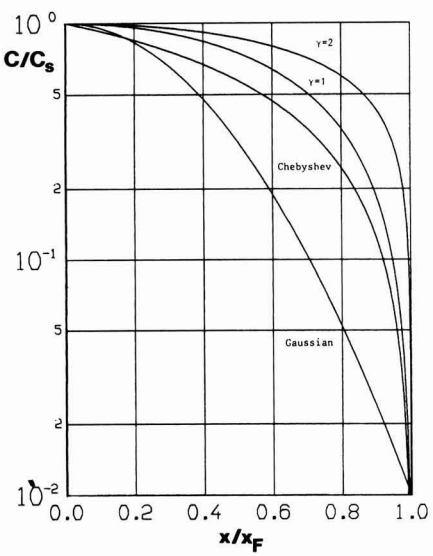


Fig. 1. Normalized doping profiles for $\gamma = 1$ and $\gamma = 2$. The Gaussian profile is given for comparison together with the Chebyshev polynomial approximation (9-13).

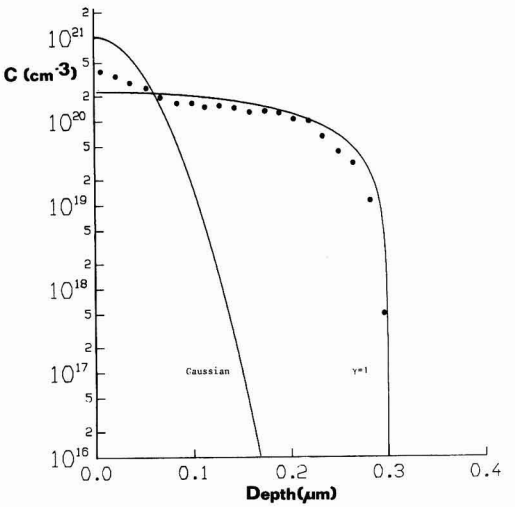


Fig. 2. Doping profile for shallow implanted arsenic compared with experimental results of Hill (16). The Gaussian profile for a constant diffusion constant is given for comparison.

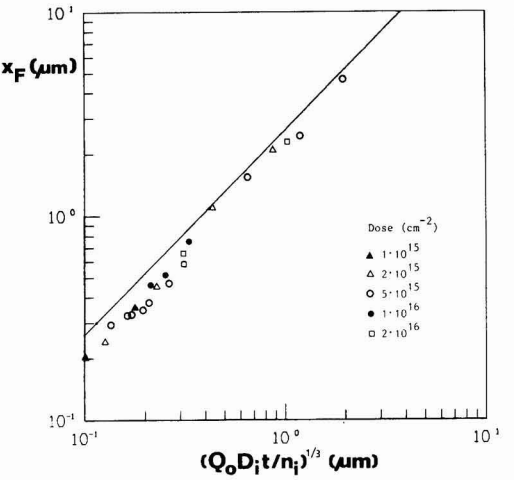


Fig. 4. The dependence of the junction depth of time, temperature, and dose (Eq. [13]) for implanted As compared with experimental results of Fair and Tsai (13) for dry ambients.

doping profile of shallow ion-implanted arsenic, after 30 min of diffusion in argon at 1000°C, measured by Hill (13), has been compared to our theoretical curve calculated from Eq. [10] and [11]. Excellent agreement is found between the two curves. The Gaussian profile for the same conditions is also shown for comparison. In this plot, the value of $D_i = 24 \exp(-4.08/kT)$ has been used together with the value of n_i according to Morin and Maita (17).

The diffusion of ion-implanted arsenic in silicon has also been extensively studied by Fair and Tsai (12, 13), using secondary ion mass spectroscopy (SIMS). In Fig. 3, their experimental data for the surface concentration as a function of $(Q_o^2 n_i/D_i t)^{1/3}$ is compared to our theoretical result as given by Eq. [13]. Very good agreement is found. In particular, we note that for a given dose and temperature, the surface concentration will decrease as $t^{-1/3}$, as theoretically predicted by Eq. [13].

In Fig. 4, the junction depth, x_F, as described theoretically by Eq. [13], is plotted against $(Q_oD_it/n_i)^{1/3}$, together with the experimental data of Fair and Tsai (12, 13), in the temperature range 1000°-1250°C. Again, good agreement is found, especially for deeper junction depths. In particular, the junction depth is clearly seen to increase as $t^{1/3}$.

Finally, Eq. [13] may also be rewritten as the following simple relation between surface concentration, dose, and junction depth, *viz.*

$$C_S = 1.5Q_o/x_F \qquad [19]$$

This relation, together with the experimental data of Fair and Tsai, is shown in Fig. 5, again with good agreement.

The characteristic scaling of surface concentration and junction depth has previously been pointed out by Fair and Tsai (13), using a semiempirical approach. However, in this paper, we have demonstrated that the observed scalings are exact consequences of the properties of the nonlinear diffusion equation. The similarity method clearly shows that, for arsenic and boron diffusion at high impurity concentrations when the diffusion constant is concentration dependent (with $\gamma = 1$), the impurity profile is a function of $x/(D_it)^{1/2}$ for diffusion with constant surface concentration and a function of $x/(D_it)^{1/3}$ for diffusion with a constant number of shallow implanted impu-

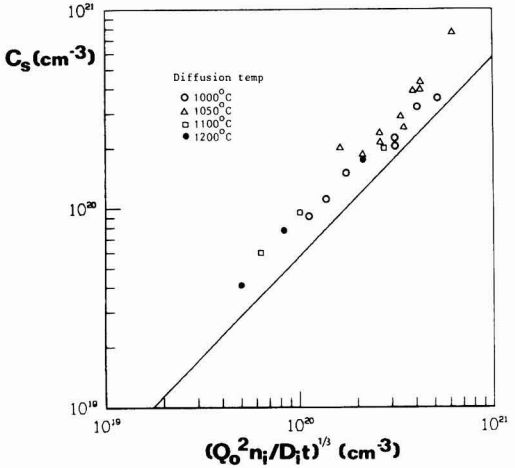


Fig. 3. The dependence of the surface concentration on time, temperature, and dose (Eq. [13]) for implanted As compared with experimental results of Fair and Tsai (13).

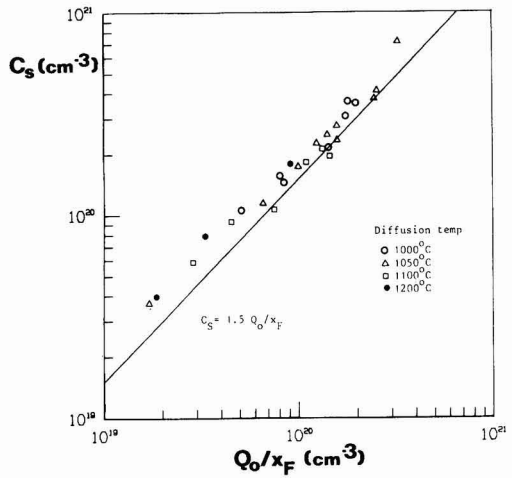


Fig. 5. The surface concentration of implanted As vs. average doping compared with experimental data from Fair and Tasi (13).

rities. In earlier papers, this fact has only been obtained indirectly, as shown in Appendix A. Any function of $x/(C_S D_i t/n_i)^{1/2}$, describing a doping profile with a constant surface concentration (and $\gamma = 1$), will be turned into a function of $x/(Q_o D_i t/n_i)^{1/3}$ if instead the total number of impurities are assumed constant, since integration of the impurity profile over x yields

$$Q_o = \text{const.} \cdot C_S x_F \qquad [20]$$

This constant is empirically determined by Fair and Tsai (13) to be 0.53 for arsenic, as compared to our theoretical value of 0.67 from Eq. [19], which is a 20% difference. For boron, this constant is 0.4 (11).

As shown in Fig. 2, the exact solution of the nonlinear diffusion equation is an excellent description of the arsenic doping profile, except very close to the surface. In this region, the theoretical profile tends to underestimate the surface concentration. This is also evident from the experimental data in Fig. 3. This is probably due to the reduced arsenic diffusivity at concentrations above 10^{20} cm^{-3} (6, 7). Hence, the implanted profile close to the surface is not redistributing as fast as theoretically expected, owing to complex impurity-vacancy pair formation, clustering, and strain effects. This effect is also more evident at lower diffusion temperatures.

This is probably also the explanation for why the Chebyshev approximation, with its nonvanishing slope at the surface, may result in just as good, or even better, doping profiles as compared to the theoretical solution in this paper. This is, then, not a natural result of the nonlinear diffusion itself, but rather a consequence of the deviations from ideal conditions, such as reduced surface diffusivity. The nonvanishing slope is, then, a residue of the originally implanted profile.

Manuscript submitted Feb. 9, 1984; revised manuscript received July 16, 1984.

Chalmers University of Technology assisted in meeting the publication costs of this article.

APPENDIX A

For nonlinear diffusion with $\gamma = 1$ and a constant surface concentration C_S, Nakajima *et al.* (9) approximated the doping profile with the Chebyshev polynominal

$$C/C_S = 1.00 - 0.87\ Y - 0.45\ Y^2 \qquad [A\text{-}1]$$

where $Y = x/(8C_S D_i t/n_i)^{1/2}$. This profile approximation may be simplified to

$$C/C_S = 1 - 0.70\frac{x}{x_J} - 0.30\left(\frac{x}{x_J}\right)^2 \qquad [A\text{-}2]$$

where $x_J = 2.3\ (C_S D_i t/n_i)^{1/2}$ is the junction depth. This expression does not include the background concentration because of the large doping gradient at the diffusion front. Integrating Eq. [A-2] over x gives the total amount of dopants as

$$Q_o = K C_S x_J \qquad [A\text{-}3]$$

where K is a constant. This approximation is used by Fair and Tsai (13) also for the case of implanted arsenic diffusion with a constant amount of impurities. In this case, Q_o is assumed constant in Eq. [A-3] instead of C_S, which is now assumed slowly varying. Insertion of Eq. [A-3] into the junction depth expression yields

$$x_J = 2(Q_o D_i t/n_i)^{1/3} \qquad [A\text{-}4]$$

$$C_S = 0.94\ (Q_o^2 n_i/D_i t)^{1/3} \qquad [A\text{-}5]$$

which has turned the doping profile in Eq. [A-2] into a $t^{1/3}$ dependence instead of the original $t^{1/2}$ dependence.

For boron diffusion with $\gamma = 1$ and a constant surface concentration C_S, the doping profile may be approximated by (11)

$$C/C_S = 1 - \left(\frac{x}{x_J}\right)^{2/3} \qquad [A\text{-}6]$$

where the junction depth $x_J = 2.45\ (C_S D_i t/n_i)^{1/2}$. Integrating Eq. [A-6] over x yields the total amount of boron impurities

$$Q_o = 0.4\ C_S x_J \qquad [A\text{-}7]$$

Now assuming Q_o constant for implanted boron diffusion, yields

$$C_S = 0.53\ (Q_o^2 n_i/D_i t)^{1/3} \qquad [A\text{-}8]$$

where 0.53 is an empirical constant.

APPENDIX B

The purpose of this Appendix is to give a more detailed presentation of the similarity approach as applied to the nonlinear diffusion equation obtained by combining Eq. [6] and [7], *i.e.*

$$\frac{\partial C}{\partial t} = D_o \frac{\partial}{\partial x}\left(\left(\frac{C}{n_i}\right)^\gamma \frac{\partial C}{\partial x}\right) \qquad [B\text{-}1]$$

It is convenient to normalize Eq. [B-1] by introducing $\tilde{C} = C/n_i$ and $\tau = D_o t$. Equation [B-2] then becomes

$$\frac{\partial \tilde{C}}{\partial \tau} = \frac{\partial}{\partial x}\left(\tilde{C}^\gamma \frac{\partial \tilde{C}}{\partial x}\right) \qquad [B\text{-}2]$$

In order to investigate Eq. [B-2] by similarity methods, we write the solution as (11)

$$\tilde{C}(x, \tau) = \tau^\alpha \phi(\xi)$$

$$\xi = \frac{x}{\tau^\beta} \qquad [B\text{-}3]$$

Inserting this ansatz into Eq. [B-2] we find that the powers of τ match if α and β are related by

$$\alpha = \frac{2\beta - 1}{\gamma} \qquad [B\text{-}4]$$

and the resulting equation for $\phi(\xi)$ is then

$$\alpha\phi - \beta\xi\frac{d\phi}{d\xi} = \frac{d}{d\xi}\left(\phi^\gamma \frac{d\phi}{d\xi}\right) \qquad [B\text{-}5]$$

A further relation between α and β is obtained from the fact that the total number of diffusing particles is conserved, *i.e.*

$$\int_o^\infty \tilde{C}(x, \tau)dx = \tau^{\alpha+\beta}\int_o^\infty \phi(\xi)d\xi = \tilde{Q}_o = \text{const.} \qquad [B\text{-}6]$$

This obviously requires $\alpha = -\beta$, which, together with relation [B-4], determines α and β to be

$$\alpha = -\beta = -\frac{1}{\gamma + 2} \qquad [B\text{-}7]$$

Note that constant surface concentration requires $\alpha = 0$ and consequently $\beta = 1/2$. With α and β given by Eq. [B-7], Eq. [B-5] for $\phi(\xi)$ can be integrated explicitly to yield

$$\phi(\xi) = \phi_o\left(1 - \frac{\xi^2}{\xi_o^2}\right)^{1/\gamma} \qquad [B\text{-}8]$$

where the characteristic penetration depth, ξ_o, is related to the integration constant, ϕ_o, by

$$\xi_o^2 = \frac{2(\gamma + 2)}{\gamma}\phi_o^\gamma \qquad [B\text{-}9]$$

Furthermore, ϕ_o is determined from the conservation condition, Eq. [B-6]. This yields

$$\phi_o = \left(\frac{\gamma}{2(\gamma + 2)I_\gamma^2}\tilde{Q}_o^2\right)^{1/(\gamma+2)} \qquad [B\text{-}10]$$

where I_γ denotes the integral

$$I_\gamma = \int_o^1 (1 - x^2)^{1/\gamma}\,dx = \frac{\sqrt{\pi}}{2}\frac{\Gamma(1 + 1/\gamma)}{\Gamma(3/2 + 1/\gamma)} \qquad [B\text{-}11]$$

and $\Gamma(x)$ is the complete elliptic integral. In particular, $I_1 = 2/3$ and $I_2 = \pi/4$.

Using Eq. [B-10] in Eq. [B-9], ξ_o is obtained as

$$\xi_o = \left(\frac{2(\gamma+2)}{\gamma I_\gamma^{\gamma}}\,\tilde{Q}_o^{\gamma}\right)^{1/(\gamma+2)} \qquad [B\text{-}12]$$

Collecting our results, we find that $C(x, \tau)$ can be written

$$\tilde{C}(x,\tau) = \tilde{C}_S(\tau)\left(1 - \frac{x^2}{x_F^2(\tau)}\right)^{1/\gamma} \qquad [B\text{-}13]$$

i.e., in terms of a decaying maximum concentration, $\tilde{C}_S(\tau)$, given by

$$\tilde{C}_S(\tau) = \left(\frac{\gamma}{2(\gamma+2)I_\gamma^2}\,\frac{\tilde{Q}_o^2}{\tau}\right)^{1/(\gamma+2)} \qquad [B\text{-}14]$$

and a well-defined diffusion front at $x = x_F(\tau)$, where

$$x_F(\tau) = \left(\frac{2(\gamma+2)}{\gamma I_\gamma^{\gamma}}\cdot\tilde{Q}_o^{\gamma}\tau\right)^{1/(\gamma+2)} \qquad [B\text{-}15]$$

In order to incorporate the feature of a finite width of the initial profile, we note that the fundamental nonlinear diffusion equation, Eq. [B-2], is invariant under time translations. This implies that a more general similarity solution is obtained through an arbitrary time translation of the previously obtained solution, *i.e.*

$$\tilde{C}(x,\tau) = \phi_o(\tau+\tau_o)^{-1/(\gamma+2)}\left(1 - \frac{x^2}{\xi_o^2(\tau+\tau_o)^{2/(\gamma+2)}}\right)^{1/\gamma} \qquad [B\text{-}16]$$

The arbitrary constant, τ_o, can be related to the width of the original profile as follows: As $\tau \to 0$, the solution given by Eq. [B-16] does not approach a delta function, but rather

$$\lim_{\tau\to 0}\tilde{C}(x,\tau) = \tilde{C}(x,0) = \phi_o\tau_o^{1/(\gamma+2)}\left(1 - \frac{x^2}{\xi_o^2\tau_o^{2/(\gamma+2)}}\right)^{1/\gamma} \qquad [B\text{-}17]$$

This implies that, for an initial profile of the form given by Eq. [B-17], the subsequent diffusive evolution is determined exactly by Eq. [B-16]. Admittedly, we cannot expect the initial profile to correspond to a similarity profile, as given by Eq. [B-17]. However, it is possible to approximate realistic initial profiles by functions of the form of Eq. [B-17], provided we choose τ_o properly. Thus, Eq. [B-16] yields an approximate solution for the subsequent development, and, furthermore, this solution asymptotically approaches the correct solution, as the influence of the original profile width diminishes.

To be more specific, we note that if we characterize the initial profile simply by its width, x_o, this determines τ_o as

$$\tau_o = (x_o/\xi_o)^{\gamma+2} = \frac{\gamma}{2(\gamma+2)}\left(\frac{I_\gamma}{\tilde{Q}_o}\right)^{\gamma} x_o^{\gamma+2} \qquad [B\text{-}18]$$

which implies that the maximum concentration, C_S, and the location of the diffusion front, x_F, can be written as

$$C_S = \left(\frac{\gamma}{2(\gamma+2)I_\gamma^2}\,\frac{\tilde{Q}_o^2}{\tau}\right)^{1/(\gamma+2)}\left(1+\frac{\tau_o}{\tau}\right)^{1/(\gamma+2)}$$

$$x_F = \left(\frac{2(\gamma+2)}{\gamma I_\gamma^{\gamma}}\,\tilde{Q}_o^{\gamma}\tau\right)^{1/(\gamma+2)}\left(1+\frac{\tau_o}{\tau}\right)^{1/(\gamma+2)} \qquad [B\text{-}19]$$

REFERENCES

1. A. B. Glaser and G. E. Subak-Sharpe, "Integrated Circuit Engineering," Addison-Wesley, Reading, England (1979).
2. R. Shrivastava and A. Marshak, *Proc. IEEE*, **65**, 1614 (1977).
3. W.-S. Wang, *ibid.*, **71**, 179 (1983).
4. J. Crank, "The Mathematics of Diffusion," Chap. 2, 2nd ed. Clarendon Press, Oxford, England (1975).
5. A. S. Grove, "Physics and Technology of Semiconductor Devices," p. 58, John Wiley and Sons, New York (1967).
6. R. B. Fair, in "Impurity Doping Processes in Semiconductors," F. F. Y. Wang, Editor, Chap. 7, North-Holland Publishing Co., Amsterdam (1981).
7. R. B. Fair, in "Silicon Integrated Circuits," Part B, D. Kahng, Editor, Applied Solid State Science, Supplement 2, pp. 1-108, Academic Press, New York (1981).
8. See *e. g.* G. J. Declerck, in "Large Scale Integrated Circuits Technology; State of the Art and Prospect," L. Esaki and G. Soncini, Editors, p. 112, NATO Advanced Study Institutes Series, Vol. E55, Martinus Nijhoff Publishers, The Hague (1982).
9. Y. Nakajima, S. Ohkawa, and Y. Fukukawa, *Jpn. J. Appl. Phys.*, **10**, 162 (1971).
10. R. B. Fair, *J. Appl. Phys.*, **43**, 1278 (1972).
11. R. B. Fair, *This Journal*, **122**, 800 (1975).
12. R. B. Fair and J. C. C. Tsai, *ibid.*, **122**, 1689 (1975).
13. R. B. Fair and J. C. C. Tsai, *ibid.*, **123**, 583 (1976).
14. W. F. Ames, "Nonlinear Partial Differential Equations," p. 133, Vol. 1, Academic Press, New York (1965).
15. M. Ghezzo, *This Journal*, **119**, 977 (1972).
16. C. Hill, Lecture notes, see p. 124 in Ref. (8).
17. F. J. Morin and J. P. Maita, *Phys. Rev.*, **96**, 28 (1954).

Carrier Lifetime Reduction in Silicon by Proton Implantation Through MOS Structures

A. Mogro-Campero* and R. P. Love

General Electric Research and Development Center, Schenectady, New York 12301

ABSTRACT

Ion implantation provides a versatile technique for lifetime control in silicon. Localized penetration and damage profiles provide means for the creation of regions of low lifetime within device structures. Protons of 80 keV were implanted 0.5 μm into silicon through a MOS structure, with doses up to 10^{14} cm^{-2}. The generation lifetime can be reduced by several orders of magnitude, and varies linearly with dose. Changes in oxide quality, surface generation velocity, and doping concentration were also studied. Low temperature annealing repairs the oxide degradation while maintaining substantial lifetime reduction.

The methods currently used to reduce carrier lifetime in silicon (the diffusion of gold or platinum, and electron irradiation) produce effects throughout the silicon wafer. Because of their well-defined range, implanted ions make possible the spatial localization of regions of reduced lifetime. Masking can be used to provide planar selectivity; depth control can be attained by energy selection or epitaxial overgrowth. Argon implantation provides an effective way of reducing lifetime, and is resistant to high temperature annealing (1-3). This makes it particularly appropriate for use during the early steps of device processing. In this paper, we explore the use of ion implantation to reduce lifetime in silicon during the late

*Electrochemical Society Active Member.

stages of device processing. Depth control can be implemented by varying the energy of the ion. Most of the damage occurs near the end of range, so that a considerable degree of localization is still possible. Protons were used in our study; for singly ionized atoms and a given maximum implanter energy, they provide the greatest choice of depth. Since MOS structures are present in many of the devices of interest, the implantation was performed into the silicon through the metal and oxide layers.

Procedure

n-Type CZ silicon wafers of (111) orientation and doping density of 10^{15} phosphorus atoms cm^{-3} were used. The backs of the wafers were implanted with 10^{15} cm^{-2} phosphorus of 100 keV to ensure a low resistance contact to the back-side aluminum. 100 nm of dry oxide were grown at 1000°C. A set of 300 nm thick aluminum dots was then evaporated to form MOS capacitors, and sintered at 450°C for 30 min in nitrogen.

Using energy-loss and range tables (4), we calculate that the 80 keV protons implanted through the MOS structures penetrated 0.5 μm into the silicon. The maximum depletion depth under inversion is 1 μm, so that the high frequency (1 MHz) capacitance-voltage and capacitance-transient measurements used in this experiment should be affected by the implantation. A portion of each sample was left unimplanted to serve as a control area. The damage produced by the protons has been estimated (5) to be such that at 0.35 μm into the silicon, the fraction of silicon atoms displaced from their crystalline positions is about 4×10^{-4} for the maximum proton dose of 10^{14} cm^{-2} used in this experiment.

Generation lifetime was measured at room temperature by the Zerbst technique (6, 7). A MOS capacitor is pulsed into deep depletion, and the formation of the inversion layer is observed via the capacitance transient. By this method it is possible to deduce the generation lifetime (τ_g) in the depleted zone, and the parameter s due to minority carriers whose current is independent of the time varying depth of the depletion zone. Because the lifetime is not constant with depth within the sampling volume, an average value dependent on depletion voltage will be obtained (3). The lifetime values reported here have been obtained with a −10V depletion pulse. The parameter s is the sum of the surface generation velocity and a term corresponding to diffusion of carriers into the depletion zone from the quasi-neutral regions (3). A typical variation of τ_g by a factor of 2 and parameter s by a factor of 3 was found across a given sample.

Results

Generation lifetime as a function of proton dose is shown in Fig. 1. Functional dependence with dose is close to linear. At 10^{14} cm^{-2}, analysis by the capacitance transient technique was no longer reliable, but the duration of the capacitance transient continued to follow an inverse dose dependence, as shown by the dotted line extension in the figure. The superlinear dependencies (reverse leakage current of diodes approximately proportional to dose squared) for helium and carbon implantation within the range of doses in our experiment (8) were not observed.

The generation lifetime as a function of proton dose has been reported to drop more than three orders of magnitude in the dose range 10^{12}-10^{13} cm^{-2} for similar experimental conditions (9). We find no evidence for this precipitous drop in lifetime. In that experiment, the lifetime was also deduced from a capacitance transient analysis, but the surface contribution was not taken into account. It has been shown that for irradiated samples, this procedure can lead to large errors (3).

The parameter s as a function of proton dose is shown in Fig. 2. Since the implantation damage region includes the oxide/Si interface, a linear dose dependence suggest the predominance of the surface generation velocity in the parameter s [the diffusion term would be either independent of dose if arising from deeper than the implant range, or proportional to the square root of dose if related to the lateral component (3)]. In a separate study of the temperature variation of τ_g and s for the sample with a dose of 10^{11} cm^{-2}, we have also come to the conclusion that the surface generation velocity is the dominant term in s at room temperature.

Doping profiles were obtained by a pulsed C-V method (10), using a pulse width of 1 ms. The result is shown in Fig. 3. The rise in doping density at shallow depths is most likely due to the interface proximity limitation (10). The rise in doping density due to the redistribution of

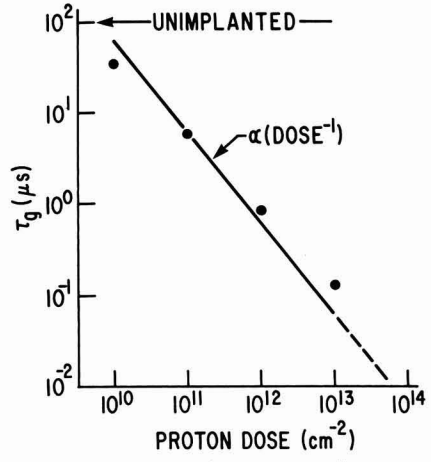


Fig. 1. Generation lifetime vs. proton dose

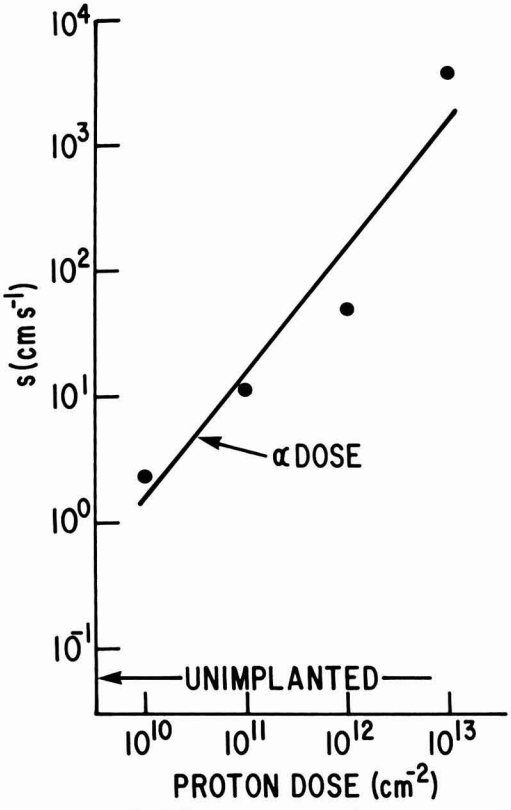


Fig. 2. Parameter s vs. proton dose

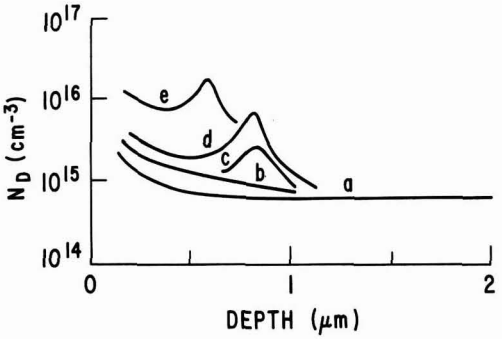


Fig. 3. Donor density vs. depth from C-V measurements. Portions of the curves have been omitted for clarity. All curves merge at depths >1.3 μm. Curve a corresponds to a control sample and to a sample with a proton dose of 10^{10} cm^{-2}. Curves b-e correspond to proton doses 10^{11}-10^{14} cm^{-2}.

phosphorus during thermal oxidation (11) is only a small effect in our case. The peaks in Fig. 3 correspond approximately to the expected range of the protons, and they indicate an increase in doping density with proton dose. However, interface traps can produce apparent changes in doping density profiles (10). Therefore, an average value of doping density within the equilibrium depletion depth under inversion (0.3-0.8 μm for doping densities 10^{16}-10^{15} cm^{-3}) was obtained by the maximum-minimum C-V method, which is free of interface trap effects (10). A doping density increase is again observed (Fig. 4), but only for the highest proton dose.

Doping concentration changes after proton implantation into n-type silicon have been reported; carrier concentration decreases were found after implantation, but increases appeared after annealing at around 300°C (12). This indicates a competition between the dominance of deep and shallow levels, which should depend on the energy level spectrum within the silicon bandgap. Since various point defect complexes and/or defect-impurity associations are probably responsible for the levels, the details in a particular situation are bound to be different. It is important to note in this respect that we have used Czochralski samples, whereas the other experimenters (12) have worked with float-zoned material. It is well known that there is a large difference in impurity concentrations in these two types of crystals, notably with respect to oxygen concentration, which in Czochralski samples is many orders of magnitude higher (in the 10^{18} cm^{-3} range). Sample differences are presumably also partly responsible for the variety of energy levels reported by different investigators after proton bombardment (13).

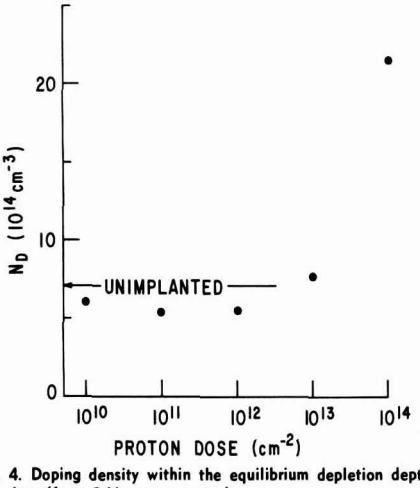


Fig. 4. Doping density within the equilibrium depletion depth vs. proton dose (from C-V measurements).

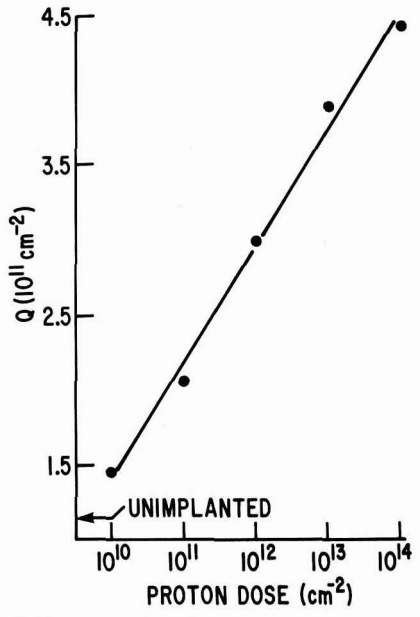


Fig. 5. Charge associated with the oxide in units of the electron charge as a function of proton dose.

Charge associated with the oxide was computed from flatband voltage shift (14): the results are shown in Fig. 5. The associated shift in threshold voltage for inversion is 2V for a dose 10^{14} cm^{-2}. C-V curves for a control sample, and one with a dose of 10^{14} cm^{-2} are shown in Fig. 6. The

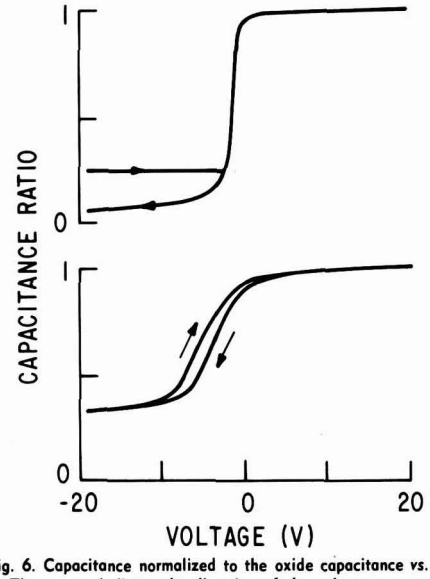


Fig. 6. Capacitance normalized to the oxide capacitance vs. voltage. The arrows indicate the direction of the voltage sweeps (at a rate of 0.4 V s^{-1}). The top graph is for the control region of the sample, and the bottom one for a proton dose of 10^{14} cm^{-2}. Measurements are carried out in the dark, except that the sample is brought to equilibrium by a brief exposure to light after the positive-to-negative voltage sweep.

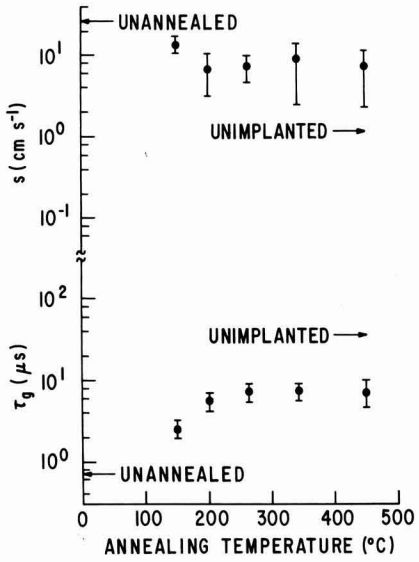


Fig. 7. Surface generation velocity and generation lifetime as function of annealing temperature for samples implanted with 10^{12} protons cm^{-2}. All anneals for 30 min. Average values are indicated with arrows for an unimplanted sample annealed at 450°C and for an implanted sample prior to annealing.

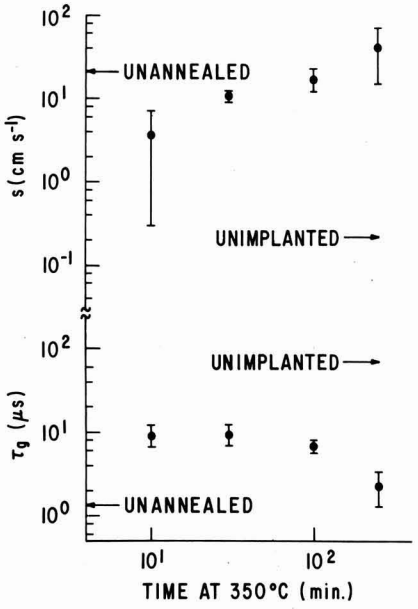


Fig. 8. Surface generation velocity and generation lifetime as a function of time at 350°C for samples implanted with 10^{12} protons cm^{-2}. Average values are indicated by arrows for an unimplanted sample annealed for 250 min and for an implanted but unannealed sample.

hysteresis and stretch out after irradiation are characteristic of interface charge trapping near the oxide/Si interface (15).

Annealing experiments in nitrogen were carried out for samples with a proton dose of 10^{12} cm^{-2}. Half-hour anneals showed that the oxide parameters referred to in the previous paragraph returned to their preimplanted condition after the 350°C anneal. The doping density increase deduced from the pulsed C-V method discussed earlier was reduced by the 150°C anneal, and disappeared after the higher temperature annealing treatments.

The results for annealing of the generation lifetime and surface generation velocity are shown in Fig. 7. Both parameters achieve stable values, but do not regain the unimplanted levels. It is interesting to note that the lifetime in the case of electron irradiation has returned to the unirradiated value after a 450°C anneal step for 30 min (16). Lifetime reduction by proton implantation is thus more thermally stable.

Further evidence for persistent lifetime reduction after annealing is provided in Fig. 8. For longer annealing times both τ_g and s move further away from the unimplanted values. This phenomenon of negative annealing has been observed in the reverse leakage current after carbon ion implantation in a similar temperature regime (8), and attributed to complexes that do not act to suppress lifetime annealing out at these temperatures, and freeing mobile defects which can recombine to form lifetime-active centers.

Conclusions

The generation lifetime of silicon samples can be reduced by several orders of magnitude by proton implantation, as deduced from measurements prior to annealing treatments. The implantation can be carried out near the end of the device processing sequence, so that only low temperature steps are left. Oxide degradation in MOS structures can be repaired with low temperature annealing treatments, which also serve to stabilize the lifetime. The relatively high value of surface generation velocity will tend to increase surface leakage current and decrease channel mobility. The severity of oxide and interface related effects will also depend on the ion energy used, since ion energy-loss rates depend on energy. Well-defined range and damage profiles allow localization of regions of low lifetime within device structures, so that ion implantation is emerging as a versatile tool for lifetime control in silicon.

Acknowledgments

We are indebted to G. Gidley and M. Lazzeri for carrying out various processing steps; phosphorus implantations were performed by W. Whitney, and proton implantation at the State University of New York at Albany with Professor H. Bakhru. We thank P. Chow for making us aware of Ref. (9).

Manuscript submitted May 18, 1984; revised manuscript received July 26, 1984. This was Paper 81 presented at the Cincinnati, Ohio, meeting of the Society, May 6-11, 1984.

General Electric Company assisted in meeting the publication costs of this article.

REFERENCES

1. H. F. Kappert, G. Sixt, and G. H. Schwuttke, *Phys. Status Solidi A*, **52**, 463 (1979).
2. A. Mogro-Campero and R. P. Love, in "Defects in Semiconductors," W. M. Bullis and L. C. Kimerling, Editors, p. 595, The Electrochemical Society Softbound Proceedings Series, Pennington, NJ (1983).
3. A. Mogro-Campero and R. P. Love, *This Journal*, **131**, 655 (1984).
4. B. Smith, "Ion Implantation Range Data for Silicon and Germanium Device Technologies," Research Studies Press, Inc., Forest Grove, OR (1977).
5. A. Mogro-Campero and R. P. Love, in "Ion Implantation and Ion Beam Processing of Materials," G. K. Hubler, O. W. Holland, C. R. Clayton, and C. W. White, Editors, p. 537, Elsevier, New York (1984).
6. M. Zerbst, *Z. Angew. Phys.*, **22**, 30 (1966).
7. D. K. Schroder and J. Guldberg, *Solid State Electron.*, **14**, 1285 (1971).
8. K. A. Pickar and J. V. Dalton, *Rad. Eff.*, **6**, 89 (1970).
9. Y. Wada and M. Ashikawa, *Jpn. J. Appl. Phys.*, **14**, 1405 (1975).
10. E. H. Nicollian and J. R. Brews, "MOS Physics and Technology," pp. 380-408, John Wiley and Sons,

Inc., New York (1982).
11. A. S. Grove, O. Leistiko, Jr., and C. T. Sah, *J. Appl. Phys.*, **35**, 2695 (1964).
12. Y. Ohmura, Y. Zohta, and M. Kanazawa, *Phys. Status Solidi A*, **15**, 93 (1973).
13. J.-W. Chen and A. G. Milnes, *Ann. Rev. Mater. Sci.*, **10**, 157 (1980).
14. S. M. Sze, "Physics of Semiconductor Devices," p. 395, John Wiley and Sons, Inc., New York (1981).
15. P. V. Gray, *Proc. IEEE*, **57**, 1543 (1969).
16. R. O. Carlson, Y. S. Sun, and H. B. Assalit, *IEEE Trans. Electron Devices*, **ed-24**, 1103 (1977).

The System AgI-AgBr: Energetic Consequences of Defect Equilibria in Single-Phase and Two-Phase Regions

A. Khandkar,* V. B. Tare, A. Navrotsky, and J. B. Wagner, Jr.**

Center for Solid State Science, Arizona State University, Tempe, Arizona 85287

ABSTRACT

The enthalpy of solution of various single-and two-phase AgI-AgBr compositions in $AgNO_3$ at 518 K has been determined using a Calvet-type twin microcalorimeter. The enthalpy ($H_{518} - H_{298}$) of melted and unmelted mixtures of AgI and AgBr of various compositions within two-phase regions of the phase diagram has also been obtained using the same calorimeter. The effect of AgBr on the temperature and enthalpy of transformation of β-AgI to α-AgI has been investigated using a Perkin Elmer Differential Scanning Calorimeter. The terminal compositions at 518 K of the two-phase region of AgI-AgBr system has been found to be $AgI_{0.85}Br_{0.15}$ and $AgI_{0.3}Br_{0.7}$. The excess enthalpy, the difference in ($H_{518} - H_{298}$) values of the unmelted and melted mixtures in the two-phase region of the AgI-AgBr system, has been found to be maximum at the equivolume concentration of the two terminal phases and is suggested to be due to the generation of silver ion vacancies at the interfaces due to a space-charge layer.

During the past few years, several investigators have reported anomalous electrical conduction in materials containing finely divided particles dispersed as a second phase. The systems investigated include the dispersion of submicron-sized insulating particles in an ionically conducting matrix [LiI + Al_2O_3 (1), AgI + Al_2O_3 (2), AgCl + Al_2O_3 (3)], of insulating particles in materials with predominant electronic conduction [SiO_2 in TiO_2 (4)], of metallically conducting particles in a semiconductor [Ni_3S_2 (5) or Ni (6) in NiO], and of ionically conducting materials in an ionically conducting matrix [AgBr in AgI (7)]. The observed changes in the electrical conductivity could not be explained on the basis of classical theories alone. Several alternative explanations have been proposed (8-10); however, the explanation based on the presence of additional defects at the interface because of the space-charge layer appears to be most satisfactory (8)]. The AgI-AgBr system was chosen for the present study because of its relative physical and chemical simplicity and because of the extensive investigations carried out in this laboratory regarding its electrical conductivity (2, 7, 11). Silver iodide is known to exist in at least two stable crystallographic modifications with a transition at 420 K from a low temperature wurtzite β form to a high temperature, body-centered cubic α form. Silver bromide, on the other hand, is stable only in the rocksalt-type cubic structure up to its melting temperature.

Electrical conductivity of α-AgI is several orders of magnitude higher than that of β-AgI and AgBr. Partial replacement of iodine in AgI with bromine has been found to lower the transition temperature (11). Anomalous changes in electrical conductivity of several single-phase and two-phase compositions in the AgI-AgBr system have also been reported (7). Since the changes in the electrical conductivity are presumably associated with the changes in number and the mobility of the transporting species, present investigations were undertaken to see whether these changes are reflected in the energetics of this system as well.

Experimental

Sample preparation.—AgI and AgBr, (99.999% pure from Apache Chemicals) in powder form, were mixed together in appropriate proportions and sealed in 6 mm diam evacuated silica tubes. The mixture was melted at 873 K for 1h. To ensure complete solution and homogenization, the melt was shaken from time to time. The sample was then quenched to room temperature, removed from the silica tube, and cut into small pieces of 500-600 mg each. Some of these pieces were annealed in air at 533 K for times varying from 2 to 15h before using them for drop calorimetry. Other pieces were ground to a fine powder (~200 mesh), and 50-60 mg of the powder was used for solution calorimetry in molten $AgNO_3$. A few milligrams of the same powder was used in a Perkin-Elmer DSC-2 Differential Scanning Calorimeter.

Compositions of the samples were assumed to be the same as those of the starting mixtures. X-ray powder diffraction technique was used on samples at 298 K to confirm that no phases other than wurtzite-type AgI and rocksalt-type AgBr were present.

Calorimetry

Solution calorimetry.—A Calvet-type twin-microcalorimeter as described elsewhere (12), was used. Samples were dissolved in molten $AgNO_3$ at 518 K. 50g of $AgNO_3$ were premelted in silica crucibles and then put in each calorimeter chamber. The Ag(I, Br) samples (about 50 mg of powder) were placed in a platinum cup, which was suspended just above the solvent by means of a movable quartz assembly. After the system attained thermal equilibrium (as seen by a steady baseline signal), the platinum cup with the powder was immersed in the solvent and, after a quick up-and-down stirring action, raised to the original level above the solvent. This procedure was repeated several times until the baseline returned to the original value. The area under the peak representing the enthalpy changes associated with the dissolution process was proportional to the heat generated. Calibration was achieved by dropping pieces of platinum, of known weight and heat content, into the melt.

To check whether the stirring contributed to the heat, several experiments were performed using empty platinum cups. No change in baseline was detected, indicating negligible heat due to stirring. The heat effects in each experiment were approximately 0.1 cal; the heat of solution ranged from +1000 to −4200 cal/mol.

Heat content measurement.—($H_{518} - H_{298}$) was measured by dropping ~250 mg cylindrical samples from 298 K into

* Electrochemical Society Student Member.
** Electrochemical Society Active Member.

the same calorimeter at 518 K using empty crucibles. The calorimeter was calibrated by dropping Al_2O_3 rods of similar dimensions, the heat content of which is tabulated by Barin and Knacke (13).

Differential scanning calorimetry (DSC).—A Perkin-Elmer Differential Scanning Calorimeter Model DSC-2 was used to obtain the temperature and enthalpy of transformation of various AgI-AgBr samples. Since the transformation occurs at temperatures close to the melting of indium (429.6 K), the instrument was calibrated using the melting point of indium, which was found to be within ± 0.5 K of the reported value (13).

The heating rate of 5 K/min was found to be most suitable. The temperature was varied from 350 to 450 K at this rate. The enthalpy changes associated with the transformation were recorded on a strip chart recorder and integrated using a planimeter. The reproducibility of the temperature measurement was ± 0.5 K and of the enthalpy measurement ± 50 cal for at least ten different indium samples.

Results

The data (H_{518} - H_{298}) obtained by drop calorimetry for pure AgI and various AgI-AgBr compositions are listed in Table I. To see any effects of change in grain size or grain boundary structure during annealing, some of the samples were annealed for periods varying from 2 to 15h at 533 K. The enthalpy values obtained for annealed and unannealed samples were the same within experimental error. Our value of 4720 ± 125 cal/mol for pure AgI is comparable to 4558 cal/mol reported by Barin and Knacke (13).

Table II lists the excess enthalpy values which were obtained for two-phase mixtures by taking the difference between the experimentally determined (H_{518} - H_{298}) values for various compositions obtained by melting and the values estimated for the same composition by taking the weighted average of the experimentally determined values for the terminal solid solutions. The phase diagram of the AgI-AgBr system has been reported by Stasiw and Teltow (14). However, subsequent investigations are not consistent with the solubility limits reported in the phase diagram. Shahi and Wagner (11) suggested from the conductivity measurements that the end members of the two-phase region of the AgI-AgBr system are $AgI_{0.9}Br_{0.1}$ and $AgI_{0.3}Br_{0.7}$. These terminal compositions were therefore used to estimate excess enthalpy. The excess enthalpy values are shown in Fig. 1 as a function of mole percent (m/o) $AgI_{0.3}Br_{0.7}$. A maximum in excess enthalpy is observed at about 50 m/o $AgI_{0.3}Br_{0.7}$. The unmelted samples (mechanical mixtures) show no excess heat content.

The enthalpies of solution of various compositions in $AgNO_3$ at 518 K are listed in Table III. For some compositions in the two-phase region, the enthalpies of solution were also obtained by preparing mechanical mixtures (without melting) of the end compositions. These values are also shown in this table. The difference in enthalpies of solution between the two-phase melted and unmelted compositions is within the experimental scatter.

The enthalpies of solution are plotted in Fig. 2 as a function of m/o AgBr. This figure indicates that the variation of the enthalpy of solution with composition shows some curvature in the AgBr-rich single-phase region, while it is approximately linear in the AgI-rich single-phase region. The enthalpy values of the compositions in the two-phase region fall approximately on a straight line joining the enthalpy values of the two terminal compositions.

The enthalpy and temperature of the β to α transformation of various compositions, as determined by

Table I. Values of (H_{518} − H_{298}) in cal/mol for various AgI-AgBr compositions

Mole fraction of AgI	Annealing time at 533 K (h)	H_{518} − H_{298} cal/mol of composition	Average with standard deviation
1.0	0	4740	
	0	4924	
	0	4564	
	0	4712	
	0	4658	4720 ± 125
0.9	0	4450	
	0	4532	
	0	4459	
	0	4517	
	0	4399	
	15	4556	
	15	4511	4489 ± 55
0.8	0	4495	
	15	4422	
	15	4359	
	15	4320	4399 ± 66
0.7	2	4627	
	15	4645	4638 ± 11
0.6	0	4366	
	0	4506	
	15	4616	
	15	4645	
	15	4526	4508 ± 124
	15	4393	
0.5	0	4308	
	2	4423	
	5	4114	
	15	4301	
	15	4151	4259 ± 113
0.4	0	3883	
	2	3932	3907 ± 25
0.3	0	3424	
	0	3467	
	15	3389	
	15	3442	3430 ± 28

Table II. Excess enthalpy for various two-phase AgI-AgBr compositions

	1	2	3	4	5	6	7	8	9
A. m/o AgI	1.0	0.90	0.85	0.80	0.70	0.60	0.50	0.40	0.30
B. H_{518} − H_{298} cal/mol Experimental	4720	4489	4364*	4339	4638	4508	4529	3907	3430
C. H_{518} − H_{298} cal/mol Assuming mixing of 2 and 9		4489		4313	4136	3959	3783	3606	3430
D. H_{518} − H_{298} cal/mol Assuming mixing of 3 and 9			4364*	4279	4109	3905	3765	3599	3430
E. Mol fraction $AgI_{0.9}Br_{0.1}$		1.00		0.83	0.67	0.50	0.33	0.166	0
F. Mol fraction $AgI_{0.85}Br_{0.15}$			1.00	0.91	0.73	0.54	0.36	0.18	0
G. Excess enthalpy cal/mol (B-C)		0		86	502	549	476	301	0
(B-D)			0	120	529	603	490	308	0

* Estimated by linear extrapolation.

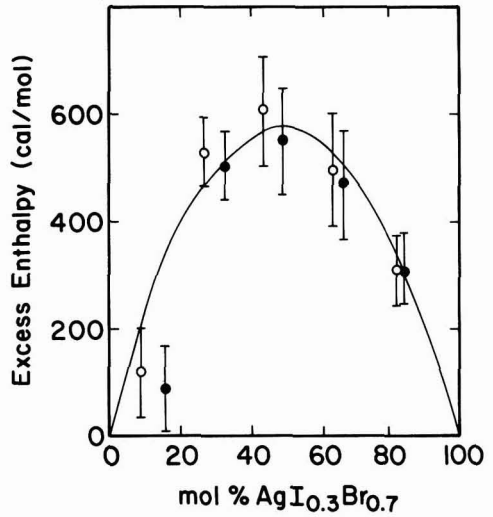


Fig. 1. Excess enthalpy, $[(H_{518} - H_{298})_{melted} - (H_{518} - H_{298})_{unmelted}]$ as a function of $AgI_{0.3}Br_{0.7}$ in $AgI_{0.9}Br_{0.1}$(●), and $AgI_{0.85}Br_{0.15}$(○).

differential scanning calorimetry are listed in Table IV. For pure AgI, these values are 1420 ± 30 cal/mol and 420 ± 0.5 K, respectively, in excellent agreement with the literature value (13).

A plot of transformation temperature as a function of composition is shown in Fig. 3. The temperature varies linearly up to 15 m/o AgBr in AgI and then remains constant. A plot of transformation enthalpy per mole of composition shown in Fig. 4 also indicates that the enthalpy varies linearly with a change in slope occurring at 15 m/o AgBr. No transformation was detected for the composition 30 m/o AgI-70% AgBr. These data indicate that the terminal compositions of the two-phase region of AgI-AgBr system at 518 K are $AgI_{0.85}Br_{0.15}$, which undergoes the $\beta \rightarrow \alpha$ transformation at 403.5 K with a transformation enthalpy of 1200 cal/mol, and $AgI_{0.3}Br_{0.7}$, which does not undergo a crystalline transformation. The enthalpy values obtained for the composition in the two-phase region are therefore entirely due to the $\beta \rightarrow \alpha$ transformation of $AgI_{0.85}Br_{0.15}$ and are converted to values per mole of

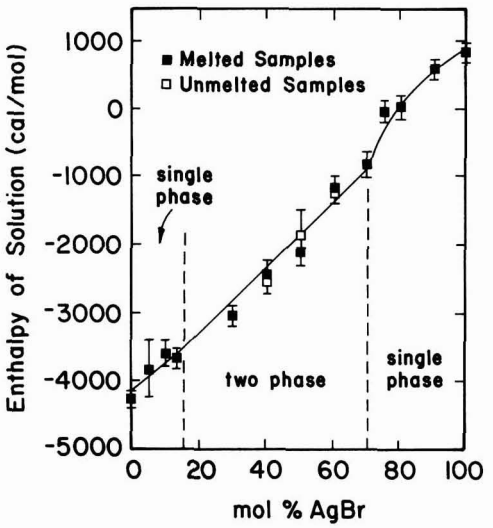


Fig. 2. Enthalpy of solution in $AgNO_3$ as a function of composition at 518 K.

Table III. Enthalpy of solution of various AgI-AgBr compositions in $AgNO_3$ at 518 K

Mole fraction of AgI	Enthalpy of solution (cal/mol) Melted	Unmelted
1.00	−4150	
	−4343	
	−4087	
	−4501	
	avg. −4270 (±188)	
0.95	−3623	
	−3237	
	−4438	
	−4085	
	avg. −3846 (±525)	
0.90	−3299	
	−3714	
	−3557	
	−3356	
	−3936	
	avg. −3572 (±262)	
0.87	−3599	
	−3796	
	−3636	
	avg. −3677 (±105)	
0.60	−2432	−2553
	−2581	−2543
	avg. −2506 (±105)	avg. −2548 (± 7)
0.50	−1717	−1598
	−2051	−1316
	−1893	−2247
	−2267	−2241
	avg. −1982 (±233)	avg. −1850 (±469)
0.40	−1216	−1271
	− 996	− 973
	avg. −1106 (±155)	avg. −1122 (±211)
0.30	− 605	
	− 884	
	− 625	
	− 787	
	− 688	
	avg. −718 (±116)	
0.25	− 162	
	+ 275	
	− 108.25	
	+ 75	
	avg. + 20 (±198)	
0.20	0	
	+ 89	
	+ 159	
	+ 123	
	avg. + 93 (± 68)	
0.10	+ 777	
	+ 678	
	+ 609	
	+ 519	
	avg. + 646 (±109)	
0.00	+ 716	
	+1012	
	+ 692	
	+1075	
	+ 896	
	avg. + 878 (±172)	

$AgI_{0.85}Br_{0.15}$ and plotted in Fig. 4. These values are constant within experimental error.

Discussion

The results obtained by differential scanning calorimetry and solution calorimetry indicate that at 518 K the terminal compositions in the two-phase region of the AgI-AgBr system correspond to 15 m/o AgBr for the α-AgI type cubic phase and 70 m/o AgBr for the AgBr-type cubic phase. The excess enthalpy values shown in Fig. 1, therefore, need to be modified. Assuming a linear variation with composition in the AgI-rich single-phase region, the enthalpy of solution for the $AgI_{0.85}Br_{0.15}$ terminal composition was calculated. This value was used to estimate the modified excess enthalpy values which are also shown in the same figure. The maximum in excess enthalpy value is still around 50 m/o. $AgI_{0.85}Br_{0.15}$ and 50 m/o $AgI_{0.3}Br_{0.7}$. However, whatever terminal compositions are assumed for the solid solutions, the rather surprising observation remains that the enthalpy $(H_{518} - H_{298})$ is much larger for the melted and solidified two-phase mixture

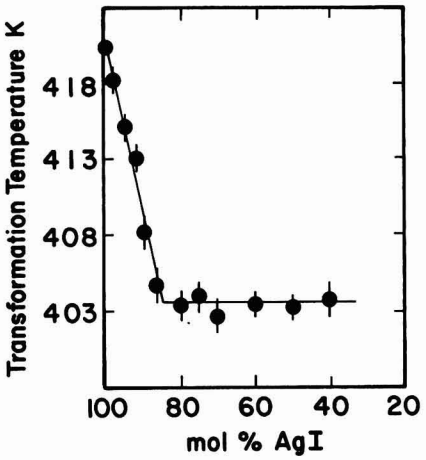


Fig. 3. Transformation temperature as a function of composition. The break in the curve corresponds to the solubility limit of AgBr in AgI.

than for a mechanical mixture of the two terminal solid solutions, while the enthalpies of solution at 518 K are similar for both types of two-phase compositions. Since the maximum in excess heat content occurs near an equimolar mixture of the two-terminal solid solutions, and since their densities are not very different, the maximum also corresponds to 50 volume percent (v/o) of each. Because of the identical methods of preparation, the grain sizes in different compositions are expected to be similar. The maximum in excess enthalpy at equivolume concentrations of each of the terminal compositions suggests that the excess enthalpy may be related to changes at the interface between these two phases. Since interfacial enthalpies reported for other systems in the literature (15) are two to three orders of magnitude smaller than the values measured in the present investigation, an additional explanation for the origin of this enthalpy is necessary.

The measured enthalpy ($H_{518} - H_{298}$) for various compositions may be considered to be the sum of (i) the enthalpy change associated with the heating of the sample from 298 K to the transformation temperature, (*ii*) the enthalpy of the $\beta \rightarrow \alpha$ transformation, and (*iii*) the enthalpy change associated with heating the sample from the transformation to the calorimetric temperature, 518 K.

The measurement of the $\beta \rightarrow \alpha$ transformation enthalpy by DSC and the enthalpy of solution in $AgNO_3$ of melted

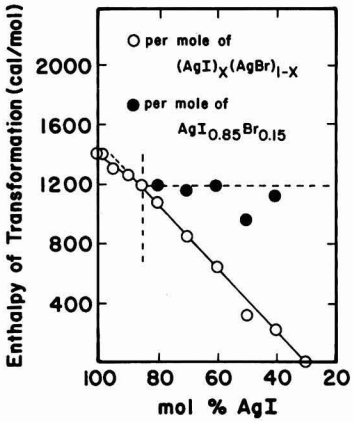


Fig. 4. Enthalpy of transformation as a function of m/o AgI in AgBr

Table IV. Temperature and enthalpy of transformation of various AgI + AgBr compositions

Mol fraction of AgI	Transition temperature K [±0.5 K]	Enthalpy of transformation (cal/mol)
1.00	420.75	1461
	420.25	1413
		1411
		1433
		1412
0.98		1411
0.95	416	1306
	414.25	1376
		1348
		1335
0.92	413.2	1116
	413.6	1135
0.90	407.75	1093
	407.75	1368
	407.25	993
	408.4	1277
	409	1350
0.85		1198
0.80	402.5	1180
	402.5	946
	402.75	1060
	404	997
0.70	404	878
	401.75	693
	402.5	656
0.60	404.2	619
	404	647
		582
0.50	402.75	347
	403	184
	403.6	323
0.40	403.5	161
	405.2	226

and unmelted samples in the two phase region at 518 K indicates that contributions from (*ii*) and (*iii*) are small. The excess enthalpy may therefore be considered to be predominantly due to the effects below the $\beta \rightarrow \alpha$ transition in the AgI-rich phase.

An anomalous increase in electrical conductivity in the two-phase region of the system at temperatures below the $\beta \rightarrow \alpha$ transformation was observed by Shahi and Wagner (2). The maximum in conductivity was reported to be at 20 m/o AgI-80 m/o AgBr. This enhanced conduction was suggested to be due to the presence of additional defects generated at the two-phase interface due to the space charge layer. AgI is an ionic conductor in which Frenkel-type defects predominate (16). Although the enthalpy of formation of silver interstitials and silver vacancies in AgI is not known, a comparison of similar values reported for AgCl suggests that the enthalpy of formation of silver vacancies is smaller than that of silver interstitials. The presence of silver vacancies as the predominant transporting species at lower temperatures has been suggested by Khandkar and Wagner (3) in the case of AgCl-Al_2O_3 composites and by Shahi and Wagner (2) in the case of AgI-Al_2O_3 composites. The latter authors inferred the predominance of silver vacancies from the sign of thermoelectric EMF.

The definite qualitative correlation observed between the anomalous conductivity enhancement and the excess enthalpy in the two-phase region suggests that the same mechanism may be responsible for both effects. It is suggested that the origin of this excess enthalpy is the excess vacancy concentration at the interface in the melted two-phase compositions of the AgI-AgBr system.

The observation that maxima in the electrical conductivity and in the excess enthalpy occur at different compositions suggests that the presence of a second phase not only affects the concentration of mobile species taking part in conduction, but also affects their mobility as well. Changes in mobility would not be reflected in the measured excess enthalpy, but could shift the maximum conductivity away from the composition of presumed maximum defect concentration and maximum enthalpy.

Enthalpies of solution of the AgI and the AgBr-rich single-phase compositions can be used to obtain enthal-

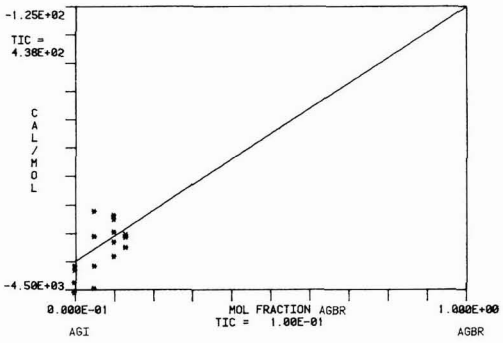


Fig. 5. Linear extrapolation of the enthalpy of solution of AgI-rich single-phase compositions to pure AgBr.

pies of solution of their metastable polymorphs by a method similar to that described by Davies and Navrotsky (17) for NiO-ZnO solid solutions. In this approach, one fits the enthalpy of solution within a single-phase region by an appropriate polynomial. Extrapolation to mole fraction of the solute equal to one gives the enthalpy of solution of the solute in the hypothetical polymorph having the structure of the terminal solid solution. The difference between that value and the heat of solution of the pure solute in its normal structure gives the enthalpy of transformation. A linear fit to the enthalpy of solution data implies that the solid solution is ideal when referred to standard states having the same structure; a quadratic fit that the solution is regular. The least squares computer fit for the data is shown in Fig. 5 and 6 for AgI-rich and AgBr-rich compositions, respectively. In each case the fit was obtained using all the data points for each composition rather than averages for each composition. Linear extrapolation of the data to pure AgBr gives a value for the enthalpy of solution of AgBr with the α-AgI-type cubic structure as -125 ± 150 cal/mol. From Table III, the enthalpy of solution of AgBr having rocksalt-type cubic structure is 870 ± 170 cal/mol. Therefore, the enthalpy of transformation of AgBr from its stable rocksalt-type cubic structure to α-AgI-type bcc structure is estimated to be 1000 ± 300 cal/mol. The variation of enthalpies of solution of AgBr-rich single phases with composition shows a small curvature. Because of the large scatter in the data obtained and small composition range of the single-phase region, the extrapolation of the data to pure AgI is quite uncertain. The linear fit (ideal solution) gives a near-zero enthalpy of transformation for AgI ($\alpha \rightarrow$ rocksalt). A quadratic fit implies negative heats of mixing in the rocksalt solid solutions and an enthalpy of transformation of 12,500 cal/mol. These two fits may represent an underestimate and overestimate, respectively, of the curvature of the data and may place a lower and upper bound on the enthalpy of transformation. Thus, ΔH for AgI ($\alpha \rightarrow$ rocksalt) may lie in the range 0-12 kcal/mol. No data are available for comparison.

Conclusions

1. The excess enthalpy, as defined by the difference in (H_{518} - H_{298}) values between the melted and solidified two-phase compositions and the mechanical mixtures of the terminal solid solutions of the AgI-AgBr system, exhibits maxima at equivolume concentrations of the terminal compositions and is suggested to be due to the excess silver ion vacancies generated at the interfaces due to the space-charge layer.

2. The terminal composition of the two-phase region of AgI-AgBr system at 518 K are $AgI_{0.85}Br_{0.15}$ and $AgI_{0.3}Br_{0.7}$.

3. The enthalpy of transformation of AgBr from its stable rocksalt-type cubic structure to α-AgI-type bcc structure is estimated to be 1000 ± 300 cal/mol, while the enthalpy for the transformation of α-AgI to the rocksalt structure lies between 0 and 12 kcal/mol.

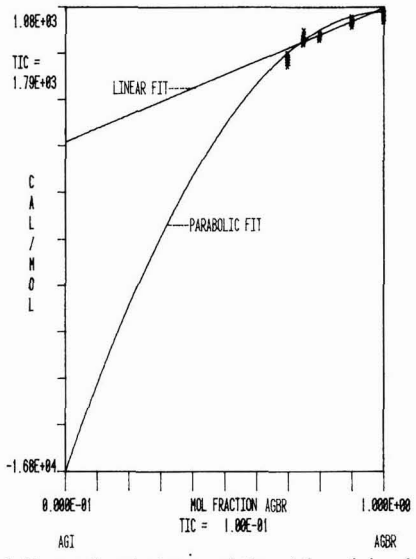


Fig. 6. Linear and quadratic extrapolations of the enthalpy of solution of AgBr-rich single-phase compsitions to pure AgI.

Acknowledgments

The authors thank DOE for providing financial support to A. Khandkar under Contract DE-ACO2-82ER12091, NSF for Grant DMR8106027 to A. Navrotsky, and The Center for Solid State Science for providing funds to V. B. Tare and J. B. Wagner, Jr. to carry out this research.

Manuscript submitted March 26, 1984; revised manuscript received June 15, 1984. This was Paper 832 presented at the San Francisco, California, Meeting of the Society, May 8-13, 1983.

Arizona State University assisted in meeting the publication costs of this article.

REFERENCES

1. C. C. Liang, *This Journal*, **120**, 1289 (1973).
2. K. Shahi and J. B. Wagner, Jr., *ibid.*, **128**, 6 (1981).
3. A. Khandkar and J. B. Wagner, Jr., Abstract 833, p. 1236, The Electrochemical Society Extended Abstracts, Vol. 83-1, San Francisco, CA, May 8-13, 1983.
4. G. Crosbie, *J. Solid State Chem.*, **25**, 367 (1978).
5. V. B. Tare and J. B. Wagner, Jr., *J. Appl. Phys.*, **154**, 252 (1983).
6. V. B. Tare and J. B. Wagner, Jr., *ibid.*, **154**, 6459 (1983).
7. K. Shahi and J. B. Wagner, Jr., *Appl. Phys. Lett.*, **37**, 757 (1980).
8. J. B. Wagner, Jr., *Mater. Res. Bull.*, **15**, 1691 (1980).
9. T. Jow and J. B. Wagner, Jr., *This Journal*, **126**, 1963 (1972).
10. A. Hooper, Paper 76 presented at the International Conference on Fast Ionic Transport in Solids, Gatlinburg, TN, May 18-22, 1981.
11. K. Shahi and J. B. Wagner, Jr., *Phys. Rev. B*, **23**, 6417 (1981).
12. A. Navrotsky, *Phys. Chem. Min.*, **2**, 89 (1977).
13. "Thermochemical Properties of Inorganic Compounds," compiled by I. Barin and O. Knacke, Springer-Verlag, Berlin (1973).
14. O. Stasiw and J. Teltow, *Z. Anorg. Allg. Chem.*, **259**, 150 (1949).
15. J. J. Kramer, G. M. Pound, and R. F. Mehl, *Acta Metall.*, **6**, 763 (1958).
16. K. Shahi, *Phys. Status Solidi A*, **41**, 11 (1977).
17. P. Davies and A. Navrotsky, *J. Solid State Chem.*, **38**, 264 (1981).

Phase Relations and Thermochemistry of Iron-Aluminum-Sulfur System at 1173 K

P. C. Patnaik* and W. W. Smeltzer**

Department of Metallurgy and Materials Science, McMaster University, Hamilton, Ontario, Canada L8S 4M1

ABSTRACT

The compositions were determined of alloy and sulfide phases in the Fe-Al-S system equilibrated with one another at 1173 K. These evaluations were used to construct the ternary Fe-Al-S isotherm, which was comprised of three sulfide phases coexisting with alloy: FeS containing up to 0.61 atomic percent (a/o) Al, $FeAl_2S_4$ of Fe/Al ratio 0.766 to 0.518 in the alloy composition range 0.84 to 5.86 a/o Al, and Al_2S_3 containing 0.30 a/o Fe. These results were combined with available thermodynamic data to determine the ternary equilibrium diagram in the form of sulfur activity *vs.* aluminum metal atom fraction of the alloy and sulfide phases. The sulfur activity over the ternary univariant coexistence alloy + $FeAl_2S_4$ + Al_2S_3 is 5.35×10^{-6}.

Phase relations and thermodynamic properties of the Fe-Al-S solid-gas system at high temperatures are not known. In this investigation, the ternary Fe-Al-S isotherm at 1173 K is constructed using the compositions of equilibrated phases. The sulfur activities coexisting with aluminum sulfide and alloys were evaluated using the value for the standard free energy of formation of Al_2S_3 (1) and the available aluminum activity data for the binary Fe-Al alloys (2, 3). These sulfur activity evaluations, in conjunction with compositions of the sulfide and alloy phases, were utilized to construct the ternary equilibrium sulfur activity diagram.

Experimental

A number of ternary compositions in the Fe-Al-S system were synthesized from the elements. The starting materials were powders of iron and aluminum of 99.99% purity and sulfur of 99.999% purity supplied by Cerac, Incorporated. Several overall compositions (P1 to P6), as shown in Fig. 1, were chosen. In each case, the elements were thoroughly mixed, compressed to a pellet, and then placed in a high purity (99.9%) alumina crucible which was sealed in a quartz tube under vacuum (1-2 Pa). This method avoided SiO_2 contamination of the sample pellet resulting from its bonding to the quartz wall, which has been shown previously to occur (4).

Previous workers using aluminum and sulfur to obtain Al_2S_3 in a quartz ampul have encountered explosions while determining a suitable heating schedule (5). This behavior was due to the autocatalytic nature of aluminum sulfidation by which the exothermic sulfidation reaction increased the sulfur pressure in the ampul. With an increased sulfur pressure, the reaction rate increased, releasing additional heat, which led to excessive sulfur pressures and rupture of the quartz tube. This problem was not encountered in the present case, owing to rapid reaction between iron and sulfur. However, for a successful experiment, combinations of slow and step heatings were used.

Figure 2 shows a typical heating schedule of samples placed in alumina crucibles encased in quartz ampuls. Initially, they were heated for 2 days in steps at 423 and 509 K (total P_{S_2} at 509 K = 10^3 Pa) to permit combination of the sulfur with metals. All the samples contained 35 atomic percent (a/o) sulfur with varying amounts of the metals. The completeness of reaction was indicated by the absence of visible sulfur in the quartz tube. After approximately 240h at 1173 ± 2 K, the ampuls were quenched in water. The quenched samples were mounted for metallographic observation. In addition to metallography, x-ray powder diffraction with Ni-filtered CuK_α radiation was also employed to identify the various phases present in each sample. Compositions of various phases were determined using electron probe microanalyses (EPMA) with Fe-Al alloys, FeS, and $FeAl_2S_4$ of known compositions as standards. These compositions could be determined to within ± 0.05 a/o.

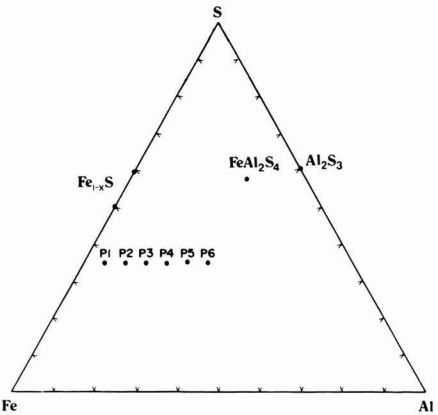


Fig. 1. Overall compositions of Fe, Al, and S (P1-P6) considered for the analysis of the ternary Fe-Al-S isotherm.

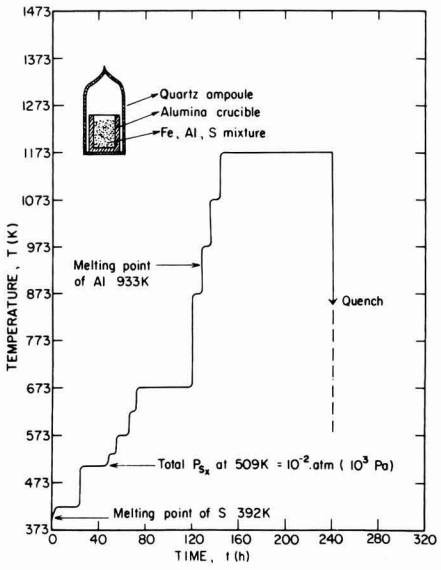


Fig. 2. Sample heating schedule for phase equilibration to determine the ternary Fe-Al-S isotherm.

*Electrochemical Society Student Member.
**Electrochemical Society Active Member.

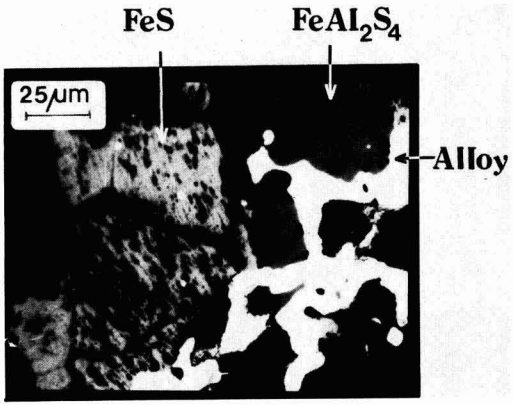


Fig. 3. Optical photomicrograph of polished-annealed alloy + FeS + $FeAl_2S_4$ pellet.

Results

Figure 3 shows three equilibrated phases, FeS + Fe-0.84Al (a/o) + $FeAl_2S_4$. Table I summarizes the equilibrated phases in pellets P1 through P6 as identified by metallography and x-ray diffraction. The x-ray intensity plots *vs.* diffraction angle 2θ for several pellets are shown in Fig. 4. The correspondence of these diffraction patterns to ASTM standards for FeS, Al_2S_3, and Fe-Al alloys and to independent diffraction measurements made on synthesized $FeAl_2S_4$ support the inferences drawn from the metallographic observations (4, 6).

Compositions of alloys and coexisting sulfide phases determined by EPMA are reported in Table II. These analyses demonstrated the following findings of phase equilibria at 1173 K: (*i*) in the FeS + alloy + $FeAl_2S_4$ univariant equilibrium, FeS contained 0.61 a/o Al and the alloy contained 0.84 a/o Al, (*ii*) the double sulfide phase, $(Fe_{1.24}Al_{1.618})S_4$, in equilibrium with $(Fe_{0.96}Al_{0.012})S$ and the Fe-0.84 Al alloy was rich in iron, and its iron content decreased to $(Fe_{0.99}Al_{1.91})S_4$ as the double sulfide was equilibrated with higher aluminum containing alloys, and (*iii*) the solubility of iron in Al_2S_3 equilibrated with double sulfide and alloy containing 5.86 a/o Al was 0.30 a/o. This solubility of iron in Al_2S_3 was found to decrease with increasing aluminum contents of the alloy.

Discussion

The Fe-Al-S isotherm, Fig. 5, was constructed from results of this investigation using the binary Fe-Al, Fe-S, and Al-S phase extents (3). Pure iron and aluminum dissolve up to 0.05 and 5 a/o of sulfur, respectively. These concentrations were used to represent the sulfur solubility in the alloy, as indicated by a dotted line on the ternary isotherm. Solubilities of aluminum and iron in FeS and Al_2S_3 were determined to be 0.61 and 0.3 a/o, respectively, when each phase was equilibrated with alloy and $FeAl_2S_4$. The phase field of double sulfide, $(Fe_{1.24}Al_{1.618})S_4$-$(Fe_{0.99}Al_{1.91})S_4$, was obtained from the microprobe analyses. Construction of two-phase regions containing alloy + $FeAl_2S_4$, alloy + Al_2S_3, and three-phase triangles consisting of alloy + FeS + $FeAl_2S_4$, alloy + $FeAl_2S_4$ + Al_2S_3 were made using the compositions as given in Table II of the appropriate equilibrated phases. The tie lines (dotted) shown in the two-phase regions are those determined experimentally. Dotted lines in the upper portion of the isotherm are schematic.

Aluminum activities in solid Fe-Al alloys over the range 5-80 a/o at 1173 K were determined by Eldridge and Komarek (2) and the values are recorded in Table III. Sulfur activities upon equilibrating Al_2S_3 with alloys containing

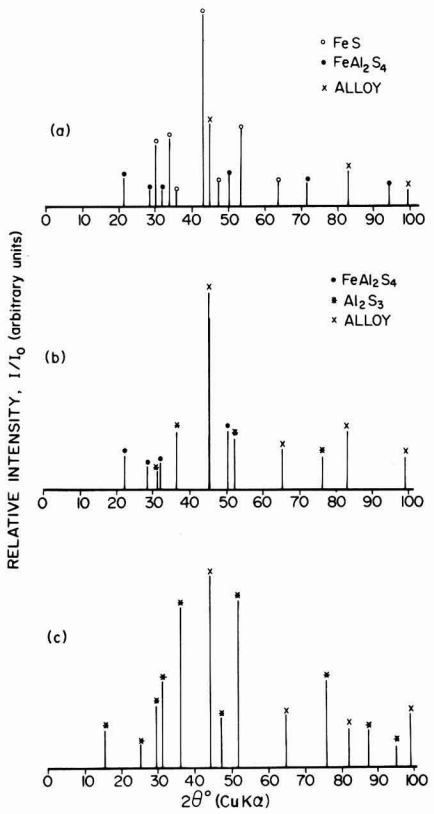


Fig. 4. Powder x-ray diffractograms of various sulfide phases in the pellets P1-P6 (Fig. 1) of increasing Al content. (a): FeS + $FeAl_2S_4$ + alloy. (b): $FeAl_2S_4$ + Al_2S_3 + alloy. (c): Al_2S_3 + alloy.

Table I. Summary of phase identification by metallographic observations and powder x-ray diffraction of the equilibrated pellets

Points on isotherm	Overall composition S	Al	Fe	Inference
P1	35	5	60	Three-phase region: alloy, FeS and $FeAl_2S_4$
P2	35	10	55	Three phases: alloy + FeS + $FeAl_2S_4$
P3	35	15	50	Two-phase region: alloy + $FeAl_2S_4$
P4	35	20	45	Two-phase region: alloy + $FeAl_2S_4$
P5	35	25	40	Three-phase region: alloy + Al_2S_3 + $FeAl_2S_4$
P6	35	30	35	Two-phase region: alloy + Al_2S_3

Table II. Electron probe microanalyses of equilibrated phases in the Fe-Al-S system

Pellet no. (Fig. 1)	Phases	Al and Fe a/o in the alloy Al	Fe	Chemical formula of the sulfide
2	Alloy	0.84	99.15	
	Iron sulfide			$(Fe_{0.96}Al_{0.012})S$
	Double sulfide			$(Fe_{1.24}Al_{1.618})S_4$
3	Alloy	2.73	97.25	
	Double sulfide			$(Fe_{1.14}Al_{1.653})S_4$
4	Alloy	3.42	96.54	
	Double sulfide			$(Fe_{1.10}Al_{1.846})S_4$
5	Alloy	5.86	94.11	
	Double sulfide			$(Fe_{0.99}Al_{1.910})S_4$
	Aluminum sulfide			$(Fe_{0.015}Al_{1.955})S_3$
6	Alloy	21.05	78.94	
	Aluminum sulfide			$(Fe_{0.009}Al_{1.982})S_3$

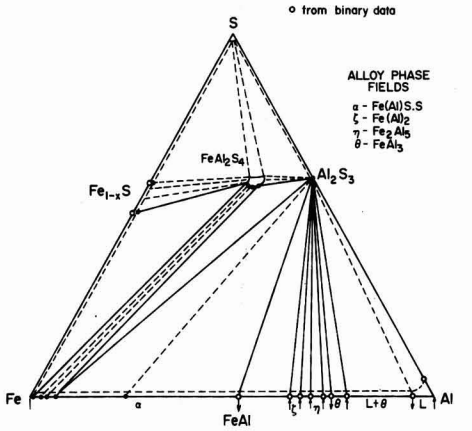


Fig. 5. The experimentally determined ternary Fe-Al-S isotherm at 1173 K.

6-80 a/o Al can be calculated as follows. If one considers the reaction

$$2Al_{(alloy)} + \frac{3}{2} S_2 = Al_2S_3 \qquad [1]$$

the equilibrium constant is given by

$$K = \exp - \frac{\Delta G^\circ_f}{RT} = \frac{a_{Al_2S_3}}{a_{Al}^2 P_{S_2}^{3/2}} \qquad [2]$$

where $a_{Al_2S_3}$ and a_{Al} are the activities of Al_2S_3 and aluminum in the alloy, respectively, P_{S_2} is the dissociation pressure of Al_2S_3, and ΔG°_f is the standard free energy of formation of Al_2S_3. Since $a_{Al_2S_3} \approx 1$, the sulfur pressure relationship is given by

$$\log P_{S_2}\,(\text{Pa}) = \frac{2}{3}\left(\frac{\Delta G^\circ_f(Al_2S_3)}{2.303\,RT} - 2 \log a_{Al}\right) + \log (101{,}300) \qquad [3]$$

Upon substituting the most recently determined value for $\Delta G^\circ_f(Al_2S_3) = -507{,}883 \pm 500$ J/mol (1), the sulfur activity is given by

$$\log a_S = 1/2\,[\log \{P_{S_2}\,(\text{Pa})/1.013 \times 10^5\,(\text{Pa})\}]$$

$$= -7.54 - \frac{2}{3} \log a_{Al} \qquad [4]$$

Sulfur activities for alloy-Al_2S_3 equilibria were then calculated using the aluminum activity values and these evaluations are given in Table III.

An aluminum cation (or metallic) fraction of each phase is defined as

$$\xi_{Al} = \frac{g \text{ ions (atoms) of aluminum}}{g \text{ ions (atoms) of iron} + g \text{ ions (atoms) of aluminum}}$$

For the three-phase equilibrium, alloy + $FeAl_2S_4$ + Al_2S_3, ξ_{Al} (alloy) was determined to be 0.059, corresponding to an activity of 3.9×10^{-4}. The corresponding sulfur activity was calculated to be 5.35×10^{-6}. It was not possible to evaluate the sulfur activity over the FeS + alloy + $FeAl_2S_4$ equilibrium because the free energy of formation of $FeAl_2S_4$ is unknown.

Figure 6 shows the sulfur activity equilibrium diagram, ln a_S *vs.* ξ_{Al}, for the Fe-Al-S system at 1173 K. This diagram is semischematic and it has been compiled insofar as possible from the results given in Tables II and III. For clarity, dissociation pressures of the sulfides are also shown in this diagram.

Table III. The thermodynamic activity of Al in solid Fe-Al alloys (2) and the sulfur activities calculated from Eq. [4] for the alloy + Al_2S_3 equilibria at 1173 K

a/o Al	$\frac{(\xi_{Al})}{\eta_{Al}} = \frac{}{\eta_{Al} + \eta_{Fe}}$	a_{Al} at 1173 K	$-\log a_S$
5	0.05	3.8×10^{-4}	
6	0.06	3.9×10^{-4}	5.27
10	0.10	8.1×10^{-4}	5.47
15	0.15	1.5×10^{-3}	5.65
20	0.20	2.5×10^{-3}	5.79
25	0.25	3.7×10^{-3}	5.91
30	0.30	5.5×10^{-3}	6.03
35	0.35	8.3×10^{-3}	6.15
40	0.40	1.4×10^{-2}	6.28
45	0.45	2.6×10^{-2}	6.47
50	0.50	5.5×10^{-2}	6.69
52	0.52	9.8×10^{-2}	6.86
60	0.60	9.8×10^{-2}	6.86
65	0.65	9.8×10^{-2}	6.86
67	0.67	1.3×10^{-1}	6.94
70	0.70	1.3×10^{-1}	6.94
75	0.75	4×10^{-1}	7.26
80	0.80	7×10^{-1}	7.42
100	1	1	7.54

The sulfur activity decreased from 1.2×10^{-4} imposed by the Fe-FeS coexistence to a lower value presently not determined associated with the univariant alloy + FeS + $FeAl_2S_4$ equilibrium. The fractions, ξ_{Al}, in each phase of this coexistence, are 0.0084, 0.012, and 0.566, respectively. The sulfur activity of the alloy + $FeAl_2S_4$ + Al_2S_3 coexistence was determined to be 5.35×10^{-6}. ξ_{Al} in each phase is 0.059, 0.658, and 0.992 respectively. $FeAl_2S_4$ equilibrated with alloys containing 0.84 to 5.86 a/o Al. The results indicate that Al_2S_3 exists with alloys containing greater than 5.86 a/o Al. Sulfur activity decreases with increasing aluminum contents of the alloy until it reaches 2.9×10^{-8}, corresponding to that of Al + Al_2S_3 equilibrium.

Summary

The ternary Fe-Al-S isotherm at 1173 K was constructed by determining the composition of equilibrated alloy and

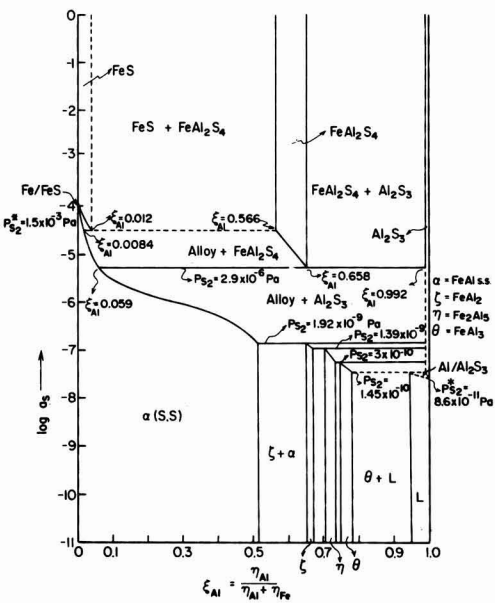


Fig. 6. The ternary equilibrium sulfur activity diagram at 1173 K, log a_S *vs.* Al cation (metallic) fraction. The dissociation pressures calculated for the sulfides are given by

$$a_s = \{P_{S_2}\,(\text{Pa})/1.013 \times 10^5\,(\text{Pa})\}^{1/2}$$

sulfide phases. Equilibrium sulfur activities were determined for the alloy + $FeAl_2S_4$ + Al_2S_3 univariant equilibrium and alloy + Al_2S_3 coexistences. These results in conjunction with thermochemical data for Fe-Al alloys and Al_2S_3 were used to determine the equilibrium diagram of sulfur activity as a function of aluminum metallic fraction of each phase.

Acknowledgments

Financial assistance for this research by the Natural Sciences and Engineering Research Council of Canada is gratefully acknowledged. P. C. Patnaik wishes to acknowledge the award of a graduate scholarship in Metallurgy and Materials Science to carry out this research as a part of his Ph.D. studies at McMaster University.

Manuscript submitted April 19, 1984; revised manuscript received July 6, 1984.

McMaster University assisted in meeting the publication costs of this article.

REFERENCES

1. M. J. Ferrante, J. M. Stuve, H. C. Ko, and R. R. Brown, *High Temp. Sci.*, **14**, 91 (1981).
2. J. Eldridge and K. L. Komarek, *Trans. Metall. Soc. AIME*, **230**, 236 (1964).
3. P. Hultgren, P. D. Desai, D. T. Hawkins, M. Gleiser, and K. K. Kelly, "Selected Values of the Thermodynamic Properties of Binary Alloys," p. 156, American Society for Metals, Metals Park, OH (1973).
4. K. Nishida and T. Narita, *Bull. Fac. Eng. Hokkaido U.*, **81**, 1 (1976).
5. E. E. Hellstrom and R. A. Huggins, *Mater. Res. Bull.*, **14**, 127 (1979).
6. J. Flahaut, *Ann. Chim. (Paris)*, **63**, 632 (1952).

Preparation and Properties of Amorphous Boron Films Deposited by Pyrolysis of Decaborane in the Molecular Flow Region

K. Nakamura

Department of Chemistry, Nihon University, Sakurajosui Setagaya-ku, Tokyo 156, Japan

ABSTRACT

Boron films of 0.1-1.5 μm thickness have been prepared on sapphire, silicon, and tantalum as substrates by the pyrolysis of decaborane ($B_{10}H_{14}$) in the molecular flow region ($\leqq 10^{-4}$ torr) and in a temperature range of 350°-1200°C. It is found that the deposition rate of the boron films is proportional to the decaborane partial pressure and the substrate temperature. Below 416°C, the deposition rate D is given as a function of the substrate temperature and partial pressure of decaborane. This relation is

$$D = 7.16 \times 10^9 \cdot P \cdot \exp(-39000/RT_s)$$

where T_s is the substrate temperature, P is the pressure of decaborne, and R is the gas constant. The apparent activation energy for the decomposition of decaborane is found to be 39 kcal/mol. X-ray and electron diffraction study indicates that the films are amorphous. The electrical conductivities vary from 3×10^{-5} S · cm^{-1} at 77 K to 30 S · cm^{-1} at 1000 K, and the activation energy is 1.07 eV in the intrinsic temperature range (700-1000 K). The maximum value of thermoelectric power is about 420 μV · deg^{-1} at 700 K, and its polarity is positive between 500 and 1000 K. The absorption coefficient, refractive index, and extinction coefficient of boron films are obtained from the measured transmittance and reflectance. The energy of the indirect allowed transition is estimated to be 1.28 ± 0.08 eV.

Boron is one of the elemental semiconductors. However, the resistivity of boron is several hundred times larger than that of Si and Ge at room temperature. Although many studies (1-3) on the properties of boron have been done, the physical properties reported are not in agreement with each other because it is very hard to obtain high-purity bulk boron. However, we can obtain pure and uniform boron in film form. Boron films have been prepared by means of chemical vapor deposition (4-6) or vacuum evaporation using electron bombardment of boron (7-9). Croft (10) has obtained high-purity boron films by pyrolysis of diborane. However, diborane is a very dangerous gas which requires much care in handling. Pentaborane (B_5H_9; −46.5°C mp, 60°C bp) and decaborane ($B_{10}H_{14}$; 99.6°C mp, 213°C bp) can be used as alternative boron hydride sources. Decaborane is safer and more stable than pentaborane and diborane. Furthermore, decaborane has advantages as a source material for boron films because high purity decaborane is easy to obtain with a sublimation purification process.

Many studies on the electrical (6, 11, 12, 14) and optical (8, 9, 13, 14) properties of boron films prepared by vacuum evaporation (12, 13) and CVD (5, 14) have been reported. However, reported properties scatter widely (e.g., the values of electrical conductivity and optical gap energy at room temperature).

In this report, high quality boron films have been prepared by pyrolysis of decaborane in the molecular flow region at temperatures between 350° and 1200°C. The deposition mechanism is discussed in terms of the dependence of the deposition rate on the substrate temperature and the impingement frequency of decaborane molecules onto the substrate surface.

The temperature dependencies of the electrical conductivity and of the thermoelectric power of the boron films deposited on sapphire substrates have been measured. The energy-band gap and optical constant ($n \cdot k$) of boron have been estimated from the results of the optical transmittance and reflectance in the visible and infrared spectral regions.

Experimental

The schematic diagram of the apparatus in this study is shown in Fig. 1. The vacuum chamber was evacuated by an oil diffusion pump system, and the ultimate pressure was 2×10^{-6} torr. Sapphire and silicon were used as the substrates. The substrate was fixed on the tungsten sheet heater (0.05 mm thickness) and was heated from 600° to 1200°C (Fig. 2). Tantalum sheet was also used as a substrate and was heated between 350° and 700°C by direct resistance heating. The sapphire substrate temperature was estimated from the heater temperature, which was measured with an optical pyrometer. The relation between the substrate and the heater temperatures was previously obtained. The tantalum substrate temperature was measured directly by a welded thermocouple.

Decaborane (Arfa Product) was sublimated by heating at abut 70°C and was introduced to the vacuum chamber through a variable leak valve. Boron films were deposited on the heated substrate by thermal decomposition of

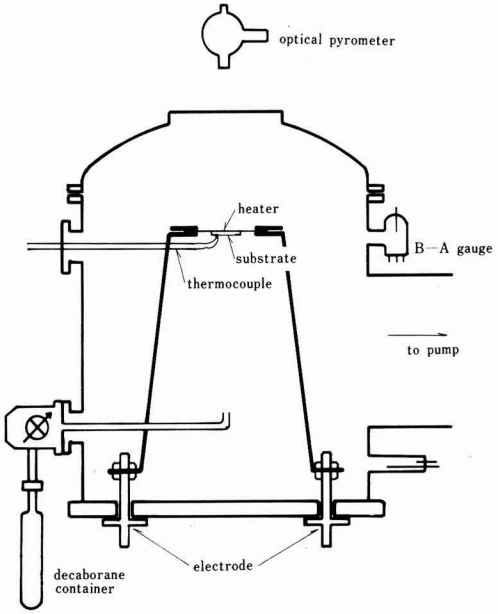


Fig. 1. Schematic diagram of the apparatus used for deposition of boron films by pyrolysis of decaborane.

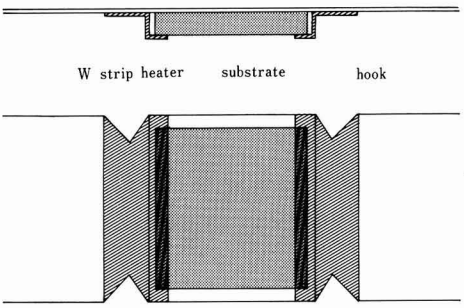


Fig. 2. Assembly of the substrate and the heater

the decaborane. The pressure of decaborane was measured as a corresponding of nitrogen pressure by a B-A type ionization gauge and was kept between 1×10^{-5} torr and 2×10^{-4} torr. Deposition time varied from 0.5-60 min, depending on the gas pressure and the substrate temperature. The thicknesses of the films on the sapphire substrates were measured with a multiple-beam interferometer and ranged from 442 to 4740Å. In the case of the films deposited on tantalum, the film thickness could not be measured optically because of the rough surface of the tantalum substrate. The film thickness of the boron films on tantalum substrates was estimated from the measured x-ray fluorescence of boron deposited using EPMA with a 7 kV acceleration voltage, a 0.1A sample current, and a 100 μm beam-diameter. The relation between the x-ray intensity and the film thickness was previously obtained using boron films on a sapphire substrate.

The crystal structure of boron films was studied by reflection electron and x-ray diffraction techniques. The electrical conductivity and its temperature dependence were measured by a two-probe technique at temperatures ranging from 300 to 1000 K in vacuum. A gold film, deposited on the boron films by vacuum evaporation, was used as an electrode. Thermoelectric power of the films was measured by using a Pt-PtRh (10%) thermocouple which was 0.2 mm in diameter. The distance between two thermocouples was 10 mm. The size of the boron films measured were 5×13 mm^2, and the film thicknesses were 1.2 and 1.5 μm. The thermoelectric power could not be measured below 250°C because it was too small in comparison with the electrical noise in this temperature range.

The transmission and the reflection spectra of the boron films on sapphire were measured over a wavelength range of 200-2500 nm using a spectrophotometer MPS-50 (Shimazu). In the transmission and the reflection measurements, an uncoated sapphire and an evaporated aluminum film were used as the references, respectively. Absorption coefficient, refractive index, and extinction coefficient of the boron films were calculated from the measured transmittance and reflectance at normal incidence.

Infrared transmittance at normal incidence on boron films deposited on high resistivity silicon wafers was measured in a wavelength range of 2.5-50 μm using an infrared spectrophotometer, DS-701G (Jasco).

Results and Discussion

Influence of the deposition parameters on the deposition rate.—The deposition rate of boron, D (Å/s), is linearly dependent on the decaborane pressure, P (torr), as shown in Fig. 3, and is given as $D = 3.57 \times 10^{-3} \cdot P$ for substrate temperatures of 750° and 1000°C.

It is thought that the deposition rate of boron films obtained by pyrolysis of decaborane depends on the impingement frequency of decaborane onto the substrate. From gaseous molecular dynamics, the impingement frequency, S, of decaborane on the substrate surface is given as

$$S = P\,(M/2\pi RT_g)^{1/2} = 5.8 \times 10^{-2} \cdot P\,(M/T_g)^{1/2} \quad (\mathrm{g/cm^2 \cdot s}) \qquad [1]$$

where $R = 62.36$ torr · l/mol · deg is the gas constant, P is the decaborane pressure in torr, M is the molecular weight of decaborane, and T_g is the gas temperature considered to be at room temperature (*i.e.*, $T_g = 300$ K).

The rate of chemisorption depends on the impingement frequency, S, of the decaborane molecules on the surface, the condensation coefficient, γ, and the fraction of collisions that take place at available sites $f(\theta)$, where θ is the fractional surface coverage. The rate of chemisorption, U is given as

$$U = S\gamma f(\theta) \exp\,(-E_c/RT_s) \qquad [2]$$

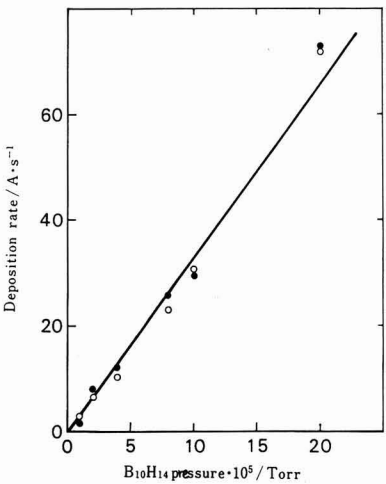


Fig. 3. Deposition rates of pyrolytic boron films as a function of $B_{10}H_{14}$ pressure. The films were deposited at substrate temperatures of T_s = 750°C (●) and T_s = 1000°C (○).

where T_s is the substrate temperature, and E_c is the activation energy for chemisorption.

As shown in Fig. 3, the deposition rate is independent of temperature, and the chemisorption is nonactivated; hence, the activation energy $E_c = 0$. Under the experimental conditions, we suppose that $f(\theta) \fallingdotseq 1$ and $\gamma \fallingdotseq 1$, hence, the rate of chemisorption is equal to the impingement frequency, S. The theoretical deposition rate, D_t, in this high temperature range is

$$D_t = 1.66 \times 10^{-2} \cdot P \quad \text{(cm/s)} \qquad [3]$$

taking into account the ratio of boron weight to decaborane molecular weight (0.9) and the density of boron (2.0 g/cm^3). Comparison with the experimental values of Fig. 3 shows that D_t must be multiplied by a factor of 0.22. This factor is due to either $f(\theta)$, γ, or the sensitivity difference of decaborane and nitrogen in the ionization gauge.

Figure 4 shows the temperature dependence of the deposition rate of boron films in a temperature range of 350°-700°C at two decaborane partial pressures, 2×10^{-5} torr and 8×10^{-5} torr. In each case, the deposition rate increases steeply, with an increase in temperature of up to 416°C, and then saturates.

In the low temperature range, $T_s \leqq 416$°C, the activation energy is found to be 39 kcal/mol from the slope, and the deposition rate is given as

$$D = 7.16 \times 10^9 \cdot P \cdot \exp(-39000/R \cdot T_s) \quad \text{(cm/s)} \qquad [4]$$

The saturated deposition rate above 416°C can be explained by Eq. [2]. The activation energy of 39 kcal/mol is in agreement with 41.4 kcal/mol (15) and 41.6 ± 0.5 kcal/mol (16), both reported for the activation energy of the decomposition of decaborane at temperatures below 250°C.

Characterization of the films (structure, impurities).—The x-ray diffraction pattern of a boron film deposited on sapphire at a substrate temperature of 700°C and a decaborane pressure of 2×10^{-5} torr for 15 min is shown in Fig. 5. The x-ray and electron diffraction analysis indicates that the films are amorphous.

The ESCA spectrum of the boron film deposited at a decaborane pressure of 4.4×10^{-5} torr and a substrate temperature of 700°C is shown in Fig. 6. Figure 6 shows

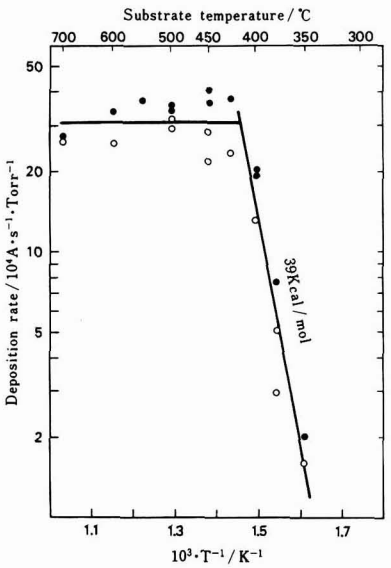


Fig. 4. Logarithm of the deposition rate divided by the decaboran pressure as a function of reciprocal absolute temperature of the substrate. The films were deposited at decaborane pressures of $P = 2 \times 10^{-5}$ torr (●) and $P = 8 \times 10^{-5}$ torr (○).

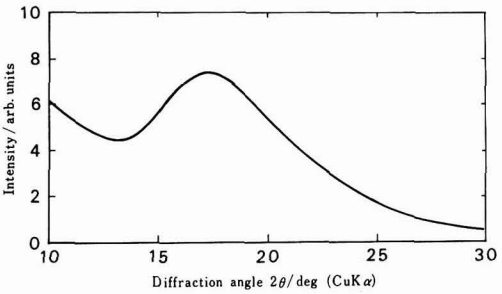


Fig. 5. X-ray diffraction pattern of a pyrolytic boron film

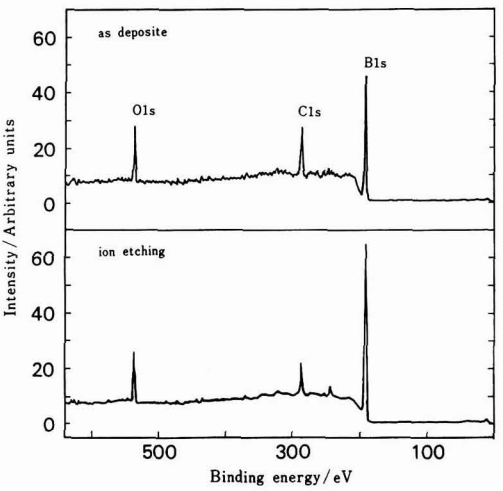


Fig. 6. ESCA spectra of a pyrolytic boron film

the spectrum of the film before and after ion etching. The peaks at the binding energies of 191, 288, and 512 eV correspond to boron 1s, carbon 1s, and oxygen 1s, respectively. The amounts of carbon and oxygen at the surface were estimated from the observed peak intensities multiplied by the photo-ionization cross-section, factor (B: 0.486, C: 1.00, O: 0.293) and are shown in Table I. The table shows that oxygen decreases little by ion etching, even though the apparent carbon content decreases to almost one third its original content. These results indicate that it is difficult to remove oxygen from the film surface by ion etching alone. The boron films were analyzed by EPMA because this method was not influenced by surface impurities. The amounts of impurities in three films deposited on sapphire substrates at decaborane pressures of 1.4×10^{-5}, 3.3×10^{-5}, and 4×10^{-5} torr are shown in Table II. This table shows that carbon decreases with increasing deposition rate. Oxygen impurities in boron films on sapphire substrates cannot be analyzed by EPMA because the primary electrons penetrate the film and extend into the oxygen bearing substrate. On the contrary, no oxygen was found in the films on tantalum substrates by EPMA. The EPMA and the ESCA analyses suggest that oxygen impurity localized near the surface is due to the exposing air, while carbon impurities are incorporated in the films from a residual gas.

Electrical properties.—The conductivities of boron films as a function of reciprocal absolute temperature are shown in Fig. 7. Conductivity varied from 3×10^{-3} S · cm^{-1} at room temperature to 30 S · cm^{-1} at 1000 K. The conductivity at room temperature is in agreement with that for amorphous boron films deposited by CVD and vacuum evaporation (1×10^{-3} S · cm^{-1}) (12), but much larger than that of single crystal ($\fallingdotseq 10^{-6}$ S · cm^{-1}) (17, 18).

Table I. ESCA data for a boron film deposited at a $B_{10}H_{14}$ pressure of 4.4×10^{-5} torr and a substrate temperature of 700°C

Sample	Intensity (arbitrary units) Boron	Carbon	Oxygen	C/B	O/B
As deposited	95	28	6.1	0.298	0.065
After argon etching	131	12	5.7	0.092	0.044

Table II. Data for boron films analyzed by EPMA

$B_{10}H_{14}$ pressure (torr)	Deposition rate (Å/s)	Characteristic x-ray intensity (CPS) Boron	Carbon	C/B
2×10^{-5}	7	1740	18	0.0103
4×10^{-5}	14	1020	6	0.0059
1×10^{-4}	33	1320	4	0.0030

The conductivity decreases slightly with increasing deposition temperature and is not affected by the carbon impurities.

Generally, the conductivity of semiconductors in the intrinsic conduction region is written as

$$\sigma = \sigma_0 \exp(-E_g/kT) \quad [5]$$

where σ_0 is a constant, E_g the bandgap energy, k the Boltzmann constant, and T the absolute temperature. E_g can be determined from the slope of the straight line in the plot of log σ against $1/T$. By applying this method to Fig.7, we obtained E_g = 1.07 eV. This value is in agreement with values reported for amorphous boron films (1.0-1.16 eV) (14, 19, 20), but is smaller than those for polycrystalline and single crystal boron (1.3-1.4 eV) (20-22). On the other hand, because the boron films obtained are amorphous,

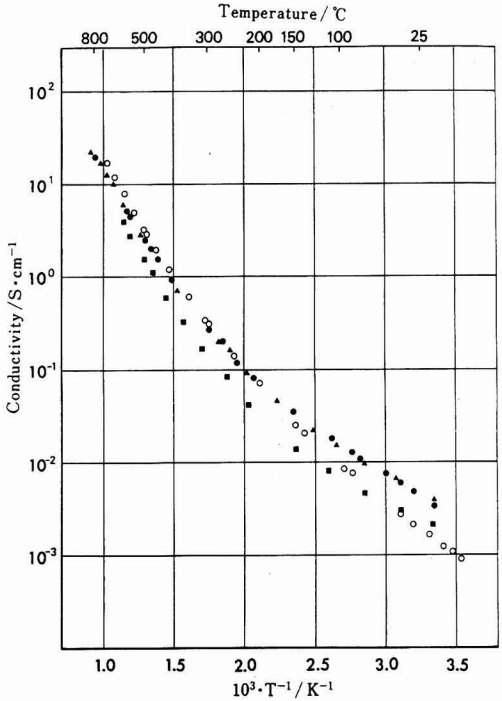


Fig. 7. Temperature dependence of the conductivity of pyrolytic boron films. The films were deposited at substrate temperatures and $B_{10}H_{14}$ pressures of T_s = 700°C and $P = 1.4 \times 10^{-5}$ torr (▲), T_s = 700°C and $P = 2 \times 10^{-5}$ torr (●), T_s = 800°C and $P = 3.3 \times 10^{-5}$ torr (■), and T_s = 750°C and $P = 1.5 \times 10^{-5}$ torr (○).

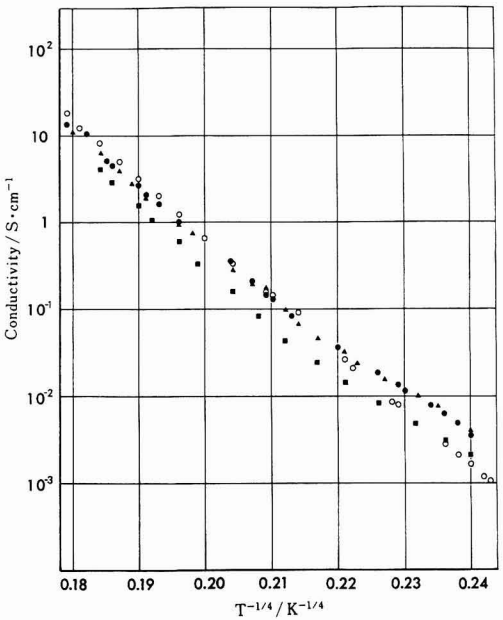


Fig. 8. Dependence of conductivity S on $T^{1/4}$; symbols correspond to those in Fig. 7.

the electric conduction is considered to be due to hopping conduction. Mott (23) has derived the equation for hopping conduction

$$\sigma = \sigma_0 \exp(-(T_0/T)^{1/4}) \quad [6]$$

where σ_0 and T_0 are constants.

The plots of log σ of the boron films as a function of $T^{1/4}$ are shown Fig. 8. The observed values show a good linear relation between log σ and $T^{1/4}$, and values of $\sigma_0 = 3.2 \times 10^{11}$ $S \cdot$ cm and $T_0 = 3.5 \times 10^{-8}$ K are obtained. According to Mott, T_0 is given as a function of the density of localized states at Fermi level, N (E_F)

$$T_0 = 16\,\epsilon^3/kN\,(E_F) \quad [7]$$

where ϵ is the exponential decay factor of localized states ($\epsilon^{-1} \fallingdotseq 5$Å) (6), and k is the Boltzmann constant. From the value of T_0 and Eq. [7], $N(E_F) = 3.8 \times 10^{18}$ cm$^{-3} \cdot$ eV^{-1} is obtained. This value is in agreement with the value for amorphous boron films, 5×10^{17}-10^{19} cm$^3 \cdot$ eV^{-1} (6), and the value for amorphous bulk, $\fallingdotseq 10^{18}$ cm$^{-3} \cdot$ eV^{-1} (24). As mentioned above, the conduction of the boron films can be explained successfully by two conduction mechanisms. We cannot decide which mechanism is valid within our experimental accuracy.

Figure 9 shows the temperature dependence of the thermoelectric power of the films. All the films obtained show p-type conduction. The thermoelectric power increases rapidly from 107 μV $\cdot$ deg^{-1} at 230°C to a maximum value of 400 μV $\cdot$ deg^{-1} at 427°C; it then decreases gradually to 310 μV $\cdot$ deg^{-1} at 730°C. As the positive carrier concentration increases with increasing temperature, the thermoelectric power also increases with increasing temperature. However, at higher temperature, the thermoelectric power decreases with increasing temperature because the hole mobility decreases. The thermoelectric powers reported for bulk boron (17, 18, 25) show a large peak at a lower temperature, compared with those for the boron films we obtained (420 μV at 700 K). These results can be explained by the assumption that the concentration of the impurities or defects in the boron films should be much higher than that in bulk boron. Middleton and Johnson have explained the same results for germanium by the higher concentration of aluminum (26).

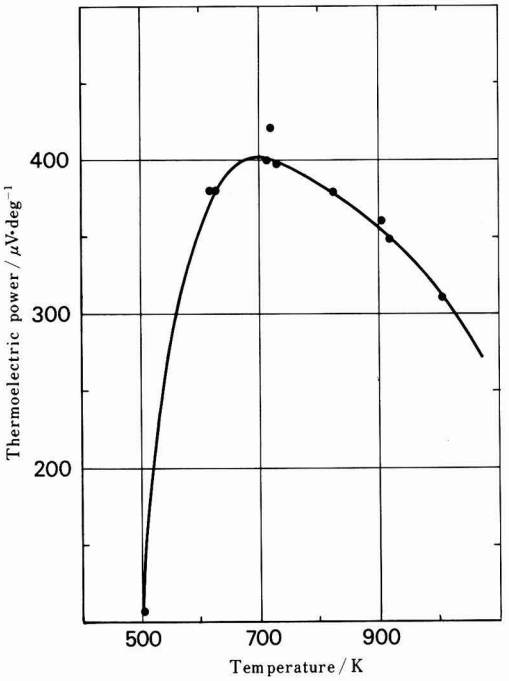


Fig. 9. Temperature dependence of the thermoelectric power

The figure of merit for thermoelectric materials, Z, is given as

$$Z = \tau^2\sigma/\kappa \ (\mathrm{deg}^{-1}) \qquad [8]$$

where τ is the thermoelectric power, σ is the electrical conductivity, and κ is the thermal conductivity. The thermal conductivity of boron is assumed to be 0.05 W · cm^{-1} · deg^{-1} (27, 28). The figure of merit of the boron films as a function of temperature are shown in Fig. 10. The value Z increases steeply with an increase of temperature. However, the Z values of the boron films are smaller than those reported for the amorphous bulk material (29). A figure of merit higher than 10^{-3} deg^{-1} is required for the material of a practical thermoelectric converter. Figure 10 suggests that boron films deposited by pyrolysis of decaborane are useful for thermoelectric devices at over 2000 K.

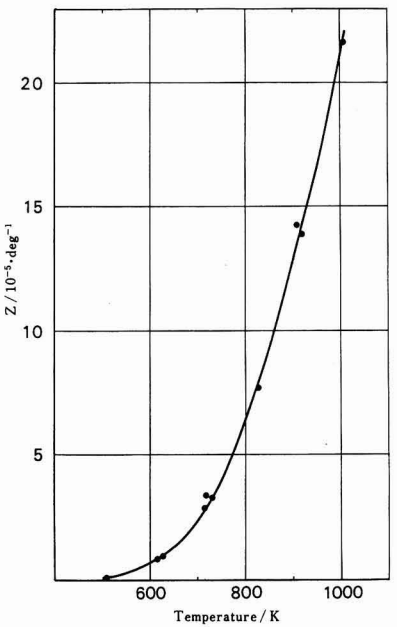


Fig. 10. EMF figure of merit Z of pyrolytic boron films as a function of absolute temperature.

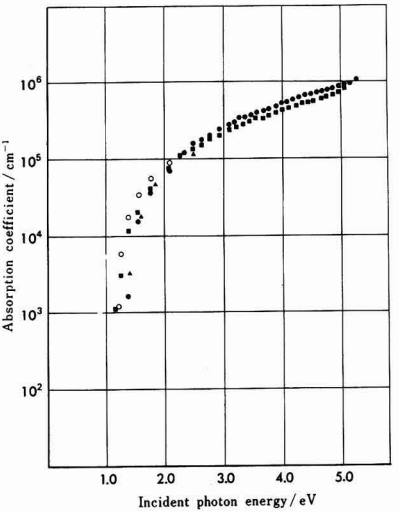


Fig. 11. Absorption coefficient of pyrolytic boron films as a function of incident photon energy.

Optical properties.—The absorption coefficient of the boron films, α, is shown in Fig. 11 as a function of incident photon energy, $h\nu$. The absorption coefficient increases rapidly at about 1.3 eV.

It is well known that boron is an indirect energy-gap type material. The absorption coefficient α near the ab-

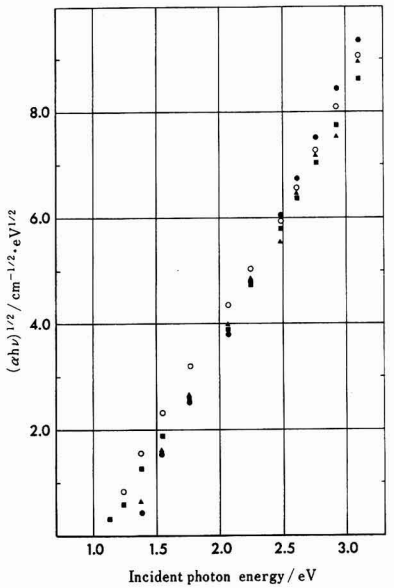


Fig. 12. The absorption edge fitted to the indirect allowed transition.

sorption edge E_g for the indirect allowed transition can be described as a function of the photon energy $h\nu$

$$\alpha h\nu \propto (h\nu - E_g)^2 \quad [9]$$

The variation of the square root of adsorption coefficient multiplied by photon energy $(\alpha h\nu)^{1/2}$ for the boron films with the incident photon energy is shown in Fig. 12. The figure shows that the boron film is an indirect energy-gap type material. The energy gap E_g is estimated to be 1.28 ± 0.08 eV by extrapolation of the linear part to the horizontal axis in Fig. 12. This value is larger than the value obtained by the electrical measurement (1.07 eV) and the values reported for amorphous films by Adirovich (19) and Morita (14).

The refractive index n and the extinction coefficient k of the boron films are shown as a function of wavelength in Fig. 13 and 14, respectively. These results agree well with the values obtained by Murphy (9) and Morita (14) for amorphous films deposited by vacuum evaporation. The hillock of the refractive index at the wavelength around 1 μm corresponds to the absorption edge. An increase in the extinction coefficient is also shown at wavelengths below 1 μm.

Figure 15 shows the infrared transmission spectrum of the boron film deposited on a silicon substrate. As shown in Fig. 15, the absorption of the boron film in the IR spectral region increases at about 8 μm and reaches a maximum at 12.5 μm. Blum (30) has studied the effect of impurities such as carbon and hydrogen on the infrared absorption of amorphous boron films and has shown that the narrow band at 2560 cm^{-1} observed in hydrogen-doped samples is due to B-H bond vibration. Also, the broad strong band from 1000 to 1200 cm^{-1}, which is correlated strongly with the amount of carbon in the films, is due to an overlapping and broadening of various B-C bond vibrations. Therefore, the absorption band from 8 to 12.5 μm observed in our films is not considered to be due to hydrogen and carbon impurities. Although many absorption bands caused by the complex crystal structure of boron have been reported, they are all in the wavelength region shorter than 8 μm (31). Werheit *et al.* (32, 33) have studied the optical properties of β-rhombohedral boron single-crystals in detail and have shown that absorption has a peak at 8 μm. According to Decker (34), the absorption spectra of α-rhombohedral boron have absorption peaks at 18.2, 10.9, 9.3, and 8.2 μm. These absorption bands are not in agreement with those observed for boron films deposited by pyrolysis of the decaborane. On the basis of studies made by Golikova (21), it can be considered that the absorption at 12.5 μm is associated with the short-range lattice structure in the boron films.

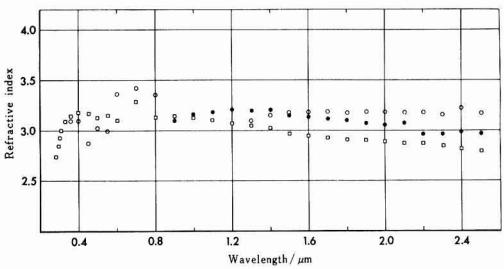


Fig. 13. Refractive index of pyrolytic boron films as a function of wavelength.

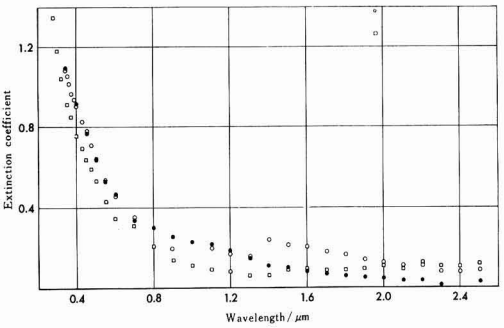


Fig. 14. Extinction coefficient of pyrolytic boron films as a function of wavelength.

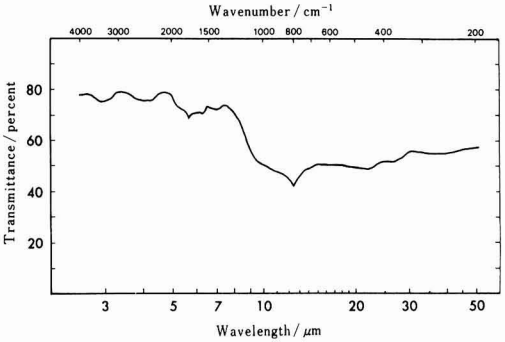


Fig. 15. Infrared transmission spectrum of a pyrolytic boron film deposited on a silicon substrate.

Conclusion

Amorphous boron films have been deposited by pyrolysis of decaborane in the molecular flow region. On the assumption that the deposition rate of boron films is determined by the impingement frequency of the decaborane molecules onto the substrate surface, we have derived the equation for the deposition rate D at temperatures lower than 416°C. The equation, $D = 7.16 \times 10^9 \cdot P \cdot \exp(-39000/RT_s)$ (cm/s), explains the experimental results successfully.

Electrical conductivity of these boron films is ≒ 10^3 larger than that for single-crystal boron and is in agreement with that for amorphous films deposited by CVD and vacuum evaporation. The influence of impurities on the conductivity is not clear. The activation energy for conduction of the boron films is estimated to be 1.07 eV in the intrinsic temperature range. The temperature dependence of the electrical conductivity can also be explained by a hopping conduction mechanism of amorphous materials. The plots of log σ against $T^{1/4}$ show a good linear relation, and the density of localized states at the Fermi level, $N(E_F)$, is estimated to be 3.8×10^{18} $cm^{-3} \cdot eV^{-1}$. However, we cannot decide which mechanism is valid within our experimental accuracy.

The thermoelectric power of the boron films obtained shows a small peak at a higher temperature, compared with those for bulk boron. This may be attributed to the fact that the concentration of the acceptors in amorphous boron films is higher than that in boron crystals.

From the measurements of optical absorption, it is found that boron films are an indirect bandgap type material and have an energy gap of 1.28 ± 0.08 eV. The refractive indexes and the extinction coefficients of the boron films in the wavelength range of 0.27-2.5 μm were obtained. In the infrared spectral region, an absorption peak was observed at 12.5 μm, which is considered to be associated with short-range order in the boron lattice.

Acknowledgments

The author would like to thank Professor K. Yoshimura and A. Itoh for suggesting this study and for their continuous encouragement. He wishes to express his thanks to S. Nakagawa, S. Misawa, and Dr. S. Gonda for helpful contributions and support of this work. Numerous valua-

ble and stimulating discussions with Professor A. Amano, Dr. S. Yoshida, and Dr. F. Shinoki are also acknowledged with many thanks.

Manuscript submitted Oct. 25, 1983; revised manuscript received May 15, 1984.

Nihon University assisted in meeting the publication costs of this article.

REFERENCES

1. H. Werheit, *Festkoerperprobleme*, **10**, 189 (1970).
2. O. A. Golikova, *Phys. Status Solidi A*, **51**, 11 (1979).
3. W. C. Shaw, *Phys. Rev.* **107**, 419 (1957).
4. L. Vandenbulke and G. Vuillard, *This Journal*, **123**, 278 (1976).
5. J. O. Carlsson, *J. Less-Common Met.*, **70**, 69 (1980).
6. M. Prudenziati, *Thin Solid Films*, **36**, 97 (1976).
7. V. S. Postnikov, *J. Less-Common Met.*, **47**, 255 (1976).
8. J. S. Lannin, *Solid State Commun.*, **25**, 363 (1978).
9. A. M. Murphy, *J. Opt. Soc. Am.*, **57**, 845 (1967).
10. W. J. Croft, *Mater. Res. Bull.*, **5**, 489 (1970).
11. G. Caserta and A. Serra, *Thin Solid Films*, **20**, 91 (1974).
12. C. Feldman, H. K. Charler, Jr., F. G. Statkiewicz, and J. Bohandy, *J. Less-Common Met.*, **47**, 141 (1976).
13. K. Moorjani and C. Feldman, *Electron Technol.*, **3**, 265 (1970).
14. N. Morita and A. Yamamoto, *Jpn. J. Appl. Phys.*, **14**, 825 (1975).
15. H. C. Beachell and J. F. Haugh, *J. Am. Chem. Soc.*, **80**, 2939 (1958).
16. A. J. Owen, *J. Chem. Soc.*, **1961**, 5438.
17. J. Cueilleron, J. C. Viala, F. Thevenot, C. Brodhag, J. M. Dusseal, and A. Elbiach, *J. Less-Common Met.*, **59**, 27 (1978).
18. H. Werheit and H. G. Leis, *Phys. Status Solidi*, **41**, 247 (1970).
19. E. I. Adirovich and L. M. Gol'dshtein, *Sov. Phys. Semicond.*, **3**, 196 (1969).
20. Sh. Z. Dzhamagidze, Yu. A. Mal'tsev, and R. R. Shvangiradze, *ibid.*, **2**, 320 (1968).
21. O. A. Golikova, D. N. Mirlin, A. S. Umarov, and T. Khomidov, *ibid.*, **7**, 1091 (1974).
22. A. Zareba and M. Maszkiewicz, *Phys. Status Solidi A*, **3**, K207 (1970).
23. N. F. Mott, *J. Non-Cryst. Solids*, **1**, 1 (1968); *Philos. Mag.*, **19**, 835 (1969).
24. A. A. Berezin, O. A. Golikova, M. M. Kazanin, T. Khomidov, D. N. Mirlin, A. V. Petrov, A. S. Umarov, and V. K. Zaitsev, *ibid.*, **16**, 237 (1974).
25. G. Majini and M. Prudenziati, *Phys. Status Solidi A*, **5**, K129 (1971).
26. V. A. Johnson and K. Lark-Horonitz, *Phys. Rev.*, **92**, 226 (1953).
27. O. A. Golikova, V. K. Zaitsev, V. M. Orlov, L. S. Stilbans, and F. S. Tkalenko, *Phys. Status Solidi A*, **21**, 405 (1974).
28. G. A. Slack, D. W. Oliver, and F. H. Horn, *Phys. Rev. B*, **4**, 1714 (1971).
29. O. A. Golikova, V. K. Zaitsev, A. V. Petrov, L. S. Stil'bonds, and E. N. Tkalenko, *Sov. Phys. Semicond.*, **6**, 1488 (1973).
30. N. A. Blum, C. Feldman, and F. G. Satkiewicz, *Phys. Status Solidi A*, **41**, 481 (1977).
31. O. A. Golikova, *Sov. Phys. Solid State*, **11**, 1341 (1969).
32. J. Jaumann and H. Werheit, *Phys. Status Solidi*, **33**, 587 (1969).
33. H. Werheit, A. H. Ausen, and H. Binnenbruck, *Phys. Status Solidi B*, **51**, 115 (1972).
34. B. F. Decker and J. H. Kasper, *Acta Crystallogr.*, **13**, 1030 (1960).

Electrical Properties of Organometallic Chemical Vapor Deposited GaAs Epitaxial Layers

Temperature Dependence

Douglas H. Reep*,[1] and Sorab K. Ghandhi*

Department of Electrical, Computer, and Systems Engineering, Rensselaer Polytechnic Institute, Troy, New York 12181

ABSTRACT

Electrical characteristics are presented for unintentionally doped GaAs epitaxial films, grown by the pyrolysis of trimethylgallium (TMG) and arsine at atmospheric pressure. The depositions were carried out on (100) substrates, from 450° to 1050°C, for a wide variety of growth conditions. Growth rates and morphology have been presented elsewhere. Films grown at 1050°C were found to be p-type, with the hole concentration falling at lower growth temperatures. Conversion to n-type occurred for growth below 975°C, independent of the arsine overpressure. At still lower temperatures, the film became increasingly n-type, with a peak in free electron concentration occurring at 850°C. Further reduction in growth temperature resulted in lower electron concentrations until eventually the films became p-type at around 550°C, depending on the arsine overpressure. The electrical behavior of these films correlates well with predictions from the growth model and thus provides additional insight into the organometallic growth process.

Much attention has been paid recently to the growth of thin epiaxial layers of GaAs by the organometallic CVD technique. Promising results have been obtained with the use of these layers for optoelectronic (1, 2), microwave (3, 4), and high speed digital applications (4). In addition, organometallic CVD grown layers which approach the purity and electron mobility of the best layers produced by the chloride-based techniques have been reported (4). The organometallic technique has also generated much interest due to its flexibility and its apparent simplicity.

Little has been published in regard to the mechanisms of growth by this process, as compared to the halide and hydride growth systems. In fact, the growth of GaAs films by this technique is generally described as a simple pyrolysis of trimethylgallium (TMG) and arsine. However, many complex processes and intermediate reactions are involved, and the subject is far from understood at the present time.

Recently, based on experiments employing different substrate orientations [(100), (110), (111)Ga, and (111)As] performed over a wide range of temperatures (450°-1050°C), we have proposed (5, 6) a growth model for this process. A brief review of this model is as follows: the dis-

*Electrochemical Society Active Member.
[1]Present address: General Electric Company, Electronics Laboratory, Syracuse, New York 13221.

sociation activation energy for the first, second, and third ($Ga-CH_3$) bonds is 59.5, 35.4, and 77.5 kcal/mol, respectively (7). This fact, together with an analysis of the rate constant data for this dissociation, leads to the conclusion that the rate limiter for the thermal decomposition of TMG is in all probability the breaking of the last ($Ga-CH_3$) bond. Studies of the decomposition of AsH_3, in like manner, lead to the conclusion that the primary surface-adsorbed arsenic species is (As-H). The growth model which we have described is the result of a Langmuir-Hinshelwood-type reaction involving these species. Although the actual reactions which take place are very complex, and are still the subject of much controversy, this relatively simple model fits the observed growth characteristics for a wide range of crystal orientations, reactant partial pressures, and growth temperatures. Thus, it serves as a useful starting point for developing further insight into the growth process. In this paper, we describe the electrical characteristics of these layers. It is shown that they, too, can be explained in terms of this growth model. Thus, they provide support for it and help in its further development.

Experimental Procedure

Epitaxial layers of GaAs were deposited by the pyrolysis of arsine and trimethylgallium (TMG), using hydrogen as the carrier gas. Anhydrous hydrogen chloride was available for *in situ* etching of the substrates prior to layer growth. Layer deposition was performed at temperatures from 450°-1050°C, for input TMG partial pressures ranging from 4.6 to 37 $\times$ 10^{-5} atm. The arsine flow was varied over a wide range, corresponding to AsH_3/TMG ratios of 4.7-75 at the reactor inlet. The hydrogen carrier gas flow through the reaction chamber was fixed at 5 l/min for all of the data reported here.

Single-crystal, semi-insulating GaAs substrates[2,3] used in this study were (100) oriented or 3° off (100) towards the [110] direction, and were received lapped and chem-mechanically polished on one side. Prior to loading into the epitaxial reactor, the wafers were degreased sequentially in trichloroethylene, acetone, and methanol. A chemical polishing etch of 1 min duration in hot (60°C) Caro's etch (H_2SO_4:H_2O_2:H_2O = 3:1:1 by volume) produced mirror-like surfaces, and removed 15-25 μm of material from the substrate surface. The substrates were quenched in DI water immediately following removal from the Caro's etch, rinsed with methanol, and blown dry in filtered nitrogen.

The epitaxial reactor consisted of an atmospheric pressure, horizontal, RF-heated, cold wall system of the type described previously (8). Gases were delivered to the 50 mm id quartz reaction chamber through 316 stainless steel or Monel tubing. The substrate temperature was monitored with a Pt/Pt-13% Rh thermocouple, sheathed in quartz, and inserted into a well in the back of the graphite susceptor.

A 10% mixture of arsine[4] in hydrogen was used in this work. TMG[5] vapor was provided by bubbling hydrogen through this liquid, which was held at 0°C in a stainless steel bubbler. A 1% mixture of electronic-grade hydrogen chloride in hydrogen[4] was available for *in situ* etching of the substrates. Ultrapure hydrogen carrier gas was obtained by passing commercial-grade hydrogen[4] through a Pd-Ag alloy purifier. In all cases, the reactant gases were thoroughly mixed prior to entry into the reaction chamber.

The substrate wafers were loaded into the reactor after chemical etching and microscopic inspection of the surface. The reaction chamber was evacuated and purged with argon,[4] followed by hydrogen gas. Next, the required flows of hydrogen and arsine were set. For experiments involving an *in situ* etch prior to growth, the susceptor was heated and stabilized at the etch temperature (typically 945°C). After a period of 5 min, which was sufficient to remove any surface oxide left by the chemical cleaning procedure (9), the wafers were given an *in situ* etch of the type described previously (10). The temperature of the susceptor was then reset and allowed to stabilize at the growth temperature for 2 min prior to commencement of growth by the introduction of the TMG vapor.

For experiments where no *in situ* etch was performed, the susceptor was heated to the growth temperature[6] and stabilized there for a period of 5 min, before the TMG flow was established. At the end of the growth interval, the TMG flow was terminated, and the system held at the growth temperature for an additional 3 min. The susceptor and substrates were then cooled to 200°C in the AsH_3/H_2 ambient, followed by an argon purge of sufficient duration for the susceptor to reach room temperature.

The growth rate of the epitaxial layer was determined either by weight change, in the case of no pregrowth *in situ* etch, or by cleaving and staining, followed by inspection with an optical microscope fitted for Nomarski differential interference contrast. Surface morphology was studied using scanning electron microscopy.

The free carrier concentration and mobility of the GaAs films were measured using the Hall effect. In particular, the van der Pauw technique was employed. All of the results presented are calculated directly from the Hall coefficient, following the common practice of assigning a unity value to the scattering factor (*i.e.*, r_H = 1). Ionized acceptor and donor concentrations were determined from the free carrier and mobility measurements (11) at liquid nitrogen temperature (77 K) for the n-type layers.

Results and Discussion

Only the (100) orientation was considered, because of the extreme difficulty of growing device-quality layers of other orientations by OMCVD. Moreover, a study of this orientation is of greatest interest, since it is commonly used in device fabrication. All of the (100) layers (oriented as well as misoriented) exhibited smooth, specular surfaces over the full range of deposition temperatures. Moreover, the morphology was found to be essentially in-

[6]A minimum of 700°C was used for the pregrowth heat-treatment, as this is sufficient to remove any traces of surface oxide (9). Thus, for the depositions performed below 700°C, the susceptor temperature was dropped (from 700°C) and allowed 2 min to stabilize at the growth temperature.

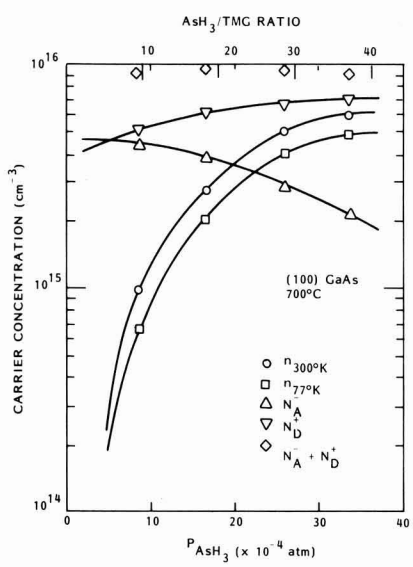


Fig. 1. Carrier concentration vs. p_{AsH_3} for (100) GaAs epitaxial layers grown at 700°C.

[2]Crystal Specialties, Incorporated, Monrovia, California 91016.
[3]Cambridge Instruments, Incorporated, Monsey, New Jersey 10952.
[4]Air Products, Tamaqua, Pennsylvania 19252.
[5]Alpha Products, Danvers, Massachusetts 01923.

dependent of the reactant flows over this temperature range, as was observed (6) for film growth at 700°C.

The majority of the epitaxial layers were grown for this investigation on substrates which were given no *in situ* etch, so that reliable growth rate data could be obtained. All of the data reported here were taken on layers which were 5-6 μm thick, so that the electrical measurements were not affected by the inclusion, or absence, of this etch step.

The electrical data reported here were made on samples grown using one lot of TMG and one cylinder of AsH_3, so that meaningful comparisons could be made. In addition, the nature of the contaminants in the starting materials was first determined so that the results could be meaningfully interpreted.

Figure 1 shows the electrical properties of undoped samples grown at 700°C as a function of the arsine overpressure. Here, it is seen that N_D (the ionized donor concentration) increases with arsine pressure, where N_A (the ionized acceptor concentration) falls. These results are what would be expected if the primary contaminant in the starting chemicals came from column IV of the periodic table. Moreover, $(N_A + N_D)$ is independent of arsine pressure for these samples, indicating that the contaminant comes mainly from the TMG source, whose partial pressure was held constant for this series of experiments. Thus, to a first order, the inherent contaminant in the combination of starting chemicals used here can be attributed to column IV impurities[7] related to the TMG, with relatively little contamination coming from the arsine. It is probable that silicon is this contaminant in our case, as this was detected by metallic impurity analysis.[8] It has been shown that this dopant, although amphoteric, always results in n-type material in the OMCVD of GaAs (12).

We have proposed a growth model (5) based on the results of measurements made over a wide range of temperature, reactant partial pressures, and crystal orientations. Growth data, taken for the purpose of model development, is presented in Fig. 2 for the (100) orientation, and for AsH_3/TMG inlet pressure ratios from 9.3 to 36.9. A study of this figure, in the light of the growth model we have proposed, shows the following features: (*i*) at high temperatures (above the point A at 850°C), growth is limited by the desorption of (Ga-CH_3) from the surface since the presence of the methyl radical significantly reduces the effective Ga-As bond strength. The temperature at which the growth rate fall-off occurs is independent of the AsH_3/TMG ratio. (*ii*) At low temperatures, (below the point B at 600°C), the growth is limited by the decomposition of arsine, and by the increased desorption of (Ga-CH_3) resulting from this effect. (*iii*) Growth in the mid region, between A and B, is relatively independent of the temperature or the AsH_3/TMG ratio. Although this region is important from a device viewpoint, it sheds little light on the growth mechanism since diffusion through the boundary layer is the limiting factor, as opposed to surface dependent effects.

Figure 3 shows the electrical characteristics of layers grown on (100) GaAs for AsH_3/TMG ratios of 37, 19, and 9.3, respectively. (Here, the points A and B are the same as those indicated in Fig. 2.) As mentioned earlier, these divide the growth into three regions, which are now considered.

The high temperature region.—Here, falloff in carrier concentration (and peak value as well) occurs at the same temperature for all reactant partial pressure ratios. Even-

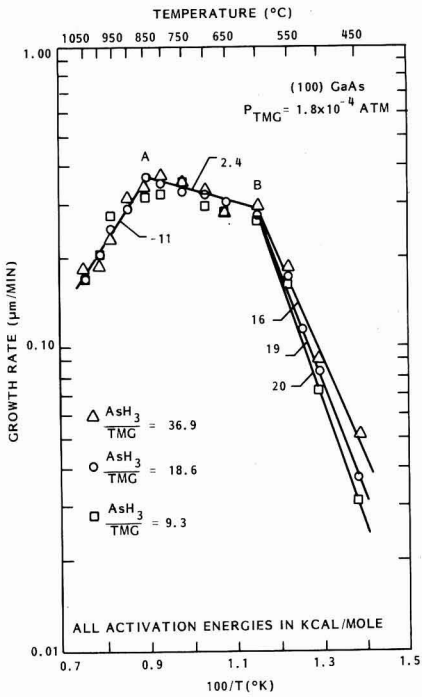


Fig. 2. Growth rate vs. reciprocal temperature for (100) GaAs epitaxial layers, as a function of P_{AsH_3} and for $P_{TMG} = 1.8 \times 10^{-4}$ atm.

tually, the layer becomes p-type, at a conversion temperature which is also independent of the AsH_3/TMG ratio. This behavior can be explained as follows: both the gallium and arsenic vacancy concentrations increase with increasing temperature, from thermodynamic considerations (14, 15). Additionally, however, the V_{Ga} increases because of increasing desorption of (Ga-CH_3) as postulated in our previous growth model; this in turn leads to increased acceptor formation, by the well-established complexing reaction of gallium vacancies and donors

$$V_{Ga} + \text{donors} \rightarrow \text{acceptor complex}$$

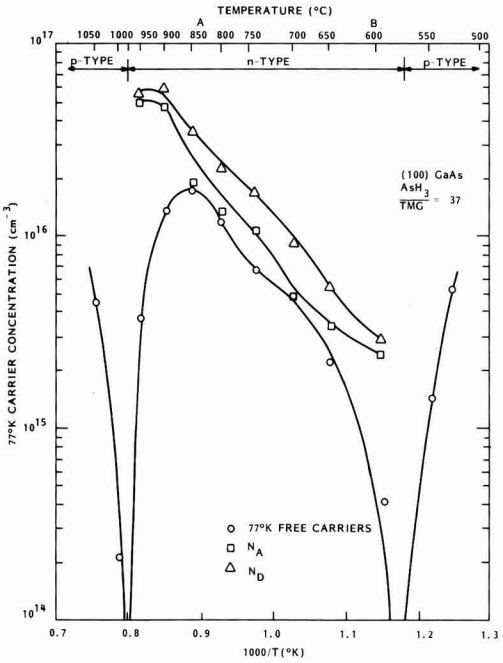
which has been confirmed by various workers (15, 16). Results of their annealing experiments on n-doped GaAs are reproduced in Fig. 4, and indicate that acceptor formation by this reaction is significant and can result in converting the layers to p-type. Moreover, the acceptor concentration is not a function of the arsenic overpressure for the range of growth conditions ($p_{AsH_3} \simeq$ 1-5 torr) reported in this paper. Hence, we can expect the falloff in electron concentration, as well as the conversion temperature (n → p) to be independent of p_{AsH_3}. Note that the data of Fig. 4 are for thermal annealing of bulk samples for long times (8-16h). We believe the analysis is applicable to this situation as well, since the layer growth is carried out in a strong excess arsine overpressure environment.

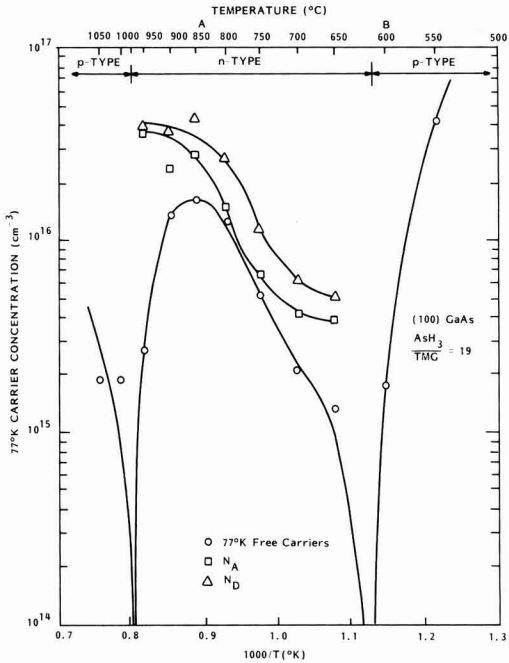
Our model leads us to conclude that this falloff in growth rate is primarily due to increased desorption of (Ga-CH_3). As a result, carbon contamination is most probably not the dominant factor at elevated temperatures. This has been verified by secondary ion mass spectroscopy (SIMS) data taken on a layer grown at 1000°C, and shown in Fig. 5. Here, the carbon level in the sample is the same as that of the substrate (except for a small perturbation at the epi-substrate interface).[9] Thus, the amount of carbon incorporated during growth at these el-

[7]As a point of interest, the usual situation at the present state of the art is that the TMG is considered to be relatively pure, and the contaminant is thought to come primarily from the arsine source. However, this was not the case with the sources used here. In fact, this controversy has received additional fuel recently with the identification of Ge as the dominant residual acceptor impurity in OMCVD GaAs, which as indeed traced to the TMG in at least one case (13).

[8]Contaminant data for TMG was 1 ppm Si, 2 ppm Al, and 1 ppm Fe with Mg and Zn not detectable. Data on the AsH_3 was not available.

[9]Layers grown with an *in situ* HCl etch did not show this peak. All the SIMS results in this paper are for layer growth without this etch step.





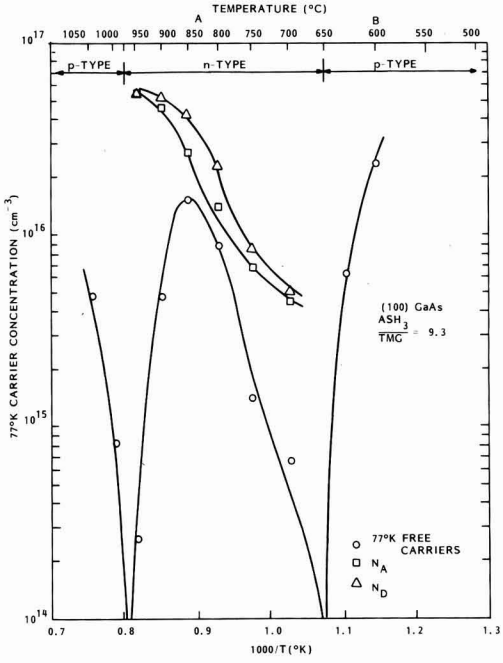


Fig. 3. 77 K carrier concentration *vs.* reciprocal temperature for (100) GaAs layers grown at $P_{TMG} = 1.8 \times 10^{-4}$ atm. a(top left): $P_{AsH_3} = 6.7 \times 10^{-3}$ atm. b(top right): $P_{AsH_3} = 3.3 \times 10^{-3}$ atm. c(left): $P_{AsH_3} = 1.7 \times 10^{-3}$ atm.

evated temperatures is below the detectability limit of the SIMS.

Low temperature region.—Here we note that the electron concentration falls for temperatures below A (Fig. 3a), with the layers eventually becoming p-type in the vicinity of, or slightly above, point B. This behavior differs from that in the high temperature region in many important respects. First, the n → p conversion point is a strong function of the arsine overpressure, and occurs at higher temperatures as p_{AsH_3} is decreased (Fig. 3b, 3c). Next, films grown at low temperatures are not entirely single crystal in nature, with strong evidence of twinning noted by x-ray diffraction analyses (but were still shiny). Finally, there is direct evidence of a large amount of carbon incorporation in these films, as seen from the SIMS data of Fig. 6.

We believe that these observations can be explained as follows: the decomposition rate of arsine, and hence the arsenic overpressure, falls with falling temperature. This results in an increased residence time of (Ga-CH_3) on the surface of the slice, and an increased possibility of the strongly bonded carbon incorporating in the film. More-

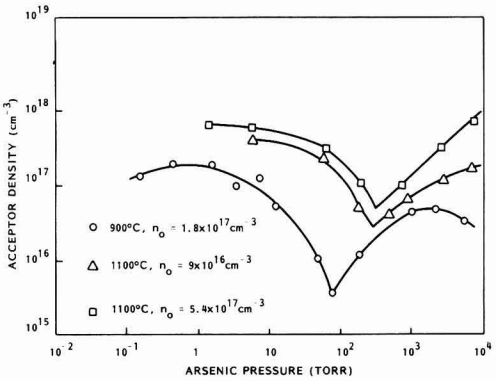


Fig. 4. Acceptor density in heat-treated n-type GaAs, as a function of arsenic overpressure, annealing temperature, and initial free electron concentration. After Ref. (15).

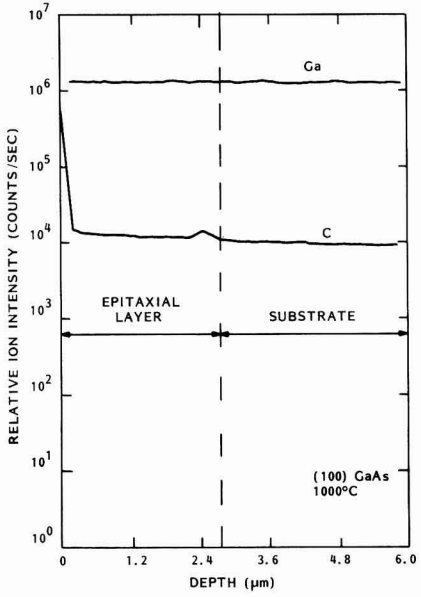


Fig. 5. SIMS trace of relative ion intensity for gallium and carbon vs. depth into sample, for 2.7 μm thick (100) GaAs epitaxial layer grown at 1000°C.

over, the reduction in effective arsenic overpressure at these temperatures increases the possibility of incorporating this carbon into arsenic sites, (increased V_{As} in this case) where it behaves as an acceptor and, in sufficient concentration, causes the layers to grow p-type. Finally, following the reactant attachment scheme previously proposed (6), we expect the methyl radical to occupy an arsenic site until the (Ga-CH_3) bond is broken, again supporting the high probability of carbon acceptor incorporation for low temperature growth.

Mid temperature region.—Here, both N_A and N_D fall with temperature. However, growth occurs in an excess arsenic overpressure, so that there is a net reduction in (N_D-N_A) with falling temperature. We believe that this explains the change in carrier concentration that we note over this temperature region, consistent with other reports in the literature (4, 17). Note, however, that an analysis of electrical behavior in this region sheds little light on the growth model, since the actual growth process is limited by diffusion through the boundary layer at these temperatures, and is independent of surface-related phenomena.

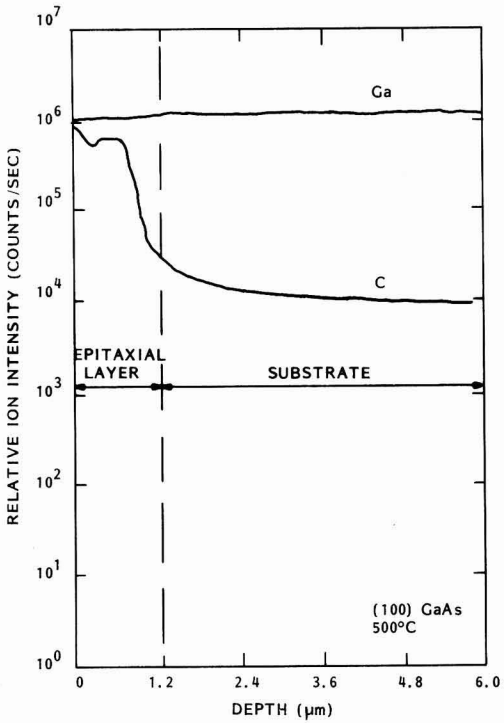


Fig. 6. SIMS trace of relative intensity for gallium and carbon vs. depth into sample for a 1.2 μm thick (100) GaAs epitaxial layer grown at 500°C.

Summary

Gallium arsenide layers have been grown over a wide range of input reactant partial pressures, and for a broad range of deposition temperatures. Electrical properties of these layers have been measured, and are described in this paper. Reasons for their behavior with temperature and reactant partial pressure have been advanced; it has been shown that the observed behavior can be explained in terms of a growth model proposed earlier.

Conversion from n to p at high temperatures (> 975°C) is shown to result from an increased desorption of (Ga-CH_3) at these temperatures, and from acceptor formation by the gallium vacancy-donor reaction. Moreover, carbon incorporation is relatively unimportant at these temperatures, as compared to the complexing reaction.

It has also been shown that the electrical characteristics of films grown in the low temperature region shift from n → p type with falling temperature. This behavior can be explained by noting that arsine decomposition falls off at low temperatures, resulting in an increased possibility of carbon incorporation in the films. Evidence for this increased carbon incorporation is presented as well.

The electrical measurements thus support the growth model proposed earlier, and help to provide further insight into the growth process.

Acknowledgments

The authors wish to thank A. Hayner for manuscript preparation, and Dr. W. Katz, General Electric CRD, Schenectady, New York, for SIMS analysis. This work was supported by the Solar Energy Research Institute, Golden, Colorado, under Contract no. XS-0-9002-4. This support is gratefully acknowledged.

Manuscript submitted Feb. 6, 1984; revised manuscript received May 10, 1984.

Rensselaer Polytechnic Institute assisted in meeting the publication costs of this article.

REFERENCES

1. R. R. Bradley, *J. Cryst. Growth*, **55**, 223 (1981).
2. J. P. Andre, P. Guittard, J. Hallais, and C. Paiget, *ibid.*, **55**, 235 (1981).
3. M. Bonnet, N. Visentin, G. Bessonneau, and J. P. Duchemin, *ibid.*, **55**, 246 (1981).
4. T. Nakanisi, T. Udagawa, A. Tanaka, and K. Kamei, *ibid.*, **55**, 255 (1981).
5. D. H. Reep and S. K. Ghandhi, *This Journal*, **130**, 675 (1983).
6. D. H. Reep and S. K. Ghandhi, *J. Cryst. Growth*, **61**, 449 (1983).
7. M. G. Jacko and S. J. W. Price, *Can. J. Chem.*, **41**, 1560 (1963).
8. B. J. Baliga and S. K. Ghandhi, *This Journal*, **122**, 683 (1975).
9. M. Otsubo, T. Oda, S. Mitsui, and H. Miki, *ibid.*, **124**, 1970 (1977).
10. R. Bhat, B. J. Baliga, and S. K. Ghandhi, *ibid.*, **122**, 1378 (1975).
11. G. E. Stillman and C. M. Wolfe, *Thin Solid Films*, **31**, 69 (1976).
12. S. J. Bass, *J. Cryst. Growth*, **47**, 613 (1979).
13. G. E. Stillman, Personal communication (Jan. 1984).
14. R. M. Logan and D. T. J. Hurle, *J. Phys. Chem. Solids*, **32**, 1739 (1971).
15. D. T. J. Hurle, *ibid.*, **40**, 613 (1979).
16. J. Nishizawa, H. Otsuka, S. Yamakoshi, and K. Ishida, *Jpn. J. Appl. Phys.*, **13**, 46 (1974).
17. S. J. Bass and P. E. Oliver, in "Gallium Arsenide and Related Compounds, 1976," p.1, Institute of Physics Conference Series, Institute of Physics, London (1977).

Low Pressure Chemical Vapor Deposition of Tungsten on Polycrystalline and Single-Crystal Silicon via the Silicon Reduction

K. Y. Tsao[1,*] and H. H. Busta[**]

Gould Research Center, Rolling Meadows, Illinois 60008

ABSTRACT

High purity metallic tungsten films are deposited on phosphorus-doped and undoped polycrystalline and single-crystal silicon by the silicon reduction of WF_6. Depositions are performed in a commercial LPCVD hot wall reactor at temperatures ranging from 310°-540°C. Film formation is self-limiting, meaning that after a given film thickness any further reaction between WF_6 and the underlying silicon is inhibited. Obtainable film thickness depends strongly on the doping condition of silicon and on surface preparation prior to LPCVD. Conventional wet chemical cleaning limits the maximum obtainable film thickness to approximately 400Å, whereas with a low power argon plasma treatment approximately 900Å thick films can be obtained reproducibly. The resistivity of these films is 18.3 ± 4.5 μΩcm. This corresponds to a minimum sheet resistance of the thickest films of approximately 2 Ω/□. The depositions are completely selective; no detectable amount of tungsten can be observed on thermal field oxide.

Low pressure chemical vapor deposition (LPCVD) of tungsten is currently under intense investigation for its potential application in VLSI circuits. These include shunting of polycrystalline silicon gate and interconnect lines with a lower resistivity tungsten film to reduce the interconnect RC time constant (1, 2), formation of a barrier between silicon and aluminum to reduce aluminum spike-induced failures (2, 4), planarization of the multilevel interconnect process (3, 4), low resistance contact formation to drain and source regions (1, 4), and formation of a Schottky barrier p-channel MOS transistor to form latch up-free CMOS (4).

An attractive feature of LPCVD tungsten is its selectivity. For appropriate deposition conditions, tungsten forms only on silicon and not on surrounding thermally grown SiO_2. Thus, for polycrystalline gate shunting this eliminates one etching step in the processing sequence, as compared to shunting with a sputter-deposited silicide. However, some nucleation of tungsten can occur on thermally grown SiO_2 when films in excess of 2000Å are deposited (5) or when the SiO_2 is formed by sputter deposition, plasma-assisted CVD, or on borophosphosilicate glass (BPSG) (3).

Tungsten can be deposited via the hydrogen reduction of WF_6 (1-3, 6, 7, 9)

$$WF_6 + 3H_2 \rightarrow W + 6HF \uparrow \quad [1]$$

or the silicon reduction of WF_6 (3, 7-9)

$$2WF_6 + 3Si \rightarrow 2W + 3SiF_4 \uparrow \quad [2]$$

With the hydrogen reduction, films of any thickness can be deposited, whereas with the silicon reduction the reaction ceases after formation of a given film thickness, because WF_6 cannot further react with the underlying silicon (9). Even in the hydrogen reduction, initial film growth proceeds via silicon reduction (3).

Since, according to reaction [2], 3 mol of silicon are needed to create 2 mol of tungsten, a certain thickness loss of silicon is experienced. It is given by

$$\frac{t_W}{t_{Si}} = \frac{2M_W \rho_{Si}}{3M_{Si}\rho_W} = 0.525 \quad [3]$$

and has to be taken into account during the device design stages. Here, t_W is the tungsten film thickness to be formed, t_{Si} the silicon thickness to be consumed, M_W, M_{Si} the molecular weights, and ρ_W = 19.35 g/cm³ and ρ_{Si} = 2.33 g/cm³ the densities of tungsten and silicon, respectively. Experimental verification of this fact is reported in Ref. (9).

In this paper, the LPCVD of tungsten using the silicon reduction method will be presented. The substrates are phosphorus-doped and undoped polycrystalline silicon and phosphorus-doped and undoped p-type single-crystal silicon.

The success of the LPCVD method in terms of obtaining reproducible films depends strongly on the surface preparation prior to film deposition (3) and hence on the native oxide characteristics (9). With the silicon reduction method, approximately 400Å thick films can be achieved at 350°C (3). By using standard wet chemical cleaning procedures we confirmed this result. With the addition of a low power argon plasma treatment, 900Å thick films can be deposited reproducibly with a sheet resistance of approximately 2 Ω/□. Film properties as a

* Electrochemical Society Member Representative.
** Electrochemical Society Active Member.
[1] Current address: AT&T Teletype Corporation, Skokie, Illinois 60077.

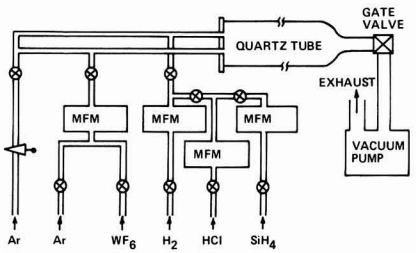


Fig. 1. Schematic of the LPCVD apparatus

function of the argon plasma treatment and deposition parameters such as WF_6 flow rate, deposition time, and deposition temperature will be presented in the following sections.

Experimental

The apparatus used for the depositions is a commercially available 4 in. hot-wall LPCVD quartz reactor whose plumbing system has been modified to allow Ar, WF_6, H_2, HCl, and SiH_4 to enter the system through mass flowmeters (MFM). This is indicated in Fig. 1. Not shown in Fig. 1 is a heating tape wrapped around the WF_6 cylinder, the gas lines, and the mass flowmeter. This is necessary to prevent the WF_6 from liquifying. The temperature of the WF_6 is controlled to provide a pressure of approximately 7-10 psi.

Argon is used as a carrier gas with a flow rate of 335 cm³/min and a pressure of 0.3 torr. For most experiments, the WF_6 flow rate is 12.4 cm³/min. In some cases, where the sheet resistance as a function of flow rate is determined, it is varied from 1.55 to 24.8 cm³/min. Deposition temperatures range from 310° to 540°C.

Sample preparation consists of growing approximately 1000Å of thermal SiO_2 on 3 in. diam silicon wafers. Approximately 4500Å thick polycrystalline silicon is then deposited via LPCVD at 610°C. For the phosphorus-doped samples, doping is performed at 950°C in PH_3 for 50 min, resulting in a sheet resistance of approximately 24 Ω/□.

The single-crystal (100) p-type wafers used in this work have a boron concentration of approximately 2×10^{15} cm^{-3}. Doping is performed at 950°C in PH_3 for 50 min. This is followed by an *in situ* nitrogen anneal for 10 min, which results in a sheet resistance of approximately 15 Ω/□.

For selectivity studies, standard photolithographic methods are used to delineate the polycrystalline silicon lines into the appropriate patterns. After photoresist (AZ1450J) stripping, the samples are cleaned at 95°C for 10 min in a mixture of three parts H_2SO_4 and one part H_2O_2. This is followed by a 6s 10:1 HF etch, followed by a DI rinse and nitrogen spin dry.

Loading of the samples takes place within several minutes after the argon plasma treatment. The LPCVD reactor is at deposition temperature and is purged with argon at approximately 3 liter/min. After loading and sealing, the system is pumped to approximately 0.03 torr and then refilled with argon to approximately 1 torr. This is followed by one more pumping and refilling cycle. The argon flow and chamber pressure are then adjusted to the appropriate values. WF_6 is then metered into the system. After deposition, the WF_6 flow is turned off and the system is allowed to cool to approximately 250°C, at which point the wafers are removed from the system.

A conventional stylus thickness monitor and the Auger elemental depth profiling technique are used for film thickness evaluations and a four-point probe for sheet resistance measurements. For the stylus measurements, a tungsten step is etched using positive photoresist or protective wax and an alkaline ferricyanide solution at room temperature to etch the tungsten. The solution consists of 5g $K_3Fe_6(CN)_6$, 5g KOH, and 100 ml DI water. All the samples are being etched for 1 min. After tungsten etching, the photoresist or wax are being stripped.

Results and Discussion

Polycrystalline silicon substrates.—Surface plasma treatment.—Initial experiments have been performed using the H_2SO_4/H_2O_2 and HF clean prior to the tungsten deposition. Depending on the surface conditions, *i.e.*, ion implanted *vs.* nonimplanted, different sheet resistances for identical deposition parameters have been obtained. From this, it has been conjectured that formation of a uniform distribution of nucleation sites will aid in the initiation of the surface reaction. Several wet and dry surface treatments have been investigated, and good results have been obtained with a short, low power argon plasma treatment in a barrel plasma etching system from which the shielding tunnel is removed. Some of the results are shown in Fig. 2. It shows five samples deposited at 410°C for 5 min at a WF_6 flow rate of 12.4 cm³/min. Sample A is a phosphorus-implanted (50 keV, 5×10^{15} cm^{-2}) polycrystalline silicon substrate, sample B is the same as A except it is annealed in N_2 at 1000°C for 30 min after the implantation, sample C is phosphorus-doped polycrystalline silicon, sample D is undoped polycrystalline silicon, and sample E phosphorus-doped p-type single-crystal silicon. Sheet resistances range from approximately 5 to 24 Ω/□, indicating a strong sensitivity of film formation to surface conditions. Sample F is from the same wafer as sample C but is subjected to a plasma treatment at 2W for 5 min. The sheet resistance differences of the samples are caused by different film thicknesses. This has been experimentally confirmed by stylus measurements. The corresponding film thickness scale is indicated on the right side of Fig. 2.

The power dependence of the plasma treatment on film thickness formation (sheet resistance) is shown in Fig. 3. From 2 to 50W, no change in sheet resistance can be observed, indicating that even at the lowest power enough nucleation sites are being created on the polycrystalline surface for optimum film formation. Little dependence of sheet resistance on plasma treatment time in the range of 1-10 min is observed. Figure 4 shows the effect of a 2W, 5 min argon plasma treatment on the sheet resistance as a function of WF_6 flow rate for phosphorus-doped polycrystalline silicon. The top curve shows the results without the plasma treatment.

Below a flow rate of 6.2 cm³/min, not enough WF_6 is supplied to fully react with the available silicon, thus

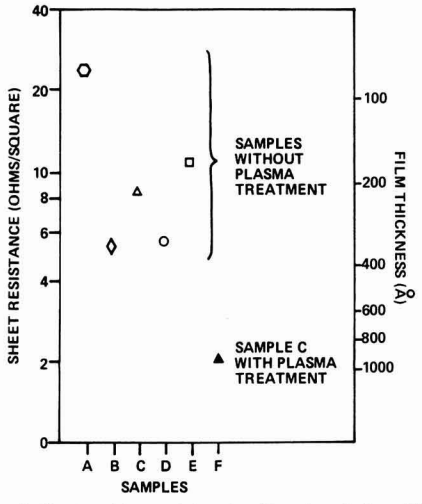


Fig. 2. Sheet resistance of tungsten films deposited on different samples with the silicon reduction method. Samples A to E are deposited without the plasma treatment. Sample F is part of the same substrate as sample C, but is being subjected to the plasma treatment.

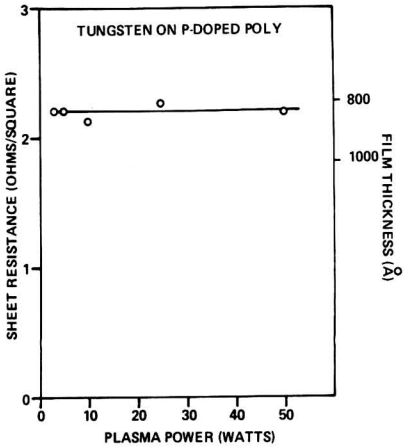


Fig. 3. Sheet resistance *vs.* argon plasma power for a phosphorus doped polycrystalline silicon sample. The tungsten deposition parameters are: 410°C, 5 min, WF_6 flow rate of 12.4 cm^3/min. The plasma treatment time per data point is 5 min.

causing thinner films. Above 6.2 cm^3/min, the difference in the sheet resistance between the treated and untreated samples is approximately a factor of three. This corresponds to a film thickness of approximately 900Å for the treated and 300Å for the untreated samples. Figure 5 shows the effect of a 2W, 5 min plasma treatment on sheet resistance as a function of the tungsten deposition time for phosphorus-doped polycrystalline silicon. The deposition is performed at a WF_6 flow rate of 12.4 cm^3/min. Otherwise, the same deposition parameters prevail as in Fig. 4. Very little dependence on deposition time is observed, indicating a self-limiting reaction. This is in agreement with the results presented in Ref. (9). Similar to Fig. 4, the difference in sheet resistances between the treated and untreated films is approximately a factor of 3, corresponding to thinner films (~300Å) for the untreated samples. In addition to the possible creation of nucleation sites, the argon plasma treatment also changes the thickness of the discontinuous native oxide. Wafers removed

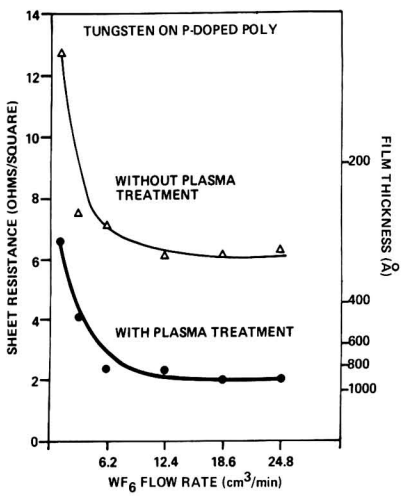


Fig. 4. Effect of the argon plasma treatment of sheet resistance (film thickness) for phosphorus-doped polycrystalline silicon as a function of WF_6 flow rate. The tungsten deposition parameters are: 410°C, 5 min, Ar pressure of 0.3 torr. Above a flow rate of 6.2 cm^3/min, the thickness of the treated films are approximately 1000Å, those of the untreated films 330Å.

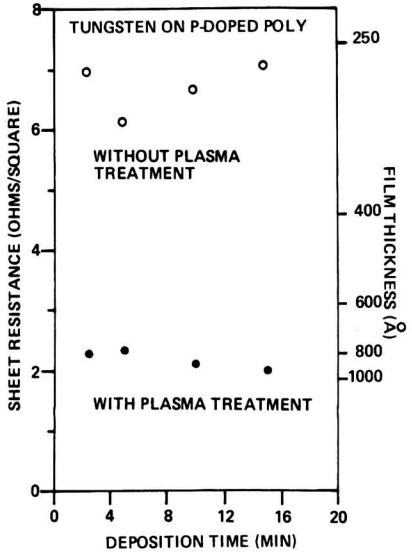


Fig. 5. Effect of the argon plasma treatment on sheet resistance as a function of tungsten deposition time for phosphorus-doped polycrystalline silicon. The tungsten deposition parameters are: 410°C, argon pressure of 0.3 torr, WF_6 flow rate of 12.4 cm^3/min.

from the storage container possess a native oxide of approximately 22 ± 2Å as measured with a Gaertner Scientific Instruments automatic ellipsometer. After cleaning and HF dip, this thickness is reduced to approximately 6 ± 4Å. After the plasma treatment, the native oxide is approximately 14 ± 4Å. At least qualitatively, this observation agrees with the discussion given in Ref. (9), where the argument is made that the thinner the native oxide the thinner a continuous tungsten film is formed, owing to a more homogeneous rate of reaction between WF_6 and silicon across the wafer surface. Similar results have been obtained with polycrystalline samples. Since the ellipsometer does not yield accurate results, the Auger technique has been used to estimate the thickness of the native oxide. HF-treated phosphorus-doped samples possess a discontinuous oxide of approximately 4-8Å, which increases after the plasma treatment to approximately 8-16Å. Results reported in the following sections are from substrates which have been subjected to a 2W, 5 min argon plasma treatment prior to tungsten deposition.

Deposition parameters.—Figure 6 shows resistance of tungsten/phosphorus doped polycrystalline silicon composite films at three different deposition temperatures as a function of deposition time. The data for the 367° and 419°C deposition temperatures show the self-limiting behavior, similar to the result shown in Fig. 5. At a deposition temperature of 469°C, the sheet resistance increases with deposition time. Stylus and Auger thickness measurements performed for the 5 and 30 min deposition time samples clearly indicate a decrease in the film thickness from approximately 330 to 235Å during this time period. This result suggests a slow etching of the films (~ 4Å/min) by WF_6. Figure 7 shows the sheet resistance of tungsten/polycrystalline silicon composite films as a function of temperature for phoshporus-doped and undoped polycrystalline silicon. Deposition time in all cases is 20 min. In the undoped case, a shallow minimum is observed at approximately 420°C. Below this minimum, very little dependence on sheet resistance (film thickness) with deposition temperature is observed. Above the minimum, the sheet resistance increases from 2 to 4 Ω/□. A strongly enhanced effect in terms of sheet resistance increase below and above a minimum is observed for the

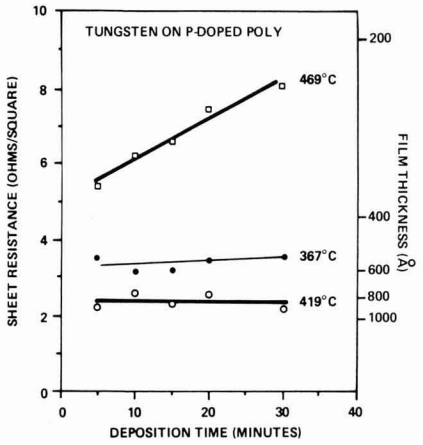


Fig. 6. Sheet resistance of tungsten/phosphorus-doped polycrystalline silicon composite films at three deposition temperatures as a function of deposition time.

phosphorus-doped case, indicating a strong participation of phosphorus in the kinetics of film formation.

From stylus and Auger thickness measurements taken of several samples below, above, and at the minima of the two curves shown in Fig. 7, a film resistivity of 18.3 ± 4.5 $\mu\Omega$cm was deduced. This is in good agreement with the data given in Ref. (4) for film thicknesses ranging from 200 to 900Å.

To investigate film surface morphology at different deposition temperatures, SEM micrographs have been prepared for samples deposited on phosphorus-doped polycrystalline silicon at 367°, 419°, and 469°C, and for a sample deposited on undoped polycrystalline silicon at 419°C. These samples are marked as A, B, C, and D in Fig. 7. Figure 8 shows the 367°C deposited film (A), which is approximately 460Å thick. Figure 9 shows the 419°C deposited film (B, 740Å), and Fig. 10 the 469°C deposited film (C, 250Å). As can be seen, the roughness of the tungsten film and of the polycrystalline interface increases with increasing film thickness. Figure 11 shows the 419°C

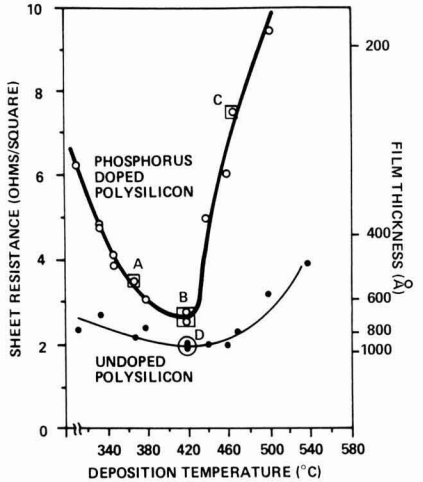


Fig. 7. Sheet resistance of tungsten/phosphorus-doped and undoped polycrystalline silicon composite films as a function of temperature. Film deposition time is 20 min. The thickness of the polycrystalline silicon is approximately 4500Å.

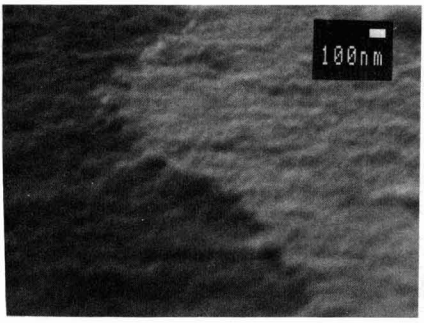


Fig. 8. SEM micrograph of a 460Å thick tungsten film deposited on phosphorous-doped polycrystalline silicon at 367°C. The film has been etched with the alkaline ferricyanide solution described in the "Experimental" section. This is sample A in Fig. 7.

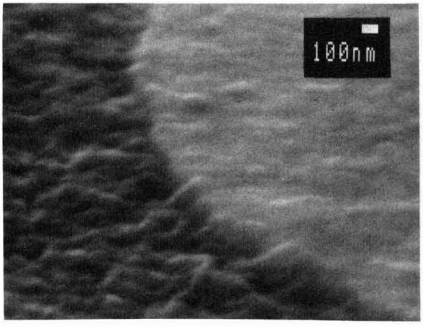


Fig. 9. SEM micrograph of a 740Å thick tungsten film deposited on phosphorus-doped polycrystaline silicon at 419°C. This is sample B in Fig. 7.

deposited film (D) on undoped polycrystalline silicon. The film thickness is 915Å. The roughness is similar to its doped counterpart (B). Auger elemental depth profiles (AEDP) of samples A, B, and C are shown in Fig. 12-14. Figure 12 shows the 367°C deposition temperature sample. Film thickness is defined at the 50% tungsten signal. The relatively broad interface between tungsten and polycrystalline silicon is an indication of film roughness, which, by taking the 10% and 90% points of the tungsten signal, is approximately equal to the film thickness. From Fig. 12, the consumption of polycrystalline silicon can also be deduced. According to Eq. [3], for a 460Å

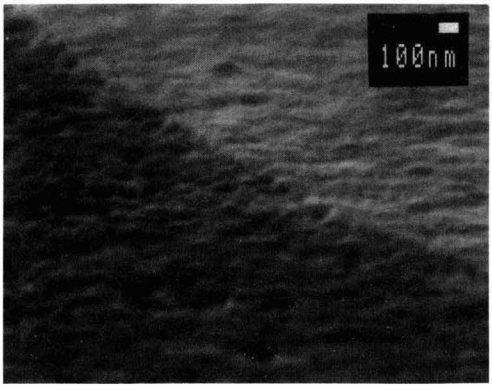


Fig. 10. SEM micrograph of a 250Å thick tungsten film deposited on phosphorus-doped polycrystalline silicon at 469°C. This is sample C in Fig. 7.

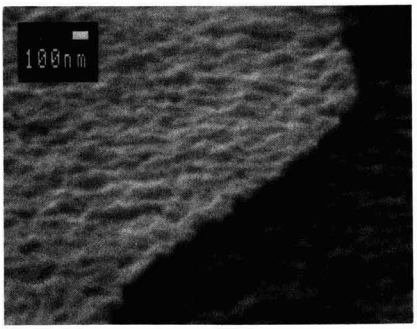


Fig. 11. SEM micrograph of a 915Å thick tungsten film deposited on undoped polycrystalline silicon at 419°C. This is sample D in Fig. 7.

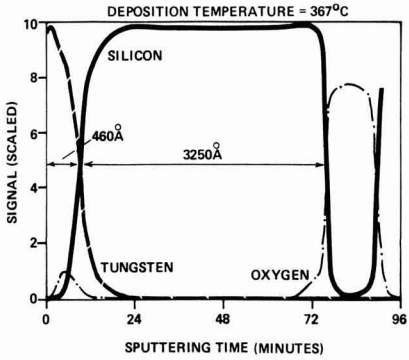


Fig. 12. Auger elemental depth profile of a tungsten/phosphorus-doped polycrystalline silicon/SiO_2 sandwich. The tungsten deposition is performed at 367°C. The deposition time is 20 min. This is sample A in Fig. 7.

thick tungsten film to be formed, approximately 900Å of silicon will be consumed. This then results in a thickness of the polycrystalline layer of 900 + 3250 = 4150Å, in fair agreement with 4500Å, the initial polycrystalline layer thickness. Some uncertainty exists in defining the interface due to the film roughness. Figure 13 shows the 419°C deposition sample. The film thickness is 740Å, with a roughness of approximately the same value. Also, the consumption of the polycrystalline silicon, similar to the previous sample, can be seen. Figure 14 shows the 469°C deposition sample. The film is 250Å thick, and the interface is the smoothest of the three samples, which is in

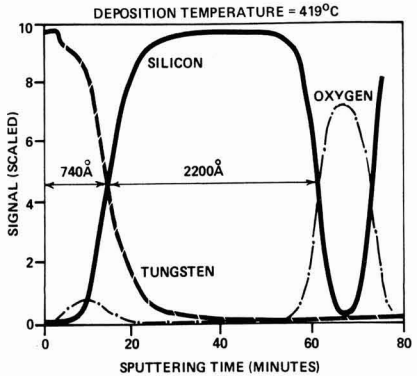


Fig. 13. Auger elemental depth profile of a tungsten/phosphorus-doped polycrystalline silicon/SiO_2 sandwich. The tungsten is deposited at 419°C. The deposition time is 20 min. This is sample B in Fig. 7.

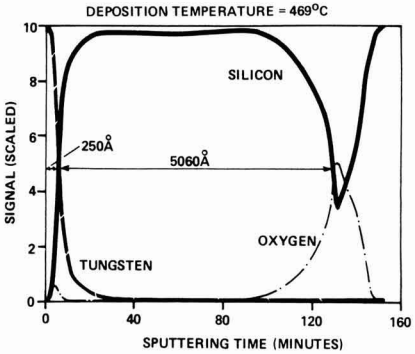


Fig. 14. Auger elemental depth profile of a tungsten/phosphorus-doped polycrystalline silcicon/SiO_2 sandwich. The tungsten deposition is performed at 469°C. The deposition time is 20 min. This is sample C in Fig. 7.

agreement with the SEM micrographs shown in Fig. 8-10. In deducing the film thickness of these three samples, it was assumed that their density, and thus the sputtering rate, did not vary significantly from each other. From Fig. 12-14, it can be seen that some oxygen is incorporated into the films. A similar result is presented in Ref. (3). Assuming that this oxygen corresponds to the native oxide on the silicon surface prior to film formation (10), an estimate of its thickness can be performed. The area under the oxygen curve is determined and equaled to the height of the oxygen signal expected for SiO_2 times the thickness (sputtering time) of the to be determined native oxide layer. The height of the oxygen signal of SiO_2 is approximately 70% of the scaled signal scale. This can be seen in Fig. 12, where the polycrystalline silicon/SiO_2 interface is shown. The results yield approximately 30Å for sample A, 60Å for sample B, and 13Å for sample C. This agrees, at least qualitatively, with the conclusions made in Ref. (9) that film thickness and roughness depend strongly on the characteristics of the native oxide, with thinner tungsten films being formed for less native oxide. AEDP taken from other samples confirmed this observation: namely, that the oxygen incorporation is proportional to film thickness.

Figure 15 shows the SIMS phosphorus concentration profile of sample B in Fig. 7. Near the tungsten/polycrystalline silicon interface, the phosphorus concentration in

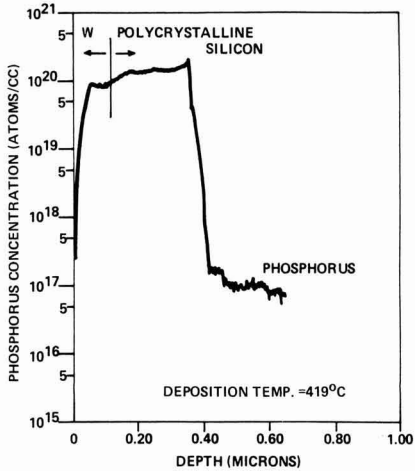


Fig. 15. Phosphorus concentration of a tungsten/phosphorus-doped polycrystalline silicon sample as measured by SIMS. The deposition temperature is 419°C. This is sample B in Fig. 7.

the tungsten film is approximately 1×10^{20} cm^{-3}. The surface concentration is approximately 4×10^{17} cm^{-3}. A similar profile has been obtained for sample A. Sample C exhibits a surface concentration of approximately 4×10^{18} cm^{-3}. Within experimental error (±20%) the resistivity of the phosphorus containing tungsten films is not different from the undoped samples.

From the presented material it is clear that phosphorus takes an active part in tungsten film formation. From Fig. 7, it can be seen that at least two deposition mechanisms are present. For the undoped samples, the film thickness increases slightly, from 320° to 420°C, and then decreases from 420° to 540°C. A similar result is obtained for the films deposited on phosphorus-doped polycrystalline silicon except that it is accentuated. Film formation depends very strongly on the native oxide condition just prior to the WF_6 release into the LPCVD reactor. It is known that all the samples at the moment of insertion into the reactor have a native oxide of approximately 13 to 15Å. However, changes in oxide thickness can take place during pumpdown due to unavoidable oxygen traces present in the reactor. This change depends on temperature and sample doping conditions (11). This makes interpretation of the results shown in Fig. 6 and 7 difficult. Nevertheless, the results presented in these figures are very reproducible, sheet resistance across the 3 in. diam wafers do not vary by more than 5%. No film "cloudiness" or streaking phenomena are observed.

Single-crystal silicon substrates.—Similar results in terms of plasma treatment and film formation as described for polycrystalline substrates are obtained for p-type and phosphorus-doped p-type single-crystal substrates. Figure 16 shows the effect of the plasma treatment on n$^+$-doped samples. Doping conditions are given in the "Experimental" section of this paper. The results are similar to Fig. 4, except that, without the plasma treatment, films of only approximately 200Å can be deposited under the given conditions of 410°C deposition temperature and a deposition time of 20 min. The sheet resistances of the plasma-treated samples (2W, 5 min) are almost identical to Fig. 4. Again, from stylus and Auger measurements, the thickness of the films has been obtained. The thickness scale is indicated on the right side of Fig. 16. The resistivity of the tungsten films is the same as of the tungsten films deposited on polycrystalline silicon, *i.e.*, 18 μΩcm. Figure 17 shows the

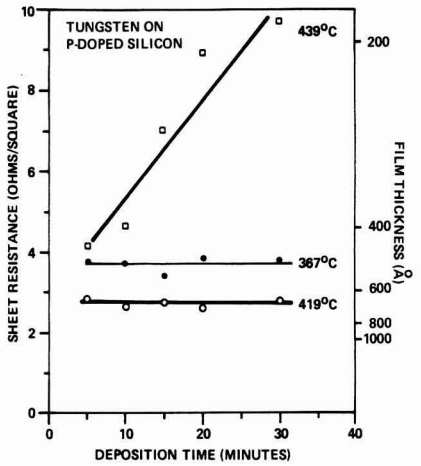


Fig. 17. Sheet resistance of tungsten deposited on phosphorus-doped p-type single-crystal silicon at three different deposition temperatures as a function of deposition time.

sheet resistance as a function of deposition time for n$^+$-doped p-type samples. Strong similarity of the data with Fig. 6 is observed. For deposition temperatures of 367° and 419°C, the films form in less than 5 min after which film thickness is independent of deposition time. At a deposition temperature of 439°C, a strong decrease in film thickness from an initial value of approximately 500Å at 5 min to approximately 200Å at 30 min is observed. This again suggests etching of the films (~12 Å/min) by WF_6 as a function of deposition time.

Figure 18 shows the sheet resistance for p-type single-crystal silicon as a function of temperature and for a film deposition time of 20 min. For the non-phosphorus-doped samples, very little change in sheet resistance and thus thickness is observed over the temperature range 330°-460°C, which is similar to the undoped polycrystalline data given in Fig. 7. For the phosphorus-doped case, a minimum is reached at approximately 420°C. Above this minimum, a sharp increase in sheet resistance (decrease in film thickness) is observed. This decrease in film thickness is due to the onset of film etching above 420°C. The data in Fig. 18 are plotted for a deposition time of 20

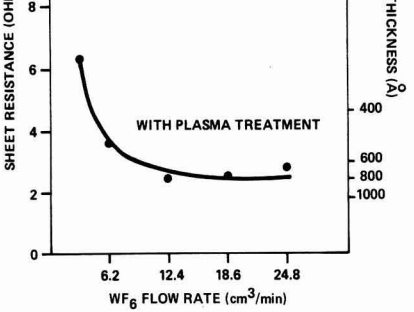


Fig. 16. Effect of the argon plasma treatment on sheet resistance for phosphorus-doped p-type single-crystal silicon as a function of WF_6 flow rate. The tungsten deposition parameters are: deposition temperature of 410°C, deposition time of 5 min, Ar pressure of 0.3 torr. Argon plasma treatment: 2W, 5 min.

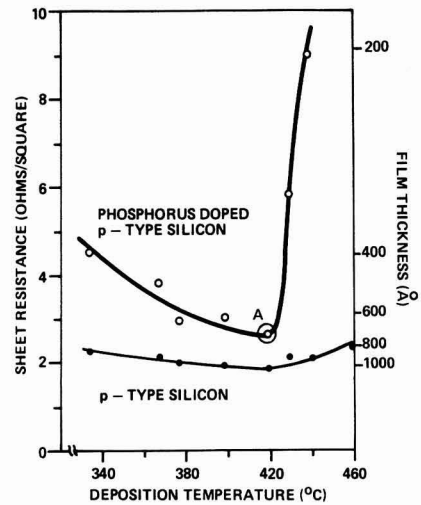


Fig. 18. Sheet resistance of tungsten deposited on phosphorus-doped p-type and on p-type single-crystal silicon as a function of temperature. Film deposition time is 20 min.

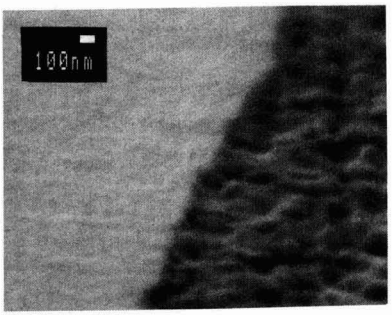


Fig. 19. SEM micrograph of a 670Å thick tungsten film deposited on phosphorus-doped single-crystal p-type silicon at 419°C. This is sample A in Fig. 18.

min. According to Fig. 17, at this time period, etching of the film is already taking place for a deposition temperature of 439°C. This behavior is similar to the data shown in Fig. 7. Insufficient data exist at this time to explain the accentuated increase in film thickness from 320° to 420°C of the phosphorus containing samples (Fig. 7 and 17).

Figure 19 shows the SEM micrograph of a 670Å thick tungsten film deposited on phosphorus-doped single-crystal p-type silicon at 419°C. This is sample A in Fig. 18. The degree of surface roughness at the W/Si interface is similar to Fig. 9 and 11. The surface roughness of the tungsten film is less, probably owing to the smoother initial surface of single-crystal *vs.* polycrystalline silicon.

Selectivity.—From AEDP, it is verified that tungsten deposited by the LPCVD method is 100% selective. Prior to tungsten deposition, 5 μm wide polycrystalline lines are photoshaped and etched on top of thermally grown SiO_2 regions, and no tungsten (< 10Å) can be detected. Selectivity has been observed for all deposition conditions reported in this paper.

Applications.—The primary purpose of this work has been to develop deposition conditions yielding low sheet resistance for a W/phosphorus-doped polycrystalline composite film to be used for IC gate and interconnects. The best results are obtained using a deposition temperature of 420°C. This results in a 700Å thick film with a sheet resistance of approximately 2.6 Ω/□ (see Fig. 7, upper curve). The initial polycrystalline silicon thickness has to be at least 4500Å. Below this value, film lifting due to the stress created by the tungsten film is observed. Note that approximately 1400Å of the polycrystalline silicon are consumed during the tungsten film formation.

For low resistance source/drain contact formation to n^+ silicon, a temperature of 420°C gives the lowest resistance films. However, to avoid film encroachment at the Si/SiO_2 pattern edges (3, 12) a deposition temperature of 350°C is needed. This results in a sheet resistance of approximately 4 Ω/□. However, the suitability of this approach has to be investigated by electrical measurements. Due to the tungsten protrusions into silicon, excessive leakage currents might result for Schottky barrier structures and tungsten on shallow n^+ source/drain structures.

Summary

Tungsten films have been deposited via the silicon reduction of WF_6 in a low pressure chemical vapor deposition system on phosphorus-doped and undoped polycrystalline silicon and on phosphorus-doped p-type and undoped p-type single-crystal silicon. Deposition temperatures range from 310° to 540°C.

For the non-phosphorus-doped substrates (polycrystalline and single crystal), film thickness of approximately 200-400Å can be obtained using a H_2SO_4/H_2O_2, HF dip clean prior to film deposition. With the introduction of a low power argon plasma treatment, film thickness can be increased, for the same deposition conditions, to a maximum of approximately 900Å. This treatment increases the native oxide thickness of all samples from 6Å (chemical clean only) to 14Å. Over the temperature range, the thicknesses of the tungsten films deposited on undoped polycrystalline silicon range from 500 to 900Å, those deposited on lightly p-type doped silicon from 800 to 1000Å.

A drastically different behavior is observed for the phosphorus-doped substrates. Here, a maximum film thickness of approximately 700Å can only be reached at 420°C. Below this temperature, film thickness decreases to approximately 400Å at 340°C for both substrates. Above 420°C, film thickness reduces to 200Å at 500°C (on polycrystalline silicon) and at 440°C (single-crystal silicon). This decrease is due to etching of the films by WF_6, which is catalyzed by the presence of phosphorus.

Acknowledgments

The authors wish to thank R. Joy, AMI, for suggesting work on LPCVD tungsten, Professor K. Saraswat, Stanford University, for many helpful comments, A. Saxena, AMI, for alerting us to the encroachment problem, E. Butler, C. Strandberg, O. Wu, and J. Kao for the AEDP measurements, and A. Brandes and D. M. Chen for the SEM and stylus profilometer work.

Manuscript submitted Feb. 29, 1984; revised manuscript received June 1, 1984. This was Paper 97 presented at the Cincinnati, OH, Meeting of the Society, May 6-11, 1984.

Gould Research Center assisted in meeting the publication costs of this article.

REFERENCES

1. P. A. Gargini and I. Beinglass, *IEDM Tech. Dig.*, CH 1708-7/81, 54 (1981).
2. N. E. Miller and I. Beinglass, *Solid State Technol.*, **25**, 85 (1982).
3. T. Moriya, S. Shima, Y. Hazuki, M. Chiba, and M. Kashiwagi, *IEDM Tech. Dig.*, CH 1973-7/83, 550 (1983).
4. K. C. Saraswat, S. Swirhun, and J. P. McVittie, in "VLSI Science and Technology 1984," K. E. Bean and G. A. Rozgonyi, Editors, p. 409, The Electrochemical Society Softbound Proceedings Series, Pennington, NJ (1984).
5. K. Y. Tsao and H. H. Busta, Unpublished data.
6. N. E. Miller and I. Beinglass, *Solid State Technol.*, **23**, 79 (1980).
7. C. E. Morosanu and V. Soltuz, *Thin Solid Films*, **52**, 181 (1978).
8. E. K. Broadbent and C. L. Ramiller, Abstract 420, p. 657, The Electrochemical Society Extended Abstracts, Vol. 83-1, San Francisco, CA, May 8-13, 1983.
9. E. K. Broadbent and C. L. Ramiller, *This Journal*, **131**, 1427 (1984).
10. D. Pramanik, A. N. Saxena, O. K. Wu, G. G. Peterson, and M. Tanielian, *J. Vac. Sci. Technol.*, To be published.
11. C. P. Ho and J. D. Plummer, *This Journal*, **126**, 1516 (1979).
12. T. Moriya, K. Yamada, T. Shibata, H. Iizuka, and M. Kashiwagi, "1983 Symposium on VLSI Technology," Maui, HI, p. 96 (1983).

Charge Transfer via Interface States at Polycrystalline Cadmium Selenide Electrodes

Ron Haak* and Dennis Tench*

Rockwell International Science Center, Thousand Oaks, California 91360

Michael Russak

Grumman Aerospace Corporation, Bethpage, New York 11714

ABSTRACT

Polycrystalline cadmium selenide thin film electrodes prepared by coevaporation of the elements were investigated *in situ* by electrochemical photocapacitance spectroscopy (EPS) in aqueous basic electrolytes, with and without added polysulfide redox species. An interface state lying about 0.2 eV below the conduction bandedge was directly detected for material prepared at low substrate temperature and was demonstrated to mediate charge transfer between the semiconductor and the electrolyte.

Interface states are known to play an important role in charge transfer processes at both single-crystal and polycrystalline CdSe electrodes. For example, Fermi level pinning has been observed for n-CdSe in neutral sulfate electrolytes (1); for fast, one-electron redox species in nonaqueous electrolytes, the open-circuit voltage varies in a nearly ideal fashion as the redox potential is changed (over a limited range) (2). It has been proposed (3) that Fermi level pinning can result from interface-state densities as low as 10^{12} cm^{-2}. Interface-state effects in the thin-film n-CdSe/aqueous polysulfide system have been investigated by Rajeshwar (4). He reports that interface states associated with adsorbed sulfide ions mediate electron transfer and limit the open-circuit voltage; no change in V_{oc} was observed when the electrolyte composition was varied so as to change the redox potential over a 250 mV range.

In the present work, electrochemical photocapacitance spectroscopy (EPS) (5, 6) and ac impedance measurements were applied to further elucidate charge transfer processes associated with interface states at cadmium selenide electrodes prepared by coevaporation of the elements (7). Such thin film material was chosen for study because of its potential practical applications, *e.g.*, in photoelectrochemical cells. Results obtained previously for such electrodes in polysulfide electrolytes can be summarized as follows. Data are variable, but, in general, films prepared at low substrate temperatures (~ 100°C) yield higher photocurrents but lower open-circuit voltages (~ 100 mV less) than those prepared at high substrate temperatures (~ 400°C) (8). For low substrate temperature films, the open-circuit voltage is increased by 50-100 mV and the fill factor is improved (with no loss in short-circuit photocurrent) when the electrode is soaked in $ZnCl_2$ solution and potential cycled (under illumination) in aqueous polysulfide (9). Based on Auger depth profile studies and impedance/polarization measurements, this improvement has been attributed to a negative shift in U_{FB} (flatband potential) caused by incorporation of Zn in the CdSe film.

Experimental Details

Thin film CdSe electrodes were prepared by vacuum coevaporation of Cd and Se from independently controlled sources, as described previously (7, 8). Two types of films were prepared (on titanium substrates). Low substrate temperature films were deposited at 100°C with a Se-to-Cd ratio in the vapor of 3:1. These films, which were only partially crystalline in the as-deposited state, were subsequently heat-treated at 400°C for 15 min in air to maximize their photovoltaic response. High substrate temperature films were deposited at 400°C with a Se-to-Cd ratio of 1:1. Although fully crystalline as deposited, these films still required heat-treatment at 450°C for 15 min for maximum photovoltaic output. After attachment of a wire lead to the titanium substrate with silver-epoxy resin, the electrode was sealed in Torr Seal® (Varian Associates, Palo Alto, California) so that the front (CdSe) face was exposed to the electrolyte. The geometric area of the electrodes ranged from 0.2-0.7 cm^2. Before evaluation, films of both types were etched in 25% HNO_3 and dipped in polysulfide solution (0.1*M* S + 2.5*M* Na_2S + 1.0*M* KOH) to remove excess selenium from the surface.

The procedures and apparatus used to perform EPS measurements have been described previously (6). Impedance measurements were performed using the same apparatus.

*Electrochemical Society Active Member.

Results and Discussion

For n-CdSe, which has a bandgap of 1.76 eV, four donor states (onsets at 1.04, 1.21,[1] 1.34, and 0.2 eV below the conduction bandedge) have been detected by EPS (10). As discussed in this earlier work, the 1.04 and 1.21 eV levels correspond to interface states associated with oxygen adsorption and play major roles in determining the electrical properties of CdSe devices. The 1.04 eV state predominates in aqueous solution and under vacuum conditions, resulting in a negative surface charge. At positive electrode potentials in acetonitrile solution, the 1.21 eV state occurs in higher concentrations, but can be electrochemically reduced to the 1.04 eV state at voltages near U_{FB}.

The 0.2 eV state in CdSe is of particular interest to the present work because it occurs in relatively high concentrations only in thin film materials prepared at low substrate temperature (100°C). As shown in Fig. 1a, this state ionizes at sufficiently positive electrode potentials and is detected as a sharp capacitance decrease beginning at about 1.5 eV (820 nm), corresponding to a transition from the valence band to the state. Such ionization, which increases the capacitance by increasing the positive charge at the interface (reduces the space charge thickness), is also reflected in Mott-Schottky plots as a sharp decrease in C^{-2} at more positive potentials. This is apparent above −0.5V in the plot given in Fig. 2; deviation from linearity, which apparently signals some ionization, is evident even at −0.7V. At potentials closer to U_{FB}, which according to Fig. 2 lies at −0.9V *vs.* SCE, the 0.2 eV state is nonionized in KOH solution and is, therefore, not detected. In this case, the capacitance is lower and the EPS spectrum (Fig. 1b) is similar to that for single-crystal electrodes; the 1.04 and 1.34 eV states are clearly evident, only slightly shifted in energy. As shown in Fig. 3, the 0.2 eV state is not detected at any appreciable concentration in coevaporated films prepared at high substrate temperature (400°C). This is an important result, indicating that the 0.2 eV

[1]A slightly higher apparent onset is observed for this state in specimens having a high concentration of the 1.04 eV state.

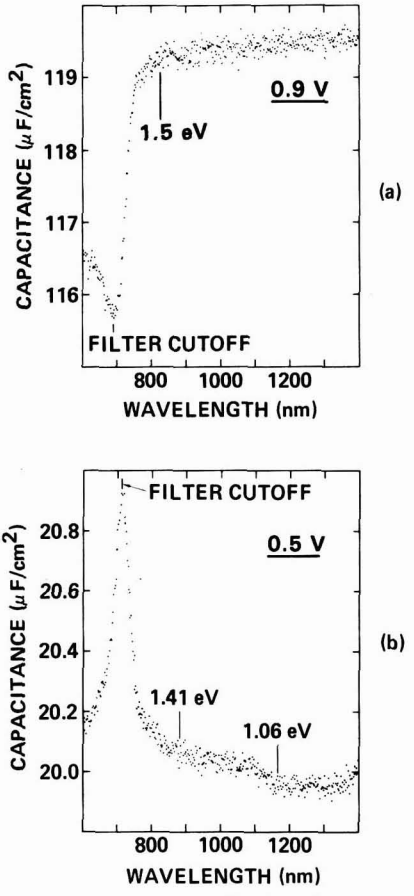


Fig. 1. EPS spectra (7 Hz) measured for a low substrate temperature film in 0.5M KOH at (a) 0.9V and (b) 0.5V vs. μ_{FB}.

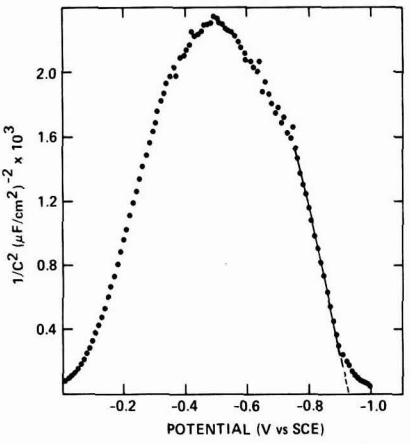


Fig. 2. Mott-Schottky plot (7 Hz) in 0.5M KOH for the same low substrate temperature CdSe electrode as in Fig. 1.

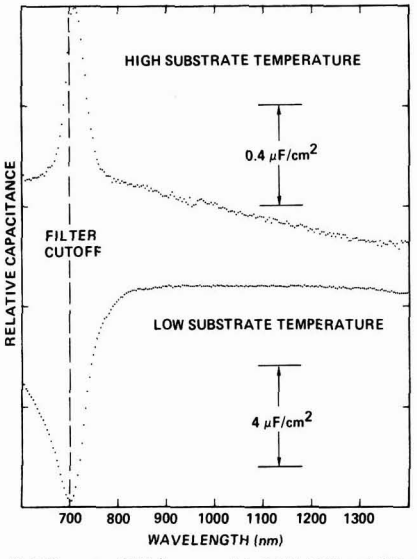


Fig. 3. EPS spectra (7 Hz) measured in 0.5M KOH at 1.0V vs. U_{FB} for coevaporated films prepared at low (100°C) and high (400°C) substrate temperatures.

level, by functioning as a charge transfer mediator/recombination center or by changing the interfacial potential distribution, is responsible for the observed limitations on the attainable open-circuit voltage for low substrate temperature material (8).

It should be mentioned that, as discussed previously (7), these thin film materials have a significant number of pinholes and cracks, through which a portion of the titanium substrate is exposed to the electrolyte. Thus, the measured capacitance includes a parallel contribution associated with the many small metal-electrolyte interfaces, which is likely to be large. In addition, the films are porous, so that the actual surface area of the electrode is much greater than the geometric area. Because of these combined effects, the capacitance values reported here tend to be large, even when the 0.2 eV state is nonionized. Hence, Mott-Schottky plots are of little value in determining carrier concentrations for these materials, but still provide useful information concerning the potential dependence of interfacial processes. Likewise, the absolute photocapacitance values reported have little quantitative significance.

Electrode porosity further complicates the situation by introducing frequency dispersion into the measured capacitance. Essentially, because of current distribution problems within pores, less of the surface of a porous electrode responds to the measurement perturbation at high frequencies. Thus, whereas the measured capacitance for an ideal planar electrode is frequency independent, that for an electrode with cylindrical pores that can be considered infinitely deep (in a given frequency range) decreases with increasing frequency. Specifically, the impedance for a porous electrode in this case is proportional to the square root of that for an ideal flat electrode (13). Consequently, low frequency measurements are preferable for porous electrodes because their capacitance behavior approaches that for ideal planar electrodes as the perturbation frequency is decreased. The relatively low perturbation frequencies used in the present work (7 and 70 Hz) were also chosen to provide optimum sensitivity to capacitance changes. Since it was not necessary, no attempt was made to normalize the data to permit determination of absolute densities of states.

The 0.2 eV state in CdSe apparently resides at the interface, since it is not observed for electrodes transferred from aqueous KOH to acetonitrile electrolytes, as shown in Fig. 4. An interface state is also consistent with the high associated EPS capacitance change (several μF/cm^2) and its potential dependence.

Because of the importance of the aqueous polysulfide for stabilization of CdSe photoanodes in photoelectro-

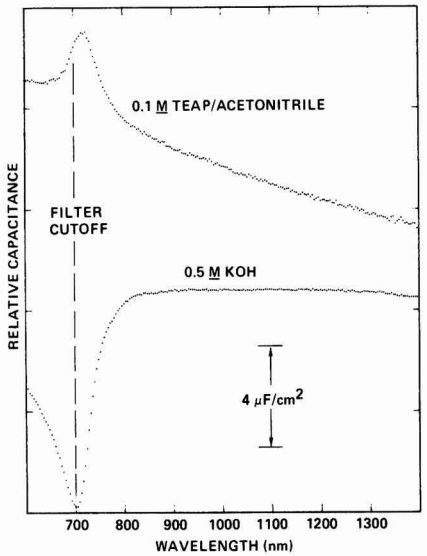


Fig. 4. EPS spectra (7 Hz) for the same low substrate temperature CdSe thin film electrode at 1.0V vs. U_{FB} in 0.5M KOH and in 0.1M tetraethylammonium perchlorate/acetonitrile solution.

chemical cells, appreciable effort was devoted to *in situ* investigation of various CdSe materials in the polysulfide electrolyte. Considerable quantitative variation in EPS results was observed from electrode to electrode (batch to batch), which can be attributed to differences in the material itself, since results for a given electrode were reproducible. In spite of the observed variation, some important general conclusions can be drawn from the data.

Exchange of electrons between the 0.2 eV state in CdSe and polysulfide species in solution is dramatically evident from the time dependence of the photocapacitance under intermittent illumination, as illustrated by the curves in Fig. 5. The response time for attainment of population/depopulation equilibrium for the state is on

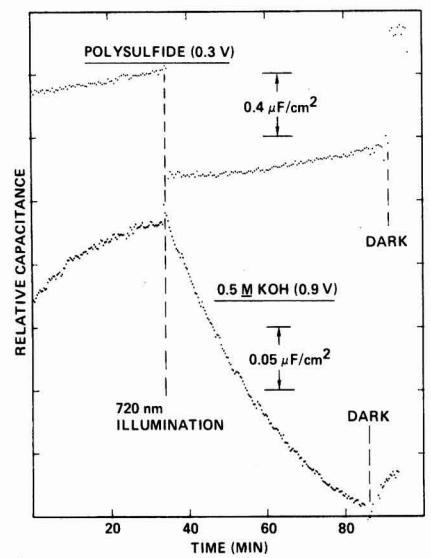


Fig. 5. Transient photocapacitance (7 Hz) for a low substrate temperature CdSe thin film electrode with and without 720 nm illumination in 0.5M KOH solution (0.9V vs. U_{FB}) and in polysulfide solution (0.3V vs. U_{FB}), *i.e.*, 0.1M KOH + 2.5M Na_2S + 1.0M S.

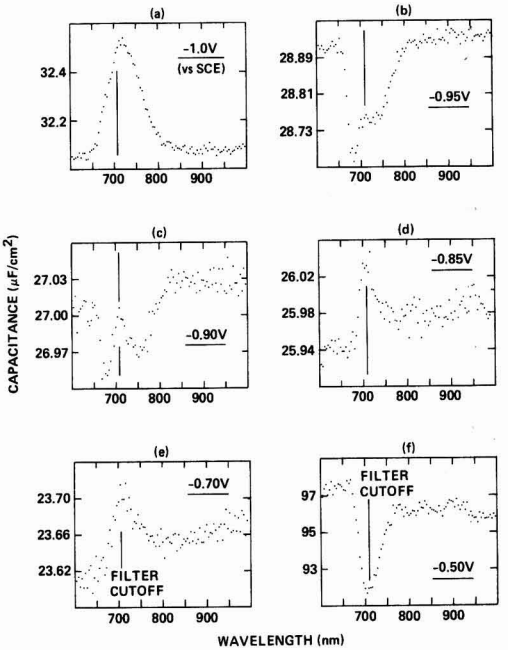


Fig. 6. EPS spectra (70 Hz) for a low substrate temperature n-CdSe electrode in polysulfide solution (0.1M KOH + 2.5M Na_2S + 1.0M S) at various electrode potentials: (a) −1.0; (b) −0.95; (c) −0.90; (d) −0.85; (e) −0.70; and (f) −0.50V vs. SCE.

the order of hours in pure KOH solution, whereas in the presence of polysulfide, equilibrium is attained in less than 2s.

As is evident from the EPS spectra[2] in Fig. 6, the population of the 0.2 eV state in the presence of polysulfide is strongly dependent on the electrode potential. Ionized 0.2 eV states, which upon photoneutralization are reflected in a capacitance decrease beginning at 1.5 eV (820 nm), are not observed at −1.0V *vs.* SCE (Fig. 6a), are evident at −0.95 and −0.90V (Fig. 6b and 6c), are practically undetectable between −0.85 and −0.7V (Fig. 6d and 6e), but are present in very high concentration at −0.5V (Fig. 6f, note that absolute capacitance and photocapacitance are both large). It should be emphasized that all features of this complicated behavior are not observed for all specimens. This is not surprising since, as discussed below, the ionization/neutralization processes for the 0.2 eV state are complex and depend strongly on the density of states and U_{FB}, both of which vary appreciably from specimen to specimen.

The complex behavior illustrated in Fig. 6 can be understood in terms of interface-state (surface-state) reactions involving electron tunneling from the semiconductor bulk to ionized interface states (ss^+) or the reverse tunneling process from neutral interface states (ss^o), *i.e.*

$$e^-_{bulk} + ss^+ \underset{(b)}{\overset{(a)}{\rightleftarrows}} ss^o \qquad [1]$$

and reactions involving the reduced (R_{red}) and oxidized (R_{ox}) redox species, *i.e.*

$$ss^+ + R_{red} \underset{(b)}{\overset{(a)}{\rightleftarrows}} ss^o + R_{ox} \qquad [2]$$

These reactions and the relative energies (approximately to scale) of the conduction band, semiconductor Fermi level, 0.2 eV interface states, and electrolyte redox level (E_R) are depicted for various bias voltages in Fig. 7. Based

[2]Note that the perturbation frequency in this case is 70 instead of 7 Hz; frequency dispersion effects are discussed below.

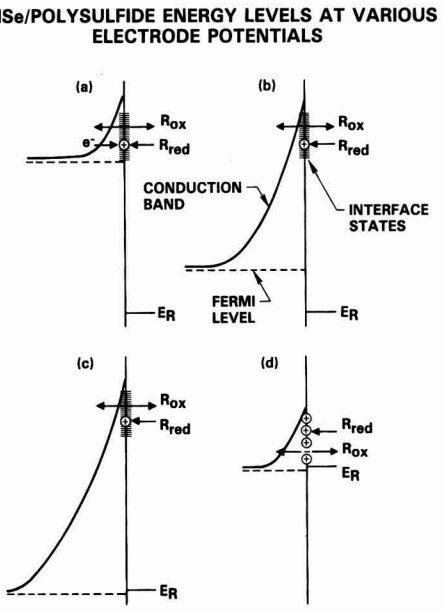


Fig. 7. Energy level diagrams for n-CdSe showing the relative positions of the conduction band, Fermi level, and polysulfide redox potential for $U_{FB} = -1.5$V at various electrode potentials: (a) −1.1; (b) −0.95; (c) −0.8; and (d) −0.5V *vs.* SCE.

on photocurrent onset and ac impedance measurements for single-crystal CdSe, U_{FB} is taken as −1.5V *vs.* SCE, which is also consistent with the highest open-circuit voltage reported for this system (0.7V) (11) and a redox potential of −0.8V; apparent variations from this value for polycrystalline electrodes are discussed below. It should be kept in mind that exchange of electrons between the 0.2 eV interface state and polysulfide species is conclusively evident from the much faster time constant for both ionization and neutralization of the state in the polysulfide electrolyte compared to pure KOH solution (Fig. 5). For Fig. 7a-7c, all of the electrode potential drop is assumed to fall within the semiconductor space-charge region, which is consistent with the relatively low capacitance values.

Population of the interface states is determined by the relative rates of reactions [1a] and [2a] compared to [1b] and [2b], which in turn are influenced by the electrode potential. At potentials of less than about 0.4V *vs.* U_{FB} (Fig. 7a), interface states are filled by electron tunneling through the relatively thin space-charge layer (Eq. [1a]) and by reaction with reduced redox species (Eq. [2a]); although some cathodic dark current is observed, transfer of electrons to electrolyte species is relatively slow (compared to the tunneling/capture rates) at this electrode potential so that no ionized interface states are detected (Fig. 6a). It is important to note that even when the formal E_R value lies far below the interface-state energy, electron transfer from reduced redox species (filled states) is still possible since the energy barrier is greatly reduced by the high local electric field associated with ionized interface states and by specific orbital interactions between the redox species and interface states. Because of such localized effects, E_R in the vicinity of interface states is effectively shifted negatively. At somewhat more positive potentials (Fig. 7b), electron tunneling is suppressed (Fermi level too low) so that some ionized states exist in equilibrium with electrolyte redox species (Fig. 6b-6c). When the Fermi level reaches the electrolyte redox potential (Fig. 7c), net electron transfer from reduced electrolyte redox species to the semiconductor is thermodynamically favored and the ionized interface states are filled (Fig. 6d and 6e). As the electrode potential is made sufficiently positive of the redox potential (Fig. 7d), a large fraction of the interface states ionize by electron tunneling to the semiconductor bulk (Eq. [2b]), so that a large fraction of the electrode potential drops across the electrolyte Helmholtz layer, increasing E_R relative to E_F and giving rise to an appreciable anodic dark current. In this case, the tunneling process is again relatively fast compared to interfacial charge transfer, so that the overall capacitance is large and a high density of ionized 0.2 eV interface states is detected (Fig. 6f).

The lower open-circuit voltage obtained for materials containing a high concentration of the 0.2 eV interface state can readily be explained within this model. That is, at potentials closer to U_{FB} than depicted in Fig. 7a, the Fermi level energy rises above that of the interface states, greatly increasing the probability of electron transfer to electrolyte species and, consequently, the cathodic dark current. In this case, the semiconductor bands cannot unbend further because of charge leakage to the electrolyte, so that a voltage loss, corresponding to the energy of the interface states below the conduction bandedge (0.2 eV), results. This is also reflected in photocurrent onset measurements, which yield apparent U_{FB} values for low substrate temperature films of typically −1.3V *vs.* SCE rather than the −1.5V obtained for single-crystal material. Values of U_{FB} measured for such films by the ac impedance method ranged from −1.0 to −1.4V, apparently reflecting, at least to some extent, variations in the density of ionized interface states. It should be mentioned that Reichman and Russak (8) have previously reported that Mott-Schottky plots are of questionable value in determining U_{FB} for thin film materials of this type.

The dark current-voltage behavior of thin-film CdSe electrodes correlates well with the EPS results and the proposed charge transfer model. Typical plots of log current *vs.* electrode potential for low and high substrate temperature electrodes are given in Fig. 8. High temperature films, for which the 0.2 eV state is not detected by EPS, exhibit very low forward and reverse dark currents (comparable to those observed for single-crystal electrodes) over a wide potential range. At −1.0V *vs.* SCE, the dark current for low temperature films is an order of magnitude greater, presumably because of conventional electron tunneling associated with the decreased band bending (shift in U_{FB}) for this type of material (8). This is consistent with the energy level diagram in Fig. 7a. Also, the fact that the forward dark currents for the both types of materials have the same ideality factor (1.5) indicates a simple change in barrier height, *i.e.*, a shift in U_{FB} for the low temperature material. In addition, the dark saturation current for the low temperature film is 8×10^{-8} A/cm², as compared to 9×10^{-9} A/cm² for the high temperature material, indicating that the former passes more current at the zero bias point. The anodic dark current under re-

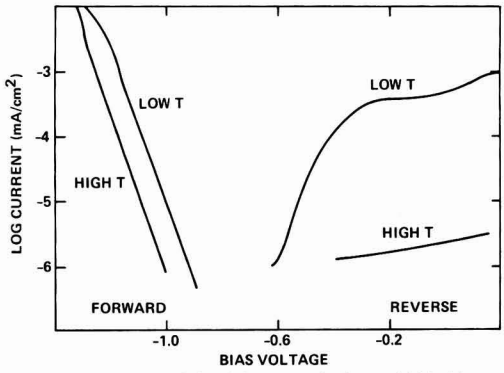


Fig. 8. Dependence of the dark current for low and high substrate temperature CdSe films in polysulfide electrolyte on the electrode bias potential (*vs.* SCE).

verse bias (−0.5V *vs.* SCE) is also much larger for the low temperature films, as expected from the proposed model (Fig. 7d).

Frequency dispersion of the photocapacitance also appears to reflect, in addition to porosity effects, the potential-dependent population/depopulation of the 0.2 eV interface state in aqueous polysulfide electrolytes. For example, in some relatively narrow potential regions, the photocapacitance decrease associated with this state was often much different in magnitude at the lower perturbation frequency (7 Hz) than at the higher frequency (70 Hz); in some cases, the 0.2 eV state was not observed at all at one of the frequencies. Such results indicate that the population of the interface state is affected by the perturbation voltage itself but only at sufficiently low frequencies for which electrons are induced to exchange between the state and electrolyte redox species or the semiconductor bulk (via tunneling). It should be mentioned that measurements of the photocapacitance frequency dispersion could ultimately yield rate constants for specific processes.

To further elucidate the role of the 0.2 eV interface state in charge transfer processes at n-CdSe electrodes, ac impedance measurements were performed over a broad frequency range (10,000 to 0.1 Hz), both in the dark and under illumination with 750 nm (1.65 eV) light. The data will be discussed in terms of the equivalent circuit given in Fig. 9, where R_s is the series resistance, C_p is the parallel capacitance, and R_{CT} is the charge-transfer resistance. Note that, ideally, C_p is a series combination of the space-charge (C_{sc}) and Helmholtz layer (C_H) capacitances, but in the present case there is also a contribution from the portion of the titanium substrate surface exposed to the electrolyte via pinholes and cracks in the CdSe film. In complex impedance plots of the imaginary (Z'') *vs.* real (Z') impedance components, generally R_{CT} is the diameter of the semicircle and $C_p = 1/2\pi f_m R_{CT}$, where f_m is the frequency at the maximum in the semicircle.

Complex impedance plots and calculated C_p and R_{CT} values for a low substrate temperature n-CdSe electrode in aqueous polysulfide at three electrode potentials are shown in Fig. 10, and the corresponding EPS spectra at two perturbation frequencies (7 and 70 Hz) are given in Fig. 11. At −1.0V, which is near U_{FB}, the semiconductor space-charge capacitance is relatively large and 0.2 eV states are readily filled via electrons tunneling from the semiconductor bulk. In this case, the 1.5 eV (820 nm) transition is not observed in the EPS spectrum for either frequency and well-defined semicircles, presumably associated with double layer charging and charge transfer/adsorption processes at the interface,[3] are observed in the complex impedance plots. Although the subbandgap light (750 nm) has no appreciable effect on C_p, as expected when C_H is dominant, R_{CT} is decreased by almost a factor of two by such illumination. This effect is probably the result of electron-hole pair photogeneration, *i.e.*, band tailing. Note that the presence of the 0.2 eV state might be expected to give rise to photocurrent band tailing associated with thermal emission of electrons photoexcited to the state from the valence band. This would explain the long wavelength difference in the action spectra for low and high substrate temperature material given in Fig. 12.

At −0.8V *vs.* SCE, the situation is quite different. In this case, the 0.2 eV state is at least partially ionized and the 1.5 eV (820 nm) transition is observed in the EPS spectra (note that the magnitude of the capacitance decrease is smaller at the higher perturbation frequency). In the dark, the complex impedance plot is a straight line inclined at 78°, indicating that the impedance is dominated by a somewhat "leaky" capacitor (an ideal nonporous capacitor would yield an angle of 90°), presumably the space-

[3]Since no linear region, *i.e.*, Warburg impedance, is observed, diffusional processes are apparently unimportant over the frequency range and light intensity studied.

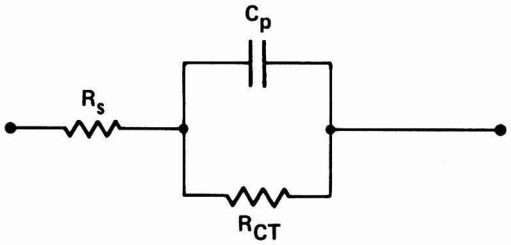


Fig. 9. Simple equivalent circuit for n-CdSe/polysulfide system

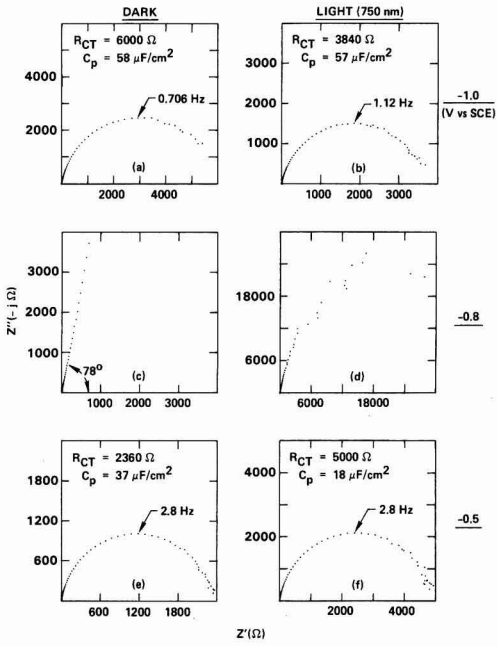


Fig. 10. Complex impedance plots for a low substrate temperature n-CdSe electrode at three bias potentials in polysulfide solution (0.1M KOH + 2.5M Na_2S + 1.0M S), with and without 750 nm illumination.

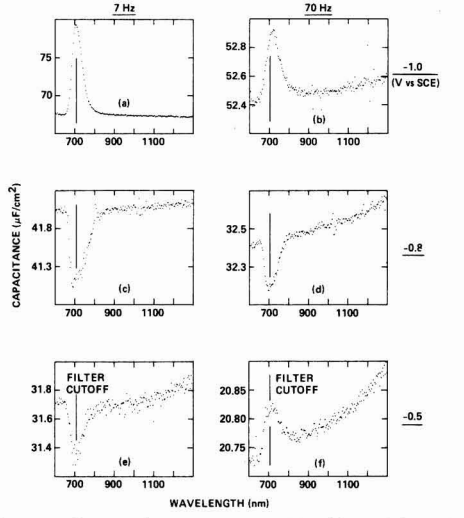


Fig. 11. EPS spectra (measured at 7 and 70 Hz) for n-CdSe at three bias potentials in polysulfide solution (same electrode and electrolyte as for Fig. 10).

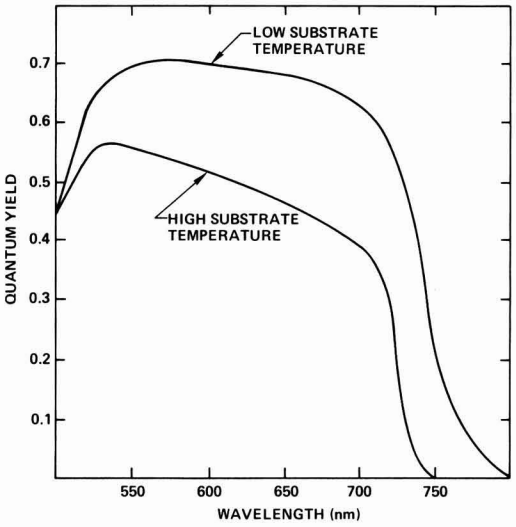


Fig. 12. Spectral response of low and high substrate temperature CdSe materials in polysulfide electrolyte at −1.0V *vs.* SCE.

charge capacitance (C_{sc}). This is consistent with the model presented above, according to which electron tunneling from the semiconductor bulk to 0.2 eV interface states does not occur at this bias voltage so that interfacial charge transfer processes are subdued. With 750 nm illumination, the complex impedance plot exhibits significant curvature (the radius corresponding to 10^5 Ω), presumably associated with interfacial reaction of electrons photoexcited to the interface states. Since photogenerated holes are rapidly consumed at the interface, such interfacial reaction of electrons corresponds to charge-carrier recombination via electrolyte species. These results, therefore, provide strong evidence for the participation of the 0.2 eV state in recombination.

At −0.5V *vs.* SCE, which is positive of the polysulfide redox potential, faradaic processes once again dominate the impedance, yielding a well-defined semicircle in the complex impedance plots. In this case, electrons are transferred from the reduced redox species to the interface states, then tunnel to the semiconductor bulk, resulting in an anodic dark current. The lower value of C_p compared to that at potentials near U_{FB} indicates a significant contribution from C_{sc}; under illumination, which populates and thus reduces the density of ionized interface states, the contribution is larger (C_p is smaller). Illumination also increases R_{CT} in this case because fewer sites are available for interfacial charge transfer, *i.e.*, states are filled via the 1.5 eV phototransition. In addition, neutralization of the 0.2 eV state effectively increases the space-charge layer thickness, as seen by the decrease in C_p, which will inhibit tunneling and thus increase R_{CT}. Although the 0.2 eV state is detected in the EPS spectrum at 7 Hz (as expected), it is not observed at 70 Hz. This is probably a consequence of the relative rates of tunneling and charge transfer and the effect the perturbation voltage has in populating/depopulating the state.

EPS was also used to investigate the mechanism by which zinc treatment improves the performance of n-CdSe photoanodes (9). Although this treatment (soaking in 0.1*M* $ZnCl_2$ solution) apparently reduces the concentration of the 0.2 eV interface state in some cases — results of one set of experiments are summarized in Table I — the effect is not consistently observed and is apparently related only incidentally to the performance improvement. This interpretation is consistent with the findings of Reichman and Russak (9) that Zn, which is incorporated in the CdSe lattice, improves the open-circuit voltage by shifting U_{FB} negatively.

Table I. Effect of $ZnCl_2$ treatment on photocapacitance change for 0.2 eV state in thin film CdSe

Electrode preparation	$\Delta C(\mu F/cm^2)$*
Untreated (etched/cycled in polysulfide)	−0.80
30 min soak in 0.1*M* $ZnCl_2$	−0.70
Additional 30 min soak in $ZnCl_2$ solution	−0.60
4 days in $ZnCl_2$ solution	−0.47

* Measured at 7 Hz and 0.4V *vs.* U_{FB}.

Some speculation concerning the origin of the 0.2 eV state is in order. A chemical impurity seems unlikely, since the 0.2 eV state is observed in small concentrations even for single-crystal material. Also, secondary ion mass spectroscopy (SIMS) profiling of low substrate temperature films indicated that impurity levels are as low as those of the best high substrate temperature films, for which the 0.2 eV state is not detected by EPS. Since the concentration of the state in single-crystal material is enhanced by mechanical polishing, participation of a lattice defect is implied. This is consistent with the findings of Brillson (12) that the feature corresponding to the 0.2 eV state in surface photovoltage spectra is enhanced by argon bombardment. Frese (1) has inferred the presence of an interface state in CdSe centered about 0.2 eV below the conduction bandedge and attributed it to excess selenium. Although free Se would be expected to dissolve in aqueous polysulfide, a Se species bound to a lattice defect would appear to be a likely prospect as the origin of the 0.2 eV interface state. The occurrence of such a selenium-defect state would not be surprising, because as-deposited low temperature films contain a 3:1 molar ratio of Se to Cd and are only partially crystalline. It is only after heat-treatment and removal of excess Se that such films are crystalline and exhibit favorable photovoltaic characteristics. This type of defect is also consistent with our inference that this state shifts U_{FB} anodic by interfering with polysulfide adsorption, which should be favored on Cd sites but inhibited on Se.

Acknowledgments

This work was supported by the Solar Energy Research Institute (SERI) under Subcontract no. XE-2-02126-01 and XB-3-03108-01. The authors are also indebted to Dr. John Dick of SERI, who performed the SIMS profiling analyses.

Manuscript submitted Oct. 24, 1983; revised manuscript received May 14, 1984.

Rockwell International Science Center assisted in meeting the publication costs of this article.

REFERENCES

1. K. W. Frese, Jr., *J. Appl. Phys.*, **53,** 1571 (1982).
2. A. Aruchamy, J. A. Bruce, S. Tanaka, and M. S. Wrighton, *This Journal*, **130,** 359 (1983).
3. A. J. Bard, A. B. Bocarsly, F. F. Fan, E. G. Walton, and M. S. Wrighton, *J. Am. Chem. Soc.*, **102,** 3671 (1980).
4. K. Rajeshwar, *This Journal*, **129,** 1003 (1982).
5. R. Haak, C. Ogden, and D. Tench, *ibid.*, **129,** 891 (1982).
6. R. Haak and D. Tench, *ibid.*, **131,** 275 (1984).
7. M. A. Russak, J. Reichman, H. Witzke, S. K. Deb, and S. N. Chen, *ibid.*, **127,** 725 (1980).
8. J. Reichman and M. A. Russak, *ibid.*, **128,** 2025 (1981).
9. J. Reichman and M. A. Russak, *J. Appl. Phys.*, **53,** 708 (1982).
10. R. Haak and D. Tench, *This Journal*, **131,** 1442 (1984).
11. B. Miller, A. Heller, M. Robbins, S. Menezes, K. C. Chang, and J. Thompson, Jr., *This Journal*, **124,** 1019 (1977).
12. L. J. Brillson, *Surf. Sci.*, **69,** 62 (1977).
13. R. de Levie, in "Advances in Electrochemistry and Electrochemical Engineering," Vol. VI, P. Delahay, Editor, p. 329, Interscience, New York (1967).

Activity Coefficients of Electrons and Holes in Semiconductors

Mark E. Orazem*,[1] and John Newman**

Materials and Molecular Research Division of Lawrence Berkeley Laboratory, and Department of Chemical Engineering, University of California, Berkeley, California 94720

ABSTRACT

Dilute-solution transport equations with constant activity coefficients are commonly used to model semiconductors. These equations are consistent with a Boltzmann distribution and are invalid in regions where the species concentration is close to the respective site concentration. A more rigorous treatment of transport in a semiconductor requires activity coefficients which are functions of concentration. Expressions are presented for activity coefficients of electrons and holes in semiconductors for which conduction- and valence-band energy levels are given by the respective bandedge energy levels. These activity coefficients are functions of concentration and are thermodynamically consistent. The use of activity coefficients in macroscopic transport relationships allows a description of electron transport in a manner consistent with the Fermi-Dirac distribution.

The concentrations of holes and electrons in a semiconductor are given by the Fermi-Dirac distribution (1, 2). A Boltzmann distribution is frequently used as an approximation to this distribution in statistical-mechanical analyses of semiconducting systems. Dilute-solution transport equations with constant activity coefficients, consistent with a Boltzmann distribution, are also used in characterizing the behavior of semiconducting systems. These approximate methods are popular because of their relative mathematical simplicity, but are invalid when electron or hole concentrations are close to the respective site concentrations in any region.

Calculation of individual ionic activity coefficients for electrons and holes has been proposed as a means of identifying the regions in which these approximations are justified. Rosenberg (3), Panish and Casey, Jr. (4, 5), and Hwang and Brews (6) have presented activity coefficients for electrons and holes that are functions of potential as well as concentration. Harvey (7) discusses the separation of the activity coefficient into parts due to chemical and electrical effects. Landsberg and Guy (8) present an activity coefficient based upon an Einstein relation that includes within it the nonidealities associated with the activity coefficient (9).

Activity coefficients are derived here that are functions of concentration. This derivation is independent of the Einstein relation. These activity coefficients are thermodynamically consistent and can be used to check the validity of the Boltzmann function as an approximation to the Fermi-Dirac distribution. These coefficients can also be used in the application of macroscopic transport equations to semiconducting systems in a way that is generally valid.

Theoretical Development

The electrochemical potential of a given species can arbitrarily be separated into terms representing a reference state, a chemical contribution, and an electrical contribution (10)

$$\mu_i = \mu_i^\theta + RT \ln (c_i f_i) + z_i F \Phi \qquad [1]$$

where Φ is a potential which characterizes the electrical state of the phase and can be defined in a number of ways. The potential used here is the electrostatic potential which is obtained through integration of Poisson's equation (11). Equation [1] can be viewed as the defining equation for the activity coefficient, f_i.

Under the assumption of a dilute solution, the flux of an individual species within the semiconductor is driven by a gradient of electrochemical potential

$$N_i = -c_i u_i \nabla \mu_i \qquad [2a]$$

or

$$f_i N_i = -u_i RT \nabla (c_i f_i) - z_i u_i \mathbf{F} (c_i f_i) \nabla \Phi \qquad [2b]$$

where N_i is the flux of species i. Introduction of $A = c_i f_i e^{z_i F \Phi / RT}$ yields

$$f_i N_i = -u_i RT e^{-z_i F \Phi / RT} \nabla A \qquad [3]$$

Under equilibrium conditions, $\nabla A = 0$, and

$$c_i f_i = A e^{-z_i F \Phi / RT} \qquad [4]$$

where A is a constant. Under the assumption of a constant activity coefficient, Eq. [4] is consistent with a Boltzmann distribution.

The distribution of electrons in a semiconductor is characterized by the Fermi-Dirac function

$$\frac{n_i}{g_i} = [1 + \exp [(E_i - E_f)/RT]]^{-1} \qquad [5]$$

where n_i is the number of electrons within an energy level E_i with degeneracy g_i. The Fermi energy E_f is a statistical parameter given the units of J/mol and defined as the energy at which the probability of occupancy of a state is one-half. The Fermi-Dirac distribution enters into the transport development (Eq. [2], [3], and [4]) through introduction of individual ionic activity coefficients: one for electrons and one for holes.

Through Fermi-Dirac statistics the concentration of conduction electrons is given by

$$n = \int_{E_c}^{\infty} \frac{N(E)}{1 + \exp [(E - E_f)/RT]} \, dE \qquad [6]$$

and the concentration of holes by

$$p = \int_{-\infty}^{E_v} \left[1 - \frac{1}{1 + \exp [(E - E_f)/RT]}\right] N(E) dE \qquad [7]$$

The concentrations defined above are consistent with the concentrations c_i used in Eq. [1]-[4]. If the distribution of available energy levels is narrow or RT is small, the valence and conduction electrons can be characterized by single-valued energy levels, E_v (the highest energy level of the valence band) and E_c (the lowest energy level of the conduction band), respectively. Thus

$$n = \frac{1}{1 + \exp [(E_c - E_f)/RT]} \int_{E_c}^{\infty} N(E) dE \qquad [8]$$

or

$$n = \frac{N_c}{1 + \exp [(E_c - E_f)/RT]} \qquad [9]$$

where N_c is the concentration of conduction-energy sites for electrons. A similar term, N_v, is defined as the concentration of valence-band sites.

From the definition of the electrochemical potential, the chemical activity

*Electrochemical Society Student Member.
**Electrochemical Society Active Member.
[1]Present address: Department of Chemical Engineering, University of Virginia, Charlottesville, Virginia 22901.

$$a_i = c_i f_i \quad [10]$$

can be expressed as

$$a_i = \exp\left[\frac{\mu_i - \mu_i^\theta - z_i F\Phi}{RT}\right] \quad [11]$$

Note that the activity has units of concentration (see Eq. [1]). In Eq. [9], the concentration of conduction electrons is given as a function of the Fermi energy level. The energy E_c in this equation depends upon potential as

$$E_c = E_c^* + z_i F\Phi \quad [12]$$

where E_c^* is a constant, independent of potential. The electrochemical potential of conduction electrons and the Fermi energy are related by an arbitrary constant

$$\mu_{e^-} = E_f + \mu^*_{e^-} \quad [13]$$

Equations [11] through [13] can be combined to yield

$$f_{e^-} = \frac{\exp\left[(\mu^*_{e^-} - \mu^\theta_{e^-} + E_c^*)/RT\right]}{N_c}\left[\frac{1}{1 - n/N_c}\right] \quad [14]$$

where f_{e^-} is dimensionless. The secondary reference state quantities, E_c^*, $\mu^*_{e^-}$, and $\mu^\theta_{e^-}$, are chosen to allow the activity coefficient to approach unity as the concentration of conduction electrons approaches zero. Thus, the activity coefficient is obtained as a function of composition

$$f_{e^-} = \frac{1}{1 - n/N_c} \quad [15]$$

The activity coefficient of conduction electrons is equal to 2 for a dimensionless concentration n/N_c equal to 0.5.

A similar activity coefficient can be obtained for the holes as

$$f_{h^+} = \frac{1}{1 - p/N_v} \quad [16]$$

The assumption of unity activity coefficients is in harmony with the assumption of the Boltzmann limits to the Fermi-Dirac distribution. Use of the Fermi-Dirac distribution results in activity coefficients that are functions of concentration.

Discussion

Equations [15] and [16] are consistent with the form of the activity coefficients

$$f_{e^-} = \frac{N_c}{n} e^{(E_f - E_c)/RT} e^{\Delta E/RT}$$

presented by Hwang and Brews (6) and Landsberg and Guy (8). These authors include a term $e^{\Delta E/RT}$ for the shift in electron energy due to the occupation of energy levels above E_c at high electron concentrations (12). Under the assumption that $\Delta E = 0$, Eq. [15] is recovered by introduction of the Fermi-Dirac distribution function for electrons. Calculation of ΔE requires knowledge of the electron site distribution $N(E)$.

The activity coefficients defined above can be checked for consistency with the Fermi-Dirac function. Introduction of the activity coefficient presented for electrons in Eq. [15] into the respective Boltzmann distribution

$$nf_{e^-} = N_c e^{-(E_c - E_f)/RT} \quad [17]$$

recovers the Fermi-Dirac distribution

$$\frac{n}{N_c} = \frac{1}{1 + e^{(E_c - E_f)/RT}} \quad [18]$$

The same is true for the activity coefficient for holes.

A measure of internal thermodynamic consistency is obtained from the second cross-derivative of the Gibbs function, *i.e.*

$$\left(\frac{\partial \mu_i}{\partial c_k}\right)_{T,P,c_j \neq k} = \left(\frac{\partial \mu_k}{\partial c_i}\right)_{T,P,c_j \neq i} \quad [19]$$

where i and k represent components of the system that are not the solvent. This necessary condition for thermodynamic consistency is expressed for the system described here as

$$\frac{RT}{f_{e^-}}\left(\frac{\partial f_{e^-}}{\partial p}\right)_{T,P,n} = \frac{RT}{f_{h^+}}\left(\frac{\partial f_{h^+}}{\partial n}\right)_{T,P,p} \quad [20]$$

This condition is satisfied. (Equation [19] is properly stated in terms of mole numbers rather than concentrations. For the dilute systems involved here, lattice expansion is ignored, and the two are equivalent.)

Use of macroscopic relations for thermodynamics and transport in regions of nonzero electric charge density raises some interesting philosophical questions because transport and thermodynamic properties are not easily measurable as functions of composition including arbitrary departures from electroneutrality. Fortunately, the semiconductors of interest are extremely dilute compared to even dilute aqueous solutions, and theoretical expressions such as the Fermi-Dirac distribution can be used with some confidence. Note that individual ionic activity coefficients are here being introduced in regions of net charge.

The extreme dilution of the semiconductors is also a justification for using the simple transport Eq. [2a] rather than the multicomponent diffusion equation (10), which includes interactions of solute species, and for using the approximate thermodynamic test embodied in Eq. [19].

Conclusions

Activity coefficients are derived here that are functions of concentration. These activity coefficients are thermodynamically consistent and can be used to check the validity of the Boltzmann function as an approximation to the Fermi-Dirac distribution. These coefficients can also be used in the application of macroscopic transport equations to semiconducting systems.

The use of constant activity coefficients in modeling semiconductor systems is valid for dimensionless concentrations n/N_c and p/N_v less than 0.1. Use of the activity coefficients presented in Eq. [15] and [16] allows treatment of systems with dimensionless concentrations ranging from 0 to 1. This approach is restricted, however, by the assumption that valence- and conduction-band electrons are characterized by their respective bandedge energies. Relaxation of this assumption involves integration of Eq. [6] and [7] for a specific distribution of electron energy levels.

Acknowledgment

This work was supported by the United States Department of Energy under Contract no. DE-AC03-76SF00098 through the Director, Office of Energy Research, Office of Basic Energy Sciences, Chemical Sciences Division, and through the Assistant Secretary of Conservation and Renewable Energy, Office of Advanced Conservation Technology, Electrochemical Systems Research Division.

Manuscript submitted Nov. 21, 1983; revised manuscript received June 6, 1984.

The University of California assisted in meeting the publication costs of this article.

REFERENCES

1. A. S. Grove, "Physics and Technology of Semiconductor Devices," John Wiley and Sons, New York (1967).
2. S. M. Sze, "Physics of Semiconductor Devices," Wiley-Interscience, New York (1969).
3. A. J. Rosenberg, *J. Chem. Phys.*, **33**, 665 (1960).
4. M. B. Panish and H. C. Casey, Jr., *J. Phys. Chem. Solids*, **28**, 1673 (1976).
5. M. B. Panish and H. C. Casey, Jr., *ibid.*, **29**, 1719 (1968).
6. C. J. Hwang and J. R. Brews, *ibid.*, **32**, 837 (1971).
7. W. W. Harvey, *ibid.*, **23**, 1545 (1962).

8. P. T. Landsberg and A. G. Guy, *Phys. Rev. B*, **28**, 1187 (1983).
9. P. T. Landsberg, "Thermodynamics and Statistical Mechanics," Oxford University Press, Oxford, England (1978).
10. J. Newman, "Electrochemical Systems," Prentice-Hall, Englewood Cliffs, NJ (1973).
11. R. Parsons, in "Modern Aspects of Electrochemistry," Vol. 1, J. O'M. Bockris, Editor, Chap. 3, Academic Press, New York (1954).
12. F. A. Lindholm and J. G. Fossum, *IEEE Trans. Electron. Devices Lett.*, **edl-2**, 230 (1981).

Technical Notes

Polarization Effects in Polyimides

G. Samuelson

Solavolt International, Phoenix, Arizona 85040

S. Lytle*

Motorola, Incorporated, Mesa, Arizona 85202

Polyimide is a class of high temperature, stable organic polymers that has found widespread use in the semiconductor industry. It has been used as an interlevel dielectric in multilevel discrete transistors (1), and as a final passivant (2). More recently, its role in silicon and aluminum MOS integrated circuits has been demonstrated (3).

Some limited-reliability data on polyimide films have been described in the literature. For example, the effect of incomplete cure on device performance was discussed by Gregoritsch (4). The via resistance and leakage current of a multilevel bipolar LSI chip was reported by Mukai *et al.* (5). Finally, the effects of ionic contamination and electrical conduction in polyimide was discussed by Brown (6).

The present work extends the discussion of charge instability within polyimide films by using standard C-V techniques to probe charge effects that are inherent in the polyimide film or are induced by certain processes. Evidence is presented to show that differences in inherent polarizability of several commercially available polyimides exist. Evidence is presented to show that absorbed water causes increases in the polarization time constants. It may be possible to distinguish different kinds of water, based on the fact that different dehydration conditions are required to restore the original time constants of polarization, depending on the relative humidity to which the polyimide film was exposed. Finally, evidence is presented to show that plasmas routinely used in the semiconductor industry may influence the polarization of polyimide films. For example, standard isotropic O_2 plasma etching of polyimide was shown to cause a decrease in the polarization time constant and activation energy.

Experimental

Polarization effects intrinsic to polyimide.—MIS structures were constructed of 8-12 Ωcm phosphorus-doped Si, 1000Å thermally grown MOS-quality SiO_2, 0.8-4.8μ polyimide (du Pont PI2545, PI2555, PI2562, PSH61453, and Hitachi PIQ-13), and 4000Å pure evaporated aluminum, patterned using conventional lithographic techniques. The resulting test wafer was subjected to a 200°C, 20 min dehydration bake immediately prior to measurement. The measurement system consisted of a Temptronic TP350A thermally controlled chuck, an HP4275A LCR meter, and a Fluke 8502A multimeter. A "standard" room temperature trace was performed at 100 kHz from −100V to +100V using a ramp rate of 1 V/s. The stress conditions used to compare measured ΔV_{FB} values against ΔV saturation calculated from classic polarization theory were −5V, 200°C, and 20 min, with cooling to room temperature under bias. At room temperature, the "standard" trace was repeated and the ΔV_{FB} measured. The stress conditions used to determine the time constants of polarization were −5V, 200°C, and times varying from 1 to 40 min, depending on the polyimide under test. Following stress, the MIS structure was cooled to room temperature under bias, the "standard" trace was repeated, and ΔV_{FB} was measured.

Humidity effects on polarization.—C-V analysis was performed on MIS structures which consisted of 4-7 Ωcm p-type Si substrates, 1000Å thermally grown MOS quality SiO_2, 1000Å CVD Si_3N_4, and 1.5μ polyimide, followed by 12 kÅ of sputtered Al-Cu-Si. An MDC computerized semiconductor measurement system consisted of a Boonton 72B capacitance meter, a HP7010B XY recorder, current monitors, and power supplies supported by an 8080S microcomputer system. Standard C-V traces of unstressed samples were made at room temperature over a voltage range of −75 to +25V at 1 MHz. Stressing was done at 225°C under a +5V bias for times ranging from 2 to 20 min. The MIS structure was brought to room temperature under bias, and the ΔV_{FB} was measured as a function of stress time. The time constant of polarization, τ, was calculated from the slope of the ln ΔV_{FB} *vs.* time curves for MIS structures exposed to various humidity ambients. 100% humidity ambient was achieved by placing wafers in an airtight wafer box with water. At no time was the water in contact with the polyimide. All other relative humidities were obtained by exposing wafers to the clean room ambient. Typically, control wafers were stored at 200°C at N_2.

Results and Discussion

Polarization effects vs. polyimide chemistry.—It has been noted by Brown (6) that charge effects in polyimide can cause inversion of underlying silicon and consequent undesired communication between doped areas. An effort was made to distinguish among the various commercially available polyimides with respect to charge instabilities by subjecting them to −5V, 200°C, and 20 min stress, conditions which mimicked realistic operating conditions for certain devices. The ΔV_{FB} of the stressed

*Electrochemical Society Active Member.

Table I. ΔV_{FB} measured and calculated for various polyamides

Polyamide	Thickness (μm)	ΔV_{FB} meas. (volts)	ΔV_{sat} (volts)	ΔV_{FB} meas./ΔV_{sat}	ΔV_{FB} meas./μm (volts/μm)
PI2566	4.76	4	216.0	0.018	0.840
PI2562	0.79	18	35.9	0.501	22.800
PIQ-13	1.15	34	52.3	0.650	29.600
40%PSH 61453	1.95	78	88.6	0.880	40.000
PI2545	1.68	80	76.4	1.000	47.600

profile was compared with the ΔV_{FB} of the unstressed profile. The results are presented as ΔV_{FB}, measured in Table I for numerous polyimides. The saturating shift was calculated from classic polarization theory where

$$\Delta V_{sat} = -(k_o x_p / k_p x_o) V_p^{7}$$

V_p is the polarizing voltage, k_o and k_p are the dielectric constants of oxide and polyimide, respectively, and x_p and x_o are the thicknesses of polyimide and oxide. The ratio of the ΔV_{FB} measured and the calculated ΔV saturation is a reflection of the relative polarizability of the polyimides tested, as is the parameter ΔV_{FB} measured/μm. From Table I, it is clear that PI2566 is the least polarizable. du Pont *PI2545* and *PSH61453* are both rapid polarizers, and the other polyimides fall intermediately between these two extremes.

An attempt was made to measure the time constant of polarization. Figure 1 shows the C-V trace under −5V, 200°C stress for times varying from 1 to 15 min for PSH61453. The undulating C-V profiles made it difficult to measure a single meaningful time constant. An attempt was made to "freeze" out polarization events by reducing the stress temperature to as low as −10°C. Even under these conditions, the most rapid polarizers continued to exhibit nonlinear ln ΔV *vs.* time curves. In fact, under conditions of no applied stress other than that imposed by the standard trace, considerable hystersis in the C-V characteristics was observed for all polyimides, except for the slowest polarizer, PI2566. Figure 2 shows the comparable family of C-V traces for PI2566, also stressed at −5V and 200°C, though now for 15-40 min. The family of curves exhibits uniform, conventional C-V behavior. A plot of ln ΔV *vs.* time, as shown in Fig. 3, gives a straight line with correlation coefficient 0.984. The time constant τ was determined from the slope of the curve in Fig. 3 and the equation

$$\Delta V = \frac{K_o x_p}{K_p x_o} V_p \left(1 - e^{-t/\tau}\right)^{7}$$

The calculated τ for PI2566 was 840 min.

Polarization effects due to absorbed water.—The specific contribution of water to polarization effects in polyimide films was studied. MIS structures using PIQ or PI2566 were "soaked" for varying times in either a clean room environment where the relative humidity varied from 17 to 35% or a 100% relative humidity environment. The structures were stressed at +5V and 225°C following humidity exposure, and C-V profiles were measured as a function of stress time. Figure 4 is an example of the results for a MIS structure using PIQ and SiO_2 where the stress times were 2-16 min. The figure illustrates the typical finding that, initially, a rapid shift in ΔV_{FB} occurred which correlated directly with the relative humidity of the soak period. The term ΔV_{H_2O} was defined as the ΔV_{FB} that arose between the zero-stress C-V profile for a dehydrated film (the dotted line in Fig. 4) and the zero-stress C-V profile for a water-"soaked" film. The magnitude of ΔV_{FB} appeared to be a direct function of the relative humidity and the time of exposure to that humidity, as indicated in Fig. 5. The ΔV_{H_2O} occurred almost instantaneously upon temperature and bias stressing and disappeared following a 200°C, 30 min dehydration bake in dry N_2. After ΔV_{H_2O} occurred, a family of C-V curves resulted, with continued stressing from which ΔV_{FB} values could be measured and used to calculate a time constant of polarization, τ. If such a time constant was measured as a function of exposure time in a 100% RH ambient, τ was seen to increase, as shown in Fig. 6 for PIQ MIS structures. Samples which exhibited increasing τ with time at 100%

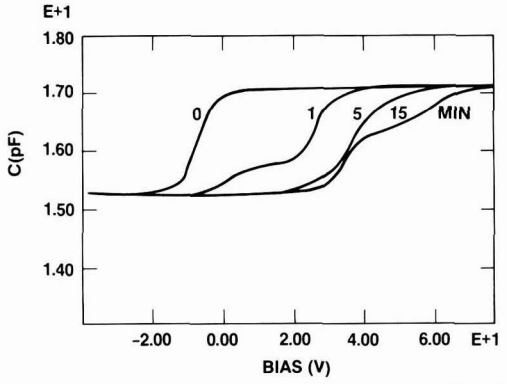


Fig. 1. C-V characteristics for PSH61453 stressed at −5V and 200°C for 1-15 min.

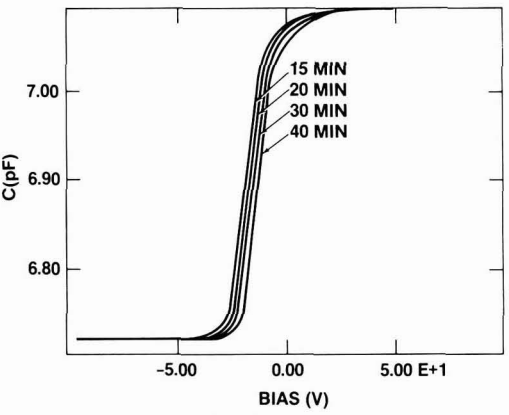


Fig. 2. C-V characteristics for PI2566 stressed at 5V and 200°C for 15-40 min.

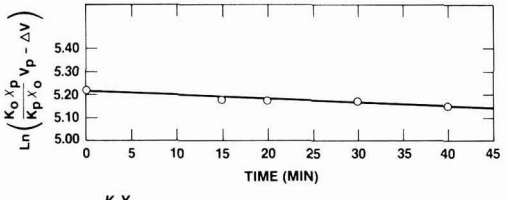


Fig. 3. Ln $\left(\frac{K_o X_p}{K_p X_o} V_p - \Delta V\right)$ *vs.* time for PI2566 stressed at −5V and 200°C.

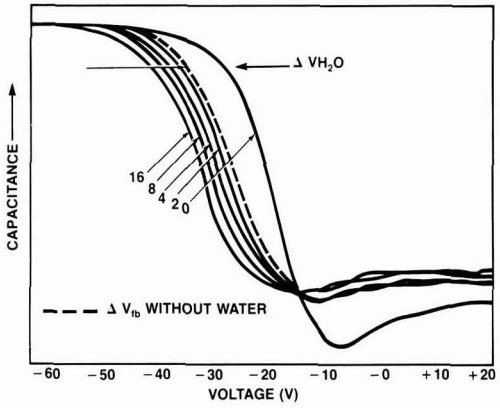


Fig. 4. C-V characteristics of PIQ-3 exposed to a 17% RH ambient for 22h and stressed at +5V and 225°C for 2-16 min.

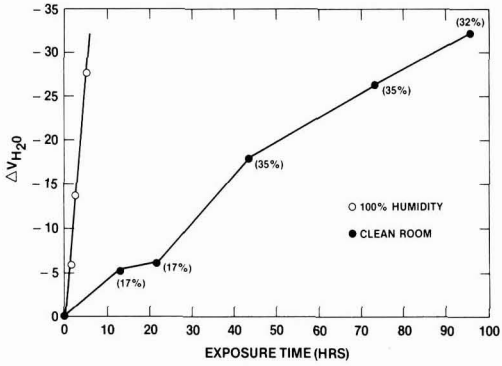


Fig. 5. Magnitude of ΔV_{H_2O} vs. exposed time for PIQ-13 at 100% RH and clean room humidity, varying as indicated in the parentheses.

RH did not revert to the original τ values following 200°C dehydration bake in dry N_2 atmosphere for as long as 72h. They did, however, revert to original τ values following 450°C dehydration bake in dry N_2 for 30 min. Such high temperature dehydration conditions were consistent with the release of H-bonded water. Samples exposed to lower relative humidities (*i.e.*, 17-35%) for as long as 120h also

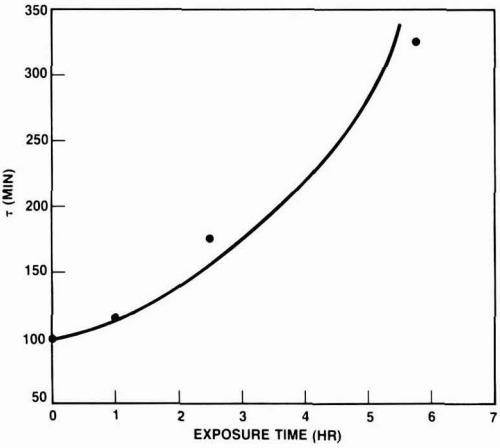


Fig. 6. The time constant of polarization for PIQ-13 as a function of exposure time to 100% RH conditions and +5V, 225°C stress conditions.

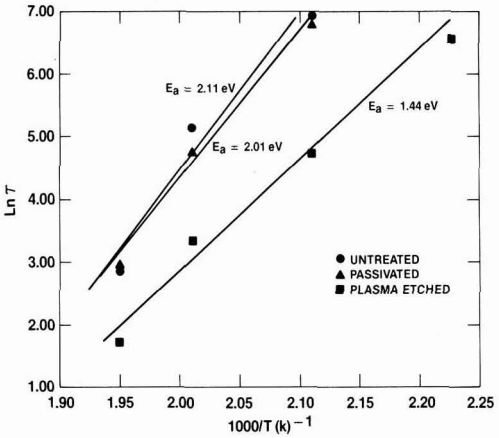


Fig. 7. Arrhenius plots for untreated, plasma-etched, and passivated PIQ-13 films.

exhibited increased τ values which reverted to original values on lower temperature, 200°C dehydration bake.

Processing effects on polarization.—A brief study was done to determine the effects of highly energetic UV irradiation associated with plasma processing on the polarization behavior of polyimide films. Two plasma processes were performed on deposited polyimide films: plasma etching of the polyimide film itself and passivation with a plasma-enhanced CVD film of silicon oxide.

Films with a thickness of ~ 3.0 μm of cured PIQ-13 polyimide were etched to half their original thickness in a Dionex 3000 barrel reactor. Etching took place at 150°C and 0.5 torr in an O_2 plasma at 500W. The approximate etching time was 30 min. After etching, 1.5 μm of Al-Cu-Si was deposited, and C-V analysis was performed as previously described. For passivation, a 1000Å-thick film of plasma oxide was deposited on wafers which had 1.5 μm of cured PIQ-13 and Al-Cu-Si metallization. Passivation was performed in an AMT Plasma II reactor at 300°C and 0.3 torr. A plasma energy of 150W was used to react SiH_4 and N_2O in a carrier gas to form the silicon oxide film. Deposition time was approximately 5 min. The plasma oxide film was then selectively removed from the metal-patterned polyimide film, and C-V analysis was done.

Figure 7 shows Arrhenius plots for untreated, plasma-etched, and passivated PIQ films. While no significance beyond measurement error could be attributed to the differences in activation energy between the passivated film and the untreated control, there was a significant lowering of the activation energy for the plasma-etched film. In addition, this effect increased with increasing exposure and/or intensity of the plasma. This change in polarization could not be reversed by annealing the plasma-treated films at 450°C in N_2 for 1h.

Oxygen plasma treatments have been shown in the literature to affect other properties of polymer films, particularly in a 1-10 μm thick region at the surface. For example, general trends of increases in wettability and decreases in molecular weight have resulted for a number of different polymer films (8). Also, mechanical strength of surface layers has been altered as a result of exposing polypropylene to O_2-containing and N_2O-containing plasmas (9). In general, the mechanism responsible for changes in these properties has been scissioning of polymer chains due to UV irradiation, with subsequent rapid termination of free radicals with oyxgen (8). Such a mechanism may have been responsible for the changes in polarization behavior which occurred in the thin polyimide films studied.

Manuscript submitted Sept. 19, 1983; revised manuscript received June 5, 1984.

Solavolt International assisted in meeting the publication costs of this article.

REFERENCES

1. K. Mukai, A. Saiki, S. Harada, and S. Shoji, International Electron Devices Meeting, p. 16 (1977).
2. A. Saiki, K. Mukai, S. Takahashi, K. Tamanaka, and S. Harada, "Reliability of Semiconductor Devices Using a Resin Insulation Structure," Hitachi Central Research Laboratories Bulletin, Japan.
3. R. Larsen, *IBM J. Res. Dev.*, **24**, 268 (1980).
4. A. Gregoritsch, Polyimide Passivation Reliability Study, Rel. Physics, 14th Annual Proceedings, 228 (1976).
5. G. Samuelson, *Organic Coatings and Plastics Chemistry*, **43**, 446 (1981).
6. G. Brown, Rel. Physics, 19th Annual Proceedings, Orlando, FL, 282 (1981).
7. E.H. Snow and M. E. Dumesnil, *J. Appl. Phys.*, **37**, 2123 (1966).
8. M. Hudis, "Plasma Treatment of Solid Materials," John Wiley and Sons, New York (1974).
9. H. Schonhorn, S. W. Ryan, and R. H. Hansen, *J. Adhesion*, **2**, 93 (1970).

Dependences of Magnetron-Sputtered SiO_2 Film Properties on Argon Pressure

Toshiaki Yachi and Tadashi Serikawa

Nippon Telegraph and Telephone Public Corporation, Musashino Electrical Communication Laboratory, 3-9-11 Midori-cho, Musashino-shi, Tokyo 180, Japan

Planar magnetron-sputtered SiO_2 films have been found to be desirable as insulating materials in integrated circuits, such as aluminum multilevel interconnections, because of their high deposition rates, very low deposition temperature, and good step coverage (1). Some studies on deposition rates and step coverage, as well as on applications for device fabrication, of such planar magnetron-sputtered SiO_2 films have been reported (2-5). However, dependences of the film properties on deposition conditions have yet to be made sufficiently clear (6). This note describes the dependences of the RF planar magnetron-sputtered SiO_2 film properties on argon pressure.

Experimental

SiO_2 film about 1 μm thick was deposited on (100)-oriented p-type 10 Ω cm resistivity silicon wafers of 3 in. diam by a RF planar magnetron sputtering apparatus with two targets. The system was pumped down to 3×10^{-4} Pa prior to in-bleeding of the argon, and sputtering was carried out at 0.3-2.0 Pa in argon. The barrel-type substrate holder, electrically at floating potential, had a 10 rpm rotation rate during deposition. The minimum spacing between the substrate and the target was 50 mm, and the targets used were 99.99% pure SiO_2 sheets, 5×15 in. and 1/8 in. thick. The RF forward power was held at 2.0 kW/target. The substrate temperature was also kept at 200°C. Some samples were annealed at 900°C for 20 min in nitrogen gas.

Film properties were evaluated by etching rate, transmission electron microscope (TEM) surface replica observation, and stress. Etching rates were determined by the film thickness decrease in 15:10:1 (H_2O:NH_4F:HF) buffered hydrofluoric acid solution at 30°C, which was measured by creating a step and then using the Talystep Height Reader. Film stresses were determined by comparing wafer curvatures before and after deposition, which were measured by the Newton rings method. Film densities were also measured by a gravimetric technique.

Results and Discussion

The SiO_2 film deposition rate *vs.* argon pressure is shown in Fig. 1. The deposition rate is maximum at 0.40 Pa. At an argon pressure above 0.40 Pa, the deposition rate decreases with regularity with an increase in argon pressure. The deposition rate at 2.00 Pa amounts to only about 60% of its maximum. At the higher pressures, this drop is due mainly to increased sputtered-particle scattering resulting from the discharge gas (7).

The dependence of the buffered HF etching rate on argon pressure is shown in Fig. 2, where the samples indicated are deposited and annealed. The etching rates change markedly at the "critical pressure" of about 0.5 Pa. In the as-deposited samples, the etching rate of the film depos-

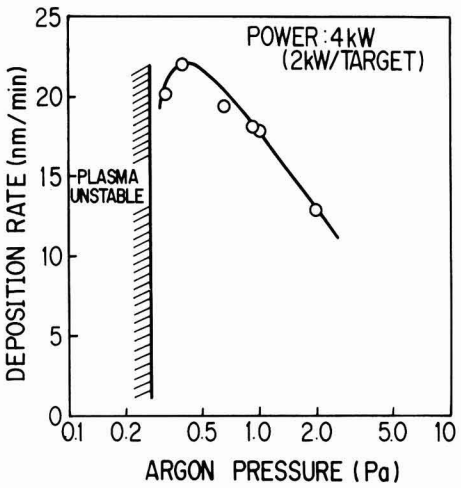


Fig. 1. SiO_2 film deposition rate *vs.* argon pressure

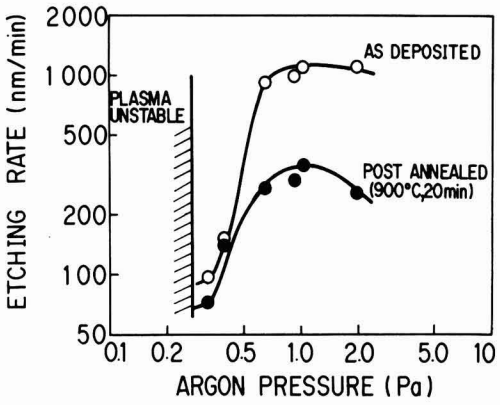


Fig. 2. SiO_2 film etching rates *vs.* argon pressure

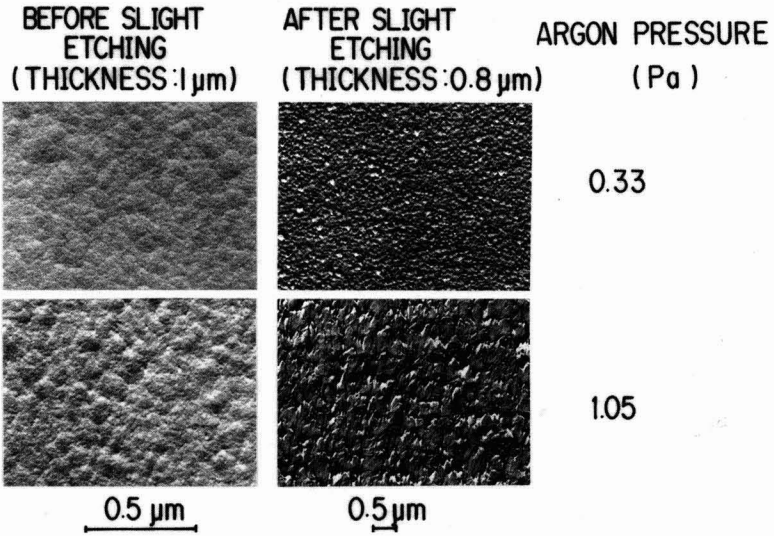


Fig. 3. TEM micrographs of as-deposited SiO_2 films.

ited at an argon pressure of 0.95 Pa is about 12 times greater than that for the film deposited at a pressure of 0.33 Pa. Although these etching rates are reduced over the entire argon pressure by annealing, the etching rate still exhibits a marked dependence on argon pressure.

TEM micrographs for as-deposited film before and after slight etching by buffered HF are shown in Fig. 3. Before slight etching the surfaces of the films deposited at both 0.33 and 1.05 Pa argon pressures show partial undulation. The surface of the film deposited at 1.05 Pa, however, has very small, shallow pits. The slightly etched film surfaces are markedly different for the two pressures. The film surface deposited at 0.33 Pa (below the critical pressure) shows comparatively shallow spherelike pits of about 0.1 μm diam, while the surface of the film deposited at 1.05 Pa (about the critical pressure) shows a deep leaflike roughness of about 0.5 μm overall.

TEM micrographs of annealed film before and after slight etching are also provided in Fig. 4. The films prior to etching indicate a scalelike surface, corresponding to the undulations in the as-deposited film surface. After slight etching, the surface of the annealed film deposited at 0.40 Pa shows spherelike pits as in the as-deposited film, while the surface of the annealed film deposited at 2.00 Pa shows a marked roughness.

The SiO_2 film density also depends on the argon pressure. The density of film deposited at 0.33 Pa is 2.23 g/cm^3, while the density of film deposited at 2.00 Pa is 2.10 g/cm^3. Film density at 0.40 Pa corresponds to the thermally oxidized film density of 2.2 g/cm^3 (8).

TEM micrographs and film density suggest that the marked increase in the etching rate of film deposited above the critical pressure arises mainly from the large amount of internal surface area associated with the microvoids present in these films.

The dependence of SiO_2 film intrinsic stress on argon pressure is shown in Fig. 5. The stresses are compressive. The stress also changes greatly at the critical pressure of about 0.5 Pa.

In a sputter deposition system the sputtered particles are emitted from the target, follow the cosine emission distribution and have an energy value of a few electron

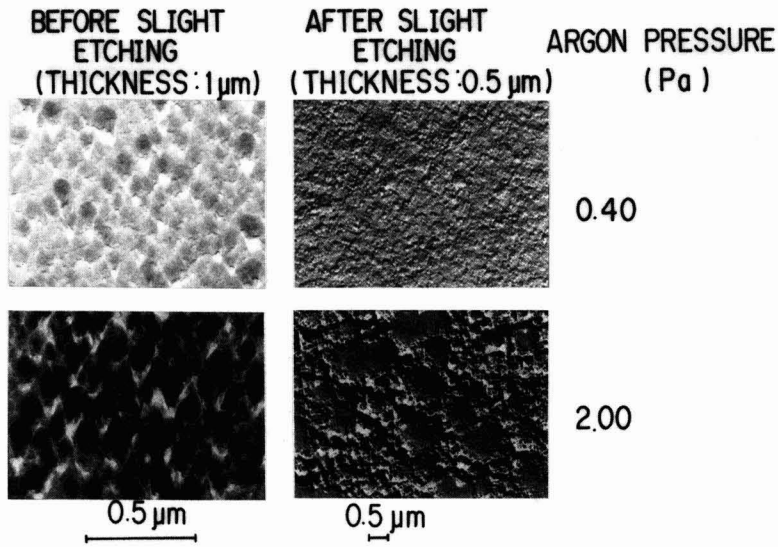


Fig. 4. TEM micrographs of annealed SiO_2 films.

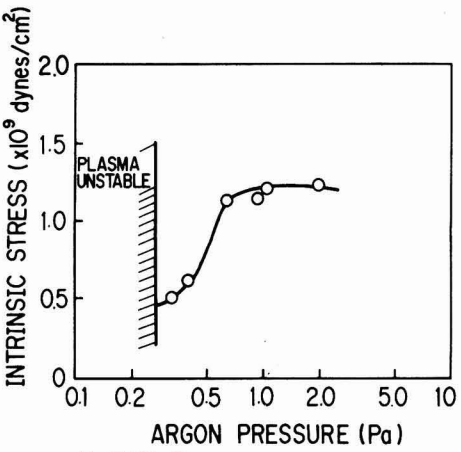


Fig. 5. SiO_2 film stress vs. argon pressure

volts (9). The energy of the emitted particles is reduced, and the direction of the particles changes as a result of gas-phase collisions with the argon atoms, as indicated in Fig. 1, and then reach the substrate. In this way, the energy of the sputtered particles is finally reduced so that it corresponds to the thermal energy of the gas.

Westwood calculated the distances which the particles travel normal to the sputtering target before their energies are reduced to the thermal energy of the gas. The distance increases with the mass and energy of the sputtered particle and with a decrease in argon gas pressure; for a 5 eV particle with a mass 60, the distance is about 8 cm at an argon pressure of 0.5 Pa (10).

The distance of 8 cm is near the space between the target and the substrate. At an argon pressure below the critical pressure 0.5 Pa, many SiO_2 particles reaching the substrate have an energy higher than the thermal energy of the gas. These SiO_2 particles with a higher energy migrate on the substrate; thus, the film contains few microvoids, and the film density increases. At an argon pressure above the critical pressure 0.5 Pa, however, the SiO_2 particle energy is thermalized before the particles reach the substrate and the SiO_2 incident angle distribution is broad. This broad incident angle distribution produces a self-shadowing effect (11). The SiO_2 films contain microvoids, on account of both the low energy of the SiO_2 particle reaching the substrate and the self-shadowing effect. Thus, film density is low. Owing to etching along the microvoids, the films deposited at an argon pressure above the critical pressure 0.5 Pa have a markedly large etching rate. These microvoids can be partially removed by annealing.

In conclusion, the following results are demonstrated: (*i*) The SiO_2 films deposited below the critical pressure are dense (2.23 g/cm³) and have a low etching rate. (*ii*) The SiO_2 films deposited above the critical pressure contain many microvoids and film density decreases to 2.10 g/cm³. Moreover, the etching rate of the films deposited by buffered HF is 12 times greater than that of films deposited below the critical pressure. (*iii*) The stress of SiO_2 film is compressive and increases rapidly with the critical pressure.

Acknowledgment

The authors would like to thank A. Ishimoto and T. Wada for their valuable suggestions and encouragement.

Manuscript received June 11, 1984.

Nippon Telegraph and Telephone Public Corporation assisted in meeting the publication costs of this article.

REFERENCES

1. J. S. Chapin, *IBM J. Res. Dev.*, **18**, 37 (1974).
2. K. Urbanek, *Solid State Technol.*, **20**, 87 (1977).
3. R. A. Larsen, *IBM J. Res. Dev.*, **24**, 268 (1980).
4. T. Serikawa, *Jpn. J. Appl. Phys.*, **19**, L259 (1980).
5. T. Serikawa and T. Yachi, *This Journal*, **128**, 918 (1981).
6. K. Hara, Y. Suzuki, and Y. Taga, *Jpn. J. Appl. Phys.*, **18**, 2027 (1979).
7. S. Schiller, U. Heisig, and K. Goedicke, *Thin Solid Films*, **40**, 327 (1977).
8. A. S. Grove, "Physics and Technology of Semiconductor Devices," Chap. 2, John Wiley and Sons, Inc., New York (1967).
9. G. K. Wehner and G. S. Anderson, in "Handbook of Thin Film Technology," Chap. 3, L. I. Maissel and R. Glang, Editor, McGraw-Hill, New York (1970).
10. W. D. Westwood, *J. Vac. Sci. Technol.*, **15**, 1 (1978).
11. N. G. Nakhodkin and A. I. Shaldervan, *Thin Solid Films*, **10**, 109 (1972).

The Growth of Epitaxial Layers of $Ga_{0.47}In_{0.53}As$ by the Vapor-Phase Epitaxy-Hydride Method Using a Gallium-Indium Alloy Source

Thomas E. Erstfeld and Kenneth P. Quinlan*

Rome Air Development Center, Solid State Sciences Division, Hanscom Air Force Base, Massachusetts 01731

Epitaxial structures of the ternary system, $Ga_{0.47}In_{0.53}As$, have found wide application in the fields of optoelectronic and microwave devices. These epitaxial layers have been prepared by various techniques: liquid-phase epitaxy (1), vapor-phase epitaxy (2), molecular beam epitaxy (3), and metal-organic chemical vapor deposition (4). All these methods have produced $Ga_xIn_{1-x}As$ layers with room temperature mobilities in the 10,000 cm²/V-s range, with a high of 13,000 cm²/V-s for the liquid-phase epitaxy (3, 5-7). Carrier concentrations ranged from 10^{15} cm^{-3} to the mid-10^{16} cm^{-3}.

The vapor-phase epitaxy (VPE) technique uses either $AsCl_3$ (chloride method) or AsH_3 (hydride method) as the source of arsenic. Higher mobilities have usually been achieved with the chloride method (8, 9) but the hydride method has many advantages that the chloride method lacks, *e.g.*, ease of control, group V reactants are gaseous, etc. Most work with the VPE-hydride technique for the preparation of $Ga_{0.47}In_{0.53}As$ have concentrated on the use of separate metallic sources for the group III elements with a double-barrel reactor. The use of an alloy source in the VPE-hydride technique offers two distinct advantages over the use of two separate metal sources: (*i*) the flow of hydrogen chloride over the source does not have to be as finely controlled as is necesssary with separate metallic sources, and (*ii*) only a single-barrel reactor is needed. A study of the preparation of $Ga_xIn_{1-x}As$ ternaries using an alloy source (Ga-In) with the VPE-hydride technique was carried out in order to evaluate the technique. This paper reports the effect of various parameters, *e.g.*, source composition, hydrogen chloride pressure, deposition temperature, and operation time on the ternary compositions and growth rates.

*Electrochemical Society Active Member.

The use of an alloy source for the preparation of $Ga_xIn_{1-x}As$ by the VPE technique has been studied by a number of investigators. In 1965, Minden (10) used an alloy source of gallium and indium in a modified VPE-chloride method to prepare epitaxial layers of the ternary. Recently, Chatterjee *et al.* (11) studied the use of the alloy with a modified VPE-chloride technique and presented a thermodynamic model describing the system. They demonstrated that a low doped, lattice-matched gallium indium arsenide epilayer could be obtained in a reproducible and controlled manner. Kordos *et al.* (12) studied the growth of $Ga_xIn_{1-x}As$ with the VPE-hydride system using a Ga-In alloy. Their results differ from those reported in this paper.

Experimental

The preparation of the epitaxial layers of the ternaries, $Ga_xIn_{1-x}As$, was studied in the quartz reactor previously described (9). The quartz reactor has three temperature zones, source, mixing, and deposition, which are heated by "clam shell" resistance heaters. The reactor has three inlet flow systems for AsH_3/H_2, HCl/H_2, and H_2. The flow rates are regulated by Tylan mass flow controllers. The reactants are the highest purity products obtainable: arsine (99.998%), as a 10% mixture in hydrogen (99.999%), hydrogen carrier gas (99.999%), hydrogen chloride (99.995%), indium (99.9999%), and gallium (99.9999%). The hydrogen carrier gas was further purified by a hydrogen purifier (Palladium Diffusion Process-Engelhard). The alloys were prepared by putting the appropriate amounts of the metals into a quartz boat. The masses of the alloys used varied between 99 and 107g. The surface areas of the alloys in the quartz boats were approximately 26 cm^2. The alloys were prebaked for 50h in a hydrogen atmosphere before any runs were performed. This procedure as reported by Kordos *et al.* (12) lowers the carrier concentrations in the resulting epitaxial layers.

Compositions of the grown ternaries of $Ga_xIn_{1-x}As$ were determined from Vegard's law plots of lattice constants *vs.* compositions. The lattice constants were determined by x-ray diffractometry with the CuKα irradiation using InP as an internal standard. Microprobe analyses verified this method of determining the composition. The growth rates were determined from the surface area of the substrate, mass of deposit, density of the ternary, and time duration of growth. The time of growth was usually 225 min.

The substrates were prepared from a liquid-encapsulated Czochralski (LEC)-grown InP(Fe-doped) boule. Slices were cut 3° off the (100) plane towards the (111) plane. The preparation of the InP substrates are described in Ref. (9).

Carrier concentrations (n) and mobilities (μ) were obtained from resistivity and Hall measurements at room temperature with the van der Pauw technique (13). A permanent magnet provided a field of 3 kG for the Hall measurements.

The residual compositions of the Ga-In alloys were determined by atomic absorption spectroscopy. The alloys for the analyses were remelted and quenched at 0°C to prevent formation of Ga-In solid solutions. During the course of a series of runs, the alloy becomes richer in indium content.

Results and Discussion

Various parameters were studied initially to determine the parameter values which produce high quality epitaxial layers with consistent growth rates. Superior quality epitaxial layers of the ternary, $Ga_xIn_{1-x}As$, were obtained when the source, mixing, and deposition temperatures were 800°C, 850°C, and 700°C, respectively. The partial pressures of hydrogen chloride in these preliminary experiments were in the vicinity of 233 Pa. The partial pressure of AsH_3 was 1013 Pa, while the flow rate of hydrogen carrier gas was 980 cm^3/min. The arsine and hydrogen were maintained at these values throughout the study. The x-ray diffractometry studies used for the determination of the lattice constants showed that the layers were normally of high quality and uniform composition. After these preliminary results were obtained, the determination of the alloy composition required to give a specific ternary composition of $Ga_xIn_{1-x}As$ was undertaken. Growth rates of the ternary systems were determined as function of hydrogen chloride partial pressure and deposition temperature.

Figure 1 shows the composition of the ternary, $Ga_xIn_{1-x}As$, obtained as a function of the alloy composition. The values depicted are for a deposition temperature of 700°C and a hydrogen chloride partial pressure of 233 Pa. The plot of the experimental data intersecting the $Ga_{0.47}In_{0.53}As$ composition line gives a value of 12.2 mole percent (m/o) gallium-87.8 m/o indium as the alloy necessary to prepare this ternary. The theoretical curve (Fig. 1) calculated from thermodynamic data shows that kinetic factors probably play a role in the deposition process. The differences between theory and experiment may not only be due to kinetic factors but may also be due to errors in the literature used in the calculation of thermodynamic values. Faktor and Haigh (14) have shown that errors in the literature can result in derived thermodynamic values that are inaccurate. Kordos *et al.* (12) reported that 7 m/o in the alloy produces the $Ga_{0.47}In_{0.53}As$ ternary. This large discrepancy between 7 m/o and that found in the present work (12.2 m/o) is not understood.

The compositions of the ternaries were studied as a function of the number of runs with an alloy. The plots obtained are shown in Fig. 2 and are typical of the ternary composition found for various alloys. Figure 2 shows the ternary compositions obtained from the two alloy compositions, 11.5 m/o Ga and 11.9 m/o Ga. The data show that the average composition of the ternaries exhibits a slight increase in the indium content as more runs are performed. An increase in the indium content of the ternary was expected since an analysis of an alloy after 30h of reaction time showed that the mole fraction of indium had increased by 4%. This is in agreement with the extrapolated value of 2% from the data of Chatterjee *et al.* (11). The data presented in Fig. 2 show that at least 14 samples lattice-matched to InP can be obtained with the same alloy.

Epitaxial layers with a value of $|\Delta a/a| < 10^{-3}$ are considered to be lattice-matched to InP. These values of $\Delta a/a$ correspond to $Ga_xIn_{1-x}As$ layers that range in composition from $Ga_{0.45}In_{0.55}As$ to $Ga_{0.49}In_{0.51}As$. Inspection of Fig. 1 illustrates that alloy compositions with a gallium content between 11.9 and 12.9 m/o are capable of producing

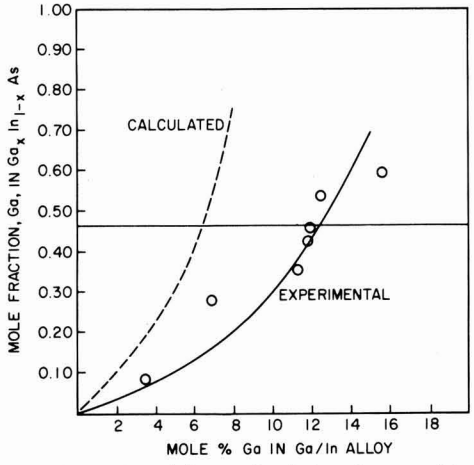


Fig. 1. Compositions of the ternaries, $Ga_xIn_{1-x}As$, prepared from various alloy (Ga-In) mixtures. ---: Theory. ○——○: Experimental. AsH_3 = 1013 Pa; HCl = 233 Pa; H_2 = 980 cm^3/min. Deposition temp. = 700°C; mixing temp. = 850°C; source temp. = 800°C.

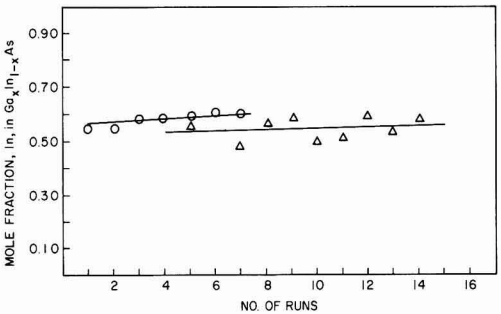


Fig. 2. Mole fraction of indium in $Ga_xIn_{1-x}As$ as a function of the number of runs. ○——○: Alloy composition = 11.5 m/o Ga + 88.5 m/o In. △——△: Alloy composition = 11.9 m/o Ga + 88.1 m/o In. AsH_3 = 1013 Pa; HCl = 233 Pa; H_2 = 980 cm³/min. Deposition temp. = 700°C; mixing temp. = 850°C; source temp. = 800°C.

$Ga_xIn_{1-x}As$ epitaxial that are lattice-matched to InP. The series of runs shown in Fig. 2 with an alloy composition of 11.9 m/o gallium produced epitaxial films that were lattice-matched to InP only one-third of the time. The values for the indium mole fraction in these samples ranged from 0.48 to 0.60, indicating the lack of reproducibility in these types of experiments. An important aspect of this type of work is depicted in these results, where a certain amount of scatter is observed in the composition of the epitaxial layers from one run to the next. This scatter may be attributed to the free radical nature of these reactions. Various workers (15) have shown that changes in the surfaces of a reactor greatly influence the course of free radical reactions. The surfaces of the reactors used for epitaxial growth undergo constant change when the different parameters of the system are varied. This scatter may account for the lack of observation of the increase in indium content for the ternaries obtained in the series of 25 runs reported by Kordos *et al.* (12).

The growth rates of the ternary, $Ga_xIn_{1-x}As$, were determined as functions of the source hydrogen chloride partial pressure and deposition temperature. Hydrogen chloride reacts with gallium and indium in the alloy to form GaCl(g) and InCl(g). The metal chlorides react with As_4(g) at the InP-substrate surface in the deposition zone to form $Ga_xIn_{1-x}As$. The growth rates of various epitaxial layers grown from different alloy compositions as a function of HCl partial pressure are shown in Fig. 3. These results were obtained at a source temperature of 800°C a mixing temperature of 850°C, and a deposition temperature of 700°C. The decrease in growth rate below ~ 233 Pa is probably due to the corresponding decrease in the concentration of the monochlorides of the group III elements being formed. The decrease in growth at HCl partial pressures greater than ~ 233 Pa may be due to the occupancy of the available arsenic adsorption sites by either the metallic monochlorides or hydrogen chloride molecules or both which inhibit the deposition reactions. This mechanism has been clearly described by Shaw (16, 17).

The maximum growth rates for the ternaries were obtained when the partial pressure of the hydrogen chloride was in the vicinity of 233 Pa. These growth rates for the various ternary compositions were investigated at 700°C and 725°C, and the results are presented in Table I. The growth rate increases when the temperature is increased from 700° to 725°C, indicating that the growth is occurring in the kinetic-limited region. The table shows that the growth rates of $Ga_xIn_{1-x}As$ ternaries having indium mole fractions of 0.42-0.63 remain relatively constant at the two temperatures. These ternaries were prepared from alloy source compositions ranging from 15.9 to 11.1 m/o gallium. The ternaries, $Ga_{0.29}In_{0.71}As$ and $Ga_{0.08}In_{0.92}As$, produced from alloy sources of 6.9 and 3.2 m/o gallium, respectively, exhibited higher growth rates. InAs (18) has been shown to have a higher growth rate than GaAs (19)

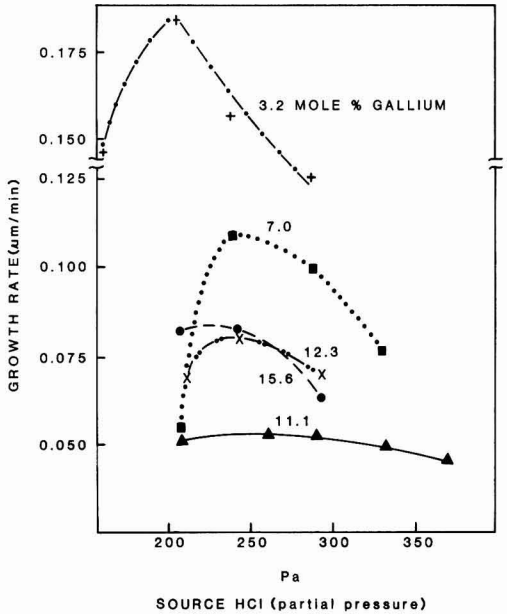


Fig. 3. Growth rate of epitaxial layers of $Ga_xIn_{1-x}As$ as a function of source HCl partial pressure using different alloys. AsH_3 = 1013 Pa; H_2 = 980 cm³/min. Deposition temp. = 700°C; mixing temp. = 850°C; source temp. = 800°C. Compositions of layers prepared from the various alloys given in Table I.

in their homoepitaxial growth by the VPE-chloride technique.

Data showed that varying the partial pressure of the source hydrogen chloride had no effect on the composition of the epitaxial layer which is formed. This would be expected, because the ratio of GaCl(g) to InCl(g) would be independent of HCl partial pressures. No definite trend could be found in our work for the effect of deposition temperature on the composition of the epitaxial layer. Experiments carried out at 750°C showed no effect on the composition. This was not surprising since the temperature coefficient of the compositional ratio of GaAs/InAs is very small (11). Kordos *et al.* (12) reported a 0.1% increase in gallium content of the ternary per degree.

The average energy of activation for the data presented in Table I is 170 kJ/mole. Activation energies of the formation of the epitaxial layers were obtained from Arrhenius plots of growth rates *vs.* reciprocal of the deposition temperatures. A value of 180 kJ/mol was found for the energy of activation for $Ga_{0.53}In_{0.47}As$ prepared from a 12.3 m/o Ga alloy. This value is in close agreement with the value of 44 kcal/mol (184 kJ/mol) reported by Hyder *et al.* (20). These authors used the VPE-hydride technique with separate metal sources.

Table I. Growth rates of $Ga_xIn_{1-x}As$ formed from various alloy compositions at two deposition temperatures. HCl partial pressure = 233 Pa, AsH_3 partial pressure = 1013 Pa, and H_2 flow rate = 980 cm³/min. Source temp. = 800°C, mixing temp. = 850°C, and deposition temp. = 700° and 725°C.

Alloy composition (m/o Ga)	$Ga_xIn_{1-x}As$	Growth rate at 700°C (μ/min)	Growth rate at 725°C (μ/min)
15.6	$Ga_{0.58}In_{0.42}As$	0.08	0.13
12.3	$Ga_{0.53}In_{0.47}As$	0.08	0.14
11.9	$Ga_{0.46}In_{0.54}As$	0.08	0.12
11.5	$Ga_{0.43}In_{0.57}As$	0.08	0.11
11.1	$Ga_{0.37}In_{0.63}As$	0.05	0.11
7.0	$Ga_{0.29}In_{0.71}As$	0.11	—
3.2	$Ga_{0.08}In_{0.92}As$	0.19	—

Table II. Carrier concentrations (n) and mobilities (μ) of various ternaries at room temperature

Ternary	n (cm^{-3})	μ (cm^2/V-s)
$Ga_{0.56}In_{0.44}As$	2.6×10^{15}	3982
$Ga_{0.52}In_{0.48}As$	4.4×10^{15}	4164
$Ga_{0.51}In_{0.49}As$	2.0×10^{15}	6601
$Ga_{0.45}In_{0.55}As$	2.4×10^{15}	5947
$Ga_{0.44}In_{0.56}As$	5.6×10^{15}	3064
$Ga_{0.41}In_{0.59}As$	3.4×10^{15}	7204
$Ga_{0.40}In_{0.60}As$	5.8×10^{15}	4991
$Ga_{0.39}In_{0.61}As$	8.4×10^{15}	3722

The carrier concentrations (n) and mobilities (μ) were determined for a series of samples and are reported in Table II. The results represent the average of a number of determinations for many of the ternaries. The carrier concentrations all fall in the vicinity of 4.0×10^{15} cm^{-3}, while the mobilities range 3064-7204 cm^2/V-s. A plot of the mobility *vs.* layer composition exhibits a curve with the appearance of two maxima. Whiteley and Ghandhi (21) reported a similar-type plot with less pronounced maxima and observed their highest mobility with a layer composition corresponding to $Ga_{0.42}In_{0.58}As$. The best values obtained in the present study for n and μ were 2.8×10^{15} cm^{-3} and 8852 cm^2/V-s, respectively, for a sample whose composition was $Ga_{0.41}In_{0.59}As$. These higher mobilities when In > 0.53 have been attributed to less dislocation formation in layers under compressive stress (22). The present results compare favorably to the values previously reported: Kordos *et al.* (12) reported a value of 4000 cm^2/V-s for the mobility for the $Ga_{0.41}In_{0.59}As$. Towe (23, 24) obtained a value of 9400 cm^2/V-s for the mobility with a carrier concentration of 6.4×10^{15} cm^{-3} at room temperature for the composition $Ga_{0.47}In_{0.53}As$. Towe prepared the ternary with the VPE-hydride technique using two metal sources. Cheng and Cho (3) prepared $Ga_{0.47}In_{0.53}As$ (Si-doped) by the MBE method and reported values of μ = 8500 cm^2/V-s and $n = 1 \times 10^{16}$ cm^{-3} at room temperature. A high value of 13,800 cm^2/V-s for the mobility (with $n = 1.9 \times 10^{15}$ cm^{-3}) at room temperature has been reported by Oliver and Eastman (6) for LPE prepared $Ga_xIn_{1-x}As$. The MOCVD technique for the growth of $Ga_{0.47}In_{0.53}As$ used by Whiteley and Ghandhi (21) gave values of 5800 cm^2/V-s and mid-10^{16} cm^{-3} for μ and n at room temperature, respectively. These comparisons show that the system using the alloy source can be used to grow high quality $Ga_xIn_{1-x}As$ epitaxial layers.

Recent analyses of the different techniques to grow epitaxial layers of the III-V compounds have shown that the roles of VPE, MOCVD, and MBE are expected to increase greatly (25) in the future. The present study shows that the VPE-hydride technique can be simplified by the use of an alloy source with no loss in the quality of the epitaxial layers. Further work with this system should give carrier concentrations and mobilities equal to those produced by the LPE technique.

Acknowledgments

The authors gratefully acknowledge the help provided by Jane A. Horrigan in performing x-ray analyses of these samples. Van der Pauw measurements were performed by Joseph P. Lorenzo and Captain Kenneth J. Soda. Single-crystal InP substrates were grown and polished by Brian S. Ahern. The authors also wish to acknowledge the help and advice obtained from William D. Potter and John K. Kennedy through discussions with them. Finally, the authors wish to thank the team of A. K. Chatterjee, M. M. Faktor, M. H. Lyons, and R. H. Moss and the team of P. Kordos, P. Schumbera, M. Heyen, and P. Balk, both of whom were kind enough to send us preprints of their work on the growth of InGaAs from an alloy source.

Manuscript submitted Nov. 14, 1983; revised manuscript received June 11, 1984. This was paper 344 presented at the San Francisco, California, Meeting of the Society, May 8-13, 1983.

Rome Air Development Center assisted in meeting the publication costs of this article.

REFERENCES

1. N. Chand, A. V. Syrbu, and P. A. Houston, *Electron. Lett.*, **18,** 613 (1982).
2. N. Susa, Y. Yamauchi, H. Ando, and H. Kanbe, *Jpn. J. Appl. Phys.*, **19,** L17 (1979).
3. K. Y. Cheng and A. Y. Cho, *J. Appl. Phys.*, **53,** 4411 (1982).
4. J. S. Whiteley and S. K. Ghandhi, *This Journal*, **129,** 383 (1982).
5. S. Y. Narayan, T. P. Paczkowski, S. T. Jolly, E. P. Bertin, and R. T. Martin, *RCA Rev.*, **42,** 491 (1981).
6. J. D. Oliver and L. F. Eastman, *J. Electron, Mater.*, **9,** 693 (1981).
7. M. Razeghi, M. A. Poisson, P. Hirtz, B. de Cremoux, and J. P. Duchemin, Abstract I-2, p. 49, Electronic Materials Conference, Technical Abstracts, Colorado State University, Fort Collins, CO, June 23-25, 1982.
8. K. Fairhurst, D. Lee, D. S. Robertson, H. T. Parfitt, and W. H. E. Wilgross, in "Proceedings of the 1980 NATO Sponsored InP Workshop, RADC-TM-80-07 (June, 1980)," Rome Air Development Center, Hanscom AFB, MA (1980)
9. T. E. Erstfeld and K. P. Quinlan, *J. Electron. Mater.*, **11,** 647 (1982).
10. H. T. Minden, *This Journal*, **112,** 300 (1965).
11. A. K. Chatterjee, M. M. Faktor, M. H. Lyons, and R. H. Moss, *J. Cryst. Growth*, **56,** 591 (1982).
12. P. Kordos, P. Schumbera, M. Heyen, and P. Balk, in "Proceedings of the International Conference on GaAs and Related Compounds," T. Sugano, Editor, p. 131, The Institute of Physics (Bristol), No. 63, Japan (1981).
13. L. J. van der Pauw, *Philips Res.* Rep., **13,** 1 (1958).
14. M. M. Faktor and J. Haigh, *J. Cryst. Growth*, **58,** 291 (1982).
15. A. F. Trotman-Dickenson, "Gas Kinetics," p. 152, Academic Press, New York (1955).
16. D. W. Shaw, *This Journal*, **117,** 683 (1970).
17. D. W. Shaw, *J. Cryst. Growth*, **31,** 130 (1975).
18. O. Mizuno, H. Watanabe, and D. Shinoda, *Jpn. J. Appl. Phys.*,**14,** 184 (1975).
19. M. Makagawa and H. Ikoma, *ibid.*, **10,** 1345 (1971).
20. S. B. Hyder, R. R. Saxena, S. H. Chiao, and R. Yeats, *Appl. Phys. Lett.*, **35,** 787 (1979).
21. J. S. Whiteley and S. K. Ghandhi, *This Journal*, **130,** 1191 (1983).
22. B. I. Miller and J. H. McFee, *ibid.*, **125,** 1310 (1978).
23. E. Towe, *J. Appl. Phys.*, **53,** 5136 (1982).
24. E. Towe, M. S. Thesis, MIT, Cambridge, MA (1981).
25. J. M. Woodall, *Science*, **208,** 908 (1980).

Hot Wall Si-CVD at Reduced Pressures

C. Domínguez,[1] G. Pastor, E. Lora-Tamayo, and E. Domínguez

U.E.I. Microelectrónica, I.E.C. (C.S.I.C.), Madrid, Spain

In this technical note, results are given for silicon deposition in a hot-wall reactor at basic pressures of 10 and 76 torr and a temperature of 1223 K. Various initial gas mixtures were used (SiH_2, $Cl_2/HCl/H_2$, $SiH_2Cl_2/SiHCl_3/SiCl_4/HCl/H_2$, $SiHCl_3/H_2$, and SiH_2Cl_2/H_2).

The system used for our experiments consisted of a reaction chamber, a vacuum system, and a gas system. The reaction chamber contained a 100 mm id quartz tube heated by a conventional diffusion furnace. The four heating zones this system provided guaranteed constant temperature over a length of 70 cm (with variations below 0.2%). The temperature profile was measured using a thermocouple (Pt-Pt 10% Rh) located inside the reactor under deposition conditions. The vacuum system consisted of a rotary pump in series with a variable-speed roots blower with a throttle valve. This provided a wide range of working pressures. The pressure was measured using two Baratron MKS pressure gauges, one for high ranges and one for low ranges. Chlorosilanes used for our experiments were SiH_2Cl_2, $SiHCl_3$, and $SiCl_4$, as well as HCl and H_2. Flow was measured and regulated using a mass-flow controller for gases and a vaporizer-type controller for liquid sources. All gases used were electronic-grade pure. For H_2, a palladium cell purifier was used.

The depositions were made at a maximum flow of 2500 sccm, total pressures of 10 and 76 torr, and a gas temperature of 1223 K. Wacker Chemitronic silicon (100) wafers were placed vertically parallel or perpendicular to the gas flow, and no significant variations in the growth rate were observed.

The experiments were performed taking as a base the results obtained through a model (1) analogous to the one used by Sirtl and Hunt (2) and Van der Putte *et al.* (3). This program calculated the partial pressures of all the components of a gaseous mixture in equilibrium with solid silicon for the Si-H-Cl system. Results were obtained through the solution of a nonlinear system of equations generated by the application of the mass-action law to the formation reactions of the different components, starting from the elements. The pressure, temperature, and Cl/H ratio were used to define the composition of the gaseous phase.

To determine which type of thermodynamic equilibrium existed in the Si-H-Cl system, different series of experiments were performed, based on data provided by the model.

Series A: $SiH_2Cl_2/HCl/H_2$.—For the first group of experiments, a mixture of SiH_2Cl_2, HCl, and H_2 was introduced into the system at the appropriate flow, under the equilibrium condition for each Cl/H ratio, and under successive situations of Si supersaturation at normal pressures of 10 and 76 torr. None of the experiments, despite having reached Si supersaturation levels [values above the equilibrium given by the model (1)] of close to 100%, revealed appreciable deposition or significant etching of the wafers. These results did not agree with model (1) for these conditions.

Series B: $SiH_2Cl_2/SiHCl_3/SiCl_4/HCl/H_2$.—These compounds were introduced simultaneously in the reactor in a proportion that anticipated this equilibrium (although the Si supersaturation was gradually increased). The experiments in this case continued to provide negative results.

Series C: SiH_2Cl_2/H_2.—Figure 1 shows the silicon growth rate for different SiH_2Cl_2 and H_2 flows (without HCl) at a total pressure of 10 torr. Growth rates were much higher than those observed when HCl was present.

Series D: $SiHCl_3/H_2$.—Figure 2 shows the results of these experiments, together with those of SiH_2Cl_2 and H_2 at 76 torr. We found growth that was different from the series $SiH_2Cl_2/H_2/HCl$ under the same total pressure, temperature, and Cl/H ratio conditions. The crystalline structure was determined using x-ray diffraction, and polycrystalline silicon was obtained in every case.

It can be deduced from the analysis of prior experiments that, at equal or lower pressures of 76 torr, the growth rate is almost zero in the presence of HCl in the initial mixture and is considerably higher in the absence of HCl. Hence, the introduction of HCl in the initial mixture can be said to cause a drastic decrease of the growth rate.

We found that the growth rate, G, depends on the total flow in equilibrium, C_T^e, and on partial pressures of $SiCl_2$, H_2, P_{SiCl_2}, and P_{H_2}. The dependence can be expressed as

$$G = k(C_T^e)^{\beta} (P_{SiCl_2})^{\gamma} (P_{H_2})^{\delta} \quad [1]$$

where e expresses equilibrium values, k is a constant that depends on nucleation, and β, γ, and δ are exponents to be determined. Total flow in the equilibrium can be expressed as

$$C_T^e = C_{SiCl_2}^e + C_{H_2}^e \quad [2]$$

where $C_{SiCl_2}^e$ is equal to the initial dichlorosilane flow because, under experimental conditions, the equilibrium dissociation constant of equation

$$SiH_2Cl_{2(g)} \rightarrow SiCl_{2(g)} + H_{2(g)} \quad [3]$$

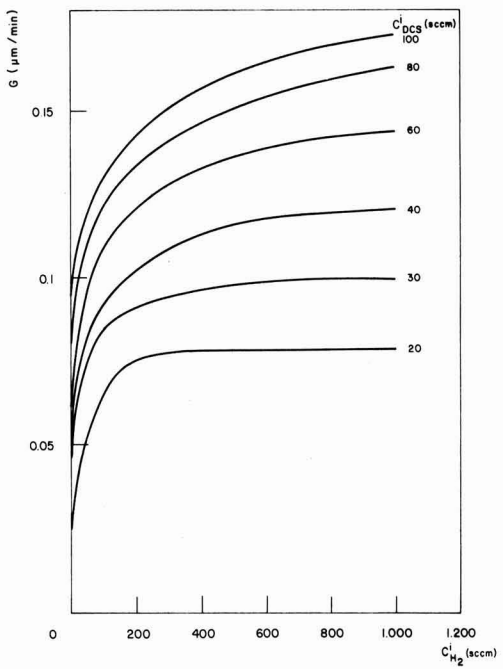


Fig. 1. Silicon growth rate under hydrogen flows for different dichlorosilane flows at 10 torr and 1223 K.

[1]Present address: Department of Inorganic Chemistry, Complutense University, Madrid, Spain.

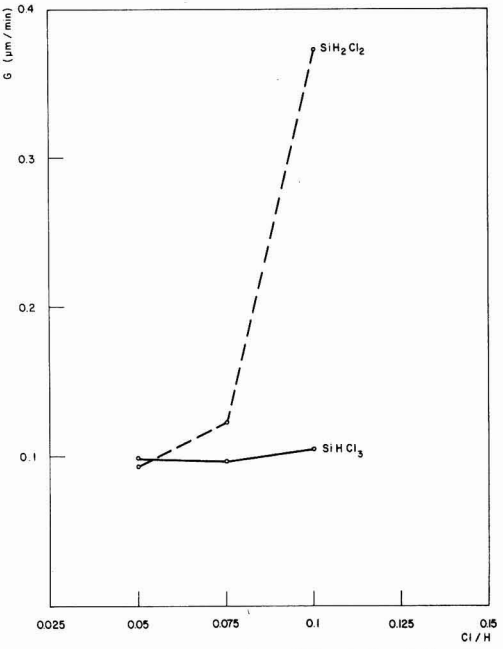


Fig. 2. Silicon growth rate under a Cl/H ratio for dichlorosilane-hydrogen and trichlorosilane-hydrogen at 76 torr and 1223 K.

is 3.322, and the degree of dissociation, without hydrogen and with it, is about 100%. $C_{H_2}{}^e$ is therefore

$$C_{H_2}{}^e = C_{H_2}{}^i + C_{DCS}{}^i \qquad [4]$$

In other words, it is the sum of the initial hydrogen flows, i, and those obtained from the dissociation of dichlorosilane as a result of the dissociation reaction [3]. Equation [1] can be expressed as

$$G = k' C_T{}^{e\beta} \left(\frac{C_{SiCl_2}{}^e}{C_T{}^e}\right)^{\gamma} \left(\frac{C_{H_2}{}^e}{C_T{}^e}\right)^{\delta} \qquad [5]$$

where $(C_T{}^e)^\beta$ reflects diffusion dependence, and $(C_{SiCl_2}{}^e/C_T{}^e)^\gamma$ $(C_{H_2}{}^e/C_T{}^e)^\gamma$ reflects superficial adsorption of $SiCl_2$ and H_2. The experimental values of the exponents are $\beta = 0.54$, $\gamma = 0.56$, and $\delta \simeq 1$.

In summary, it has been confirmed that, at low pressures, the presence of HCl in the initial mixture produces silicon growth rates that are practically nil or negative for a supersaturation range of 0% to 120%. This result does not agree with the data based on the classic model of calculating the equilibrium for the Si-H-Cl system. In addition, a change in the silicon growth rate has been noted, according to the source of the silicon used in the initial mixture, so that a growth rate three times higher is obtained when SiH_2Cl_2/H_2 mixtures are used instead of $SiHCl_3/H_2$.

Finally, the silicon growth rate has been studied at a pressure of 10 torr and a temperature of 1223 K, with SiH_2Cl_2/H_2 mixtures and an LPCVD system modified in accordance with experimental conditions. The experimental results make it possible to determine the dependence of the silicon growth rate on the total flow and the partial pressures of $SiCl_2$ and H_2 in equilibrium. We have assumed that $SiCl_2$ comes mainly from the thermal decomposition of SiH_2Cl_2.

Manuscript submitted Jan. 3, 1983; revised manuscript received May 25, 1984.

U.E.I. Microelectrónica IEC assisted in meeting the publication costs of this article.

REFERENCES

1. G. W. H. Staarink and F. Jakma, Private communication.
2. E. Sirtl, L. P. Hunt, and D. H. Sawyer, *This Journal*, **121**, 919 (1974).
3. P. Van der Putte, L. J. Giling, and J. Bloem, *J. Cryst. Growth*, **31**, 299 (1975).

JOURNAL OF THE ELECTROCHEMICAL SOCIETY

COMMENTS

NOVEMBER 1984

Each issue of the **Journal** will have a section of "Comments." In this section, we provide a means via short pieces, *i.e.*, one column or less, to applaud, dispute, or otherwise discuss the papers published in the **Journal.** Space will be provided for one response by the paper's author(s) to each comment.

Since space available in each issue for the "Comments" section is limited; it is important to be concise.

Comments should be sent to the Editor, Dr. Norman Hackerman, President's Office, Rice University, P.O. Box 1892, Houston, TX 77251.

This is the second appearance of the "Comments" section.

Norman Hackerman
Editor

Sputter-Etching Planarization for Multilevel Metallization

H. Kotani, H. Yakushiji, H. Harada, K. Tsukamoto, and T. Nishioka
(pp. 645-648, Vol. 130, no. 4)

J. H. Thomas III and J. L. Vossen:[1] We should like to point out that the model employed by the authors for the variation of the sputtering yield with the angle of incidence of the bombarding ions is not applicable as a general model for all materials and bombarding species and energies.

The Sigmund theory[2] predicts a change in sputtering yield that rises as the angle of incidence increases, peaks, and then falls to zero at glancing incidence. The rate of increase and the angular position of the peak value depend upon the energy of the incident ions, the mass of the incident ion (as compared to the target atoms), and the target material. It has been verified both by computer simulation and experiment that the angle at which the peak sputtering yield occurs is between about 45° and 80°, depending on the conditions and materials involved.[3]

The authors' finding that the 45° facet angle developed in their experiment should be considered specific to the material being etched (SiO_2) and to the bombarding conditions used (which were not specified), and should not be extrapolated to other materials and bombarding conditions.

H. Kotani, H. Yakushiji, K. Tsukamoto, T. Nishioka,[4] and H. Harada:[5] We agree with the comments that the values of our results are specific and are not necessarily applicable to all materials and bombarding conditions. We consider the exact value of the facet angle in our experiments insignificant. It should be emphasized that the sputter etching in our experiment provides smooth surfaces and develops facets with angles of around 45°.

[1]RCA Laboratories, Princeton, New Jersey 08540.

[2]P. Sigmund, *Phys. Rev.*, **184**, 383 (1969).

[3]P. D. Townsend, J. C. Kelly, and N. E. W. Hartley, "Ion Implantation, Sputtering and their Applications," p. 126, Academic Press, New York (1976); M. Kaminsky, "Atomic and Ionic Impact Phenomena on Metal Surfaces," pp. 159-163, Academic Press, New York (1965); H. H. Anderson and H. L. Bay, in "Sputtering by Particle Bombardment," Vol. 1, R. Behrisch, Editor, pp. 200-203, Springer-Verlag, Berlin (1981); C. M. Melliar-Smith and C. J. Mogab, in "Thin Film Processes," J. L. Vossen and W. Kern, Editors, pp. 523-525, Academic Press, New York (1978); J. P. Ducommun, M. Cantagrel, and M. Moulin, *J. Mater. Sci.*, **10**, 52 (1975); J. L. Vossen, *J. Phys. E*, **12**, 159 (1979); H. Dimigen, H. Luthje, H. Hubsch, and V. Convertini, *J. Vac. Sci. Technol.*, **13**, 976 (1976); P. G. Glöerson, *ibid.*, **12**, 28 (1975); H. Dimigen and H. Luthji, *Philips Tech. Rev.*, **35**, 199 (1975).

[4]Mitsubishi Electric Corporation, LSI Research and Development Laboratory, 4-1 Muzuhara, Itami, Hyogo 664, Japan.

[5]Mitsubishi Electric Corporation, Kitaitami Works, 4-1 Mizuhara, Itami, Hyogo 664, Japan.

Electrical Properties of Post-Annealed Thin SiO_2 Films

S. S. Cohen
(pp. 929-932, Vol. 130, no. 4)

P. A. Heimann:[6] The author of this paper does not mention any checks for the presence of sodium, which might be present since the oxidations were done without HCl. In fact, the hysteresis of the C-V curves is in the direction which would be expected for mobile ions in the oxide. He assumes that this hysteresis is due to a layer of SiO at the oxide/silicon interface. However, stoichiometric SiO is not known to exist in the solid phase. The author does not give any reason for expecting that an oxygen-deficient layer (SiO_x) should contain "slow" charge trapping sites.

The author describes a cold trap for removing residual water from the oxygen, but he does not mention whether any other precautions were taken to keep water out. For instance, a double-walled quartz tube is often used to prevent atmospheric moisture from diffusing through the hot fused-silica furnace tube. Irene[7] has shown that low concentrations of moisture can improve the breakdown voltages of thin oxides. This effect becomes probable for the very long annealing times described in this paper, so it is uncertain whether the improvement seen here is due to the annealing ambient or to trace moisture. This residual moisture could also affect the results of the second oxidation step, even if dry oxygen is being used.

The author might be underestimating the actual breakdown fields by choosing a breakdown definition of 1 μA. It is easy to pass currents much greater than 1 μA through thin oxides by Fowler-Nordheim tunneling without having catastrophic breakdown. The author should use a breakdown criterion that distinguishes between Fowler-Nordheim tunneling and irreversible breakdown.[8] The breakdown histograms in his Fig. 3-5 probably should show higher breakdown fields.

S. S. Cohen:[9] The following clarifications are provided to answer the comments made by P. A. Heimann about my paper.

1. Routine bias-temperature stress measurements were made in the course of the investigations to demonstrate that sodium was at a low level of $\leq 10^{10}$ cm^{-2}. Also, one who carefully reads the paper would notice that a re-oxidation treatment removed the observed hysteresis. Such a treatment is not known as capable of driving sodium out of the oxide film.

[6]AT&T Bell Laboratories, Murray Hill, New Jersey 07974

[7]E. A. Irene, *This Journal*, **125**, 1708 (1978).

[8]P. A. Heimann, *IEEE Trans. Electron Devices*, To be published.

[9]General Electric Company, Corporate Research and Development, Schenectady, New York 12301.

2. The possibility that water molecules made part of our ambient atmosphere was not ignored; it was clearly mentioned in the paper. The effects of these on the breakdown field was also discussed in view of Irene's paper.

3. Like most of the researchers in this field, we are well aware of the ability of thin SiO_2 films to withstand high level tunneling currents without suffering a destructive breakdown.[10] We have, therefore, verified experimentally that in our case a 1 μA current level could only be obtained after an irreversible breakdown of the MOS capacitors under study.

[10]D. A. Baglee and P. L. Sah, in "VLSI Electronics," Vol. 7, N. G. Einspruch, Editor, Academic Press, New York (1983); G. Gildenblat, D. M. Brown, C. A. Becker, and S. S. Cohen, "The Influence of Traps on the Conduction and Breakdown of the MOS Structure," General Electric Report no. 83CRD207 (1983).

JOURNAL OF THE ELECTROCHEMICAL SOCIETY

ACCELERATED

—BRIEF COMMUNICATIONS—

NOVEMBER 1984

Oxygen Reduction on Ruthenium Electrode Modified by Foreign Metal Adsorbates

R. R. Adžić, N. A. Anastasijević, and Z. M. Dimitrijević[1]

Institute of Electrochemistry, ICTM and Center for Multidisciplinary Studies, University of Belgrade, Belgrade, Yugoslavia

Ruthenium is a metal of considerable importance in electrochemical technology, especially in combination with an oxidized Ti substrate as an electrocatalyst for Cl_2 evolution (1). A few studies of oxygen reduction on Ru(2) and RuOx/Ti (3) and RuO_2 (4) electrodes have been reported. Under certain conditions its activity for oxygen reduction is similar to that of the other noble metals(2). The oxidized surface of Ru, which would be encountered at potentials of practical oxygen cathodes, is completely inactive for O_2 reduction (2). This has been confirmed in the present work. Improving electrocatalytic properties of Ru for O_2 reduction appears interesting from both academic and practical viewpoints. In this work we have shown that a completely inactive surface of oxidized Ru can be modified by thallium and lead adsorbates in such a way as to show a pronounced activity for O_2 reduction. Also, these adsorbates catalyse O_2 reduction on the Ru surface which shows a high activity when cycled in the potential range encompassing H adsorption/absorption.

The effects are of fundamental interest in developing an understanding of the relation of O_2 electrocatalysis to the surface oxide properties. They could furnish also some information on the properties of ruthenium oxides per se. Considering the importance of Ru as an electrode material these effects seem to have an applicative side.

Ru rod 99.999%, 4 mm diam x 6 mm was supplied by Metal Crystals Ltd, Cambridge, England. It was embedded in a Teflon holder to serve as a rotating electrode and polished in the standard way with a final polishing performed with 0.3 μm diamond paste. The solution, 0.1 M NaOH, was prepared from triply distilled water and "carbanate free" Barker's NaOH.

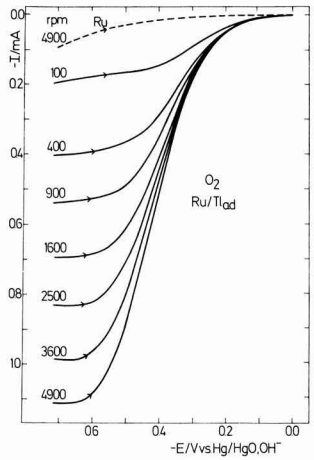
Fig. 1 gives a comparison of O_2 reduction on Ru and Ru modified by Tl adsorbate. An oxidized Ru surface, obtained by a repetitive cycling in the potential range (-) 0.7 V < E < 0.1 V does not show any activity for O_2 reduction. Almost identical curves have been obtained in the presence of N_2 or O_2 in this electrolyte. At high rotation rates a small reduction current is observed at the negative potential limit. Upon addition of Tl^+ into the electrolyte the adatoms of Tl are formed at E = -0.6 V. At more positive potentials the Tl^+ ions adsorb on the surface oxide layer. These two adsorbates change the properties of the oxide layer sufficiently to make it a good catalyst for O_2 reduction. A similar effect is caused by addition of Pb ions to the electrolyte (Fig. 2).

Fig. 3 shows O_2 reduction on Ru electrode when cycled in the potential range encompassing hydrogen adsorption/absorption. Under these conditions Ru shows a pronounced activity. This is in agreement with the data reported in reference (2). Tl adsorbates cause an enhancement of the reaction rate, causing a shift of half-wave potential by ~0.1 V. Oxygen reduction is strongly influenced by foreign metal adatoms obtained by underpotential deposition. The adatoms of Pb, Tl and Bi catalyse O_2 reduction on Au (5-9) and Pt (10). Besides adatoms, it has been shown that ions of the above metals, interacting with the oxidized layers of Au (6) and Pt(10), also cause a catalytic effect. This has been ascribed to the modification of the oxidized layers of Au and Pt which become better catalysts for O_2 reduction.

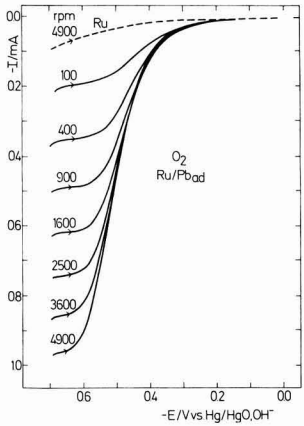
---

[1] Permanent address: Institute of Chemical Power Sources, Belgrade, Yugoslavia.

Key words: oxygen reduction, ruthenium, modified surfaces, adatoms.



ig.1. O_2 reduction on Ru and Ru/Tl_{ad} in 0.1M NaOH and 0.1M NaOH+$1x10^{-4}$M Tl^+. Sweep rate 50 mVs^{-1}.



ig. 2. Same as in Fig. 1 but for $1x10^{-5}$M Pb^{2+} in 0.1 M NaOH.

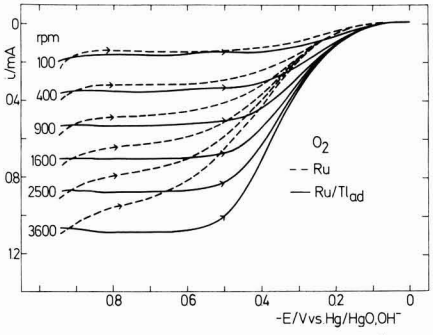


Fig.3. Same as in Fig.1 but for $1x10^{-5}$M Pb^{2+} in 0.1 M NaOH and E_{cat}=-0.95 V.

These data show, for the first time, that foreign metal adatoms can modify an oxidized surface completely inactive for O_2 reduction and present further strong evidence of the modification of the oxide layer by ionic adsorption. Further work is in progress to determine the nature of the interaction of the oxidized Ru with foreign metals adsorbates, the extent of modification and kinetics and mechanism of O_2 reduction on such surface.

Acknowledgements: The authors are grateful to the Research Fund of the Republic of Serbia, Yugoslavia and the National Science Foundation, USA, grant No. Y0R81/037, for financial support.

Manuscript submitted June 28, 1984; revised manuscript received August 27, 1984.

References:

1. S. Trasatti and W.E. O'Grady in "Advances in Electrochemistry and Electrochemical Engineering" vol. 12, H. Gerischer and C. Tobias, Editors, pp 177-249, J. Wiley and Sons, Inc., New York (1982.)

2. L. N. Nekrasov and E. I. Khruscheva, Elektrokhimiya, 3, 166 (1967).

3. W. O. 'Grady, C. Iwakura, J. Huang and E. Yeager, In "Proceedings of the Symposium on Electrocatalysis", M. W. Breiter, Editor p. 286, The Electrochemical Society Inc., Princeton, N. J. (1974).

4. J. Horkans and M.W. Shafer, This Journal, 124, 1202 (1977).

5. R.R. Adžić and A.R. Despić, Zeit. Phys. Chem., N.F., 98, 95 (1975).

6. R.R. Adžić, A.V. Tripković, N.M. Marković J. Electroanal. Chem., 114, 37 (1970).

7. R. Amadelli, N. Marković, R. Adžić and E. Yeager, ibid, 159, 391 (1983).

8. J.D.E. Mc Intyre and W. F. Peck, Proc. 3rd Symp. Electrode Processes, pp. 332-349, The Electrochemical Society Inc. Pennington, N. J. (1979).

9. A. Zwetanova and K. Jüttner, J. Electroanal. Chem., 119, 149 (1981).

10. R. Amadelli, J. Molla and E. Yeager, ibid, 126, 265 (1981).

A New Transition-Metal Penta-Chalcogenide Cathode for Secondary Lithium Cells

S. Okada, H. Ohtsuka, and T. Okada

Nippon Telegraph and Telephone Public Corporation, Ibaraki Electrical Communication Laboratory, Tokai, Ibaraki-ken, 319-11, Japan

INTRODUCTION

Low-dimensional van der Waals-bonded materials have been intensively studied for cathodes of secondary batteries based on rechargeable Li intercalation. In particular, transition-metal poly-chalcogenides, MX_n (M: transition-metal, X: chalcogen), have been supplying many candidates by combination of the elements (M,X) and stoichiometry (n). Dichalcogenides, typified by TiS_2, exhibit relatively deep rechargeability and high rate capability due to the presence of straight Li diffusion pathways (1). On the other hand, higher chalcogenides such as $NbSe_3$ and $NbSe_4$ tend to exhibit highly specific capacities due to the presence of polychalcogen bonds which are reducible for Li intercalation (2).

Here, we report $ZrTe_5$ and $HfTe_5$ cathode properties in MX_5 for the first time. MX_5 ($ZrTe_5$ and $HfTe_5$) is the highest chalcogenide in MX_n and the atomic arrangement induces some expectation for a rechargeable high-capacity cathode material. MX_5 contains both layer and chain structures with the extra "X_2" atoms linking the "MX_3" chains into layers (3). These layers are weakly held together by van der Waals type forces. Correspondingly, a single crystal has cleavage properties along the a-c plane (X_2-layer) with the longest dimension parallel to the a-axis (MX_3-chain). Furthermore, $ZrTe_5$ and $HfTe_5$ show the lowest resistivity along the a-axis, $\sim 7 \times 10^{-4}$ Ωcm at room temperature (4), and anisotropy in the a-c plane, $\rho_c / \rho_a = 2 \sim 3$, is quite small compared with that of typical MX_3, e.g., 16 of $NbSe_3$ (5).

EXPERIMENTAL

MX_5 was synthesized from stoichiometric amounts of 99.9% Zr (99.8% Hf) and 99.999% Te by iodine vapor transport (5 mg per cc of the quartz ampule volume) in a 470 ∿ 420 ℃ thermal gradient for a month. Most of the material were confirmed by X-ray powder diffraction analysis as $ZrTe_5$ ($HfTe_5$) with the same lattice parameters given by Furuseth et al (3), that is, a = 3.9876 Å, b = 14.502 Å and c = 13.727 Å for $ZrTe_5$, a = 3.9743 Å, b = 14.492 Å and c = 13.730 Å for $HfTe_5$.

The cathode pellet (250 mg/cell) was prepared by mixing the sieved MX_5 powder (35 mesh) with carbon powder (Ketjen black) and polytetrafluoroethylene powder in a weight ratio of 78:20:2. The surface area of the cathode pellet in a coin type cell (23 mm diameter, 2 mm thickness) was 2 cm^2. The Li content in each cell was 200 mAh. The electrolyte, used here, was 1M $LiClO_4$-propylene carbonate/1,2-dimethoxyethane (1:1 vol%) with a water content of less than 50 ppm. The cell properties were measured galvanostatically and the open circuit voltages (OCV) were determined by discharge at regular intervals (discharging at 0.5 mA/cm^2 for 7 hr and resting for 50 hr). All set-up operations and measurements were carried out in a dry box filled with Ar gas.

RESULTS AND DISCUSSION

Figure 2 shows open circuit voltages and several discharge curves of $ZrTe_5$. Though the cell capacity above 1.5 V gradually decreased (260, 200, 100 and 50 Ah/kg) with an increasing current density (OCV, 0.5, 1.5 and 5 mA/cm^2), there are intrinsic similarities in each profile. In addition, the profiles of $HfTe_5$ agree with those of $ZrTe_5$.

This common $ZrTe_5$ and $HfTe_5$ behavior suggests that the MX_5 structure itself plays an important role in the cell reaction. The first plateau region on the open circuit voltage curve corresponds to 7 Li/MX_5 (260 Ah/kg-$ZrTe_5$, 230 Ah/kg-$HfTe_5$), compared with 5 Li/MX_4 (e.g., $NbSe_4$), 3 Li/MX_3 (e.g., $NbSe_3$) and 1 Li/MX_2 (e.g., $NbSe_2$) (6). The stoichiometry of Li_7MX_5 is accounted for by reduction of both the chalcogenide and the metal ions as follows;

Key Words: $ZrTe_5$, $HfTe_5$, Secondary Li cell, Intercalation.

$$MX_5 : M^{4+}(X^{2-})(X_2^{2-})(X_2) + 7\,Li^+ + 7\,e^- \rightleftarrows (Li^+)_7M^{3+}(X^{2-})_5$$

Although the cell reaction mechanism beyond 7 Li/MX_5 is not clear, MX_5 cathodes show rechargeability for several cycles at least within this depth. The typical cycling behavior of $ZrTe_5$ at 1 Li/$ZrTe_5$ depth and 0.5 mA/cm^2 rate is given in Fig. 3. In terms of rechargeability, $ZrTe_5$ and $HfTe_5$ were also much the same. The cycle number was about 20 times to 2 Li/MX_5, but to 1 Li/MX_5 it exceeded 180 times. Commonly, most higher chalcogenides except $NbSe_3$ show over 100 cycles within the limits of 1 Li/MX_n. This good rechargeability to 1 Li/MX_5 may be mainly attributed to metal ion reduction/oxidation ($M^{4+} \rightleftarrows M^{3+}$) with Li intercalation/deintercalation.

In summary, the cathode properties of MX_5 are shown in Table I, compared with the other types of MX_n. It is worth while noting that the capacity of MX_5 reaches 7 Li/MX_5 for the 1.5 V cutoff, though a rechargeability of over 100 times is so far restricted to 1 Li/MX_5. This result involves a new possibility, that is, if a lighter MX_5 like TiS_5 can be synthesized and reacted with up to 7 Li in the same manner as $ZrTe_5$ or $HfTe_5$, the theoretical capacity is estimated to be 900 Ah/kg for TiS_5. Such MX_5 cathode properties are still open to future study.

ACKNOWLEDGEMENTS

The authors would like to thank Dr. A. Yamaji, C. Uemura, M. Kakuchi and A. Shibukawa for their helpful discussion. We are also grateful to Prof. T. Sambongi and Assistant Prof. M. Ido of Hokkaido University for their kind support.

REFERENCES

1) G.L. Holleck and J.R. Driscoll, Electrochim. Acta, 22, 647(1977).
2) D.W. Murphy, F.A. Trumbore and J.N. Carides, Electrochem. Soc., 124, 325 (1977)
3) S. Furuseth, L. Brattas and A. Kjekshus, Acta. Chem. Scand., 27, 2367(1973)
4) S. Okada, T. Sambongi, M. Ido, Y. Tazuke, R. Aoki and O. Fujita, J. Phys. Soc. Jpn. , 51, 460(1982)
5) N.P. Ong and J.W. Brill, Phys. Rev., B15, 5265(1978)
6) D.W. Murphy and F.A. Trumbore, J. Cryst. Growth., 39, 185(1977)

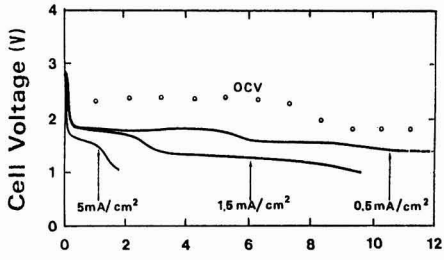


Fig. 1. Current dependence of $ZrTe_5$ discharge characteristics.

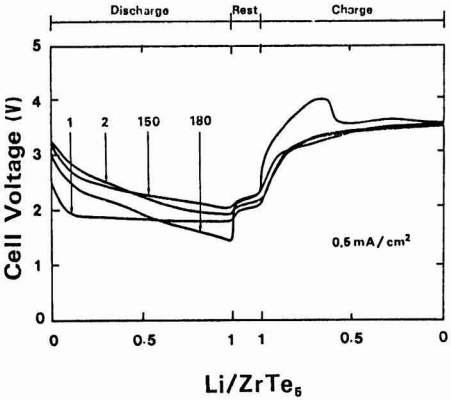


Fig. 2. Typical cycling behavior of $ZrTe_5$ at 1 Li/$ZrTe_5$ depth and 0.5 mA/cm^2 rate.

Table I. Approximate theoretical cathode capacities for MX_n.

Cathode	Li/mole[a)]	Ah/kg[b)]	Ah/cc[c)]
TiS_2	1	240	0.8
$NbSe_3$	3	240	1.6
$NbSe_4$	5	330	-
$ZrTe_5$	7	260	1.6
$HfTe_5$	7	230	1.6

a: 1.5V cutoff
b: Calculated on the basis of MX_n weight.
c: Calculated on the basis of MX_n density.

Manuscript submitted August 21, 1984.
Nippon Telegraph and Telephone Public Corporation assisted in meeting the publication costs of this article.

Electrochemical Conversion of CrO_2

D. Fousse, V. Jovancicevic,[1] and F. Tissier

Centre de Recherches du Fer Blanc, 57103 Thionville, France

Despite a number of interesting properties, such as ferromagnetism and "metallic" electrical conductivity ($10^4\ \Omega^{-1}\ cm^{-1}$), CrO_2 is not well known by the electrochemists. This situation may be explained by relative chemical and electrochemical instability of the oxide and by difficulty in the preparation of the solid electrodes. One can suppose that its oxido-reduction properties (chromium valence IV) and/or metallic character can play a role in the electrocatalysis or in the chromate-passivated films behavior.

In the solid state chemistry, CrO_2 formed by the thermal decomposition of CrO_3 was extensively studied (1 - 3). In particular, the interconversion of CrO_2 to CrOOH and/or Cr_2O_3 was examined as a function of the temperature and is summarized by means of the equation :

$$CrO_2 \underset{O_2(400°C)}{\overset{H_2\ (330°C)}{\rightleftharpoons}} CrOOH \xrightarrow{(>330°C)} Cr_2O_3$$

The interconversion process was explained by the analogy between a tetragonal structure of CrO_2 and an orthorhombic distortion of rutile structure of CrOOH (2).

Besides, some literature results on the composition of the passive film on chromium (4) and chromate-passivated film on iron (5) allow to design a non-stoichiometric close to CrO_2 and a double layer chromium oxide structure, respectively. Nevertheless, a prevalent model of chromate passivation films is chromium trivalent oxide-hydroxide structure (6 - 8). In XPS spectroscopy, it is fairly difficult to obtain conclusive evidence of CrO_2 presence in the film since this compound is easily reduced to Cr_2O_3 by electron, ion or prolonged X-ray bombardment (9).

As a part of investigation on the composition of the electrolytically chromium coated steel (an industrial packaging material), the electrochemical behavior of CrO_2 in neutral NaH_2PO_4 (pH = 7) solution have been studied in the relation with those of Cr_2O_3 and $Cr(OH)_3$, using cyclic voltammetry. Considerable attention has been paid on the procedure of preparation of the oxide layers. The specimens were made from pressed (greater than 98 % pure) powder on platinum "soft" substrate to provide a 0.1 mm thin solid layer. The chromium dioxide (CrO_2) was obtained by courtesy of Kodak Pathé France.

The cyclic voltammograms on CrO_2 are shown in Fig. 1. In the region preceeding oxygen evolution reaction at 0.35 V/SSE one can observe two characteristic features relative to CrO_2 layer ; an oxido-reduction process at about 0.2 V/SSE (sweep increasing currents) and a reduction process at - 0.2 V/SSE (sweep decreasing current) in the oxide. The "steady state" voltammetric curve obtained after ten sweeps (Fig. 1b) indicated that two steps reversible oxido-reduction reactions take place. No cathodic reduction peak at -0.2 V/SSE means that the transformation of the oxide produced in the course of the potential cycling is stopped. The same voltammogram was obtained with the previously potentiostatically reduced (- 0.2 V/SSE) CrO_2.

1. Present address : Texas A & M University, College Station, Texas 77843

Key words : chromium dioxide, chromium-passivated film, electroconversion.

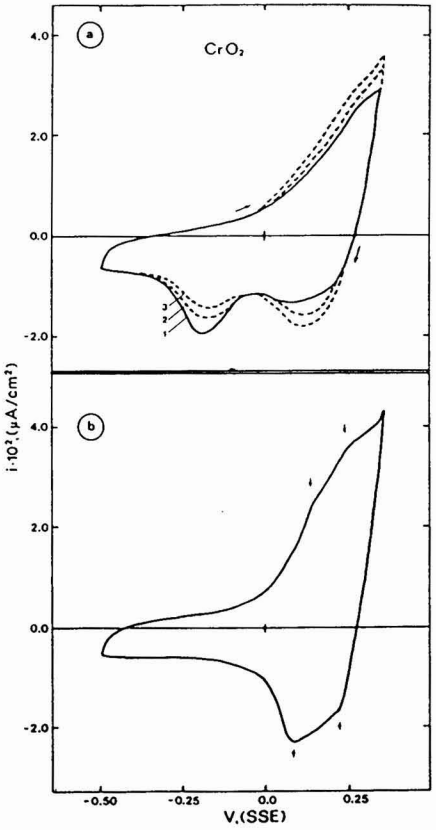


Fig. 1 : Cyclic voltammograms of CrO_2 for three first sweeps (a) and "steady state" curve after ten sweeps (b) ; scan rate = 20 mV/sec.

The double-peak feature of CrO_2 (arrows in Fig. 1b) was examined in relation with the cyclic voltammograms on Cr_2O_3 and $Cr(OH)_3$ oxides obtained in the same conditions (Fig. 2). Cr_2O_3 shows the same marked less than 0.05 V reversible double-anodic peak (second peak is more reversible than the first one). Conversely, $Cr(OH)_3$ presents only double layer behavior.

Two steps reversible oxidation of Cr_2O_3 can be assigned to the consecutive oxidation to CrO_2 and CrO_3.

Then the electrochemical conversion (Fig. 1) of CrO_2 can be summarized in terms of the following reactions :

$$CrO_2 \longrightarrow Cr_2O_3$$

$$Cr_2O_3 \rightleftharpoons CrO_2 \rightleftharpoons CrO_3$$

the first one is irreversible reduction of CrO_2 and the second one is a reversible oxido-reduction of formed Cr_2O_3. The chromium dioxide participates in both reactions, as a bulk oxide and an intermediate oxide product, respectively. At the beginning of the cycling of the potential (Fig. 1a), the reduction of CrO_2 is produced at two different potentials separated by 0.35 V. One can assume that this difference is due to the different crystallographic structures of CrO_2.

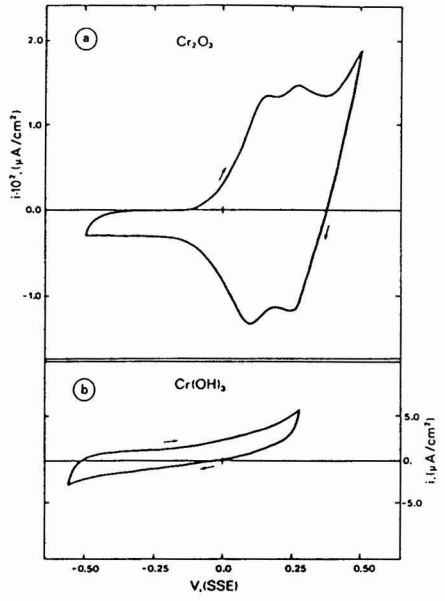


Fig. 2 : Cyclic voltammograms of Cr_2O_3 (a) and $Cr(OH)_3$ (b) ; scan rate = 20 mV/sec.

In this paper we give the evidence of the electrochemical stability of CrO_2 and the role that it can play as a component of the chromate passivation film. In the case of chromium coated steel a subsequent anodic oxidation allows to reduce the porosity of the chromium oxide film, more than by ten times (10). The improvement of the passivating properties may be ascribed

to the formation of the high conducting CrO_2.

Besides, the metallic conductivity of CrO_2 and its electrochemical stability could be used to promote it, for example, as an electrocatalyst for oxygen evolution reaction.

REFERENCES

1. N.C. Tombs, W.J. Croft, J.R. Carter and J.F. Fitzgerald, Inorg. Chem., 3, 1791 (1964).

2. I. Ikemoto, K. Ishii, S. Kinoshita, H. Kuroda, M.A. Alario-Franco and J.M. Thomas, J. Solid State Chem., 17, 425 (1976).

3. R. Saes-Puche and M.A. Alario-Franco, J. Solid State Chem., 38, 87 (1981).

4. A.M. Sukhotin, E.I. Antonovskaya and A.A. Pozdeeva, Zh. Fiz. Khim., 36, 2368 (1962).

5. A.T. Vagramyan and D.N. Usachev, Zh. Fiz. Khim., 32, 1900 (1958).

6. I. Inui, K. Saijyo and N. Shimizu, Kinzoku Hyomen Gitjutsu, 32, 80 (1981).

7. T. Hiroshi and K. Yoshitaka (Nippon Kokan K.K.), German Pat. 2,600,654 (1976).

8. S. Maeda, T. Asai, H. Omata and H. Okada, Proceedings of 10th Congress on Metal Finishing, Interfinish 80, ed. by S. Haruyama, p. 432, Kyoto (1980).

9. D. Fousse and F. Tissier, unpublished results.

10. V. Jovancicevic (Centre de Recherches du Fer Blanc), Patent applied for.

Manuscript submitted March 19, 1984.
Centre de Recherches du fer Blanc assisted in meeting the publication costs of this article.

JOURNAL OF THE ELECTROCHEMICAL SOCIETY

REVIEWS AND NEWS — NOVEMBER 1984

Abstracts of Recent News Papers

Presented at the New Orleans, Louisiana, Meeting of the Society, October 7-12, 1984

661 SOA High Speed/High Frequency Gallium Arsenide Transistors for Integrated Circuits: *L. F. Eastman*, Electrical Engineering School, Cornell University, Ithaca, NY 14853

The band width of transistors is determined directly by the ratio of the transconductance to the input capacitance and thus directly on electron velocity. At room temperature, GaAs MESFET's doped at $1 \times 10^{17}/cm^3$ have 1.2×10^7 cm/s saturated electron velocity, while modulation doped heterojunction (Al, GaAs) FET's have 1.8×10^7 cm/s saturated electron velocity, all compared with 0.6×10^7 cm/s saturated electron velocity for silicon. The latter GaAs devices under 0.5 μm length will be shown to have nearly 4×10^7 cm/s average electron velocity. The FET structures required and the physical electronics for devices operating with less than 5 ps switching time or over 100 GHz operating frequency are described.

662 SOA Compound Semiconductor Material Preparation for High Speed/High Frequency: *D. W. Shaw*, Texas Instruments Incorporated, Materials Science Laboratory, MS 147, Dallas, TX 75265

As the first commercial GaAs integrated circuits are becoming available, the materials technology is undergoing a series of transitions. Large wafers of uniform size and shape with predictable behavior with respect to ion implantation are demanded; unprecedented uniformities in material properties are essential for the complex, large area chips; and new approaches, such as heterojunction bipolar transistors and HEMT-based IC's, are requiring multilayer epitaxial structures with exceptionally precise thickness and composition control. This presentation attempts to describe these evolving trends in materials preparation and critically assesses the major issues currently associated with GaAs substrate preparation, ion implantation, and epitaxial growth.

663 SOA The Growth of Undoped Semi-Insulating GaAs Crystals by the Horizontal Gradient Freeze Method: *M. S. Young, R. Caruso, J. M. Parsey, Jr.*, and *A. P. Kinsella*, AT&T Bell Laboratories, Murray Hill, NJ 07974

Undoped semi-insulating GaAs single crystals were grown by the horizontal gradient freeze method. The D-shaped, <111>-oriented crystals weighing 1 kg were grown in PBN boats. High resistivity GaAs material can be obtained consistently when the melt has been doped with oxygen to suppress Si contamination. Uniform etch pit densities in the range of 2-4000/cm^2 were obtained. The (100) wafers were found to be stable against thermal conversion after ion implantation and subsequent heat-treatment. Results of SIMS analysis and electrical characterization are discussed.

664 SOA Molecular Beam Epitaxial Growth on Radiation-Heated GaAs Substrates: *S. C. Palmateer, B. R. Lee*, and *J. C. M. Hwang*, General Electric Company, Electronics Laboratory, Syracuse, NY 13221

Growth on GaAs substrates without indium mounting is essential for improvements in substrate backside morphology and throughput of molecular beam epitaxy. By coating the substrate with a thin Ti-W layer and by mounting the substrate on a ring-shaped holder with clips, we have succeeded in performing the growth on radiation-heated GaAs substrates. The surface morphology of the epitaxial layers was comparable to that grown with indium mounting. Electrochemical C-V measurements show the doping and thickness were uniform within ± 3% across a 2 in diam wafer. Photoluminescence and Hall measurement were also uniform and comparable to the case with indium mounting.

665 SOA Characterization of MBE-Grown AlGaAs Layers for Charge-Coupled Devices: *M. J. Holtzman, R. T. Chen, R. Sahai, D. L. Miller, J. A. Higgins, R. L. Pierson*, and *S. Pittman*, Rockwell International Corporation, Microelectronics Research and Development Center, Thousand Oaks, CA 91360

Charge-coupled devices with good charge-transfer efficiency (>0.999) have been fabricated on MBE-grown $Al_xGa_{1-x}As$ layers. Layers grown with different substrate temperatures (610 – 700°C), arsenic species (As_2 and As_4), and Al content (x = 0-0.3) were studied. Energy levels and densities of deep electron traps were measured both by DLTS and by measuring the charge loss in CCD's as a function of device temperature. Trap levels were observed from 0.26 to 0.78 eV below the conduction band and trap densities ranged from less than 10^{13} cm^{-3} for 10% Al to 3×10^{15} cm^{-3} for 30% Al. A substantial reduction in trap concentration and corresponding improvement in CCD performance were seen in layers grown at 700°C with As_2, compared to layers grown at 610°C with As_4.

666 SOA A New Method to Supply Solute Elements into Growth Solutions: Demonstration by LPE of $In_{1-x}Ga_xAs$: *K. Nakajima, S. Yamazaki*, and *T. Kotani*, Atsugi Laboratories, Fujitsu Laboratories Limited, 1677 Dannoki, Ono, Atsugi 243-01, Japan

We have developed a new controllable method to supply solute elements into growth solutions. A dc electric current was passed through binary semiconductor compounds used as source materials, and the compounds were dissolved into the growth solutions due to Peltier and Joule heating. We found that the composition of $In_{1-x}Ga_xAs$ LPE layers could be varied by the electric current because solute elements were supplied from the source compounds into the growth solutions.

667 SOA Gallium Contamination of InP Epitaxial Layer in InP/InGaAsP Multilayer Structure Grown by Hydride Transport Vapor-Phase Epitaxy: *S. N. G. Chu, A. T. Macrander, R. F. Karlicek, C. C. Chang, C. M. Jodlauk, K. E. Strege, D. L. Mitcham*, and *W. D. Johnson, Jr.*, AT&T Bell Laboratories, Murray Hill, NJ 07974, and *F. A. Stevie*, AT&T Bell Laboratories, Allentown, PA 18103

Gallium contamination of InP epitaxial layers grown in CVD reactors designed for InGaAsP/InP multilayer structures was observed by secondary ion mass spectrometry (SIMS). By presaturating the reactor with PH_3, the amount of the gallium which was incorporated into the InP was found to be reduced. SIMS profiles of gallium on layers grown after the withdrawal of the gallium source from the reactor indicated that the indium melt was cross-contaminated even though the reactor was designed to physically exclude the gallium source from the indium source. The possible mechanisms which lead to the cross contamination are discussed.

668 SOA TEM Cross-Sectional Sample Preparation Technique for III-V Compound Semiconductor Device Materials by Chemical Thinning: *S. N. G. Chu* and *T. T. Sheng*, AT&T Bell Laboratories, Murray Hill, NJ 07974

A cross-sectional sample preparation technique is described for the TEM studies of III-V compound semiconductor device materials. In this technique, a grid masking method is introduced for selective-area perforation using chemical etching. Examples of the use of this technique for InP/InP (substrate) single-layer and p$^+$InGaAsP/p-InP/InGaAsP/n-InP/InP (substrate) multilayer laser device structures grown by vapor-phase epitaxy are demonstrated. The technique is also applicable for selective perforation of plan-view TEM samples.

669 SOA Transmission Electron Microscopy Study of Cross Sections of 1.3 μm InGaAsP-Etched Mesa Heterostructure Lasers: *R. B. Marcus*, Bell Communications Research, Inc., Murray Hill, NJ, *T. T. Sheng* and *D. M. Maher*, AT&T Bell Laboratories, Murray Hill, NJ, and *P. D. Wright*, Bell Communications Research, Inc., Murray Hill, NJ 07974

Transmission electron microscopy studies made of cross sections of InGaAsP-etched mesa buried heterostructure (EMBH) lasers show the presence of a thin layer of atomic disorder at the {III} A sidewall/epi interface. This disordered layer is thought to relate to a previously discovered dependence of lasing threshold on vertical position of the active layer.

670 SOA The Contribution of Surface States to Electrochemical CV-Profiling of GaAs and InP: *P. Wennekers*, Fraunhofer-Institute for Solid State Physics, D-7800 Freiburg, Germany

This electrochemical CV profiling method gives stable results for various semiconductor/electrolyte pairs, but the accuracy is questionable owing to simultaneously measured surface charge. Admittance measurements at different fixed semiconductor electrode potentials in the frequency range 100 Hz-1 MHz separate space charge from surface charge contribution. For some GaAs$^-$,InP/electrolyte pairs, the frequency range and electrode potentials are determined, where space-charge capacitance can be measured with minimum error.

671 SOA Growth and Characterization of II-VI Alloy Crystals: *K. Y. Lay, B. Breithaupt, N. C. Giles-Taylor, J. Schetzina,* and *K. J. Bachmann,* North Carolina State University, Raleigh, NC 27695

The preparation of single crystals of $Cd_xMn_{1-x}Te$, $Zn_xCd_{1-x}Te$, and $CdSe_yTe_{1-y}$ by zone leveling is described. The electrical transport properties of these alloys are characterized by Hall effect measurements in the temperature range $20K \leq T \leq 300K$. Photoluminescence measurements are used for supplementing the Hall measurements of shallow dopants and to probe for deep emission. Preliminary data are presented on the defect structure in the above materials.

672 SOA The Optical Properties of $CuInSe_2$ and Related Compounds: *P. Lange, H. Neff, M. Fearheiley,* and *K. J. Bachmann,* Department of Chemistry, North Carolina State University, Raleigh, NC 27695-8204

The optical properties of $CuInSe_2$, including off-stoichiometric crystals within the existence range of this compound, are reported, including $Cu_3In_5Se_9$, the maximum melting point compound in the Cu, In, Se system. Modulation spectroscopy techniques and photoluminescence were employed to probe the density of states at critical points for these materials and to elucidate the shift in the fundamental edge with composition.

673 SOA The Potential Distribution at $CuInSe_2$/Aqueous Electrolyte Interfaces: *M. Tomkiewicz, W. M. Shen,* Brooklyn College of CUNY, Brooklyn, NY 11210, and *D. Cahen,* Weizmann Institute of Science, Rehovot, Israel

We report the results of a detailed investigation, using electrolyte electroreflectance (EER) and impedance spectroscopy, that was aimed at elucidating the changes that take place in the chemistry and potential distribution at the n-$CuInSe_2$ interface with aqueous electrolytes, following optimized etching and controlled surface oxidation. We correlate these results with the previously reported enhancement in the photovoltaic response of this system.

674 SOA III-V Compound Semiconductor Device Technology for Future Space Communication Applications: *D. J. Connolly,* NASA Lewis Research Center, Cleveland, OH 44135

III-V compound semiconductor device technology is an all-pervasive element in modern and future space communication systems. Under development for future systems are GaAs FET low noise receivers, GaAs FET and impatt transmitters, microwave matrix switches, and high-speed, high-throughput, on-board processors. Hoped-for performance improvements in these systems center on performance of the III-V devices around which they are designed. The influence of materials and processes on these devices is reviewed.

675 SOA III-V Integrated Circuit Technology: Some Things Old and Some Things New: *C. L. Allyn,* AT&T Bell Laboratories, Murray Hill, NJ 07974

III-V integrated circuits are relatively new types of semiconductor devices. Digital circuits began appearing in research laboratory reports in 1978 and have just recently become commercially available. The observed increase in demonstrated complexity pays eloquent tribute to an effective marriage between the IC fabrication knowledge from the silicon experience and the novel aspects of III-V devices. The talk will review and compare some of the process technologies used to fabricate III-V integrated circuits.

676 SOA Stabilization of Deep UV Lithographic Definition of 0.5 μm Gates for GaAs Microwave Integrated Circuits: *N. Dandekar, L. Pobedinsky, P. C. Chao,* and *J. C. M. Hwang,* General Electric Company, Syracuse, NY 13221, and *P. Thompson,* Karl Suss, Inc., Waterbury Center, VT 05677

0.5 μm line definition using deep UV lithography has been improved upon by investigation of stability of the deep UV source and the development conditions of the double-layer resist. Direct linewidth measurement by scanning electron microscopy as well as electrical resistance measurement of the metallized lines demonstrate a narrow distribution of the statistical data. Application of this high yield process in GaAs microwave integrated circuit fabrication is presented.

677 SOA Plasma Reactor Cleaning and Plasma Damage in GaAs Annealing Encapsulation: Part I: *G. J. Valco* and *V. J. Kapoor,* Solid State Electronics Laboratory, Department of Electrical and Computer Engineering, University of Cincinnati, Cincinnati, OH 45221, and *J. E. Dickman,* NASA Lewis Research Center, Cleveland, OH 44135

Substrate and reactor preparation prior to plasma deposition of Si_3N_4 films for encapsulated annealing of implanted GaAs and plasma damage of the GaAs have been investigated. A substrate cleaning process including a HCl/H_2O solution was selected by Auger electron spectroscopy studies. Reactor preparations including bakeout and plasma pretreatment yielded repeatable Si_3N_4 depositions with very low oxygen content. CF_4 plasma cleaning of the chamber walls required steps to prevent flourine contamination of the substrate-film interface. Schottky diode characteristics on substrates subjected to plasma deposition indicated no significant plasma damage. The films were deposited in a planar reactor with various N_2/SiH_4 ratios, flow rates, pressures, RF powers, and substrate temperatures.

678 SOA Silicon Nitride for Annealing GaAs: Part II: *G. J. Valco* and *V. J. Kapoor,* Solid State Electronics Laboratory, Department of Electrical and Computer Engineering, University of Cincinnati, Cincinnati, OH 45221

Silicon nitride films have been deposited on Si-implanted GaAs for use as an annealing encapsulant. The thickness and refractive indices of the films were measured by ellipsometry. Etch rates in 1:1 deionized water to hydrofluoric acid were determined before and after annealing. Auger electron spectroscopy and the XPS technique were used to determine film composition before and after annealing. The film properties were studied as a function of film deposition conditions. Schottky diode current-voltage characteristics indicated how well the GaAs was protected during annealing, and electron concentration profiles and implant activations were determined after annealing.

679 SOA Novel Open-Tube Method for Zn Diffusion: *I. Camlibel, A. K. Chin, H. Guggenheim, S. Singh, L. G. Van Uitert,* and *G. J. Zydzik,* AT&T Bell Laboratories, Murray Hill, NJ 07974

Diffusion into III-V compounds generally requires closed systems that maintain the vapor pressure of the highly volatile group V element. In this talk, we describe a novel, open-tube method for diffusion Zn into III-V compounds. The dopant source is composed of an evaporated film of ZnF_2 encapsulated with a film of either SiO_2, borosilicate, or Al_2O_3. Localized p-n junctions can be formed by patterning the ZnF_2 using standard photolithography prior to encapsulation. Planar photodiodes of InP or $In_{0.53}Ga_{0.47}As$, fabricated with this diffusion technique, showed state-of-the-art performance. For 75 μm diam devices, dark currents as low as 5×10^{-12} A and 3×10^{-10}A at 10V reverse bias were achieved for InP and $In_{0.57}Ga_{0.47}As$ photodiodes, respectively.

680 SOA Simulation of Concentration-Dependent Diffusion During the Annealing of Ion-Implanted Compound Semiconductors: *B. Streetman* and *C. Farley,* Department of Electrical Engineering, University of Texas at Austin, Austin, TX 78712

This paper discusses several models used in the simulation of anomalous redistribution commonly observed during the annealing of ion-implanted compound semiconductors. These models include the effects of temperature, impurity concentration, and outdiffusion and produce post-anneal impurity profiles consistent with experimental observations. These models have accurately simulated the retrograde annealing behavior of Be in InP and have been generalized to allow simulation of the annealing behavior of all impurities which show concentration-dependent diffusion similar to Zn in GaAs. These simulations should be applicable to most acceptors implanted into compound semiconductors. Additional abstracts of papers presented in the symposium "III-V Semiconductor for High Speed Applications" were published in the August issue of the Journal, p. 315C.

681 RNP A New View on the Equilibrium Diagram Potential-*p*H of the System Manganese Dioxide-H_2O: *J. P. Brenet* and *P. C. Piquet,* SEDEMA, B-7340 Tertre, Belgium

Based on new data available on manganese oxides, the potential-pH diagram is surveyed again. New suggestions are proposed in the interpretation of the diagram. These concern the theoretical conditions of formation of manganese oxides, the manufacture of manganese dioxide cells, and also the manufacture of the metal itself. Better ways are suggested to look at the role of such diagrams in predicting possible or impossible reactions from at least the thermodynamic point of view.

682 RNP Behavior of MnO_2 Cathodes in Nonaqueous Electrolytes: *J. Ruch, P. Schmoede,* and *D. Katryniok,* Carl Zoellner & Sohn GmbH, KG, Accumulatorenwerke Hoppecke D-5790 Brilon 2, Germany

Among the various systems of nonaqueous lithium cells under development, those using MnO_2 as active material have long been considered as not sufficient in power to really compete with those based, for instance, on SO_2, $SOCl_2$, or SO_2Cl_2. The characteristics of our present production standard indeed more than meet the requirements for common cells of the D, C, 2/3A, AAA, or 1/2 AA sizes, so that we can ascertain that MnO_2 is not only competitive, but even combines to good electric characteristics a number of advantages, among which corrosion behavior, passivation problems, or safety aspects are not to be minimized. Principally, we present characteristics of cells for various conditions of discharge rates or temperature ranges. Then we compare them with alternative lithium systems under the aspects of specific energy and power density, and finally we give some results on further improvements which have been achieved more recently.

683 RNP High Resolution Transmission Electron Microscopy of Natural and Lithiated Manganese Oxides: *P. R. Buseck, B. Miner,* and *S. Turner,* Department of Geology, Arizona State University, Tempe, AZ 85287

Using transmission electron microscopy, it is possible to examine the structural details of crystals on a subunit scale. Many manganese oxides are highly disordered and poorly crystalline, and so TEM provides a unique means for studying these materials. Results are reviewed briefly obtained from minerals. Samples of lithiated EMD were obtained from Union Carbide Corporation (Parma, Ohio). The samples were given to us with the following percentage of lithiation: 100, 75, 50, 36. High resolution transmission electron microscopy (HRTEM) was used to image the samples using the

same procedures as we used on natural manganese oxides (Turner and Buseck, 1979, 1981, 1983) and other minerals (Buseck, 1983). Selected-area electron diffraction (SAED) patterns were routinely obtained, both to identify phases and to orient crystals for HRTEM imaging. A Philips 400T 120kV and a JEOL 200CX 200kV TEM were used for the measurements. Results are shown and discussed.

684 RNP Recent Studies on the Variance of the Equilibrium Potential of EMD due to Crystal Structure and Combined Water: *Kiyoshi Shimizu*, and *Junji Koshiba*, Toyo Soda Manufacturing Company, Limited, Akasaka, Minato-ku, Tokyo 107, Japan

The water contained in the structure which could be related with the equilibrium potential of EMD was studied in concentrated alkaline solution. It was found that the equilibrium potential is indirectly influenced to a small degree by H atoms and directly by the content and the activation energy of the water. The H atoms correspond to the Mn(III) atoms in EMD. The water is released at about 250°C and apparently exists in the form of H_2O molecules.

685 RNP Recent Studies on Crystal Structures of the Moanda (Gabon) Battery Active Natural Manganese Dioxide: *R. Giovanoli* and *D. Thirouin*, Compagnie Miniere deL'Ogooue, 92521 Neuilly, France

The use of x-ray diffraction for determining the most battery-active natural manganese dioxide should become a means of selection at the mine level by providing information on the crystal structure itself. A natural ore is, of course, a collection of many chemical species, and the reading of an x-ray diagram is something which has to be done with utmost care. Nevertheless, the identity and size of the different peaks of the diagram should provide a powerful way of control at the production level.

686 RNP Tunnelling Through Structural Linkages in MnO_2: *R. G. Burns* and *V. M. Burns*, Department of Earth, Atmospheric, and Planetary Sciences, Massachusetts Institute of Technology, Cambridge, *MA 02139*

Tetravalent Mn and Ti form a variety of oxide polymorphs containing chains of edge-shared $[Mn^{IV}O_6]$ or $[Ti^{IV}O_6]$ octahedra in their crystal structures. The MnO_2 polymorphs exhibit a greater diversity in number and extent of edge-shared octahedra than TiO_2, owing to the higher covalent bonding in Mn(IV) oxides. The linked $[MnO_6]$ octahedra provide a variety of tunnels which contribute to cation exchange, ion mobility, proton transfer, Mn^{4+} vacancies in the tunnel walls, structural defects and cryptocrystallinity, all of which influence the electrochemical properties of Mn(IV) oxides. Molecular orbital calculations using the α scattered wave method were performed on the clusters $[MnO_6]^{8-}$ and $[MnO_4]^{4-}$, representing Mn^{4+} ions in octahedral and tetrahedral coordinations with O^{2-} ions, respectively. The calculated energy levels demonstrate that Mn^{4+} ions are considerably more stable in octahedral rather than tetrahedral coordination by about 2.8 eV. The charge distributions in bonding and antibonding molecular orbitals indicate that bonding in Mn(IV) oxides is about 80% covalent, compared to 50% covalent character in Ti(IV) oxides. These results lead to the conclusions that, although Mn^{4+}-Mn^{4+} repulsions are reduced by covalency effects in oxides, they are further alleviated by vacancies in edge-shared $[MnO_6]$ octahedra and the facility with which the structural linkages are disrupted to provide cryptocrystallinity in Mn(IV) oxides polymorphs. Such vacancies and broken bonds result in structural defects and large specific surface areas, all of which contribute to the chemical reactivities and electrochemical behavior of MnO_2 polymorphs.

687 RNP Solvent-Deposited Chalcogenide Glasses: *G. C. Chern*, *B. Singh*, and *I. Lauks*, Center for Chemical Electronics, Department of Electrical Engineering, University of Pennsylvania, Philadelphia, PA 19104

Chalcogenide glasses, conventionally prepared by melt quenching or vapor deposition, can also be formed by deposition from organic solution. The mechanism of reaction between binary chalcogenides and low molecular weight primary amines (RNH_2) has been investigated. The continuous network of the solid glass is attacked by amine only at selected sites, and macromolecules of chalcogenide (MW 100,000s) terminated at their surfaces by $-S^-RNH_3^+$. For applications in multilayer resist systems, solvent-deposited As_2S_3 has been used as a barrier layer in a trilevel scheme and a planarizer in a bilevel scheme. Submicron lines and spaces without width variation over steps have been successfully replicated.

688 RNP A Novel Metallization Structure for Silicon and Gallium Arsenide Power Devices: *G. Csanky* and *S. McCluskey*, Hughes Research Laboratories, Malibu, CA

A novel multilayered metallization structure specifically useful for metallization of microwave power devices is proposed. It consists of chrome-gold-chrome-gold layers (500:7000:750:500Å, respectively). This novel structure allows the use of O_2 plasma to etch chrome. Using the combination of ion milling of gold and oxygen plasma etching of chrome fine-line interdigitated metallization patterns have been produced. A description of the process and recipe are presented.

688A RNP Large Area Photodeposition of Tungsten: *J. M Marrs* and *H. Zarnani*, Tektronix, Incorporated, Solid State Research Laboratory, Beaverton, OR 98962

Large area, wafer-scale, thin films of tungsten metal have been deposited in a photochemical CVD system utilizing a microwave discharge ultraviolet light source. Photodeposited films of W have the properties of conformal coverage, good adhesion, and low temperature of deposition. This is believed to be the first report of a photolytic deposition of a thin film metal utilizing a source other than a laser. The technique, apparatus, and films are discussed.

689 RNP LPCVD Tungsten Interconnect: *C. Arena*, Matra Harris Semiconducteurs, 38243 Meylan Cedex, France, *M. Papapietro*, Institut National des Sciences Appliquees de Lyon, 69621 Villeurbanne, France

LPCVD Tungsten used as an interconnect metal provides the following advantages over aluminum/silicon alloys: small grain deposits, good stepcoverage, no hillock formation, and a superior electromigration resistance. Using 900Å thick polysilicon films as adhesion promoting layers, 7000Å thick tungsten films have been deposited in a hot-wall reactor from a WF6 source. The tungsten-polysilicon layers have been chemically and/or SF6 plasma patterned. Diffusional thermal treatments to get appropriate N^+P^+ ohmic contacts have been investigated, and results are presented. Tungsten interconnected integrated circuits have been fabricated and electrically characterized.

690 RNP Electromigration Mass Transport in Aluminum Conductors on TiN and Polysilicon Surfaces: *E. Kinsbron*, AT&T Bell Laboratories, Murray Hill, NJ 07974

The Blech-Kinsbron (1) edge displacement technique has been used to measure the electromigration mass transport of Al 0.5% Cu films evaporated from various sources on TiN or polysilicon substrates. In tests between 200° and 400°C, average drift velocities of 0.01-10 m/h, depending on the temperature and grain size, were measured in the films lying on TiN. No Al edge displacement could be detected in the films lying on polysilicon. The Si electrotransport in Al is much faster compared to the Al self-electromigration rate. The failure mechanisms and the lifetime dependence on temperature, current density, and linewidth have been established.

References: 1. I. A. Blech and E. Kinsbron, *Thin Solid Films*, **25**, 327 (1975).

691 RNP Physical and Electrical Characteristics of LPCVD Si-Rich Nitride: *A. Bhattacharyya*, *R. Bass*, *W. Tice*, *R. Baxter*, and *T. Derenthal*, IBM, Essex Junction, VT 05452

Silicon-rich nitride films were deposited by varying the ratio of SiH_2Cl_2 to NH_3 in a LPCVD system. The refractive indices of these films varied from 2.0 to 3.0. Auger and NBS analyses were used to obtain the stoichiometry of the films; they were characterized in terms of excess silicon content. In order to characterize the silicon-rich regions, structural analysis was carried out by TEM. Physical (refractive index and dielectric constant), chemical (etch rate), and electrical (charge transport and charge trapping) properties were correlated with the stoichiometry and structure of these unique films.

692 RNP Rapid Growth of Thin Film Silicon Oxides: *G. Grant*, *G. Brown*, *J. Shu*, *E. Lee*, and *J. Reynolds*, Texas Instruments, Incorporated, Dallas, TX 75265

Results of thin oxide growth in the range of 40-300Å on single-crystal silicon wafers using an incoherent light source are presented. Classical linear growth rates for temperatures from 1000° to 1150°C were observed in different oxygen concentrations. Electrical characteristics of the oxide such as breakdown voltage, Q_{ss}, I-V, and electron injection are investigated. Parametric analysis indicates that this method could provide a reproducible and more controllable alternative to convection furnaces in thin film oxide growth for IC fabrication.

693 RNP Sputtered Thin Films of Barium Titanate Alloys: *D. W. Ormond* and *I. B. Cadoff*: IBM, General Technology Division - East Fishkill, Hopewell Junction, NY 12533.

High dielectric films of composition ranges (Ba_x, Sr_{1-x}) TiO_3, where x = 0.75 to ~0.1, and $Ba(Sn_x, Ti_{1-x})$ O_3, where x = 0.86 to 0.1, were deposited on Pd-coated, SiO_2/Si substrates by RF cosputtering in a 0.01 torr Ar atmosphere. Pressed-powder targets composed of butted half-moon segments, one target of $BaTiO_3$//$SrTiO_3$, the other of $BaTiO_3$//$BaSnO_3$, were used in an RF diode configuration to cosputter the source material. With direct radiation heating, substrate temperatures as high as 1000°C were attained. The films were found to be single phase with continuous compositional variation $<x>$ across the 2 in. exposed surface of the sample substrate. Lattice parameter data correlated with composition data. Anomalously large lattice parameter values were found with $BaTiO_3$-rich films deposited on low temperature substrates. We obtained dielectric constant, ϵ, ranging from 200 to 1000 on MIM structures of Pd/insulating alloy/Pd. Highest values at room temperature were obtained for Sr-rich Ba/$SrTiO_3$ compositions.

This research performed in partial fulfillment of the degree requirements for D. W. O. for Doctor of Philosophy in Metallurgy and Materials Science, Polytechnic Institute of New York.

694 RNP Redistribution of Implanted Zn and Mg in GaAs under Different Annealing Conditions: *I. K. Naik* and *J. W. Tully*, Northrop Research and Technology Center, Palos Verdes Peninsula, CA 90274

Redistribution of ion-implanted Zn and Mg in semi-insulating GaAs resulting from two different annealing methods was investigated. Individual implantations of Zn^+ and Mg^+ were carried out at 200 and 80 KeV, respectively. In one annealing method, unencapsulated GaAs wafers were rapid thermally annealed using a

bank of halogen lamps as heating source. In the second method, annealing was done by placing the unencapsulated wafers on a RF-power-heated graphite susceptor in a 1.6% AsH_3-98.4% H_2 environment. The annealed GaAs wafers were characterized by means of differential Hall effect measurements and secondary ion mass spectrometry to determine the redistribution behavior of the dopants during annealing. Both capless annealing techniques were effective in restricting the spread of dopant profiles while yielding high activation efficiencies.

695 RNP Silicon Cells by Ion Implantation: *R. Galloni*, CNR-Istituto LAMEL, 40126 Bologna, Italy

To make photovoltaics competitive with other energy sources, not only for special or remote applications, costs of energy production must be further decreased either by decreasing solar cell manufacturing costs or by increasing the device conversion efficiency. The application of ion implantation to the solar cell fabrication process, together with thermal treatments in a transient regime obtained by laser, electron beam, or incoherent light pulses, could be profitably used to reach this goal. Computer models have been used to optimize solar cell geometrical factors and to understand which physical parameters still need improving. Emitter shape and effect of residual damage are specifically analyzed and compared with experimental values.

696 RNP Solar Cell Performance Assessment of Elkem HPMS-Silicon: *J. P. Dismukes, J. A. Amick, P. S. Ravishankar, E. E. Shipp,* and *L. B. Younghouse*, Exxon Research and Engineering Company, Annandale, NJ 08801, *J. Blake* and *R. Sylvain*, Solar Power Corporation, Boston, MA 01801, *G. Halvorsen, K. Larsen,* and *A. Schei*, Elkem A/S Research and Development Center, N-4620 Vagsbygd, Norway

In-module solar cell efficiencies up to 13% have been measured on production-size solar cells made from Bridgman-recrystallized, high purity metallurgical silicon (HPMS-Si). This exceeds previously reported results from this type of material and compares favorably with the 14% value typical in the photovoltaic industry for high quality Czochralski cells. In order to verify this performance and to assess variations in performance for a variety of silicon materials and recrystallization processes, we submitted a number of Elkem-Exxon silicon wafers to Applied Solar Energy Corporation (ASEC) for solar cell fabrication and measurement. Since 1976, this organization has been a recognized authority within the photovoltaic industry for both comparative and absolute solar cell performance testing on silicon wafer materials. The ASEC data show that cells prepared in twice Bridgman-recrystallized Elkem HPMS-Si are equal to or superior to cells made in competitive polycrystalline materials processed at ASEC in the 1983 time frame. Their data, in conjunction with our own measurements, have also helped in the analysis of mechanisms which can degrade performance of solar cells prepared in polycrystalline Bridgman silicon.

697 RNP Ambient Effects on Oxygen Precipitation in Silicon: *J. D. Peng*, Fairchild Semiconductor, Silicon Materials Division, Healdsburg, CA 85548, and *L. Forbes*, Dept. of Electrical and Computer Engineering, Oregon State University, Corvallis, OR 97331

Many fundamental studies have been made and several conflicting theories presented in the literature on the nucleation and precipitation of interstitial oxygen in silicon. Part of these differences might be explained by virture of the fact that we have found the precipitation rate of oxygen in silicon to be critically dependent on the ambient used in the first step. The results of a large number of single-step, two-step, and three-step heat-treatments are summarized and this ambient effect explained.

698 RNP Characterization of Lightly Doped Drain (LDD) Device Fabricated with Self-Aligned Titanium Disilicide: *F. S. Lai, S. H. Dhong, E. J. Petrillo, Y. C. Sun, M. R. Polcari, C. Y. Ting,* and *Y. Taur*, IBM T. J. Watson Research Center, Yorktown Heights, NY 10598

An As-P double-diffused LDD device was designed and fabricated for the 1 μm CMOS technology. In this device, a self-aligned titanium disilicide is formed over the polysilicon gate and source/drain by using a two-step process. The sheet resistance of both the poly gate and source/drain is dramatically reduced. The avalanche breakdown voltage gained 2V improvement over the conventional device. However, transconductance degradation is observed, owing to the introduction of n- region series resistance. A detailed description of experimental results and hot electron characteristics is discussed.

699 RNP Boron Diffusion through Gate Oxides: *C. Y. Wong, F. S. Lai, V. R. Deline,* and *J. C. Deluca*, IBM, T. J. Watson Research Center, Yorktown Heights, NY 10598

As device dimensions of CMOS continue to be scaled down, the demand for better performance of PMOS dictates the use of p$^+$ polysilicon gate. Consequently, diffusion of boron through thin gate oxide becomes a major concern in this technology. In our study, the diffusion of ion-implanted boron in thermally oxidized silicon is compared with the diffusion of boron through thin gate oxides, using ion-implanted polysilcon as a dopant source. Secondary ion mass spectroscopy (SIMS) was used to monitor the boron distribution profiles in these oxides. Diffusion coefficients are calculated by fitting the data with Sah's diffusion model. The values are obtained as a function of annealing temperature and ambient. Large discrepancies are found for boron diffusion in thick thermal oxide *vs.* diffusion through thin gate oxide. A proposed model based on enhanced diffusion through interfacial regions in thin oxides is presented.

700 RNP Self-Aligned Silicided Shallow P+ Junctions for CMOS Applications: *L. K. Wang, Y. Taur, V. R. Deline,* and *C. Y. Ting*, IBM, Thomas J. Watson Research Center, Yorktown Heights, NY 10598

Shallow P+ junctions have been fabricated by using a silicon amorphorization implant prior to boron on BF_2 implants to eliminate channeling effect. By incorporating a self-aligned titanium disilicide process over both the diffusion and the polysilicon gate regions, the sheet resistance can be dramatically reduced. The SIMS depth profile of the silicided junctions as well as the electrical characteristics of the MOSFET devices fabricated using this technology are presented.

701 RNP Ion Implant Dose Windows for Generation of Silicon Crystal Defects: *B. Waller*, United Technologies Mostek, Process R&D Department, Carrollton, TX 75006

A study was made of the formation of high densities of surface stacking faults by a particular sequence of processing steps involving intermediate dose ion implantation. These defects are known to be both very detrimental to device yield and, once formed, very difficult to remove during subsequent normal thermal processing. The dependence of defect density on implant species, energy, dose, and subsequent thermal treatment is discussed.

702 RNP Empirical Range Statistics for Low Energy Boron Implants in Silicon: *C. Slaby* and *M. Simard-Normandin*, Northern Telecom Electronics Limited, Nepean, Ontario, Canada K2H 8G1

Extensive SIMS profiling studies were undertaken for B^+ and BF_2^+ implants in silicon. The data gathered covers the 10-30 keV energy range for B^+ and the 25-120 keV range for BF_2^+, with doses from 5×10^{14} to $3 \times 10^{15} cm^{-2}$. Empirical range statistics are extracted, and modeling of as-planted boron profiles is discussed. It is shown that Pearson IV distribution correctly describes boron profiles, provided empirical range statistics are used.

703 RNP Characteristics of BCl Ion-Implanted Silicon: *M. Delfino* and *M. E. Lunnon*, Philips Research Laboratories Sunnyvale, Sunnyvale, CA 94088

Shallow p$^+$/n junction diodes are formed by the furnace annealing or rapid-incoherent light annealing of BCl ion-implanted <100> silicon. The diodes exhibit excellent I-V characteristics with reverse-bias leakage currents comparable to those of diodes fabricated with equivalent energy BF_2 ions. However, chlorine, unlike fluorine, is found to inhibit the electrical activation of boron and contribute to some minority recombination within the depletion layer. A band of dislocation loops, that remains near the as-implanted amorphous-crystalline interface after annealing, does not adversely affect the devices.

704 RNP Emitter-Base Leakage in Boron-Implanted Transistors: *D. C. Ahlgren*, IBM Corporation, General Technology Division, East Fishkill Facility, Hopewell Junction, NY 12533

Various methods of ion implanting boron for base doping of shallow NPN transistors have been studied. Diodes of various areas and perimeter-to-area ratios were fabricated using BBr deposition, BF_2^+ and B^+ implantation of base, followed by As^{+3} ion implanation for emitter formation. Dose and anneal experiments were performed to find reverse bias leakage and junction breakdown voltage dependence on geometry, species, dose, and annealing conditions. TEM was performed to correlate leakage with residual defects.

705 RNP Autodoping of Thin Si Epi Layers Deposited on Heavily Doped Substrates: *J. R. Abernathey*, IBM, General Technology Division, Essex Junction, VT 05452

The deposition and characterization of thin ($0.5 < T_{epi} < 15.0\ \mu m$) epi layers deposited on heavily doped substrates were investigated with respect to VLSI CMOS requirements. Conventional CMOS "well" formation processes induce epi/substrate outdiffusion which narrows the epi flat region. In this case, control of backside autodoping (which affects resistivity in the flat) is of primary concern. Reduced time-temperature well formation processes are discussed which allow much thinner epi layers. With these processes, the as-deposited epi transition region is a more significant component of the final epi/substrate vertical doping profile. Control of frontside autodoping, which affects the transition width, becomes a more important concern with thinner epi layers.

706 RNP Modeling Reactive Sputter-Etched Profiles: *R. J. Schutz*, AT&T Bell Laboratories, Murray Hill, New Jersey 07974

We have modeled the edge profile of reactive sputter-etched features. The model takes into account vertical and horizontal etching of the masking layer, the material to be etched, and a layer which continually redeposits during etching. By empirically fitting modeled results to observed profiles, information about the redeposited layer is obtained. The etching of a deep trench in silicon is modeled as an example.

707 RNP Dry Etching of Tapered Contact Holes Using Multilayer Resist: *R. J. Saia* and *B. Gorowitz*, General Electric Company, Corporate Research and Development, Schenectady, NY 12301

Optimum coverage of contact hole sidewalls by sputtered metals typically requires tapering of the holes. A number of resists and dry (reactive ion and plasma) etch processes have been examined for this purpose. These include (*i*) replication of the presloped single-layer AZ-type photoresist profile by anisotropically etching the resist and the SiO_2 at comparable rates, and (*ii*) controlled lateral etching of the vertical walls of a multilayer resist while anisotropically etching the SiO_2. The latter process, which will be discussed in detail, preserves the inherent accurate resolution the multilayer resist while providing an opportunity for tailored and reproducible sidewall angles.

708 RNP Plasma Interactions with Photoresist during Metal Etch: *M. ter Beek*, IMP, San Jose, CA 95134

There is a growing industry trend towards plasma metal etching. The plasma environment can have detrimental effects on the photoresists, owing to ion bombardment and resist surface heating. In addition to these phenomena, plasma metal etching can cause other effects not seen when etching other films. Most aluminum alloy etch processes are based on chlorine chemistry which results in $AlCl_3$ as the etch product. $AlCl_3$ is highly reactive and it is thought to be responsible for the additional interactions. This phenomenon is especially true with high power densities during etch and is shown to lead to resist removal problems and bondability problems.

709 RNP Etching Al-Si with Neglibible CD Loss: *K. M. Monahan, D. Livingston*, and *B. Richardson*, GCA Corporation, West Coast Technology Center, Sunnyvale, CA 94086

The perceived difficulty of dry etching aluminum for VLSI micorelectronic applications has led to the development of some very complex processing chemistries, each designed to enhance one or more performance parameters, such as etch rate, mask selectivity, substrate selectivity, etch uniformity, and critical dimension control. The purpose of this work is to show how a simple two-gas process in a triode etch reactor can be used to maintain precision linewidth control associated with reactive ion etching and the selectivities associated with plasma etching.

710 RNP Transient Behavior during Film Removal in Diffusion-Controlled Plasma Etching: *R. C. Alkire* and *D. J. Economou*, Department of Chemical Engineering, University of Illinois, Urbana, IL 61801

A mathematical model was formulated to analyze transient behavior during film removal from closely spaced wafers in a barrel plasma etcher. The model incorporates diffusion and simultaneous reactions which include the etching process and also recombination reactions of both volume and surface types. The analysis relates the effect of geometric and operating variables to process behavior, including etch uniformity, over-etch exposure, and throughput. Optimum settings for interwafer spacing and reactor pressure to achieve maximum throughput were also identified. Dimensionless system parameters were used to express calculated results in general form for any system which conforms to the model assumptions.

711 RNP Polyimide Etching in O_2/CF_4 RF Plasmas: *T. Yogi, K. Saenger, S. Purushothaman*, and *C. P. Sun*, IBM, Thomas J. Watson Research Center, Yorktown Heights, NY 10598

Polyimide etch rates (ER) and optical data were obtained as a function of gas composition (0-40% CF_4) and flow rate for a wide range of conditions relevant to plasma processing. The CF_4 percentage giving the maximum ER varies with power, temperature, and loading; the O/F ratio at this optimum CF_4 percentage is nearly constant. Factors affecting the O/F ratio and simplifying generalizations based on it are discussed.

712 RNP Microwave Plasma Downstream Chemical Etching: *B. Robinson* and *S. A. Shivashankar*, IBM, T. J. Watson Research Center, Yorktown Heights, NY 10598

A microwave downstream etcher has been built to determine the etching characteristics of organic materials in a CF_4/O_2 discharge. Arrhenius plots (etch rate *vs.* inverse temperature) as a function of percent CF_4 suggests that hydrogen extraction from the organic structure lowers the activation energy and increases the density of etching sites. Substrate temperature is an important parameter for controlling the etch rate.

713 RNP Low Temperature Epitaxial Silicon Growth Kinetics in a Low Pressure Plasma-Enhanced CVD Reactor: *J. H. Comfort, R. Reif*, and *H. Sawin*, Department of Electrical Engineering and Computer Science and Department of Chemical Engineering, Massachusetts Institute of Technology, Cambridge, MA 02139

An extensive kinetic study of silicon growth in a novel plasma enhanced chemical vapor deposition (PECVD) reactor has been carried out. The effects of plasma power, gas composition [$\%H_2$], and pressure have been studied for growth temperatures from 600° to 800°C. In particular, the growth of epitaxial silicon films at very low gas pressures (~1 mtorr) and low temperatures (650°-800°C) will be discussed in this paper. The dependencies of the silicon growth rate and crystallinity on silane and hydrogen partial pressures are presented as are the observed activation energies.

This work was supported by Semiconductor Research Corporation under Contract no. 83-01-033.

714 RNP A Simple Method to Control the Bias Voltage during Reactive Ion Etching (RIE): *G. Csanky* and *S. L. McCluskey*, The Aerospace Corporation, Los Angeles, CA 90009

In a standard RIE system, the upper electrode is grounded and RF power is supplied to the lower electrode. Plasma is generated between these two electrodes; etching is done at low pressures (≅ 10-20 mtorr). During etching, the lower electrode develops a negative bias voltage possibly exceeding −1000V. A simple solution is proposed which allows the bias voltage to be set semi-independently of the RF input power and process pressure without affecting the etch-rate. Experiments performed with a modified Plasma-Therm RIE system is presented and results discussed.

715 RNP Planar Plasma Etching of Molybdenum Polycide: *S. A. Agamy, T. Abraham*, and *H. M. Naguib*, Semiconductor Components Group, Northern Telecom Electronics Limited, Ottawa, Ontario, Canada

The etching of molybdenum polycide was investigated using a Drytek DRIE-100 planar plasma etcher. Reasonably good etch profiles were obtained in a one-step etching process using a gas throughputs were obtained by applying a two-step etching process in which a high percentage of SF_6 (> 60) was used to etch the $MoSi_2$ films, followed by a second etching cycle with high percentage of Freon-115 (> 50%) for the underlying polysilicon. The implications of these results on VLSI applications are discussed.

716 RNP Luminescence of YAG:Tm, YAG:Tb, and YAG:Tm:Tb: *M. S. Scholl* and *J. R. Trimmier*, Sperry Corporation, Corporate Technology Center, Displays, Phoenix, AZ 85036

Two rare earth elements thulium (Tm) and terbium (Tb) have been used to synthesize a blue yttrium aluminum garnet (YAG) phosphor. Tm with concentration of up to 5% produces dark saturated blue with low efficiency. For Tm YAG, the highest efficiency is achieved at Tm concentration of 2%. Tb with a concentration of approximately 0.5% produces unsaturated blue light with an appreciably higher efficiency than that of Tm alone (by a factor of 15). The cathodoluminescence spectrum of YAG:Tm:Tb displays features of mostly Tb-doped YAG even when using low concentration of Tb (0.5%). The light emitted by phosphors codoped by Tm and Tb show a clear shift toward green color. There appears to be a resonant transfer of energy from the $^1G_4$ state of Tm^{3+} to the $^5D_4$ state of Tb^{3+}. At least in the case of low terbium concentration in YAG, the thulium acts as a sensitizer for cathodoluminescence.

PEOPLE

ASTM Honors Society Members

Florian B. Mansfeld, Shu-Yuan C. Tsai, and **Cameron A. Ogden** have been honored as three of the recipients of the Sam Tour Award of the American Society for Testing Materials.

The three, along with their co-authors, E. Meyer, S. Jeanjaquet, and K. Fertig, were given the award for their paper titled "Reproducibility of Electrochemical Measurements of Atmospheric Corrosion Phenomena," which was published in "Atmospheric Corrosion of Metals" (1982).

The Sam Tour Award is presented annually to the author(s) of a technical paper of outstanding merit in the field of improvements and evaluation of corrosion testing methods.

Mansfeld was born in Leipzig, Germany. He received his Ph.D. degree from the University of Munich in 1967 and was a postdoctoral fellow at MIT from 1967 to 1977. He is currently a group manager for Rockwell International Science Center, Thousand Oaks, California. He has been a member of The Electrochemical Society since 1969.

Tsai was born in Taiwan and received her M.S. degree in materials science from Rensselaer Polytechnic Institute in 1970. She now works as a manager for Matech, Incorporated, Sylmar, California. Tsai joined The Electrochemical Society in 1973.

Ogden was born in Vancouver, British Columbia. He was awarded his B.S. degree in chemistry by UCLA in 1974. He is currently acting as technical director for Photocircuits, Glen Cove, New York. He has been a member of The Electrochemical Society since 1978.

POSITION AVAILABLE

Post Doctoral Fellows or Senior Technicians for fundamental research, one position each: Radiolysis of water; High Temp decomposition of water. Salary range 16,000-20,000 and 10,000-12,000, respectively. Send resumes to: Dr. M. A. Habib, Department of Chemistry, Texas A&M University, College Station, Texas 77843 MF/EOE.

Call for Nominations for the Henry B. Linford Award for Distinguished Teaching

Nominations are solicited for the Henry B. Linford Award for Distinguished Teaching of The Electrochemical Society, Inc. The third presentation of this biennial award will be made at the 1986 Spring Meeting of the Society in Boston, Massachusetts.

The nominee shall be distinguished for excellence in teaching in subject areas of interest to the Society. The nominee need not be a member of the Society, nor shall there be any restrictions or reservations regarding age, sex, race, citizenship, or place of origin or residence.

The award shall consist of a silver metal and bronze replica thereof both bearing the recipient's name and the sum of one thousand dollars. The recipient shall receive the award in person at the 1986 Spring meeting of the Society. The award will be presented by the President of the Society at the Awards and Recognition Session. Expenses involved in the acceptance of the award shall be assumed by the recipient.

To be considered for the Henry B. Linford Award, nominations must be accompanied by supporting documents, such as a biography, list of recent pertinent courses taught, list of publications, professional activities, and other appropriate supporting material. Letters of support by distinguished colleagues and former students are also welcome.

Nomination documents in 8 copies should be submitted to the Chairman of the Selection Committee, Dr. P. N. Ross, Jr., University of California, Materials and Molecular Research Division, Lawrence Berkeley Laboratory, Berkeley, CA 94720. Deadline for receipt of nominations by the Selection Committee Chairman is **May 1, 1985.**

Nominations Solicited for the 1984 Vittorio de Nora-Diamond Shamrock Award of The Electrochemical Society, Inc. in Electrochemical Engineering and Technology

Nominations are solicited by the Honors and Awards Committee for the Vittorio de Nora-Diamond Shamrock Award in Electrochemical Engineering and Technology. The next Award will be presented at the Spring 1986 Meeting of the Society in Boston, Massachusetts.

The recipient shall be distinguished for outstanding contributions to electrochemical engineering and technology. Nominees need not be members of the Society to be considered and there are no distinctions, restrictions, or reservations regarding age, sex, race, citizenship, or place of origin or residence.

The Award consists of a gold medal and a bronze replica, both bearing the recipients name, and the sum of $1500. The recipient is required to deliver an address to the Society on a subject related to the contributions for which the Award is presented.

Previous recipients of the Vittorio de Nora-Diamond Shamrock Award are:

1974—Abner Brenner	1980—Henri B. Beer
1976—Robert B. MacMullin	1982—Joseph C. Schumacher
1978—Francis T. Bacon	1984—Donald E. Danly

This is one of The Electrochemical Society's most prestigious awards, and all members are urged to give serious consideration to nominating possible candidates. Please send letters of nomination and supporting documentation to: Brooke Schumm, Jr., Union Carbide Corp., Battery Products Division, Technical Laboratory, 25225 Detroit Rd., Westlake, OH 44145, U.S.A. Supporting documentation should include a biography, a list of publications and patents, and a brief summary of the outstanding contributions on which the Award is to be based. Letters of support from experts in electrochemical engineering and technology will be welcomed. If possible, please submit nominations by April 1, 1985, to facilitate consideration by the Award Committee. Nominations will be closed at the beginning of the Spring 1985 meeting.

F. M. Becket Memorial Award

The Electrochemical Society will offer the F. M. Becket Memorial Award to a qualified graduate student for the summer of 1985. This award commemorates F. M. Becket, a man of great research and administrative ability, and a former President of the Society, whose accomplishments in science and industry were outstanding. The stipend, valued at $2000, provides a grant-in-aid toward a summer's (at least two months) research and study overseas in the laboratory of a recognized research institute or institution of higher learning, selected from the approved list maintained by the F. M. Becket Memorial Award Committee.

The objectives of this award are to stimulate and encourage education and participation in the fields of electrochemical science and industry concerned with specialty materials and processes as follows:

a) **Materials** such as refractory metals and compounds, intermetallics, graphite, fused salts, and rare earth metals;

b) **Equipment** for the utilization of electrical energy in materials synthesis;

c) **Processes** using arcs, vacua, plasmas, and electron and ion beams; and

d) **High temperature kinetics and thermodynamic and related phenomena** such as melting, vaporization, reactions, sintering, diffusion or oxidation occurring at high temperatures, high pressures, or vacua involving high temperature materials.

To be eligible for the award, the entrant must qualify in one of the two following categories. He or she must be either (1) a graduating senior of demonstrated ability, regularly enrolled in any recognized college, university, or institute of technology in continental United States or Canada, who intends to seek an advanced degree, or (2) a graduate student, similarly enrolled, who is seeking an advanced degree. No limitations of sex, race, nationality, or religion are to be imposed by the Award Committee in determining the recipient of the award.

The award shall be presented on the basis of the following material:

1. A complete transcript of the student's academic record.
2. Two copies of a letter, over the signature of the head of the College or Department in which the student is enrolled, describing briefly his or her academic work, his or her campus activities, and presenting an estimate of his or her abilities.
3. Two copies of a letter, over the student's signature, containing a brief biographical sketch, a detailed description of the nature and extent of his or her academic work, particularly as it may relate to the field of the award, and an outline of future plans. The student's letter should also contain a statement signifying willingness to fulfill the further requirements of the award as described in the Award Rules. The student shall indicate, from the list provided by the Award Committee, a choice of a place of residence under the award.

Application forms are available from the Executive Secretary, V. H. Branneky, The Electrochemical Society, Inc., 10 South Main St., Pennington, N.J. 08534-2896. Deadline for receipt of completed applications will be January 1, 1985 and the award winner will be announced on March 30, 1985.

$LiAsF_6$

(Lithium Hexafluoroarsenate)

USS LECTRO-SALT™

The superior electrolyte salt for nonaqueous lithium cells. Available in commercial quantities.

Pure $LiAsF_6$ is not toxic by dermal absorption, and is only slightly toxic when ingested. Ames test results indicate $LiAsF_6$ is not a carcinogen.

ELECTROCHEMICAL GRADE 99.9+%

1. Less than 100 ppm H_2O
2. Completely soluble in organic solvents
3. Acid equivalent near zero

For technical bulletins, and price information, call or write:

USS Agri-Chemicals
Division of United States Steel

Atlanta Technical Center
685 DeKalb Industrial Way
Decatur, GA 30033
Phone: 404/292-2525

NEW MEMBERS

It is a pleasure to announce the following new members of The Electrochemical Society as recommended by the Admissions Committee and approved by the Board of Directors in June 1984.

Active Members

Arafat, E. S. S., Holly Springs, MS
Baldwin, R. P., Louisville, KY
Bolch, N. A., Greensboro, NC
Burcin, W. A., Research Triangle Park, NC
Crooke, M., Brakpan, South Africa
Demunda, G. P., Sanborn, NY
Donaldson, K. T., Austin, TX
Dunham, O. O., Jr., Corbin, KY
Ho, K., Denver, CO
Hoenigman, J. R., Dayton, OH
Hosokura, S., New York, NY
Ihantola, H. K. J., Halikko, Finland
Johnson, R., Munford, AL
Kao, W.-H., Madison, WI
Kinney, R., Phoenix, AZ
Kirtley, S., Milpitas, CA
Lamb, S., Huntington, WV
MacDiarmid, A. G., Philadelphia, PA
Malahat, T., Santa Clara, CA
Mattis, J. J., Hackettstown, NJ
Medelko, M. C., Islington, Ont., Canada
Moquin, J. F., Eagan, MN
Nuerenberg, D., Nampa, ID
Ohfuji, S.-I., Kanagawa, Japan
Okkonen, H., Espoo, Finland
Opila, R. L., Aberdeen, NJ
Pampalone, T. R., Branchville, NJ
Papadakis, N., Painesville, OH
Passaniti, J. L., Madison, WI
Price, J., Owing Mills, MD
Rieke, P. C., Los Alamos, NM
Ro, S. K., Puchun City, Kyungki Do, Korea
Rodgers, T., Sunnyvale, CA
Roedel, R. J., Tempe, AZ
Schnurnberger, W. F., Stuttgart, Germany
Schuler, A. M., Upton, NY
Soriaga, M. P., Santa Barbara, CA
Stucki, F., Balzers, Liechtenstein
Van Nice, G. V., Santa Clara, CA
Van Roosmalen, A. J., Eindhoven, The Netherlands
Wojciechowski, M., Catonsville, MD

Student Members

Backs, S. J., Edmonton, Alb., Canada
Coffman, M. A., Terre Haute, IN
Daubenspeck, T., Potsdam, NY
Goodenough, M. R., London, England
Grubb-Hewlett, D., Arlington, VA
Han, M. K., Salt Lake City, UT
Kathare, M., Akron, OH
Kim, H. J., Raleigh, NC
Leu, J., Gainesville, FL
Mariani, R. D., Ithaca, NY
Mathcock, R. S., Cambridge, MA
McVay, L., Berkeley, CA
Meissner, P. L., Kensington, CA
Orfield, M., Menomonie, WI
Sider, M., Montreal, Que., Canada
St-Pierre, J., Boucherville, Que., Canada
Willis, J. D., Columbus, OH
You, J., Fuzhou, Fujian, China
Zappia, M. J., Cleveland, OH

Reinstatements

Crouch, D. A., Jr., Corvallis, OR
Kugimiya, K., Osaka, Japan
Ranadive, D. K., San Ramon, CA
Verdet, L. J., New York, NY

Announcement of Energy Research Summer Fellowships

The Board of Directors of The Electrochemical Society has announced that there will be additional summer fellowships in 1985 supported by the Department of Energy. Each fellowship grant will be $2000. The Summer Fellowship Award subcommittee, with the approval of the Department of Energy, shall have the discretion of deciding the number of recipients and the amount granted to each, within the limits of the appropriation.

The purpose of the award is to assist a student in continuing his/her graduate work during the summer months in a field relating to energy research or technology of interest to The Electrochemical Society. Such field shall address energy-related aspects of electrochemical science and engineering as well as solid state science and engineering and shall involve the areas of batteries, fuel cells, photoelectrochemistry, photovoltaics, and electrochemical processes of materials aimed at reducing energy consumption.

Candidate's qualifications: "The award shall be made without regard to sex, citizenship, race, or financial need. It shall be made to a graduate student pursuing work between the degree of B.S. and Ph.D., in a college or university in the United States or Canada, and who will continue their studies after the summer period. A previous holder of an award is eligible for reappointment."

Qualified graduate students are invited to apply for these fellowship awards. Applicants must complete an application form and supply the following information:

1. A brief statement of educational objectives.
2. A brief statement of the thesis research problem including objectives, work already accomplished, and work planned for the summer of 1985.
3. A transcript of undergraduate and graduate academic work.
4. Two letters of recommendation, one of which should be from the applicant's research adviser.
5. Successful recipients of fellowships shall agree not to hold other appointments or other fellowships during the summer of 1985.

Application forms are available from the Chairman of the Fellowship Awards Subcommittee, to whom completed applications and letters of recommendation should be sent: Dr. B. E. Conway, Department of Chemistry, University of Ottawa, Ottawa, Ontario, Canada K1N 9B4.

The deadline for receipt of completed applications for these Summer Fellowships will be January 1, 1985 and award winners will be announced on May 1, 1985.

Summer Fellowship Award Program of The Electrochemical Society

The Board of Directors of The Electrochemical Society has voted to allocate $6,000 for summer fellowships in 1985. The Award subcommittee shall have the discretion of deciding the number of recipients and the amount granted to each, within the limits of the appropriation.

The purpose of the award is to assist a student in continuing his/her graduate work during the summer months in a field of interest to The Electrochemical Society. According to the rules for the Society Summer Fellowship Program, if one award is given it shall be called the Edward G. Weston Fellowship Award; if two awards are given, the second one shall be designated the Colin Garfield Fink Fellowship Award; if more than two are given, the third award shall be called the Joseph W. Richards Fellowship Award.

Candidate's qualifications: "The award shall be made without regard to sex, citizenship, race, or financial need. It shall be made to a graduate student pursuing work between the degree of B.S. and Ph.D., in a college or university in the United States or Canada, and who will continue their studies after the summer period. A previous holder of an award is eligible for reappointment."

Qualified graduate students are invited to apply for these fellowship awards. Applicants must complete an application form and supply the following information:

1. A brief statement of educational objectives.
2. A brief statement of the thesis research problem including objectives, work already accomplished, and work planned for the summer of 1985.
3. A transcript of undergraduate and graduate academic work.
4. Two letters of recommendation, one of which should be from the applicant's research adviser.
5. Successful recipients of fellowships shall agree not to hold other appointments or other fellowships during the summer of 1985.

Application forms are available from the Chairman of the Fellowship Awards Subcommittee, to whom completed applications and letters of recommendation should be sent: Dr. B. E. Conway, Department of Chemistry, University of Ottawa, Ottawa, Ontario, Canada K1N 9B4.

Deadline for receipt of completed applications will be January 1, 1985 and award winners will be announced on May 1, 1985.

MEETINGS CALENDAR

Gordon Research Conferences
in
California
Winter 1985

January 7-11
Fibronectin
Polymers
January 14-18
Composites
January 21-25
Renin-Angiotensin
Electrochemistry
January 28-February 1
Agricultural Science
Protons and Membrane Reactions
February 4-8
Polymers for Biomedical and Medical Application
Multiple Opiate Receptors
February 11-15
Biology of Aging
Oxygen Radicals in Biological Systems
February 18-22
Chemistry of Electronic Materials

For further information, contact A. M. *Cruickshank, Director, Gordon Research* Conferences, University of Rhode Island, Kingston, RI 02881-0801. Telephone: (401) 783-4011 or (401) 783-3372.

REVIEWS & NEWS INDEX

Abstracts of Recent News Papers—New Orleans, Louisiana, Meeting 467C-471C
People 472C
New Members 473C
Meetings Calendar . 474C
Call for Papers—Toronto, Ontario, Canada Meeting 491C-496C

ADVERTISERS' INDEX

Bioanalytical Systems 490C
Combustion Engineering, Inc. 476C
Electrosynthesis Co., Inc. 488C
Elsevier 484C
Gaertner Scientific Corp. 487C
Hewlett Packard 483C
JEC Press 485-486C
Kerr McGee Corp. 481C
Life Systems, Inc. 482C
Princeton Applied Research .. 489C
Standard Oil Co. 480C
Texas A&M University 472C
USS Agri-Chemicals 473C

APPLICATION FOR AWARDED STUDENT MEMBERSHIP
TO
THE ELECTROCHEMICAL SOCIETY, INC.
AND
THE ELECTRONICS DIVISION OF THE ELECTROCHEMICAL SOCIETY, INC.

Includes subscriptions to the JOURNAL OF THE ELECTROCHEMICAL SOCIETY and Electronics Division Newsletter.

Limited to: undergraduate students in final two years; graduate students in science or engineering; or education majors in science or engineering

1. Name: _____

2. Home address: _____

_____

_____

3. School, Division, and Department: _____

4. School address: _____

_____

5. Undergraduate year beginning in September 1985 (check one):

Next to final year:_____ Final year:_____

Graduate year beginning in September 1985 (circle one): 1 2 3 4 5

6. Current or future major subject: _____

7. Undergraduate grade point average:_____out of possible_____

Graduate school grade point average:_____out of possible_____

8. Have you won this award before? (check one) Yes_____ No_____

If yes, how many times?_____

9. Are you a member of a Local Section of The Electrochemical Society? Yes_____ No_____

Signature of student: _____

Faculty member signature attesting to full-time enrollment of student:

Signature: _____

Department: _____ Date: _____

APPLICATIONS MUST BE POSTMARKED BY OCTOBER 31, 1985

Send application to: A. Reisman, Professor
Microelectronics Center of North Carolina
and North Carolina State University
P.O. Box 12889
Research Triangle Park, NC 27709

AWARD RULES

This award is available to qualified full-time students worldwide, who will be starting, or are already in, their final two years as undergraduates or who are graduate students in science, engineering, or education (with a science or engineering degree). It is renewable for up to a total of four years. Qualifiers will be determined by a committee of the Electronics Division of The Electrochemical Society, Inc. Qualifiers and nonqualifiers will be notified by January 1, 1985. Membership will begin on January 1, 1986.

MANAGER
APPLIED RESEARCH OPERATION

C-E Power Systems, a Division of Combustion Engineering located in Windsor, Connecticut is involved in the crucial business of supplying energy to meet growing worldwide demands. The work is important and we treat it that way, with innovative technology and the wide range of professionals needed to implement it. Right now, a career is available for a Scientist-Manager to aggressively lead applied research activities in advanced electrochemical applications.

Necessary credentials must include a PhD in Physical Science with a minimum of 4 years successful Research Management and proven research ability in one or more of the following areas: ELECTROCHEMICAL ENERGY CONVERSION, SOLID STATE MATERIALS RESEARCH, SOLID ION CONDUCTORS, THIN FILM TECHNOLOGY INCLUDING SURFACE MODIFICATION.

Excellent communicative skills (ORAL and WRITTEN) and the ability to generate and create a climate for innovative research are requisites.

Salary is excellent and we offer a comprehensive fringe benefits package including a thrift investment plan, 11 paid holidays and free group insurance including a medical and dental plan. Please send a detailed resume including salary requirements to: **Robert G. Greene. Combustion Engineering, Inc., Power Systems Group, P.O. Box 500, Windsor, Connecticut 06095-0500.** An Equal Opportunity Employer M/F/H/V.

POWER SYSTEMS

COMBUSTION ENGINEERING, INC

CHANGES OF ADDRESS SHOULD BE PROMPTLY REPORTED.

ATTACH LABEL HERE

Change of Address

To change your address, place address label here for proper identification. Print your NEW address below.

Mail to the Circulation Department, The Electrochemical Society, Inc., 10 South Main St., Pennington, N.J. 08534.

name

address

city state zip code

The Electrochemical Society, Inc.
10 South Main Street, Pennington, New Jersey 08534 • Telephone: 609-737-1902

Instructions to Authors

The **JOURNAL OF THE ELECTROCHEMICAL SOCIETY** is the official monthly journal of the Society. It contains three sections: Electrochemical Science and Technology, Solid-State Science and Technology, and Reviews and News. Technical Papers, Technical Notes, and Accelerated Brief Communications are published in the first two sections and Review Papers in the third. **All manuscripts (in English) submitted are considered for publication, with the understanding that they have not been submitted, accepted for publication, or published elsewhere. Material, e.g., figures and tables, may not be reproduced from another publication unless it absolutely cannot be described in words. If this material must be used, it must be properly referenced and acknowledged, and permission to reproduce it must be obtained from the publisher.** A wide range of subject matter is acceptable. Manuscripts can be handled promptly and efficiently if these instructions are followed.

TYPES OF PAPERS

Technical Papers describe fundamental or applied studies in depth. They contain new data and/or new interpretations of existing data. Abstracts summarizing the results are required.

Technical Notes report briefly on limited research or development that is not being pursued further. No abstracts are required.

Accelerated Brief Communications present, in camera-ready format of limited length, scientific or technological information warranting rapid dissemination. No abstracts are required.

Review Papers furnish critical analyses of topical subjects. Abstracts are required.

SUBMISSION

Submit three complete, clear copies of each manuscript and the originals of all figures and illustrations to:

Editorial Office
The Electrochemical Society, Inc.
10 South Main Street
Pennington, New Jersey 08534

A letter accompanying the manuscript should give (a) the name and mailing address of the author to whom correspondence should be sent, (b) reference to any presentation of the work at a meeting of The Electrochemical Society, (c) the Division or Group of the Society or the Divisional or Group Editor (both are listed in the front of each issue of the Journal) whose interests are most closely related to the work being discussed, (d) the section of the Journal in which the work should appear, and (e) the names and addresses of people able to act as reviewers.

EDITORIAL PRACTICES

Following receipt by the Editorial Office, each manuscript is sent to a Divisional or Group Editor with knowledge of the subject matter. This editor arranges for review of the manuscript and communicates with the author(s) regarding revisions. Final acceptance or rejection of a manuscript is determined by the Editor.

Accelerated Brief Communications are handled as rapidly as possible, ordinarily with a response to the author(s) from the Divisional Editor, the Group Editor, or the Editor within three weeks of their arrival at Pennington. Response to the authors of other manuscripts usually takes place within six weeks. Following acceptance, authors are notified of the Journal issue in which publication is scheduled; about one month before publication, page proofs and an order blank for reprints are provided. Proofs must be promptly corrected and returned. Extensive alterations by the author may delay publication; their cost will be billed to the author(s).

PUBLICATION CHARGE

To help meet publication costs, a payment of $65.00 per printed page is requested for the publication of technical material. If at least one author is a Society member or an employee of a Patron or Sustaining member, a 10% reduction is allowed. Acceptance of manuscripts for publication is, however, based on merit and is in no way dependent on such payment, which may be waived in individual cases upon request.

PRESENTATION

Organization and clarity are essential elements of successful written communication. Identify the subject matter in the title, using words useful in indexing. State the purpose of the work early in the text. Avoid introductory and explanatory material that is overly familiar to those in the field. Present the work and the arguments in an order that leads naturally to clearly specified conclusions. Provide enough information for the work to be reproduced and the logic behind it to be understood. Identify and justify any assumptions that are made; avoid tacit assumptions. Omit details that are generally known or that can be covered by reference to other publications. Give the magnitude and define the significance of experimental errors. Use headings and subheadings as appropriate. Avoid proprietary and trade names, but capitalize them where their use is necessary. Define unusual technical terms and abbreviations. Where symbols are used extensively, list them with their definitions at the end of the paper. Avoid repetition in the text and duplication of material in figures and tables. Be brief but clear.

Edit and proofread the manuscript carefully; these are not the responsibilities of the editors or reviewers.

MANUSCRIPT PREPARATION

Accelerated Brief Communications must be typewritten or printed on standard forms obtained, with detailed instructions for their use, from the Pennington Editorial Office.

All other manuscripts must be typewritten or printed, double-spaced throughout, on one side only of white 21.6 x 27.0 cm paper, with 2.5-3.8 cm margins. Do not use single spacing anywhere, in title, abstract, text, references, tables, or figure captions.

For general matters of style and format, see papers in recent issues of the **Journal** and consult a style manual such as that of the American Chemical Society or that of the American Institute of Physics. These also provide lists of common abbreviations and units. The following specific items should be noted:

(a) Système Internationale (SI) units are to be used; a description may be found in NBS Special Publication 330 or ASTM Metric Practice Guide E-380-72.

(b) The signs of cell and electrode potentials are to follow the IUPAC conventions of 1953.

(c) **Mathematical equations** should be written on a single line, if possible, using parentheses, brackets, the solidus, negative exponents, etc.

(d) **References** are to be listed separately at the end of the paper in the order they are cited in the text, being sure that each listed reference is cited. Authors' initials must be given, and Chemical Abstracts abbreviations must be used. Citations of other than the generally available literature should be avoided if possible.

(e) **Tables** are to be presented on individual sheets, with both captions and body double-spaced.

(f) **Figure captions** and numbers are to be included on a separate sheet and must not appear in the body of any figure or illustration.

(g) **Drawings** and **graphs** will ordinarily be reduced to column width (8.3 cm) and after such reduction should have lettering at least 0.15 cm high. Lettering must be of letter-guide quality. Originals in India ink on tracing cloth or paper are preferred, but India ink on coordinate paper with blue ruling is acceptable. When several curves are shown, each may be lettered and identified in the caption. The Editorial Office will not make corrections or additions to figures.

(h) **Photographs** should be used sparingly. The originals supplied must be glossy prints and should be protected against bending. Micrographs must have a labeled unit length within the body of the picture; reduction for printing makes magnifications meaningless.

Revised August 1, 1984

Printed in the United States of America

THE ELECTROCHEMICAL SOCIETY, INC.

The Electrochemical Society is an international society concerned with a broad range of phenomena related to electrochemical science and technology and solid state science and technology.

OBJECTIVES

1. The advancement of the theory and practice of electrochemistry, electrometallurgy, electrothermics, electronics, and allied subjects.
2. The encouragement of research and the dissemination of knowledge in the fields of electrochemical science and technology and solid state science and technology.
3. The assurance of the availability of adequate training in the fields of electrochemistry and solid state science for chemists, engineers, metallurgists, physicists, solid state scientists, and others in related subjects.

BENEFITS OF MEMBERSHIP

1. The assurance of being kept aware of pertinent scientific and technical developments through the JOURNAL OF THE ELECTROCHEMICAL SOCIETY and other Society publications.
2. The opportunity to contribute to the advancement of science and technology through support of Society activities.
3. The stimulation of personal association and technical exchange with fellow scientists and engineers.

DIVISIONS

The activities of the Society are carried on by its nine Divisions and two Groups as follows:

Battery
Corrosion
Dielectrics and Insulation
Electrodeposition
Electronics
  New Electronic Technologies
  Semiconductors
Energy Technology Group
High Temperature Materials
Industrial Electrolytic
Luminescence and Display Materials Group
Organic and Biological Electrochemistry
Physical Electrochemistry

SECTIONS

Local Sections of the Society have been organized in the following cities and regions:

Boston
Canadian
Chicago
Cleveland
Columbus
Detroit
European
Indianapolis
Japan
Metropolitan New York
Midland (Michigan)
National Capital Area
North Texas
Oregon
Pacific Northwest
Philadelphia
Pittsburgh
Rocky Mountain
San Francisco
Southern California-Nevada
Southern Wisconsin
Twin Cities

OUT-OF-PRINT SOCIETY VOLUMES

The following volumes sponsored or published by The Electrochemical Society, Inc. are now out-of-print. Xerographic copies* or reprints† of these volumes are available.

* **Vapor Plating.** C. F. Powell, I. E. Campbell, and B. W. Gonser, Editors. A 1955 symposium. 158 pages.
* **The Structure of Electrolytic Solutions.** W. J. Hamer, Editor. A 1957 symposium. 441 pages.
* **Technology of Columbium (Niobium).** B. W. Gonser and E. M. Sherwood, Editors. A 1958 symposium. 120 pages.
* **Surface Chemistry of Metals and Semiconductors.** H. C. Gatos, J. W. Faust, Jr., and W. J. LaFleur, Editors. A 1959 symposium. 526 pages.
* **Electrode Processes,** First Conference. E. Yeager, Editor. A 1959 symposium. 374 pages.
* **Mechanical Properties of Intermetallic Compounds.** J. H. Westbrook, Editor. A 1959 symposium. 435 pages.
* **Zirconium and Its Alloys.** J. P. Pemsler, E. C. W. Perryman, and W. W. Smeltzer, Editors. A 1965 symposium. 205 pages.
† **Measurement Techniques for Thin Films.** B. Schwartz and N. Schwartz, Editors. 1965 and 1966 symposia. 347 pages.
† **Electrode Processes,** Second Conference. E. Yeager, H. Hoffman, and E. Eisenmann, Editors. A 1966 symposium. 190 pages.
* **Electrolytic Rectification and Conduction Mechanisms in Anodic Oxide Films.** P. F. Schmidt and D. M. Smyth, Editors. A 1967 symposium. 230 pages.
* **Electrets and Related Electrostatic Charge Storage Phenomena.** L. M. Baxt and M. M. Perlman, Editors. A 1967 symposium. 150 pages.
* **Dielectrophoretic and Electrophoretic Deposition.** E. F. Pickard and H. A. Pohl, Editors. A 1967 symposium. 138 pages.
* **Electron and Ion Beam Science and Technology,** Third International Conference. R. Bakish, Editor. A 1968 symposium. 725 pages.
* **Optical Properties of Dielectric Films.** N. Axelrod, Editor. A 1968 symposium. 325 pages.
* **The Film Dielectrics.** F. Vratny, Editor. A 1968 symposium. 680 pages.
* **Ohmic Contacts to Semiconductors.** B. Schwartz, Editor. A 1968 symposium. 356 pages.
* **Semiconductor Silicon.** R. R. Haberecht and E. L. Kern, Editors. A 1969 symposium. 750 pages.
* **Chemical Vapor Deposition,** Second International Conference. J. M. Blocher, Jr. and J. C. Withers, Editors. A 1970 symposium. 872 pages.
* **Marine Electrochemistry.** J. B. Berkowitz, M. Banus, M. J. Pryor, R. Horne, P. L. Howard, G. C. Whitnack, and H. V. Weiss, Editors. A 1972 symposium. 416 pages.
* **Semiconductor Silicon 1973.** H. R. Huff and R. R. Burgess, Editors. A 1973 symposium. 936 pages.
* **High Temperature Oxidation of Metals.** By P. Kofstad. The Corrosion Monograph Series. 340 pages.
* **Chemical Vapor Deposition,** Fourth International Conference. G. F. Wakefield and J. M. Blocher, Jr., Editors. A 1973 symposium. 595 pages.
* **Electrets, Charge Storage and Transport in Dielectrics.** M. M. Perlman, Editor. A 1973 symposium. 675 pages.
* **Fine Particles.** W. E. Kuhn and J. Ehretsmann, Editors. A 1974 symposium. 352 pages.
* **Corrosion Problems in Energy Conversion and Generation.** C. S. Tedmon, Editor. A 1974 symposium. 484 pages.
* **Electrocatalysis.** M. W. Breiter, Editor. A 1974 symposium. 378 pages.
* **Electron and Ion Beam Science and Technology,** Sixth International Conference. R. Bakish, Editor. A 1974 symposium. 594 pages.
* **Energy Storage.** H. P. Silverman and J. B. Berkowitz, Editors. A 1975 symposium. 258 pages.
* **Chemical Vapor Deposition,** Fifth International Conference. J. M. Blocher, Jr., H. E. Hintermann, and L. H. Hall, Editors. A 1975 symposium. 848 pages.
* **Etching.** H. G. Hughes and M. J. Rand, Editors. A 1976 symposium. 203 pages.
* **Electrode Materials and Processes for Energy Conversion and Storage.** J. D. E. McIntyre, S. Srinivasan, and F. G. Will, Editors. A 1977 symposium. 340 pages.
* **Electron and Ion Beam Science and Technology,** Eighth International Conference. R. Bakish, Editor. A 1978 symposium. 297 pages.
* **International Symposium on Solar Energy.** J. B. Berkowitz and I. A. Lesk, Editors. A 1976 symposium. 372 pages.
* **High-Temperature Metallic Corrosion of Sulfur and Its Compounds.** Z. A. Foroulis, Editor. A 1969 symposium. 276 pages.
* **Properties of Electrodeposits—Their Measurement and Significance.** R. Sard, H. Leidheiser, Jr., and F. Ogburn, Editors. A 1974 symposium. 430 pages.
* **Chemical Vapor Deposition,** Sixth International Conference. L. F. Donaghey, P. Rai-Choudhury, and R. N. Tauber, Editors. A 1977 symposium. 596 pages.
* **The Electrocatalysis of Fuel Cell Reactions.** W. E. O'Grady, S. Srinivasan, and R. F. Dudley, Editors. A 1978 workshop. 228 pages.
* **Electron and Ion Beam Science and Technology,** Fourth International Conference. R. Bakish, Editor. A 1970 symposium. 680 pages.
* **Plasma Processing.** R. G. Frieser and C. J. Mogab, Editors. A 1980 symposium. 360 pages.
* **Oxide-Electrolyte Interfaces.** R. S. Alwitt, Editor. A 1972 symposium. 312 pages.
* **Industrial Water Electrolysis.** S. Srinivasan, F. J. Salzano, and A. R. Landgrebe, Editors. A 1978 symposium. 297 pages.
* **Semiconductor Characterization Techniques.** P. A. Barnes and G. A. Rozgonyi, Editors. A 1978 symposium. 532 pages.
* **Fundamentals of Electrochemical Machining.** A 1970 symposium. 365 pages.
* **Electron and Ion Beam Science and Technology,** Seventh International Conference. R. Bakish, Editor. A 1976 symposium. 632 pages.
* **Thin Film Phenomena—Interfaces and Interactions.** J. E. E. Baglin and J. M. Poate, Editors. A 1977 symposium. 525 pages.
* **Electrochemical Contributions to Environmental Protection.** T. R. Beck, O. B. Cecil, C. G. Enke, J. McCallum, and S. T. Wlodek, Editors. A 1972 symposium. 173 pages.

* Order from University Microfilms, Inc., 300 North Zeeb Street, Ann Arbor, Mich. 48106. Specify an Electrochemical Society volume.

† Order from Johnson Reprint Co., 355 Chestnut St., Norwood, N.J. 07648. Specify an Electrochemical Society volume.

1/84

ELECTROCHEMISTRY
SR. R&D CHEMIST

SOHIO RESEARCH & DEVELOPMENT

SOHIO's new Corporate Research Center, located in a pleasant suburban Cleveland community, is dedicated to continuning research in production of oil, mining, industrial products and solar energy.

When you join us you will become a vital part of our company's strong commitment to solar energy research, building on our unique electrochemical storage system (double-layer capacitors, Redox systems).

As a strongly motivated scientist, you will formulate, model, synthesize and evaluate novel and proprietary electronic and ionic conducting materials for electrochemical systems. You will establish an R&D program within the corporate energy storage group and initiate collaborative efforts with our other business research groups.

You probably now are a materials or surface scientist or a physical chemist involved in electrochemical research. You should have a PhD in Chemistry or Physics and 1-3 years' industrial experience with experimental background in synthetic and electrochemical techniques.

An attractive total compensation plan including comprehensive benefits accompanies this position. **SOHIO's comprehensive relocation package for new hires includes all normal moving expenses. Homeowners also qualify for mortgage interest differential allowance, third party home purchase and other features typically restricted to internal transfers.**

Ready for the challenge of a fast growing, results-oriented Fortune 25 company? Start by sending your resume detailing your experience to:

David B. Crow, Senior Executive Recruiter
THE STANDARD OIL COMPANY (Ohio)
1424 Midland Building – 694JE • Cleveland, Ohio 44115
An Equal Opportunity Employer
NO THIRD PARTY INQUIRES, PLEASE
"Help us Help to Assure America's Energy Future"

SOHIO

ELECTROCHEMISTS AND ELECTROCHEMICAL ENGINEERS

Immediate professional opportunities exist for electrochemists and electrochemical engineers challenged by the need to improve industrial electrolytic processes. The competitive business environment demands improvements that minimize energy consumption and improve product quality.

We presently produce an array of electrochemical products including:

- Sodium Chlorate
- Sodium Perchlorate (and subsequently
- Ammonium Perchlorate)
- Manganese Dioxide
- Manganese Metal

We prefer a Ph.D. with a good academic background who is a strong experimentalist, has the ability to work with others on related electrochemical problems, and is results oriented.

A competitive salary and benefits program is offered with this position. If you are a qualified applicant and interested in a challenging industrial research and development opportunity, please send resume including education, experience and salary requirements to:



Julius C. Hilburn
KERR-McGEE CORPORATION
P. O. Box 25861
Oklahoma City, OK 73125

An Equal Opportunity Employer M/F/H/V

ELECTROCHEMICAL OPPORTUNITIES

AEROSPACE SYSTEMS

Life Systems, Inc., is a high-tech aerospace R&D company with the following immediate openings for individuals possessing proven talents and experience in Electrochemistry. Current and long-term projects, including life support and power storage systems (i.e. regenerative fuel cell) for space station applications, has created the need for more of the highly skilled people responsible for our success. These positions require a Ph.D. and 5 + years of related experience and strong communication skills.

ELECTROCHEMICAL ENGINEER

Direct activities to develop water electrolysis systems technology for multiple applications. Examples include regenerative fuel cells, O_2 generation and bulk H_2 generation. Sizes vary from 0.1 ft^2 to 1.0 ft^2 with modules to >30 cells. Focus is on new applications of recent technology, logical development cycles, and high quality results.

ELECTROCHEMIST

Responsible for creatively applying electrochemistry to various systems and components (i.e. water electrolysis, air cathodes, O_2 anodes, sensors and biocide generation). Focus is expanding our technology base on electrocatalysis, electrodes matrices and cells.

Our interdisciplinary approach to R&D has made us a leader in advanced aerospace and new product development. Our team is strong in sophisticated system and subsystem integration and unique control/monitoring instrumentation. We offer an above average compensation package coupled with challenging assignments and respect for good work. If you're interested in the challenges we can provide, send resume with salary history to:

Manager, Recruitment

Life Systems, Inc.

24755 Highpoint Road
Beachwood, OH 44122

An Equal Opportunity Employer M/F/H/V

Hewlett-Packard Laboratories

Hewlett-Packard Laboratories has opportunities for the following scientists to join our progressive R&D team in Palo Alto, California.

Surface Scientist

Your focus will be on understanding adhesion between metal-polymer and polymer-polymer interfaces for the purpose of optimizing processes in printed circuit board fabrication. You will be involved in developing test procedures for surface cleanliness and adhesion for photoresist processes. Requirements include an MS or Ph.D. in chemistry, metallurgy, materials science or equivalent; proven research skills in testing materials and surfaces are desirable.

Electrochemist

Your duties will focus on the fabrication of plated through holes on printed circuit boards. You will investigate electrochemical parameters necessary to fabricate high aspect ratio and reliable plated through holes. Requirements include a BS, MS or Ph.D. in fields related to electrochemistry. Experience with printed circuit boards is desirable.

Both positions involve extensive interaction with chemists, physicists, process engineers, PC fabricators and vendors.

Hewlett-Packard provides its employees with an excellent salary and benefits package which includes stock purchase plan, profit sharing, medical, dental and life insurances and retirement plans. We also offer a tax deferred savings plan (401-K).

Please send your resume to Barbara D. Kaufmann, Hewlett-Packard Laboratories, 1501 Page Mill Road, Palo Alto, CA 94304. We are an equal opportunity/affirmative action employer.



HEWLETT PACKARD

FOR YOUR BOOKSHELF

POWER SOURCES FOR ELECTRIC VEHICLES

B.D. McNICOL, *Shell Research Ltd., Chester, UK and* **D.A.J. RAND**, *CSIRO, Division of Mineral Chemistry, Port Melbourne, Australia (editors)*

Studies in Electrical and Electronic Engineering, 11

Electric road vehicles, operating on alternative fuels to oil, are an attractive means of alleviating oil problems in the transportation sector. This is the first definitive account of recent progress in the development of electrochemical power sources (secondary battery and fuel-cells) for traction applications. Advantages and disadvantages of electric vehicles are compared. The lead/acid battery - currently the only suitable power source in commercial production - is fully discussed. Present and possible future performance of the electric vehicle, in the laboratory and on the road, is assessed. Of interest to: vehicle developers, battery/fuel-cell scientists and engineers, governmental authorities, industries, and those concerned about the prospect of scarce, expensive petroleum and the accompanying problems it will cause the transportation sector.

1984 xxvi + 1066 pages
US $ 211.50/Dfl. 550.00
ISBN 0-444-42315-X

PHYSICS OF SOLID DIELECTRICS

I. BUNGET, *University of Bucharest and* **M. POPESCU**, *Institute of Physics and Technology of Materials, Bucharest, Romania*

Materials Science Monographs, 19

A detailed coverage of the fundamentals of solid-state dielectrics. After a detailed description of the structure of various dielectrics including glasses and polymers, a comprehensive view of chemical bonding and electron energy states in dielectrics is given. The most important properties of solid dielectrics are treated from the theoretical point of view: polarization, relaxation, electrical conduction, dielectric breakdown, ferroelectricity and principles of main dielectric devices. In support, experimental data and numerous examples of various dielectric materials are provided. Written primarily for physicists involved in solid state physics in general and in dielectric physics in particular and for students keen to enter these fields. The problems discussed may be of interest to engineers working in various industrial projects.

1984 446 pages
US $ 94.25/Dfl. 245.00
ISBN 0-444-99632-X

ELECTROCHEMISTRY: THE INTERFACING SCIENCE

Proceedings of the Sixth Australian Electrochemistry Conference, Geelong, Victoria, 19-22 February 1984

D.A.J. RAND, *CSIRO Division of Mineral Chemistry, Melbourne, and* **A.M. BOND**, *Deakin University, Waurn Ponds, Australia (editors)*

Studies in Physical and Theoretical Chemistry, 34

(Reprinted from Journal of Electroanalytical Chemistry and Interfacial Electrochemistry, Vol. 168)

Analytical, industrial, inorganic, organic, physical and theoretical chemists from university, governmental and industrial laboratories around the world attended this international and interdisciplinary conference. The programme underlined the wide range of disciplines associated with electrochemistry. Sessions were held in the fields of electrode surface studies, semi-conductor and photoelectrochemistry, mineral processing and electrometallurgy, trace electroanalysis, organic and bioelectrochemistry, physical electrochemistry, solid electrolytes, electrochemical power sources, corrosion and teaching electrochemistry.

This volume contains a selection of the papers presented. It indicates both progress and problems in the field of electrochemistry and will therefore have a broad appeal to the scientific community at large.

1984 x + 482 pages
US $ 113.50/Dfl. 295.00
ISBN 0-444-42304-4

PROGRESS IN ELECTROCHEMISTRY

Proceedings of the Fifth Australian Electrochemistry Conference, Perth, W.A., 18-22 August 1980

D.A.J. RAND, *CSIRO Division of Mineral Chemistry, Melbourne,* **G.P. POWER** *and* **I.M. RITCHIE** *(editors)*

Studies in Physical and Theoretical Chemistry, 15

(Reprinted from Journal of Electroanalytical Chemistry and Interfacial Electrochemistry, Vol. 118)

This conference - one of the major world events in the electroanalytical calendar, attracted participants and contributors from internationally recognised laboratories. Reports cover the studies on fuel cells and secondary batteries for electric vehicle and electric utility storage applications as well as photoelectrochemical and photovoltaic devices for solar energy conversion.

Contributions in the area of electrochemical research into energy conservation include investigations concerned with prevention and control of corrosion, processing of sulphide minerals, and electrowinning of aluminium and zinc.

1981 x + 470 pages
US $ 106.50/Dfl. 250.00
ISBN 0-444-41955-1

FURTHER INFORMATION WILL BE SENT BY THE PUBLISHER ON REQUEST.

Order from your bookseller or direct from:

For the USA & Canada
P.O. Box 1663
Grand Central Station
New York, NY 10163, USA

Elsewhere
P.O. Box 211
1000 AE Amsterdam
The Netherlands

7309

ELSEVIER

Advertisement

New Materials Developed in Japan (1984 Edition)

about 650 pages
Price: $980

This new English book on Japanese new materials is edited by Toray Research Center (Japan) and distributed by JEC Press Inc. (U.S.A.). Toray Research Center has been publishing the new material book annually for years. This is the first time to publish the English edition. All the 237 materials selected for this book have significant applications in industries and many of these are being used in Japanese new products. Each chapter contains the company name and address, so the reader can inquire immediately about the new material. Please order now so that you can receive the book directly from the printer in Japan as soon as the book is completed some time in June 1984.

Table of Contents

( ): The number in parenthesis shows number of articles in this book.

(A) Building and Construction (14)
Asphalt (3)
Board (4)
Concrete (5)
Miscellaneous (2)

(B) Ceramic, Glass and Carbon (23)
Carbon (4)
Ceramic (13)
Glass (5)
Miscellaneous (1)

(C) Electronic and Electric (70)
Conductor (2)
Dielectric (2)
Electrochromic (1)
Electrode (1)
Electrolite (2)
Electroluminescence (1)
Electromagnetic Wave Absorber, Shield (5)
Insulator (5)
Laser (3)
Light Emitting Diode (2)
Liquid Crystal (2)
Magnetic (8)
Optical Fiber (6)
Optoelectronic (Excluding EL, Laser, LED and OF) (2)
Photoconductor (3)
Photoelectromagnetic (2)
Resist (4)
Semiconductor (2)
Sensor (9)
Super Conductor (3)
Surface Acoustic Wave Device (2)
Thermoelectric (1)
Miscellaneous (2)

(D) Energy (9)
Solar (5)
Storage (4)

(E) Fiber and Paper (13)
Ceramic and Carbon (6)
Metallic (1)
Organic (6)

(F) Medical (7)

(G) Metal (31)
Aluminum (6)
Chromium (1)
Copper (3)
Iron (14)
Molybdenum (2)
Nickel (2)
Titanium (2)
Miscellaneous (1)

(H) Optical (3)

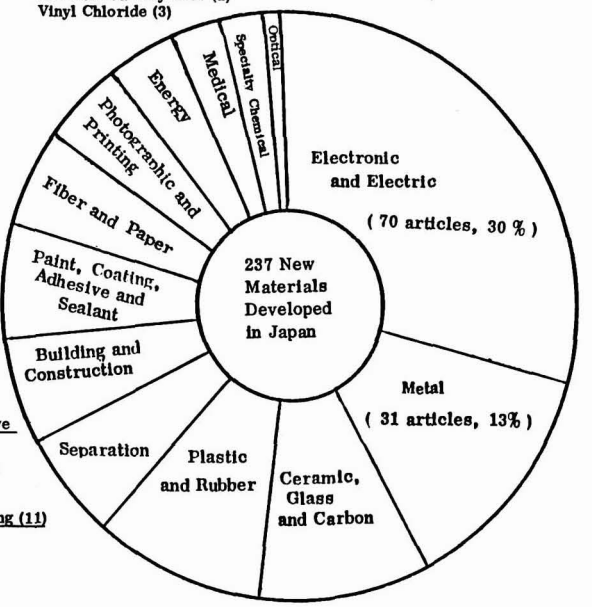
(I) Paint, Coating, Adhesive Sealant (14)
Adhesive and Sealant (6)
Paint and Coating (8)

(J) Photographic and Printing (11)
Heat Sensitive (3)
Photosensitive (7)
Miscellaneous (1)

(K) Plastic and Rubber (22)
Acrylic (2)
Amide (1)
Carbonate (1)
Fluoric (1)
Olefinic (6)
Rubber (1)
Silicone (1)
Styrene (1)
Unsaturated Polyester (1)
Vinyl Chloride (3)

(L) Separation (14)
Absorbent (1)
Adsorbent (2)
Filter (6)
Ion Separation (5)

(M) Specialty Chemical (6)



How to Order Fill out the order form below and send to JEC Press Inc.

---------- Cut out and mail ----------

To: JEC Press Inc.
14731 Sprengel Ave
Cleveland, Ohio 44135 USA

Date _____

Re: Purchase Order

Please send us a copy of "New Materials Developed in Japan" (1984 Edition) ($980) by
☐ Air ($65)
☐ Surface ($15)

We are enclosing
☐ Purchase order (this form)
☐ A bank cheque payable to JEC Press Inc.
(If payment is enclosed, ignore the shipping charge. We will pay the air shipping charge.)

Company _____

Name Attn: (Tel:)

Address _____

Advertisement



New Books and Meetings on Batteries and New Materials

1 "Progress in Batteries & Solar Cells" Vol. 5 (1984), 400 Pages

Edited by Dr. H. Shimotake, Dr. E. Voss, Mrs. H.M. Friend, etc. Published by JEC Press. About 400 pages $65. Shipping: $18 (air), $6 (surface). Contents: View From The Top, Lithium Batteries, MnO_2 and MnO_2 Dry Batteries, Lead-Acid Batteries, Electric Car Batteries, Fuel Cells, Ni-Cd Batteries, Energy Storage Systems, Battery Patents (90 articles).

2 Battery Active MnO_2 Samples and New Carbon Samples for Batteries

New MnO_2 Samples, New Acetylene Black Samples, New CF_x and C_2F Samples for Lithium Cells, New Separator Papers Samples are available as I.C. (International Common) samples. These samples are being distributed by IBA (International Battery Material Association). The price is $18 each for MnO_2 (1 Kg bottle), for C_2F and CF_x (25g each) and carbon (500g

3 Battery Material Symposium, Vol. 1, Brussels, 1983

Compiled and Edited by A. Kozawa and M. Nagayama, 300 pages, $45. Published by IBA (International Battery Material Assoc)

Contents (1) Opening Remarks on MnO_2, Zn, carbon etc (A. Kozawa), (2) EMD Deposits from Cl^-, NO_3^-, $SO_4^=$ Baths (K. Matsuki), (3) Dry Cell Dynamics (Atlung), (4) $ZnCl_2$-type cells (Furumi and Smets), (5) MnO_2 (L.F. DeVries), (6) Discharge Mechanism (Hirai, Ozuku), (7) MnO_2 (Brenet), (8) Surface of MnO_2: Zn^{++} adsorption (Tamura, Nagayama), (9) Potential of MnO_2 (Tari, Hirai), (10) Sintered Ti Anode (Bewer), (11) Zinc Powder (Meeus), (12) Carbon Rod, Acetylene Black (Denki Kagaku Kogyo), (13) Separator for Dry Cells and NiOOH, $AgNiO_2$, etc, (14) New CMD (Tanabe), (15) MnO_2 Cells (Kordesch), (16) New EMD and Activated MnO_2 (Takahashi), (17) Rechargeable MnO_2 Cells (Kwasnik), (18) CMD (Piquet, Tye, Van der Poorten).

4 New Materials Developed in Japan (1984 Edition)

about 650 pages Price: $980

Compiled by Toray Research Center Inc, about 600 pages, $980. Shipping: $60 (air) and $10 (surface). This new English book on Japanese new materials is edited by Toray Research Center (Japan) and distributed by JEC Press Inc. (U.S.A.). Toray Research Center has been publishing the new material book annually for years. This is the first time to publish the English edition. All the 237 materials selected for this book have significant applications in industries and many of these are being used in Japanese new products. Each chapter contains the company name and address, so the reader can inquire immediately about the new material. Please order now so that you can receive the book directly from the printer in Japan as soon as the book is completed some time in June 1984.

5 Recent Carbon Technology by T. Ishikawa and T. Nagaoki

By T. Ishikawa and T. Nagaoki, English edited by Dr. I.C. Lewis, 400 pages, $55 (+ shipping) Published by JEC Press Inc.

Contents (1) Preface: Carbon and Industry, (2) Basic Section: Carbon and graphite, standard production methods (pulverizing, sieving, kneading, forming, baking, impregnation, graphitization, machining), Fillers and Binders; Carbonization and graphitization, special treatment and compounding, fiber reinforcing, laminating, carbon fibers (cellulose carbon, polymer carbon, glassy carbon, vitreous carbon, PAN-based fibers, pitch-based fibers, carbon paper, carbon film, chemical and physical properties. (3) Applications: electric furnace electrode, carbon blocks, carbon paste, carbon cement, dies, molds, crucible, alloying, arc carbon, carbon raiser, denuder, electrodes for electric discharge machining, pantagraph shoe

6 Other Books on Carbon, Battery and Electrochemistry in English

1. Surface Electrochemistry by T. Takamura and A. Kozawa, $50, 250 pages (Hard cover book)
2. Rechargeable Batteries in Japan by Y. Miake and A. Kozawa, $45, 528 pages (Hard cover book)
3. Manganese Dioxide Symposium Vol. 1 by A. Kozawa and R.J. Brodd, $48, 535 pages
4. Progress in Batteries & Solar Cells, Vol. 2, 3, 4, $55, 300-400 pages
5. Electrochemistry of MnO_2 and MnO_2 Batteries, $35, 400 pages
6. Applications of Solid Electrolyte by T. Takahashi and A. Kozawa, $48, 210 pages
7. New Materials & New Processes Vol. 2 (1983) Edited by Nagayama, Yeager etc., 560 pages, $55

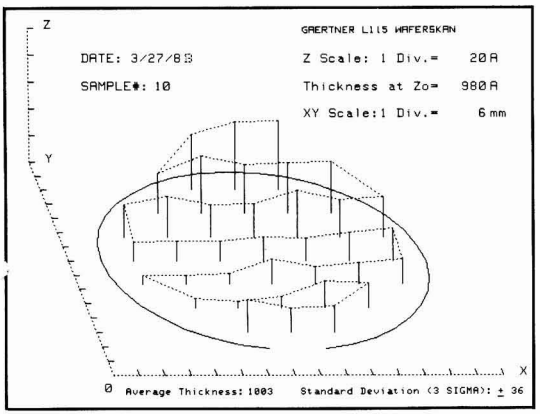
7 Meetings on Battery Materials : (1) Sept. 21, 1984, (2) Sept. 16&17, 1985

(1) The Discussion Meeting on Battery Materials (Sept. 21, 1984) in England. Organized by Dr. F.L. Tye. Registration: 40 pounds. Topics: Alkaline Manganese Dioxide Cells and Other Materials on Primary Cells. Contact Dr. Tye (Middlesex Polytechnic, Bounds Green Rd, London N11 2NQ England. Telex: 8954762.

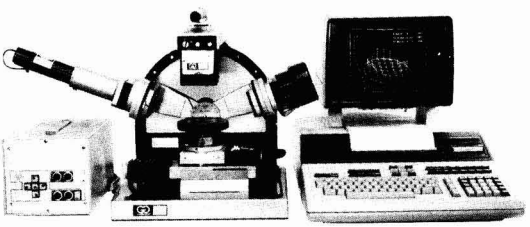
(2) The 3rd MnO_2 Symposium (Sept. 16 & 17, 1985) in Graz, Austria. Organized by Prof. K.V. Kordesch. Registration: $150 (including proceedings and two dinners). Inquire to IBA U.S. Office, 14731 Sprengel Ave, Cleveland, Ohio 44135 USA

How To Order Send Your Order To:
JEC Press & IBA, 14731 Sprengel Ave., Cleveland, Ohio. 44135 U.S.A.
(Telephone: 216-835-7695)

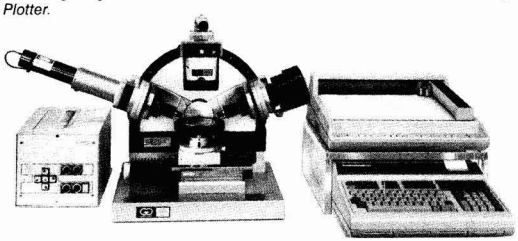
Gaertner Waferskan™ systems for automated photoresist/oxide/nitride thickness and index.



L115-45B WAFERSKAN System simultaneous printout of CRT display measuring photoresist thickness at 29 locations on 3" wafer.



L115-45B WAFERSKAN System. Automatic Ellipsometer with Precision Scanning Stage Driver and Hewlett-Packard 9845B Calculator with Integral Plotter.



L115-25B WAFERSKAN System. Automatic Ellipsometer with Precision Scanning Stage Driver, Hewlett-Packard 9825B Calculator and 7225A Plotter. (Also available for HP9835A Calculator.)

Choose from three flexible, high performance, easy-to-operate ellipsometry systems for semiconductor engineering and production control. Measure film thicknesses from 0-60,000Å with an accuracy of ±5Å and a repeatability of ±1Å. Get refractive index readings accurate to ±.01. Get automatic thin-film measurements at 5 points, 9 points, or complete XY surface profiling of wafers up to 5 inches in diameter. Get six easily adaptable and updateable operating programs in a single tape cassette. Get both numerical hard-copy and graphical scan display readouts with pushbutton ease and simplicity. Get full details now. 81212

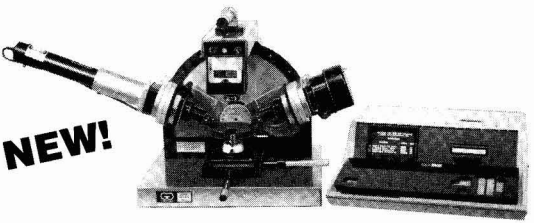
GAERTNER®

Gaertner *is* ellipsometry.

GAERTNER SCIENTIFIC CORPORATION
1201 Wrightwood Avenue, Chicago, IL 60614
Phone: (312) 281-5335 TELEX: 206136

Gaertner L116A Dual Mode Automatic Ellipsometer

Automatically measures film thickness and refractive index using both linearly and circularly polarized light.

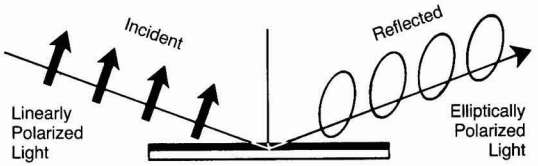


Improved accuracy. Gaertner's new model L116A Dual Mode Ellipsometer incorporates a laser light source, automatic C-Slide, rotating analyzer and desk-top computer to measure samples utilizing 72 data points with circularly polarized projected light, and 72 points with linearly polarized projected light. It's programmed to select measurements from the most accurate mode, providing extremely precise measurements of very thin to thick films.

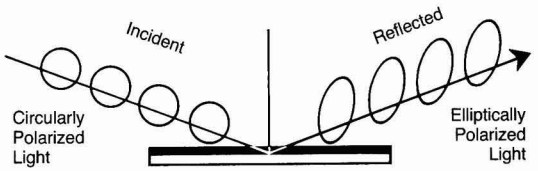
Improved automation. Operation of the L116A is automatic, including insertion and withdrawal of the C-Slide. Pushbutton-activated operation limits user error. Measurements are displayed on a CRT screen and printed on tape.

Improved versatility. The Dual Mode Automatic Ellipsometer is ideal for extremely accurate, repeatable measurement of films ranging from very thin to thick, including difficult-to-measure films for the semiconductor industry. Any L116 Gaertner Automatic Ellipsometer can be upgraded to the L116A Dual Mode model.

Linearly Polarized Projection Mode



Circularly Polarized Projection Mode



Both **circularly** *and* **linearly polarized light** *is projected on the sample and provides readings utilizing 144 data points, with computer selection of the most accurate set of readings.*

82213

Call or write for information and literature.

GAERTNER®

Gaertner *is* ellipsometry.

GAERTNER SCIENTIFIC CORPORATION
1201 Wrightwood Avenue, Chicago, IL 60614
Phone: (312) 281-5335 TELEX: 206136

INTRODUCING THE ESC MODEL 680 COMPUTING COULOMETER

• The most powerful and versatile digital coulometer available today. •

The ESC model 680 can integrate currents spanning 14 decades and accurately display coulometric values from 10^{-9} to 10^{19} Coulombs.

A RS-232-C data interface permits the 680 to act as a smart coulometric front end for your data acquisition system or as a stand alone data logger when used with any RS-232-C compatible data terminal.

Call us today for details.



THE ELECTROSYNTHESIS CO., INC.

P.O. Box 16, E. Amherst, N.Y. 14051 • 716-684-0513

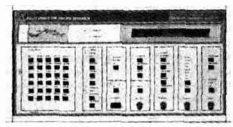
EUROPE: SWEDISH NATIONAL DEVELOPMENT CO. P.O. BOX 94 S-194 22 Upplands Vasby

The elegant touch for electrochemical corrosion measurements



Under the elegantly simple exterior of the new Model 351 Corrosion Measurement System lies the world's most advanced technology for corrosion measurements. Touch your way through self-explanatory menus (the buttons on the screen are live!). Run up to eight different types of experiments simultaneously, viewing each data plot as it's being generated. Use PARCalc™, our latest and most sophisticated data reduction routine, to calculate the results. For more customized applications you can add the capability for BASIC programming.

The Model 351 System can be configured with up to *eight* of our new Model 272/273 Potentiostat/Galvanostats for multiplexed operation. These high performance potentiostats can also be incorporated into our other computer-assisted systems or used as stand-alone instruments.



Want to take a closer look? Just give us a call.

EG&G
PRINCETON APPLIED RESEARCH
P.O. BOX 2565 • PRINCETON, NJ 08540, U.S.A. • 609/452-2111 • TELEX: 843409

HIRE TECHNOLOGY

PUT ELECTROCHEMISTRY TO WORK!

BAS introduced the first commercial liquid chromatography/electrochemistry instrument in 1974. LCEC has become the fastest growing electrochemical technique. Thousands of our systems are in routine use for environmental, pharmaceutical, biomedical, industrial, and forensic applications. Nitro compounds, phenols, aromatic amines, thiols, and many heterocycles are ideal candidates for trace determination by LCEC. Detection limits of well below 1 picomole can now be achieved in a few minutes using apparatus of very modest cost.

The latest addition to our family is the BAS 100 ELECTROCHEMICAL ANALYZER. This interactive microprocessor based instrument is capable of performing over 25 electroanalytical techniques including cyclic voltammetry, chronocoulometry, differential pulse voltammetry, phase selective AC voltammetry, electrocapillary measurements, and virtually all forms of polarography. The BAS 100 is the first commercial instrument capable of square wave voltammetry, a powerful new technique for both analytical and fundamental studies. The first "smart" iR compensation approach is included, as are various statistical and background subtraction routines. Experimental parameters and data are available on a video screen and publishable figures are rapidly plotted.

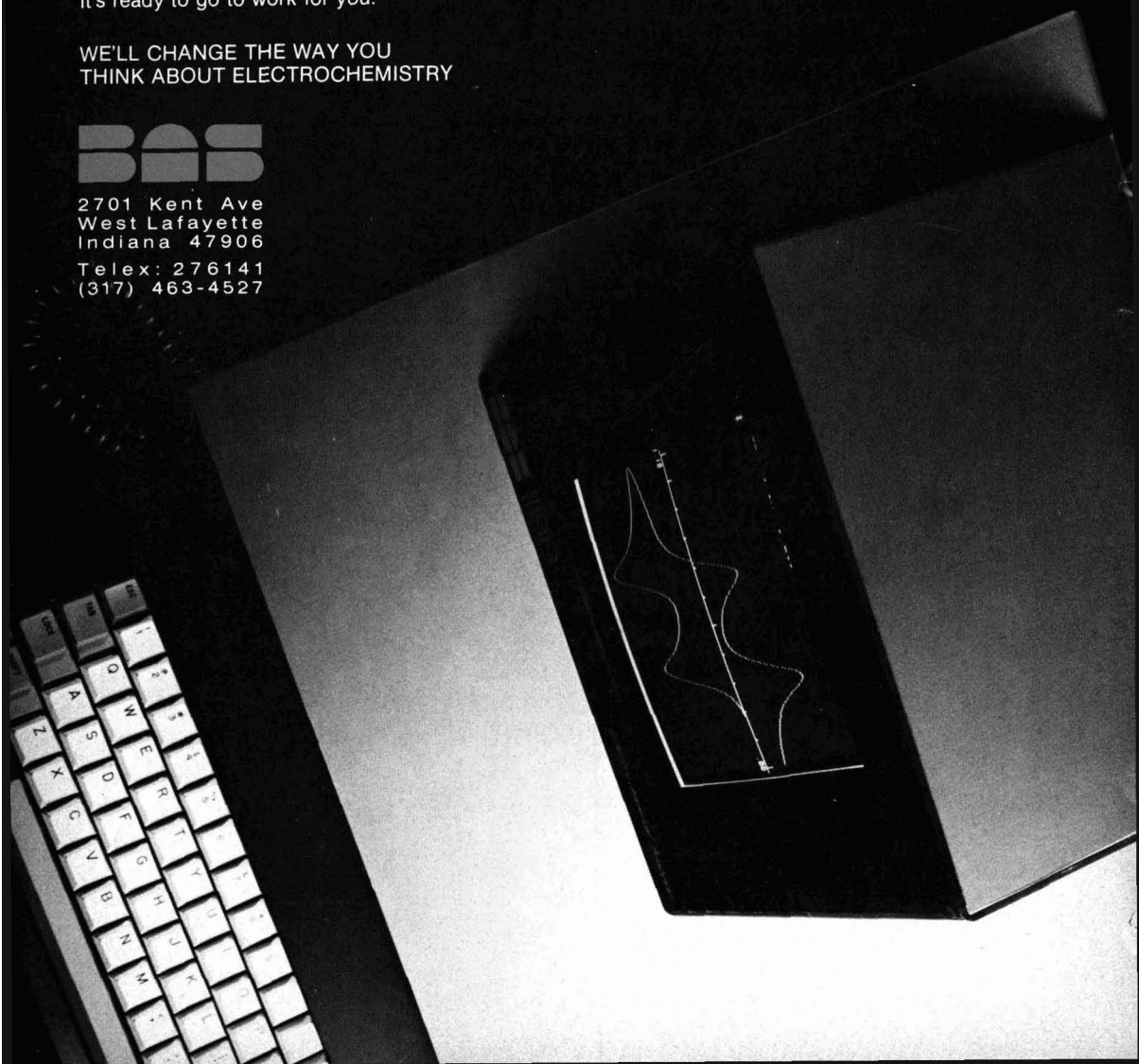
The BAS 100 was designed by and for chemists. It's ready to go to work for you.

WE'LL CHANGE THE WAY YOU
THINK ABOUT ELECTROCHEMISTRY

BAS

2701 Kent Ave
West Lafayette
Indiana 47906

Telex: 276141
(317) 463-4527



Call for Papers
167th Meeting
Toronto, Ontario, Canada, May 12-17, 1985

New procedure and deadlines have been established.

Selected symposium topics and planned General Sessions are described in the following pages:

Procedure for Submitting Papers

1. Submit one original 75-Word Abstract on the attached form or a facsimile together with one original Extended Abstract to The Electrochemical Society, Inc., 10 South Main St., Pennington, NJ 08534-2896. The deadline for receipt of **both** the 75-Word and Extended Abstracts at The Electrochemical Society Headquarters Office is **December 1, 1984.**

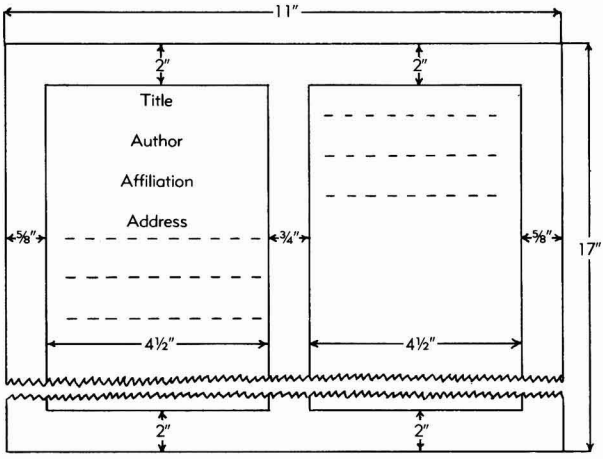
2. Send a copy of **both** the 75-Word and Extended Abstract to the appropriate organizing symposium or General Session chairman listed.

No paper will be considered unless both the 75-Word and Extended Abstract are received at Society Headquarters by December 1, 1984. Both abstracts and the oral presentation are required in English.

Instructions for Preparation of Extended Abstract

1. New Deadline—Extended Abstract must be submitted with the 75-Word Abstract by **December 1, 1984.**

2. All scheduled papers will be published in the EXTENDED ABSTRACTS volume for this meeting. The volume is published photo-offset directly from typewritten copy submitted by the author. The volume will be 7" × 10"; therefore, it is essential that the typing be clear and all lettering should be the size of ordinary type or at least 1/16 inch high so that it will be legible after reduction. The EXTENDED ABSTRACTS volume is in a double-column format. Camera-ready typing mats may be obtained from The Electrochemical Society, Inc., 10 South Main St., Pennington, NJ 08534-2896, or you may use any white bond paper 11" × 17". The diagram below gives the dimensions of the Extended Abstract form.



A. Use black typewriter ribbon only; type single-spaced.

B. Opaque lacquer may be used for corrections.

C. Type title, author(s), affiliation(s), and address(es) at top of first column (see diagram).

D. Tables and figures must be securely mounted within the margins with rubber cement.

E. Place references and figures after text.

3. The text of the abstract, including references, must not exceed one page (two columns) in length. An additional two columns are permitted for figures, if necessary. Papers exceeding this limit will be returned or rejected.

Mailing Instructions

Mail the original Extended Abstract together with the original 75-Word Abstract to The Electrochemical Society, Inc., 10 South Main St., Pennington, NJ 08534-2896 and a copy to the organizing chairman **for receipt before December 1, 1984.**

Notification of Paper Acceptance

Programming for this meeting will occur in early January. Organizing chairmen will notify those authors whose papers have not been accepted. In early March, a complete packet of program materials, including an Advance Program, will be sent to the presenting authors. Coauthors will receive a meeting packet without an Advance Program.

Manuscript Publication in the JOURNAL OF THE ELECTROCHEMICAL SOCIETY

Upon presentation, all meeting papers become the property of The Electrochemical Society, Inc. However, presentation incurs no obligation to publish. If publication in the JOURNAL OF THE ELECTROCHEMICAL SOCIETY is desired, papers should be submitted as promptly as possible in full manuscript form in order to be considered. "Instructions to Authors" for JOURNAL publication are available from the Society Headquarters office. If publication elsewhere is desired after presentation, written permission from Society Headquarters is required.

Toronto, Ontario, Canada, Meeting Symposia Plans—Spring 1985 May 12-17, 1985

New Deadline—Extended Abstract must be submitted with the 75-Word Abstract by December 1, 1984.

CORROSION

General Session

Papers on all aspects of low and high temperature corrosion and associated phenomena will be considered. Experimental techniques for the study of corrosion processes and corrosion products are also of interest.

Suggestions and inquiries should be sent to the Session Chairman: R. A. Rapp, Dept. of Metal Engineering, Ohio State University, 116 West 19th Ave., Columbus, OH 43210.

CORROSION/DIELECTRICS AND INSULATION/ELECTRODEPOSITION

Anodic Oxidation

Papers dealing with the growth and properties of anodic oxide films on metals, alloys, and semiconductors as well as the role of these surface films in electrochemical processes and electronic devices are invited. The symposium is intended to serve as a forum for discussion, where participants can express and exchange their views on both the nature of anodic oxide films and the crucial role these films play in their field of interest.

Suggestions and inquiries should be sent to the Symposium Co-Chairmen: B. MacDougall, National Research Council, Div. of Chemistry, Ottawa, Ont., Canada K1A 0R9; L. Young, University of British Columbia, Vancouver, BC, Canada V6T 1W5; or R. H. Muller, Lawrence Berkeley Labs., M/S 62-203, Berkeley, CA 94720.

DIELECTRICS AND INSULATION

Adhesion

This symposium will aim at covering a broad range of application areas involving adhesion problems and/or solutions related to electronic device fabrication. Process-related areas are of particular interest, as are instances where increasing resolution and reliability needs are creating new standards for adhesion performance. Papers on methods of measuring adhesion in a practical sense in electronic device application are also invited.

Suggestions and inquiries should be sent to the Symposium Chairman: C. A. Deckert, Shipley Company, Inc., 2300 Washington St., Newton, MA 02162.

DIELECTRICS AND INSULATION/ELECTRONICS

Defects and Related Electronic Effects in Insulators

This symposium will be concerned with defects in insulators and dielectrics and their effects on electronic processes for solid-state devices, including IC's, VLSI and hybrid devices, components, and packages.

Materials of particular interest include oxides, nitrides, glasses, silicates, ceramics, high-dielectric constant solids, insulators for compound semiconductors, and organic polymers.

Papers are solicited on topics concerned with chemical and structural defects and their effects on electrical breakdown, drift in electronic properties, electron trapping, current leakage phenomena, and electrostatic charging and discharge. Types of chemical defects include local inhomogeneity, nonstoichiometry, surface and bulk contamination, gas inclusions, hydrogen and water content, foreign particles, and phase separation. Structural defects include pinholes, cracks, thin spots, poor step coverage, excessive stress, and mismatch of lattices and interfaces. Other aspects may concern: 1. effects of radiation, moisture, stress, ambients, etc. on insulator properties; 2. influence of defects on device yield, reliability, and manufacturing processes; and 3. methods of characterization of defects.

Suggestions and inquiries should be sent to the Symposium Co-Chairmen: W. Kern, RCA Laboratories, Princeton, NJ 08540; R. B. Comizzoli, AT&T Bell Laboratories, Crawfords Corner Rd., Holmdel, NJ 07733; or Y. H. Wong, AT&T Bell Laboratories, Murray Hill, NJ 07974.

DIELECTRICS AND INSULATION/NEW TECHNOLOGY

Conducting Organic Polymers

Papers are requested concerning recent advances in applications and preparation and characterization of electrically conducting organic solids. Materials of specific interest include: 1. conductive polymeric charge-transfer complexes; 2. polymers with high intrinsic conductivity; 3. conductive ionomers; and 4. conductive molecular charge-transfer salts. The applications will focus on organic conductors such as: *(i)* reversible electrodes in batteries, fuel cells, and electrochromic devices; and *(ii)* components of thermal and voltaic switches and photoelectric cells. Of special interest are novel materials and original applications.

Suggestions and inquiries should be directed to the Symposium Chairman: M. Maxfield, Allied Corp., MRC, P.O. Box 1021R, Morristown, NJ 07960.

ELECTRONICS

Automated IC Manufacturing (AIM)

This symposium will primarily focus on all aspects of automation related to front-end IC fabrication and manufacture. In this context, the phrase "automation" is meant to imply computer control of equipment, mechanized/automated material handling, computer network architecture for equipment communication/control, IC factory planning and logistics, in-process monitoring, and data collection and analysis. By "front-end IC fabrication and manufacture," it is meant those operations involved in the development, prototyping, and volume manufacturing of IC circuits in the "clean room."

Original technical work or substantial review papers are solicited. Also being planned for this symposium are: 1. plenary session with invited presentations by industry and university leaders in the field of IC fabrication automation; and 2. an evening panel discussion on technical and strategic issues facing the industry. Publication of a proceedings volume is planned.

Papers are being solicited for the following sessions and topics: 1. CAM systems architecture and network, information systems for wafer/lot tracking, and process and operations management and control; 2. IC factory modeling, simulation, and capacity planning systems, on-line lot/batch dispatching and scheduling systems; 3. chemical and wafer/cassette handling in the lab, with emphasis on cleanliness, reliability, flexibility, and maintainability of such systems; the impact of such systems on clean room design; 4. contamination detection sensors and systems for particles, organics, etc., contamination detection and monitoring procedures, personnel and garment requirements and control, electrostatic, ionic and radiation induced "contamination"; 5. interface to equipment for process control and data collection; local, real-time data reduction and feed-forward control; 6. engineering data collection, analysis, correlation; engineering feedback and process feed forward; 7. development and use of standards for equipment communication interfaces, material handling, chemicals, wafer marking, safety, etc.

Suggestions and inquiries should be sent to the Symposium Co-Chairmen: M. Parikh, Hewlett Packard Laboratories, 3500 Deer Creek Rd., Palo Alto, CA 94304; or V. Atkins, Motorola, M-120, Box 20906, Phoenix, AZ 85036.

First International Symposium on Silicon Molecular Beam Epitaxy

This symposium will deal with the growth and application of silicon, silicides, and related materials produced by molecular beam deposition. It will include all techniques utilizing high vacuum deposition of silicon and related materials to ultimately produce epitaxial crystal growth. These techniques include not only direct epitaxial growth by evaporation, but also ionized and partially ionized deposition, and deposition of amorphous or disordered layers combined with subsequent crystallization processes. "Related materials" denotes any material which can be epitaxially combined with silicon and as such includes a range of semiconductors, insulators, and metals. The scope of the symposium will include: 1. substrate preparation and characterization; 2. layer synthesis and evaluation; 3. experimental apparatus and techniques; 4. device fabrication; 5. modeling of crystal growth; and 6. proposals for silicon MBE-based devices.

Suggestions and inquiries should be sent to the Symposium Co-Chairmen: J. C. Bean, AT&T Bell Laboratories, Rm 1D-366, Murray Hill, NJ 07974; or S. S. Iyer, IBM, T. J. Watson Research Center, Rm 1D-120, P.O. Box 218, Yorktown Heights, NY 10598.

Growth- and Processing-Induced Defects in Compound Semiconductors

The principal objective of this symposium is to bring together scientists who are pursuing research related to growth- and processing-induced defects in compound semiconductors. The following topics will be considered for presentation and discussion: 1. dislocations in as-grown crystals and their origin; 2. generation of defects during epitaxy; 3. growth of compound semiconductors on insulators; 4. shallow and deep impurities; 5. strained superlattices and interfacial studies; 6. metal-semiconductor interactions; 7. recombination-enhanced defect reactions; and 8. role of defects in device reliability. Invited speakers will highlight each of the topics. Contributed papers are solicited for presentation.

A proceedings volume is planned, and papers must be available in camera-ready form at the time of presentation.

Suggestions and inquiries should be sent to the Symposium Co-Chairmen: S. Mahajan, Carnegie-Mellon University, Pittsburgh, PA 15213; and V. G. Keramidas, Bell Communications Research, Murray Hill, NJ 07974.

Amorphous Materials for Electronic Applications

This symposium, consisting of invited and contributed papers, will deal with the current and potential use of amorphous materials as electronic devices. Materials covered will include amorphous chalcogenides, molecular solids, and amorphous tetrahedral materials including hydrogenated amorphous silicon. Applications to be discussed will include solar photovoltaic cells, thin film transistors, image sensors, and electrophotography.

Suggestions and inquiries should be sent to the Symposium Chairman: J. Mort, Xerox Webster Research Center, 800 Phillips Rd.—114, Webster, NY 14580.

ELECTRONICS/DIELECTRICS AND INSULATION

Third International Symposium on VLSI Science and Technology

This symposium will focus on advanced processing suitable for high density, high performance integrated circuits. It will cover a wide variety of topics, including: 1. yield limiting aspects of VLSI; 2. substrate materials; 3. low temperature and rapid-anneal processing; 4. process-induced radiation damage; 5. fine feature patterning; 6. scaling of circuit elements; 7. gates and interconnects; 8. novel device structures; 9. process and device modeling; 10. IC technologies; 11. VLSI packaging; and 12. reliability.

Detailed instructions concerning participation in this symposium appear in the special Call for Papers appearing in the March, May, June, and July 1984 issues of the **Journal.** The publication of a proceedings volume, which will be available at the symposium, is being planned.

Authors must send the title, address, and telephone number of the senior author and the topic area to be covered to the organizing chairmen by September 1, 1984. They should also include their response (yes or no) to the question: "If not accepted for the VLSI Symposium, do you want the paper to be transferred to an appropriate General Session?"

Camera-ready manuscripts must be submitted no later than November 1, 1984. Paper selection will be based on the camera-ready copy submitted. Authors will be notified by December 15 whether their paper has been accepted.

Suggestions and inquiries should be sent ot the Symposium Co-Chairmen: W. Murray Bullis, Siltec Corp., Silicon Div., 423 National Ave., Mountain View, CA 94043; or Samuel Broydo, Zymos Corp., 477 North Mathilda St., Sunnyvale, CA 94088.

Joint General Session

Papers that deal with all aspects of materials of interest for electronic devices, including their preparation, characterization, interactions, and device applications,

and whose subject matter is not covered by the special symposia, are invited to be submitted to this session. Also invited are papers on the basic chemistry and physics of materials, processing, and computer modeling of the formation and of the characterization of materials and devices. Of particular interest are new materials and processes.

Suggestions and inquiries should be sent to the Session Co-Chairmen; P. L. Castro, Hewlett Packard Laboratories, 3500 Dear Creek Rd., Palo Alto, CA 94304; P. Rai-Choudhury, Westinghouse Research and Development Center, Beulah Rd., Pittsburgh, PA 15235; or G. C. Schwartz, IBM Corp., Dept. 206, Bldg. 300-48A, Hopewell Junction, NY 12533.

Joint Recent News Papers Session

Recent News Papers and Extended Recent News Papers consisting of topics covered by the symposia and sessions being sponsored or cosponsored by the Electronics and Dielectrics and Insulation Divisions are invited for presentation.

A special Call for Recent News Papers will appear in the January, February, and March 1985 issues of the **Journal.**

Suggestions and inquiries should be sent to the Session Chairman: W. A. Pliskin, IBM Corp., Dept 04A, Zip 48A, Hopewell Junction, NY 12533.

ELECTRONICS/INDUSTIRAL ELECTROLYTIC

On-line Solid-State Sensors for Process Monitoring

A symposium focusing on solid-state sensor devices for on-line process monitoring is planned. Papers are solicited in the following areas: 1. applications of solid-state sensors to process monitoring; 2. requirements for solid-state sensors used in process monitoring; 3. design and development of solid-state sensors; 4. advances in materials and devices used in solid-state sensors; and 5. the future of solid-state sensors in process monitoring.

Detailed instructions concerning participation in this symposium appear in a special Call for Papers in the **Journal.** The publication of a proceedings volume is being planned.

Prospective authors must submit five copies of a 500-word summary before October 1, 1984. This summary will be used as the basis for selecting papers for presentation at the symposium. Acceptance of a paper for presentation at this symposium obligates the authors to submit a typed camera-ready copy of their talk, including a list of key words for the subject index, by April 1, 1985. A paper published in the proceedings volume may also be submitted to the **Journal.**

Suggestions and inquiries should be sent to Symposium Co-Chairmen: S. J. Fonash, 127 Hammond Bldg., The Pennsylvania State University, University Park, PA 16802; and Marino Woo, 930 Brown Rd., Bridgewater, NJ 08807.

ENERGY TECHNOLOGY

General Session

Papers are solicited in areas of energy conversion and storage not covered by current symposia. Of particular interest are new developments in photoelectrochemistry and novel methods for energy storage, conversion, and transmission.

Suggestions and inquiries should be sent to the Session Co-Chairmen: V. K. Kapur, ARCO Solar, Inc., P.O. Box 4400, Woodland Hills, CA 91356; or H. C. Maru, 1 Coach Dr., Brookfield Center, CT 06805.

ENERGY TECHNOLOGY/BATTERY

Requirements of Components and Systems for Energy Conversion and Storage

This symposium emphasizes the requirements, both existing and projected, for all types of energy conversion and storage systems, as well as requirements for individual components within these systems. A broad spectrum of contributed papers is being sought on all aspects of energy conversion system and system component requirements for commercial, industrial, and military applications. It is anticipated that these papers will provide information to focus future research and development efforts on critical, high payoff areas. The papers should emphasize the electrochemical aspects of the requirement and critical parameters (*e.g.*, weight, volume, cost, life, environmental extremes) for the requirement. While the electrochemical aspects of the papers are emphasized, other concepts and/or alternate approaches should be described and their advantages and disadvantages provided.

Papers are solicited on the following general topics: 1. energy conversion system requirements; 2. energy storage system requirements; 3. component requirements for energy conversion and storage systems and 4. special material requirements for energy conversion and/or storage systems.

Suggestions and inquiries should be sent to the Symposium Co-Chairmen: A. R. Landgrebe, U.S. Dept. of Energy, Electrochemical Storage Branch, Div. of Storage Technology, M/S 5E-052, Forrestal Bldg., Washington, DC 20585; or W. S. Bishop, Air Force Wright Aeronautical Laboratories, Aero Propulsion Lab., AFWAL/POOC-1, Wright-Patterson Air Force Base, OH 45433.

ENERGY TECHNOLOGY/HIGH TEMPERATURE MATERIALS

The Chemistry and Physics of Composite Media

This symposium will focus on physical and chemical properties of random media which are effected by interfacial and electrochemical phenomena. A number of keynote lectures will be delivered by invited speakers on experimental and theoretical aspects of composite media which have not yet found their way into the electrochemical literature. These topics may include: 1. the physics of porous rock; 2. theories of transport properties in heterogeneous media; 3. critical phenomena in crystal growth and the roughening transition; and 4. fractional characterization of rough interfaces. Contributed papers are solicited on these and related topics.

Publication of a proceedings volume is planned.

Suggestions and inquiries should be sent to the Symposium Co-Chairmen: M. Tomkiewicz, Dept. of Physics, Brooklyn College of CUNY, Brooklyn, NY 11210; or P. N. Sen, Schlumberger—Doll Research Center, Old Quarry Rd., P.O. Box 307, Ridgefield, CT 06877.

HIGH TEMPERATURE MATERIALS

Ceramics for Heat Engine and Energy Applications

The theme of this session will be control of microstructure in ceramics through powder preparation and processing, fabrication, and sintering, and evaluation of ceramic parts for mechanical and thermal properties and reliability. Contributions may take the form of review articles concerning the state of the art or may concern research work in an appropriate field.

Suggestions and inquiries should be sent to the Symposium Chairman: B. C. Mutsuddy, Ceramics and Glass Technology Section, Battelle Columbus Laboratories, 505 King Ave., Columbus, OH 43201.

HIGH TEMPERATURE MATERIALS/INDUSTRIAL ELECTROLYTIC/ENERGY TECHNOLOGY

Hydrogen Production and Storage

This symposium will consider all aspects of electrolytic hydrogen production, including photoelectrolysis, hydrogen storage, and hydrogen utilization and chemical use and energy conversion methods. The results of experimental, theoretical, and applications-oriented work will be included. Papers are solicited on the following or related topics: 1. electrolytic hydrogen production including electrolysis of steam; 2. fuel cells; 3. future prospects and economics of hydrogen production/use; 4. hydride and other storage methods; 5. hydrogen recovery in the electrochemical process industry; 6. new technologies for both production and storage; and 7. materials problems in hydrogen systems.

Suggestions and inquiries should be sent to the Symposium Co-Chairmen: Martin Hammerli, Div. of Energy, National Research Council, M-55 Montreal Rd., Ottawa, Ont., Canada K1A 0R6; D. E. Hall, American Cyanamid Co., Chemical Div., Research Labs, 1937 West Main St., Stanford, CT 06904-0060; or S. Srinivasan, Institute for Hydrogen Systems, 2480 Dunwin Dr., Mississauga, Ont., Canada L5L 1J9.

HIGH TEMPERATURE MATERIALS/LUMINESCENCE AND DISPLAY MATERIALS

Science and Technology of High Temperature Light Sources

This symposium will focus on fundamental and applied aspects of the high temperature chemistry in incandescent and high intensity discharge lamps, specifically tungsten halogen, metal halide, and high pressure sodium lamps. Topics of specific interest include: 1. chemical effects of gaseous and condensed phase halides in discharges; 2. metal halide reaction kinetics and thermodynamics; 3. phase equilibria, vaporization phenomena, complex molecules; 4. transport chemistry; 5. dose-electrode-wall impurity interactions; 6. emission material and seal glass chemistry; 7. diagnostic techniques; 8. spectroscopic properties of gaseous and condensed-phase metal halides and oxyhalides; 9. thermochemical modeling; and 10. metal halide laser systems.

Publication of a proceedings volume for the symposium is being considered.

Suggestions and inquiries should be sent to the Symposium Chairman: E. G. Zubler, General Electric Co., Lighting Research and Technical Service Operation, Nela Park, Cleveland, OH 44112.

INDUSTRIAL ELECTROLYTIC

Engineering of Industrial Electrolytic Processes

This symposium focuses on the application of engineering science and principles in the development and design of industrial electrolytic processes. Those areas of special focus include new synthesis or separation process technology and computer-aided design of electrochemical systems. Papers are solicited on the following topics: 1. design, development, optimization, and scale-up of cells and cell components; 2. methods of engineering evaluation of process alternatives; 3. economic analyses of electrochemical processes; 4. factors involved in plant layout and design; 5. mathematical modeling; and 6. current and potential distribution phenomena.

Publication of a proceedings volume is planned.

Suggestions and inquiries should be sent to the Symposium Co-Chairmen: U. Landau, Dept. of Chemical Engineering, Case Western Reserve University, Smith Bldg., Cleveland, OH 44106; R. D. Varjian, Dow Chemical Co., Louisiana Applied Science and Technology Lab., P.O. Box 400, Bldg. 2512, Plaquemine, LA 70765; or R. E. White, Dept. of Chemical Engineering, Texas A&M University, College Station, TX 77843.

Advances in Electrodes

This symposium will focus on advances in anodes and cathodes used in electrochemical processes. Theoretical and experimental aspects dealing with laboratory studies, engineering work, and applications in industrial production will be included.

Papers are solicited on the following topics: 1. new types of insoluble anodes for the generation of gases and electrosynthesis of organic and inorganic compounds; 2. new types of soluble anodes for electroplating and other applications; 3. recent improvements in existing anodes or cathodes used in commercial applications; 4. advances in gas depolarized electrodes, fluidized bed electrodes and catalytic cathode coatings; and 5. new applications for electrodes.

Suggestions and inquiries should be sent to the Symposium Co-Chairmen: M. R. Tighe, ELTECH Systems Corp., 470 Center St., Chardon, OH 44024; or G. Fisher, 35 Alcott Rd., Mahwah, NJ 07430.

LUMINESCENCE AND DISPLAY MATERIALS

Laser Materials

We invite those who study the electronic processes of importance to laser action, those who search for new laser systems, and those whose use of lasers require improvements in materials' properties to contribute to this symposium. All three states of matter and the whole spectral range covered by lasers can be addressed. Excited-state absorption, Auger de-excitations, other nonradiative processes, pumping mechanisms, and optical nonlinearities are a sampling of our interests.

Suggestions and inquiries should be sent to the Symposium Chairman: L. Andrews, GTE Laboratories, 40 Sylvan Rd., Waltham, MA 02154.

Luminescence in Amorphous Materials

Papers are invited for this symposium both on the technological uses of the luminescence of amorphous materials and on the structural information that is gleaned by studying the luminescence of amorphous materials. Papers are acceptable on glasses, liquids, polymers, and any other disordered material. Topics of particular interest are site multiplicities, energy transfer among sites, and inhomogeneous broadening.

Suggestions and inquiries should be sent to the Symposium Co-Chairmen: C. W. Struck, GTE Laboratories, 40 Sylvan Rd., Waltham, MA 02254; or A. R. Spowart, NIHE, Dublin 9, Ireland.

General Session

Papers are invited on the preparation and the properties of materials for every lighting technology and display technology. Examples are photoluminescence, cathodoluminescence, electrochromics, controlled light scattering, x-ray detectors, IR sources and detectors, gas discharges, electroluminescence, etc. Moreover, papers are welcome on the technologies themselves, especially as they impose requirements on materials. Papers are especially desired which share studies of the fundamental processes determining the material properties of interest.

Suggestions and inquiries should be sent to the Session Chairman: Ronald Karam, GTE Products Corp., Towanda, PA 18848.

Recent News Papers

Recent News Papers and Extended Recent News Papers consisting of topics covered by the symposia and sessions being sponsored or cosponsored by the Luminescence and Display Materials Group are invited for presentation.

A special call for Recent News Papers will appear in the January, February, and March 1985 issues of the **Journal.**

Suggestions and inquiries should be sent to the Session Chairman: T. E. Peters, GTE Laboratories, 40 Sylvan Rd., Waltham, MA 02154.

ORGANIC AND BIOLOGICAL ELECTROCHEMISTRY

Electrical Double Layers in Biology

This symposium will be devoted to papers on the role of electrical double layers in a variety of biological processes. Relevant topics include: the stability of natural membranes, membrane-membrane interactions, biopolymer interactions (*e.g.*, in striated muscle), ion transport across membranes and excitation, electrokinetic effects (*e.g.*, streaming potentials in biological tissues), and the effects of imposed electromagnetic fields. Both invited and contributed papers are planned.

Suggestions and inquiries should be sent to the Symposium Chairman: M. Blank, Dept. of Physiology, Columbia University, 630 West 168th St., New York, NY 10032.

Electrochemical Aspects of Biocompatibility

This symposium will be devoted to papers on the role of electrochemical interactions in the biocompatibility of biomaterials. The materials for consideration are polymers, metals, and nonmetals (carbon). Relevant topics include: 1. surface charge and biocompatibility; 2. blood interfacial interactions; 3. blood cell surface chemistry; 4. biomaterial surface modification; 5. lipid bilayer cell membrane analogs; and 6. biomaterial surface energy. Both invited and contributed papers are planned.

Suggestions and inquiries should be sent to the Symposium Chairman: Gary S. Margules, Cordis Research Corp., P.O. Box 025700, ATC-2M, Miami, FL 33102-5700.

Organometallic Electrochemistry

Papers are solicited from all areas pertaining to electrochemical properties of transition metal complexes. Suggested topic areas include: 1. electrochemical generation of reactive intermediates; 2. application of electrochemically prepared intermediates to synthesis; 3. selective mediated transformations of organic substrates; 4. kinetics and mechanism of redox processes; and 5. investigations of reversible redox couples and electrochemically induced processes (insertion, elimination, rearrangement, ligand substitution, etc.).

Both invited and contributed papers are planned. The publication of a proceedings volume is being considered. Papers published in a proceedings volume may also be submitted to the **Journal.**

Suggestions and inquiries should be sent to the Symposium Chairman: Joseph J. Bozell, Monsanto Co., 800 North Lindbergh Blvd., Q1A, St. Louis, MO 63167.

PHYSICAL ELECTROCHEMISTRY

Electrochemical Techniques for Thermodynamic and Kinetic Measurements

This symposium will focus on the development and application of electrochemical methods for the determination of thermodynamic properties (such as activities, free energies, phase boundaries, solubilities, and equilibrium constants), transport properties in liquids or solids, and interfacial kinetic parameters (rate constants, exchange current densities, reaction orders). Papers are solicited in the following and closely-related areas: development of electrochemical techniques and application of electrochemical techniques for the measurement of thermodynamic properties, transport properties, and interfacial kinetic parameters.

Emphasis will be given to new techniques and novel applications of existing techniques. Applications using aqueous, nonaqueous, molten salt, and solid electrolyte systems are all suitable for inclusion in this symposium. Publications of a proceedings volume is being considered.

Suggestions and inquiries should be sent to the Symposium Co-Chairmen: E. J. Cairns, Applied Science Div., Lawrence Berkeley Laboratory, Berkeley, CA 94720; or R. A. Huggins, Dept. of Materials Science and Engineering, Stanford University, Stanford, CA 94305.

Physicochemical Hydrodynamics in Electrochemistry

This symposium will provide a forum for those interested in the effect of interactions of physical chemical hydrodynamics phenomena with electrochemical processes. Specifically, we shall concentrate our attention on the electrode/electrolyte interface. The following two basic aspects will be the focus of this symposium: 1. interaction of the physical and/or chemical changes with mass transport and the current distribution of the interface; and 2. the effect of interfacial chemical and/or physical changes on polarization characteristics of the electrode.

Physical changes include new phase formation or electrode geometry variations caused by the nature of the process itself or by the electrode design. Chemical changes imply all interfacial chemical composition variations from the bulk electrolyte, including the changes of the coordination shell composition of the electrochemically active species. Original works that deal with either one or both of the above topics are solicited.

A proceedings volume is being considered. Papers published in a proceedings volume may also be submitted to the **Journal.**

Suggestions and inquiries should be sent to the Symposium Chairman: I. V. Kadija, Olin Corp., Metals Research Laboratories, 91 Shelton Ave., New Haven, CT 06511.

General Session

Papers concerning any aspect of physical electrochemistry not included in the topic areas of the symposia are welcome.

Suggestions and inquiries should be sent to the Session Chairman: L. R. Faulkner, Dept. of Chemistry, University of Illinois, 1209 West California St., Urbana, IL 61801.

PHYSICAL ELECTROCHEMISTRY/BATTERY

Characterization of Battery Electrodes

Papers are solicited for a symposium which will focus on new approaches and techniques for characterizing battery electrodes. Of particular interest are papers which correlate physical and/or chemical characteristics of the electrode to performance parameters, such as capacity, energy density, or cycle life. Suggested characterization techniques include: spectroscopy, micrography, mathematical modeling, forced convection, and chemical and electrochemical analysis. Both theoretical as well as experimental studies are invited. Publication of a proceedings volume is being considered.

Suggestions and inquiries should be sent to the Symposium Co-Chairmen: G. H. Brilmyer, Johnson Controls, Inc., P.O. Box 591, Milwaukee, WI 53201; or D. Bennion, Dept. of Chemical Engineering, 350-CB, Brigham Young University, Provo, UT 84602.

PHYSICAL ELECTROCHEMISTRY/ENERGY TECHNOLOGY/ELECTRONICS

Semiconductor-Electrolyte Interfaces

This symposium will address the chemistry, electrochemistry, and physics of semiconductor-electrolyte contacts. Papers considering the relationship between the interfacial chemistry and carrier recombination, charge transport or corrosion behavior, photoetching of semiconductors, photoelectrochemical cells, electroluminescence at semiconductor-electrolyte contacts, or electrocatalysis and surface modification of semiconductor electrodes are invited.

Suggestions and inquiries should be sent to the Symposium Co-Chairmen: Arthur J. Nozik, Solar Energy Research Institute, 1617 Cole Blvd., Golden, CO 80401; or Adam Heller, AT&T Bell Laboratories, Rm 6D-321, Murray Hill, NJ 07974.

PHYSICAL ELECTROCHEMISTRY/ORGANIC AND BIOLOGICAL ELECTROCHEMISTRY

Spectroelectrochemistry and Electroanalysis

Contributions dealing with all aspects of research in spectroelectrochemistry or electroanalysis are invited. The symposium will include theoretical and experimental work related to the development and application of new techniques or to the improvement and extension of established methods.

Suggestions and inquiries should be sent to the Symposium Co-Chairmen: W. R. Heineman, Dept. of Chemistry, University of Cincinnati, Cincinnati, OH 45221; or L. R. Faulkner, Dept. of Chemistry, University of Illinois, 1209 West California St., Urbana, IL 61801.

PHYSICAL ELECTROCHEMISTRY/BATTERY/ ENERGY TECHNOLOGY

Electrocatalysis in Energy Conversion Systems

This symposium is concerned with the role of electrocatalysis in various energy conversion systems, including batteries, fuel cells, solar-photoelectrochemical systems, electrolyzers, and electrosynthesis. Special emphasis will be placed on reducing energy losses associated with the electrocatalysts. High efficiency for free energy conversion requires reaction rates as close to reversible as possible, together with minimized concentration gradients and electronic resistance losses. The symposium will include several invited papers reviewing the status of the electrocatalysts used in various energy conversion applications. Contributed papers are solicited dealing with the fundamental electrochemical and electrochemical engineering aspects of electrocatalysis as they relate to energy conversion.

Specific topics are expected to include mechanistic aspects of electrocatalysis, new electrocatalysts, optimization of presently available electrocatalysts, electrocatalyst-support interactions, the electrolyte factor in electrocatalysis, optimization of mass transport and electronic conduction on electrocatalyst systems, and factors involved in the degradation of electrocatalytic activity, including area loss and poisoning phenomena.

Suggestions and inquiries should be sent to the Symposium Co-Chairmen: A. J. Appleby, Electric Power Research Institute, P.O. Box 10412, Palo Alto, CA 94303; or E. B. Yeager, Case Center for Electrochemical Sciences, Case Western Reserve University, Cleveland, OH 44106. Titles and abstracts for contributed papers should be submitted to the Society Office in the usual manner with a copy also going to E. B. Yeager.

PHYSICAL ELECTROCHEMISTRY/NEW TECHNOLOGY

Electrochemical Characteristics of Amorphous Materials

The purpose of this symposium is to provide an interdisciplinary forum which permits researchers in the diverse areas of electrochemistry and materials science to discuss problems of mutual interest. This symposium will cover a range of topics in the preparation, characterization, physical aspects, and applications of amorphous materials. Papers are being solicited that focus on: 1. the fundamental understanding of the microscopic and macroscopic properties of glasses, glassy metals, and other amorphous materials; 2. the preparation of these materials; 3. their surface and bulk properties; and 4. their potential and real applications.

Suggestions and inquiries should be sent to the Symposium Chairman: A. R. Landgrebe, Dept. of Energy, MS 5E-052, Forrestal, Washington, DC 20585.

New Deadline—Extended Abstract must be submitted with the 75-Word Abstract by December 1, 1984.

75-Word Abstract Form

(New Deadline—Extended Abstract must be submitted with the 75-Word Abstract by December 1, 1984)

Toronto, Ontario, Canada—May 12-17,1985

Submit to: The Electrochemical Society, Inc.
10 South Main Street, Pennington, NJ 08534-2896

Abstract No. .....
(to be assigned by the Society)

Schedule for .....
(Title of Symposium)

Sponsored by .....
(Division/Group)

Title of paper .....

.....

Authors (Underline name of author presenting paper.) .....

.....

Business affiliation and address .....

.....

..... (State or Country) (ZIP Code) (Telephone No.)

(Type abstract in this area—double-spaced.)

Do you require any audiovisual equipment?

- ☐ **35 mm (2 x 2 in.) slide projector**
- ☐ **Vu-Graph**
- ☐ **other (specify)**

Has the information in this abstract been presented verbally, submitted for publication, or published?

☐ **Yes** ☐ **No**

If the answer is yes, please provide the reference (except in the case of invited review presentations). _____

Is a full length paper on this work to be submitted for Society Journal publication? ☐ **Yes** ☐ **No**

Papers presented before a Society technical meeting become the property of the Society and may not be published elsewhere without written permission of the Society. Papers presented at Society technical meetings must be authored by a member or sponsored by an active member.

..... Insert name of Society member author or sponsor

This form should accompany your Extended Abstract.

SUSTAINING MEMBERS (CONTINUED)

Fairchild Camera & Instrument Corp.
Research & Development Laboratory
Palo Alto, CA

Ford Motor Co.
Dearborn, MI

The Gates Corporation
Denver, CO

General Motors Corp.
Delco-Remy Div., Anderson, IN
Research Laboratories Div.
Warren, MI

Gould Inc.
Gould Research Center
Rolling Meadows, IL

Grelcon, Inc.
Niagara Falls, NY

GTE Laboratories
Waltham, MA

GTE Sylvania Inc.
Chemical & Metallurgical Div.
Towanda, PA

Heliotronic GmbH
Burghausen, Germany

Hewlett Packard Co.
Loveland, CO

Hewlett Packard Laboratories
Palo Alto, CA

Hill Cross Co., Inc.
West New York, NJ

Hitachi, Ltd.
Central Research Laboratory
Tokyo, Japan

Hoechst-Uhde Corp.
Englewood Cliffs, NJ

Honeywell, Inc.
Power Sources Center
Horsham, PA

Hughes Research Laboratories
Div. of Hughes Aircraft Co.
Malibu, CA

IMI Marston Limited
Wolverhampton, England

INCO ElectroEnergy Corp.
Engineering & Development Center
Ray-O-Vac Corp.
Madison, WI

International Lead Zinc Research Organization, Inc.
New York, NY

S. C. Johnson & Son, Inc.
Racine, WI

Johnson Controls, Inc.
Milwaukee, WI

Kaiser Aluminum & Chemical Corp.
Pleasanton, CA

KBI
a division of Cabot Corp.
Boyertown, PA

Lockheed Missiles & Space Co., Inc.
Research Laboratory
Palo Alto, CA

LSI Logic Corp.
Santa Clara, CA

Marathon Battery Co.
Waco, TX

Medtronic Energy Technology
Minneapolis, MN

Mepco/Electra, Inc.
Columbia, SC

Microwave Associates, Inc.
Burlington, MA

Molycorp, Inc.
New York, NY

Monsanto Co.
St. Louis, MO

Motorola Inc.
Phoenix, AZ

M&T Chemicals Inc.
Detroit, MI

Nippon Telegraph and Telephone Public Corporation
Tokyo, Japan

Noranda Research Centre
Pointe Claire, Que., Canada

North American Philips Lighting Corp.
Bloomfield, NJ

Northern Telecom
Ottawa, Ont., Canada

Occidental Chemical Corporation
Research & Development
(2 memberships)
Grand Island, NY

Olin Corp.
Metals Research Laboratories
New Haven, CT

OMI International Corp.
Udylite/Sel-Rex
Warren, MI

Perkin-Elmer Corp.
Norwalk, CT

Philips Laboratories, Inc.
Briarcliff Manor, NY

Prototech Co.
Newton Highlands, MA

Public Service Electric and Gas Co.
PSE&G Research Corp.
Newark, NJ

RCA Corp.
Color Picture Tube Div.
Lancaster, PA

Reynolds Metals Co.
Reduction Research Div.
Sheffield, AL

Rockwell International
El Segundo, CA

SAFT America, Inc.
Power Sources Division,
Valdosta, GA
Advanced Battery Systems Division,
Cockeysville, MD

Sandia National Laboratories
Albuquerque, NM

Sanyo Electric Co., Ltd.
Osaka, Japan

J. C. Schumacher Co.
Oceanside, CA

Shipley Company, Inc.
Newton, MA

Siemens Aktiengesellschaft
Munich, Germany

Signetics Corp.
Sunnyvale, CA

Siltec Corp.
Menlo Park, CA

Sprague Electric Co.
North Adams, MA

Standard Telecommunication Laboratories Ltd.
Essex, England

St. Joe Minerals Corp.
Monaca, PA

Tektronix, Inc.
Beaverton, OR

Teletype Corp.
Skokie, IL

Texas Instruments Inc.
Attleboro, MA
Dallas, TX

Toshiba Corp.
Toshiba Research and
Development Center
Kawasaki, Japan

Toyota Central Research and Development Labs, Inc.
Nagoya, Japan

Varian Associates
Palo Alto, CA

VARTA Batterie AG
Kelkheim, Germany

Wacker Chemitronic
Burghausen, Germany

Xerox Corp.
Webster Research Center
Rochester, NY

Yardney Corp.
Pawcatuck, CT

Yuasa Battery Co., Ltd.
Osaka, Japan

THE ELECTROCHEMICAL SOCIETY PATRON MEMBERS

AT&T Bell Laboratories
Murray Hill, NJ

Dow Chemical Co.
Inorganic Chemicals Dept.
Midland, MI

ELTECH Systems Corp.
Chardon, OH

Exxon Research and Engineering Co.
Corporate Research
Advanced Energy Systems Laboratory,
Materials and Catalysis Sciences Laboratory
Linden, NJ
Technology Department
Chemical Engineering Technology Div.
Materials Technology Div.
Florham Park, NJ

General Electric Co.
Chemical Laboratory, Knolls Atomic Power Laboratory,
Schenectady, NY
Lamp Div., Cleveland, OH
Materials & Process Laboratory, Large Steam
Turbine-Generator Dept., Schenectady, NY
Research and Development Center,
Inorganic Materials Laboratory
Schenectady, NY

General Electric Co. (continued)
Signal Processing & Communication Laboratory,
Schenectady, NY
Semiconductor Products Dept.,
Syracuse, NY

International Business Machines Corp.
New York, NY

Olin Corp.
Chemicals Div.
Charleston Technology Center
Charleston, TN

Philips Research Laboratories
Eindhoven, The Netherlands

Tadiran, Israel Electronics Industries, Ltd.
Tel Aviv, Israel

Union Carbide Corp.
Battery Products Div.
Corporate Research Dept.
Danbury, CT

Westinghouse Electric Corp.
Electronic Tube Div., Elmira, NY
Nuclear Center, Monroeville, PA
Semiconductor Div., Youngwood, PA
Research Laboratories, Pittsburgh, PA

THE ELECTROCHEMICAL SOCIETY SUSTAINING MEMBERS

The Aerospace Corp.
Los Angeles, CA

Airco Industrial Gases
Murray Hill, NJ

Allen Clark Research Centre
Plessey Research (Caswell) Ltd.
Towcester, Northants, England

Allied Corporation
C & D Power Systems
Plymouth Meeting, PA

Aluminum Co. of America
New Kensington, PA

AMAX Inc.
Greenwich, CT

AMP Inc.
Harrisburg, PA

Analog Devices, Inc.
Norwood, MA

Applied Materials, Inc.
Santa Clara, CA

ASARCO, Inc.
South Plainfield, NJ

AT&T Technologies
Princeton, NJ

Battelle Memorial Institute
Columbus, OH

Bioanalytical Systems Inc.
West Lafayette, IN

Boeing Co.
Seattle, WA

BP Research Centre
Middlesex, England

Brown, Boveri & Co., Ltd.
Research Center
Baden, Switzerland

C-I-L Inc.
Industrial Chemicals Div.
Montreal, Que., Canada

Comdial Semiconductor, Inc.
Sunnyvale, CA

Cominco Ltd.
Trail, B.C., Canada

Corning Glass Works
Corning, NY

Crawford & Russell Inc.
Stamford, CT

CSIRO Division of Mineral Chemistry
Port Melbourne, Victoria, Australia

Diamond Shamrock Chemicals Co.
Painesville, OH

Duracell Inc.
A Division of Duracell International
Tarrytown, NY (2 memberships)

Duro-Test Corp.
North Bergen, NJ

Eagle-Picher Industries, Inc.
Electronics Div.
Joplin, MO

Eastman Kodak Co.
Rochester, NY

ECO Energy Conversion
Newton, MA

EG&G Princeton Applied Research Corp.
Princeton, NJ

Elcap Electronics Ltd.
Tai Po, Hong Kong

Electric Power Research Institute
Palo Alto, CA

Electrochemical Technology Corp.
Seattle, WA

Energy Conversion Devices, Inc.
Troy, MI

Energy Development Associates
A Gulf and Western Co.
Madison Heights, MI

Engelhard Corp.
Engelhard Industries Div.
Iselin, NJ

Ever Ready Co. (Holdings) Ltd.
Whetstone, London, England

Exmet Corp.
Bridgeport, CT

29 NOV 2528